A journal o

Published by the American Institute
for the
AMERICAN PHYSICAL

Officers

President

H. A. BETHE
Cornell University
Ithaca, New York

Vice-President

R. T. BIRGE
University of California
Berkeley, California

Secretary

K. K. DARROW
Bell Telephone Laborat
Office:
Columbia University
New York 27, New York

Treasurer

G. B. PEGRAM
Columbia University
New York 27, New York

Local Secretary
for the Pacific Coa

J. KAPLAN
University of Californ
Angeles
Los Angeles, California

Managing Editor

S. A. GOUDSMIT
Brookhaven National L
Upton, Long Island
New York

The Physical

Entered as second-class m

Acceptance for mailing at special

THE
PHYSICAL REVIEW

A journal of experimental and theoretical physics established by E. L. Nichols in 1893

SECOND SERIES, VOL. 94, NO. 6 JUNE 15, 1954

Variational Principles for the Acoustic Field*

E. GERJUOY, *University of Pittsburgh, Pittsburgh, Pennsylvania*

AND

DAVID S. SAXON,† *National Bureau of Standards, Los Angeles, California*

(Received December 24, 1953)

Variational principles are presented for the scattering amplitude in the general acoustic scattering problem, and, for spherically symmetric scatterers, for the phase shifts. Integral equations for the acoustic field are also given and the properties of the scattering matrix are developed. The entire formulation remains valid in the presence of discontinuities of density and/or velocity in the medium.

I. INTRODUCTION

IN recent years variational expressions have been developed for the total cross section and for the phase shifts of the partial waves, in a variety of scattering problems.[1] In many instances these variational expressions have led to accurate estimates of the scattering cross section.[1] To our knowledge, however, the scattering problems for which explicit variational formulations have been developed are confined to those in which the wave function and its normal derivative are both continuous across a surface of discontinuity. Consequently, these formulations are not applicable in acoustic scattering problems, where, using the customary definitions, the acoustic potential is discontinuous across a surface bounding two media of differing constant density.

It seemed worth while, therefore, to derive Schwinger-type[1] variational principles for acoustic scattering problems. We present a variational principle for the total scattering amplitude and, for spherically symmetric scatterers, variational principles for the phase shifts; the derivations of these variational principles are not trivial, as will be seen. We present also a general integral equation formulation of the acoustic scattering problem and determine explicitly the elements of the scattering matrix. These results do not seem to have been previously given and are required for proofs of the variational principles and of the cross-section theorem, Eq. (34), in the following.

Applications of these variational principles are not reported here, but are being considered. It seems likely that techniques similar to those we have used will lead to variational principles applicable to nonabsorptive electromagnetic scattering problems involving arbitrary variations of dielectric constant and magnetic permeability.

II. THE ACOUSTIC FIELD

We start from the equations

$$\rho\partial\mathbf{v}/\partial t=-\operatorname{grad}p,$$
$$\rho\operatorname{div}\mathbf{v}=-(1/c^2)\partial p/\partial t. \tag{1}$$

Equation (1) describes the sound pressure p and the sound velocity $\mathbf{v}$ at all points of space which are free of acoustic sources. The equilibrium density at any point $\mathbf{r}$ is $\rho(\mathbf{r})$ and $c(\mathbf{r})$ is the local velocity of sound. Equation (1) is valid for an ideal fluid, with p and $\mathbf{v}$ small time-dependent increments about p_0 and zero, respectively, where p_0 is time independent.[2] The boundary conditions, that p and $\mathbf{v}_n$, the normal component of $\mathbf{v}$, remain continuous as ρ and/or c approach functions discontinuous across a surface, are implied by Eq. (1). The rate of flow of acoustic energy across the

* The preparation of this paper was sponsored (in part) by the U. S. Office of Naval Research.

† Present address, University of California, Los Angeles, California.

[1] B. A. Lippman and Julian Schwinger, Phys. Rev. **79**, 469 and 481 (1950), and references therein.

[2] In the presence of body forces, Eq. (1) is correct only at sufficiently high frequencies. In particular, in the gravitational field of the earth, we must have $\omega\gg g/c$, which is satisfied above a tenth of a cycle in air or water. See P. G. Bergmann, J. Acoust. Soc. Am. **17**, 329 (1946).

surface element $d\mathbf{S}\equiv dS\mathbf{n}$ is $p\mathbf{v}\cdot\mathbf{n}dS$. It is presumed that p and $\mathbf{v}$ are real.

When the fields are harmonic, we write in Eq. (1)

$$\begin{aligned} p(\mathbf{r},t)&=p(\mathbf{r})e^{-i\omega t}+p^*(\mathbf{r})e^{i\omega t},\\ \mathbf{v}(\mathbf{r},t)&=\mathbf{v}(\mathbf{r})e^{-i\omega t}+\mathbf{v}^*(\mathbf{r})e^{i\omega t}, \end{aligned} \tag{2}$$

the asterisk denoting complex conjugate. Then

$$\begin{aligned} \operatorname{grad}p-i\omega\rho\mathbf{v}&=0,\\ (i\omega/c^2)p-\rho\operatorname{div}\mathbf{v}&=0. \end{aligned} \tag{3}$$

In Eq. (3) $p\equiv p(\mathbf{r})$ and $\mathbf{v}\equiv\mathbf{v}(\mathbf{r})$ of Eq. (2). The average rate of radiation across the surface element $dS\mathbf{n}$ is $(p^*\mathbf{v}+p\mathbf{v}^*)\cdot\mathbf{n}dS$. If ρ and c are everywhere constant, $\rho=\rho_0$ and $c=c_0$, Eq. (3) yields upon elimination of $\mathbf{v}$

$$\begin{aligned} \Delta p+k^2p&=0,\\ \mathbf{v}&=(1/i\omega\rho_0)\operatorname{grad}p, \end{aligned} \tag{4}$$

where

$$k=\omega/c_0.$$

Equation (4) is entirely equivalent to the customary formulation in terms of the acoustic potential:

$$\begin{aligned} \mathbf{v}&=-\operatorname{grad}\varphi,\\ p&=-i\omega\rho_0\varphi, \end{aligned} \tag{5}$$

together with

$$\Delta\varphi+k^2\varphi=0. \tag{6}$$

Equation (5) continues to be useful if c varies, but no longer solves the first of Eq. (3) when ρ is not constant. Nor does replacing the first of Eq. (5) by $\rho\mathbf{v}=-\rho_0\operatorname{grad}\varphi$ yield any particular simplification. Moreover, Eq. (5) simply makes φ proportional to p. It is apparent therefore that for our purposes, developing generally applicable variational principles, there is no advantage to introducing an acoustic potential. Consequently, our results are given in terms of the directly observable quantities p and $\mathbf{v}$.

The typical acoustic scattering problem is to find a solution of Eq. (3) of the form

$$\begin{aligned} p&=p_0+p_s=\exp(ik\mathbf{n}_0\cdot\mathbf{r})+p_s,\\ \mathbf{v}&=\mathbf{v}_0+\mathbf{v}_s=\frac{\mathbf{n}_0}{\rho_0c_0}\exp(ik\mathbf{n}_0\cdot\mathbf{r})+\mathbf{v}_s, \end{aligned} \tag{7}$$

where p_s and $\mathbf{v}_s$ are outgoing at infinity and represent the scattered wave, while p_0 and $\mathbf{v}_0$ represent a plane wave incident along $\mathbf{n}_0$ and are solutions of Eq. (4). The quantities ρ_0 and c_0 are the values of ρ and c at infinity. Of course, p and the normal component of $\mathbf{v}$ are continuous across any surface of discontinuity of ρ and/or c.

We now seek to replace Eq. (3) by a pair of integral equations incorporating the conditions (7). For this purpose, we first derive from Eq. (3),

$$\begin{aligned} \Delta p+k^2p&=k^2(1-\mu^2)p+i\omega\mathbf{v}\cdot\operatorname{grad}\rho,\\ \Delta\mathbf{v}+k^2\mathbf{v}&=k^2(1-\mu^2)\mathbf{v}\\ &\quad+i\omega p\operatorname{grad}\frac{1}{\rho c^2}-\operatorname{curl}\left(\operatorname{grad}\frac{1}{\rho}\times\rho\mathbf{v}\right), \end{aligned} \tag{8}$$

where

$$\mu=c_0/c.$$

Then as shown in Appendix A, using the outgoing free-space Green's function

$$G(\mathbf{r},\mathbf{r}')=-\frac{1}{4\pi}\frac{e^{ik|\mathbf{r}-\mathbf{r}'|}}{|\mathbf{r}-\mathbf{r}'|}, \tag{9}$$

which satisfies

$$(\Delta+k^2)G(\mathbf{r},\mathbf{r}')=\delta(\mathbf{r}-\mathbf{r}'), \tag{10}$$

we obtain, whether or not there are surfaces of discontinuity of ρ and/or c,

$$\begin{aligned} p(\mathbf{r})&=p_0+k^2\int d\mathbf{r}'G(\mathbf{r},\mathbf{r}')(1-\alpha'\mu'^2)p(\mathbf{r}')\\ &\quad+i\omega\operatorname{div}\int d\mathbf{r}'G(\mathbf{r},\mathbf{r}')(\rho'-\rho_0)\mathbf{v}(\mathbf{r}'),\\ \mathbf{v}(\mathbf{r})&=\mathbf{v}_0+k^2\int d\mathbf{r}'G(\mathbf{r},\mathbf{r}')\left(1-\frac{1}{\alpha'}\right)\mathbf{v}(\mathbf{r}')\\ &\quad-\frac{i\omega}{\rho_0c_0^2}\operatorname{grad}\int d\mathbf{r}'G(\mathbf{r},\mathbf{r}')(1-\alpha'\mu'^2)p(\mathbf{r}')\\ &\quad-\operatorname{curl}\operatorname{curl}\int d\mathbf{r}'G(\mathbf{r},\mathbf{r}')\left(1-\frac{1}{\alpha'}\right)\mathbf{v}(\mathbf{r}'), \end{aligned} \tag{11}$$

where

$$\alpha=\rho_0/\rho.$$

In Eq. (11) we have introduced the convention, which we shall use consistently, that functional dependence on $\mathbf{r}'$ is indicated by a prime. Thus $\mu'=c_0/c(\mathbf{r}')$ and $\alpha'=\rho_0/\rho(\mathbf{r}')$. As written, Eq. (11) is to be regarded as a pair of simultaneous integral equations for the unknown functions p and $\mathbf{v}$, which functions, as verified in Appendix A, properly satisfy Eq. (3). An apparent simplification is readily obtained if $\mathbf{v}$ is eliminated from the first of Eq. (11) using the first of Eq. (3) since in this case one need consider only a single integral equation for the scalar function p. However, this equation explicitly involves $\operatorname{grad}p$ and it turns out that in deriving the variational principles we seek, it would still be necessary to construct an expression for $\operatorname{grad}p$ equivalent to the second of Eq. (11). Thus no real simplification is attained.

We prove[3] in Appendix B that the solutions to Eq.

[3] In Eq. (11) and in subsequent equations we assume that ρ, c, p, and $\mathbf{v}$ remain finite, and that ρ and c are different from zero, to keep α and μ finite. If these assumptions are not made, the question of the existence of the integrals in Eq. (11), and therefore of the existence of a solution to Eq. (11), has to be examined. In any

(11) satisfy the requirements of continuity of p and $\mathbf{v}_n$. To establish the behavior of p and $\mathbf{v}$ at infinity, we note that to terms of higher order

$$\lim_{r\to\infty} G(r\mathbf{n},\mathbf{r}') = -\frac{1}{4\pi}\frac{e^{ikr}}{r}\exp(-ik\mathbf{n}\cdot\mathbf{r}'), \tag{12}$$

whence Eq. (11) yields

$$\lim_{r\to\infty} p(r\mathbf{n}) = p_0 - \frac{k^2}{4\pi}\frac{e^{ikr}}{r}\int d\mathbf{r}'\exp(-ik\mathbf{n}\cdot\mathbf{r}') \times\left[(1-\alpha'\mu'^2)p' + \rho_0 c_0\left(1-\frac{1}{\alpha'}\right)\mathbf{n}\cdot\mathbf{v}'\right], \tag{13}$$

$$\lim_{r\to\infty} \mathbf{v}(r\mathbf{n}) = \mathbf{v}_0 - \frac{1}{4\pi}\frac{k^2}{\rho_0 c_0}\frac{e^{ikr}}{r}\mathbf{n}\int d\mathbf{r}'\exp(-ik\mathbf{n}\cdot\mathbf{r}') \times\left[(1-\alpha'\mu'^2)p' + \rho_0 c_0\left(1-\frac{1}{\alpha'}\right)\mathbf{n}\cdot\mathbf{v}'\right].$$

By comparison with Eq. (8), Eq. (13) demonstrates that the solutions $p(\mathbf{r})$, $\mathbf{v}(\mathbf{r})$ of Eq. (11) are such that p_s and $\mathbf{v}_s$ are everywhere outgoing at infinity. This, together with Appendices A and B, proves that Eq. (11) is equivalent to Eq. (3) plus the boundary conditions p and $\mathbf{v}_n$ continuous and p_s and $\mathbf{v}_s$ outgoing at infinity. Incidentally Eq. (13) shows that the scattered field is longitudinal, $\mathbf{v}_s$ parallel to $\mathbf{n}$ at infinity, and that the acoustic impedance for the scattered field is $\rho_0 c_0$, $|\mathbf{v}_s| = p_s/\rho_0 c_0$ at infinity.

actual problem ρ and c are bounded and different from zero. Thus, since in the scattering problems which we treat there are no sources at a finite distance from the origin, it is most reasonable on physical grounds to expect that $p(\mathbf{r})$ and $\mathbf{v}(\mathbf{r})$ are finite everywhere, although a general proof may be difficult to construct. For the proof of Appendix B it is necessary to assume that various derivatives of ρ, c, p, $\mathbf{v}$, α, and μ remain finite as a surface of discontinuity; is approached from either side of the surface. In other words, except right at the discontinuity, the field variables p and $\mathbf{v}$, and the medium itself, are well behaved. Again these assumptions are reasonable for any actual problem and are made to simplify the argument in Appendix B, which is already complicated enough. If finiteness of the derivatives is not assumed Eq. (11) may remain valid in various circumstances, but another proof that the boundary conditions are satisfied will have to be devised. We stress that we are not assuming the derivatives exist at the discontinuity; this would be an unreasonable assumption. To illustrate, as the everywhere continuous $\rho(\mathbf{r})$ becomes in the limit discontinuous with a finite jump across a surface, gradρ becomes infinite at the surface, although it remains finite on either side. Because the integrands in Eq. (11) do not involve derivatives the integrals may be and are extended over all space. If derivatives or other expressions which cannot be assumed finite at the discontinuity are included in the integrand, the volume of integration must omit thin strips on either side of the surfaces of discontinuity, generally with the consequent complication of adding compensating surface integrals to the integral equation, as in Eqs. (1B) and (7B). It should be added that in the event that ρ and/or c are idealized to be zero in an extended region, as for example in the scattering of sound from a bubble in water, then p and $\mathbf{v}$ are zero within this region, and a reformulation in terms of surface integrals is necessary.

III. THE SCATTERING AMPLITUDE. RECIPROCITY

We define $A(\mathbf{n},\mathbf{n}_0)$ as the pressure amplitude at infinity of the outgoing spherical wave proceeding along $\mathbf{n}$, which results from an incident plane wave of unit amplitude along $\mathbf{n}_0$. From Eq. (13),

$$A(\mathbf{n},\mathbf{n}_0) = -\frac{k^2}{4\pi}\int d\mathbf{r}'\exp(-ik\mathbf{n}\cdot\mathbf{r}')\left[(1-\alpha'\mu'^2)p(\mathbf{r}',\mathbf{n}_0) + \rho_0 c_0\left(1-\frac{1}{\alpha'}\right)\mathbf{n}\cdot\mathbf{v}(\mathbf{r}',\mathbf{n}_0)\right], \tag{14}$$

where $p(\mathbf{r},\mathbf{n}_0)$ and $\mathbf{v}(\mathbf{r},\mathbf{n}_0)$ represent the fields resulting from an incident unit plane wave along $\mathbf{n}_0$. The average rate of flow of acoustic energy across the surface element $dS\mathbf{n} = r^2 d\Omega\mathbf{n}$ at infinity is, from Eqs. (13) and (14) and the definition following Eq. (3),

$$I(\mathbf{n})d\Omega = \frac{2|A(\mathbf{n},\mathbf{n}_0)|^2}{\rho_0 c_0}d\Omega. \tag{15}$$

The incident intensity is $2/\rho_0 c_0$, so the differential cross section is $\sigma(\mathbf{n}) = |A(\mathbf{n},\mathbf{n}_0)|^2$.

Replacing $\mathbf{n}$ and $\mathbf{n}_0$ in Eq. (14) by $-\mathbf{n}_0$ and $-\mathbf{n}$, respectively, we obtain an expression for $A(-\mathbf{n}_0,-\mathbf{n})$ in terms of $p(\mathbf{r},-\mathbf{n})$ and $\mathbf{v}(\mathbf{r},-\mathbf{n})$, where $p(\mathbf{r},-\mathbf{n})$, the pressure resulting from an incident wave along $-\mathbf{n}$, satisfies, according to Eq. (11),

$$p(\mathbf{r},-\mathbf{n}) = \exp(-ik\mathbf{n}\cdot\mathbf{r}) + k^2\int d\mathbf{r}'G(\mathbf{r},\mathbf{r}')(1-\alpha'\mu'^2)p(\mathbf{r}',-\mathbf{n}) - i\omega\rho_0\,\mathrm{div}\int d\mathbf{r}'G(\mathbf{r},\mathbf{r}')\left(1-\frac{1}{\alpha'}\right)\mathbf{v}(\mathbf{r}',-\mathbf{n}). \tag{16}$$

Multiplying Eq. (16) by $(1-\alpha\mu^2)p(\mathbf{r},\mathbf{n}_0)$, and the corresponding equation for $\mathbf{v}(\mathbf{r},-\mathbf{n})$ by $\rho_0 c_0(1-\alpha^{-1})\mathbf{v}(\mathbf{r},\mathbf{n}_0)$, adding and integrating, we get, by virtue of Eq. (14), another expression for $A(\mathbf{n},\mathbf{n}_0)$, namely,

$$\begin{aligned} A(\mathbf{n},\mathbf{n}_0) = {} & \frac{-1}{4\pi}\int d\mathbf{r}[\beta p(\mathbf{n}_0)p(-\mathbf{n}) - \omega\rho_0\gamma\mathbf{v}(\mathbf{n}_0)\cdot\mathbf{v}(-\mathbf{n})] \\ & -\frac{i}{4\pi}\int d\mathbf{r}\beta p(\mathbf{n}_0)\,\mathrm{div}\int d\mathbf{r}'G\gamma'\mathbf{v}'(-\mathbf{n}) \\ & +\frac{i}{4\pi}\int d\mathbf{r}\gamma\mathbf{v}(\mathbf{n}_0)\cdot\mathrm{grad}\int d\mathbf{r}'G\beta'p'(-\mathbf{n}) \\ & +\frac{1}{4\pi}\int d\mathbf{r}\gamma\mathbf{v}(\mathbf{n}_0)\cdot\mathrm{curl}\,\mathrm{curl}\int d\mathbf{r}'G\gamma'\mathbf{v}'(-\mathbf{n}) \\ & +\frac{1}{4\pi}\int d\mathbf{r}d\mathbf{r}'\Big[p(\mathbf{n}_0)\beta G\beta'p'(-\mathbf{n}) \\ & \qquad -k^2\gamma G\gamma'\mathbf{v}(\mathbf{n}_0)\cdot\mathbf{v}'(-\mathbf{n})\Big], \end{aligned} \tag{17}$$

where we have used $G \equiv G(\mathbf{r},\mathbf{r}')$ and

$$\beta(\mathbf{r}) = k^2(1-\alpha\mu^2),$$
$$\gamma(\mathbf{r}) = \omega\rho_0\left(1-\frac{1}{\alpha}\right). \tag{18}$$

From Eq. (17) and the corresponding expression for $A(-\mathbf{n}_0,-\mathbf{n})$ follows the principle of reciprocity,

$$A(\mathbf{n},\mathbf{n}_0) = A(-\mathbf{n}_0,-\mathbf{n}). \tag{19}$$

The proof is given in Appendix C.

IV. THE SCATTERING MATRIX

In Eq. (11) p_0 and $\mathbf{v}_0$ need not be a plane wave but may be any solution of the homogeneous equations, namely Eq. (3) with $\rho = \rho_0$ and $c = c_0$. Presumably the solution to Eq. (11) remains unique for any such choice of p_0 and $\mathbf{v}_0$. It follows therefore from Eq. (11) that the amplitudes at infinity of the outgoing spherical waves are wholly determined by the incoming waves. In fact, since $\mathbf{v}_0 = (\text{grad}\, p_0)/i\omega\rho_0$, p_s and $\mathbf{v}_s$ at infinity are solely determined by the incoming spherical waves in p_0. Consequently, since the solutions are linear, we infer[4] the existence of a scattering matrix $S(\mathbf{n},\mathbf{n}')$ defined as follows. At infinity p_0 is composed of incoming and outgoing spherical waves. Hence, by Eq. (13), neglecting terms of order $1/r^2$

$$\lim_{r\to\infty} p(r\mathbf{n}) = F_1(\mathbf{n})\frac{e^{ikr}}{r} + F_2(\mathbf{n})\frac{e^{-ikr}}{r}, \tag{20}$$

where

$$F_1(\mathbf{n}) = -\int d\Omega' S(\mathbf{n},\mathbf{n}')F_2(-\mathbf{n}'). \tag{21}$$

$\mathbf{n}'$ is the unit vector along the element of solid angle $d\Omega'$. As will be seen this definition, Eq. (21), of the scattering matrix has the virtue that $S(\mathbf{n},\mathbf{n}')$ reduces to the unit matrix when there is no scattering.

We now derive some general properties of the scattering matrix. Since energy conservation is a ready consequence of Eq. (3), as it must be, we have, for any solution of that equation

$$\int dS\mathbf{n}\cdot(p^*\mathbf{v}+p\mathbf{v}^*) = 0, \tag{22}$$

where the integration extends over the sphere at infinity. Recalling that $\mathbf{v} = (\text{grad}\, p)/i\omega\rho_0$ at infinity, substitution of Eq. (20) in Eq. (22) yields

$$\frac{2}{\rho_0 c_0}\int d\Omega[|F_1(\mathbf{n})|^2 - |F_2(\mathbf{n})|^2] = 0. \tag{23}$$

[4] Although the assertion that the outgoing waves are determined by the incoming waves is intuitively obvious, a satisfactory proof is not easily obtained. This question is discussed by Friedrichs, Marcuvitz, and John in Sec. III of "Recent developments in the theory of wave propagation," lecture notes, New York University Institute for Mathematics and Mechanics, 1949–1950 (unpublished).

Since $F_2(\mathbf{n})$ may be chosen arbitrarily, Eq. (21) implies

$$\int d\Omega S(\mathbf{n},\mathbf{n}')S^*(\mathbf{n},\mathbf{n}'') = \delta(\mathbf{n}'-\mathbf{n}''). \tag{24}$$

Next we observe that Eq. (3) is invariant when its complex conjugate is taken and $\mathbf{v}$ is simultaneously replaced by $-\mathbf{v}$. That is, if p and $\mathbf{v}$ are any solutions of Eq. (3), then so are p^* and $-\mathbf{v}^*$. Thus from Eq. (20) we infer the behavior of p^* at infinity, namely,

$$\lim_{r\to\infty} p^*(r\mathbf{n}) = F_2^*(\mathbf{n})\frac{e^{ikr}}{r} + F_1^*(\mathbf{n})\frac{e^{-ikr}}{r}, \tag{25}$$

whence, from the definition (21) of the scattering matrix,

$$F_2^*(\mathbf{n}) = -\int d\Omega' S(\mathbf{n},\mathbf{n}')F_1^*(-\mathbf{n}'). \tag{26}$$

Substitution of the conjugate of Eq. (26) into Eq. (21) then yields, after rearrangement of the dummy variables,

$$\int d\Omega S(-\mathbf{n}',-\mathbf{n})S^*(\mathbf{n},\mathbf{n}'') = \delta(\mathbf{n}'-\mathbf{n}''). \tag{27}$$

Comparison of Eqs. (24) and (27) implies, as can be shown by multiplying Eq. (27) by $S^*(-\mathbf{n}',-\mathbf{n}''')$, and integrating over $\mathbf{n}'$, that

$$S(-\mathbf{n}',-\mathbf{n}) = S(\mathbf{n},\mathbf{n}'), \tag{28}$$

a result which can be regarded as an extension of the reciprocity relation (19). Equations (27) and (28) yield

$$\int d\Omega S(\mathbf{n}',\mathbf{n})S^*(\mathbf{n}'',\mathbf{n}) = \delta(\mathbf{n}'-\mathbf{n}''), \tag{29}$$

which, together with Eq. (24), expresses the fact that S is unitary.[5]

Finally, we relate the scattering amplitude $A(\mathbf{n},\mathbf{n}_0)$, which is defined only for plane wave excitation, to the general scattering matrix. For plane wave excitation, the field at infinity has the form

$$\lim_{r\to\infty} p(r\mathbf{n}) = \exp(ik\mathbf{n}_0\cdot r\mathbf{n}) + A(\mathbf{n},\mathbf{n}_0)\frac{e^{ikr}}{r}$$
$$= \frac{2\pi i}{k}\sum_{l,m}(-1)^l Y_l^m(\mathbf{n}_0)Y_l^{m*}(\mathbf{n})\frac{e^{-ikr}}{r}$$
$$+\left[A(\mathbf{n},\mathbf{n}_0) - \frac{2\pi i}{k}\sum_{l,m}Y_l^m(\mathbf{n}_0)Y_l^{m*}(\mathbf{n})\right]\frac{e^{ikr}}{r}, \tag{30}$$

where the Y_l^m are normalized spherical harmonics. Since these form a complete orthonormal set, we thus

[5] As in reference 1, for a spherically symmetric scatter S is expressible in terms of the usual phase shifts and is diagonal in a representation in which the spherical harmonics are the basis vectors.

have

$$\lim_{r\to\infty} p=\frac{2\pi i}{k}\delta(\mathbf{n}_0+\mathbf{n})\frac{e^{-ikr}}{r}$$

$$+\left[A(\mathbf{n},\mathbf{n}_0)-\frac{2\pi i}{k}\delta(\mathbf{n}_0-\mathbf{n})\right]\frac{e^{ikr}}{r}. \quad (31)$$

If we regard Eq. (31) as that special case of Eq. (20) for which

$$F_1(\mathbf{n})=A(\mathbf{n},\mathbf{n}_0)-(2\pi i/k)\delta(\mathbf{n}_0-\mathbf{n}),$$
$$F_2(\mathbf{n})=(2\pi i/k)\delta(\mathbf{n}_0+\mathbf{n}), \quad (32)$$

Equation (21) yields at once

$$A(\mathbf{n},\mathbf{n}_0)=(2\pi i/k)\delta(\mathbf{n}_0-\mathbf{n})-(2\pi i/k)S(\mathbf{n},\mathbf{n}_0), \quad (33)$$

which is the desired relation.[6] Equation (33) and the unitary character of S lead directly to the cross-section theorem[1]

$$\sigma=\int d\Omega|A(\mathbf{n},\mathbf{n}_0)|^2=\frac{4\pi}{k}\,\mathrm{Im}A(\mathbf{n}_0,\mathbf{n}_0). \quad (34)$$

V. VARIATIONAL PRINCIPLE FOR $A(n,n_0)$

Suppose A_1, A_2, and A_3 are three functions of pressure and velocity which are exactly equal for correctly chosen pressure and velocity, but are not necessarily equal when the pressure and velocity are varied about their correct values. Then for correct p, $\mathbf{v}$

$$A_1=A_2=A_3=B=A_1A_2/A_3, \quad (35)$$

and

$$\delta B=(A_1/A_3)\delta A_2+(A_2/A_3)\delta A_1-(A_1A_2/A_3^2)\delta A_3$$
$$=\delta A_2+\delta A_1-\delta A_3. \quad (36)$$

From Eq. (14) introduce

$$A(-\mathbf{n}_0,-\mathbf{n})=\frac{-k^2}{4\pi}\int d\mathbf{r}$$
$$\times\exp(ik\mathbf{n}_0\cdot\mathbf{r})\Big[(1-\alpha\mu^2)p(\mathbf{r},-\mathbf{n})$$
$$-\rho_0c_0\left(1-\frac{1}{\alpha}\right)\mathbf{n}_0\cdot\mathbf{v}(\mathbf{r},-\mathbf{n})\Big]. \quad (37)$$

Denote $A(\mathbf{n},\mathbf{n}_0)$ from Eq. (14) by A_1, $A(-\mathbf{n}_0,-\mathbf{n})$ from Eq. (37) by A_2, and $A(\mathbf{n},\mathbf{n}_0)$ from Eq. (17) by A_3. Then, as shown in Appendix D, B defined by Eq. (35) is stationary for arbitrary variations $\delta p(\mathbf{r},\mathbf{n}_0)$, $\delta\mathbf{v}(\mathbf{r},\mathbf{n}_0)$, $\delta p(\mathbf{r},-\mathbf{n})$, $\delta\mathbf{v}(\mathbf{r},-\mathbf{n})$. We mention specifically that these variations need not satisfy the boundary conditions, although of course they must be so chosen that the integrals converge.

Since the right side of Eq. (35) is stationary, Eq. (36) shows $B'=A_1+A_2-A_3$ is also stationary. If we define $A_4=A(-\mathbf{n}_0,-\mathbf{n})$ of Eq. (17) then by symmetry the expressions

$$B=A_1A_2/A_4,$$
$$B'=A_1+A_2-A_4, \quad (38)$$

are stationary for arbitrary variations $\delta p(\mathbf{r},\mathbf{n}_0)$, $\delta\mathbf{v}(\mathbf{r},\mathbf{n}_0)$, $\delta p(\mathbf{r},-\mathbf{n})$, $\delta\mathbf{v}(\mathbf{r},-\mathbf{n})$.

Since B and B' are stationary for arbitrary variations they are stationary for the special choice

$$\delta\mathbf{v}(\mathbf{r},\mathbf{n}_0)=(1/i\omega\rho)\,\mathrm{grad}\delta p(\mathbf{r},\mathbf{n}_0),$$
$$\delta\mathbf{v}(\mathbf{r},-\mathbf{n})=(1/i\omega\rho)\,\mathrm{grad}\delta p(\mathbf{r},-\mathbf{n}). \quad (39)$$

Hence, comparing with Eq. (3), the above expressions for B and B' are stationary for arbitrary $\delta p(\mathbf{r},\mathbf{n}_0)$ and $\delta p(\mathbf{r},-\mathbf{n})$ when, in B and B', $\mathbf{v}$ is everywhere replaced by $(\mathrm{grad}p)/i\omega\rho$. Similarly the expressions are stationary for arbitrary $\delta\mathbf{v}(\mathbf{r},\mathbf{n}_0)$ and $\delta\mathbf{v}(\mathbf{r},-\mathbf{n})$ when p is everywhere replaced by $(\rho c^2\,\mathrm{div}\mathbf{v})/i\omega$.

VI. ABSTRACT FORMULATION OF THE VARIATIONAL PRINCIPLE

The difficulties involved in obtaining a variational principle for $A(\mathbf{n},\mathbf{n}_0)$ are more readily recognized when the problem is given a more general abstract formulation,[4] with a condensed notation. Suppose

$$Kx=z, \quad (40)$$

where K is a given operator, z is known, and x is unknown. Suppose further that we are interested in determining

$$A=z'^TLx, \quad (41)$$

where L is a given operator and z' is known. If K and L are matrices, then x and z' are single column matrices, and z'^T, the transpose of z', is a single row matrix. If now we can determine operators K' and L' such that

$$K'L=L'K, \quad (42)$$

and for which there exists a solution y, not necessarily known, to the equation

$$y^TK'=z'^T, \quad (43)$$

then it is easily verified, by virtue of Eqs. (40)–(43), that

$$A=y^TK'Lx=y^TL'Kx=y^TL'z, \quad (44)$$

and moreover that either of the expressions

$$B'=y^TL'z+z'^TLx-y^TK'Lx,$$
$$B'=y^TL'z+z'^TLx-y^TL'Kx, \quad (45)$$

is stationary for arbitrary δx and δy^T. We note that Eqs. (40), (43), and (44) alone, without Eq. (42), are not sufficient to prove B' of Eq. (45) stationary. It is sufficient to replace Eq. (42) by the requirements

$$K'Lx=L'Kx,$$
$$y^TL'K=y^TK'L. \quad (46)$$

[6] With Eq. (19), Eq. (33) provides an alternative proof of Eq. (28).

When $\rho'=\rho_0$ in Eq. (11) derivatives of the Green's function do not appear in the integral equation for $p(\mathbf{r})$, and the problem reduces to the type which has been treated previously.[1] In this event in Eq. (40) we identify x with $p(\mathbf{r},\mathbf{n}_0)$, z with $p_0(\mathbf{n}_0)$. Also, in conformity with matrix notation,

$$K=1-GM, \tag{47}$$

where $\mathbf{r}$ and $\mathbf{r}'$ index, respectively, the rows and columns of the continuous matrix $G(\mathbf{r},\mathbf{r}')$, $1\equiv\delta(\mathbf{r}-\mathbf{r}')$ is the unit matrix, and from Eq. (11), M is the diagonal matrix

$$M(\mathbf{r},\mathbf{r}')=k^2(1-\mu^2)\delta(\mathbf{r}-\mathbf{r}'), \tag{48}$$

if we remember that we are presently assuming $\alpha=1$. We then identify $A(\mathbf{n},\mathbf{n}_0)$ with A of Eq. (41). Because of Eq. (12) and the way in which $A(\mathbf{n},\mathbf{n}_0)$ is defined, we see that z' of Eq. (41) must be identified with $p_0(-\mathbf{n})$, and $L\equiv -M/4\pi$. The only equation involving $p_0(-\mathbf{n})$ which is immediately at hand is, again by Eq. (11),

$$(1-GM)p(-\mathbf{n})=p_0(-\mathbf{n}). \tag{49}$$

Hence, in Eq. (43),

$$K'=(1-GM)^T=1-M^TG^T=1-MG, \tag{50}$$

since M and G are both symmetric. Consequently $L'=L=-M/4\pi$ satisfies Eq. (42). The resultant variational principle, corresponding to Eq. (45), is the usual one.[1]

We observe that when derivatives of the Green's function do not appear in the integral equation, i.e., when p and $(\mathrm{grad}p)_n$ are continuous, the variational principle is a necessary and natural consequence of the simple relationship between the form of K, Eq. (47), and the expression for $A(\mathbf{n},\mathbf{n}_0)$, which makes $L=-M/4\pi$. This simple relationship no longer obtains in the more general case when ρ is not constant. In the first place there are now four independent quantities in Eq. (11), $p(\mathbf{r})$ and the three components of $\mathbf{v}(\mathbf{r})$, corresponding to the elements x_i, $i=1$ to 4, in Eq. (40). Consequently, K in Eq. (40) is a supermatrix of continuous submatrices $K_{ij}(\mathbf{r},\mathbf{r}')$, $i,j=1$ to 4. Further, since derivative terms enter, off diagonal elements of the continuous submatrices enter in a complicated way. Moreover, because of these derivative terms, alternative expressions are possible, by virtue of partial integrations, for K and for $A(\mathbf{n},\mathbf{n}_0)$. However, the integral equations (11) and Eq. (14) appear to give the only reasonably simply obtained formulation of the problem in terms of volume integrals which extend over all space and assuredly remain well defined even when discontinuities of ρ and/or c exist, thereby obviating any necessity for the inclusion of surface integrals. Thus it is interesting to note that this formulation is also the only one from which we have been able to derive a variational principle for $A(\mathbf{n},\mathbf{n}_0)$, even when surfaces of discontinuity are in fact absent. For example, when all functions and their derivatives are well behaved, derivatives of $G(\mathbf{r},\mathbf{r}')$ may be avoided by using Eqs. (1A) and (4A), yielding the integral equation

$$p(\mathbf{r},\mathbf{n}_0)-\int d\mathbf{r}'G(\mathbf{r},\mathbf{r}')[k^2(1-\mu'^2)p'(\mathbf{n}_0)+i\omega\mathbf{v}'(\mathbf{n}_0)\cdot\mathrm{grad}'(\rho'-\rho_0)]=\exp(ik\mathbf{n}_0\cdot\mathbf{r}), \tag{51}$$

for $p(\mathbf{n}_0)$, with corresponding equations for $\mathbf{v}(\mathbf{n}_0)$, $p(-\mathbf{n})$, and $\mathbf{v}(-\mathbf{n})$ and, for $A(\mathbf{n},\mathbf{n}_0)$, the equation

$$A(\mathbf{n},\mathbf{n}_0)=-\frac{1}{4\pi}\int d\mathbf{r}'\exp(-ik\mathbf{n}\cdot\mathbf{r}')[k^2(1-\mu'^2)p'(\mathbf{n}_0)+i\omega\mathbf{v}'(\mathbf{n}_0)\cdot\mathrm{grad}'(\rho'-\rho_0)], \tag{52}$$

with a corresponding equation for $A(-\mathbf{n}_0,-\mathbf{n})$. However, Eqs. (51) and (52), which correspond to Eqs. (40) and (41), do not lead to a variational principle for $A(\mathbf{n},\mathbf{n}_0)$, as is readily verified. This does not mean that a variational principle based on Eqs. (51) and (52) does not exist, but demonstrates that the obvious equations involving $\exp(-ik\mathbf{n}\cdot\mathbf{r})$, which corresponds to z' of Eq. (41), do not satisfy Eq. (42) or Eq. (46). Similar remarks pertain to the other combinations of integral equations and expressions for $A(\mathbf{n},\mathbf{n}_0)$ which we have tried,[7] excepting of course the combination of Eqs. (11) and (14). Evidently it would be most helpful to have a deeper comprehension of the kinds of formulations of the scattering problem which can yield variational principles for $A(\mathbf{n},\mathbf{n}_0)$.

We add that the two distinct variational principles obtained from Eqs. (35) and (38) correspond to the pair of stationary expressions of Eq. (45), and that the content of Appendix D is essentially the demonstration of Eq. (42).

VII. SPHERICALLY SYMMETRIC SCATTERER

When ρ and c are spherically symmetric, the pressure p of Eq. (8) can be written in the form

$$p(\mathbf{r})=\textstyle\sum_l R_l(r)P_l(\cos\theta), \tag{53}$$

where P_l are the Legendre polynomials and θ is the angle between $\mathbf{r}$ and $\mathbf{n}_0$. By Eqs. (3) and (8) R_l satisfies

$$\frac{1}{r^2}\frac{d}{dr}r^2\frac{dR_l}{dr}-\frac{l(l+1)}{r^2}R_l+k^2R_l=k^2(1-\mu^2)R_l+\frac{1}{\rho}\frac{d\rho}{dr}\frac{dR_l}{dr}. \tag{54}$$

In Eq. (54) we have used $\rho=\rho(r)$, $c=c(r)$.

[7] Nor have we succeeded in finding any different variational principles when the condition that the variations be unrestricted is relaxed. More precisely, the restrictions on the variations turn out to be complicated and difficult to interpret or achieve, at least in the cases we have examined.

In Appendix E we derive an integral equation for $R_l(r)$, namely

$$R_l(r)=i^l(2l+1)j_l(kr)+\frac{1}{r}\int_0^\infty dr'r'G_l\left\{\left[(1-\alpha')\frac{l(l+1)}{r'^2}-k^2(1-\alpha'\mu'^2)\right]R_l'-(1-\alpha')\frac{\dot{R}_l'}{r'}\right\}+\frac{1}{r}\int_0^\infty dr'r'(1-\alpha')\dot{R}_l'\frac{dG_l}{dr'}. \quad (55)$$

In Eq. (55) the dot signifies the derivative, the prime continuing to denote functional dependence on r'. Thus $\dot{R}_l=dR_l/dr$, $\dot{R}_l'=\dot{R}_l(r')$. $G_l(r,r')$ is defined by

$$\begin{aligned} G_l(r,r')&=ikrr'j_l(kr)h_l^{(1)}(kr'), \quad r<r',\\ G_l(r,r')&=ikrr'j_l(kr')h_l^{(1)}(kr), \quad r'<r, \end{aligned} \quad (56)$$

where j_l and $h_l^{(1)}$ are spherical Bessel functions.[8] Equation (55) is valid whether or not there are discontinuities in ρ and/or c. As in Eq. (11), derivatives of $\rho(r)$ and $c(r)$ have been eliminated in Eq. (55). As explained in Sec. II, ρ and $\mathbf{v}$ are presumed finite, so that Eq. (53) and the first of Eq. (3) imply $\dot{R}_l$ is finite. The integrals in Eq. (55) extend over all values of r' from 0 to ∞, with the understanding that α', μ', R_l', and $\dot{R}_l'$ may be assigned arbitrary finite values at discontinuities of ρ' and/or c'. The boundary conditions on R_l are inferred from the boundary conditions on p and $\mathbf{v}_n$, using Eqs. (3) and (8), and remembering that in the present case the surfaces of discontinuity are spheres centered at the origin. We conclude that R_l and $\dot{R}_l/\rho$ are continuous at the discontinuities $r=r_d$, and that except for its incoming part, obtained from the expansion of p_0 in Eq. (8), R_l is outgoing at infinity.[9]

From Eqs. (55) and (65) and the asymptotic forms[8] of $j_l(kr)$ and $h_l^{(1)}(kr)$ we find that for large r

$$R_l(r)\sim\frac{i^l(2l+1)e^{i\delta_l}}{kr}\sin\left(kr-\frac{l\pi}{2}+\delta_l\right), \quad (57)$$

where

$$\frac{i^l(2l+1)e^{i\delta_l}\sin\delta_l}{k}=X_l=\int_0^\infty dr'r'^2\times\left[\sigma'R_l'j_l(kr')+\tau'\dot{R}_l'\frac{d}{dr'}j_l(kr')\right], \quad (58)$$

and we use the abbreviations

$$\sigma=\frac{l(l+1)(1-\alpha)}{r^2}-k^2(1-\alpha\mu^2), \quad \tau=1-\alpha. \quad (59)$$

As usual,[10] by virtue of Eqs. (8), (53), (57), and the definition of $A(\mathbf{n},\mathbf{n}_0)$,

$$A(\mathbf{n},\mathbf{n}_0)=k^{-1}\sum_l(2l+1)e^{i\delta_l}\sin\delta_l P_l(\cos\theta)=\sum_l(-i)^l X_l P_l(\cos\theta). \quad (60)$$

In order to eliminate the inconsequential imaginary part of R_l, we introduce

$$S_l(r)=\frac{R_l(r)}{i^l(2l+1)e^{i\delta_l}\cos\delta_l}. \quad (61)$$

Then Eq. (57) shows that for large r,

$$S_l(r)\sim\frac{\sin(kr-\frac{1}{2}l\pi)}{kr}+\tan\delta_l\frac{\cos(kr-\frac{1}{2}l\pi)}{kr}; \quad (62)$$

and, from Eqs. (58) and (61),

$$\frac{1}{k}\tan\delta_l=\int_0^\infty drr^2\left[\sigma S_l j_l(kr)+\tau\dot{S}_l\frac{d}{dr}j_l(kr)\right]. \quad (63)$$

$S_l(r)$ satisfies Eq. (54) and the same boundary conditions at a discontinuity $r=r_d$ as does $R_l(r)$, since it is merely proportional to $R_l(r)$.

Define $\bar{G}_l(r,r')$ by

$$\begin{aligned} \bar{G}_l(r,r')&=-krr'j_l(kr)n_l(kr'), \quad r<r';\\ \bar{G}_l(r,r')&=-krr'j_l(kr')n_l(kr), \quad r'<r. \end{aligned} \quad (64)$$

$\bar{G}_l(r,r')$ satisfies the same differential Eq. (2E) as does $G_l(r,r')$, but behaves like $[\cos(kr-\frac{1}{2}l\pi)]/kr$ as r approaches infinity, i.e., like the second or scattering term in Eq. (62). Consequently, just as in Appendix E, $S_l(r)$ can be shown to obey the integral equation,

$$S_l(r)=j_l(kr)+\frac{1}{r}\int_0^\infty dr'r'\bar{G}_l\left[\sigma'S_l'-\tau'\frac{\dot{S}_l'}{r'}\right]+\frac{1}{r}\int_0^\infty dr'r'\tau'\dot{S}_l'\frac{d\bar{G}_l}{dr'}. \quad (65)$$

Equation (65) also can be demonstrated directly from Eq. (55).

[8] J. A. Stratton, *Electromagnetic Theory* (McGraw-Hill Book Company, Inc., New York, 1941), pp. 404–406.

[9] Since in Appendix E Eq. (55) is shown to follow directly from Eq. (54), we expect, and can prove without much difficulty, that the solutions to Eq. (55) do in fact satisfy Eq. (54). A proof directly from Eq. (55) that its solutions satisfy the boundary conditions can be furnished along the lines of Appendix F. However neither of these proofs is necessary here in view of the proportionality between $R_l(r)$ and the function $S_l(r)$ which we define immediately below, and for which we do give proofs.

[10] L. I. Schiff, *Quantum Mechanics* (McGraw-Hill Book Company, Inc., New York, 1949), p. 105.

Differentiating Eq. (65), we obtain

$$\dot{S}_l(r)=\frac{d}{dr}j_l(kr)$$
$$-\frac{1}{r^2}\int_0^\infty dr'\bar{G}_l[r'\sigma' S_l'-\tau'\dot{S}_l']$$
$$+\frac{1}{r}\frac{d}{dr}\int_0^\infty dr'\bar{G}_l[r'\sigma' S_l'-\tau'\dot{S}_l']$$
$$-\frac{1}{r^2}\int_0^\infty dr'r'\tau'\dot{S}_l'\frac{d\bar{G}_l}{dr'}$$
$$+\frac{1}{r}\frac{d}{dr}\int_0^\infty dr'r'\tau'\dot{S}_l'\frac{d\bar{G}_l}{dr'}. \quad (66)$$

Equations (65) and (66) may now be regarded as a pair of coupled integral equations in the independent variables $S_l(r)$, $\dot{S}_l(r)$. As is proved in Appendix F, the solutions to Eqs. (65) and (66), with $S_l(r)$ and $\dot{S}_l(r)$ regarded as independent, satisfy the requisite boundary conditions and

$$\dot{S}_l(r)=\frac{d}{dr}S_l(r), \quad (67)$$

$$\frac{d\dot{S}_l}{dr}+\frac{2}{r}\dot{S}_l-\frac{l(l+1)}{r^2}S_l+k^2S_l=k^2(1-\mu^2)S_l+\frac{1}{\rho}\dot{\rho}\dot{S}_l. \quad (68)$$

Equation (68) implies S_l satisfies the original differential Eq. (54). Therefore Eqs. (65) and (66), with S_l and $\dot{S}_l$ regarded as independent quantities, solve the scattering problem for the lth partial wave. We may therefore infer also that $S_l(r)$ of Eq. (65), with $\dot{S}_l$ defined as the derivative of S_l, satisfies Eq. (54) and the boundary conditions, and similarly for $R_l(r)$ of Eq. (55). Evidently Eqs. (65) and (66) are the analogs, for the lth partial wave, of Eq. (11) which held for the total fields $p(\mathbf{r})$ and $\mathbf{v}(\mathbf{r})$.

We are now finally in a position to formulate the variational principle which we have been seeking. Denote the right side of Eq. (63) by A_{1l}. Define

$$A_{2l}=\int_0^\infty dr r^2\left[\sigma S_l^T j_l(kr)+\tau\dot{S}_l^T\frac{d}{dr}j_l(kr)\right], \quad (69)$$

where S_l^T and $\dot{S}_l^T$ are independent functions whose variations are independent of the variations of S_l and $\dot{S}_l$, but such that the unvaried (correct) values of S_l^T and $\dot{S}_l^T$ satisfy the same Eqs. (65) and (67) as do S_l and $\dot{S}_l$. In other words, for $\delta S_l=\delta S_l^T=\delta\dot{S}_l=\delta\dot{S}_l^T=0$, $S_l=S_l^T$, $\dot{S}_l=\dot{S}_l^T$, $A_{1l}=A_{2l}$. From Eqs. (63), (65), and (66), and the corresponding equations for S_l^T, $\dot{S}_l^T$, we obtain directly[11]

$$\frac{1}{k}\tan\delta_l=A_{3l}=\int_0^\infty dr r^2(\sigma S_l^T S_l+\tau\dot{S}_l^T\dot{S}_l)$$
$$-\int_0^\infty dr r\sigma S_l^T\int_0^\infty dr'\bar{G}_l[r'\sigma' S_l'-\tau'\dot{S}_l']$$
$$-\int_0^\infty dr r\sigma S_l^T\int_0^\infty dr'r'\tau'\dot{S}_l'\frac{d\bar{G}_l}{dr'}$$
$$+\int_0^\infty dr r\tau\dot{S}_l^T\int_0^\infty dr'\bar{G}_l[r'\sigma' S_l'-\tau'\dot{S}_l']$$
$$-\int_0^\infty dr r\tau\dot{S}_l^T\frac{d}{dr}\int_0^\infty dr'\bar{G}_l[r'\sigma' S_l'-\tau'\dot{S}_l']$$
$$+\int_0^\infty dr r\tau\dot{S}_l^T\int_0^\infty dr'r'\tau'\dot{S}_l'\frac{d\bar{G}_l}{dr'}$$
$$-\int_0^\infty dr r\tau\dot{S}_l^T\frac{d}{dr}\int_0^\infty dr'r'\tau'\dot{S}_l'\frac{d\bar{G}_l}{dr'}. \quad (70)$$

Moreover the quantities

$$B_l=A_{1l}A_{2l}/A_{3l},$$
$$B_l'=A_{1l}+A_{2l}-A_{3l} \quad (71)$$

are stationary for arbitrary variations δS_l, δS_l^T, $\delta\dot{S}_l$, $\delta\dot{S}_l^T$. These variations need not satisfy the boundary conditions. By symmetry, S_l, $\dot{S}_l$ and S_l^T, $\dot{S}_l^T$ can be interchanged in Eq. (70), yielding in Eq. (71) the second, though equivalent, variational principle we have learned to expect from Eq. (45) and the discussion in Sec. VI.

The proof that B_l' in Eq. (71) is stationary is given in Appendix G. Since it is stationary for arbitrary variations it is stationary for $\delta S_l=\delta S_l^T$ and $\delta\dot{S}_l=\delta\dot{S}_l^T$, as well as for $\delta\dot{S}_l=d(\delta S_l)/dr$. That Eqs. (65) and (66) extend over the entire interval $0\leq r'<\infty$, without endpoint sums over $r'=r_d$, whether or not there are discontinuities, has already been remarked. As in the preceding section, we have not been able to construct variational principles from various alternative equations [to Eqs. (63), (65), and (66) for $\tan\delta_l$, S_l and/or $\dot{S}_l$] which can be shown to hold even when discontinuities are absent.

APPENDIX A

The simplest way to derive Eq. (11) is to assume first that there are no discontinuities in ρ and/or c. Let $p=p_0+p_s$ on the left side of Eq. (8) and, for convenience in the manipulations which follow, replace gradρ

[11] We introduce this seemingly awkward distinction between S_l and S_l^T merely to emphasize that in applications of the variational principle it is legitimate to use different trial functions for S_l and S_l^T, a procedure which might be useful in obtaining tractable integrals.

by grad$(\rho-\rho_0)$ on the right side of Eq. (8). Then

$$p_s(\mathbf{r})=\int d\mathbf{r}'G(\mathbf{r},\mathbf{r}') \times[k^2(1-\mu'^2)p'+i\omega\mathbf{v}'\cdot\text{grad}'(\rho'-\rho_0)], \quad (1A)$$

as may be verified by direct application of $(\Delta+k^2)$ to p_s, by using Eq. (10). In Eq. (1A)

$$G(\mathbf{r},\mathbf{r}')\mathbf{v}'\cdot\text{grad}'(\rho'-\rho_0)=\text{div}'G(\mathbf{r},\mathbf{r}')(\rho'-\rho_0)\mathbf{v}' -(\rho'-\rho_0)\mathbf{v}'\cdot\text{grad}'G(\mathbf{r},\mathbf{r}')-\frac{i\omega}{c'^2}G(\mathbf{r},\mathbf{r}')(1-\alpha')p', \quad (2A)$$

by use of Eq. (3). The integral of $\text{div}'G(\rho'-\rho_0)\mathbf{v}'$ vanishes since $\rho'-\rho_0$ is zero at infinity. The other terms yield

$$p_s(\mathbf{r})=k^2\int d\mathbf{r}'G(\mathbf{r},\mathbf{r}')(1-\alpha'\mu'^2)p(\mathbf{r}') -i\omega\int d\mathbf{r}'(\rho'-\rho_0)\mathbf{v}'\cdot\text{grad}'G(\mathbf{r},\mathbf{r}'). \quad (3A)$$

By noting $\text{grad}'G=-\text{grad}G$, Eq. (3A) and Eq. (7) are seen to be identical with Eq. (11) for $p(\mathbf{r})$.

Similarly, from Eq. (8)

$$\mathbf{v}_s(\mathbf{r})=\int d\mathbf{r}'G(\mathbf{r},\mathbf{r}')\Big[k^2(1-\mu'^2)\mathbf{v}' +i\omega p'\,\text{grad}'\Big(\frac{1}{\rho'c'^2}-\frac{1}{\rho_0c_0^2}\Big) -\text{curl}'\Big\{\text{grad}'\Big(\frac{1}{\rho'}-\frac{1}{\rho_0}\Big)\times\rho'\mathbf{v}'\Big\}\Big]. \quad (4A)$$

The derivative terms in Eq. (4A) can be in effect integrated by parts by manipulations similar to those of Eq. (2A), remembering always that, because the surface integrals at infinity vanish, any integral of a pure divergence, a pure curl, or a pure gradient, is zero. Thus, using Eq. (3) to eliminate $\text{grad}'p'$, Eq. (4A) becomes

$$\mathbf{v}_s(\mathbf{r})=k^2\int d\mathbf{r}'G(\mathbf{r},\mathbf{r}')\Big(1-\frac{1}{\alpha'}\Big)\mathbf{v}' -\frac{i\omega}{\rho_0c_0^2}\,\text{grad}\int d\mathbf{r}'G(\mathbf{r},\mathbf{r}')(1-\alpha'\mu'^2)p' -\text{curl}\int d\mathbf{r}'G(\mathbf{r},\mathbf{r}')\,\text{grad}'\Big(\frac{1}{\rho'}-\frac{1}{\rho_0}\Big)\times\rho'\mathbf{v}'. \quad (5A)$$

Because of Eq. (3), $\text{curl}\rho\mathbf{v}=0$, so that, in Eq. (5A),

$$\text{grad}'\Big(\frac{1}{\rho'}-\frac{1}{\rho_0}\Big)\times\rho'\mathbf{v}'=\text{curl}'\Big(\frac{1}{\rho'}-\frac{1}{\rho_0}\Big)\rho'\mathbf{v}'. \quad (6A)$$

With the aid of Eq. (6A), and of course another integration by parts, Eq. (5A) becomes identical with Eq. (11) for $\mathbf{v}(\mathbf{r})$.

The integrals in Eq. (11) do not involve derivatives of ρ' and/or c'. Hence Eq. (11) remains valid as the continuous functions $\rho(\mathbf{r})$ and/or $c(\mathbf{r})$ are permitted to have sharper and sharper gradients, becoming, in the limit, discontinuous with a finite jump across one or more surfaces. Consequently Eq. (11) holds whether or not such surfaces of discontinuity exist. Of course Eq. (11) can be established directly, but also more awkwardly, without making the initial assumption that ρ and/or c are everywhere continuous. Green's theorem and Eqs. (8) and (10) imply that

$$\int dS\mathbf{n}\cdot[G(\mathbf{r},\mathbf{r}')\,\text{grad}p_s(\mathbf{r})-p_s\,\text{grad}G(\mathbf{r},\mathbf{r}')] =\int d\mathbf{r}G(\mathbf{r},\mathbf{r}')[k^2(1-\mu^2)p(\mathbf{r}) +i\omega\mathbf{v}\cdot\text{grad}(\rho-\rho_0)]. \quad (7A)$$

The volume integral in Eq. (7A) runs over the space exterior to a small sphere about the point $\mathbf{r}=\mathbf{r}'$, not including an infinitesimal strip on either side of any surface of discontinuity of ρ and/or c. The surface integral in Eq. (7A) is over the sphere at infinity, the sphere around $\mathbf{r}=\mathbf{r}'$, and both sides of every strip; the normal $\mathbf{n}$ points out of the volume of integration of the right-hand side. The surface integral at infinity vanishes because G and p_s are both outgoing so that, shrinking the radius ρ of the small sphere to zero,

$$p_s(\mathbf{r}')+\int dS\mathbf{n}\cdot\{G(\mathbf{r},\mathbf{r}')[\text{grad}p_{si}-\text{grad}p_{se}] -\text{grad}G(\mathbf{r},\mathbf{r}')[p_{si}-p_{se}]\} =\int d\mathbf{r}G(\mathbf{r},\mathbf{r}')[k^2(1-\mu^2)p+i\omega\mathbf{v}\cdot\text{grad}(\rho-\rho_0)]. \quad (8A)$$

The surface integral in Eq. (8A) runs only over the surfaces of discontinuity. These are assumed to be finite closed surfaces, with $\mathbf{n}$ in Eq. (8A) directed out of the surface, toward the exterior, and i and e referring respectively to the interior and exterior sides. The volume integral in Eq. (8A) is over all space excluding infinitesimal strips on either side of the surfaces of discontinuity. Since p_0 and $\mathbf{v}_0$, Eq. (8), are everywhere continuous, the subscript s may be dropped in Eq. (8A). Also, according to the boundary conditions, p and $\mathbf{v}_n$ are continuous across S. Hence, using Eq. (3), Eq. (8A) becomes

$$p_s(\mathbf{r}')=\int d\mathbf{r}G(\mathbf{r},\mathbf{r}')[k^2(1-\mu^2)p+i\omega\mathbf{v}\cdot\text{grad}(\rho-\rho_0)] -i\omega\int dS\mathbf{n}\cdot G(\mathbf{r},\mathbf{r}')\mathbf{v}(\mathbf{r})(\rho_i-\rho_e). \quad (9A)$$

By interchanging $\mathbf{r}$ and $\mathbf{r}'$, and employing Eq. (2A), the volume integral in Eq. (9A) is integrated by parts just as previously, except that the integral of $\mathrm{div}'G(\rho'-\rho_0)\mathbf{v}'$ gives a surface integral on either side of S which just cancels the surface integral already in Eq. (9A). We are left with Eq. (3A), integrated over all of space exterior to the strips. In Eq. (3A) the integrands remain finite on S, since derivatives of ρ and c, and p and $\mathbf{v}$ for that matter, do not appear. Consequently, in Eq. (3A) the integral over an infinitesimal strip surrounding S is infinitesimal, and Eq. (9A) is seen to yield Eq. (11) for $p(\mathbf{r})$. With much more labor Eq. (11) for $\mathbf{v}(\mathbf{r})$ can be similarly deduced directly, without assuming ρ and c everywhere continuous. However it is apparent from a comparison of the above two derivations of $p(\mathbf{r})$ that our original simpler derivation of Eq. (11) was quite legitimate.

From Eq. (11), using Eq. (7), Eq. (10), and curl curl $\equiv$ grad div $-\Delta$,

$$\begin{aligned} &\mathrm{grad}\,p-i\omega\rho_0\mathbf{v}=-i\omega(\rho_0-\rho)\mathbf{v}, \\ &(i\omega/c_0^2)p-\rho_0\,\mathrm{div}\mathbf{v}=(i\omega/c_0^2)(1-\alpha\mu^2)p. \end{aligned} \tag{10A}$$

Equation (10A) is identical with Eq. (3), proving that the solutions p and $\mathbf{v}$ to Eq. (11) satisfy the original differential relations Eq. (3).

APPENDIX B

To prove $p(\mathbf{r})$ of Eq. (11) is continuous across a surface of discontinuity S we first eliminate the derivatives of the Green's function in Eq. (11). Differentiating under the integral sign, Eq. (11) for $p(\mathbf{r})$ yields Eq. (3A). The integrals in Eq. (3A) exist for all $\mathbf{r}$. Consequently for any point $\mathbf{r}$ not actually in S, exclusion from the region of integration in Eq. (3A) of an arbitrarily thin strip on either side of S modifies $p(\mathbf{r})$ by an arbitrarily small amount. Excluding such a region then, the last integral in Eq. (3A) can be integrated by parts, and we obtain

$$\begin{aligned} p(\mathbf{r})=p_0(\mathbf{r})&+k^2\int d\mathbf{r}'G(\mathbf{r},\mathbf{r}')(1-\alpha'\mu'^2)p' \\ &+i\omega\int d\mathbf{r}'G(\mathbf{r},\mathbf{r}')\,\mathrm{div}'(\rho'-\rho_0)\mathbf{v}' \\ &-i\omega\int dS'\mathbf{n}'\cdot G[(\rho_i'-\rho_0)\mathbf{v}_i'-(\rho_e'-\rho_0)\mathbf{v}_e']. \end{aligned} \tag{1B}$$

In Eq. (1B) $\mathbf{n}'$, the normal to dS', and the subscripts i and e are defined as in Eq. (8A). The volume integrals in Eq. (1B) are over all space except for a thin strip on either side of S. However these volume integrals may be extended over all space by assigning an arbitrary finite value to $\mathrm{div}'(\rho'-\rho_0)\mathbf{v}'$ on S'.

Let $\mathbf{r}_0$ lie in S. We wish to show that given any ϵ it is possible to choose δ sufficiently small that $|p(\mathbf{r}_0+z_1\mathbf{n})-p(\mathbf{r}_0-z_2\mathbf{n})|<\epsilon$ whenever $0<z_1<\delta$ and $0<z_2<\delta$. $p_0(\mathbf{r})$, Eq. (8), is a continuous function of $\mathbf{r}$. There is no difficulty in demonstrating this inequality for the volume integrals in Eq. (1B), since the factors multiplying $G(\mathbf{r},\mathbf{r}')$ in the integrands are assumed bounded. There remains to be proved continuous only the surface integral of Eq. (1B). Draw a sphere of radius $\alpha\epsilon$ about $\mathbf{r}_0$, α to be determined, which sphere, for small $\alpha\epsilon$, intersects S in some nearly circular closed curve. (We assume of course that S possesses all the usual attributes of a well-behaved surface, e.g., a tangent plane.) The surface integral of Eq. (1B), integrated over points $\mathbf{r}'$ outside the sphere for $\mathbf{r}=\mathbf{r}_0+z_1\mathbf{n}$, can be made as nearly equal as desired to the surface integral integrated over the same $\mathbf{r}'$ for $\mathbf{r}=\mathbf{r}_0-z_2\mathbf{n}$. This is accomplished by choosing δ sufficiently small, since the integrand is finite and continuous as $\delta\to 0$ for points $\mathbf{r}'$ outside the sphere. We now prove that for sufficiently small $\alpha\epsilon$ and δ the contribution to the surface integral from points on S' within the sphere vanishes. The factors multiplying $G(\mathbf{r},\mathbf{r}')$ in the integrand are bounded, so that, within the sphere,

$$\left|\int dS'\mathbf{n}'\cdot G[(\rho_i'-\rho_0)\mathbf{v}_i'-(\rho_e'-\rho_0)\mathbf{v}_e']\right| \leq\beta\int dS'\frac{1}{|\mathbf{r}-\mathbf{r}'|}, \tag{2B}$$

where β is some upper bound to $|\mathbf{n}'\cdot[(\rho_i'-\rho_0)\mathbf{v}_i'-(\rho_e'-\rho_0)\mathbf{v}_e']|$ within the sphere. Write

$$\mathbf{r}'-\mathbf{r}_0=x'\mathbf{t}'+y'\mathbf{n}, \tag{3B}$$

with $\mathbf{t}'$ a unit vector in the tangent plane. Then with $z=z_1$ or z_2

$$|\mathbf{r}'-\mathbf{r}|=(x'^2+z^2)^{\frac{1}{2}}\left[1+\frac{y'^2\pm 2zy'}{x'^2+z^2}\right]^{\frac{1}{2}}. \tag{4B}$$

Since $\mathbf{t}'$ lies in the tangent plane, $y'\sim x'^2$ for sufficiently small $\alpha\epsilon$. For sufficiently small $\alpha\epsilon$ therefore

$$\left|\frac{y'^2\pm 2zy'}{x'^2+z^2}\right|\sim\frac{x'^4}{x'^2+z^2}+\frac{2zx'^2}{x'^2+z^2} =\frac{x'^2}{1+z^2/x'^2}+\frac{2z}{1+z^2/x'^2}, \tag{5B}$$

which can be made arbitrarily small by choosing $\alpha\epsilon$ and δ sufficiently small, for any x' within the circle of radius $\alpha\epsilon$ in the tangent plane, and for all $0<z<\delta$. In Eq. (2B), therefore, we may write

$$\beta\int dS'\frac{1}{|\mathbf{r}-\mathbf{r}'|}=2\pi\beta\int_0^{\alpha\epsilon}dx'\frac{x'}{(x'^2+z^2)^{\frac{1}{2}}} =2\pi\beta[(z^2+\alpha^2\epsilon^2)^{\frac{1}{2}}-z]. \tag{6B}$$

The right side of Eq. (6B) can be made $<\epsilon$ by choosing δ arbitrarily small and $\alpha<1/2\pi\beta$. We conclude that $p(\mathbf{r})$ is continuous across S.

Equation (11) for $\mathbf{v}(\mathbf{r})$ yields, corresponding to Eq. (1B),

$$\begin{aligned}\mathbf{v}(\mathbf{r})=\mathbf{v}_0(\mathbf{r})&+k^2\int d\mathbf{r}'G(\mathbf{r},\mathbf{r}')\left(1-\frac{1}{\alpha'}\right)\mathbf{v}'\\&-\frac{i\omega}{\rho_0c_0^2}\int d\mathbf{r}'G(\mathbf{r},\mathbf{r}')\,\mathrm{grad}'(1-\alpha'\mu'^2)p'\\&-\int d\mathbf{r}'G(\mathbf{r},\mathbf{r}')\,\mathrm{curl}'\,\mathrm{curl}'\left(1-\frac{1}{\alpha'}\right)\mathbf{v}'\\&+\frac{i\omega}{\rho_0c_0^2}\int dS'\mathbf{n}'G(\mathbf{r},\mathbf{r}')\\&\times[(1-\alpha'\mu'^2)_ip_i'-(1-\alpha'\mu'^2)_ep_e']\\&+\int dS'\mathbf{n}'G(\mathbf{r},\mathbf{r}')\\&\times\left[\mathrm{curl}'\left(1-\frac{1}{\alpha'}\right)_i\mathbf{v}_i'-\mathrm{curl}'\left(1-\frac{1}{\alpha'}\right)_e\mathbf{v}_e'\right]\\&-\int dS'\,\mathrm{grad}'G(\mathbf{r},\mathbf{r}')\\&\times\left\{\mathbf{n}'\times\left[\left(1-\frac{1}{\alpha'}\right)_i\mathbf{v}_i'-\left(1-\frac{1}{\alpha'}\right)_e\mathbf{v}_e'\right]\right\}.\end{aligned}\tag{7B}$$

In Eq. (7B) it is possible that $[1-(1/\alpha')]\mathbf{v}'$ is discontinuous or nondifferentiable on a curve C on one or both sides of S, in which case $\mathrm{curl}'[1-(1/\alpha')]\mathbf{v}'$ would not exist on C on one or both sides of S. For example, $\mathbf{v}_e$ might be discontinuous on the rim of a plane piston source. However the value of the surface integral is not changed by assigning arbitrary finite values to $\mathrm{curl}'[1-(1/\alpha')]\mathbf{v}'$ on C, so that such discontinuities do not affect the validity of Eq. (7B). Moreover, in deriving the boundary conditions it is assumed that $p(\mathbf{r}_0)$ and $\mathbf{v}_n(\mathbf{r}_0)$ on either side of S differ infinitesimally from the values of $p(\mathbf{r})$ and $\mathbf{v}_n(\mathbf{r})$ at points $\mathbf{r}$ on the same side of S in the neighborhood of $\mathbf{r}_0$. This assumption need not be correct at points $\mathbf{r}_0$ where $[1-(1/\alpha')]\mathbf{v}'$ is discontinuous or nondifferentiable on either side of the surface. Consequently we are required to demonstrate the boundary conditions only at points $\mathbf{r}_0$ where $[1-(1/\alpha')]_i\mathbf{v}_i$ and $[1-(1/\alpha')]_e\mathbf{v}_e$ are well behaved. It can now be seen that in Eq. (7B) all integrals except the surface integral involving $\mathrm{grad}'1/|\mathbf{r}-\mathbf{r}'|$ (arising from $\mathrm{grad}'G$) are of the same types as those in Eq. (1B) and can be proved continuous in a like manner. As before, drawing a sphere of radius $\alpha\epsilon$ about $\mathbf{r}_0$, we observe that the contribution to the $\mathrm{grad}'1/|\mathbf{r}-\mathbf{r}'|$ surface integral from points $\mathbf{r}'$ outside the sphere is continuous on $\mathbf{r}$. It follows that the continuity of $\mathbf{v}_n$ will be assured if

$$\left|\mathbf{n}\cdot\int dS'\frac{e^{ik|\mathbf{r}-\mathbf{r}'|}}{|\mathbf{r}-\mathbf{r}'|^3}(\mathbf{r}-\mathbf{r}')\times\left\{\mathbf{n}'\times\left[\left(1-\frac{1}{\alpha'}\right)_i\mathbf{v}_i'-\left(1-\frac{1}{\alpha'}\right)_e\mathbf{v}_e'\right]\right\}\right|<\epsilon,\tag{8B}$$

for $\mathbf{r}=\mathbf{r}_0\pm z\mathbf{n}$ and sufficiently small α and δ, the integral running over points on S' lying within the sphere, and the integrand well behaved, i.e., differentiable, at $\mathbf{r}_0$.

Replace $\mathbf{r}'$ by $\mathbf{r}_0$ in the integrand of Eq. (8B), except in $(\mathbf{r}-\mathbf{r}')/|\mathbf{r}-\mathbf{r}'|^3$, which is equivalent to making a Taylor expansion with remainder term of order of magnitude

$$\int dS'\frac{\mathbf{r}-\mathbf{r}'}{|\mathbf{r}-\mathbf{r}'|^3}\times\{(\mathbf{r}'-\mathbf{r}_0)\cdot\mathrm{grad}'\}\left\{\exp ik|\mathbf{r}-\mathbf{r}'|\times\mathbf{n}'\left[\left(1-\frac{1}{\alpha'}\right)_i\mathbf{v}_i'-\left(1-\frac{1}{\alpha'}\right)_e\mathbf{v}_e'\right]\right\}.\tag{9B}$$

By using Eqs. (3B)–(5B) and remembering $y'\sim x'^2$, each of the components of the expression (9B) can be seen to have an upper bound involving sums of integrals such as

$$\int_0^{\alpha\epsilon}dx'\frac{zx'^2}{(x'^2+z^2)^{\frac{1}{2}}},\quad\int_0^{\alpha\epsilon}dx'\frac{zx'^3}{(x'^2+z^2)^{\frac{1}{2}}},\quad\int_0^{\alpha\epsilon}dx'\frac{x'^3}{(x'^2+z^2)^{\frac{1}{2}}},\tag{10B}$$

each of which can be made as small as desired by choosing $\alpha\epsilon$ and δ sufficiently small. Consequently the remainder term Eq. (9B) is negligible, and, again using Eqs. (3B)–(5B) and examining integrals like those of (10B), Eq. (8B) is seen to be equivalent to the condition that

$$\left|\mathbf{n}\cdot\int_0^{\alpha\epsilon}dx'\int_0^{2\pi}d\theta'x'\frac{e^{\pm ikz}}{(x'^2+z^2)^{\frac{1}{2}}}\times[x'\mathbf{t}'+(y'\pm z)\mathbf{n}]\times\{\mathbf{n}\times\mathbf{q}(\mathbf{r}_0)\}\right|<\epsilon,\tag{11B}$$

where

$$\mathbf{q}(\mathbf{r}_0)=\left(1-\frac{1}{\alpha'}\right)_i\mathbf{v}_i'-\left(1-\frac{1}{\alpha'}\right)_e\mathbf{v}_e',\tag{12B}$$

evaluated at $\mathbf{r}'=\mathbf{r}_0$. In Eq. (11B) y' and $\mathbf{t}'$ are the only quantities depending on θ'. The region of integration is

a circle in the tangent plane, centered at $\mathbf{r}_0$, with θ' the azimuth of $\mathbf{t}'$. Thus the terms involving $\mathbf{t}'$ in Eq. (11B) vanish when integrated over θ'. The remaining terms in the integrand, in $(y'\pm z)\mathbf{n}$, are perpendicular to $\mathbf{n}$. We conclude therefore that the normal component of any $\mathbf{v}(\mathbf{r})$ solving Eq. (11) is continuous at $\mathbf{r}=\mathbf{r}_0$ on S.

We remark that our procedure in referring the demonstration of the continuity of $\mathbf{v}_n(\mathbf{r})$ to the preceding proof of the continuity of $p(\mathbf{r})$ means that the rather lengthy argument used in proving $p(\mathbf{r})$ continuous really did not involve any extra work. Actually $p(\mathbf{r})$ can be readily proved continuous directly from Eq. (3A), but this proof cannot be extended to proving $\mathbf{v}_n(\mathbf{r})$ continuous. We see no obvious way to avoid the detailed examination of the surface integrals in Eq. (7B).

APPENDIX C

Corresponding to Eq. (17) we have

$$\begin{aligned}A(-\mathbf{n}_0,-\mathbf{n})&=-\frac{1}{4\pi}\int d\mathbf{r}[\beta p(-\mathbf{n})p(\mathbf{n}_0)-\omega\rho_0\gamma\mathbf{v}(-\mathbf{n})\cdot\mathbf{v}(\mathbf{n}_0)]\\&\quad-\frac{i}{4\pi}\int d\mathbf{r}\beta p(-\mathbf{n})\,\mathrm{div}\int d\mathbf{r}'G\gamma'\mathbf{v}'(\mathbf{n}_0)\\&\quad+\frac{i}{4\pi}\int d\mathbf{r}\gamma\mathbf{v}(-\mathbf{n})\cdot\mathrm{grad}\int d\mathbf{r}'G\beta'p'(\mathbf{n}_0)\\&\quad+\frac{1}{4\pi}\int d\mathbf{r}\gamma\mathbf{v}(-\mathbf{n})\cdot\mathrm{curl\ curl}\int d\mathbf{r}'G\gamma'\mathbf{v}'(\mathbf{n}_0)\\&\quad+\frac{1}{4\pi}\int d\mathbf{r}d\mathbf{r}'[p(-\mathbf{n})\beta G\beta'p'(\mathbf{n}_0)\\&\qquad-k^2\gamma G\gamma'\mathbf{v}(-\mathbf{n})\cdot\mathbf{v}'(\mathbf{n}_0)],\quad(1C)\end{aligned}$$

where G is symmetric, $G(\mathbf{r},\mathbf{r}')=G(\mathbf{r}',\mathbf{r})$, and $\mathrm{grad}'G=-\mathrm{grad}G$. Moreover

$$\begin{aligned}\int d\mathbf{r}\beta p(\mathbf{n}_0)\,\mathrm{div}\int d\mathbf{r}'G\gamma'\mathbf{v}'(-\mathbf{n})&=\int d\mathbf{r}d\mathbf{r}'\beta p(\mathbf{n}_0)\gamma'\mathbf{v}'(-\mathbf{n})\cdot\mathrm{grad}G\\&=\int d\mathbf{r}d\mathbf{r}'\beta'p'(\mathbf{n}_0)\gamma\mathbf{v}(-\mathbf{n})\cdot\mathrm{grad}'G,\quad(2C)\end{aligned}$$

interchanging the dummy variables $\mathbf{r}$ and $\mathbf{r}'$. It follows that the second integral on the right of Eq. (17) equals the third integral on the right of Eq. (1C). Similarly, the second integral on the right of Eq. (1C) equals the third integral on the right of Eq. (17). Consequently, comparing Eqs. (17) and (1C), to prove Eq. (19) it is only necessary to show

$$\begin{aligned}\int d\mathbf{r}\gamma\mathbf{v}(\mathbf{n}_0)\cdot\mathrm{curl\ curl}\int d\mathbf{r}'G\gamma'\mathbf{v}'(-\mathbf{n})&=\int d\mathbf{r}\gamma\mathbf{v}(-\mathbf{n})\cdot\mathrm{curl\ curl}\int d\mathbf{r}'G\gamma'\mathbf{v}'(\mathbf{n}_0).\quad(3C)\end{aligned}$$

By elementary manipulations using Stokes' theorem, it can be seen that the left side of Eq. (3C) equals

$$\begin{aligned}&\int dS\mathbf{v}\cdot\gamma\mathbf{v}(\mathbf{n}_0)\times\int dS'\mathbf{v}'\times G\gamma'\mathbf{v}'(-\mathbf{n})\\&\quad-\int dS\mathbf{v}\cdot\gamma\mathbf{v}(\mathbf{n}_0)\times\int d\mathbf{r}'G\,\mathrm{curl}'\gamma'\mathbf{v}'(-\mathbf{n})\\&\quad-\int d\mathbf{r}[\mathrm{curl}\gamma\mathbf{v}(\mathbf{n}_0)]\cdot\int dS'\mathbf{v}'\times G\gamma'\mathbf{v}'(-\mathbf{n})\\&\quad+\int d\mathbf{r}[\mathrm{curl}\gamma\mathbf{v}(\mathbf{n}_0)]\cdot\int d\mathbf{r}'G[\mathrm{curl}'\gamma'\mathbf{v}'(-\mathbf{n})].\quad(4C)\end{aligned}$$

In (4C) $\mathbf{v}$ is the normal to dS, and the surface integrals run over the interior and exterior of each surface of discontinuity, with $\mathbf{v}_i=\mathbf{v}$ as previously defined in Eq. (8A) on the interior surface and $\mathbf{v}_e=-\mathbf{v}$ on the exterior surface. A similar expression for the integral on the right of Eq. (3C) is obtained by interchanging $\mathbf{n}_0$ and $-\mathbf{n}$ in (4C). But interchanging the dot and first cross in each of the first two integrals on the right side of (4C), and then interchanging the dummy variables $\mathbf{r}$ and $\mathbf{r}'$, it is seen that the right side of (4C) is symmetric in $\mathbf{n}_0$ and $-\mathbf{n}$. It follows that Eq. (3C) is true, and therefore that Eq. (19) is proved.

APPENDIX D

From Eqs. (14), (17), and (37):

$$\begin{aligned}\delta A_1&=\frac{-k^2}{4\pi}\int d\mathbf{r}\exp(-ik\mathbf{n}\cdot\mathbf{r})\Big[(1-\alpha\mu^2)\delta p(\mathbf{n}_0)\\&\qquad+\rho_0c_0\Big(1-\frac{1}{\alpha}\Big)\mathbf{n}\cdot\delta\mathbf{v}(\mathbf{n}_0)\Big],\quad(1D)\\\delta A_2&=\frac{-k^2}{4\pi}\int d\mathbf{r}\exp(ik\mathbf{n}_0\cdot\mathbf{r})\Big[(1-\alpha\mu^2)\delta p(-\mathbf{n})\\&\qquad-\rho_0c_0\Big(1-\frac{1}{\alpha}\Big)\mathbf{n}_0\cdot\delta\mathbf{v}(-\mathbf{n})\Big],\quad(2D)\end{aligned}$$

$$\delta A_3=\frac{-1}{4\pi}\int d\mathbf{r}[\beta p(\mathbf{n}_0)\delta p(-\mathbf{n})+\beta p(-\mathbf{n})\delta p(\mathbf{n}_0)$$
$$-\omega\rho_0\gamma\mathbf{v}(\mathbf{n}_0)\cdot\delta\mathbf{v}(-\mathbf{n})-\omega\rho_0\gamma\mathbf{v}(-\mathbf{n})\cdot\delta\mathbf{v}(\mathbf{n}_0)]$$
$$-\frac{i}{4\pi}\int d\mathbf{r}\beta\delta p(\mathbf{n}_0)\ \mathrm{div}\int d\mathbf{r}'G\gamma'\mathbf{v}'(-\mathbf{n})$$
$$-\frac{i}{4\pi}\int d\mathbf{r}d\mathbf{r}'[\beta p(\mathbf{n}_0)\gamma'\ \mathrm{grad}G]\cdot\delta\mathbf{v}'(-\mathbf{n})$$
$$+\frac{i}{4\pi}\int d\mathbf{r}\gamma\delta\mathbf{v}(\mathbf{n}_0)\cdot\mathrm{grad}\int d\mathbf{r}'G\beta'p'(-\mathbf{n})$$
$$+\frac{i}{4\pi}\int d\mathbf{r}d\mathbf{r}'\gamma\beta'[\mathbf{v}(\mathbf{n}_0)\cdot\mathrm{grad}G]\delta p'(-\mathbf{n})$$
$$+\frac{1}{4\pi}\int d\mathbf{r}\gamma\delta\mathbf{v}(\mathbf{n}_0)\cdot\mathrm{curl\ curl}\int d\mathbf{r}'G\gamma'\mathbf{v}'(-\mathbf{n})$$
$$+\frac{1}{4\pi}\int d\mathbf{r}\gamma\mathbf{v}(\mathbf{n}_0)\cdot\mathrm{curl\ curl}\int d\mathbf{r}'G\gamma'\delta\mathbf{v}'(-\mathbf{n})$$
$$+\frac{1}{4\pi}\int d\mathbf{r}d\mathbf{r}'[\delta p(\mathbf{n}_0)\beta G\beta'p'(-\mathbf{n})$$
$$+p(\mathbf{n}_0)\beta G\beta'\delta p'(-\mathbf{n})$$
$$-k^2\gamma G\gamma'\mathbf{v}'(-\mathbf{n})\cdot\delta\mathbf{v}(\mathbf{n}_0)$$
$$-k^2\gamma G\gamma'\mathbf{v}(\mathbf{n}_0)\cdot\delta\mathbf{v}'(-\mathbf{n})]. \quad (3D)$$

By substituting Eqs. (1D)–(3D) in Eq. (36) and collecting terms, it is found that the terms in $\delta p(\mathbf{n}_0)$ vanish by virtue of Eq. (16). The terms in $\delta\mathbf{v}(\mathbf{n}_0)$ vanish by virtue of the equation for $\mathbf{v}(-\mathbf{n})$. The terms in $\delta p'(-\mathbf{n})$ vanish because of the first of Eq. (11), after interchanging the dummy variables $\mathbf{r}$ and $\mathbf{r}'$ in the double integrals of Eq. (3D). We similarly interchange $\mathbf{r}$ and $\mathbf{r}'$ in the terms in $\delta\mathbf{v}'(-\mathbf{n})$, with the exception of the curl curl term where this interchange is of no utility. However, by following the procedure used to demonstrate Eq. (3C), it is seen that

$$\int d\mathbf{r}\gamma\mathbf{v}(\mathbf{n}_0)\cdot\mathrm{curl\ curl}\int d\mathbf{r}'G\gamma'\delta\mathbf{v}'(-\mathbf{n})$$
$$=\int d\mathbf{r}\gamma\delta\mathbf{v}(-\mathbf{n})\cdot\mathrm{curl\ curl}\int d\mathbf{r}'G\gamma'\mathbf{v}'(\mathbf{n}_0). \quad (4D)$$

Moreover the proof of Eq. (4D) does not necessitate using the boundary conditions. With the aid of Eq. (4D) the terms in $\delta\mathbf{v}'(-\mathbf{n})$ are thereby all converted to integrals over $\delta\mathbf{v}(-\mathbf{n})$, and at once are observed to vanish because of the second of Eq. (11). This completes the desired proof.

APPENDIX E

The simplest way to derive Eq. (55) is to assume first that ρ and c are continuous. Introduce $u_l=rR_l$ into Eq. (54), which yields

$$\frac{d^2u_l}{dr^2}-\frac{l(l+1)}{r^2}u_l+k^2u_l=k^2(1-\mu^2)u_l+\frac{1}{\rho}\dot{\rho}\left(\dot{u}_l-\frac{u_l}{r}\right). \quad (1E)$$

The function $G_l(r,r')$ of Eq. (56) is the outgoing Green's function satisfying

$$\frac{d^2G_l}{dr^2}-\frac{l(l+1)}{r^2}G_l+k^2G_l=-\delta(r-r'), \quad (2E)$$

where $\delta(r-r')$ is a one-dimensional δ function over the interval $0\leq r<\infty$. It may then be directly verified that

$$u_l=u_{l0}-\int_0^\infty dr'G_l(r,r')\times\left[k^2(1-\mu'^2)u_l'+\frac{1}{\rho'}\left(\dot{u}_l'-\frac{u_l'}{r'}\right)\dot{\rho}'\right], \quad (3E)$$
$$u_{l0}=i^l(2l+1)rj_l(kr),$$

satisfies Eq. (1E) and consequently that

$$R_l=i^l(2l+1)j_l(kr)-\frac{1}{r}\int_0^\infty dr'r'G_l(r,r')\left[k^2(1-\mu'^2)R_l'+\frac{\dot{R}_l'}{\rho'}\dot{\rho}'\right], \quad (4E)$$

satisfies Eq. (54). Now use the identity,

$$r'G_l\dot{\rho}'\frac{\dot{R}_l'}{\rho'}=\frac{d}{dr'}\left[r'G_l(\rho'-\rho_0)\frac{\dot{R}_l'}{\rho'}\right]-(\rho'-\rho_0)\frac{\dot{R}_l'}{\rho'}\frac{d}{dr'}(r'G_l)-r'G_l(\rho'-\rho_0)\frac{d}{dr'}\left(\frac{\dot{R}_l'}{\rho'}\right), \quad (5E)$$

and substitute in Eq. (4E). The total derivative term contributes nothing since $r'G_l$ vanishes at the origin while $\rho'-\rho_0$ vanishes at infinity. Thus there results

$$R_l=i^l(2l+1)j_l(kr)-\frac{1}{r}\int_0^\infty dr'r'G_l(r,r')\times\left[k^2(1-\mu'^2)R_l'-(\rho'-\rho_0)\frac{d}{dr'}\frac{\dot{R}_l'}{\rho'}\right]+\frac{1}{r}\int_0^\infty dr'(1-\alpha')\dot{R}_l'\frac{d}{dr'}(r'G_l). \quad (6E)$$

Equation (54) implies

$$\frac{d}{dr}\left(\frac{\dot{R}_l}{\rho}\right)=-\frac{2}{r}\frac{\dot{R}_l}{\rho}+\frac{l(l+1)}{r^2}\frac{R_l}{\rho}-\mu^2k^2\frac{R_l}{\rho}. \quad (7E)$$

Substitution of Eq. (7E) into Eq. (6E) then yields Eq. (55). Just as in Appendix A, we now argue that since Eq. (55) does not involve derivatives of ρ' and/or c', it remains valid in the limit in which ρ' and/or c' becomes discontinuous across one or more surfaces. Eq. (55) can also be deduced without assuming ρ' and/or c' continuous, either directly from Eq. (54) or via the integral equation (9A), in either case with rather more labor.

APPENDIX F

We regard S_l and $\hat{S}_l$ as independent quantities in Eqs. (65) and (66). Since Eq. (66) was obtained by differentiating Eq. (65), Eq. (67) is evidently true. To demonstrate Eq. (68), differentiate Eq. (66) to get $d\hat{S}_l/dr$ and, combining this with Eqs. (65) and (66), evaluate the left side of Eq. (68). By using the differential equation[4] for $j_l(kr)$, the results obtained are

$$\frac{d\hat{S}_l}{dr}+\frac{2}{r}\hat{S}_l-\frac{l(l+1)}{r^2}S_l+k^2S_l=\frac{1}{r}\left[\frac{d^2}{dr^2}-\frac{l(l+1)}{r^2}+k^2\right]\times\left[\int_0^\infty dr'\bar{G}_l(r'\sigma'S_l'-\tau'\hat{S}_l')+\int_0^\infty dr'r'\tau'\hat{S}_l'\frac{d\bar{G}_l}{dr'}\right]. \quad (1F)$$

We integrate by parts the second integral in Eq. (1F). Thereby we convert the right side of Eq. (1F) to integrals to which Eq. (2E) can be applied under the integral sign, plus a sum over $r'=r_d$ which vanishes after application of Eq. (2E), since the delta function vanishes for the only points in which we are now interested, namely points r not equal to any r_d. Thus we find

$$\frac{d\hat{S}_l}{dr}+\frac{2}{r}\hat{S}_l-\frac{l(l+1)}{r^2}S_l+k^2S_l=-\sigma S_l+\frac{\tau\hat{S}_l}{r}+\frac{1}{r}\frac{d}{dr}(r\tau\hat{S}_l), \quad (2F)$$

which, after some manipulation, reduces to Eq. (68).

In Eq. (65) the first integrand is bounded. The second integral when integrated by parts yields an integral excluding infinitesimal intervals surrounding the points $r'=r_d'$, and therefore one for which the integrand is again bounded. The integration by parts also yields a well-behaved sum over $r'=r_d'$, and we infer that $S_l(r)$ is continuous. We similarly integrate by parts the integrals involving $d\bar{G}_l/dr$ in Eq. (66), perform the d/dr operation indicated in the last integral of Eq. (66), and observe that discontinuities in $\hat{S}_l$ can arise only from the terms in $d\bar{G}_l/dr$ in the sum over r'. In this way we find that

$$\hat{S}_{le}(r_d)-\hat{S}_{li}(r_d)=\frac{1}{r_d}\left[\frac{d}{dr}G_l(r_d+\epsilon,r_d)-\frac{d}{dr}G_l(r_d-\epsilon,r_d)\right]\{[r'\tau_i'\hat{S}_{li}'-r'\tau_e'\hat{S}_{le}']\}_{r'=r_d}. \quad (3F)$$

Since from Eq. (2E)

$$\frac{dG_l(r_d+\epsilon,r_d)}{dr}-\frac{dG_l(r_d-\epsilon,r_d)}{dr}=-1, \quad (4F)$$

we get $\alpha_e\hat{S}_{le}=\alpha_i\hat{S}_{li}$, which is the desired boundary condition.

APPENDIX G

The proof that B_l', Eq. (71), is stationary is straightforward. Appendix D is a guide. The coefficients of δS_l^T and $\delta\hat{S}_l^T$ are readily seen to vanish by virtue of Eqs. (65) and (66). Similarly the coefficient of $\delta S_l'$ vanishes. There is a complication in the coefficient of $\delta\hat{S}_l$. It is seen that this coefficient will not vanish by Eq. (66) unless it is true that

$$\int_0^\infty dr r\tau\hat{S}_l^T\frac{d}{dr}\int_0^\infty dr'r'\tau'\frac{d\bar{G}_l(r,r')}{dr'}\delta\hat{S}_l'=\int_0^\infty dr'r'\tau'\delta\hat{S}_l'\frac{d}{dr'}\int_0^\infty dr r\tau\hat{S}_l^T\frac{d\bar{G}_l(r,r')}{dr}. \quad (1G)$$

Equation (1G) can be proved however. The left side of Eq. (1G) is

$$\begin{aligned}&-k\int_0^\infty dr r\tau\hat{S}_l^T\frac{d}{dr}\left\{\int_0^r dr'r'\tau'\delta\hat{S}_l'rn_l(kr)\frac{d}{dr'}r'j_l(kr')+\int_r^\infty dr'r'\tau'\delta\hat{S}_l'rj_l(kr)\frac{d}{dr'}r'n_l(kr')\right\}\\&=-k\int_0^\infty dr r\tau\hat{S}_l^T r\tau\delta\hat{S}_l'\left[rn_l(kr)\frac{d}{dr}rj_l(kr)-rj_l(kr)\frac{d}{dr}rn_l(kr)\right]\\&-k\int_0^\infty dr r\tau\hat{S}_l^T\left\{\int_0^r dr'r'\tau'\delta\hat{S}_l'\frac{d}{dr}rn_l(kr)\frac{d}{dr'}r'j_l(kr')+\int_r^\infty dr'r'\tau'\delta\hat{S}_l'\frac{d}{dr}rj_l(kr)\frac{d}{dr'}r'n_l(kr')\right\}.\end{aligned} \quad (2G)$$

We evaluate the right side of Eq. (1G) as we did the left side and observe the expression so obtained is identical with the result of interchanging the order of integration in the double integrals on the right side of Eq. (2G). Hence Eq. (1G) is true.

Film Flow in Liquid Helium II at Low Level Differences*

GERALD S. PICUS†‡
Institute for the Study of Metals, University of Chicago, Chicago, Illinois
(Received March 15, 1954)

Observations of the flow of the liquid helium II film have been made at very low level differences. To produce the flow a plunger is displaced vertically at an accurately controlled rate inside of a beaker of internal diameter of about one centimeter. By this means the initial behavior when flow is started, the eventual steady-state behavior, and the oscillations around the final equilibrium position after the plunger is stopped, are observed. The results obtained fit the form of equations derived by Atkins if, in addition, the existence of an upper limit to the velocity of flow is postulated. However, the period of the final oscillations is always found to be shorter than that deduced from the initial effects. The final periods also vary more slowly with temperature and more rapidly with the total length of the helium film than do the initial periods. Assuming the film thickness d varies with height h according to a relation $d=D/h^n$, we find from the initial periods that $n\cong\frac{1}{3}$ and from the final oscillations $n\cong1$. D, the thickness at a height of one centimeter, is approximately 2.5×10^{-6} cm, somewhat smaller values being obtained from the initial periods than from the final periods.

These results are taken as evidence for the existence of a difference between the moving and the stationary film. Various mechanisms for producing the necessary redistribution of the material of the film, if this difference is simply a change in shape, are discussed.

I. INTRODUCTION

AMONG the most striking of the anomalous properties of liquid helium below the lambda temperature are those associated with its unusual transport properties. The best example of the latter is the flow which takes place between a beaker and the surrounding bath if the liquid levels are at different heights. In isothermal conditions, the direction of flow is always toward the region of lower gravitational potential. The first quantitative investigations of the properties of this mass transport were carried out by Daunt and Mendelssohn,[1] who established the existence of a limiting transfer rate, independent of the level difference and varying only with temperature. Their results have been confirmed by many later experimenters,[2–5] some of whom[2,3] have also noted that the critical transfer rate decreases slightly for level differences between 2 and 3 mm.

To date the only experiments at level differences less than 2 mm are the oscillation studies of Atkins.[6] When the beaker level approaches its equilibrium position, the momentum in the film results in an overshoot which produces an oscillation of the beaker level about its equilibrium position. The period of these oscillations depends on the inertia of the film, and this in turn varies with the height of the beaker rim above the bath level. From a study of these oscillations, Atkins deduced a relation for the film thickness as a function of height. The oscillation amplitude, which depends somewhat on the geometry of the apparatus, is only several tenths of a millimeter.

It appeared, therefore, that information on the behavior, and possibly the structure, of the film might be obtained from a study of its flow properties at low level differences, both in the steady state and in the oscillations. To achieve the former condition, the customary capillary beaker was replaced by one with an internal diameter of about one centimeter, inside of which was suspended a plunger, leaving an annular space one millimeter wide. Flow was initiated by moving the plunger up or down.

II. THE APPARATUS

The experiments were performed in a separate chamber suspended in the helium bath. This inner chamber, shown in detail in Fig. 1, is made from a 2-inch copper-glass seal F, soldered at K with Rose's metal to a brass cap D, and sealed at the bottom. Hanging from the rods N is a thin-walled brass cup M which supports the beaker L. This beaker is a $4\frac{3}{4}$-in. length of precision bore tubing of i.d. 0.960 ± 0.003 cm, the bottom of which has been very carefully sealed so that its dimensions were distorted for no more than a half-inch of its length. The top of the beaker was ground to a smooth finish on a carborundum wheel. Before assembly into the apparatus, the beaker was cleaned in hot chromic acid, rinsed with distilled water, and carefully dried.

Suspended in the beaker is the Lucite plunger I which was lapped to a diameter of 0.7625 ± 0.0003 cm along its entire length. It is kept centered in the beaker

* This paper is based on a thesis submitted to the Physics Department of the University of Chicago in partial fulfillment of the requirements for the degree of Doctor of Philosophy.

† This work was performed while the author held a U. S. Atomic Energy Commission predoctoral fellowship.

‡ Present address: Naval Research Laboratory, Washington, D. C.

[1] J. G. Daunt and K. Mendelssohn, Proc. Roy. Soc. (London) **A170**, 423, 439 (1939).

[2] K. Mendelssohn and G. K. White, Proc. Phys. Soc. (London) **A63**, 1328 (1950).

[3] K. R. Atkins, Proc. Roy. Soc. (London) **A203**, 240 (1950).

[4] J. G. Dash and H. A. Boorse, Proceedings of the National Bureau of Standards Symposium on Low Temperature Physics, 1951, National Bureau of Standards Circular 519 (U. S. Government Printing Office, Washington, D. C., 1952), p. 169.

[5] B. Smith and H. A. Boorse, Phys. Rev. **92**, 505 (1953).

[6] K. R. Atkins, Proc. Roy. Soc. (London) **A203**, 119 (1950).

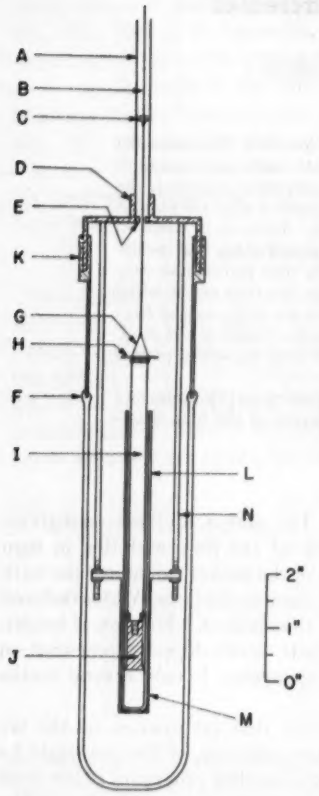

FIG. 1. The inner chamber, showing details of the beaker and plunger.

by the small projections on the brass extension J. This brass piece also serves to give the plunger sufficient weight to keep taut the linen string B from which it hangs. The plunger does not hand directly from the string, but from a loop G of No. 40 Be-Cu wire to which the string is tied. The string passes to the upper part of the cryostat through the $\frac{1}{4}$-inch Monel tube A from which the entire inner chamber hangs.

The inset E and baffle C shield the plunger and beaker from room temperature radiation coming down the Monel tube. The beaker is further protected from vertical radiation by a polished copper disk H mounted on top of the plunger.

At the top of the cryostat the string from which the plunger hangs is attached to a stainless steel shaft which passes vertically through a vacuum seal and then connects with a micrometer screw. The latter is driven vertically by a dc motor through a speed reducer and worm gear. A magnetic amplifier circuit powers the motor and enables control of its speed to within ± 0.5 percent, in the range from 350 rpm to 1550 rpm.

Special care was taken to isolate the cryostat from any sources of vibration to protect the helium levels from mechanical disturbances during an experiment.

The liquid levels were illuminated by a mercury vapor lamp filtered so that only the green 5641A line was passed with its intensity reduced to the lowest level compatible with comfortable observation. A pair of condenser lenses, with their optic axis directed slightly upward so as to make an angle of about three degrees with the horizontal, concentrated the light at the center of the cryostat in such a way that the helium level in the beaker appeared as a bright, sharp line.

The liquid levels were viewed with a telescope mounted on a Gaertner vertical traveling microscope stage. A timer was mounted directly above the microscope drum so that both instruments could be photographed simultaneously by a 35-mm movie camera operated as an automatically advancing single exposure device. The camera was tripped by a solenoid actuated through a relay-operated control circuit by a hand-held microswitch. By means of this circuit, the timer and the motor operating the plunger were not started until the microswitch was tripped to take the first picture. Thereafter the timer ran until the circuit was turned off, but the plunger motor could be stopped or its speed changed at any subsequent operation of the microswitch that the operator chose. Since the camera photographed the timer and microscope drum each time the switch was closed, the times of coincidence of the crosshairs and the helium levels were accurately recorded along with the times of any changes in conditions.

III. PROCEDURE AND ERRORS

A. Procedure During a Run

For at least three days before each helium run, the inner chamber was pumped to a pressure of 3 or 4×10^{-6} mm mercury, thus insuring that the beaker and other parts in the inner chamber were reasonably free of adsorbed gases. The vacuum was maintained until just before liquid helium was transferred into the cryostat, at which time helium gas, specially purified over charcoal at 2000 lb/in.^{2} and at liquid N_2 temperature, was admitted through a charcoal trap at liquid N_2 temperature.

After the transfer was completed, helium was condensed into the inner chamber to the desired level, and the system was closed off completely by means of a stopcock on the vacuum line. The temperature of the helium bath was then adjusted to the desired value and when equilibrium with the inner chamber, as indicated on a differential manometer, had been attained, the actual taking of data was begun.

To measure film transfer rates over large level differences of the order of several millimeters or more, the motor was disengaged from the driving screw and the desired difference in levels was produced by manually raising or lowering the plunger. The subsequent level motion was followed in the telescope and recorded on film.

The data on the behavior of the film transfer at very low level differences were taken with the motor engaged

to drive the plunger. With the telescope lined up on the level in the beaker and the motor control circuits set for the desired speed, the first picture was taken. This recorded the equilibrium position of the level and simultaneously started the timer and the plunger motor. The level was then tracked with the telescope and its position as a function of height was recorded by the camera. When desired, the motor control circuits were switched to the motor off position; thus at the instant of the next photograph, the plunger was stopped, and the process of the level settling back to its equilibrium position was recorded.

B. Flow Rate Measurements

The rate σ, in units of cubic centimeters per second per centimeter perimeter of the beaker, is given by

$$\sigma=\frac{1}{2\pi r_b}(A_b\dot{y}+A_p\dot{x})=\frac{r_b^2-r_p^2}{2r_b}\dot{y}+\frac{r_p^2}{2r_b}\dot{x}, \qquad (1)$$

where r_b is the inner radius of the beaker, A_b is the area of the helium surface in the beaker, A_p is the cross-section area of the plunger, $\dot{y}$ is the velocity of the helium level, and $\dot{x}$ is the velocity of the plunger (see Fig. 2). From the values for r_b and r_p (radius of the plunger) corrected for thermal contraction to liquid helium temperatures, we find $(r_b^2-r_p^2)/2r_b=0.0922\pm0.0019$ cm and $r_p^2/2r_b=0.1474\pm0.0006$ cm. The speed of the driving motor, which determines the plunger velocity $\dot{x}$, could be measured to within 0.5 percent with a General Radio Strobotac that had been calibrated against the ac line frequency. The largest total uncertainty that can result in the term $(r_p^2/2r_b)\dot{x}$ from the combined effects of instability in the motor speed and strobotac calibration and the variations in the radii is ±1.3 percent.

Sighting on the helium levels is a more important source of error. In sighting on the tenth-millimeter divisions of a precision scale, it was found that settings could be reproduced to within 0.002 mm, no matter from which direction they were approached. Since, during a run, extreme care in sighting had to be sacrificed so that readings could be taken more rapidly, it is estimated that helium level positions are accurate to about ±0.005 mm. Consequently, an accuracy of 1 percent can be expected in level velocities measured over level differences of the order of 1 mm. But in the low level difference runs, where flow is observed over intervals less than 0.10 mm, errors as large as ±20 percent can occur.

An experimental check on the validity of these estimates of precision was made by means of runs at a temperature of 2.17°K where the film transfer rate is very small. From Eq. (1) it is evident that the ratio $\dot{y}/\dot{x}$ should equal $r_p^2/(r_b^2-r_p^2)=1.60\pm0.04$ when $\sigma=0$. The observed values of this ratio for five different plunger speeds were 1.58, 1.61, 1.59, 1.60, and 1.61. In addition, these runs indicated that the plunger started moving as soon as the motor was started, and this fact was confirmed by direct observations on the plunger.

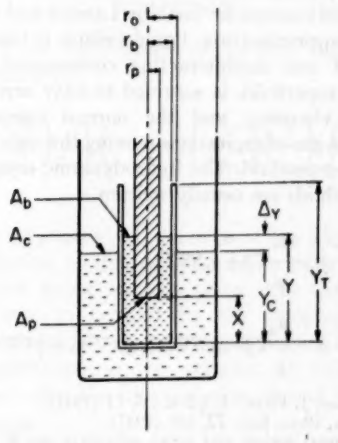

FIG. 2. Schematic representation of the inner chamber.

C. Film Path Length and Temperature

There are two other parameters which are measured: temperature T and film path length H. By the latter is meant the total length of the helium film measured from the level inside the beaker to the level outside. In the low level difference runs, H is equal to twice the height of the rim of the beaker above the liquid levels.

Vapor pressures read on the oil manometer connected to the helium bath were converted to temperatures on the 1948 scale.[7] The estimated errors in the measured temperatures were ±0.03°K at 1.30°K, ±0.01° at 1.50°K, and ±0.004° at 1.70°K and above. Temperature was controlled with an even greater precision, the maximum observed variation during a flow rate measurement having been 0.004°K. In most cases it was only several ten-thousandths of a degree.

D. Effect of the Illuminating Radiation

Increasing or decreasing the level of illumination by a factor of two produced no observable effect on any of the flow rate measurements. Although the range of intensities covered is not large, the results are in agreement with the findings of other investigators,[3,8] that even the complete absence of radiation does not affect film flow.

IV. EXPERIMENTAL RESULTS

A. Gross Flow Rates

Results of determinations of the temperature dependence of the film flow rate for level differences up to six millimeters are shown in Fig. 3. At each tempera-

[7] H. van Dijk and D. Shoenberg, Nature **164**, 151 (1949).
[8] R. Bowers and K. Mendelssohn, Proc. Phys. Soc. (London) **A63**, 1318 (1950).

ture it was found that the beaker emptied at a rate rougly ten percent faster than it filled; and that the rate of emptying was slightly lower when the level difference was less than 2.5 mm. The filling rate was constant over the range of level differences used. The general form of the temperature dependence of the film transfer rate agrees with that found by previous investigators;[1,3,4] and the decrease in flow when the levels are very close has also been reported.[2,3] Atkins[4] also found a ten percent greater emptying rate, but Mendelssohn and White[2] reported that their emptying rate was 5 percent lower than their filling rate. No satisfactory explanation has been given for these differences in rates under different conditions of flow.

B. Film Flow at Low Level Differences

Figure 4 is an example of a run conducted at low level differences. A better understanding of the significant features of such a run can be had from a consideration of the behavior of the level in two limiting cases.

First, consider a liquid in which there is no film transfer. With the plunger moving, the level inside the beaker would rise at a rate given by $\dot{y}=-(A_p/A_b)\dot{x}$ [see Eq. (1) and Fig. 2] which is the maximum possible level velocity, and is represented in Fig. 4 by the dashed line a. In the second case, the film transfer rate is such that the levels inside and outside the beaker are always equal. This represents ideal superfluidity where flow can be maintained at any rate with no difference in level. In this case $\dot{y}=-(A_p/(A_b+A_c))\dot{x}$, and is represented by line b in Fig. 4. (A_c is the area of the liquid surface in the inner chamber.)

The following features of the curve actually obtained are the most significant. When the plunger is first started, the level rises very sharply almost along the line a, until a peak is reached at a time t_p. Sometimes the peak is broad, as shown in Fig. 4, and at other times it is quite well defined, as can be seen in some of the runs in Fig. 5. After the peak, the level falls, and along this downswing the highest rate of film flow out of the beaker is reached. The transfer rate along this portion of the curve never exceeds that found in the measurements made at large level differences.

After the downswing there are two possible ways in which the curve may progress. One is illustrated in Fig. 4 where the level is seen to rise slowly, following the line b, but remaining a small distance above it. The other is shown in the upper runs of Fig. 5, most clearly in No. 7, where the liquid level oscillates about line b as an axis. The oscillations are damped, and the later portion of the plot (not shown in Fig. 5) looks very much like that in Fig. 4.

When the plunger is stopped (indicated by the leveling off of line b in Fig. 4), a damped oscillation of the level is observed. The period of these oscillations and the rate at which they are damped have also been measured.

It is sometimes possible to discern a step-like structure in the rapid downswing that follows the initial peak at t_p. This effect appears only in runs performed at relatively high plunger speeds where the slope of the downswing is small. Since the scale of the steps is also small, no good quantitative data can be obtained. A somewhat broader, but similar effect can be observed in the gentle rise of the level following the downswing.

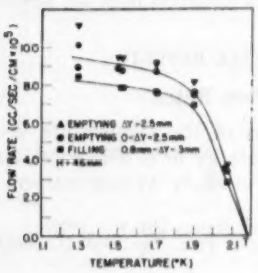

FIG. 3. Film transfer rates for large level differences.

C. Theory

Before trying to interpret the results of the low level difference runs, some discussion of the hydrodynamics

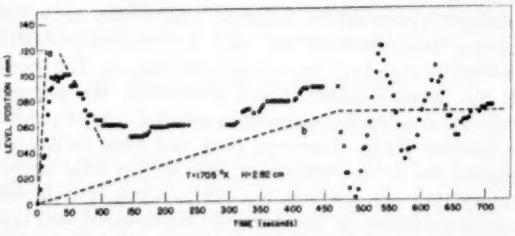

FIG. 4. Results of a typical low level difference run.

of helium II and its application to film flow is necessary. Many authors have given derivations of the hydrodynamic equations of motion of liquid helium, based on the two-fluid concept set forth by Landau and Tisza.[9–11] As a first approximation, liquid helium is treated as a mixture of two noninteracting components. One of these, the superfluid, is assumed to have zero entropy and zero viscosity, and the normal component is treated as a gas of excitations moving through the background of superfluid. The hydrodynamic equations for these two fluids are usually written

$$\rho_s\frac{d\mathbf{v}_s}{dt}=-\frac{\rho_s}{\rho}\nabla p+\rho_s S\nabla T, \tag{2}$$

$$\rho_n\frac{d\mathbf{v}_n}{dt}=-\frac{\rho_n}{\rho}\nabla p-\rho_s S\nabla T+\eta_n(\nabla^2\mathbf{v}_n+\tfrac{1}{3}\nabla\nabla\cdot\mathbf{v}_n). \tag{3}$$

[9] L. Landau, J. Phys. (U.S.S.R.) **5**, 71 (1941).
[10] L. Tisza, Phys. Rev. **72**, 838 (1947).
[11] For general review and other references see R. B. Dingle, Advances in Physics, Phil. Mag. Suppl. **1**, 111 (1952).

ρ_s and ρ_n are the densities of the superfluid and normal fluids, respectively, while $\rho=\rho_s+\rho_n$ is the density of the liquid as a whole. v_s and v_n are the velocities of the two fluids, S is the entropy per unit mass, and p is the pressure. η_n is the viscosity of the normal component.

In the film the viscosity of the normal fluid prevents it from moving so that Eq. (3) may be neglected. Assuming isothermal conditions and irrotational flow, Eq. (2) reduces to

$$\frac{\partial \mathbf{v}_s}{\partial t}+(\mathbf{v}_s\cdot\nabla)\mathbf{v}_s=-\frac{1}{\rho}\nabla p. \tag{4}$$

Atkins[6] used this equation as the starting point to derive expressions describing the oscillations of a liquid helium level about its equilibrium position. His procedure will be applied to find the equations of motion of the beaker level in the present experiments.

Besides those already mentioned, Atkins adds the assumption that the shape of the film is independent of its velocity. The irrotational character of the motion is approximated by assuming that at a given height and time, the velocity of the film is constant throughout its thickness. Dropping the subscript s, let v represent the upward velocity of the superfluid component at some point on the inner wall of the beaker, and let d be the thickness of the film at that point. Then, since σ is negative when the beaker is emptying,

$$\sigma=-(\rho_s/\rho)vd, \tag{5}$$

and so from Eq. (1) and Fig. 2 we have

$$v=-\frac{1}{d}\frac{\rho}{\rho_s}\frac{1}{2\pi r_b}(A_b\dot{y}+A_p\dot{x}). \tag{6}$$

Substituting into Eq. (4) and following Atkins' procedure, we find for the equation of motion of the helium level

$$\ddot{y}+\omega^2 y=\omega^2 bt, \tag{7}$$

where y is the displacement of the level from its equilibrium position,

$$\omega^2=g\left(1+\frac{A_b}{A_c}\right)\Big/\left[\left(1+\frac{r_b}{r_0}\right)\left(\frac{A_b}{2\pi r_b}\right)\left(\frac{\rho}{\rho_s}\right)\int_0^{H/2}\frac{dz}{d}\right], \tag{8}$$

and $b=-\dot{x}A_p/(A_b+A_c)$, the slope of line b in Fig. 4.

The solution of this equation is an undamped harmonic wave about an axis rising with slope b. The simplest way to account for the damping actually observed is to add to the right side of Eq. (4) a retarding term proportional to the velocity. If this term is written as $-2kv$, the equation of motion of the beaker level becomes

$$\ddot{y}+2k\dot{y}+\omega^2 y=\omega^2 bt+2ka, \tag{9}$$

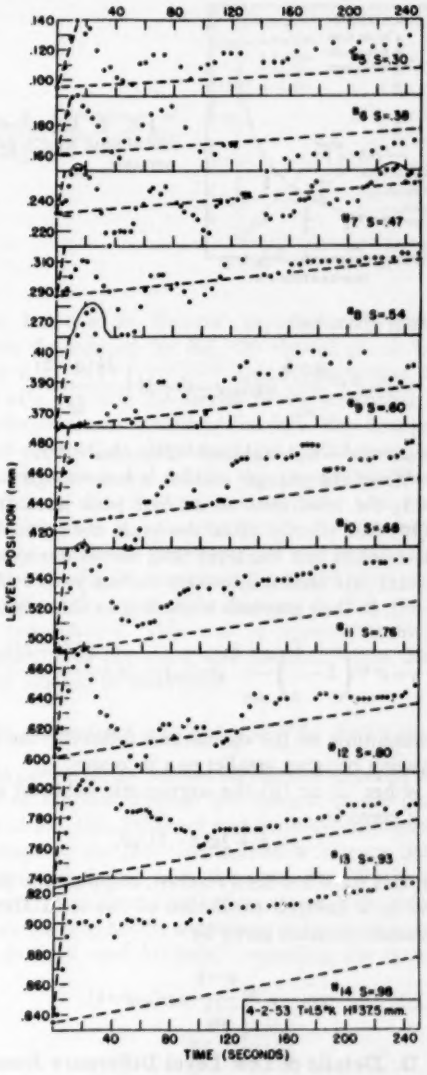

FIG. 5. Example of the variation of low level difference runs with relative plunger speed s.

where $a=-(A_p/A_b)\dot{x}$, the slope of line a in Fig. 4. The existence of a critical flow rate is taken into account by postulating that σ can never exceed σ_c. Since the magnitude of the plunger speed is significant only in terms of the motion it produces, it is represented through the quantity $s=\sigma_b/\sigma_c$. σ_b is the flow rate necessary to maintain a fixed level difference between the beaker and the bath (the slope of line b in Fig. 4).

If at time $t=0$, when the plunger is started downward at some speed $\dot{x}$, the level is stationary in its equilibrium position, its subsequent motion is as follows:

(i) For rates $\dot{x}$ such that the relative plunger speed s is between 0 and $\frac{1}{4}$, the position of the level as a function

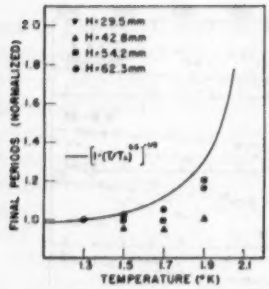

FIG. 6. Dependence of initial peak time t_p on temperature.

of time is given by

$$y=e^{-kt}\frac{a-b}{\omega_0}\sin(\omega_0 t-\delta)+bt+\frac{2k(a-b)}{\omega^2}, \qquad (10)$$

where $\omega_0=(\omega^2-k^2)^{\frac{1}{2}}$ and $\tan\delta=2k\omega_0/(\omega_0^2-k^2)$.

(ii) When the plunger motion is fast enough so that $\frac{1}{2}<s<1$, the level rises to its first peak according to Eq. (10) but shortly after the peak the critical flow rate is reached and the level then moves downward at a constant rate until it intersects the line $y=bt+(2k/\omega^2)\times(a-b)$. It then proceeds according to the relation

$$y=e^{-kt}\left(1-\frac{1}{s}\right)\frac{a-b}{\omega_0}\sin(\omega_0 t)+bt+\frac{2k(a-b)}{\omega^2}. \qquad (11)$$

The amplitude of the oscillations following the linear downswing becomes smaller as s increases.

In either (i) or (ii) the asymptotic behavior of the level is given by

$$y=bt+2k(a-b)/\omega^2. \qquad (12)$$

When this state has been reached, stopping the plunger results in a damped oscillation of the level about its equilibrium position given by

$$y=-e^{-kt}\frac{a-b}{\omega_0}\sin(\omega_0 t-\delta). \qquad (13)$$

D. Details of Low Level Difference Runs

(1) *Variation of Level Behavior with s*

The behavior of the helium level in the beaker as a function of time for various rates of plunger motion is, in general form, the same as that predicted by the theory of the preceding section. An example of the variation of the results with relative plunger speed at a particular temperature and film path length is shown in Fig. 5. Within the estimated error, the values of the flow rate calculated from the slope of the downswing following the initial peak increase with relative plunger speed s until the latter reaches a value of ~ 0.6. For larger s the flow is constant at the rate found in runs at large level differences. The difference from the expected value, $s=0.5$, is thought to be due to the fact that the linear portion of the downswing is very short for s only slightly greater than one-half, so that the slope cannot be accurately measured.

Only the initial features of the various plots of level position against time are illustrated in Fig. 5. In most of the runs the plunger was not stopped until at least 600 seconds had passed, and in some cases the slow upward trend of the level was observed for as long as 1400 seconds. In the total of more than seventy runs of this type which were made, there are only three in which the observed level difference falls below the line b. In the rest y_p, the average level difference between the observed points and b is positive and usually of the order of 0.002 mm to 0.020 mm. It has already been noted that in this region the level progresses upward in broad irregular steps and so the instantaneous value of y_p varies over even wider limits. Because of these effects, it is impossible to make an accurate comparison of this level difference with the value to be expected from the last term in Eq. (10). The order of magnitude of this term can be quickly estimated from data obtained from the final oscillations. For example, for $T=1.50$°K and $H=43$ mm, $k=0.009$ sec^{-1} and $\omega=0.107$ sec^{-1}. For $s=0.80$ at this temperature and path length, the plunger speed is such that $a-b$ is about 95×10^{-4} cm/sec. The calculated value of y_p is then 0.015 mm, which is of the same order of magnitude as the observed values.

TABLE I. Comparison of measured and computed values of the differences between initial peak times and final periods. $t_p-t_f/4$ is the measured value and $k/\omega_0^2+0.034/\omega_0$ is the value calculated from the data for the final oscillations only.

H (mm) \ T		1.30°K		1.50°K		1.70°K		1.90°K	
62.3	$t_p-t_f/4$	···	6.3	···	8.3	···	7.7	···	9.3
	$k/\omega_0^2+0.034/\omega_0$	0.80	0.84	1.01	1.32	1.82	2.01	···	5.2
54.2	$t_p-t_f/4$	···	5.6	···	4.2	···	5.5	···	8.8
	$k/\omega_0^2+0.034/\omega_0$	0.66	0.71	···	1.21	1.36	1.44	···	3.03
42.9	$t_p-t_f/4$	···	3.2	···	6.2	···	6.9	···	12.7
	$k/\omega_0^2+0.034/\omega_0$	···	0.68	0.74	1.09	···	1.50	···	···
29.5	$t_p-t_f/4$	···	4.9	···	6.2	···	5.6	···	9.6
	$k/\omega_0^2+0.034/\omega_0$	0.52	0.77	0.67	0.44	0.57	0.51	···	···

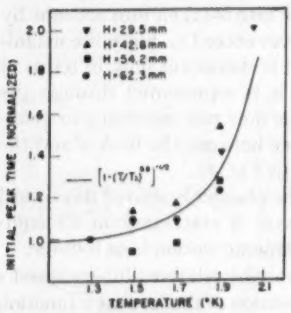

FIG. 7. Dependence of final periods t_f on temperature.

(2) *The Initial Peak and Final Oscillations*

Measurements on the group of experiments from which the results of the preceding section are taken, indicated that the periods of the final oscillations and the initial peak times were not related as the theory predicted. t_p may be calculated from the equation $\dot{y}=0$, which from Eq. (10) is seen to be

$$\cos(\omega_0 t_p-\gamma)=-(\omega_0/\omega)[b/(a-b)]\exp(kt_p), \quad (14)$$

where $\tan\gamma=k/\omega_0$ and the period of the final oscillations is involved through $\omega_0=2\pi/t_f$. From the geometry of the apparatus we have $b/(a-b)=A_b/A_c=0.017$, so that the right side of Eq. (14) is small. For A_c infinite, this term would be zero, and the initial peak time would be $t_p=(\frac{1}{2}\pi+\gamma)/\omega_0$. If we assume that the actual peak differs from this value by only a small interval, τ, Eq. (14) becomes

$$\sin\omega_0\tau=(\omega_0 A_b/\omega A_c)\exp(kt_p). \quad (15)$$

The largest value of k/ω_0 observed was 0.27; in most runs values of the order of 0.10 and less were found. Therefore $\omega_0\cong\omega$, and $\exp(kt_p)$ lies somewhere between 1 and 2. Under these conditions, the right side of Eq. (15) will never be larger than $2A_b/A_c=0.034$. Approximating the sine with its argument, we get $\omega_0\tau<0.034$. In terms of the quantities actually measured from the final oscillations—namely the period $t_f=2\pi/\omega_0$, and the damping coefficient, k—the results of this paragraph may be summarized in the inequality

$$t_p-t_f/4<k/\omega_0^2+0.034/\omega_0. \quad (16)$$

Because the results of the first group of experiments indicated that this relation was not obeyed, a second set was undertaken to check this point specifically. At each temperature and film path length, at least five independent determinations of the initial peak time were made and the final oscillations were observed at the end of two of these runs. The results are presented in Table I. The striking feature of the data presented in this table is that, far from obeying Eq. (16), $t_p-t_f/4$ is actually larger than $(k/\omega_0^2)+0.034/\omega_0$—in a majority of cases by an order of magnitude.

(3) *Temperature Dependence of t_p and t_f*

The dependence of the initial peak times and the final period on temperature are shown in Figs. 6 and 7. The results obtained at various film path lengths are comprised in one graph by using normalized times defined as $t_p(T)/t_p(1.30°\text{K})$ and $t_f(T)/t_f(1.30°\text{K})$.

It is evident from Fig. 6 that t_p rises with temperature much more rapidly than does t_f, and, in fact, follows the scaled reference line corresponding to $[1-(T/T_\lambda)^{5.5}]^{-\frac{1}{2}}$ reasonably well. In Eq. (8) there are two factors to which we may look for the source of the temperature variation of t_p and t_f: namely, ρ/ρ_s and $\int_0^{H/2}dz/d$. If it is assumed that the film thickness d is independent of temperature—there is experimental evi-

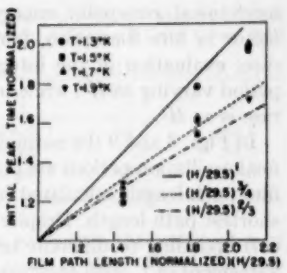

FIG. 8. Dependence of initial peak time t_p on film path length.

dence for this in Bowers' experiments[12]—then the periods determined by Eq. (8) should go as $(\rho/\rho_s)^{\frac{1}{2}}$, which is $[1-(T/T_\lambda)^{5.5}]^{-\frac{1}{4}}$.[13] This suggests that at the start of a run it is the inertia of the superfluid which must be overcome to initiate film flow. The final periods should presumably show the same variation with temperature, unless we admit the possibility that the geometry of the film becomes slightly temperature-dependent when it is moving. Atkins,[6] whose measurements of oscillation frequencies lie within the range of the points in Fig. 6, combined his results with the data for ρ/ρ_s and found a slight increase in film thickness with temperature. This was in agreement with the experiments of Henshaw and Jackson,[14] who used an optical method to measure d.

(4) *Dependence of t_p and t_f on Film Path Length*

The period of the helium oscillations depends on the shape of the film through the integral in the denominator of Eq. (8). Frenkel[15] and Schiff[16] considered that the shape of the film results from a balance between gravitational forces and the van der Waals forces between the walls and the helium atoms. Film thickness then varies with height according to the relation $d\propto h^{-\frac{1}{3}}$. Bijl, de Boer, and Michels,[17] regarding the quantum-

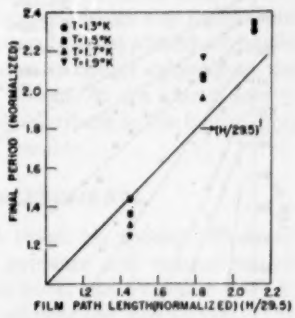

FIG. 9. Dependence of final periods t_f on film path length.

[12] R. Bowers, Phil. Mag. **44**, 1309 (1953).
[13] E. L. Andronikashvili, J. Phys. (U.S.S.R.) **10**, 201 (1946).
[14] D. G. Henshaw and L. S. Jackson, Proceedings of the National Bureau of Standards Symposium on Low Temperature Physics, 1951, National Bureau of Standards Circular 519 (U. S. Government Printing Office, Washington, D. C., 1952), p. 183.
[15] J. Frenkel, J. Phys. (U.S.S.R.) **2**, 365 (1940).
[16] L. I. Schiff, Phys. Rev. **59**, 838 (1941).
[17] Bijl, de Boer, and Michels, Physica **8**, 655 (1941).

mechanical zero-point energy as the most important factor in film formation, found $d \propto h^{-\frac{1}{3}}$. In the former case, evaluation of the integral in Eq. (8) leads to a period varying as $H^{\frac{1}{2}}$, while in the latter case the variation is as $H^{\frac{1}{3}}$.

In Figs. 8 and 9 the normalized initial peak times and final oscillation periods are plotted against a normalized film path length calculated by dividing H by 29.5, the shortest path length. Despite the wide spread in values corresponding to different temperatures, there is some agreement of t_p with the curve of $(H/29.5)^{\frac{1}{2}}$, whereas t_f lies above the straight line $H/29.5$. Such linear dependence of period on film path length would result from Eq. (8) if film thickness were inversely proportional to height. Probably neither t_p nor t_f obey the simple laws given here because the points at $H=42.8$ mm are in both cases slightly below the indicated curves, while the points for larger film path lengths are somewhat higher.

(5) *The Retardation Coefficient*

The retardation coefficient k was evaluated by plotting the logarithm of the amplitudes of the maxima and minima of the final oscillations against the number of elapsed periods. k is the slope of the line obtained multiplied by the period. The data for the 62.3-mm film path length are shown in Fig. 10. The various plots have been displaced vertically to prevent overlap.

The fact that the decay is exponential does not necessarily mean that the source of the damping lies in the velocity-dependent retardation term introduced into Eq. (9). Robinson,[18] in a detailed analysis of helium superfluid oscillations in narrow channels, has shown that if there is imperfect heat exchange between the bath and beaker, so that conditions are not completely isothermal, an exponential decay will occur. In this situation, the behavior of the level will still be described by an expression similar to Eq. (13), but the finite level difference necessary to maintain a steady subcritical flow—expressed by the last term in that equation—will depend on the lack of complete heat exchange and on the fountain effect. An upper limit to the magnitude of this level difference can be estimated by considering the case where the only means for heat transfer between the inside and outside of the beaker is through the vapor phase. It ranges from 0.009 mm at 1.30°K to 0.126 mm at 1.90°K, corresponding to temperature differences of 10^{-6} °K. For subcritical transfer rates such as are obtained when the relative plunger speed is less than one, these level differences will be proportionately smaller. Since even at the highest temperatures, level differences of this magnitude were not observed, it is concluded that there was good thermal contact through the walls of the glass beaker and its brass supporting cup. However, the fact that a temperature difference of 10^{-7} °K between the contents of the beaker and the bath could produce the observed exponential decay of the oscillations, makes it impossible to draw any definite conclusions concerning the existence of velocity-dependent retardation terms.

Robinson's analysis indicates that not only does imperfect thermal contact between the bath and beaker introduce damping, but that it also affects the frequency of the oscillations. For the largest value of k/ω_0 observed, the period would be increased by only 2 percent, and for most of the experiments the effect is less than 1 percent and has been neglected.

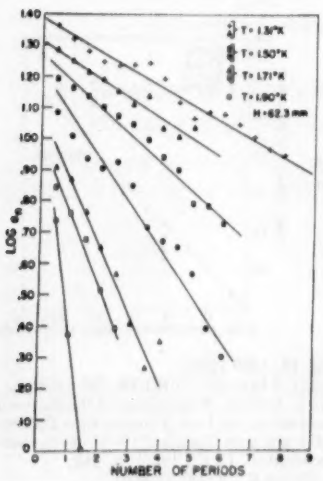

FIG. 10. Decay of the amplitude of final oscillations with time. The lines have been displaced vertically to prevent overlap.

V. DISCUSSION

The experiments in Sec. IV enabled us to study the motion of the helium film under two different sets of conditions. At the beginning of a run, the film is at rest and in *static* equilibrium with its surroundings. After the oscillations set up by the initiation of the flow have been damped, the level settles into an essentially steady state of motion, indicating that the flowing film has attained *dynamic* equilibrium with its surroundings. The essential result of our experiment is that the behavior of the film is different in the two sets of conditions. While it is true that the equations derived on the basis of the simple theory here presented describe both situations adequately, the most important parameter—the oscillation frequency—and its dependence on temperature and film path length differ for the two cases. The simplest hypothesis which will account for these differences between the first peak and the final oscillations, is that the static film differs from the moving film. At the beginning of a run the necessary changes in the film must take place in addition to the acceleration of the superfluid. From Eq. (8) there are two possible changes that can occur to produce the observed result.

(1) The superfluid content of the moving film might

[18] J. E. Robinson, Phys. Rev. 82, 440 (1951).

increase. If we assume that at a given temperature ρ/ρ_s in the static film is the same as for the bulk liquid, then below 1.80°K (where $\rho/\rho_s=0.70$) the observed change could not be produced even if the moving film became completely superfluid. At higher temperatures, such an increase would imply the existence of an unreasonably large temperature difference between the film and bulk liquid, because of the unique relation between ρ/ρ_s and the temperature.

(2) The film might alter its shape. The exact nature of this change in terms of the assumption that the film shape is represented by $d=D/h^n$ has been discussed in a preceding paragraph. The time necessary for such a change must be of the order of magnitude of the oscillation periods observed, or longer, and would be the interval necessary to redistribute the normal component of the film into the shape corresponding to dynamic equilibrium. This can be accomplished in several ways: flow of the normal fluid; exchange of material with the gas phase through evaporation and condensation; or flow of the superfluid with consequent transitions into or from the normal state to establish the right ratio of ρ/ρ_s.

The drift velocity of the normal fluid in the film is limited by its viscosity to only 10^{-6} that of the superfluid as deduced from the flow rate σ. From this it can be estimated that at least 10^3 seconds would be required to change the film thickness by 1 percent by flow of normal fluid over a distance of 1 cm. Because of the low heat capacities of the film and the substrate, evaporation will be effective only if there is available some other source of the comparatively large latent heat. A possibility is de-excitation of normal fluid into the superfluid state, but in the range of temperatures used, the heat so liberated per particle is less than one-tenth the latent heat of vaporization. Of course, similar considerations apply to condensation and consequent excitation of the normal fluid. To redistribute the film in this manner would therefore require the transfer of at least ten times as much material as would be necessary to accomplish the same effect by superflow and consequent transitions. In addition, the rate of either process would be ultimately limited by the rate of such transitions—i.e., by the interaction between normal and superfluid. Since the experimental results fit the form predicted by the simple two-fluid hydrodynamics which neglects this interaction, it is assumed to be small.

Such a slow change in the film characteristics might be expected to produce a gradual decrease in the periods t_i of the oscillations following the initial downswing. In the series of runs conducted to compare t_p and $t_f/4$, there were only three in which these oscillations were sufficiently well defined so that their periods could be measured accurately. The reason for this is that the factor $(1-1/s)$ in Eq. (11) limits the amplitude, particularly when large s values are used. In the three cases observed, the values found for $4t_p$, t_i, and t_f are given in Table II. In each case the value of t_i is intermediate between $4t_p$ and t_f, just what our considerations would lead us to expect.

TABLE II. Comparison of periods t_p of the observed initial oscillations with the corresponding initial peak times t_p and final oscillations t_f.

T (°K)	H (mm)	$4t_p$	t_i	t_f
1.30	54.2	106.8	91.7	84.3
1.50	54.2	100.8	95.3	84.1
1.50	62.3	128.8	108.5	95.5

There are several theories of the structure of the static film, but none of the mechanism of film flow. It is interesting to speculate on whether modifications introduced into existing theories of the film might lead us to expect an alteration in its shape when it is flowing. Bijl, de Boer, and Michels[17] attributed the existence of the film to a balance between gravitational forces and those resulting from the zero-point energy of the atoms condensed in their lowest state. The atoms are treated essentially as particles in a box, but it is possible that if a wave function adequate to describe their motion when flow is taking place were available, the corresponding zero-point energy would be altered in such a way as to change the stability conditions. Temperley[19] calculates the energy of the bound states of an atom in the van der Waals field of the wall and of the remaining helium atoms, and balances this against the gravitational energy to determine the shape of the film. He attributes film flow to the fact that not all the bound states that exist in the outer layers of the film are occupied. Atoms may move by transitions between these states. In this theory the possibility of an alteration in film shape arises from the perturbing effects on the bound states of the interaction which produces the transitions. The present state of the theory does not permit a calculation of such an effect. Even the more complete quantum-mechanical treatment of the He II problem by Feynman[20] has not yielded any insight into the nature of the film. Generally, from a thermodynamic point of view, the problem is one of minimizing the total free energy of the system. As the kinetic energy of the moving film would contribute to the free energy, a change in shape seems possible.

ACKNOWLEDGMENTS

The author wishes to thank his sponsor, Professor Lothar Meyer, for his guidance and encouragement during the course of this work, and Professor Earl A. Long for his valuable advice and suggestions. The cooperation of various members of the staff of the Institute for the Study of Metals, and particularly the Low Temperature Laboratory, is also gratefully acknowledged.

[19] H. N. V. Temperley, Proc. Roy. Soc. (London) **A198**, 438 (1949).
[20] R. P. Feynman, Phys. Rev. **91**, 1291, 1301 (1953).

General Relativistic Variational Principle for Perfect Fluids

A. H. TAUB
Digital Computer Laboratory, University of Illinois, Urbana, Illinois
(Received January 4, 1954)

The field equations for the gravitational field of a perfect compressible fluid and the equations of motion of the fluid in its own gravitational field are derived from a single variational principle in which the variations of the various field quantities are restricted so that mass is conserved.

1. INTRODUCTION

IN general relativity, the gravitational field due to matter is determined by the field equations.

$$R_{\mu\nu}-\tfrac{1}{2}g_{\mu\nu}R=-\kappa T_{\mu\nu}, \tag{1.1}$$

where the tensor $T_{\mu\nu}$ describes the stress energy tensor of the matter. If the matter is a perfect fluid (i.e., one with no viscosity or heat conductivity), the stress energy tensor is

$$T^{\mu\nu}=\rho^0\lambda u^\mu u^\nu-pg^{\mu\nu}, \tag{1.2}$$

where u^μ are the components of the four-dimensional velocity vector,

$$\lambda=c^2+\epsilon+p/\rho^0, \tag{1.3}$$

$$g_{\mu\nu}u^\mu u^\nu=1, \tag{1.4}$$

ρ^0 is the rest density of the fluid (i.e., the number of particles per unit volume as measured by an observer moving with the mean velocity of these particles) p the pressure, and ϵ is the specific internal energy of the fluid as measured by an observer at rest with respect to the fluid. The equations of motion of the fluid are

$$T^{\mu\nu}{}_{;\nu}=0, \tag{1.5}$$

where the semicolon denotes covariant differentiation.

Equations (1.5) are a consequence of (1.1). However, if the $g_{\mu\nu}$ are known, Eqs. (1.5) together with the equation of conservation of mass, namely,

$$(\rho^0u^\nu)_{;\nu}=0, \tag{1.6}$$

serve to determine the kinematical variables u^σ and two thermodynamic variables ρ^0 and p (or any function of these two) which describe the motion of the fluid in the gravitational field given by the $g_{\mu\nu}$.

It is the purpose of this paper to give a variational principle which uses a Lagrangean which is a function of the hydrodynamic variables u^σ, ρ^0, and T^0, the rest temperature of the fluid, and the gravitational field variables $g_{\mu\nu}$. We shall consider variations of all of these field quantities such that (1.4) and (1.6) are satisfied, and shall show that Eqs. (1.1) and (1.2) are the Euler equations due to the variation of $g_{\mu\nu}$, and that Eqs. (1.5) with $T^{\mu\nu}$ given by (1.2) are the Euler equations due to the variation of the hydrodynamical field variables, namely ρ^0, T^0, and the world lines of elements of the fluid. Thus, from a single variational principle, we shall obtain both the field equations for the gravitational field created by the fluid and the equations of motion of the fluid in this gravitational field.

2. THE LAGRANGEAN

Consider the integral

$$I=\int[R-2\kappa\rho^0(c^2+H^0+\tfrac{1}{2}\mu g_{\mu\nu}u^\mu u^\nu)]\sqrt{(-g)}d^4x, \tag{2.1}$$

where R is the scalar curvature formed from the metric tensor $g_{\mu\nu}$, κ is the Einstein gravitational constant, μ is a Lagrange multiplier which must be chosen so that Eq. (1.4) is satisfied, and H^0 is the Helmholtz free energy defined as

$$H^0=\epsilon-T^0S^0, \tag{2.2}$$

where S^0 is the entropy as measured by an observer at rest with respect to the fluid. The integration in Eq. (2.1) is over a volume in space-time swept out by the world lines of an arbitrary member of "particles" of the fluid.

When we consider ρ^0 and T^0 as the independent thermodynamic variables, we have

$$\delta H^0=\left(\frac{\partial\epsilon^0}{\partial\rho^0}-T^0\frac{\partial S^0}{\partial\rho^0}\right)\delta\rho^0+\left(\frac{\partial\epsilon}{\partial T^0}-S^0-T^0\frac{\partial S^0}{\partial T^0}\right)\delta T^0.$$

However, from the equation defining entropy, namely

$$T^0dS^0=d\epsilon^0+pd(1/\rho^0), \tag{2.3}$$

it follows that

$$\delta H^0=(p/\rho^{02})\delta\rho^0-S^0\delta T^0. \tag{2.4}$$

The world lines which are to be varied may be written as

$$x^\mu=x^\mu(u,v,w,s), \tag{2.5}$$

where u, v, w are variables labelling a particular world line and s is the proper time along this world line. It follows from (2.5) that

$$u^\mu=\partial x^\mu/\partial s,$$

and hence the variation in the velocity vector δu^μ produced by a variation δx^μ in the world lines is

$$\delta u^\mu=\partial\delta x^\mu/\partial s. \tag{2.6}$$

When we consider Eqs. (2.5) as a transformation in space time from the coordinates x^μ to the coordinates

u, v, w, s, we may evaluate all the quantities in the integrand of (2.1) as functions of the latter variables and write

$$I=\int[R^*-2\kappa\rho^{0*}(c^2+H^{0*}+\tfrac{1}{2}\mu g_{\mu\nu}{}^*u^{\mu*}u^{\nu*})]\times\sqrt{(-g^*)}dudvdwds, \quad (2.7)$$

where the starred quantities in the brackets are obtained from the unstarred ones by use of the scalar transformation law:

$$f^*(u)=f(x(u)),$$

and the tensor transformation laws. Further, we know that R^* is the same function of the $g_{\mu\nu}{}^*$ as R is of the $g_{\mu\nu}$.

In addition, it is a consequence of the transformation laws that

$$[-g^*(u)]^{\frac{1}{2}}=[-g(x)]^{\frac{1}{2}}\epsilon_{\mu\nu\sigma\tau}\frac{\partial x^\mu}{\partial u}\frac{\partial x^\nu}{\partial v}\frac{\partial x^\sigma}{\partial w}\frac{\partial x^\tau}{\partial s}, \quad (2.8)$$

where $\epsilon_{\mu\nu\sigma\tau}$ is the numerical tensor density which vanishes unless all its indices are different. If this is so it has the value plus one if the indices are an even permutation of 1, 2, 3, 4 and minus one, if the indices are an odd permutation of these numbers.

3. THE CONSERVATION OF MASS

Equation (1.6), the equation which states that mass is conserved may be written as

$$\frac{1}{\sqrt{(-g^*)}}\frac{\partial}{\partial x^{\sigma*}}(\sqrt{(-g^*)}\rho^{0*}u^{\sigma*})=0,$$

where $x^{1*}=u$, $x^{2*}=v$, $x^{3*}=w$, $x^{4*}=s$. Multiplying this equation by $\sqrt{(-g^*)}dudvdwds$ and integrating over a region of space-time swept out by world lines of the particles, we obtain

$$\int\frac{\partial}{\partial x^{\sigma*}}(\sqrt{(-g^*)}\rho^{0*}u^{\sigma*})dudvdwds=0.$$

This equation is equivalent to the statement that the three-dimensional integral,

$$\int\rho^0u^\tau[g(x(u))]^{\frac{1}{2}}\epsilon_{\lambda\mu\nu\sigma\tau}\frac{\partial x^\lambda}{\partial u}\frac{\partial x^\mu}{\partial v}\frac{\partial x^\nu}{\partial w}dudvdw,$$

is independent of s. That is, the requirement of conservation of mass for arbitrary amounts of fluid may be written as the condition

$$\rho^{0*}[-g^*(u)]^{\frac{1}{2}}=\rho^0[-g(x)]^{\frac{1}{2}}\epsilon_{\lambda\mu\nu\tau}\frac{\partial x^\lambda}{\partial u}\frac{\partial x^\mu}{\partial v}\frac{\partial x^\nu}{\partial w}\frac{\partial x^\tau}{\partial s}=M(u,v,w), \quad (3.1)$$

where M is not a function of s.

The variation in proper density $\delta\rho^0$ may be determined in terms of the variation in the metric field and the variation in the particle paths by the requirement that mass be conserved. Thus, from the requirement that $\delta M=0$, it follows from (3.1) that

$$\frac{\delta\rho^0}{\rho^0}+\tfrac{1}{2}g^{\mu\nu}\delta g_{\mu\nu}+\frac{1}{\sqrt{(-g)}}\frac{\partial}{\partial x^\sigma}(\sqrt{(-g)}\delta x^\sigma)=0. \quad (3.2)$$

The derivation of (3.2) follows from (3.1), and the fact that the quantity,

$$\epsilon_{\lambda\mu\nu\tau}\frac{\partial x^\lambda}{\partial u}\frac{\partial x^\mu}{\partial v}\frac{\partial x^\nu}{\partial w}\frac{\partial x^\tau}{\partial s},$$

is the Jacobian of the transformation (2.5). Equation (3.2) may also be written in the u, v, w, s coordinate system as

$$\delta\rho^{0*}/\rho^{0*}+\tfrac{1}{2}g^{\mu\nu*}\delta g_{\mu\nu}{}^*+(\delta x^{\sigma*})_{;\sigma}=0, \quad (3.3)$$

where

$$\delta x^{\sigma*}=\delta x^\tau(\partial x^{*\sigma}/\partial x^\tau), \quad (3.4)$$

and

$$\delta g_{\mu\nu}{}^*=\delta g_{\sigma\tau}\frac{\partial x^\sigma}{\partial x^{\mu*}}\frac{\partial x^\tau}{\partial x^{\nu*}}. \quad (3.5)$$

It should be observed that $\delta g_{\mu\nu}{}^*$ is the variation in the metric tensor in the starred coordinate system. There is a variation in $g_{\mu\nu}{}^*$ due to a variation of the particle paths which may be computed from the definition of $g_{\mu\nu}{}^*$, namely

$$g_{\mu\nu}{}^*=g_{\sigma\tau}\frac{\partial x^\sigma}{\partial x^{\mu*}}\frac{\partial x^\tau}{\partial x^{\nu*}},$$

to be

$$\delta_x g_{\mu\nu}{}^*=(\delta x_\mu{}^*)_{;\nu}+(\delta x_\nu{}^*)_{;\mu}, \quad (3.6)$$

where the covariant derivatives are computed in the starred coordinate system and $\delta x_\mu{}^*$ are the covariant components of $\delta x^{\mu*}$.

For the purposes of the next section we shall need to evaluate

$$\begin{aligned}\delta_x(g_{\mu\nu}{}^*u^{\mu*}u^{\nu*})&=\delta_x(g_{\mu\nu}u^\mu u^\nu)\\&=(\partial g_{\mu\nu}/\partial x^\rho)\delta x^\rho u^\mu u^\nu+2g_{\mu\nu}u^\mu(\partial\delta x^\nu/\partial s)\\&=(\partial g_{\mu\nu}/\partial x^\rho)\delta x^\rho u^\mu u^\nu+2g_{\mu\nu}u^\mu u^\rho(\partial\delta x^\nu/\partial x^\rho)\\&=2g_{\mu\nu}u^\mu(\delta x^\nu)_{;\rho}u^\rho\\&=2g_{\mu\nu}{}^*u^{\mu*}(\delta x^{\nu*})_{;\rho}u^{\rho*}.\end{aligned}$$

4. THE EULER EQUATIONS

In order to compute the variation of I subject to the restrictions (1.4) and (1.6), we use the form of I given by Eq. (2.7). From this equation and the fact that

$\delta M=0$, it follows that

$$\delta I=\int\Big\{(-R^{*\mu\nu}+\tfrac{1}{2}g^{\mu\nu*}R)[\delta g_{\mu\nu}{}^{*}+(\delta x_{\mu}{}^{*})_{;\nu}+(\delta x_{\nu}{}^{*})_{;\mu}]$$
$$-2\kappa\rho^{0*}\Big[\Big(\frac{p}{\rho^{0*2}}\delta\rho^{0*}-S^{0*}\delta T^{0*}\Big)+\tfrac{1}{2}\mu u^{\mu*}u^{\nu*}\delta g_{\mu\nu}{}^{*}$$
$$+\mu g_{\mu\nu}{}^{*}u^{\mu*}u^{\nu*}(\delta x^{\nu*})_{;\rho}\Big]\Big\}\sqrt{(-g^{*})}dudvdwds.$$

On using Eq. (3.3) to eliminate $\delta\rho^{0*}$ from this expression, we have

$$-\delta I=\int\{(R^{\mu\nu*}-\tfrac{1}{2}g^{\mu\nu*}R^{*}+\kappa\theta^{\mu\nu*})[\delta g_{\mu\nu}{}^{*}+2(\delta x_{\mu}{}^{*})_{;\nu}]$$
$$-2\kappa\rho^{0*}S^{0*}\delta T^{0*}\}\sqrt{(-g^{*})}dudvdwds, \quad (4.1)$$

where

$$\theta^{\mu\nu*}=\rho^{0*}\mu u^{\mu*}u^{\nu*}-pg^{\mu\nu*}. \quad (4.2)$$

If we now introduce a new variable by the equation

$$\delta T^{0}=(\delta\alpha^{*})_{,\rho}u^{\rho*}=\partial\delta\alpha/\partial s,$$

where the comma denotes the ordinary derivative, Eq. (4.1) may be written after integration by parts as

$$-\delta I=\int[(R^{\mu\nu*}-\tfrac{1}{2}g^{\mu\nu*}R+\kappa\theta^{\mu\nu*})\delta g_{\mu\nu}{}^{*}-\kappa\theta^{\mu\nu*}{}_{;\sigma}\delta x_{\mu}{}^{*}$$
$$+2\kappa(\rho^{0*}S^{0*}u^{\sigma*})_{;\sigma}\delta\alpha^{*}]\sqrt{(-g^{*})}dudvdwds \quad (4.3)$$

for variations which vanish on the three-dimensional hypersurface bounding the region of integration.

The Euler equations for $\delta I=0$ for variations which vanish on the bounding hypersurface are then

$$R^{\mu\nu}-\tfrac{1}{2}g^{\mu\nu}R+\kappa\theta^{\mu\nu}=0, \quad (4.4)$$

$$\theta^{\mu\nu}{}_{;\nu}=0, \quad (4.5)$$

$$(\rho^{0}S^{0}u^{\sigma})_{;\sigma}=0, \quad (4.6)$$

where we have written the unstarred quantities since the equations are tensor equations. The last of these equations may be written as

$$\rho^{0}S^{0}{}_{;\sigma}u^{\sigma}=0, \quad (4.6')$$

in view of Eq. (1.6).

Equation (4.5) may be written as

$$\rho^{0}u^{\nu}(\mu u^{\mu})_{;\nu}=p_{,\nu}g^{\mu\nu}, \quad (4.7)$$

as a consequence of (4.2) and (1.6). The quantity μ entering into this equation must be determined so that (1.4) is satisfied. Multiplying Eq. (4.7) by u_{μ} and summing, we obtain

$$2\rho^{0}\mu d(g_{\mu\nu}u^{\mu}u^{\nu})=dp-\rho^{0}g_{\mu\nu}u^{\mu}u^{\nu}d\mu, \quad (4.8)$$

where $df=f_{,\sigma}u^{\sigma}$.

It follows from Eq. (2.3) that

$$dp/\rho^{0}=d\epsilon^{0}+d(p/\rho^{0})-T^{0}dS^{0}.$$

Hence,

$$2\rho^{0}\mu d(g_{\mu\nu}u^{\mu}u^{\nu})=\rho^{0}[d\epsilon^{0}+d(p/\rho^{0})]-\rho^{0}g_{\mu\nu}u^{\mu}u^{\nu}d\mu,$$

where we have used (4.6'). Hence, (1.4) will be satisfied if

$$d\mu=d\epsilon^{0}+d(p/\rho^{0}).$$

That is,

$$\mu=c^{2}+\epsilon^{0}+p/\rho^{0},$$

where the constant of integration has been chosen to be c^{2} in order that the stress-energy tensor be correctly given when $p=0$. If this is done, then Eqs. (4.4), (4.2), and (4.5) become (1.1), (1.2), and (1.5), respectively. Equation (4.6') is then a consequence of Eqs. (1.2) to (1.6), which may be seen as follows: Eq. (4.7) with μ given by (1.3) follows from Eqs. (1.2), (1.5), and (1.6). Multiplying (4.7) by u_{μ}, summing, and using (1.4), we obtain

$$\rho^{0}d\mu=dp, \quad (4.9)$$

that is,

$$d\epsilon^{0}+d(1/\rho^{0})=0;$$

but in view of Eq. (2.3) this may be written as (4.6).

If Eq. (4.9) is substituted into (4.7), the latter equation may be written as

$$\rho^{0}\mu u^{\nu}u^{\mu}{}_{,\nu}=p_{,\nu}(g^{\mu\nu}-u^{\mu}u^{\nu}). \quad (4.10)$$

Equations (1.6), (4.10), and (4.6) are a set of five linearly independent equations equivalent to the five equations (1.5) and (1.6).

Thus we have shown that the variational principle $\delta I=0$, where the field variables ρ^{0}, T^{0}, $g_{\mu\nu}$ and the particle paths are varied so that (1.6) is always satisfied and the Lagrange multiplier is chosen so that (1.4) is satisfied, has as Euler equations the field equations for the gravitational field created by the fluid and the equations of motion of the fluid. This variational principle is an extension of a nonrelativistic one previously given[1] for compressible fluids alone. In the previous work it was shown that the Rankine-Hugoniot equations could be derived from considerations involving the existence of singular surfaces in the fluid and the variations of these surfaces. A derivation of the relativistic Rankine-Hugoniot equations should follow from the variational principle given above.

[1] A. H. Taub, in *Proceedings of First Symposium of Applied Mathematics* (American Mathematical Society, New York, 1949), pp. 148–57.

An Instance in Thermal Convection of Eddington's "Overstability"*

D. Fultz, Y. Nakagawa, and P. Frenzen
Hydrodynamics Laboratory, Department of Meteorology, University of Chicago, Chicago, Illinois

(Received December 28, 1954)

The existence of modes of cellular convection driven by thermal instability which are oscillatory in type, rather than steady, has been predicted theoretically for systems that are rotating as a whole. Such modes are of a type called "overstable" by Eddington in a different connection. The result of an initial successful experiment with mercury is given.

THE theoretical study of the convective fluid motions due to thermal instability stems from Rayleigh's 1916 attempt[1] to explain the experimental observations of Benard on cellular convection. The standpoint in Rayleigh's and the subsequent studies has uniformly been to investigate the conditions just sufficient for the initiation of motions of a cellular type by means of perturbation techniques relative to a state of rest. All dependent variables in the perturbations are assumed proportional to a factor $e^{\sigma t}$. When σ is real, the conditions are investigated for σ first to become positive. The critical dividing point is taken at marginal stability $\sigma=0$, thus corresponding to a neutral or steady perturbation. The steady cells observed experimentally when the work is done carefully are then expected first at the physical conditions corresponding to the marginal stability point.

While the possibility that σ may be complex had at least been noted by Rayleigh himself[1] and by Jeffreys,[2] none of the published work in this area until recently dealt with problems in which σ could actually be complex in such a way as to give amplified motions. Pellew and Southwell[3] for example, show that in ordinary Benard convection problems, motions corresponding to such complex σ's are always damped. It is apparent that in more general problems of cellular motion the possibility may occur of first attaining a positive real part for σ with a nonzero imaginary part. The corresponding perturbation will be an exponentially amplifying oscillation or, at the point where the real part$=0$, a neutral oscillation. The former type of behavior has been named "overstability" by Eddington[4] who made some controversial applications of the idea to astrophysics. His reasons for the name are best described in his own words: "In the usual kind of *instability* a slight displacement provokes forces tending away from equilibrium; in *overstability* it provokes restoring forces so strong as to overshoot the corresponding position on the other side of equilibrium and set up an increasing oscillation." In the last two years Chandrasekhar[5] and, independently, Frenzen and Nakagawa[6] have shown theoretically that overstability can occur for cellular convection in a *rotating* system and Chandrasekhar has shown that the same is true of certain cases in hydromagnetics. The perturbation system governing rotating cellular convection can be arranged so as to depend on three nondimensional parameters: the Rayleigh number $R=g\alpha\beta d^4/\kappa\nu$, the Taylor number $T=4\Omega^2d^4/\nu^2$, and the Prandtl number $P=\nu/\kappa$, where g is the acceleration of gravity, α the volume coefficient of expansion of the fluid, β the vertical adverse temperature gradient, d the depth of the fluid, ν the kinematic viscosity of the fluid, κ the thermometric conductivity, and Ω the basic rotation rate of the system. The above authors show in one particular case that, provided $P<0.6766$, for all sufficiently large T the criterion for overstability (oscillating cells) is reached before the marginal stability criterion for ordinary cells.

Mercury is a liquid whose Prandtl number is about 0.025 at ordinary temperatures and consequently it is suitable for a search for overstable motions. In addition, convection cells in a rotating system have at the top surface individual rotations about their axes which depend in sign on whether the motion at the center of the cell is up or down. This gives a very simple means of detecting whether oscillating cells are occurring simply by noting whether particles floating on the top free surface show periodic reversals of the axial rotation.

A trial carried out with preliminary equipment on November 20, 1953 showed rather conclusively that overstable (oscillating) cellular motions are obtained at approximately the expected conditions. A glass cylinder of 14½-cm diameter containing 5.0 cm of mercury was rotated at about 10 rpm. Heating was applied uniformly from below by means of a Corning electrically-conducting glass plate. The estimated data for the point where the cells first became visible in the particle motions at the free surface and in the temperature gradient measurements were:

$$P=0.024, \quad T=2.2\times10^9; \quad R=7.6\times10^5,$$

* The research reported herewith has been made possible through support and sponsorship extended by Air Force Cambridge Research Center under a contract.

[1] Lord Rayleigh, Phil. Mag. (6) **32**, 529 (1916).
[2] H. Jeffreys, Phil. Mag. (7) **2**, 833 (1926), see p. 834.
[3] A. Pellew and R. V. Southwell, Proc. Roy. Soc. (London) **A176**, 312 (1940), see p. 322, ff.
[4] A. S. Eddington, *Internal Constitution of the Stars* (Cambridge University Press, London, 1926), p. 201.
[5] S. Chandrasekhar, Proc. Roy. Soc. (London) **A217**, 306 (1952).
[6] P. Frenzen and Y. Nakagawa, Tellus (to be published).

corresponding to a temperature difference over 5 cm of 1.7°C. While the field of motion at the top was somewhat irregular and not strictly cellular, some cells of about 2-cm diameter were always visible in the overstable range and at least two were observed to go through two full cycles of reversal of the axial rotation without moving away or deforming appreciably. The period of oscillation of the cells ranged from 15.1 to 16.2 sec in a set of several determinations. The theoretical data available at present are not strictly applicable because the boundary conditions are slightly different but the above values may roughly be compared with theoretical values for the given P and T of $R=2.1\times10^5$ and oscillation period = 13.9 sec. Systematic experiments along these lines are planned at this laboratory and should be the subject of later reports.

PHYSICAL REVIEW VOLUME 94, NUMBER 6 JUNE 15, 1954

Theory of Elementary Particles in General Relativity

M. M. HATALKAR*
The Institute of Science, Bombay, India
(Received April 9, 1952; revised manuscript received March 10, 1954)

The matrices of elementary particles are generalized to general coordinates, and a new covariant displacement operator is defined, in order to generalize the theory of elementary particles to general relativity, and obtain general commutation rules. The elementary particle is considered as a singularity, with spin-structure of a gravitational field which gives Riemannian structure to the space-time. It is shown that the transformation properties of the space-time are determined not only by the affine structure due to the gravitational field but also by the spin-structure of the particle singularity.

INTRODUCTION

DIRAC'S equation has been generalized by Bhabha[1] to describe elementary particles of any integral or half-integral spin. However, in his theory of elementary particles[2] Bhabha assumes that his theory is valid in the framework of special relativity only.

Since a particle and its gravitational field are inseparable, it is desirable to extend the theory of elementary particles to general relativity by making it covariant for general continuous groups of transformation of Riemannian space-time. Even though, for particles of integral spin, tensor formalism is easier to handle, the spinor form will be retained here in order to keep the underlying unity of the theory for particles of integral and half-integral spins always evident. Pauli[3] has generalized Dirac's equation (for spin $\frac{1}{2}$) to general coordinates; we shall show that Bhabha's equation can be generalized in a similar manner. To do this we have to modify Einstein's idea of considering a particle as a singularity in its gravitational field which gives a Riemannian structure to space-time. The spin structure will be described by the operation of a set of spin matrices β^μ on the spin variables which are components of a wave function ψ. It will be shown that the β^μ satisfy a certain commutation relation (dependent upon the spin of the particle) which we shall for the moment write in the symbolic functional form:[4]

$$\mathbf{G}(\beta^\mu,\beta^\nu,\beta^\sigma,\cdots;g^{\mu\nu},g^{\sigma\tau},\cdots)=0, \tag{1}$$

where $g^{\mu\nu}g_{\nu\sigma}=\delta^\mu{}_\sigma$, $g_{\mu\nu}$ being the metric tensor of Riemannian space-time.

SPIN AFFINE TRANSFORMATIONS

In Eq. (1) we assume that the matrices β^μ are contravariant components of a vector point function whose operation on ψ is determined by $g_{\mu\nu}$ at each point of space-time. The effect of the gravitational field is to make this operation nonintegrable, i.e., dependent upon the path chosen. Hence, under a parallel displacement along a path, the increment in β^μ is

$$\delta\beta^\mu=-\Gamma_{\alpha\nu}{}^\mu\beta^\alpha dx^\nu,$$

where $\Gamma_{\alpha\nu}{}^\mu$ is the affine connection constructed from the gravitational potentials $g_{\mu\nu}$.

Under an infinitesimal affine transformation, the β^μ transform as

$$\beta'^\mu=\beta^\mu+\epsilon^\tau[\beta^\mu{}_{,\tau}+\Gamma_{\alpha\tau}{}^\mu\beta^\alpha]=\beta^\mu+\epsilon^\tau\beta^\mu{}_{;\tau}, \tag{2}$$

where $\beta^\mu{}_{,\tau}=\partial\beta^\mu/\partial x^\tau$, ϵ^τ is an infinitesimal parameter, and $\beta^\mu{}_{;\tau}$ defines the covariant derivative of β^μ.

Under a local infinitesimal spin-space rotation

$$S=1+\epsilon^\tau\Omega_\tau,$$

β^μ transforms as

$$\beta'^\mu=S^{-1}\beta^\mu S=\beta^\mu+\epsilon^\tau[\beta^\mu,\Omega_\tau], \tag{3}$$

* Fellow, The Institute of Science, Bombay, India. Deceased August 29, 1953. This research was completed while the author was doing graduate work at Harvard University.

[1] H. J. Bhabha, Revs. Modern Phys. 17, 200 (1945).
[2] H. J. Bhabha, Revs. Modern Phys. 21, 451 (1949).
[3] W. Pauli, Ann. Physik 18, 337 (1933).

[4] $\mathbf{G}$ is a rational integral function of β^μ and $g^{\mu\nu}$.

where the usual commutator notation is used, as in

$$[\beta^\mu,\Omega_\tau]=\beta^\nu\Omega_\tau-\Omega_\tau\beta^\mu.$$

On varying $g_{\mu\nu}$, we assume β^μ to vary as

$$\delta\beta^\mu=\tfrac{1}{2}\beta_\nu\delta g^{\mu\nu};\quad \delta\beta_\mu=\tfrac{1}{2}\beta^\nu\delta g_{\mu\nu}. \tag{4}$$

This variation is also nonintegrable in general.

Definition A

Commutation rules $\mathbf{G}(\beta^\mu,\beta^\nu,\beta^\sigma,\cdots,g^{\mu\nu},g^{\sigma\tau},\cdots)=0$ will be called consistent under the operation of variation (4), if

$$\delta\mathbf{G}(\beta^\mu,\beta^\nu,\beta^\sigma,\cdots,g^{\mu\nu},g^{\sigma\tau},\cdots)=0,$$

that is if

$$\frac{1}{2}\left[\frac{\partial\mathbf{G}}{\partial\beta^\mu},\beta_\alpha\right]\delta g^{\alpha\mu}+\frac{1}{2}\left[\frac{\partial\mathbf{G}}{\partial\beta^\nu},\beta_\sigma\right]\delta g^{\sigma\nu}+\cdots=-\frac{\partial\mathbf{G}}{\partial g^{\mu\nu}}\delta g^{\mu\nu}-\cdots.$$

(Here square brackets mean that $\delta\beta^\mu$ must replace the differentiated β^μ without change of order.)

It can be shown easily that the following theorem always holds:

Theorem I: The commutation relation,

$$\mathbf{G}(\beta^\mu,\beta^\nu,\cdots g^{\mu\nu})=0,$$

remains invariant (i) under any local infinitesimal spin space rotation, (ii) under any infinitesimal affine transformation, provided it is consistent in the sense of definition A.

This theorem at once tells us that there always exists a spin-space rotation S which annuls the change in β^μ due to the affine transformation (2). Hence, equating the coefficients of ϵ^τ in (2) and (3), we get

$$\beta^\mu{}_{|\tau}=\beta^\mu{}_{,\tau}+\Gamma^\mu{}_{\alpha\tau}\beta^\alpha+[\Omega_\tau,\beta^\mu]=0. \tag{5}$$

Thus we have defined a new derivative which we may call the coefficient of covariant displacement (abbreviated as c.c.d.). Hence the c.c.d. of the fundamental matrix $\beta^\mu{}_{|\tau}=0$ determines the spin-space structure Ω_τ, just as the covariant derivative of the metric tensor $g^{\mu\nu}{}_{;\tau}=0$ determines the affine structure of Riemannian space. Therefore, $g_{\mu\nu}$ and β^ν both have fundamental significance in our combined spinor-tensor formalism.

The c.c.d. of the covariant β_μ is

$$\beta_{\mu|\tau}=\beta_{\mu,\tau}-\left\{\begin{matrix}\alpha\\ \mu,\tau\end{matrix}\right\}\beta_\alpha+[\Omega_\tau,\beta_\mu]. \tag{6}$$

Theorem I also tells us that there exists an infinitesimal spin-space transformation, $\mathbf{S}=1+\mathfrak{F}^{\sigma\alpha}\delta g_{\sigma\alpha}$, such that it makes the variation $\delta\beta_\mu$ integrable, i.e.,

$$d\beta^\mu=\delta\beta^\mu-[\mathfrak{F}^{\alpha\sigma},\beta^\mu]\delta g_{\sigma\alpha},$$

where $d\beta^\mu$ is a total differential. Hence the integrability condition,

$$\frac{\partial^2\beta^\mu}{\partial g_{\alpha\sigma}\partial g_{\lambda\delta}}=\frac{\partial^2\beta^\mu}{\partial g_{\lambda\delta}\partial g_{\alpha\sigma}},$$

gives

$$\frac{\partial\mathfrak{F}^{\alpha\sigma}}{\partial g_{\lambda\delta}}-\frac{\partial\mathfrak{F}^{\lambda\delta}}{\partial g_{\alpha\sigma}}-[\mathfrak{F}^{\alpha\sigma},\mathfrak{F}^{\lambda\delta}]\equiv\tfrac{1}{4}[g^{\alpha\nu}g^{\sigma\delta}+g^{\sigma\delta}g^{\alpha\nu}+g^{\alpha\delta}g^{\sigma\nu}+g^{\sigma\nu}g^{\alpha\delta}],$$

where the matrices $g^{\mu\nu}$ represent a transformation

$$T=1+\epsilon_{\mu\nu}g^{\mu\nu}, \tag{7}$$

($\epsilon_{\mu\nu}=-\epsilon_{\nu\mu}$ are infinitesimal parameters) and form an infinitesimal algebra, defined over underlying Riemannian space-time, as follows:

$$\begin{aligned}[g^{\mu\nu},g^{\sigma\tau}]&=-g^{\mu\sigma}g^{\nu\tau}-g^{\nu\tau}g^{\mu\sigma}+g^{\mu\tau}g^{\nu\sigma}+g^{\nu\sigma}g^{\mu\tau},\\ [\beta^\mu,g^{\sigma\tau}]&=g^{\mu\sigma}\beta^\tau-g^{\mu\tau}\beta^\sigma,\\ g^{\mu\nu}&=-g^{\nu\mu}.\end{aligned} \tag{8}$$

Taking variations of (5) and (6) and using (8), one obtains

$$\delta\Omega_\tau=\tfrac{1}{2}g_{\alpha\sigma}g^{\sigma\nu}\delta\Gamma^\alpha{}_{\nu\tau}. \tag{9}$$

Hence the variation of spin-space structure is linearly connected with that of affine structure.

That the matrices $g^{\mu\nu}$ are fundamental, i.e., $g^{\mu\nu}{}_{|\tau}=0$ can be seen by taking the c.c.d. of (8), which gives

$$g^{\mu\nu}{}_{|\tau}=g^{\mu\nu}{}_{,\tau}+\Gamma_{\alpha\tau}{}^\mu g^{\alpha\nu}+\Gamma_{\alpha\tau}{}^\nu g^{\mu\alpha}+[\Omega_\tau,g^{\mu\nu}]=0.$$

GENERALIZED WAVE FUNCTION ψ

Since the components of ψ are spinors, ψ transforms under a spin-space rotation as $\psi'=S^{-1}\psi$. We assume that there exists a Hermitian matrix D defined by $\bar\psi=\psi^\dagger D$, where $\psi^\dagger$ = Hermitian conjugate of ψ and $\bar\psi$ = Pauli conjugate of ψ. It can be verified that

$$\begin{aligned}&\beta^{\mu\dagger}=D\beta^\mu D^{-1},\quad \beta'^{\mu}=D'\beta^\mu D'^{-1},\\ &D'=S^{-1}DS,\quad \bar\psi'=\bar\psi S\end{aligned} \tag{10}$$

imply the invariance of $(\bar\psi\psi)$ and $(\bar\psi\beta^\mu\psi)$ under spin-space rotation. But under an affine transformation $\bar\psi\beta^\mu\psi$ transforms as a contravariant vector, hence its c.c.d. gives

$$\begin{aligned}\psi_{|\tau}&=\psi_{,\tau}+\Omega_\tau\psi,\\ \bar\psi_{|\tau}&=\bar\psi_{,\tau}-\bar\psi\Omega_\tau,\\ \psi^\dagger{}_{|\tau}&=\psi^\dagger{}_{,\tau}+\psi^\dagger\Omega^\dagger{}_\tau.\end{aligned} \tag{11}$$

The c.c.d. of β^μ gives

$$\Omega_\tau'=S^{-1}\Omega_\tau S+S^{-1}S_{,\tau}.$$

Hence for the invariance of Ω_τ we have $S_{,\tau}=-[\Omega_\tau,S]$. The $\psi_{|\tau}$ transforms as $\psi'_{|\tau}=S^{-1}\psi_{|\tau}$, and

$$\psi_{|\tau|\sigma}=\psi_{|\tau,\sigma}-\Gamma_{\tau\sigma}{}^\alpha\psi_{|\alpha}+\Omega_\sigma\psi_{|\tau}. \tag{12}$$

Hence, $\psi_{|\tau}$ is a covariant spinor-tensor of rank one. Equations (5) and (10) show that

$$D_{|\tau}=D_{,\tau}-D\Omega_\tau-\Omega^\dagger D=0, \tag{13}$$

i.e., the matrix D is fundamental. If we define a matrix Λ_s so that $\bar{\psi}\cdot\Lambda_s$ transforms like a vector,[5] then

$$\Lambda_{s|\tau}=\Lambda_{s,\tau}-\Gamma_{s\tau}{}^{\sigma}\Lambda_{\sigma}+\Omega_{\tau}\Lambda_{s}. \tag{14}$$

From (12) and (15) one obtains

$$\psi_{|\mu\nu}-\psi_{|\nu\mu}=(\Omega_{\mu,\nu}-\Omega_{\nu,\mu}-[\Omega_{\mu}\Omega_{\nu}])\psi, \tag{15}$$

$$\begin{aligned}O&=\beta^{\tau}{}_{|\mu\nu}-\beta^{\tau}{}_{|\nu\mu}\\&=\{\Gamma^{\tau}{}_{\alpha\mu,\nu}-\Gamma^{\tau}{}_{\alpha\nu,\mu}+\Gamma^{\tau}{}_{\sigma\nu}\Gamma^{\sigma}{}_{\alpha\mu}-\Gamma^{\tau}{}_{\sigma\mu}\Gamma^{\sigma}{}_{\alpha\nu}\}\beta^{\alpha}\\&\quad+[(\Omega_{\mu,\nu}-\Omega_{\nu,\mu}-[\Omega_{\mu}\Omega_{\nu}]),\beta^{\tau}].\end{aligned} \tag{16}$$

The quantity in curly brackets is just the curvature tensor $R^{\tau}{}_{\mu\nu\alpha}$. Hence,

$$\psi_{|\mu\nu}-\psi_{|\nu\mu}=-\tfrac{1}{2}R_{\mu\nu\sigma\tau}I^{\sigma\tau}\psi, \tag{17}$$

i.e.,

$$\Delta\psi=(\partial_1\partial_2-\partial_2\partial_1)\psi=-\tfrac{1}{2}R_{\mu\nu\sigma\tau}g^{\sigma\tau}\psi.$$

Hence the total increment $\Delta\psi$ of a wave function ψ in an elementary circuital displacement depends linearly on the curvature and the matrices $g^{\mu\nu}$ of the infinitesimal algebra generated locally in that region.

We shall therefore interpret ih times the c.c.d. as a displacement operator, covariant under any spin-affine transformations of Riemannian space-time in the presence of the gravitational field, and shall define $\mathfrak{P}_\mu$ by

$$\mathfrak{P}_\mu\psi=ih\psi_{|\mu}. \tag{18}$$

$\mathfrak{P}$ will be seen to satisfy the following covariant commutation rules in general relativistic quantum mechanics:

$$\begin{aligned}&[x_\nu,\mathfrak{P}_\mu]=ih\delta_{\mu\nu},\\&[x_\mu,x_\nu]=0,\\&[\mathfrak{P}_\mu,\mathfrak{P}_\nu]=-\tfrac{1}{2}h^2R_{\mu\nu\sigma\tau}g^{\sigma\tau},\\&[\mathfrak{F}_\tau,\mathfrak{P}_\tau]=ih\mathfrak{F}_{|\tau},\end{aligned} \tag{19}$$

which may be compared with the noncommutation of the electromagnetic field displacement operator Π_μ,[6]

$$[\Pi_\mu,\Pi_\nu]=f_{\mu\nu}=\frac{ih}{c}e\left(\frac{\partial\varphi_\mu}{\partial x^\nu}-\frac{\partial\varphi_\nu}{\partial x^\mu}\right).$$

This can be interpreted as follows: In general the matter and its field produce a topological deformation of the space-time by modifying its local properties so as to introduce nonintegrability. General relativity tells us that in the case of a gravitational field this topology can be metrized so that nonintegrability becomes related with the curvature.

[5] In case of spin 0 and 1, Λ_s is just the generalization of Harish-Chandra's γ_s matrix which is useful in going from the particle to the wave aspect of mesons and photons [Harish-Chandra, Proc. Roy. Soc. (London) **186**, 503 (1946)].

[6] W. Pauli and M. Fierz, Proc. Roy. Soc. (London) **173**, 230 (1939).

LAGRANGIAN FORMULATION

Postulate

Laws of physics are covariant under any general spin-affine transformations of the space-time.

Taking this as our fundamental postulate, and assuming that a wave function ψ contains the maximum knowledge of the system, we observe that the wave equation must be linear in the derivatives of ψ and that an irreducible wave equation represents an elementary particle. We set up an invariant Lagrangian density as follows:

$$\begin{aligned}\mathfrak{L}=&\frac{1}{16\pi}G^{-1}c^4(-g)^{\frac{1}{2}}g^{\mu\nu}[\Gamma^{\sigma}{}_{\rho\mu}\Gamma^{\rho}{}_{\mu\nu}-\Gamma^{\sigma}{}_{\mu\rho}\Gamma^{\rho}{}_{\nu\sigma}]\\&+ic(-g)^{\frac{1}{2}}\bar{\psi}(\beta^\mu\mathfrak{P}_\mu{}^{(s)}+\chi)\psi,\end{aligned} \tag{20}$$

where $\mathfrak{P}_\mu{}^{(s)}$ is the symmetrized covariant displacement operator, i.e.,

$$\mathfrak{P}_\mu{}^{(s)}=\tfrac{1}{2}(\mathfrak{P}_\mu+\mathfrak{P}_\mu{}^{(\tau)}),$$

also where

$$\bar{\psi}\mathfrak{P}_\mu{}^{(\tau)}=-ih\bar{\psi}_{|\mu}=-\mathfrak{P}_\mu\bar{\psi},$$

and G is the universal gravitational constant.

Variation of $\mathfrak{L}$ with respect to ψ, $\bar{\psi}$, and $g_{\mu\nu}$ gives the Euler-Lagrange equation

$$\beta^\mu\mathfrak{P}_\mu\psi+\chi\psi=0,\quad \mathfrak{P}_\mu\bar{\psi}\beta^\mu-\chi\bar{\psi}=0, \tag{21}$$

and[7]

$$\begin{aligned}&(-g)^{\frac{1}{2}}(R_{\mu\nu}-\tfrac{1}{2}g_{\mu\nu}R)\\&\quad=\frac{4\pi G}{c^3}(-g)^{\frac{1}{2}}\bar{\psi}(\mathfrak{P}_\mu{}^{(s)}\beta_\nu+\beta_\mu\mathfrak{P}_\nu{}^{(s)})\psi,\end{aligned} \tag{22}$$

from which by putting

$$\mathcal{S}^\mu=(-g)^{\frac{1}{2}}c(\bar{\psi}\beta^\mu\psi),$$

and

$$\Theta_{\mu\nu}=\tfrac{1}{2}(-g)^{\frac{1}{2}}c\bar{\psi}(\mathfrak{P}_\mu{}^{(s)}\beta_\nu+\beta_\mu\mathfrak{P}_\nu{}^{(s)})\psi,$$

one obtains

$$\mathfrak{P}_\mu\mathcal{S}^\mu=0,\quad \text{i.e.,}\quad \mathcal{S}^\mu{}_{|\mu}=0,$$

and

$$\mathfrak{P}_\mu\Theta^{\mu\nu}=0,\quad \text{i.e.,}\quad \Theta^{\mu\nu}{}_{|\mu}=0. \tag{23}$$

These are the conservation equations of the charge current vector $\mathcal{S}^\mu$ and the conservation equations of the symmetric stress energy tensor $\Theta_{\mu\nu}$ of an elementary particle in its gravitational field.

Introducing the operators $\mathfrak{P}=\beta^\mu\mathfrak{P}_\mu$ and $\mathfrak{P}^2=\mathfrak{P}_\mu\mathfrak{P}^\mu$, one sees that they satisfy the characteristic equation of even degree:

$$(\mathfrak{P}^2-\alpha_1{}^2\mathfrak{P}^2)(\mathfrak{P}^2-\alpha_2{}^2\mathfrak{P}^2)\cdots=0, \tag{24}$$

or, of odd degree:

$$\mathfrak{P}(\mathfrak{P}^2-\alpha_1{}^2\mathfrak{P}^2)(\mathfrak{P}^2-\alpha_2{}^2\mathfrak{P}^2)\cdots=0; \tag{25}$$

i.e.,

$$\mathfrak{P}_\mu\mathfrak{P}_\nu\mathfrak{P}_\sigma\cdots(\beta^\mu\beta^\nu-\alpha_1{}^2g^{\mu\nu})(\beta^\sigma\beta^\tau-\alpha_2{}^2g^{\sigma\tau})\cdots=0,$$

[7] This equation can also be written as

$$(-g)^{\frac{1}{2}}(R_{\mu\nu}-\tfrac{1}{2}g_{\mu\nu}R)=(8\pi G/c^4)\Theta_{\mu\nu}+\lambda g_{\mu\nu},$$

where λ = Einstein's cosmological constant. The conservation equation of $\Theta_{\mu\nu}$ remains unaffected.

which gives for even and odd degrees, respectively:

$$\Sigma(\beta^\mu\beta^\nu-\alpha_1{}^2g^{\mu\nu})(\beta^\sigma\beta^\tau-\alpha_2{}^2g^{\sigma\tau})\cdots=0,$$
$$\Sigma\beta^\mu(\beta^\nu\beta^\sigma-\alpha_1{}^2g^{\nu\sigma})\cdots=0. \quad (26)$$

These are the general relativistic commutation relations previously written symbolically as **G** in (1) and in their irreducible form their degree represents the spin of the elementary particle as given by (8).[8] It may be noted that they are consistent according to definition A and hence satisfy theorem I. From (21) and (25) one gets,

$$(\chi^2-\alpha_1{}^2\mathfrak{M}^2)(\chi^2-\alpha_2{}^2\mathfrak{M}^2)\cdots=0.$$

Hence χ^2/α^2, the eigenvalues of $\mathfrak{M}^2$, are squares of masses of elementary particles.

The matrices $\mathcal{S}^{\mu\nu}$ defined by (8) reduce to the nucleus of the representation of Lorentz transformation in a locally Cartesian frame; hence we can define an infinitesimal transformation $\mathcal{T}$ whose representation transforms as $\psi'=\mathrm{T}\psi=[1+\frac{1}{2}\epsilon_{\mu\nu}\mathcal{S}^{\mu\nu}]\psi$, where T is a representation matrix of $\mathcal{T}$ which may be called a local Lorentz transformation, and $\mathcal{S}_{\mu\nu}$ the nucleus of representation of $\mathcal{T}$. T forms a local group embedded in the general transformation group S and (9) shows us that S can be built up by successive variation of $\Gamma_{\sigma\tau}{}^\mu$ if we know the infinitesimal algebra of $\mathcal{S}^{\mu\nu}$ and β^μ defined by (8) and (26). In the particular case of spin $\frac{1}{2}$, $\mathcal{S}^{\mu\nu}=\frac{1}{4}[\beta^\mu,\beta^\nu]$, and for spin 0 and 1, $\mathcal{S}^{\mu\nu}=[\beta^\mu,\beta^\nu]$.

In the case of spin 2, ψ in (20), (21), (22) represents the wave function of gravitons (gravitational quanta). Now the metrical structure of physical space has been considered to be due to gravitation. One may ask how to reconcile this representation of gravitation with the one in terms of gravitational quanta. The apparent contradiction is resolved by considering matter with its field as causing a (topological) deformation of physical space-time and having the duality of metricity and discreteness, as observed by experiments which also deform space-time. We can observe metrical properties only on the macroscopic level, where approximate rigid bodies and local frames of reference exist, but in the case of the microscopic world where there exist no rigid rods to define distance (since the uncertainty principle applies) the other aspect of duality (discreteness) becomes apparent.

[8] For degrees two and three, these commutation rules reduce to the generalizations of Dirac's and Kemmer's commutation relations:

$$\beta^\mu\beta^\nu+\beta^\nu\beta^\mu=2g^{\mu\nu}$$

for spin $\frac{1}{2}$, and

$$\beta^\mu\beta^\sigma\beta^\nu+\beta^\nu\beta^\sigma\beta^\mu=g^{\mu\sigma}\beta^\nu+g^{\sigma\nu}\beta^\mu$$

for spins 0 and 1.

PHYSICAL REVIEW VOLUME 94, NUMBER 6 JUNE 15, 1954

Electron Energy Distributions in Stationary Discharges

IRA B. BERNSTEIN* AND T. HOLSTEIN
Westinghouse Research Laboratories, East Pittsburgh, Pennsylvania

(Received March 3, 1954)

Calculations of the electron distribution function are presented for some simple examples of a stationary discharge in a dc space charge field. The treatment is valid when the predominant mechanism of energy exchange arises from motion in the dc space charge field. The computations indicate that the effect of dc space charge is, for a given external field strength, to increase the proportion of high energy electrons over that computed neglecting space charge. This results in a larger specific ionization rate, but the effect is not so great as to account for the low maintenance potentials observed in positive columns and in microwave discharges in inert gases.

I. INTRODUCTION

PAST theoretical analyses[1] of the energy distribution of electrons in gases have generally ignored the presence of space charge fields. In the microwave discharge, for example, the electric field is usually assumed to be of external origin; in positive columns of dc discharges, the relevant field is taken to be the longitudinal gradient. Now, in both these examples, the removal of charged particles takes place via the mechanism of ambipolar diffusion. This process requires the presence of a space charge field sufficiently strong to retard the motion of electrons, and to accelerate that of the positive ions to the boundary. Such fields are often comparable to or even larger than the external fields.

In order to obtain some idea of the effect of a space charge field (of the type prevalent in ambipolar diffusion) on electron energy distributions and associated quantities, such an average ionization rates, it has been deemed of interest to investigate the situation in which the space charge field is much larger than the applied field. This case represents the opposite extreme to that already treated, namely, space charge field very much less than external field. By this procedure one may hope to achieve an understanding of the generally encountered intermediate case by interpolation between the two extremes.

* Present address: Forrestal Research Center, Princeton, New Jersey.

[1] Morse, Allis, and Lamar, Phys. Rev. **48**, 412 (1935); J. A. Smit, Physica **3**, 543 (1936); T. Holstein, Phys. Rev. **70**, 367 (1946), to be referred to hereafter as I.

A special feature of interest arises in connection with the question of low maintenance voltages in positive columns and microwave discharges.[2] In these discharges the essential problem is to account for the extraordinary ionization efficiency. A possible contributing mechanism might involve just the phenomenon under discussion. This possibility has in fact been investigated by Davydov[3] who comes to the conclusion that an ambipolar field large compared to the longitudinal gradient "Maxwellianizes" the energy distribution, thereby providing a relatively large number of "tail" (i.e., high-energy) electrons capable of direct ionization. In this paper the analysis of Davydov will be shown to be incorrect; furthermore, it will turn out that the effect of space charge fields upon average ionization rates, while not negligible, is completely unable to account for the observed low maintenance voltages.

II. BASIC ENERGY DISTRIBUTION EQUATION

The rigorous starting point of any energy distribution treatment is, of course, the Boltzmann transport equation,

$$\frac{\partial f}{\partial t}=-\mathbf{v}\cdot\operatorname{grad}_{\mathbf{r}}f-\mathbf{a}\cdot\operatorname{grad}_{\mathbf{v}}f=\frac{\partial f}{\partial t}\Big)_{\text{coll}}. \tag{1}$$

Here, $f=f(\mathbf{r},\mathbf{v},t)$ gives the distribution of electrons in position and velocity space, $\mathbf{a}=-e\mathcal{E}/m$, where the electric field, $\mathcal{E}$, is in general a function of position $\mathbf{r}$ and time t. The first two terms on the right-hand side represent the change in f arising from the velocities of the elcctrons and from the action of the electric field. The last term represents the change in f due to collisions.

At this point it is to be remarked that, apart from the consideration of the space-charge field, the present analysis will be based on essentially the same assumptions as the previous treatments. This implies, first of all, that collisions other than those between electrons and normal atoms will be ignored. In this event $\partial f/\partial t$ has the form[4]

$$\begin{aligned}\partial f/\partial t)_{\text{coll}}=&Nv\int_\Omega d\omega'[f(\theta',\varphi',v,\mathbf{r},t)-f(\theta,\varphi,v,\mathbf{r},t)]q_{el}(\psi,v)\\&+(Nv/v^2)(m/M)(\partial/\partial v)\\&\times\int_\Omega d\omega' f(\theta',\varphi',v,\mathbf{r},t)(1-\cos\psi)q_{el}(\psi,v)v^4\\&+\sum_h\int_\Omega d\omega'\{f(\theta',\varphi',[v^2+v_h^2]^{\frac12},\mathbf{r},t)\\&\times(1+v_h^2/v^2)q_h(\psi,[v^2+v_h^2]^{\frac12})\\&-f(\theta,\varphi,v,\mathbf{r},t)q_h(\psi,v)\}+\partial f/\partial t)_{\text{ion}}.\end{aligned} \tag{2}$$

In Eq. (2), N is the density of normal gas atoms; v, θ, and φ are polar coordinates in velocity space (the integrals being carried out over the total solid angle Ω in this space, i.e., over-all values of θ' and φ'); $q_{el}(\psi,v)$ is the differential cross section for elastic scattering through an angle ψ of an electron of velocity v; and $q_h(\psi,v)$ the corresponding inelastic differential cross section involving excitation of the h'th atomic level. The first term gives the change in f due to elastic scattering with neglect of recoil loss. The second term takes this loss into account. The third term describes the effect of excitation collisions. In it the summation is extended over all discretely excited levels. Finally, $\partial f/\partial t)_{\text{ion}}$ denotes the change in f due to ionizing collisions. This term will be written down explicitly later.

A second assumption which characterizes the existing theoretical treatments of electron energy distributions is that the distribution is essentially isotropic in velocity space, with only small anisotropies arising from the actions of external fields and diffusion gradients. One thus has

$$f(\mathbf{r},\mathbf{v},t)\approx f_0(\mathbf{r},v,t)+\mathbf{v}\cdot\mathbf{f}_1(\mathbf{r},v,t), \tag{3}$$

where $f_0(\mathbf{r},v,t)$ and $\mathbf{f}_1(\mathbf{r},v,t)$ are scalar and vector functions of $\mathbf{r}$, t and the magnitude of $\mathbf{v}$, and where it is to be presumed that

$$f_0(\mathbf{r},v,t)\gg|\mathbf{f}_1(\mathbf{r},v,t)|. \tag{4}$$

Upon substituting (3) into (2), multiplying the result by $1/4\pi$ or by $3\mathbf{v}/4\pi$, integrating over the velocity angles (as is done in I, pp. 371–372), and transforming the velocity variable from v itself to $u=v^2$, one obtains the following equations[5] for $\partial f_0/\partial t$ and $\partial\mathbf{f}_1/\partial t$.

$$\begin{aligned}u^{\frac12}\partial f_0/\partial t=&-(u/3)\operatorname{div}_{\mathbf{r}}\mathbf{f}_1-(2\mathbf{a}/3)\cdot(\partial/\partial u)(u\mathbf{f}_1)\\&+(2m/M)(\partial/\partial u)(u^2f_0/\lambda_e)\\&+\sum_h\{(u+u_h)f_0(u+u_h,\mathbf{r})/\lambda_h(u+u_h)\\&-uf_0(u,\mathbf{r})/\lambda_h(u)\}+u^{\frac12}\partial f_0/\partial t)_{\text{ion}},\end{aligned} \tag{5}$$

$$u^{\frac12}\partial\mathbf{f}_1/\partial t=-u\operatorname{grad}_{\mathbf{r}}f_0-2a u\partial f_0/\partial u-u\mathbf{f}_1/\lambda_e, \tag{6}$$

where

$$1/\lambda_e(u)=2\pi N\int_0^\pi d\psi\sin\psi(1-\cos\psi)q_{el}(\psi,u), \tag{7}$$

and

$$1/\lambda_h(u)=2\pi N\int_0^\pi d\psi\sin\psi q_h(\psi,u). \tag{8}$$

$\lambda_e(u)$ and $\lambda_h(u)$ are, respectively, the mean free paths for elastic scattering and for excitation of the h'th atomic level.

Equations (5) and (6) will be applied to the positive column of a dc discharge. For the sake of simplicity the usual cylindrical geometry will be replaced by plane

[2] See, for example, Krasik, Alpert, and McCoubrey, Phys. Rev. 76, 722 (1949), especially p. 730 and Fig. 12.
[3] B. Davydov, Physik Z. Sowjetunion 12, 269 (1937).
[4] See, for example, I, Eqs. (10), (11), and (13).
[5] These equations are vector generalizations of (21) and (22) of I, the only further change being the use of $u=v^2$ rather than v itself as the velocity variable.

parallel geometry, i.e., the boundary will be assumed to consist of two parallel walls separated by a distance $2d$. The vector acceleration $\mathbf{a}$ consists of a longitudinal component a_l parallel to the walls, and a transverse component a_t perpendicular to the walls, arising from the ambipolar space charge field. Whereas a_l is constant, a_t must be considered a function of x (the x axis being directed perpendicular to the walls). In addition, the positive column is assumed homogeneous in directions parallel to the walls, i.e., the dependence of f_0 and $\mathbf{f}_1$ on $\mathbf{r}$ is limited to the x coordinate. Under these conditions (6) reduces to

$$o=u^{\frac{1}{2}}\partial f_{1t}/\partial t=-2a_tu\partial f_0/\partial u-uf_{1t}/\lambda_e-u\partial f_0/\partial x, \quad (9)$$

$$o=u^{\frac{1}{2}}\partial f_{1l}/\partial t=-2a_tu\partial f_0/\partial u-uf_{1l}/\lambda_e, \quad (10)$$

where f_{1t} and f_{1l} are the transverse and longitudinal components of $\mathbf{f}_1$. These equations may be used immediately to eliminate $\mathbf{f}_1$ from (5), whence one obtains

$$o=u^{\frac{1}{2}}\partial f_0/\partial t=\tfrac{1}{3}(\partial/\partial x+2a_t\partial/\partial u)(u\lambda_e)\times(\partial/\partial x+2a_t\partial/\partial u)f_0(x,u,t)+L\{f_0(x,u,t)\}, \quad (11)$$

where

$$L\{f_0(x,u,t)\}=(4/3)a_t^2(\partial/\partial u)(u\lambda_e\partial f_0/\partial u)+(2m/M)(\partial/\partial u)(u^2f_0/\lambda_e)+\sum_h\{(u+u_h)f_0(x,u+u_h,t)/\lambda_h(u+u_h)-uf_0(x,u,t)/\lambda_h(u)\}+u^{\frac{1}{2}}\partial f_0/\partial t)_{\text{ion}}. \quad (12)$$

For the sake of reference the explicit form of $u^{\frac{1}{2}}\partial f_0/\partial t)_{\text{ion}}$ given in I, Eq. (32), will be recorded here. It is

$$u^{\frac{1}{2}}\partial f_0/\partial t)_{\text{ion}}=\int_{u+u_i}^{\infty}du'u'f_0(u')/\lambda_i(u',u)-uf_0(u)\int_0^{(u-u_i)/2}du'/\lambda_i(u,u'), \quad (13)$$

where u_i is the ionization potential, and where $1/\lambda_i(u,u')$ is the "differential" probability per cm for ionization in which one of the two resultant electrons has an energy between u' and $u'+du'$ (the energy of the other being necessarily contained between $u-u_i-u'$ and $u-u_i-u'-du'$). As is the case in the standard treatments,[1] $u^{\frac{1}{2}}\partial f_0/\partial t)_{\text{ion}}$ plays a negligible role in determining the energy distribution, and will henceforth be neglected. It is to be noted that $u^{\frac{1}{2}}f_0dudx$ is proportional to the fraction of electrons at x with kinetic energy u.

The development of (11) from (5) and (6), which has been given in the preceding paragraphs for the case of the positive column, can also be applied under certain conditions to the microwave discharge. The geometry of the discharge, as before, will be assumed plane-parallel. However, both the ambipolar space charge field $\mathcal{E}_t$, and the applied microwave field $\mathcal{E}_0\cos\omega t$, are in the x direction, perpendicular to the walls. Just as in I, it will be assumed that the microwave frequency ω is high enough so that f_0 does not change appreciably in a cycle of field oscillation: For the steady state, (6) then yields

$$f_1=-\lambda_e\{\partial f_0/\partial x+2a_t\partial f_0/\partial u\}-2a_0\lambda_e\{(\cos\omega t+\omega\lambda_eu^{-\frac{1}{2}}\sin\omega t)/(1+\omega^2\lambda_e^2u^{-1})\}\partial f_0/\partial u. \quad (14)$$

Substituting (14) into Eq. (5) and time-averaging over a cycle of field oscillation (in which f_0 is still to be considered time-independent), one obtains, with the further assumption that $\omega^2\lambda_e^2u^{-1}\ll1$ (many elastic collisions per oscillation), an equation of precisely the same form as (11). The sole difference is that a_t^2 is to be replaced by $\frac{1}{2}a_0^2$, i.e., the longitudinal field of the dc positive column is equivalent to the root-mean-square field of the microwave discharge.[6]

Equation (11) constitutes the basic equation for the electron energy distribution in the presence of an external and an ambipolar space charge field; its approximate solution for the case of external field very much less than ambipolar field will be developed in the next section. Henceforth the subscript o will be suppressed.

III. METHOD OF SOLUTION OF BASIC EQUATION

An integral feature of the method for solving (11), to be given here, is the transformation from u to a new variable

$$w=u+\varphi(x), \quad (15)$$

where

$$\varphi(x)=-2\int_0^x dxa_t(x). \quad (16)$$

Physically (apart from the factor $\frac{1}{2}m$), $\varphi(x)$ is the potential energy associated with the space charge field. Thus w represents the sum of kinetic energy and space charge potential energy. In what follows, w will be referred to as "total energy."

From (15) and (16) one readily derives the relationships

$$\partial/\partial u)_x=\partial/\partial w)_x, \quad (17)$$

$$\partial/\partial x)_u=\partial/\partial x)_w-2a_t\partial/\partial w)_x, \quad (18)$$

the combination of which yields

$$\partial/\partial x)_w=\partial/\partial x)_u+2a_t\partial/\partial u)_x. \quad (19)$$

With the use of these relations, Eq. (12) assumes the form

$$o=\tfrac{1}{3}(\partial/\partial x)[(w-\varphi)\lambda_e\partial f/\partial x]+L\{f(w,x)\}, \quad (20)$$

where f is now to be considered a function of x and w, and where

$$L\{f(w,x)\}=(4/3)a_t^2(\partial/\partial w)[(w-\varphi)\lambda_e\partial f/\partial w]+(2m/M)(\partial/\partial w)[(w-\varphi)^2f/\lambda_e]+\sum_h\{(w-\varphi+u_h)f(w+u_h,x)/\lambda_h(w-\varphi+u_h)-(w-\varphi)f(w,x)/\lambda_h(w-\varphi)\} \quad (21)$$

with λ_e a function of $(w-\varphi)$.

[6] This result is also given in I.

Equations (20) and (21) describe a type of diffusion-drift motion in w,x space. In fact, by defining two diffusion coefficients

$$D_x=\tfrac{1}{2}(w-\varphi)\lambda_e(w-\varphi), \tag{22}$$

and

$$D_w=(4/3)a_i^2(w-\varphi)\lambda_e(w-\varphi), \tag{23}$$

one may write (20) and (21) in the form

$$\begin{aligned}0=&(\partial/\partial x)[D_x(\partial f/\partial x)]+(\partial/\partial w)[D_w(\partial f/\partial w)]\\&+(2m/M)(\partial/\partial w)[(w-\varphi)^2 f/\lambda_e]\\&+\textstyle\sum_h\{(w-\varphi+u_h)f(w+u_h,x)/\lambda_h(w-\varphi+u_h)\\&-(w-\varphi)f(w,x)/\lambda_h(w-\varphi)\},\end{aligned} \tag{24}$$

in which it is seen that the first term describes a diffusion in x, the second a diffusion in w, and the remaining terms a degradation in total energy w, which is continuous for the recoil term and takes place in jumps of u_h in the case of the inelastic collision term.

The diffusion coefficients, D_x and D_w are of course functions of the coordinates. In particular, as illustrated in Fig. 1, they vanish on the curve of zero kinetic energy $w=\varphi(x)$ which, since electrons must have positive kinetic energies, constitutes one of the boundaries of the available region of w,x space.

In an analogous fashion, curves of $\varphi(x)$, uniformly displaced upwards by amounts u_h, define the lower boundaries of regions of inelastic collisions of various types. Finally, the curve

$$w=\varphi(x)+u_{\text{ion}}$$

[where $u_{\text{ion}}=(2/m)$ ionization potential] gives the lower boundary of the ionization region.

To complete the description in w,x space, it is to be considered that $\varphi(x)$, as pictured in Fig. 1, is symmetrically disposed with respect to the enclosure geometry—an assumption which will be employed in all that follows—and attains a finite value φ on the enclosure

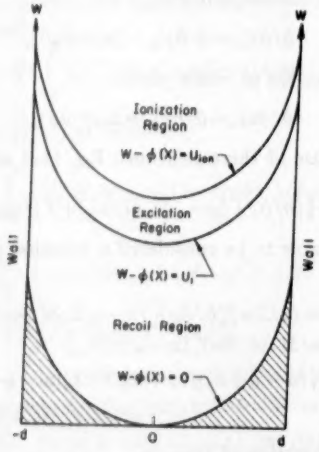

FIG. 1. Diagram of total energy w *versus* position x showing regions of the various classes of collisions.

walls. For $w>\varphi_{\text{wall}}$ the boundary is no longer $w=\varphi(x)$, but the walls themselves. If the latter are assumed absorbing, as is usually the case, the boundary condition

$$f(w,\pm d)=0, \tag{26}$$

($d=\frac{1}{2}$ wall spacing) appropriate to diffusion theory, is to be employed.[7]

It turns out that the inclusion of wall effects leads to special difficulties in the analysis of Eq. (24). The treatment will therefore be limited to situations in which the significant range of w lies below φ_{wall}; this restriction is equivalent to assuming an infinite "space charge well."

With the transformation from the u,x to the w,x system of variables, the stage has been reached where one may profitably make use of the basic assumption, discussed in the introduction of this paper, that the ambipolar field $\mathcal{E}_t$ is much larger than the "applied" longitudinal field $\mathcal{E}_l$. As a preliminary step, it will be helpful to consider the extreme case in which it is imagined that there is a longitudinal field and no collision-induced energy losses, i.e., the electrons move in a space charge field of the type illustrated in Fig. 1, undergoing elastic collisions with infinitely massive atoms. In this case (20) reduces to

$$0=\tfrac{1}{2}(\partial/\partial x)[(w-\varphi)\lambda_e\partial f/\partial x]. \tag{27}$$

A first integration yields

$$\partial f/\partial x=C(w)/(w-\varphi)\lambda_e(w-\varphi).$$

Let it be supposed that $\lambda_e(0)$ is finite. Then the requirement of regularity of f (and $\partial f/\partial x$) at $w=\varphi(x)$ leads to the conclusion that $C(w)$ is zero. Thus $\partial f/\partial x=0$ and

$$f(w,x)=F(w), \tag{29}$$

where $F(w)$ is an arbitrary function of w.

The arbitrariness of $F(w)$ arises from the circumstance that, with neglect of the longitudinal field and collision losses, the sole mechanism for changing kinetic energy is the motion in the ambipolar field. Obviously, a constant of this motion is the total energy, w. Thus, in the approximation represented by Eq. (27), transitions between different w levels do not take place with the consequence that an arbitrary distribution in w of electrons is stationary.

It has been remarked above that the consideration of (27) as an approximation to (20) is in line with the basic point of view of this paper, which regards the effect of the space charge field in determining the electron energy distribution as "dominant." The results just obtained demonstrate that this dominance is necessarily incomplete in the sense that the space charge field cannot determine the distribution in w. It is therefore necessary to proceed to a higher stage of

[7] In contrast to the situation at the physical boundary $x=\pm d$, only regularity of $f(x,w)$ is required at $w=\varphi(x)$.

approximation. This is done by considering the terms designated in (21) by the notation $L\{f(w,x)\}$ as a small but nevertheless nonvanishing perturbation. The introduction of these terms will correspond physically to permitting transitions to take place between the different w levels; these transitions will then determine[8] the form of $F(w)$.

Considering, then, $L\{f(w,x)\}$ in (20) as a perturbation, one attempts a solution of the form

$$f(w,x)=F(w)+G(w,x), \tag{30}$$

where $G(w,x)$ is to be presumed small. Inserting (30) into (20), one has, approximately,

$$0=\tfrac{1}{2}(\partial/\partial x)[(w-\varphi)\lambda_e\partial G/\partial x]+L\{F(w)\}, \tag{31}$$

where the higher-order term $L\{G(w,x)\}$ has been dropped. Upon integration of (31) from $-x_0$ to $+x_0$, x_0 being defined by the relation[9]

$$\varphi(x_0)=\varphi(-x_0)=w, \tag{32}$$

the first term of (31) drops out, and one is left with

$$0=\int_{-x_0}^{x_0} dx L\{F(w)\} \tag{33}$$

as the basic equation[10] for the determination of $F(w)$. Equation (33) may be written more explicitly as

$$\begin{aligned} o=&(4/3)a_i^2(d/dw)[p(w)dF/dw] \\ &+(2m/M)(d/dw)[q(w)F] \\ &+\sum_h\{r_h(w+u_h)F(w+u_h)-r_h(w)F(w)\}, \end{aligned} \tag{34}$$

where

$$p(w)\equiv\int_{-x_0}^{x_0} dx(w-\varphi)\lambda_e(w-\varphi), \tag{35}$$

$$q(w)\equiv\int_{-x_0}^{x_0} dx(w-\varphi)^2\lambda_e(w-\varphi), \tag{36}$$

$$r_h(w)\equiv\int_{-x_0}^{x_0} dx(w-\varphi)/\lambda_h(w-\varphi). \tag{37}$$

It is to be noticed that the form of (34) is quite similar to that of the corresponding equation for the case of no space charge field [see I, (54′)]. Hence, the general technique developed in I for solving that equation will also be applicable here. In the following section (34) will be solved for a number of specific examples and the results compared with those obtained in I for the case of no space charge field.

IV. ILLUSTRATIVE EXAMPLES

1. Elastic Collision Case

The first example to be considered is that in which the electron energies are low enough so that inelastic collisions may be neglected. Equation (34) then reduces to

$$\begin{aligned} &(4/3)a_i^2(d/dw)[p(w)dF/dw] \\ &\quad+(2m/M)(d/dw)[q(w)F]=0. \end{aligned} \tag{38}$$

A first integration yields

$$d\ln F/dw=-(3m/2Ma_i^2)[q(w)/p(w)], \tag{39}$$

the constant of integration being eliminated by the requirement of regularity of F and dF/dw at the origin. A second integration gives

$$F=C\exp\left[-(3m/2a_i^2)\int_0^w dwq(w)/p(w)\right]. \tag{40}$$

In order to proceed further, it is necessary to make some assumptions concerning both the energy dependence of the mean free path, λ_e, and the spatial dependence of the space charge potential φ. In what follows, it shall be assumed that (a) λ_e=constant, and (b) φ varies parabolically with distance,[11] i.e.,

$$\varphi=\alpha x^2. \tag{41}$$

[8] In the language of perturbation theory the situation may be described as follows. The solutions of the equation $(1/3)(\partial/\partial x)\times[(\omega-\varphi)\lambda_e\partial f/\partial x]=-\beta f$ which belong to the "eigenvalue" $\beta=0$ are degenerate. A complete set of the eigenstates, for example, is given in terms of the Dirac delta function, namely $f_{w_1}(w,x)=\delta(w-w_1)$. The general solution, equivalent to (29) is then, $f(w,x)=\int dw_1F(w_1)f_{w_1}(w,x)$. According to the general methods of perturbation theory, the degeneracy is to be removed by a secular perturbation procedure which considers $L\{f(w,x)\}$ as the perturbation. In such a procedure, one will expect to have to evaluate integrals of the type $\int dxdwf_{w_1}(w,x)L\{f(w,x)\}$. This in fact is just what is done in the text below. (See also reference 10.)

[9] It has already been assumed that $\varphi(x)$ is an even function of x, with the plane $x=0$ chosen to lie midway between the two walls.

[10] With reference to the remarks of footnote 8, the above procedure is fully equivalent to that followed in secular perturbation theory. Namely, one constructs the solution as a linear superposition of degenerate unperturbed functions, i.e., $f(w,x)\approx\int dw_1F(w_1)f_{w_1}(w,x)=F(w)$ [since $f_{w_1}(w,x)=\delta(w-w_1)$] in accordance with footnote 8, and substitutes into the basic Eq. (20), thereby obtaining $o=L\{F(w)\}$. Then, upon multiplying with one of the "eigenfunctions" and integrating with respect to x and w, one obtains

$$o=\int_0^\infty dw\int_{-x_0}^{x_0} dx\delta(w'-w)L\{F(w)\}=\int_{-x_0(w')}^{x_0(w')} dxL\{F(w')\},$$

as is given by (33) of the text.

[11] It is felt that the actual functional form of the space charge potential is contained between two extremes, one of which is represented by (41); the other extreme is a step-like potential given by $\varphi=0$ for $|x|<d$, followed by a discontinuous jump at $x=\pm d$ to the value $\varphi=\varphi_{\text{wall}}$. In particular, it is readily shown that a field of the type occurring in the conventional theory of ambipolar diffusion is contained between these two extremes (apart from a small region in the neighborhood of the wall in which ambipolar theory is not applicable anyway). Now, the "step" field, when applied to Eq. (34), is essentially equivalent to no space charge field. Hence (41) should give an extreme indication of the effect of space charge fields on the electron energy distribution and related statistical quantities.

With these assumptions, (35) and (36) are readily evaluated and yield

$$p(w)=(4/3)\lambda_e w^{\frac{1}{2}}/\alpha^{\frac{1}{2}}, \tag{42}$$

$$q(w)=(16/15)w^{5/2}/\lambda_e\alpha^{1/2}, \tag{43}$$

which, when substituted into (40), give

$$F=C\exp[-(3m/5M)(w^2/a_i^2\lambda_e^2)]. \tag{44}$$

(44) is to be compared to the so-called "Druyvesteyn" distribution obtained for the elastic collision case in the absence of the space charge field. This distribution is[12]

$$F_D=C_D\exp[-(3m/4M)(u^2/a_i^2\lambda_e^2)]. \tag{45}$$

The comparison of (44) with (45) demonstrates a characteristic effect of the space charge field on electron energy distributions, namely, a relative enhancement of the tail. This feature will, in particular, be again encountered in the next example to be treated, in which inelastic collisions are taken into account.

2. Inelastic Collisions

The extension of the electron energy distribution into the inelastic collision region will now be considered. The specific example to be treated is that for which: (a) λ_e=constant (as in the previous example); (b) there exists only one excitation level, $u_1\equiv u_{ex}$ with the corresponding free path, $\lambda_1\equiv\lambda_{ex}$ independent of electron energy;[13] (c) the energy loss due to recoil collisions is negligible; (d) the space charge well is of the form[14]

$$\varphi(x)=\alpha x^{2r};\quad r=1,2,\cdots. \tag{46}$$

It should be pointed out that (a), (b), and (c) characterize the first example treated in I, Sec. 7. The results of the present treatment will therefore be directly comparable to those of I.

Utilizing these assumptions in the evaluation of the integrals in (35) and (37), one obtains

$$p(w)=2\alpha^{-1/2r}[2r/(2r+1)]w^{1+1/2r}, \tag{47}$$

$$r_{ex}(w)=r_1(w)=2\alpha^{-1/2r}[2r/(2r+1)](w+u_{ex}/2r)\times(w-u_{ex})^{\frac{1}{2}}S(w-u_{ex}), \tag{48}$$

where $S(x)$ is the conventional step function. Substituting (47) and (48) into (34) and dropping the recoil term, one has

$$O=(4/3)\lambda_e\lambda_{ex}a_i^2(d/dw)(w^{1+1/2r}dF/dw)+\{(w+u_{ex}/2r+u_{ex})w^{1/2r}F(w+u_{ex})-(w+u_{ex}/2r)(w-u_{ex})^{1/2r}F(w)S(w-u_{ex})\}. \tag{49}$$

As in the treatment of I, (49) is first solved for the excitation region $w>u_{ex}$. Here, for fields which are not too strong, the distribution function falls off sufficiently rapidly with increasing energy so that the "production" term, proportional to $F(w+u_{ex})$, may be neglected. In this case, and with the introduction of the dimensionless quantities

$$\zeta=w/u_{ex}, \tag{50}$$

$$\gamma^2=\tfrac{3}{4}(u_{ex}/a_i\lambda_e)^2(\lambda_e/\lambda_{ex}), \tag{51}$$

Eq. (49) may be written as

$$o=(d/d\zeta)[\zeta^{1+1/2r}dF(\zeta)/d\zeta]+\gamma^2\zeta^{1/2r}(\zeta+1+1/2r)F(\zeta+1),\quad \zeta\leqslant 1, \tag{52}$$

$$o=(d/d\zeta)[\zeta^{1+1/2r}dF(\zeta)/d\zeta]-\gamma^2(\zeta-1)^{1/2r}(\zeta+1/2r)F(\zeta),\quad \zeta\geqslant 1. \tag{53}$$

The region $\zeta\geqslant 1$ will be considered first. Introducing the substitution

$$G(\zeta)=\zeta^{\frac{1}{2}+1/2r}F(\zeta), \tag{54}$$

one may write (53) as

$$G''(\zeta)=[\gamma^2(1-1/\zeta)^{1/2r}(1+1/2r\zeta)-(2r+1)/16r\zeta^2]G(\zeta). \tag{55}$$

Here primes indicate differentiation with respect to ζ.

A considerable simplification of (55) may be achieved if the last term in the square bracket is neglected, a step which is permissible for sufficiently large γ (low field). Actually in the present paper, the range of field for which specific calculations is such that[15]

$$\gamma\geqslant 10. \tag{56}$$

For the range defined by (56) the second term in the bracket of (55) is quite small and will be dropped forthwith. Equation (55) then becomes

$$G''(\zeta)-k^2(\zeta)G(\zeta)=0, \tag{57}$$

where

$$k(\zeta)=\gamma(1-1/\zeta)^{1/4r}(1+1/2r\zeta)^{\frac{1}{2}}. \tag{58}$$

Equation (57) will be solved by an approximate method based on the circumstance that, because of (56), $G(\zeta)$ attains its asymptotic form, as given by the W.K.B. method[16] for $\zeta-1\ll 1$, which solution is then readily joined to one which is specially valid for the

[12] Equation (45) is readily obtained by taking $\varphi=0$ in (35) and (36) [the procedure being equivalent to assuming the "step field" of reference 10].

[13] This assumption corresponds to a "step function" cross section, the step occurring at $u=u_{ex}$. An energy dependence of this type is actually not unreasonable. In particular, the excitation cross sections of metastable levels (which is a number of gases are the lowest excited levels) often exhibit a rather sharp initial rise, followed by a plateau, or even by a diminishing characteristic.

[14] It will be noticed that the previously employed parabolic space charge potential $\varphi=\alpha x^2$ is a special case of (46) with $r=1$. Higher values of r represent cases intermediate between the parabolic potential and the square well potential of footnote 10.

[15] In a typical case such as argon, $\lambda_e/\lambda_{ex}\sim 50$, $\lambda_e p\sim(1/60)$ cm mm (where p is the gas pressure in mm Hg), and the excitation potential, $V_{ex}\sim 15$ volts. With these numbers, and with $\mathcal{E}$=longitudinal field in volts/cm, the limitation expressed by (56) is equivalent to $\mathcal{E}/p\lesssim 23$. This limit is considerably higher than the values of $\mathcal{E}/p$ commonly encountered in maintenance discharges (see Fig. 12 of reference (2)).

[16] H. F. Jeffries and B. S. Jeffries, *Methods of Mathematical Physics* (Cambridge University Press, Cambridge, 1950), second edition, p. 522.

immediate neighborhood of $\zeta=1$. Thus, the asymptotic solution of (57), as given by the W.K.B. method,[16] is

$$G(\zeta)=Ak(\zeta)^{-1/2}\exp\left[-\int_1^{\zeta}d\zeta' k(\zeta')\right]. \quad (59)$$

On the other hand, in the immediate neighborhood of $\zeta=1$, (57) may be approximated by

$$G''(\zeta)-(1+1/2r)\gamma^2(\zeta-1)^{1/2r}G(\zeta)=0, \quad (60)$$

the appropriate solution of which is

$$G(\zeta)=(\zeta-1)^{\frac{1}{2}}K_{2r/(4r+1)}[(1+1/2r)^{\frac{1}{2}} \times(1+1/4r)^{-1}\gamma(\zeta-1)^{1+1/4r}], \quad (61)$$

where $K_\nu(z)$ denotes the modified Bessel function of the second kind.[17]

Comparison of (60) with the asymptotic form of (61) in the neighborhood of $\zeta=1$ then gives

$$A=(\pi/2)^{\frac{1}{2}}(1+1/4r)^{\frac{1}{2}}. \quad (62)$$

Equations (54), (59), (61), and (62) give $F(\zeta)$ in the region $\zeta\geqslant 1$. For $\zeta\leqslant 1$, the combination of (52) and (53) yields

$$\zeta^{1+1/2r}F'(\zeta)=F'(1)-(\zeta+1)^{1+1/2r}F'(\zeta+1), \quad (63)$$

from which

$$F(\zeta)=F(1)-\int_{\zeta}^{1}d\zeta\zeta^{-(1+1/2r)}F'(1) -(\zeta+1)^{1+1/2r}F'(\zeta+1), \quad (64)$$

where $F(1)$ and $F'(1)$ are obtained[18] from the solution in (61). Thus, $F(\zeta)$ is given for the whole energy region. Specific calculations are carried out by numerical evaluation of (64).

The fraction of electrons with energy between w and $w+dw$ is given by

$$N(w)=\int_{-x_0}^{x_0}dx(w-\varphi)^{\frac{1}{2}}f(w,x)$$

$$=\int_{-x_0}^{x_0}dx(w-\alpha x^{2r})^{\frac{1}{2}}F(w)$$

$$=2[\Gamma(1+1/2r)/\Gamma(\tfrac{3}{2}+1/2r)]w^{\frac{1}{2}+1/2r}\alpha^{-1/2r} \times\alpha w^{\frac{1}{2}+1/2r}F(w). \quad (65)$$

Curves of $N(w)$, normalized to unity, are given in Fig. 2 for the case of $r=1$ (parabolic space charge field), and for various values for γ (corresponding to various values of the applied longitudinal field).

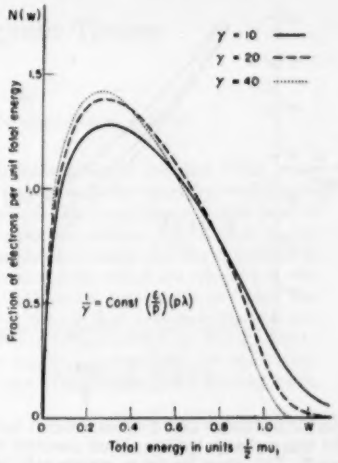

FIG. 2. Normalized distribution in total energy $N(w)$ *versus* w for various values of ε/p. The space charge well has been assumed to be parabolic.

Now that the distribution function has been determined, it is of interest to calculate the specific ionization rate β. For this computation, it is assumed that the ionization cross section is a linear function of the electron kinetic energy, an assumption that is quite good near threshold. Thus

$$1/\lambda_{\text{ion}}=(K_{\text{ion}}/\lambda_e)[(u-u_{\text{ion}})/u_{\text{ion}}]S(u-u_{\text{ion}}). \quad (66)$$

β is then given by

$$\beta=\frac{\displaystyle\int_{u_{\text{ion}}}^{\infty}dw\int_{-x_{\text{ion}}}^{x_{\text{ion}}}dx(w-\varphi)f(w,x)/\lambda_{\text{ion}}}{\displaystyle\int_0^{\infty}dw\int_{-x_0}^{x_0}dx(w-\varphi)^{\frac{1}{2}}f(w,x)}, \quad (67)$$

where x_{ion} is defined by the relation

$$w-\varphi(x_{\text{ion}})=u_{\text{ion}}. \quad (68)$$

Taking $f(x,w)=F(w)$ and using (46), one obtains, after some manipulation, the expression

$$\frac{\beta}{K_{\text{ion}}u_{\text{ion}}^{\frac{1}{2}}}=\frac{I}{J} \quad (69)$$

where

$$I=\int_{u_{\text{ion}}/u_{ex}}^{\infty}d\zeta F(\zeta)\{8r^2(\zeta-u_{\text{ion}}/u_{ex})^{2+1/2r} +2r(4r+1)(u_{\text{ion}}/u_{ex})(u-u_{\text{ion}}/u_{ex})^{1+1/2r}\}, \quad (69a)$$

and

$$J=[2(2r+1)(4r+1)\Gamma(1+1/2r)/\Gamma(\tfrac{3}{2}+1/2r)] \times\int_0^{\infty}d\zeta\zeta^{1+1/2r}F(\zeta), \quad (69b)$$

which may be evaluated numerically.

[17] G. N. Watson, *A Treatise on the Theory of Bessel Functions* (Cambridge University Press, Cambridge, 1948), second edition, p. 78. The solution involving the modified Bessel function of the first kind, $I_\nu(z)$, is excluded because it would represent an energy distribution which increases exponentially with increasing ζ.

[18] This is done conveniently with the aid of the series representation of $K_\nu(z)$.

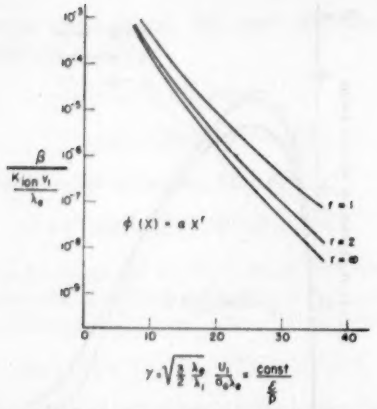

FIG. 3. Specific ionization rate β *versus* external field parameter $\gamma \propto p/\mathcal{E}$. The space charge well has been assumed to be of the form $\varphi(x)=\alpha x^r$. The curve for $r=\infty$ corresponds to the case of vanishing space charge field, that for $r=0$ a square potential well.

The results of the computation are presented in Fig. 3. The principal feature to be noted is that, for a given external field, i.e., a given value of γ, the specific ionization increases as the parameter r is varied from ∞—the case of a square-well potential, equivalent to no space charge field—to unity, the parabolic case, representing the extreme manifestation of a space charge field. However, and this qualification is of particular significance with regard to the low-voltage problem mentioned in the introduction of this paper, the "space charge" reduction of the longitudinal field required to achieve a *given* rate of ionization, is rather limited. Specifically, inspection of Fig. 3 indicates that this reduction is at most of the order of thirty percent. With reference to Fig. 12 of the paper of Krasik, Alpert, and McCoubrey,[2] it is immediately obvious that the effect is much too small to explain the discrepancy between theory and experiment. It is therefore necessary to invoke some other mechanism, such as cumulative or secondary ionization.

V. VALIDITY OF GENERAL METHOD

At this point some remarks on the validity of the general method are in order. It will be recalled that the basis of this method is contained in the assumption that, for a given total energy w, the distribution function is, to a sufficiently good approximation, independent of the spatial coordinate, x, i.e.,

$$f(w,x) \approx F(w). \tag{70}$$

It was implied in the text that (70) is a suitable approximation provided that the space charge field is large compared to the applied field. When this situation prevails, one may infer that the rate of energy change due to motion in the space charge field is large compared to that arising from the applied field. Now, as is exemplified in Sec. IV, it is necessary (for equilibrium) that the energy gain associated with motion in the applied field be compensated by loss due to collisions. Hence, one would expect (70) to be valid provided that the rate of energy change due to motion in the space charge field is large compared to the rate of energy loss due to collisions.

In the case of inelastic collisions, in which most of the energy is lost in one encounter, this condition is equivalent to the requirement that the time for an electron to diffuse throughout the accessible region of the space charge well ($w \gtrsim \varphi$) be small compared to the mean time between inelastic collisions, λ_{ex}/v.

In the case of recoil loss, an electron loses, on the average, a fraction $2m/M$ of its energy per collision. Hence, the requirement would be that the electron diffuses throughout the well in a time small compared to $(M/2m)(\lambda_e/v)$.

These intuitive expectations have been confirmed by a detailed analysis presented in a Westinghouse Research Report.[19]

VI. SUMMARY

In this paper the theoretical treatment of electron energy distributions has been extended to include the case in which—in addition to a spatially homogeneous applied field—there exists a dc space charge field of the type associated with ambipolar diffusion. The method is valid in the limiting case that the dominant mechanism for changing the energy of an electron is its motion in the space charge field. The equation determining the energy distribution [Eq. (34)] is then found to be of a form similar to that prevalent in the absence of the space charge field [Eq. (54′), I]. Illustrative calculations (Sec. V) demonstrate that the principal effect of the space charge field is an enhancement of the tail of the distribution function, with a consequent increase in specific ionization. The magnitude of the latter effect, however, is found to be much too small to account for the large ionization rates required in steady state discharges, such as the positive column of a noble gas dc discharge.

The treatment presented above applies both to the positive column and to low-frequency microwave discharges. The sole difference is that in the latter case one uses the rms microwave field in place of the dc longitudinal field of the positive column.

[19] T. Holstein, Westinghouse Research Report, R-94411-9-0, Higher-Order Approximations to Electron Energy Distributions in D. C. Space Charge Fields; reprints available upon written request.

Reaction Concept in Electromagnetic Theory

V. H. RUMSEY
Ohio State University, Columbus, Ohio

(Received September 21, 1953; revised manuscript received March 8, 1954)

A physical observable called the reaction is defined to simplify the formulation of boundary value problems in electromagnetic theory. To illustrate its value it is used to obtain formulas for scattering coefficients, transmission coefficients, and aperture impedances. An approximate solution to problems of this type is obtained by replacing the correct source (of the scattered field for example) with an approximate source which is adjusted so that its reaction with certain "test" sources is correct. This insures that the approximate source "looks" the same as the correct source according to the physical tests which are inherent in the problem. The formulas so obtained have a stationary character (for the cases considered) and thus the results could also be obtained from a variational approach. However the physical approach has two important advantages. It is general whereas the variational technique has to be worked out for each problem. It is conceptually simple and leads directly to results which might not be uncovered by the variational approach because of the complexity of the mathematical formulation. The problem of scattering by a dielectric body is used to illustrate this latter point.

INTRODUCTION

THE classical analysis of electromagnetic waves is based on the theory of fields which satisfy Maxwell's equations. It is interesting to examine this concept from the point of view of an experimenter whose objective is to use the theory to correlate his measurements. Suppose that we attempt to measure the field radiated by some source of electromagnetic energy by observing the signal received at the terminals of an antenna placed at the point of observation. By moving the antenna around we can obtain a considerable amount of information about the given field, but it is very difficult to relate this information to the classical field parameters, e.g., the electric field. Indeed from a literal point of view the postulate of electric field might be questioned on the grounds that any experiment designed to measure the electric field at a point must necessarily consist of measuring the effect of the field over a small but finite region, and therefore the postulate is incompatible with the process of performing an observation. This suggests that it is desirable to introduce into the theory a fundamental observable which represents measurements which can actually be performed.

DEFINITIONS AND PROPERTIES OF REACTION

We introduce a quantity, called the "reaction," which is defined as follows. Let the source of a monochromatic electromagnetic field consist of the volume distributions of electric and magnetic current $d\mathbf{J}$ and $d\mathbf{K}$ (i.e., the electric dipole moment contained in a volume V is equal to the vector $\int\int\int_V d\mathbf{J}$). (The word source is used in the sense that everywhere in the given region there is no field when the source is absent. Thus currents which may be induced in various parts of the region are not counted as sources because they vanish when the true source is turned off.) Let $\mathbf{E}(a)$ and $\mathbf{H}(a)$ represent the electric and magnetic fields generated by the source distributions $d\mathbf{J}(a)$ and $d\mathbf{K}(a)$, which we call the source a for simplicity. Similarly for some other source b, which generates a field at the same frequency and in the same environment. Define a complex number [the usual $\exp(\pm i\omega t)$ time convention is employed], denoted by $\langle a,b\rangle$ as follows:

$$\langle a,b\rangle=\int\int\int_V[\mathbf{E}(b)\cdot d\mathbf{J}(a)-\mathbf{H}(b)\cdot d\mathbf{K}(a)], \quad (1)$$

where the volume V contains the source a.

The reciprocity theorem[1] states that

$$\langle a,b\rangle=\langle b,a\rangle, \quad (2)$$

provided that all media are isotropic and that a and b can be contained in a finite volume.

The scalar $\langle a,b\rangle$ is a measure of the reaction (or coupling) between the sources a and b. We think of "reaction" as a physical observable like mass, length, charge, etc.: Eq. (1) is to be understood as a formula for the measure of reaction. For example, in electrostatic theory, let the source a consist of the volume distribution of charge $dq(a)$: similarly for the source b. Then we could define the static reaction (a,b) by the relation

$$(a,b)=\int\int\int\mathbf{E}(b)dq(a), \quad (3)$$

which is analogous to Eq. (1). In this case the physical observable which (a,b) represents is the resultant force exerted by a on b. In the oscillating case let the source a consist of a unit current generator connected to the terminals of some antenna. Then it follows from Eq. (1) that $\langle a,b\rangle$ is equal to the open circuit voltage generated at the antenna terminals by the source b. Again for static fields the electric field is equal to (u,a) the reaction between the given source a and an infinitesimal unit charge u placed at the point of observation.

[1] S. A. Schelkunoff, *Electromagnetic Waves* (D. Van Nostrand Publishing Company, New York, 1943), p. 477. The proof given applies here with a minor extension.

For oscillating fields the component of electric field in a particular direction is equal to $\langle u,a\rangle$, the reaction between the given source a and an infinitesimal electric dipole u, of unit moment, placed parallel to this direction at the point of observation.

The complex number $\langle a,b\rangle$ consists of the sum of products of the form $V(a)I(b)$ where $V(a)$ represents the voltage generated by a across the terminals of a current generator of strength $I(b)$. If

$$V(a)=|V(a)|\exp(i\alpha),\quad I(b)=|I(b)|\exp(i\beta),$$

then the corresponding explicit time functions which these complex numbers represent are

$$V(a,t)=|V(a)|\cos(\omega t+\alpha),\quad I(b,t)=|I(b)|\cos(\omega t+\beta),$$

and the complex number,

$$V(a)I(b)=|V(a)I(b)|\exp[i(\alpha+\beta)],$$

represents the explicit time function,

$$|V(a)I(b)|\cos(2\omega t+\alpha+\beta)$$
$$=|V(a)I(b)|[2\cos(\omega t+\alpha)\cos(\omega t+\beta)-\cos(\alpha-\beta)].$$

The first term in the square brackets is the instantaneous rate at which b works against a, and the second term is the average rate per cycle at which b works against a. Thus, $\langle a,b\rangle$ represents the instantaneous minus the average rate at which b expends energy on a. Note that if $\langle a,b\rangle=0$, then no energy is transferred from a to b at any time.

Observe that

$$\langle a,(b+c)\rangle=\langle a,b\rangle+\langle a,c\rangle, \tag{4}$$

where a, b, and c represent any three sources radiating at the same frequency in the same region. Note also that if A represents any scalar and Aa represents the source a increased in strength by the factor A, then

$$\langle Aa,b\rangle=A\langle a,b\rangle. \tag{5}$$

Before proceeding any further with the formal development let us now discuss how the concept of reaction can be used, in order to see what further developments are needed.

APPLICATIONS OF THE REACTION CONCEPT

Consider the problem of scattering by a perfectly conducting body, of surface S, which is irradiated by the source g (see Fig. 1). Let $\mathbf{J}(c)$ represent the surface distribution of electric current which is induced on the scatterer by g. The scattered field, $\mathbf{E}(c)$, is defined as the field that would be generated by $\mathbf{J}(c)$ (acting as a source) if the scatterer were absent (the total field is then the superposition of the incident and scattered fields). We postulate that if $\mathbf{J}(c)$ were known the scattered field $\mathbf{E}(c)$ could be calculated. It is known that the tangential component of $\mathbf{E}(c)$ on S is equal to minus the tangential component of the incident electric field, because the scatterer is a perfect conductor. Thus, although $\mathbf{J}(c)$ is unknown it is possible to calculate the reaction between the source $\mathbf{J}(c)$ and some known current distribution, $\mathbf{J}(a)$, on the surface S, for

$$\langle a,c\rangle=\int\int_S \mathbf{J}(a)\cdot\mathbf{E}(c)\,dS \tag{6}$$

and the tangential component of $\mathbf{E}(c)$ on S is known.

FIG. 1. A hypothetical surface S in the presence of a source g.

Suppose that we wish to calculate the "echo," i.e., the signal at g due to the scattered field. If we think of g as a unit current generator connected to the terminals of some antenna, the open circuit voltage at these terminals generated by the scattered field is equal to $\langle g,c\rangle$. Thus the problem is to calculate $\langle g,c\rangle$. Let $\mathbf{J}(a)$ represent an assumed distribution of electric current on S which we propose to adjust so that it approximates $\mathbf{J}(c)$. We would like to adjust $\mathbf{J}(a)$ so that

$$\langle g,a\rangle=\langle g,c\rangle, \tag{7}$$

for then the echo obtained by substituting $\mathbf{J}(a)$ for $\mathbf{J}(c)$ would be correct. Obviously this is too much to expect: indeed we find that Eq. (7) cannot be enforced because we cannot calculate $\langle g,c\rangle$. We can interpret Eq. (7) as the condition that the approximate source a (i.e., $\mathbf{J}(a)$) should "look" the same as the correct source c (i.e., $\mathbf{J}(c)$) to the source g, in the sense that a and c produce the same signal at g. Thus we can think of g as a "test" source which is used to test for any difference between a and c. This suggests that we regard Eq. (7) as a special case of the more general restriction

$$\langle x,a\rangle=\langle x,c\rangle, \tag{8}$$

which expresses the condition that a and c should "look" the same to an arbitrary test source x. The problem is now a matter of trying to enforce Eq. (8) for every "available" test source, i.e., every x for which $\langle x,a\rangle$ and $\langle x,c\rangle$ can be calculated. The only sources in the problem are g, c and a. We have seen that g is not "available" because $\langle g,c\rangle$ cannot be calculated and we find that c is not available because $\langle c,c\rangle$ cannot be calculated. Thus a is the only "available" test source. We therefore adjust the approximation a to satisfy the condition

$$\langle a,a\rangle=\langle a,c\rangle \tag{9}$$

and use the value of a so obtained in place of the correct source c.

To carry out the calculation of the echo we assume some current distribution $\mathbf{J}(a)$ whose level can be adjusted, i.e., let

$$\mathbf{J}(a)=U\mathbf{J}(u),\quad\text{or}\quad a=Uu, \tag{10}$$

where $\mathbf{J}(u)$ is fixed and U is an adjustable constant. Substituting for a in Eq. (9) gives

$$U=\langle u,c\rangle/\langle u,u\rangle. \tag{11}$$

Now the echo $\sim-\langle c,g\rangle$, where

$$\begin{aligned}-\langle c,g\rangle&=\int\int_S \mathbf{J}(c)\cdot\mathbf{E}(c)dS\\&=\langle c,c\rangle\doteq\langle a,a\rangle=U^2\langle u,u\rangle=\langle u,c\rangle^2/\langle u,u\rangle\\&=\left[\int\int_S \mathbf{J}(u)\cdot\mathbf{E}(c)dS\right]^2\Big/\int\int_S \mathbf{J}(u)\cdot\mathbf{E}(u)dS.\end{aligned} \tag{12}$$

In Eq. (12) $\mathbf{J}(u)$ represents the assumed current distribution, $\mathbf{E}(u)$ represents the electric field generated by $\mathbf{J}(u)$ (in the absence of the scatterer), and $\mathbf{E}(c)$ represents the tangential component at S of the incident electric field.

The approximation can be improved by starting from an assumed distribution $\mathbf{J}(a)$ which contains a number of adjustable constants. Thus, let

$$a=Ll+Mm+\cdots, \tag{13}$$

where L, M, $\cdots$, represent adjustable constants and, l, m, $\cdots$ represent fixed source distributions which are assumed. The problem is to find the linear combination of l, m, $\cdots$, denoted by a, which best approximates the correct source $\mathbf{J}(c)$, denoted by c. Here we can enforce the conditions:

$$\begin{aligned}\langle a,l\rangle&=\langle c,l\rangle,\\\langle a,m\rangle&=\langle c,m\rangle,\\&\cdots\end{aligned} \tag{14}$$

which ensure that a and c "look" the same to l, m, $\cdots$. If the assumed set of source distributions l, m, $\cdots$ constitute a complete orthogonal set, the equations (14) represent the condition that a and c are identical in every respect. Substituting for a from (13) in (14) gives the following equations for the constants:

$$\begin{aligned}L\langle l,l\rangle+M\langle m,l\rangle+\cdots&=\langle c,l\rangle,\\L\langle l,m\rangle+M\langle m,m\rangle+\cdots&=\langle c,m\rangle,\\&\cdots\end{aligned} \tag{15}$$

In terms of a matrix notation, the constants L, M, $\cdots$ are given explicitly by

$$\begin{bmatrix}L\\M\\\cdot\\\cdot\\\cdot\end{bmatrix}=\begin{bmatrix}\langle l,l\rangle & \langle l,m\rangle & \cdots\\\langle m,l\rangle & \langle m,m\rangle & \cdots\\\cdot & \cdot & \\\cdot & \cdot & \\\cdot & \cdot & \end{bmatrix}^{-1}\begin{bmatrix}\langle l,c\rangle\\\langle m,c\rangle\\\cdot\\\cdot\\\cdot\end{bmatrix}. \tag{16}$$

By substituting for L, M, $\cdots$ in (13), the approximate value of the echo is given by (see Eq. (12)):

$$\begin{aligned}\langle a,a\rangle=\langle a,c\rangle=(&\langle l,c\rangle\langle m,c\rangle\cdots)\\&\times\begin{bmatrix}\langle l,l\rangle & \langle l,m\rangle & \cdots\\\langle m,l\rangle & \langle m,m\rangle & \cdots\\\cdot & \cdot & \\\cdot & \cdot & \\\cdot & \cdot & \end{bmatrix}^{-1}\begin{bmatrix}\langle l,c\rangle\\\langle m,c\rangle\\\cdot\\\cdot\\\cdot\end{bmatrix}.\end{aligned} \tag{17}$$

These results can also be obtained by means of the variational technique. For example, let δa represent a slight change of the source distribution represented by a. If both a and $a+\delta a$ satisfy Eq. (9), then $2\langle a,\delta a\rangle=\langle a,\delta a\rangle+\langle\delta a,a\rangle=\langle\delta a,c\rangle$ to the first order. If δa represents a slight change about the correct distribution c, we can substitute c for a in this equation and thus obtain $\langle\delta a,c\rangle=0$. Hence, the expressions $\langle a,a\rangle$ and $\langle a,c\rangle$ are stationary for variations of a about c, if a satisfies Eq. (9), i.e., if $a=u\langle u,c\rangle/\langle u,u\rangle$ [see Eqs. (10) and (11)]. Thus the expression $x=\langle a,c\rangle=\langle a,a\rangle=\langle u,c\rangle^2/\langle u,u\rangle$ is stationary for variations of the assumed distribution $\mathbf{J}(u)$ about the correct distribution $\mathbf{J}(c)$, and Eqs. (14) and (15) can be obtained by setting $\partial x/\partial L=0$, $\partial x/\partial M=0$, etc. However, the fact that an expression is stationary for variations of an assumed distribution about the correct distribution does not justify the assumption that it will yield the "best" approximation when the assumed distribution is completely arbitrary. The reaction approach does show that the approximation is the best in a physical sense, i.e., in the sense that the approximate source "looks" the same as the correct source to any source in the problem which can be used for such an observation. More precisely, the reaction between the approximate source and every available test source is correct, it being understood that a test source is "available" if its reaction with the correct source can be calculated. Note that this comparison of the variational method with the reaction method is, so far, based on the specific problem of scattering by a perfect conductor. There are other problems (some of which we consider later) where a number of different approximations can be obtained from the variational method, and there is no way of deciding which approximation is best. In the reaction approach such problems yield an excessive number of test sources, i.e., the number of independent test sources exceeds the number of adjustments which can be made in the approximation, so that it is not possible to make the reaction with every test source correct. In this case it is necessary to decide what selection of the available test sources is most likely to yield the best approximation. From the physical point of view the answer is clearly that selection which most nearly represents the actual physical observation which we are trying to approximate. The physical approach has the added advantages of being general (whereas the stationary formulation has to be established for each specific problem), and of providing a simple understanding of the type of approximation

which is being used. In short, the fundamental advantage of the reaction method is its conceptual simplicity which leads directly to results which might not be uncovered by the variational approach because of the complexity of the mathematical formulation. These points are illustrated by the examples which follow.

TRANSMISSION CALCULATIONS

The problem of scattering by a perfect conductor can be used to illustrate the formulation of transmission problems. We are now interested in the signal received at an arbitrary point whereas in the echo problem the point of reception was at the given source g. As before the total field is represented as the sum of contributions from g and c (the induced electric current distribution on S) radiating as if the scatterer were absent. The contribution from g can be calculated easily since g is given. We therefore put up a source h at the point of observation (see Fig. 2) and the problem is to calculate the reaction $\langle c,h\rangle$ evaluated in the absence of the scatterer. Let the notation be as follows: c generates the same field as g inside of S (as before), d generates the same field as h inside of S, a is the approximation for c (as before), b is the approximation for d. The sources a, b, c, and d are all distributions of electric current on S, and all sources radiate as if the scatterer were absent. We therefore adjust the approximations a and b to satisfy the conditions:

$$\langle a,x\rangle=\langle c,x\rangle, \tag{18}$$

and

$$\langle b,y\rangle=\langle d,y\rangle, \tag{19}$$

where x and y represent any test sources inside of S. The available test sources are represented by $x=a$, $x=b$, $y=a$ and $y=b$. Since Eq. (18) cannot be satisfied for both values of x, we have to decide which value is likely to give the better approximation: similar remarks apply to Eq. (19). Now the quantity which we are trying to approximate is $\langle c,h\rangle$ where

$$\langle c,h\rangle=\int\int_S \mathbf{J}(c)\cdot\mathbf{E}(h)dS = \int\int_S \mathbf{J}(c)\cdot\mathbf{E}(d)dS=\langle c,d\rangle. \tag{20}$$

To approximate $\langle c,d\rangle$ we replace c by its approximation a, or d by b, or both. Thus there are three possible approximations which are represented by $\langle a,d\rangle$, $\langle c,b\rangle$ and $\langle a,b\rangle$. We see that these are all the same if we

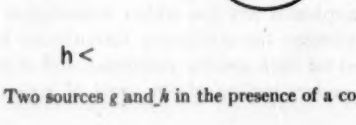

FIG. 2. Two sources g and h in the presence of a conductor.

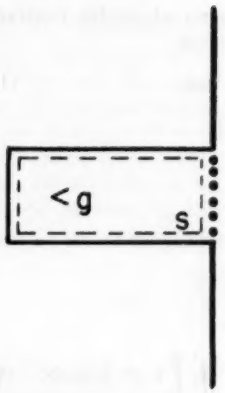

FIG. 3. A source g radiating through a waveguide.

choose $x=b$ and $y=a$ which is therefore the best choice.

An explicit formula for $\langle c,d\rangle$ is obtained by setting

$$a=Uu \quad \text{and} \quad b=Vv, \tag{21}$$

where U and V are adjustable constants. Proceeding as before [see Eq. (10)], we obtain

$$\langle c,d\rangle\simeq\langle c,v\rangle\langle d,u\rangle/\langle u,v\rangle, \tag{22}$$

where u and v represent assumed electric current distributions. In terms of integrals over S, Eq. (22) becomes

$$\langle c,d\rangle\simeq\left[\int\int_S \mathbf{E}(g)\cdot\mathbf{J}(v)dS\right]\left[\int\int_S \mathbf{E}(h)\cdot\mathbf{J}(u)dS\right]\Big/ \int\int_S \mathbf{E}(u)\cdot\mathbf{J}(v)dS, \tag{23}$$

where $\mathbf{J}(u)$ and $\mathbf{J}(v)$ are the current distributions which we assume to approximate the current distributions induced on the scatterer by g and h, respectively.

IMPEDANCE CALCULATIONS

Suppose that the given source g radiates into space through a length of uniform wave guide as shown in Fig. 3. This represents a type of problem which has been treated successfully by means of the variational approach.[2]

We postulate that it is impractical to calculate the field which is radiated through the aperture (the aperture is shown as the line of dots in Fig. 3), but that it is practical to calculate the field (in the waveguide) that would be obtained if the aperture were covered with a conducting plate.

Let $\mathbf{J}(c)$ represent the electric current distribution that would be induced by g on a conducting plate covering the aperture. Let $\mathbf{E}(g,1)$ represent the field generated by g with the plate in position, $\mathbf{E}(g,2)$ represent the field generated by g with the plate removed, and $\mathbf{E}(c,2)$ the field that would be generated

[2] *Waveguide Handbook*, edited by N. Marcuvitz (McGraw-Hill Book Company, Inc., New York, 1951).

by $\mathbf{J}(c)$ (acting as a source) with the plate removed. Then,

$$\mathbf{E}(g,1)=\mathbf{E}(g,2)+\mathbf{E}(c,2), \tag{24}$$

for points in the wave-guide region (inside of the dashed curve S shown in Fig. 3). If g consists of a unit current generator connected to a pair of terminals, then it follows from (24) that

$$Z_1=V_1=V_2+\langle c,g\rangle=Z_2+\langle c,g\rangle, \tag{25}$$

where V_1 and V_2 are the voltages at these terminals with and without the plate respectively, Z_1 and Z_2 are the corresponding impedances, and $\langle c,g\rangle$ is evaluated with the plate removed. The problem is to calculate an approximation for Z_2, assuming that Z_1 is known. For example, suppose that the wave-guide structure consists of a biconical horn as illustrated in Fig. 4. The source g consists of a unit current generator connected to the input. Then

$$Z_1=-i\mu^{\frac{1}{2}}\epsilon^{-\frac{1}{2}}\pi^{-1}\log(\cot\alpha/2)\tan\omega l\mu^{\frac{1}{2}}\epsilon^{-\frac{1}{2}},$$
$$\mathbf{J}(c)=[2\pi l\cos\omega l\mu^{\frac{1}{2}}\epsilon^{\frac{1}{2}}\sin\theta]^{-1}\boldsymbol{\theta},$$

where l and θ are given in Fig. 4, ω represents the frequency, μ and ϵ represent the permeability and inductive capacity of the medium inside of S, and $\boldsymbol{\theta}$ represents a unit vector in the spherical coordinate system shown in Fig. 4.

The specific example which we have chosen to illustrate impedance calculations is representative of the general problem in which g is inside of as illustrated in Fig. 5. It is essentially the same as the scattering problem in which g is outside of S. Here, as in the scattering problem, $-\mathbf{J}(c)$ generates the same field as g on the source-free side of S. Here, $\langle g,c\rangle$ cannot be calculated because tangential $\mathbf{E}(g)$ at S is unknown, whereas $\langle g,c\rangle$ cannot be calculated in the scattering problem because $\mathbf{J}(c)$ is unknown. In this problem we therefore assume some approximation for $\mathbf{E}(c)$, the tangential component of electric field in the aperture (or over S in the more general terminology). We postulate that it is possible to calculate $\mathbf{E}(a)$, the field which fits this assumed distribution of tangential $\mathbf{E}(c)$ on both sides of S. By definition the tangential component of $\mathbf{E}(a)$ at S is continuous but the tangential component of $\mathbf{H}(a)$ obviously is not continuous. In short, the field $\mathbf{E}(a)$ is generated by a certain distribution of electric currents $\mathbf{J}(a)$ on S which can be calculated from the assumed distribution of tangential electric field. If this assumed distribution were correct, then $\mathbf{J}(a)$ would turn out to be identical to $\mathbf{J}(c)$. We can see now that the impedance problem is formally identical to the scattering problem, with the modification that the approximate source a is now required to look the same as the correct source c to a test source x which is outside of S. Thus Eq. (9) applies again:

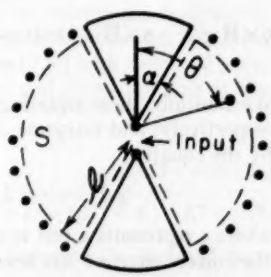

FIG. 4. A biconical horn.

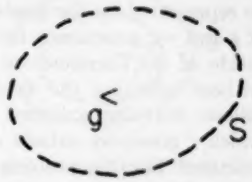

FIG. 5. A source g inside of a closed surface S.

$$\langle a,a\rangle=\langle a,c\rangle. \tag{9}$$

Instead of Eq. (10), we now put

$$\mathbf{E}(a)=U\mathbf{E}(u), \tag{10a}$$

where $\mathbf{E}(u)$ represents the assumed distribution of tangential $\mathbf{E}(c)$ over S and U is an adjustable constant. Equation (10a) is equivalent to Eq. (10) because it implies that

$$a=Uu, \tag{10}$$

as before. The approximation for $\langle c,g\rangle$ given by (12) also applies except that we express $\langle u,c\rangle$ in the form $\iint_S\mathbf{E}(u)\cdot\mathbf{J}(c)dS$. Thus, the approximation for the impedance obtained from Eq. (25) (replacing c by a) is

$$Z_2=Z_1-\langle u,c\rangle^2/\langle u,u\rangle. \tag{26}$$

The problem of transmission through the aperture can be treated by placing a test source h at the point of observation outside of S and proceeding as in Eqs. (18)–(23).

SCATTERING BY A DIELECTRIC

The problem of scattering by a dielectric brings out some interesting features which have not been encountered up to this point. Let the given source g radiate in the presence of a dielectric scatterer of surface S, as in Fig. 1. The scattered field is again defined as the difference between the fields generated by g with and without the scatterer. The problem is to find a source, a, which generates a field outside of S which is approximately equal to the scattered field (and such that it is possible to calculate the field generated by a).

Let $\mathbf{E}(g,1)$ represent the field generated by g in the presence of the scatterer, and

$$\mathbf{J}(c)=\mathbf{n}\times\mathbf{H}(g,1),\quad \mathbf{K}(c)=\mathbf{E}(g,1)\times\mathbf{n}, \tag{27}$$

where $\mathbf{n}$ represents a unit vector normal to S pointing inwards. The surface distributions of electric and magnetic current $\mathbf{J}(c)$ and $\mathbf{K}(c)$, are the equivalent currents of Schelkunoff.[3] Let the combination of $\mathbf{J}(c)$ and $\mathbf{K}(c)$

[3] S. A. Schelkunoff, Phys. Rev. **56**, 308 (1939).

be represented by the symbol c. Then the combination of g and $-c$ generates a field which is zero everywhere inside of S. Therefore we can remove the scatterer without affecting the field generated by $(g-c)$. It follows that the scattered field is equal to the field which c generates outside of S, in the absence of the scatterer. Thus the problem is to find an approximation for c. Observe that c generates the same field as g inside of S, regardless of the medium inside of S. Thus we require that the approximation for c, represented by a, should look the same as g to a test source x inside of S, and for the purpose of simplifying calculations we can perform this test in "free space" (see Fig. 6).

At this point it is desirable to extend the notation [introduced in Eq. (24)] in which a number represents the environment, as follows. Let $\langle p,1,q\rangle$, $\langle p,2,q\rangle$, and $\langle p,3,q\rangle$ represent the reaction between sources p and q in the presence of the scatterer, in free-space, and in an infinite homogeneous dielectric medium, respectively. Thus the test illustrated by Fig. 6 is represented by the equation

$$\langle g,2,x\rangle=\langle a,2,x\rangle. \tag{28}$$

Observe that c generates zero field outside of S, in the presence of the scatterer. The region outside of S can therefore be filled with the same material as the inside of S without affecting the result. We therefore require a to satisfy the requirement,

$$\langle a,3,y\rangle=0, \tag{29}$$

where y represents any test source outside of S (see Fig. 7).

The coarsest approximation is obtained by representing a in the form

$$a=Ll+Mm, \tag{30}$$

where l and m represent the assumed distributions of electric and magnetic current on S respectively, and L and M are adjustable constants. Then the possible choices of x and y are represented by $x=l$, $x=m$, $x=a$, $y=l$, $y=m$, and $y=a$ (only four of which are independent). Observe that if we set $x=l$ in the expression $\langle a,2,x\rangle$, we must interpret this as the limit obtained as l approaches a from the inside of S as illustrated in Fig. 8. Similarly, the substitute for y must be taken just outside of S. An expression of the form $\langle a,2,a\rangle$ is evaluated by imagining two sources a slightly displaced from each other in the manner of Fig. 8. Considering the symmetry of Eqs. (28) and (29), the obvious choice appears to be $x=a$ and $y=a$. A further point in support of this choice is the fact that the echo $=\langle g,2,c\rangle=\langle c,2,c\rangle$ is approximated by $\langle c,2,a\rangle$ or $\langle a,2,a\rangle$ and the choice $x=a$ makes these two results the same. The choice $y=a$ is also supported by the fact that if a were correct (i.e., if $y=c$), its radiation would be confined to the region occupied by the source under test (which is also a), thus producing, in a sense, the maximum irradiation of the source under test.

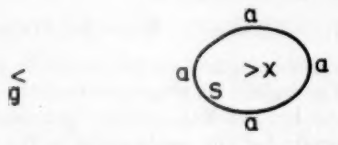

FIG. 6. A test source x set up to detect the difference between sources a and g.

Substituting $x=a$ in Eq. (28) and $y=a$ in Eq. (29) gives the following equations for the constants L and M:

$$L\langle g,2,l\rangle+M\langle g,2,m\rangle=L^2\langle l,2,l\rangle+LM\langle(l),2,m\rangle+LM\langle l,2,(m)\rangle+M^2\langle m,2,m\rangle, \tag{31}$$

$$0=L^2\langle l,3,l\rangle+LM\langle(l),3,m\rangle+LM\langle l,3,(m)\rangle+M^2\langle m,3,m\rangle, \tag{32}$$

where the notation (l) in $\langle(l),2,m\rangle$ indicates that l is just inside of m (see Fig. 8), e.g.,

$$\langle(l),2,m\rangle=\int\int_S \mathbf{J}(l)\cdot\mathbf{E}(m,2,\text{internal})dS, \tag{33}$$

where

$$\mathbf{n}\times[\mathbf{E}(m,2,\text{internal})-\mathbf{E}(m,2,\text{external})]=\mathbf{K}(m) \quad [\text{see Eq. (27)}]. \tag{34}$$

The approximation for the echo is then given by substituting a for c in $\langle g,2,c\rangle$.

It can be shown that the formula for the echo obtained in this way is stationary for variations of the assumed distribution of electric current $\mathbf{J}(l)$ and magnetic current $\mathbf{K}(m)$ about the correct distribution. The interesting point is that a number of stationary formulas for the echo can be derived, all of which are based on assumed distributions $\mathbf{J}(l)$ and $\mathbf{K}(m)$ and involve the same "free space" calculations, but differ in the way that the calculations are combined. Here is a case where the physical approach through the reaction concept leads to a result which probably would not have been uncovered by the variational technique, although, once the result has been established, it is possible to see how it could have been obtained by means of a variational approach.

Another approach is to set down the equations for continuity of tangential $\mathbf{E}$ and $\mathbf{H}$ which are:

$$\begin{aligned}\mathbf{n}\times\mathbf{E}(g,2)-\mathbf{n}\times\mathbf{E}(c,2,\text{external})&=\mathbf{n}\times\mathbf{E}(c,3,\text{internal}),\\ \mathbf{n}\times\mathbf{H}(g,2)-\mathbf{n}\times\mathbf{H}(c,2,\text{external})&=\mathbf{n}\times\mathbf{H}(c,3,\text{internal}).\end{aligned} \tag{35}$$

We multiply these equations by tangential $\mathbf{H}$ and $\mathbf{E}$, respectively, and integrate over S. This is represented by the equation

$$\langle g,2,z\rangle-\langle(a),2,z\rangle=\langle a,3,(z)\rangle, \tag{36}$$

where z represents a test source distributed over S and the correct source c has been replaced by the approxi-

mate source a. Here it is necessary to use every available test source, i.e., $z=l$ and $z=m$ in order to evaluate L and M. We then obtain two equations which are essentially the same as those used by Crowley[4] for a certain class of impedance calculations. The formula for the echo obtained from Eq. (36) is stationary but it is different from that given by Eqs. (28) and (29). An important point of difference is that the approximation given by Eq. (36) does not give the same value for the two possible approximations for the echo, $\langle g,2,a\rangle$ and $\langle a,2,a\rangle$.

There is a simple connection between Eqs. (28), (29), and (36). It is obtained from the relation

$$\langle(a),2,b\rangle-\langle a,2,(b)\rangle=\langle(a),3,b\rangle-\langle a,3,(b)\rangle, \qquad (37)$$

which we shall establish [see Eq. (47)]. In Eq. (37), a and b represent any two sources, and 2 and 3 represent any two environments. Thus, Eq. (36) can be written in the form

$$\langle g,2,z\rangle=\langle a,2,(z)\rangle+\langle(a),3,z\rangle. \qquad (38)$$

Bearing in mind that in Eqs. (28) and (29) x is inside of S and y is outside of S, we see that Eq. (36) is satisfied if Eq. (28) is satisfied for $x=z$ and Eq. (29)

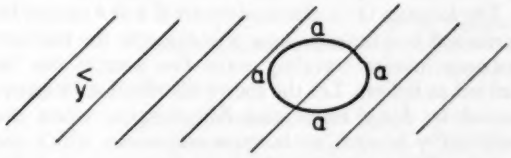

FIG. 7. A test source y set up to detect the external field from a.

for $y=z$. In this sense, Eqs. (28) and (29) embody the information contained in Eq. (36). We obtain different formulas for the echo because we choose to enforce Eq. (36) for two different values of z, $z=l$ and $z=m$, whereas we enforce Eqs. (28) and (29) for $x=a$ and $y=a$. To put it another way, if $x=y=z=a$ then the same value of a is obtained from any two of the three equations (28), (29), and (36). It is interesting to note that the value of $\langle g,2,a\rangle$ (the echo) obtained from (36) is stationary provided Eq. (36) is enforced for the single value of z, $z=a$. On the other hand, if (28) and (29) are enforced for $x=a$ and $y=a$, then all three quantities $\langle g,2,a\rangle$, $\langle a,2,a\rangle$ and $\langle a,3,a\rangle$ are stationary.

To give a specific comparison between these two approaches, the echo from an infinite plane dielectric slab for a plane wave at normal incidence, has been computed from Eqs. (28) and (29) with $x=a$ and $y=a$, and from Eq. (36) with $z=l$ and $z=m$. We note at the

FIG. 8. The source l just inside of the source a.

outset that the results of this comparison must be regarded as suggestive rather than conclusive for not only is the example specific, as opposed to general, but the assumed distribution is also specific. Note also that the assumed distribution, which is usually a function of position, in this case consists of four discrete values corresponding to the front and the back faces of the slab. Thus, if our approximation contains four independent adjustable constants, any set of tests which determines them uniquely is bound to yield the correct solution.

The two methods were compared on the basis of the type of approximation represented by Eq. (30), which contains two adjustable constants. A crude approximation is obtained by assuming equal and opposite electric and magnetic currents on the front and back faces, e.g., the distributions l and m can be represented by the pair of values $(+1,-1)$. For thin slabs and low dielectric constants both methods give an echo which is four times the correct value, and for low dielectric constants, the maximum echo, as a function of slab thickness, is about twice the correct value. The situation here is that the differences between the two methods are overshadowed by the crudeness of the assumed distribution, which emphasizes the overriding importance of starting from an assumed distribution which is nearly correct. A better approximation is obtained by assuming that l and m are represented by the distribution $(+1,-\exp it)$ where t represents the electrical thickness, i.e., $t=\omega\mu^{\frac{1}{2}}\epsilon^{\frac{1}{2}}d$, where $d=$thickness of slab and μ and ϵ are the constants of the dielectric. This is the type of assumption used in physical optics and neglects reflection from the back face. For an incident field of one volt per meter the following formulas are obtained. The correct solution is

$$|\langle g,2,c\rangle|=\frac{2K|1-\exp 2it|}{\eta_0|1-K^2\exp 2it|}. \qquad (39)$$

The approximation given by Eqs. (28) and (29) is

$$|\langle g,2,a\rangle|=\frac{2K|1-\exp(it/1+K)|^2}{\eta_0|1-2\exp(2it/1+K)+\exp 2it|}. \qquad (40)$$

The approximation given by Eq. (36) is

$$|\langle g,2,a\rangle|=\frac{2K|1-\exp it/1+K|^2|1-\exp 2it|}{\eta_0|1-2\exp(2it/1+K)+\exp(4it/1+K)-K^2\exp(4it)+2K^2\exp[2it(2+K)/1+K]-K^2\exp(4it/1+K)|}. \qquad (41)$$

[4] T. H. Crowley, "Variational Impedance Calculations," Antenna Laboratory Report 478-5, Ohio State University (unpublished).

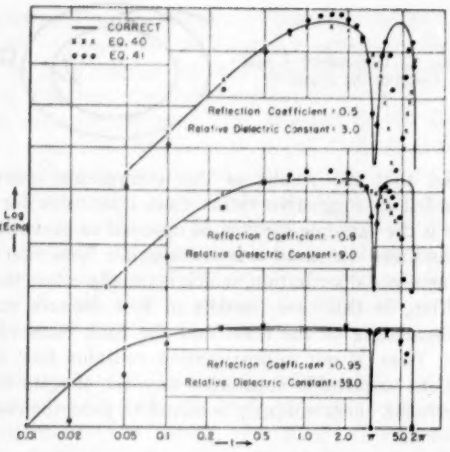

FIG. 9. The echo from a dielectric slab *versus* thickness.

In Eqs. (39), (40), and (41), K represents the reflection coefficient for $t=\infty$; i.e.,

$$K=(\epsilon_r-1)/(\epsilon_r+1), \tag{42}$$

where ϵ_r = relative dielectric constant of the dielectric.

These results are plotted in Fig. 9. It can be seen that the error in Eq. (40) is insignificant for $t\leqslant 1$ but becomes progressively worse for larger values of t until there is practically no correlation with the correct result. Equation (41) is in error for small values of t by the factor $(K+1)$, but, unlike Eq. (40), it is correct in the vicinity of $t=\pi$, although otherwise it shows practically no correlation with the correct result for large values of t. The behavior at $t=\pi$ is interesting because the assumed distribution is correct at this value of t, and therefore both (40) and (41) might be expected to reduce to the correct result at $t=\pi$. The failure of Eq. (40) at $t=\pi$ is due to the fact that the external field generated by l or m in a homogeneous dielectric is zero. Thus, while Eq. (29) is certainly satisfied it does not yield any information about the constants L and M, i.e., for $t=\pi$ the test represented by Eq. (29) turns out to be trivial for the particular assumed distribution under consideration. This suggests that instead we should put the test source y inside of S, but then we find that in order to arrive at an enforceable condition we are brought back to Eq. (36).

FURTHER PROPERTIES OF THE REACTION

The foregoing example of scattering by a dielectric shows the need for a more elaborate formulation to handle cases where Eq. (1) is inadequate. When a and b [see Eq. (1)] consist of surface distributions over the same surface S the field at a due to b is discontinuous and consequently the integral in Eq. (1) is not defined. In this case there are two possible values for the reaction which are obtained by imagining that a and b are slightly separated. If a is imagined to be just outside of b, we have

$$\langle a,(b)\rangle=\int\int_S[\mathbf{J}(a)\cdot\mathbf{E}(b,\text{external})-\mathbf{K}(a)\cdot\mathbf{H}(b,\text{external})]dS; \tag{43}$$

and for b just outside of a, we have

$$\langle(a),b\rangle=\int\int_S[\mathbf{J}(a)\cdot\mathbf{E}(b,\text{internal})-\mathbf{K}(a)\cdot\mathbf{H}(b,\text{internal})]dS. \tag{44}$$

It can be shown[5] that

$$\langle a,(b)\rangle=\langle(b),a\rangle, \tag{45}$$

under the same conditions as are required for the usual reciprocity theorem [see Eq. (2)]. It follows that

$$\langle(a),b\rangle-\langle a,(b)\rangle=\int\int_S[\mathbf{J}(a)\times\mathbf{K}(b)-\mathbf{J}(b)\times\mathbf{K}(a)]\cdot\mathbf{n}dS. \tag{46}$$

Thus

$$\langle(a),1,b\rangle-\langle a,1,(b)\rangle=\langle(a),2,b\rangle-\langle a,2,(b)\rangle, \tag{47}$$

where 1 and 2 represent any two environments.

The formula (1) is also inadequate if a or b cannot be contained in a finite volume. For example the reaction between infinite traveling wave line sources can be defined as follows. Let the source distribution be represented by $\mathbf{J}(x,y)\exp\gamma z$ and $\mathbf{K}(x,y)\exp\gamma z$, where the constant γ is such as to represent waves which are attenuated as they travel along the z axis, and the medium is independent of z but is otherwise heterogeneous. Then

$$\langle a,b\rangle=\int\int_\Sigma[\mathbf{J}(a,x,y)\sigma\mathbf{E}(b,x,y)+\mathbf{K}(a,x,y)\sigma\mathbf{H}(b,x,y)]dxdy, \tag{48}$$

where σ represents the matrix

$$\sigma=\begin{bmatrix}1&0&0\\0&1&0\\0&0&-1\end{bmatrix},$$

and the surface Σ contains all sources.[6] This formula differs from Eq. (1) but can be applied in the same way: it represents the same physical observable. Modifications similar to Eqs. (43) and (44) apply if a and b are at the same place.

Returning to the case where a and b are at different places, let S represent any surface which separates a and b (e.g., all parts of a are inside of S and all parts of b are outside of S). Then

$$\langle a,b\rangle=\int\int_S[\mathbf{H}(a)\times\mathbf{E}(b)-\mathbf{H}(b)\times\mathbf{E}(a)]\cdot\mathbf{n}dS, \tag{49}$$

[5] T. H. Crowley, J. Appl. Phys. **25**, 119 (1954).
[6] V. H. Rumsey, J. Appl. Phys. **24**, 1358 (1953).

where $\mathbf{n}$ points away from a towards b. This illustrates another aspect of the reaction concept, for Eq. (49) states that the flux of the vector in brackets is conserved (provided S separates a and b), and $\langle a,b\rangle$ represents the conserved property. This principle of conservation is self-evident from a physical point of view, for Eq. (42) can be interpreted as stating that the reaction between a and b is the same as the reaction between a and the equivalent sources $\mathbf{n}\times\mathbf{E}(b)=\mathbf{K}(b)$ and $\mathbf{H}(b)\times\mathbf{n}=\mathbf{J}(b)$ which generate the same field as b at a. It is apparent that the reaction between a and b is the same as the reaction between a and any source which produces the same field as b at a.

The reaction concept can be extended to anisotropic media by using a more general form of the reciprocity theorem (which was brought to the author's attention by M. H. Cohen). Let $[\mathbf{E}(a),\mathbf{H}(a)]$ represent the field generated by the source distribution $[d\mathbf{J}(a),d\mathbf{K}(a)]$ as before. Let $[\mathfrak{E}(a),\mathfrak{H}(a)]$ be the field generated by the same source when all media are replaced by the corresponding media whose macroscopic constants μ (permeability), ϵ (dielectric constant), and σ (conductivity), are the transposes of the original constants. [If $\tilde{\epsilon}$ represents the transpose of ϵ, and $\mathbf{A}$ and $\mathbf{B}$ represent any two vectors, then the scalar product $\mathbf{A}\cdot(\epsilon\mathbf{B})\equiv\mathbf{B}\cdot(\tilde{\epsilon}\mathbf{A})$]. Then the formula for the reaction is

$$\langle a,b\rangle=\int\int\int[\mathbf{E}(b)\cdot d\mathbf{J}(a)-\mathbf{H}(b)\cdot d\mathbf{K}(a)], \quad (50)$$

subject to the same conditions as Eq. (1) except that the media need not be isotropic.

ACKNOWLEDGMENT

It is a pleasure to acknowledge many helpful discussions with T. H. Crowley, and the partial support of a contract between the Signal Corps and the Ohio State University Research Foundation.

PHYSICAL REVIEW VOLUME 94, NUMBER 6 JUNE 15, 1954

Point Source Kernel for Diffusion with Small-Angle Scattering

W. E. Drummond and C. S. Gardner
Livermore Research Laboratory, California Research and Development Company, Livermore, California

(Received January 18, 1954)

Analytical expressions are derived for the particle flux from a point source which emits particles with an angular distribution $(1/\pi\beta)\exp[-\theta^2/\beta]$. The emission is into an infinite medium characterized by a strongly forward differential scattering cross section which can be approximated by a Gaussian $\Sigma(\theta)=(\Sigma/\pi\alpha)\exp[-\theta^2/\alpha]$, and in which all cross sections are energy independent. In particular, an asymptotic expression is obtained for large Σr, *viz.*

$$\phi(r,\theta)\sim\frac{\exp[-(\Sigma_t-\Sigma)r]}{\pi r^2(\beta+\frac{1}{2}\alpha\Sigma r)}\exp\left\{-\frac{\theta^2}{\beta+\frac{1}{2}\alpha\Sigma r}\right\}.$$

INTRODUCTION

A DIFFERENTIAL scattering cross section which has a strong forward scattering peak can in some cases be approximated by a Gaussian, $\sigma(\theta)=[\sigma/(\pi\alpha)]\times\exp[-\theta^2/\alpha]$. This approximation is physically realized in several different cases, among which are the differential Compton scattering cross section for γ rays and the differential scattering cross section of high Z materials for very high-energy neutrons ($E>100$ Mev).

It is the purpose of this paper to show that under the small-angle approximation, $\theta^2\ll1$, for the energy-independent case an expression can be derived for the particle flux at x, y, z, from a point source emitting particles with an angular distribution $[1/\pi\beta]\exp[-\theta^2/\beta]$ into an infinite medium which is characterized by a total cross section, Σ_t, and a differential scattering cross section, $\Sigma(\theta)=[\Sigma/(\pi\alpha)]\exp[-\theta^2/\alpha]$. It will further be shown that an analytic expression for the distribution function at a distance z from an infinite plane source can be derived.

SMALL-ANGLE APPROXIMATION

The differential elastic scattering cross section of several materials has been measured for 83-Mev neutrons[1] and for 300-Mev neutrons.[2] The experimental results can be easily fitted by a Gaussian $[\sigma/\pi\alpha]\times\exp[-\theta^2/\alpha]$. The Gaussian character of the scattering is also displayed by the "opaque" theory of scattering. The "opaque" model gives an angular dependence $[J_1(KR\theta)/\theta]^2$ which upon expansion in a power series gives, neglecting terms in θ^4 and higher powers,

$$[\tfrac{1}{2}KR]^2[1-\tfrac{1}{2}(KR\theta)^2]\sim[\tfrac{1}{2}KR]^2\exp[-\tfrac{1}{2}(KR\theta)^2].$$

The total cross section for neutrons of >200 Mev seems to be roughly geometric and therefore independent of energy. Thus, considering the total cross section to be constant and the differential scattering

[1] Bratenahl, Fernbach, Hildebrand, Leith, and Moyer, Phys. Rev. **77**, 597 (1950).
[2] W. P. Ball, University of California Radiation Laboratory Report 1938 (unpublished).

cross section to be $[\sigma/\pi\alpha]\exp[-\theta^2/\alpha]$ seem to be valid assumptions for neutrons in this energy region.

For the case of Compton scattering, if one defines $\epsilon=E/mc^2$, the photon energy after collision, ϵ, is related to the photon energy before collision, ϵ', by

$$\epsilon=\epsilon'/[1+\epsilon'(1-\cos\theta)],$$

where θ is the angle of scattering. The differential cross section for Compton scattering is given by the Klein-Nishina formula;

$$\sigma(\theta)=(r_0^2/2)(\epsilon/\epsilon')^2[(\epsilon'/\epsilon)+(\epsilon/\epsilon')-\sin^2\theta],$$

where $r_0=e^2/mc^2$. For small-angle scattering, $\theta^2\ll 1$, $\epsilon\cong\epsilon'$, $\sigma(\theta)$ may be written as

$$\sigma(\theta)=\tfrac{1}{2}r_0^2[1/(1+\tfrac{1}{2}\epsilon\theta^2)]\{1+\tfrac{1}{2}(\epsilon\theta^2)+[1/(1+\tfrac{1}{2}\epsilon\theta^2)]-\theta^2\}$$
$$\cong r_0^2[1-(\epsilon+\tfrac{1}{2})\theta^2]\cong r_0^2\exp[-(\epsilon+\tfrac{1}{2})\theta^2].$$

Consider the following problem: given a unit point source at $x=y=z=0$ with angular distribution $(\pi\beta)^{-1}\exp(-\theta^2/\beta)$, where θ is the angle with the z axis. Assume that the particles from the source enter an infinite medium characterized by a total cross section Σ_t and a macroscopic differential scattering cross section $\Sigma(\theta)=(\Sigma/\pi\alpha)\exp[-\theta^2/\alpha]$.

The problem is to compute the flux/cm^2 through a plane $z=$constant at a point (x, y, z).

POINT-SOURCE ENERGY-INDEPENDENT CROSS SECTIONS

Since a one-velocity model is used, one can represent the vector velocity of a particle by a point on the surface of a unit sphere. The x and y components of the velocity, ξ, η, can then be represented by the projections

$$\xi=\sin\theta\cos\phi, \quad \eta=\sin\theta\sin\phi. \tag{1}$$

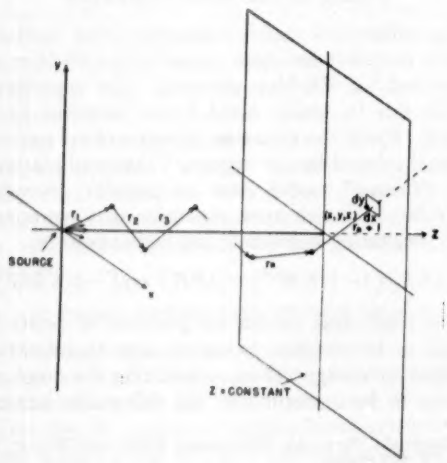

FIG. 1. Path of particle from source to element $dxdy$ in plane $z=$constant.

One finds then that $\sin^2\theta=\xi^2+\eta^2$. Using the approximation that $\theta^2\ll 1$, one then obtains

$$\theta^2\cong\xi^2+\eta^2, \quad d\Omega=\sin\theta d\theta d\phi\cong d\xi d\eta, \tag{2}$$

and the differential scattering cross section is given by

$$\Sigma(\theta)=[\Sigma/(\pi\alpha)]\exp[-\theta^2/\alpha]$$
$$\cong[\Sigma/(\pi\alpha)]\exp[-(\xi^2+\eta^2)/\alpha]. \tag{3}$$

Since the scattering function is strongly peaked around $\xi=\eta=0$, no further error will be introduced if ξ and η vary from $-\infty$ to $+\infty$.

If a particle with velocity coordinates ξ_0, η_0 travels a distance r_1 before having a collision the position, coordinates of the particle will be $x=r_1\xi_0$, $y=r_1\eta_0$. If the collision changes the velocity coordinates by ξ_1, η_1, the new velocity coordinates will be $\xi_0+\xi_1$, $\eta_0+\eta_1$, and if the particle travels a distance r_2 to its next collision its position coordinates will be $x=r_1\xi_0+r_2(\xi_0+\xi_1)$, $y=r_1\eta_0+r_2(\eta_0+\eta_1)$. After n collisions the position coordinates will be

$$\begin{aligned}
x&=r_1\xi_0+r_2(\xi_0+\xi_1)+r_3(\xi_0+\xi_1+\xi_2)+\cdots\\
&\qquad+r_{n+1}(\xi_0+\xi_1+\xi_2+\cdots\xi_n),\\
x&=r\xi_0+\xi_1(r-r_1)+\xi_2(r-r_1-r_2)+\xi_3(r-r_1-r_2-r_3)\\
&\qquad+\cdots+\xi_n(r-r_1-r_2-r_3-\cdots-r_n),\\
y&=r_1\eta_0+r_2(\eta_0+\eta_1)+r_3(\eta_0+\eta_1+\eta_2)+\cdots\\
&\qquad+r_{n+1}(\eta_0+\eta_1+\eta_2+\cdots+\eta_n),\\
y&=r\eta_0+\eta_1(r-r_1)+\eta_2(r-r_1-r_2)+\eta_3(r-r_1-r_2-r_3)\\
&\qquad+\cdots+\eta_n(r-r_1-r_2-r_3-\cdots-r_n),
\end{aligned} \tag{4}$$

where owing to the small angles of scattering it is assumed that

$$\sum_1^{n+1} r_i=r=(x^2+y^2+z^2)^{\frac{1}{2}}. \quad \text{(See Fig. 1.)} \tag{5}$$

Now letting $x/r=p$, $y/r=q$, $(r-r_1-r_2-r_3-\cdots-r_i)/r=\mu_i$,

$$p=\xi_0+\sum_1^n \xi_i\mu_i, \tag{6}$$

$$q=\eta_0+\sum_1^n \eta_i\mu_i,$$

$$dp=(dx)/r=d\xi_0,$$

$$dq=(dy)/r=d\eta_0,$$

$$dr_1dr_2dr_3\cdots dr_n=r^n d\mu_1d\mu_2d\mu_3\cdots d\mu_n. \tag{7}$$

To calculate the probability that a particle from a point source which is emitting particles with an angular distribution $[1/(\pi\beta)]\exp[-\theta^2/\beta]$ about the z axis will reach a position x, y at a distance r from the source, we proceed as follows: Since $\xi^2+\eta^2\cong\theta^2$, the probability of a particle entering the medium with velocity coordinates in $d\xi_0d\eta_0$ about ξ_0, η_0 is $[1/(\pi\beta)]\exp[-(\xi_0^2+\eta_0^2)/\beta]d\xi_0d\eta_0$. The probability that the particle will then

travel a distance r_1, and have a collision in dr_1, which results in a change of velocity coordinates into $d\xi_1 d\eta_1$, about $\xi_0+\xi_1$, $\eta_0+\eta_1$ is $\exp[-\Sigma_t r_1]\Sigma dr_1[1/(\pi\alpha)]d\xi_1 d\eta_1 \times\exp[-(\xi_1^2+\eta_1^2)/\alpha]$. The probability of the particle reaching x, y, r, after having n collisions, is

$$\phi_n(r,x,y)dxdy=\int\{[1/\pi\beta]\exp[-(\xi_0^2+\eta_0^2)/\beta]d\xi_0 d\eta_0\}$$

$$\times\{\exp[-\Sigma_t r_1]\Sigma dr_1[1/\pi\alpha]\exp[-(\xi_1^2+\eta_1^2)/\alpha]d\xi_1 d\eta_1\}$$

$$\times\{\cdots\}\{\exp[-\Sigma_t r_n]\Sigma dr_n[1/\pi\alpha]$$

$$\times\exp[-(\xi_n^2+\eta_n^2)/\alpha]d\xi_n d\eta_n\}\exp[-\Sigma_t r_{n+1}], \quad (8)$$

where:

$$x=r_1\xi_0+r_2(\xi_0+\xi_1)+r_3(\xi_0+\xi_1+\xi_2)+\cdots$$
$$+r_{n+1}(\xi_0+\xi_1+\cdots+\xi_n),$$
$$y=r_1\eta_0+r_2(\eta_0+\eta_1)+r_3(\eta_0+\eta_1+\eta_2)+\cdots$$
$$+r_{n+1}(\eta_0+\eta_1+\eta_2+\cdots\eta_n).$$

The limits on ξ_i and η_i are, as discussed above, $-\infty$ to $+\infty$, and the r_i's vary so that $0\leq r_1\leq r_1+r_2\leq r_1+r_2+r_3\leq\cdots\leq r_1+r_2+\cdots r_n\leq r$.

By using Eqs. (5) and (7), Eq. (8) becomes

$$\phi_n=[(\Sigma r)^n/(\pi^{n+1}\alpha^n\beta)][1/r^2]\exp[-\Sigma_t r]$$

$$\times\int\exp\{-[(\xi_0^2+\eta_0^2)/\beta]-(1/\alpha)\sum_1^n\xi_i^2+\eta_i^2\}$$

$$\times d\xi_1\cdots d\xi_n d\eta_1\cdots d\eta_n d\mu_1\cdots d\mu_n, \quad (9)$$

where $0<\mu_n<\mu_{n-1}<\cdots<\mu_1<1$. Substituting (6) into (9), one obtains:

$$\phi_n(r,p,q)=\frac{\exp[-\Sigma_t r](\Sigma r)^n}{(\pi\beta)(\pi\alpha)^n r^2}$$

$$\times\int\exp\{-1/\beta[(p-\sum_1^n\xi_i\mu_i)^2+(q-\sum_1^n\eta_i\mu_i)^2]$$

$$-(1/\alpha)\sum_1^n\xi_i^2+\eta_i^2\}d\xi_1\cdots d\xi_n d\eta_1\cdots$$

$$\times d\eta_n d\mu_1\cdots d\mu_n. \quad (10)$$

Making orthogonal transformations of the type

$$\xi_1'=[\sum_1^n\mu_i\xi_i]/[\sum_1^n\mu_i^2]^{\frac{1}{2}}, \quad \eta_1'=[\sum_1^n\mu_i\eta_i]/[\sum_1^n\mu_i^2]^{\frac{1}{2}}, \quad (11)$$

$$\xi_2'=\sum_1^n\alpha_i\xi_i, \qquad \eta_2'=\sum_1^n\beta_i\eta_i.$$

Setting

$$\rho=[\sum_1^n\mu_i^2]^{\frac{1}{2}},$$

we obtain

$$\phi_n(r,p,q)=\frac{\exp[-\Sigma_t r](\Sigma r)^n}{(\pi\beta)(\pi a)^n r^2}$$

$$\times\int\exp\{-(1/\beta)[(p-\xi_1'\rho)^2+(q-\eta_1'\rho)^2]$$

$$-(1/\alpha)\sum_1^n\xi_i'^2+\eta_i'^2\}$$

$$\times d\xi_1'\cdot d\xi_n' d\eta_1'\cdot d\eta_n' d\mu_1\cdots d\mu_n. \quad (12)$$

The terms for $i=2$ to $i=n$ can be integrated directly. A sample term is

$$\int_{-\infty}^{\infty}\exp[-(1/\alpha)(\xi_i^2+\eta_i^2)d\xi_i d\eta_i=\pi\alpha.$$

$\phi_n(r,p,q)$ now becomes

$$\phi_n(r,p,q)=\frac{\exp[-\Sigma_t r](\Sigma r)^n}{(\pi\beta)(\pi\alpha)r^2}$$

$$\times\int\exp\{-(1/\beta)[(p-\xi_1'\rho)^2+(q-\eta_1'\rho)^2$$

$$-(1/\alpha)(\xi_1'^2+\eta_1'^2)\}d\xi_1' d\eta_1' d\mu_1\cdots d\mu_n. \quad (13)$$

Upon completing the square and integrating over ξ_1', η_1' this becomes:

$$\phi_n(r,p,q)=\frac{\exp[-\Sigma_t r](\Sigma r)^n}{\pi r^2}$$

$$\times\int\frac{\exp[-(p^2+q^2)/(\beta+\alpha\rho^2)]}{\beta+\alpha\rho^2}d\mu_1\cdots d\mu_n$$

$$0<\mu_n<\mu_{n-1}<\cdots<\mu_1<1. \quad (14)$$

Since μ_i only appears as $\sum_1^n\mu_i^2=\rho^2$, the integration is unchanged by permuting the μ_i's. Dividing by the number of permutations, $n!$, and letting $0<\mu_i<1$, one obtains

$$\phi_n(r,p,q)=\frac{\exp[-\Sigma_t r](\Sigma r)^n}{\pi r^2 n!}$$

$$\times\int_0^1\frac{\exp[-(p^2+q^2)/(\beta+\alpha\rho^2)]}{\beta+\alpha\rho^2}d\mu_1 d\mu_2\cdots d\mu_n. \quad (15)$$

Now, since $p^2+q^2\cong\theta^2$, then

$$\phi_n(r,\theta)=\Gamma_n(r)\psi_n(r,\theta),$$

where

$$\Gamma_n(r)=\frac{\exp[-\Sigma_t r](\Sigma r)^n}{r^2 n!},$$

$$\psi_n(r,\theta)=(1/\pi)\int_0^1\frac{\exp[-\theta^2/(\beta+\alpha\rho^2)]}{\beta+\alpha\rho^2}d\mu_1 d\mu_2\cdots d\mu_n.$$

Now performing a double Fourier transformation with respect to the variables p and q,

$$\Omega_n(r,\omega_1,\omega_2)=[1/(2\pi)^2]\int_{-\infty}^{\infty}\int_{-\infty}^{\infty}\psi_n(r,p,q)\times\exp[i(\omega_1 p+\omega_2 q)]dpdq,$$

$$\psi_n(r,p,q)=\int_{-\infty}^{\infty}\int_{-\infty}^{\infty}\Omega_n(r,\omega_1,\omega_2)\times\exp[-i(\omega_1 p+\omega_2 q)]d\omega_1 d\omega_2,$$

one obtains

$$\Omega_n(r,\omega_1,\omega_2)=\frac{1}{(2\pi)^2\pi}\int_{\mu_i}\int_{-\infty}^{\infty}\int_{-\infty}^{\infty}\times\frac{\exp[-(p^2+q^2)/(\beta+\alpha\rho^2)+i(\omega_1 p+\omega_2 q)]}{\beta+\alpha\rho^2}\times dpdqd\mu_1\cdots d\mu_n. \quad (16)$$

Now,

$$[1/(\pi)^{\frac{1}{2}}]\int_{-\infty}^{\infty}\frac{\exp[-p^2/(\beta+\alpha\rho^2)+i\omega_1 p]}{(\beta+\alpha\rho^2)^{\frac{1}{2}}}dp=\exp-\tfrac{1}{4}\omega_1^2(\beta+\alpha\rho^2),$$

so

$$\Omega_n(r,\omega_1,\omega_2)=[1/(2\pi)^2]\int_0^1\exp[-\tfrac{1}{4}(\omega_1^2+\omega_2^2)(\beta+\alpha\rho^2)]\times d\mu_1 d\mu_2\cdots d\mu_n$$

$$=[1/(2\pi)^2]\exp(-\tfrac{1}{4}\lambda^2\beta)\int_0^1\int_0^1\int_0^1\cdots\int_0^1\times\exp(-\tfrac{1}{4}\lambda^2\alpha\mu_1^2\cdots-\tfrac{1}{4}\lambda^2\alpha\mu_n^2)d\mu_1\cdots d\mu_n,$$

where

$$\lambda^2=\omega_1^2+\omega_2^2,$$

$$\Omega_n(r,\omega_1,\omega_2)=[(1/2\pi)^2]\exp(-\lambda^2\beta/4)\times\{[\pi^{\frac{1}{2}}/(\lambda\alpha^{\frac{1}{2}})]\operatorname{Erf}(\alpha^{\frac{1}{2}}\lambda/2)\}^n,$$

where

$$\operatorname{Erf}(x)=[2/\pi^{\frac{1}{2}}]\int_0^x\exp[-x^2]dx,$$

$$\psi_n(r,p,q)=[1/(2\pi)^2]\int_{-\infty}^{\infty}\int_{-\infty}^{\infty}\exp[-\tfrac{1}{4}\lambda^2\beta-i(\omega_1 p+\omega_2 q)]\times\{[\pi^{\frac{1}{2}}/(\lambda\alpha^{\frac{1}{2}})]\operatorname{Erf}(\tfrac{1}{2}\alpha^{\frac{1}{2}}\lambda)\}^n d\omega_1 d\omega_2.$$

Now introducing the coordinates

$$p=\theta\cos\phi,\quad \omega_1=\lambda\cos\psi,$$
$$q=\theta\sin\phi,\quad \omega_2=\lambda\sin\psi,$$
$$p\omega_1+q\omega_2=\lambda\theta\cos(\phi-\psi),$$

one obtains

$$\psi_n(r,\theta)=[1/(2\pi)^2]\int_0^{\infty}\int_0^{2\pi}\{[\pi^{\frac{1}{2}}/\lambda\alpha^{\frac{1}{2}}]\operatorname{Erf}(\tfrac{1}{2}\alpha^{\frac{1}{2}}\lambda)\}^n\times\exp[-\tfrac{1}{4}\lambda^2\beta-i\lambda\theta\cos(\phi-\psi)]\lambda d\lambda d\psi$$

$$=[1/(2\pi)]\int_0^{\infty}\{[\pi^{\frac{1}{2}}/\lambda\alpha^{\frac{1}{2}}]\operatorname{Erf}(\tfrac{1}{2}\alpha^{\frac{1}{2}}\lambda)\}^n\times\exp[-\tfrac{1}{4}\lambda^2\beta]J_0(\lambda\theta)\lambda d\lambda,$$

letting $\alpha^{\frac{1}{2}}\lambda/2=\kappa$;

$$\psi_n(r,\theta)=[2/\pi\alpha]\int_0^{\infty}J_0(2\theta\kappa/\alpha^{\frac{1}{2}})\{[\pi^{\frac{1}{2}}/(2\kappa)]\operatorname{Erf}(\kappa)\}^n\times\exp[-\beta\kappa^2/\alpha]\kappa d\kappa \quad (17)$$

$$\phi_n(r,\theta)=\frac{2(\Sigma r)^n\exp[-\Sigma_t r]}{(\pi\alpha)r^2 n!}\int_0^{\infty}J_0(2\theta\kappa/\alpha^{\frac{1}{2}})\times\{[\pi^{\frac{1}{2}}/(2\kappa)]\operatorname{Erf}(\kappa)\}^n\exp[-\beta\kappa^2/\alpha]\kappa d\kappa, \quad (18)$$

which is the number of particles reaching, r, θ after having had n collisions. To find the total number of particles reaching r, θ one obtains the sum $\phi_n(r,\theta)$ from $n=0$ to $n=\infty$:

$$\phi(r,\theta)=\sum_0^{\infty}\phi_n(r,\theta)=\frac{2\exp[-\Sigma_t r]}{\pi\alpha r^2}\int_0^{\infty}J_0(2\theta\kappa/\alpha^{\frac{1}{2}})\times\exp\{-[\beta\kappa^2/\alpha]+[\pi^{\frac{1}{2}}\Sigma r/(2\kappa)]\operatorname{Erf}(\kappa)\}\kappa d\kappa, \quad (19)$$

which is the desired result.

ASYMPTOTIC SOLUTIONS

An asymptotic solution of (19) can be obtained by noting that

$$f(\kappa)=[\pi^{\frac{1}{2}}/(2\kappa)]\operatorname{Erf}(\kappa)=\int_0^1\exp[-\kappa^2 t^2]dt \quad (20)$$

is equal to unity at $\kappa=0$ and decreases monotonically to 0 as κ approaches infinity.

Near $\kappa=0$, one has

$$f(\kappa)\sim 1-\tfrac{1}{3}\kappa^2. \quad (21)$$

If Σr is large, then $\exp[\Sigma r f(\kappa)]$ decreases very rapidly as κ increases. Thus it can be expected that the integral, (19), depends in the main on the values of $\exp[\Sigma r f(\kappa)]$ for small values of κ.

One obtains

$$\exp[\Sigma r f(\kappa)]\sim\exp[\Sigma r-\tfrac{1}{3}\Sigma r\kappa^2];$$

TABLE I. Comparison at several angles of the exact, asymptotic, and approximate values of the probability $\phi(r,\theta)$.

θ	ϕ_{exact}	ϕ_{asym}	ϕ_{approx}
0	$1.532\times10^{7}\dfrac{\exp[-\Sigma_t r]}{\pi r^2}$	$1.510\times10^{7}\dfrac{\exp[-\Sigma_t r]}{\pi r^2}$	$1.404\times10^{7}\dfrac{\exp[-\Sigma_t r]}{\pi r^2}$
0.158 (9.06°)	$1.460\times10^{7}\dfrac{\exp[-\Sigma_t r]}{\pi r^2}$	$1.445\times10^{7}\dfrac{\exp[-\Sigma_t r]}{\pi r^2}$	$1.348\times10^{7}\dfrac{\exp[-\Sigma_t r]}{\pi r^2}$
0.316 (18.1°)	$1.268\times10^{7}\dfrac{\exp[-\Sigma_t r]}{\pi r^2}$	$1.264\times10^{7}\dfrac{\exp[-\Sigma_t r]}{\pi r^2}$	$1.198\times10^{7}\dfrac{\exp[-\Sigma_t r]}{\pi r^2}$
0.474 (27.2°)	$1.008\times10^{7}\dfrac{\exp[-\Sigma_t r]}{\pi r^2}$	$1.014\times10^{7}\dfrac{\exp[-\Sigma_t r]}{\pi r^2}$	$0.984\times10^{7}\dfrac{\exp[-\Sigma_t r]}{\pi r^2}$

thus

$$\phi(r,\theta)\sim[2/(\pi\alpha r^2)]\exp[-(\Sigma_t-\Sigma)r]\int_0^\infty J_0(2\theta\kappa/\alpha^{\frac{1}{2}})\times\exp\{-[(\beta/\alpha)+\tfrac{1}{4}\Sigma r)]\kappa^2\}\kappa d\kappa. \quad (22)$$

This last integral can be evaluated explicitly. The calculation yields

$$\phi(r,\theta)\sim\frac{\exp[-(\Sigma_t-\Sigma)r]}{\pi r^2(\beta+\frac{1}{4}\alpha\Sigma r)}\exp\left(-\frac{\theta^2}{\beta+\frac{1}{4}\alpha\Sigma r}\right), \quad (23)$$

for large values of Σr.

APPROXIMATE SOLUTIONS

It is interesting to note the effect of assuming that the particle travels the same distance between each collision, i.e., $[r_i=r/(n+1)]$. In this case,

$$\mu_i=(r-r_1-r_2-r_3-\cdots r_i)/r=(n+1-i)/(n+1),$$

$$\rho^2=\sum_1^n\mu_i^2=\sum_1^n\frac{(n+1-i)^2}{(n+1)^2}=n\frac{(n+1)(2n+1)}{6(n+1)^2}.$$

One obtains from (15),

$$\phi_n(r,\theta)=\frac{\exp[-\Sigma_t r](\Sigma r)^n}{\pi r^2 n!\alpha_n}\exp[-\theta^2/\alpha_n], \quad (24)$$

where

$$\alpha_n=\beta+\alpha\frac{n(2n+1)}{6(n+1)},$$

and

$$\phi_{\text{approx}}(r,\theta)=\sum_0^\infty\phi_n(r,\theta),$$

$$\phi(r,\theta)=\frac{\exp[-\Sigma_t r]}{\pi r^2}\sum_0^\infty\frac{(\Sigma r)^n}{n!}(1/\alpha_n)\exp[-\theta^2/\alpha_n]. \quad (25)$$

To test the accuracy of the approximate and asymptotic solutions, $\phi_{\text{exact}}\phi_{\text{asym}}$, ϕ_{approx} have been calculated for $\Sigma r=16$, $\alpha=\beta=0.1$, $\theta=0°$, 10°, 20°, 30° as shown in Table I.

That the approximation, $r_i=r/(n+1)$, has qualitative physical basis can be seen in the following manner. The coefficient of $(1/\alpha_n)\exp[-\theta^2/\alpha_n]$ in Eq. (25) contains the term $(\Sigma r)^n/n!$ which has a maximum in the neighborhood of $\Sigma r\cong n+1$ or, $r/(n+1)=\lambda$, where λ is the mean free path for scattering. Thus in Eq. (25) the term in $(1/\alpha_n)\exp[-\theta^2/\alpha_n]$ which has the largest coefficient is the term in which assuming $r_i=r/(n+1)$ is simply equivalent to assuming that the particles travel one scattering mean free path between each collision. Therefore, it is not too surprising that the approximate solution is fairly close to the exact solution.

PLANE SOURCE—DISTRIBUTION FUNCTION

If we use the small angle approximation, the transport equation for an infinite plane source can be written as

$$\partial\psi/\partial z+\Sigma_t\psi=\int\psi(z,\xi',\eta')\Omega(\xi-\xi',\eta-\eta')d\xi'd\eta',$$

where

$$\psi=\psi(z,\xi,\eta),$$

$$\Omega(\xi-\xi'\eta-\eta')=[\Sigma/\pi\alpha]\exp\{-[(\xi-\xi')^2+(\eta-\eta')^2]/\alpha\}.$$

Performing a double Fourier transformation with respect to ξ and η, and making use of the convolution theorem leads to a differential equation which has the solution

$$\bar{\psi}(z,\omega_1,\omega_2)=[1/2\pi]\exp\{-\tfrac{1}{4}\beta(\omega_1^2+\omega_2^2)-[\Sigma_t-2\pi\bar{\Omega}]z\},$$

where $\bar{\psi}(z,\omega_1,\omega_2)$, $\bar{\Omega}(\omega_1,\omega_2)$ are the double Fourier transforms of $\psi(z,\xi,\eta)$, $\Omega(\xi,\eta)$, respectively.

Performing the inverse transformation leads to a distribution function of the form[3]

$$\psi(z,\xi,\eta)=\psi(z,\theta,\phi)=\sum_0^\infty\psi_n(z,\theta),$$

[3] Using somewhat different assumptions, similar results were obtained by L. L. Foldy and R. K. Osborn, Phys. Rev. **81**, 400 (1951).

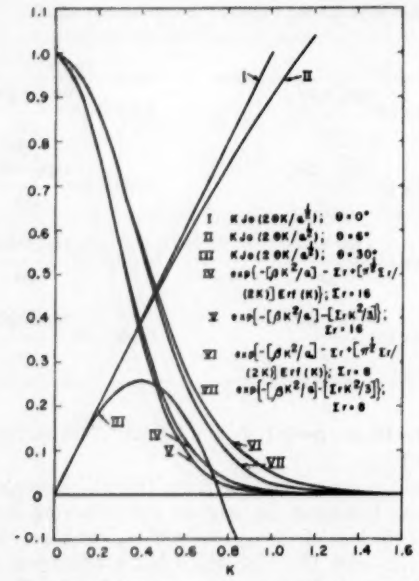

FIG. 2. Factors occurring in integrands of Eqs (19), (22) for $\alpha=\beta=0.1$ and various values of Σr, θ, plotted as functions of K.

where

$$\psi_n(z,\theta)=\frac{\exp[-\Sigma_t z](\Sigma z)^n}{\pi n!(n\alpha+\beta)}\exp[-\theta^2/(n\alpha+\beta)].$$

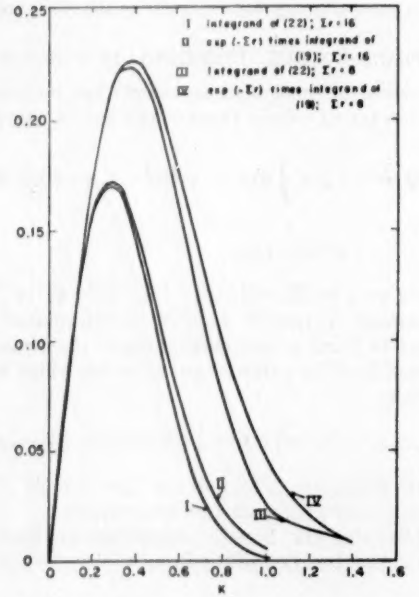

FIG. 3. Integrands of exact expression, Eq. (19), and asymptotic expression, Eq. (22), for $\alpha=\beta=0.1$; $\Sigma r=8$, 16; $\theta=0$ plotted as functions of K.

$\psi_n(z,\theta)$ describes the distribution of particles at z which have had exactly n collisions. This can be seen by noting that

$$\int\psi_n(z,\theta)d\Omega=[(\Sigma z)^n/n!]\exp[-\Sigma z]$$

is just the integral of (15) over an infinite plane source.

CONCLUSION

The error introduced into the asymptotic solution, ϕ_{asym}, by approximating $\exp\{-(\beta\kappa^2/\alpha)+[\pi^{\frac{1}{2}}\Sigma r/(2\kappa)]\times\text{Erf}(\kappa)\}$ by $\exp\{-(\beta\kappa^2/\alpha)+\Sigma r(1-\frac{1}{4}\kappa^2)\}$ can be judged by considering Fig. 2, which is a plot of the different parts of the integrands of Eqs. (19) and (22) for different values of θ and Σr. The entire integrands for some of the different cases are plotted in Fig. 3.

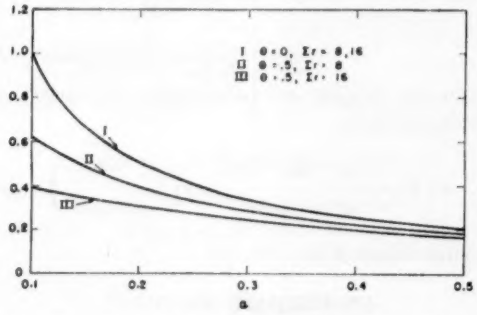

FIG. 4. Plot of $\phi_{\text{asym}}(r,\theta)$ times $\{\pi r^2\cdot\frac{1}{2}\Sigma r\cdot\exp[(\Sigma_t-\Sigma)r]\}$ as a function of the parameter α, for various values of Σr, θ.

For the case of $r=1\delta$, it is easily seen that the error is quite small for $\theta=0°$, 6°, 30°. In fact the above approximation is good to even larger θ, however, as is shown below, the accuracy of the "exact" solution is not good for very large θ. For the case of $r=8$, the accuracy seems to be lower than for $r=16$, but is still quite good.

It is interesting to note the sensitivity of ϕ_{asym} to the constant which appears in the scattering cross section, $(\theta)=1/(\pi\alpha)\exp(-\theta^2/\alpha)$. Figure 4 shows ϕ_{asym} plotted as a function of α for different values of θ and Σr. The curve for $\theta=0$ is independent of Σr, and, as can be seen from the graph, is the most sensitive function of α.

The assumption that the position angle, θ, is small is made in the transformations leading to Eq. (17). This approximation could have been avoided and, using somewhat different transformations, a result similar to Eq. (17) could have been obtained. However, the utility of such a calculation is limited because an earlier approximation [Eq. (15)], implicitly assumed that θ is not large.

Dielectric Properties of Colored KCl Crystals

T. SUITA*
Department of Electrical Engineering, Osaka University, Osaka, Japan
(Received January 20, 1954)

The dielectric properties of colored KCl crystals were measured from 20° to 600°C by the resonance method at 3 Mc/sec, and the number of color centers by the conduction method. The dissociation energy of the color centers in KCl was roughly calculated to be 0.36 ev from the data thus obtained.

THE optical properties of colored crystals have been extensively studied from the theoretical and experimental points of view, but little has been published on their dielectric properties. We have previously observed an expansion of alkali halide crystals irradiated by x-rays,[1] a change of resonance frequency of piezoelectric crystals caused by coloration,[2] and have measured the dielectric breakdown voltage of colored NaCl crystals.[3] Some dielectric properties of additively colored KCl crystals are reported here.

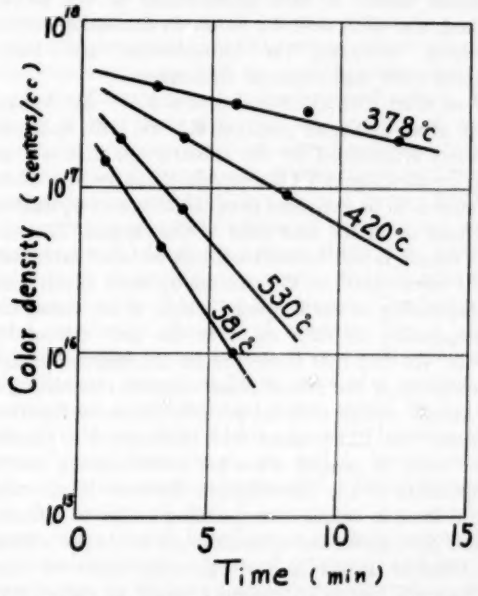

FIG. 1. Time dependence of density of color centers in KCl crystal.

The density of color centers in the sample was measured by means of conduction current at about 600°C, and were found to be 10^{17} to 10^{18} centers/cc. The sample dimension was 20×20×1 mm and the electrodes used were platinum plates of 10×10×2 mm.

The change of density of color centers N *versus* time t at constant temperature was determined (Fig. 1). It may be seen that log$N$ decreases almost linearly with the time t, as in a first-order reaction. We found it very difficult, however, to measure the color density by the conduction method owing to the time required to raise the crystal to the higher temperature at which the conduction measurement was carried out. Using Fig. 1, the dissociation energy of the color centers is calculated to be about 0.36 ev.

The dielectric constant and loss tangent were measured at 3 Mc/sec in the temperature range from 20° to 600°C (Fig. 2). These show an interesting behavior; ϵ and tanδ increase rather rapidly at about 250° with temperature and decrease at about 500°C. However, on cooling, the crystal showed no large increase in ϵ and tanδ, as it does on heating; it behaved like a noncolored crystal. The colored crystal after this thermal cycle was transparent at room temperature. The dielectric properties of the noncolored crystal, as is well known, increase monotonically with increasing temperature except for a number of Breckenridge-type dispersions.[4] We found small dielectric dispersions near 500°C, which we are now investigating. It is important to note that the color density decreases while the dielectric measurements are being carried out, especially at high temperatures.

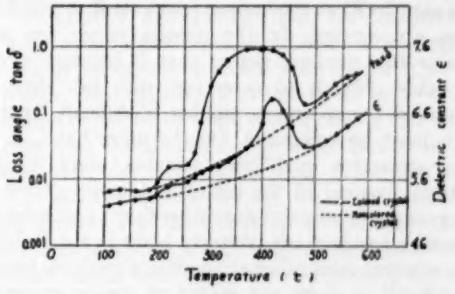

FIG. 2. Temperature dependence of dielectric constant and tanδ for colored KCl crystal.

Our results show clearly that the rapid increase of ϵ and tanδ in the previously mentioned temperature region is due to the color centers in the crystal. Because of the large orbitals of trapped electrons in the crystal, we may expect the centers or aggregations of centers to influence one another at very low concentrations.

The author wishes to express his appreciation to Mr. S. Kondo and Mr. H. Okura for assistance in carrying out the experiments.

* Present address; Laboratory for Insulation Research, Massachusetts Institute of Technology, Cambridge, Massachusetts.

[1] K. Sakaguchi and T. Suita, Technol. Repts. Osaka Univ. 2, 177 (1952): similar measurements have been made by Estermann, Leivo, and Stern, Phys. Rev. 75, 627 (1949).

[2] T. Suita and K. Sakaguchi, Kansai Meeting of Electrical Engineers of Japan, No. 71, 1947 (unpublished).

[3] T. Suita, J. Inst. Elec. Engrs. (Japan) 69, 190 (1949).

[4] S. Kondo and T. Suita, J. Phys. Soc. Japan 5, 375 (1950); R. G. Breckenridge, J. Chem. Phys. 16, 959 (1948).

Simplified LCAO Method for the Periodic Potential Problem*

J. C. SLATER AND G. F. KOSTER†
Massachusetts Institute of Technology, Cambridge, Massachusetts
(Received February 17, 1954)

The LCAO, or Bloch, or tight binding, approximation for solids is discussed as an interpolation method, to be used in connection with more accurate calculations made by the cellular or orthogonalized plane-wave methods. It is proposed that the various integrals be obtained as disposable constants, so that the tight binding method will agree with accurate calculations at symmetry points in the Brillouin zone for which these calculations have been made, and that the LCAO method then be used for making calculations throughout the Brillouin zone. A general discussion of the method is given, including tables of matrix components of energy for simple cubic, face-centered and body-centered cubic, and diamond structures. Applications are given to the results of Fletcher and Wohlfarth on Ni, and Howarth on Cu, as illustrations of the fcc case. In discussing the bcc case, the splitting of the energy bands in chromium by an antiferromagnetic alternating potential is worked out, as well as a distribution of energy states for the case of no antiferromagnetism. For diamond, comparisons are made with the calculations of Herman, using the orthogonalized plane-wave method. The case of such crystals as InSb is discussed, and it is shown that their properties fit in with the energy band picture.

I. THE LCAO METHOD FOR SOLIDS

ONE of the standard methods for solving the periodic potential problems met in the theory of the electronic motions in solids is the LCAO (linear combination of atomic orbitals) or Bloch or tight binding method. This was originally proposed by Bloch,[1] and consists of making a linear combination of atomic orbitals located on the various atoms of the crystal, the coefficients being the values of the plane wave $\exp(i\mathbf{k}\cdot\mathbf{R})$ at the various positions $\mathbf{R}$ at which the atoms are located. In the present paper, we shall examine this method, noting that it becomes almost impossibly difficult to carry out with full rigor, on account of the enormous number of difficult integrals which must be computed. On the other hand, it has many attractive qualitative features, since it gives solutions showing all the correct symmetry properties of the energy bands, and it is rather easy to get solutions for energy bands at an arbitrary point in the Brillouin zone, whereas most other approximate methods become too difficult to carry out except at certain symmetry points of the Brillouin zone. With this in mind, we shall suggest using the LCAO method, not as a primary method of accurate calculation, but rather as an interpolation method. We shall arbitrarily discard many of the terms which make trouble with the accurate calculation, but shall retain those which are necessary to give qualitative correctness to the method. Instead of computing the various integrals analytically, we shall use them as disposable constants, to be chosen so that we shall fit the results of more accurate calculation made by other methods, such as the cellular method or the method of orthogonalized plane waves, which are capable of more accurate results, but only at restricted symmetry points of the Brillouin zone. We shall give formulas useful in such applications of the LCAO method, and shall describe its use in discussing certain problems, including the face-centered and body-centered cubic and diamond structures.

If we start with an atomic orbital $\phi_n(\mathbf{r}-\mathbf{R}_i)$, located on an atom at vector position $\mathbf{R}_i$, and with quantum numbers symbolized by the subscript n, then we can form the Bloch sum $\sum(\mathbf{R}_i)\exp(i\mathbf{k}\cdot\mathbf{R}_i)\phi_n(\mathbf{r}-\mathbf{R}_i)$, where the sum is to be extended over the atoms in equivalent positions in all the unit cells of the crystal. The sum as it stands is not normalized, but we shall later take up its normalization. We can set up such Bloch sums corresponding to each atomic orbital of an atom, and corresponding to each atom in the unit cell of the crystal. We find that there are no nondiagonal matrix components of the Hamiltonian operator, consisting of the kinetic energy and the periodic potential function, between two Bloch sums with different $\mathbf{k}$'s. On the other hand, in general there are nonvanishing matrix components of the Hamiltonian between Bloch sums of the same $\mathbf{k}$ value, corresponding either to different atomic orbitals on the same atom, or to atomic orbitals on different atoms in the unit cell. Some of these nondiagonal matrix components vanish at special symmetry points of the Brillouin zone, or special values of $\mathbf{k}$, and it is this vanishing which leads to the special properties of the energy bands at these symmetry points.

We can then set up an approximate solution of the periodic potential problem in the following way. We take a finite set of atomic orbitals on each of the atoms of the unit cell, going up from the lowest atomic states to those concerned in the highest levels occupied in the crystal, or somewhat higher. From each of these atomic orbitals, we construct a Bloch sum. For a given $\mathbf{k}$ value, we can then set up a wave function consisting of a linear combination of all these Bloch sums. In general, except at special $\mathbf{k}$ values, there will be matrix

* Supported in part by the U. S. Office of Naval Research, in part by the Army, Navy, and Air Force.
† Staff member, Lincoln Laboratory, Massachusetts Institute of Technology, Cambridge, Massachusetts.
[1] F. Bloch, Z. Physik 52, 555 (1928).

components of energy between all these Bloch sums, so that we shall have a secular problem whose order equals that of the total number of atomic orbitals concerned, though at special $\mathbf{k}$ values there will be factoring of the secular equation, and resulting simplification. With modern digital computers, such secular equations can be solved, and the resulting wave functions and energy levels form useful approximations to the solution of the periodic potential problem. At a general $\mathbf{k}$ value, all roots of the secular equation will be distinct, and we group together the functions of different $\mathbf{k}$ value having the lowest energy as the lowest-energy band, those having the second lowest energy as the second-energy band, and so on, though at special symmetry points several energy bands can be degenerate with each other. This is, in principle, a quite good method for approximating the periodic potential problem. Its practical difficulties arise only from the enormous amount of numerical work involved in computing rigorously the various matrix components of energy, and as mentioned earlier, we shall later suggest certain simplications which make it practical.

It is rather surprising that many writers who have considered this method in the literature have not understood certain rather fundamental points. Thus, many writers have felt that in crystals of certain symmetry there were sets of wave functions which did not combine with each other, resulting in splitting of energy bands, which in fact do not occur. Bloch, in his original paper, only computed the diagonal matrix component of energy for a single Bloch sum, and gave no thought to setting up a secular problem relating to the combination of several Bloch sums. The first writer who specifically thought of anything but s atomic orbitals seems to have been Wilson,[2] who computed the diagonal energy of Bloch sums of p orbitals, but erroneously concluded that there would be no nondiagonal matrix components of energy between Bloch sums formed from the p_x, p_y, and p_z atomic orbitals. He made this error on account of a misinterpretation of the results of Bethe[3] concerning the symmetry properties of wave functions in crystals in which the potential has various types of rotational and inversion symmetry, as well as translational symmetry. Bethe had shown that electronic wave functions in such crystals can be chosen to transform under the symmetry operations of the point group like the various irreducible representations of this group, and by using such arguments had been able to derive results on the splitting of energy levels in the crystal, and on the vanishing of certain nondiagonal matrix components of energy. Some of the early writers on energy band theory failed to note the fact, pointed out later by Bouckaert, Smoluchowski, and Wigner,[4] that one cannot, in general, choose wave functions in this way and simultaneously diagonalize the translational operations in the crystal.

A wave function which diagonalizes the translational operations is one which, like a Bloch sum, is multiplied by the factor $\exp i(\mathbf{k}\cdot\mathbf{R})$ when we make a translation $\mathbf{R}$ which carries the lattice into itself; the factor $\exp i(\mathbf{k}\cdot\mathbf{R})$ is the eigenvalue connected with the translational operation. Bouckaert, Smoluchowski, and Wigner pointed out that associated with one $\mathbf{k}$ vector are several others, into which the first one transforms by one of the symmetry operations of the point group of the crystal. Thus, for instance, a general $\mathbf{k}$ vector in a cubic crystal is one of 48 vectors derived from the first one by interchanging x, y, and z, or changing signs; such vectors are said to form a star. It now proves necessary to make linear combinations of Bloch-type wave functions corresponding to all $\mathbf{k}$ vectors in this star, in order to form a wave function transforming according to Bethe's prescription, according to an irreducible representation of the point group of the crystal. Conversely, in order to build up a function connected with one $\mathbf{k}$ value, and hence diagonalizing the translational operations, one must make a linear combination of functions transforming according to the various irreducible representations of the point group. Put more simply, a wave function of a given $\mathbf{k}$ value must be made up as a linear combination of functions having the symmetry properties of s, p_x, p_y, p_z, $\cdots$ orbitals, and will not have the characteristics of any one of these types of orbitals. The exceptions come only for certain special $\mathbf{k}$ values, such as $\mathbf{k}=0$.

We see, then, that Bethe's rules do not apply to wave functions of the Bloch type, corresponding to a definite $\mathbf{k}$, except at special values like $\mathbf{k}=0$. But as we have pointed out, this fact was not clear to various writers at first. In the LCAO method, we make up suitable wave functions at an arbitrary $\mathbf{k}$ value by making linear combinations of the Bloch sums made up of different atomic orbitals, in the way already described, and in general we have contributions coming from all the Bloch sums. The first paper in which it was realized that a secular equation must be solved between the various Bloch sums formed from different atomic orbitals seems to have been that of Jones, Mott, and Skinner[5] dealing with x-ray emission bands of metals, in which wave functions were made up by solving a secular problem between s, p_x, p_y, and p_z Bloch functions. Oddly enough, however, in a later paper by Jones and Mott[6] the error was made of thinking that a threefold d band, formed from the functions of symmetry xy, yz, zx, was separated from a twofold band formed from functions like x^2-y^2 and $3z^2-r^2$; no nondiagonal matrix components of energy between the Bloch sums formed from these two types of atomic

[2] A. H. Wilson, Proc. Roy. Soc. (London) **A133**, 458 (1931).
[3] H. Bethe, Ann. Physik **3**, 133 (1929).
[4] Bouckaert, Smoluchowski, and Wigner, Phys. Rev. **50**, 58 (1936).
[5] Jones, Mott, and Skinner, Phys. Rev. **45**, 379 (1934).
[6] H. Jones and H. F. Mott, Proc. Roy. Soc. (London) **A162**, 49 (1937).

orbitals were considered. Actually, here as in other cases, there are nondiagonal matrix components of energy between all these types of Bloch functions, at an arbitrary $\mathbf{k}$ value, and the d band does not split into two subbands. This unwarranted simplification is also found in the first work of Fletcher and Wohlfarth[7] on nickel, though it is removed in their second paper,[8] which seems to be the first proper treatment of the structure of the d band by the LCAO method.

In addition to the misunderstanding which we have just been describing, there is another widespread misconception about the method. This is the supposition that it is desirable for some reason to start by hybridizing the atomic orbitals, for instance, to introduce directed orbitals of some sort suggested by the symmetry of the crystal. This misconception occurs particularly in the writings of those who, like for instance Pauling[9] and Ganzhorn,[10] do not make it clear whether they are using an energy band calculation, or a modified Heitler-London method. In the case of Lennard-Jones and his associates,[11] using their equivalent orbitals, one gathers that they feel that there is some virtue in using hybridized orbitals of one type or another (that is, linear combinations of several atomic orbitals, on the same or adjacent atoms) for a straightforward calculation of energy bands, or of molecular orbitals in a molecular problem. This procedure is in fact of no value in most cases.

One can start with atomic orbitals of the ordinary sort, space quantized with respect to a particular direction in space, or can use orbitals set up with reference to cubic axes, such as the p_x, p_y, p_z combinations of the p orbitals and the d orbitals varying as xy, yz, zx, x^2-y^2, and $3z^2-r^2$, or finally one can use more complicated hybridized orbitals, such as the four tetrahedral directed orbitals formed from the s and the three p functions. With any one of these starting points, one can set up the Bloch sums of the atomic orbitals, and then can solve the secular problem between these Bloch sums. The final result will obviously be the same no matter which set of atomic orbitals we start with. In fact, if we were going to use n atomic orbitals per unit cell, we could make any n linear combinations of the original orbitals, form Bloch sums of these modified orbitals, and solve a secular problem using the modified Bloch sums, and in every case come out with the same answer in the end. The only advantage in one choice of atomic orbitals over another is convenience in calculating the matrix components or solving the secular equation. We shall be dealing in the present paper with cubic crystals, and shall use orbitals of the p_x, p_y, p_z, xy, yz, etc., type, since they give about as much simplification as we can get. But in addition, these are just as useful in discussing the diamond structure as tetrahedral orbitals would be. At an arbitrary point of $\mathbf{k}$ space, in any case the matrix components will not simplify, no matter what form of atomic orbitals we use. Along special symmetry lines and planes, we can sometimes choose atomic orbitals leading to a factoring of the secular equation, and this is obviously useful; but the choice is different for different symmetry lines and planes.

For solving the one-electron problem, in other words, there is no advantage in using hydridized or directed orbitals when dealing with crystals, or similarly in using directed or equivalent orbitals in solving the molecular orbital problem in a molecule. The advantages of such orbitals, if there are any, seem to lie in treating the many-electron problem, either by methods of configuration interaction or by other methods. It seems likely that by using directed or hybridized or equivalent orbitals, one can set up approximate treatments of electron correlation which express the preference of two electrons of opposite spin to be found in an orbital representing a covalent bond. But this use of such orbitals lies entirely outside the scope of the present paper, which deals with energy band theory, or one-electron solutions of Schrödinger's equation for a periodic potential.

II. SIMPLIFICATION OF THE LCAO METHOD

We have seen in the preceding section the general outlines of the LCAO method for solids. We shall now examine it in more detail, show how complicated it is when applied rigorously, but indicate the simplifications which can be made if we treat it as an interpolation method. There is one complication which we can remove at the outset. If we start with the atomic orbitals ϕ_n, located on the various atoms of a unit cell, and make Bloch sums from them, then we shall find that these Bloch sums are not orthogonal to each other. The reason is that the ϕ_n's connected with orbitals on different atoms are not orthogonal to each other. We can remove this difficulty by immediately setting up new atomic orbitals, linear combinations of the original ones, which are orthogonal to each other. This can be done most symmetrically by the method of Löwdin.[12] We shall assume that this is done, and shall call the resulting orbitals ψ_n. By this procedure we still have not solved the periodic potential problem. We shall still find nondiagonal matrix components of energy between the Bloch sums formed from different Löwdin

[7] G. C. Fletcher and E. P. Wohlfarth, Phil. Mag. **42**, 106 (1951).
[8] G. C. Fletcher, Proc. Phys. Soc. (London) **A65**, 192 (1952).
[9] L. Pauling, Phys. Rev. **54**, 899 (1938).
[10] K. Ganzhorn, "Gruppentheorie und Quantenmechanik der Übergangs metall-Strukturen," thesis, Technischen Hochschule, Stuttgart, 1952 (unpublished); Z. Naturforsch. **7a**, 291 (1952); Z. Naturforsch. **8a**, 330 (1953).
[11] J. Lennard-Jones, Proc. Roy. Soc. (London) **A198**, 1, 14 (1949); J. Lennard-Jones and G. G. Hall, Proc. Roy. Soc. (London) **A202**, 155 (1950); J. Lennard-Jones and J. A. Pople, Proc. Roy. Soc. (London) **A202**, 166 (1950); G. G. Hall, Proc. Roy. Soc. (London) **A202**, 336 (1950); Proc. Phys. Soc. (London) **A66**, 1162 (1953). (This last reference, which was not available when the present paper was written, has some resemblance to it in its general point of view.)
[12] P.-O. Löwdin, J. Chem. Phys. **18**, 365 (1950).

functions ψ_n. But the technique of solving the secular problem will be much simplified. These Löwdin functions ψ_n show symmetry properties like those of the atomic orbitals ϕ_n from which they were derived. (See the Appendix for a proof of this.) For instance, if we start with a p_x atomic orbital and construct orthogonalized atomic orbitals according to Löwdin's prescription, in a cubic crystal, we shall find that the orthogonalized orbital formed from p_x and from contributions of other orbitals on adjacent atoms, will still have the symmetry of a p_x function.

From these Löwdin functions, we can now construct Bloch sums, and if we write them in the form $N^{-\frac{1}{2}}\sum(\mathbf{R}_i)\exp i(\mathbf{k}\cdot\mathbf{R}_i)\psi_n(\mathbf{r}-\mathbf{R}_i)$, where $\mathbf{R}_i$ is the vector position of the atom on which the orbital is located, we shall find that these Bloch sums are normalized and orthogonal. We are assuming periodic boundary conditions, and the number of unit cells in the repeating region is N; the normalization is over this repeating region. The sum is over unit cells. That is, a Bloch function is to be formed from just one atomic orbital per unit cell. If we have several atoms per unit cell, even if some are identical with each other, as the two atoms per unit cell in the diamond structure, we are to use different Bloch sums for each atom in the unit cell. On the other hand, we are to choose our unit cells as small as possible. For instance, in the face-centered or body-centered cubic structures, we are to choose unit cells containing only one atom in the unit cell, instead of the conventional cube, which holds four atoms per cube in the face-centered structure, two per cube in the body-centered structure.

We must now find the matrix component of energy between two such Bloch sums. If H is the Hamiltonian operator, this matrix component is clearly

$$N^{-1}\sum(\mathbf{R}_i,\mathbf{R}_j)\exp i\mathbf{k}\cdot(\mathbf{R}_j-\mathbf{R}_i)\times\int\psi_n^*(\mathbf{r}-\mathbf{R}_i)H\psi_m(\mathbf{r}-\mathbf{R}_j)dv. \quad (1)$$

The sum is over the N unit cells. We must remember that $\mathbf{R}_i$ ranges over the positions of the atoms on which orbitals ψ_n are located, while $\mathbf{R}_j$ ranges over the positions of orbitals ψ_m. These may well be different, for these orbitals may be located on different atoms in the unit cell. But now we notice that one of the summations in the double sum of (1) can be eliminated, for it merely amounts to multiplying the single summation by N, which cancels the factor N^{-1}. In particular, let us eliminate the summation over $\mathbf{R}_i$, letting it be for instance the position of the atom in the central unit cell on which the orbital ψ_n is located, and carrying out a single sum over $\mathbf{R}_j$, which amounts to summing over all neighbors of the original atom. Then in place of (1) we have

$$\sum(\mathbf{R}_j)\exp i\mathbf{k}\cdot(\mathbf{R}_j-\mathbf{R}_i)\int\psi_n^*(\mathbf{r}-\mathbf{R}_i)H\psi_m(\mathbf{r}-\mathbf{R}_j)dv. \quad (2)$$

In this formula, $\mathbf{R}_j-\mathbf{R}_i$ is the vector displacement from the atom on which the orbital ψ_n is located, to one of its neighbors on which an orbital ψ_m is located.

The convenient feature which we observe from (2) is the very simple way in which each term depends on the propagation constant $\mathbf{k}$, and the fact that each term of the summation can be identified with a pair of orbitals on neighboring atoms. The actual calculation of the integrals, however, can be extremely difficult. First we must find the orthogonalized Löwdin functions, from the atomic orbitals, and this is a very considerable task. When this is done, each ψ_n in (2) is a combination of atomic orbitals on many nearby atoms. Thus the integral in (2) can be made up as a linear combination of many integrals of the form of $\int\phi_n^*(\mathbf{r}-\mathbf{R}_i)\times H\phi_m(\mathbf{r}-\mathbf{R}_j)dv$. Now the Hamiltonian H, involving a periodic potential, can be written as the sum of a kinetic energy operator, and a potential, which is approximately a sum of spherically symmetrical potential wells located at all the atoms of the crystal. Hence our integral is a linear combination of integrals of a product of an atomic function $\phi_n^*(\mathbf{r}-\mathbf{R}_i)$ located on the atom at position $\mathbf{R}_i$, another atomic function $\phi_m(\mathbf{r}-\mathbf{R}_j)$ on the atom at $\mathbf{R}_j$, and a spherical potential function located on still a third atom. In other words, we have three-center integrals, of the form which are being worked on so extensively in the present study of molecules, and whose calculation is very difficult. All these complications add up to make the rigorous calculation of the matrix components of energy an almost impossible task, not only because the individual terms are difficult to work out, but also because there are so many of them, combined in such complicated ways. The possibility is not excluded that eventually ways will be found to do this work by means of high-speed computers, but it will certainly be quite out of the question without such help. No calculations which have yet been made by the LCAO method for crystals approach real rigor, and Dr. R. H. Parmenter, in this laboratory, who has tried to estimate the labor involved in such a rigorous calculation, has concluded that by present methods it would be quite out of the question.

We now come to the point where it is desirable to introduce our simplifications, which convert the method from a rigorous one to a rather simple interpolation method. We merely use the form (2) for the matrix components of energy, but replace the integrals by disposable constants, which we choose to fit accurate determination of energies at particular $\mathbf{k}$ values. We must be more precise about the way this is done, however. We wish only a finite number of arbitrary constants, for we have to fit only a finite number of accurate calculations of energy. To choose a finite number, we proceed as follows. We note first that there is every reason to think that the integrals in (2) will get smaller numerically as the atoms in question get farther apart. If the functions ψ_n were atomic orbitals, instead of Löwdin's orthogonalized combinations, then

such an integral would be zero unless the two atoms were close enough so that their orbitals overlapped to an appreciable extent. The orthogonalized Löwdin functions contain contributions located on neighboring atoms, and hence extend outward farther than atomic orbitals, so that the actual integrals in (2) will be appreciable for greater interatomic distances than if they were formed from simple atomic orbitals. Still our general statement almost certainly remains true, that the integrals will decrease fairly rapidly as the interatomic distance decreases. A first natural simplification, then, is to assume arbitrarily that all integrals are to be disregarded except those for neighbors lying closer than a certain minimum distance. We can use only nearest neighbors, or only nearest and second nearest, or only nearest and second and third nearest, according to how many disposable constants we wish to use.

There is one thing to be noticed about the integrals in (2). Many of them must be related, through demands of crystal symmetry. Thus, if symmetry operations of rotation and inversion about the atom at position $\mathbf{R}_i$, where the orbital ψ_n is located, will carry the atom at $\mathbf{R}_j$ into another similar atom, in the same or another unit cell, then there will be relations between the integrals between the orbital ψ_n and orbitals of type ψ_m on these various atoms, which clearly must all be at the same distance from the first atom. As a very simple example, in a simple cubic crystal the interaction integrals between an s orbital on the atom at the origin and s orbitals on atoms displaced by equal distances along the $\pm x$, $\pm y$, and $\pm z$ axes must all be equal. Rules like this, which can be studied by inspection or by the group theory, decrease greatly the number of independent integrals. When we take account of such rules, we find in some important practical cases, which we shall mention later, that if we use the integrals between nearest neighbors, or nearest and second-nearest neighbors, we have about the right number of disposable constants to fit the results of accurate calculation at the various symmetry points in the Brillouin zone for which calculations have been made. This results in rather simple formulas for matrix components of energy, set up according to (2).

Another simplification which we can make is to consider only atomic orbitals whose energy is somewhere near that of the energy bands we are interested in. Thus, if we are dealing with diamond, we can reasonably disregard the $1s$ atomic orbitals, treating only the $2s$ and $2p$. Or, with an element in the $3d$ transition group, we can consider $3d$, $4s$, and possibly $4p$ atomic orbitals, but can disregard the rest, when we are concerned with the valence and conduction bands. We could not make such an approximation if we were making a rigorous calculation; we remember that one hazard of such calculations is that, if we use wave functions for outer electrons which are not orthogonal to those of the inner electrons and then apply the variation method, we can arrive at entirely erroneous results. We are saved from such difficulties in our present method. By choosing our parameters so as to fit certain accurately determined energies, we know that we cannot possibly make a serious error. The use of relatively few atomic orbitals then reduces the order of the secular problem to a point where we can handle it without serious difficulty. Thus, for instance, in diamond, we need eight orbitals: $2s$ and the threefold degenerate $2p$, on each of the two atoms of the unit cell. Hence we have an eighth-order secular equation, which is not difficult to solve with a digital computer. For an element of the iron group, the five d functions and the one $4s$ lead to a sixth-order secular equation and give quite good results; under some circumstances, we can simplify even further, disregarding the $4s$, and having a fifth-order equation.

There is a still further simplification which is sometimes desirable, sometimes not, involving the neglect of three-center integrals. This is complicated enough so that we devote the next section to its discussion. Then we shall go on to the application of our method to several specific cases.

III. THE TWO-CENTER APPROXIMATION

Many writers on molecular problems have assumed that three-center integrals were negligible compared to two-center integrals. This is not really the case. Nevertheless they are certainly smaller than the two-center integrals. And since we are neglecting many terms, and trying to reduce our problem to a form where it has just enough arbitrary constants to fit whatever information we may have, there may be cases where it is desirable to assume that we can disregard three-center integrals, thereby simplifying the situation even further. If we treat the potential energy in H as being the sum of spherical potentials located on the various atoms and disregard three-center integrals, then the only part of the potential energy we retain in (2) is the sum of spherical potentials located on the two atoms on which the atomic orbitals are located. Thus the integral becomes similar to the type which we should have in a diatomic molecule. If we consider the vector $\mathbf{R}_j-\mathbf{R}_i$, stretching from one atom to the other, to be an axis like that of a diatomic molecule, we can express each of the functions ψ as a sum of functions space quantized with respect to that axis. Thus if ψ were an atomic p orbital, we could express it as a linear combination of a $p\sigma$ and a $p\pi_\pm$ function with respect to the axis, and if it is a d function it is a combination of $d\sigma$, $d\pi_\pm$, and $d\delta_\pm$, where as usual σ, π, and δ refer to the component of angular momentum around the axis. Actually, the ψ's are not atomic orbitals, but rather the Löwdin orthogonalized functions, but we have seen that they still have the same symmetry properties with respect to the crystal as the atomic orbitals, and it is not a bad approximation to assume that they can

be expanded in the same way. In the integral (2), we shall get a nonvanishing contribution only if we are dealing with σ components of both ψ_n and ψ_m, or π_+ components of both, or π_- components of both, etc. Hence we can reduce all the various integrals appearing in (2) to a relatively small number.

It is a straightforward matter of rotating axes and transforming spherical harmonics in terms of one set of axes into spherical harmonics with respect to another set, to find the nature of these integrals. Thus, let the atomic orbitals be set up with respect to a set of rectangular axes. We shall symbolize the p_x, p_y, p_z functions by x, y, z; the various d functions by xy, yz, zx, x^2-y^2, and $3z^2-r^2$, which stand for the various functions whose dependence on angle is like that of the polynomials we have written, multiplied by appropriate functions of r. Then to set up the integrals in (2), we need contributions consisting of a product of an atomic orbital of this type on the atom located at $\mathbf{R}_i$, another atomic orbital on the atom at $\mathbf{R}_j$, and spherical potentials centered on these two atoms. Let the direction cosines of the direction of the vector $\mathbf{R}_j-\mathbf{R}_i$, pointing from one atom to the other, be l, m, n. Then we can symbolize one of the integrals by such a symbol as $E_{x,xy}(l,m,n)$, meaning an integral in which the function ψ_n is a p_x-like function; ψ_m, a d function with symmetry properties like xy. This particular function can be written approximately in terms of two integrals: that between a $p\sigma$ orbital on the first atom and a $d\sigma$ orbital on the second; and that between a $p\pi$ on the first and a $d\pi$ on the second. Let the first of these be symbolized by $(pd\sigma)$ and the second by $(pd\pi)$; we shall assume that the first index, such as p, refers to the first orbital, the second, as d, to the second, and note that interchanging the order of the indices has no effect if the sum of the parities of the two orbitals is even, but changes the sign if the sum of the parities is odd. We now find, by carrying out the analysis mentioned earlier, that $E_{x,xy}(l,m,n)=\sqrt{3}l^2m(pd\sigma)+m(1-2l^2)(pd\pi)$. Similar formulas can be worked out for each of the combinations of functions, and are listed in Table I for all combinations of s, p, and d functions. The entries not given in the table can be found by cyclically permuting the coordinates and direction cosines. It is to be realized, of course, that the integrals like $(pd\sigma)$ are functions of the distance between the atoms, so

TABLE I. Energy integrals for crystal in terms of two-center integrals.

$E_{s,s}$	$(ss\sigma)$
$E_{s,x}$	$l(sp\sigma)$
$E_{x,x}$	$l^2(pp\sigma)+(1-l^2)(pp\pi)$
$E_{x,y}$	$lm(pp\sigma)-lm(pp\pi)$
$E_{x,z}$	$ln(pp\sigma)-ln(pp\pi)$
$E_{s,xy}$	$\sqrt{3}lm(sd\sigma)$
E_{s,x^2-y^2}	$\frac{1}{2}\sqrt{3}(l^2-m^2)(sd\sigma)$
$E_{s,3z^2-r^2}$	$[n^2-\frac{1}{2}(l^2+m^2)](sd\sigma)$
$E_{x,xy}$	$\sqrt{3}l^2m(pd\sigma)+m(1-2l^2)(pd\pi)$
$E_{x,yz}$	$\sqrt{3}lmn(pd\sigma)-2lmn(pd\pi)$
$E_{x,zx}$	$\sqrt{3}l^2n(pd\sigma)+n(1-2l^2)(pd\pi)$
E_{x,x^2-y^2}	$\frac{1}{2}\sqrt{3}l(l^2-m^2)(pd\sigma)+l(1-l^2+m^2)(pd\pi)$
E_{y,x^2-y^2}	$\frac{1}{2}\sqrt{3}m(l^2-m^2)(pd\sigma)-m(1+l^2-m^2)(pd\pi)$
E_{z,x^2-y^2}	$\frac{1}{2}\sqrt{3}n(l^2-m^2)(pd\sigma)-n(l^2-m^2)(pd\pi)$
$E_{x,3z^2-r^2}$	$l[n^2-\frac{1}{2}(l^2+m^2)](pd\sigma)-\sqrt{3}ln^2(pd\pi)$
$E_{y,3z^2-r^2}$	$m[n^2-\frac{1}{2}(l^2+m^2)](pd\sigma)-\sqrt{3}mn^2(pd\pi)$
$E_{z,3z^2-r^2}$	$n[n^2-\frac{1}{2}(l^2+m^2)](pd\sigma)+\sqrt{3}n(l^2+m^2)(pd\pi)$
$E_{xy,xy}$	$3l^2m^2(dd\sigma)+(l^2+m^2-4l^2m^2)(dd\pi)+(n^2+l^2m^2)(dd\delta)$
$E_{xy,yz}$	$3lm^2n(dd\sigma)+ln(1-4m^2)(dd\pi)+ln(m^2-1)(dd\delta)$
$E_{xy,zx}$	$3l^2mn(dd\sigma)+mn(1-4l^2)(dd\pi)+mn(l^2-1)(dd\delta)$
E_{xy,x^2-y^2}	$\frac{3}{2}lm(l^2-m^2)(dd\sigma)+2lm(m^2-l^2)(dd\pi)+\frac{1}{2}lm(l^2-m^2)(dd\delta)$
E_{yz,x^2-y^2}	$\frac{3}{2}mn(l^2-m^2)(dd\sigma)-mn[1+2(l^2-m^2)](dd\pi)+mn[1+\frac{1}{2}(l^2-m^2)](dd\delta)$
E_{zx,x^2-y^2}	$\frac{3}{2}nl(l^2-m^2)(dd\sigma)+nl[1-2(l^2-m^2)](dd\pi)-nl[1-\frac{1}{2}(l^2-m^2)](dd\delta)$
$E_{xy,3z^2-r^2}$	$\sqrt{3}lm[n^2-\frac{1}{2}(l^2+m^2)](dd\sigma)-2\sqrt{3}lmn^2(dd\pi)+\frac{1}{2}\sqrt{3}lm(1+n^2)(dd\delta)$
$E_{yz,3z^2-r^2}$	$\sqrt{3}mn[n^2-\frac{1}{2}(l^2+m^2)](dd\sigma)+\sqrt{3}mn(l^2+m^2-n^2)(dd\pi)-\frac{1}{2}\sqrt{3}mn(l^2+m^2)(dd\delta)$
$E_{zx,3z^2-r^2}$	$\sqrt{3}ln[n^2-\frac{1}{2}(l^2+m^2)](dd\sigma)+\sqrt{3}ln(l^2+m^2-n^2)(dd\pi)-\frac{1}{2}\sqrt{3}ln(l^2+m^2)(dd\delta)$
$E_{x^2-y^2,x^2-y^2}$	$\frac{3}{4}(l^2-m^2)^2(dd\sigma)+[l^2+m^2-(l^2-m^2)^2](dd\pi)+[n^2+\frac{1}{4}(l^2-m^2)^2](dd\delta)$
$E_{x^2-y^2,3z^2-r^2}$	$\frac{1}{2}\sqrt{3}(l^2-m^2)[n^2-\frac{1}{2}(l^2+m^2)](dd\sigma)+\sqrt{3}n^2(m^2-l^2)(dd\pi)+\frac{1}{4}\sqrt{3}(1+n^2)(l^2-m^2)(dd\delta)$
$E_{3z^2-r^2,3z^2-r^2}$	$[n^2-\frac{1}{2}(l^2+m^2)]^2(dd\sigma)+3n^2(l^2+m^2)(dd\pi)+\frac{3}{4}(l^2+m^2)^2(dd\delta)$

that we shall have different values for nearest neighbors, second-nearest neighbors, and so on; these can be indicated by subscripts 1, 2, etc. Sometimes it is more convenient to indicate the argument of $E_{x,xy}$, and similar quantities, not by l, m, n, but by the actual coordinates of the second atom with respect to the first, perhaps expressed as a multiple of the lattice spacing. Such notations will be given later for the various special cases we consider.

By the use of Table I, we can approximately express the various E integrals concerned in the problem in terms of a smaller number of integrals like $(pd\sigma)$, etc. In some cases, we shall find that the number of integrals like $(pd\sigma)$ is exactly equal to the number of E integrals involved with neighbors of a particular interatomic distance, and in such a case one method has no advantage over the other; we can compute one set of integrals from the other. In other cases, however, there are considerably more E integrals than integrals of the two-center type. In such a case, we must be guided by convenience as to which method to use. If we have to fit a considerable number of points by means of our disposable constants, we shall normally want to use the E integrals, since we have more of them. When we do this, we find in practice that they cannot be accurately derived from the smaller number of two-center integrals, showing that the two-center approximation is not very good. However, if we have fewer points to fit, it may happen that we cannot determine all the E integrals from the information at hand. In such a case, we may choose to assume that they can be expressed according to Table I in terms of two-center integrals, thereby having a smaller number of disposable constants, which we may be able to determine from the available information. Certainly the results will not be as reliable as if we do not make the two-center approximation; but the two-center approximation may not be very bad and such a procedure may be better than nothing. Another use for Table I is that in some cases there are existing calculations using the LCAO approximation, which almost invariably assume two-center integrals; our table will make it convenient to compare our method with these existing calculations.

IV. THE SIMPLE CUBIC STRUCTURE

Though real crystals do not ordinarily show the simple cubic structure, nevertheless it is convenient to begin with it, both on account of its simplicity, and also because from the results of it we can immediately derive the behavior of the face-centered and body-centered cubic structures. Our task is to express the matrix components of the Hamiltonian, which we have written in (2), in a form convenient for use in the simple cubic case. As before, we use s, p, and d atomic orbitals, which we choose so as to form basis functions for irreducible representations of the cubic point group. These s, p, and d functions will have transformation properties like the sets s; x, y, z; xy, yz, zx; x^2-y^2, $3z^2-r^2$. We let the atoms be located at the vector positions $pa\mathbf{i}+qa\mathbf{j}+ra\mathbf{k}$, where p, q, r are integers, a is the lattice spacing of the simple cubic crystal, and $\mathbf{i}$, $\mathbf{j}$, $\mathbf{k}$ are unit vectors along the x, y, z axis. Let the subscripts n, m refer to two out of the set of symbols s, x, y, z, xy, etc. Then we shall denote our integrals by the expression

$$E_{n,m}(p,q,r)=\int\psi_n^*(\mathbf{r})H\psi_m(\mathbf{r}-pa\mathbf{i}-qa\mathbf{j}-ra\mathbf{k})dv. \quad (3)$$

That is, in this case, rather than using l, m, n as the arguments of the E symbols, it is more convenient to use actual atomic coordinates, so that $l=p(p^2+q^2+r^2)^{-\frac{1}{2}}$, etc. The integrals occurring in (3) are the ones to be inserted in formula (2) for the matrix components of energy.

We now wish to express our matrix components of energy between the Bloch sums in terms of the smallest set of integrals of this nature that is possible. We make use of all relations between integrals which symmetry permits to reduce the number of atomic integrals which appear in the matrix elements of Bloch functions. Making use of these relations, the matrix elements for the simple cubic crystal are given in Table II. A symbol like (n/m), such as (s/x), etc., denotes the matrix component of the Hamiltonian between a Bloch sum of atomic functions of symmetry type n and one of symmetry type m. We have also used the abbreviation $\xi=ak_x$, $\eta=ak_y$, $\zeta=ak_z$.

The various E symbols occurring in Table II are all independent, so that in fitting known energy values, we may treat them all as disposable constants. On the other hand, in some cases we may wish to express these symbols in terms of the smaller number of two-center integrals, as discussed in the preceding section. In this case, we may use Table I to write all of the E's in terms of these two-center integrals. In doing this, we must remember that the direction cosines in Table I are proportional to, but not equal to, the p, q, r of Table II. It is not hard to introduce the expressions of Table I into Table II, and we give in Table III the results of this substitution. Comparison of these tables allows us to see the considerable reduction in the number of disposable parameters introduced by using the two-center approximation. Thus, for instance, for interactions of d electrons on second-nearest neighbors, we have six independent integrals in Table II: $E_{xy,\,xy}(110)$, $E_{xy,\,xy}(011)$, $E_{xy,\,xz}(011)$, $E_{xy,\,3z^2-r^2}(110)$, $E_{3z^2-r^2,\,3z^2-r^2}\times(110)$, and $E_{x^2-y^2,\,x^2-y^2}(110)$. In Table III, these are all expressed in terms of three two-center integrals: $(dd\sigma)_2$, $(dd\pi)_2$, $(dd\delta)_2$. In some cases the reduction in number is less, or there is no reduction at all, as we have mentioned earlier. Each case is different, and must be separately examined by comparison of Tables II and III.

There are obviously many different independent

TABLE II. Matrix components of energy for simple cubic crystals.

(s/s)	$E_{s,s}(000)+2E_{s,s}(100)(\cos\xi+\cos\eta+\cos\zeta)+4E_{s,s}(110)(\cos\xi\cos\eta+\cos\xi\cos\zeta+\cos\eta\cos\zeta)+8E_{s,s}(111)\cos\xi\cos\eta\cos\zeta$
(s/x)	$2iE_{s,x}(100)\sin\xi+4iE_{s,x}(110)(\sin\xi\cos\eta+\sin\xi\cos\zeta)+8iE_{s,x}(111)\sin\xi\cos\eta\cos\zeta$
(s/xy)	$-4E_{s,xy}(110)\sin\xi\sin\eta-8E_{s,xy}(111)\sin\xi\sin\eta\cos\zeta$
(s/x^2-y^2)	$\sqrt{3}E_{s,3z^2-r^2}(001)(\cos\xi-\cos\eta)+2\sqrt{3}E_{s,3z^2-r^2}(110)(-\cos\xi\cos\zeta+\cos\eta\cos\zeta)$
$(s/3z^2-r)$	$E_{s,3z^2-r^2}(001)(-\cos\xi-\cos\eta+2\cos\zeta)-2E_{s,3z^2-r^2}(110)(-2\cos\xi\cos\eta+\cos\xi\cos\zeta+\cos\eta\cos\zeta)$
(x/x)	$E_{x,x}(000)+2E_{x,x}(100)\cos\xi+2E_{y,y}(100)(\cos\eta+\cos\zeta)+4E_{x,x}(110)(\cos\xi\cos\eta+\cos\xi\cos\zeta)+4E_{x,x}(011)\cos\eta\cos\zeta$ $+8E_{x,x}(111)\cos\xi\cos\eta\cos\zeta$
(x/y)	$-4E_{x,y}(110)\sin\xi\sin\eta-8E_{x,y}(111)\sin\xi\sin\eta\cos\zeta$
(x/xy)	$2iE_{x,xy}(010)\sin\eta+4iE_{x,xy}(110)\cos\xi\sin\eta+4iE_{x,xy}(011)\sin\eta\cos\zeta+8iE_{x,xy}(111)\cos\xi\sin\eta\cos\zeta$
(x/yz)	$-8iE_{x,yz}(111)\sin\xi\sin\eta\sin\zeta$
$(x/x-y^2)$	$\sqrt{3}iE_{s,3z^2-r^2}(001)\sin\xi+2\sqrt{3}iE_{s,3z^2-r^2}(011)(\sin\xi\cos\eta+\sin\xi\cos\zeta)+2iE_{s,x^2-y^2}(011)(\sin\xi\cos\eta-\sin\xi\cos\zeta)$ $+8iE_{x,x^2-y^2}(111)\sin\xi\cos\eta\cos\zeta$
$(x/3z^2-r^2)$	$-iE_{s,3z^2-r^2}(001)\sin\xi-2iE_{s,3z^2-r^2}(011)(\sin\xi\cos\eta+\sin\xi\cos\zeta)+2\sqrt{3}iE_{s,x^2-y^2}(011)(\sin\xi\cos\eta-\sin\xi\cos\zeta)$ $-(8/\sqrt{3})E_{x,x^2-y^2}(111)\sin\xi\cos\eta\cos\zeta$
$(z/3z^2-r^2)$	$2iE_{s,3z^2-r^2}(001)\sin\zeta+4iE_{s,3z^2-r^2}(011)(\cos\xi\sin\zeta+\cos\eta\sin\zeta)+(16/\sqrt{3})iE_{x,x^2-y^2}(111)\cos\xi\cos\eta\sin\zeta$
(xy/xy)	$E_{xy,xy}(000)+2E_{xy,xy}(100)(\cos\xi+\cos\eta)+2E_{xy,xy}(001)\cos\zeta+4E_{xy,xy}(110)\cos\xi\cos\eta$ $+4E_{xy,xy}(011)(\cos\xi\cos\zeta+\cos\eta\cos\zeta)+8E_{xy,xy}(111)\cos\xi\cos\eta\cos\zeta$
(xy/xz)	$-4E_{xy,xz}(011)\sin\eta\sin\zeta-8E_{xy,xz}(111)\cos\xi\sin\eta\sin\zeta$
(xy/x^2-y^2)	zero
$(xy/3z^2-r^2)$	$-4E_{yz,3z^2-r^2}(110)\sin\xi\sin\eta-8E_{xy,3z^2-r^2}(111)\sin\xi\sin\eta\cos\zeta$
(xz/x^2-y^2)	$2\sqrt{3}E_{xy,3z^2-r^2}(110)\sin\xi\sin\zeta+4\sqrt{3}E_{xy,3z^2-r^2}(111)\sin\xi\cos\eta\sin\zeta$
$(xz/3z^2-r^2)$	$2E_{xy,3z^2-r^2}(110)\sin\xi\sin\zeta+4E_{xy,3z^2-r^2}(111)\sin\xi\cos\eta\sin\zeta$
(x^2-y^2/x^2-y^2)	$E_{3z^2-r^2,3z^2-r^2}(000)+\frac{3}{4}E_{3z^2-r^2,3z^2-r^2}(1001)(\cos\xi+\cos\eta)+2E_{x^2-y^2,x^2-y^2}(001)(\frac{1}{4}\cos\xi+\frac{1}{4}\cos\eta+\cos\zeta)$ $+3E_{3z^2-r^2,3z^2-r^2}(110)(\cos\xi\cos\zeta+\cos\eta\cos\zeta)+4E_{x^2-y^2,x^2-y^2}(110)(\cos\xi\cos\eta+\frac{1}{4}\cos\xi\cos\zeta+\frac{1}{4}\cos\eta\cos\zeta)$ $+8E_{3z^2-r^2,3z^2-r^2}(111)\cos\xi\cos\eta\cos\zeta$
$(3z-r/3z-r^2)$	$E_{3z^2-r^2,3z^2-r^2}(000)+2E_{3z^2-r^2,3z^2-r^2}(001)(\frac{1}{4}\cos\xi+\frac{1}{4}\cos\eta+\cos\zeta)+\frac{3}{4}E_{x^2-y^2,x^2-y^2}(001)(\cos\xi+\cos\eta)$ $+4E_{3z^2-r^2,3z^2-r^2}(110)(\cos\xi\cos\eta+\frac{1}{4}\cos\xi\cos\zeta+\frac{1}{4}\cos\eta\cos\zeta)+3E_{x^2-y^2,x^2-y^2}(110)(\cos\xi\cos\zeta+\cos\eta\cos\zeta)$ $+8E_{3z^2-r^2,3z^2-r^2}(111)\cos\xi\cos\eta\cos\zeta$
$(x^2-y^2/3z^2-r^2)$	$\frac{1}{4}\sqrt{3}E_{3z^2-r^2,3z^2-r^2}(001)(-\cos\xi+\cos\eta)-\frac{1}{2}\sqrt{3}E_{x^2-y^2,x^2-y^2}(001)(-\cos\xi+\cos\eta)$ $+\sqrt{3}E_{3z^2-r^2,3z^2-r^2}(110)(\cos\xi\cos\zeta-\cos\eta\cos\zeta)-\sqrt{3}E_{x^2-y^2,x^2-y^2}(110)(\cos\xi\cos\zeta-\cos\eta\cos\zeta)$

integrals and types of atomic functions in Tables II and III, and we should not try in any case to set up a problem so complicated as to include all types. In special cases, the problem will simplify greatly by the omission of many types of orbitals. In such cases, it may well be that the secular equation set up from these matrix components will be simple enough along certain special directions or in certain special planes so that it can be solved by elementary means; this arises mostly because many of the nondiagonal matrix components have factors $\sin\xi$, etc., which vanish in special cases. However, since real crystals do not show the simple cubic structure, we shall not try to set up special cases and discuss them here, but shall rather go on to the structures which actually occur in nature, starting with the face-centered cubic structure.

V. THE FACE-CENTERED CUBIC STRUCTURE

The face-centered cubic structure is that in which the atoms are located at points $p\mathbf{a}i+qa\mathbf{j}+ra\mathbf{k}$, where $p+q+r$ is an even integer. The nearest neighbors of a given atom are located at the twelve points whose p, q, r are like (110). The second-nearest neighbors are at the six points like (200), and the third nearest at the 24 points like (211). We see that as far as the nearest and second-nearest neighbors are concerned, the problem is very similar to what we have already met with the simple cubic structure. That is, the nearest neighbors with the face-centered structure are precisely the same as the second-nearest neighbors with the simple cubic structure, and the second-nearest neighbors with the face-centered structure are like the nearest neighbors with the simple cubic structure, only twice as far away. Thus, if we are interested only in nearest and second-nearest neighbors, we can deduce the matrix components of energy immediately from the results of Tables II and III. For the diagonal matrix component of an s state, for instance, the quantity (s/s) of Tables II and III, the corresponding formulas are

$$\begin{aligned}(s/s)&=E_{s,s}(000)+4E_{s,s}(110)(\cos\xi\cos\eta+\cos\xi\cos\zeta\\&\quad+\cos\eta\cos\zeta)+2E_{s,s}(200)(\cos2\xi+\cos2\eta+\cos2\zeta)\\&=E_{s,s}(000)+4(ss\sigma)_1(\cos\xi\cos\eta+\cos\xi\cos\zeta\\&\quad+\cos\eta\cos\zeta)+2(ss\sigma)_2(\cos2\xi+\cos2\eta+\cos2\zeta).\quad(4)\end{aligned}$$

In a similar way, we can find all the other matrix components of energy.

From the matrix components of energy, we can easily demonstrate all the various cases of symmetry found at various points of the Brillouin zone with a crystal of this type. For instance, at the center of the Brillouin zone, where $\xi=\eta=\zeta=0$, we see by inspection that all nondiagonal matrix components of energy vanish, so that our original Bloch functions are the correct wave functions to form solutions of Schrödinger's equation. We find, of course, that the diagonal energies of the three p states are all equal, so that they are degenerate at the origin. The d states, however, split into a threefold degenerate and a twofold degenerate set, as we should expect from Bethe's rules. The reason why Bethe's rules apply is that at this symmetry point, the star of $\mathbf{k}$ vectors contains only one member, and as a result we can diagonalize the symmetry operations of the point group and the translation operation at the same time. The energies of the two d states at $\mathbf{k}=0$ are found to be

$$\begin{aligned}(xy/xy)&=(yz/yz)=(zx/zx)\\&=E_{xy,\,xy}(000)+4E_{xy,\,xy}(110)+8E_{xy,\,xy}(011)\\&\qquad+4E_{xy,\,xy}(200)+2E_{xy,\,xy}(002),\\(x^2-y^2,\,x^2-y^2)&=(3z^2-r^2,\,3z^2-r^2)\\&=E_{3z^2-r^2,\,3z^2-r^2}(000)+6E_{3z^2-r^2,\,3z^2-r^2}(110)\\&\quad+6E_{x^2-y^2,\,x^2-y^2}(110)+3E_{3z^2-r^2,\,3z^2-r^2}(002)\\&\qquad+3E_{x^2-y^2,\,x^2-y^2}(002).\end{aligned}\tag{5}$$

As we depart from $\mathbf{k}=0$, however, nondiagonal matrix components of energy between the various functions appear, proportional to k for small $\mathbf{k}$ values, and the degeneracy is removed. If we expand the matrix components in power series in ξ, η, ζ, and retain only the lowest terms, we can find the behavior of the energy bands in the neighborhood of $\mathbf{k}=0$, and are led to secular equations of the type discussed by Shockley.[13] Our method, however, is not limited to small k values, and we can solve for the behavior of the energy bands throughout the Brillouin zone.

The Brillouin zone for the face-centered cubic structure if of course identical with the Wigner-Seitz cell for the body-centered structure. We can easily demonstrate this fact from our matrix components of energy. By examining the reciprocal lattice, we find that the origin of the Brillouin zone, and the points $\xi=\pm\pi$, $\eta=\pm\pi$, $\zeta=\pm\pi$, lying at the corners of the cube, must be equivalent points. The first Brillouin zone includes the region closer to the origin than to these points. To demonstrate the body-centered nature of the reciprocal lattice, we must show that when we increase ξ, η, ζ, by $\pm\pi$ each, the energy is unchanged. When we examine the matrix components of energy, like those given in (4), we find that in fact each of them is unchanged when we make this change. Each of the components relating to a second-nearest neighbor in the simple cubic case, or a nearest neighbor in the face-centered structure, has a product of two sines or cosines in the expression in Table II or III, whereas each component relating to a nearest neighbor for the simple cubic case, or a second-nearest neighbor for the face-centered structure, has a single cosine, or the product of three, and these relations are just such as to assure the periodicity in the momentum space. The same thing would hold, of course, if more distant neighbors were included. Such simple considerations allow us to study all the symmetry properties of the wave functions and energy levels, and show that the LCAO method is particularly well suited for pedagogical purposes, in discussing the degeneracy properties of wave functions. Since such deductions are very elementary in nature, we shall not carry them further.

Many important crystals have the face-centered cubic structure, and the type of treatment we have sketched can be very useful for discussing their energy bands. A beginning in this direction is furnished by the discussion of Fletcher and Wohlfarth,[7,8] of the energy bands of nickel. They have considered the five d electrons of nickel, omitting discussion of the $4s$ band which really overlaps the d bands. They have considered only nearest neighbors, and have computed the integrals $(dd\sigma)$, $(dd\pi)$, $(dd\delta)$, using a two-center approximation, and suitable atomic orbitals and spherical potentials. They do not state their result in terms of these two-center integrals, but rather in terms of six quantities, which they call A_1, A_2, $\cdots A_6$, which are very closely related to our quantities $E_{xy,\,xy}(110)$, etc. We have already stated that for the interaction of d electrons on second-nearest neighbors in the simple cubic structure, there are six such integrals, and these are simply related to Fletcher and Wohlfarth's A's. However, since they were determined from a two-center approximation, we should be able to work back from these A's to find $(dd\sigma)$, etc. When we examine the numerical values of Fletcher and Wohlfarth's A's, we find that in fact they satisfy the relations necessary to be derived from two-center integrals, and working backward from them, we find that they must be given by $(dd\sigma)=-0.2504E_0$, $(dd\pi)=0.1348E_0$, $(dd\delta)=-0.0204E_0$, where $E_0=1.349$ ev. It is interesting to see the rapid decrease in the numerical values of these integrals, as we go from the σ orbital, which of course will overlap the most, through the π to the δ orbital, which overlaps the least. The alternation of sign of the integrals is demanded by the symmetry of the orbitals.

If we use these values of the integrals and the matrix components of energy from Table III for the nearest neighbors in a face-centered cubic structure (that is, the second-nearest neighbors in a simple cubic structure), and consider the five d states, we then find precisely the matrix components of energy considered by Fletcher and Wohlfarth. They have solved the five-by-five secular equation at many points throughout

[13] W. Shockley, Phys. Rev. 78, 173 (1950).

TABLE III. Matrix components of energy for simple cubic crystals, two-center approximation.

(s/s)	$s_0+2(ss\sigma)_1(\cos\xi+\cos\eta+\cos\zeta)+4(ss\sigma)_2(\cos\xi\cos\eta+\cos\xi\cos\zeta+\cos\eta\cos\zeta)+8(ss\sigma)_3\cos\xi\cos\eta\cos\zeta$
(s/x)	$2i(sp\sigma)_1\sin\xi+2\sqrt{2}i(sp\sigma)_2(\sin\xi\cos\eta+\sin\xi\cos\zeta)+(8/\sqrt{3})i(sp\sigma)_3\sin\xi\cos\eta\cos\zeta$
(s/xy)	$-2\sqrt{3}(sp\sigma)_2\sin\xi\sin\eta-(8/\sqrt{3})(sd\sigma)_3\sin\xi\sin\eta\cos\zeta$
(s/x^2-y^2)	$\sqrt{3}(sd\sigma)_1(\cos\xi-\cos\eta)+\sqrt{3}(sd\sigma)_2(\cos\xi\cos\zeta-\cos\eta\cos\zeta)$
$(s/3z^2-r^2)$	$(sd\sigma)_1(-\cos\xi-\cos\eta+2\cos\zeta)+(sd\sigma)_2(-2\cos\xi\cos\eta+\cos\xi\cos\zeta+\cos\eta\cos\zeta)$
(x/x)	$p_0+2(pp\sigma)_1\cos\xi+2(pp\pi)_1(\cos\eta+\cos\zeta)+2(pp\sigma)_2(\cos\xi\cos\eta+\cos\xi\cos\zeta)$ $+2(pp\pi)_2(\cos\xi\cos\eta+\cos\xi\cos\zeta+2\cos\eta\cos\zeta)+[(8/3)(pp\sigma)_3+(16/3)(pp\pi)_3]\cos\xi\cos\eta\cos\zeta$
(x/y)	$-2[(pp\sigma)_2-(pp\pi)_2]\sin\xi\sin\eta-(8/3)[(pp\sigma)_3-(pp\pi)_3]\sin\xi\sin\eta\cos\zeta$
(x/xy)	$2i(pd\pi)_1\sin\eta+(\sqrt{6})i(pd\sigma)_2\cos\xi\sin\eta+2\sqrt{2}i(pd\pi)_2\sin\eta\cos\zeta+[(8/3)(pd\sigma)_3+(8/3\sqrt{3})(pd\pi)_3]i\cos\xi\sin\eta\cos\zeta$
(x/yz)	$[-(8/3)(pd\sigma)_3+(16/3\sqrt{3})(pd\pi)_3]i\sin\xi\sin\eta\sin\zeta$
(x/x^2-y^2)	$\sqrt{3}(pd\sigma)_1\sin\xi-(3/2)^{\frac{1}{2}}(pd\sigma)_2i\sin\xi\cos\zeta+2\sqrt{2}(pd\pi)_2i[\sin\xi\cos\eta+\frac{1}{2}\sin\xi\cos\zeta]+(8/\sqrt{3})(pd\pi)_3i\sin\xi\cos\eta\cos\zeta$
$(x/3z^2-r^2)$	$-(pd\sigma)_1i\sin\xi+\sqrt{2}(pd\sigma)_2i[\sin\xi\cos\eta-\frac{1}{2}\sin\xi\cos\zeta]-(\sqrt{6})(pd\pi)_2i\sin\xi\cos\zeta-(8/3)(pd\pi)_3i\sin\xi\cos\eta\cos\zeta$
$(z/3z^2-r^2)$	$2i(pd\sigma)_1\sin\zeta+[(1/\sqrt{2})(pd\sigma)_2+(\sqrt{6})(pd\pi)_2]i[\cos\xi\sin\zeta+\cos\eta\sin\zeta]+(16/3)(pd\pi)_3i\cos\xi\cos\eta\sin\zeta$
(xy/xy)	$d_0+2(dd\pi)_1(\cos\xi+\cos\eta)+2(dd\delta)_1\cos\zeta+3(dd\sigma)_2\cos\xi\cos\eta+2(dd\pi)_2(\cos\xi\cos\zeta+\cos\eta\cos\zeta)$ $+(dd\delta)_2(\cos\xi\cos\eta+2\cos\xi\cos\zeta+2\cos\eta\cos\zeta)+[(8/3)(dd\sigma)_3+(16/9)(dd\pi)_3+(32/9)(dd\delta)_3]\cos\xi\cos\eta\cos\zeta$
(xy/xz)	$2[-(dd\pi)_2+(dd\delta)_2]\sin\eta\sin\xi\sin\zeta+[-(8/3)(dd\sigma)_3+(8/9)(dd\pi)_3+(16/9)(dd\delta)_3]\cos\xi\sin\eta\sin\zeta$
(xy/x^2-y^2)	zero
$(xy/3z^2-r^2)$	$\sqrt{3}[(dd\sigma)_2-(dd\delta)_2]\sin\xi\sin\eta+(16/3\sqrt{3})[(dd\pi)_3-(dd\delta)_3]\sin\xi\sin\eta\cos\zeta$
(xz/x^2-y^2)	$-\frac{3}{4}[(dd\sigma)_2-(dd\delta)_2]\sin\xi\sin\zeta-(8/3)[(dd\pi)_3-(dd\delta)_3]\sin\xi\cos\eta\sin\zeta$
$(xz/3z^2-r^2)$	$\frac{1}{2}\sqrt{3}[-(dd\sigma)_2+(dd\delta)_2]\sin\xi\sin\zeta-(8/3\sqrt{3})[(dd\pi)_3-(dd\delta)_3]\sin\xi\cos\eta\sin\zeta$
(x^2-y^2/x^2-y^2)	$d_0+\frac{1}{2}(dd\sigma)_1(\cos\xi+\cos\eta)+(dd\delta)_1(\frac{1}{2}\cos\xi+\frac{1}{2}\cos\eta+2\cos\zeta)+4(dd\pi)_2\cos\xi\cos\eta$ $+[\frac{1}{4}(dd\sigma)_2+(dd\pi)_2+(9/4)(dd\delta)_2](\cos\xi\cos\zeta+\cos\eta\cos\zeta)+[(16/3)(dd\pi)_3+(8/3)(dd\delta)_3]\cos\xi\cos\eta\cos\zeta$
$(3z^2-r^2/3z^2-r^2)$	$d_0+(dd\sigma)_1(\frac{1}{2}\cos\xi+\frac{1}{2}\cos\eta+2\cos\zeta)+\frac{3}{4}(dd\delta)_1(\cos\xi+\cos\eta)+(dd\sigma)(\cos\xi\cos\eta+\frac{1}{4}\cos\xi\cos\zeta+\frac{1}{4}\cos\eta\cos\zeta)$ $+3(dd\pi)_2(\cos\xi\cos\zeta+\cos\eta\cos\zeta)+3(dd\delta)_2(\cos\xi\cos\eta+\frac{1}{4}\cos\xi\cos\zeta+\frac{1}{4}\cos\eta\cos\zeta)$ $+[(16/3)(dd\pi)_3+(8/3)(dd\delta)_3]\cos\xi\cos\eta\cos\zeta$
$(x^2-y^2/3z^2-r^2)$	$\frac{1}{2}\sqrt{3}[-(dd\sigma)_1+(dd\delta)_1](\cos\xi-\cos\eta)+[\frac{1}{4}\sqrt{3}(dd\sigma)_2-\sqrt{3}(dd\pi)_2+\frac{3}{4}\sqrt{3}(dd\delta)_2](\cos\xi\cos\zeta-\cos\eta\cos\zeta)$

the unit cell of reciprocal space, obtaining the distribution of energy levels in energy in this way. They also show that the secular equation can be factored, leading to no factor worse than a quadratic equation, in the 100, 110, and 111 directions. This of course is to be expected. We can consider the symmetry of the wave functions for $\mathbf{k}$ vectors in these directions and can see that if we combine the various d functions to give combinations belonging to the appropriate irreducible representations for these directions, we shall get the factoring of the secular equation which they have found.

The results of this calculation of Fletcher and Wohlfarth are very interesting, but the reader will see that they are not carried out exactly according to the spirit of the present discussion. Our present view would be that more accurate values of the energies at certain symmetry points could probably be found by other methods, such as the method of orthogonalized plane waves, and that it would be better to use the present method as an interpolation, determining the integrals as disposable constants. Fortunately, we have such a calculation of a crystal having the face-centered structure. Recent results of Howarth[14] on copper, by the cellular method, provide us with some of the necessary information. Howarth's calculations are very accurate but unfortunately are carried out only at $\mathbf{k}=0$ and at the edge of the Brillouin zone in the 001 direction or at the point $\zeta=\pi$, $\xi=\eta=0$. We shall examine these calculations and see what information they can give us, using this as an illustration of the application of the method.

If we let ζ be arbitrary but assume $\xi=\eta=0$, the matrix components of energy for the face-centered structure take on the following form:

$$
\begin{aligned}
&(s/s)=E_{s,s}(000)+4E_{s,s}(110)+8E_{s,s}(110)\cos\zeta,\\
&(xy/xy)=E_{xy,xy}(000)+4E_{xy,xy}(110)\\
&\qquad\qquad+8E_{xy,xy}(011)\cos\zeta,\\
&(xz/xz)=(yz/yz)=E_{xy,xy}(000)+4E_{xy,xy}(011)\\
&\qquad+4E_{xy,xy}(110)+4E_{xy,xy}(011)\cos\zeta,\\
&(x^2-y^2/x^2-y^2)\\
&\quad=E_{3z^2-r^2,3z^2-r^2}(000)+4E_{x^2-y^2,x^2-y^2}(110)\\
&\qquad+6E_{3z^2-r^2,3z^2-r^2}(110)+2E_{x^2-y^2,x^2-y^2}(110)\cos\zeta,\\
&(3z^2-r^2/3z^2-r^2)\\
&\quad=E_{3z^2-r^2,3z^2-r^2}(000)+4E_{3z^2-r^2,3z^2-r^2}(110)\\
&\qquad+6E_{x^2-y^2,x^2-y^2}(110)+2E_{3z^2-r^2,3z^2-r^2}(110)\cos\zeta,\\
&(s/3z^2-r^2)=4E_{s,3z^2-r^2}(110)-4E_{s,3z^2-r^2}(110)\cos\zeta.
\end{aligned}
\tag{6}
$$

All other nondiagonal matrix components vanish. We see that at $\mathbf{k}=0$, where $\cos\zeta=1$, all nondiagonal matrix

[14] D. J. Howarth, Proc. Roy. Soc. (London) **A220**, 513 (1953).

components vanish, so that we are left with three energy levels: the nondegenerate s level; the threefold degenerate state formed from the functions xy, yz, zx; and the twofold degenerate state formed from x^2-y^2 and $3z^2-r^2$. A twofold degeneracy between the states xz, yz persists for all ζ values, but otherwise the degeneracy is all removed when ζ departs from zero, so that at $\zeta=\pi$ we have five distinct energies. Howarth has determined the three energy values we have just described at $\zeta=0$, and the five at $\zeta=\pi$. Let us see what information this gives us about the E integrals.

When we count up in Eq. (6), we find that there are nine independent E integrals concerned in the formulas. Hence it is clear that we can determine all but one of these from Howarth's calculations. When we examine the numbers, we see that we can proceed as follows. The nondiagonal matrix component $(s/3z^2-r^2)$ serves only to push apart the diagonal energies (s/s) and $(3z^2-r^2/3z^2-r^2)$ at $\zeta=\pi$. But the numerical values indicate that these two states are already far apart at this point in the Brillouin zone, so that a small nondiagonal matrix component would have almost no effect in pushing them further apart. We can then assume with very slight error that this nondiagonal matrix component is negligible at $\zeta=\pi$. We then use Eq. (6) to determine the eight integrals aside from $E_{s,\,3z^2-r^2}(110)$, which we neglect. This integral would become important only over the relatively small range of ζ where the s function was having an energy close to that of the $3z^2-r^2$ function; it would determine the details of the interaction of s and d functions where their energies cross. We cannot get information about this from calculations at the center and edges of the Brillouin zone.

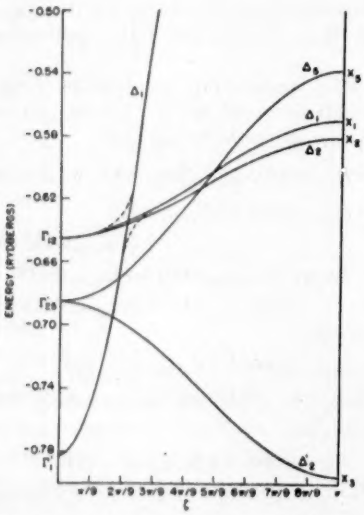

FIG. 1. Variation of energy with wave vector in the 001 direction for Cu calculated using Howarth's energy values at the center and boundary of the zone. (Symmetry symbols are taken from reference 4.)

Proceeding in this way, from Howarth's numerical values, we can compute the values of the remaining eight integrals. These are tabulated in Table IV in rydbergs. The reader can find Howarth's values, if he wishes, by substituting these integrals in Eq. (6). We plot the functions of ζ, given from Eq. (6), in Fig. 1. We see the way in which the s function cuts across the d band steeply; we recall that if the matrix component $(s/3z^2-r^2)$ were known, we should be able to show that the s function does not cut the d function $3z^2-r^2$, but that their energies are pushed apart in the immediate neighborhood of the crossover point as schematically indicated by the dotted line in Fig. 1. Since, however, the energy of the s state varies so rapidly with $\mathbf{k}$, we expect that this effect will not be felt far from this crossover point. It is this fact which makes it a rather good approximation to treat the problem of the five d electrons in a transition metal as independent of the s electron, merely superposing their final energy bands, as Fletcher and Wohlfarth have done.

Comparison of Fig. 1 with Fig. 1 of Fletcher and Wohlfarth's paper (reference 8) shows that the energies, as a function of $\mathbf{k}$, in the 100 direction, show a surprising similarity though one energy level, that arising from the $3z^2-r^2$ state, behaves quite differently, rising with increasing ζ in Howarth's case, falling in Fletcher and Wohlfarth's. But nevertheless the similarities are close. This is shown from Table IV, where we have given not only Howarth's values of the integrals, but also those computed from Fletcher and Wohlfarth's integrals $(dd\sigma)$, etc., which we have already mentioned, expressed in rydberg units so that they are comparable with Howarth's integrals. The agreement of the integrals $E_{xy,\,xy}(110)$ and $E_{xy,\,xy}(011)$ is surprisingly good. The disagreement of the other two integrals computed by both methods is, of course, a result of the discrepancy between the behavior of the $3z^2-r^2$ state, showing that the behavior of this state cannot be described in terms of two-center integrals. Fletcher and Wohlfarth's calculations, of course, assume identical values for the quantities $E_{xy,\,xy}(000)$ and $E_{3z^2-r^2,\,3z^2-r^2}(000)$, since these must be equal in the two-center approximation. Since this quantity merely appears as an additive constant in Fletcher and Wohlfarth's calculation, we cannot determine it in their case. It is interesting to see that the difference between the two integrals as determined by Howarth's calculations, though appreciable, is by no means large. Fletcher and Wohlfarth's calculations of course give no information about the s state, and neither theirs nor Howarth's give information about the interaction between s and d states, as we have pointed out.

This discussion of the resemblances and differences between the calculations of Fletcher and Wohlfarth on nickel, and of Howarth on copper, carried out by quite different methods, suggests that in the future, when more accurate calculations are made for more metals showing the face-centered structure, comparisons of

this type may prove quite valuable in discussing the variation of the energy bands from one element to the next. Further calculations now being carried out in this laboratory by Howarth on copper, if successful, should provide more complete information about this substance, perhaps filling in some of the gaps in Table IV.

VI. THE BODY-CENTERED CUBIC STRUCTURE

The body-centered cubic structure can be handled by methods similar to those we have just used for the face-centered structure. It has atoms at points $pa\mathbf{i}+qa\mathbf{j}+ra\mathbf{k}$, where p, q, r are all even, or all odd, integers. The nearest neighbors of a given atom are the eight of type (111), the second nearest are the six of type (200), and the third nearest are the twelve of type (220). We see that all three of these types are similar to those met in the simple cubic structure, the first being equivalent to the third-nearest neighbors in the simple cubic structure, the second to the nearest neighbors in the simple cubic structure, but twice as far away, and the third being equivalent to the second-nearest neighbors in the simple cubic structure, but twice as far away. Thus we can read the matrix components of the energy for all these types of neighbors directly from the results of Tables II and III. For the s state, for instance, we have

$$(s/s)=E_{s,s}(000)+8E_{s,s}(111)\cos\xi\cos\eta\cos\zeta+4E_{s,s}(200)(\cos2\xi\cos2\eta+\cos2\xi\cos2\zeta+\cos2\eta\cos2\zeta)+2E_{s,s}(220)(\cos2\zeta+\cos2\eta+\cos2\zeta). \quad (7)$$

As with the face-centered structure, it is interesting to check the relationship between these energy expressions and the periodicity in the reciprocal lattice and the structure of the Brillouin zone. The reciprocal space must show a face-centered cubic type of symmetry, the points such as $\xi=0, \eta=\zeta=\pi$ being equivalent to the origin. If we make this transformation, we see that the expression (7) is unchanged, and examination of Tables II and III shows that the same thing will be true of each matrix component. We can also easily check the special symmetry properties at the center and other symmetry points of the Brillouin zone.

There are a number of important metals which show the body-centered structure: the alkalies, on the one hand, and some of the transition metals, on the other. The alkalies have of course been the subject of much study, and the indications from both the cellular method and the method of orthogonalized plane waves are that the conduction band is rather closely like that characteristic of free electrons, explaining the success of the free-electron model in treating these simple metals. The fact that the alkali metal energy band is so nearly free-electron-like throws some interesting light on our approximation method. The fact appearing from the free-electron nature is that the curvature of the energy surface at $\mathbf{k}=0$ is much less than that at the boundaries of the Brillouin zone. We see from Eq. (7) that in the 100 direction, for $\eta=\zeta=0$, the energy is given by $8E_{s,s}(111)\cos\xi+[8E_{s,s}(200)+2E_{s,s}(220)]\times\cos2\xi+$constant. Now if the quantities $E_{s,s}(200)$ and $E_{s,s}(220)$ were determined as real energy integrals from atomic orbitals, they would have to be negative, just as $E_{s,s}(111)$ is. We then see at once that these terms would increase the curvature already present from the first term at $\xi=0$ but would decrease it at $\xi=\pi$. In other words, if we had this sign for $E_{s,s}(200)$ and $E_{s,s}(220)$, we should have a curvature of the energy surface which (numerically) would be greater at $\mathbf{k}=0$ than at the boundary of the zone, which is contrary to our other information. It must be, then, that to fit the known properties of the energy surface, we must choose the quantities $E_{s,s}(200)$ and $E_{s,s}(220)$ of opposite sign to what we should find if we regarded them as energy integrals between atomic orbitals, and we may by no means neglect them. This emphasizes the importance of our principle that these quantities are really to be regarded as disposable parameters rather than atomic integrals; we may be led seriously astray if we disregard this fact. On the other hand, if we computed the integrals properly from Löwdin functions, we might well get this opposite sign for the integrals for more distant neighbors; for the characteristic of the orthogonalized functions is that they must have contributions on rather distant atoms, of opposite sign to those on the central atom where the orbital is located, which might change the sign of the integral.

The greatest interest of the body-centered structure comes not from the alkali metals, however, but from the tight bound transition metals showing this structure, vanadium, chromium, one of the forms of iron, molybdenum, tantalum, and tungsten. These metals, on account of their tight binding, and on account of the slight antiferromagnetic properties of chromium and the ferromagnetic behavior of body-centered iron, have a very great interest and practical importance. Unfortunately, we do not have any really reliable determination of the structure of their energy bands, by any method.

TABLE IV. Energy integrals (in rydbergs) for face-centered cubic structure of Ni (Fletcher and Wohlfarth) and Cu (Howarth).

Integral	Fletcher and Wohlfarth (Ni)	Howarth (Cu)
$E_{s,s}(000)$		+0.0366
$E_{s,s}(110)$		−0.0683
$E_{xy,xy}(000)$		−0.6388
$E_{3z^2-r^2,3x^2-r^2}(000)$		−0.5925
$E_{xz,xy}(110)$	−0.01928	−0.0253
$E_{xy,xy}(011)$	+0.00574	+0.00683
$E_{3z^2-r^2,3x^2-r^2}(110)$	−0.00786	−0.00375
$E_{x^2-y^2,x^2-y^2}(110)$	+0.01353	−0.00500
$E_{xy,xz}(011)$	−0.03116	
$E_{xy,3x^2-r^2}(110)$	−0.03917	

Lacking such information, it is tempting to ask how much our simplified LCAO method can tell us. Accordingly, we shall give here a treatment of the behavior of the *3d* band in such a metal, though, since we have no correct calculation to start with, we must arbitrarily assume values for the various integrals. Even in this way we can derive interesting results, and our present work can form a framework for more accurate treatments of this structure, when calculations by better methods become available in the future.

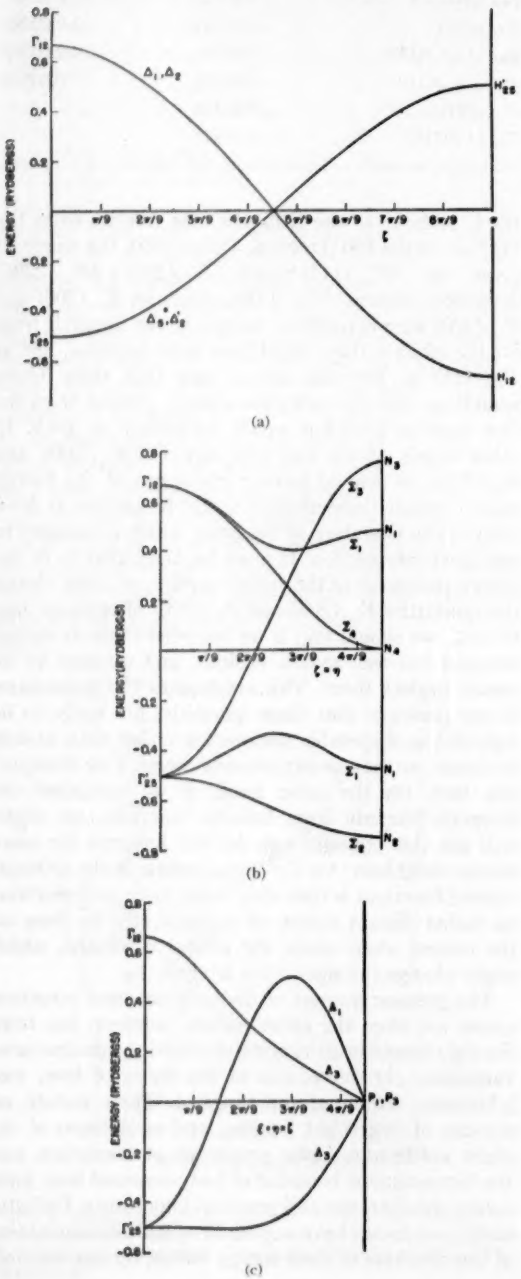

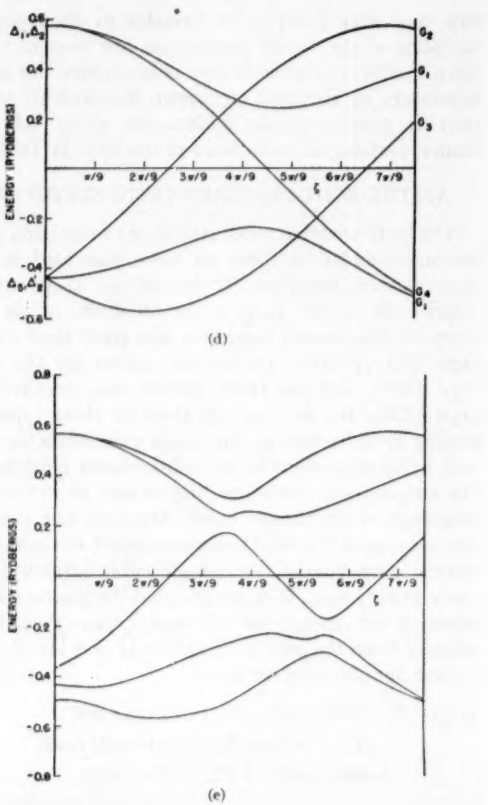

FIG. 2. Variation of energy with wave vector along various lines in reciprocal space calculated for body-centered structure using Fletcher and Wohlfarth's values for the nearest-neighbor *d* interactions. (a) 001 direction; (b) 011 direction; (c) 111 direction; (d) parallel to 001 direction with $\xi=0$, $\eta=\pi/6$; (e) parallel to 001 direction with $\xi=\pi/18$, $\eta=\pi/6$. (Symmetry symbols are taken from reference 4.)

Since we have no better information, we shall use the two-center approximation, and since we have no values for the integrals $(dd\sigma)$, $(dd\pi)$, $(dd\delta)$, we shall use the same ones determined by Fletcher and Wohlfarth for nickel. The absolute values of these integrals would certainly be different for the elements having the body-centered structure, but very likely the ratios of the three integrals would not be very different. Hence it seems likely that our treatment can give some idea of the general form of the energy bands, though not of the absolute width. We assume, of course, only nearest-neighbor interactions, as Fletcher and Wohlfarth did for nickel. Then the matrix components of energy are found from Table III, using the values appropriate for third-nearest neighbors in the simple cubic case.

We have taken the secular equation and values of the integrals which we have just described, and have solved the five-by-five secular equation at many points through

the Brillouin zone. This calculation was made on the Whirlwind digital computer, and we wish to thank the authorities in charge of that computer, and in particular to thank Dr. Alvin Meckler, who assisted in the programming, for their help in making the calculations. Energy levels were computed on a network of points 10 degrees apart along the axes (that is, for intervals of $\pi/18$) for ξ, η, and ζ. Calculations had to be made at 220 independent points in the Brillouin zone:[15] for $\xi<\eta\leq\zeta\leq\pi/2$. The limitation that ξ, η, ζ be less than $\pi/2$ will be discussed in a later paragraph; it proves to be the case that the roots for larger values of these quantities can be obtained at once from values when they are less than $\pi/2$.

Calculations at these points did not all have to be made by solving the secular equation, since it proves to to be possible to get an analytical solution at all points in the xy plane, or for $\zeta=0$. If we take the matrix components, and insert this value of ζ, we find that the only nondiagonal matrix components of energy which do not vanish are (xz/yz) and $(xy/3z^2-r^2)$. Thus the secular equation factors into a quadratic equation, involving the functions xz and yz; another quadratic, involving xy and $3z^2-r^2$; and the function x^2-y^2, which is a solution as it stands.

In Fig. 2,[15a] we show the energy levels as computed in this way, along a number of lines in the reciprocal lattice. In Fig. 2a, 2b, and 2c we show the energy along the 001, 011, and 111 directions. By comparison with Fig. 1, or with the figures in Fletcher and Wohlfarth's papers, we see that the arrangement of energy bands is quite different in the body-centered structure from what it is in the face-centered structure: at the origin, the energy levels are near the top and bottom of the band rather than near the center, as in the face-centered structure. This would lead us to expect a large density of levels near the top and bottom of the band, with a dip in the middle, which as we shall show in a moment really occurs. We also show two curves indicating the way in which the degeneracy is removed as we move away from symmetry positions in the Brillouin zone. In Fig. 2d, we show curves for the energy levels for $\xi=0$, $\eta=\pi/6$, ζ arbitrary. By comparison with Fig. 2a, we see that the double and triple degeneracies found in the 001 direction are split, but that an accidental degeneracy is still permitted, since we are still in a symmetry plane. In Fig. 2e, we have $\xi=\pi/18$, $\eta=\pi/6$, ζ arbitrary. The accidental degeneracy present in Fig. 2d is now removed, the energy levels being modified so that they cannot cross at all. This is a sample of what happens in other general directions in the Brillouin zone.

From these calculations, we have found values of $N(E)$, the number of states in a given energy range. We have done this in the following way. We have set up curves, like Figs. 2a, 2d, and 2e, for all the calculated values of ξ and η. In each of these curves, we have subdivided the energy range into small intervals (0.05 unit) and have measured the relative extent of the ζ axis for which the curve lay within each of these intervals. This results in a step curve for $N(E)$ determined from each of these energy curves. We have finally added these step curves for all the various energy curves, weighting each one properly. Since we have used a finite net, and a finite energy interval, this of course does not give a smooth curve, and one could get better results by more elaborate methods of calculation; but since our problem is only illustrative anyway, it did not seem worth while to take greater pains in calculating the energy distribution. The results of this calculation are shown in Fig. 3. We see, as we suspected, that there is a decided dip in the density of states curve in the center. There is a good deal of experimental evidence, based on electronic specific heat and other evidence, for such a dip, though we shall not go into the details here. The curve of Fig. 3 is symmetrical about its midpoint, for reasons which we shall now discuss.

The reason for this symmetry is the existence of a type of reflection symmetry of the whole problem

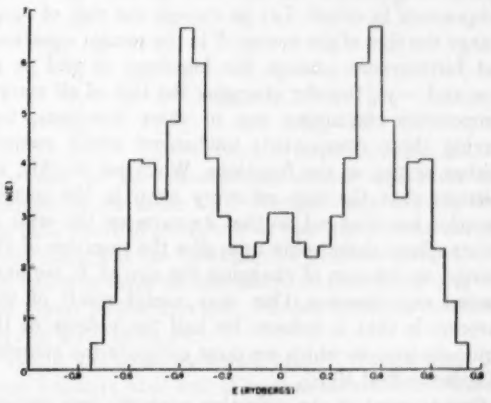

FIG. 3. Density of states curve for body-centered structure calculated using Fletcher and Wohlfarth's parameters for the nearest-neighbor d interactions. The total area under the $N(E)$ curve is five corresponding to five states.

[15] A complete table of the eigenvalues of the 220 secular equations, in hectographed form, may be obtained by writing the authors. This table has also been deposited as Document No. 4225 with the ADI Auxiliary Publications Project, Photoduplication Service, Library of Congress, Washington 25, D. C. A copy may be secured by citing the Document number and by remitting $1.25 for photoprints or $1.25 for 35-mm microfilm. Advance payment is required. Make checks or money orders payable to: Chief, Photoduplication Service, Library of Congress.

[15a] In the ordinates of Figs. 2 and in the abscissa of Fig. 3, the unit of energy is incorrectly indicated. Instead of the rydberg the unit of energy should be $E_0=1.349$ ev. (The unit of energy in terms of which Fletcher and Wohlfarth express their nearest-neighbor interactions between d functions for the face-centered structure.) In any case, the scale of energy in these diagrams should not be taken seriously. There is little reason to believe anything but the ratios of the nearest-neighbor d interactions is correct as we have used them. We expect that the broad features of the curves are correct but do not believe that the actual numerical values of the energies are significant.

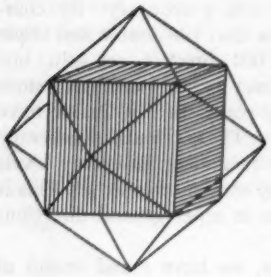

FIG. 4. First Brillouin zone for the body-centered cubic structure showing the inscribed cube bounded by the planes $\xi=\pm\pi/2$, $\eta=\pm\pi/2$, $\zeta=\pm\pi/2$.

about the planes $\xi=\pm\pi/2$, or $\eta=\pm\pi/2$, etc. These planes enclose a cubic volume half the volume of the Brillouin zone. This is made clear from Fig. 4 in which we show the whole Brillouin zone and the cube under discussion. The Brillouin zone consists of the cube and of pyramids extending outward from each face of the cube. If these pyramids were reflected in the faces of the cube, so that they extended inside rather than outside the cube, they would just fill the cube. The symmetry property to which we have referred can then be stated as follows: the energies of the five states at a point in one of the pyramids, outside the cube, and at the mirror image of this point reflected in the face of the cube, therefore located in the corresponding pyramid inside the cube, are the negatives of each other. (In this statement, we are assuming that the additive term in the energy, $E_{xy,xy}(000)$, is zero.) Thus all the energies inside the cube occur with the opposite sign at corresponding points outside the cube, proving the symmetry of the $N(E)$ curve to which we have just referred.

To prove this theorem, we wish to show that the roots of the secular equation are unchanged if, for instance, we change ζ to $\pi-\zeta$, and leave ξ and η unchanged. That is, we change the sign of $\cos\zeta$ but leave all other sines and cosines unchanged in our matrix components. We can now examine the matrix components in detail. Let us change the sign of $\cos\zeta$; change the sign of the energy E in the secular equation; and furthermore, change the functions xz and yz to $-xz$ and $-yz$, thereby changing the sign of all matrix components containing one of these functions, but leaving those components unchanged which contain neither or two of the functions. When we do this, we discover that the sign of every term in the secular equation has changed, so that its roots are the same as before. Since these roots now give the negative of the energy, on account of changing the sign of E, we have proved our theorem. One very useful result of this theorem is that it reduces by half the volume of the Brillouin zone in which we must compute the energies, in order to find $N(E)$.

One account of the reflection property just proved, we see that on the faces of the cube equal positive and negative energy levels must occur in pairs. That is, since there are five levels, one must be zero, and the others must be plus and minus two values. This suggests that the secular equation should factor into quadratics along these faces, and this is in fact the case. It does not follow from the vanishing of matrix components, but if we multiply out the whole secular equation, we find that it has a factor E, and the remaining fourth-order equation becomes a quadratic for E^2, leading to the properties described. We shall not write down this quadratic equation, but it is not hard to derive and it obviously leads to additional points in the Brillouin zone where we can solve the secular equation analytically, rather than having to use the digital computer.

The cube which we have introduced in Fig. 4 has a special significance. Suppose we considered the problem in which the atom at the center of our body-centered cubic structure was of one type, but its eight nearest neighbors were of another sort. We should then have a simple cubic structure with two atoms in the unit cell, the cube having a side of $2a$, in our present notation, and one atom being at the corner, the other at the center, of the unit cell. The cube in the Brillouin zone which we have been discussing is then just the Brillouin zone for this simple cubic structure. It is now easy to modify our discussion so as to take up this case of two unlike atoms. This case is of considerable importance. It is met in some alloys; for instance, in the ordered form of CuZn, though in that case we should be more interested in the $4s$ and $4p$ levels than in the $3d$. But in particular, it is probably met in chromium, on account of the antiferromagnetic nature of that element. It has been suggested by one of the writers[16] that electrons of one spin, in an antiferromagnetic substance, may see an alternating potential, having one value in atoms whose spin is preponderately in the same direction as the spin of the electron in question, but having a higher value in atoms of opposite spin. We know from the work of Shull and Wilkinson[17] that chromium appears to show a small antiferromagnetism, corresponding to about 0.4 Bohr magneton per atom. Thus we must conclude that the electrons feel such an alternating potential, and that as far as they are concerned the crystal is made of two unlike centers of force, forming the simple cubic structure with two unlike atoms per unit cell, of the type which we have just described. This situation is somewhat similar to that suggested by Ganzhorn (reference 10), though his discussion is so confused, as between energy band and Heitler-London approaches, that it is hard to understand the details of his argument.

Let us now ask how our problem is to be formulated in terms of the simple cubic structure containing two atoms per unit cell. We must set up ten Bloch functions, the first five corresponding to the five d orbitals on the atoms at the corners of the cubic unit cells, the second

[16] J. C. Slater, Phys. Rev. **82**, 538 (1951).
[17] C. G. Shull and M. F. Wilkinson, Revs. Modern. Phys. **25**, 100 (1953).

five corresponding to the five d orbitals on the atoms at the centers. The nearest neighbor of an atom of one type is now an atom of the other type. Hence since we are considering only interactions between nearest neighbors, the only nonvanishing matrix components of energy will be nondiagonal components between an atom of one type and an atom of the other type. Thus, for instance, the nondiagonal matrix component between an xy orbital on the atom of one type, and the xy on the atom of the other type, will be the expression (xy/xy) which we have already considered; and so on. For convenience in writing, let us label these matrix components H_{11}, H_{12}, $\cdots H_{15}$, H_{21}, $\cdots H_{55}$. There will be no nondiagonal matrix components between Bloch functions formed from two types of orbital on the same type of atom, for such nondiagonal matrix components would involve interactions between second-nearest neighbors, which we are disregarding. The diagonal matrix component of energy of one of the Bloch wave functions will be independent of $\mathbf{k}$ for the same reason. If the atoms of the two types are really identical, then the diagonal matrix components of atoms of either type will be the same; but, if they are not identical, these diagonal components will be different, and it is just the effect of this difference which we wish to investigate.

Let the diagonal energies of the two types of atoms be H_a and H_b. Then the secular equation can be written as given in Eq. (8). We can solve this equation, if we assume that we have already solved the corresponding five-by-five secular equation whose matrix components are $H_{11}\cdots H_{55}$. For that solution tells us how to find linear combinations of our five functions, which diagonalize this matrix,

$$\begin{vmatrix} H_a-E & 0 & 0 & 0 & 0 & H_{11} & H_{12} & H_{13} & H_{14} & H_{15} \\ 0 & H_a-E & 0 & 0 & 0 & H_{21} & H_{22} & H_{23} & H_{24} & H_{25} \\ 0 & 0 & H_a-E & 0 & 0 & H_{31} & H_{32} & H_{33} & H_{34} & H_{35} \\ 0 & 0 & 0 & H_a-E & 0 & H_{41} & H_{42} & H_{43} & H_{44} & H_{45} \\ 0 & 0 & 0 & 0 & H_a-E & H_{51} & H_{52} & H_{53} & H_{54} & H_{55} \\ H_{11} & H_{12} & H_{13} & H_{14} & H_{15} & H_b-E & 0 & 0 & 0 & 0 \\ H_{21} & H_{22} & H_{23} & H_{24} & H_{25} & 0 & H_b-E & 0 & 0 & 0 \\ H_{31} & H_{32} & H_{33} & H_{34} & H_{35} & 0 & 0 & H_b-E & 0 & 0 \\ H_{41} & H_{42} & H_{43} & H_{44} & H_{45} & 0 & 0 & 0 & H_b-E & 0 \\ H_{51} & H_{52} & H_{53} & H_{54} & H_{55} & 0 & 0 & 0 & 0 & H_b-E \end{vmatrix} = 0. \tag{8}$$

Let the eigenvalues be E_1, E_2, $\cdots E_5$. Let us now apply this linear transformation to the five d functions on atom a, and the same transformation to the five on atom b. This will diagonalize the upper right corner and lower left corner of the matrix in (8). It will not interfere, however, with the other two corners of the matrix, on account of the degeneracy of the problem, the fact that all five functions have the same diagonal energy. When we have made this transformation, Eq. (8) will be transformed into

$$\begin{vmatrix} H_a-E & 0 & 0 & 0 & 0 & E_1 & 0 & 0 & 0 & 0 \\ 0 & H_a-E & 0 & 0 & 0 & 0 & E_2 & 0 & 0 & 0 \\ 0 & 0 & H_a-E & 0 & 0 & 0 & 0 & E_3 & 0 & 0 \\ 0 & 0 & 0 & H_a-E & 0 & 0 & 0 & 0 & E_4 & 0 \\ 0 & 0 & 0 & 0 & H_a-E & 0 & 0 & 0 & 0 & E_5 \\ E_1 & 0 & 0 & 0 & 0 & H_b-E & 0 & 0 & 0 & 0 \\ 0 & E_2 & 0 & 0 & 0 & 0 & H_b-E & 0 & 0 & 0 \\ 0 & 0 & E_3 & 0 & 0 & 0 & 0 & H_b-E & 0 & 0 \\ 0 & 0 & 0 & E_4 & 0 & 0 & 0 & 0 & H_b-E & 0 \\ 0 & 0 & 0 & 0 & E_5 & 0 & 0 & 0 & 0 & H_b-E \end{vmatrix} = 0. \tag{9}$$

We can now immediately solve Eq. (9). Let us rearrange the rows and columns so that first we have the first row and column, then the sixth, then the second, then the seventh, and so on. Then we see that it factors into a set of two-by-two secular equations, the first one being

$$\begin{vmatrix} H_a-E & E_1 \\ E_1 & H_b-E \end{vmatrix} = 0. \tag{10}$$

The solution of this is

$$E=\tfrac{1}{2}(H_a+H_b)\pm[E_1^2+\tfrac{1}{4}(H_a-H_b)^2]^{\frac{1}{2}}. \tag{11}$$

The rest of the two-by-two secular equations are handled in the same way. We shall now discuss first the case where $H_a=H_b=0$, so that the two atoms are really alike, but are handling the problem using a unit cell twice as large as necessary, so that there are two like atoms in the unit cell. In this case, the solutions are $E=\pm E_1$, $\pm E_2$, etc.

This is just what we should expect. We are using the cubic Brillouin zone, half as large as the correct Brillouin zone for the body-centered structure. We must describe, in this smaller zone, all the energy levels which should properly be found inside the larger zone. But we have

already found that the energy levels at any point of one of the pyramids extending outside the cube are the negatives of the values found at the point inside the cube which is the mirror image in a cube face. Alternatively, the energy levels at any point of one of the pyramids are the negatives of those at the point inside the cube to which this pyramid would be shifted by a translation of π along the x, y, or z axes. Thus the solution E_1, E_2, etc., of our secular equation give the energies which belong inside the cubic part of the Brillouin zone, and the solutions $-E_1$, $-E_2$, etc., are those corresponding to the pyramids outside the cube, in the body-centered cubic case. We see the way, then, in which our present description leads to just the same energy levels as before, for the case where the two atoms are really identical. This shows us that our requirement, which we stated earlier, that the unit cell be chosen as small as possible, in applying the LCAO method, is dictated by convenience, not by necessity. It leads to a smaller secular equation, but the final results are the same in either case.

Now let us consider the case where the atoms are really different, so that H_a is not equal to H_b. For convenience, we may take $H_b=-H_a$, so that the center of gravity of the band is not disturbed by making the atoms unlike. Then we see from Eq. (11) that the effect of a nonvanishing value of H_a-H_b is to push the two energies $\pm E_1$ apart, enough so that the higher one is always greater than $\frac{1}{2}(H_a-H_b)$, the lower one always less than the negative of this quantity. In other words, the effect of this perturbation is to make a real energy gap, holding throughout the Brillouin zone, such that no energy levels whatever will be found within a gap of width H_a-H_b. This of course has an effect over the bounding planes of the new cubic Brillouin zone. We have already seen that in the absence of our perturbation, there would always be one energy level equal to zero on these planes. With our doubled number of energy levels, this level now splits into two, one of positive and one of negative energy. But there is a similar situation wherever, inside the Brillouin zone, an energy level of the unperturbed problem is equal to zero. In Fig. 3, under the action of this perturbation, a gap where $N(E)$ is zero appears in the center of the figure, of width H_a-H_b. Of course, the area under the curve cannot be changed, and it is not hard to show that $N(E)$ will become infinite at the edges of the gap, and rapidly fall to approximately its original value at a distance from the gap of the order of the gap width, the added height of the curve near the gap being just enough to keep the original area. Such a gap has been considered by Ganzhorn (reference 10); but it is not clear from his argument whether he realizes that it exists only for unlike atoms, vanishing when the two atoms a and b become alike.

It is interesting next to ask what is the effect of this perturbation on the wave functions, with particular reference to the problem of the antiferromagnetism of chromium. There are two cases: first, for those energy levels far from the gap; secondly, for those close to the gap. For those far from the gap E_1, which plays the part of the nondiagonal matrix component of energy in Eq. (10), is large compared to H_a-H_b. That is, as far as the secular equation is concerned, we have almost a degenerate problem, and the solutions are almost exactly the sum or difference of the two unperturbed wave functions. The sum gives a solution involving equal amplitudes of disturbances on the atoms of both types, with phase relations just like those arising from the Bloch sums for the problem where the atoms are alike. That is, it reduces to our former solution, and the wave functions are unperturbed far from the gap. The difference is similar to this, except for the difference in phase, which is just what is needed to describe the former solution for ζ between $\pi/2$ and π, or in the pyramidal region of the Brillouin zone of Fig. 4. Close to the gap, however, E_1, the nondiagonal matrix component of energy in Eq. (10), is small compared to the diagonal component, and the solution consists largely of the one unperturbed solution or the other. The wave functions corresponding to energies below the gap, and near to it, consist of contributions coming almost entirely from the lower potential wells, while those corresponding to energies just above the gap consist of contributions from the atoms with higher potential wells.

We can now ask what is the application of this situation to the antiferromagnetic case, as found in chromium. We must assume that a gap of this type really exists in the d band of chromium, as a result of an alternating potential arising from the antiferromagnetism itself. This would give a lower band capable of accommodating five d electrons per atom. We must further assume that the s band, which will overlie the d band, is located at such a height that the Fermi level, coming when one electron per atom is located in the s band, lies within the gap in the d band. This would amount to a numerical coincidence, which would not be particularly improbable. If we had this situation, then in the ground state of chromium, we should have one electron in the s band, five in the lower d band. At the Fermi level, the electron density $N(E)$ would arise only from the s electron, and hence would be quite small, consistent with the known low electronic specific heat of chromium. The upper occupied d levels would correspond to a considerable concentration of electrons of one spin in sites of one type, electrons of the other spin in sites of the other type, thus leading to the type of antiferromagnetism observed. The lower occupied d levels would have no such alternation of spin, so that the net magnetic moment on each atomic site would be far less than five Bohr magnetons. The magnitude of the net magnetization would depend on the ratio of the gap width to the whole band width, and the observed small value would be consistent with a rather narrow gap width. All of these predictions

seem to be consistent with what is known about chromium.

This type of argument is not able to lead to a prediction as to the expected magnitude of the gap width or magnetic moment per atom. To do that, we should calculate the energy of the whole crystal, as a function of the magnitude of the antiferromagnetic moment, and find that value of antiferromagnetic moment which minimizes the energy. This would demand finding the cohesive energy very accurately as a function of magnetic moment, and the calculation of cohesive energy, involving a many-electron problem, is very much more difficult than a discussion of one-electron energies, which alone can be handled by the present simplified methods. It is surely not adequate merely to identify the cohesive energy of the crystal with the sum of the one-electron energies, which is all that can be found by the present methods. We can see qualitatively, however, by considering the one-electron energies, why we should expect a result such as is observed. If we start with a model in which there is no antiferromagnetism, there would be no gap. If we now introduce an antiferromagnetic moment and alternating potential, the gap will appear, and as a result the energies of the upper energy levels of the lower occupied d band will decrease. It certainly seems likely that this decrease of one-electron energy is the feature of the problem which stabilizes the antiferromagnetic state. On the other hand, if we used only our simple one-electron arguments, we should conclude that the one-electron energies, and hence the energy of the crystal, would continue to decrease as the gap width increased. This would suggest that the stable state was one with a complete antiferromagnetic effect, with a moment of five Bohr magnetons per atom, as was once suggested by Zener.[18] This is known not to occur by the results of Shull and Wilkinson (reference 17).

The reason for this is moderately clear, if we ask what happens to our prediction of energy bands as the antiferromagnetic moment gets large. In Eq. (11), this is the limit where $H_a - H_b$ is large compared to any of the E_1's, or where the effect of the alternating potential, arising from exchange, is large compared to the effect of band splitting on account of the interaction of neighboring atoms. Then Eq. (11) shows us that, though the two halves of the d band are split widely apart, each half-band is greatly narrowed (since in this limit the effect of E_1 is found only as a second-order correction to the energy). This narrowing is real and has a perfectly simple physical meaning. In this limit, all electrons of plus spin are found on atomic sites of one type, those of minus spin on sites of the other type. The energy bands are set up only from electrons of one spin, and as far as these are concerned, the electrons are found only on atoms forming a simple cubic lattice of side $2a$. These atoms are much further apart than the nearest neighbors in the nonmagnetic case, so that we expect practically no broadening of the bands. The energy difference between the two half-bands will be independent of interatomic distance, and the broadening of the bands, being very small, will hardly vary with interatomic distance.

We shall thus lose, in this limit, the principal feature undoubtedly contributing to the cohesive energy of chromium. The fact that the body-centered transition metals are so tightly bound unquestionably arises on account of the contribution of the d electrons to the binding energy.[19] On our interpretation, the lower half of the d band is occupied, consisting of those wave functions contributing most strongly to the bonding, while the upper half, containing the antibonding orbitals, is empty. This view implies that it is the change in average energy of the occupied d levels with internuclear distance which is the important feature in the binding. Clearly we lose this binding if the occupied d band shrinks to a very narrow width, as it does for very large antiferromagnetism. But a quantitative calculation of these effects demands a thorough study of the many-electron problem, as we have stated. In the limit of large antiferromagnetism, the energy difference between the two d bands, the occupied and the unoccupied ones, will come entirely from an intra-atomic exchange integral of a type which can only be properly treated by a study of the energy of the many-electron problem and of the configuration interaction involved in the correct behavior of the system as the interatomic distance increases to infinity. We do not feet that there is any simplified way to estimate these effects and must hope that at some future time a sufficiently exact treatment of the cohesive energy of chromium can be given so that a reliable estimate of the antiferromagnetic moment can be made. In the meantime, it seems quite legitimate to use the observed magnitude of this quantity to derive results, as we have done here, regarding the energy bands, and to use these results in a qualitative way to correlate information on such quantities as electronic specific heat.

If our views are correct, the case of chromium can be rather unique. It is known from the work of Shull and Wilkinson, quoted above, that molybdenum and tungsten, which have the same electronic structure as chromium, are not antiferromagnetic and that vanadium, lying before chromium in the periodic table, also is not antiferromagnetic. Molybdenum and tungsten would have to be explained by supposing that the coincidence by which the Fermi edge for the s electrons lay within the gap for d electrons did not occur in those elements. Thus the d band would be either more or less than half-filled (it does not seem to make much difference which), and we could not get a stabilizing effect

[18] C. Zener, Phys. Rev. 81, 440 (1951).

[19] This is in agreement with the views of Pauling (reference 9). Pauling in that reference intimated that those who believe in the energy band theory of the d band did not accept this view but this is by no means the case.

by introducing the gap, since if the band were more than half-filled there would be approximately equal numbers of electrons increasing and decreasing their energy, and if it were less than half-filled the energies of the occupied levels would hardly be changed. According to the remarks made earlier, we feel that the tight binding of these elements arises from the fact that the d band is approximately half-filled and that it is strongly bonding; but the antiferromagnetic effect would have small effect on this, and we do not feel that the present methods are adapted to making a calculation of the cohesive energy. As for vanadium, with one less electron than chromium, the energy levels in the neighborhood of the middle of the d band are empty in any case, and there would be no stabilizing effect from introducing an antiferromagnetic moment, so that we expect a complete lack of antiferromagnetism, and a very close approximation to an ordinary energy band picture, for this element.

As we proceed in the other direction in the periodic table from chromium, we come to manganese, which has a different crystal structure and so cannot be treated by the present discussion. Its structure is unfortunately so complicated that it would be very difficult to handle it even by the present simplified method, since it has many atoms in the unit cell. One would guess, from the fact that it is known to be slightly antiferromagnetic, that proper treatment, if it could be given, would perhaps lead to a gap in this case too, somewhat similar to that in chromium, but separating the occupied from the unoccupied levels; but this is entirely speculative. The next element is iron, which of course is ferromagnetic in its body-centered form. Surely our arguments would not lead to antiferromagnetism for it; and one should be able to apply a rather straightforward energy-band argument to its ferromagnetism.

The only difference between this case and the standard one is that, if we ask what is probably the saturation magnetization to be expected, we can conclude that very likely it should be less than the value of approximately 2.6 Bohr magnetons which would be deduced by extrapolating the well-known curve of saturation magnetization of nickel and cobalt *versus* atomic number. The probable reason is that as enough electrons have their spin reversed so that electrons of plus spin will come somewhere near filling the d band, those of minus spin will be reduced to something like 2.5 per atom, so that their one-electron energies will lie near the minimum of the distribution curve of Fig. 3. In this case, it will require quite a large one-electron energy to reverse the spin of an electron, so that the magnetization will probably stop at this point, rather than continuing until there are quite five electrons per atom in the d band with plus spin. This could well lead to the observed moment of something like 2.2 Bohr magnetons. This argument, as we seen, is not very different from Pauling's.[9] However, it is based on an energy-band theory rather than an attempted Heitler-London explanation. Furthermore, unlike Pauling, we believe that the proper quantitative discussion of the problem would involve an accurate calculation of cohesive energy as a function of magnetization, just as in the case of chromium, and we are of the opinion that no simple and easy argument can lead to a reliable calculation of the saturation magnetization, such as Pauling attempted in his paper already quoted or in a more recent and entirely different discussion.[20]

In this section we have attempted to show that rather simple arguments can lead to a qualitative interpretation of some of the features of the body-centered metals, though those properties depending on cohesive energy are necessarily hard to treat. Our discussion of chromium has depended on the very simplified tight binding approximation involving only nearest neighbors. It is easy to see that if second nearest-neighbor interactions are included, the gap arising from the alterating potential can disappear. In such a case, in Eq. (8), the upper-left and lower-right corners of the secular determinant would no longer have the simple form assumed, and our arguments would entirely break down. Of course, we should still have energy gaps appearing at each point of the face of the cubic Brillouin zone of the simple cubic structure, but these gaps would no longer all be centered at the same energy, and they could well not result in a gap in the $N(E)$ curve as a whole. To maintain our explanation, then, we must assume that these terms are at least small. It does not seem absurd that this should be the case, so that our treatment really might represent a valid approximation to the facts. The d electrons have rather concentrated wave functions and second-nearest neighbor interactions would really be expected to be small. This would be in entire contrast to the $4s$ electrons, whose interactions surely are so great that no gap would appear in the $4s$ band. Only later calculations by more accurate methods can answer these questions properly.

VII. THE DIAMOND STRUCTURE

The diamond structure may most conveniently be described as a face-centered cubic structure, but with two atoms in the unit cell, rather than one. That is, we have atoms at the points $p\mathbf{a}+q\mathbf{a}\mathbf{j}+r\mathbf{a}\mathbf{k}$, where p, q, r are integers, and $p+q+r$ is an even integer, just as in the face-centered structure; but also we have atoms at points identical with the first, but displaced by a vector $\frac{1}{2}a(\mathbf{i}+\mathbf{j}+\mathbf{k})$. The first lattice we shall denote by 1, the second by 2. We must now set up Bloch functions of s, p_x, p_y, p_z orbitals on each of the two types of atomic sites, so that we shall have eight Bloch sums. By the methods we have previously used, we can find the matrix components of energy between these Bloch sums. We shall denote these matrix components by such symbols as $(s/x)_{11}$, signifying a matrix component

[20] L. Pauling, Proc. Natl. Acad. Sci. 39, 551 (1953).

TABLE V. Matrix components of energy for diamond structure.

$(s/s)_{11}=(s/s)_{22}$	$E_{s,s}(000)+4E_{s,s}(110)(\cos\xi\cos\eta+\cos\eta\cos\zeta+\cos\xi\cos\zeta)$
$(x/x)_{11}=(x/x)_{22}$	$E_{x,x}(000)+4E_{x,x}(110)(\cos\xi\cos\eta+\cos\xi\cos\zeta)+4E_{x,x}(011)\cos\eta\cos\zeta$
$(s/s)_{12}=(s/s)_{21}^*$	$4E_{s,s}(\frac{1}{2}\frac{1}{2}\frac{1}{2})(\cos\frac{1}{2}\xi\cos\frac{1}{2}\eta\cos\frac{1}{2}\zeta-i\sin\frac{1}{2}\xi\sin\frac{1}{2}\eta\sin\frac{1}{2}\zeta)$
$(s/x)_{12}=-(s/x)_{21}^*$	$4E_{s,x}(\frac{1}{2}\frac{1}{2}\frac{1}{2})(i\sin\frac{1}{2}\xi\cos\frac{1}{2}\eta\cos\frac{1}{2}\zeta-\cos\frac{1}{2}\xi\sin\frac{1}{2}\eta\sin\frac{1}{2}\zeta)$
$(s/x)_{11}=-(s/x)_{22}^*$	$-4E_{s,x}(011)\sin\xi\sin\eta+4iE_{s,x}(110)(\sin\xi\cos\eta+\sin\xi\cos\zeta)$
$(x/x)_{12}=(x/x)_{21}^*$	$4E_{x,x}(\frac{1}{2}\frac{1}{2}\frac{1}{2})(\cos\frac{1}{2}\xi\cos\frac{1}{2}\eta\cos\frac{1}{2}\zeta-i\sin\frac{1}{2}\xi\sin\frac{1}{2}\eta\sin\frac{1}{2}\zeta)$
$(x/y)_{12}=(x/y)_{21}^*=(y/x)_{12}$	$4E_{x,y}(\frac{1}{2}\frac{1}{2}\frac{1}{2})(i\cos\frac{1}{2}\xi\cos\frac{1}{2}\eta\sin\frac{1}{2}\zeta-\sin\frac{1}{2}\xi\sin\frac{1}{2}\eta\cos\frac{1}{2}\zeta)$
$(x/y)_{11}=(x/y)_{22}^*$	$-4E_{x,y}(110)\sin\xi\sin\eta-4iE_{x,y}(011)(\sin\xi\cos\zeta-\sin\eta\cos\zeta)$

between an s and a p_x Bloch sum on the sites 1, or $(s/x)_{12}$ for the component between an s function on site 1, a p_x on site 2. We shall include interactions between nearest and second-nearest neighbors. The nearest neighbors of a given atom are four forming a tetrahedral array around it, belonging to the other lattice. Thus the four nearest neighbors of the atom at the origin are located at the positions $(\frac{1}{2}\frac{1}{2}\frac{1}{2})$, $(\frac{1}{2}-\frac{1}{2}-\frac{1}{2})$, $(-\frac{1}{2}\frac{1}{2}-\frac{1}{2})$, $(-\frac{1}{2}-\frac{1}{2}\frac{1}{2})$, all times a. The second-nearest neighbors of a given atom belong to the same lattice, and are the twelve neighbors of type $a(110)$. When we include these interactions, and use the same notation as previously, we find the matrix components given in Table V.

From the two-center approximation, we can derive values which the various integrals of Table V would have to have if this approximation were valid. We find the following results:

$$\begin{aligned}
&E_{s,s}(\tfrac{1}{2}\tfrac{1}{2}\tfrac{1}{2})=(ss\sigma)_1,\\
&E_{x,x}(\tfrac{1}{2}\tfrac{1}{2}\tfrac{1}{2})=\tfrac{1}{3}(pp\sigma)_1+\tfrac{2}{3}(pp\pi)_1,\\
&E_{x,y}(\tfrac{1}{2}\tfrac{1}{2}\tfrac{1}{2})=\tfrac{1}{3}(pp\sigma)_1-\tfrac{1}{3}(pp\pi)_1,\\
&E_{s,x}(\tfrac{1}{2}\tfrac{1}{2}\tfrac{1}{2})=3^{-\frac{1}{2}}(sp\sigma)_1,\\
&E_{s,s}(110)=(ss\sigma)_2,\\
&E_{x,x}(011)=(pp\pi)_2,\\
&E_{x,y}(110)=\tfrac{1}{2}(pp\sigma)_2-\tfrac{1}{2}(pp\pi)_2,\\
&E_{x,x}(110)=\tfrac{1}{2}(pp\sigma)_2+\tfrac{1}{2}(pp\pi)_2,\\
&E_{s,x}(110)=2^{-\frac{1}{2}}(sp\sigma)_2,\\
&E_{s,x}(011)=E_{x,y}(011)=0.
\end{aligned}\tag{12}$$

For the nearest-neighbor interactions, we see that we have four of the E integrals, and also four of the two-center integrals, so that either scheme gives the same degree of generality. For the second-nearest neighbors, we have seven E integrals, and only four two-center integrals, so that we lose disposable constants by using the two-center approximation.

We can now use the results of Table V to investigate propagation in special directions, in particular the 100 and 111 directions, in which the secular equations simplify enough so that we can get part of the solution analytically. First we shall consider the origin, the case $\mathbf{k}=0$. Here it is clear that the secular equation factors into four two-by-two secular equations, one each for the s, p_x, p_y, and p_z functions. Furthermore, the diagonal matrix components of energy of the two lattices are the same, so that the energies equal the diagonal component, plus or minus the nondiagonal component, and the wave functions are the sums and differences of the atomic orbital functions on the two lattices. The energies are the following: for the s states, $E_{s,s}(000)+12E_{s,s}(110)\pm 4E_{s,s}(\frac{1}{2}\frac{1}{2}\frac{1}{2})$; (+ sign, Γ_1 symmetry,[21] − sign, Γ_2') and for the p states, which of course are threefold degenerate, $E_{x,x}(000)+8E_{x,x}(110)+4E_{x,x}(011)\pm 4E_{x,x}(\frac{1}{2}\frac{1}{2}\frac{1}{2})$. (+ sign, Γ_{15} symmetry, − sign, Γ_{25}').

Next let us consider the 100 direction, so that $\eta=\zeta=0$. We then find by inspection of Table V that there are no nondiagonal matrix components between any of the four Bloch functions formed from the s or p_x functions on either lattice, and those formed from the p_y or p_z functions on either lattice. We have thus, in the first place, a fourth-order secular equation for the s and p_x like functions. Let us denote the s function on the first lattice as function 1, the p_x on the first lattice as function 2, the s on the second lattice as function 3, the p_x on the second lattice as function 4. When we write out the secular equation, we find that certain terms are imaginary; but these can all be made real by multiplying the second and fourth columns by $-i$, the second and fourth rows by i, which has the effect of using imaginary coefficients for the x functions, real coefficients for the s functions. When we do this, the modified matrix components prove to be

$$\begin{aligned}
&H_{11}=H_{33}=E_{s,s}(000)+4E_{s,s}(110)+8E_{s,s}(110)\cos\xi,\\
&H_{22}=H_{44}=E_{x,x}(000)+4E_{x,x}(011)+8E_{x,x}(110)\cos\xi,\\
&H_{12}=H_{34}=8E_{s,x}(110)\sin\xi,\\
&H_{13}=4E_{s,s}(\tfrac{1}{2}\tfrac{1}{2}\tfrac{1}{2})\cos\tfrac{1}{2}\xi,\\
&H_{14}=H_{23}=4E_{s,x}(\tfrac{1}{2}\tfrac{1}{2}\tfrac{1}{2})\sin\tfrac{1}{2}\xi,\\
&H_{24}=4E_{x,x}(\tfrac{1}{2}\tfrac{1}{2}\tfrac{1}{2})\cos\tfrac{1}{2}\xi.
\end{aligned}\tag{13}$$

The matrix in this form, since it is real, is symmetric about the diagonal.

The biquadratic equation determined from these matrix components can now be further factored into a

[21] For the meaning of symmetry symbols for diamond structure see C. Herring, J. Franklin Inst. **233**, 525 (1942).

form giving two quadratic equations. To do this, we need only assume that $S_3=S_1$, $S_4=S_2$ (Δ_1 symmetry), or $S_3=-S_1$, $S_4=-S_2$ (Δ_2' symmetry), where the S's are the coefficients of the functions. These quadratic equations are

$$\begin{vmatrix} H_{11}+H_{13}-E & H_{12}+H_{14} \\ H_{12}+H_{14} & H_{22}+H_{24}-E \end{vmatrix}=0, \tag{14}$$

and a similar equation in which the signs of H_{13}, H_{14}, and H_{24} are to be changed each time they appear. There is a very interesting feature regarding this quadratic. If we take Eq. (14), but use values of ζ between π and 2π, we find that it becomes identical with the other quadratic equation in the range from 0 to π. Specifically, if we find the solutions of (14) for a value of ξ between π and 2π, this solution equals the solution of the other quadratic for a value $2\pi-\xi$. The energy is a smooth function of ξ for this whole range, and this means that the two quadratics have common roots for $\xi=\pi$, which is the edge of the Brillouin zone in this direction. This is similar to a case of accidental degeneracy; the roots separate as we depart from this point in any direction in the momentum space. Another result is that at this special point, the energy, regarded as a function of ξ, approaches the edge of the Brillouin zone with a finite slope, instead of with a zero slope as we usually find.

At this special point $\xi=\pi$, since we have degeneracy, the wave functions are not uniquely determined. There is one way to set them up, however, which is interesting and informing. We can set up one wave function as a combination of the s functions on lattice 1 and the p_x on lattice 2, and the other as a combination of the s functions on lattice 2 and the p_x on lattice. 1. This situation seems very peculiar at first sight, but when we consider it we see that it is entirely reasonable. If $\xi=\pi$, the wavelength equals $2a$. Now the x component of the distance between an atom of the first lattice and one of the second is $a/2$, and hence a quarter wavelength. If we have, then, a wave function which goes to a maximum on the atoms of one lattice, represented by s atomic orbitals, this wave function must be passing through zero on the atoms of the other lattice, so that it must be made up on that lattice out of p_x orbitals, with a nodal plane through the atoms. There will be, of course, two degenerate states of this type (symmetry type X_1).

We have now considered the four nondegenerate levels formed from the s and p_x functions for propagation along the 100 direction, and the special degeneracy that occurs for $\xi=\pi$, at the edge of the Brillouin zone. Next let us consider the doubly degenerate levels formed from the p_y and p_z functions on the two lattices. Let us denote the p_y function on the first lattice as function 1, the p_z on the first lattice as function 2, the p_y on the second as function 3, the p_z on the second as function 4. Then the matrix components of energy between these four functions are

$$\begin{aligned} H_{11}&=H_{22}=H_{33}=H_{44}=E_{x,x}(000)+4E_{x,x}(110) \\ &\quad+[4E_{x,x}(110)+4E_{x,x}(011)]\cos\xi, \\ H_{13}&=H_{24}=4E_{x,x}(\tfrac{1}{2}\tfrac{1}{2}\tfrac{1}{2})\cos\tfrac{1}{2}\xi, \\ H_{14}&=H_{23}=4iE_{x,y}(\tfrac{1}{2}\tfrac{1}{2}\tfrac{1}{2})\sin\tfrac{1}{2}\xi, \\ H_{12}&=H_{34}=0. \end{aligned} \tag{15}$$

We find at once that the secular problem given by (15) can be solved by assuming either that the coefficients S_1 and S_2 of the first two functions are the same, and similarly that $S_3=S_4$, or by assuming that $S_2=-S_1$, $S_4=-S_3$. Either solution leads at once to a quadratic, and the energies are the same: $E=H_{11}\pm(H_{13}^2+H_{14}H_{14}^*)^{\frac{1}{2}}$. One of these solutions corresponds to a function of type p_y+p_z, and the other to a function of type p_y-p_z (Δ_5 symmetry). We verify at once that these solutions lead to the value already found at $k=0$. At the edge of the Brillouin zone, $\xi=\pi$, the solutions are $E_{x,x}(000)-4E_{x,x}(011)\pm4E_{x,y}(\frac{1}{2}\frac{1}{2}\frac{1}{2})$ (X_4 symmetry).

We have now finished our discussion of propagation along the 100 direction, and have found that in this direction, out of our eight energy levels, there are four single levels, which however join to form two doubly degenerate levels at the edge of the Brillouin zone, and two doubly degenerate levels. Next we may take up in a similar way the solutions in the 111 direction. We shall not give such a complete discussion of this case, though it is carried through in a similar way. We first set up matrix components of energy, using Table V, and setting $\xi=\eta=\zeta$. We may then take advantage of our knowledge of the symmetry properties of the solution along the trigonal 111 axis to factor the resulting secular equation. We know that all solutions must belong to one of the irreducible representations of the threefold rotation group. One of these representations is one-dimensional. This is a function which is unchanged when we make a rotation of 120° about the threefold axis; that is, when we cyclically permute the letters x, y, z. In other words, for this type of function, the p_x, p_y, p_z functions must have equal coefficients. We may set up such a solution by assuming that the s function on one lattice has one coefficient; the p_x, p_y, p_z functions on that lattice have a second coefficient, all equal; the s on the other lattice has a third coefficient; and the p_x, p_y, p_z on the second lattice have a fourth coefficient (Λ_1 symmetry). When we make these substitutions, we find that all the eight linear equations leading to the eight-by-eight secular equation reduce to four independent equations, leading thus to a fourth-order secular equation with four roots.

This fourth-order secular equation for the four nondegenerate functions cannot be further simplified, except at the boundary of the Brillouin zone, which in this direction comes for $\xi=\eta=\zeta=\pi/2$. For this propagation vector, as often at the midpoints of faces of Brillouin zones, we have a symmetry relation which

we lack otherwise: the wave function must be symmetric or antisymmetric with respect to inversion in the midpoint of the line joining the atom at the origin, and the atom at position $a/2$, $a/2$, $a/2$, which is displaced from it along the direction of propagation. If we assume that the coefficients of the atomic orbital on the two lattices are related in such a way that we have either this symmetry or antisymmetry, we find that we have an additional simplification of the secular equation. It breaks down into two quadratic equations, each of which can be solved by formula, though no additional degeneracies are introduced: the four roots are still distinct. The solutions of these quadratics is given in Eq. (16). The solutions with the upper sign (aside from the sign in front of the radical, which is $\pm$ in either case) refer to the symmetric (L_1 symmetry), those with the lower sign to the antisymmetric (L_2' symmetry), functions with respect to the inversion mentioned.

$$\begin{aligned}E=&\tfrac{1}{2}[E_{s,s}(000)+E_{x,x}(000)]\mp E_{s,x}(\tfrac{1}{2}\tfrac{1}{2}\tfrac{1}{2})\\&\pm E_{x,x}(\tfrac{1}{2}\tfrac{1}{2}\tfrac{1}{2})\mp 2E_{x,y}(\tfrac{1}{2}\tfrac{1}{2}\tfrac{1}{2})-4E_{x,y}(110)\\&\pm\{[\tfrac{1}{2}[E_{s,s}(000)-E_{x,x}(000)]\mp E_{s,s}(\tfrac{1}{2}\tfrac{1}{2}\tfrac{1}{2})\\&\mp E_{x,x}(\tfrac{1}{2}\tfrac{1}{2}\tfrac{1}{2})\pm 2E_{x,y}(\tfrac{1}{2}\tfrac{1}{2}\tfrac{1}{2})+4E_{x,y}(110)\}^2\\&+3\{\pm 2E_{s,x}(\tfrac{1}{2}\tfrac{1}{2}\tfrac{1}{2})+4E_{s,x}(011)\}^2]\}. \quad (16)\end{aligned}$$

In addition to these four nondegenerate solutions in the 111 direction, we also have twofold degenerate solutions. We can build up the wave functions by using only the p_x, p_y, and p_z functions, omitting the s, and using two arbitrary linear combinations of p_x, p_y, and p_z which are orthogonal to the sum $p_x+p_y+p_z$ which is used in the solution which we have already discussed. The method of making these linear combinations is arbitrary; we can, for instance, use the combination p_x-p_y, and $p_z-\frac{1}{2}(p_x+p_y)$. If we do this, we find a quadratic equation for the energy, identical in either case, leading to twofold degenerate energy values (Λ_3 symmetry). The roots of this quadratic, at the edge of the Brillouin zone, where $\xi=\eta=\zeta=\pi/2$, are

$$\begin{aligned}E=&E_{x,x}(000)+4E_{x,y}(110)\\&\pm[2E_{x,x}(\tfrac{1}{2}\tfrac{1}{2}\tfrac{1}{2})+2E_{x,y}(\tfrac{1}{2}\tfrac{1}{2}\tfrac{1}{2})] \quad (17)\end{aligned}$$

(+ sign L_3 symmetry, − sign L_3' symmetry).

We have now found formulas for the energies of all eight bands, at the center of the Brillouin zone, and at the edges of the zone along the 100 and 111 directions. Fortunately, for this problem we have good calculations of the energy bands of diamond at these points in the Brillouin zone, carried out by Herman[22] by the method of orthogonalized planes waves. We therefore can make a good quantitative application of our method. Herman's calculations provide enough information to determine uniquely the parameters listed in Table VI. These parameters are sufficient to fit all of Herman's calculations. The parameters $E_{s,x}(110)$ and $E_{x,y}(011)$ cannot be determined from Herman's calculations.

[22] F. Herman, Phys. Rev. **88**, 1210 (1952); F. Herman and J. Callaway, Phys. Rev. **89**, 518 (1953). We are indebted to Dr. Herman for supplying numerical data regarding his calculations.

TABLE VI. Energy integrals (in Rydbergs) for diamond, from Herman's calculations.

$E_{s,s}(000)$	−1.37
$E_{x,x}(000)$	−0.378
$E_{s,s}(\frac{1}{2}\frac{1}{2}\frac{1}{2})$	−0.325
$E_{x,x}(\frac{1}{2}\frac{1}{2}\frac{1}{2})$	0.0563
$E_{x,y}(\frac{1}{2}\frac{1}{2}\frac{1}{2})$	0.277
$E_{s,x}(\frac{1}{2}\frac{1}{2}\frac{1}{2})$	0.122
$E_{s,s}(110)$	0.019
$E_{x,x}(011)$	−0.064
$E_{x,y}(110)$	−0.022
$E_{s,x}(110)$	−0.006
$E_{s,x}(011)$	0.119

It is interesting to take the parameters from Table VI, and see how accurately they fit in with the two-center approximation, and also to what extent they justify us in feeling that the integrals decrease as we go to more and more distant neighbors. From Eq. (12), we see that as far as the nearest neighbors are concerned, we can derive the integrals uniquely from the values of Table VI: we have $(ss\sigma)_1=-0.325$ rydbergs, $(pp\sigma)_1=0.610$, $(pp\pi)_1=-0.221$, $(sp\sigma)_1=0.211$. These values are reasonable. They all have the right signs for two-center integrals of the corresponding atomic orbitals, and the right order of magnitude: the largest interaction is $(pp\sigma)_1$, between two p orbitals pointing along the bond, while $(ss\sigma)_1$, the interaction of s orbitals, is considerably smaller, and the other interactions still smaller.

As far as second-nearest neighbors are concerned, we cannot derive two-center integrals uniquely from the values of Table VI, showing that the two-center approximation is not valid. We can, however, test its correctness and get orders of magnitude for the integrals. From Eq. (12), we know that $E_{s,s}(110)$, which equals 0.019, uniquely equals $(ss\sigma)_2$, and it is encouraging to find it so much smaller than $(ss\sigma)_1$. It is also interesting to find it of the opposite sign; this is in line with earlier remarks made in connection with the body-centered structure in the alkalies, where we pointed out that the s interaction between second-nearest neighbors might often be of the opposite sign to the nearest-neighbor interactions. The integral $E_{x,x}(011)$ should equal $(pp\pi)_2$, and its value -0.064 shows that this quantity is considerably smaller than $(pp\pi)_1$, so that again we verify that the second-nearest neighbor interaction is considerably smaller than the nearest-neighbor terms. But from Eq. (12), we see that we can also solve for $(pp\pi)_2$, as well as $(pp\sigma)_2$, from $E_{x,y}(110)$ and $E_{x,x}(110)$. When we do this, we find $(pp\sigma)_2=-0.028$, $(pp\pi)_2=0.016$. These are both small, in line with the fact that they represent second-nearest neighbor interactions, but the value of $(pp\pi)_2$ determined in this way does not agree at all with the value found from $E_{x,x}(011)$. This shows that the two-center approximation is not valid. This is shown even more by the

considerable value of the integral $E_{x,x}(011)$, which is 0.119, the largest of the second-nearest neighbor terms. For this is an integral which would vanish entirely if we used the two-center approximation and can appear only because the tetrahedral surroundings of each atom in the diamond structure do not have the complete cubic symmetry. In spite of this failure of the two-center approximation, still it is possible to choose integrals of a two-center type which form a passable approximation to Herman's results; but since they cannot be chosen uniquely, but only as a compromise between various errors, it does not seem worth while pursuing this matter further.

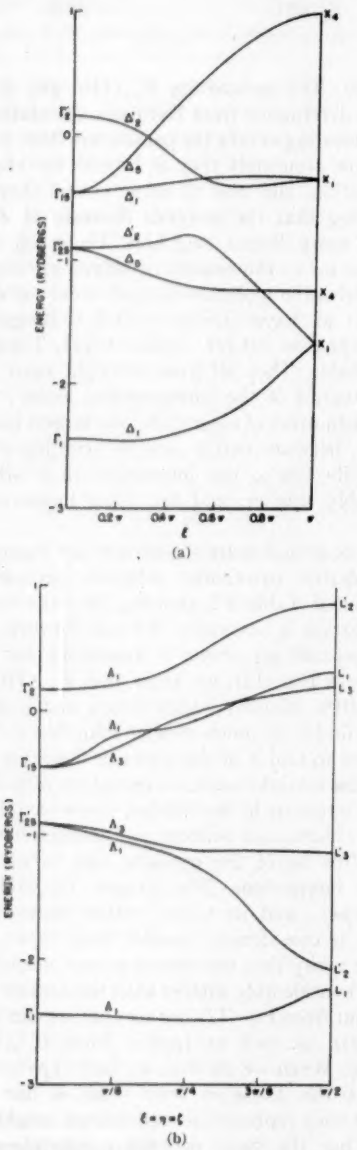

FIG. 5. Variation of energy with wave vector for diamond calculated using Herman's values at the center and boundaries of the zone. (a) 100 direction; (b) 111 direction; (see reference 21 for the meaning of the symmetry symbols).

It is interesting to use the integrals given in Table VI to calculate the energy at other points in the Brillouin zone than those symmetry points for which Herman has made calculations; this after all is the fundamental object of the present study. To do this, we need the two integrals $E_{x,x}(110)$ and $E_{x,y}(011)$ which cannot be determined from Herman's values. Lacking further information, we have arbitrarily chosen the values 0.021 and 0 for these two integrals; these are of the order of magnitude of what would be deduced from a two-center approximation. We have then used these values (which are of small importance in the final calculations) and the values of Table VI, and have calculated the curves of Fig. 5, giving the energy as a function of $\mathbf{k}$ along the 100 and 111 directions. This demanded solving the fourth-order secular equation in the 111 direction numerically. These curves of course reduce exactly to Herman's values at the edges of the zone. Herman has made interpolations in his paper, but our computed curves differ from his in some significant details, such as in the peculiar nature of the nondegenerate levels in the conduction band in the 100 direction, in which we have found accidental degeneracy to occur. Nevertheless, the general form of energy bands is similar to that deduced by Herman, giving of course the energy gap between the four lower occupied bands and the four higher empty bands. Similar calculations of course could be made for germanium, since Herman and Callaway[22] have made orthogonalized plane-wave calculations for this material too. However, we understand that they are improving the published numerical values for germanium, and feel it better to wait for the revised values before making numerical calculations. It is clear from Fig. 5 that we have the possibility, as has been frequently suggested, that the top of the valence band and bottom of the conduction band should not lie at $\mathbf{k}=0$. In our case, it appears that the top of the valence band would lie at six equivalent points along the 100 directions

It is interesting to compare these results for diamond with various other calculations which have been made for crystals of this type. The first calculation by the tight binding method is by Morita.[23] His calculations are like those of the present section, in most respects; his values for the various integrals are just like those of Table V. He does not express his integrals in terms of two-center integrals, though he calculates them by a two-center approximation. His results are known to come out very differently from the results of Herman and of the present study in that he finds the nondegenerate level in the conduction band lying below the threefold degenerate level at the center of the

[22] A. Morita, Sci. Rep. Tôhoku Univ. 33, 92 (1949).

Brillouin zone. This discrepancy is so serious that it has thrown considerable doubt on the use of the tight binding approximation for diamond. It appears to us likely, however, that this discrepancy is the result of some unfortunate numerical error in Morita's work. If we work back from the numerical values of his integrals, we find that some of the two-center integrals which we derive from them are surprisingly close to those which we have found from Herman's calculations; for instance, the values of $(ss\sigma)_1$ are almost exactly the same. However, Morita's value for $(pp\sigma)_1$ comes out to be 0.179 and for $(pp\pi)_1$, -0.349, as compared to our values of 0.61 and -0.22, respectively. We should certainly expect that $(pp\pi)$ would be smaller numerically than $(pp\sigma)$, since the $p\pi$ wave functions will overlap less than the $p\sigma$'s, so that it seems likely that Morita's calculations of these quantities are in error. This probably ties in with the fact that Morita finds that the s-like level is the lowest in the conduction band, which we have already mentioned. This is largely a result of the integrals which seem to be in error. We therefore suspect that a tight binding calculation made correctly by the method Morita used might well give a good account of the conduction as well as the valence band in diamond and germanium.

Another, and quite different, calculation of diamond by the tight binding approximation has been made by Hall.[24] Hall has used the equivalent orbitals which have been discussed by him, Lennard-Jones, and others. In the present case, he interprets these equivalent orbitals as being the symmetric, or bonding, combinations of directed orbitals on adjacent pairs of atoms. He sets up Bloch functions made from each such directed orbital, and solves the secular equation between these Bloch functions. Each bond in the unit cell then has a directed symmetric orbital along it. There are four such bonds in the unit cell (each of the two atoms in unit cell has four bonds attached to it, but each bond is shared between two atoms), so that we have a four-by-four secular equation, and we may expect in this way to get four states, and a description of the valence band, but not of the conduction band. If Hall had chosen to do so, he could also have set up a four-by-four secular equation involving combinations of antisymmetric or antibonding orbitals on each bond and have thus got a description of the conduction band.

The results which Hall obtains are not in very good agreement with experiment, or with the results which we have so far been discussing. In particular, he finds the levels at $\mathbf{k}=0$ to be split essentially as in Fig. 5, but the twofold degenerate level in the 100 or 110 direction proves to have an energy independent of $\mathbf{k}$, or to be a zero-width band, a peculiarity found also in the cellular treatment[25] of this problem, to which Hall's results have close resemblance. There is no physical reason to think that the band really has this property and this is a shortcoming of Hall's calculation.

It is useful to consider the relation of Hall's calculation to the one which we have been describing earlier in this section, since at first sight one might think them equivalent; Hall[26] clearly feels that his calculation has a fundamental significance which we do not believe that it possesses. In our discussion, we have already seen that the lower band is made up at $\mathbf{k}=0$ of symmetric combinations of s and p functions on the two lattices, and the upper band of antisymmetric combinations. From the s and p functions we can of course build up tetrahedral directed orbitals, so that for $\mathbf{k}=0$ we can build up the wave function properly for the valence band from the symmetric combinations of directed orbitals. In other words, Hall's method would give the same values for the energy at $\mathbf{k}=0$ that we have found by our more general treatment. However, as $\mathbf{k}$ departs from zero, we have seen that the correct combinations for the lower band are no longer the symmetric combinations of orbitals on the two lattices. By solving our eight-by-eight secular equation we have automatically found the correct combinations, and our results depart increasingly from Hall's as $\mathbf{k}$ increases. Of course, our energies will be lower than Hall's, since we are making a better approximation to a solution of the Schrödinger equation. In particular, the band which Hall finds to be of zero width is depressed in the more accurate calculation, as $\mathbf{k}$ increases.

If we had carried out the calculations by Hall's method of equivalent orbitals, using his calculation of the valence band by symmetric orbitals, and a similar calculation of the conduction band by antisymmetric orbitals, we should then find that there were nondiagonal matrix components of energy between the two bands, which vanished for $\mathbf{k}=0$, but increased with $\mathbf{k}$. By including these nondiagonal matrix components, we should find an eight-by-eight secular equation which would have the same roots as our secular equation, since the symmetric and antisymmetric equivalent orbitals are linear combinations of the s and p orbitals on the two lattices which we have used as our starting point. It might be convenient to use Hall's procedure, as amplified in this way, to make an actual calculation. For by using Hall's equivalent orbitals, but disregarding the nondiagonal matrix components of energy between valence and conduction band, we find an energy gap between these two bands. Introduction of the nondiagonal matrix components will then have the effect of pushing certain levels apart, push the levels of the valence band down and those of the conduction band up. Since these levels are not degenerate, even in the absence of nondiagonal matrix components, it is possible that a second-order perturbation calculation would be adequate for considering the effect of these nondiagonal matrix components of energy, thereby making possible

[24] G. G. Hall, Phil. Mag. **43**, 338 (1952).
[25] G. E. Kimball, J. Chem. Phys. **3**, 560 (1935).
[26] G. G. Hall, Phys. Rev. **90**, 317 (1953).

an approximation to the exact solution of the correct secular equation. Since this secular equation is not very difficult to handle anyway, however, it seems better to use it directly, and in this case there is no advantage in Hall's procedure. In any case, Hall's calculation for the valence band alone is clearly a poorer approximation than the one considered in the present section.

Before leaving the problem of the diamond structure, we should say a few words about the compounds, such as InSb, crystallizing in the zincblende structure. This is the case in which the two interpenetrating face-centered lattices are no longer equivalent. For instance, the atom at the origin might be In, that at the point $a/2$, $a/2$, $a/2$ might be Sb. We shall lose, then, any results depending on symmetry or antisymmetry between these two lattices, but otherwise the results of the calculations will be essentially unchanged. We can introduce the modification by using one set of diagonal energy values, $E_{s,s}(000)$ and $E_{x,x}(000)$, for the atoms of one type, another set for the atoms of the other type, much as we did in our earlier treatment of the body-centered cubic structure when modified to have unlike atoms at the centers and corners of the cube. Here, however, in contrast to that case, the treatment we have already given has the correct unit cell, holding two atoms, even if the atoms are unlike.

We shall still have eight bands arising from our s and p orbitals on the two lattices. At $\mathbf{k}=0$, we shall still have two nondegenerate bands of s-like type and two threefold degenerate bands of p-like type, and the other consequences of symmetry will mostly be the same as for diamond. One exception is the degeneracy between the two bands formed from s and p_x functions, at the point $\xi=\pi$, $\eta=\zeta=0$. We remember that the wave functions for one of these bands consisted of s orbitals on one lattice, p_x on the other, and for the other band the role of the two lattices was interchanged. If the two lattices are no longer equivalent, it is quite clear that these two wave functions will have different energies. This is one of the few qualitative differences between the energy band structures in the two cases, however. The general situation, according to which we have a lower set of bands capable of holding eight electrons per unit cell, and an upper set of bands holding the same number, will still hold, so that since we have just eight electrons per cell in any of these crystals, we shall in every case fill the valence band, leaving the conduction band empty, and shall have an insulator or semiconductor as with the diamond group of elements. The situation is quite different from what we had in the body-centered cubic case, where making the two types of atoms unlike introduced an energy gap which was not present previously. Here, we have an energy gap anyway, on account of the lack of equivalence of the two atoms in unit cell even in diamond, and this gap can be modified in width by making the two atoms unlike, but no new gaps are introduced.

There can be a good deal of qualitative difference between the wave functions for diamond and for a crystal forming the zincblende structure, however, and in some cases there can be reversals of the order of the bands, which we can understand from general qualitative arguments. To have a specific example, let us take InSb, formed from the elements on the two sides of Sn. The potential wells about the Sb atoms will be deeper than around the In atoms, and if the atoms were electrically neutral, there would be three outer electrons around each In atom, five around each Sb atom. We cannot of course guarantee this neutrality; the chemists often speculate in such cases whether the crystal is formed from neutral atoms or ions, and in a case like this we could even speculate as to which sign the charges on the ions were. We could take extreme points of view. We could say that the crystal was completely ionic, the In forming a positive ion with triple charge, losing its three electrons, which would go onto the Sb to form a closed shell of eight electrons. Or we could take a quite opposite point of view, supposing that the In took up an extra electron, forming a negative ion, so as to have four outer electrons like a tetravalent atom, and that similarly the Sb lost an electron, again so as to have four outer electrons. There is no good reason for thinking that either of these extreme points of view has any close relation to the actual facts of the situation. We can, however, from our general approach, get a much sounder view of the charge distribution in this crystal, which points the way to an interpretation of many other crystals in which there is an ambiguity between different points of view.

We remember that our determination of one-electron wave functions is one part of a self-consistent field calculation, and that the final decision as to how much charge lies on each type of atom is one that is to be made by carrying through a self-consistent problem. Let us assume that at a given stage of this calculation we are given a periodic potential and are trying to find the wave functions, that is, we are solving our eight-by-eight secular equations. When we have done this, for each $\mathbf{k}$ value, we find the total charge density of electrons distributed in the lower or valence band, leaving the conduction band empty, and we use this charge density in computing a potential to use in the next stage of the self-consistent calculation. If, for instance, as seems highly likely, the final result of the self-consistent method should be that each of the atoms is approximately electrically neutral in the crystal, then the charge distribution corresponding to the valence band would actually correspond to three electrons per atom in the In atoms, five per atom in the Sb atoms. We shall now show that such a result is altogether probable.

For any particular $\mathbf{k}$ value, we have to determine the eight wave functions corresponding to the various energy bands. As a very simple example, let us consider $\mathbf{k}=0$; the other $\mathbf{k}$ values, though more complicated, will not be different in principle. We know that at $\mathbf{k}=0$,

our problem factors on account of symmetry, so that we find two s-like states, two p_x like, two p_y like, two p_z like. Each of these is handled in a similar way. In the s-like states, for instance, we know that if we are dealing with the diamond structure we have a quadratic secular equation in which the two diagonal matrix components are equal, since the diagonal energies will be the same whether the atomic orbitals are on the one face-centered lattice or on the other. The two linear combinations, then, will be the sum and difference of the unperturbed functions, so that in either case the resulting charge density will have equal values on the atoms of both lattices.

With the InSb, however, this secular problem for the two s-like states no longer has this property of degeneracy. The diagonal energy of an s orbital on an In atom will be considerably higher than that of an s orbital on an Sb atom, since the Sb has a deeper potential well. The nondiagonal matrix component between the two states may well be much as in the diamond case, but the perturbation will have a very different effect, on account of the lack of degeneracy. It will separate the energies of the two states somewhat. But the wave function of the lower of the two resulting states will be a mixture of a large fraction of that unperturbed wave function whose diagonal energy is lower (that is, an s function on the Sb) and a much smaller fraction of that function whose diagonal energy is higher (that is, an s function on the In). Conversely, for the upper state, we shall have a combination in which most of the charge density is on the In, a lesser amount on the Sb. Only the lower state is filled, however, so that we are left with more charge on the Sb, less on the In. The same situation will hold for the p states with $\mathbf{k}=0$, and in fact for every $\mathbf{k}$ value; so that it is quite certain that the charge distribution corresponding to the electrons in the valence band will have a good deal more charge on the Sb than on the In. It is entirely possible, as has been suggested above, that the final result would come out with almost complete electrical neutrality, about five-eighths of the charge being on the Sb, three-eights on the In. Certainly we should have something much closer to this than to either of the extreme ionic states which we discussed earlier.

The final type of wave function, and charge distribution, which we have found in this case can throw a good deal of light on the question of ionic or nonionic crystals in general. We have different amounts of charge on the atoms of the two types; we do not even have to have integral charges, on the average, on each type of atom. And yet our total charge distribution consists of the entirely filled valence bands, entirely empty conduction bands, just as in diamond. The total charge density has the same sort of spherical symmetry about each atom (modified by overlap with the neighboring atoms) which we should have in diamond, and which we should find from filling s, p_x, p_y, p_z bands. The interesting feature is the way in which, by making up our energy band functions as linear combinations of atomic orbitals, we can simultaneously achieve these two results of variable total charge, and yet the characteristics of a closed shell of electrons. Our wave function for the crystal as a whole is set up as a single determinant, since we have only filled energy bands. We have all the advantages which we meet in the molecular orbital model of molecules, including the way in which that model leads naturally to the interpretation of the polarity of molecules, and the possibility of having fractional amounts of electronic charge on each atom. We must now forget that we have the drawbacks of the molecular orbital model as well; we could get better results if we took a certain amount of configuration interaction into account. Thus, in particular, if we wished to give a proper account of the energy bands in our crystals of the diamond or zincblende type as a function of internuclear separation, we should have to consider a configuration interaction, of a practically impossible degree of difficulty, between the single determinantal state we have been describing, and other configurations in which varying numbers of electrons are excited to the antibonding energy bands. Even in the absence of such configuration interaction, however, our energy band method gives a good general account of the situation.

From the discussion which we have given of the zincblende structure, we can see that in certain cases the order of energy levels may be different in it from what it is in the diamond structure, as shown in Fig. 5. In Fig. 5, we saw that the lowest state of the valence band and the highest of the conduction band were of the s-like type, while the top of the valence band and the bottom of the conduction band were of the p-like type. The reason for this arrangement is seen in the magnitudes of the various matrix components of energy. Thus we found that the energies of the s states, for $\mathbf{k}=0$, were $E_{s,s}(000)+12E_{s,s}(110)\pm 4E_{s,s}(\frac{1}{2}\frac{1}{2}\frac{1}{2})=-1.14 \pm 1.30$ rydbergs, and for the p states we had $E_{x,x}(000)+8E_{x,x}(110)+4E_{x,x}(011)\pm 4E_{x,x}(\frac{1}{2}\frac{1}{2}\frac{1}{2})=-0.68\pm 0.23$. The smaller nondiagonal matrix component for the p states is responsible for the fact that these two states are not widely separated. On the other hand, as we go to a compound like InSb, where we shall no longer have a degenerate problem, the diagonal s and p components on the Sb sites will lie considerably below those on the In sites. Furthermore, we may expect that the diagonal energy of the s state, on either site, will lie considerably below that of the p state on the same site, on account of the general rule that s states lie lower than p states; this is consistent with our value of -1.14 for the s energy, -0.68 for the p, above. Hence as far as diagonal energies are concerned, the lowest level of all will be the s Sb orbital, next the p Sb orbitals, next the s In orbital, with the p In orbitals highest. If the orbitals on the two sites are considerably separated in energy, the nondiagonal matrix components,

even if they are still of the same general magnitude as those given above, still will not produce nearly as much displacement of the energy as in the diamond case, since they will produce only a second-order change in energy rather than a first-order change in a nondegenerate problem. Consequently, it may well be that they will not invert the order of the s and p states in the conduction band, but will rather leave the lowest state in the conduction band an s-like rather than a p-like state. This would explain an observation of Pearson and Tanenbaum,[27] according to which the conduction band of InSb appears to be nondegenerate at its lowest energy value.

Many of the properties of the crystals like InSb, then, seem to be interpreted easily in terms of our approximate tight binding method. In fact, the diamond structure appears to be the one in which, at the moment, we are able to make the best use of it, partly on account of the results of Herman by means of the orthogonalized plane-wave method. This, in particular, is the only case in which we are at present able to evaluate the effect of second-nearest neighbors, by comparison of our LCAO method with values calculated by other methods; and it is particularly gratifying that the contributions of second-nearest neighbors appear to be a good deal less than those of nearest neighbors, lending support to our hypothesis that we really are dealing with a series of terms which decrease rapidly as we go to more distant neighbors. If this turns out to be a general situation, it really may be that the method possesses a rather fundamental significance and need not be regarded merely as a convenient interpolation method.

APPENDIX

We wish to show in this appendix that the transformation properties of the Löwdin functions ψ_n are the same as those of the nonorthogonal functions ϕ_n from which they arise. Let us suppose that under some operation O, of the group of the crystal, the transformation properties of the nonorthogonal functions are given by

$$O\phi_n=\sum(m)\phi_m\Gamma(O)_{mn}. \tag{A1}$$

Here $\Gamma(O)_{mn}$ is a unitary matrix ($[\Gamma(O)^{-1}]_{mn}=\Gamma(O)^*_{nm}$). We must show that the transformation properties of the ψ_n's are the same; that is,

$$O\psi_n=\sum(m)\psi_m\Gamma(O)_{mn}. \tag{A2}$$

[27] G. L. Pearson and M. Tanenbaum, Phys. Rev. **90**, 153 (1953).

The relation between the ψ_n's and the ϕ_n's is given by Löwdin,[12]

$$\psi_n=\sum(m)\phi_m(\Delta^{-\frac{1}{2}})_{mn}. \tag{A3}$$

Here $(\Delta^{-\frac{1}{2}})_{mn}$ is the mnth matrix element of the reciprocal of the square root of the overlap matrix Δ_{mn},

$$\Delta_{mn}=\int\phi_m^*\phi_n d\tau. \tag{A4}$$

[The same orbitals are included in this summation in Eq. (A3) as in the summations expressing the transformation properties of the ϕ_n's.] Applying the operator O to Eq. (A3) we see that

$$O\psi_n=\sum(l)\sum(m)\phi_l\Gamma(O)_{lm}(\Delta^{-\frac{1}{2}})_{mn}. \tag{A5}$$

In order to prove our theorem, we must show that the right-hand sides of Eq. (A5) and Eq. (A2) are equal. Explicitly, we must prove the equality

$$\sum(l)\sum(m)\phi_l(\Delta^{-\frac{1}{2}})_{lm}\Gamma(O)_{mn}=\sum(l)\sum(m)\phi_l\Gamma(O)_{lm}(\Delta^{-\frac{1}{2}})_{mn}. \tag{A6}$$

In Eq. (A6), the left-hand side was obtained from Eq. (A2) through the use of Eq. (A5). To establish the validity of Eq. (A6), it suffices to show that

$$\sum(m)(\Delta^{-\frac{1}{2}})_{lm}\Gamma(O)_{mn}=\sum(m)\Gamma(O)_{lm}(\Delta^{-\frac{1}{2}})_{mn}. \tag{A7}$$

Multiplying both sides by $[\Gamma(O)^{-1}]_{ql}$ and summing over l yields the result

$$\begin{aligned}\sum(l)\sum(m)[\Gamma(O)^{-1}]_{ql}(\Delta^{-\frac{1}{2}})_{lm}\Gamma(O)_{mn}&=\sum(l)\sum(m)[\Gamma(O)^{-1}]_{ql}\Gamma(O)_{lm}(\Delta^{-\frac{1}{2}})_{mn}\\&=\sum(l)\sum(m)\delta_{qm}(\Delta^{-\frac{1}{2}})_{mn}=(\Delta^{-\frac{1}{2}})_{qn}.\end{aligned} \tag{A8}$$

In other words, we have established our theorem if we can show that the reciprocal of the square root of the overlap matrix is invariant with respect to the unitary matrix $\Gamma(O)_{mn}$. Under certain very general conditions, this is true if the overlap matrix itself is invariant with respect to the unitary transformation. This, however, is easily seen to be true since

$$\begin{aligned}\Delta_{mn}&=\int\phi_m^*\phi_n d\tau=\int O\phi_m^* O\phi_n d\tau\\&=\sum(q)\sum(l)\Gamma(O)_{qm}^*\Gamma(O)_{in}\int\phi_q^*\phi_l d\tau\\&=\sum(q)\sum(l)[\Gamma(O)^{-1}]_{mq}\Delta_{ql}\Gamma(O)_{ln}.\end{aligned} \tag{A9}$$

Thus we have established our theorem.

Conductivity and Hall Effect in the Intrinsic Range of Germanium

F. J. MORIN AND J. P. MAITA
Bell Telephone Laboratories, Murray Hill, New Jersey
(Received February 4, 1954)

Conductivity and Hall effect have been measured in the intrinsic range of germanium from 250° to 1000°K. From lattice-scattering mobility and conductivity below 500°K, a new empirical expression for carrier concentration is determined: $np=3.10\times10^{32}T^3\exp(-0.785/kT)$. An estimate is made of the contribution of optical modes to the lattice-scattering mobility. Conductivity from 500° to 1000° and Hall effect from 250° to 1000° are computed and compared with experiment. Included in the computation are: the empirical expression for carrier concentration modified by the change in intrinsic ionization energy produced by electrostatic interaction of charge carriers, extrapolated empirical lattice scattering mobility, scattering by electron-hole collisions, and an extrapolation of the ratio Hall mobility/conductivity mobility.

1. INTRODUCTION

EFFORTS to understand the semiconducting properties of germanium have been confined for the most part to the range of impurity conductivity; literature on the intrinsic range is meager. Theory is incomplete, but enough is known to say that the number of processes involved in conduction are too numerous to be separated empirically from measurements of conductivity and Hall effect. This paper, therefore, is not a complete analysis of the intrinsic range but tries to indicate the relative importance of some of the conduction processes by comparing experiment with available theory.

Conductivity and Hall effect in the intrinsic range of germanium are reported for the temperature range 250° to 1000° Kelvin. The data are analyzed in two steps, the results below 500°K being considered first. It is believed that below 500° the conduction mechanism contains fewer unknowns and that a reliable expression for carrier concentration can be obtained from conductivity and lattice-scattering mobility. The temperature dependence of lattice-scattering mobility has been determined[1] from 100° to 300°K and found to deviate from the $T^{-1.5}$ law predicted by theory. It is shown that all of the deviation found for electrons and some of the deviation found for holes can be accounted for by assuming the presence of optical mode scattering. Most of the deviation from the $T^{-1.5}$ law found for holes may arise because the band edge is not at the center of the Brillouin zone. However, when the carriers have gained enough thermal energy, this scattering mechanism will have a $T^{-1.5}$ temperature dependence and acoustical mode scattering can be expected to return to the $T^{-1.5}$ law at some temperature above 300°K. Since this temperature is not known, the effect has been neglected and measured lattice scattering mobility is extrapolated from 300° to 1000°K. From lattice-scattering mobility and conductivity below 500° an empirical expression for carrier concentration is determined.

Conductivity above 500° is computed and compared with experiment. Included in the computation are the empirical expression for carrier concentration modified by the change in intrinsic ionization energy produced by electrostatic interaction of charge carriers; extrapolated lattice-scattering mobility; and scattering by electron-hole collisions. Hall effect from 250° to 1000° is computed and compared with experiment, making use of information obtained in computing conductivity plus an extrapolation of the ratio: Hall mobility/conductivity mobility. This ratio has been determined between 100° and 300° and found for holes to be increasing with temperature above the theoretically predicted constant 1.18. Along with the departure from the $T^{-1.5}$ law, this effect is expected to disappear at some temperature above 300° and the ratio to decrease to some constant value. Since the actual behavior of the ratio has not been determined, a linear extrapolation of the measured ratio from 300° to 1000°K is used in computing the Hall coefficient. Computed conductivity and Hall effect agree well with experiment. This is encouraging in view of the large number of assumptions made in the analysis.

2. METHODS

Conductivity and Hall effect were measured on bridge shape[2] samples having rhodium plated contact areas. All samples were cut from recently grown single crystal germanium. Measurements above 350°K were made using a ceramic holder fitted with pressure contacts of platinum 10 percent rhodium wire and platinum-platinum 10 percent rhodium couples. Samples were heated in a small electric furnace and an atmosphere of nitrogen.

3. SYMBOLS

σ = conductivity in ohm^{-1} cm^{-1},
R_H = Hall coefficient in cm^3/coulomb,
n, p = electron and hole concentration in cm^{-3},
n_i, p_i = carrier concentration when all impurities are ionized (the difference between donor and acceptor concentration),
μ_{cn}, μ_{cp} = electron and hole conductivity mobility in cm^2/volt sec,

[1] F. J. Morin, Phys. Rev. **93**, 62 (1954).

[2] P. P. Debye and E. M. Conwell, Phys. Rev. **93**, 693–706 (1954).

μ_{Ln}, μ_{Lp} = electron and hole lattice scattering mobility,
μ_{Hn}, μ_{Hp} = electron and hole Hall mobility,
μ_{ac} = lattice-scattering mobility acoustical modes,
μ_{op} = lattice-scattering mobility optical modes,
μ_{np} = electron-hole scattering mobility,
T = temperature in degrees Kelvin,
k = Boltzmann constant,
κ = dielectric constant,
m_n, m_p = electron and hole effective mass,
m = electron rest mass,
$\hbar$ = Planck's constant/2π,
E_G = intrinsic ionization energy in electron volts,
β = temperature coefficient of E_G in ev /degree.

4. CONDUCTIVITY FROM 250 TO 500°K

In this section an empirical expression for carrier concentration is determined using conductivity and lattice-scattering mobility. The measurements to be described were made on samples of such purity that impurity scattering was negligible above ~100°. Analysis of the conductivity is restricted here to the range below 500° where extrapolated empirical results only are used. Above 500° the analysis depends upon extrapolated empirical results and theory. Another empirical expression for carrier concentration has been determined from conductivity and mobility.[3] The determination, however, made use of early values of drift mobility and assumed lattice scattering to have a temperature dependence of $T^{-1.5}$. The expression to be obtained in this paper is significantly different from the old one because recent mobility values are higher at room temperature, and it is known that the temperature dependence of lattice-scattering mobility departs from the $T^{-1.5}$ law.

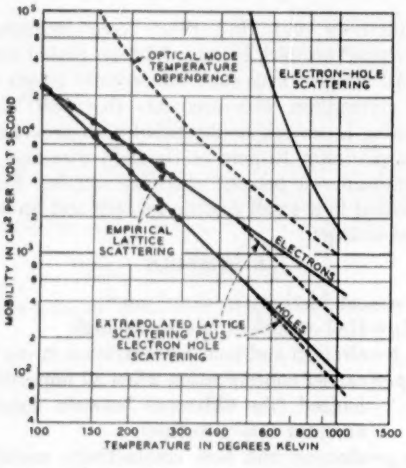
OPTICAL MODE TEMPERATURE DEPENDENCE
ELECTRON-HOLE SCATTERING
EMPIRICAL LATTICE SCATTERING
ELECTRONS
HOLES
EXTRAPOLATED LATTICE SCATTERING PLUS ELECTRON HOLE SCATTERING
MOBILITY IN CM² PER VOLT SECOND
TEMPERATURE IN DEGREES KELVIN
100 150 200 300 400 600 800 1000 1500

FIG. 1. Conductivity mobility *vs* temperature.

[3] J. Bardeen and W. Shockley, Phys. Rev. **80**, 72–80 (1950).

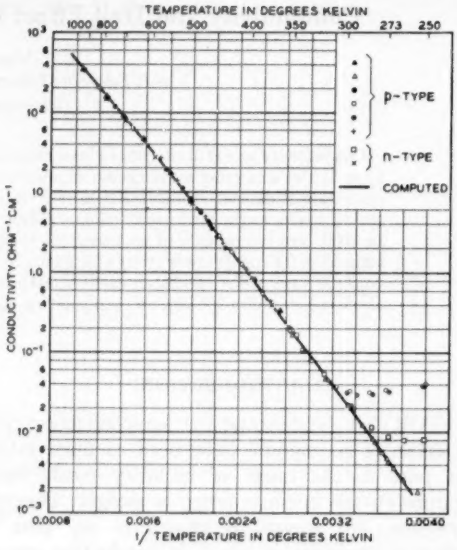

FIG. 2. Conductivity *vs* reciprocal temperature.

4.1 LATTICE-SCATTERING MOBILITY

Theory predicts for lattice scattering by acoustical modes:

$$\mu_{ac} = AT^{-1.5}, \tag{1}$$

and for lattice scattering by optical modes:

$$\mu_{op} = BT^{-0.5}(e^{\Theta/T} - 1), \tag{2}$$

where A, B, and Θ are constants. Lattice-scattering mobility has been determined[1] between 100° and 300°K and the temperature dependence of mobility found to be $T^{-1.66}$ for electrons and $T^{-2.33}$ for holes. These results are shown as plotted points in Fig. 1. For comparison the temperature dependence of μ_{op} is also shown in Fig. 1. This has been computed using $\Theta = 520°$ as determined by Shockley.[4] An absolute value for μ_{op} is not given because the value for B is unknown. It is probable, however, that optical mode scattering is comparable with acoustical mode scattering at temperatures as high as 1000°. Therefore, since the curves for μ_{op} and μ_{ac} do not diverge rapidly with decreasing temperature, it is also probable that optical modes make an appreciable contribution to the scattering over the temperature range where lattice-scattering mobility has been measured. If it is assumed that the departure from the $T^{-1.5}$ law found for electrons is due to an optical mode contribution, the two scattering processes are separable. Lattice-scattering mobility is given approximately by

$$\mu_L^{-1} = \mu_{ac}^{-1} + \mu_{op}^{-1}. \tag{3}$$

When Eqs. (1), (2), and (3) are combined and measured values of μ_L and T inserted, the constants A and B

[4] W. Shockley, Bell System Tech. J. **30**, 1025 (1951).

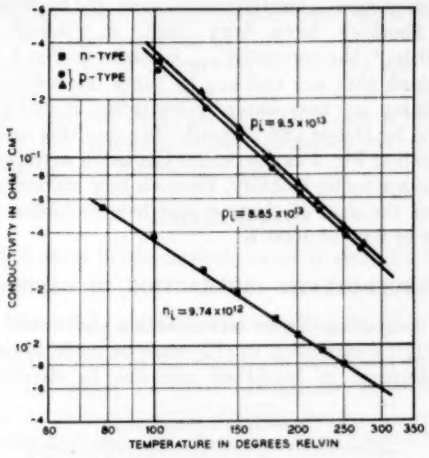

FIG. 3. Conductivity *vs* temperature in the range where carrier concentration is constant.

can be evaluated by solving two simultaneous equations. The results for electrons are

$$\mu_{ac} = 2.4 \times 10^7 T^{-1.5}, \tag{4}$$

$$\mu_{op} = 7.8 \times 10^4 T^{-0.5}(e^{520/T} - 1). \tag{5}$$

These equations generate μ_L *vs* T which coincides with measured μ_L to within the experimental error of ~2 percent. This is because so small a contribution from μ_{op} is required to go from $T^{-1.5}$ to $T^{-1.66}$ that the curvature in the μ_{op} temperature dependence (see Fig. 1) does not appear in measured μ_L. However, the contribution from μ_{op} required to go from $T^{-1.5}$ to $T^{-2.33}$ found for holes is so large that the curvature becomes evident and computed μ_{op} differs from measured μ_{op} by 6 percent at 200°. Assuming the maximum contribution by optical modes possible within the 2 percent experimental error leads to the following results for holes:

$$\mu_{ac} = 2.5 \times 10^8 T^{-2.0}, \tag{6}$$

$$\mu_{op} = 1.9 \times 10^4 T^{-0.5}(e^{520/T} - 1). \tag{7}$$

The departure from the $T^{-1.5}$ law shown by Eq. (6) may be due to the location of the valence band at some point other than the center of the Brillouin zone.

The results obtained by this analysis are highly speculative. Furthermore, mobility predicted for the range 300° to 1000° by Eqs. (3), (4), (5), (6), and (7) does not differ importantly from the straight line extrapolation of measured mobility shown in Fig. 1. Therefore, for the purpose of analyzing conductivity and Hall effect, lattice-scattering mobility is taken to be that given by the solid lines of Fig. 1 which represent the equations

$$\mu_{Ln} = 4.90 \times 10^7 T^{-1.66}, \tag{8}$$

$$\mu_{Lp} = 1.05 \times 10^9 T^{-2.33}. \tag{9}$$

4.2 CARRIER CONCENTRATION FROM 250 to 500°K

Conductivity for a number of samples is shown in Fig. 2. At low temperatures the conductivity extends into a range which contains both impurity and intrinsic conductivity. In determining carrier concentration here two procedures are used. Where impurity conductivity is negligible carrier concentration is determined from conductivity and lattice-scattering mobility using Eqs. (8) and (9) and the equation

$$\sigma = e(\mu_{Ln} n + \mu_{Ln} p) = e(np)^{1/2}(\mu_{Ln} + \mu_{Lp}). \tag{10}$$

Where impurity conductivity is important two additional equations are necessary:

$$n = n_i + p \quad \text{for } n\text{-type samples,}$$
$$p = p_i + n \quad \text{for } p\text{-type samples.} \tag{11}$$

The values for n_i and p_i are determined from latttice-scattering mobility and conductivity measured in the range where impurity centers are all ionized. Conductivity in this range is shown for some samples in Fig. 3. The lines drawn through the measured points represent the product

$$e\mu_L n_i (\text{or } p_i).$$

Carrier concentration has been computed as described using Eqs. (8), (9), (10), and (11) in the 250–500° range and is shown as plotted points in Fig. 4. The best fit to these points gives the empirical expression for carrier concentration in the 250–500° range

$$np = 3.10 \times 10^{32} T^3 \exp(-0.785/kT). \tag{12}$$

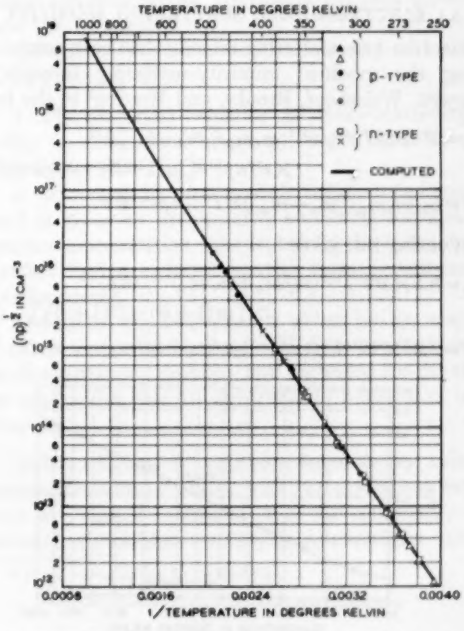

FIG. 4. Square root of the product of electron and hole concentration *vs* reciprocal temperature.

This differs from the old relation[3] in both the constant coefficient and the exponential term. The value of 0.785 is the width of the forbidden gap at $T=0$. The assumption that $\mu_L \propto T^{-1.5}$ made in obtaining the old relation led to a gap width of 0.75 at $T=0$. From lattice-scattering mobility and carrier concentration between 250 to 500° the intrinsic conductivity has been computed and is shown as the solid line in Fig. 2. Equation (12) gives the carrier concentration up to 500° shown as the solid line in Fig. 4.

5. CONDUCTIVITY FROM 500 TO 1000°K

The conductivity obtained from Eqs. (8), (9), and (12) is a factor of 1.30 higher than measured conductivity at 1000°. Above 500° the difference between measured and predicted conductivity increases with increasing temperature at a rate which is much too high to be explained on the basis of optical mode scattering. These results led Shockley to suggest that electron-hole scattering might become effective in reducing mobility when carrier concentration becomes large enough. It was also suggested by Herring that at high carrier concentration the electrostatic interaction of carriers would effectively decrease the intrinsic ionization energy and, therefore, increase the carrier concentration above that predicted by Eq. (12). Consequently, conductivity from 500 to 1000° is computed from mobility adjusted for electron-hole scattering and from carrier concentration adjusted for electrostatic interaction of the carriers. Conductivity computed in this way is to be compared with measured conductivity.

5.1 ELECTRON-HOLE SCATTERING MOBILITY

Electron-hole scattering mobility has been computed using the modified impurity-scattering formula of Conwell, Weisskopf, Brooks, and Herring[2] in the form

$$\mu_{np}=2^{7/2}k^2(kT)^{3/2}/\pi^{3/2}(m_nm_p/[m_n+m_p])^{1/2} \times e^3(np)^{1/2}[\ln(1+B)-B/(1+B)],$$

$$B=6\kappa(m_nm_p/[m_n+m_p])k^2T^2/(np)^{1/2}\hbar^2e^2.$$

Evaluating this gives

$$\mu_{np}=8.5\times10^{17}T^{3/2}(m/m_n+m/m_p)^{1/2}/(np)^{1/2} \times[\ln(1+B)-B(1+B)], \quad (13)$$

$$B=2.07\times10^{15}T^2/(np)^{1/2}(m/m_n+m/m_p).$$

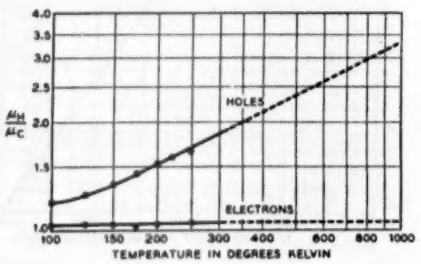

FIG. 5. Hall mobility/conductivity mobility *vs* temperature.

In computing μ_{np}, inertial masses measured by Benedict and Shockley have been used, $m_n=0.6m$,[5] and $m_p=0.3m$.[6] The computed μ_{np} is shown in Fig. 1. It is combined with μ_{Ln} and μ_{Lp} by using the method for combining μ_L and impurity-scattering mobility described by Debye and Conwell.[2] The resulting mobility is shown in Fig. 1 as the dotted line below extrapolated lattice-scattering mobility. Electron-hole scattering decreases the sum of electron and hole mobilities by a factor of 0.60 at 1000°K.

5.2 ELECTROSTATIC INTERACTION OF CARRIERS

In computing carrier concentration above 500° from Eq. (12), a correction to (12) must be made to include the decrease in forbidden gap due to electrostatic

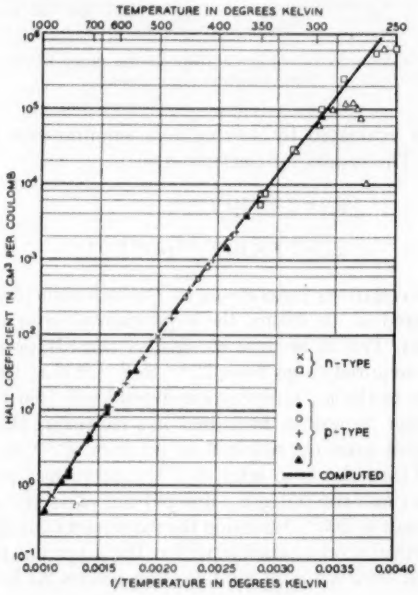

FIG. 6. Hall coefficient *vs* reciprocal temperature.

interaction of carriers. This correction,[7] as suggested by Herring and given in terms of the change in electrochemical potential of the carriers, is

$$\Delta\bar{\mu}=-(e^2/2\kappa)[4\pi e^2(n+p)/\kappa kT]^{1/2},$$

and

$$\Delta E_G=\Delta\bar{\mu}\text{ (for electrons)}+\Delta\bar{\mu}\text{ (for holes)}.$$

Evaluating:

$$\Delta E_G=-4.61\times10^{-10}(np)^{1/4}T^{-1/2}. \quad (14)$$

By use of Eqs. (12) and (14), $(np)^{1/2}$ has been computed and is shown in Fig. 4. The electrostatic interaction

[5] T. S. Benedict and W. Shockley, Phys. Rev. **89**, 1152 (1953).
[6] T. S. Benedict, Phys. Rev. **91**, 1565 (1953).
[7] See, for example, the Debye-Hückel theory in W. J. Moore, *Physical Chemistry* (Prentice-Hall, Inc., New York, 1950), p. 447.

increases carrier concentration at 1000° by a factor of 1.25 over that predicted by (12).

Using mobility determined in Sec. 5.1 and carrier concentration determined in Sec. 5.2, conductivity has been computed from 500 to 1000°K and is shown in Fig. 2. The agreement between measured and computed conductivity is surprisingly good.

6. HALL EFFECT

Hall effect in the intrinsic range is given by the expression[8]

$$R_H=(np)^{1/2}e[-\mu_{en}^2(\mu_{Hn}/\mu_{en})+\mu_{ep}^2(\mu_{Hp}/\mu_{ep})]/\sigma^2. \quad (15)$$

All of the terms in this expression have been evaluated over the range 250–1000° except the ratio of Hall mobility to conductivity mobility μ_H/μ_e. The conductivity mobility is that obtained in Sec. 5.1 and used to compute σ and is written as μ_e in expression (12) to distinguish it from Hall mobility μ_H. The mobility ratio has been determined[1] up to 250° and is shown as plotted points in Fig. 5. The values of μ_H/μ_e used to compute R_H are shown in Fig. 5 as a dashed extrapolation of the measured values. Hall coefficient has been computed using Eq. (15) and is shown compared to measured R_H in Fig. 6. The agreement between experiment and theory is very good but may be accidental. According to Herring, theory suggests that μ_H/μ_e for holes decreases at high temperature to some constant value rather than increasing as assumed in the extrapolation.

7. TEMPERATURE DEPENDENCE OF E_G

The theoretical formula for carrier concentration in the intrinsic range can be written

$$np=2.33\times10^{31}(m_nm_p/m^2)^{3/2}T^3\exp-E_G/kT. \quad (16)$$

This equation has the same form as empirical Eq. (12), but the numerical factor in (12) is larger than the theoretical value by a factor of 13.3 if we assume that effective mass equals rest mass. This can be explained as resulting from a change in E_G with temperature. If a linear variation is assumed,

$$E_G(T)=E_G(0)-\beta T. \quad (17)$$

Then $\beta=k\ln13.3=2.23\times10^{-4}$ ev/degree for $m_nm_p/m^2=1$. Bardeen and Shockley[3] find $\beta=1\times10^{-4}$ by this method. The different result is to be expected because the carrier concentration used by Bardeen and Shockley depended upon early drift mobility measurements and the assumption that $\mu_e\propto T^{-1.5}$.

At the present time, the values of m_n and m_p are uncertain. From thermoelectric effect measurements Geballe[9] finds $m_n=m_p=0.6m$ for the mass parameters in Eq. (16). From the assumption $m_n=m_p=0.6m$,

$$\beta=k\ln13.3\times4.6=3.5\times10^{-4}\text{ ev/degree.}$$

$E_G(0)$ was found in Sec. 4.2 to be 0.785 ev.

Equation (17) must be modified above $T=500°$ to include the effect on E_G by the electrostatic interaction of charge carriers. This can be done by combining (14), (17), and the results above to give

$$E_G=0.785-3.5\times10^{-4}T-4.61\times10^{-10}(np)^{1/4}T^{-1/2}. \quad (18)$$

E_G computed from (18) is shown in Fig. 7.

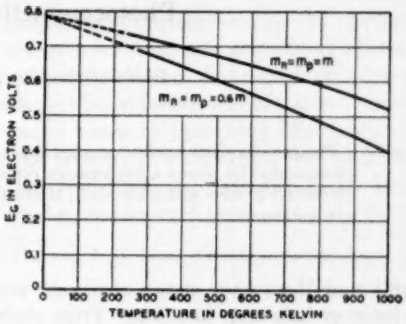

FIG. 7. Intrinsic ionization energy vs temperature.

8. SUMMARY

Conductivity and Hall effect have been measured in the intrinsic range of germanium and the results are compared with theory. Agreement between experiment and theory is good.

Conductivity is computed from theory with the following assumptions:

1. The empirical behavior of lattice-scattering mobility as determined between 100–300° can be extrapolated to 1000°.

2. Scattering by electron-hole collisions is important and is given by an impurity-scattering formula with carrier concentration substituted for impurity concentration and a reduced inertial mass substituted for carrier mass.

3. Carrier concentration is given by an empirical formula determined below 500°K from conductivity and lattice-scattering mobility and corrected for the change in gap width due to electrostatic interaction of the carriers.

Hall coefficient is computed from theory using the assumptions listed above with the additional assumption of a simple extrapolation of the empirically determined ratio of Hall mobility to conductivity mobility.

[8] W. Shockley, *Electrons and Holes in Semiconductors* (D. Van Nostrand Company, Inc., New York, 1950), first edition, p. 279.

[9] T. H. Geballe (to be published).

Photoconductivity in Gold-Doped Silicon

R. NEWMAN
General Electric Research Laboratory, Schenectady, New York
(Received March 8, 1954)

Photoconductivity has been studied in p- type gold-doped silicon at 20°K, 77°K, and 195°K. The impurity photoconduction shows a temperature dependence. At 20°K and 77°K, the data indicate a simple photoconductive process with a threshold at about 0.33 ev. At 195°K, the data indicate a complex photoconductive spectrum.

TAFT and Horn have shown that gold acts as a donor or hole trap in silicon.[1] From their resistivity-temperature data they find that a level is located 0.33 ev above the filled band. It was of interest to determine whether the corresponding result could be obtained from a study of the photoconductive response of gold-doped silicon. Preliminary experiments by Taft showed the presence of a photoconductive effect at low temperatures.[2]

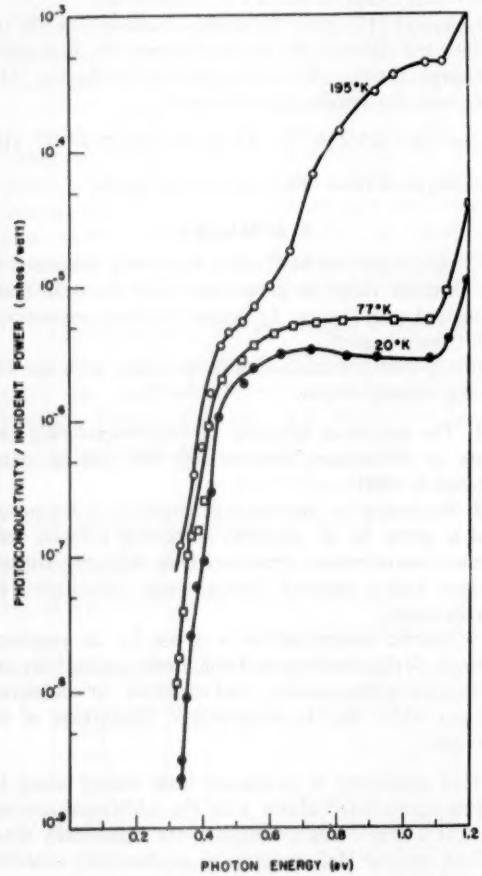

FIG. 1. Photoconductivity in gold-doped silicon at 195°K, 77°K, and 20°K. Sample thickness 2.5 mm. Estimated $n_{Au} \sim 5 \times 10^{15}$/cc.

Photoconductivity was measured using a conventional series circuit. A Perkin-Elmer thermocouple amplifier with a high input impedance preamplifier was used for chopped light measurements (13 cycle). A "Vibrating Reed Electrometer" was used for dc measurements. Over the range studied here, the photocurrents were linear in voltage and light intensity. A Perkin Elmer monochromator with a CaF_2 prism was employed. Samples were mounted in a cryostat equipped with a NaCl window. The illumination was substantially uniform over their length.

Figure 1 shows the photoconductivity spectra of a sample of p-type gold-doped silicon at liquid hydrogen, liquid nitrogen, and dry ice temperatures. This sample had high resistance (i.e., greater than 5 megohm) at these temperatures. The curves shown are typical of those obtained from similar samples cut from three different gold-doped ingots. The curves, which were obtained from chopped light data, were normalized by a measurement of dc photocurrent at a particular wavelength (0.8 ev). The division of the photoconductive spectra into an intrinsic region at energies above about 1.1 ev and an impurity region below this value seems obvious. The data for 77°K and 20°K seem interpretable in a simple fashion. The form of the response at these temperatures suggests a simple photoionization process. There is an uncertainty as to what value should be adopted to define the low-energy threshold. If in somewhat arbitrary analogy to the intrinsic case, we define the edge as the energy for which the response is $\sim 10^{-3}$ of the plateau value then the present data give an optical activation energy of 0.32 to 0.33 ev in agreement with the energy determined thermally.

The data for dry ice temperature cannot be explained as simply. The curve of impurity photoconduction appears to be a superposition of at least two simple photoconduction curves, the first of these having the previously determined threshold of ~0.33 ev and a second with a threshold in the vicinity of 0.7 ev.

It might be suggested that the dry ice data indicate the presence of a second gold donor level at about ~0.7 ev above the filled band. This level would exist

[1] E. A. Taft and F. H. Horn, Phys. Rev. **93**, 64 (1954).

[2] E. A. Taft (private communication).

only when the lower donor level was filled. However, a rough calculation of the Fermi level from the resistivity data indicated that it is "locked-in" at the 0.33 ev donor level, even at dry ice temperature. If there is only a negligible change in Fermi level in going from say 195°K to 77°K, then it would seem difficult to explain the data in terms of a two-level model. At present we have no alternative to suggest. If both resistivity and optical data were available for samples which could be made *n*-type by gold-doping, perhaps more complete information would be forthcoming on the energy level scheme in gold-doped silicon.

Response times of the gold-doped samples are of order 10 μsec.[3] No evidence was found in this work of long response times or quenching effects that would indicate the presence of stable traps even at 20°K.

I am indebted to E. A. Taft and F. H. Horn for furnishing the samples used here.

[3] E. A. Taft and F. H. Horn (private communication).

PHYSICAL REVIEW VOLUME 94, NUMBER 6 JUNE 15, 1954

Diffusion of Impurities in Germanium*

W. C. Dunlap, Jr.
General Electric Research Laboratory, Schenectady, New York
(Received February 26, 1954)

A method is described for the study of diffusion of impurities in semiconductors; results are obtained by the observation of the *p-n* junction formed as the diffusing impurity penetrates the specimen. Studies have been made upon germanium using this technique, and comparisons with the radioactive tracer method have shown the *p-n* junction method to give valid results. Measurements on indium, gallium, aluminum, arsenic, boron, phosphorus, antimony, and zinc are described. The diffusion coefficients of these elements in germanium range, at 900°C, from 10^{-12} cm²/sec to 10^{-9} cm²/sec. The activation energy for bulk diffusion in germanium is about 2.5 ev, or 57 000 cal/mole. Applications are given for the study of the *p-n* junction method to the study of surface and grain-boundary diffusion. The method has also been applied to the study of new elements and their electrical activity in germanium. It is concluded that the rapidity with which results can be obtained by the junction method, and its applicability to elements not conveniently available in radioactive form make it a valuable adjunct to the radioactive tracer method for studying diffusion.

INTRODUCTION

THE problem of the diffusion of atoms through a crystalline lattice is an old one, and one which has been approached in many different ways, both theoretically and experimentally.[1] Most of the past work has been done on metals, and much of the recent work on metals has been done with the radioactive tracer technique.[2]

In the present study, a new method has been applied to the study of diffusion in semiconducting crystals. These crystals have the property that their electrical properties are determined, in most cases, by the presence of very minute traces of impurities. In many of these crystals, some impurities render them *p* type, whereas others make them *n* type semiconductors. The type of conduction refers to the carrier present; in *n* type semiconductors, the current is carried by electrons, in *p* type semiconductors, the current is carried by positive holes.

The type of carrier can be determined by several methods: (1) Hall effect; (2) thermoelectric measurements; and (3) rectification probe measurements. The latter two methods are particularly suitable to the present purpose, since the desired information can be made to apply to very localized regions of the specimen, by the use of fine whiskers for probes. In particular, the region of transition between *p* and *n* type material can be located with a high degree of precision, even though it may be localized very close to the surface of the specimen.

In the present work, diffusion has been studied by means of the change in type of conductivity. To do this, one chooses the base material to be one of the type opposite to that prevailing when the impurity has diffused in. Thus, for studying the diffusion of indium into germanium, one chooses samples of *n* type material, heats them in contact with indium, and measures the depth of the *p-n* junction formed by the diffusion of indium into the germanium.

The plan of the present work, then, was to put various impurity elements of interest in contact with germanium, and to diffuse them in at different tem-

* Preliminary accounts have appeared by W. C. Dunlap, Jr., **86**, 615 (1952); D. E. Brown and W. C. Dunlap, Jr., Phys. Rev. **86**, 616 (1952); and W. C. Dunlap, Jr., and D. E. Brown, Phys. Rev. **86**, 417 (1952).

[1] R. M. Barrer, *Diffusion in and Through Solids* (Cambridge University Press, Cambridge, 1951).

[2] For a discussion of the radioactive method, see R. Hoffman, in *Atom Movements* (American Society of Metals, Cleveland, 1951).

peratures for different times, in order to determine their diffusion coefficients as a function of temperature. Information about the lattice structure can be obtained by means of the equation:

$$D=D_0\exp(-E/kT). \tag{1}$$

Here D_0 is a constant of the material, E is the activation energy for diffusion, and k is Boltzmann's constant. The activation energy is a measure of the stiffness of the lattice, since it is the energy jump that an impurity atom must acquire before it can make a motion into a nearby vacancy. Details of the theory of diffusion can be found in reference 1.

In particular, a study was made of the diffusion rates of donor as compared to acceptor atoms, and some interesting conclusions were drawn.

Attempts were also made to apply the p-n junction method to the study of other types of diffusion, such as surface and grain boundary diffusion.

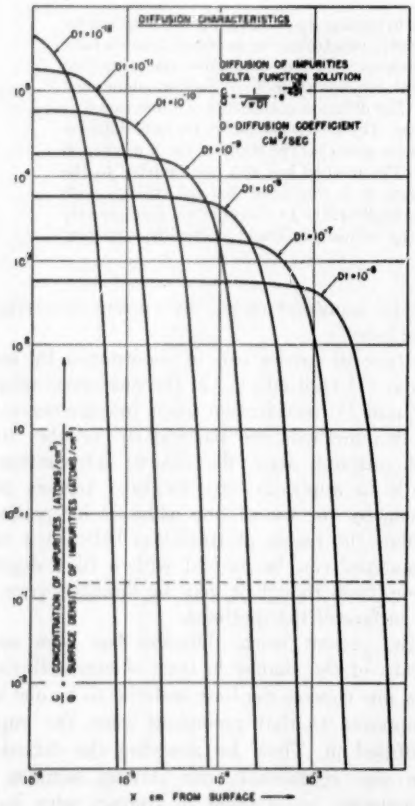

FIG. 1. Theoretical diffusion curves for one-dimensional diffusion, based upon the "constant-source" solution to the diffusion equation. The plot is on a log-log scale, with x being measured from the surface of the slab. The p-n junction, in the case of a semiconductor, is formed at the point where the curve crosses the horizontal line representing the impurity concentration in the base material.

As part of the work, a systematic study was made of the p-n junction method as compared to the radioactive tracer method, for reliability, accuracy, and rapidity.

METHODS OF MEASUREMENT

A basic assumption in this work was that of one-dimensional geometry; that is, the penetrations dealt with were always small compared to the lateral dimensions of the samples, and to the thickness of the samples. It was also assumed that the initial impurity distribution, at time zero, was zero except at the surface of the sample. This we can call the "constant-source"[2] problem, if we assume we are dealing with a constant number of impurity atoms Q present in or on the sample.

The diffusion equation is:

$$D[\partial^2C(x)/\partial x^2]=\partial C(x)/\partial t, \tag{2}$$

where D is the diffusion coefficient, $C(x)$ is the concentration of the diffusing impurity; $C(x)$ is related to the total Q by the relation

$$Q=\int_0^\infty C(x)dx. \tag{3}$$

The solution of the diffusion equation for the constant-source problem is

$$C(x)=Q(\pi Dt)^{-\frac{1}{2}}\exp(-x^2/4Dt). \tag{4}$$

A plot of the form of the advancing diffusion front at various times (actually the parameter $(Dt)^{\frac{1}{2}}$ makes a more useful one for plotting) is shown in Fig. 1. Both the concentration and the distance are on a logarithmic scale. On this scale the shape of the curve does not change with time. The curve is simply translated down and to the right. The concentration representing that of the impurities in the base material is shown as a straight horizontal line. At the point where the curve crosses this line, the p-n junction occurs. If the p-n junction depth is x_0, and the base concentration C_0, then

$$x_0=2(Dt)^{\frac{1}{2}}\{\ln[Q/C_0(\pi Dt)^{\frac{1}{2}}]\}^{\frac{1}{2}}. \tag{5}$$

For example, if $C_0=10^{16}$, $Q=10^{17}$, $(Dt)^{\frac{1}{2}}\sim10^{-3}$ cm, then we can approximate

$$x_0\approx 8(Dt)^{\frac{1}{2}}. \tag{6}$$

The quantity C_0 is easily determinable with good accuracy from Hall effect measurements. While the Hall measurement gives actually the density of electrical carriers, for germanium at room temperature these are all ionized, so that this is also the number of impurity centers.

$$C_0=7.4\times10^{18}/R, \tag{7}$$

where R is the Hall coefficient in cm³/coulomb.

[2] See reference 1, p. 44.

It is seen from Eq. (6) and Eq. (5) that the p-n junction moves very nearly according to a $\sqrt{t}$ law. This gives a means of checking the theory experimentally.

For exact solutions for the diffusion coefficient from Eq. (4), a method of successive approximations has been used. Since the complicating term $(Dt)^{\frac{1}{2}}$ enters logarithmically into the solution for D, the process rarely requires more than two such steps. Indeed, for an accuracy satisfactory in many experiments, a simple guess at C_0, Q, and D suffices to give D accurate to better than a factor of 2.

Another diffusion problem to which the present one is related is the "step-function" problem. In the application of this method, the diffusing impurity is present in large quantities at the plane $x=0$. As diffusion proceeds, the diffusing impurity enters the crystal, but the concentration at the surface presumably does not change. This method leads to the following solution of the diffusion equation.

$$C(x)=C_0'\{1-\text{erf}[x/2(Dt)^{\frac{1}{2}}]\}, \tag{8}$$

where C_0' is the concentration at the surface.

For the case that we have here, $C=C_0$, $x=x_0$, with $C_0 \ll C_0'$, the error function can be replaced by the form:

$$\exp(-x^2)/\pi^{\frac{1}{2}}x. \tag{9}$$

Thus, the solution in the step-function case reduces to the form very similar to that for the constant-source case,

$$x_0 \approx 2(Dt)^{\frac{1}{2}}[\ln(C_0'/C_0)]^{\frac{1}{2}} \approx 6(Dt)^{\frac{1}{2}}, \tag{10}$$

if $C_0' \sim 10^{20}$, $C_0 \sim 10^{16}$. It is interesting that for many practical cases, the "constant source" and the "step-function" approximations yield the same result [compare Eqs. (10) and (6)].

In general, we are not able to use the step-function solution for measurements of diffusion by the depth of the p-n junction. The major reason is that the quantity of diffusing impurity must be kept small. This is important because we wish the entire layer from the surface to the p-n junction to be a true diffusion zone. This means, presuming that the impurity may alloy with or dissolve into the germanium, that all secondary phases, alloy regions, etc., must be negligible in thickness compared to the true diffusion zone. If the amount of impurity is limited to a few micrograms/cm^2, simple calculations show that the "alloy zone" is actually thin compared to the diffusion zone.

For example, if 5 micrograms of indium are heated in contact with 1 cm^2 of germanium wafer, at 700°C, it can be estimated from a phase diagram, such as that of Fig. 2, that at that temperature the indium will dissolve germanium until a concentration of ~20 percent indium is reached. This will mean an "alloy zone" of about 2 microns. In the design of the experiment then, one must heat for a sufficiently long time so that the diffusion distance x_0 is large compared to micron. This is hardly a limitation, since much larger diffusion distances than this must be used to attain reasonable experimental accuracy.

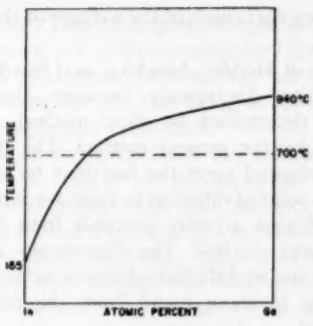

FIG. 2. Phase diagram showing the liquidus curve of indium-germanium.

The fact that the surface layer, even though liquid initially, attains a state very shortly in which the impurity is in saturated solid solution with the germanium, means that we can be sure that the observed p-n junction arose by diffusion and not by liquid penetration.

Thus, for measurement purposes, one uses techniques that are somewhat complementary to those used when junctions are made for technical purposes.[4] There the "step-function" solution is more applicable, because large amounts of impurity are applied, there is a considerable penetration by solution and alloying, and usually conditions are chosen to make the diffusion zone thin in comparison with the alloy region. In technical fused junctions, also, the "recrystallization" region plays a major part, whereas, for measurement work, it can be neglected, as long as Q is small.

The step-function solution may apply to diffusion in a grown p-n junction, where the impurity of interest changes its concentration abruptly as a result of the doping procedure used. McAfee, Shockley, and Sparks[5] studied diffusion in germanium using such junctions. In their work, the motion of impurities was studied through the changes of capacity of the p-n junction used as a rectifier. Although in principle the same problem could be studied by the p-n technique dealt with in the present paper, there is a major drawback, the lack of a reference for measurement. In the case of measurements from the surface, the surface itself serves as a convenient base. In the grown junction, there is no such base. Although a base from which to measure can be set up, all the schemes for doing so that have been envisioned to date, suffer from such

[4] A discussion of "fused-impurity contact" or "alloy" junctions is given by J. S. Saby and W. C. Dunlap, Jr., Phys. Rev. **90**, 630 (1953).

[5] McAfee, Shockley, and Sparks, Phys. Rev. **86**, 137 (1952).

poor accuracy that much of the validity of the measurement is lost.

The work of McAfee, Shockley, and Sparks revealed an interesting discrepancy between the diffusion coefficients determined by their method, and those determined by the present method. The discrepancy appears to depend upon the fact that no surface was close to the point of diffusion in their *p-n* junction bars, whereas diffusion actually proceeds from the surface in the present method. The discrepancy is about a factor 1000 smaller diffusion coefficient in their measurements, than in those found from the present type measurement.

EXPERIMENTAL

Samples

The diffusion studies reported here were made, in the main, with single crystal samples of germanium, some kindly furnished by R. N. Hall, others made by the author. These samples were in the form of flat plates, cut square, ground, polished, and etched. For the study of donor elements, high-resistivity *n* material was often used for starting material, and the thermal conversion arising from the diffusion heating was used to give *p* type specimens of about 1 ohm cm resistivity.

For the study of acceptor elements, generally, low-resistivity *n* type material, in the range 0.1–0.2 ohm cm was used. These values were used to minimize thermal conversion effects such as occur with higher-resistivity samples.

Determination of the Depth of the *p–n* Junction

Determination of the depth of the *p-n* junction was generally done by cutting off the sample at a small angle, generally 5 or 10°, and measuring the distance along the slope from the original surface to the junction.

The method requires the use of flat, highly polished plates. These were accurately ground, and the angular surface was also prepared, using the hand grinding machine shown in Fig. 3. The hand grinder contains a piston of polished, hardened steel, turning in a cylinder of similar metal. The sample is mounted on an end piece, which may be a flat, or it may be a beveled piece of the proper angle. Some preliminary information is generally needed so that the cut is deep enough and of the right angle that the junction is actually exposed, and at a suitable distance for accurate measurement.

A problem that may be severe in some cases, is the warpage of some germanium surfaces at high temperatures of diffusion. This effect is, presumably, similar to that reported by Gallagher,[6] namely that the stress of supporting their own weight, while inside a cylindrical tube, at temperatures of 900°C or so for periods of days can lead to a curvature of the originally flat surface. Again, this does not appear as an error of alarming degree for measurements of the accuracy desired here. However, support for the sample on a flat surface is generally desirable.

[6] C. J. Gallagher, Phys. Rev. 88, 721 (1952).

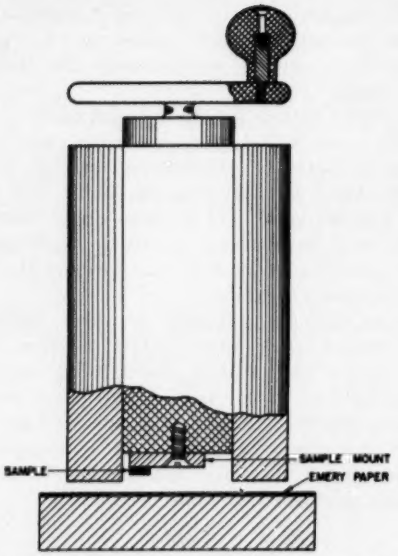

FIG. 3. Cut-away view and section of hand-operated precision grinder used in diffusion measurements, both in the radioactive tracer work and in the *p-n* junction work.

Figure 4 shows the arrangement for making the tests on detection and location of the *p-n* junction. The test probe was mounted on a micromanipulator originally designed for work with point-contact transistors, and having a sensitivity of 0.1 mil per division.

Most of the measurements were made with a thermoelectric probe as the detector of the *p-n* junction. The point used was a tungsten carbide needle, sharpened to a fine point. The needle was mounted in a pin vise, close to a small heating coil. The base of the sample and the pin vise were connected to a recording dc millivoltmeter, whose direction of deflection indicated the type of germanium.

Some considerations in the use of the method are:

1. The diffusion coefficient depends upon the square of the *p-n* junction depth, and care must be exercised all through the measurement for best results.

2. The junction depth is determined from the distance to the junction, relative to the point of intersection of the ground surface and the original surface. This location had to be done visually, through the binocular microscope; the location is based upon the difference in visual appearance of the original polished surface and the new ground surface. The larger the angle for the cutting, the more clear the line of intersection; and, conversely, attempts to increase sensitivity by decreasing the angle of grinding are partially self-defeating because of increased fuzziness of the line of intersection.

3. Considerable attention must be given the location of the p-n junction itself. Besides the expected uncertainties due to roughness of the ground surface, there is a tendency of ground surfaces on the n type material to show up p type. This leads the measured value of the junction depth to be somewhat too small for measurements on donors, too large for acceptors. The effect is minimized if low-resistivity material is used for the base.

4. It is estimated that the p-n junction depth can be measured to about 10 percent accuracy at 10 mils penetration, 25 percent at 1 mil penetration. In most experiments, the heating time was chosen to produce penetrations of at least 1 mil.

Evaluation of Q

It is assumed that the quantity Q, the total number of impurity atoms deposited on the sample/cm², remains constant, in order to use Eq. (4) and its derivatives. This assumption is in general not valid. Evaporation often leads to departure of much of the volatile impurities in the first few seconds or minutes of heating, and surface diffusion can also lead to a spreading of the impurity around the sample. Evaporation, followed by chemical reaction or diffusion, can lead to a loss of most of the impurity into the walls of the heating chamber, in this work, quartz.

A virtue of the method used here, however, is the insensitivity of the method to the exact value Q. This point was demonstrated experimentally in the following way. Two similar specimens of germanium were prepared, each evaporated with radioactive antimony at the same time, in the same way. A third similar specimen was also used, but unevaporated. One evaporated specimen was sealed in a quartz tube by itself, the other two in another quartz tube. Both tubes were heated together at the same temperature, for the same time. The tubes were cut open, and each sample was measured for penetration of the n type layer into the p type base. All three were equal, to

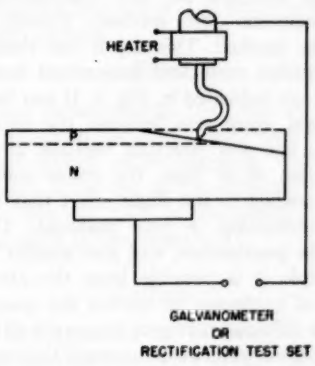

FIG. 4. Schematic diagram showing the method used for locating the p-n junction on germanium samples.

±10 percent. Thus, the pure sample acquired from the evaporated one sufficient antimony to receive the same depth of junction. Likewise, the loss of antimony did not prevent the junction being at the same depth as in the sample heated by itself.

The loss of impurity from the sample has been checked for a number of the important impurities, particularly antimony, zinc, and indium, which were available in radioactive form. It was found by etching out the insides of the quartz tubes used for heating, and checking both samples and etching residues, that at least 50 percent of antimony could be found on the sample after the typical diffusion experiment, heating at 850°C for 16 hours. Zinc, however, and particularly indium, combine with or diffuse into the quartz walls at such a rate that only a small fraction of the originally deposited material is found on the sample. Attempts to counteract this by increasing Q may well lead to errors because of increased alloy penetration, contamination and roughening of the surface, etc.

Further information on the evaluation of Q is given under the headings for each impurity in the next section.

OTHER FACTORS IN DIFFUSION EXPERIMENTS

Two important factors for all diffusion experiments are the exact manner of heating the specimens, the atmosphere, and the type, uniformity, and degree of temperature control and measurement of the furnaces used.

The diffusion measurements were carried out almost exclusively with small quartz tubes to hold the samples and protect them from oxidation. Each sample was sealed in a separate quartz tube, about 4 inches long and $\frac{3}{8}$ inch in diameter. These tubes were all cleaned in hydrofluoric acid and well rinsed and dried before sealing in the samples. They were then baked out at 350°C, and 15 cm pure dry argon added. The tubes were then sealed off. Cleanliness of the tubes was of extreme importance, but very difficult to guarantee. Because of the extreme sensitivity of germanium to impurities, even a trace of an element that diffuses faster than the one under study may lead to a completely erroneous result.

The furnaces in which the heating was done were nichrome wound, tubular furnaces, with a single winding whose density of turns increased towards the ends to compensate for end losses. These furnaces were found to hold up well for long periods when used at temperatures of 1000°C and below. The length, 24 inches, was sufficient to furnish a zone about 6 inches long in which temperature was uniform to several degrees C.

Temperatures were controlled from iron-constantan thermocouples, placed very close to the sample tube. These couples were used only for control of the regulators. Actual furnace temperatures were obtained

periodically during the diffusion run, by use of a separate calibrated thermocouple. This was one of a group of six iron-constantan thermocouples, each used for a short period of time, discarded, and replaced by a new calibrated thermocouple. This procedure was done in order to avoid errors due to drift in calibration of thermocouples. All thermocouples were calibrated by the thermal standards section of the General Engineering Laboratory, General Electric Company.

The furnaces were all regulated by means of Brown Pyrovane electronic controllers. To each had been added an "anticipator," consisting of a dummy thermocouple, and a flashlight bulb. This device, which is a standard one, permits a greater degree of control of furnace temperature, if properly used. Even with these precautions, it was found very difficult to maintain a uniform measured temperature in a diffusion furnace for a period of a week or so at, say, 900°C, with uncertainties of less than ±2°C. The over-all temperatures specified are thought to be accurate to about ±5°C.

COMPARISON OF THE *p-n* JUNCTION METHOD WITH THE RADIOACTIVE TRACER METHOD

It was desirable to compare diffusion results obtained with the *p-n* junction method, with results on the same specimens obtained with the radioactive tracer method. For this purpose several wafers of single crystal germanium were ground to a high degree of polish and flatness, and coated with a thin evaporated layer of antimony, about 1000A thick. This antimony was Sb^{124}, a radioactive isotope with half-life of 60 days. The samples were heated in the usual way at temperatures ranging from 600 to 900°C. The heating times were chosen to give a reasonable penetration; because of the difficulty of removing thin layers accurately, the penetration was chosen to be at least several mils on all samples.

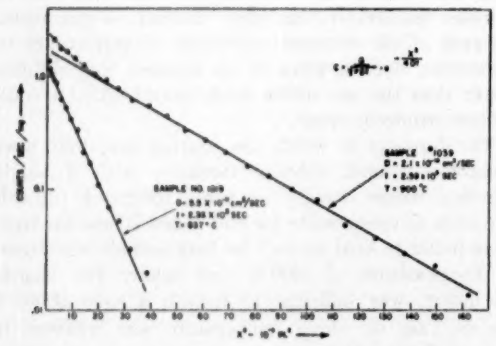

FIG. 5. Diffusion results on germanium obtained by radioactive tracer technique using Sb^{124}. The counting rate per unit weight of germanium is plotted against the square of the distance from the surface. According to Eq. (4) of the text, this should be a straight line. The diffusion coefficient is determined only by the slope of the line.

The samples were then ground on the grinder of Fig. 3. The grinding head was the one normal to the axis, so that the layers parallel to the surface could be removed. The face opposite the one to be ground off was first itself ground slightly to minimize effects of lack of parallelism. The activity was also removed from the opposite face and all the edges. Layers generally 0.2–0.3 mil were removed at a time. The amount removed was determined by micrometric measurements of the sample and base to which it was waxed. Also the weight of this combination was measured after each grinding. Weighing was found to give the most accurate results.

The grinding was done into sheets of fine grade emery paper. Care was taken that all the ground material was actually in or on the paper. The activity of the paper was determined by placing in a standard position in a scintillation counter, using an anthracene crystal for counting beta rays.

No corrections were made for the absorption of the activity in the powder while on the paper. It was found that if the layers removed were equal in thickness, the absorption would introduce a constant factor to be applied to give the correct activity. This corresponds to a translation of the log activity *versus* x^2 curve without change of slope and hence without effect on D.

The activity in the sample could be reduced to an absolute basis by using standards consisting of dilute solutions placed on similar pieces of emery paper, dried and coated with plastic to prevent loss of loose material.

The results of the radioactive tracer studies are summarized in Figs. 5 and 6. Figure 5 shows the counting rate per unit weight of germanium removed, plotted against the square of the distance from the original surface. This is based upon the formula of Eq. (4) and the assumption that the counting rate is proportional to the concentration of the antimony in the germanium. The good linearity in Fig. 5 is an excellent check on the validity of the theory.

Each time the surface was ground off, the new surface was checked for *p-n* characteristic, using the thermoelectric test method. Finally, the *p-n* junction was reached. This depth was then recorded, and the diffusion coefficient determined from Eq. (5). The results are indicated in Fig. 6. It can be seen that there is good agreement between the two methods. In general, the *p-n* junction method gave slightly smaller values of D than the tracer method. This might be ascribed to the slight effect that the surface has in contributing *p* type material. This would minimize the penetration, and give smaller D.

In principle it is possible from the absolute concentration of antimony to answer the question as to whether the diffusing antimony atoms are all electrically active. The good agreement between the two methods of measurement is one indication of this. Actually, direct comparison is difficult because of the large

errors of determining the absolute antimony concentration in thin layers, particularly when the concentration is varying rapidly.

MEASUREMENTS ON THE VARIOUS IMPURITIES

Antimony

In this section is given a short discussion of the particular techniques applicable to each element.

In the case of antimony, which was more extensively studied than any other element, the major problem was determination of Q. Most the work with antimony was done with radioactive antimony 124. Use of the radioactive tracer is convenient for measurement of Q, even though the standard techniques for getting D by the tracer method are replaced by the p-n junction method.

When ordinary antimony was used, the evaporation was usually done upon a glass slide holding the sample. The slide was weighed on a micro balance before and after evaporation. Generally, the weights involved were about 10 microgram/cm^2, or about 200 microgram for the typical slide.

Because of the good retention of antimony on the sample, the values of Q obtained were relatively significant, and Eq. (5) could be used with safety.

Arsenic

Arsenic was studied less extensively than antimony. In most of the experiments, a tiny speck of arsenic was simply added to the quartz tube at the time of sealing. Equation (6) was used to determine D.

Phosphorus

A similar procedure to that of arsenic was used in the case of phosphorus. In these three cases above, ordinary cp chemicals were found to be of adequate purity. Their segregation characteristics and diffusion coefficients are such that the only element likely to cause trouble is one of the other two, and it would have to be present as a rather high percentage impurity to cause much trouble.

Zinc

For the zinc measurements, Zn^{65} was available, and some work was also done with high purity Johnson-Mathey zinc (about 99.99 percent). Unfortunately, zinc was found to be one of the elements most likely to disappear into the walls of the quartz tube during heating. Equation (6) was used.

Gallium

Gallium was deposited as an evaporated film on most of the samples. Weighing of the film was used for most of the experiments. Gallium has a lower vapor pressure than indium or zinc, but much of it is still lost to the quartz at the higher temperatures of diffusion heating.

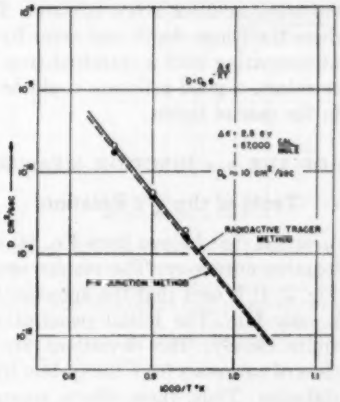

FIG. 6. Diffusion coefficient of antimony in germanium plotted vs the reciprocal temperature. Results were obtained both by the p-n junction method and radioactive tracer method on the same samples. Agreement between the two methods is seen to be good.

Equation (5) and Eq. (6) were both used for measurements on gallium.

Aluminum

A number of attempts were made to determine the diffusion coefficient of aluminum into germanium, without success. The troubles apparently lay in the oxidation of the very small amounts of aluminum deposited by evaporation on the samples. Very high resistance layers were generally observed when probe tests were attempted on these surfaces.

Indium

As in the case of antimony, most of the work with indium was done with radioactive material, in this case In^{114}, which has a 48-day half-life. The surface activity of the sample before diffusion again could be used for accurate determination of the initial Q. In the case of indium, however, so much of the indium was lost to the quartz during diffusion, that the utility of this value is questionable. Equation (5) was used, however, on the belief that at most temperatures the indium would not be lost so fast that the initial penetration, which determines the final penetration, to a great extent, is that given by the initial Q, Eq. (5) was used for most of the work.

Boron

Boron was deposited pyrolytically upon the germanium samples. Although weighings were made in order to determine Q, it was found more precise to determine thickness of the films from their interference properties. For this purpose, one of the samples was etched at one end to remove the boron, using hot

concentrated nitric acid for a few minutes. This made a region where the fringe depth was zero. By counting fringes, and comparing with a standard step gauge for interference colors, a good estimate could be obtained for the Q in the case of boron.

RESULTS OF THE p-n JUNCTION MEASUREMENTS

Tests of the $\sqrt{t}$ Relation

The $\sqrt{t}$ relation that follows from Eq. (4) was tested using radioactive antimony. The results obtained are shown in Fig. 7. It is seen that the agreement with the $\sqrt{t}$ law is only fair. The initial penetration follows this law quite closely. The deviations are probably due to the loss of antimony from the system by evaporation and diffusion. Thus, these effects appear to be a limitation on the accuracy of the measurements.

Results of Measurements on Various Impurities

Figure 8 shows results obtained on the various impurities at temperatures ranging from 600°C to 900°C. The lines describe the results to a good approximation, considering the rather large errors in measurement of x_0, the uncertainty in Q values, uncertainties in temperature measurement and control, and other effects already discussed.

The lines shown are nearly parallel, and have a slope about the same found for antimony by the radioactive tracer method, i.e., 2.5 ev, or 57 000 cal/mole.

Boron appears to give somewhat anomalous results, in contrast to all the others. Boron diffusion appears to be rather rapid at high temperatures, slow at low temperatures; thus the activation energy appears to be higher. A possible reason for this behavior lies in the fact that boron does not alloy easily with germanium, as do all the other elements studied here. Thus, some of the slowness of diffusion at the lower temperatures, may be due to lack of good "contact" between the film of boron and the crystal.

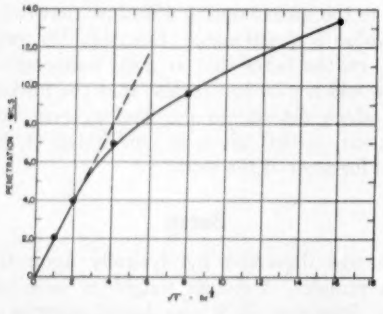

FIG. 7. Penetration of the p-n junction into germanium as a function of time of heating. The dashed line is the theoretical $\sqrt{t}$ law predicted by diffusion theory. Agreement is considered fair.

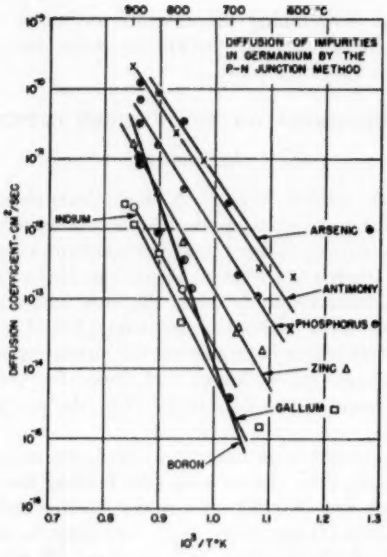

FIG. 8. Diffusion results for various elements, based upon p-n junction measurements.

DISCUSSION

Besides the activation energy E, another parameter of interest is D_0, the "frequency factor" in the diffusion equation. This value is obtained by extrapolating the diffusion curve to the axis $1/T=0$. From Fig. 6 it is found that D_0 is about 10 cm²/volt sec for germanium. A similar value is found from Fig. 7, although this is probably not as accurate.

A use of the experimental value of D_0 is in checking validity of diffusion data, as described by Nowick.[7] Thus, diffusion through cracks, imperfections, or other agencies than the pure bulk diffusion effect show up as a departure from the "Langmuir-Dushman equation,"[8] or one of its successors. The equation used by Langmuir and Dushman was

$$D_0=a^2E/N_0h, \qquad (11)$$

where a is the interatomic spacing in cm, E is the experimental activation energy, N_0 is Avogadro's number 6.06×10^{23}, and h= Planck's constant. Although this equation has been supplanted by more rigorous equations, most of them involving such parameters as the entropy of diffusion and the rigidity modulus, it still remains a useful tool for qualitative evaluation of diffusion data.

According to Eq. (11), D_0 for germanium should be about 0.3 cm²/sec. The agreement with the experimental extrapolated value of 10 cm²/sec is satisfactory, considering that in many cases of invalid data, the disagreement is many orders of magnitude.

[7] A. S. Nowick, J. Appl. Phys. **22**, 1182 (1951).
[8] I. Langmuir and S. Dushman, Phys. Rev. **20**, 113 (1922).

Another factor of importance in considering D_0 is the possibility of a temperature dependence of the activation energy E. If E has a component depending linearly upon the temperature,

$$E=E_0+\alpha T, \tag{12}$$

then the expression for D should be written

$$D=D_0e^{-\alpha/k}e^{-E_0/kT}=D_0'e^{-E_0/kT}. \tag{13}$$

Thus, in this case, the experimental D_0' actually contains the parameter (α/k) as well as the proper component D_0. There is some likelihood that there is such a temperature dependence of the activation energy.

Comparison of the Diffusion Coefficients

It is seen from Fig. 8 that the various elements differ greatly in their diffusion coefficients. In particular, the donors are seen to diffuse much more rapidly than the acceptors. This can be interpreted qualitatively in terms of Fig. 9. Here are shown the "Goldschmidt ionic radii" for various ionic charges, as determined from x-ray studies of compounds in which these elements assume different valencies. As is expected, the negative ions of an element are considerably larger than the positive ions. In germanium, of course, the donor ions become positively charged on giving up their electrons, whereas the acceptors become negatively charged. These differences, even apart from the natural differences of ionic radius for the various elements, lead naturally to higher diffusion coefficients for donor elements.

No great success has followed attempts to correlate to a higher degree the specific values of diffusion coefficient with the values of ionic radii. The ionic radii themselves do not apply well enough, and there

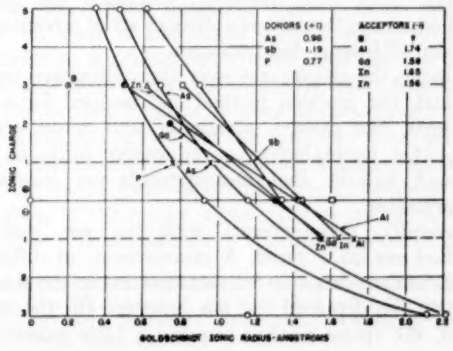

FIG. 9. Ionic radii for various ions of interest, determined from "Goldschmidt ionic radii." These values were obtained from various compounds of these elements and unfortunately do not have direct application without serious error to the substitutional solution of the elements in germanium, where their bonding relations are not the same as in their compounds. This hinders their use in more than rough correlations between ionic charge and diffusion coefficient.

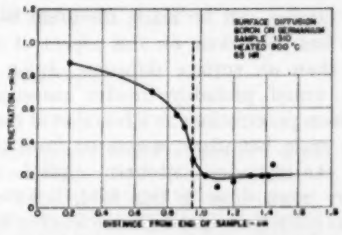

FIG. 10. Surface diffusion of boron on germanium. The plot of bulk penetration *vs* distance from end of boron coating indicated that appreciable time elapsed before sufficient boron reached points indicated, and thus before bulk penetration could proceed. Because of the large distances, however, it was concluded that surface diffusion proceeds at a rate probably 100 times the bulk penetration in this experiment.

is question as to whether the data on diffusion are accurate enough to justify serious attempts in this direction.

APPLICATION OF THE *p–n* JUNCTION METHOD TO SURFACE AND GRAIN BOUNDARY DIFFUSION

Studies of Boron Surface Diffusion

Figure 10 illustrates some preliminary results on study of surface diffusion of boron on germanium, using the *p-n* junction method. The technique was as follows: polished samples on which boron had been deposited pyrolytically, were used. The boron was removed from about half the sample by etching in hot concentrated nitric acid. The sample was then sealed and heated at 800°C for 65 hours in argon. The sample was next ground off at a 5° angle, starting at the edge of the sample, in steps. After about eight of these steps, the sample had been cut beyond the point at which the boron layer had stopped.

The first thing noticed on checking the sample after diffusion was that the surface was *p* type. In a check experiment, with an *n* type sample in the same tube, the *n* type sample showed no corresponding *p* type layer. This is evidence that the *p* layer was due to boron surface diffusion, and not evaporation.

The depth of penetration was measured as a function of the distance from the original boron coating. This should give some measure of the time required to move along the surface, because the boron cannot begin its penetration into the bulk until it has diffused along the surface to the point in question.

The curve of Fig. 10 gives this bulk penetration as a function of distance along the sample. The location of the original boron coating is indicated by the dashed line. As expected, the penetration falls off rather rapidly in the region of this line and reaches nearly a constant value farther out. While it is rather difficult to estimate surface diffusion velocities from this type of data, it appears that surface diffusion proceeds, at 800°C, at a rate of about 100 times its average penetration into the bulk in this experiment, namely 1 or 2 mil/hr.

Similar studies can be made for grain boundaries. Even less has been done on this aspect of the work, however, than on surface diffusion. Again the best technique would probably involve measurement of bulk diffusion penetrations as a function of the distance along the grain boundary, measured from that point at which the impurity had been applied. From the preliminary work done in this field, however, it appeared that grain boundary diffusion was not sufficiently more rapid than bulk diffusion to make it possible to get good data easily.

OTHER WORK ON THE *p-n* JUNCTION METHOD FOR MEASURING DIFFUSION

In addition to the papers of the author (and D. E. Brown) on the measurement of diffusion by the *p-n* junction method, papers by Fuller and others on similar applications of the method have appeared. Fuller[9] measured diffusion of antimony, arsenic, indium, and zinc in germanium by the junction method, and obtained results in agreement with those of the author. Even more interesting, however, has been the application of the method to the very rapid diffusion of copper and lithium, both studied by Fuller *et al.*[10]

At this point we might mention the somewhat different though related methods of measuring diffusion coefficient described by Fuller. He assumed the step function solution, which we have seen is not completely valid for very small amounts of added impurity, but which should give satisfactory approximations.

In Fuller's technique, the diffusion coefficient is measured by study of two samples of germanium, both exposed to the same amount of impurity, as for example by exposing them together in a closed tube to the vapor of arsenic.

The two samples can be described by impurity concentrations C_1 and C_2, determined from conductivity or Hall measurement. The depth of the *p-n* junction is determined in the two cases to be x_1 and x_2. Application Eq. (8) leads then, according to Fuller, to the relation:

$$\frac{C_1}{C_2}=\frac{1-\mathrm{erf}[x_1/2(Dt)^{\frac{1}{2}}]}{1-\mathrm{erf}[x_2/2(Dt)^{\frac{1}{2}}]}. \tag{14}$$

If one then replaces the error function by its approximate value from Eq. (9), one finds for the diffusion coefficient the relation

$$4Dt=\frac{x_2^2-x_1^2}{\ln(C_1x_1/C_2x_2)}. \tag{15}$$

Thus, the diffusion coefficient is determined by the difference in the squares of the penetrations of the *p-n* junction for two different resistivities. It removes C_0 (or Q) as a variable in the measurement, but requires the measurement of two junction depths. Since the error in each "squared depth" is double the error in the depth measurement itself, additional care must be taken regarding accuracy of measurement.

An additional assumption involved in Fuller's approach is that C_0 remain constant during the diffusion. This is a rather doubtful assumption, since we have seen that the impurity either evaporates from the sample, and reacts with the walls, or it alloys with the germanium until there is no longer a second phase at the surface. Furthermore, if enough diffusing impurity is added until there is always a supply of impurity at the surface, then the penetration by the liquid alloy will, in general, be considerable, and will lead to erroneous ideas of the diffusion penetration.

The method of Fuller is somewhat similar to that in which the $\sqrt{t}$ law is assumed to be correct, the sample is diffused for two successive periods, and again the determination of two junction depths permits of the measurement of the diffusion coefficient without knowledge of the C_0, or Q value.

Results by the method of Fuller are best obtained by use of two samples having the greatest possible range of resistivity. As in all applications of the *p-n* junction method, accuracy is improved if the diffusion depth is as large as possible.

SUMMARY AND CONCLUSIONS

In the long history of the study of diffusion in solids, many physical properties have been used for indication of the extent of diffusion. The radioactive tracer, among the most modern of these, has also proved one of the most universally effective. In the field of semiconductors, however, it is possible to use the extreme sensitivity of the material to impurities, both in type and quantity, to establish a new and sensitive method for studying diffusion. Comparison of this *p-n* junction method with other methods, including the tracer method, shows that it has a distinct set of advantages, coupled with some disadvantages.

Among the advantages over the radioactive tracer method, the junction method can be used for some elements, like gallium, aluminum, and boron, which are either unobtainable in radioactive form, or are of such half-life that measurements are somewhat inconvenient.

Secondly, measurements with the *p-n* junction method are quite rapid. A measurement of diffusion coefficient requires only one measurement on the sample, namely the depth of the *p-n* junction. On the other hand, the tracer method requires a large number of time consuming operations and measurement before a corresponding value of similar precision is obtained.

A disadvantage of the junction method is the fact that is works only for electrically active elements. For inactive elements, it cannot be used at all. And of course, it is used only for semiconductors.

[9] C. S. Fuller, Phys. Rev. **86**, 136 (1952).
[10] C. S. Fuller and J. D. Struthers, Phys. Rev. **87**, 526 (1952); C. S. Fuller, Phys. Rev. **91**, 193 (1953).

Search for *F*-Center Luminescence

CLIFFORD C. KLICK
Solid State Division, Naval Research Laboratory, Washington, D. C.
(Received February 26, 1954)

Measurements have been made on the quantum efficiency of luminescence from *F* centers in x-rayed LiF and additively colored KCl at 4°K. In the wavelength range from 3000A to 20 000A an upper limit of 3 percent efficiency is found for the LiF *F*-band emission, if it exists. At 25 000A the upper limit is 10 percent. Similar results are found for *F* centers in KCl in the wavelength range from 6500A to 25 000A. These results are in disagreement with theoretical predictions that the *F* center should luminesce with high efficiency in the wavelength region near 10 000A.

INTRODUCTION

THE *F* center in the alkali halides is probably the most widely investigated and best understood imperfection in insulators.[1] It is generally agreed that the *F* center consists of an electron trapped at a negative ion vacancy. Using this model of the *F* center, Gurney and Mott[2] have suggested that absorption in the *F* band raises an electron from the ground state to an excited state and that at high temperatures thermal energy raises the electron from the excited state to the conduction band. This view is supported by several investigations. First, measurements by Glaser and Lehfeldt[3] on the variation of photoconductivity of the *F* center with temperature show a reasonably constant value in the room temperature range followed by a large decrease at low temperatures. Second, Kleinschrod[4] discovered a small absorption band on the high-energy side of the *F*-band absorption. This band may be interpreted as due to a direct transition from the ground state of the *F* center to the conduction band. Finally, Dexter[5] has computed the absorption strength of the *F*-center band and the short wavelength band on the basis of the model of Gurney and Mott and finds agreement with the experimental results of Kleinschrod.

At sufficiently low temperatures then, light absorption in the *F* band raises the electron to an excited state but there is insufficient thermal energy to free the electron. A problem of interest, and the one with which this investigation is concerned, is to determine how the excited *F* center returns to its ground state. If luminescence occurs, as has generally been anticipated,[6] the measurement of the luminescent emission spectrum should yield important information about the relaxation of the lattice around the excited *F* center and allow a determination of configuration coordinate curves for the center from experimental data alone.[7] If, however, there is a radiationless transition of the excited *F* center to its ground state, it will be important to attempt to identify the mechanism for this transition.

Luminescence in alkali halides has been observed in supposedly pure materials under a variety of conditions, such as bombardment by high-energy radiation or heating from low temperatures after x-raying. In most cases, however, the possibility cannot be excluded that the luminescence may arise from impurities since minute concentrations of a large number of metal ions act as luminescent centers in alkali halides,[8] and the reported emission in these cases is frequently of low intensity. In order to avoid the difficulties associated with excitation methods which produce free electrons and holes, the author has previously looked for emission from *F* centers in LiF and NaCl upon irradiating into their absorption bands at 4°K.[9] No emission was found, but the results were limited in the range of wavelengths covered. In addition, no quantitative estimate was made as to the minimum detectable signal in terms of quantum efficiency. Ghormley and Levy[10] have found an emission at 10 000A from colored KCl at 77°K upon exciting with light in the region of the *F*-band absorption. These investigators state, however, that it is not possible to determine from their experiments whether the emission is true *F*-center fluorescence or results from interactions with other centers such as *M* centers. This uncertainty arises from the fact that *M* centers in LiF and NaF are known to luminesce,[11] and that, in the case of LiF at room temperature, irradiation in the *F* band produces a feeble *M*-center luminescence.[9] At 77°K there may be some photoconductivity from *F* centers in KCl, thus permitting the formation or excitation of *M* centers. Also, the range of exciting light used by Ghormley and Levy is sufficiently large so that there may be a small overlap of this light with the *M*-absorption band, thus

[1] For reviews of the properties of *F* centers see F. Seitz, Revs. Modern Phys. **18**, 384 (1946), and N. F. Mott and R. W. Gurney, *Electronic Processes in Ionic Crystals* (Oxford University Press, London, 1940), Chap. IV.
[2] R. W. Gurney and N. F. Mott, Proc. Phys. Soc. (London) **A49**, 32 (1937).
[3] G. Glaser and W. Lehfeldt, Nachr. Akad. Wiss. Göttingen Math. physik. Kl. **2**, 91 (1936).
[4] F. G. Kleinschrod, Ann. Physik **27**, 97 (1936).
[5] D. L. Dexter, Phys. Rev. **83**, 435 (1951).
[6] N. F. Mott and R. W. Gurney, *Electronic Processes in Ionic Crystals* (Oxford University Press, London, 1940), pp. 136, 222.
[7] C. C. Klick, Phys. Rev. **85**, 154 (1952).
[8] It has been found in this laboratory, for instance, that the addition of 40 parts per billion of copper to NaCl causes measurable luminescence.
[9] C. C. Klick, Phys. Rev. **79**, 894 (1950).
[10] J. A. Ghormley and H. A. Levy, J. Phys. Chem. **56**, 548 (1952).
[11] J. P. Molnar, thesis, Physics Department, Massachusetts Institute of Technology (1948) (unpublished).

exciting the M center directly. These investigators do not estimate the quantum efficiency of the luminescence they measure; and, since their experimental measuring technique will detect as little as ten photons per second, they may be measuring a weak or secondary emission.

Theoretical investigations concerning the F center have largely been concerned with the determination of wave functions for the F center and the computation of the F-center absorption band. Recent work by Huang and Rhys[12] considers, in addition, the relative probabilities of radiationless to radiative transitions from the excited to the ground state of the F center. For KBr at a temperature of 28°K they compute this ratio to be 4×10^{-19}. Similar results should be expected for other alkali halides at low temperatures. These figures support the general opinion that the quantum efficiency of luminescence from F centers at low temperatures should be essentially one hundred percent.

There are several ways in which estimates may be made concerning the position of the emission band from F centers. Experience with luminescent centers such as Ag^+, Tl^+, Cu^+, Pb^{++}, and M centers in alkali halides indicates that the ratio of emitted wavelength to absorbed wavelength is less than two.

Pekar[13] has derived relationships between the absorption peak wavelength, the emission peak wavelength, and the half-widths of the peaks for simple centers which may be used to predict the wavelength at which emission from the F center should occur. Using these relations and previous results from a theoretical investigation of F centers,[14] Pekar predicts that luminescence from F centers in NaCl, KCl, KBr, and KI all lie between 9000A and 10 000A. The relations derived by Pekar may have somewhat limited accuracy, however. They predict, for instance, that the half-widths, in energy units, of the absorption and the emission bands are identical, but for KCl:Tl at room temperature the ratio of emission to absorption band width is approximately two.

Using both experimental and theoretical results, it is possible to compute the configuration coordinate curves for F centers in KBr, and from these curves determine the emission spectrum. The method used has been described.[7,15] In the case of KBr the data employed are the peak wavelength of absorption, the absorption half-width at low temperatures, the variation of this half-width with temperature,[16] and the number of vibrational quanta given off in absorption as determined theoretically by Huang and Rhys.[12] The effective mass of the system is taken to be that of the six potassium ions surrounding the center. The results of this computation are illustrated in Fig. 1, and from these results the F-center emission would be expected at 12 000A.

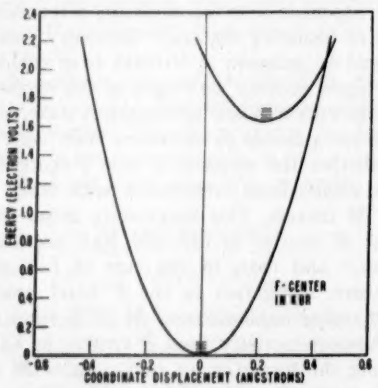

FIG. 1. Configuration coordinate curves for the ground and excited states of the F center in KBr, computed as described in the text. The coordinate is the separation between the F center and a nearest neighbor potassium ion. The horizontal lines indicate the vibrational energy levels of the system as computed. Using cgs units, the energy of the ground state is given by $U_g=1.76\times10^8X^2$, where X is the coordinate displacement; the excited state is given by $U_e=2.61\times10^{-12}+1.5\times10^8(X-0.214\times10^{-8})^2$.

EXPERIMENTAL PROCEDURE

For this work LiF and KCl were chosen as the alkali halides to be investigated. LiF has its F band at 2500A, thus allowing an experimental search over an eight to one range of wavelengths from 3000A to 25 000A. However, LiF can be colored conveniently only by x-rays which also produce the full gamut of other color centers. Since the interaction of the F band with other centers was considered unlikely for low F-center concentrations but not impossible, it was felt advisable also to investigate an alkali halide colored by heating in the alkali metal vapor which produces only the F band.

Of the alkali halides which can be conveniently colored by this means, KCl has the shortest wavelength F band and could be investigated over a four to one range of wavelengths. KCl has the added advantage that Pekar has included it as one of the alkali halides for which he predicts F-center luminescence in the wavelength region from 9000A to 10 000A.

Single crystals of LiF, grown commercially, were used. Considerable variation in the luminescent background of untreated crystals was found in various samples from the same producer. Therefore, samples with low background under 2537A excitation were chosen and were colored by exposure to heavily filtered x-rays from a 50-kvp machine. The coloration appeared uniform to the eye. By using Smakula's[17] equation relating the optical absorption to the number of centers

[12] K. Huang and A. Rhys, Proc. Roy. Soc. (London) **A204**, 406 (1950).
[13] S. I. Pekar, J. Exptl. Theoret. Phys. (U.S.S.R.) **22**, 641 (1952).
[14] S. I. Pekar, J. Exptl. Theoret. Phys. (U.S.S.R.) **20**, 510 (1950).
[15] C. C. Vlam has called to our attention an error in the constant of Eq. (4) of reference 7 which is too high by $\sqrt{2}$. Similar corrections should be made in Eqs. (10) and (11) of C. C. Klick and J. H. Schulman, J. Opt. Soc. Am. **42**, 910 (1952).
[16] R. Hilsch and R. W. Pohl, Z. Physik **64**, 606 (1930).
[17] See, for instance, F. Seitz, *Modern Theory of Solids* (McGraw-Hill Book Company, Inc., New York, 1940), p. 662.

and assuming an oscillator strength of unity, the density of F centers could be computed. For the samples used in investigating luminescence in the range from 3000A to 6000A, the density was 3.5×10^{17} cm^{-3}; other samples, investigated in the range from 4500A to 26 000A, had a density of 6.6×10^{16} cm^{-3}. These densities correspond, respectively, to concentration of 6 and 1 parts per million of negative ion sites. In each case reported in this investigation the sample thicknesses were such that more than 90 percent of the exciting light was absorbed.

F centers were formed in commercial crystals of KCl by heating in potassium vapor at 450°C. After this treatment the crystals were heated briefly to 600°C and quenched to remove colloid bands. The density of color centers was computed to be 9×10^{16} cm^{-3} using Smakula's equation and an oscillator strength of 0.81. This corresponds to a concentration of 6 parts per million of negative ion sites.

In all cases the alkali halides to be measured were submerged in liquid helium at 4.2K°. The Dewar used was an unsilvered glass double Dewar with the inner Dewar painted black except for a small window at the level of the crystal. The exciting light entered the Dewar vertically through a quartz plate, passed through the liquid helium, and fell on the crystal. When a photomultiplier was used as a detector in the 3000A to 6000A range, it observed the crystal through a second quartz plate placed at the top of the Dewar. When a lead sulfide photoconductive cell was used, the crystals were held at an angle of 45° from the vertical and were observed through the window by the detector placed exterior to the Dewars.

For the investigation of F centers in LiF, the exciting source was a low-pressure mercury arc with a Corning 9863 filter. This radiates almost all of its energy in the 2537A mercury line, which falls well within the F-center absorption band. In the investigation of KCl, an A-H6 high-pressure 1000-watt mercury arc was used as the exciting source. The light was filtered through a Baird filter 7-2970-3 and Corning filters 4303 and 3484 to pass only light near the F-band absorption peak.

A 1P28 photomultiplier tube with a Corning 7740 filter was used to look for luminescence in the range from 3000A to 6000A for LiF F centers. For the longer wavelength investigations, an Eastman Kodak lead sulfide cell with dimensions 1 cm by 2 cm was used. For the LiF investigation, no filter was used with the PbS cell other than the filtering action of the Pyrex glass Dewars; for KCl, a Corning 2412 filter was placed before the cell in order to pass only wavelengths greater than 6100A. When the PbS detector was used, the exciting light was chopped at a rate of 10 cycles per second and the detector output amplified by a 10-cycle amplifier. The relative response of both detectors was determined as a function of wavelength by the use of suitable monochromators, chopped light sources, a fast response thermocouple, and an alternating current amplifier.

A measurement of the quantum efficiency of luminescence for some material implies a determination of the number of quanta absorbed by the material and of the number emitted. This involves measurements of the intensity of the exciting light, the fraction of light reflected by the material, the intensity of the emitted light, its angular dependence, and the amount of self absorption of the emitted light by the material. Measurements have been made with fair accuracy on a number of phosphors[18] but it was concluded that the difficulties introduced by the use of complicated Dewars would greatly reduce the accuracy of the measurements. Instead, a substitution method was used in which a material either of known reflectivity or quantum efficiency was substituted for the material to be measured. For LiF in the range where a photomultiplier was used as a detector, the standard was magnesium carbonate for which the reflectivity at 2537A was taken as 72 percent.[19] For the wavelength range in which LiF was investigated with the PbS detector, the standard used was the luminescence of $CaWO_4$. Jones and Fonda[18] give a quantum efficiency at room temperature of 73 percent for this material and Kröger[20] has shown that its brightness increases about 20 percent as the temperature is reduced. It was assumed that this material had a quantum efficiency of 90 percent at 4°K. For the investigation of KCl the standard used was the reflectivity of MgO which was taken to be[19] 95 percent at the wavelength of the F-center peak. From the experimentally determined detector responses to these substituted standards, from their known reflectivities or quantum efficiencies and emission spectra, from the measured relative response of the detectors to equal numbers of incident quanta, and from the computed fraction of exciting light absorbed in the sample it was possible to compute at any wavelength what the detector response would be to a material luminescing at this wavelength with an efficiency of 100 percent. Several other corrections have been made to obtain the quantum efficiency data; the fraction of incident light reflected at the front surface of the alkali halide was computed and included in the calculations as was the effect on the angular distribution of luminescent light from a crystal due to refraction at the surface. However, these corrections are of somewhat minor importance in determining the unexpectedly low quantum efficiency.

RESULTS

In no case was efficient F-center luminescence found. The results are given in Fig. 2 for both the LiF and

[18] S. Jones and G. R. Fonda, Electrochemical Society, enlarged abstract, spring meeting, 1952 (unpublished).
[19] S. Schwartz and G. Lloyd, J. Opt. Soc. Am. 38, 964 (1948).
[20] F. A. Kröger, Nature 159, 674 (1947).

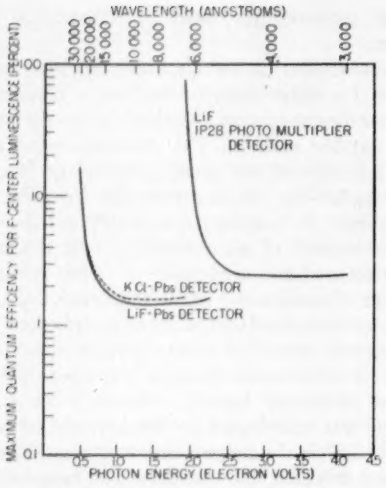

FIG. 2. Experimentally determined upper limit for the quantum efficiency of the F centers in LiF and KCl as a function of wavelength. Each point on the curve is computed assuming that the luminescence is concentrated at the wavelength corresponding to the point.

KCl investigations. These curves are obtained by converting the observed detector response, when the colored alkali halide is investigated, into a quantum efficiency at each of various wavelengths by assuming that the detector response is due to F-center luminescence concentrated at each wavelength. At wavelengths for which the detector sensitivity is poor, the small observed response corresponds to a higher possible quantum efficiency. The results may be summarized by saying that the efficiency of luminescence of F centers in LiF is less than 3 percent if the emission occurs in the wavelength range from 3000A to 20 000A. For KCl the F-center luminescence efficiency is less than 3 percent for the range from 6500A to 20 000A. For both materials the efficiency is less than 10 percent at 25 000A. For an emission which extends over a range of wavelengths, the maximum quantum efficiency is given by an appropriately weighted average over this range. If the whole emission spectrum of F centers in LiF were included in the range from 3000A to 20 000A, the maximum efficiency would be less than 3 percent.

Because of these low efficiencies no attempt was made to investigate the emission as a function of wavelength; the measurement itself would be difficult and the assignment of apparent emission bands to the F center would be open to question because of the possibility of complicating factors such as stray light. In the case of LiF with the photomultiplier detector, for instance, emission from the mercury arc in the 3000A to 4000A range was not filtered from the detector. This is known to be a few percent of the total emission but was tolerated here in order to extend the range of investigation as close as possible to the F-center absorption. Similarly with LiF and the PbS detector, some of the red and infrared lines of the mercury arc were not filtered out. Furthermore, there is evidence that excitation in the F center leads to weak luminescence in the M center. Finally there are the effects of small concentrations of impurities which frequently are troublesome in visible and ultraviolet emission investigations and which might also give rise to infrared emission.

Considering all of these difficulties which arise when such low light levels are investigated, it is possible that the efficiency of luminescence of the F center itself is really much less than that given in Fig. 2; these curves should be taken only as upper limits of the efficiency.

DISCUSSION

This investigation indicates that within the rather wide wavelength range investigated, the luminescence of the F center, if it exists at all, is one to two orders of magnitude less than expected. Two possible explanations may be examined.

First, the concentration of color centers may be so high that the luminescence is quenched. This phenomenon is well known in phosphors but begins to occur at concentrations above 100 parts per million even in materials with high dielectric constants such as the sulfides. In KCl:Tl the efficiency has decreased less than a factor of 2 because of concentration quenching even at concentrations of 7000 parts per million. Theory[21] also indicates that this effect should become important at concentrations of 1000 parts per million. Therefore the low F-center concentrations used here, less than 10 parts per million, avoid this difficulty.

Second, the luminescence may not appear because of the presence of "poisons." In nonphotoconducting phosphors the effect of poisons in concentrations as low as 10 parts per million may be detected. The mechanism for efficient poisoning is probably that of dipole-dipole transfer of energy discussed by Dexter[22] who concludes that concentrations of the order of 100 parts per million are required and that the poison should have an allowed absorptive transition in the wavelength range of the emission which it quenches. Therefore a poison should have a large oscillator strength and even in concentrations of only 10 parts per million should show an absorption band comparable with the F bands investigated here. No such bands were found nor does there appear to be any reference in the literature to such effects.

The conclusion then appears to be that current

[21] D. L. Dexter and J. H. Schulman (to be published).
[22] D. L. Dexter, J. Chem. Phys. 21, 836 (1953).

F-center theory, which predicts luminescence near 10 000A with 100 percent efficiency, is not correct. It is possible that a more detailed theoretical investigation of the configuration coordinate curves for the *F* center, both in its ground state and in its excited state, might lead to a better understanding of these results.

ACKNOWLEDGMENTS

It is a pleasure to acknowledge the assistance of Robert J. Ginther in preparation of the materials and of Clifford J. Grebenkemper in supplying the liquid helium; the author is especially indebted to Dr. David L. Dexter and Dr. James H. Schulman for numerous discussions of this work.

PHYSICAL REVIEW VOLUME 94, NUMBER 6 JUNE 15, 1954

Theory of Thermodielectric Effect

B. GROSS
Instituto Nacional de Tecnologia, Rio de Janeiro, Brazil
(Received July 13, 1953; revised manuscript received October 26, 1953)

A theory is put forth to explain the electrical effects which accompany phase changes occurring in dielectrics and aqueous solutions. Ionic movement in the interface is treated as a transition between energy levels separated by potential barriers. The height of the barriers and the value of the energy levels are supposed to be different for positive and negative ions. Such a model results in a net current flow across the solid-liquid interface. When the interface moves during a phase change of the system, the excess electric charges thus produced constitute space charges in the solid and surface charges in the liquid. The field of the global charge distribution causes the appearance of the currents and potential differences which have been observed between the plates of a condenser containing the dielectric.

INTRODUCTION

COSTA RIBEIRO, a Brazilian physicist, while studying electret behavior and related effects, discovered in 1944 that solidification and melting of many dielectrics are accompanied by charge separation.[1] He found that the phenomenon is observed only if the phase change proceeds in an orderly fashion, that is, if a definite phase boundary (or interface) exists between the solid and liquid phase. Displacement of the interface in one direction corresponds to solidification, and displacement in the opposite direction to melting. A system in which such a process occurs, has properties similar to those of a primary cell with very high internal resistance. Measurements were made of the short circuit current and the total charge separation. The first observations concerned dielectrics like carnauba wax, naphthalene (where the effect is particularly strong), and paraffin; however, occurrence in ice was also mentioned. Costa Ribeiro concluded that the effect was a general one: Production of currents and charge separation in dielectrics during phase changes. Later Workman and Reynolds[2] and Alfrey and Gill[3] found that orderly solidification of many aqueous solutions gives rise to the appearance of considerable open-circuit potentials (of the order of hundreds of volts) which become measurable when the freezing is observed inside a condenser in open circuit. These authors also give astonishingly high values for the total charge separation in aqueous solutions, and this was thought to be significant for the interpretation of atmospheric electricity. For this reason the effect, besides its theoretical interest, is likely to become of practical importance. Recently Krause and Renninger[4] found that individual crystals of pentaerythren become electrically charged during crystallization from a supersaturated solution. Numerous other papers have been published since 1944 on similar matters, partly in continuation of the previously mentioned ones,[5] partly independently.[6] It is also worth mentioning that as early as 1940 some observations along the same line were reported in meteorological papers.[7] It has already been asserted that the findings of Costa Ribeiro and Workman and Reynolds refer to the same effect[8] as does, in the author's opinion, the evidence contained in all previously mentioned papers. It is therefore justified to call

[1] J. Costa Ribeiro, thesis, Universidade do Brasil, 1945; Anais acad. brasil. cienc. **17**, No. 2, 2, 3 (1945); **22**, 321 (1950).
[2] E. J. Workman and S. E. Reynolds, Phys. Rev. **74**, 709 (1948); **78**, 254 (1950).
[3] E. W. B. Gill and S. A. Alfrey, Nature **169**, 203 (1952); E. W. B. Gill, Nature **169**, 1109 (1952); Brit. J. Appl. Phys. Supplement 2, 16 (1953).
[4] B. Krause and M. Renninger, Naturwiss. **40**, 52 (1953).
[5] J. Costa Ribeiro, Abstracts of Simposio sobre Novas Técnicas da Física, Rio de Janeiro, 1952 (unpublished), p. 23; L. Cintra do Prado, Anais acad. brasil. cienc. **18**, 145, 149 (1946); L. Cintra do Prado and P. Saraiva, Anais acad. brasil. cienc. **19**, 30 (1947); P. Saraiva, Anais acad. brasil. cienc. **18**, 161 (1946); A. Dias Travares, Anais acad. brasil. cienc. **25**, 53, 91 (1953).
[6] I. Clay and C. Kramer, Physica **13**, 508 (1947); A. Becker and I. Schaper, Z. Naturforsch. **4a**, 194 (1949); W. Rau, Z. Naturforsch. **6a**, 649 (1951); V. J. Schaefer, Phys. Rev. **77**, 721 (1950).
[7] W. Findeisen, Z. Meteorol. **57**, 6, 201 (1940); E. Lange, Z. Meteorol. **57**, 12, 429 (1940); A. Klumm, Arch. Meteorol., Geophys. u. Bioklimatol., Ser. **A3**, 382 (1951).
[8] J. D. Hoffman, Dig. of Lit. Dielectrics (Nat. Research Council) **14**, 13 (1950).

the whole complex of phenomena with which we are here concerned the "thermodielectric effect," as it was called by its discoverer.

It has been mentioned by Costa Ribeiro that electrical phenomena occurring in the interface must be primarily responsible for the effect. However, an interface mechanism alone would not explain the production of voltages and currents in the external circuit. An additional mechanism is necessary to provide the macroscopic electric fields that force the charge carriers through the dielectric and raise the potential difference between the plates. This was found by Gill and Alfrey[8] in the production of space-charge distributions in the nonconducting (or at least badly conducting) solid phase. According to these authors, charge separation occurs primarily at the interface. Part of the charge produced there is, however, imprisoned in the ice, thus constituting a "frozen-in" space charge.[9] The charge carriers responsible are most likely the ions which are known to exist in considerable number in solid and liquid dielectrics unless they are purified to an extreme degree. Existing evidence about the influence of impurities on the effect corroborates this idea. However, in consequence of the rather general nature of the assumptions made, the pattern of the theory would not change basically if the carriers were electrons.

So far, no theory has been advanced that would allow correlation of the macroscopically observable quantities —current and voltage in the external circuit—with the potentials that must exist across the interface. In the present paper we shall attempt to do this, and shall show that available evidence about the behavior of ions in the dielectric and the structure of the interface leads one to expect the appearance of electrical effects during phase changes. The treatment is still approximate, applying only to "good" dielectrics such as were examined by Costa Ribeiro, in which the conductivity of the solid phase can be disregarded. The theory does not consider in detail the process of fusion or solidification, but is exclusively a "conductance" theory.

The basic mechanism is explained as follows. A contact potential difference—whether for ions or electrons makes no material difference—exists between the solid and the liquid. This contact PD results in the formation of a double layer at the interface under static conditions. If the interface moves, as in solidification or melting, the double layer would have to move with it. However, owing to the low conductivity of the solid site, the solid component of the charge cannot dissipate fast enough to keep up with the interface; hence, as the interface advances, it leaves behind a trail of space charge in the solid which builds up a potential difference between the region deep in the solid and the liquid (electrolyte) which can be many orders of magnitude larger than the contact PD. Thus the interface behaves like a selectively permeable membrane, allowing one kind of charge carrier to pass through more easily than the other, and "pushing along" with it a surface charge consisting of the excess charge left in the liquid. The combined fields of space and surface charges result in a counter emf at the interface which gradually neutralizes the contact PD, so that the trail of space charge decreases as the interface advances, and a limiting interface field is reached. The fraction of the double-layer charge which is actually left behind as space charge depends upon the velocity of advance of the interface and the rate at which charge is dissipated across the interface by back-diffusion. Mathematical formulation of these assumptions would lead directly to an expression for the conduction current across the interface corresponding to Eq. (15) and could be made the starting point for the theory.

In the present paper, however, a molecular model is introduced and the concept of a contact PD interpreted in terms of potential barriers and transition probabilities; rate theory is applied for obtaining the expression of the current through the interface. In this model the contact PD is shown to contain a term proportional to the speed of the phase change. This explains the experimentally found proportionality between equilibrium external current and speed of solidification or melting. But it must be emphasized that the simple analysis in terms of a contact PD, as outlined above, does not depend on such an explicit model; the mathematical restrictions introduced in the discussion for the sake of getting simple expressions are more severe than necessary for carrying out the calculations.

I. MODEL OF INTERFACE

A condenser with plane plates contains a dielectric that is partly in the solid, partly in the liquid state. The phase boundary is assumed to run parallel to the surfaces of the electrodes. The conductance of the solid is supposed to be negligible, that of the liquid finite. The dielectric contains positive and negative ions, the relative concentration of which in the neutral state is the same. Thus no net charge exists under normal conditions. In the solid phase, as a consequence of the previously made assumptions of zero conductance, the ions are unable to move. In the liquid they can move more or less freely, having mobilities that depend on temperature and viscosity of the liquid. Thus conduction in the liquid can be described by the introduction of a specific conductance σ. In the interface the conductance changes from σ to 0. It is just this zone that is of decisive importance.

Fröhlich[10] has applied rate theory to the problem of the movement of ions in solid dielectrics. He considers the existence of potential barriers which oppose the movement of ions within the dielectric. The probability of transition is given by a Boltzmann factor. Applying

[9] See B. Gross and L. F. Denard, Phys. Rev. **67**, 253 (1945).

[10] H. Fröhlich, *Theory of Dielectrics* (Clarendon Press, Oxford, 1949).

this picture to the present case, we see that the potential barriers in the solid will have to be high to give sufficiently low conductance. In the liquid the barriers are practically absent. Then the phase boundary is characterized as a zone of finite extension where the height of the barriers decreases from its very high value inside the solid to its very low value inside the liquid. Within the interface the movement of the ions may be described in the way shown by Fröhlich.

The detailed picture of the interface is of no importance. It is sufficient to represent it schematically by a single potential barrier of finite height and the introduction of two potential minima on either side of the interface, one in the solid and the other in the liquid. The difference in the behavior of positive and negative ions in conducting dielectrics obliges one to assume that the height of the barrier and the energy difference between the minima are different for positive and negative ions. Thus one obtains Fig. 1 which gives the model of the interface used here. The height of the barrier at level I is U_1^+ for positive and U_1^- for negative ions, and at level II it is, respectively, U_2^+ and U_2^-. The differences U_1-U_2 give the work functions. The levels running parallel to the phase boundary have an area A and are separated by a distance $2d_0$. The surface densities of the ions in the levels are, respectively, N_1^+/A, N_1^-/A and N_2^+/A, N_2^-/A. Probabilities of transitions from I to II and from II to I are, respectively, w_{12}^+, w_{12}^- and w_{21}^+, w_{21}^-. The temperatures are T_1 and T_2.

The assumption of zero conductance in the solid makes it unnecessary to consider any transfer of ions to level I from the side of the solid. Thus the number of ions in I changes only by transport through the interface. It decreases by jumps from I to II and increases by jumps from II to I. Applying the equations of rate theory, one obtains

$$dN_1^+/dt=-w_{12}^+N_1^++w_{21}^+N_2^+, \tag{1a}$$

$$dN_1^-/dt=-w_{12}^-N_1^-+w_{21}^-N_2^-. \tag{1b}$$

If e is the charge of the ions, then the conduction current across the interface is given by

$$i=e\frac{d}{dt}(N_1^+-N_1^-). \tag{2}$$

The transition probabilities are given by

$$w=w_0\exp(-U/kT), \tag{3}$$

where U is the height of the potential barrier. In general, one has to consider the existence of an electrical field E^* set up by the surface and space charges that build up in the system in consequence of the transport of ions through the interface. The presence of the field E^* changes the height of a potential barrier from its value $U(0)$ without field to $U(0)\pm ed_0E^*$, the sign depending on the polarities of the ions and the direction of the jumps. Therefore,

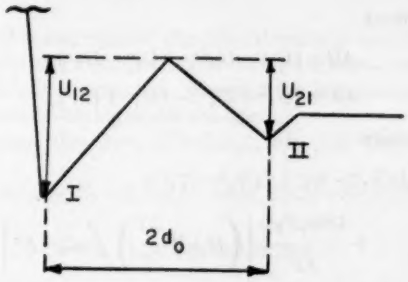

FIG. 1. Model of interface.

$$U=U(0)\pm ed_0E^*. \tag{4}$$

Finally, we expand Eq. (3) into a series and consider the first two terms only. This means linearization of the theory and therefore represents a considerable simplification for all following developments. We believe that within the framework of the present still semi-empirical theory this procedure is justified. (It could be made more rigorous by introducing the differences between the values U^+ and U^- and expanding only the part containing them, but the final result would not differ significantly from the following.) Substituting (4) into (3) and designating the energy values without field by U_1^+, U_1^-, U_2^+, U_2^- gives, finally

$$w_{12}^+=w_0[1-(U_1^+-ed_0E^*)/kT_1], \tag{5a}$$

$$w_{12}^-=w_0[1-(U_1^-+ed_0E^*)/kT_1], \tag{5b}$$

$$w_{21}^+=w_0[1-(U_2^++ed_0E^*)/kT_2], \tag{5c}$$

$$w_{21}^-=w_0[1-(U_2^--ed_0E^*)/kT_2]. \tag{5d}$$

Substituting (5) and (1) into (2) gives for the conduction current across the interface, the expression

$$\begin{aligned} i=ew_0[&\{(N_2^+-N_2^-)-(N_1^+-N_1^-)\}\\ &+\{(N_1^+U_1^+-N_1^-U_1^-)/kT_1\\ &-(N_2^+U_2^+-N_2^-U_2^-)/kT_2\}\\ &-ed_0E^*\{(N_1^++N_1^-)/kT_1+(N_2^++N_2^-)/kT_2\}]. \end{aligned} \tag{6}$$

We now make the following two assumptions:

(a) The temperature gradient across the interface is very low, so that one can introduce the mean temperature

$$T=(T_1+T_2)/2,\quad T_1=T-\Delta T,\quad T_2=T+\Delta T; \tag{7a}$$

(b) The difference in the number of positive and negative ions in each level is small compared with the total number of ions of each species. This is equivalent to saying that one has a rather small effect in a medium where under normal conditions the concentration of ions is relatively large. Under these conditions the values of N_1 and N_2 can be replaced by a mean value N_0 except in the first term of Eq. (6) which otherwise would cancel out. Introducing, furthermore, the

coefficients

$$4H=(U_1^+-U_2^+)-(U_1^--U_2^-), \tag{8a}$$

$$4W=(U_1^++U_2^+)-(U_1^-+U_2^-), \tag{8b}$$

one obtains

$$i=ew_0\{(N_2^+-N_2^-)-(N_1^+-N_1^-)\}+\frac{4e^2w_0N_0d_0}{kT}\left\{\left(H+W\frac{\Delta T}{T}\right)\Big/ed_0-E^*\right\}. \tag{9}$$

II. THE CONDUCTION CURRENT ACROSS THE INTERFACE

a. The Electromotive Force

The primary cause of the current flow through the interface is the spontaneous jumping of the ions over the potential barrier. This mechanism is described by the term containing H and W. It represents an electrochemical force. In Maxwell's theory one takes such forces into account by the introduction of an intrinsic electric field E_0. Applying this concept to the present case, one has

$$E_0=(H+W\Delta T/T)/ed_0. \tag{10}$$

The constant factor multiplying E_0 is an equivalent conductance of the interface. Thus,

$$\sigma_0=4e^2d_0w_0N_0/AkT. \tag{11}$$

The expression for the intrinsic field can be correlated with the speed of the phase change. Considering solidification, the experiment is conducted in such a way that one electrode is cooled while the other is kept at constant temperature. The heat exchange with the surroundings will be disregarded. Then heat is removed from the liquid across the interface only. The quantity of heat removed from the liquid per unit time is $-A\lambda\Delta T/2d_0$, where λ is the coefficient of thermal conduction of the liquid and $\Delta T/2d_0$ is the temperature gradient. In consequence of the cooling, the mass of the liquid decreases per unit time by the amount $-cdm/dt$, where c is the latent heat. Equalizing both quantities allows one to express the temperature gradient in terms of the amount of solidified material, giving

$$\Delta T=(2d_0c/A\lambda)dm/dt \tag{12}$$

and, therefore,

$$E_0=[H+W(2d_0c/A\lambda T)dm/dt]/ed_0. \tag{13}$$

The speed of the phase change v is proportional to dm/dt. Therefore, E_0 consists of two components; one is constant and exists already under equilibrium conditions, the other appears only during phase changes and is directly proportional to the speed of the phase change. One can, therefore, write $E_0=c_1+c_2v$.

The current J, that in a shorted condition flows in the external circuit, will be proportional to E_0. Costa Ribeiro[5] has measured J for various (constant) velocities of melting and solidification. He found that J reaches an equilibrium value some time after the phase change has attained constant speed and that this equilibrium value is very nearly proportional to dm/dt. This suggests that the coefficient c_1 must be much smaller than c_2. Therefore a constant PD, independent of the temperature gradient, would not suffice to explain this result. The bulk of the intrinsic electromotive force must be due to the appearance of a temperature gradient across the interface. The introduction of the corresponding term in Eq. (10) was therefore relevant.

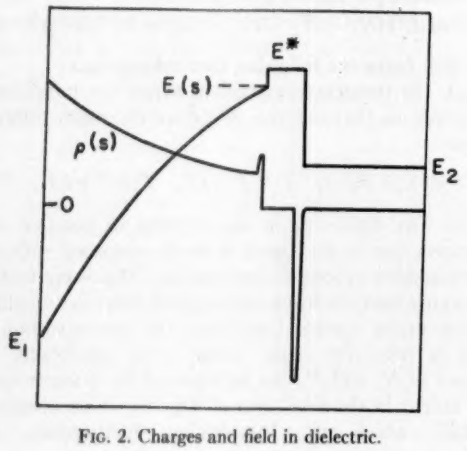

FIG. 2. Charges and field in dielectric.

b. The Surface Charge

The term $e(N_2^+-N_2^-)/A$ is the density of the surface charge on level II and $e(N_1^+-N_1^-)/A$ the same for level I. Existence of a surface charge means discontinuity of the displacement field. Let $E(s)$ be the field in the solid adjacent to the interface, E_2 the field in the liquid, and E^* the field in the interface (Fig. 2). Then

$$e(N_2^+-N_2^-)=A\epsilon(E_2-E^*),$$

$$e(N_1^+-N_1^-)=A\epsilon[E^*-E(s)],$$

and

$$e[(N_2^+-N_2^-)-(N_1^+-N_1^-)]=A\epsilon[E_2-2E^*+E(s)], \tag{14}$$

where ϵ is the dielectric constant of the system which for the sake of simplicity is taken to be the same for solid and liquid.

c. The Current

Substituting (10), (11), and (14) into (9) gives

$$i=A\sigma_0(E_0-E^*)-Aw_0\epsilon[2E^*-E_2-E(s)]. \tag{15}$$

This equation has a direct physical significance. Consider again the distribution of fields and charges as shown in Fig. 2, the thickness of the solid deposit being s, electrode I being in contact with the solid, and electrode II being in contact with the liquid. The electric fields at the surfaces of the electrodes are,

respectively, E_1 and E_2. According to previous assumptions, no space charge forms in the liquid; therefore, inside the liquid the field is constant and given everywhere by E_2. In the solid, space charge will exist. Therefore here the field is not in general constant, but varies from its boundary value E_1 at electrode I to the value $E(s)$ at a point close to the interface. Both sides of the interface carry surface charges of opposite sign. Therefore discontinuities of the field do appear. Inside the boundary layer, the field consists of the intrinsic field E_0 and the surface and space charge field E^*, the total field being E_0-E^*.

The mechanism of the interface current can now be described in the following way. Originally there exists an intrinsic field E_0. Starting from a neutral condition, this gives rise to an ionic current $\sigma_0 E_0$. In consequence, surface charges are set up at both sides of the interface and, eventually, space charges in the solid. The combined field of these charges is superposed on the intrinsic field and reduces the acting field in the interface from E_0 to E_0-E^*. The current produced falls off from its initial value $\sigma_0 E_0$ to $\sigma_0(E_0-E^*)$. Introducing the electromotive force $V_0=2d_0E_0$, the process can be thought of as a polarization phenomenon, with polarization voltage $V_p=2d_0E^*$. However, the accumulation of surface charge at both sides of the interface has still another consequence. This is the appearance of a back-current directly proportional to the differences in concentration of ions in the solid and the liquid, as given by the second term in Eq. (15). Like a diffusion current, it tends to equalize the ionic concentrations across the interface. Of course all terms are already implicitly contained in the fundamental equations. The electromotive force is associated with the existence of finite potential barriers and the thermal movement of the ions, the polarization with changes in the height of the potential barriers by the field, and the diffusion current with the proportionality between the number of jumps and concentration of ions in each potential minimum. The linearity of the expression follows from the series expansion of the Boltzmann factor. The fields E_1 and E_2 are functions of time, and the field $E(s)$ is a function of time and distance. Therefore, i is a function of t and s and has to be written $i(t,s)$.

Equation (15) contains both the field E^* inside the boundary layer and the field $E(s,t)$ in the solid adjacent to the interface. In the present case one can, however, neglect the difference between both fields. During solidification a continuous flow of current i goes through the interface. After the interface has advanced a certain distance, say a, an excess charge q_a is found in the solid and an excess charge of the same amount, but contrary polarity, is found in the liquid. However, while in the solid the charge is distributed over the distance a in the form of a space charge, in the liquid it constitutes a surface charge adhering to the interface. It becomes therefore understandable, that the value of the surface charge at the solid site can be disregarded. With this assumption, the discontinuity of the field at the solid site disappears and $E(s,t)$ becomes identical with E^*. Of course, this consideration is valid only for processes involving phase changes.

Putting, therefore, $E^*=E(s,t)$, Eq. (15) transforms into

$$i=A\sigma_0[E_0-E(s,t)]-Aw_0\epsilon[E(s,t)-E_2(t)]. \quad (16)$$

d. The Space Charge

The total amount of charge carried across the interface in time dt is $dq=idt$. With the interface in a fixed position, the result of the charge transfer would be only the formation of an electric double layer. Here, however, we are interested in phase transitions where the interface advances with velocity $v=ds/dt$. To cover the distance ds, the interface needs the time $dt=ds/v$. The charge transferred through the interface while the latter has advanced by ds, is, therefore,

$$dq=ids/v. \quad (17)$$

This charge, however, does not any longer constitute a surface charge, but is distributed over ds and constitutes a space charge. The assumption of zero conduction for the solid makes consideration of charge decay unnecessary. The density of space charge is

$$\rho=\frac{1}{A}\frac{dq}{ds}, \quad (18a)$$

or

$$\rho=i/Av, \quad (18b)$$

with i given by (16). Poisson's equation for the field in the solid at a point close to the interface then is

$$\epsilon\partial E(s,t)/\partial s=i(s,t)/Av(t). \quad (19)$$

III. THE SPACE-CHARGE FIELD

The value of the current in (19) must now be replaced by its explicit expression (16). We assume that the phase change proceeds with constant speed $v=$constant. Then, making the substitutions, one gets finally

$$\frac{\partial E(s,t)}{\partial s}+\frac{E(s,t)}{s_0}=\frac{E_0+kE_2(t)}{s_0(1+k)}, \quad (20)$$

with

$$1/s_0=(1+k)\sigma_0/\epsilon v, \quad (21a)$$

and

$$k=\epsilon w_0/\sigma_0. \quad (21b)$$

This equation must be integrated with the initial condition

$$s=0: \quad E(0,t)=E_1(t). \quad (22)$$

The solution is given by

$$E(s,t)=\frac{E_0+kE_2(t)}{1+k}-\left\{\frac{E_0+kE_2(t)}{1+k}-E_1(t)\right\}e^{-s/s_0}. \quad (23)$$

Integrating once more between 0 and x, one obtains the space-charge potential $V(x,t)$ at time t and the point x, where the interface is found at that time; that is,

$$x=vt. \tag{24}$$

This gives

$$V(x,t)=x\frac{E_0+kE_2(t)}{1+k}$$
$$-s_0\left(\frac{E_0+kE_2(t)}{1+k}-E_1(t)\right)(1-e^{-x/s_0}), \tag{25}$$

or, substituting x from (24),

$$V(t,t)=vt\frac{E_0+kE_2(t)}{1+k}$$
$$-vt_0\left(\frac{E_0+kE_2(t)}{1+k}-E_1(t)\right)(1-e^{-t/t_0}), \tag{26}$$

where

$$t_0=\epsilon/\sigma_0(1+k). \tag{27}$$

IV. THE DIFFERENTIAL EQUATIONS FOR CURRENT AND VOLTAGE

We are now in a position to establish the equations for the observable quantities, i.e., currents and voltages in the external circuit, under different conditions of the experiment. Let $U(t)$ be the total potential difference between the plates, D the distance between the plates, and $J(t)$ the external current.

The total current must be the same in the solid and the liquid. In the latter it contains a conduction and a displacement component, in the former it is purely displacement current. Writing the equations for the surfaces of both electrodes gives

$$J(t)=A\epsilon dE_1(t)/dt, \tag{28a}$$
$$J(t)=A\epsilon dE_2(t)/dt+A\sigma E_2(t), \tag{28b}$$

and, therefore,

$$\epsilon dE_1(t)/dt=\epsilon dE_2(t)/dt+\sigma E_2(t). \tag{29}$$

This is the differential equation connecting the field values at the two electrodes.

The total voltage drop across the plates is constituted by the space charge potential in the solid, the potential drop across the interface, and the voltage loss in the liquid. Disregarding the voltage drop across the interface, this gives

$$U(t)=V(t,t)+(D-x)E_2(t). \tag{30}$$

Equations (26), (29), and (30) together constitute a system that permits determination of E_1, E_2, and J. Different experiments are characterized by different boundary conditions. For the measurement of the short circuit current one has $U(t)=0$; for the measurement of the open circuit voltage one has $J(t)=0$.

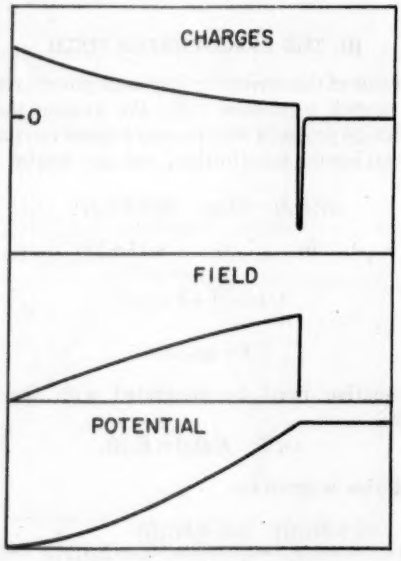

FIG. 3. Open-circuit behavior.

V. OPEN-CIRCUIT VOLTAGE

We shall give here only the calculation of the open-circuit voltage as it would be measured by an electrometer of negligible capacitance. From the condition

$$J(t)=0 \tag{31}$$

it follows that both $E_1(t)$ and $E_2(t)$ are equal to 0. The absence of a voltage drop in the liquid makes the measured potential difference equal to the space charge potential. From (26) one gets

$$U(t)=\frac{vE_0}{1+k}\{t-t_0(1-e^{-t/t_0})\}. \tag{32}$$

Expanding for small and large values of t/t_0 gives

$$t/t_0\ll 1: \quad U(t)=\frac{vt_0E_0}{2(1+k)}(t/t_0)^2, \tag{33a}$$

$$t/t_0\gg 1: \quad U(t)=vE_0t/(1+k). \tag{33b}$$

The voltage increases at first quadratically, later linearly. The maximum voltage reached when the entire system has solidified is approximately equal to $DE_0/(1+k)$. The ratio of the maximum open-circuit voltage to the interfacial potential is therefore $D/2d_0(1+k)$. This shows that the external voltage can exceed the electromotive force by a great amount, provided k is not exceedingly high. The space charge mechanism then represents a voltage amplification system. Supposing for dimensional reasons that k is of

the order of 1, and taking the thickness of the interface as equal to 10^{-6} cm, gives for a 1-cm cell a total voltage of about 50 v, as corresponding to an electromotive force E_0 equal to $\frac{1}{10}$ of a millivolt. A comparison with the measurements of Workman and Reynolds is unfortunately not possible because in their case the assumption of zero conduction for the solid does not hold. However, it is gratifying to see that a mechanism of the type considered here can cause the appearance of the potential differences, and generally of the effects of the kind found by the observers.

In the present case (open circuit) the total amount of surface charge in the liquid adhering to the interface is equal to the total amount of space charge, the entire system remaining neutral. The space charge distribution in the solid is exponential (see Fig. 3). According to (23), the field is given by

$$E(s)=E_0(1-e^{-s/s_0})/(1+k), \quad s\leq x \tag{34}$$

and

$$\rho(s)=\epsilon E_0 e^{-s/s_0}/s_0(1+k), \quad s\leq x. \tag{35}$$

The voltage is at any time proportional to vE_0. Since we found $E_0=c_1+c_2v$, one has

$$U(t)=(c_1v+c_2v^2)f(t). \tag{36}$$

Thus voltage curves obtained with different speeds of phase change differ only by a factor lying roughly between v and v^2.

VI. CONCLUSIONS

The foregoing exposition shows that a relatively simple theory based on existing evidence about interface potentials and behavior of ions in dielectrics can account for charge separation, and the production of voltages and currents during phase changes. The theory leads to expressions for the space-charge distribution in the solid and the voltage-time curves in open circuit that eventually may be compared with experimental data. The differential equation for the short-circuit current can be obtained in a straightforward manner; it is omitted here because it is not easily integrated. In the present form the theory is still incomplete. Among the factors it does not take into account are (a) the conductivity of the solid that affects the reversibility of the effect and the form of the voltage-time curves in aqueous solutions, and (b) the diffusion of ions in the liquid that may also play a rôle when a solid dielectric is dissolved in a solvent. However, we believe that the theory describes correctly the principal mechanism of interface conduction and presents already the basis for a more precise and complete treatment.

PHYSICAL REVIEW VOLUME 94, NUMBER 6 JUNE 15, 1954

Stored Energy Measurements in Irradiated Copper

ALBERT W. OVERHAUSER*
Department of Physics, University of Illinois, Urbana, Illinois
(Received March 10, 1954)

Thin copper foils, cooled to liquid nitrogen temperature, were subjected to bombardment by 12-Mev deuterons. The stored energy released due to annealing of the radiation damage was measured as the foils warmed to room temperature. Below −40°C the stored energy released per °C was approximately uniform and is presumed to result from annihilation of closely spaced interstitial-vacancy pairs produced by the bombardment. A prominent maximum in the annealing spectrum occured at −15°C and is interpreted as binary recombination of interstitial atoms and vacancies by means of interstitial diffusion. Changes in residual electrical resistivity were also measured. The stored energy to resistivity ratio was found to be 1.7±0.2 cal/gram per micro-ohm-cm, both for the low-temperature processes and the −15°C annealing peak. If the energy of formation of an interstitial-vacancy pair is 5 ev, a value of 11 micro-ohm-cm for the resistivity of one atomic percent of pairs is obtained. The atomic concentration of interstitial atoms and vacancies produced by an irradiation of 10^{17} deuterons/cm² at liquid nitrogen temperature is, accordingly, 5×10^{-5}.

I. INTRODUCTION

CHANGES in the physical properties of a metal resulting from irradiation with fast particles are difficult to interpret because the types and numbers of imperfections produced by the bombardment are unknown. Interstitial atoms and vacant lattice sites are expected[1] to be the predominant types produced, and this view is supported by the observed annealing properties[2] of the damage. The resulting decrease in electrical resistivity upon anneal has received the greatest amount of experimental study, but the inherent difficulties of corresponding theoretical calculations have prevented a determination of the number of interstitial-vacancy pairs that occur.

The measurement of a fundamental quantity, such as energy, should provide a more reliable method of

* Present address: Department of Physics, Cornell University, Ithaca, New York.
[1] F. Seitz, Discussions Faraday Soc. **5**, 271 (1949).
[2] A. W. Overhauser, Phys. Rev. **90**, 393 (1953).

counting interstitial-vacancy pairs. Such a method depends upon knowledge of the energy of formation of a pair. This energy is stored in the lattice after formation and is released in the form of lattice phonons and degraded into heat upon annihilation of the pair. If, then, one can identify the annealing stages of an irradiated material that are due to annihilation of interstitial atoms and vacancies and can measure the quantity of heat that is released during the process, one can determine the number of defects that were destroyed. If changes in electrical resistivity are measured for the same annealing stages, one can determine also the resistivity increase per atomic percent of interstitial-vacancy pairs.

The present interpretation of the annealing behavior of copper, irradiated at low temperature, is based on measurements of electrical resistivity changes. It is observed[2] that the residual resistivity increase recovers about an equal amount at all temperatures above that of bombardment, as the sample is allowed to warm to room temperature, with the exception of a prominent annealing peak at about $-35°C$. This peak was found to obey second-order reaction kinetics and to have a unique activation energy of 0.68 ev. This process is attributed, therefore, to binary annihilation of interstitial atoms and vacancies, made possible by the diffusion of either of the defects. Recent experiments[3] on the energy of formation of vacancies in copper yield a value of 0.9 ev. Since the activation energy for self-diffusion[4] is about 2.1 ev and is assumed to be due to a vacancy mechanism, the energy for vacancy motion is 1.2 ev. By elimination, it follows that the 0.68-ev activation energy is to be associated with interstitial motion.

The low-temperature annealing processes do not have a unique activation energy and are interpreted as the recombination of very close interstitial-vacancy pairs, of which there are several types. Such pairs are expected to constitute a large fraction of the damage, and to recombine at low temperatures by slip-back of the vacancy towards the interstitial. This action is made possible by large elastic strains about the nearby interstitial atom, which open up the lattice in such a way that the activation energy for motion of the vacancy towards the interstitial is greatly reduced. (Elastic strains due to a vacancy are such as to impede slightly the approach of an interstitial.) Quantitative estimates of such strain effects indicate that they are sufficiently large to account for the observed activation energies.

The foregoing description, though difficult to establish conclusively, is supported by the results of the present study. The major contribution is the observation that the stored energy to resistivity ratio is the same for the low temperature processes and the second-order reaction peak. This result would be fortuitous if the basic processes (e.g., annihilation of pairs) were not the same for both parts of the spectrum.

In order to determine the number of interstitial-vacancy pairs present in the damaged material, it is necessary to know the energy of formation of such a pair. Recent calculations of Huntington[5] indicate that the energy of formation of an interstitial atom in copper is about 4 ev. If this result is combined with the measured value associated with vacancy formation, one obtains about 5 ev for the energy of a pair. We shall adopt this tentative value when interpreting the results of the present experiment. An experimental determination of this quantity is very desirable. Unfortunately, threshold measurements for production of pairs by electron bombardment do not yield this quantity, since an interstitial atom must travel more than a lattice constant in order to form a stable pair, and consequently needs extra energy to expend in collisions.

The principle difficulty in measuring the stored energy that is released during the anneal of a damaged sample is one of sensitivity. Irradiation with 12-Mev deuterons, having a range of 0.008 inch in copper, was used. It is necessary, then, to use thin foils in order to achieve a fairly uniform distribution of damage. Consequently, the mass of a specimen is small (0.2 g for 2 cm^2 of a 0.005-inch foil) and the total stored energy available is, as the results indicate, of the order of 0.01 calorie for a deuteron irradiation of $10^{17}/cm^2$. Furthermore, this small quantity of heat does not appear in a narrow temperature interval as the sample is heated, but is liberated over the entire temperature spectrum between liquid nitrogen and room temperature. It follows that an absolute sensitivity of better than 10^{-5} cal/°C is required if an accuracy of 10 percent is to be achieved. A differential technique was employed and is described in Sec. III.

II. DESIGN OF CALORIMETER

A schematic diagram of the calorimeter, which was machined from a solid block of copper, is shown in Fig. 1. The purpose of the double wall construction was to provide as far as possible an isothermal enclosure for the foils. The outer cylindrical shell provided a heat path to the inner one and served also as a thermal shield. The inner shell was supported by the outer one through an annular ring halfway between the top and the bottom. The calorimeter came apart at this midpoint so as to provide access to the interior.

The formidable problem of transfering an irradiated foil from a cyclotron target to a calorimeter, all at liquid nitrogen temperature, was eliminated by allowing the foil to be irradiated within the calorimeter. The

[3] C. J. Meechan and R. R. Eggleston, Phys. Rev. **93**, 953 (1954). See also: Brinkman, Dixon, and Meechan, Acta Metallurgica **2**, 38 (1954).

[4] M. S. Maier and H. R. Nelson, Trans. Am. Inst. Mining Met. Engrs. **147**, 39 (1942).

[5] H. B. Huntington, Phys. Rev. **91**, 1092 (1953).

deuteron beam passed through a rectangular hole in the calorimeter wall and this hole was covered with a 0.0005-inch copper foil in order to restore the integrity of the outer shell as a thermal shield. The foil to be irradiated was held in place over the hole in the inner shell by means of a spring and plunger shown in Fig. 1. A length of fuse wire provided tension to the device and was blown out after the bombardment so as to allow the damaged foil to drop into place alongside the dummy foil.

The calorimeter was mounted on the base of a liquid nitrogen flask, as shown in Fig. 1, and was cooled by conduction to about -190°C. The foil in the deuteron beam was considerably hotter since a pressure contact at one point between the foil and jacket is not a very good thermal path. With a deuteron beam of 5×10^{-8} amp/cm^2 the foil temperature increased to about -150°C. The flask and calorimeter were enclosed in an evacuated chamber. After bombardment dry nitrogen was admitted to the chamber at atmospheric pressure and the system was allowed to warm up freely. If the system were allowed to warm up in a vacuum, the warmup rate was found to be extremely erratic due to the liberation of gases that had condensed on the system during the week-long irradiation.

Two copper foils were suspended inside the calorimeter with 0.002-inch copper wire. Prior to bombardment the foils (of at least 99.95 percent purity) were annealed in vacuum at 450°C for four hours. A 10-cm length of 0.002-inch constantan wire joined the two foils so as to form a copper-constantan differential thermocouple that measured the temperature difference between the irradiated and dummy foils. Another length of 0.002-inch constantan wire joined the copper wall of the jacket and the midpoint of the constantan wire connecting the two specimens, so that a differential thermocouple between either of the foils and the wall of the calorimeter was provided. A third thermocouple was attached to the outside wall for measuring the temperature of the calorimeter. All leads were brought through the vacuum jacket by means of wax seals.

The three measurements made during the warmup of the system were, (a) the temperature difference between the irradiated and dummy foils, (b) the temperature difference between the calorimeter wall and the dummy foil, and (c) the temperature of the calorimeter. Since the temperature difference between the foils was of the order of 0.01°C, a thermal potential of about 3×10^{-7} volt was produced. This potential was amplified by a Leeds and Northrup stabilized dc amplifier operating at a gain of 1000 and the output voltage was measured with a potentiometer. The amplifier was found to reproduce readings to 10^{-8} volt over a 24-hour period for the small potential range that was required. The temperature difference between the calorimeter wall and the dummy foil was about 1°C and the resulting thermal potential was measured with a Leeds and Northrup type K2 potentiometer.

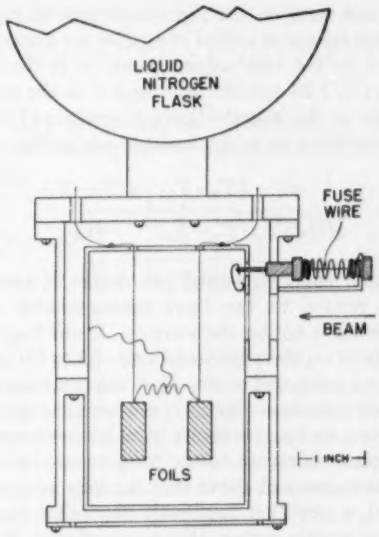

FIG. 1. Schematic diagram of calorimeter. The unit has cylindrical symmetry about a vertical axis.

Measurements of electrical resistivity changes were made during the experiment also. A copper specimen cut from the same foil as used for the thermal measurements was mounted on a bracket adjoining the rectangular hole in the calorimeter wall and received the same irradiation as the foil inside. Resistance measurements were made by standard potentiometric techniques.

III. THEORY OF MEASUREMENT

We must consider the variation with time of the foil temperature during the warmup of the system. Let T_1 and T_2 be the temperatures of the dummy and bombarded foils, respectively, and T_w the temperature of the inner wall of the calorimeter, which at any instant is assumed to be an isothermal enclosure. We shall discuss later the effects of temperature gradients in the calorimeter. Since the temperature differences between the foils and the jacket are small ($\sim$1°C), Newton's law of cooling applies and, consequently, the variation in temperature of the dummy foil with time t is

$$dT_1/dt=\alpha(T_w-T_1), \tag{1}$$

where the coefficient α is a function of temperature. We have neglected any thermal contact between the dummy and bombarded foils and shall justify this omission later. Let us assume, temporarily, that the dummy and bombarded foils are perfectly balanced and have the same thermal contact with the caloirmeter wall. The variation in temperature of the bombarded foil is then,

$$dT_2/dt=\alpha(T_w-T_2)+(MC)^{-1}dU/dt. \tag{2}$$

The second term on the right-hand side of Eq. (2) is due to the release of stored energy as the imperfections produced by the irradiation anneal. M is the mass of the foil, $C(T)$ its specific heat, and U is the energy of formation of the imperfections. Equations (1) and (2) can be combined so as to eliminate αdt, giving

$$\frac{1}{MC}\frac{dU}{dT_1}=\frac{(T_2-T_1)}{(T_w-T_1)}+\frac{d(T_2-T_1)}{dT_1}. \quad (3)$$

The stored energy released per degree is seen to be directly related to the three measurements of temperature made during the warmup. If one neglects the second term on the right-hand side of Eq. (3), which is very small compared to the first, the resulting relation seems quite obvious. The ratio of stored energy released per degree to heat capacity equals the ratio of the temperature difference to the temperature lag.

We have assumed above that the foils were perfectly balanced, a condition manifestly impossible to achieve, and must modify our equations accordingly. It is sufficient to introduce an extra parameter into Eq. (2) as follows:

$$dT_2/dt=\alpha(T_w-T_2)/(1-\beta)+(MC)^{-1}dU/dt. \quad (4)$$

Here, $\beta(T)$ is a parameter that measures the unbalance of the foils due to differences in mass and thermal contact with the surroundings, and must be determined experimentally. If one eliminates αdt from Eqs. (1) and (4), one obtains

$$\frac{1-\beta}{MC}\frac{dU}{dT_1}+\beta=\frac{(T_2-T_1)}{(T_w-T_1)}+(1-\beta)\frac{d(T_2-T_1)}{dT_1}. \quad (5)$$

It is clear that measurements taken during one warmup are no longer sufficient to determine dU/dT_1. After the first warmup is completed, the system must be cooled to liquid nitrogen temperature and allowed to warm up again. Since the imperfections have already annealed, the stored energy term in Eq. (4) will be absent, and we can assume (and shall show later) that $\beta(T)$ has not changed appreciably as a result of the first anneal. Equation (1) will remain unchanged and Eq. (5) will appear the same except for the absence of the stored energy term. The second warmup provides, therefore, a measurement of $\beta(T)$. Observed values of the unbalance between the foils were of the order of a few percent. Figure 2 shows a plot of $(T_2-T_1)/(T_w-T_1)$ for three successive warmups of one specimen. The agreement of the data for the second and third warmups suggests that the experimental method gave results that were adequately reproduceable. Such a check was made for each bombardment.

We shall consider next a number of systematic errors associated with the measurement. In writing Eqs. (1) and (2) we assumed that the thermal enclosure was at a unique temperature T_w for any instant in time. Since measurements are made while the system is warming up, temperature gradients due to thermal conduction will exist along the inner wall of the calorimeter, and T_w must be considered as some appropriate average temperature seen by the foils. For a rate of warmup of 1°C per minute, one can calculate an average temperature gradient along the vertical wall of the inner jacket of about 0.05°C/cm. For such a warmup rate T_w-T_1 was about 1°C. The foils were suspended in the lower half of the calorimeter and the thermal junction that was soldered to the inner wall was at a distance above the plane of symmetry equal to the distance that the foil midpoints were below the plane. Measurements indicated that there was never an appreciable temperature difference across the joint between the halves of the calorimeter, so that one can assume a symmetric temperature distribution about the bisecting plane of the inner jacket. A liberal estimate of the error in measurement of T_w-T_1 due to such gradients is 5 percent.

In writing the basic equations we neglected any thermal contact between the two foils. Since the rate of release of stored energy is proportional to the difference of $(T_2-T_1)/(T_w-T_1)$ for successive warmups, the measurements will be in error to the extent that the stored energy released by the irradiated foil is

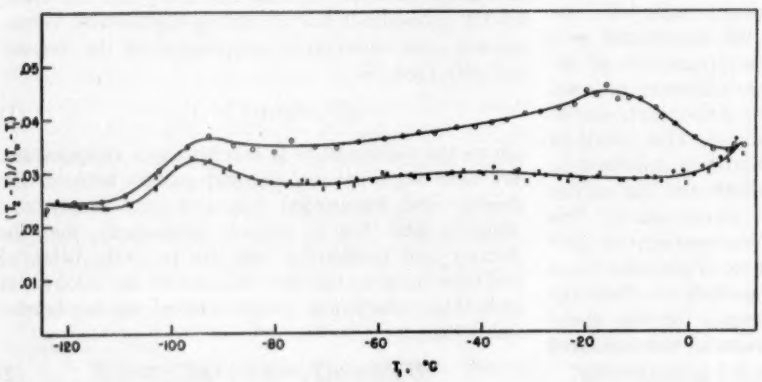

FIG. 2. Plots of $(T_2-T_1)/(T_w-T_1)$ for three successive warmups of one specimen. ○—first warmup; ×—second warmup; ●—third warmup.

transferred to the other foil instead of to the wall of the calorimeter. We must estimate the stored energy lost to the dummy foil per second and compare it with the total rate of release of stored energy, which was about 5×10^{-6} cal/sec. An estimate of the heat transfer through the constantan wire joining the foils yields 5×10^{-10} cal/sec, and is therefore negligible. However, an estimate of the thermal transfer through the nitrogen atmosphere yields about 10^{-7} cal/sec, so that an error of about 3 percent is possible due to neglect of such effects.

Since temperatures were measured thermoelectrically, errors will be introduced by the presence of stray thermal emf's. Let us consider first the effect of a stray potential in the circuit measuring T_2-T_1. A consideration of the analysis by which U is determined shows that stray thermals here will not affect the numerical results provided that they are not too large and are equal for each warmup, and provided that T_1 *versus* time is approximately the same for successive warmups. This result follows from the fact that dU/dT is obtained, essentially, by subtracting $(T_2-T_1)/(T_w-T_1)$ for two warmups. Stray thermals were not observed, the warmup rates were almost identical, and large stray emf's, introduced artificially by running leads through solder seals instead of wax seals, were found to be reproduceable. On the other hand, stray emf's in the circuit measuring T_w-T_1 will cause a proportional error. The potentiometer used for this measurement was checked for internal emf's before and after each warmup, and no appreciable potentials were observed when the calorimeter and foils were in thermal equilibrium at -190°C or room temperature.

We have heretofore neglected any changes in the specific heat of the sample due to the presence of imperfections. In order to demonstrate that such effects are not important in the present experiment, we shall derive the appropriate equations for the case of a dummy and bombarded foil that are otherwise perfectly matched. For the purpose of discussion we shall assume that the damaged foil contains only interstitial atoms and vacancies and that they anneal out completely during the first warmup. Let f be the atomic fraction of interstitial-vacancy pairs. For $f\ll1$ (and constant) the specific heat per gram will be given with sufficient approximation by,

$$C(f,T)=C_0(T)[1+fs(T)],$$

where

$$s(T)=\frac{1}{C_0(T)}\left[\frac{\partial C(f,T)}{\partial f}\right]_{f=0}.$$

Here, $C_0(T)$ is the specific heat of the undamaged material. Let E_0 be the energy of formation of an interstitial-vacancy pair at 0°K and $U(T)$ be the internal energy per gram. Then, if N is the number of atoms per gram,

$$U(f,T)=U_0(T)+f\left[NE_0+\int_0^T C_0(T')s(T')dT'\right], \quad (6)$$

where $U_0(T)$ is the corresponding function for $f=0$. The rate of warmup of the bombarded foil is, instead of Eq. (2),

$$\frac{dT_2}{dt}=\frac{\alpha(T_w-T_2)}{1+fs(T_2)}+\frac{NE_0+\int_0^{T_2} C_0(T')s(T')dT'}{C_0(T_2)[1+fs(T_2)]}\left(-\frac{df}{dt}\right). \quad (7)$$

The first term on the right side of Eq. (7) accounts for thermal transfer from the surroundings, whereas the second term results from the *adiabatic* annealing of the damage and is obtained by equating the total derivative of Eq. (6) to zero. As before, αdt can be eliminated by the use of Eq. (1) and we obtain after manipulation,

$$NE_0\left(-\frac{df}{dT_1}\right)=C_0\left[\frac{T_2-T_1}{T_w-T_1}+(1+fs)\frac{d(T_2-T_1)}{dT_1}+fs\right]+\frac{df}{dT_1}\int_0^{T_2} C_0(T')s(T')dT'. \quad (8)$$

This expression is to be compared with Eq. (3). It is seen that there are two extra terms on the right side of Eq. (8), both of magnitude fsC_0, which must be compared with the leading term, $C_0(T_2-T_1)/(T_w-T_1)$. It is sufficient to estimate the magnitude of f and s. From the results of the following section it follows that $f\sim2\times10^{-5}$ for the measured portion of the stored energy spectrum. A rough estimate of s can be made as follows. Consider the specific heat as given by the Einstein model. If one assumes that the vibrational frequencies of the six nearest neighbors of and interstitial atom are altered 100 percent, then s might be of order of magnitude 6. This is, undoubtedly, an overestimate in spite of our neglect of other neighbors and neighbors of vacancies, since the temperature region of interest is not much lower than the Debye temperature of the lattice, where the specific heat is nearly 6 cal/mole and, consequently, not strongly frequency dependent. Furthermore, partial cancellation will occur since the frequency of some modes will increase, whereas others will decrease. The magnitude of fs is therefore not greater than 10^{-4}, which is smaller by a factor of 100 than the term $(T_2-T_1)/(T_w-T_1)$. The two extra terms in Eq. (8) always tend to cancel, so that the stored energy spectrum is probably in error by less than one percent as a result of their omission. If the stored energy spectrum were integrated from 0°K to a temperature at which annealing is complete, one can show that all of the terms in Eq. (8) involving s cancel identically.

We have shown that the neglect of any variations in the specific heat due to annealing of the radiation damage is justified to a good degree of approximation. It follows from Eq. (8) that in the same approximation the energy U in Eqs. (2) through (5) can be interpreted as the energy of formation of the imperfections at 0°K.

Radioactive heating of the damaged sample as a result of bombardment induced activities could produce a spurious source of stored energy. The foil temperatures were measured, therefore, for several hours after irradiation, when they were still in a vacuum, and no heating effects were observed. Changes in the properties of thermal junctions were avoided by shielding all junctions from the deuteron beam.

The foregoing considerations, if complete, indicate that the over-all experimental uncertainty of the stored energy measurements is about 10 percent.

IV. RESULTS AND DISCUSSION

The stored energy spectrum obtained for two samples is shown in Fig. 3. Both samples weighed 0.219 g and they received an irradiation of 0.9 and 1.5×10^{17} deuterons/cm², respectively. The fact that the spectrum does not extend below −140°C for the first specimen is due to the sample being heated to about −150°C by the deuteron beam, so that annealing processes occurring at lower temperatures were already complete. The second specimen received a larger irradiation in an equal length of time so that the beam current and heating effects were correspondingly greater and also more erratic. The two curves can be compared above −80°C and are seen to be almost identical except for a constant ratio equal to the ratio of the integrated fluxes. This result is to be expected since, for copper, bombardment saturation effects are not apparent for irradiations of 10^{17}/cm². The annealing peak at −15°C, most likely due to annihilation of interstitial atoms and vancancies as a result of interstitial diffusion, is quite prominent.

The total stored energy released between −80°C and room temperature is found by integrating the curves in Fig. 3, and is 1.03×10^{-2} and 1.68×10^{-2} cal for specimens 1 and 2, respectively. If these results are normalized to an irradiation of 1.0×10^{17} and unit mass, one finds 0.052 cal/gram for the heat released in this temperature range. This result can be compared with the (residual) electrical resistivity increase that anneals out in the same temperature interval in order to obtain the stored energy to resistivity ratio that characterizes the imperfections. From reference 2, we find a resistivity decrease of 3.1×10^{-8} ohm-cm (normalized to 1.0×10^{17} deuterons/cm²) between −80°C and room temperature. Thus, the U/ρ (stored energy to resistivity) ratio is 1.7 cal/gram per micro-ohm-cm. This value is, perhaps, the most important and unambiguous result of the present study.

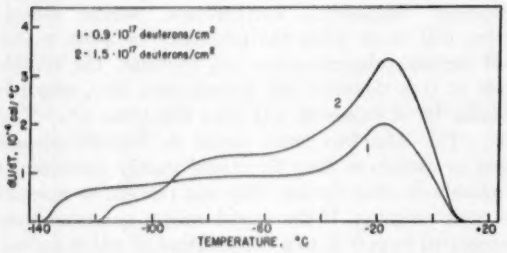

FIG. 3. Stored energy annealing spectrum observed for two irradiated samples, both weighing 0.219 gram.

It is interesting to compare the U/ρ ratio obtained here with that obtained in copper as a result of plastic deformation. Stored energy measurements[6] of heavily cold-worked polycrystaline copper yield about 0.5 cal/gram. On the other hand, the resistivity change[7] is only 3.6×10^{-8} ohm-cm. Hence, the U/ρ ratio for imperfections resulting from cold work is 14 cal/gram per micro-ohm-cm, an order of magnitude larger than the result obtained for radiation damage.

The U/ρ ratio we have determined above was for the integrated U and the total $\Delta\rho$ between −80°C and room temperature. Since this temperature region includes (at least) two distinct annealing processes, the −15°C annealing peak and the low-temperature processes, one must examine the U/ρ ratio for both. This ratio should be the same for both if the low-temperature processes are due to the annihilation of close interstitial-vacancy pairs and the −15°C, second-order reaction is due to annihilation of separated pairs as a result of volume diffusion. This comparison could be made by comparing directly the corresponding annealing spectra for stored energy and resistivity. The spectrum for the latter was obtained[2] by successive isothermal anneals instead of by continuous warmup, as in the present experiment. Some calculation, therefore, is needed to effect the comparison.

For anneal of the resistivity, the second-order reaction process was found[2] to obey the following equation.

$$df/dt=-ae^{-E/kT}f^2e^{bf}, \tag{9}$$

where f is the concentration of imperfections, E is an activation energy=0.68 ev, and a and b are constants. The factor $\exp(bf)$ appeared[8] (theoretically) as an enhancement in the diffusion process resulting from elastic strains in the lattice due to interstitial atoms, and such a factor was needed to fit the isothermal annealing data. Using Eq. (9) with the values of a and b determined from the resistivity curves, an annealing spectrum was computed for this process

[6] H. Quinney and G. I. Taylor, Proc. Roy. Soc. (London) **A163**, 157 (1933); H. Kanzaki, J. Phys. Soc. Japan **6**, 90 (1951); **6**, 456 (1951).

[7] K. Takahasi, Science Repts. Tôhoku Univ. **19**, 265 (1930).

[8] The detailed theory given in reference 2 applies to vacancy motion. Similar results are obtained for interstitial motion.

if it were subjected to the thermal treatment occuring in the stored energy experiments. This spectrum was converted to energy units by use of the U/ρ ratio obtained for the *entire* spectrum. The result of the calculation is shown as curve 2 in Fig. 4, and should be compared with the experimental energy spectrum, curve 1. Since no arbitrary constants were available, the good agreement in the region of the peak proves that the U/ρ ratio is the same for the low-temperature processes and for the second-order reaction. This result is consistent with the interpretation that interstitial-vacancy annihilation is the mechanism in both parts of the spectrum. The agreement obtained for the position of the peak provides an additional check of the 0.68-ev activation energy measured during the resistivity study since, then, the effective warmup rate was about 20 times slower and the annealing peak occured 20°C lower in temperature.

For comparison, similar curves were computed assuming pure second-order reaction kinetics and first-order kinetics, and are shown in Fig. 4 as curves 3 and 4, respectively. The necessary constants were determined by best fit of the resistivity data and converted to energy units in the foregoing manner. It is apparent that a pure second-order reaction [Eq. (9) without the factor $\exp(bf)$] is not as satisfactory and that a first-order process has an entirely different shape. It should be noted, however, that the high-temperature tail of the experimental curve is cut off like that of the first-order reaction curve. This behavior is due likely to interstitial traps in the copper that compete with vacancies so as to impose first-order kinetics when the concentration of interstitials and vacancies becomes small. It should be emphasized, though, that the transition to first-order kinetics occurs only after the second-order process has proceeded about 90 percent towards completion, so that any residual damage at room temperature due to trapped interstitials and vacancies can be but a small fraction in magnitude of the damage associated with the second-order reaction. Experimentally the residual resistivity at room temperature due to damage is about equal in magnitude to the resistivity change of the second order reaction. The origin and nature of the imperfections that remain at room temperature is, at present, unknown. They anneal out only at relatively high temperatures.[9]

Further results can be obtained if one uses a specific value, say 5 ev, for the energy of formation of an interstitial-vacancy pair. The stored energy per atomic percent of pairs would be 18 cal/gram. Using the measured U/ρ ratio (1.7 cal/gram per micro-ohm-cm) one obtains a value of 11 micro-ohm-cm for the resistivity due to one percent of pairs. Jongenburger[10] has

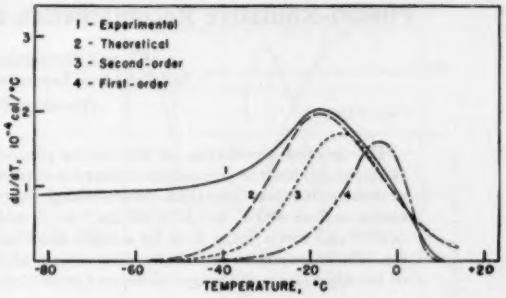

FIG. 4. Experimental annealing spectrum and three computed spectra for the 0.68-ev activation energy annealing process.

calculated the resistivity associated with one percent of vacancies. His result, 1.3 micro-ohm-cm, together with the above value would imply that the resistivity of an equal number of interstitial atoms is about 10 micro-ohm-cm.

The number of interstitial-vacancy pairs produced by bombardment can now be estimated. An irradiation of 10^{17} deuterons/cm^2 (average energy=9 Mev) at -180°C causes a residual resistivity increase of 7×10^{-8} ohm-cm. Presumably, only 75 percent of this increase is due to interstitial atoms and vacancies, the remaining fraction being associated with imperfections that remain at room temperature. The total concentration of pairs resulting from such a bombardment is, then, 5×10^{-5}. This value is smaller by a factor of 50 then the concentration, 2.5×10^{-3}, obtained from Seitz's theory,[1] using the observed[11] energy threshold (25 ev) for formation of imperfections stable at -170°C. The origin of this discrepancy seems to be the approximation of letting a knocked-on copper atom of energy E have unit probability to form a stable interstitial-vacancy pair if E is greater than the threshold. Rough calculations indicate that this probability increases from 0 only very slowly with increasing E above the threshold. Consequently, the number of stable pairs resulting from secondary atoms that recoil from the primary deuteron is drastically reduced, especially since the energy distribution of secondaries is inversely proportional to E^2. A further consequence is that production of more than one interstitial-vacancy pair as a result of a primary collision and subsequent secondary or tertiary collisions is unlikely.

In conclusion the writer would like to thank J. W. Henderson and H. G. Cooper for their kind assistance in conducting the bombardment and annealing measurements The encouragement and interest of J. S. Koehler and F. Seitz is gratefully acknowledged. This research was supported by the U. S. Atomic Energy Commission.

[9] R. R. Eggleston, Acta Metallurgica **1**, 679 (1953).
[10] P. Jongenburger, Phys. Rev. **90**, 710 (1953).
[11] D. T. Eggen and M. J. Laubenstein, Phys. Rev. **91**, 238 (1953).

Photon-Radiative Recombination of Electrons and Holes in Germanium

W. VAN ROOSBROECK AND W. SHOCKLEY
Bell Telephone Laboratories, Murray Hill, New Jersey

(Received February 19, 1954)

The spectral distribution of the rate of photon generation for the photon-radiative recombination of electrons and holes in germanium is determined from known optical properties by application of the principle of detailed balance. Quantities characterizing the process are evaluated: The thermal equilibrium recombination rate at 300°K is 1.57×10^{13} cm^{-3} sec^{-1}, which corresponds to a recombination cross section of 2.9×10^{-21} cm^2 and a decay time for a small disturbance in carrier concentration in intrinsic material of 0.75 sec. The extension to the steady-state case of added current carriers is given, and estimates are included of the dependence of the quantities on temperature.

IT has been established that in the wavelength range from 1 to 2 microns photons absorbed in germanium produce electron-hole pairs with unit quantum efficiency.[1] The inverse process—the production of photons by electron-hole recombination—has also been observed.[2] In this paper, quantities characterizing this radiative recombination process are estimated for germanium by application of the principle of detailed balance to the thermal equilibrium rate of photon absorption estimated from the optical constants[3] at room temperature.

It should be remarked that recombination in germanium is in general so enhanced by imperfections, which have been referred to as "deathnium," that the lifetime of injected carriers is predominantly a structure-sensitive property and is much less than the lifetime for the radiative process alone.[4] Perhaps even in pure and perfect germanium crystals processes involving phonons and long-wavelength photons also occur and contribute materially to the reduction of lifetime. There is at present neither theoretical nor experimental information from which such contributions can be estimated.

From the principle of detailed balance, the rate of radiative recombination at thermal equilibrium for an elementary frequency interval $d\nu$ at frequency ν is equal to the corresponding rate of generation of electron-hole pairs by thermal radiation. This rate is $P(\nu)\rho(\nu)$ per unit volume and unit frequency interval, where $\rho(\nu)d\nu$ is the density in the crystal of photons in the range $d\nu$, and $P(\nu)$ is the probability per unit time that a photon of frequency ν be absorbed. The total rate $\mathcal{R}$ per unit volume is obtained by integrating over ν as follows:

$$\mathcal{R}=\int P(\nu)\rho(\nu)d\nu. \tag{1}$$

While the range of integration is nominally all values of ν, the principal contribution to the integral for germanium comes, as will be seen, from a comparatively narrow frequency range near the absorption edge.

With added current carriers, the total rate of radiative recombination $\mathcal{R}_e$ per unit volume in the steady state is given by

$$\mathcal{R}_e=(np/n_i^2)\mathcal{R}, \tag{2}$$

since[5] it must be proportional to the product of electron concentration n and hole concentration p and be equal to $\mathcal{R}$ when this product has its thermal equilibrium value, the square of the concentration n_i of electrons or holes in the intrinsic semiconductor.

From the expression for $\mathcal{R}_e$, the decay time for a small disturbance in concentration if radiative recombination alone were operative may readily be calculated.[6] If δn and δp are small concentrations in excess of the steady-state values, (2) gives for the net recombination rate,

$$\delta\mathcal{R}_e=(\delta n/n+\delta p/p)\mathcal{R}_e, \tag{3}$$

whence the decay time for a relatively small[7] disturbance for which $\delta n=\delta p$ is

$$\tau=np/(n+p)\mathcal{R}_e. \tag{4}$$

For sufficiently strongly extrinsic n- or p-type material initially at thermal equilibrium, with $n=n_0$ and $p=p_0$, τ from Eq. (4) equals, respectively, the microscopic lifetimes for minority holes or electrons.[6] With the thermal equilibrium minority carrier concentration negligible in each case, these lifetimes are

$$\begin{aligned}\tau_p&=p_0/\mathcal{R}=2(p_0/n_i)\tau_i=2(n_i/n_0)\tau_i,\\ \tau_n&=n_0/\mathcal{R}=2(n_0/n_i)\tau_i=2(n_i/p_0)\tau_i,\end{aligned} \tag{5}$$

where, from (4),

$$\tau_i=n_i/2\mathcal{R} \tag{6}$$

[1] F. S. Goucher, Phys. Rev. 78, 816 (1950); Goucher, Pearson, Sparks, Teal, and Shockley, Phys. Rev. 81, 637 (1951).
[2] J. R. Haynes and H. B. Briggs, Phys. Rev. 86, 647 (1952); R. Newman, Phys. Rev. 91, 1313 (1953).
[3] H. B. Briggs, Phys. Rev. 77, 287 (1950); J. Opt. Soc. Am. 42, 686 (1952).
[4] W. Shockley, *Electrons and Holes in Semiconductors* (D. Van Nostrand Company, Inc., New York, 1950), p. 69; Proc. Inst. Radio Engrs. 40, 1289 (1952), pp. 1297 ff.
[5] Tacit in this reasoning is the assumption that the velocity distributions of electrons and holes are independent of the concentrations. Hence, (2) is strictly applicable only if the electron and hole gases are nondegenerate.
[6] W. van Roosbroeck, Phys. Rev. 91, 282 (1953).
[7] It is assumed that δn and δp are small compared with $(n+p)$, in accordance with (35) of reference 6 written in terms of the steady-state concentrations n and p.

is the decay time in material of intrinsic conductivity. The recombination cross section σ is given by

$$\sigma = \mathfrak{R}/n_0 p_0 v = \mathfrak{R}/n_i^2 v, \tag{7}$$

where v is a relative velocity of thermal motion.

The thermal equilibrium distribution of photon density, $\rho(\nu)$, may be calculated in the usual way from the density distribution of normal modes in wave number or in K space, by applying the partition function for the harmonic oscillator to each mode. Since wave number is

$$K = n\nu/c, \tag{8}$$

where n is refractive index and c the speed of light, the density of modes in the frequency range $d\nu$ is given by

$$2\times 4\pi K^2 dK = (8\pi/c^3)[n^3(1+d\ln n/d\ln\nu)]\nu^2 d\nu, \tag{9}$$

which is that for free space multiplied by the quantity in square brackets. The photon density distribution is accordingly given by

$$\rho(\nu) = (8\pi\nu^2/c^3)[n^3 d\ln n\nu/d\ln\nu]/[\exp(h\nu/kT)-1]. \tag{10}$$

The probability of absorption of a photon per unit time $P(\nu)$ is calculated as follows: The absorption coefficient,

$$\alpha \equiv 4\pi n\kappa\nu/c, \quad \kappa \equiv \text{absorption index}, \tag{11}$$

is defined and measured in terms of the relative decrease in intensity for given thickness of material along the optical path. A wave packet moving along the path has a group velocity of

$$v_g = d\nu/d(1/\lambda) = (c/n)(d\ln\nu/d\ln n\nu). \tag{12}$$

Hence,[8]

$$P(\nu) = \alpha v_g = 4\pi\kappa\nu(d\ln\nu/d\ln n\nu). \tag{13}$$

From (10) and (13),

$$P(\nu)\rho(\nu) = (32\pi^2\kappa n^3/c^3)\nu^3/[\exp(h\nu/kT)-1]. \tag{14}$$

The total rate $\mathfrak{R}$ of radiative recombination per unit volume at thermal equilibrium may, from (1) and (14), be written as

$$\mathfrak{R} = 32\pi^2 c(kT/ch)^4 \int_0^\infty \frac{n^3\kappa u^3 du}{e^u-1}$$

$$= 1.785\times 10^{22}(T/300)^4 \int_0^\infty \frac{n^3\kappa u^3 du}{e^u-1} \text{ cm}^{-3}\text{ sec}^{-1}, \tag{15}$$

in which $u \equiv h\nu/kT$ is the variable of integration. The lower limit u_0 corresponds to the long-wavelength limit of the characteristic absorption band, about 2.2μ for germanium, at wavelengths exceeding which other mechanisms of absorption, such as absorption by conduction electrons, predominate.[9]

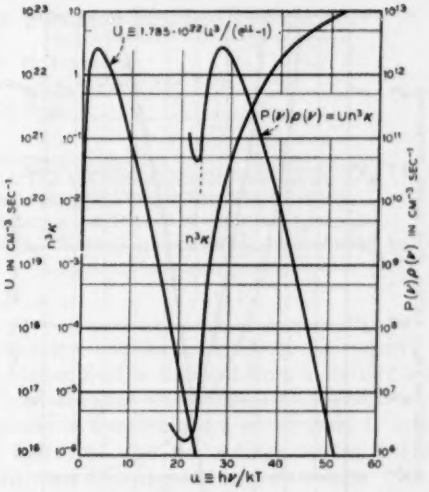

FIG. 1. The dependence for germanium of $n^3\kappa$ and the radiative recombination rate per unit frequency $P(\nu)\rho(\nu)$ on $u \equiv h\nu/kT$.

Values have been determined over the characteristic absorption band of germanium of the refractive index n and of the extinction coefficient $n\kappa$ for high-purity single crystals.[3] Using these values, the rate of recombination is found by numerical evaluation of the integral in (15) to be given by

$$\mathfrak{R} = 1.57\times 10^{13} \text{ cm}^{-3}\text{ sec}^{-1} \tag{16}$$

at 300°K. While only the small fraction 7.7×10^{-3} of the photons at 300°K possess wavelengths below the long-wavelength limit for germanium,[10] it appears from the dependence on u of the integrand $P(\nu)\rho(\nu)$, shown in Fig. 1, that there is no appreciable contribution to $\mathfrak{R}$ from the long-wavelength photons, the integrand possessing a sharp peak which occurs in wavelength just below the long-wavelength limit. In evaluating the integral, the contribution of carrier absorption, which causes the sharp increase in $n^3\kappa$ at the longer wavelengths, was obviated by using the dashed extrapolation shown in the figure.

In accordance with[11]

$$n_i^2 = 3.1\times 10^{33} T^3 \exp(-9100/T), \tag{17}$$

the corresponding lifetime and recombination cross

[8] This expression for $P(\nu)$ in terms of optical constants is readily derived also by considering the decay of a spatially unattenuated wave of given wavelength.

[9] J. Bardeen, Phys. Rev. **79**, 216 (1950); H. Y. Fan and M. Becker, in *Semi-Conducting Materials*, edited by H. K. Henisch (Butterworths Scientific Publications Ltd., London, 1951).

[10] U. S. National Bureau of Standards, *Miscellaneous Physical Tables: Planck's Radiation Function and Electronic Functions* (U. S. Government Printing Office, Washington, D. C., 1941), Applied Mathematics Series, Vol. MT-17.

[11] F. J. Morin (private communication); Phys. Rev. **93**, 62 (1954). At 300°K, n_i equals 2.4×10^{13} cm^{-3}, corresponding to an intrinsic resistivity of 47 ohm-cm for electron and hole mobilities of 3800 and 1820 cm^2 volt^{-1} sec^{-1}. See also reference 6, p. 288.

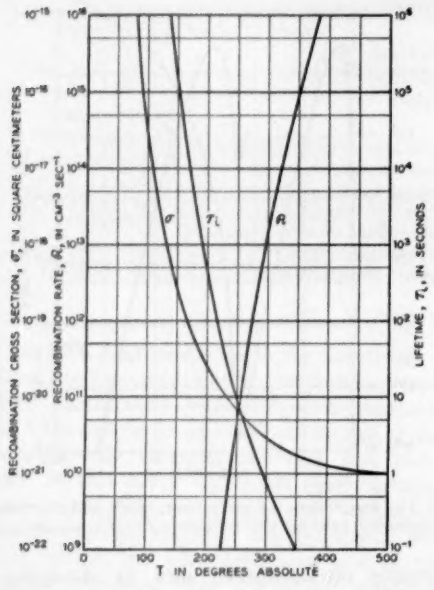

FIG. 2. The temperature dependence for germanium of the radiative recombination rate $\mathcal{R}$, of the lifetime τ_i for intrinsic germanium, and of the recombination cross section σ.

section are, from (6) and (7),

$$\tau_i = 0.75 \text{ sec}, \quad \sigma = 2.9\times10^{-21} \text{ cm}^2, \tag{18}$$

at 300°K. For 10 ohm-cm n-type germanium at this temperature, τ_p is accordingly about 0.22 sec. Photon-radiative recombination thus has but slight influence in general on the observed lifetimes, which seldom exceed 10^{-2} sec.

Recombination radiation should be generated at the rate $(np/n_i^2)P(\nu)\rho(\nu)$ per unit volume per unit frequency interval, and such radiation from germanium was observed by Haynes and Briggs under conditions in which the emergent radiation should have essentially the same spectral distribution as that generated.[2,12] Their results are in good agreement with the $P(\nu)\rho(\nu)$ distribution of Fig. 1. Making correction for thickness of intervening material, Newman found radiation from germanium to be substantially in accord with theory.[2]

When the coupling between the electrons and the photons is large, application of the calculated $P(\nu)$ to a photon of frequency ν is not strictly correct. This approximation, however, introduces only relatively small error. For, it is evident from Fig. 1 that the principal contribution to $\mathcal{R}$ comes from values of u less than 32; and for $u=32$, the photon intensity is attenuated in one wavelength in germanium by the factor[2]

$$\exp(-4\pi n\kappa/\lambda)(\lambda/n) = \exp(-4\pi/n)(n\kappa) \sim \exp(-2.4\times10^{-2}). \tag{19}$$

Thus, a photon is absorbed on the average in about 40 wavelengths, and the broadening of the photon levels by coupling with the electrons is only about 1.5 percent. It might also be remarked that the linearity resulting from quantum electrodynamics is such that absorption coefficients measured for cases in which there may be several photons in each mode are applicable to the present case, in which less than 10^{-7} of the modes are excited above the ground state.

Estimates of $\mathcal{R}$, σ, and τ_i in their dependence on temperature are shown in Fig. 2. These estimates are based on the approximation that temperature changes the dependence of $n^3\kappa$ on ν only through the shift of long-wavelength limit associated with the temperature coefficient of the energy gap E_g. The data provide, with this assumption, the dependence at 300°K of $n^3\kappa$ on $h\nu/E_g$. With[13]

$$E_g = 0.785 - 1.0\times10^{-4}T \text{ ev}, \tag{20}$$

the curve of Fig. 1 of $n^3\kappa$ *versus* $u \equiv h\nu/kT$ is thus shifted along u axis in accordance with

$$u/u_{300} = 300/T + 0.040(300/T - 1). \tag{21}$$

The rapid increase of photon density with temperature produces the corresponding increase in $\mathcal{R}$ and decrease in τ_i shown in Fig. 2; but it is the more rapid increase of n_i^2 that produces the decrease in σ, which appears to become substantially constant at the higher temperatures shown.

We are particularly indebted to Miss D. J. Oxman for evaluation of the integrals and to Mr. H. B. Briggs for his assistance with the optical data.

[12] Visible recombination radiation of a broad band width from silicon carbide, with photons of energies in general somewhat less than the value of the energy gap, has been observed: Lehovec, Accardo, and Jamgochian, Phys. Rev. **83**, 603 (1951); Phys. Rev. **86**, 615 (1952). See also K. Lehovec, Proc. Inst. Radio Engrs. **40**, 1407 (1952).

[13] See the text of reference 4, pp. 335–336.

Domain Clamping Effect in Barium Titanate Single Crystals

M. E. Drougard and D. R. Young
International Business Machines Corporation, Poughkeepsie, New York

(Received February 26, 1954)

We have found that the dielectric constant of good single crystals of barium titanate decreases as the average polarization is decreased by means of an electric field. This has been interpreted as being due to a domain clamping effect arising from the multidomain situation in the crystal that accompanies the reduction in polarization. These measurements give a value for the coefficient of coupling of 0.50 which is in agreement with Caspari and Merz's value of d_{33} and our measurement of S_{33}. The coupling coefficient has been studied as a function of temperature using this clamping effect.

I. INTRODUCTION

IN view of the possible applications of $BaTiO_3$ for memory devices, it is desirable to know more about the phenomena which take place as the polarization is reversed from one direction to the other. Dielectric constant measurements can be used as one means of giving useful information about the nature of this process.

The effect on the dielectric constant that is to be described depends on the magnitude of the average polarization and can only be observed in a simple form if crystal plates are used in which the polarization is always normal to the surface of the plate. In addition, the polarization must be reversed at a slow rate, otherwise additional effects enter that are to be described in a subsequent publication.

The plots shown were obtained using crystals grown by J. Remeika of Bell Telephone Laboratories. We have observed similar effects using crystals grown in our laboratory. They are characterized as having a low dielectric constant ($k=185$) in the c direction normal to the surface of the plate and a low 60 cycle per second coercive field strength (675 v/cm).

II. DIELECTRIC CONSTANT MEASUREMENTS

A. Equipment

As illustrated by Fig. 1, the crystal under study is subjected at the same time to a slowly varying biasing field and to an audio-frequency (20 kc) sine wave of constant low amplitude (1/500 of the coercive field). The biasing field is obtained from a rectifier which is fed from a Variac transformer. This Variac is driven by means of a motor and a set of gears at extremely slow speed, so that the voltage coming out of the rectifier can be considered as a dc voltage (the corresponding field across the crystal varies at the rate of 30 v/cm per minute). A complete cycle usually requires three hours. Under such conditions it is known from previous measurements that the imaginary part of the dielectric constant remains negligible even during the switching time, so that the fraction of the high-frequency voltage appearing across the series measuring condenser is a measure of the real part of this dielectric constant. This voltage is amplified, rectified, and fed into the y axis of an x-y recorder, the x axis of which is used for the low-frequency field. A battery is interposed between the rectifier and the crystal, so that the zero field point can be brought to mid-scale of the recorder x axis.

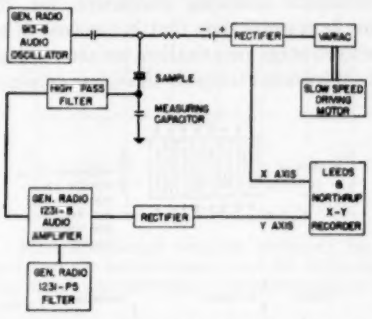

FIG. 1. Arrangement for recording the dielectric constant as a function of applied field.

B. Results

The plots obtained have the aspect shown by Fig. 2. The sample had been "depolarized" by "walking" it down its hysteresis loop using 60-cycle ac and was plugged in at A, in the absence of any dc field. The low-frequency field was then increased to about twice the value of the coercive field, which is shown by the solid line ABC. The dotted line CDE corresponds to the reversal of this field to the opposite value. In the

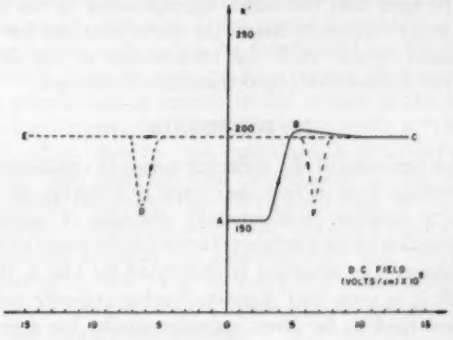

FIG. 2. Dielectric constant as a function of dc field.

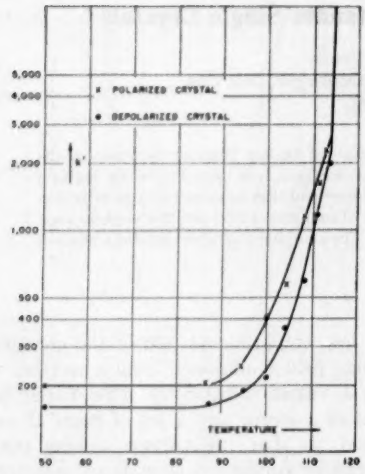

FIG. 3. Dielectric constant as a function of temperature for depolarized and saturated crystals.

region D, the polarization of the crystal reverses itself, and the dielectric constant goes to a minimum, then comes back to its initial value. The low-frequency field is then reversed, and the plot obtained is the dotted line EFC.

It is apparent from the figure that the effect is completed for a smaller value of the field for the case of the initially "depolarized" crystal than it is when we start from a saturated crystal. The minimum values of the dielectric constant are also somewhat different. The slight overshoot which appears at B in the case of an initially "depolarized" crystal has not been explained.

The experimental arrangement described in section A has been used to record the variation of the dielectric constant of the same sample with temperature. (This was done by feeding into the x axis of an x-y recorder the output of a thermocouple and slowly increasing the temperature by means of the same automatically controlled Variac.) The two plots shown in Fig. 3 have been obtained, respectively, from a depolarized crystal and from the same sample polarized to saturation. It can be seen that the curve corresponding to the first case stays constantly below the curve obtained for the polarized crystal until the temperature of the ferroelectric to nonferroelectric transition is reached.

III. DISCUSSION

This behavior of the dielectric constant can easily be understood if we picture the crystal as breaking up into a large number of elementary domains of opposite polarization as the average polarization decreases during switching. This situation is illustrated by Fig. 4, from which it is seen that domains having opposite orientations tend to be given opposite strains for a given half-cycle of the high-frequency field. The elementary domains, therefore, mutually clamp each other, and we measure the "thickness-clamped" dielectric constant.

For a tetragonal crystal such as barium titanate, the equations relating the electric displacement D, the stress T, the strain X, and the field E using nonrationalized units are:

$$D_3=4\pi d_{33}T_3+\epsilon_{33}E_3, \tag{1}$$

$$X_3=S_{33}T_3+d_{33}E_3, \tag{2}$$

where d_{33}, S_{33}, and ϵ_{33} are, respectively, the corresponding piezoelectric and elastic compliance coefficient and the permittivity of the material (or dielectric constant in cgs units).

For two domains having opposite polarity, the coefficient d_{33} takes opposite values. If we have the same number of such domains, addition of the corresponding Eq. (2) shows that

$$\sum X_3=S_{33}\sum T_3.$$

Since there is no external applied stress, $\sum T_3=0$ which shows that the strain must be zero. Then, for either kind of region,

$$T_3=-(d_{33}/S_{33})E_3$$

and from (1)

$$\frac{D_3}{E_3}=\epsilon_{33}-4\pi\frac{d_{33}^2}{S_{33}}=\epsilon_{33}\left(1-\frac{4\pi}{\epsilon_{33}}\frac{d_{33}^2}{S_{33}}\right), \tag{3}$$

while, if all domains had the same orientations, the electrical displacement would be given by:

$$D_3=\epsilon_{33}E_3.$$

For a crystal having zero average polarization, we then measure a dielectric constant

$$K_c'=\frac{D_3'}{\epsilon_0 E_3}=\frac{\epsilon_{33}}{\epsilon_0}\left(1-\frac{4\pi d_{33}^2}{\epsilon_{33}S_{33}}\right)=K_f'(1-C^2), \tag{4}$$

where K_f' is the "free" dielectric constant and C is the electromechanical coupling coefficient for thickness vibrations. It appears then that in the case of a crystal having zero average polarization we are measuring the so-called "thickness-clamped" dielectric constant.

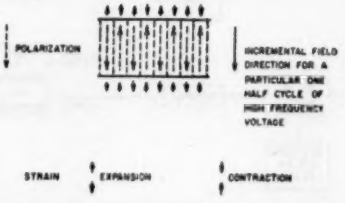

FIG. 4. Tendency of oppositely oriented domains to develop opposite strains in response to the same increment of field.

Bond, Mason, and McSkimmin,[1] working on $BaTiO_3$ single crystals, have found for C a value of 0.67. If we use this value in Eq. (4), we find:

$$K_c'=0.55K_f',$$

obviously not in good agreement with the results shown in Fig. 2. However, the crystals available to those authors were certainly different from ours (they had a very high low-frequency dielectric constant[1] of 2890).

Measurements have been taken, however, in this laboratory on the thickness piezoelectric resonance mode; these measurements, described in Sec. IV of this paper, have given for S_{33} the approximate value

$$S_{33}=4.5\times10^{-12}\ \text{cm}^2/\text{dyne}.$$

In an earlier study, Caspari and Merz[2] found

$$d_{33}=396\times10^{-8}\ \text{cgs units}.$$

If we put these values into Eq. (3), the corrective term $4\pi(d_{33}^2/S_{33})$ becomes equal to 45, while the largest difference we observed is 40, indicating almost complete clamping. The coefficient of coupling is about 0.50.

From the plots shown on Fig. 3 it is possible to study the variation of the electromechanical coupling coefficient C with temperature. C can be determined from Eq. (4), which gives

$$C^2=1-(K_c'/K_f').$$

The results are illustrated by the solid line on Fig. 5. No data were available to us on the temperature dependence of the thickness electromechanical coupling coefficient, but we can compare our results to Caspari and Merz's earlier studies of piezoelectric longitudinal modes.[2] The electromechanical coupling coefficient for

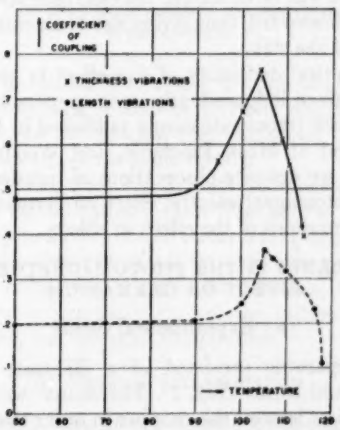

FIG. 5. Electromechanical coupling coefficient for thickness vibrations (from our measurements) and for longitudinal vibrations [from Merz's (see reference 2) measurements] as a function of temperature.

[1] Bond, Mason, and McSkimmin, Phys. Rev. 82, 443 (1951).
[2] M. E. Caspari and W. J. Merz, Phys. Rev. 80, 1084 (1950).

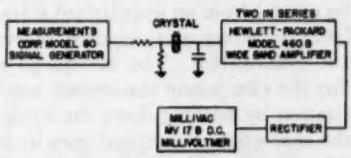
MEASUREMENTS CORP MODEL 80 SIGNAL GENERATOR
CRYSTAL
TWO IN SERIES
HEWLETT-PACKARD MODEL 460 B WIDE BAND AMPLIFIER
MILLIVAC MV 17 B D.C. MILLIVOLTMER
RECTIFIER

FIG. 6. Experimental arrangement for investigation of thickness piezoelectric modes.

the samples used by these authors can be approximately determined from the data shown in Fig. 10 of their article by using the relation:

$$K=\tfrac{1}{2}\pi(\Delta\nu/\nu_R)^{\frac{1}{2}}.$$

The curve obtained has been drawn in dotted lines on Fig. 5, and it can be seen that its aspect is quite similar to that of our thickness coupling coefficient curve.

IV. ELASTIC-CONSTANT MEASUREMENTS

The experimental arrangement shown by Fig. 6 is the classical arrangement for investigations of the piezoelectric resonances of a crystal. The high-frequency voltage applied to the crystal is of the order of one thousandth of the coercive voltage.

Few crystals have been found to be uniform enough in thickness to give a very sharp and well-defined thickness resonance. For the same reason, the accuracy in the measurement of the frequency constant for such modes is at present no better than 10 percent. It is about 10^5 cps-cmp, yielding for S_{33} the value

$$S_{33}=\frac{1}{4(tF_r)^2\rho}=4.5\times10^{-12}\ \text{cgs units}.$$

(t is the thickness, F_r is the resonant frequency, and ρ is the density.)

V. SUMMARY

We have found that if a $BaTiO_3$ single crystal goes slowly from one state of polarization to the opposite state, the dielectric constant decreases noticeably with a minimum at zero average polarization. This low value is also observed if the crystal is initially at zero polarization and it can be interpreted as being the "initial" dielectric constant for a crystal plate in which the polarization is normal to the surface of the place. We have interpreted this behavior as being a "clamping" effect due to the multidomain situation that arises. The clamped case corresponds to the initial dielectric constant, the unclamped case is for the dielectric constant at saturation. There is a satisfactory agreement between our measurements and the value expected on this basis by using Merz and Caspari's[2] values of the piezoelectric coefficient d_{33} and our value for the elastic coefficient S_{33}.

A field strength of 350 volts/cm was required to

polarize the crystal from an unpolarized state, whereas a field of 675 volts/cm was required to reverse the direction of polarization. The clamping was more complete for the case where the crystal was forced to zero polarization by walking down the hysteresis loop than for the case where the crystal goes to zero polarization while traversing the hysteresis loop. This indicates that the elementary domains are smaller in the former case than in the latter case. It is interesting to note that the configuration with the smaller domains is less stable than for the larger domains as is evidenced by the observation that a smaller field is required to change the configuration.

Our measurements show no indication of the elementary domain walls moving to any appreciable extent in response to the high-frequency field. Otherwise, the dielectric constant would be expected to increase in the multidomain region.

The temperature dependance of the coefficient of coupling is similar to that computed from earlier measurements.

VI. ACKNOWLEDGMENT

We are indebted to Dr. S. O. Morgan and J. Remeika of the Bell Telephone Laboratories for the crystals used in this study. Our crystals were grown by C. Karan and B. Skinner and the samples were prepared by H. Dunn and E. Davin of our laboratory.

PHYSICAL REVIEW VOLUME 94, NUMBER 6 JUNE 15, 1954

Photomagnetoelectric Effect in Germanium and Silicon

HUBERT BULLIARD*
Electrical Engineering Research Laboratory, University of Illinois, Urbana, Illinois
(Received March 8, 1954)

The transient part of the photomagnetoelectric (p.m.e.) voltage in germanium has been studied. It has been observed that the p.m.e. voltage reached its steady-state value by passing through a maximum instead of reaching it by progressive increase. The p.m.e. effect in silicon has been observed and a few experimental results are given.

I. INTRODUCTION

THE photomagnetoelectric effect first reported by Kikoin and Noskow,[1] and by Groetzinger[2] in cuprous oxide has been observed recently by Aigrain and Bulliard[3] and independently by Moss, Pincherle, and Woodward[4] in germanium. A communication on the effect has been given by Oberly[5] at the 1953 Thanksgiving Meeting at Chicago. It has been observed also in lead sulfide by Moss,[6] and, as will be reported here, in silicon. The effect is the following:

If a slab of semiconductor is illuminated on one face and introduced in a magnetic field parallel to the plane of the slab, then an emf arises in a direction perpendicular to both the light and the magnetic field (Fig. 1). If the light is oriented parallel to the x axis and the field parallel to the y axis, the emf appears along the z axis.

The action of the light is to produce hole-electron pairs near the surface of the semiconductor sample, provided that the wavelength is shorter than 1.8 μ, thus producing a very high concentration of carriers next to the surface. These added carriers tend to diffuse towards the interior of the slab. If a magnetic field is introduced in the direction previously described, the carriers will be deflected, the electrons upward and the holes downward, thus giving rise to an emf between the ends of the slab.

A theoretical derivation of this effect in germanium has been given independently in the papers of Aigrain and Bulliard[3] (more extensively published in Bulliard's thesis[7]) and of Moss, Pincherle, and Woodward.[4] In this paper we describe observations of transient effects in the photomagnetoelectric effect on germanium and some observations of the effect on silicon.

II. TRANSIENTS IN THE PHOTOMAGNETOELECTRIC EFFECT ON GERMANIUM

(a) Experimental Study

The apparatus consisted of a 500-watt lamp, a chopper, and lenses (Fig. 2). The source was focused with the first lens on the chopper in order that the rise time of the light pulse be as short as possible compared to the pulse duration. With the second lens, the source was focused again on the germanium sample. The signal developed across the sample was amplified with a

* On leave from Laboratoire de Physique-Ecole Normale Superieure, Paris, France.

[1] K. Kikoin and M. Noskov, Physik. Z. Sowjetunion **5**, 586 (1934).

[2] G. Groetzinger, Physik. Z. (5), **36**, 169–179 (1935).

[3] P. Aigrain and H. Bulliard, Compt. rend. **236**, 595 and 672 (1953).

[4] Moss, Pincherle, and Woodward, Proc. Phys. Soc. (London) **B66**, 743 (1953).

[5] John J. Oberly, Phys. Rev. **93**, 911 (1954).

[6] T. S. Moss, Proc. Phys. Soc. (London) **B66**, 993 (1953).

[7] Hubert Bulliard, Ann. phys. **9**, 52 (1954).

broad-band amplifier and then displayed on an oscilloscope. The germanium samples had the following characteristics: p type, resistivity; 40 ohms/cm; body lifetime greater than or equal to 600 μsec according to a measurement made by the Valdes method. The thickness was 3 mm, which is of the same order as the diffusion length of the carriers in such a sample. The sample was etched with the *C-P*-4 on both sides.

It was observed that the photomagnetoelectric voltage, instead of reaching the steady-state value by progressive increase, as might be expected, passed through a maximum value and then decreased to reach the steady-state value.

In Fig. 3 are illustrated the wave shapes of the photomagnetoelectric effect and of the photoconductivity.

The transient part was also studied as a function of the light intensity (Fig. 4). The light intensity was

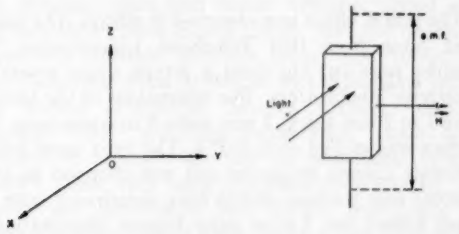

FIG. 1. Orientation of light, magnetic field, and p.m.e. voltage.

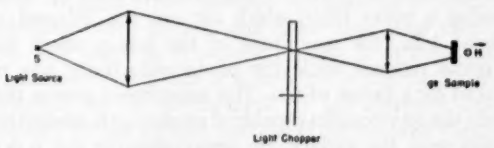

FIG. 2. Optical setup for transient response determination of p.m.e. effect.

varied by increasing the current through the lamp and also by interposing screens of different apertures so as not to change the spectral distribution of the lamp. Both methods gave the same results.

As can be seen from Fig. 2, there is an increase of the ratio peak value to steady value from zero at low light intensity up to a value of four under strong illumination.

It was also observed that if the dark side was ground instead of etched under strong illumination, the value of the photomagnetoelectric voltage increased by a factor of ten, but the peak disappeared.

(b) Physical Interpretation

The p.m.e. voltage gives a current which compensates the one arising from the deflection of carriers due to the magnetic field.

If j_x is the density of current of minority carriers, diffusing in the germanium from the illuminated surface towards the dark surface, and if H = magnetic field and

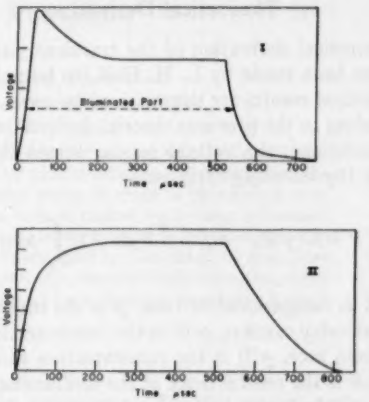

FIG. 3. Typical wave shapes for the photomagnetoelectric effect (I) and photoconductivity (II).

μ = average mobility, the net current arising from the deflection of both types of carriers by a small magnetic field is then

$$2\mu Hh\int_0^l j_x dx,$$

which should be equal to $V_{\text{p.m.e.}}\times G$, where l = thickness of the sample, h = height of the sample, and G = conductance of the sample. One has then:

$$V_{\text{p.m.e.}}=2\mu Hh\int_0^l j_x dx \Big/ G.$$

The p.m.e. voltage increases with the diffusion flow of carriers and decreases with induced photoconductance.

Initially, the diffusion flow builds up more rapidly than the photoconductance and later on is overtaken by the growth of the photoconductance, thus giving rise to an initial increase followed by a drop to an equilibrium value.

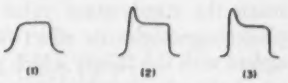

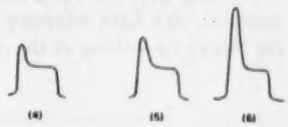

FIG. 4. Wave shape for the photomagnetoelectric effect as a function of light intensity.

Resistance of Original Sample 580 ohms

Average Value of Signal	Resistance of Illuminated Sample
1 - 0.3 mv	550 ohms
2 - 1.8 mv	410 ohms
3 - 5.8 mv	340 ohms
4 - 6.5 mv	250 ohms
5 - 10 mv	180 ohms
6 - 14 mv	50 ohms

(c) Theoretical Derivation

A theoretical derivation of the transient part of the effect has been made by L. H. Hall (to be published). The principal results are summarized below.

According to the previous theories derived for steady-state conditions, the voltage arising across the slab is given by the following expression:

$$V=K|p(0)-p(l)|\Big/N\mu le+2e\int_0^l pdx,$$

where K is independent of time. p is the concentration of the minority carriers, $p(0)$ is the concentration at the illuminated face, $p(l)$ is the concentration at the dark face, $N\mu le$ is the conductance of the unilluminated slab, and $2e\mu\int_0^l pdx$ is the induced conductance due to the illumination.

Both $p(0)-p(l)$ and the induced conductance increase with time. The formula derived for the transient part takes the form:

$$V=K[1-\sum_0^\infty a_i e^{-v_i(t/t_0}]/\{G_0+B[1-\sum_0^\infty b_i e^{-v_i(t/t_0}]\},$$

where G_0 if the conductance of the unilluminated sample and t_0 the lifetime of the minority carriers. It is generally necessary to include only the first few terms. The parameters a_i, b_i, and v_i depend on the characteristics of the sample. With suitable values of the body lifetime and surface recombination, the numerator increases more rapidly than the induced conductance but is then overtaken by the growth of the latter, so that the voltage passes through a maximum and then decreases to the steady-state value.

(d) Correlation between Theory and Experiment

Because of the complicated nature of the theoretical formula, no attempt has been made to correlate the values between the experimental and theoretical values. However, a few remarks can be made.

The fact that the time for the photoconductivity to reach the steady-state value is the same as for the photomagnetoelectric effect (as can be seen in Fig. 3), agrees with the theory which predicts that the building up of the photoconductivity accounts for the decrease from the maximum value.

The fact that the ratio peak value to steady value increases with light intensity can be accounted for by the theory by looking at the denominator of expression 1. Under low illumination, the conductance of the unilluminated slab is far greater than the induced conductance. Thus the denominator of this expression is practically constant, and one should not observe any maximum but a progressive increase.

The greater the illumination, the more important the induced conductance compared with the conductance of the unilluminated sample and thus the greater the ratio of the peak to steady-state value.

The last remark concerns the fact that when the dark surface is ground so as to increase surface recombination, the value of the p.m.e. effect increases and the peak disappears. The increase of the p.m.e. effect is due to the fact that the term $p(0)-p(l)$ is greater for a dark surface ground than etched, and the fact that the peak disappears can be accounted for by a reduction of the average lifetime of the sample.

III. PHOTOMAGNETOELECTRIC EFFECT IN SILICON

The p.m.e. effect was observed in silicon. The silicon used came from Bell Telephone Laboratories. The samples were cut out from a p-type single crystal of resistivity 20 ohms/cm. The dimensions of the samples were 1 to 2 mm thick, 2 mm wide, 8 to 6 mm long. The surface was etched with *C-P-4*. The light came from a 500-watt cinema projector and was chopped so as to prevent any thermal effects from interfering with the effect looked for. Under quite intense illumination of the sample, the magnitude of the p.m.e. voltage was of the order of 1 Mv. It was observed that by interposing a water filter, which cut out the infrared at about 1.2μ, the magnitude of the p.m.e. effect was slightly reduced while the photoconductivity was reduced by a factor of ten. This experiment proves that only the wavelengths capable of producing hold-electron pairs near the surface are responsible for the p.m.e. effect.

A remark should be made as to the application to silicon of the theoretical derivation worked out for germanium. In this derivation the space-charge of trapped electrons is neglected, and this may not be a good approximation for silicon.

ACKNOWLEDGMENTS

The author is very grateful to Professor John Bardeen for permitting him to work in his laboratory, and for fruitful discussions and guidance all along the course of this work, as well as to L. H. Hall for the theoretical derivation mentioned in part II.

Energy Transfer in Organic Phosphors*

J. B. Birks†
Physics Department, Rhodes University, Grahamstown, South Africa
(Received June 29, 1953; revised manuscript received March 12, 1954)

A quantitative theory is developed of the photofluorescence and scintillation properties of organic materials. On this theory the intermolecular energy transfer occurs by photon emission and absorption; the molecular emission spectrum extends continuously from the ionization energy E_I down to the strong fluorescence band normally observed; the emission of primary photons $\sim E_I$ is excited by ionizing radiations; and the subsequent scintillation process consists of a photon cascade, through the emission spectrum. The theory is in agreement with the experimental data on the photofluorescence and scintillations from pure and mixed crystals, and on the scintillations from solutions. It is shown that, because of self-absorption, many of the existing data refer only to the technical fluorescence properties, and a preliminary assessment is made of the molecular properties of the more important organic phosphors.

1. INTRODUCTION

VARIOUS studies[1] of the photofluorescence and scintillation properties of different organic phosphor systems—pure and mixed crystals, liquid and solid solutions—have shown clearly that the observed fluorescence emission generally occurs from molecules other than those initially excited by the incident radiation. Several alternative theories, notably "exciton migration"[2] and "sensitized fluorescence,"[3] have been proposed to account for this intermolecular energy transfer. These have been discussed elsewhere by the author,[1] and they have been shown inadequate to explain the full range of experimental data now available. In particular these theories postulate *strong* electronic coupling either between neighboring or distant molecules, while spectral and other data show clearly that such coupling in organic crystals is so *weak* that the electronic structure of a molecule is practically unperturbed by its environment. It has therefore been proposed by the author[1] that the intermolecular energy transfer occurs by the simple process of *photon emission and absorption*.

In this paper the photon theory is developed further, and compared with the experimental results. It is shown that many of the previous observations on the photofluorescence and scintillation properties of organic materials refer only to the *technical* properties of the materials. Such observations, made on relatively thick specimens, give little direct information about the true *molecular* fluorescence, due to the strong self-absorption which occurs.

2. PHOTOFLUORESCENCE OF MIXED CRYSTALS

We consider initially the photofluorescence of mixed organic crystals (e.g., anthracene in naphthalene, naphthacene in anthracene). On the photon emission and absorption theory, the processes listed in Table I occur in a mixed crystal containing solute molecules Y in a solvent of molecules X. It is assumed for simplicity and clarity that the incident radiation is absorbed entirely by X, and that X is transparent to the fluorescence emission of Y. These conditions correspond to those normally obtaining in relatively dilute solid solutions. Square brackets indicate concentrations in molecules/solvent molecule (i.e., $[X]=1$), X^* and Y^* represent molecules of X and Y with the excitation energy, and $k(=1/t)$ represents the probability of a process of decay time t.

The *molecular* quantum efficiency q_{0X} of fluorescence by X is given by

$$q_{0X}=\frac{1}{1+(k_{iX}/k_{fX})}, \tag{1}$$

as a result of the competitive processes (2) and (3). The quantum efficiency of the *escape* of the fluorescence of X from the crystal, i.e., the *technical* fluorescence quantum efficiency, is given by

$$q_{eX}=\frac{q_{0X}}{1+(k_X/k_{eX})+(k_Y/k_{eX})[Y]} + \frac{k_X}{k_{eX}}\left(\frac{q_{0X}}{1+(k_X/k_{eX})+(k_Y/k_{eX})[Y]}\right)^2 + \left(\frac{k_X}{k_{eX}}\right)^2\left(\frac{q_{0X}}{1+(k_X/k_{eX})+(k_Y/k_{eX})[Y]}\right)^3 + \cdots \tag{2}$$

$$=\frac{q_{0X}}{1+(1-q_{0X})(k_X/k_{eX})+(k_Y/k_{eX})[Y]} \tag{3}$$

due to the competitive processes (2), (3), (4), (5), and (9). Terms 1, 2, 3, $\cdots$ in (2) represent the escape of light from the crystal after 1, 2, 3, $\cdots$ molecular emissions.

* This paper forms part of a thesis accepted for the degree of Doctor of Science by the University of Glasgow.
† Now at British Dielectric Research, London W. 12, England.
[1] J. B. Birks, *Scintillation Counters* (Pergamon Press, London; McGraw-Hill Book Company, Inc., New York, 1953).
[2] Bowen, Mikiewicz, and Smith, Proc. Phys. Soc. (London) **A62**, 26 (1949).
[3] J. Franck and R. Livingston, Revs. Modern Phys. **21**, 505 (1949).

TABLE I. Photon transfer processes.

Process	Relative rate	Description of process
1. $X+h\nu\rightarrow X^*$	1	Excitation by light
2. $X^*\rightarrow X+h\nu_X$	$k_{fX}[X^*]$	Fluorescence of X
3. $X^*\rightarrow X$	$k_{iX}[X^*]$	Internal quenching of X
4. $X+h\nu_X\rightarrow X^*$	$k_X k_{fX}[X^*]$	Self-absorption of X
5. $Y+h\nu_X\rightarrow Y^*$	$k_Y k_{fX}[X^*][Y]$	Absorption of Y
6. $Y^*\rightarrow Y+h\nu_Y$	$k_{fY}[Y^*]$	Fluorescence of Y
7. $Y^*\rightarrow Y$	$k_{iY}[Y^*]$	Internal quenching of Y
8. $Y+h\nu_Y\rightarrow Y^*$	$k_Y' k_{fY}[Y^*][Y]$	Self-absorption of Y
9. $h\nu_X\rightarrow$	$k_{eX}k_{fX}[X^*]$	Escape of $h\nu_X$
10. $h\nu_Y\rightarrow$	$k_{eY}k_{fY}[Y^*]$	Escape of $h\nu_Y$

In these relations (k_{iX}/k_{fX}) describes the internal quenching, which reduces the molecular quantum efficiency q_{0X} below unity. $(1-q_{0X})(k_X/k_{eX})$ represents the effect of self-absorption of X, which together with the internal quenching produces "self-quenching." $(k_Y/k_{eX})[Y]$ describes the relative probability of photon capture by Y, i.e., energy transfer from X to Y. In the absence of internal quenching $q_{0X}=1$, and (3) becomes

$$q_{eX}=\frac{1}{1+(k_Y[Y]/k_{eX})}. \tag{4}$$

The *molecular* fluorescence quantum efficiency q_{0Y} of Y is, similarly,

$$q_{0Y}=\frac{1}{1+(k_{iY}/k_{fY})}, \tag{5}$$

and the *technical* quantum efficiency q_{eY} of the escape of the fluorescence of Y is given by

$$q_{eY}=\frac{q_{eX}q_{0Y}(k_Y/k_{eX})[Y]}{1+(1-q_{0Y})(k_Y'/k_{eY})[Y]}. \tag{6}$$

(k_{iY}/k_{fY}) describes the internal quenching of Y. $(1-q_{0Y})(k_Y'/k_{eY})[Y]$ represents the effect of self-absorption, which together with the internal quenching produces "concentration quenching." In the absence of internal quenching, $q_{0X}=q_{0Y}=1$, and (6) becomes

$$q_{eY}=q_{eX}(k_Y/k_{eX})[Y]=1-q_{eX}. \tag{7}$$

The quantities k_{eX}, k_X, and $k_Y[Y]$ are not independent, but are related by

$$k_{eX}+k_X+k_Y[Y]=1. \tag{8}$$

Their magnitudes depend on the relative absorption coefficients of X and Y for the fluorescence of X, and on the size of the crystal. For a pure crystal ($[Y]=0$) of anthracene of thickness $\geqslant 1$ mm, values of $k_{eX}=0.2$, $k_X=0.8$ have been obtained from spectral measurements,[4] and similar observations on thick naphthalene crystals indicate that k_{eX} is even smaller for this material. The effect of this self-absorption of X is to increase the "energy transfer" parameter (k_Y/k_{eX}), since the molecules of Y may absorb not only the primary emission of X, but subsequent re-emissions following self-absorption. The observations of Bowen *et al.*[2] that the transfer effect disappears when the mixed crystals are dissolved in benzene are readily explained, since the effective concentration of Y for photon absorption should now be expressed in molecules/*benzene* molecule, so that $[Y]\rightarrow 0$ and $k_{eX}\rightarrow 1$.

A further factor contributing to the efficient $(X\rightarrow Y)$ energy transfer in the crystal is the directional alignment of the molecules of X and Y, and of the polarizations of the emission of X and the absorption of Y.[1] If the molecular alignment is destroyed, as in homogeneous mixed sols of X and Y, the effective absorption coefficient of Y for the emission of X will be reduced due to the random molecular orientation, by a factor

$$f=\frac{\int_0^{\frac{1}{2}\pi}\int_0^{\frac{1}{2}\pi}\cos^2\theta\cos^2\phi\,d\theta d\phi}{\int_0^{\frac{1}{2}\pi}\int_0^{\frac{1}{2}\pi}d\theta d\phi}=0.25, \tag{9}$$

relative to that for alignment of Y parallel to X. Bowen and Mikiewicz[5] have measured the intensities of the two fluorescence components L_X and L_Y for anthracene-naphthacene crystals, and for homogeneous anthracene-naphthacene sols. They find that $L_X=L_Y$ at a concentration of $\sim 1.8\times 10^{-5}$ g naphthacene/g anthracene in the crystals, and at a concentration of $\sim 9\times 10^{-5}$ g/g in the sols, giving $f\sim 0.2$ in agreement with (9).

The equations obtained on the photon theory are in general agreement with the available experimental data on mixed organic crystals[2,6,7] though further observations on the effect of crystal size are desirable. The theory gives a clear physical interpretation of the processes of "resonance energy transfer," self-quenching, and concentration quenching, for which several more complex and less satisfactory mechanisms have been proposed.[2,3,6-10]

3. SCINTILLATIONS FROM MIXED CRYSTALS AND SOLUTIONS

An extension of the photon theory has been proposed by the author[1] in considering the excitation of the fluorescence by ionizing radiation, i.e., scintillations. It is proposed that the ionization and excitation of the molecules by the ionizing particle cause the emission of photons whose energy is $\sim$ the molecular ionization energy. This primary photon emission is discussed in more detail later. The absorption coefficient for these

[4] J. B. Birks and W. A. Little, Proc. Phys. Soc. (London) **A66**, 921 (1953).

[5] E. J. Bowen and E. Mikiewicz, Nature **159**, 706 (1947).

[6] G. T. Wright, Ph.D. thesis, University of Birmingham, 1952 (unpublished).

[7] G. T. Wright, Proc. Phys. Soc. (London) **A66**, 777 (1953).

[8] P. Pringsheim, *Fluorescence and Phosphorescence* (Interscience Publishers, New York, 1949).

[9] H. Kallmann and M. Furst, Phys. Rev. **79**, 857 (1950).

[10] H. Kallmann and M. Furst, Phys. Rev. **81** 853 (1951).

primary photons is relatively low (molar extinction coefficient $\epsilon \sim 10^2$) and they are reabsorbed at $\sim 10^4$ molecular distances from the ionization column.

In a mixed crystal, or in a liquid solution of Y in a solvent X, the primary photons will excite the photofluorescence of X and Y. If p primary photons are produced and are completely absorbed within the phosphor, the number of fluorescence photons $h\nu_X$, $h\nu_Y$ escaping are given by pq_{eX} and pq_{eY}, respectively. Hence for mixed crystals it is to be expected that the relative intensities of the two fluorescence components will be independent of the manner of excitation. This has been confirmed experimentally for naphthalene-anthracene crystals by Wright[6,7] who compared the fluorescence excited by α rays and by 254-mμ ultraviolet radiation, and by the author,[1] who has compared the fluorescence excited by α rays and by the internal conversion electrons from In^{114}. In each case the ratio of the intensities of the naphthalene and anthracene components was found to be independent of the mode of excitation.

For liquid organic solution phosphors pq_{eX}, the solvent fluorescence, is small because of strong self-absorption and internal quenching. The solute fluorescence, which is observed, is given by

$$L_Y = pq_{eY} = \frac{pq_{0X}q_{0Y}(k_Y/k_{eX})[Y]}{[1+(1-q_{0X})(k_X/k_{eX})+(k_Y/k_{eX})[Y]][1+(1-q_{0Y})(k_Y'/k_{eY})[Y]]} \tag{10}$$

$$= \frac{P[Y]}{(Q+[Y])(R+[Y])}, \tag{11}$$

where P, Q, and R are parameters depending on the mode of excitation, and on the properties of the solvent and solution. Equation (11) is the empirical equation found by Furst and Kallman[11] to be in excellent agreement with their experimental observations on the dependence of relative scintillation efficiency L_Y on concentration $[Y]$ for a wide range of organic solutions, excited by γ rays or by α rays.

It should be noted however that (10) is derived from (6), which is based on the initial postulate that the incident radiations, in this case the p primary photons, are absorbed entirely by the solvent molecules X. If the absorption coefficient of Y for the primary photons is high compared with that of X, direct excitation of Y by the primary photons will also occur. It may be readily shown by a similar analysis to that in Sec. 2, that the additional fluorescence component is also of the form

$$L_Y' = \frac{P'[Y]}{(Q'+[Y])(R'+[Y])}, \tag{12}$$

the first term in the denominator representing the competition between absorption by X and by Y, and the second term the competition between concentration quenching and the escape of the fluorescence emission.

All the efficient solvents used (e.g., xylene, toluene, benzene) possess molecules which fluoresce in dilute solution, although this fluorescence is not normally observed from the bulk liquid due to "self-quenching." This association of solvent molecular fluorescence with scintillation efficiency suggests that the main process in liquid phosphors is the initial excitation of the solvent molecules leading to fluorescence emission, which is absorbed and re-emitted by the solute molecules, as described by (10) and (11). The much lower scintillation efficiency[9] of solutions of terphenyl in "nonfluorescent" solvents (paraffin oil, hexane, etc.) is attributable to the fact that the solute fluorescence will only be excited directly by primary photon absorption, as described by (12). Since the scintillation efficiency of terphenyl in a nonfluorescent solvent is only about 15 percent of that from a terphenyl solution in a fluorescent solvent, it appears that about 85 percent of the solute emission in the latter case is excited by the solvent emission. The alternative possibility, that the differences between the two classes of solvent are due to differences in the primary photon emission efficiency (which may be associated with the fluorescence efficiency) and in the absorption coefficients for these primary photons [P' and Q' in (12)], cannot however be discarded on the existing experimental evidence.

[11] M. Furst and H. Kallmann, Phys. Rev. **85**, 816 (1952).

4. PHOTOFLUORESCENCE OF PURE CRYSTALS

In pure crystal phosphors only processes (1), (2), (3), (4), and (9) in Table I are operative. The molecular quantum efficiency q_0 (suffix X will be omitted since only one molecular species is present) is given by (1) as before, but the technical quantum efficiency q_e from (2) becomes

$$q_e = \frac{q_0}{1+(1-q_0)(k/k_e)} = \frac{1}{1+(k_i/k_e k_f)}, \tag{13}$$

since $(k+k_e)=1$.

In the absence of internal quenching, the molecular photofluorescence decay time $(t_f)_{00}=1/k_f$. Due to internal quenching, the actual *molecular* decay time $(t_f)_0$ is reduced to

$$(t_f)_0 = \frac{(t_f)_{00}}{1+[(t_f)_{00}/t_i]} = q_0(t_f)_{00}. \tag{14}$$

The *technical* photofluorescence decay time t_f of a thick crystal is increased,[4] due to the self-absorption, to

$$t_f=\frac{(t_f)_{00}}{k_e+[(t_f)_{00}/t_i]}. \tag{15}$$

If the internal quenching is small, i.e., $(t_f)_{00}\ll t_i$, then (15) and (13) may be approximated to

$$t_f=n(t_f)_0, \tag{16}$$

$$q_e=(q_0)^n, \tag{17}$$

where

$$n=1/k_e \tag{18}$$

represents the average number of molecular fluorescence emissions of decay time $(t_f)_0$, quantum efficiency q_0, that occur prior to the escape of the fluorescence from the crystal. These approximate relations provide a simple physical model of the photon cascade process that occurs.

For anthracene at room temperature, values of $q_0=0.9$ and $(t_f)_0=3.5\pm1.0$ mμ sec have been observed for microcrystalline specimens, $t_f=14\pm2$ mμ sec has been measured for a thick crystal, and $k_e=0.2$ has been obtained from the ratio of the areas under the thick crystal (technical) and micro-crystalline (molecular) fluorescence spectra.[4] Substitution in (13)–(15) gives $(t_f)_{00}=3.9\pm1.2$ mμ sec, $t_i=35\pm10$ mμ sec, $q_e=0.58$ and $t_f=12.6\pm3.5$ mμ sec, this last value agreeing within the experimental error with that observed directly. The approximate Eqs. (16)–(18) give $n=5$, $t_f=17.5\pm5.0$ mμ sec and $q_e=0.59$.

The photofluorescence quantum efficiency q_0 is practically independent of the excitation wavelength down to at least 250 mμ, i.e., into the second and higher electronic absorption bands. This effect has been interpreted previously[6] as due to internal conversion with 100 percent efficiency from the higher electronic states into the first electronic excited state, from which the observed emission occurs. This explanation is not completely satisfactory, since it fails to explain why the absorption from the ground state into the higher electronic states should be highly "allowed" ($\epsilon\sim10^4-10^5$) while the reverse transition, corresponding to emission, should be completely "forbidden." The photon theory suggests a simple alternative description of the effect. Fluorescence emission from these higher electronic states may occur with an ultra-short decay time $\sim10^{-11}$ sec, since the oscillator strengths are $\sim10^2-10^3$ that of the normal photofluorescence emission corresponding to the 1st electronic absorption band ($\epsilon\sim10^5$). The internal quenching will be negligible, owing to the very short lifetime of the excited state compared with $t_i\sim35$ mμ sec, and the quantum efficiency will be practically 100 percent. Such emitted photons will be very strongly reabsorbed by neighboring molecules, and after several repetitions of the process, during which thermal degradation of the excess energy occurs, the normal fluorescence from the 1st excited state will be observed.

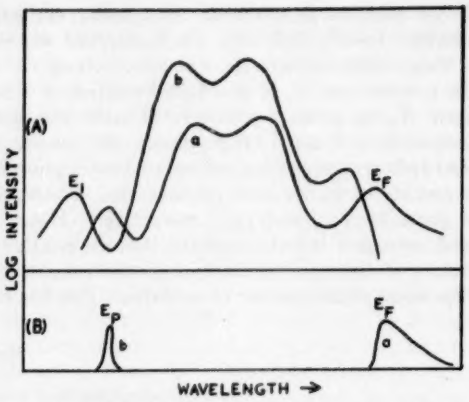

FIG. 1 (A). Molecular spectrum; (*a*) fluorescence, (*b*) absorption. (B). Technical fluorescence spectrum of crystal of a few μ thickness; (*a*) normal emission, (*b*) primary photon emission.

It is proposed therefore that the *complete* molecular fluorescence spectrum corresponds to the *complete* absorption spectrum, and not just to the first electronic band, which is all that has been observed previously. This failure to observe the complete emission spectrum may be due to various causes: (a) the use of relatively thick crystals or solutions, (b) inadequate exposure times or detection sensitivity, and (c) excitation of the fluorescence by irradiation in the first electronic absorption band (e.g., by 365-mμ radiation). Each emission band would be expected to be approximately the mirror image of the corresponding absorption band, but with its maximum intensity shifted by about 50 mμ towards longer wavelengths. A schematic diagram of the proposed *molecular* fluorescence and absorption spectrum is shown in Fig. 1(A). Both spectra extend from about the molecular ionization energy E_I down to the energy E_F of the first electronic transition. Measurements on the molecular spectra of microcrystalline fluorescent organic compounds are in progress in the author's laboratory.

Because of the overlap of the molecular absorption and emission spectra, the *technical* fluorescence from a relatively thick specimen ($>1\mu$) will only be observed in spectral regions of low absorption. Apart from the region near E_F, where the normal technical fluorescence is observed, there is a further region of low absorption ($\epsilon\leqslant10^2$) in the vacuum ultraviolet[12] near E_I. Photons emitted in this region have a relatively long mean free path $\sim7\mu$ in the crystal, so that when near the crystal surface they are able to escape without reabsorption. These are the primary photons of energy E_P, whose emission is excited by ionizing radiation, according to the theory.[1] The decrease of specific fluorescence near the phosphor surface[13] is attributed to the escape of the primary photons.[14,1] The *technical* fluorescence spectrum

[12] H. B. Klevens and J. R. Platt, J. Chem. Phys. **17**, 470 (1949).
[13] J. W. King and J. B. Birks, Phys. Rev. **86**, 568 (1952).
[14] J. B. Birks, Phys. Rev. **86**, 569 (1952).

of a crystal a few microns thick is shown schematically in Fig. 1(B). It will be noted that there are *two* main regions of emission, E_P and E_F.

5. SCINTILLATIONS FROM PURE CRYSTALS

In a thicker crystal, excited by ionizing radiation, the emission E_P is unable to escape. The scintillation process corresponds to the reabsorption of the primary photons E_P, followed by a cascade of photon emissions and absorptions, culminating in the normal emission E_F which ultimately escapes from the crystal. For excitation by fast electrons, the ion pairs are produced ~100 molecular distances apart, so that quenching in the ionization column is negligible. Under these conditions the decay of the scintillation pulses has been observed to be exponential and of technical scintillation decay time t_I. We may therefore, by analogy with the previous photofluorescence results, take

$$t_I = t_P + t_f, \tag{19}$$

where t_f is the technical photofluorescence decay time, and t_P the technical decay time of the primary photon emission. The decay times of the emission in the intermediate region of high absorption are negligible, compared with t_f and t_P. Liebson, Bishop, and Elliot[15] have measured t_I for γ-ray excitation and for several organic phosphors, and they find in general that $t_I > t_f$ in accordance with (19). Typical values of t_f and t_P obtained from their results, using (19), are listed in Table II.

It is seen that in general $t_P \sim t_f$. It is of importance to note that t_P is a property of the phosphor, similar to t_f. This suggests strongly that the primary photon emission is not due simply to ion recombination, which should take about the same time in similar organic materials, but that it is due to a definite electronic transition of the molecule, as proposed above. The similarity of t_P and t_f is attributable to the similarity of the extinction coefficients and oscillator strengths of the absorption bands E_P and E_F associated with the two transitions. We may therefore take as a working approximation, that

$$(t_P)_0 = (t_f)_0, \tag{20}$$

where $(t_P)_0$ is the molecular decay time of the primary photon emission. Hence, provided t_i, the internal quenching decay time, does not differ appreciably for the two excited states, corresponding to E_P and E_F, the molecular quantum efficiency of the primary photon emission will also be equal to q_0.

By analogy with (16),

$$t_I = m(t_f)_0, \tag{21}$$

where m is the average number of photon emissions of molecular decay time $(t_f)_0$, molecular quantum efficiency q_0, occurring in the photon cascade. Hence the technical scintillation quantum efficiency is

$$q_I = (q_0)^m, \tag{22}$$

expressed as the number of escaping fluorescence photons per initial primary photon.

TABLE II. Decay time components.

	Anthracene	Carbazole	Stilbene	Quaterphenyl	Diphenylacetylene
t_f (mμ sec)	17	7	3.1	3.8	2.5
t_P (mμ sec)	13	6	4.9	3.2	1.5

The energy expenditure per ion pair in gaseous organic materials (e.g., ethylene, methane) is $E_i = 30$ ev/ion pair. It is a reasonable assumption that one primary photon is produced per ion pair (in the absence of quenching in the ionization column) so that $E_i = 30$ ev/primary photon. These primary photons are absorbed and ultimately emitted as the technical fluorescence emission, of mean photon energy E_F, with an over-all technical quantum efficiency of q_I. Hence for excitation by radiation of low specific ionization the over-all technical energy conversion efficiency,

$$C_{IF} = E_F q_I / E_i. \tag{23}$$

Expressed alternatively, the energy expenditure per emitted photon is

$$E_{IF} = E_i / q_I. \tag{24}$$

6. DISCUSSION OF THE ORGANIC PHOSPHORS

For anthracene crystals at room temperature, values of $t_I = 27$ mμ sec, $(t_f)_0 = 3.5$ mμ sec and $q_0 = 0.9$ have been observed. Hence from (21) and (22), $m = 7.7$ and $q_I = 0.44$. The mean wavelength[16,17] of the technical emission spectrum is 469 mμ, corresponding to a mean photon energy $E_F = 2.65$ ev. Hence from (23) and (24), $C_{IF} = 4.0$ percent, $E_{IF} = 68$ ev/photon. This value for the absolute scintillation efficiency of anthracene at room temperature is in excellent agreement with the experimental values of 65 ev/photon measured by Harrison,[17] and of 70.5 ev/photon measured by Birks and Szendrei.[16]

The technical scintillation efficiency q_I is increased by reducing the crystal thickness. For anthracene microcrystals m tends to 2, corresponding to one primary photon emission and one photofluorescence emission, and E_{IF} tends to a lower limit of 36 ev/photon. Because of the surface escape of primary photons this optimum efficiency cannot be attained, but thin anthracene flakes have a higher scintillation efficiency than thick crystals, tending towards this value. The effect has been observed in this laboratory.

Reduction of the temperature also causes an increase in q_I due to (a) the reduced overlap of the absorption and emission spectra, giving a decrease in m, and (b) the decrease in the internal quenching so that q_0

[15] Liebson, Bishop, and Elliot, Phys. Rev. **80**, 907 (1950).

[16] J. B. Birks and M. E. Szendrei, Phys. Rev. **91**, 197 (1953).

[17] F. B. Harrison, Nucleonics **10**, No. 6, 40 (1952).

tends to unity, as the temperature approaches absolute zero. For thick anthracene crystals (a) is the major effect, since q_0 only increases from 0.9 towards 1.0, while m decreases from 7.7 towards 2. Liebson[18] has observed that t_I for anthracene decreases by about 56 percent in cooling from 10°C to −70°C. Neglecting the small change in q_0, we obtain from (21) and (22) that at −70°C $m=4.3$, $q_I=0.64$, corresponding to a 44 percent increase over the scintillation efficiency at 10°C. Sangster[19] has observed directly that the scintillation efficiency increases by 40 percent in cooling over this temperature range.

Anthracene is the most efficient of the known organic scintillators at room temperature. It is of interest therefore to consider the reasons for the inferiority of the other organic phosphors. If we denote the properties of anthracene by $(q_I)_A$, $(q_0)_A$, and m_A, the other phosphors may be divided into 4 possible categories:

(A) $q_0\sim(q_0)_A$, $m>m_A$, $q_I<(q_I)_A$;
(B) $q_0<(q_0)_A$, $m<m_A$, $q_I<(q_I)_A$;
(C) $q_0<(q_0)_A$, $m>m_A$, $q_I<(q_I)_A$;
(D) $q_0\sim(q_0)_A$, $m<m_A$, $q_I>(q_I)_A$.

Examples of each of the first 3 categories are known. So far no organic members of the desirable category (D) have been identified, although sodium iodide (thallium) is an inorganic member of this class.

Naphthalene probably belongs to class (A). Taking $q_0=0.9$, $(t_f)_0=3.5$ mμ sec, by analogy with anthracene, and combining these with the experimental values of $t_I=80$ mμ sec and $E_F=3.6$ ev, we obtain $m=23$, $q_I=0.09$, $C_{IF}=1.0$ percent, and $E_{IF}=341$ ev/photon, in excellent agreement with the direct experimental value[17] of $E_{IF}=350$ ev/photon. The major difference between the technical and microcrystalline emission spectra of naphthalene, due to the self-absorption associated with the high value of m, has been observed.[20] It is to be expected that a major increase in q_I for naphthalene will be produced by reducing the thickness or the temperature. The former effect has been observed for naphthalene flakes by the author, and has previously been reported by Kallmann.[21] The temperature effect, which is pronounced, has been observed by Liebson.[18] At low temperatures the scintillation efficiency of naphthalene approaches that of anthracene.

Stilbene, terphenyl, diphenylacetylene, and quaterphenyl belong to class (B). The reduced overlap of the absorption and emission spectra ($m<m_A$) accounts for their low scintillation decay time t_I of 6 to 10 mμ sec, since their molecular decay time $(t_f)_0$ is similar to anthracene.[4] Although the experimental data for stilbene are less comprehensive than for anthracene, they may be used to estimate the other properties of the material. Birks and Little[4] have observed $(t_f)_0=1.7$ mμ sec, $t_f=3.0$ mμ sec, and Post and Shiren[22] and Lundby[23] have observed $t_I=6.0$ mμ sec, so that $m\sim3.5$. Sangster[19] has observed that C_{IF} for stilbene at room temperature is 0.45 that of anthracene, giving $C_{IF}=1.8$ percent, and that the mean wavelength of the technical emission spectrum is 410 mμ, so that $E_F=3.0$ ev. These values substituted in the appropriate equations give $q_I\sim0.18$, $q_0\sim0.6$, $(t_f)_{00}\sim3$ mμ sec. Different values of t_I and C_{IF} have been reported by other observers, and it is hoped to obtain more accurate data by observations of the main parameters for single specimens. It is to be expected that the decay time and scintillation efficiency of stilbene would show a smaller variation with temperature than anthracene, due to the smaller value of m, and this has been observed experimentally.[18,19,22]

Terphenyl and diphenylacetylene have rather similar properties to stilbene, but data on $(t_f)_0$ are not yet available so that q_0 cannot be evaluated. Quaterphenyl is of interest, as C_{IF} is 0.83 that of anthracene, while t_I is only 8.5 mμ sec.[19] The very slight increase[19] of only 7 percent in C_{IF} in cooling from 30°C to −70°C suggests that the self-absorption is negligible, and hence the experimental value[15] of $t_f=3.8$ mμ sec may be taken as approximately equal to $(t_f)_0$. Hence $m\sim2.2$, $q_I\sim0.38$, giving $q_0\sim0.65$. If q_0 increases with molecular chain length while m remains small, then the higher compounds quinquephenyl and sexiphenyl may have a higher scintillation efficiencies than anthracene as suggested by Sangster,[19] and hence belong to category (D). The existing experimental evidence suggests, however, that at room temperature $q_0\sim0.6$ for the polyphenyl compounds, compared with $q_0\sim0.9$ for the polycyclic compounds like naphthalene and anthracene.

The following tentative allocations are suggested for other phosphors for which data on q_I and t_I are available:[19] phenanthrene (B), chrysene (C), pyrene (A), fluoranthene (C), or (A), fluorene (C), carbazole (B), diphenylene oxide (B), bibenzyl (B), diphenylbutadiene (B).

7. CONCLUSION

The discussion above, based on existing experimental data, represents a preliminary attempt to compare the *molecular* properties of the different compounds. Now that these can be differentiated from the technical data reported hitherto, it is hoped to correlate the fluorescence properties of the organic molecules with their π-electron configurations.

The molecular properties $(t_f)_0$ and q_0 can be obtained from measurements on microcrystalline specimens, and from these $(t_f)_{00}$ and t_i can be deduced. The technical photofluorescence properties t_f and q_e can be obtained

[18] S. H. Liebson, Nucleonics **10**, No. 7, 41 (1952).
[19] R. C. Sangster, Massachusetts Institute of Technology Technical Report 55, January 1, 1952 (unpublished).
[20] W. A. Little and J. B. Birks, Congress of the South African Association for the Advancement of Science, Cape Town, South Africa, July, 1952 (unpublished).
[21] H. Kallmann, Conference on Scintillation Counting, 1949 (unpublished).
[22] R. F. Post and H. S. Shiren, Phys. Rev. **78**, 80 (1950).
[23] A. Lundby, Phys. Rev. **80**, 477 (1950).

from similar measurements on thick crystals, and by comparison with the molecular properties, $n=1/k_e$ can be found. n may also be determined from a comparison of the molecular and technical photofluorescence spectra. The technical scintillation properties l_I and q_I can also be observed directly, and the related quantities m, l_P, and $(l_P)_0$ deduced. The direct measurement of these latter parameters is difficult. An experimental investigation is in progress to determine the main properties of interest for a large group of related organic fluorescent compounds.

The photon cascade theory provides a quantitative description of the fluorescence and scintillation properties of organic phosphors which is in excellent agreement with experiment. When considered in conjunction with the other experimental data discussed elsewhere,[1] the results provide strong evidence of the validity of the photon theory of energy transfer.

PHYSICAL REVIEW VOLUME 94, NUMBER 6 JUNE 15, 1954

Moduli and Internal Friction of Magnetite as Affected by the Low-Temperature Transformation

M. E. FINE AND NANCY T. KENNEY
Bell Telephone Laboratories, Murray Hill, New Jersey

(Received March 15, 1954)

The low-temperature ordering transformation in magnetite is the source of large nonelastic effects. For example, Young's modulus for the ⟨111⟩ direction at 108°K is 30 percent lower than the value one would estimate from higher-temperature measurements; an internal friction peak occurs near 95°K. We have attributed the nonelastic effects to stress-induced ordering of Fe^{++} and Fe^{+++} among the octahedral sites in the lattice.

A SECOND-ORDER transformation with critical temperature near 115°K occurs in magnetite[1–14] and has been attributed to ordering[2,3] of Fe^{++} and Fe^{+++} among the octahedral sites of the magnetite structure (spinel type). The symmetry changes from cubic to orthorhombic on cooling.[5] In certain crystallographic directions this transformation, we find, is accompanied by large effects in the moduli and internal friction. Stress-induced ordering is proposed as the explanation.

For our measurements two rods were prepared from a natural occurring magnetite single crystal containing 20.7 percent Fe^{++} and, as an impurity, 1.2 percent Zn (stochiometric Fe_3O_4 has 24.2 percent Fe^{++}). The long direction of one rod was parallel to a ⟨100⟩ direction; the long direction of the other was parallel to a ⟨111⟩ direction. Young's modulus of ⟨111⟩ and ⟨100⟩, the torsion modulus of ⟨100⟩, and the internal friction in each case were determined as functions of temperature and external magnetic field by the resonant vibration method. Both electromagnetic[15,16] and piezoelectric[17,18] excitation and detection of vibrations were employed. The strain amplitudes were approximately 10^{-7}, the frequency range, 50 to 130 kc/sec.

DATA AND INTERPRETATION

The moduli of crystalline solids are expected to increase on cooling approaching asymptotically a maximum value at very low temperatures, provided there is no change of state and all of the strains are elastic. Magnetite has a transformation. Furthermore, two sources of nonelastic strain are probably present, stress-induced domain motion (magnetostriction)[19,20] and stress-induced ordering of Fe^{++} and Fe^{+++} among the octahedral sites. Thus, for a given applied stress (σ), the total strain (ϵ) is given by (1).

$$\epsilon=\epsilon_{\text{elastic}}+\epsilon_{\text{domain-motion}}+\epsilon_{\text{ordering}}=\epsilon_1+\epsilon_2+\epsilon_3. \quad (1)$$

The observed modulus,

$$M=\frac{\sigma}{\epsilon}=\frac{\sigma}{\epsilon_1+\epsilon_2+\epsilon_3}, \quad (2)$$

is thus less than the truly elastic value.

[1] E. J. W. Verwey, Nature **144**, 327 (1939).
[2] E. J. W. Verwey and P. W. Haayman, Physica **8**, 979 (1941).
[3] Verwey, Haayman, and Romeijn, J. Chem. Phys. **15**, 181 (1947).
[4] C. A. Domenicali, Phys. Rev. **78**, 458 (1950).
[5] S. C. Abrahams and B. A. Calhoun, Acta Cryst. **6**, 105 (1953).
[6] R. W. Millar, J. Am. Chem. Soc. **51**, 215 (1929).
[7] G. S. Parks and K. K. Kelley, J. Phys. Chem. **30**, 47 (1926).
[8] P. Weiss and R. C. Forrer, Ann. Physik [10] **12**, 279 (1929).
[9] T. Okamura, Science Repts. Tôhuku Univ. **21**, 231 (1932).
[10] T. Okamura and S. Ogawa, Proc. Phys. Math. Soc. Japan **23**, 363 (1941).
[11] L. R. Bickford, Phys. Rev. **78**, 449 (1950).
[12] Williams, Bozorth, and Goertz, Phys. Rev. **91**, 1107, 1115 (1953).
[13] L. R. Bickford, Rev. Modern Phys. **25**, 75 (1953).
[14] C. H. Li, Phys. Rev. **40**, 1002 (1932).
[15] R. L. Wegel and H. Walther, Physics **6**, 141 (1935).
[16] M. E. Fine and W. C. Ellis, Trans. Am. Inst. Mining Met. Engrs. **188**, 1120 (1950).
[17] F. C. Rose, Phys. Rev. **49**, 50 (1936).
[18] W. P. Mason, *Piezoelectric Crystals and Their Application to Ultrasonics* (D. Van Nostrand Company, Inc., New York, 1950), pp. 83, 90, 151.
[19] R. M. Bozorth, *Ferromagnetism* (D. Van Nostrand Company, Inc., New York, 1951), pp. 684–699.
[20] R. Becker and W. Döring, *Ferromagnetismus* (Julius Springer, Berlin, 1939).

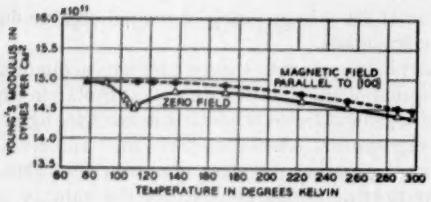

FIG. 1. Young's modulus of ⟨100⟩ in magnetite. Length = 3.8 cm, $w = t = 0.4$ cm. Frequency of measurement—approximately 70 kc sec^{-1}.

Domain motion ϵ_2 may be prevented by measuring specimens in a saturating magnetic field; the field has little effect on elastic strains and would not prevent ordering.

The moduli of magnetite, Figs. 1, 2, and 3, do not vary with temperature in the usual manner. The moduli are minima near the critical temperature of the transformation. Furthermore, positive temperature coefficients of G_{100} (the torsion modulus in ⟨100⟩), and E_{111} (Young's modulus in ⟨111⟩), are observed substantially above the critical transformation temperature. Stress-induced ordering ϵ_3, we propose, is an important strain contribution to these two moduli.

Domain motion ϵ_2 is totally responsible for the abnormal temperature variation of E_{100}, Fig. 1, because when a saturating field is applied parallel to [100] the long direction of the rod, Young's modulus behaves normally. The internal friction is independent of magnetic field and is small throughout the temperature range, Fig. 4. The temperature variation of the domain motion effect, the difference between the two curves in Fig. 1, may arise as follows: At room temperature ϵ_2 for a given applied stress is small because ⟨111⟩ is the direction of easy magnetization[11] and the four ⟨111⟩'s are inclined equally to the stress direction ⟨100⟩. But on cooling the anisotropy constant diminishes reaching zero near 130°K; below 130°K ⟨100⟩ is the direction of easy magnetization.[9–12] When ⟨100⟩ is the magnetic axis, the relative lowering of modulus by ϵ_2[19,20] is proportional to $\mu_0\lambda^2$ (μ_0 is the initial permeability, λ is the magnetostriction). Maximum μ_0 occurs near 130°K but then λ is small.[11] As the temperature is lowered, λ increases but μ_0 becomes small.[11,13] Consequently, the maximum product, that is the minimum modulus, is expected at an intermediate temperature. The minimum occurs at 118°K.

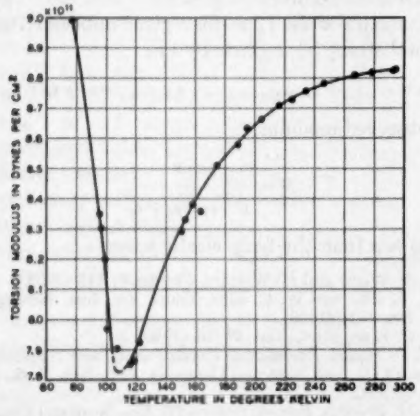

FIG. 2. Torsion modulus of ⟨100⟩ in magnetite. Length = 3.1 cm, diam. = 0.4 cm. Frequency of measurement—approximately 50 kc sec^{-1}.

The transformation has a much larger effect on G_{100}, Fig. 2, and E_{111}, Fig. 3. The slope of the E_{111} curve is positive well above room temperature and both slopes increase on cooling until a sharp minimum near 108°K. Furthermore, the internal friction for the ⟨111⟩ rod in longitudinal vibration and the ⟨100⟩ rod in torsional vibration are maximum near 95°K, Figs. 4 and 5. Neither the internal friction peaks nor the moduli minima are removed by placing the rods in a magnetic field parallel to their long directions. Actually the minimum in E_{111} is even sharper for the saturated condition. Thus the principal effect is not domain wall motion; another source of nonelasticity is indicated.[21]

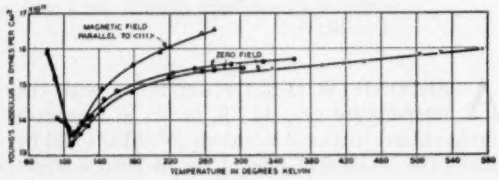

FIG. 3. Young's modulus of ⟨111⟩ in magnetite. Length = 2.1 cm, $w = t = 0.4$ cm. Frequency of measurement—approximately 130 kc sec^{-1}.

As previously mentioned stress-induced ordering ϵ_3 is probably present. On first consideration it may seem unreasonable to conclude that effects in the moduli occurring several hundred degrees above the critical ordering temperature arise from stress-induced ordering. However, the low resistivity at room temperature and above has been attributed[2,3] to a change in the distribution of Fe^{++} and Fe^{+++} induced by an applied electric field and occurring by electron motion. Increase in local ordering of Fe^{++} and Fe^{+++} interferes with this electron motion, and consequently, the increase in resistivity due to cooling below 360°K is evidence for a building up of order.

We next consider the question of how the local order changes to give a strain component. Figure 6(a) shows the stacking of octahedral sites in consecutive {100} planes in the magnetite (spinel) structure. In the ordered arrangement suggested by Verwey and Haay-

[21] The true elastic modulus may be affected from temperature variation by change in the average configuration of local order. However, this would not be a source of internal friction. Furthermore, the elastic modulus would be expected to gradually change from that for the disordered to that for the ordered phase and give an inflection in the modulus-temperature curve at the critical temperature, not a sharp minimum as observed.

man[2] alternate (001) layers are Fe^{++} and Fe^{+++}. Such ordering would change the symmetry to orthorhombic in the manner shown in Fig. 6(b). This was verified experimentally.[5,13] When the crystal becomes orthorhombic, the dimensions of the cubic lattice change, according to Bickford,[13] as follows: The c axis, direction of easy magnetization in the orthorhombic phase and normal to the plane of Fig. 6, shrinks 0.03 percent. One face diagonal AC shrinks 0.07 percent becoming the a axis of the orthorhombic phase while the other face diagonal DB increases 0.06 percent becoming the b axis of the orthorhombic phase. The changes in body diagonals are -0.06 percent (AF and CG) and $+0.03$ percent (BE and DH).

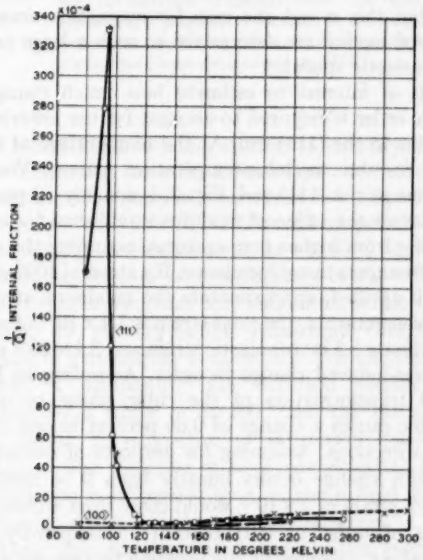

FIG. 4. Internal friction of ⟨111⟩ and ⟨100⟩ in magnetite, longitudinal vibrations. ×⟨100⟩, no external magnetic field. ○⟨111⟩, no external magnetic field. +⟨111⟩, large magnetic field parallel to the ⟨111⟩ of the rod. Frequency for ⟨100⟩ approximately 70 kc sec^{-1}. Frequency for ⟨111⟩ approximately 130 kc sec^{-1}.

Bickford[13] further concludes that if a single crystal is cooled through the transformation in a demagnetized condition, below T_c it is not a true single crystal; different cubic axes became the orthorhombic c axis in different regions. Furthermore, the regions may be twinned since the a and b axes can be interchanged. A cubic single crystal will remain a single crystal after transformation if it is cooled in a magnetic field parallel to a ⟨100⟩ (that ⟨100⟩ direction becomes the orthorhombic c axis) and tension or compression is applied in one of the ⟨110⟩ directions perpendicular the magnetic field direction. The hybrid orthorhombic crystals revert back to single cubic crystals on heating above T_c.[5,13]

At temperatures considerably above the critical ordering temperature a longitudinal stress applied

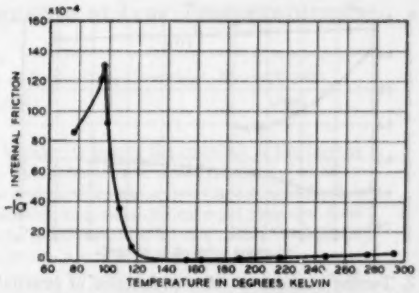

FIG. 5. Internal friction of ⟨100⟩ in magnetite for torsional vibrations. Frequency approximately 50 kc sec^{-1}.

along a ⟨110⟩, AC or DB in Fig. 6 changes the distribution of Fe^{++} and Fe^{+++} to give an additional strain component ϵ_3. Compression along AC, for example, would cause more of the smaller Fe^{+++} ions to populate the sites whose rows are parallel to AC, that is the second and fourth layers in Fig. 6(a). The larger Fe^{++} ions prefer rows parallel to DB, that is the first and third layers. Tension along AC or compression along DB reverse the preferred arrangement.

Tension-compression stresses applied in a ⟨100⟩ direction would not deform the structure in the manner shown in Fig. 6.[22] Consequently, no evidence for stress-induced ordering is expected in Young's modulus of ⟨100⟩ and none is observed, Fig. 1.

Consider a stress system causing torsion of the ⟨100⟩ rod with the long dimension of the rod as the stress axis. In this case stress-induced ordering is large, Fig. 2, because the stress induces atomic motions in ⟨110⟩ directions in certain areas of the rod. The effect of applying a magnetic field parallel to the ⟨100⟩ that is the long direction of the rod is shown in Fig. 7 and will be discussed later.

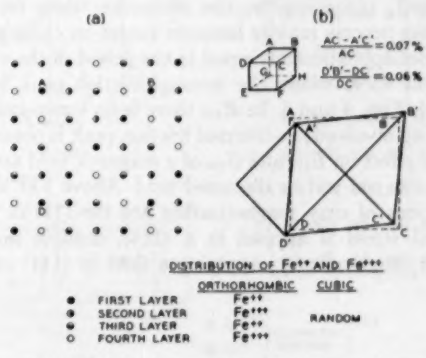

FIG. 6. (a) Stacking of successive {100} layers of octahedral sites in the spinel structure. (b) The relation between the cubic and orthorhombic phases in magnetite.

[22] Near T_c a normal stress applied in ⟨100⟩ may determine the c axis of the orthorhombic phase (see reference 13), with a strain component resulting. This is essentially a domain motion effect and would be absent if an external magnetic field determines the c axis of the orthorhombic phase.

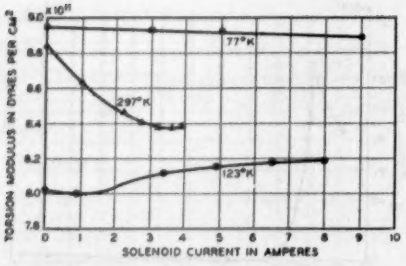

FIG. 7. Torsion modulus of ⟨100⟩ as function of external magnetic field. H at center of solenoid = 288 I gauss. Solenoid is 10.5 cm long, 12.5-cm o.d., and has 325 turns per cm.

The decrease in E_{111} on cooling and the minimum near 108°K, Fig. 3, probably also derive from stress-induced ordering. A normal stress applied in a ⟨111⟩ direction probably transforms the structure to orthorhombic. The resulting orientation of the orthorhombic cell is determined by the relative change in lengths of the body diagonals upon transforming. For example compression applied in the direction of AF, Fig. 6(b) would tend to make AF and CG the short diagonals and favors the ordered arrangement shown in Fig. 6. A strain component results, lowering the modulus.

The change in degree of order caused by a constant applied stress increases as the temperature is lowered toward T_c the critical ordering temperature and is maximum at T_c, where the free energy would be most sensitive to state of stress. G_{100} and E_{111} have their lowest values at 108°K. The relaxation time for the ordering process is also an important consideration. Above T_c where local order is involved, diffusion of electrons takes place very rapidly compared to the periods of the vibrations used in this investigation. The relaxed modulus is measured; the internal friction is low. Below the critical temperature long range order is involved; consequently, the relaxation time for the ordering process rapidly becomes longer on cooling and becomes approximately equal to the period of the vibrations at 95°K where the internal friction peak is observed, Figs. 4 and 5. In E_{100} there is no stress-induced ordering involved; no internal friction peak is observed.

The effect on E_{111} and G_{100} of a magnetic field applied along the rod will be discussed next. Above 130°K the directions of easy magnetization are the ⟨111⟩'s. If a normal stress is applied in a ⟨111⟩, domain motion occurs; consequently, applying a field in ⟨111⟩ causes E_{111} to increase, Fig. 3. Below 130°K when ⟨100⟩ is the magnetic axis, the domain motion component of E_{111} is small. In the case of torsional vibrations of the ⟨100⟩ rod the effects of applying an external magnetic field along the rod, Fig. 7, are difficult to explain. At 297°K the torsion modulus decreases 5.5 percent when a field[23] of 980 gauss is applied; further increase of the field to 1130 gauss increases the modulus slightly. Ordinarily one expects application of a magnetic field to increase the torsion modulus since the external field impedes domain motion.[24] The observed decrease in modulus seems to imply that the field aids stress-induced ordering.

Ordinarily in cubic substances the elastic constants (c_{11}, c_{12}, c_{44}) could be calculated from E_{100}, E_{111}, and G_{100}, but this is not the case for magnetite since the observed moduli are determined to such a large extent by nonelastic strains.

It is of interest to estimate how much change in atomic order is required to account for the lowering of modulus in the ⟨111⟩ rod. At the temperature of minimum in the modulus-temperature curve, Young's modulus of the ⟨111⟩ rod, Fig. 2, is roughly 30 percent lower than the value of modulus established by extrapolating from higher temperatures, assuming the usual sort of temperature dependence. If a stress of 1000 grams cm^{-2} is applied, approximately the maximum stress in the measurements, the total strain is 7.4×10^{-7} of which we estimate 5.3 is true elastic strain and 2.1×10^{-7} is due to stress-induced change in order. According to Bickford,[13] transformation of the cubic phase to orthorhombic causes a change of 0.06 percent in one of the ⟨111⟩ directions. Assuming for purposes of calculation that this change occurs linearly from 0 to complete order, a strain of 2×10^{-7} would come from a change in degree of order of 0.03 percent; consequently, the dimensional changes in the ordering process are ample to account for the observed moduli.

ACKNOWLEDGMENTS

We are grateful for the assistance of H. E. Johnson and J. P. Wright for furnishing the chemical analyses; J. Andrus for orienting the magnetite crystal; F. J. Schnettler, E. E. Schumacher, and Mrs. E. A. Wood for helpful discussion and encouragement.

[23] These values of field are for the center of the solenoid.
[24] W. F. Brown, Jr., Phys. Rev. **50**, 1171 (1936).

Magnetic and Electric Properties of Magnetite at Low Temperatures*

B. A. CALHOUN†
Laboratory for Insulation Research, Massachusetts Institute of Technology, Cambridge, Massachusetts

(Received March 1, 1954)

The low-temperature transition in magnetite, according to Verwey, is due to the ordering of the ferrous and ferric ions in the octahedral interstices of the spinel lattice. This arrangement would require a symmetry change from cubic to orthorhombic. X-ray diffraction indicates and electric conductivity and magnetization measurements confirm that the transition leads to an orthorhombic structure. An external magnetic field applied while cooling through the transition establishes a preferred orientation for the c axis throughout the whole crystal. Below the transition this c axis can be switched to a new direction by a strong magnetic field, a process involving a co-operative rearrangement of the ferrous ions in new sites and relatively large changes in dimensions. In stoichiometric, synthetic, single crystals the transition occurs at 119.4°K and is marked by an abrupt decrease in the conductivity by a factor of 90 in a temperature interval of 1°. No thermal hysteresis is observed. The conductivity of a crystal cooled in a strong magnetic field is anisotropic below the transition as given by the relation $\sigma=A+B(1+\cos^2\theta)$, where θ is the angle between the c axis and the direction of measurement. The ratio $B/(A+B)$ increases rapidly as the crystal is cooled to 90°K, indicating a progressive increase in the long-range order. The c axis is the direction of easy magnetization below the transition, and the anisotropy energy is very much larger below than above; the anisotropy constants have been determined at 85°K.

MAGNETITE is being studied intensively in this laboratory both as a prototype of the ferrites and because of its unusual behavior at low temperatures (from $-140°$ to $-190°$C).[1,2] The initial permeability passes through a maximum at *ca* $-140°$C and then decreases rapidly to a very small value below $-155°$C. Bickford[1] has shown that this maximum is due to the vanishing of the crystalline anisotropy energy. At *ca* $-155°$C a transition is observed. The specific heat traverses a maximum;[3] the electrical conductivity decreases by a factor of *ca* 100;[4] and the material is much harder to magnetize to saturation below the transition.[5] The direction of easy magnetization below the transition is influenced by a magnetic field applied as the sample is cooled through the transition.[6]

Verwey[4] proposed that above the transition magnetite has the inverse spinel structure, and that the transition itself is due to an ordering of the random distribution of ferrous and ferric ions in the octahedral lattice sites. The ordered arrangement of Fig. 1 appeared as the most likely one,[7] and Verwey suggested that the c axis of this ordered structure would lie along the cube edge closest to the direction of the external field applied during cooling.

The object of the present research was to study this unusual type of transition by electric and magnetic means as well as by x-ray analysis on single crystals of magnetite grown in this laboratory.[8]

CRYSTAL STRUCTURE

The ferrites have the same crystal structure as spinel ($MgOAl_2O_3$), space group $Fd3m$-O_h^7. The unit cell contains 32 oxygen ions in an almost cubic close-packed arrangement; the cations occupy 8 tetrahedral and 16 octahedral interstices in this oxygen lattice. Simple ferrites show two variations: a normal spinel structure, where each type of ion occupies only one type of site and the inverse spinel structure, where both kinds of cations occur in the octahedral

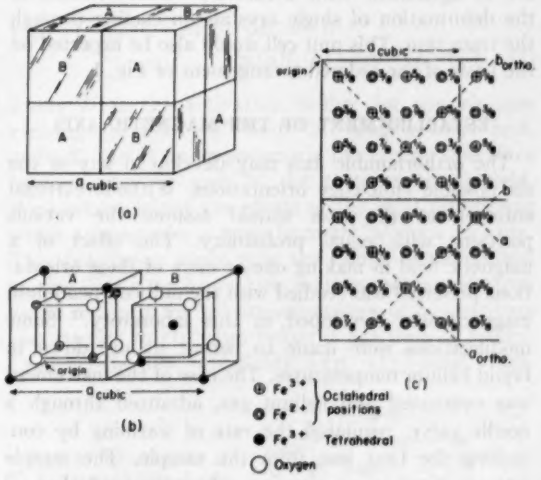

FIG. 1. Verwey's ordered structure: (a) the cubic unit cell; (b) subcells A and B; (c) projection of ions in octahedral sites on the a-b plane.

* Sponsored by the U. S. Office of Naval Research, the Army Signal Corps, and the Air Force.

† Now at Westinghouse Electric Corporation, Research Laboratories, East Pittsburgh, Pennsylvania.

[1] L. R. Bickford, Jr., Phys. Rev. **78**, 449 (1950).

[2] C. A. Domenicali, Phys. Rev. **78**, 458 (1950).

[3] R. W. Millar, J. Am. Chem. Soc. **51**, 215 (1929).

[4] E. J. W. Verwey, Nature **144**, 327 (1939); E. J. W. Verwey and P. W. Haayman, Physica **8**, 979 (1941).

[5] P. Weiss and R. Forrer, Ann. Physik. [10] **12**, 279 (1929).

[6] C. H. Li, Phys. Rev. **40**, 1002 (1932).

[7] Verwey, Haayman, and Romeijn, J. Chem. Phys. **15**, 181 (1947).

[8] J. Smiltens, J. Chem. Phys. **20**, 990 (1952).

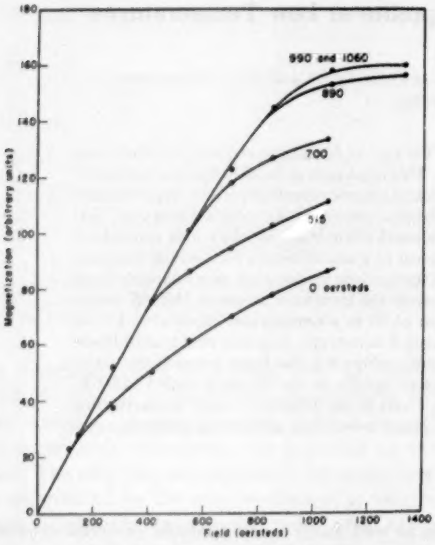

FIG. 2. Magnetization curves in the cubic [001] direction at 78°K after cooling in magnetic fields parallel to [001]; field strength as indicated.

sites. Neutron diffraction measurements[9] have confirmed the inverse structure for magnetite.

An x-ray study, undertaken in connection with the present investigation,[10] indicates the symmetry of magnetite below the transition as orthorhombic (unit cell dimensions: $a=5.912$, $b=5.945$, $c=8.388$A at 78°K), with the c axis orientated along one of the original cube edges, and the a and b axes along the cubic face diagonals normal to the c axis. These results are in agreement with Bickford's[11] measurements of the deformation of single crystals on cooling through the transition. This unit cell would also be expected on the basis of the ordered arrangement of Fig. 1.

ESTABLISHMENT OF THE MAGNETIC AXIS

The orthorhombic axis may develop in any of the six possible cube-edge orientations. Without external enforcement the axes should assume the various positions with equal probability. The effect of a magnetic field in making one or more of these orientations preferred was studied with the null-coil pendulum magnetometer developed in this laboratory.[12] Some modifications were made to permit its use down to liquid helium temperatures. The case of the instrument was evacuated and helium gas, admitted through a needle valve, regulated the rate of warming by controlling the heat loss from the sample. The sample was mounted in an aluminum boat in good thermal contact with the null coil, which also served as a heat source. The measurements were made on a circular disk cut from a (100)-plane slice of a single crystal of magnetite and ground to an oblate spheroid with axes of 4.55 and 0.89 mm.

The smallest magnetic field that establishes a magnetic axis was determined by cooling this (100) sample through the transition with magnetic fields of various strengths applied parallel to the [001] direction. The sample was then demagnetized and the magnetization curve in the [001] direction measured at −195°C (Fig. 2). The minimum field for completely establishing the magnetic axis is *ca* 1000 oersteds; approximately the same field is needed to produce technical saturation. The external field aligns the individual domains throughout the sample along the previous cube-edge direction establishing this as a unique magnetic axis, the c axis of the orthorhombic structure.

When such a sample is demagnetized, the c axis remains the direction of easy magnetization and the domain pattern consists of antiparallel domains aligned along this axis. This was verified by measuring the longitudinal magnetostriction in a [100] bar after cooling through the transition in a field parallel to its length and then demagnetizing the bar. The longitudinal magnetostriction in fields up to *ca* 10 000 oersteds was extremely small ($\delta l/l<10^{-6}$), indicating that the magnetization in this direction was almost entirely due to the motion of 180° walls.

In additional experiments the (100) sample was cooled through the transition in a field of 4700 oersteds, directed in the (100) plane at angles of 0°, 40°, 45°, 55°, and 90° to the [001] direction. The warming curves (magnetic moment as a function of temperature at constant applied field) are shown in Figs. 3 and 4. When the field is within 40° of the [001] direction, this [001] becomes the c axis. When the field is within 40° of the [010] direction, i.e., more than 50° from [001], [010] becomes the c axis and the [001] direction is magnetically hard. When the cooling field is applied at 45° to [001], warming curves show that in approximately one half the sample [001] is the c axis and in the remainder [010] is the c axis.

The effect of applying a magnetic field at various angles in the cubic (110) plane was investigated with a quasi-static B-H loop tracer for an oblate spheroidal sample prepared from a (110) slice of a magnetite

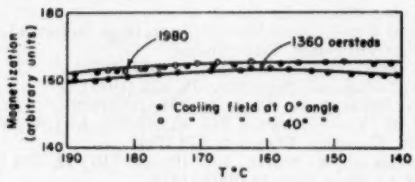

FIG. 3. Warming curves in [001] direction after cooling in field of 4700 oersteds orientated 0° and 40° to [001].

[9] Shull, Wollan, and Koehler, Phys. Rev. **84**, 912 (1951).
[10] S. C. Abrahams and B. A. Calhoun, Acta Cryst. **6**, 105 (1953).
[11] L. R. Bickford, Jr., Revs. Modern Phys. **25**, 75 (1953).
[12] C. A. Domenicali, Rev. Sci. Instr. **21**, 327 (1950).

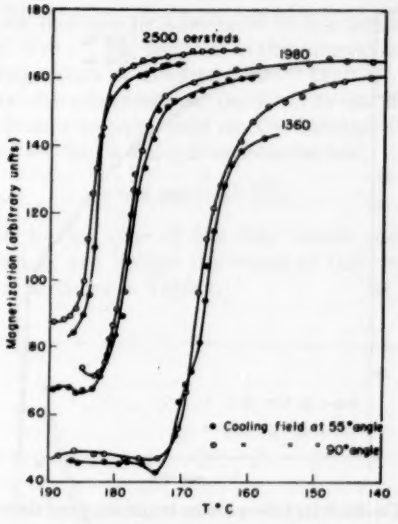

FIG. 4. Warming curves in [001] direction after cooling in field of 4700 oersteds orientated 55° and 90° to [001].

crystal. Magnetization curves were measured in the [001] direction of this sample, after cooling in a field of 10 000 oersteds directed in the (110) plane at angles of 0°, 25°, and 40° to [001]. The indentity of the curves shows that, in each case, the c axis is established along the [001] direction. All results are consistent with the picture that the c axis is established along the cube edge nearest the direction of the magnetization in each domain. Similar results have been obtained with natural crystals of magnetite by Williams and Bozorth.[13]

SWITCHING OF THE MAGNETIC AXIS

The phenomenon of axis-switching, i.e., the change of the c axis from one cube edge to another below the transition, was first observed by Bickford[1] in microwave resonance experiments at liquid nitrogen temperature. The effect is apparent in the warming curves of Fig. 4. The magnetic axis was established along the [010] direction so that [001] was magnetically hard, as shown by its small magnetic moment. At some temperature below the transition, there is an abrupt increase in the magnetic moment indicating that the [001] direction has suddenly become an easy direction. The external field necessary to cause axis-switching at various temperatures was determined by cooling the (100) spheroid through the transition with a field of 4700 oersteds along the [010] direction and then measuring the warming curves with fields from 1000 to 5000 oersteds applied in the [001] direction (see Fig. 4).

Axis-switching was also observed in the (110)-plane sample. An unexpected result was that axis-switching occurred only with the field applied in the $[1\bar{1}0]$ direction and in a direction at 15° to it in the (110) plane. From measurements of the change in length of a [100] bar accompanying the axis-switching, it was evident that relatively large changes in dimensions ($\delta l/l \simeq 10^{-4}$) and correspondingly, in elastic energy, are involved in this situation. This elastic energy apparently suffices, in the case just mentioned, to prevent the axis-switching from occuring at the field indicated by Eq. (2) (see below), although it may still occur in a sufficiently high field.

Transfer of the c axis from one cube edge to another requires an electron exchange from ferrous to neighboring ferric ions in the tetrahedra formed by the iron ions in the octahedral interstices (Fig. 5). A crystal in which the c axis has been established along the [010] direction, placed in a magnetic field directed along the [001] direction, can reduce its energy considerably if [001] becomes the easy direction. The dependence of this energy difference on the magnetic induction is complicated since it is determined by the anisotropy energy. Let us consider an electron and its two possible positions, an "a" site corresponding to the c axis in the [010] direction and a "b" site corresponding to the c axis in the [001] direction. Initially, there is a high probability that an electron will be at an "a" site, since the process of cooling the crystal in a field directed along [010] has lowered the energy of the "a" site relative to that of the "b" site. The application of a magnetic field in the [001] direction lowers the energy of site "b". If the change in the energy of the "b" sites is proportional to the internal magnetic induction, the net probability that an electron will jump from an "a" to a "b" site is given as

$$\exp(-U/kT)(1-\exp[-\mu B_i/kT]) \simeq (\mu B_i/kT)\exp(-U/kT), \quad (1)$$

where U is the activation energy for the electron exchange between "a" and "b" sites without field, and μB_i (μ = Bohr magneton) is the energy difference between sites "a" and "b" due to the magnetic field. We have neglected the effects of the local disordering which accompanies a jump from an "a" to a "b" site. This disordering would raise the energy of an electron in the "b" site; hence, we may expect an electron would return to an "a" site unless some of its neighbors also jumped to "b" sites before it has time to return. Crudely, the net probability [Eq. (1)] must reach

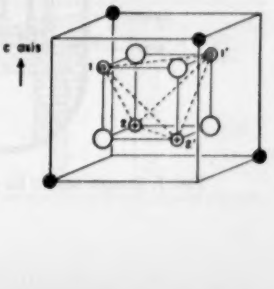

FIG. 5. Tetrahedron 1, 1', 2, 2' establishing c axis vertical; exchange of 1 and 2' or 1' and 2' turns c axis 90°.

[13] H. J. Williams and R. M. Bozorth, Revs. Modern Phys. **25**, 79 (1953).

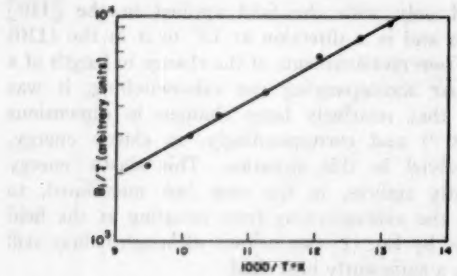

FIG. 6. Induction required to switch the c axis.

some critical value before the "b" sites become stable and the axis switches; that is,

$$B_i = CT(\exp U/kT), \qquad (2)$$

where B_i is the internal induction prior to the axis-switching and T the temperature at the midpoint of the switching. Figure 6 shows that the experimental data calculated from curves similar to Fig. 4 fit this equation with $U = 0.033$ ev.

CONDUCTIVITY OF MAGNETITE AND ITS RELATION TO THE TRANSITION

If the conductivity of magnetite is due to the exchange of electrons between the ferrous and ferric ions in the octahedral lattice sites, the random distribution above the transition should lead to an isotropic conductivity, but belo the transition the conductivity should be anisotropic. This anisotropy and its dependence on crystallographic orientation and magnetic field direction during cooling have been studied in detail.

The four-terminal sample holder (Fig. 7) was designed to maintain sample and contacts in as nearly an isothermal region as possible in order to minimize

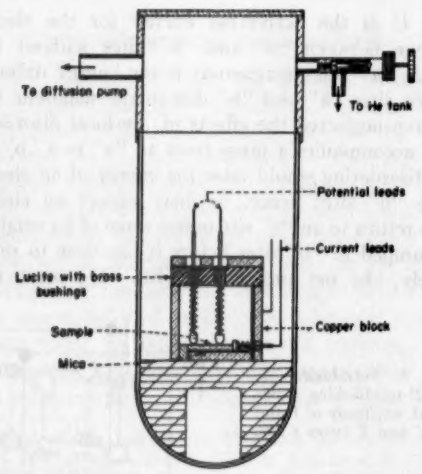

FIG. 7. Sample holder for conductivity measurements.

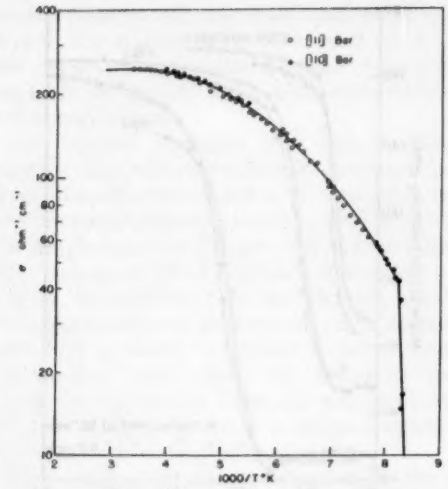

FIG. 8. Conductivity between room temperature and the transition.

spurious thermal emf. Helium gas, admitted through a needle valve, allowed the pressure to be adjusted from 10^{-2} to 10^{-5} mm. Thus, the warming and cooling rates could be controlled from 3° to 50°C per hour. The temperature was measured potentiometrically by a copper-constantan thermocouple.[14] The samples were cut from two synthetic crystals in the form of rectangular bars about 1 cm in length and with a cross-sectional area of about 3 sq mm. The length direction of the bars was oriented parallel to the cubic [100], [110], and [111] directions, respectively.

The conductivity of two of the specimens from room temperature through the transition is shown in Fig. 8. Warming and cooling data coincide; no thermal hysteresis marks the transition. The conductivity is 250 ohm^{-1} cm^{-1} at room temperature and has a broad maximum at *ca* 15°C; previous investigators[2,4] have reported this maximum for natural crystals to be at a higher temperature (*ca* 80°C). At the transition the

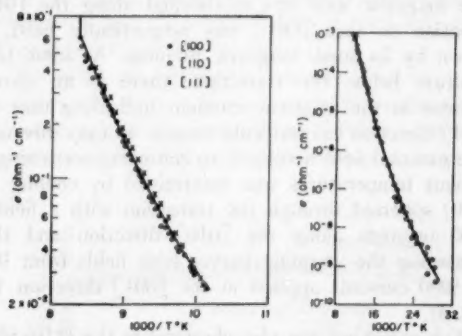

FIG. 9. Conductivity of the [111] bar below the transition after cooling in zero magnetic field.

[14] See R. P. Teele and S. Schuhmann, J. Research Natl. Bur. Standards **22**, 431 (1939).

resistivity increases by a factor of 90 in a temperature interval of *ca* 1°. The midpoint of this interval occurred at a temperature of 119.4±0.3°K (−153.8°C).

Below the transition the conductivity for samples cooled in zero magnetic field remains isotropic (Fig. 9) but does not follow a simple exponential law,

$$\sigma = A \exp(-U/kT).$$

If fitted to this type of law over certain ranges of temperature, one obtains the values of the constants A and U as shown in Table I.

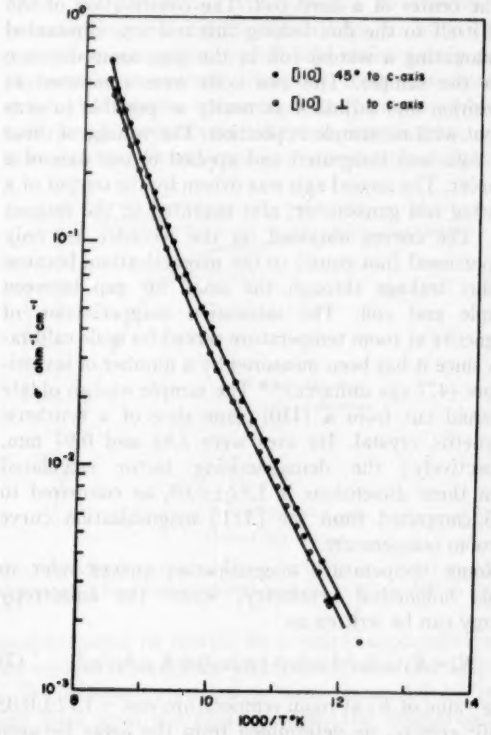

FIG. 10. Conductivity of [110] sample after cooling in two differently orientated magnetic fields.

When the samples are cooled through the transition in a magnetic field (*ca* 9000 oersteds) the conductivity is anisotropic and depends on the orientation of both the sample and the magnetic field (Fig. 10). The anisotropy increases as the sample is cooled from the transition to *ca* 95°K, and then remains practically constant at lower temperatures. Table II gives the ratios of the conductivities for a number of combinations of electrode orientation and c axis direction.

The observed anisotropy in the conductivity agrees well with that which can be predicted from Verwey's model of the low-temperature structure of magnetite. Although the exchange of electrons between ferrous and ferric ions has become much more difficult below the transition, it is still the dominant mechanism of conduction. In the ordered structure this will lead to an anisotropy since ferrous and ferric ions occupy adjacent sites in only four of the cubic [110] directions. Although the ordered structure has orthorhombic symmetry, its conductivity anisotropy corresponds to tetragonal symmetry (neglecting the small departure of the b/a axial ratio from unity). The conductivity of a tetragonal crystal in an arbitrary direction is given by

$$\sigma = \sigma_{11} \sin^2\theta + \sigma_{33} \cos^2\theta, \tag{3}$$

where θ is the angle between the direction and the c axis, σ_{33} the conductivity along the c axis, and σ_{11} the conductivity normal to the c axis. It can be seen easily from the ordered structure that the ratio $\sigma_{33}/\sigma_{11}=2$. Thus we can write the conductivity below the transition as

$$\sigma = B(1+\cos^2\theta). \tag{4}$$

In case the order is not perfect, we would expect the conductivity to contain in addition, an isotropic term

$$\sigma = A+B(1+\cos^2\theta). \tag{5}$$

The quantity $B/(A+B)$ should be a measure of the amount of order. The values of A, B, and $B/(A+B)$ derived from our conductivity data for a number of temperatures are given in Table III. This table shows that with decreasing temperature the order increases, as one would expect, since the ordering process involves an activation energy.

TABLE I. Conductivity of magnetite below the transition.

Temperature	A (ohm^{-1} cm^{-1})	U (ev)
78 to 90°K	8200	0.11
56 to 77°	1400	0.09
40 to 52°	1.5	0.06

MAGNETIC ANISOTROPY

The magnetic anisotropy energy is the difference between the energy required to magnetize a sample in an arbitrary direction and in the direction of easy magnetization. The angular dependence of this anisotropy energy is determined by the symmetry of the crystal. In the ordered structure of magnetite a determination of the angular dependence of the anisotropy

TABLE II. Ratio of conductivities of magnetite in different directions below the transition.

T	$\frac{\sigma[100]\|H}{\sigma[100]\perp H}$	$\frac{\sigma[100]\|H}{\sigma[110]\perp H}$	$\frac{\sigma[100]\|H}{\sigma[110]45°H}$	$\frac{\sigma[110]45°H}{\sigma[110]\perp H}$	$\frac{\sigma[100]\|H}{\sigma[111]}$
117.6°K	1.44	1.40	1.25	1.12	···
111.1	1.63	1.51	1.21	1.25	···
105.3	1.79	1.59	1.27	1.25	···
100.0	1.87	1.59	1.24	1.28	···
95.2	1.88	1.61	1.25	1.28	1.56
90.9	···	1.61	1.27	1.27	···
87.0	···	1.60	1.26	1.27	···
83.3	···	1.60	1.26	1.26	···

TABLE III. Anisotropy of conductivity below the transition.

T,°K	A	B	$B/(A+B)$
117.6	0.2660	0.1270	0.324
111.1	0.0718	0.0741	0.508
105.3	0.0202	0.0396	0.662
100.0	0.0079	0.0194	0.711
95.2	0.0026	0.01155	0.816

energy is particularly important since the actual deformation of the crystal structure at the transition is very small and therefore difficult to determine directly, while the anisotropy energy below the transition is very large. Consequently, the determination of the anisotropy energy provides a sensitive method for checking the crystal symmetry.

The method of calculating the dependence of the anisotropy energy on orientation for any type of crystal symmetry is well known. The anisotropy energy is expanded as a power series in the direction cosines relative to the crystallographic axes, only those terms consistent with the symmetry being retained. The existence of a plane of symmetry normal to a crystallographic axis requires the direction cosine relative to that axis to appear only in even powers. Since the ordered structure of magnetite seems to belong to the orthorhombic holohedral crystal class, it has three such symmetry planes (one normal to each axis). The remaining symmetry elements of this crystal class, i.e., the three twofold axes and the center of symmetry, can be compounded from appropriate sequences of reflections in the three symmetry planes and therefore do not impose any additional restrictions on the form of the anisotropy energy. Thus we have

$$E_a = K_1\alpha_1^2 + K_2\alpha_2^2 + K_{11}\alpha_1^4 + K_{12}\alpha_1^2\alpha_2^2 + K_{22}\alpha_2^4, \quad (6)$$

where the K's are the anisotropy constants, and the α's the direction cosines relative to the crystallographic axes. The identity $\alpha_1^2+\alpha_2^2+\alpha_3^2=1$ has been used to eliminate all the terms containing α_3. For magnetite below the transition, the c axis is the easy direction and magnetization along one of the a and b axes appears to be much more difficult than along the other. Since this difficult axis could not be experimentally identified uniquely with the a or b direction because of twinning, the b axis was arbitrary chosen as the difficult one. If this choice should prove to be incorrect, only the subscripts 1 and 2 of the anisotropy constants would have to be interchanged.

TABLE IV. Anisotropy constants of magnetite at low temperature.

Constants ergs/cc	Method: Magnetization curves	Method: Torque curves
K_1	4.0×10^5	2.8×10^5
K_2	9.0×10^5	7.5×10^5
K_{11}	2.2×10^5	2.2×10^5
K_{12}	13.0×10^5	12.4×10^5
K_{22}	10.2×10^5	7.4×10^5

The anisotropy constants were computed from the areas between the magnetization curves taken in different crystallographic directions. Fields as high as 15 000 oersteds are required to saturate magnetite below the transition. Because the pendulum magnetometer, at present, is limited to fields of less than 5000 oersteds, the quasistatic B-H loop tracer constructed in this laboratory[15] was modified to trace the magnetization curves of samples mounted in the gap of our large electromagnet. The sample was mounted at the center of a fixed coil. The contribution of the field itself to the flux linking this coil was eliminated by mounting a second coil in the gap, some distance from the sample. The two coils were connected in opposition and adjusted as nearly as possible to zero output with no sample in position. The voltage of these two coils was integrated and applied to one axis of a recorder. The second axis was driven by the output of a rotating coil gaussmeter, also mounted in the magnet gap. The curves obtained on the recorder are only proportional (not equal) to the magnetization, because of flux leakage through the small air gap between sample and coil. The saturation magnetization of magnetite at room temperature served for scale calibration since it has been measured by a number of investigators (477 cgs units/cc).[2,5] The sample was an oblate spheroid cut from a (110)-plane slice of a synthetic magnetite crystal. Its axes were 3.84 and 0.97 mm, respectively; the demagnetizing factor calculated from these dimensions is 1.82 ± 0.08, as compared to 1.75 computed from the [111] magnetization curve at room temperature.

Room temperature magnetization curves refer to cubic holohedral symmetry, where the anisotropy energy can be written as

$$E_a = K_1(\alpha_1^2\alpha_2^2+\alpha_2^2\alpha_3^2+\alpha_3^2\alpha_1^2) + K_2\alpha_1^2\alpha_2^2\alpha_3^2. \quad (7)$$

The value of K_1 at room temperature was $-1.12\pm0.05\times10^5$ ergs/cc, as determined from the areas between the [100] and [110], as well as between the [100] and [111] curves. This is in good agreement with the value of -1.12 for K_1 from microwave resonance measurements[1] and -1.22 from torque magnetometer measurements.[13] K_2 is zero, within the limits of experimental error.

The low-temperature curves were obtained by immersing the sample and the surrounding coil in liquid air. The sample reached equilibrium very quickly at a temperature of *ca* -188°C. The saturation magnetization of magnetite at this temperature was 508 cgs units/cc, in excellent agreement with the value of 510 at -195°C obtained by Domenicali.[2] Magnetization curves were obtained in the cubic [100],

[15] Developed by D. J. Epstein and B. Frackiewicz after P. P. Cioffi, Rev. Sci. Instr. 21, 624 (1950).

[110], and [111] directions, and also 15°, 30°, 45° and 75° to [100] after cooling in a parallel or a perpendicular magnetic field of *ca* 10 000 oersteds. Curves were also obtained in the cubic [100] and [110] directions after cooling in zero field.

The twinning that occurs in magnetite when it is cooled through the transition introduces a number of complications. A magnetic field applied to the sample as it is cooled will align the *c* axis along the cube edge nearest the applied field. Since the anisotropy energy is considerably lower along the *a* axis than along *b*, the *a* axis will tend to lie closer to the external field.[16] These two conditions are sufficient to remove the twinning only in certain orientations. In some cases, particularly when the applied field makes nearly equal angles with two or three cube edges, there is uncertainty about the relative volumes of the sample assuming each possible orientation. Because interactions occur between the different regions of the sample, a twinned

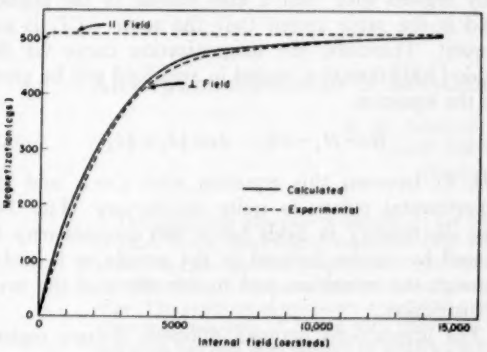

FIG. 11. Magnetization curves at 85°K in the [100] direction after cooling in a field of 10 000 oersteds at 0° and 90° to [100].

sample cannot be treated by a simple superposition of the various orientations which it contains (see below).

The anisotropy constants were calculated by trial and error from the areas between the magnetization curves. Due to the uncertainties introduced by twinning, a simple fitting of the measured areas between the various magnetization curves was not considered a sufficient check on the actual values of these constants. The anisotropy constants obtained from the areas were therefore used to compute the magnetization curves for the cubic [100] and [111] directions after cooling in a perpendicular field and adjusted to improve the fit between the calculated and the experimental curves. The values of the constants finally obtained by this two-step approximation are given in Table IV under "Magnetization curves." The calculated and experimental curves for the cubic [100] and [111] directions are shown in Figs. 11 and 12. The anisotropy energy, as a function of crystallographic orientation, is shown in Fig. 13. The complicated path followed

[16] Williams, Bozorth, and Goertz, Phys. Rev. **91**, 1107 (1953).

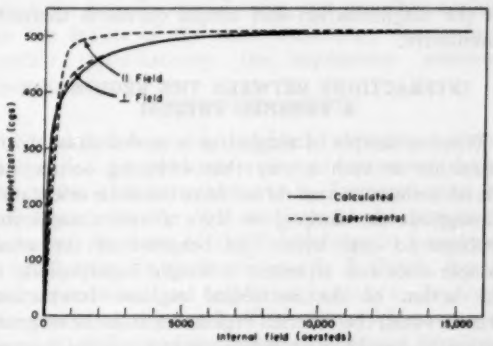

FIG. 12. Magnetization curves at 85°K in the [111] direction after cooling in a field of 10 000 oersteds at 0° and 90° to [111].

by the magnetization vector and its experimental confirmation by magnetization curves lend strong support to the assumption of an orthorhombic structure for magnetite below the transition.

Williams and Bozorth[15,16] have measured torque curves on samples of natural magnetite at liquid nitrogen temperature, i.e., at about −195°C. When their results are expressed in terms of our constants (Table IV) the agreement between the two sets is relatively good, considering the differences in temperature and crystals used. The natural crystals are not exactly stoichiometric and consequently would not have as perfect an ordered structure as the synthetic crystals. The amount of order increases rapidly as a crystal is cooled below the transition (Table III). Thus the 7° difference in temperature between the two sets of measurements partially compensates for the inherent difference in the crystals. The differences in all constants are in the same direction; their effect

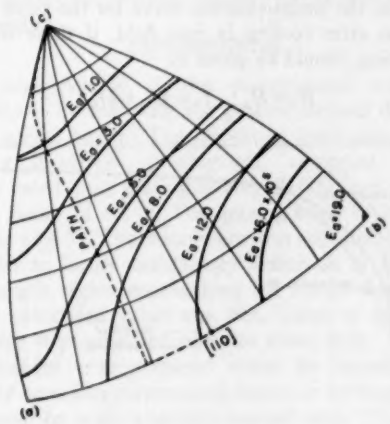

FIG. 13. Anisotropy energy of magnetite, showing the path followed by the magnetization when a field is applied in the orthorhombic [110] direction. The projections of the orthorhombic *a*, *b*, and *c* axis are at the corners (a), (b), and (c) (E_a = anisotropy energy [ergs/cc]).

on the magnetization and torque curves is therefore cumulative.

INTERACTIONS BETWEEN THE REGIONS OF A TWINNED CRYSTAL

When a sample of magnetite is cooled through the transition in such a way that twinning occurs, i.e., the orthorhombic axes do not have the same orientation throughout the sample, we have a very complicated problem to deal with. The behavior of the whole sample does not represent a simple superposition of the action of the individual regions. Interactions arise between the different regions because the magnetization in neighboring regions exerts mutual torque; each region is strained owing to the distortions experienced by its neighbors, and free poles on the boundaries between the regions cause discontinuities in the internal field. The effects due to the last two causes could be very complex; lacking the information needed to even estimate them, we can only assume here that they do not greatly alter the magnetization curves.

The effect of torques exerted by the magnetization in one region on that in neighboring regions is particularly large in two of the experimental magnetization curves: the cubic [100] direction cooled in zero field, and the cubic [111] direction cooled in a parallel field. When a sample is cooled through the transition in a demagnetized state, the cubic [100] direction will become the orthorhombic [001] in $\frac{1}{3}$ of the sample, the orthorhombic [110] in $\frac{1}{3}$, and the orthorhombic [1$\bar{1}$0] in $\frac{1}{3}$, since the orthorhombic a and b axes develop along face diagonals of the cubic unit cell. The magnetization curves in the orthorhombic [110] and [1$\bar{1}$0] directions will be identical. The orthorhombic [110] curve can be obtained by cooling with a field normal to the cubic [100] direction, and the [001] curve with a parallel field. Since the c axis [001] is the easy direction, the magnetization curve for the cubic [100] direction after cooling in zero field, if there were no interaction, should be given by

$$H_0=H_\perp;\quad I_0=\tfrac{1}{3}I_\parallel+\tfrac{2}{3}I_\perp. \tag{8}$$

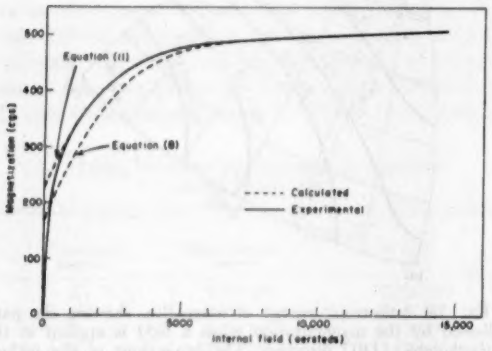

FIG. 14. Magnetization curve at 85°K in the [100] direction after cooling in zero field.

The curve calculated from Eq. (8) on the basis of the measurements in Fig. 11 is compared in Fig. 14 with the measured characteristic. Let us analyze the discrepancy on the basis that torque interaction between the different regions affects the magnetization. In part of the sample the magnetization I_s is orientated parallel to the field, in the remainder at an angle θ to the field. The torque energy will be of the form $I_s^2\cos\theta$. Thus, the energy of a region with the c axis perpendicular to the applied field will be

$$E_T=E_a-HI_s\cos\theta-CI_s^2\cos\theta, \tag{9}$$

where E_a is the anisotropy energy, H the internal field, I_s the saturation magnetization, and C an empirical constant. To find the equilibrium position of the magnetization, we set $dE_T/d\theta=0$ and obtain

$$H-CI_s=-(dE_a/d\theta)/(I_s\sin\theta). \tag{10}$$

The corresponding equation for a sample containing only regions with their c axes normal to the applied field is the same except that the term $-CI_s$ is not present. Therefore, the magnetization curve for the cubic [100] direction cooled in zero field will be given by the equation

$$H_0=H_\perp-CI_s;\quad I_0=\tfrac{1}{3}I_\parallel+\tfrac{2}{3}I_\perp. \tag{11}$$

The fit between this equation with $C=1$, and the experimental curve, is quite satisfactory (Fig. 14). The discrepancy in fields below 800 oersteds may be caused by strains induced in the sample as it cooled through the transition, and to the effects of the magnetostriction.

The interactions between different domain regions probably account for the fact that the anisotropy constants obtained by static methods do not explain quantitatively the microwave resonances observed by Bickford.[1] The twinning at the transition accounts qualitatively for the multiple resonances observed [in the case of the cubic (100) plane discrepancies may be due to lack of magnetic saturation in the sample]. If one calculates from the anisotropy constants the positions of the resonance peaks, the values do not agree with those observed. Interactions of the type described above produce torques which would affect the precession of the magnetization and hence the position of the resonance. The resonance experiments must be repeated under conditions excluding twinning to determine whether the static anisotropy constants will account for the observed resonance frequencies.

SUMMARY AND CONCLUSIONS

A large amount of experimental evidence indicates that the structure of magnetite below the transition is orthorhombic. Direct determination of the unit cell size, both x-rays[10] and strain-gauge measurements,[11] show that the c axis lies along one of the original cube

edges, and the a and b axes along the perpendicular cubic face-diagonal directions. The magnetic anisotropy energy gives convincing evidence for orthorhombic symmetry. The anisotropy of the conductivity agrees well with that to be expected from Verwey's ordered structure. The increase in conductivity anisotropy with decreasing temperature (Table III) appears to be directly related to the increase in long-range order.

In addition to accounting for the anisotropic properties below the transition, Verwey's model explains the influence of a magnetic field applied during cooling on the properties of the crystal below the transition. The axis-switching effect, not previously predicted, can be readily explained. Twinning at the transition greatly complicates the magnetic behavior at lower temperatures because the different regions of a twinned crystal interact in a complex way. These interactions are quite large in special cases and probably account for the failure of the static anisotropy constants to predict quantitatively the microwave resonance frequencies.

ACKNOWLEDGMENTS

The author is greatly indebted to Professor A. von Hippel for his guidance and encouragement during the course of this research; to B. Frackiewicz for his assistance with the B-H loop tracer measurements; to many members of this laboratory, in particular, D. J. Epstein, D. O. Smith, and L. B. Smith, for the many discussions and helpful suggestions made during the course of this work. The author wishes also to thank R. P. Teele of the National Bureau of Standards for the loan of a "thermo-free" reversing key, and L. R. Bickford, Jr., and R. M. Bozorth for the privilege of seeing their results prior to publication.

PHYSICAL REVIEW VOLUME 94, NUMBER 6 JUNE 15, 1954

Absorption Spectrum of Beryllium in the Neighborhood of the K Edge*

R. W. JOHNSTON† AND D. H. TOMBOULIAN
Cornell University, Ithaca, New York

(Received March 3, 1954)

The absorption spectrum of metallic Be has been investigated in the soft x-ray region extending from 60A to 250A. The K discontinuity appears at 111A and coincides with the K edge observed in the emission spectrum. Over the spectral range studied, the values of the linear absorption coefficient range from 0.25×10^5 to 2.8×10^5 cm^{-1}. Characteristic secondary structure is also noticeable on the short wavelength side of the edge. The positions of secondary absorption maxima are compared with those previously found in the K absorption spectrum of Al and with theoretical calculations based on the Hayasi model. The absorption spectrum has also been studied by irradiating Be absorbers with the continuous far ultraviolet radiation emitted by relativistic electrons accelerated in the Cornell synchrotron. Partial reduction of the data indicates good agreement with determinations based on the use of line spectra as the incident radiation.

INTRODUCTION

THE electronic structure of Be ($1s^22s^2$) indicates that the initial state in an absorption transition must either be a K level or a level belonging to the filled portion of the conduction band. A study of the K emission band of Be shows that the photon energy required for the ejection of a K electron should be nearly 112 ev. In the absence of previous information on the absorption spectrum of this metal, an investigation was undertaken to measure the absorption in the spectral region extending from 60A to 250A. The energy of photons in this wavelength region ranges from 50 to 200 ev. Thus, a sample of Be irradiated by photons possessing the above energy spread, should reveal the behavior of the spectrum in the region of the K discontinuity. The present paper offers an extension of the preliminary measurements reported on previously.[1]

EXPERIMENTAL

A large portion of the experimental work was carried out by following the general method described in an earlier paper.[2] The dispersing instrument was a grazing incidence spectrograph, equipped with a lightly ruled glass grating having 30 000 lines per inch and a radius of 1.5 m. The grazing angle of incidence was set at 4.5°. The instrument was adjusted carefully in order to insure satisfactory definition in the short wavelength region approaching the cut-off wavelength whose calculated value was 30A. Lines of reasonable intensity were observed down to about 60A.

Absorbers were prepared either by depositing Be directly on a thin substrate of Zapon or by evaporating the metal on a glass surface treated with "Victawet."

* Supported in part by the Office of Ordnance Research, U. S. Army.

† Present address: Electronics Laboratory, The General Electric Company, Syracuse, New York.

[1] D. H. Tomboulian and R. W. Johnston, Phys. Rev. 83, 220 (1951).

[2] D. H. Tomboulian and E. M. Pell, Phys. Rev. 83, 1196 (1951).

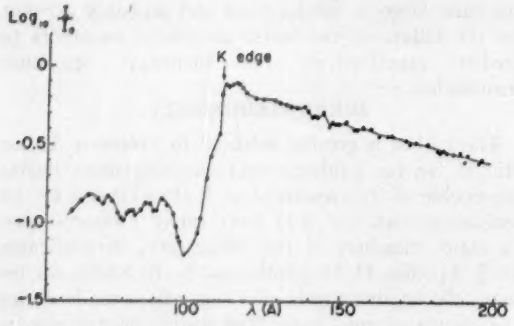

FIG. 1. A typical absorption curve of a metallic Be absorber 1000A in thickness.

The film so condensed was subsequently floated off and mounted on suitable holders. The second procedure resulted in unusually good samples with a bright metallic sheen remarkably free from pin-holes. In all evaporation processes, great care was exercised to prevent contamination.

Thicknesses of the foils were arrived at by taking into account the mass of the metal evaporated and the geometry of the arrangement. The foil density was assumed to be that of the bulk material. It is known that this procedure results in thickness determinations which agree within 5 percent with those obtained by direct weighing on a microbalance when the foil thickness exceeds 3000A. Since the errors in the photometric reductions are of this order, more refined measurements of thickness were not attempted.

The spectrograms consisted of three juxtaposed spectra. One was taken without an absorber while the remaining two represented the spectra transmitted by the absorber under varying times of exposure. This procedure enables one to calibrate each individual plate and to obtain two determinations of the absorption

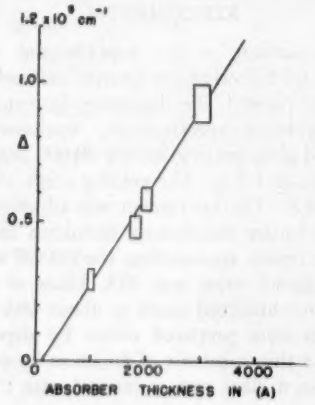

FIG. 2. A graph which shows Δ, the change in $\log_{10}(I_0/I)$, as a function of absorber thickness. The change was evaluated between two wavelengths located respectively on the short and long wavelength side of the edge.

curve. Admittedly a more desirable procedure would have consisted in obtaining contiguous spectra of two absorbers which are prepared under identical conditions but differ in the thickness of the deposited layer. Measurements based on such absorbers would be free from effects due to interface penetration or surface contamination. Since the differential thickness of absorbing material is not readily available, this scheme is not suitable for testing the consistency of a series of measurements or for evaluating the absorption coefficient. However, it affords a means for detecting in an absorption curve those features which are due to surface effects.

The continuum emitted from targets is very feeble in the soft x-ray region, and until recently one was limited to the use of line spectra as a source of incident radiation. However, within the past year, the continuous electromagnetic radiation emitted by relativistic electrons accelerated in the Cornell synchrotron has been investigated[3] and found to be sufficiently intense to serve as a suitable source. Though the major portion of the data reported in this paper is based on the radiation emitted by condensed spark discharges, an absorption spectrum of Be has also been obtained using the synchrotron radiation as a source. The possibility of utilizing this remarkable source as a tool in absorption spectroscopy shows promise. The details of the method will be published at a later date. Microphotometer traces showing the incident intensity distribution as well as the absorption by Be are included. Complete reduction of the traces is not possible at the present time for reasons to be offered later.

RESULTS

The Absorption Curve

Figure 1 shows the $\log_{10}(I/I_0)$ curve for a sample whose thickness was 1000A. (Here, I_0 is the incident intensity and I that transmitted by the absorber.) An application of the relation $I=I_0e^{-\mu x}$, indicates that the greatest difference in transmitted intensity on either side of an absorption edge occurs when the absorber thickness x has the optimum value given by

$$x_{\text{opt}}=(\ln\mu_1-\ln\mu_2)/(\mu_1-\mu_2),$$

where μ_1 and μ_2 represent the linear absorption coefficients on the short and long wavelength side of the edge. For Be, $x_{\text{opt}}=1100$A, hence a considerable part of the measurements were carried out with samples having this thickness. The values of $\log_{10}(I/I_0)$ represent weighted averages of the results of several spectrograms taken with different samples and exposure ratios. The K edge appears at 111A. As in the case of other light metallic elements, such as Li, Mg, Al, a secondary structure is also observable. The intense absorption dip at 100A appeared on all spectrograms including

[3] P. L. Hartman and D. H. Tomboulian, Phys. Rev. **91**, 1577 (1953).

those obtained with absorbers free from Zapon. Except for the small likelihood of an interface effect at the metal "Victawet" boundary, this feature of the absorption curve may be regarded as characteristic of the metal. As a check on the consistency of the measurements, the magnitude of the change in $\log_{10}(I_0/I)$ at the K edge was plotted as a function of absorber thickness. The change was measured between the wavelength $\lambda=110$A and $\lambda=118$A, located respectively on the high- and low-energy side of the edge. The plot is shown in Fig. 2, where the sides of the rectangles indicate the estimated errors in thickness x and in $\log_{10}(I_0/I)$. If the four different samples were free from a layer of BeO, then the linear plot should go through the origin and possess a slope proportional to the change in the absorption coefficient between the wavelengths mentioned above. On the other hand if a surface layer of thickness x_0 is oxidized, and if this thickness is the same for all absorbers, the straight line should yield an x-intercept equal to x_0. Due to appreciable errors as indicated it is not possible to estimate x_0 with certainty. However, inspection reveals that the oxide thickness cannot be in excess of a few hundred angstroms.

The linear absorption coefficient μ was determined for a number of wavelengths on the basis of the absorption data given in Fig. 1. A plot of these results appears on the graph of Fig. 3. The values of μ range from $2.8\times10^{+5}$ to 0.25×10^{5} cm^{-1}.

The K-emission band of Be has been studied by Skinner and O'Bryan.[4] The intensity distribution in this band shows a sharp emission edge at 110.9A, corresponding to a photon energy of 112 ev, the latter being emitted when an electron makes a transition from the Fermi level to a vacant K state. The present measurements yield the value of 111A for the position of the K absorption edge, that is, the emission and absorption edges coincide. This result is in agreement with expectation, since in a metal like Be, there should be no forbidden zone of energies between the filled and unfilled portions of the valence band. On the theoretical side, Herring and Hill[5] have applied the method of orthogonalized plane waves to beryllium and have calculated the level density curve for energies up to and somewhat in excess of the Fermi energy.

The experimental emission curve, and the theoretical level density curve are reproduced in Fig. 4, which also shows the new measurements of $\log_{10}(I_0/I)$ here plotted as a function of the energy of incident photons. The agreement between the shape of the observed emission curve and that of the level density curve is good. Also, the theoretical curve, suggests a rapid rise in the density of unoccupied states. This feature of the theoretical curve may have its counterpart in the intense absorption that is observed to the high-energy side of the edge.

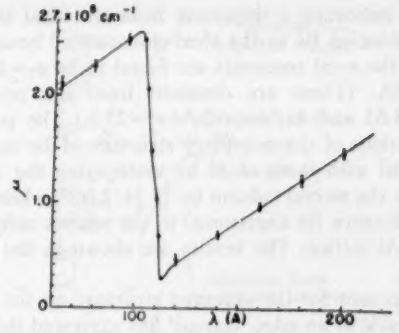

FIG. 3. A plot of linear absorption coefficients as determined from the curve shown in Fig. 1.

Secondary Structure

In common with other studies of this type, a series of secondary absorption maxima are observed on the high energy side of the K edge. The observed energy differences between the edge and the various peaks are given in the second column of Table I. The Be lattice is of the hexagonal close-packed variety. Coster[6] has pointed out that a correlation should exist in the secondary structure exhibited by elements having this symmetry and those which possess a face-centered cubic lattice. It is therefore of interest to compare the fine structure found in the case of Be with the corresponding structure associated with the K edge of an element such as Al which has a face-centered cubic lattice. The fourth column lists the energy differences between the K edge and secondary maxima as found in the K absorption spectrum of Al.[7]

For the ideal close-packed hexagonal lattice the axial ratio (c/a) should be 1.63. In Be, $c/a=3.59/2.28$

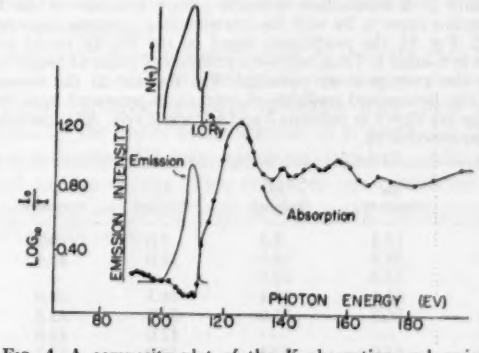

FIG. 4. A composite plot of the K absorption and emission spectra of Be as a function of incident or emitted photon energy. The upper curve shows the calculated density of states $N(\eta)$ as a function of the energy parameter η expressed in Rydbergs.

[4] H. W. B. Skinner and H. M. O'Bryan, Trans. Roy. Soc. (London) **239**, 95 (1940).
[5] C. Herring and A. G. Hill, Phys. Rev. **58**, 132 (1940).
[6] D. Coster, Physica **2**, 606 (1935).
[7] Munier, Bearden, and Shaw, Phys. Rev. **58**, 537 (1940).

$=1.58$, indicating a departure from the ideal lattice. Upon reducing Be to the ideal close-packed hexagonal lattice, the axial constants are found to be $a_1=2.24$A, $c_1=3.65$A. (These are obtained from the relations $c_1/a_1=1.63$ and $2a_1^2+c_1=2a^2+c^2=23.3$.) The present observations of the secondary structure of Be may be compared with those of Al by multiplying the values given in the second column by $(2.24/2.86)^2$, where 2.86 is the distance (in angstroms) to the nearest neighbors in the Al lattice. The results are shown in the third column.

To account for the observed structure on the high-energy side of an edge, Hayasi[8] has suggested that the structure may be considered as a series of absorption maxima superimposed on the absorption curve as a background. According to this view, the secondary maxima represent transitions in which the final state of an electron ejected photoelectrically from a sharp inner level is a so-called quasi-stationary state. Hayasi points out that such energy states are produced when the waves associated with the ejected electron form a standing wave pattern in the immediate vicinity of the atom from which the electron was emitted.

In the case of an electron ejected from a K shell, the specification of the final state ($l=1$) requires that the wave function shall have a twofold axis of symmetry. This consideration imposes a condition on the propagation sphere in the reciprocal lattice. Such a sphere must pass through two points so located that the sum of the propagation vectors is zero. Thus, the requirement in the case of K absorption is that the ejected electron shall move at right angles to a set of parallel crystal planes and undergo 90° Bragg reflection.

The comparison with experiment is facilitated, since on the basis of this model it becomes possible to select a relatively small set of absorption maxima which are expected to be most intense. The selection is carried out by estimating the relative amplitude of waves backscattered from nearby atoms. The relative intensity is found to depend on (1) the number of equivalent neighboring atoms (2) the magnitude of the distance of such atoms from the one which has lost a photoelectron and (3) the coherence of the scattered waves.

The energy, in ev, of electrons reflected normally from crystal planes in a cubic lattice is given by $V=150(\alpha^2+\beta^2+\gamma^2)/4a^2$, where α, β, γ are the reflection indices of cooperating planes, and a is the lattice constant in A. The relation follows directly from the particular Bragg condition $n\lambda=2d$ which must be satisfied in the case of the K absorption spectrum.

The first column in Table I gives the magnitudes of V calculated for the Al lattice corresponding to absorption peaks of high intensity. (The values of the reflection indices are subject to the appropriate condition for the nonvanishing of the atomic structure factor. For a face-centered cubic lattice α, β, γ must be all even or all odd.) The calculated values of V are measured from the average inner potential V_0. The tabulated position of observed peaks represent energy differences from the K edge and correspond to $(V+V_0)-V_K$ where V_K is the energy of the final state corresponding to the K absorption edge. Since V_0 and V_K are not equal the calculated values should be corrected by (V_K-V_0) before comparison with the observed values listed in the fourth column. The value of the inner potential for Al is not known reliably. In any case the correction should be a constant not exceeding a few ev. The last column in the table gives the calculated values corrected by (V_K-V_0). The constant difference of 3 ev was estimated from the observed and calculated values for Al.

Due to the thermal vibrations of the lattice and the natural width of the stationary states[9] a secondary absorption band possesses considerable width. Accordingly, it is not possible to determine the positions of individual absorption peaks very accurately from the experimental observations. The average energy difference between successive peaks as obtained from a sequence should be a more reliable basis for comparison between theory and experiment. This difference should be constant and is found to be equal to 9.2 ev from the values of V calculated for the Al lattice. The corresponding differences obtained from the observations on Be and Al are also given at the bottom of Table I. As in the case of the K spectrum of Mg (see reference 7), the presence of additional peaks is not surprising on account of the more complex hexagonal structure of these elements. One such peak is detected in Be over the present range of measurements. The missing peak in Be falls in the very short wavelength region where the available data are inadequate.

TABLE I. A comparison of the secondary structure in the K absorption curve of Be with the corresponding structure observed in Al. For Al, the predictions based on the Hayasi model are given in column 1. These represent positions of peaks as measured from the average inner potential. For Be and Al the experimentally determined positions of maxima as measured from the K edge are shown in columns 2 and 4, respectively. All quantities are expressed in ev.

V calc	Be observed	Be reduced	Al observed	V corrected
9.2	13.4	8.3	8.0	6.2
18.4	25.9	15.9	15.0	15.4
...	35.8	22.0	...	...
27.6	43.1	26.4	24.5	24.6
36.8	56.9	35.0	34.0	33.8
46.0	...	...	42.0	43.0
55.2	85.0	52.1	52.0	52.2
Av. diff.		8.8	9.0	9.2

[8] T. Hayasi, Sci. Repts. Tôhoku Univ. 33, 123 (1949).

[9] See T. Hayasi, Science Repts. Tôhoku Univ. 34, 185 (1951) for a determination of these widths in connection with the fine structure of the K absorption edge in Li.

The Use of Synchrotron Radiation

The top curve in Fig. 5 is a reproduction of the microphotometer trace of the absorption spectrum of a 1000A Be foil in the vicinity of the K edge. The spectrogram was taken in connection with a study of the properties of the radiation emitted by electrons of maximum energy equal to 321 Mev. Due to the continuous nature of the incident radiation, the reduction of the trace involves a consideration of the energy distribution among the various orders produced by the grating.

In the spectral distribution of the radiation emitted by the source, let $P_0(\lambda)$, $P_0(\lambda/2)$, $P_0(\lambda/3)$, etc. represent the intensity per unit wavelength band centered at λ, $\lambda/2$, $\lambda/3$, etc. Radiation of each of these wavelengths will be brought to a focus on the Rowland circle at the same position x measured from the central image. The contribution to the photographic density at x will be determined by the manner in which the component incident intensities are modified by the absorber and by the grating response. The latter is defined as the fraction of the intensity incident on the grating diffracted into a given order. If $P(x)$ is the intensity per unit distance interval centered at x, we may write

$$P(x)dx/d\lambda = P_0(\lambda)e^{-\mu(\lambda)t}R(\lambda) + \tfrac{1}{2}P_0(\lambda/2)e^{-\mu(\lambda/2)t}R(\lambda/2)+\cdots,$$

where only two spectral orders have been taken into account. In this expression t is the absorber thickness, and μ, the linear absorption coefficient. The grating response is introduced through the factors $R(\lambda)$, and $R(\lambda/2)$, while $dx/d\lambda$ is the reciprocal instrumental dispersion. The factor $\frac{1}{2}$ which appears in the second term on the right is due to the change in dispersion with order.

It is possible to determine $P(x)$, $P_0(\lambda)$, $P_0(\lambda/2)$, and $dx/d\lambda$ experimentally. For a complete reduction of the trace the grating efficiency factors $R(\lambda)$ and $R(\lambda/2)$ must also be known. Our present knowledge[10] of the grating efficiency is very meager. However, in the immediate region of the edge, the absorption by the sample affects primarily the transmitted intensities associated with the first-order radiation and photometer deflections may be converted into relative intensities.

[10] Experiments utilizing various monochromatic radiations in the soft x-ray region and aimed at the determination of the grating response are now in progress.

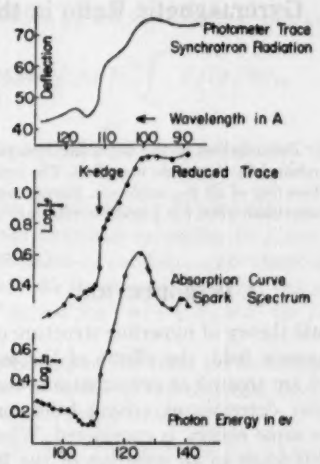

FIG. 5. The absorption curve of Be in the neighborhood of the K edge based on measurements using the far ultraviolet continuous radiation from the Cornell synchrotron.

In so doing, one neglects the variation of $R(\lambda)$ with wavelength and regards the second- and higher-order intensity components to be free from large changes over the narrow spectral range centered at the K discontinuity.

The result of a partial reduction of this sort is shown in the middle curve of Fig. 5. The corresponding portion of the absorption curve as determined by the use of spark spectra is also reproduced in the lowest graph in Fig. 5. A comparison indicates that the shapes of the two curves in the region of the edge are in good agreement. In the case of the middle curve, the less rapid drop in the low-energy side of the edge is most likely due to second order spectra of short wavelength radiations (55 to 70A) which are present in the incident beam and contribute to the observed intensity above the edge. Third-order contributions are not expected since the intensity of the incident radiation below 55A is negligible.

Additional measurements using Al indicate that the absorption curves determined by the use of the synchrotron radiation compare favorably with those obtained by the use of spark spectra. It is gratifying that two radically different types of incident radiation yield similar results. This enhances our confidence in procedures previously used in soft x-ray spectroscopy of the solid state.

Gyromagnetic Ratio in the Hyperfine Structure of Doublet States*†

W. W. CLENDENIN‡
Yale University, New Haven, Connecticut
(Received March 10, 1954)

Perturbation of the hyperfine structure of an electronic $p_{1/2}$ state by the $p_{3/2}$ state is calculated using relativistic electronic functions. The main effects are a change in apparent nuclear g factor and a common lowering of all $p_{1/2}$ sublevels. Energy corrections due to the perturbation of one level of a doublet term by the other when i is $\frac{1}{2}$ and j is arbitrary are also obtained.

I. INTRODUCTION

IN the usual theory of hyperfine structure of an atom in a magnetic field, the effects of the nucleus and applied field are treated as perturbations and the part of the secular determinant arising from unperturbed levels of the same energy is considered. When either j or i is $\frac{1}{2}$, this leads to an equation of the Breit-Rabi[1] form. Inclusion in the secular determinant of matrix elements between the components of a doublet electronic term, e.g., between $p_{\frac{1}{2}}$ and $p_{\frac{3}{2}}$ components, gives second-order corrections to this equation. Foley[2] has treated the corrections for $p_{\frac{1}{2}}$ states, using nonrelativistic wave functions, and he has shown that they lead to a change in the apparent nuclear g factor. In the present work this treatment is modified by using relativistic electronic functions and the case $i=\frac{1}{2}$ is also considered. The procedure has been to compute matrix elements of the perturbing terms of the Hamiltonian between states of definite f, m_f. These are used in the secular determinant and this determinant is solved to order $1/\delta$, where δ is the doublet separation. Expressions for the energy are thus obtained which are applicable for a range of field strengths such that the perturbing terms are small compared with δ

II. UNPERTURBED SOLUTIONS

The Dirac Hamiltonian for an electron in an electromagnetic field is

$$H=-c\boldsymbol{\alpha}\cdot(\mathbf{p}+(e\mathbf{A})/c)-eA_0-\beta mc^2, \tag{1}$$

where $-e$ is the charge on the electron and A_0 and $\mathbf{A}$ are the scalar and vector potentials, respectively. In this problem the effect of the vector potential is treated as a perturbation. The unperturbed electronic functions are solutions of the equation

$$H_0\Psi=E_0\Psi, \tag{2}$$

where

$$H_0=-c\boldsymbol{\alpha}\cdot\mathbf{p}-eA_0-\beta mc^2. \tag{3}$$

For application to a single electron outside of closed shells, A_0 is assumed to depend only on the radial distance r_e of the electron from the nucleus and the nucleus is taken to be stationary. The solutions of Eq. (2) used here are the same as those given by Darwin[3] except that a factor $\exp[\pi i(m_j-\frac{1}{2})]$ is included for $m_j>0$. This choice of phase is convenient since the operation of the electronic angular momentum $\mathbf{J}$ then takes the form

$$J_z\Psi_j(m_j)=m_j\hbar\Psi_j(m_j), \tag{4}$$

$$(J_x\pm iJ_y)\Psi_j(m_j)=\hbar[(j\mp m_j)(j\pm m_j+1)]^{\frac{1}{2}}\Psi_j(m_j\pm1). \tag{5}$$

Here $\Psi_j(m_j)$ is the solution of Eq. (2), corresponding to particular electronic quantum numbers j, m_j.

The nucleus has been treated as of negligible spatial extent and of infinite mass so that it is taken to be stationary.[4] As is well known the angular momentum operators I_x, I_y, I_z of the nucleus may be represented by noncommuting matrices and the nuclear spin functions by column vectors $N_i(m_i)$, belonging to values i and m_i of the nuclear spin quantum numbers. Wave functions of the combined system of electron plus nucleus are linear combinations of products of the type $\Psi_j(m_j)N_i(m_i)$. Combined functions belonging to particular quantum numbers f, m_f of the total angular momentum $\mathbf{F}=\mathbf{J}+\mathbf{I}$ are obtained by using the coefficients of the product functions given by Wigner.[5] These functions with definite f, m_f are the base functions used in the perturbation calculation.

III. PERTURBATIONS

The perturbing term of the vector potential is, from Eq. (1), $-e\boldsymbol{\alpha}\cdot\mathbf{A}$. The vector potential $\mathbf{A}$ has a part $[\mathfrak{H}\times\mathbf{r}_e]/2$ due to the external field $\mathfrak{H}$ and a part $[\boldsymbol{\mu}_i\times\mathbf{r}_e]/r_e^3$ due to the nuclear moment $\boldsymbol{\mu}_i$. Here $\mathbf{r}_e$ is the position vector of the electron with respect to the nucleus. An additional perturbation is the energy

* Part of a dissertation submitted for the degree of Doctor of Philosophy at Yale University.

† Assisted by the joint program of the U. S. Office of Naval Research and U. S. Atomic Energy Commission. The later part of the work was supported by the United States Air Force, through the Office of Scientific Research of the Air Research and Development Command.

‡ Now at the Department of Physics, University of Texas, Austin, Texas.

[1] G. Breit and I. I. Rabi, Phys. Rev. **38**, 2082 (1931); Millman, Rabi, and Zacharias, Phys. Rev. **53**, 384 (1938).

[2] H. M. Foley, Phys. Rev. **80**, 288 (1950).

[3] C. G. Darwin, Proc. Roy. Soc. (London) **A118**, 654 (1928).

[4] For a doublet component of a particular isotope, the main effect of the finite nuclear volume is to cause a shift in energy common to all sublevels. See, e.g., J. E. Rosenthal and G. Breit, Phys. Rev. **41**, 459 (1932); G. Breit, Phys. Rev. **42**, 348 (1932).

[5] E. Wigner, *Gruppentheorie und ihre Anwendung auf die Quantenmechanik der Atomspektren* (Vieweg und Sohn, Braunschwig, 1931).

$-\boldsymbol{\mu}_i\cdot\mathfrak{H}$ of the nuclear moment in the external field. If $\mathfrak{H}$ is taken in the z direction, the three perturbations become

$$(e/2)\mathfrak{H}_z B_z \equiv X, \tag{6}$$

$$eg_i\mu_0(\mathbf{I}\cdot\mathbf{B})/hr_e^3 \equiv Y, \tag{7}$$

$$-g_i\mu_0\mathfrak{H}_z I_z/h \equiv Z. \tag{8}$$

Here $\mathbf{B}$ is the matrix vector $\boldsymbol{\alpha}\times\mathbf{r}_e$, μ_0 is the Bohr magneton, and the nuclear moment $\boldsymbol{\mu}_i$ is $g_i\mu_0\mathbf{I}/h$, $\mathbf{I}$ being the nuclear angular momentum operator.

Matrix elements of matrix vectors of the type of (6), (7), and (8) have been given by Guettinger and Pauli[6] and by Johnson.[7] All the nonvanishing elements are diagonal in m_f, and f differs in the initial and final states by 0, ±1. The elements of (7) are diagonal in f while those of (8) are diagonal in j.

Matrix elements of (6) between states of different f are given in terms of the elements of (6) between electron states $\Psi_j(m_j)$. These are

$$(\Psi_j(m_j),\ X\Psi_j(m_j)) = \mu_0\mathfrak{H}_z g_j' m_j, \tag{9}$$

$$(\Psi_{l+\frac{1}{2}}(m_j),\ X\Psi_{l-\frac{1}{2}}(m_j)) = \mu_0\mathfrak{H}_z N\{(l+\tfrac{1}{2})^2-m_j^2\}^{\frac{1}{2}}/(2l+1). \tag{10}$$

The quantities g_j' and N are given by

$$g_j' = g_j\left[1-\{4k/(2k-1)\}\int_0^\infty F_j^2 dr_e\right], \tag{11}$$

$$N = \int_0^\infty G_{l+(1/2)}G_{l-(1/2)}dr_e. \tag{12}$$

Here g_j is the Lande g factor while k is the quantum number introduced by Dirac and equal to $-l-1$ for $j=l+\frac{1}{2}$ and to l for $j=l-\frac{1}{2}$. The functions F_j and G_j are solutions for particular j of Dirac's radial equations in the form used by Gordon,[8] with the normalization

$$\int_0^\infty (F_j^2+G_j^2)dr_e = 1. \tag{13}$$

The second term in the brackets of (11) is the relative correction to g_j discussed by Breit[9] and by Margenau.[10]

The matrix elements of (7) are most readily expressed in terms of coupling constants of the interaction between electron and nucleus. Between states of definite f, m the matrix elements are

$$(i,j,f,m_f|\,Y\,|i,j,f,m_f) = (a_{j,j}/2)[f(f+1)-j(j+1)-i(i+1)], \tag{14}$$

$$(i,j,f,m_f|\,Y\,|i,j-1,\ f,m_f) = \pm(b_{j,j-1}/2)[(f+j-i)\times(f+i-j+1)(f+j+i+1)(j+i-f)]^{\frac{1}{2}}. \tag{15}$$

Here $a_{j,j}$ and $b_{j,j-1}$ are the coupling constants

$$a_{j,j} = [2eg_i\mu_0 k/j(j+1)]\int_0^\infty F_jG_j r_e^{-2}dr_e, \tag{16}$$

$$b_{j,j-1} = -[eg_i\mu_0/2j]\int_0^\infty (F_{j-1}G_j+F_jG_{j-1})r_e^{-2}dr_e. \tag{17}$$

Choice of the double sign in (15) depends on the relative phases of the functions belonging to j and $j-1$. The coupling constants $a_{j,j}$ and $b_{j,j-1}$ are those of Breit and Wills' paper.[11] In their notation which was also that of Goudsmit[12] $a_{jj}=a'$ for $j=l+\frac{1}{2}$, $a_{jj}=a''$ for $j=l-\frac{1}{2}$, and $b_{j,j-1}=a'''$.

Matrix elements of the third perturbation, (8), may be expressed in terms of the diagonal matrix element between states $N_i(m_i)$, which is

$$(N_i(m_i),\ ZN_i(m_i)) = -g_i\mu_0\mathfrak{H}_z m_i. \tag{18}$$

All matrix elements of the perturbations between states of definite f, m_f are given in terms of (9), (10), (16), (17), and (18) by means of the Guettinger-Pauli formulas, and the secular determinant may thus be set up.

IV. ENERGY LEVELS OF $p_{\frac{1}{2}}$ STATES

Since the matrix elements are diagonal in m_f, the secular determinant breaks up into smaller determinants corresponding to a given m_f. For the $p_{\frac{1}{2}}$, $p_{\frac{1}{2}}$ doublet there are, in general, six values of f and the smaller determinants have six rows and columns. These may be solved in an approximation equivalent to the standard second-order perturbation approximation. The diagonal elements belonging to $p_{\frac{1}{2}}$ are approximated by δ, the doublet separation. Off-diagonal elements belonging to the $p_{\frac{1}{2}}$ state and elements between $p_{\frac{1}{2}}$ and $p_{\frac{1}{2}}$ states are eliminated to order $1/\delta$ by adding multiples of rows and columns. The determinant is thus reduced to one with two rows and columns, the elements of which contain second-order terms. This is solved for the energy E. The result is

$$E-E_0 = -\frac{\Delta\nu}{2(2i+1)} - g_i'\mu_0\mathfrak{H}_z m_f \pm \frac{\Delta\nu}{2}\left(1+\frac{4m_f x}{2i+1}+x^2\right)^{\frac{1}{2}} - \frac{2(a''')^2}{\delta}i(i+1) - \frac{2\mu_0^2\mathfrak{H}_z^2 N^2}{9\delta}. \tag{19}$$

Here E_0 is the unperturbed energy and $\Delta\nu$ is the zero-field separation, given by

$$\Delta\nu = (i+\tfrac{1}{2})[a''-2(a''')^2/\delta]. \tag{20}$$

The remaining undefined quantities are

$$g_i' = g_i(1+4Na'''/3g_i\delta), \tag{21}$$

$$x = (g_j'+g_i')\mu_0\mathfrak{H}/\Delta\nu. \tag{22}$$

[6] P. Guettinger and W. Pauli, Z. Physik **67**, 743 (1931).
[7] M. H. Johnson, Jr., Phys. Rev. **38**, 1635 (1931).
[8] W. Gordon, Z. Physik **48**, 11 (1928). In order to avoid double double subscripts, F is here used for Gordon's ψ_1, and G for his ψ_2.
[9] G. Breit, Nature **122**, 649 (1928).
[10] H. Margenau, Phys. Rev. **57**, 383 (1940).
[11] G. Breit and L. A. Wills, Phys. Rev. **44**, 470 (1932). In terms of φ_1, φ_2 of Breit and Wills the functions used here are $F=\varphi_1$, $G=\varphi_2$; F, G of Breit and Wills differ from those here and are expressed in terms of φ_1, φ_2 by their Eq. (15).
[12] S. A. Goudsmit, Phys. Rev. **37**, 663 (1931).

TABLE I. Values of correction terms in Eq. (28) and Eq. (27).

	$-(\Delta\nu)/[6(2i+1)g_i\delta]$	$-(\Delta\nu)\chi/[6(2i+1)g_i\delta]$
Gallium	−0.0062	−0.0058
Indium	−0.0043	−0.0035

Equation (19) is seen to have the same form as the Breit-Rabi equation except for the addition of the last two terms which are the same for all sublevels of the $p_{\frac{1}{2}}$ state. Perturbation by the $p_{\frac{1}{2}}$ state also adds a small correction term to $\Delta\nu$, but the main effect is to replace g_i with g_i'.

The magnitude of this effect may be estimated by using the values of a'' and a''' obtained by Breit and Wills.[11] Near the nucleus, where the integrands of (16) and (17) are large, a Bessel function approximation may be used for the electronic functions F and G. In this way the above authors obtain

$$(a'''/a'')=-(1/16)(\mathcal{S}/\mathcal{F}). \tag{23}$$

Here $\mathcal{F}$ and $\mathcal{S}$ are relativistic correction factors given by

$$\mathcal{F}=3/[\rho''\{4(\rho'')^2-1\}], \tag{24}$$

$$\mathcal{S}=(4/\pi Z^2\alpha^2)\sin\pi(\rho''-\rho'). \tag{25}$$

The quantity $\rho'=(4-Z^2\alpha^2)^{\frac{1}{2}}$, while $\rho''=(1-Z^2\alpha^2)^{\frac{1}{2}}$, where Z is the nuclear charge and α is the fine structure constant. The ratio $\chi=\mathcal{S}/\mathcal{F}$ is

$$\chi=1-1.396Z^2\alpha^2-0.121Z^4\alpha^4+\cdots. \tag{26}$$

Since the term $(a''')^2/\delta$ in $\Delta\nu$ is small compared with a'', one has, approximately,

$$a''\approx(2\Delta\nu)/(2i+1).$$

With these approximations the apparent nuclear g factor is

$$g_i'=g_i[1-(\Delta\nu)N\chi/\{6(2i+1)g_i\delta\}]. \tag{27}$$

V. APPLICATION TO GALLIUM AND INDIUM

Using nonrelativistic wave functions for the electron, Foley[2] found that

$$g_i'=g_i\{1-(\Delta\nu)/[6(2i+1)g_i\delta]\}. \tag{28}$$

Equation (27) is seen to be identical with this except for the factor $N\chi$ in the correction term. Taking N to be approximately unity, the effect of χ in the cases of gallium ($Z=31$) and indium ($Z=49$) is shown in Table I.

The change in apparent nuclear g factor appears experimentally in a difference in values of the g factor obtained from atomic beam experiments and those measured by magnetic resonance methods. Existence of such discrepancies has been pointed out by Kusch.[12] Using experimental values of the nuclear moments quoted by him, the ratio of the apparent moment from atomic beam work to that from magnetic resonance work is $1-0.0079\pm0.0023$ for Ga^{69} and $1-0.0077\pm0.0017$ for Ga^{71}. The theoretical values, both the nonrelativistic -0.0062 and the relativistic -0.0058 are seen to differ from the experimental ones by an amount about equal to the assigned experimental error. This difference may be due, as Foley has suggested,[2] to configuration interaction in the $p_{\frac{1}{2}}$ state.

[12] P. Kusch, Phys. Rev. 78, 615 (1950).

VI. ENERGY LEVELS FOR $i=1/2$

When $i=\frac{1}{2}$, there are just four values of f belonging to a doublet term, and the secular determinant breaks down into smaller determinants having four rows and columns. Solution of these may be carried out along the same lines as in IV. The energy E of a doublet component is

$$E-E_0=-\frac{\Delta\nu}{2(2j+1)}+g_j'\mu_0\mathcal{H}_z m_f \pm\frac{\Delta\nu}{2}\left[1-\frac{4m_f x}{2j+1}+x^2+\Gamma\right]^{\frac{1}{2}}+\Delta. \tag{29}$$

Here E_0 is the energy of the unperturbed level. The quantities Γ and Δ are second-order corrections given by

$$\Gamma=(4/\delta)\{-m_f a'''y\pm[y^2(\Delta\nu)/(j+\tfrac{1}{2}) -xya'''(l(l+1)-m_f^2)-xy^2m_f(\Delta\nu)]\}, \tag{30}$$

$$\Delta=(1/\delta)\{-(k+1)(2l+1)(a''')^2/4 \pm[a'''(\Delta\nu)y+y^2(\Delta\nu)^2(l(l+1)-m_f^2)]\}. \tag{31}$$

The upper signs in (30) and (31) apply to $j=l+\frac{1}{2}$ and the lower signs to $j=l-\frac{1}{2}$. The parameter x is $(g_j'+g_i)\mu_0\mathcal{H}_z/(\Delta\nu)$ and y is $\mu_0\mathcal{H}_z N(2l+1)(\Delta\nu)$, where $\Delta\nu$ is the zero-field separation given by

$$\Delta\nu=(j+\tfrac{1}{2})\{a''-|k+1|(a''')^2/\delta\}. \tag{32}$$

Unlike the case when $j=\frac{1}{2}$, the second-order perturbation does not take the form of a change in apparent nuclear g factor, but can only be expressed by means of the more complex correction terms Γ and Δ.

VII. SUMMARY AND CONCLUSION

The perturbation of an atomic $p_{\frac{1}{2}}$ state by the $p_{\frac{3}{2}}$ state leads to second-order corrections to the Breit-Rabi equation. The main effects of the correction terms are: 1) to change the apparent nuclear g factor, and 2) to add a term which lowers all the sublevels of the $p_{\frac{1}{2}}$ state equally. Perturbation of one component of a doublet by the other when neither j is $\frac{1}{2}$ but $i=\frac{1}{2}$ leads to the correction terms (30) and (31) to the energy equation.

The author takes pleasure in expressing his gratitude to Professor G. Breit for suggesting this problem and for valuable discussions during the course of the work.

Anomalous Dispersion and Scattering of X-Rays*

L. G. PARRATT AND C. F. HEMPSTEAD
Cornell University, Ithaca, New York
(Received January 25, 1954)

The theoretical expressions for the anomalous dispersion of x-rays have been integrated for any positive value of p_q in a $C_q\lambda^{p_q}$ term in the distribution of "dispersion" oscillators for the q shell of electrons. This distribution may be written generally as the sum of n terms of the form $C_{qn}\lambda^{p_{qn}}$ or, as is commonly done, as a single term. Damping has been retained, its effect evaluated and shown to be negligible except for λ extremely close to the wavelength of an absorption discontinuity. With damping neglected, universal dispersion curves are presented. If p_q and g_q (the oscillator strength) are known, the anomalous part of the refractive index or of the atomic scattering factor can be readily deduced from the universal curves.

Comparison of the more exact theoretical values with experiment shows less satisfactory agreement than before.

INTRODUCTION

IN comparing theoretical predictions with experimental measurements of refractive index r for x-rays,

$$r=1-(\delta+i\beta),$$

and for the atomic scattering factor f, written for very small scattering angle as

$$f=(1/A\lambda^2)(\delta^2+\beta^2)^{\frac{1}{2}},$$

where A is a constant, it has become the custom to assume that the frequency distribution of the theoretical "dispersion" oscillators follows a λ^3 relation, where λ is the wavelength.[1] This assumption makes for easy integration of the expression for δ (or for f), but it is not in accord with x-ray absorption measurements: In general, $\lambda^{11/4}$ is probably better for the photoelectric absorption by K electrons, $\lambda^{7/3}$ by L electrons,[2,3] and perhaps $\lambda^{5/2}$ by M electrons.[4] The exponent for a given electron shell varies with atomic number. Needless to say, the numerical value of the exponent is important in the region of anomalous dispersion.

As an additional complication, the exponent may vary with wavelength. Hönl[5] used a two-term expression for K electrons, viz., $C_K(\lambda/\lambda_K)^3+D_K(\lambda/\lambda_K)^4$, where $C_K=4/3$ and $D_K=-1/3$; this is equivalent to a single term with exponent $p_K(\lambda)$, such that $p_K=2.67$ at λ_K, 2.78 at $\lambda_K/2$, and 2.94 at $\lambda_K/200$. Hall[4] also discussed this expression. Victoreen[3] concluded that it expresses well the experimental data for the net effect of all the electron shells; the C/D ratio depends markedly upon the atomic number and upon the wavelength region (i.e., $\lambda<\lambda_K$ or $\lambda_K<\lambda<\lambda_L$). However, careful analysis of the available experimental data for the K electrons of copper, for example, indicates that p_K is very nearly 2.75 and does not vary significantly in the range $0.1A<\lambda<\lambda_K$. With more extensive and accurate absorption measurements, it may well be necessary to use two (or more) terms in the general sum $\sum_n C_{q_n}\lambda^{p_{qn}}$. In any case, the general integration must be carried out separately for each term.

In the present paper, the dispersion expression is integrated for a general λ^{p_q} term, where p_q may be any number greater than zero. Combinations of such terms may be made when and if desired. Typical calculations are shown for $p=2$, 7/3, 5/2, 11/4, 3, and 4. The necessity of including the anomalous effects of more than one shell of electrons is pointed out[6] with the correlative conclusion that there is practically no region of "normal" x-ray dispersion.

It has also become the custom to neglect the damping factor. In the present integrations and calculations, damping has been retained so as to allow evaluation of the error made in any specific case due to neglect of

* This research was supported in part by The United States Air Force under a contract monitored by the Office of Scientific Research, Hq. Air Research and Development Command, Post Office Box 1395, Baltimore 3, Maryland.

[1] For example, see R. W. James, *The Optical Principles of the Diffraction of X-Rays* (G. Bell and Sons, Ltd., London, 1948); and A. H. Compton and S. K. Allison, *X-Rays in Theory and Experiment* (D. Van Nostrand Company, Inc., New York, 1935). W. Heitler [*The Quantum Theory of Radiation* (Oxford University Press, London, 1944), second edition, pp. 129–137] discusses "dispersion" oscillators quantum mechanically in terms of matrix elements of transitions of the inner electron to the various bound and unbound states. This discussion includes "oscillator strength" as introduced later.

[2] K. Grosskurth, Ann. Physik **20**, 197 (1934); S. J. M. Allen, Phys. Rev. **28**, 907 (1926); Compton and Allison, reference 1; A. Jönsson, *Inaugural Dissertation* (Upsala University, Upsala, 1928); and J. Victoreen, J. Appl. Phys. **19**, 855 (1948) and **20**, 1141 (1949). These measurements refer to all types of electrons; appropriate subtractions are necessary to deduce the exponent of λ for a particular electron shell. (Subtraction must first be made for the scattering part of the measured absorption.)

[3] With damping terms neglected, the integration for δ or f has been done for $\lambda^{5/2}$ by E. J. Williams, Proc. Roy. Soc. (London) **A143**, 358 (1934). Williams, and also J. A. Bearden and C. H. Shaw [Phys. Rev. **46**, 759 (1934)] have interpolated between $\lambda^{5/2}$ and λ^3 for $\lambda^{11/4}$.

[4] No direct measurements of p in λ^p for n electrons are known. However, p_{LI} is smaller than $p_{LII,III}$, and it is the behavior of the L_I-electrons that causes p_L to be so small. Similar behavior is observed for the M_I-electrons relative to the other M electrons. See H. Robinson, Proc. Roy. Soc. (London) **A104**, 455 (1923); and H. Hall, Revs. Modern Phys. **8**, 358 (1936), and references.

[5] H. Hönl, Ann. Physik **18**, 625 (1933) and Z. Physik **84**, 1 (1933). Hönl's treatment is based on theoretical assumptions that are known to be not valid in the present range of x-ray energies. (*Note added in proof.*—H. Eisenlohr and G. L. J. Müller [Z. Physik **136**, 491 and 511 (1954)] have recently extended Hönl's treatment to L electrons).

[6] The authors note, after completion of the present work, that this point has also recently been made by H. Eisenlohr and G. L. Müller, Z. Naturforsch. **8a**, 429 (1953).

damping. It turns out that neglect of damping is well justified except in the case of λ extremely close to λ_q, the wavelength of an absorption discontinuity; and for this narrow region the difference between λ and λ_q has, as yet, very little practical meaning. With damping neglected, universal curves for anomalous dispersion are useful and convenient.

Comparison of the present calculations with experiment show less good agreement than before.

EXPRESSION FOR δ OR f

The Integral

According to quantum-mechanical dispersion theory,[1] the refractive index, in terms of various electron shells q, is

$$r=1-(\delta+i\beta)=1-A\lambda^2\sum_q\int_{\omega_q}^{\infty}\frac{\omega^2(dg/d\omega_\nu)_q}{\omega^2-\omega_\nu^2-i\eta_q\omega}d\omega_\nu. \quad (1)$$

The real unit decrement and the imaginary terms are

$$\delta=\sum_q\delta_q=A\lambda^2\sum_q\int_{\omega_q}^{\infty}\frac{\omega^2(\omega_\nu^2-\omega^2)(dg/d\omega_\nu)_q}{(\omega^2-\omega_\nu^2)^2+\eta_q^2\omega^2}d\omega_\nu, \quad (2)$$

$$\beta=\sum_q\beta_q=A\lambda^2\sum_q\int_{\omega_q}^{\infty}\frac{\eta_q\omega^3(dg/d\omega_\nu)_q}{(\omega^2-\omega_\nu^2)^2+\eta_q^2\omega^2}d\omega_\nu, \quad (3)$$

where

$$A=\frac{Ne^2}{2\pi m_e c^2}\frac{\rho}{M}=2.7019\times10^{10}\frac{\rho}{M},$$

and e = electronic charge, N = Avogadro's number, m_e = electronic mass, c = velocity of light, ρ = density, M = molecular weight, $\omega=2\pi\nu$, ν = incident x-ray frequency; $\omega_\nu=2\pi\nu_\nu$, ν_ν = frequency of dispersion oscillator, $\omega_q=2\pi\nu_q$, ν_q = frequency of the q-absorption discontinuity; $(dg/d\omega_\nu)_q$ = oscillator density of q-type electrons near ω_ν; and η_q = damping factor. Although the oscillators extend in frequency from 0 to ∞, the only ones actually operating are those[7] from ω_q to ∞. The quantity $(\delta+i\beta)$ is positive; the minus sign in Eq. (1) indicates that the phase of the scattered waves is opposite to the phase of the incident wave. The imaginary term, $i\beta$, represents a wave $\pi/2$ out of phase, and is an absorptive term. This wave has a negligible effect in angular deviations of the beam, but has a significant role in scattered intensity in the anomalous region, especially at small scattering angles.[1] The integral of Eq. (3) for β is easy to evaluate and is discussed later. The essential problem is δ.

[7] For ω very close to ω_q, we must be careful of the value we choose for ω_q. Fine structure is observed in the experimental absorption coefficient in this region, structure composed of "resonance absorption lines" [of the sort reported by L. G. Parratt, Phys. Rev. **56**, 295 (1939); J. Trischka, Phys. Rev. **67**, 318 (1945), and by Y. Cauchois and N. F. Mott, Phil. Mag. **40**, 1260 (1949)]. Transitions to unfilled outer levels in the atom (or "bands" in the solid) are properly included in the integral. It has become the custom arbitrarily to take as ω_q the frequency at the first inflection point in the absorption curve, whereas a point about midway up the absorption discontinuity is probably more realistic for use in the dispersion equations.

The operating oscillators involve the photoelectric absorption process, and the oscillator density can be written

$$(dg/d\omega_\nu)_q=(m_e c/2\pi^2e^2)\mu(\omega_\nu)_q, \quad (4)$$

where $\mu(\omega_\nu)_q$ is the atomic photoelectric absorption coefficient of q-type electrons for frequency ω_ν. For convenience we shall write the absorption coefficient as following a single term in the sum $\sum_n C_{qn}\lambda^{p_{qn}}$, then

$$\begin{aligned}\mu(\omega_\nu)_q&=(\omega_\nu/\omega_q)^{-p_q}\mu_q \quad \text{for } \omega_\nu>\omega_q,\\ &=0 \qquad\qquad\quad \text{for } \omega_\nu<\omega_q,\end{aligned} \quad (5)$$

where μ_q is the coefficient for $\omega_\nu=\omega_q$. With Eqs. (4) and (5) placed in (1), we may write

$$\delta=\sum_q\delta_q=A\lambda^2\sum_q g_q\,\mathrm{Re}(J_q), \quad (6)$$

where J_q, containing the integral to be evaluated, is

$$[J_q]_p\equiv 2\alpha x^2\omega_q^{p_q+1}\int_{\omega_q}^{\infty}\frac{\omega_\nu^{-p_q}}{\omega^2-\omega_\nu^2-i\eta_q\omega}d\omega_\nu. \quad (7)$$

The quantities α and x are defined explicitly below. If the absorption coefficient is expressed as a sum, as discussed in the Introduction, Eq. (6) becomes

$$\delta=A\lambda^2\sum_q g_q[\textstyle\sum_n C_{qn}\,\mathrm{Re}(J_q)_{pn}] \quad (6a)$$

and Eqs. (5), (8), (16) and (18) must be similarly modified.

The oscillator strength g_q in Eq. (6) may be obtained from an integration of Eq. (4), in which Eq. (5) has been inserted, *viz.*,

$$g_q=\int_{\omega_q}^{\infty}\left(\frac{dg}{d\omega_\nu}\right)_q d\omega_\nu=\frac{m_e c}{2\pi^2e^2}\frac{\omega_q}{p_q-1}\mu_q, \quad (8)$$

or g_q may be obtained by some other method.[5,8]

Evaluation of the Integral

The following relations are convenient:

$$\begin{aligned}&x\equiv\omega/\omega_q,\quad y\equiv(\omega_q/\omega_\nu)^2,\quad z\equiv\frac{1+i\zeta}{x^2(1+\zeta^2)},\\ &0<\alpha\equiv n/m\equiv\tfrac{1}{2}(p_q-1)<1,\\ &\zeta\equiv\eta_q/\omega,\\ &a\equiv|z|^{1/m}\equiv1/b,\\ &\theta\equiv\tan^{-1}\zeta,\\ &\gamma\equiv\exp(2\pi i/m).\end{aligned} \quad (9)$$

Equation (7) becomes

$$[J_q]_p=\alpha z x^2\int_0^1\frac{y^\alpha}{y-z}dy, \quad (10)$$

and this can be evaluated by contour integration.

[8] E. J. Williams, reference 3, and J. A. Wheeler and J. A. Bearden, Phys. Rev. **46**, 755 (1934).

Case I

$|z| \lesssim 1$, i.e., $x \gtrsim 1/(1+\zeta^2)^{\frac{1}{2}}$. ($|z|$ is the modulus of the complex z).

$$[J_q]_p^{\mathrm{I}} = zx^2\left[1 - \frac{\pi\alpha z^\alpha \gamma^{-n/2}}{\sin\pi\alpha} - \alpha\sum_{j=1}^{\infty}\frac{z^j}{(j-\alpha)}\right]. \quad (11)$$

The sum from $j=1$ to ∞ is easily evaluated to about 1 part in 10^6 by taking no more than 7 terms when $|z| \lesssim \frac{1}{4}$.

For $|z|$ near unity, the number of necessary terms in Eq. (11) becomes impractically large, and we need a closed form expression. When α is rational, i.e., when n and m are integers, the closed form is

$$\left[\sum_{j=1}^{\infty}\frac{z^j}{(j-\alpha)}\right]^{\mathrm{I}} = -z^\alpha\sum_{k=0}^{m-1}\gamma^{kn}\ln(1-\gamma^k z^{1/m}). \quad (12)$$

Case II

$|z| \gtrsim 1$, i.e., $x \lesssim 1/(1+\zeta^2)^{\frac{1}{2}}$,

$$[J_q]_p^{\mathrm{II}} = zx^2\left[1 - \alpha\sum_{j=0}^{\infty}\frac{1}{z^j(j+\alpha)}\right], \quad (13)$$

and the closed form of the sum of Eq. (13), with n and m integers, is

$$\left[\sum_{j=0}^{\infty}\frac{1}{z^j(j+\alpha)}\right]^{\mathrm{II}} = -z^\alpha\sum_{k=0}^{m-1}\gamma^{k(m-n)}\ln(1-\gamma^k z^{-1/m}). \quad (14)$$

Equations (12) and (14) restrict α to the range $0<\alpha<1$, i.e., $1<p<3$. Theory (with hydrogenic wavefunctions) predicts $p>3$ for $\omega \gg \omega_q$ (see Hall, reference 4), and some advantage may accrue from use of the two-term absorption expression $C_q\lambda^3 + D_q\lambda^4$ discussed in the Introduction. For $\alpha \gtrsim 1$, but for case I, α cannot be an integer, the open sums must be put into the form

$$\sum_{j=1}^{\infty}\frac{T^j}{j-\epsilon} = -T^\epsilon\sum_{k=0}^{m-1}\sigma^{kn}\ln(1-\sigma^k T^{1/m}), \quad (15)$$

where $0<\epsilon \equiv n/m<1$, and $\sigma \equiv \exp(-2\pi i/m)$, by separating the appropriate terms and adjusting the index of summation. For α an integer, integration of Eq. (10) is straightforward: The change of variable $u=y-z$ produces an elementary integral always containing as one term $\int_{-z}^{1-z} u^{-1}du$. Since the path of integration is well defined, there is no question about the argument of the resulting logarithm.

Our final expression for δ for a medium containing different atomic species s becomes

$$\delta = \sum_s A_s\lambda^2\{Z_s + \sum_q g_q[\mathrm{Re}(J_q)-1]\}, \quad (16)$$

where the real part of Eq. (11) or (13), in either open or closed form, is used for $\mathrm{Re}(J_q)$. The q summation of g_q gives the atomic number Z by the so-called sum rule;[9] the use of this rule here minimizes calculational errors due to uncertainties in the g_q values, and conveniently separates the normal and anomalous dispersion parts. The $\sum_s A_s\lambda^2 Z_s$ term is the normal dispersion term;[10] the $\sum_q$ terms are the anomalous contributions.

The expression for the modulus of the complex atomic scattering factor is

$$f = \sum_s[f_{1s}^2 + f_{2s}^2]^{\frac{1}{2}}, \quad (17)$$

where, for a single atomic species,

$$f_1 \equiv f_0 + \sum_q g_q[\mathrm{Re}(J_q)-1], \quad f_2 \equiv \beta/(A\lambda^2), \quad (18)$$

and f_0 is the "normal" (i.e., ω not near ω_q) atomic scattering factor ($=Z$ if the scattering angle is zero as is assumed for δ). Equation (17) neglects quadrupole and octopole oscillators; this neglect is justified unless the incident wavelength is small compared with the radius of the Bohr orbit B_q. Quadrupole oscillators cause an increase in f_1 of the order of $(2\pi B_q/\lambda)^2\sum_q g_q[\mathrm{Re}(J_q)-1]$ and this increase depends, as does also f_0, upon the scattering angle.[5]

The expression for f_2 requires evaluation of β. The integration of Eq. (3) is readily carried out since (a) only those dispersion oscillators respond appreciably whose frequencies are very close to the incident frequency, i.e., ω_v need be distinguished from ω only in their difference, and (b) the variation in the oscillator density is negligible in this restricted range of frequencies. Then,

$$\beta_q = \frac{\omega}{2}A\lambda^2\left(\frac{dg}{d\omega_v}\right)_q \cot^{-1}\left(\frac{2(1-x)}{\zeta}\right),$$

and, by use of Eq. (4),

$$\beta = \sum_q \beta_q = \frac{c}{2\pi\omega}\frac{N\rho}{M}\sum_q \mu(\omega)_q \cot^{-1}\left(\frac{2(1-x)}{\zeta}\right). \quad (19)$$

When x is appreciably greater or less than unity, the $\cot^{-1}$ term is π or zero for the q-type electrons, and $\beta = \lambda\mu_l/4\pi$ where μ_l,

$$\mu_l = (N\rho/M)\sum_q \mu(\omega)_q, \quad (20)$$

is the linear photoelectric absorption coefficient.

A more accurate method for evaluating β is to gather the imaginary terms in the expression for J_q. This method is usually unnecessarily cumbersome; however, it has been carried out in the case of $p=2.5$. If ζ terms are neglected compared with π, the value of β so obtained agrees with Eq. (18) except that now the $\cot^{-1}$ argument is $4(1-x^4)/\zeta$ for $x \gtrsim 1/(1+\zeta^2)^{\frac{1}{4}}$ and $4(1-x^4)/x^4\zeta$ for $x<1/(1+\zeta^2)^{\frac{1}{4}}$.

DAMPING FACTOR

There has been some ambiguity as to the proper value of η_0 for use in the above expressions. Radiation damping of a dispersion oscillator predicts $\eta_0 = 2e^2\omega^2/3m_e c^3$. This

[9] W. Kuhn, Z. Physik **33**, 408 (1925), and F. Reiche and W. Thomas, Z. Physik **34**, 510 (1925).

[10] Confirmation of the theory for the normal dispersion term is beautifully demonstrated by Bearden and Shaw, reference 3, and by J. A. Bearden, Phys. Rev. **54**, 698 (1938).

TABLE I. Universal values of $\mathrm{Re}(J_q-1)$.

λ/λ_q	$p=2.0$	$p=7/3$	$p=5/2$	$p=11/4$	$p=3$	$p=4$
0.01	−0.0001	0.0025	0.0021	0.0014	0.0009	0.0003
0.03	−0.0009	0.0097	0.0092	0.0083	0.010	0.0027
0.05	−0.0025	0.0174	0.0181	0.0197	0.013	0.0075
0.10	−0.0100	0.0368	0.042	0.048	0.046	0.0297
0.20	−0.0406	0.059	0.092	0.116	0.128	0.1151
0.30	−0.0929	0.059	0.111	0.169	0.209	0.2449
0.40	−0.1695	0.018	0.098	0.195	0.266	0.3987
0.50	−0.275	−0.061	0.033	0.169	0.275	0.544
0.60	−0.416	−0.190	−0.080	0.064	0.202	0.631
0.65	−0.504	−0.285	−0.175	−0.020	0.139	0.629
0.70	−0.607	−0.410	−0.305	−0.150	0.035	0.578
0.75	−0.730	−0.550	−0.390	−0.240	−0.150	0.456
0.80	−0.879	−0.72	−0.65	−0.52	−0.37	0.233
0.85	−1.068	−0.94	−0.89	−0.78	−0.68	−0.147
0.90	−1.325	−1.35	−1.25	−1.25	−1.23	−0.790
0.95	−1.740	−1.74	−1.74	−1.74	−1.74	−2.004
0.98	−2.252	−2.477	−2.692	−2.889	−3.062	−3.606
1.02	−2.344	−2.722	−2.888	−3.144	−3.380	−4.225
1.05	−1.93	−2.195	−2.308	−2.469	−2.619	−3.141
1.10	−1.65	−1.840	−1.91	−2.021	−2.08	−2.45
1.15	−1.51	−1.657	−1.71	−1.794	−1.83	−2.05
1.20	−1.44	−1.541	−1.58	−1.650	−1.70	−1.87
1.25	−1.36	−1.458	−1.49	−1.549	−1.60	−1.74
1.30	−1.32	−1.397	−1.43	−1.474	−1.51	−1.63
1.40	−1.25	−1.310	−1.33	−1.369	−1.40	−1.49
1.50	−1.20	−1.252	−1.270	−1.299	−1.320	−1.390
1.70	−1.15	−1.179	−1.195	−1.211	−1.225	−1.270
2.00	−1.10	−1.119	−1.13	−1.140	−1.148	−1.180
2.50	−1.06	−1.072	−1.078	−1.084	−1.091	−1.107
3.00	−1.04	−1.048	−1.051	−1.057	−1.063	−1.070
5.00	−1.014	−1.017	−1.019	−1.019	−1.02	−1.023
10.00	−1.003	−1.001	−1.002	−1.005	−1.005	−1.006
15.00	−1.00	−1.000	−1.00	−1.002	−1.00	−1.00

value gives for the full width at half maximum of the q-state $W_0=(2\pi c/\omega_q^2)\eta_0=0.118$ x.u. for all states of all atoms; whereas observed K-state widths, for example, vary from 0.70 x.u. (0.58 ev) for argon,[11] 0.15 x.u. (8 ev) for silver,[12] to 0.118 x.u. (62 ev) for gold;[13] and observed L_I widths are 4.6 x.u. (5.3 ev) for silver,[12] and 0.52 x.u. (8.7 ev) for gold.[13,14]

In general, W_0 is less than the observed widths, and two reasons are presented to account for the difference: First, the classical oscillation may be prematurely interrupted by the filling of the q-electron vacancy by another electronic transition (either radiative or non-radiative), and, second, the energy position of the q state is broadened by splitting of the state into unresolved multiplet states due to interactions between the q vacancy and outer electrons of the atom or neighboring atoms. The early interruption of the oscillation may properly be considered as contributing to η_q, but not the splitting of the state. The splitting is probably negligible for K states for atoms $Z\lesssim 16$ and for L states for $Z\lesssim 45$, except for the transition elements;[15] and, of course, if the q electrons are near the outer part of the atom in a solid the splitting may be very large.

The state width W_q has not been measured for many q's for many elements, but we may infer their values from measurements of emission line widths, making appropriate correction for the width of the final state, or by extrapolation from a nearby Z whose W_q has been measured (the energy width may be taken as proportional to Z^4 if it is not much greater than W_0). Thus, for example, W_K for copper is about 0.30 x.u.; W_{LI}, W_{LII} and W_{LIII} for wolfram, 0.56, 0.27 and 0.40 x.u., respectively. W_M and W_N values are much larger because of non-radiative transitions.

To arrive at the value of η_q for use in the above dispersion equations, we note that $\eta_0\propto\omega^2$, and may become very large for $\omega\gg\omega_q$. For large ω/ω_q, the "premature" death of the q state (filling by another process) is of no concern. For any ω/ω_q and for any ratio η_q/η_0, we may write approximately

$$\eta_q=\eta_0\left\{1+\left(\frac{\omega_q}{\omega}\right)^2\left[\frac{W_q}{0.118}-1\right]\right\}, \qquad (21)$$

where W_q is in x.u.

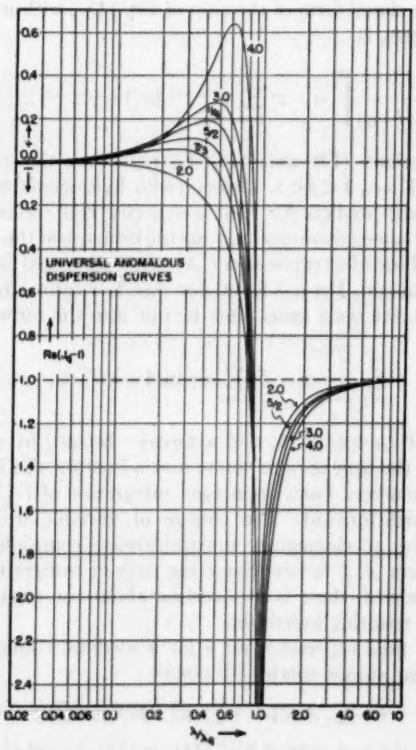

FIG. 1. The anomalous dispersion for any q shell of electrons for any atom is equal to $\mathrm{Re}(J_q-1)$ multiplied by the oscillator strength. $\mathrm{Re}(J_q-1)$ may be taken from this curve for the appropriate p_q value where p_q is the parameter in the distribution of dispersion oscillators $C_q\lambda^{p_q}$. Curves for five different p_q values are shown.

[11] L. G. Parratt, Phys. Rev. **56**, 295 (1939).
[12] L. G. Parratt, Phys. Rev. **54**, 99 (1938).
[13] F. K. Richtmyer, Revs. Modern Phys. **9**, 391 (1937). The K width for gold has not been directly measured; the value 62 ev is believed to be better than the value reported by Richtmyer.
[14] Previous discussions of the comparison of classical and observed widths have been in terms of emission lines; this is incorrect. It is evident from the integrated form of Eq. (3), that $\zeta(=\eta_q/\omega)$ refers to the width of the absorption edge or state.
[15] Widths of lines for transition elements have been measured for K lines; e.g., see Fig. 6 of L. G. Parratt, Phys. Rev. **50**, 1 (1936).

TABLE II. Dispersion calculations for copper K region.

Line	λ(A)	λ/λ_K	g_K Re(f_K-1)	g_{LI} Re$(f_{LI}-1)$	$g_{LII,III}$ Re$(f_{II,III}-1)$	g_M Re(f_M-1)	μ/ρ	f_0	$f-f_0$
Mo $K\alpha_1$	0.709	0.514	+0.209	−0.005	0.083	0.013	52	1.37	0.332
Pb $L\alpha_1$	1.175	0.852	−1.097	−0.014	0.156	0.026	198	3.16	−0.752
Ge $K\alpha_1$	1.254	0.910	−1.793	−0.016	0.168	0.029	234	3.49	−1.390
Zn $K\beta_1$	1.295	0.939	−2.358	−0.017	0.175	0.030	261	3.77	−1.906
Ir $L\alpha_1$	1.351	0.980	−3.850	−0.019	0.184	0.032	290	4.02	−3.337
Cu $K\beta_1$	1.392	1.010	−4.949	−0.020	0.190	0.034	38	0.51	−4.740
Zn $K\alpha_1$	1.435	1.041	−3.471	−0.022	0.196	0.035	42	0.55	−3.255
Cu $K\alpha_1$	1.541	1.117	−2.565	−0.025	0.213	0.039	51	0.62	−2.349
Ni $K\alpha_1$	1.658	1.202	−2.187	−0.029	0.231	0.043	62.8	0.71	−1.932
Co $K\alpha_1$	1.789	1.297	−1.965	−0.033	0.251	0.048	76	0.80	−1.688
Fe $K\alpha_1$	1.936	1.404	−1.816	−0.039	0.272	0.054	96.3	0.93	−1.513
Cr $K\alpha_1$	2.290	1.661	−1.629	−0.055	0.321	0.068	150	1.23	−1.267

$\lambda_K=1.379$A $\quad p_K=11/4 \quad g_K=1.33 \quad W_K=0.30$ x.u. $\quad \rho=8.936$
$\lambda_{LI}=12 \quad p_{LI}=2 \quad g_{LI}=1.5 \quad W_{LI}=30 \quad M=63.57$
$\lambda_{LII,III}=13.15 \quad p_{LII,III}=5/2 \quad g_{LII,III}=4 \quad W_{LII,III}=6$
$\lambda_M=160 \quad p_M=5/2 \quad g_M=20 \quad W_M=2000$

The only reliable method of knowing the relative effect of damping is to have the complete expressions and to make the necessary calculations. In the special cases of p values shown below, an effort has been made to separate the damping terms so that, with η_q known, their relative effects can be readily seen.

SPECIAL CASES OF p VALUES

For p (or α) equal to an integer, the integration for J_q is readily carried out as already discussed. In this section we shall give examples for $p=7/3$, $5/2$, and $11/4$.

In the following formulas, 2nd and higher powers of ζ have been neglected compared to unity except where important, and the terms have been written in a form intended to make calculations easy.

$p=7/3$

For this case, $n=2$ and $m=3$. For $|z|\leqslant 1$,

$$\mathrm{Re}[J_q-1]_{7/3}{}^{\mathrm{I}}=-\frac{2a^2}{3}\left[\frac{1}{2}\ln\left(\frac{1+a+a^2}{1-2a\cos\frac{1}{3}\theta+a^2}\right)+\sqrt{3}\tan^{-1}\left(\frac{\sqrt{3}a}{2+a}\right)-\frac{\pi}{\sqrt{3}}\left(1-\frac{5\zeta}{\sqrt{3}}\right)-\frac{5\zeta}{3}\tan^{-1}\left(\frac{a\sin\frac{1}{3}\theta}{1-a\cos\frac{1}{3}\theta}\right)\right]. \quad (22)$$

For $|z|\geqslant 1$,

$$\mathrm{Re}[J_q-1]_{7/3}{}^{\mathrm{II}}=-\frac{2}{3b^2}\left[\frac{1}{2}\ln\left(\frac{1+b+b^2}{1-2b\cos\frac{1}{3}\theta+b^2}\right)-\sqrt{3}\tan^{-1}\left(\frac{\sqrt{3}b}{2+b}\right)+\frac{5\zeta}{3}\tan^{-1}\left(\frac{b\sin\frac{1}{3}\theta}{1-b\cos\frac{1}{3}\theta}\right)\right]. \quad (23)$$

$p=5/2$

For this case, $n=3$ and $m=4$. For $|z|\leqslant 1$

$$\mathrm{Re}[J_q-1]_{5/2}{}^{\mathrm{I}}=-\frac{3a^3}{4}\left\{\frac{1}{2}\ln\left[\frac{(1+a)^2}{1-2a\cos\frac{1}{4}\theta+a^2}\right]+2\tan^{-1}a-\pi\left(1-\frac{7\zeta}{4}\right)-\frac{7\zeta}{4}\tan^{-1}\left(\frac{a\sin\frac{1}{4}\theta}{1-a\cos\frac{1}{4}\theta}\right)\right\}. \quad (24)$$

For $|z|\geqslant 1$,

$$\mathrm{Re}[J_q-1]_{5/2}{}^{\mathrm{II}}=-\frac{3}{4b^3}\left\{\frac{1}{2}\ln\left[\frac{(1+b)^2}{1-2b\cos\frac{1}{4}\theta+b^2}\right]-2\tan^{-1}b+\frac{7\zeta}{4}\tan^{-1}\left(\frac{b\sin\frac{1}{4}\theta}{1-b\cos\frac{1}{4}\theta}\right)\right\}. \quad (25)$$

Note that in this case $p=5/2$, if damping is assumed to be zero, Eq. (1) or (7) can be integrated directly, since p is a half-integer.[3] The value for δ_q obtained from Eqs. (25) and (16), when $\zeta=0$, is identical with the value reported by Williams.[3]

$p=11/4$

For this case, $n=7$ and $m=8$. For $|z|\leqslant 1$

$$\mathrm{Re}[J_q-1]_{11/4}{}^{\mathrm{I}}=-\frac{7a^7}{8}\left\{\frac{1}{2}\ln\left[\frac{(1+a)^2}{1-2a\cos\frac{1}{8}\theta+a^2}\right]+\frac{1}{\sqrt{2}}\ln\left(\frac{1+\sqrt{2}a+a^2}{1-\sqrt{2}a+a^2}\right)+2\tan^{-1}a+\sqrt{2}\tan^{-1}\left(\frac{\sqrt{2}a}{1-a^2}\right)-\pi\cot\tfrac{1}{8}\pi\left(1-\frac{15\zeta}{8}\tan\tfrac{1}{8}\pi\right)-\frac{15\zeta}{8}\tan^{-1}\left(\frac{a\sin\frac{1}{4}\theta}{1-a\cos\frac{1}{4}\theta}\right)\right\}. \quad (26)$$

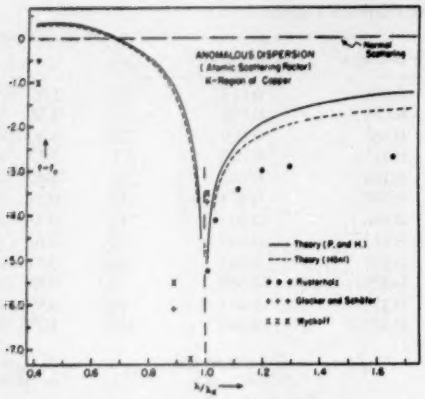

FIG. 2. Comparison of calculated and measured scattering factors (at zero angle) for copper in the K region.

For $|z| \geqslant 1$,

$$\mathrm{Re}[J_q-1]_{11/4}^{II}=-\frac{7}{8b^7}\left\{\frac{1}{2}\ln\left[\frac{(1+b)^2}{1-2b\cos\frac{1}{8}\theta+b^2}\right]\right.$$

$$+\frac{1}{\sqrt{2}}\ln\left(\frac{1+\sqrt{2}b+b^2}{1-\sqrt{2}b+b^2}\right)-2\tan^{-1}b$$

$$\left.-\sqrt{2}\tan^{-1}\left(\frac{\sqrt{2}b}{1-b^2}\right)+\frac{15\zeta}{8}\tan^{-1}\left(\frac{b\sin\frac{1}{8}\theta}{1-b\cos\frac{1}{8}\theta}\right)\right\}. \quad (27)$$

In each of these cases the closed form of the sum has been used, but the open form may be the more convenient except when x is between about $\frac{1}{2}$ and 2 depending upon the desired accuracy.

UNIVERSAL ANOMALOUS DISPERSION CURVES

By evaluation of the above equations, we see that the term ζ is of the order of 2×10^{-3} or less, sufficiently small that it can be neglected in all cases where λ/λ_q differs from unity by more than 10^{-4} (or 10^{-5} in most cases). In general, no oscillator strength g_q is meaningfully known as well as one part in 10^3, nor is the ratio λ/λ_q meaningfully known as well as about one part in 10^4 (because of the large intrinsic line width, and because of unresolved structure in the absorption edge). Thus, for practically all experimental problems in anomalous dispersion, we may write

$$a=\frac{1}{b}=\left(\frac{\lambda}{\lambda_q}\right)^{2/m}\left(1+\frac{\zeta^2}{2m}+\cdots\right)\doteq\left(\frac{\lambda}{\lambda_q}\right)^{2/m} \quad (28)$$

and

$$\cos(\theta/m)\doteq1-(\zeta^2/2m^2)\doteq1, \quad (29)$$

and introduce thereby a negligible error, less than about 0.2 percent.

With damping neglected, $\mathrm{Re}(J_q-1)$ is independent of the atomic number and of the particular electron shell, and depends upon only p_q. Curves of $\mathrm{Re}(J_q-1)$ *vs* λ/λ_q for various values of p_q are therefore universal anomalous dispersion curves; and if p_q and g_q are known, the magnitude of the anomalous dispersion for each q-shell of electrons in any atom can be readily deduced therefrom. The calculations for such curves are presented in Table I for five different p_q values, and the curves are shown in Fig. 1. Interpolation for an intermediate p_q value is possible.

If we wish numerical values of anomalous dispersion when λ/λ_q is within 10^{-4} or 10^{-5} of unity, we must revert to the equations and retain the damping factor.

CALCULATIONS

For comparison with theoretical values, we shall use experimental measurements of $f-f_0$ for iron,[16] copper[17] and for wolfram.[18] The wavelengths used in these experiments are not sufficiently close to λ_q to warrant inclusion of the damping factor.

Table II lists calculations for copper. The $f-f_0$ values are compared with experiment in Fig. 2. The constants used in the calculations are given under the table. The calculated curve from Hönl's theory for K electrons is also shown in the figure.

(For comparison with the two L subgroups listed in Table II, we have also calculated $g_L\,\mathrm{Re}(J_L-1)$ for the L electrons as a single group with $p_L=7/3$. The difference ranges from 21 percent at 0.709A to 10 percent at 2.290A.)

For the wavelengths of Table II, the largest ζ value is $\zeta_K=5.4\times10^{-4}$ at 0.709A, and smallest the is $\zeta_K=0.40\times10^{-4}$ at 2.290A.

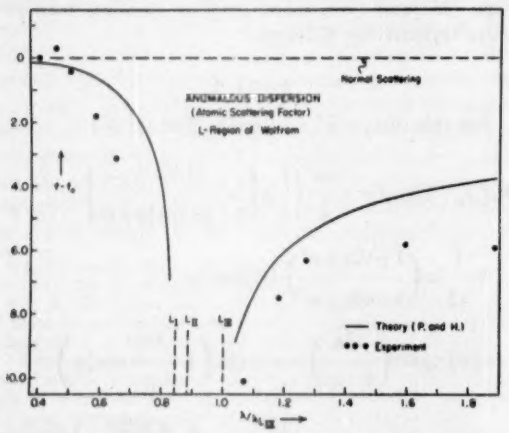

FIG. 3. Comparison of calculated and measured scattering factors (at zero angle) for wolfram in the L region.

[16] R. Glocker and K. Schäfer, Z. Physik **73**, 289 (1931) and **86**, 738 (1933); and R. W. G. Wyckoff, Phys. Rev. **36**, 1116 (1930). The corrected observed values of f are subtracted from the Thomas-Fermi $f_0=17.3$ for the (110) planes of Fe.

[17] A. A. Rusterholz, Z. Physik **82**, 538 (1933).

[18] J. Brentano and A. Baxter, Z. Physik **89**, 720 (1934).

TABLE III. Dispersion calculations for wolfram L region.

Line	λ(A)	λ/λ_{LIII}	g_K Re(J_K-1)	g_{LI} Re$(J_{LI}-1)$	g_{LII} Re$(J_{LII}-1)$	g_{LIII} Re$(J_{LIII}-1)$	g_M Re(J_M-1)	g_N Re(J_N-1)	μ_l/ρ	f_2	$f-f_0$
Sn $K\alpha_1$	0.491	0.404	−1.284	−0.052	0.086	0.234	0.679	0.061	36	3.98	0.150
Ag $K\alpha_1$	0.560	0.461	−1.266	−0.156	0.020	0.165	0.813	0.074	52	5.04	−0.178
Rh $K\alpha_1$	0.613	0.505	−1.259	−0.266	−0.049	0.082	0.902	0.084	68	6.01	−0.260
Mo $K\alpha_1$	0.709	0.584	−1.247	−0.536	−0.239	−0.143	1.059	0.104	104	7.94	−0.572
Zr $K\alpha_1$	0.786	0.647	−1.236	−0.851	−0.466	−0.411	1.179	0.120	137	9.44	−1.052
Th $L\alpha_1$	0.956	0.788	−1.222	−2.305	−1.444	−1.422	1.425	0.158	238	13.49	−3.508
Zn $K\beta_1$	1.295	1.067	−1.214	−2.014	−1.889	−5.128	1.808	0.241	107	4.48	−8.045
Zn $K\alpha_1$	1.435	1.182	−1.211	−1.833	−1.668	−3.904	1.912	0.277	141	5.32	−6.218
Cu $K\alpha_1$	1.541	1.269	−1.209	−1.750	−1.573	−3.522	1.967	0.305	172	6.05	−5.513
Fe $K\alpha_1$	1.936	1.595	−1.206	−1.591	−1.399	−2.948	1.967	0.415	303	8.48	−4.245
Cr $K\alpha_1$	2.290	1.886	−1.204	−1.529	−1.332	−2.755	1.649	0.521	470	11.12	−3.764

$\lambda_K=0.179$A $\quad p_K=11/4 \quad g_K=1.2$ $\quad \rho=19.30$

$\lambda_{LI}=1.024 \quad p_{LI}=7/3 \quad g_{LI}=1.4 \quad W_{LI}=0.56$ x.u. $\quad M=183.92$

$\lambda_{LII}=1.074 \quad p_{LII}=5/2 \quad g_{LII}=1.2 \quad W_{LII}=0.27$

$\lambda_{LIII}=1.214 \quad p_{LIII}=5/2 \quad g_{LIII}=2.4 \quad W_{LIII}=0.40$

$\lambda_M=5.51 \quad p_M=5/2 \quad g_M=18 \quad W_M=20$

$\lambda_N=56 \quad p_N=5/2 \quad g_N=36 \quad W_N=1200$

Table III lists calculations for wolfram, and comparison with experiment is shown in Fig. 3. Again the constants used are given under the table. The L electrons are subdivided; the M and N electrons are not. The oscillator strengths used here, as in the copper calculations, are selected on an arbitrary weighted average basis from theory and experiment,[5,8,19] as are also the p_q values. Since f_2 is of minor importance, the electron shells are not subdivided for β.

For the wavelengths of Table III, the largest ζ value is $\zeta_M=15.5\times10^{-4}$ at 2.290A, the smallest is $\zeta_{LII}=2.5\times10^{-4}$ at 0.786A.

For such cases as this one for wolfram, the magnitude of Re(J_K) is sometimes assumed to be zero and the normal dispersion reckoned as $\delta=A\lambda^2(Z-g_K)$ of $f_0=Z-g_K$. Were this done, the $f-f_0$ scale of Fig. 3 would be dropped by 1.2 units and the calculated curve would go above $f-f_0=0$, as it does for the copper case.

Wavelengths for both tables are taken from Cauchois and Hulubei.[20]

So-called normal dispersion refers to a region of wavelengths for which $f-f_0$ is a constant; whether this constant is zero or g_K (or g_K+g_L, etc.) is not now important. It is seen from the above calculations that the anomalous contributions from various electron shells, in addition to the particular shell whose λ_q is in the wavelength region under study, is rarely negligible—*there is practically no region of normal dispersion*. This is illustrated in Fig. 4 for the entire region $0.1<\lambda<100$A for copper.

SUMMARY

The distribution of "dispersion" oscillators in an atom can be written generally as the sum of n terms of the form $C_{qn}\lambda^{p_{qn}}$. This distribution appears in a complex integrand in the expression for x-ray dispersion (either for the refractive index or for the scattering factor). The general integration of any term of this distribution has been carried out.

Damping of the oscillators has been retained in the integration, and the resulting equations allow ready evaluation of the numerical effect of damping. For practically all of the dispersion region, the damping can be neglected with an error of less than 0.2 percent. Then, universal anomalous dispersion curves can be used to determine Re(J_q-1) which, when multiplied by the

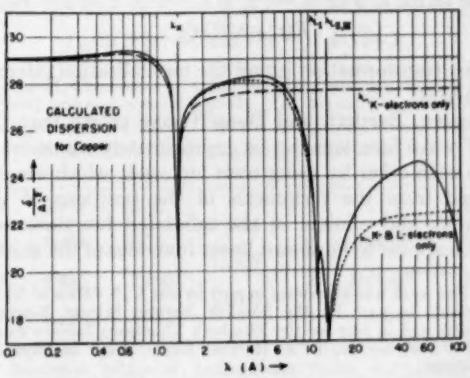

FIG. 4. There is practically no region of normal dispersion when several electron shells are included in the calculations.

[19] The M-oscillator strength is, on one hand, less than the number of M-type electrons because of virtual transitions from outer shells, but, on the other hand, it is augmented by virtual transitions to inner shells. It is estimated that the increase is greater than the reduction for copper, and about equal for wolfram.

[20] Y. Cauchois and H. Hulubei, *Longueurs d'Onde des Emissions X et des Discontinuites d'Absorption X* (Hermann and Company, Paris, 1947). For copper, λ_K is taken as 1.379A, about 9 ev less energy than is reported in this reference, for the reason mentioned in footnote 7 [also see Fig. 6 of W. W. Beeman and H. Friedman, Phys. Rev. **56**, 392 (1939)].

oscillator strength and summed over all q shells, gives easily and quickly the anomalous dispersion for any atom.

Sample calculations for the K region of copper and for the L region of tungsten have been made, using in each case only one term in the oscillator distribution for each q shell. Comparison with experiment shows less satisfactory agreement than with the previous less exact calculations. This disagreement is believed to be due to (a) the difficulties inherent in the experimental measurements, and (b) neglect of parts of the calculations in previous comparisons.

PHYSICAL REVIEW VOLUME 94, NUMBER 6 JUNE 15, 1954

Studies of Atomic Self-Consistent Fields. II. Interpolation Problems*

PER-OLOV LÖWDIN
Physics Department, Massachusetts Institute of Technology, Cambridge, Massachusetts and Institute of Mechanics and Mathematical Physics, University of Uppsala, Uppsala, Sweden
(Received November 27, 1953)

By studying the self-consistent-field (SCF) functions tabulated in the literature, it is shown that a quantity, which for a hydrogenlike function would equal the atomic number Z, for SCF functions will represent a form of "effective nuclear charge" Z_{eff}, which for a series of consecutive atoms or ions appears to be an almost linear function of the atomic number, convenient for interpolation purposes. The positions and magnitudes of maxima and minima, nodes, derivatives in origin, eigenvalues, etc., are investigated by considering the corresponding effective nuclear charges. It is important that the nodes may be interpolated separately, since the logarithm of an SCF function, divided by a polynomial having the same zero points as the function itself, may be used for interpolating SCF functions as a whole. This logarithm may also be used for defining a continuously varying effective charge $Z_{\text{eff}}(r)$, which is convenient for interpolation purposes or for estimating fields with exchange from those without exchange.

THE numerical work involved in each cycle of the integration of the Hartree-Fock equations for atomic self-consistent fields (SCF) with exchange by using the technique developed by Hartree[1] is quite large, and, in order to secure a rapid convergence of the process, it is therefore important to have as good "initial" functions as possible. For this purpose it is now possible to utilize the properties of already tabulated fields; Hartree has shown that rather good estimates of the initial functions could be obtained simply by interpolating their departures from properly scaled hydrogenlike wave functions. A function $F(r)$ is here said to be obtained from another $f(r)$ by change of a scale factor λ, if

$$F(r)=\lambda^{\frac{1}{2}}f(\lambda r), \tag{1}$$

which transformation leaves the normalization integral invariant.

Brown, Bartlett, and Dunn[2,3] have shown that the SCF wave functions can be approximately transformed into each other by using scale factors λ, which are obtained from the reciprocals of the positions of the maxima and minima of the tabulated functions and which appear to be almost linear functions of the atomic number Z. Hartree and Hartree[4] have used a similar idea for scaling the departure of the SCF functions with exchange from those without exchange. In a slightly modified form, the scaling method has recently been used also by Scherr[5] in Chicago.

Using a somewhat different approach, Arnot and McLauchlan[6] and Manning and Millman[7] have shown that, instead of the wave functions themselves, the effective nuclear charges associated with the SCF potentials may be used for interpolation purposes. On a large-scale basis, these total charges have recently been tabulated by Freeman[8] for all fields available.

In the first paper of this series,[9] it was shown that SCF wave functions could be interpolated (and to some extent extrapolated) with a surprisingly high accuracy by means of analytic expressions of Slater type. The purpose of the present paper is to investigate whether it is possible to carry out similar interpolations directly in the numerical tables of the functions involved, without the help of the analytic forms. We will first show the existence of some simple regularities for quantities like the positions and the magnitudes of maxima and minima, derivatives in origin, nodes,

* This work was supported in part by the U. S. Office of Naval Research, in part by the Swedish Natural Science Research Council, and in part by the Elizabeth Thompson Science Fund.
[1] For a survey, see D. R. Hartree, Repts. Progr. in Phys. **11**, 113 (1946).
[2] Brown, Bartlett, and Dunn, Phys. Rev. **44**, 296 (1933).
[3] See also Hartree, reference 1, p. 126, Fig. 1, for another example.
[4] D. R. Hartree and W. Hartree, Proc. Roy. Soc. (London) **A166**, 450 (1938).
[5] C. W. Scherr, J. Chem. Phys. **21**, 1237, 1241 (1953).
[6] F. L. Arnot and J. C. McLauchlan, Proc. Roy. Soc. (London) **A146**, 662 (1934).
[7] M. F. Manning and J. Millman, Phys. Rev. **49**, 848 (1936).
[8] A. J. Freeman, Phys. Rev. **91**, 1410 (1953).
[9] P. O. Löwdin, Phys. Rev. **90**, 120 (1953), in the following referred to as Part I.

TABLE I. Properties of the hydrogenlike radial wave functions $f_{nl}(Z|r)=Z^{\frac{1}{2}}NQ_{nl}(\rho)\exp(-\rho/2)$, expressed in the variable $\rho=2Zr/n$. The values of ρ_m correspond to the maxima and minima; the positions r_m and the magnitudes f_m of these extreme values are given by the relations $r_m=c_m/Z$ and $f_m=d_mZ^{\frac{1}{2}}$. The values of ρ_0 correspond to the nodes.

nl	N^{-1}	$Q(\rho)$	ρ_m	c_m	d_m	ρ_0
$1s$	1	ρ	2	1	0.73576	...
$2s_1$	$2\sqrt{2}$	$2\rho-\rho^2$	$3-\sqrt{5}$	0.76393	0.22786	2
$2s_2$			$3+\sqrt{5}$	5.23607	−0.43700	
$2p$	$2\sqrt{6}$	ρ^2	4	4	0.44200	...
$3s_1$	$6\sqrt{3}$	$6\rho-6\rho^2+\rho^3$	0.49336	0.74004	0.12179	1.26795
$3s_2$			2.79063	4.18595	−0.19667	4.73205
$3s_3$			8.71602	13.07403	0.31864	
$3p_1$	$6\sqrt{6}$	$4\rho^2-\rho^3$	2	3	0.20025	4
$3p_2$			8	12	−0.31903	
$3d$	$6\sqrt{30}$	ρ^3	6	9	0.32723	...

eigenvalues, etc., and we will then describe the general interpolation rule for the numerical wave functions themselves.

I. INTERPOLATION PROPERTIES OF THE MAXIMA AND MINIMA, THE DERIVATIVES IN ORIGIN, THE NODES, AND THE ENERGY EIGENVALUES OF THE SCF FUNCTIONS

If (n,l,m) is a fixed triple of atomic quantum numbers, there is a close connection between the normalized radial wave function $f_{nl}(\mathrm{SCF}|r)$ for a self-consistent field (SCF) with or without exchange and the corresponding hydrogen function $f_{nl}(\mathrm{H}|r)$. With increasing atomic number Z, the attraction from the nucleus on an electron in the orbital (n,l,m) will dominate entirely over the repulsion from the other electrons, and the function $f_{nl}(\mathrm{SCF}|r)$ will therefore tend to be more and more hydrogenlike. In the limit, we obtain

$$\lim_{Z\to\infty} Z^{-\frac{1}{2}}f_{nl}(\mathrm{SCF}|r/Z)=f_{nl}(\mathrm{H}|r). \tag{2}$$

A more rigorous proof[10] of this relation can be derived by considering the Hartree-Fock equations in greater detail. For large Z, we will therefore have

$$f_{nl}(\mathrm{SCF}|r)=Z^{\frac{1}{2}}\{f_{nl}(\mathrm{H}|Zr)+(Z^{-1})\}, \tag{3}$$

where the remainder (Z^{-1}) can be expressed asymptotically as a power series in Z^{-1}. In a similar way, each characteristic SCF quantity can be expressed in the corresponding hydrogenlike quantity and a power series in Z^{-1}. The explicit form of this asymptotic expansion may be useful in interpolation problems, where only one or two SCF data are available, but otherwise it seems to be simpler to use the numerical informations in a more direct way, as described below.

As basic interpolation rule, we will here use the principle that *a quantity, which for a hydrogenlike function equals the atomic number Z, for a series of SCF functions for consecutive atoms or ions will be an almost linearly varying function of the atomic number Z.* The function obtained in this way will be called the *effective nuclear charge* with respect to the SCF quantity under consideration and will be denoted by $Z(\mathrm{SCF}|\ )$ plus a suffix indicating the quantity, which is investigated. Numerically, this function is very convenient for interpolation purposes, and, physically, it will give us an idea of the effect of the screening of the electrons around the nucleus in the various atoms under consideration.

(a) The Extreme Values

In order to investigate, for instance, the properties of the maxima and minima of the SCF functions, we will start with considering the scaled hydrogenlike functions $f_{nl}(Z|r)$ having the explicit form

$$f_{nl}(Z|r)=Z^{\frac{1}{2}}f_{nl}(\mathrm{H}|Zr)=Z^{\frac{1}{2}}NQ_{nl}(\rho)\exp(-\rho/2), \tag{4}$$

where $\rho=2Zr/n$; N is a normalization constant, and Q_{nl} is a polynomial in ρ of degree n, which is explicitly given for the lowest quantum numbers[11] in Table I. The numerical values ρ_m, corresponding to the extreme values of $f_{nl}(Z|r)$, are obtained by solving the alegbraic equation $Q(\rho)=2dQ(\rho)/d\rho$. The positions r_m and the magnitudes f_m of the extreme values are then given by

$$r_m=c_m/Z, \quad f_m=d_mZ^{\frac{1}{2}}, \tag{5}$$

where the coefficients c_m and d_m are listed in Table I, too.

In investigating the numerically given SCF functions we should now, according to the analogy rule stated above, study the quantities

$$Z(\mathrm{SCF}|r_m)=c_m/r_m, \quad Z(\mathrm{SCF}|f_m)=(f_m/d_m)^2, \tag{6}$$

where the coefficients c_m and d_m are taken from Table I, whereas r_m and f_m have to be determined from the SCF functions under consideration. In order to compute r_m with some accuracy from the numerical tables, one can utilize the behavior of "quotient series" of the same type as described in Part I. We will start from the assumption that, in the neighborhood of an extreme value belonging to the slope number L in order from origin, the SCF function is of the form

$$f_{nl}(\mathrm{SCF}|r)=\text{const}\ r^p e^{-ar}, \quad p=l+L, \tag{7}$$

TABLE II. Calculation of r_m for the first maximum of $f_{3s}(r)$ for Cl^- with exchange according to Eq. (12); k = number of iterations.

Given properties of the function f_{3s}. Solution of Eq. (12).						
r	$f_{3s}(r)$	f_{3s}/r	$q(r)$	k	r_m	q_m
0.03	0.393	13.10		0		1.243
			1.2214			
0.04	0.429	10.73		1	0.04596	1.2435
			1.2413			
0.05	0.432	8.640		2	0.04589	1.2434
			1.2644			
0.06	0.410	6.833		3	0.04590	

[10] D. R. Hartree and W. Hartree, Proc. Roy. Soc. (London) **A166**, 450 (1938).

[11] Extensive tables of hydrogenlike radial wave functions $R_{nl}=f_{nl}\cdot r$ are given in L. Pauling and E. B. Wilson, *Introduction to Quantum Mechanics* (McGraw-Hill Book Company, Inc., New York, 1935), p. 135.

TABLE III. Positions r_m and magnitudes f_m of maxima and minima for SCF functions with exchange for some Ne-like ions.

		1s		2s1		2s2		2p	
Z	Element	r_m	f_m	r_m	f_m	r_m	f_m	r_m	f_m
10	Ne	0.10295	2.268	0.08088	0.4752	0.6848	1.087	0.6342	0.965
11	Na^+	0.09343	2.382	0.07333	0.5190	0.6119	1.169	0.5478	1.070
12	Mg^{+2}	0.08550	2.492	0.06672	0.5607	0.5483	1.246	0.4833	1.157
13	Al^{+3}	0.07875	2.598	0.06140	0.6019	0.4972	1.320	0.4310	1.243
14	Si^{+4}	0.07309	2.700	0.05675	0.6400	0.4555	1.390	0.3893	1.321

TABLE IV. Positions r_m and magnitudes f_m of maxima and minima for SCF functions with exchange for some A-like ions.

		1s		2s1		2s2		2p	
Z	Element	r_m	f_m	r_m	f_m	r_m	f_m	r_m	f_m
17	Cl^-	0.05992	2.982	0.04672	0.7427	0.3636	−1.575	0.3033	1.5188
18	A	0.05651	3.069	0.04390	0.7722	0.3412	−1.632	0.2825	1.5805
19	K^+	0.05351	3.157	0.04142	0.8035	0.3196	−1.687	0.2637	1.6407
20	Ca^{+2}	0.05083	3.240	0.03944	0.8341	0.3014	−1.743	0.2477	1.6979

		3s1		3s2		3s3		3p1		3p2	
Z	Element	r_m	f_m	r_m	f_m	r_m	f_m	r_m	f_m	r_m	f_m
17	Cl^-	0.04590	0.2168	0.3026	0.4036	1.3021	0.8635	0.2430	0.3175	1.4825	0.7340
18	A	0.04314	0.2397	0.2825	0.4430	1.1767	0.9242	0.2247	0.3712	1.3010	0.8208
19	K^+	0.04078	0.2621	0.2652	0.4812	1.0851	0.9813	0.2099	0.4180	1.1641	0.8933
20	Ca^{+2}	0.03877	0.2841	0.2500	0.5176	1.0010	1.036	0.1961	0.4622	1.0527	0.9578

where $a=a(r)$ is a function of r, which, in the actual computations, is found to be rather slowly varying. The extreme value is then situated in a point $r=r_m$ satisfying the relation

$$r=p/(a+ra'). \tag{8}$$

In order to determine the denominator without the explicit evaluation of the function $a(r)$, we will introduce the auxiliary functions

$$g(r)=f_{nl}(\mathrm{SCF}|r)/r^p, \tag{9}$$

$$q_h(r)=g(r-h/2)/g(r+h/2). \tag{10}$$

The functions $q_h(r)$ are called the "quotient functions" associated with the interval h, and a table for them is easily formed by taking the successive quotients between consecutive values of $g(r)$ in equidistant points having the interval h. Using a Taylor-series expansion of the exponent $ra(r)$ in (7) and Eqs. (9) and (10), we obtain

$$\log_e q_h(r)=h(a+ra')+h^3(3a''+ra''')/24+\cdots. \tag{11}$$

For the SCF functions under consideration, we have found that the function $q_h(r)$ is so slowly varying that one may use linear interpolations, and, consequently, the higher terms in the expansion (11) may be neglected in comparison to the first term. By using (11), the relation (8) may then be written in the form

$$r=ph/\log_e q_h(r). \tag{12}$$

From this equation, the position $r=r_m$ may be determined in a few steps by iteration by using only the quotient table. A typical example of the procedure is given in Table II.

The magnitude $f=f_m$ of the extreme value of the SCF function is then given by $f_m=r_m{}^p g(r_m)$, where

$$\log_e g(r_m)=\log_e g(r_1)+\frac{r_1-r_m}{h}\log_e q_h\left(\frac{r_1+r_m}{2}\right). \tag{13}$$

Two isoelectronic series have been investigated in this way, namely some Ne-like ions (Ne, Na^+, Mg^{+2}, Al^{+3}, and Si^{+4}) and some A-like ions (Cl^-, A, K^+, and Ca^{+2}), for which self-consistent-field functions with exchange are already available in the literature,[12] calculated by D. R. and W. Hartree, and others. Tables III and IV contain the results of our computations of r_m and f_m; we note the existence of such regularities as make these tables directly suitable for interpolation purposes. The corresponding effective nuclear charges $Z(\mathrm{SCF}|\ )$ with respect to r_m and f_m, calculated from Eqs. (6), are then given in Tables V and VI. These quantities may be written in the form

$$Z(\mathrm{SCF}|r_m)=Z-s_1, \quad Z(\mathrm{SCF}|f_m)=Z-s_2, \tag{14}$$

where the quantities s_1 and s_2 may be interpreted as the "shielding constants" with respect to the positions and the magnitudes of the extreme values, respectively. From the tables, we note that, at least for the inner electrons, the quantities s_1 and s_2 are approximately constant for fixed quantum numbers (nl) in each series, but also that they differ appreciably from each other: $s_1 \neq s_2$. The last fact indicates a result of importance for understanding the special character of the SCF functions in comparison to the hydrogenlike functions.

[12] The proper references to the original articles used in the calculations in this paper may be found in the extensive bibliography given by Hartree in our reference 1. However, the data for Ne and Al^{+3} are taken from our own SCF calculations (to be published).

TABLE V. Effective nuclear charges $Z(\mathrm{SCF}|\ )$ for the positions r_m and the magnitudes f_m of some Ne-like ions with exchange.

Z	Element	$1s$ $Z(r_m)$	$Z(f_m)$	$2s_1$ $Z(r_m)$	$Z(f_m)$	$2s_2$ $Z(r_m)$	$Z(f_m)$	$2p$ $Z(r_m)$	$Z(f_m)$
10	Ne	9.713	9.502	9.445	4.349	7.646	6.184	6.307	4.771
11	Na^+	10.704	10.481	10.417	5.188	8.557	7.161	7.302	5.860
12	Mg^{+2}	11.696	11.472	11.450	6.055	9.549	8.134	8.277	6.852
13	Al^{+3}	12.699	12.464	12.441	6.979	10.531	9.124	9.281	7.908
14	Si^{+4}	13.683	13.471	13.461	7.889	11.497	10.122	10.276	8.932
Average difference:		0.993	0.992	1.004	0.885	0.963	0.985	0.992	1.040

TABLE VI. Effective nuclear charges $Z(\mathrm{SCF}|\ )$ for the positions r_m and the magnitudes f_m of some A-like ions with exchange.

Z	Element	$1s$ $Z(r_m)$	$Z(f_m)$	$2s_1$ $Z(r_m)$	$Z(f_m)$	$2s_2$ $Z(r_m)$	$Z(f_m)$	$2p$ $Z(r_m)$	$Z(f_m)$
17	Cl^-	16.688	16.426	16.351	10.624	14.402	12.990	13.188	11.807
18	A	17.695	17.399	17.401	11.485	15.344	13.947	14.160	12.786
19	K^+	18.687	18.411	18.442	12.435	16.381	14.903	15.168	13.779
20	Ca^{+2}	19.673	19.392	19.368	13.400	17.371	15.909	16.146	14.756
Average difference:		0.995	0.989	1.006	0.925	0.990	0.973	0.986	0.983

Z	Element	$3s_1$ $Z(r_m)$	$Z(f_m)$	$3s_2$ $Z(r_m)$	$Z(f_m)$	$3s_3$ $Z(r_m)$	$Z(f_m)$	$3p_1$ $Z(r_m)$	$Z(f_m)$	$3p_2$ $Z(r_m)$	$Z(f_m)$
17	Cl^-	16.122	3.169	13.832	4.211	10.040	7.344	12.480	2.514	8.094	5.293
18	A	17.147	3.873	14.818	5.074	11.023	8.412	13.352	3.436	9.224	6.619
19	K^+	18.147	4.631	15.783	5.987	12.049	9.484	14.294	4.357	10.309	7.840
20	Ca^{+2}	19.089	5.441	16.748	6.943	13.061	10.571	15.296	5.312	11.400	9.073
Average difference:		0.989	0.757	0.972	0.911	1.007	1.076	0.939	0.933	1.102	1.260

In the first attempts to treat atomic wave functions, it was natural to consider them as hydrogenlike functions having an effective nuclear charge of the form $(Z-s)$, where the single shielding constants s were determined, e.g., by the rules given by Slater.[13] The results concerning the SCF functions, contained in Tables V and VI, show now that, in order to describe such a function around one of its extreme values, it is necessary to use *two* independent screening constants, s_1 and s_2, and a relation of the form

$$f_{nl}(\mathrm{SCF}|r) \approx (Z-s_2)^{\frac{1}{2}} N Q_{nl}(\rho) \exp(-\rho/2), \qquad \rho = 2(Z-s_1)r/n, \tag{15}$$

which actually corresponds to Eq. (3) with part of the remainder taken into account. This formula gives the values of the SCF function under consideration only within a small range, and, in order to describe the same function around another extreme value or in another region, different values of s_1 and s_2 are necessary. We note that, if the values of s_1 and s_2 would be kept constant from $r=0$ to $r=\infty$, the resulting function (15) would no longer be properly normalized.

As a typical example of the limited validity of formula (15), we have in Table VII listed the values of the right-hand side of this expression for the region around the maximum of f_{2p} for Na^+ with exchange in comparison to the actual values. If two effective nuclear charges Z_1 and Z_2, taken from Table V, are used, the SCF function will be correctly represented in the maximum $r=r_m$ and with the accuracy desired within a small interval $(r_m-0.05;\ r_m+0.05)$ around this point, whereas the errors, e.g., in the interval $(0;\ r_m-0.05)$, will be appreciable and amount to as much as -0.070. However, if only *one* effective nuclear charge Z_{eff} is used, for instance the compromise value $Z=(Z_1Z_2)^{\frac{1}{2}}$, the position and the magnitude of the maximum show errors of about 0.05 and 0.070, respectively, whereas the errors in the interval $(0;\ r_m)$ amount to as much as -0.110. The example shows that, even if two effective nuclear charges are used, it is desirable to have these quantities *continuously varying* in order to describe a SCF function with complete accuracy over a larger region. This idea will be further developed in Sec. II.

We have also investigated the interpolation properties of the extreme values of the SCF functions for a series of *neutral* atoms, namely C, N, and O. These atoms can

TABLE VII. Approximate representation of the $2p$ function of Na^+ with exchange around its maximum according to Eq. (15) and Table V.

r	SCF Hartree-Hartree	Eq. (15) $Z_1=7.302$ $Z_2=5.860$	Eq. (15) Compromise $Z=(Z_1Z_2)^{\frac{1}{2}}$
0	0.000	0.000	0.000
0.1	0.231	0.183	0.161
0.2	0.578	0.508	0.465
0.3	0.842	0.793	0.753
0.4	0.997	0.978	0.966
0.5	1.061	1.061	1.088
0.6	1.061	1.061	1.130
0.7	1.021	1.002	1.109
0.8	0.956	0.908	1.044
0.9	0.880	0.798	0.953
1.0	0.799	0.684	0.848

[13] J. C. Slater, Phys. Rev. **36**, 57 (1930).

TABLE VIII. Positions r_m, magnitudes f_m, and the corresponding effective nuclear charges $Z(\mathrm{SCF}|\ )$ for the maxima of the $2p$ functions of some neutral atoms, namely carbon (^1D, $\beta=0.04$), nitrogen (^2P, $\beta=0$), and oxygen (^1S, $\beta=0$).

Z	Element	State	r_m	f_m	$Z(\mathrm{SCF}\|r_m)$	$Z(\mathrm{SCF}\|f_m)$
6	C	^1D	1.221	0.7134	3.276	2.605
7	N	^2P	0.994	0.7813	4.024	3.124
8	O	^1S	0.837	0.8430	4.779	3.637
			Average difference:		0.7515	0.516

occur in several different states, characterized by Slater's[14] parameter β, and we have here treated the actual or interpolated functions belonging to $\beta=0$. The results for the $2p$ functions are given in Table VIII; again it is found that the *linearity rule* for the quantities $Z(\mathrm{SCF}|\ )$ holds with a surprisingly high accuracy. The average differences in each series are now appreciably smaller than 1.000, as one could expect from physical reasons for a sequence of neutral atoms, since one outer electron with some shielding effects is added to the system when the nuclear charge is increased by one.

(b) The Region Around $r=0$

In order to investigate the SCF functions in greater detail in the neighborhood of the point $r=0$, we will again start from the hydrogenlike functions given in Table I. The quantity $f_{nl}(Z|r)/r^{l+1}$ is nonvanishing for $r=0$, and, according to (4), we have

$$\lim_{r\to 0}\frac{f_{nl}(Z|r)}{r^{l+1}}=NZ^{l}\left\{\frac{Q_{nl}(2Zr/n)}{r^{l+1}}\right\}_{r=0}. \tag{16}$$

From this relation we can then solve the atomic number Z and obtain

$$Z=[\alpha_{nl}f_{nl}(Z|r)/r^{l+1}]_{r=0}^{2/(2l+3)}, \tag{17}$$

where α_{nl} is a constant which for the lowest quantum numbers has the following values:

$$\begin{array}{lccccccc}(nl)= & 1s & 2s & 2p & 3s & 3p & & 3d\\ \alpha_{nl}= & 0.5 & \sqrt{2} & 2\sqrt{6} & 1.5\sqrt{3} & 3.375\sqrt{6} & & 20.25\sqrt{30}.\end{array} \tag{18}$$

According to the analogy rule, stated above, the corresponding quantities for the SCF functions will then represent the effective nuclear charges $Z(\mathrm{SCF}|\ )$ with respect to the first nonvanishing derivative in origin, and, for the sake of simplicity, we will denote these quantities by the symbol K_{nl}, introduced in Part I:

$$K_{nl}=[\alpha_{nl}f_{nl}(\mathrm{SCF}|r)/r^{l+1}]_{r=0}^{2/(2l+3)}. \tag{19}$$

In publishing the results of their calculations of self-consistent fields, Hartree and Hartree have usually given the value of $f_{nl}(\mathrm{SCF}|r)/r^{l+1}$ for $r=0$, and the evaluation of K_{nl} is then straightforward. In other cases, one has to study the function $f_{nl}(r)/r^{l+1}$ in the neighborhood of $r=0$ and to extrapolate its value for $r=0$ by means of "quotient analysis" or logarithmic extrapolation.

The results of our calculations of K_{nl} for the CNO series, the Ne-like ions, and the A-like ions are condensed in Table IX, where the upper values refer to fields with exchange and the lower to fields without exchange. From this table, we conclude that the effective nuclear charge K_{nl} with striking accuracy is a *linear function* of the atomic number Z, and that therefore interpolations and extrapolations to neighboring atoms are possible as soon as two SCF data are available; the existence of additional data will, of course, increase the accuracy. A table of K_{1s} for the He-like ions was also given in Part I.

According to (19), one can determine the first nonvanishing derivative in origin for a SCF function from the corresponding effective nuclear charge K_{nl} by the relation

$$c_{l+1}=\frac{f^{(l+1)}(\mathrm{SCF}|0)}{(l+1)!}=K_{nl}^{(2l+3)/2}/\alpha_{nl}. \tag{20}$$

TABLE IX. Effective nuclear charges K_{nl} for SCF functions belonging to the CNO series, the Ne series, and the A series. The upper values refer to fields *with* exchange, the lower to fields *without* exchange.

CNO series (SCF with exchange)					
Z	Element	State	K_{1s}	K_{2s}	K_{2p}
6	C	^1D	5.760	4.115	3.85
7	N	^2P	6.757	4.971	4.66
8	O	^1S	7.751	5.787	5.50
Average difference:			0.996	0.836	0.825

Ne series				
Z	Element	K_{1s}	K_{2s}	K_{2p}
9	F^-	...	...	...
		8.746	6.516	5.913
10	Ne	9.736	7.403	7.139
		...	...	...
11	Na^+	10.725	8.382	8.168
		...	...	...
13	Al^{+3}	12.718	10.364	10.198
		12.737	10.160	10.022
14	Si^{+4}	13.735	11.368	11.206
		13.743	11.176	11.014
Average difference:		1.000	0.991	1.017
		0.999	0.932	1.202

A series						
Z	Element	K_{1s}	K_{2s}	K_{2p}	K_{3s}	K_{3p}
17	Cl^-	16.701	14.301	14.163	9.527	9.976
		16.722	14.024	13.968	9.981	9.817
18	A	17.690	15.284	15.150	10.561	11.217
		...	...	...	...	...
19	K^+	18.698	16.271	16.145	11.645	12.385
		18.712	15.979	15.946	11.898	12.273
20	Ca^{+2}	19.691	17.266	17.141	12.717	13.523
		19.706	16.955	16.925	12.888	13.420
Average difference:		0.997	0.988	0.993	1.063	1.182
		0.995	0.977	0.986	0.969	1.201

[14] J. C. Slater, Phys. Rev. 34, 1293 (1929).

This is of particular importance in the calculations of self-consistent fields *with exchange* by solving the Hartree-Fock equations, since, in this case, it is desirable to have as good estimates as possible of the initial conditions in origin in order to obtain the solutions directly in correctly normalized form. The interpolation rule based on (19) may therefore be of value for SCF calculations in the future.

We may conclude that, in a close neighborhood of $r=0$, it is possible to describe a SCF function as a hydrogenlike function with $Z_{eff}=K_{nl}$. However, the range of validity of such a representation is rather short, as is shown by the example for f_{2p} of Na^+ with exchange in Table X, where the function (4) is compared to the actual SCF function, given by Hartree and Hartree.

Table IX gives also a comparison between the values of K_{nl} for fields with and without exchange, and we note that, except for $(3s)$, the inclusion of exchange corresponds to a slight increase of the effective nuclear charge, which confirms an earlier observation by Hartree. However, a much stronger tool for investigating the influence of the inclusion of exchange will be described in a following section.

In order to give a detailed description of the SCF functions in a longer range around $r=0$, one should investigate also the next derivative of order $(l+2)$, writing the function in the form

$$f_{nl}(\mathrm{SCF}|r)=c_{l+1}r^{l+1}(1-ar+\cdots). \tag{21}$$

By substituting this expression into the Hartree-Fock equations, one finds that $a=Z/(l+1)$, where Z is the atomic number of the nucleus. This is a general result which is valid both for the hydrogenlike functions and the SCF functions. However, in their papers concerning self-consistent fields, Hartree and Hartree have usually given tables also of the quantities f_{nl}/r^{r+1} for the range around $r=0$, and by making a "quotient analysis" of this material, we have found that, in the nearest neighborhood of origin, the SCF functions are better expressed under the form

$$f_{nl}(\mathrm{SCF}|r)=c_{l+1}r^{l+1}e^{-ar}. \tag{22}$$

TABLE X. Comparison between the SCF function f_{2p} for Na^+ with exchange, given by Hartree and Hartree, and the corresponding hydrogenlike function (4) with $Z_{eff}=K_{2p}$ in the neighborhood of $r=0$. The numerical value of $K_{2p}=8.168$ is taken from Table IX.

r	SCF	Eq. (4)	r	SCF	Eq. (4)
0.00	0.000	0.000	0.2	0.578	0.688
0.01	0.004	0.004	0.3	0.842	1.029
0.02	0.014	0.014	0.4	0.997	1.216
0.03	0.030	0.031	0.5	1.061	1.263
0.04	0.050	0.053	0.6	1.061	1.209
			0.7	1.021	1.094
0.06	0.102	0.110	0.8	0.956	0.949
0.08	0.163	0.180	0.9	0.880	0.799
0.10	0.231	0.259	1.0	0.799	0.654
0.12	0.302	0.343			

TABLE XI. Example of "quotient analysis" of the numerically given functions $f_{nl}(\mathrm{SCF}|r)/r^{l+1}$ for $K^+(3s)$ and $(3p)$ with exchange.

r	f_{3s}/r	q_A	f_{3p}/r^2	q_A
0.000	15.295		65.30	
		1.1008		1.0485
0.005	13.895		62.28	
		1.1032		1.0483
0.010	12.595		59.41	
		1.1058		1.0482
0.015	11.39		56.68	
		1.1091		1.0479
0.020	10.27		54.09	

TABLE XII. Quotients $q_A(0)$ for $h=0.005$ and corresponding effective nuclear charges Z_0, defined by (24), for SCF functions of some A-like ions with exchange.

	Z	Element	$1s$	$2s$	$2p$	$3s$	$3p$
$q_A(0)$	17	Cl^-	1.0885	1.0887	1.0427	1.0929[a]	1.0429
	18	A	1.0941	1.0941	1.0462	1.0937	1.0461
	19	K^+	1.0997	1.0993	1.0488	1.0996	1.0486
	20	Ca^{++}	1.1053	1.1049	1.0514	1.1045	1.0509
Z_0	17	Cl^-	16.960	16.997	16.726	17.767[a]	16.802
	18	A	17.986	17.986	18.066	17.913	18.028
	19	K^+	19.008	18.935	19.058	18.989	18.982
	20	Ca^{++}	20.023	19.951	20.050	19.879	19.858

[a] The SCF data for $Cl^-(3s)$ contain apparently some slight error.

Here $a=a(r)$ is constant or extremely slowly varying over the interval $(0;0.02)$ under consideration, as is shown by the example in Table XI. A comparison between (21) and (22) shows then that, for $r=0$, we should simply have

$$a(0)=h^{-1}\log_e q_h(0)=Z/(l+1), \tag{23}$$

where Z is the atomic number of the nucleus, and q_A is the quotient function defined by (10).

Let us now consider the actual numerical material, given by Hartree and Hartree, from this point of view. The result of our quotient analysis for the A-like ions with exchange is condensed in Table XII, where we also have listed a quantity,

$$Z_0=(l+1)h^{-1}\log_e q_A(0), \tag{24}$$

obtained from the Hartree-Hartree quotient. Except for the case of $Cl^-(3s)$, where the SCF data apparently contain some accidental error, the quantities Z_0 are all very close to the real atomic number Z, in agreement with (23). In the following, we may, therefore, simply get an approximate idea of the behavior of $f_{nl}(\mathrm{SCF}|r)r^{l+1}$ by starting from the value of c_{l+1}, found from (20), and by using a quotient q_A, given by the three-term formula

$$q_A=1+hZ/(l+1)+\tfrac{1}{2}\{hZ/(l+1)\}^2, \tag{25}$$

for, e.g., $h=0.005$. We note that the values in the example in Table XIII are in excellent agreement with the SCF data given in Table XII.

TABLE XIII. The quotient $q_k(0)$ for $h=0.005$ for the A-like ions according to the three-term formula (25). Compare the SCF data in Table XII.

Z	$l=0$	$l=1$
17	1.0886	1.0434
18	1.0941	1.0460
19	1.0995	1.0486
20	1.1050	1.0513

TABLE XIV. Example of the procedure of evaluating the position r_0 of the node for the $2s$ function of Na^+ with exchange; $r_0^{(k)}$ gives the successive approximations for r_0 in Aitken's iteration scheme.

f_{2s}	r	$r_0^{(k)}$ $k=1$	$k=2$	$k=3$
+0.215	0.16			
+0.102	0.18	0.198 053		
−0.015	0.20	0.197 391	0.197 476	
−0.301	0.25	0.197 500	0.197 913	0.197 45

(c) The Nodes

Another characteristic property of the SCF functions is the position r_0 of their eventual nodes. For the hydrogenlike functions, the nodes are given by the zero points ρ_0 of the polynomials $Q(\rho)$ in Table I; and by solving the atomic number Z, we obtain, therefore, $Z=n\rho_0/2r_0$. According to the analogy rule, the corresponding effective nuclear charges for the SCF functions are then defined by

$$Z(\mathrm{SCF}|r_0)=n\rho_0/2r_0. \tag{26}$$

The zero points r_0 of the numerically given SCF functions may be determined by solving the equation $f_{nl}(\mathrm{SCF}|r)=0$ by inverse interpolation, and, for this purpose, we have used the Aitken iteration scheme.[15] An example of the procedure is given in Table XIV.

The final results of our calculations of the nodes of of the $2s$ functions, associated with fields with and without exchange, are condensed in Table XV. We note that the linearity rule for $Z(\mathrm{SCF}|r_0)$ holds with the same striking accuracy as before, and that therefore this auxiliary quantity is very convenient for interpolation purposes. The nodes of the $3s$ and $3p$ functions have been evaluated only for the fields with exchange, and the results are given in Table XVI.

Let us finally consider the possibility of expressing a SCF function in the form (15) in the neighborhood of a node. The quantity ρ is defined by $\rho=2Z_{eff}r/n$, but it is not *a priori* evident that the value of Z_{eff} in the polynomial $Q(\rho)$ is identical with the value of Z_{eff} in $\exp(-\rho/2)$, particularly not in the region around a zero point $r=r_0$, where the former is sharply defined. In order to describe an SCF function in such a region, it may therefore be necessary to use *three* independent shielding factors in formula (15). In considering a single continuously varying scale factor, we will meet this problem again, since the nodes will be a little bit "out of scale" and lead to sudden discontinuities.

In general, the nodes cause such complications in the interpolation problem as to make it highly desirable to transform them away. As we shall see in the next section, such a transformation can be carried out even for the numerically given SCF functions, if the nodes are evaluated with sufficient accuracy. The possibility of a separate interpolation of the nodes, based on (26), will in this way prove to be of essential importance for the solution of the interpolation problem for the function as a whole.

(d) The Energy Eigenvalues

The "tails" of the SCF functions for large r may be interpolated simply by considering the outmost Slater exponential in the analytic expressions, described in Part I. This single exponential term is quickly found by a "quotient analysis" without evaluating the whole expression, and we note that the exponents satisfy the

TABLE XV. The positions r_0 and the effective nuclear charges $Z(\mathrm{SCF}|r_0)$ of $2s$ functions belonging to self-consistent fields with and without exchange.

Z	Element	State β value	r_0 With exchange	r_0 Without exchange	$Z(\mathrm{SCF}\|r_0)$ With exchange	$Z(\mathrm{SCF}\|r_0)$ Without exchange
3	Li		0.829 96		2.4098	
4	Be		0.589 57	0.679 76	3.3923	2.9422
5	B			0.504 45		3.9647
6	C	^1D 0.04	0.375 41		5.3275	
	C^{+2}		0.370 75	0.400 45	5.3945	4.9944
7	N^-	^1S 0	0.318 15		6.2863	
	N	^2P 0	0.317 98		6.2897	
8	O^-	^2P −0.8	0.276 36		7.2369	
	O	^1S 0	0.276 11	0.289 94	7.2435	6.8980
	O^+	^2P 0	0.275 54	0.289 48	7.2585	6.9089
	O^{+2}	intp. 0	0.274 25	0.288 57	7.2926	6.9307
	O^{+3}	^2P 0	0.272 53	0.287 10	7.3386	6.9662
9	F^-			0.254 02		7.8734
10	Ne		0.218 36		9.159	
11	Na^-		0.197 45		10.129	
	Na^+		0.197 45		10.129	
12	Mg^{+2}		0.180 14	0.185 03	11.102	10.809
13	Al^{+3}		0.165 42	0.169 57	12.090	11.795
14	Si^{+2}			0.156 54		12.776
	Si^{+3}			0.156 51		12.779
	Si^{+4}		0.153 04	0.156 54	13.068	12.776
17	Cl^-		0.124 80	0.127 06	16.027	15.741
18	A		0.117 65		17.000	
19	K^+		0.111 07	0.112 91	18.007	17.713
20	Ca			0.106 91		18.707
	Ca^{+2}		0.105 30		18.993	
29	Cu^+		0.071 612	0.072 302	27.928	27.662

The positions r_0 and the effective nuclear charges $Z(\mathrm{SCF}|r_0)$ for $2s$ functions of some heavier elements for self-consistent fields *without* exchange.

Z	Element	r_0	$Z(\mathrm{SCF}\|r_0)$
30	Zn	0.069 719	28.687
31	Ca	0.067 510	29.625
32	Ge	0.065 210	30.670
33	As	0.063 236	31.628
37	Rb	0.056 155	35.616
55	Cs	0.037 342	53.559
80	Hg	0.025 454	78.573

[15] See, for instance, W. E. Milne, *Numerical Calculus* (Princeton University Press, Princeton, 1949), p. 69.

TABLE XVI. The positions r_0 and the effective nuclear charges $Z(\mathrm{SCF}|r_0)$ for $3s$ and $3p$ functions belonging to self-consistent fields *with* exchange.

		$3s$				$3p$	
Z	Element	r_0'	r_0''	$Z(\mathrm{SCF}\|r_0')$	$Z(\mathrm{SCF}\|r_0'')$	r_0	$Z(\mathrm{SCF}\|r_0)$
17	Cl^-	0.121 60	0.554 99	15.641	12.790	0.531 53	11.288
18	A	0.114 37	0.515 72	16.630	13.763	0.488 69	12.278
19	K^+	0.108 00	0.481 89	17.610	14.730	0.451 99	13.275
20	Ca^{+2}	0.102 33	0.451 62	18.586	15.717	0.420 42	14.271
29	Cu^+	0.069 238	0.292 38	27.469	24.277	0.262 63	22.846

linearity rule, whereas the coefficients satisfy Eq. (I, 7). Typical examples may be found in Part I.

Another quantity characteristics for the asymptotic behavior is the eigenvalue parameter ϵ_{nl}. For hydrogenlike functions we would have $\epsilon_{nl}=Z^2/n$, and, for SCF functions, the corresponding effective nuclear charge is then defined by

$$Z(\mathrm{SCF}|\epsilon_{nl})=n\sqrt{\epsilon_{nl}}. \tag{27}$$

Table XVII gives a survey of this quantity for some Ne-like and A-like ions, and we note that, for the outer electrons, the electronic shielding is so strong that the linearity rule for $Z(\mathrm{SCF}|\epsilon_{nl})$ holds only with a rather moderate accuracy as long as this quantity is comparatively large, whereas there are considerable deviations from this rule when $Z(\mathrm{SCF}|\epsilon)$ tends to zero on the side of the negative ions. However, if only two SCF data are available, the interpolation based on (27) gives at least a first estimate of the eigenvalue parameter, and, in actual computations, we have found that this value might be just as good as, e.g., the approximate eigenvalue obtained from the average value of the energy operator with respect to an interpolated SCF function.

If three of more SCF data are available, it is usually simpler to carry out the interpolations directly in the quantity ϵ_{nl} itself, which is then considered as being a polynomial of at least the second degree in the atomic number Z.

In our investigation of the SCF functions, we have found that the hydrogenlike behavior decreases when the point under consideration moves outwards from origin, which depends on the simple fact that the electronic screening gets an increasing importance in comparison to the nuclear attraction. The idea of the "effective nuclear charge" must consequently lose some of its validity when it is applied to the asymptotic behavior, and it is therefore probable that a more detailed description of quantities like, e.g., the eigenvalues can be given first after a closer investigation of the basic Hartree-Fock equations.

II. INTERPOLATION OF SELF-CONSISTENT-FIELD WAVE FUNCTIONS

In the previous section we have investigated the interpolation of certain point properties of the SCF functions, and will now study the problem of the interpolation of the SCF functions as a whole. Our different attempts to treat this question have shown us that the eventual nodes in the SCF functions cause considerable complications in this connection, and we will therefore take advantage of the fact that these nodes may be interpolated separately by using (26).

Let us start by dividing the function $f_{nl}(\mathrm{SCF}|r)$ by a polynomial $r^{l+1}(r_0'-r)(r_0''-r)\cdots$, where r_0', r_0'', $\cdots$ are the $(n-l-1)$ zero points of the function itself; the quotient is nodeless and monotonously decreasing with increasing r. Let us also form a table of the quantity

$$\phi_{nl}(\mathrm{SCF}|r)=\log_e\{f_{nl}(\mathrm{SCF}|r)/r^{l+1}(r_0'-r)(r_0''-r)\cdots\}. \tag{28}$$

We observe that, except for the normalization constant, the quantity $\phi_{nl}(Z|r)$ for a hydrogenlike function is linear in rZ/n, and, according to the analogy rule, we may then consider $\phi_{nl}(\mathrm{SCF}|r)$ as being the same linear function of $rZ_{eff}(r)/n$:

$$\phi_{nl}(\mathrm{SCF}|r)=\phi_{nl}(\mathrm{SCF}|0)-rZ_{eff}(r)/n. \tag{29}$$

We postulate that the effective charge $Z_{eff}(r)$ should be an almost linear function of the atomic number, convenient for interpolation purposes.

TABLE XVII. The effective nuclear charge $Z(\mathrm{SCF}|\epsilon_{nl})$ corresponding to the eigenvalue parameters ϵ_{nl} for some Ne-like and some A-like ions.

		Ne series, with exchange.				
Z	Element	$1s$		$2s$		$2p$
10	Ne	8.093		3.925		2.598
11	Na^+	9.026		4.960		3.796
12	Mg^{+2}	9.973		5.981		4.895
13	Al^{+3}	10.94		7.019		5.985
14	Si^{+4}	11.90		8.042		7.046
Average difference:		0.952		1.029		1.112

A-series, upper values with exchange, lower values without exchange.						
Z	Element	$1s$	$2s$	$2p$	$3s$	$3p$
17	Cl^-	14.46	9.049	7.846	3.617	1.635
		14.46	8.567	7.582	3.116	1.013
18	A	15.40	9.930	8.752	4.795	3.260
		...	...	...	...	...
19	K^+	16.36	10.85	9.693	5.947	4.590
		16.35	10.33	9.374	5.268	4.096
20	Ca^{+2}	17.32	11.79	10.65	7.072	5.814
		17.31	11.27	10.32	6.390	5.330
Average difference:		0.953	0.914	0.935	1.152	1.393
		0.950	0.901	0.913	1.091	1.439

The problem of interpolating an SCF function as a whole may now simply be solved by performing linear interpolations in the functions $\phi_{nl}(\mathrm{SCF}|r)$ given by (28) for each r value under consideration, with an eventual renormalization of the first preliminary result as to the entire wave function. In order to test this rule, we have applied it to the series of A-like ions, where we have interpolated the SCF functions with exchange for K^+ from the tabulated functions for Cl^- and Ca^{+2} and compared them with the correct ones. The results in Table XVIII show that the errors for the $1s$, $2s$, and $2p$ functions are hardly of the order ± 0.002, whereas the errors for the $3s$ and $3p$ functions are slightly larger.

Let us now study in greater detail the continuously varying effective charge which, according to (29), is defined by the formula

$$Z_{\mathrm{eff}}(r)/n=\{\phi_{nl}(\mathrm{SCF}|0)-\phi_{nl}(\mathrm{SCF}|r)\}/r. \quad (30)$$

By using (20) and (22), we obtain

$$\phi_{nl}(\mathrm{SCF}|0)=\frac{2l+3}{2}\log_e K_{nl}-\log_e \alpha_{nl}r_0'r_0''\cdots, \quad (31)$$

where all quantities in the right-hand member may be interpolated according to rules given in the previous section. We note, however, that the value of $\phi_{nl}(\mathrm{SCF}|0)$ is in all events rather unimportant since it corresponds only to a normalization constant in the wave function, which can always be determined afterwards. If there is an uncertainty of $\Delta\phi_0$ in the value of $\phi_{nl}(\mathrm{SCF}|0)$, there will be a corresponding uncertainty of $\Delta\phi_0/r$ in the quantity $Z_{\mathrm{eff}}(r)/n$, which is particularly large in the vicinity of $r=0$. Using (22), (23), and (28), we obtain for the point $r=0$ in particular

$$Z_{\mathrm{eff}}(0)/n=\frac{Z}{l+1}-\frac{1}{r_0'}-\frac{1}{r_0''}-\cdots. \quad (32)$$

TABLE XVIII. The error in the SCF functions for K^+ with exchange obtained from the given functions for Cl^- and Ca^{+2} by linear interpolation in the auxiliary function (28). Unit $=10^{-3}$.

r interval	$1s$	$2s$	$2p$	$3s$	$3p$
0.00					
	± 0.5	0	0	+2	+0.5
0.02					
	−1	± 1	+0.5	+3	+3
0.08					
	−1	−2	+1.5	−6	+6
0.30					
	+1	+1	−2	± 4	± 5
0.60					
		+1	−1	+5	−7
1.20					
		−0.5	−1	−6	+8
4.00					
				−1	+1

In addition to $Z_{\mathrm{eff}}(r)$, we have also studied the quantity

$$\omega_{nl}(r)=Z_{\mathrm{eff}}(r)/Z_{\mathrm{eff}}(0). \quad (33)$$

This function is monotonously decreasing with increasing r from the value $\omega(0)=1$, and it describes, therefore, in a simple way some of the essential properties of the SCF functions, particularly their deviations from the hydrogenlike form. Practically we have found that this function is very slowly varying with the atomic number and that the accuracy of the interpolations may be improved by performing them in $\omega(r)$ instead of in $Z_{\mathrm{eff}}(r)$ or in (28). In this way, the error in, for instance, the $3p$ function of K^+ with exchange derived from Cl^- and Ca^{+2} may be reduced by about 50 percent in comparison to the values given in Table XVIII.

As an example, we have given the ω functions for the series of Ne-like ions with exchange in Table XIX. The ω functions for some A-like ions (Cl^-, A, K^+, Ca^{+2}) and Cu^+ with and without exchange have also been calculated and are available on special request.[16] The tables are all affected by small normalization constant uncertainties $\Delta\phi_0/r$ of the type described above, and it is, therefore, remarkable that they still fit rather smoothly together in spite of the fact that the tables are given in their original form without being adjusted to each other.

In the results for the A-like ions and Cu^+, one can observe another characteristic feature of the ω functions, namely, that for an isoelectronic series the difference between the two ω functions for fields with and without exchange seems to be approximately the same function of r for all elements of the series. This property may be used for estimating wave functions with exchange from those without exchange in case only one field with exchange is known in the series.

A comparison of the ω functions for the $1s$, $2s$, and $2p$ functions with exchange for the Ne-like and the A-like ions, respectively, shows further the effect of adding a complete outer electronic shell.

Finally, with respect to the tables published here, we would like to emphasize that, in order to utilize the full accuracy of the given material and to avoid rounding-off errors, we have in general kept at least one figure more in the tables than is actually valid. This is particularly true for the "tails" of the wave functions.

Up till now, several fields with exchange have been determined for atoms and ions up to $Z=39(Cu^+)$, whereas quite a few additional fields without exchange have been calculated up to $Z=80$ (Hg). However,

[16] Tables of the ω functions for some A-like ions (Cl^-, A, K^+, Ca^{+2}) and Cu^+, supplementary to this article, have been deposited as Document number 4222 with the ADI Auxiliary Publications Project, Photoduplication Service, Library of Congress, Washington 25, D. C. A copy may be secured by citing the Document number and by remitting $1.25 for photoprints, or $1.25 for 35-mm microfilm. Advance payment is required. Make checks or money orders payable to: Chief, Photoduplication Service, Library of Congress.

TABLE XIX. The characteristic functions $\omega_{nl}(r)$ for the SCF functions of some Ne-like ions with exchange. These quantities, defined by $\omega(r)=Z_{eff}(r)/Z_{eff}(0)$, describe the relative decrease in the specific effective nuclear charge under consideration here. In addition, the first nonvanishing derivative in origin, the position r_0 of the node of the $2s$ function, and the values of $Z_{eff}(0)$ are tabulated for the calculation of the wave functions themselves.

	$1s$ functions with exchange.				
r	Ne	Na^+	Mg^{+2}	Al^{+3}	Si^{+4}
0.0	1.0000	1.0000	1.0000	1.0000	1.0000
0.1	0.9858	0.9851	0.9851	0.9858	0.9863
0.2	0.9735	0.9730	0.9732	0.9734	0.9735
0.3	0.9637	0.9631	0.9632	0.9629	0.9630
0.4	0.9550	0.9542	0.9537	0.9528	0.9520
0.5	0.9468	0.9452	0.9442	0.9427	0.9413
0.6	0.9381	0.9351	0.9335	0.9301	0.9287
0.7	0.9284	0.9239	0.9287	0.9148	0.9218
f_0'	60.76	70.25	80.26	90.77	101.8
Z_0	10	11	12	13	14

	$2s$ functions with exchange.				
r	Ne	Na^+	Mg^{+2}	Al^{+3}	Si^{+4}
0.0	1.0000	1.0000	1.0000	1.0000	1.0000
0.1	0.9553	0.9531	0.9533	0.9533	0.9533
0.2	0.9161	0.9128	0.9102	0.9134	0.9122
0.3	0.8831	0.8830	0.8810	0.8824	0.8817
0.4	0.8571	0.8559	0.8547	0.8558	0.8556
0.5	0.8333	0.8323	0.8313	0.8325	0.8328
0.6	0.8123	0.8109	0.8102	0.8121	0.8129
0.7	0.7928	0.7918	0.7915	0.7937	0.7953
0.8	0.7749	0.7742	0.7745	0.7774	0.7798
0.9	0.7585	0.7581	0.7589	0.7627	0.7659
1.0	0.7431	0.7434	0.7448	0.7495	0.7537
1.1	0.7288	0.7297	0.7319	0.7375	0.7427
1.2	0.7157	0.7173	0.7203	0.7269	0.7326
1.4	0.6917	0.6948	0.6998	0.7081	0.7159
1.6	0.6708	0.6756	0.6822	0.6921	0.7016
1.8	0.6522	0.6588	0.6670	0.6794	0.6890
2.0	0.6358	0.6445	0.6530	0.6677	0.6781
2.2	0.6214	0.6311	0.6400	0.6577	0.6685
2.4	0.6083	0.6191	0.6278	0.6490	0.6599
2.6	0.5959	0.6090	0.6163	0.6414	0.6520
2.8	0.5857	0.5992	0.6051	0.6348	0.6446
3.0	0.5754	0.5900	0.5943	0.6275	0.6377
3.2	0.5659	0.5829	0.5839	0.6237	0.6312
3.4	0.5583	0.5730	0.5737	0.6184	0.6245
3.6	0.5510	0.5656	0.5637	0.6110	0.6191
3.8	0.5443	0.5588	0.5538	0.6093	0.6133
4.0	0.5352	0.5552	0.5442	0.6076	0.6078
r_0	0.21836	0.19745	0.18014	0.16542	0.15304
f_0'	14.24	17.16	20.24	23.60	27.10
$Z_0/2$	5.4204	5.9354	6.4488	6.9548	7.4658

	$2p$ functions with exchange.				
r	Ne	Na^+	Mg^{+2}	Al^{+3}	Si^{+4}
0.0	1.0000	1.0000	1.0000	1.0000	1.0000
0.1	0.9489	0.9485	0.9447	0.9445	0.9444
0.2	0.9025	0.9007	0.8989	0.9008	0.8996
0.3	0.8637	0.8639	0.8630	0.8648	0.8654
0.4	0.8323	0.8327	0.8330	0.8352	0.8364
0.5	0.8046	0.8058	0.8067	0.8094	0.8117
0.6	0.7804	0.7820	0.7832	0.7870	0.7902
0.7	0.7582	0.7603	0.7626	0.7672	0.7713
0.8	0.7381	0.7409	0.7437	0.7494	0.7549
0.9	0.7192	0.7230	0.7268	0.7337	0.7401
1.0	0.7021	0.7065	0.7114	0.7193	0.7270
1.1	0.6858	0.6915	0.6975	0.7066	0.7153
1.2	0.6709	0.6777	0.6847	0.6950	0.7047
1.4	0.6439	0.6527	0.6624	0.6749	0.6866
1.6	0.6203	0.6314	0.6436	0.6581	0.6715
1.8	0.5992	0.6129	0.6271	0.6443	0.6588
2.0	0.5808	0.5970	0.6136	0.6319	0.6469
2.2	0.5643	0.5828	0.6014	0.6214	0.6351
2.4	0.5492	0.5700	0.5904	0.6122	0.6276
2.6	0.5362	0.5588	0.5806	0.6041	0.6184
2.8	0.5240	0.5490	0.5721	0.5967	0.6083
3.0	0.5129	0.5391	0.5648	0.5904	0.6016
3.2	0.5030	0.5307		0.5851	0.5918
3.4	0.4935	0.5218		0.5784	
3.6	0.4852	0.5143		0.5737	
3.8	0.4776	0.5072		0.5675	
4.0	0.4697	0.5014			
$f_0''/2$	27.79	38.92	52.00	67.81	85.80
$Z_0/2$	5.0	5.5	6.0	6.5	7.0

there are also a rather large number of atoms and ions left out in the first treatment of the periodic system where the interpolation methods described here may prove to be useful. Further applications of the theory will be given in a later paper of this series.

In conclusion, I should like to express my sincere gratitude to Professor John C. Slater for his generous support of my work and for the great hospitality I have enjoyed during my stay at Massachusetts Institute of Technology, where I also have had the advantage of many inspiring discussions with him and with the members of the Solid-State and Molecular Theory Group.

I am further greatly indebted to *Fil. Kand.* Klaus Appel, Uppsala, for his skillful cooperation in leading the computational group, and to Miss U. Areskog, Miss K. Berger, B. Anderberg, A. Fröman, R. Nilsson, E. Tenerz, M. Tideman, and L. Wik for their kind assistance in carrying out the numerical computations involved in various parts of the work.

Hyperfine Structure and Nuclear Moments of the Stable Bromine Isotopes*

JOHN GORDON KING AND VINCENT JACCARINO
Research Laboratory of Electronics, Massachusetts Institute of Technology, Cambridge, Massachusetts

(Received November 20, 1953)

The hyperfine structure of the $^2P_{\frac{3}{2}}$ state of atomic Br^{79} and Br^{81} has been investigated by the atomic-beam, magnetic-resonance method. The following values have been obtained for the nuclear magnetic dipole interaction constant, a, and the nuclear electric quadrupole interaction constant, b:

$$a^{79}=884.810\pm0.003 \text{ Mc/sec}, \quad a^{81}=953.770\pm0.003 \text{ Mc/sec},$$
$$b^{79}=-384.878\pm0.008 \text{ Mc/sec}, \quad b^{81}=-321.516\pm0.008 \text{ Mc/sec}.$$

From these data, an upper limit of 0.0001 Mc/sec can be placed on the nuclear magnetic octupole interaction constant, c. Applying the results of recent theoretical calculations by Sternheimer and Koster, the following values of the nuclear quadrupole moments were computed:

$$Q^{79}=(0.33\pm0.02)\times10^{-24} \text{ cm}^2, \quad Q^{81}=(0.28\pm0.02)\times10^{-24} \text{ cm}^2.$$

The ratios (a^{79}/a^{81}) and (b^{79}/b^{81}) are in satisfactory agreement with the ratios (μ^{79}/μ^{81}) and (eqQ^{79}/eqQ^{81}), respectively, as measured by other methods.

An experimental technique is given for combining many of the advantages of the "flop-out" resonance method with those of the "flop-in" resonance method in the analysis of complex spectra.

Increased importance can be assigned to the hyperfine structure interaction constants of pairs of isotopes in view of the available information on the ground states of nuclei and on nuclear structure, and the fact that new methods exist for precise measurements of the ratio of nuclear moments.

I. INTRODUCTION

THE present work represents an extension of the study of the hyperfine structure of various halogen atoms by the atomic-beam method to the stable isotopes of bromine. Refinements in technique have made it possible to produce and detect a steady atomic beam of bromine. The analysis of the spectra of the two almost equally abundant isotopes ($Br^{79}=50.6$ percent; $Br^{81}=49.4$ percent) is facilitated by using a mass spectrometer to separate one from the other in the negative ion beam from the surface ionization detector.

Because of the similarity in theory and method of this experiment to that performed with the stable chlorine isotopes by Davis, Feld, Zabel, and Zacharias (DFZZ), it is suggested that the reader refer to the report of their work[1] whenever further amplification of our discussion is desired. A detailed description of methods for simplifying the study of hyperfine structure and for determining the sign of the nuclear moments is given.

The atomic ground state of bromine is a $^2P_{\frac{3}{2}}$ configuration. The energy difference between the $^2P_{\frac{3}{2}}$ state and the $^2P_{\frac{1}{2}}$ metastable state is 3685 wave numbers (1.105×10^9 Mc/sec). (The inversion of the fine structure doublets in the halogens is a result of the fact that the valence electron is a "missing" electron.) As is known, and has been confirmed in this experiment, the nuclear spin I, of both isotopes is $\frac{3}{2}$ in units of $\hbar$. Thus, with $I=J=\frac{3}{2}$, the Zeeman effect of the hfs interaction of bromine is similar to that of the two isotopes of chlorine, a discussion of which is given in DFZZ.

The Hamiltonian of the hfs interaction in a magnetic field H may be expressed as[2]:

$$\mathbf{H}=ha\mathbf{I}\cdot\mathbf{J}+hbQ_{op}+hcO_{op}+\mu_0(g_J\mathbf{J}\cdot\mathbf{H}+g_I\mathbf{I}\cdot\mathbf{H}), \tag{1}$$

where

$$\mathbf{I}\cdot\mathbf{J}=[f(f+1)-j(j+1)-i(i+1)]/2, \tag{2}$$

$$Q_{op}=\frac{3(\mathbf{I}\cdot\mathbf{J})^2+\frac{3}{2}(\mathbf{I}\cdot\mathbf{J})-i(i+1)j(j+1)}{2i(2i-1)j(2j-1)}. \tag{3}$$

The hfs interaction constants a and b for the case $j=l+\frac{1}{2}$ may be written as follows:

$$a=-\frac{\mu_0^2}{h}g_I\mathfrak{F}\frac{2l(l+1)}{j(j+1)}\langle r^{-3}\rangle, \tag{4}$$

$$b=-\frac{e^2}{h}QR\frac{2l}{2l+3}\langle r^{-3}\rangle. \tag{5}$$

Where $g_I=-(m/M)(\mu/I)$, μ being the nuclear magnetic moment in nuclear magnetons, Q is the nuclear electric quadrupole moment in units of 10^{-24} cm^2, $\mathfrak{F}=1.04$ and $R=1.05$ are two relativistic correction factors,[3] and the other symbols have their usual meanings. (This choice of the diagonal form for the Hamiltonian, that is, the assumption that the eigenvalues of J^2, J_z, I^2, and I_z are good quantum numbers, presupposes that the effects of neighboring electronic and nuclear levels on the ground state are small compared to the hfs interaction in the ground state, that is, in particular

$$E_{\text{fine structure}}(^2P_{\frac{1}{2}}\leftrightarrow{}^2P_{\frac{3}{2}})\gg E_{hfs}(^2P_{\frac{3}{2}}).$$

For $I=\frac{3}{2}$, multipole interactions of higher order than the magnetic octupole are forbidden.

For atoms with $I=J=\frac{3}{2}$, the calculated hfs energy levels in an external magnetic field are plotted, for $b=0$, in Figs. 1(a) and 1(b), where μ_I is assumed positive and negative, respectively.

II. APPARATUS

Since the apparatus used in this experiment is the same as that used in the chlorine experiments,[1,4-6] the

* This work was supported in part by the Signal Corps, the Air Materiel Command, and the U. S. Office of Naval Research.

[1] Davis, Feld, Zabel, and Zacharias (referred to as DFZZ), Phys. Rev. 76, 1076 (1949).

[2] N. F. Ramsey in *Experimental Nuclear Physics* edited by E. Segrè (John Wiley and Sons, Inc., New York, 1953), Vol. 1, Chap. 3, pp. 358–467.

[3] H. B. G. Casimir, *On the Interaction Between Atomic Nuclei and Electrons* (DeErven F. Bohn N. V., Haarlem, 1936).

[4] Davis, Nagle, and Zacharias, Phys. Rev. 76, 1068 (1949).

[5] V. Jaccarino and J. G. King, Phys. Rev. 83, 471 (1951).

[6] J. G. King and V. Jaccarino, Phys. Rev. 84, 852 (1951).

papers describing the latter experiments may be consulted for general information not found in the description of the modified details of the apparatus peculiar to the bromine experiment.

A. Atomic Beam Source and Detector

The microwave-discharge atom source that was used for chlorine was found adequate for bromine. Since, however, the needle valves or metallic leaks used to control the gas flow to the discharge in the case of chlorine operated erratically after exposure to bromine, the arrangement shown in Fig. 2 was adopted. The flow of bromine vapor was determined both by the vapor pressure of the liquid bromine in the reservoir, which was maintained at a constant temperature by a water bath with an adjustable thermostat, and by a fixed leak consisting of a 40-cm length of capillary into which a wire was inserted to reduce the cross-section area to 2×10^{-4} mm^2; the entire leak was kept at 70°C to prevent condensation of the vapor. The ease with which bromine could be trapped anywhere in the system with dry ice eliminated the need for many troublesome valves.

The consumption of liquid bromine was about 0.1 cc per hour. From this value and the measured detector ion currents, the detection efficiency of the hot tungsten ribbon for bromine was estimated to be 2×10^{-5}, in agreement with previous results.[7]

It was later found that detection efficiencies more closely approaching unity could be achieved for the halogens by using a properly activated thoriated tungsten ribbon. The low detection efficiency made it desirable to increase the sensitivity of the electrometer system (particularly since we intend to investigate the hyperfine structure of the $^2P_{\frac{1}{2}}$ metastable state).

To achieve greater electrometer sensitivity, an FP54 electrometer in a conventional circuit was coupled by means of an amplifier to an L and N galvanometer of sensitivity 0.00014 μa/mm. Part of the increased sensitivity that results from the use of the amplifiers is sacrificed in an equalizer network that reduces the effective time constant of the system.

With this arrangement the sensitivity and time constant could easily be adjusted so that changes in ion beam intensity comparable to the thermal fluctuations in the grid resistor of the FP54 could be observed. A simplified schematic of the system is given in Fig. 3. The batteries shown were continuously charged at a rate that maintained them near full charge.

B. Generation and Measurement of Transition Frequencies

The low-frequency $\Delta F=0$ transitions were observed with General Radio 805-C signal generators below 50 Mc/sec. In the range from 2200 to 2600 Mc/sec, a 707-B klystron was used with a set of simple cylindrical cavities chosen to cover each of the regions predicted from the low-frequency data in which it was necessary to search for high-frequency $\Delta F=\pm1$ transitions. Two other $\Delta F=\pm1$ transitions near 1300 Mc/sec were observed with a F4800 jamming transmitter using a 2C39-A lighthouse tube. All these high-frequency oscillators were operated by batteries or by well-filtered power supplies to minimize the output signal width, which was in all cases less than 1 kc/sec. Adequate output was obtained from all oscillators when optimally

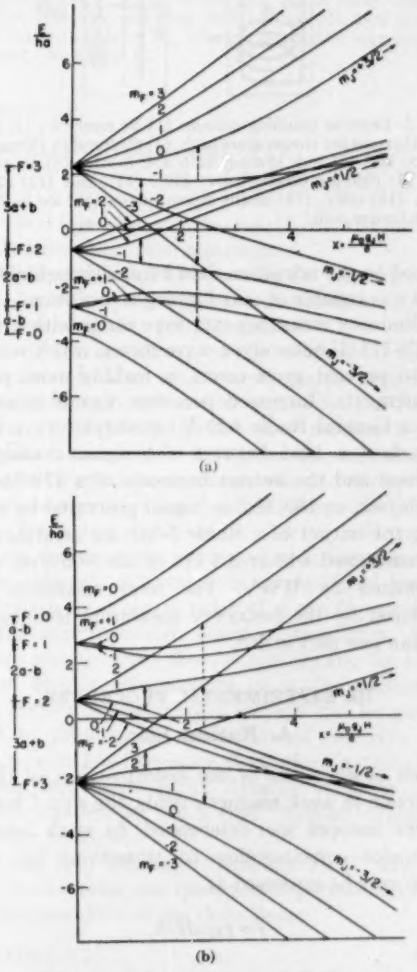

FIG. 1. Calculated hfs energy level diagrams for atoms with $I=J=(3/2)\hbar$ in an external magnetic field H. In plotting both curves, the quadrupole interaction constant b has been set equal to zero. Figure 1(a) was plotted with μ_I assumed positive, and Fig. 1(b) with μ_I assumed negative. The double arrows represent the normal $\Delta F=0$ "low-frequency," "flop-in" transitions; and the dashed arrows, the transitions observed as "flop-out on flop-in."

[7] H. H. Stroke, Massachusetts Institute of Technology, Master's thesis, 1952 (unpublished).

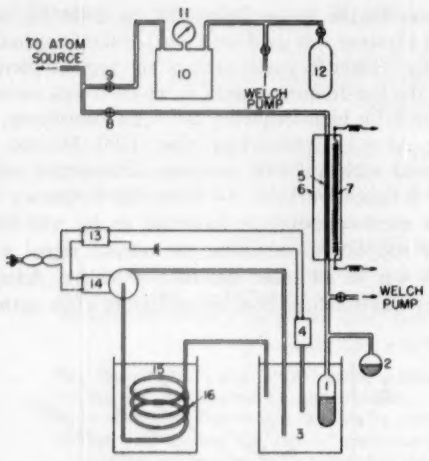

FIG. 2. Bromine handling system: (1) Br reservoir, (2) drying agent, (3) constant temperature bath, (4) thermostat, (5) capillary leak, (6) and (7) leak heating bath and heater, (8) Br shut-off valve, (9) chlorine needle valve, (10), (11), and (12) chlorine system, (13) relay, (14) motor driven pump, (15) ice bath, (16) heat exchanger coil.

matched to the transition field loop, although only the F4800 was capable of overflopping a transition.

Preliminary measurements were made with a Cardwell TS-175/U heterodyne wave meter, which was also used to prevent gross errors in making more precise measurements. Increased precision was obtained by using a General Radio 620-A heterodyne wave meter to produce a beat between the signal causing the transition and the nearest harmonic of a 120 Mc/sec, 150 Mc/sec, or 180 Mc/sec signal generated by multiplying the output of a stable 5-Mc/sec crystal, which was maintained within ± 1 cps of the 5-Mc/sec signal transmitted by WWV. The total maximum error introduced by the frequency measuring techniques is less than one part in 10^6.

III. EXPERIMENTAL PROCEDURE

A. Nuclear Spin

From observations of the Zeeman effect of the hfs interaction in weak magnetic fields, the spin I for both bromine isotopes was determined. In weak fields the frequencies corresponding to transitions for which $\Delta F=0$ may be expressed as

$$\nu = g_F \mu_0 H/h, \tag{6}$$

where

$$g_F=[(\mathbf{F}\cdot\mathbf{J})g_J+(\mathbf{F}\cdot\mathbf{I})g_I]/[f(f+1)]. \tag{7}$$

Since $g_I \ll g_J$,

$$\nu=\frac{f(f+1)+j(j+1)-i(i+1)}{2f(f+1)}g_J\mu_0 H/h. \tag{8}$$

For the case of $I=J$ the Zeeman frequencies are identical for all F levels. $\Delta F=0$ transitions at a given weak field were observed at the same frequency in both bromine isotopes and in chlorine, whence, since $g_J=4/3$ and $J=\frac{3}{2}$ for all halogens, the value of $I=\frac{3}{2}$ for both Br^{79} and Br^{81} was immediately established.

B. Determination of the HFS Intervals

In order to observe transitions which satisfy the selection rule $\Delta F=0$, $\Delta m_F=\pm 1$, a further condition must be imposed on the value of the effective magnetic moment of the atom (m_J) in the large fields ($x>7$) of the deflecting (**A**) and refocusing (**B**) magnets, depending on the relative orientation of the gradients of the two magnets. In these experiments the **A** and the **B** magnets have their gradients in the same direction, so that an atom arrives at the detector only if the sign of its effective moments is reversed by a transition in the intervening homogeneous field produced by the **C** magnet. Transitions can therefore be observed free of background due to atoms, except for that resulting from scattering. The background of molecules which have no net atomic magnetic moment, is conveniently removed by a stopping wire placed at the end of the **B** magnet. This is the "flop-in" method first used by Zacharias on K^{40}.[8] Alternatively the **A** and **B** magnets can have their gradients oppositely directed, so that all atoms reach the detector, except those whose effective magnetic moment changes sign or magnitude as a result of a transition in the **C** field. Transitions must, therefore, be observed as a small decrease of the total beam. This is the "flop-out" method.

"Flop-in," though preferable to "flop-out" when it is necessary to work with small or unsteady beams, does not allow as many transitions to be observed as can be observed with "flop-out," because of the more stringent requirements that must be satisfied by the atoms in the **A** and **B** fields. For instance, in the case

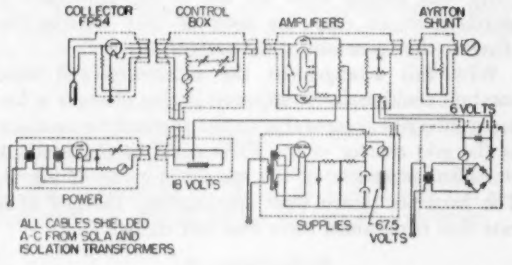

FIG. 3. Electrometer system. The total increase in sensitivity resulting from the amplifiers shown is a factor of about 100 partly due to improved matching to the galvanometer. An equalizer with an insertion loss of 10 is used to speed up the initial response of the galvanometer so that the presence of a transition may be more easily ascertained when the radio-frequency oscillator is turned on and off.

[8] J. R. Zacharias, Phys. Rev. 61, 270 (1942).

of $I=J=\frac{3}{2}$, two transitions can be seen in "flop-in," whereas six can be seen in "flop-out."

If two independent transition wires carrying rf currents of different frequency are used, both producing oscillating magnetic fields so oriented as to induce $\Delta m_F=\pm 1$ transitions, most of the advantages of the "flop-out" method may be realized in a "flop-in" apparatus. The two independent wires for inducing $\Delta m_F=\pm 1$ transitions were placed on either side of the wire used for inducing $\Delta m_F=0$ transitions as shown schematically in Fig. 4. As an illustration, consider the transition $(F=3,\ m_F=-1\leftrightarrow F=3,\ m_F=-2)$ as indicated in Fig. 1(a).

If an rf current is passed through the wire labelled f_i (see Fig. 4) at a frequency $\nu_1=E(3,\ -1\leftrightarrow 3,\ -2)/h$, "flop-in" will be observed as an increase in the negative ion current from the detector. Now when a current of frequency $\nu_2=E(3,\ -2\leftrightarrow 3,\ -3)/h$ is passed through the wire labelled f_0 with the current of frequency $E(3,\ -1\leftrightarrow 3,\ -2)/h$ still present in the wire f_i, those atoms which were in the state $(F=3,\ m_F=-1,\ m_J=\frac{1}{2})$ in the **A** magnet will be in the state $(3,\ -1,\ \frac{1}{2})$ in the **B** magnet and will consequently not be refocused at the detector.[9] The transitions induced by the current in f_0 will, therefore, be observed as a decrease of one half in the amount of "flop-in" initially observed. Reference to Fig. 1(a) shows that besides the two normal "flop-in" transitions, three additional "flop-out" transitions (shown in dashed lines) may be observed by this method. It is worth mentioning that the "flop-out on flop-in" method as described above corresponds selectively to observing either induced emission or absorption (but not to both) depending on the sign of the nuclear moment and the particular transition involved; further discussion of this point will be given in Sec. III-C.

These "flop-out on flop-in" techniques are expected to be useful in investigating radioactive nuclides such as Br^{80} because they combine the high discrimination against background of normal "flop-in" techniques with some of the flexibility of "flop-out" techniques. Using a mass spectrometer as well, should compensate for the isotopic dilution characteristic of many such experiments.

The "flop-out on flop-in" method is particularly valuable in the example given above since a relatively precise value of the zero field interval $F=3\leftrightarrow F=2$,[10] Δ, may be obtained by observing the frequency of the transition as a function of **C** field and using the exact

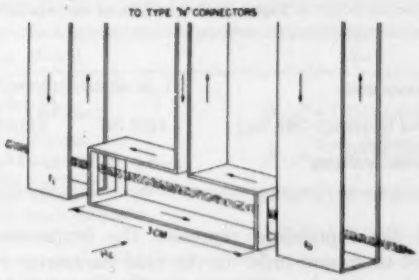

FIG. 4. Radio-frequency transition wire system. The direction of the steady homogeneous field of the **C** magnet is indicated by H_c, and is perpendicular to the direction of the beam. The wires f_i and f_0 generate oscillating field components in a direction perpendicular to that of H_c, whereas the middle wire generates components parallel to H_c.

expression:

$$\nu_2(3,\ -2\leftrightarrow 3,\ -3)=\tfrac{1}{2}(1-\gamma)ax-\tfrac{1}{2}\Delta+[\Delta^2+(1+\gamma)^2a^2x^2]^{\frac{1}{2}},\quad (9)$$

where $\gamma=-(g_I m)/(g_J M)$, $x=(\mu_0 g_J H)/ha$, and the other symbols have their usual meanings.

The field is measured by observing the same transition in Cl^{35}, for which the interaction constants are known, and by assuming that $g_J(\mathrm{Cl})=g_J(\mathrm{Br})$.

The relative complexity of the expressions for the various $\Delta m=\pm 1$ lines can be seen from the form of the solution of the general secular equation. The secular equation, for $I=J=\frac{3}{2}$, factors into one-fourth-order determinant, and pairs of first-order, second-order and third-order determinants corresponding to the low field quantum number $m_F=0,\pm 3,\pm 2,\pm 1$, respectively. Only in the case of the transition $(3,\ -2\leftrightarrow 3,\ -3)$ can the transition frequency be expressed as a function of H and the zero field interval Δ in simple closed form so that a relatively accurate value of Δ can be calculated from the experimentally observed quantities. It is, therefore, not necessary to solve numerically the rather involved secular determinants as in the method of DFZZ. Evidently the present method can be used in general to simplify the prediction of the zero field intervals from low-frequency data, since a "flop-out" transition expressible by an equation of lower order than the equation for the normal "flop-in" transition can always be found.

The zero field interval $(F=2\leftrightarrow F=1)$, Γ, was estimated by observing the quadratic departure from the linear Zeeman effect of the three lines:

$$\nu_1(3,\ -1\leftrightarrow 3,\ -2)=\tfrac{1}{2}(1-\gamma)ax+[(3/20)/\Delta](1+\gamma)^2a^2x^2,\quad (10)$$

$$\nu_3(2,\ 0\leftrightarrow 2,\ -1)=\tfrac{1}{2}(1-\gamma)ax+[(1/5)/\Gamma-(1/20)/\Delta](1+\gamma)^2a^2x^2,\quad (11)$$

$$\nu_4(2,\ -1\leftrightarrow 2,\ -2)=\tfrac{1}{2}(1-\gamma)ax+[(3/5)/\Gamma-(3/20)/\Delta](1+\gamma)^2a^2x^2,\quad (12)$$

[9] The quantum number m_I is not specified since (a) it is uniquely determined by $m_I=m_F-m_J$; (b) the physically important quantum number is m_J, which determines the path of the atom in the high fields of the **A** and **B** magnets.

[10] The following notation will be used throughout for the zero field intervals:

hfs intervals	Symbol
$(F=3\leftrightarrow F=2)$	Δ
$(F=2\leftrightarrow F=1)$	Γ
$(F=1\leftrightarrow F=0)$	Ω.

TABLE I. Frequencies of various $\Delta F=\pm 1$ transitions observed in a weak magnetic field.

	Br^{79}			Br^{81}		
Transitions used	$(1, 0\leftrightarrow 0, 0)$	$(2, 0\leftrightarrow 1, 0)$ $(2, 1\leftrightarrow 1, 1)$	$(3, -1\leftrightarrow 2, -1)$	$(1, 0\leftrightarrow 0, 0)$	$(2, 0\leftrightarrow 1, 0)$ $(2, 1\leftrightarrow 1, 1)$	$(3-1\leftrightarrow 2-1)$
Observed frequency (Mc/sec) corrected to $x=0$	1269.702	2154.499	2269.552	1275.271	2229.056	2539.794
Theoretical splitting	$a-b+100.8c$	$2a-b-50.4c$	$3a+b+14.4c$	$a-b+100.8c$	$2a-b-50.4c$	$3a+b+14.4c$

where the expressions represent the frequencies expanded to second order in the field parameter x, and the value of Δ obtained from Eq. (1) is used. A knowledge of the approximate values of the zero-field intervals facilitated finding the three corresponding $\Delta F=\pm 1$, $\Delta m_F=0$ transitions in each isotope. A transition wire which produced an oscillating magnetic field principally in the direction of the **C** field (see Fig. 4) was used. Since no "flop-in" transition exists between the levels $F=1$ and $F=0$, the ingenious method of DFZZ was used, with slight modification. The "flop-in" transition $(F=2,\ m_F=1,\ m_J=\frac{1}{2}\leftrightarrow F=1,\ m_F=0,\ m_J=-\frac{1}{2})$ was induced by loop f_1, and the transition $(1, 0, \frac{1}{2}, \rightarrow 0, 0, \frac{1}{2})$ induced by the z-component wire was observed as "flop-out" in a fashion completely analogous to the method described above in its application to $\Delta F=0$ transitions.

The $\Delta F=\pm 1$, $\Delta m=0$ transitions were observed in very weak fields (approximately 1 gauss) and, since these transitions are field independent to first order, the natural line widths were obtained. Correction of each of the measured frequencies to zero field was made as described in DFZZ. The results are summarized in Table I. A full resonance curve was obtained for each transition as a precautionary measure in interpreting the results. Representative "flop-in" and "flop-out on flop-in" curves are shown in Fig. 5. Several of the narrow field-independent transitions exhibited structure similar to that observed and interpreted by Hughes, Tucker, Rhoderick, and Weinreich in their work with atomic helium.[11] It was found possible to enhance or eliminate the structure observed in the bromine transitions by changing the strength of the oscillating field and the range of velocities of the observed atoms, but in all cases the center of the structure was unshifted in frequency as predicted by the Majorana theory.[11,12]

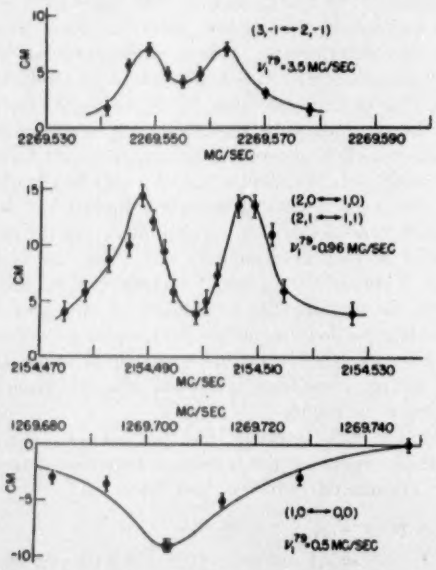

FIG. 5. Representative resonance curves in Br^{79}. These correspond to $\Delta F=\pm 1$ transitions as labeled. The field at which each transition was observed was calibrated by measuring a $\Delta F=0$ transition at the same time. The bottom curve was observed as "flop-out" on the $(2,1\leftrightarrow 1,0)$ "flop-in" transition. A galvanometer deflection of 1 cm corresponds to a collector ion current of 1.5×10^{-16} ampere.

C. Determination of the Sign of the Nuclear Magnetic Moments

The hfs energy level diagrams for $I=J=\frac{3}{2}$ appear in Figs. 1(a) and 1(b), respectively, for positive and negative nuclear moments. The important differences between these two diagrams are that the order of the hfs level is inverted with respect to energy and that all magnetic quantum numbers are reversed in sign. For purposes of this discussion the interaction of the nuclear magnetic moment with the external field can be neglected since $\mu_I \ll \mu_0$. Since the path followed by atoms in a given state in the strong fields of the **A** and **B** magnets depends on the direction of the gradient of the magnetic fields and the sign of the effective moment (e.g., atoms with $m_J>0$ are deflected toward weaker fields), atoms in a given m_J state may be removed from the observed beam by inserting an obstacle, at the exit of the **B** magnet, that extends outward from the center of the beam as indicated in Fig. 6.

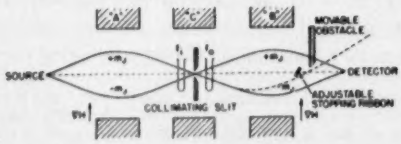

FIG. 6. Atom paths drawn exaggerated to illustrate how the sign of a nuclear moment was determined as described in Sec. IIIC of the text.

[11] Hughes, Tucker, Rhoderick, and Weinreich, Phys. Rev. **91**, 828 (1953).

[12] E. Majorana, Nuovo cimento **9**, 43 (1932).

The method used here to determine the sign of the nuclear moment requires only the observation of relatively low-frequency $\Delta F=0$ transitions. Consider the one observable $\Delta F=0$, "flop-in" transition in the $F=3$ level. Depending on the sign of the nuclear magnetic moment, this transition is $\{3, -1, \frac{1}{2}\leftrightarrow 3, -2, -\frac{1}{2}\}$ for positive moment, and $\{3, 1, -\frac{1}{2}, \leftrightarrow 3, 2, \frac{1}{2}\}$ for negative moment, as can be seen from Figs. 1(a) and 1(b). There are, in addition, the corresponding transitions $\{3, -2, -\frac{1}{2}, 3, -3, -\frac{3}{2}\}$, $(\mu_I>0)$, or $\{3, 2, \frac{1}{2}\leftrightarrow 3, 3, \frac{3}{2}\}$, $(\mu_I<0)$, observable as "flop-out on flop-in" as previously described.

The $\Delta F=0$, "flop-in" transition was reduced to half its maximum value by inserting the obstacle from the low **B** field side of the beam, so that no atoms with $m_J>0$ in the **B** magnet reach the detector. Now to determine whether the remaining atoms were in the state $(3, -2, -\frac{1}{2})$ or in the state $(3, 1, -\frac{1}{2})$, the frequency corresponding to the $\Delta F=0$, "flop-out" transition was introduced in the wire, whereupon the remaining "flop-in" disappeared. The atoms were therefore in the state $(3, -2, -\frac{1}{2})$, and it may be concluded that diagram 1(a) applies and the nuclear magnetic moment is positive. With the obstacle on the high **B** field side of the center of the beam, no "flop-out" was observed. Had the nuclear magnetic moment been negative, the same effects would have been observed with the obstacle on the high **B** field side of the beam.

IV. RESULTS

A. The Interaction Constants

From the measured intervals given in Table I the following values for the interaction constants may be calculated:

$$a_{\frac{1}{2}}^{79}=884.810\pm0.003 \text{ Mc/sec},$$
$$b_{\frac{1}{2}}^{79}=384.878\pm0.008 \text{ Mc/sec},$$
$$c_{\frac{1}{2}}^{79}\leqq 0.0001 \text{ Mc/sec},$$
$$a_{\frac{1}{2}}^{81}=953.770\pm0.003 \text{ Mc/sec},$$
$$b_{\frac{1}{2}}^{81}=321.516\pm0.008 \text{ Mc/sec},$$
$$c_{\frac{1}{2}}^{81}\leqq 0.0001 \text{ Mc/sec}.$$

Thus, as in all previous atomic beam hfs experiments, the observed nuclear-electron interaction may be described, to a high degree of accuracy, in terms of only two electromagnetic interaction parameters. This is not unexpected, since a simple theory predicts that the nuclear magnetic octupole moment should be, in order of magnitude $(a_0/R_K)^2\approx 10^{-8}$ as small as the nuclear magnetic dipole moment.

B. The Ratio of the Magnetic Dipole Interaction Constants

From the data above the ratio $a_{\frac{1}{2}}^{81}/a_{\frac{1}{2}}^{79}$ may be calculated. This ratio can be compared with the ratios, given in Table II, of the nuclear magnetic dipole moments as measured by nuclear resonance techniques. Two of the values listed agree within the experimental uncertainties with the value reported here. The result of Sheriff and Williams, however, disagrees by 18 parts in 10^5. Since the electronic wave function density for a $P_{\frac{1}{2}}$ electron at the position of the nucleus is extremely small and the two bromine isotopes have similar g_I values, the magnetic hyperfine structure anomaly to be expected in this case is far smaller than the above discrepancy (certainly less than 1 part in 10^6).[13] Professor Williams has pointed out[14] that if an error in sideband identification in the measurements of Sheriff and Williams had been made, the necessary correction would bring their result into agreement with those listed in Table II. Otherwise, it is difficult to reconcile these results.

TABLE II. Ratios of the nuclear magnetic dipole interactions.

Method	Ratio
Nuclear resonance in NaBr, LiBr solution[a]	$\mu^{81}/\mu^{79}=1.0778\pm0.0003$
Nuclear resonance in NaBr solution[b]	$\mu^{81}/\mu^{79}=1.07775\pm0.00005$
Nuclear resonance in NaBr solution[c]	$\mu^{81}/\mu^{79}=1.07796\pm0.00002$
Atomic beam magnetic resonance[d]	$a_{\frac{1}{2}}^{81}/a_{\frac{1}{2}}^{79}=1.077938\pm0.000020$

[a] R. V. Pound, Phys. Rev. **72**, 1273 (1947).
[b] R. E. Sheriff and D. Williams, Phys. Rev. **82**, 651 (1951).
[c] H. E. Walchli, Oak Ridge National Laboratory Report ORNL-1469, 1953 (unpublished), pp. 36 and 37. See reference WL 52-5 to unpublished work of H. E. Walchli.
[d] This paper.

C. The Ratio of the Electric Quadrupole Interaction Constants

In a similar fashion, the ratio $b_{\frac{1}{2}}^{79}/b_{\frac{1}{2}}^{81}$ may be compared with the ratio of the electric quadrupole moments as observed by pure nuclear quadrupole resonance in solids. (See Table III.) Since both methods are capable of great precision and are free from molecular binding effects, the agreement of these results, unique in the comparison of the quadrupole interaction ratios for two isotopes, indicates that the hfs interaction is well understood.

TABLE III. Ratios of the nuclear electric quadrupole interactions.

Method	Ratio
Quadrupole resonance in Br_2[a]	$\nu^{79}/\nu^{81}=1.1968\pm0.0002$
Molecular beams (KBr)[b]	$Q^{79}/Q^{81}=1.1977\pm0.0008$
Microwave spectroscopy[c] (average of 10 values taken with 6 compounds)	$Q^{79}/Q^{81}=1.19707\pm0.00003$
Atomic beam magnetic resonance[d]	$b^{79}/b^{81}=1.19707\pm0.00003$

[a] H. G. Dehmelt, Z. Physik **130**, 480 (1951).
[b] Fabricand, Carlson, Lee, and Rabi, Phys. Rev. **91**, 1403 (1953).
[c] A. L. Schawlow (private communication).
[d] This paper.

[13] A. Bohr and V. F. Weisskopf, Phys. Rev. **77**, 94 (1950).
[14] D. R. Williams (private communication).

TABLE IV. Nuclear electric quadrupole moments (in units of 10^{-24} cm^2).

Method	Values Uncorrected Br^{79}	Uncorrected Br^{81}	With Sternheimer correction[d] Br^{79}	With Sternheimer correction[d] Br^{81}
Microwave spectroscopy[a]	0.31	0.26	0.32	0.27
Quadrupole resonance in Br_2[b]	0.30	0.25	0.31	0.26
Atomic beam magnetic resonance[c]				
(1) calculated from Eq. (13)	0.322±0.019	0.269±0.016	0.335±0.020	0.280±0.017
(2) calculated from Eqs. (5) and (14)	0.296±0.018	0.247±0.015	0.308±0.018	0.257±0.016

[a] Gordy, Simmons, and Smith, Phys. Rev. **74**, 243 (1948).
[b] H. G. Dehmelt, Z. Physik **130**, 480 (1951).
[c] This paper.
[d] The results of Sternheimer (see reference 16) indicate that the correction should be applied to the values of Q obtained by these methods.

D. The Nuclear Electric Quadrupole Moments

From the values of $b_{\frac{1}{2}}$, $a_{\frac{1}{2}}$, μ, and I, Q may be calculated using the method of DFZZ, where it is assumed only that the angular and radial parts of the wave functions for the electron are separable, and that $\langle r^{-3}\rangle$ is the same in the electric quadrupole and magnetic dipole interactions. (Because the excited atomic states of the halogens are different from those of the gallium family it is possible, as it was not in the case of gallium,[15] to neglect the effects of configuration interaction in obtaining Q to the desired accuracy, which is limited by the relativistic corrections which are known to approximately one percent). The magnitude of Q must however be corrected for the polarization of the inner electron core by the nuclear quadrupole moment. This correction has been evaluated by Sternheimer in several articles.[16] The result may be expressed as

$$Q=-(8/3)(\mu_0/e)^2(m/M)(\mu/I)(\mathfrak{F}/R)(b/a)C, \quad (13)$$

where $C=1.040$ is the Sternheimer correction and $\mathfrak{F}/R=0.99$ is a relativistic correction.[3]

It should be noted that the sign of the nuclear magnetic moment previously confirmed to be positive (see Sec. III C) enters in determining the sign of Q.

An independent method for calculating the quadrupole moments utilizes the fact that $\langle r^{-3}\rangle$ may be evaluated from the fine structure separation δ by using the relation

$$\delta=(\mu_0^2/hc)Z_i(2l+1)H\langle r^{-3}\rangle. \quad (14)$$

For the effective value of the nuclear charge Z_i, the result of recent work of Smith and Barnes[17] for p electrons is used to write $Z_i=Z-n$, n being the radial quantum number. H here is a relativistic correction factor tabulated by Casimir.[3] Using the above relation and Eq. (5), the Q's have been calculated and are listed in Table IV for comparison with the values obtained by the aforementioned method. The agreement is good and indicates the apparent validity of quadrupole moment calculation by either method in the case of the halogens. Considering the accuracy of the experiments and the detail of the theory, we believe that ±6 percent represents an upper limit for the uncertainty in these moments.

TABLE V. The anomalous spin gyromagnetic ratio of the $P_{3/2}$ electron in bromine.

$$g_J(\mathrm{Br})/g_J(\mathrm{Cl})=0.9997\pm0.0004$$
$$g_S(\mathrm{Br})=2(1.0008\pm0.0005)$$

E. The Anomalous Spin Gyromagnetic Ratio of the $P_{3/2}$ Electron in Bromine

The ratio $g_J(\mathrm{Br})/g_J(\mathrm{Cl})$ may be determined from measurements of the transition $(3,-2\leftrightarrow 3,-3)$ in each element in the same magnetic field, once the interaction constants are known. As can be seen in Table V, the g_J's are similar in bromine and chlorine, the accuracy of the determinations being severely limited by the broadening of the transitions caused by the inhomogeneity of the C-field. From a previous investigation of the g_J's in the $J=\frac{3}{2}$ and $J=\frac{1}{2}$ states in chlorine,[18] and setting $g_L=1$, the value of g_S listed in Table V for the $P_{\frac{1}{2}}$ electron in bromine was obtained.

ACKNOWLEDGMENT

We wish to thank Professor B. T. Feld and Professor J. R. Zacharias for the interest they have shown in our work.

[15] G. F. Koster, M.I.T. Doctoral thesis (1951); Phys. Rev. **86**, 148 (1952).
[16] R. Sternheimer, Phys. Rev. **84**, 244 (1951); **86**, 316 (1952).
[17] W. V. Smith and R. G. Barnes, Phys. Rev. **91**, 457 (1953).
[18] J. G. King and V. Jaccarino, Phys. Rev. **87**, 228 (1952), and Quarterly Progress Report, Research Laboratory of Electronics, M.I.T. April 15, 1952 (unpublished), p. 33.

Mu-Mesonic X-Rays and the Shape of the Nuclear Charge Distribution

DAVID L. HILL,* *University of California, Los Alamos Scientific Laboratory, Los Alamos, New Mexico*

AND

KENNETH W. FORD, *Indiana University,† Bloomington, Indiana*

(Received March 8, 1954)

Mu-mesonic x-rays, fast electron scattering, and electronic spectra each depend on the nuclear charge distribution $\rho(r)$ in different ways. Adjoining theoretical analyses of observations on these different phenomena may therefore bracket an acceptable set of functional descriptions for $\rho(r)$. The present paper reports the dependence of the μ-mesonic x-ray spectrum of Pb on the extent and shape of the nuclear charge density. For several functional families representing conceivable forms for $\rho(r)$ we have obtained the resultant Coulomb potentials and have solved "exactly" by electronic computation the relativistic equations to yield the first four levels ($1S$, $2S$, and $2P$) and transition energies for mu mesons bound in the field of the lead nucleus. The next two levels ($3D$) have been found by perturbation theory. Effects omitted from the calculations have been examined and theoretical uncertainties estimated for each level. These results permit adjustment of the effective electric radius R, for each form of $\rho(r)$ to agree with known x-ray measurements of the $2P\rightarrow 1S$ transitions. Calculations completed for neighboring values of R permit interpolation to improved values when more precise measurements are made and when small corrections of the raw data for electrodynamic and special coupling effects have been carried through. The doublet splitting of the $2P$ levels offers an independent measure of R, as well as a check on the possible existence of an anomalous muon magnetic moment. In contrast, the $3D\rightarrow 2P$ and $2S\rightarrow 2P$ transition energies are insensitivie to R but sufficiently sensitive to the shape of the charge distribution, so that accurate measurements of the transition energies between the six lowest muon levels in the heavy nuclides will be able to provide information on both the electrical radius and the shape of nuclear electrification, independently of indications from the other phenomena mentioned above.

I. INTRODUCTION

A NUMBER of sources of evidence now give a strong indication that the electromagnetic radii of heavy nuclei are at least 15 percent smaller than the previously assumed values of $(1.4 \text{ to } 1.5)\times 10^{-13}A^{1/3}$ cm.[1] The only contrary evidence comes from the study by Schawlow and Townes[2] of the effect of the finite size of the nucleus on the electronic x-ray fine structure. The disagreement between this and other sources of evidence has not been explained, but may be due to radiative corrections to the $p_{1/2}$ electronic level. In view of the rather convincing evidence for the smaller *size* of the nuclear proton distribution, it is of interest to know whether the charge distribution is also altered in shape from our previous ideas of a nearly uniform density. (By shape we here mean the shape of the curve of nuclear proton density *vs* radius, and not the geometric shape of the nucleus.) In the present paper we show that the mu-mesonic x-ray transitions can provide a valuable tool in the determination of the shape of the charge distribution within the nucleus[3]—both alone and in conjunction with other sources of evidence.

Among known experimental results which depend on the charge distribution in the nucleus, the $2P\rightarrow 1S$ mu-mesonic transition energy[4] probably provides most unambiguously a single parameter of the charge distribution.[5] If this transition energy is the most reliable single datum that we have on the nuclear charge distribution, it can reasonably be used to delimit somewhat the set of all possible charge distributions. For example, for any assumed *shape* of distribution, the mu-mesonic transition energy can be used as a constraint to yield a radial extent, or *range* of the distribution. Other effects can then be investigated using this limited set of charge distributions.

In the present paper, we generate a set of charge distributions for the Pb nucleus more or less covering the range of reasonable shapes, limited by the requirement that for each the $2P_{3/2}\rightarrow 1S$ transition energy for the mu meson is 6.00 Mev. In order to allow for future corrections to the measured transition energy, to the mu-meson mass, or to the theoretical interpretation, we evaluate the lowest mu-meson levels in fact for each assumed shape at several ranges in the vicinity of the range which yields the transition energy of 6 Mev.

In practice, a two or three parameter family of charge distributions can rather thoroughly cover the field of reasonable possibilities. Hence, the mu-mesonic $2P\rightarrow 1S$ datum (for Pb, say) can reduce the set to a one or two parameter family. Other effects, which also depend on the nuclear charge distribution, but in a different way, can then be considered to delimit the field further and in principle to give a rather complete picture of the charge distribution. Some of these effects, which have received previous theoretical treatment, or which do not require detailed calculations, are considered in the

* On leave from Vanderbilt University, Nashville, Tennessee.

† Joint program of the U. S. Office of Naval Research and the U. S. Atomic Energy Commission.

[1] F. Bitter and H. Feshbach, Phys. Rev. **92**, 837 (1953).

[2] A. L. Schawlow and C. H. Townes, Science **115**, 284 (1952).

[3] J. A. Wheeler, Revs. Modern Phys. **21**, 133 (1949); Phys. Rev. **92**, 812 (1953).

[4] V. L. Fitch and J. Rainwater, Phys. Rev. **92**, 789 (1953).

[5] L. N. Cooper and E. M. Henley, Phys. Rev. **92**, 801 (1953).

succeeding paper.[6] It is shown that in fact in the present state of our knowledge they cast very little additional light on the question of the shape of the charge distribution.

Effects, which at present require exact numerical calculation, are

A. $3D \rightarrow 2P$ and $2S \rightarrow 2P$ mu-mesonic transitions.[3]
B. Very high energy electron scattering.[7-9]

The first of these we consider in the present paper. The second contains in principle a great deal of information and has received considerable attention already.[7-9] The freedom of choice of nuclear radius, however, has led to a great freedom in shapes[10] of charge distributions which can fit the data.[9] A principal utility of the present calculations may be providing a constraint on the radius for each shape of charge distribution and thereby in narrowing the field of shapes which can fit the electron scattering data. Detailed calculations of the electron scattering with the mu-meson-restricted charge distributions are now in progress.

Specifically, the results of the present calculations are values of the binding energy of the negative mu-meson in the lowest four states ($1S$, $2P_{1/2}$, $2P_{3/2}$, $2S$) in the field of the Pb nucleus, for a variety of assumed shapes of the nuclear charge distribution, and for a number of radii (or ranges) for each shape. The mu-mesonic wave functions are also obtained. The energies of the next two states ($3D_{3/2}$, $3D_{5/2}$) are obtained for the exponential distribution by perturbation theory, and are scaled to other shapes and sizes of charge distribution with an accuracy of about 1 kev. The main features of the pattern which emerges are the following: (1) The radius of a uniform charge distribution yielding a $2P_{3/2} \rightarrow 1S$ transition energy of 6.00 Mev is 6.94×10^{-13} cm $= 1.17 \times 10^{-13} A^{1/3}$ cm, in agreement with Fitch and Rainwater[4] and Cooper and Henley.[5] The decay length of an exponential charge distribution yielding the same transition energy is 1.78×10^{-13} cm $= 0.300 \times 10^{-13} A^{1/3}$ cm. (2) The rate of variation of transition energies with nuclear size is very different for different transitions, and is summarized in Table I. (3) The absolute values of the meson binding energies are very insensitive to change of shape of the nuclear charge distribution for fixed $2P_{3/2} \rightarrow 1S$ transition energy. (4) The $3D \rightarrow 2S$ and $2S \rightarrow 2P$ transitions are more sensitive to shape of charge distribution than to nuclear size and could be utilized to advantage to yield an indication of the shape of the nuclear charge distribution. For fixed $2P_{3/2} \rightarrow 1S$ transition energy, the $3D \rightarrow 2P$ energies vary by about 5 percent and the $2S \rightarrow 2P$ energies by about 15 percent between the uniform and exponential charge distributions. (5) The $2P$ doublet splitting is sensitive to nuclear size, and therefore provides an independent check on the nuclear radius (or a way to check for the existence of an anomalous magnetic moment of the muon). For $2P_{3/2} \rightarrow 1S$ energy $= 6.00$ Mev, the fine structure splitting is predicted to be 176 kev for the exponential charge distribution, 186 kev for the uniform charge distribution, and to lie between these figures for all other calculated distributions.

II. QUALITATIVE DESCRIPTION AND ESTIMATED PERTURBATIONS

In a first-order perturbation approximation, in which Dirac wave functions are used, the finite extension of the nucleus raises the mu-mesonic $1S$ state energy above its point-nucleus value by an amount proportional to

$$\langle r^{2\sigma} \rangle_{Av} \equiv \frac{4\pi}{Ze} \int \rho(r) r^{2\sigma+2} dr,$$

where $\rho(r)$ is the nuclear charge density, and

$$\sigma = [1-(\alpha Z)^2]^{1/2},$$

Z being the nuclear charge and $\alpha = 137.038^{-1}$ being the fine structure constant. The $2S$ and higher S-state energies are raised, in proportion to the same integral with successively smaller coefficients. The $2P_{1/2}$ energy is raised, in proportion to the same integral, with coefficient small compared to that for the $2S$ state; the $2P_{3/2}$ energy is unchanged (to first order). Hence, for light nuclei, where the perturbation approximation is valid (and for which $\sigma \cong 1$), all of the properties of the mu-mesonic x-ray spectrum are determined by the value of $\langle r^2 \rangle_{Av}$, the mean square radius integrated over the nuclear charge distribution.[1,3,5]

For heavy nuclei, the effect of the finite size of the nucleus on the mu-mesonic levels is large and exact

TABLE I. Sensitivity of energies to nulcear size. The numbers, a_i, in the table are percent changes in energies for a 1 percent increase in the radial parameter of the charge distribution in the vicinity of the "true" radius; i.e., $a_i = [(\gamma/E)(dE/d\gamma)]_i$.

Energy	Uniform distribution	Exponential distribution
$1S$	−0.514	−0.492
$2S$	−0.297	−0.268
$2P_{1/2}$	−0.158	−0.185
$2P_{3/2}$	−0.112	−0.144
$3D_{3/2}$	−0.006	−0.027
$3D_{5/2}$	−0.002	−0.011
$2P_{1/2} \rightarrow 1S$	−0.81	−0.74
$2P_{3/2} \rightarrow 1S$	−0.82	−0.75
$2S \rightarrow 2P_{1/2}$	+0.25	+0.10
$2S \rightarrow 2P_{3/2}$	+0.54	+0.36
$3D_{3/2} \rightarrow 2P_{3/2}$	−0.21	−0.26
$3D_{3/2} \rightarrow 2P_{3/2}$	−0.21	−0.25
$3D_{5/2} \rightarrow 2P_{1/2}$	−0.29	−0.32
Δ_P	−1.3	−1.3
Δ_D	−0.2	−1.0

[6] K. W. Ford and D. L. Hill, succeeding paper [Phys. Rev. 94, 1630 (1954)].
[7] Hofstadter, Fechter, and McIntyre, Phys. Rev. 92, 978 (1953).
[8] L. I. Schiff, Phys. Rev. 92, 988 (1953).
[9] Yennie, Wilson, and Ravenhall, Phys. Rev. 92, 1325 (1953).
[10] More recent analysis [R. Hofstadter, Phys. Rev. 94, 773 (T) (1954)] gives evidence of a charge distribution not greatly different from uniform.

calculation is required (Part III). The transition energy becomes relatively less sensitive to the extent of the charge distribution. We find for Pb that the shift of the $1S$ state energy from the point nucleus value varies approximately as $\langle r^{0.5}\rangle_{Av}$ rather than $\langle r^{2\sigma}\rangle_{Av}\equiv\langle r^{1.6}\rangle_{Av}$.

Possible uncertainties in the theoretical interpretation of the transition energies, most of which have already been considered by others, are here summarized, with comments. Quantitative estimates of the effects of these various perturbations on the calculated energies are summarized in Table III.

(a) *A nonelectromagnetic meson-nucleon interaction.* There is evidence that this interaction has approximately the same strength as the electron-nucleon beta decay interaction.[11] If so, it shifts the energy levels by less than 1 ev and is completely negligible.[5]

(b) *Anomalous magnetic moment of mu meson.* The electrodynamic contribution to the anomalous moment should have the same small relative value as for the electron ($\alpha/2\pi$), and increase the calculated $2P$ doublet splitting by less than 1 kev, a negligible effect. The nucleonic (pion field) contribution should be even much smaller because of the very small muon-nucleon interaction. If a sizable anomaly exists, however, only the $2P$ fine structure splitting would be appreciably affected.[3] It would of course be of great interest to look for such an effect.

(c) *Vacuum polarization—the Uehling effect.* As pointed out by Cooper and Henley[5] and by Corben,[12] the polarization of the vacuum by electron pairs produces an appreciable shift in the calculated, mu-mesonic energy levels. Because, for the levels calculated, the meson lies well within the distance of an electron Compton wavelength from the nucleus, it is a good approximation to use the limiting form of the vacuum polarization potential given by Schwinger[13] for $r\ll\lambda_e$. For a heavy nucleus this perturbing potential is, to first order in αZ,

$$V_p(r)=(2\alpha/3\pi)V_0(r)[\bar{l}(r)-(5/6)], \qquad (1)$$

where $V_0(r)$ is the unperturbed electrostatic potential

$$V_0(r)=\int|\mathbf{r}-\mathbf{r}'|^{-1}\rho(\mathbf{r}')d(\mathrm{vol}'); \qquad (2)$$

$\bar{l}(r)$ is defined by

$$\bar{l}(r)=\frac{1}{V_0(r)}\int\log\left(\gamma\frac{|\mathbf{r}-\mathbf{r}'|}{\lambda_e}\right)\frac{\rho(\mathbf{r}')}{|\mathbf{r}-\mathbf{r}'|}d(\mathrm{vol}');$$

λ_e is the reduced electron Compton wavelength; and $\gamma=1.781$. The quantity $\bar{l}(r)$ is slowly varying over the region occupied by the mu meson, and we make the simplifying assumption of replacing $\bar{l}(r)$ by a constant.

[11] E. Amaldi and G. Fidecaro, Phys. Rev. **81**, 339 (1951); J. M. Kennedy, Phys. Rev. **87**, 953 (1952).
[12] H. C. Corben, Phys. Rev. **94**, 787(A) (1954).
[13] J. Schwinger, Phys. Rev. **75**, 651 (1949).

TABLE II. Factors in the polarization energy shift, Eq. (4). The coefficient C is equal to an approximate mean value of the quantity $(2\alpha/3\pi)[\bar{l}(r)-5/6]$. The average potential energy, $\langle V_0\rangle$, was calculated for the two distributions with $2P_{3/2}\rightarrow 1S$ energy = 6.00 Mev.

Level	C	Uniform $\langle V_0\rangle$	Exponential $\langle V_0\rangle$
$1S$	0.00404	−15.63 Mev	−15.68 Mev
$2S$	0.00297	−6.27	−6.42
$2P_{1/2}$	0.00356	−9.25	−8.85
$2P_{3/2}$	0.00346	−8.76	−8.41
$3D_{3/2}$	0.002(0)	−4.6	−4.6
$3D_{5/2}$	0.002(0)	−4.3	−4.3

For $r\ll R$ (the nuclear radius), and with the assumption of a uniform charge density, $\bar{l}(r)\cong\log(\lambda_e/\gamma R)+\frac{1}{2}$. For $r\gg R$, $\bar{l}(r)\cong\log(\lambda_e/\gamma r)$. We choose as an appropriate mean value for the $1S$ state, $\bar{l}=\log(\lambda_e/\gamma R)=3.44$, and for the $2S$ and $2P$ states smaller numbers, 2.75 and 3.10, respectively. For the $3D$ states, $\bar{l}$ is taken crudely to be 2.1. Then the energy shift due to the vacuum polarization is

$$\Delta E_p=C\langle V_0\rangle. \qquad (4)$$

Values of the coefficients C and of the mean values of the potentials, $\langle V_0\rangle$, for the exponential and for the uniform distribution, are given in Table II. The energy shifts ΔE_p are included in Table III, and are estimated to be accurate to within 5 percent for the S and P states, 15 percent for the D states [the principal uncertainty arising in the choice of $\bar{l}(r)$]. This error does not include the uncertainty in the magnitude of higher order corrections, which have been ignored. Since αZ is not small compared to 1, higher order radiative effects may be appreciable. They have, however, been assumed negligible in Table III.

(d) *Other radiative effects.* Electrodynamic effects other than vacuum polarization by electrons arise from the coupling of the meson to the radiation field, and are consequently very much smaller in magnitude than the Uehling effect. Since the meson reduced Compton wavelength is substantially smaller than the radii of the meson orbits considered, a crude but presently adequate estimate for the other radiative effects (including the effect of the anomalous moment) can be made by utilizing the same approximations employed for the Lamb shift in hydrogen. One thereby obtains an estimated shift of order 1 kev for the $1S$ state and somewhat less for the $2S$ and $2P$ states.

(e) *Nuclear polarization effect.* The nuclear polarization effect has been estimated crudely by Cooper and Henley[5] for the $1S$ state by using closure over both nuclear and meson states with an average energy denominator of 20 Mev. Their result is $\Delta E=-60$ kev. Laking and Kohn[14] report an estimate of -16 ± 8 kev for the same effect. We have not attempted to improve on these estimates and include in Table III what is

[14] W. Lakin and W. Kohn, Phys. Rev. **94**, 787 (1954).

TABLE III. Summary of perturbations to calculated mu-mesonic energies. Those perturbations are included whose effect is estimated to be greater than 1 kev. Indicated uncertainties are, in all cases, intended to be upper limits to the error, rather than probable errors.

Effect	Estimated energy shifts in kev							
	$1S$	$2S$	$2P_{1/2}$	$2P_{3/2}$	$3D$	$2P\rightarrow 1S$	$2S\rightarrow 2P$	$3D\rightarrow 2P$
1. Vacuum polarization	-63 ± 5	-19 ± 2	-32 ± 3	-30 ± 3	-9 ± 3	$+32\pm8$	$+12\pm5$	$+22\pm5$
2. Other radiative effects	2 ± 2	0 ± 1	-0.6 ± 0.5	0.3 ± 0.5	...	-2 ± 3	0 ± 2	0 ± 1
3. Nuclear polarization	-50 ± 40	-8 ± 8	-7 ± 7	-4 ± 4	...	$+45\pm40$	-5 ± 10	$+5\pm5$
4. Mass of muon	0 ± 25	0 ± 12	0 ± 20	0 ± 20	0 ± 10	0 ± 5	0 ± 8	0 ± 11
5. Discrete charge	0 ± 10	0 ± 2	0 ± 2	0 ± 2	...	0 ± 10	0 ± 2	0 ± 2
Total	-110 ± 85	-27 ± 25	-40 ± 32	-34 ± 30	-9 ± 13	$+75\pm65$	$+7\pm25$	$+27\pm25$

probably a generous estimate for the uncertainty in the effect on the $1S$ state. The $2S$ state is also lowered by the nuclear polarization effect, by a lesser amount. Roughly, the ratio of $2S$ to $1S$ energy shift is equal to the ratio of $2S$ and $1S$ meson densities within the nucleus, or about 1/6. Using the same crude method to estimate the polarization effect on the $2P$ states, we find $\Delta E(2P_{1/2})/\Delta E(1S)\cong 1/7$, $\Delta E(2P_{3/2})/\Delta E(1S)\cong 1/12$, and $\Delta E(3D)$ negligible (less than 1 kev).

(f) *Mass of muon.* In the vicinity of the "true" radius, the calculated energies may be written

$$(E/mc^2)\sim(r_0/\lambda\!\!\!^{-}_{\mu})^a,$$

where m and $\lambda\!\!\!^{-}_{\mu}$ are the mass and reduced Compton wavelength of the muon. For fixed radial constant, therefore,

$$E\sim m^{a+1}.$$

Values of the exponent a for the binding energies and transition energies are given in Table I. The $2P\rightarrow 1S$ transitions are insensitive to meson mass. At somewhat larger radii, $a+1$ is even closer to zero.[4,5] We have chosen $m=207.0m_e$[15] and placed arbitrary limits of error of $\pm 1m_e$ on this value in order to determine the uncertainties given in Table III.

(g) *Nuclear quadrupole moment.* For a zero-spin nucleus, a nuclear deformation changes slightly the effective shape of the nuclear charge distribution,[16] and in particular extends the mean radius fractionally by about $(3/5)\alpha^2$, where α is a deformation parameter defined by

$$R=R_0[1+\alpha P_2(\cos\theta)].$$

For a nucleus with nonzero spin, the center of gravity of the hyperfine structure pattern reacts in the same way to the effective rounding of the edge of the charge distribution and the slight extension of the nucleus. (Wheeler[3] has considered quadrupole hyperfine patterns.) Some nuclei may have values of α as great as 0.25 but a probable upper limit for Pb^{207} is 0.05. Since for Pb the $1S$ energy varies roughly as $R^{-0.5}$, an upper limit for the quadrupole energy shift for the $1S$ state of Pb^{207} is about 5 kev. Pb^{208} is expected to have no quadrupole effect (although the zero point surface vibration will act in the same way to extend[17] slightly the charge distribution).

(h) *Granularity of nuclear charge.* Cooper and Henley[5] estimate the effect of the discrete charge distribution on the $1S$ state of Pb to be less than 10 kev. We have not attempted to improve on this estimate. The effect on the $2S$ and $2P$ levels will be smaller than the $1S$ effect by a factor of 5 to 10.

(i) *Electron shielding.* The number of K electrons within a radius of three nuclear radii is about 0.9×10^{-4}. If the total electron charge in the same volume is generously taken to be ten times this number, the total fractional effect of electrons on the potential seen by the mesons is about 10^{-5}, and may be ignored.

The relevant perturbations are summarized in Table III. We conclude that the $2P\rightarrow 1S$ transition energies can be calculated to within about 65 kev, and the $3D\rightarrow 2P$ and $2S\rightarrow 2P$ transitions to within about 25 kev. Since the $2P_{1/2}$ and $2P_{3/2}$ states are similarly perturbed by most effects, the uncertainty in the determination of the $2P$ doublet splitting is only about 5 kev. As is discussed in Part IV, these uncertainties are small enough that the possibility exists to determine in a certain sense the shape as well as the size of the nuclear charge distribution from the low mu-mesonic transitions alone.

There is strong reason to believe, therefore, that the mu meson is a probe particle sensitive to the extent of the nuclear charge distribution but relatively free of uncertainty in theoretical interpretation of transition energies.[3] As a nucleus to probe, Pb appears ideal, and we have restricted our calculations to this element. It has the greatest spacing of low-lying levels among the heavy nuclei, which serves to minimize the nuclear polarization effect. Its ground-state deformation is small. It has been already investigated with mu mesons[4] and with high energy electrons[7] and its isotope shift has been measured[18] and analyzed.[19] It is an experimentally convenient substance with which to work. It has only the disadvantage of possessing several isotopes. For future precise determinations of the mu-mesonic $2P$ fine structure splitting, for example, Au or separated Pb^{208} would be preferable.

[15] Smith, Birnbaum, and Barkas, Phys. Rev. **91**, 765 (1953).
[16] Wilets, Hill, and Ford, Phys. Rev. **91**, 1488 (1953).
[17] D. L. Hill and J. A. Wheeler, Phys. Rev. **89**, 1102 (1953).
[18] Brix, von Buttlar, Houtermans, and Kopfermann, Z. Physik **133**, 192 (1952); other references there.
[19] P. Brix and H. Kopfermann, Festschr. Akad. Wiss., Göttingen, Math.-Physik Kl. **17** (1951); Phys. Rev. **85**, 1050 (1952).

III. EXACT CALCULATIONS

Dimensionless Formulation

We consider families of charge distributions of the form

$$\rho(r)=\rho_0 f_\lambda(x), \quad x\equiv r/r_0. \tag{5}$$

Here ρ_0 is the central charge density, $f_\lambda(0)=1$; λ represents any number of parameters used to define the shape of the distribution, and r_0, the range parameter, defines the radial extent of the distribution. We define the functionals of f:

$$I_f(x)=\int_0^x f(x)x^2dx; \tag{6}$$

$$J_f(x)=[I_f(\infty)]^{-1}\int_0^x I_f(x)x^{-2}dx. \tag{7}$$

Then the normalizing condition is

$$4\pi r_0^3\rho_0 I_f(\infty)=Ze, \tag{8}$$

and the electrostatic potential is

$$V=-(Ze/r_0)J_f(x). \tag{9}$$

We further define the dimensionless energy $\epsilon=E/mc^2$, where m=mu-meson mass$=207m_e$, and the dimensionless range parameter, $\gamma=r_0/\lambda_\mu$, where $\lambda_\mu=\hbar/mc$ =reduced Compton wavelength of the mu meson. Then the radial equations for the Dirac particle in a central field[20] become

$$\begin{aligned} dG/dx&=-(k/x)G+[\gamma(\epsilon+1)+\alpha ZJ_f(x)]F,\\ dF/dx&=(k/x)F-[\gamma(\epsilon-1)+\alpha ZJ_f(x)]G, \end{aligned} \tag{10}$$

where F/x and G/x are the two components of the wave function and k is the angular quantum number. For the six levels considered, $k=-1(1S$ and $2S)$, $+1(2P_{1/2})$, $-2(2P_{3/2})$, $+2(3D_{3/2})$, and $-3(3D_{5/2})$.

Families of Charge Distributions

In order to cover the landscape of possible charge distributions, we have considered several members of each of four families of distributions.

Family I

$$f_n(x)=(1/n!)\int_x^\infty x^n e^{-x}dx=\sum_{k=0}^{n}\frac{x^k}{k!}e^{-x}, \quad n=0,1,2\cdots. \tag{11}$$

For $n=0$, this is an exponential, for $n=1$, a modified exponential (name used by Schiff[8]). As $n\to\infty$, f approaches a square distribution, but the high-n members of the family are not feasible for calculation.

For this and the succeeding families, the charge normalization integral $I_f(\infty)$ [Eq. (6)] and the dimensionless potential $J_f(x)$ [Eq. (7)] are given in Appendix I.

[20] L. I. Schiff, *Quantum Mechanics* (McGraw-Hill Book Company, New York, 1949), p. 319.

Family II

$$\text{(a)}\quad f_n(x)=\frac{1}{1-\frac{1}{2}e^{-n}}\cdot\begin{cases}1-\frac{1}{2}e^{-n}e^{x}, & x\leqslant n\\ \frac{1}{2}e^{n}e^{-x}, & x\geqslant n\end{cases}, \qquad 0\leqslant n\leqslant 1. \tag{12}$$

As n varies from 0 to 1, f varies from an exponential toward a shape roughly Gaussian in appearance.

$$\text{(b)}\quad f_n(x)=\frac{1}{1-\frac{1}{2}e^{-n}}\cdot\begin{cases}1-\frac{1}{2}e^{-n(1-x)}, & x\leqslant 1\\ \frac{1}{2}e^{-n(x-1)}, & x\geqslant 1\end{cases}, \qquad 1\leqslant n<\infty. \tag{13}$$

As n varies from 1 to infinity, f varies from a shape roughly Gaussian in appearance to a square shape (uniform distribution). Families IIa and IIb form a single connected family (being identical at $n=1$), but are distinguished in order that the range parameter r_0 may have a close relation to the size of the nucleus. For family IIa, the relevant distance is the decay length for $x>n$. For family IIb, the relevant distance is the interval out to the point where the distribution begins to fall exponentially.

Family III

$$f_{ns}(x)=\frac{\sinh sx/sx}{1-\frac{1}{2}e^{-n}}\cdot\begin{cases}1-\frac{1}{2}e^{-n(1-x)}, & x\leqslant 1\\ \frac{1}{2}e^{-n(x-1)}, & x\geqslant 1\end{cases}, \qquad n\geqslant 1,\ n>s. \tag{14}$$

This family is a generalization of family IIb and includes shapes peaked at the edge of the nucleus instead of at the center. It leads to complicated formulas, but is worth examining to discover if previous ideas about a slight depression of central charge density[21–23,16] relative to the outer part of the nucleus must be discarded.

Family IV

This family is made of various separate simple distributions, some of which are special cases of the previous three families.

A. Exponential: $f=e^{-x}$, (15)

B. Modified exponential: $f=(1+x)e^{-x}$, (16)

C. Gaussian: $f=\exp(-x^2)$, (17)

D. Modified Gaussian: $f=(1+x^2)\exp(-x^2)$, (18)

E. Square: $f=1, x<1; f=0, x>1$. (19)

Another distribution of interest for Pb is that derived theoretically by Gombas[24] from a statistical treatment:

$$f_G=(1+0.15x^2)^3\exp(-x^2). \tag{20}$$

[21] E. Wigner, Bicentennial Symposium, University of Pennsylvania, 1940 (unpublished).
[22] E. Feenberg, Phys. Rev. **59**, 593 (1941).
[23] W. J. Swiatecki, Proc. Phys. Soc. (London) **A63**, 1208 (1950).
[24] P. Gombas, Acta Phys. Acad. Sci. Hung. **1**, 329 (1952) and **2**, 223 (1952).

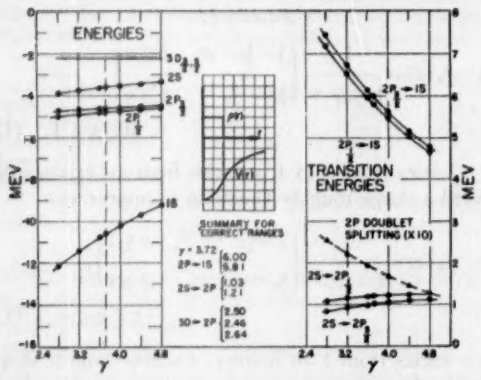

FIG. 1. Binding energies, transition energies, and $2P$ doublet splitting for the uniform charge distribution. Energies are given in Mev, assuming a meson mass of $207.0m_e$, and are plotted *vs* γ, the nuclear radius in units of the meson reduced Compton wavelength. The $3D$ levels were calculated by perturbation theory. The vertical dashed lines indicate the radius for which $2P_{3/2}\rightarrow 1S$ energy equals 6.00 Mev.

This distribution is approximately represented by intermediate members of families I and II.

Solution for Energy Levels

With the aid of one of the Los Alamos I.B.M. Type-701 electronic computers, and of its staff,[25] we have solved the radial equations (6) for various charge distributions $f(x)$ and various range parameters γ. For each choice of shape $[f(x)]$ and size (γ), the equations have been solved by successive trials with ϵ, the energy, as the eigenvalue. Some remarks on the numerical procedure are contained in an appendix. The energy values obtained are accurate to about 10^{-4} Mev.

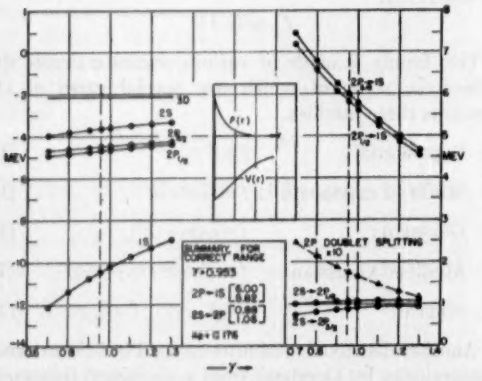

FIG. 2. Binding energies, transition energies, and $2P$ doublet splitting for the exponential charge distribution, plotted in the same way as Fig. 1. Graphs for shapes of charge distribution intermediate between uniform and exponential are qualitatively the same as Figs. 1 and 2.

[25] We express our appreciation, in particular, to Mr. Richard G. Clow and to Mr. John T. Mann for their valuable assistance on several occasions in operation of the computer.

The wave functions and energy values were found for the four lowest states. For each shape, the energy eigenvalues have been found for several ranges such that the experimental $2P_{3/2}\rightarrow 1S$ transition energy of 6 Mev is bracketed, with calculations extending to transition energies 20 percent greater and 20 percent smaller than 6 Mev.

The $3D$ levels have been calculated by perturbation theory, since the finite nucleus effect on these levels is small. The first order energy shifts away from the Dirac point nucleus values were calculated for the exponential charge distribution at the radius giving a $2P_{3/2}\rightarrow 1S$ transition energy of 6.00 Mev. The rate of variation of the energy shift with radius was found at the same point. At this radius, the $3D_{3/2}$ state is shifted by 14.9 kev and the shift varies as $r_0^{3.89}$. The $3D_{5/2}$ state is shifted by 5.7 kev and the shift varies as $r_0^{4.13}$. The energy shifts for the uniform distribution were found by assuming that the shift varies roughly as $\langle r^4\rangle_{Av}$ for different shapes of charge distribution. This crude approximation is adequate because the shifts for the uniform distribution are so small—3 ± 1 kev for the $3D_{3/2}$ state and 1 ± 0.5 kev for the $3D_{5/2}$ state. Although the $3D$ levels are insensitive to the extent of the nuclear charge, the $3D\rightarrow 2P$ transition does probe the nucleus in an important way. The $3D\rightarrow 2P$ transition should be strong. There is doubt whether the $2S\rightarrow 2P$ transition will be observable, due to the small occupation of the $2S$ state.

IV. RESULTS

In Figs. 1 and 2, sample energy level results for Pb are presented graphically. For each assumed shape of charge distribution, the lowest six energy levels are plotted as a function of the range parameter γ. The energies are given in Mev, assuming a mu-meson mass of 207.0 electron masses.[15] Since only E/mc^2 is determined by the solutions, the energies may be readily (but not linearly) scaled for a possible correction to the mu-meson mass. The dimensionless range parameter γ is equal to the range parameter r_0 divided by λ_μ, the reduced Compton wavelength of the mu meson, 1.8665×10^{-13} cm for the assumed mass of $207.0m_e$, and including a reduced mass correction.

The binding energies given in Figs. 1 and 2 and all other exactly calculated energies are presented tabularly in Table IV. The lowest four energies and transition energies are summarized in Table V for fixed $2P_{3/2}\rightarrow 1S$ transition energy. In Table VI are given the $3D$ energies and transitions, subject to the same condition, for the uniform and exponential distributions. The $3D\rightarrow 2P$ transition energies for intermediate shapes may readily be interpolated, since the major variation comes from the P states.

It is of fundamental interest to know whether the $2P$ doublet splitting and the $3D\rightarrow 2P$ and $2S\rightarrow 2P$ energies, taken together with the $2P\rightarrow 1S$ energies, can provide information on the shape of the charge distribution.

TABLE IV. All exactly calculated binding energies. The lines prefaced by arrows have in common a $2P_{3/2}\rightarrow 1S$ transition energy of 6.00 Mev. Families I through IV are defined by Eqs. (5) through (19).

Shape parameter	Range parameter γ	Binding energies in Mev $1S$	$2S$	$2P_{1/2}$	$2P_{3/2}$
		Family I			
$n=0$	0.7000	12.114	3.914	4.913	4.668
	0.8000	11.416	3.790	4.823	4.608
	0.9000	10.802	3.679	4.732	4.543
→	0.9529	10.504	3.624	4.684	4.508
	1.0000	10.257	3.577	4.641	4.475
	1.1000	9.769	3.485	4.552	4.405
	1.2000	9.330	3.399	4.465	4.334
	1.3000	8.932	3.320	4.379	4.263
$n=1$	0.5600	12.117	3.908	4.927	4.680
	0.6400	11.413	3.783	4.838	4.623
	0.7200	10.792	3.669	4.749	4.560
→	0.7577	10.525	3.620	4.706	4.529
	0.8000	10.242	3.567	4.659	4.493
	0.8800	9.749	3.473	4.571	4.424
	0.9600	9.305	3.386	4.484	4.354
	1.0400	8.904	3.306	4.399	4.283
$n=2$	0.4667	12.122	3.905	4.936	4.689
	0.5333	11.412	3.778	4.849	4.633
	0.6000	10.788	3.663	4.761	4.571
→	0.6289	10.539	3.616	4.722	4.545
	0.6667	10.233	3.559	4.672	4.506
	0.7333	9.737	3.465	4.585	4.438
	0.8000	9.290	3.377	4.498	4.368
	0.8667	8.886	3.297	4.413	4.298
$n=3$	0.4000	12.126	3.902	4.944	4.695
	0.4571	11.413	3.774	4.857	4.640
	0.5143	10.785	3.659	4.770	4.580
→	0.5376	10.550	3.615	4.734	4.554
	0.5714	10.228	3.554	4.682	4.515
	0.6286	9.729	3.458	4.595	4.448
	0.6857	9.280	3.371	4.509	4.379
	0.7429	8.874	3.289	4.424	4.309
$n=4$	0.3500	12.130	3.900	4.949	4.699
	0.4000	11.414	3.771	4.863	4.646
	0.4500	10.784	3.655	4.777	4.586
→	0.4695	10.558	3.613	4.743	4.562
	0.5000	10.224	3.550	4.690	4.523
	0.5500	9.724	3.454	4.603	4.456
	0.6000	9.273	3.365	4.517	4.388
	0.6500	8.865	3.284	4.433	4.318
$n=6$	0.2800	12.136	3.898	4.957	4.706
	0.3200	11.417	3.767	4.873	4.654
	0.3600	10.783	3.650	4.787	4.596
→	0.3746	10.570	3.610	4.755	4.574
	0.4000	10.220	3.544	4.701	4.534
	0.4400	9.717	3.447	4.615	4.468
	0.4800	9.264	3.358	4.529	4.400
	0.5200	8.854	3.275	4.445	4.331
$n=\infty$	2.8000*	12.177	3.888	4.991	4.735
	3.2000	11.442	3.752	4.913	4.690
	3.6000	10.793	3.630	4.833	4.639
→	3.7159	10.619	3.596	4.809	4.623
	4.0000	10.217	3.518	4.752	4.583
	4.4000	9.701	3.417	4.670	4.522
	4.8000	9.237	3.323	4.588	4.459
		Family II			
$n=0.5$	0.7200	11.965	3.888	4.895	4.657
	0.9000	10.800	3.678	4.731	4.543
→	0.9536	10.500	3.623	4.683	4.507
	1.0800	9.861	3.502	4.570	4.419
	1.2600	9.085	3.351	4.413	4.291
	1.4400	8.433	3.218	4.263	4.163
	1.6200	7.876	3.100	4.120	4.038
	1.8000	7.394	2.993	3.985	3.916

Shape parameter	Range parameter γ	Binding energies in Mev $1S$	$2S$	$2P_{1/2}$	$2P_{3/2}$
		Family II			
$n=1$	0.6600	12.397	3.963	4.947	4.690
	0.7700	11.592	3.821	4.848	4.626
	0.8800	10.894	3.695	4.747	4.555
→	0.9480	10.507	3.623	4.686	4.510
	0.9900	10.283	3.582	4.648	4.481
	1.1000	9.744	3.479	4.549	4.403
	1.2100	9.263	3.385	4.453	4.325
	1.3200	8.832	3.299	4.359	4.246
$n=2$	1.2000	12.647	4.002	4.983	4.713
	1.4000	11.837	3.859	4.890	4.656
	1.6000	11.133	3.732	4.796	4.593
→	1.7976	10.522	3.620	4.703	4.525
	1.8000	10.515	3.618	4.702	4.525
	2.0000	9.9676	3.515	4.608	4.453
	2.2000	9.4791	3.420	4.516	4.380
	2.4000	9.0401	3.333	4.426	4.305
$n=4$	1.9600	12.499	3.963	4.993	4.726
	2.2400	11.782	3.834	4.915	4.680
→	2.8071	10.568	3.609	4.753	4.572
	3.0801	10.074	3.515	4.675	4.514
	3.3601	9.616	3.426	4.595	4.452
	3.6401	9.200	3.343	4.516	4.389
	3.9201	8.821	3.266	4.438	4.324
$n=10$	2.4500	12.584	3.966	5.024	4.750
	2.8000	11.855	3.833	4.952	4.711
	3.1500	11.209	3.713	4.877	4.665
	3.5000	10.632	3.604	4.801	4.615
→	3.5147	10.609	3.599	4.798	4.613
	3.8500	10.115	3.504	4.725	4.561
	4.2000	9.647	3.412	4.648	4.503
	4.5500	9.223	3.327	4.508	4.377
	4.9000	8.836	3.248	4.495	4.381
$n=\infty$	Same as Family I.				

n	s	γ	$1S$	$2S$	$2P_{1/2}$	$2P_{3/2}$
		Family III				
4	2	1.4400	12.568	3.984	4.980	4.713
		1.6800	11.752	3.840	4.887	4.656
		1.9200	11.044	3.711	4.793	4.5920
	→	2.1144	10.534	3.616	4.716	4.537
		2.1600	10.422	3.594	4.698	4.524
		2.4000	9.872	3.489	4.604	4.452
		2.6400	9.381	3.392	4.512	4.379
		2.8800	8.940	3.304	4.421	4.304
5.3	2	1.9600	12.260	3.918	4.971	4.714
		2.2400	11.539	3.788	4.889	4.665
		2.5200	10.903	3.670	4.806	4.610
	→	2.6791	10.574	3.608	4.759	4.577
		2.8000	10.338	3.563	4.723	4.551
		3.0800	9.831	3.465	4.640	4.488
		3.3600	9.375	3.374	4.557	4.423
		3.6400	8.962	3.291	4.475	4.357
8	1.5	2.4500	12.170	3.892	4.981	4.726
		2.8000	11.439	3.758	4.901	4.679
		3.1500	10.795	3.637	4.819	4.626
	→	3.2628	10.603	3.600	4.792	4.607
		3.5000	10.223	3.527	4.736	4.567
		3.8500	9.711	3.427	4.653	4.506
		4.2000	9.250	3.334	4.570	4.441
		4.5500	8.833	3.249	4.488	4.374

* For uniform distribution ($n=\infty$) $\gamma=R/\lambda c$.

TABLE IV.—*Continued.*

Shape parameter		Range parameter γ	Binding energies in Mev $1S$	$2S$	$2P_{1/2}$	$2P_{3/2}$
			Family III			
8	2	2.4000	12.112	3.882	4.975	4.723
		2.7000	11.467	3.763	4.904	4.681
		3.0000	10.891	3.655	4.832	4.634
	→	3.1614	10.605	3.601	4.793	4.608
		3.3000	10.372	3.556	4.759	4.584
		3.6000	9.903	3.464	4.685	4.530
		3.9000	9.476	3.380	4.612	4.474
		4.2000	9.086	3.301	4.539	4.416
8	3	2.2400	12.065	3.874	4.969	4.719
		2.5600	11.335	3.739	4.887	4.670
		2.8800	10.692	3.617	4.803	4.615
	→	2.9276	10.602	3.600	4.791	4.606
		3.2000	10.120	3.507	4.719	4.555
		3.5200	9.610	3.406	4.634	4.491
		3.8400	9.150	3.314	4.550	4.425
12	1.5	2.4500	12.512	3.951	5.020	4.749
		2.8000	11.780	3.817	4.947	4.709
		3.1500	11.133	3.696	4.872	4.663
	→	3.4616	10.615	3.598	4.804	4.618
		3.5000	10.555	3.586	4.796	4.612
		3.8500	10.037	3.485	4.718	4.557
		4.2000	9.569	3.393	4.641	4.499
		4.5500	9.145	3.307	4.564	4.438
12	1.8	2.4500	12.448	3.939	5.015	4.747
		2.8000	11.715	3.805	4.941	4.706
		3.1500	11.067	3.684	4.865	4.659
	→	3.4200	10.616	3.598	4.805	4.619
		3.5000	10.490	3.573	4.787	4.607
		3.8500	9.972	3.472	4.709	4.551
		4.2000	9.505	3.379	4.631	4.491
		4.5500	9.081	3.293	4.553	4.430
12	2	2.4500	12.402	3.930	5.011	4.745
		2.8000	11.669	3.796	4.936	4.703
		3.1500	11.021	3.674	4.859	4.655
	→	3.3904	10.617	3.597	4.806	4.620
		3.5000	10.443	3.564	4.781	4.603
		3.8500	9.926	3.463	4.702	4.546
		4.2000	9.459	3.370	4.624	4.486
		4.5500	9.036	3.284	4.545	4.424
			Family IV			
		γ	$1S$	$2S$	$2P_{1/2}$	$2P_{3/2}$
Gaussian		1.8200	12.211	3.934	4.967	4.714
		2.0800	11.496	3.807	4.884	4.663
		2.3400	10.865	3.692	4.800	4.607
	→	2.4714	10.573	3.638	4.757	4.576
		2.6000	10.305	3.588	4.716	4.546
		2.8600	9.803	3.493	4.631	4.482
		3.1200	9.351	3.406	4.547	4.415
		3.3800	8.941	3.326	4.465	4.348
Modified Gaussian		1.4700	12.396	3.970	4.995	4.733
		1.6800	11.677	3.841	4.917	4.687
		1.8900	11.041	3.726	4.837	4.635
	→	2.0560	10.588	3.642	4.774	4.591
		2.1000	10.475	3.621	4.757	4.579
		2.3100	9.967	3.525	4.676	4.519
		2.5200	9.509	3.437	4.596	4.457
		2.7300	9.094	3.356	4.515	4.393

TABLE V. Summary of exactly calculated energies at radii chosen to yield $2P_{3/2}\rightarrow 1S$ energy $\cong$6.00 Mev. The indices n and s designate the shape of the charge distribution. The range parameter measures the size. All energies in Mev.

n	s	γ	$1S$	$2S$	$2P_{1/2}$	$2P_{3/2}$	$2P_{3/2}\rightarrow 1S$	$2P_{1/2}\rightarrow 1S$	$2S\rightarrow 2P_{3/2}$	$2S\rightarrow 2P_{1/2}$	ΔP
					Family I						
0		0.9529	10.504	3.623	4.684	4.508	5.997	5.821	0.884	1.060	0.176
1		0.7577	10.525	3.620	4.706	4.529	5.997	5.819	0.909	1.086	0.178
2		0.6289	10.540	3.617	4.722	4.543	5.997	5.818	0.926	1.105	0.179
3		0.5376	10.551	3.615	4.734	4.554	5.997	5.817	0.939	1.119	0.180
4		0.4695	10.559	3.613	4.743	4.562	5.997	5.816	0.949	1.130	0.181
6		0.3746	10.570	3.610	4.755	4.574	5.997	5.815	0.963	1.145	0.182
∞		3.7159	10.620	3.596	4.809	4.623	5.997	5.810	1.027	1.213	0.186
					Family II						
0.5		0.9536	10.500	3.623	4.683	4.507	5.993	5.817	0.884	1.060	0.176
1.0		0.9480	10.507	3.623	4.685	4.509	5.998	5.822	0.886	1.062	0.176
2.0		1.7976	10.522	3.619	4.703	4.525	5.997	5.819	0.906	1.083	0.177
4.0		2.8071	10.568	3.609	4.753	4.572	5.997	5.815	0.962	1.144	0.182
10.0		3.5147	10.609	3.599	4.798	4.613	5.997	5.811	1.013	1.199	0.186
					Family III						
n	s										
4	2	2.1144	10.534	3.615	4.716	4.537	5.997	5.818	0.922	1.101	0.179
5.3	2	2.6791	10.574	3.608	4.759	4.577	5.998	5.815	0.969	1.151	0.182
8	2	3.1614	10.605	3.601	4.792	4.608	5.997	5.813	1.007	1.192	0.185
8	1.5	3.2628	10.603	3.600	4.792	4.607	5.996	5.811	1.007	1.192	0.185
8	3	2.9276	10.602	3.600	4.791	4.606	5.996	5.811	1.006	1.191	0.185
12	1.5	3.4616	10.615	3.598	4.804	4.618	5.997	5.811	1.020	1.206	0.186
12	1.8	3.4200	10.616	3.598	4.805	4.619	5.997	5.811	1.021	1.207	0.186
12	2	3.3904	10.617	3.597	4.806	4.620	5.997	5.811	1.022	1.208	0.186
					Family IV						
Gaussian		2.4714	10.573	3.638	4.758	4.576	5.997	5.816	0.938	1.119	0.181
Modified Gaussian		2.0560	10.588	3.642	4.774	4.591	5.997	5.815	0.949	1.132	0.182

TABLE VI. $3D$ binding energies and transition energies for uniform and exponential distributions, with radii chosen as in Table V. Energies in Mev.

n	$3D_{5/2}$	$3D_{3/2}$	$3D_{5/2}\rightarrow 2P_{3/2}$	$3D_{3/2}\rightarrow 2P_{3/2}$	$3D_{3/2}\rightarrow 2P_{1/2}$	ΔD
0	2.119	2.155	2.389	2.353	2.529	0.036
∞	2.124	2.167	2.499	2.456	2.642	0.034

Figures 3 and 4 present the $3D\rightarrow 2P$ and $2S\rightarrow 2P$ transition energies and the $3D$ and $2P$ doublet splitting as a function of a suitable shape parameter for families I and II, subject to the restriction that the $2P_{3/2}\rightarrow 1S$ transition energy is 6.0 Mev. Future experiments may of course alter the value of the $2P_{3/2}\rightarrow 1S$ energy, in which case interpolation in Table III would be required, but for illustrative purposes, it is adequate to take 6.00 Mev for this transition energy and to investigate to what extent the other transitions among the low states may reveal more about the nuclear charge distribution.

Table III indicates that a calculated $2P_{3/2}\rightarrow 1S$ transition energy of 5.997 Mev corresponds to an observed transition energy of 6.072 ± 0.065 Mev. Conversely, a measured energy of 6.07 Mev corresponds to a calculated energy of 6.00 ± 0.07 Mev, which implies an uncertainty in the determination of the radial constant for any shape of charge distribution of about 1.3 percent. (It is assumed that the uncertainty in the experimental measurement is small compared to the 65 kev theoretical uncertainty.) Table I shows the relative

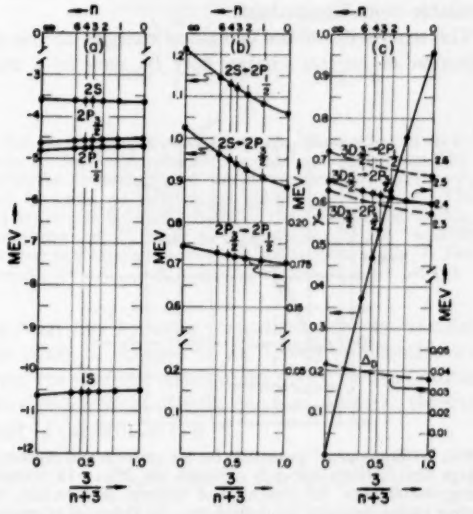

FIG. 3. Energies *vs* shape of charge distribution for family I, limited by the condition $2P_{3/2}\rightarrow 1S$ energy = 6.00 Mev. (a) Binding energies of four lowest states. (b) $2S\rightarrow 2P$ transition energies and $2P$ doublet splitting. (c) $3D\rightarrow 2P$ transition energies, $3D$ doublet splitting, and range parameter γ. The quantities are plotted *vs* an arbitrarily chosen shape parameter, $3/(n+3)$, which runs from 0 (uniform distribution) to 1 (exponential distribution).

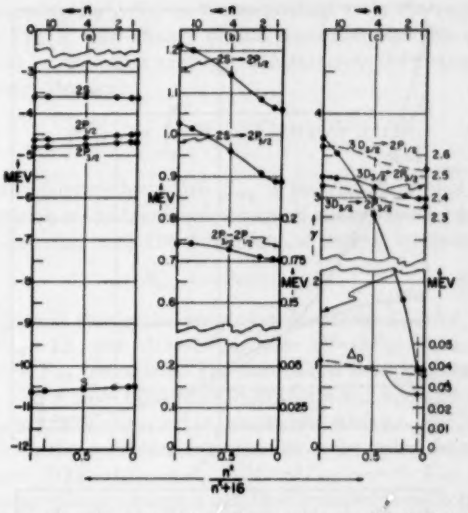

FIG. 4. Energies and radii *vs* shape of charge distribution for family II limited by the condition $2P_{3/2}\rightarrow 1S$ energy = 6.00 Mev. (a) Binding energies of four lowest states. (b) $2S\rightarrow 2P$ transition energies and $2P$ doublet splitting. (c) $3D\rightarrow 2P$ transition energies, $3D$ doublet splitting, and range parameter γ. The quantities are plotted *vs* an arbitrarily chosen shape parameter, $n^3/(n^3+16)$, which runs from 1 (uniform distribution) to 0 (exponential distribution).

sensitivity of the various measurable energies to a change of nuclear radius. For the present example, we assume a distribution intermediate between uniform and exponential. Then the 1.3 percent uncertainty in radius implies uncertainties of about 0.22 percent in the $3D\rightarrow 2P_{3/2}$ transition, 0.60 percent in the $2S\rightarrow 2P_{3/2}$ transition, and 0.26 percent in the $2S\rightarrow 2P_{1/2}$ transition. To these uncertainties must be added the (larger) theoretical uncertainty of about 25 kev from Table III. Finally then, the $3D\rightarrow 2P$ transition energies are pre-

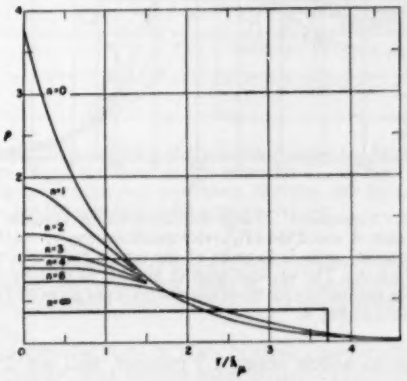

FIG. 5. "Equivalent" charge distributions for family I, for each of which the $2P_{3/2}\rightarrow 1S$ transition energy = 6.00 Mev. The horizontal scale is in units of the meson reduced Compton wavelength, λ_μ. The vertical scale is in number of protons per λ_μ^3. The range parameters for these distributions are given in Table IV and plotted in Fig. 3.

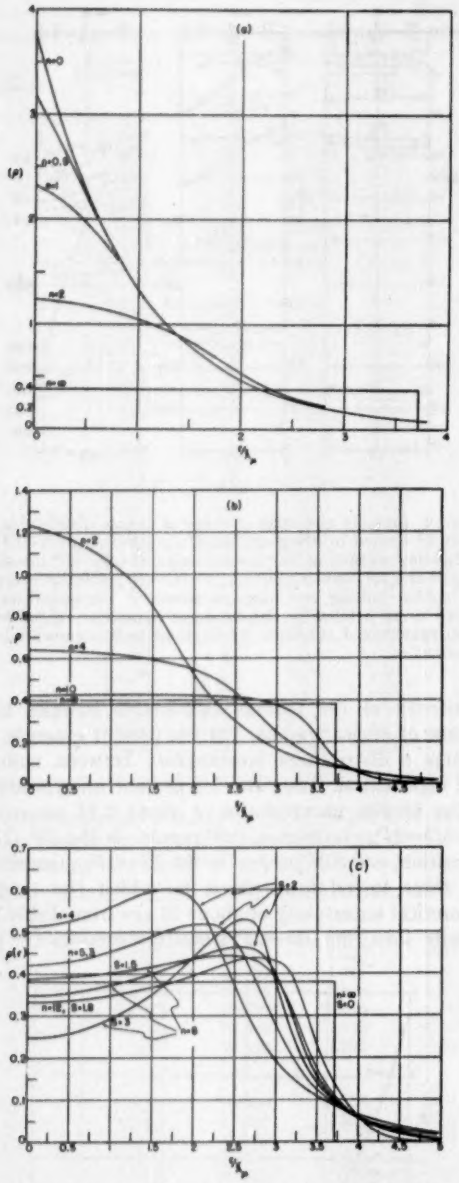

FIG. 6. "Equivalent" charge distributions for families II and III, for each of which the $2P_{3/2}\rightarrow 1S$ transition energy = 6.00 Mev. The horizontal scale is in units of the meson reduced Compton wavelength, $\lambda\!\!\!^{-}_{\mu}$. The vertical scale in number of protons per $\lambda\!\!\!^{-}_{\mu}{}^{3}$. The range parameters for these distributions are given in Table IV and plotted in Fig. 4.

dictable to within about 1.2 percent, and the $2S\rightarrow 2P$ energies to about 3 percent, for any assumed shape of charge distribution from an experimental $2P_{3/2}\rightarrow 1S$ energy measured to within a few tens of kev. The sensitivity of these transition energies to change of shape is considerably greater, however (see Figs. 3 and 4 and Tables V and VI). The change from uniform to exponential changes the $3D\rightarrow 2P$ energies by about 4.5 percent and the $2S\rightarrow 2P$ energies by about 15 percent. It therefore appears that a knowledge of these mesonic transition energies could throw considerable light on the shape of the nuclear charge distribution.

The $2P$ doublet splitting, on the other hand, is sensitive both to the radius and to the shape of the charge distribution. A 1.3 percent uncertainty in the radius introduces about a 1.6 percent uncertainty in the $2P$ doublet splitting, while the change of shape from uniform to exponential alters the $2P$ doublet splitting by about 10 kev or 5.5 percent. The determination of the $2P$ doublet splitting,[26] e.g., via the $3D\rightarrow 2P$ transitions, would be most useful in providing an independent sensitive measurement of the nuclear radius and checking for the possible existence of an anomalous muon magnetic moment. The $3D$ doublet splitting, although small ($\sim$40 kev), is sensitive to the shape of the charge distribution (Fig. 3). Its determination would provide another useful datum on which to base a firm picture of the nuclear charge distribution.

Figures 5 and 6 show the set of equivalent charge distributions for which the $2P_{3/2}\rightarrow 1S$ transition energy is 6.00 Mev. Figure 7 shows the corresponding equivalent potentials for the extreme case of uniform and exponential distributions. Sample normalized wave functions are shown in Fig. 8 for the uniform distribution. The wave functions vary little from one distribution to another, as is illustrated by the differences between uniform and exponential wave functions shown in part (c) of Fig. 8. Additional detailed numerical results are available from the authors.

The sensitivity of the transition energies to the distribution of nuclear charge may be seen in a more

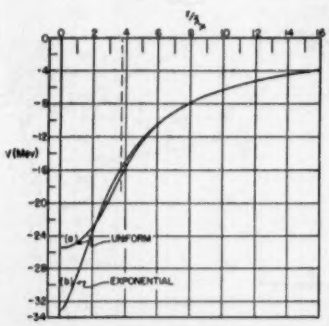

FIG. 7. "Equivalent" potentials for the uniform and exponential charge distributions, for each of which the $2P_{3/2}\rightarrow 1S$ transition energy = 6.00 Mev. (a) Potential of uniform distribution, with nuclear radius indicated by dashed line. (b) Potential of exponential distribution. Vertical scale in Mev, assuming a meson mass of $207.0m_e$. Horizontal scale in units of meson reduced Compton wavelength, $\lambda\!\!\!^{-}_{\mu}$. Corresponding charge distributions given in Figs. 5 and 6.

[26] Preliminary measurements [J. Rainwater, Phys. Rev. **94**, 773(T) (1954)] indicate a $2P$ doublet splitting of 0.18 Mev.

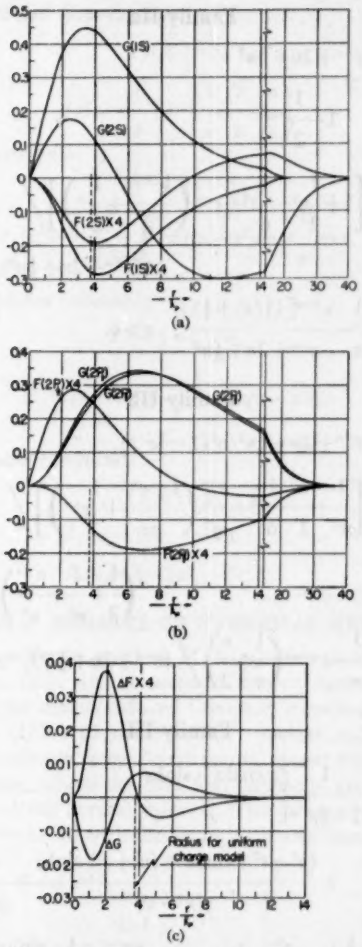

FIG. 8. Normalized wave functions. The horizontal scale is in units of the meson reduced Compton wavelength, $\lambda\!\!\!^{-}_{\mu}$. The normalization is: $(1/\lambda\!\!\!^{-}_{\mu})\int_0^\infty(F^2+G^2)dr=1$. (a) Wave functions for $1S$ and $2S$ states, uniform charge distribution, radius $R=3.716\lambda\!\!\!^{-}_{\mu}$. (b) Wave functions for $2P$ states, same charge distribution. (c) Comparison of $1S$ state wave functions for the "equivalent" uniform and exponential potentials illustrated in Fig. 7. The differences $\Delta F=F_{\text{unif}}-F_{\text{exp}}$ and $\Delta G=G_{\text{unif}}-G_{\text{exp}}$ are plotted.

pictorial way by using perturbation theory to examine the effect of changes in the charge distribution away from the uniform distribution with "correct" radius. If the altered charge distribution is $\rho_{\text{unif}}+\delta\rho(r)$, the energy shift of the mth level is

$$\Delta E_m=+4\pi\int_0^\infty v_m(r)\delta\rho(r)r^2dr, \tag{21}$$

where $v_m(r)$, the effective potential due to mu meson in the mth state (adjusted to zero at the origin), is given by

$$v_m(r)=-4\pi(e/\lambda\!\!\!^{-}_{\mu})\int_0^r y^{-2}dy\int_0^y(F_m^2+G_m^2)dx, \tag{22}$$

assuming $F_m^2+G_m^2$ to be normalized as in the caption of Fig. 8. The change of the transition energies may then be expressed as single integrals over the change of charge density:

$$\Delta E_{m\to n}=\int_0^\infty S_{mn}(r)[\delta\rho(r)/Ze]4\pi r^2dr. \tag{23}$$

The quantity by which S_{mn} is multiplied in this expression is the fractional change of charge at the radius r; and S_{mn}, with the dimensions of energy, is given by

$$S_{mn}=-Ze(v_m-v_n). \tag{24}$$

Figure 9 shows the weighting functions S_{mn} for the $2P_{3/2}-1S$, the $3D\to2P_{3/2}$, the $3D\to2P_{1/2}$, and the $2S\to2P_{3/2}$ transitions. The normalized functions shown in Fig. 8 have been used to evaluate v_{1S}, v_{2S}, and v_{2P}; v_{3D} has been neglected in comparison with v_{2P}. For light nuclei, the weighting functions have the radial dependence: $S(2P\to1S)\sim-r^2$, $S(3D\to2P_{3/2})\sim-r^4$. For Pb, the peripheral charge is weighted relatively less in relation to the central charge than for light nuclei.

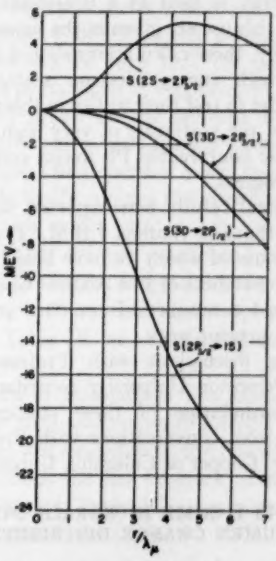

FIG. 9. The sensitivity of transition energies to distribution of nuclear charge is defined by the functions S_{mn} of Eqs. (22)–(24) and plotted here for four transitions. Entering into the calculation of S_{mn} are the expressions for μ-meson density

$$P_m(r)=4\pi(F_m^2+G_m^2).$$

When the normalized exact solutions for uniform nuclear charge were fitted to polynomials valid in the neighborhood of the nucleus, the results were, in terms of the dimensionless distance $\xi=r/\lambda\!\!\!^{-}_{\mu}$,

$$10^2P(1S)=140.71\xi^2+10.21\xi^3-24.91\xi^4+5.20\xi^5-0.32\xi^6,$$
$$10^2P(2P_{1/2})=6.565\xi^2+1.194\xi^3+3.657\xi^4-1.138\xi^5+0.086\xi^6,$$
$$10^2P(2P_{3/2})=3.423\xi^4+0.243\xi^5-0.537\xi^6+0.108\xi^7-0.007\xi^8,$$
$$10^2P(2S)=72.34\xi^2+3.12\xi^3-16.60\xi^4+3.97\xi^5-0.27\xi^6.$$

Inspection of Fig. 8 indicates that the above plotted sensitivities would not markedly change if derived for nuclear charge distributions other than uniform.

V. CONCLUSION

For light elements, the mu-mesonic transition energies determine only $\langle r^2\rangle_{Av}$ the average value of r^2 over the nuclear charge distribution.[5] This is the same quantity that is determined at low Z by most other effects sensitive to the extent of the nuclear charge distribution.

For heavy elements, the mu-mesonic spectrum is dependent upon the shape as well as the extent of the nuclear charge distribution. The present calculations for Pb serve two functions. (1) They provide predictions of the mu-meson spectrum for various charge distributions which may be compared with future, more precise, experiments on the mu-mesonic transition energies. The calculations, combined with other considerations on perturbations and uncertainties in the interpretation, indicate that the mu-mesonic transitions alone can provide a reasonable idea of the shape as well as the size of the nuclear charge distribution. (2) They limit the set of possible charge distributions which may be applied to the interpretation of other nuclear charge-sensitive experiments, if the value of the $2P\rightarrow 1S$ transition energy is used as a constraint. Some considerations of this use are given in the succeeding paper. More especially, these calculations should help in interpreting the high energy electron scattering experiments.[7] In order to test their utility in this regard, exact calculations of the scattering of very high energy electrons from the conceivable Pb nuclei considered here are now in progress.

The numerical results here reported were obtained with one of the Los Alamos I.B.M. Type 701 computers, in the use of which we have benefited from the experience of members of Los Alamos Group T-1, who have developed a number of standard programs employed in the present work.

Stimulating discussions with Professor John A. Wheeler of Princeton University contributed much to the initial formulation of these studies. We have profited also from conversations with Professor Rainwater and Dr. Cooper of Columbia University.

APPENDIX I. SOME INTEGRALS OVER THE ASSUMED CHARGE DISTRIBUTION

The normalization integral $I_f(\infty)$, defined by Eq. (6), and the dimensionless potential function $J_f(x)$, defined by Eq. (7), are here given for the various charge distribution functions, $f(x)$, defined in Part III.

Family I

$$I_f(\infty)=\tfrac{1}{3}(n+1)(n+2)(n+3),$$

$$J_f(x)=\frac{1}{x}-(1-e^{-x})-e^{-x}\sum_{k=0}^{n} b_k\frac{x^k}{k!},$$

where

$$b_k=\frac{n+1}{n+2}-\frac{k}{k+1}-\frac{\tfrac{1}{2}n(n+1)-\tfrac{1}{2}(k-1)k}{(n+1)(n+2)(n+3)}.$$

Family IIa

$$I_f(\infty)=\frac{e^{-n}+2n+\tfrac{1}{3}n^3}{1-\frac{1}{2}e^{-n}};$$

$$J_f(x)=\left[1+\frac{1}{2}n^2-\frac{1}{6}x^2+e^{-n}\left(\frac{1-e^{x}}{x}+\frac{1}{2}e^{x}\right)\right]\Big/ \times(e^{-n}+2n+\tfrac{1}{3}n^3),\quad x<n;$$

$$J_f(x)=\frac{1}{x}-\frac{e^{n-x}[(1/x)+\frac{1}{2})]}{e^{-n}+2n+\frac{1}{3}n^2},\quad x>n.$$

Family IIb

$$I_f(\infty)=e^{-n}+2n+\tfrac{1}{3}n^3/n^3(1-\tfrac{1}{2}e^{-n}),$$

$$J_f(x)=\left[\frac{1}{n^2}+\frac{1}{2}-\frac{1}{6}x^2+\frac{e^{-n}}{n^2}\left(\frac{1-e^{nx}}{nx}+\frac{1}{2}e^{nx}\right)\right]\Big/ \left(\frac{1}{3}+\frac{2}{n^2}+\frac{e^{-n}}{n^3}\right),\quad x<1;$$

$$J_f(x)=\frac{1}{x}-e^{n-nx}\left(\frac{1}{x}+\frac{n}{2}\right)\Big/(e^{-n}+2n+\tfrac{1}{3}n^3),\quad x>1.$$

Family III

$$I_f(\infty)=\frac{1}{1-\frac{1}{2}e^{-n}}\left[\frac{s\cosh s-\sinh s}{s^3}+\frac{(n^2-s^2)s\cosh s+(n^2+s^2)\sinh s}{s(n^2-s^2)^2}+\frac{ne^{-n}}{(n^2-s^2)^2}\right],$$

$$J_f(x)=\frac{1}{D}\left\{\frac{n^2}{s^2(n^2-s^2)}\cosh s+\frac{ne^{-n}}{(n^2-s^2)^2}\frac{1}{x}-\frac{\sinh sx}{s^2x}+\frac{e^{-n}}{2s(n^2-s^2)^2}\frac{e^{nx}}{x}[(n^2+s^2)\sinh sx-2ns\cosh sx]\right\},\quad x<1;$$

$$J_f(x)=\frac{1}{x}-\frac{e^{n}}{2(n^2-s^2)^2s}\frac{e^{-nx}}{x}\cdot\frac{1}{D}[2ns\cosh sx+(n^2+s^2)\sinh sx],\quad x>1;$$

where

$$D=(1-\tfrac{1}{2}e^{-n})I_f(\infty).$$

Family IV

A. *Exponential:*

$$I_f(\infty)=2,$$

$$J_f(x)=\frac{1}{x}-e^{-x}\left(\frac{1}{x}+\frac{1}{2}\right).$$

B. *Modified Exponential:*

$$I_f(\infty)=8,$$

$$J_f(x)=\frac{1}{x}-e^{-x}\left[\frac{1}{x}+\frac{5}{8}+\frac{x}{8}\right].$$

C. *Gaussian:*

$$I_f(\infty)=\tfrac{1}{4}\sqrt{\pi},$$

$$J_f(x)=\frac{1}{x}\cdot\frac{2}{\sqrt{\pi}}\int_0^x \exp(-z^2)dz=\frac{1}{x}\operatorname{erf}x.$$

D. *Modified Gaussian:*

$$I_f(\infty)=\tfrac{5}{8}\sqrt{\pi},$$

$$J_f(x)=\frac{1}{x}\operatorname{erf}x-\frac{2}{5\sqrt{\pi}}\exp(-x^2).$$

E. *Square (uniform):*

$$I_f(\infty)=\tfrac{1}{3},$$

$$J_f(x)=1/x, \quad x>1,$$

$$J_f(x)=\tfrac{3}{2}-\tfrac{1}{2}x^2, \quad x<1.$$

APPENDIX II. REMARKS ON NUMERICAL METHOD

A Runge-Kutta method of integration is used to solve Eqs. (10), with a constant interval size of two-tenths of the meson reduced Compton wavelength, $\lambda\!\!\!^{-}_{\mu}$, or about (1/19) of the "correct" nuclear radius, as defined for the uniform charge model, except very close to the origin, where the first four intervals are $\frac{1}{16}$, $\frac{1}{8}$, $\frac{1}{4}$, and $\frac{1}{2}$ of the normal interval. The integrations are begun at $r=\lambda\!\!\!^{-}_{\mu}/80$ with the asymptotic solutions of Eq. (10):

$$\left.\begin{aligned} G&=Ax^{k+1},\\ F&=\frac{2k+1}{\gamma(1+\epsilon)+\alpha ZJ_f(0)}Ax^k,\end{aligned}\right\} \qquad k>0;$$

$$\left.\begin{aligned} G&=Bx^{-k},\\ F&=-\frac{\alpha ZJ_f(0)+\gamma(\epsilon-1)}{-2k+1}Bx^{-k+1},\end{aligned}\right\} \qquad k<0.$$

Here A and B are arbitrary constants. Each trial solution is extended to whatever radius is required to determine whether the trial eigenvalue is too high or too low. If the initial values of G are taken positive for the $1S$ and $2P$ states and negative for the $2S$ state, common criteria for high or low ϵ may be applied to all four states: (a) if G exceeds a previously chosen large number, $G_{\max}$, or if dG/dr passes from negative to positive while $G>0$, then ϵ is too small (binding energy too large); (b) if G passes from positive to negative, then ϵ is too large. The initial trial binding energy for the $1S$ state was one-half of the central potential. The initial trial binding energy for the $2S$ and $2P$ states was one-half of the binding energy of the $1S$ state. Trial solutions were repeated for each assumed size and shape until the apparent eigenvalues had converged to one part in $2^{17}\cong 1.2\times 10^5$. Some experimentation with interval size indicated that for the interval above described the accuracy of the eigenvalues was also one part in 10^5.

For each shape of charge distribution, a number of values of the range parameter γ were used which led to $2P_{3/2}\rightarrow 1S$ energies of 6.00 Mev$\pm$20 percent. The initial value of γ was chosen such that the distribution in question had a mean value of r^3 approximately equal to that previously found for the uniform distribution.[4,5] Succeeding values of γ were chosen automatically by the machine, and a final value of γ was chosen by interpolating parabolically among the previous values for that range which would yield a $2P_{3/2}\rightarrow 1S$ energy of 6.00 Mev. The final energies calculated with this interpolated γ and the earlier interpolated energies agreed to about 1 kev, so that parabolic interpolation among the values of Table IV may be carried out with high accuracy.

The sequence of calculations was made automatic throughout the sizes and shapes of interest within each family. Listings are available of the potentials, and of the wave functions for the "correct" range, of each shape. Each line of Table IV represents about five minutes of automatic calculation.

Nonuniform Nuclear Charge Distributions and Measurements of Nuclear Electrical Radius*

KENNETH W. FORD, *Indiana University, Bloomington, Indiana*

AND

DAVID L. HILL,† *University of California, Los Alamos Scientific Laboratory, Los Alamos, New Mexico*

(Received March 8, 1954)

The dependence of three long wavelength electronic effects and of the nuclear Coulomb energy on the size and shape of the electrical charge distribution in heavy nuclei is examined. We note that the x-ray fine structure effect and the isotope shift effect measure the volume integral of $r^{2\sigma}$ weighted by the nuclear charge density. $[\sigma=\{1-(\alpha Z)^2\}^{\frac{1}{2}}]$. An earlier result of Feshbach—that medium-energy electron scattering measures the similarly weighted mean value of r^2—is derived more simply. For these electronic effects, therefore, exact calculations for one shape of charge distribution may easily be scaled to other shapes. The nuclear Coulomb energy has no such simple dependence, but measures very roughly the weighted mean value of $r^{0.8}$—nearly the same quantity as measured by the $2P\rightarrow 1S$ mu-mesonic transition in heavy nuclei.

The nuclear Coulomb energy sheds no light on the shape of the nuclear charge distribution because of its inherent insensitivity to change of shape. The x-ray fine structure, and the atomic isotope shift, cannot give detailed information about the nuclear charge distribution because of uncertainty in the magnitude of radiative corrections, and of nuclear compressibility, respectively. Medium-energy electron scattering results, coupled with mu-mesonic x-ray results, will in principle be able to delineate shapes. Present evidence from this source suggests a charge distribution nearly uniform or somewhat peaked toward the edge of the nucleus.

I. INTRODUCTION

IN the preceding paper[1] a set of conceivable charge distributions for the Pb nucleus was derived, limited by the requirement that for each the mu-mesonic $2P_{3/2}\rightarrow 1S$ transition energy has the observed value of 6.0 Mev.[2] In the present paper this set of charge distributions is used to calculate the contribution of the finite extent of the nuclear charge to the following phenomena:[3]

1. Electronic x-ray fine structure.[4]
2. Atomic isotope shift.[5–7]
3. "Medium" energy (5–40 Mev) electron scattering.[6]
4. Nuclear Coulomb energy.[6,8]

These effects have in common that their dependence on the nuclear charge distribution is rather easily calculable [in contrast to the mu-mesonic bound state energies[1,2,8] and the "high" energy ($\gtrsim$50 Mev) electron scattering[9–11]]. They also have in common, however, that their certainty of theoretical interpretation or their precision of measurement is less than the certainty or precision of the mu-mesonic transition energies.

We therefore adopt the mu-mesonic transition energy ($2P_{3/2}\rightarrow 1S$) as a fixed constant and find the dependence of the other phenomena on the shape of the nuclear charge distribution. The relative results are not at all sensitive to the particular choice of 6.0 Mev for the mu-mesonic transition energy. We discuss qualitatively some effects other than the finite extension of the nucleus which may contribute significantly to these phenomena, but we add no new insight into the detailed quantitative interpretation of these phenomena. It is the limited aim of this paper to demonstrate the dependence of these effects on the shape of the nuclear charge distribution, and to show to what extent a nonuniform charge distribution might explain the apparent discrepancies in values of nuclear radii found from different sources.

It is found that values of nuclear radii deduced from these sources should not differ among themselves by more than about 10 percent. Discrepancies considerably greater than this now exist, and exceed the uncertainties in the experimental data.[12] Only the electron scattering

* Supported in part by the U. S. Office of Naval Research and the U. S. Atomic Energy Commission.

† On leave from Vanderbilt University, Nashville, Tennessee.

[1] D. L. Hill and K. W. Ford, preceding paper, Phys. Rev. **94**, 1617 (1954).

[2] V. L. Fitch and J. Rainwater, Phys. Rev. **92**, 789 (1953).

[3] References 4–8 are to recent theoretical work. References to experimental work and to earlier theoretical work may be found in these papers.

[4] A. L. Schawlow and C. H. Townes, Science **115**, 284 (1952).

[5] W. Humbach, Z. Physik **133**, 589 (1952).

[6] F. Bitter and H. Feshbach, Phys. Rev. **92**, 837 (1953).

[7] Wilets, Hill, and Ford, Phys. Rev. **91**, 1488 (1953).

[8] L. N. Cooper and E. M. Henley, Phys. Rev. **92**, 801 (1953).

[9] Hofstadter, Fechter, and McIntyre, Phys. Rev. **92**, 978 (1953).

[10] L. I. Schiff, Phys. Rev. **92**, 988 (1953).

[11] Yennie, Wilson, and Ravenhall, Phys. Rev. **92**, 1325 (1953).

[12] This conclusion is somewhat at variance with that of Bitter and Feshbach in their recent report (reference 6) on nuclear radii. Since our work overlaps theirs to some extent, we mention here several points of difference. We find that the isotope shift for heavy nuclei depends on a weighted integral of $r^{2\sigma}\approx r^{(\sim 1.6)}$ rather than r^2. Their Fig. 1 consequently overestimates the effect of an altered radius on the isotope shift. Further we conclude that nuclear compressibility is important for isotope shifts and introduces a correction of about 25 ± 15 percent in the derived radius. In spite of the contrary evidence from the x-ray fine structure, we agree with the general conclusion that the weight of evidence favors a nuclear electrical radius substantially smaller than the previously accepted $1.4\text{–}1.5\times 10^{-13}A^{1/3}$ cm.

can be used at present to get an idea of the shape of the nuclear charge distribution.

II. THEORY OF EFFECTS OF EXTENDED NUCLEAR CHARGE

1. Electronic X-Ray Fine Structure

Schawlow and Townes[4] fit the experimental electronic $2p$ fine structure splitting among the heavy elements by adding to the point-nucleus formula of Christy and Keller[13] a correction term for the displacement of the $2p_{1/2}$ level by the finite extent of the nucleus. The $2p_{3/2}$ level is displaced negligibly by comparison. The $2p_{1/2}$ displacement is upward (diminishing the doublet splitting) and arises mainly from the finite value of the small component of the $2p_{1/2}$ wave function at the origin.

Although first-order perturbation theory is inadequate to give the magnitude of the energy shift, the interesting result of a number of exact calculations is that the correct dependence on the size and shape of the nuclear charge distribution is the same as given by the perturbation formula. According to first-order perturbation theory, the energy shift of the $2p_{1/2}$ level may be written:

$$\Delta E_1 = 4\pi \int_0^\infty \rho_N(r) V_e^{(0)}(r) r^2 dr, \tag{1}$$

where $\rho_N(r)$ is the nuclear charge density (assumed spherically symmetric) and $V_e^{(0)}(r)$ is the potential due to the (unperturbed) $p_{1/2}$ electron, normalized to be zero at the origin. The unperturbed electronic charge density is given by

$$\rho_e^{(0)}(r) = -(e/r^2)(F_0^2+G_0^2), \tag{2}$$

where F_0 and G_0 are the small and large components of the point nucleus solution of the radial Dirac equation, with the normalization,

$$4\pi \int_0^\infty (F_0^2+G_0^2) dr = 1. \tag{3}$$

In the vicinity of the nucleus,

$$\rho_e^{(0)}(r) = -A e r^{2\sigma-2}, \tag{4}$$

where A is a normalization constant, and

$$\sigma = [1-(Z/137)^2]^{\frac{1}{2}};$$

and

$$V_e^{(0)}(r) = [4\pi A e/2\sigma(2\sigma+1)] r^{2\sigma}. \tag{5}$$

Then the perturbation energy shift, Eq. (1), takes the form

$$\Delta E_1 = [4\pi Z e^2 A/2\sigma(2\sigma+1)] \langle r^{2\sigma}\rangle_{Av}. \tag{6}$$

Thus the property of the charge distribution determined by experiment is the average value of $r^{2\sigma}$, defined by

$$\langle r^{2\sigma}\rangle_{Av} = (Ze)^{-1} \int_0^\infty r^{2\sigma} \rho_N(r) 4\pi r^2 dr. \tag{7}$$

In spite of the small value of the energy shift, the perturbing potential is large and the modification of the wave function within the nucleus is large. A number of authors[5,14-17] have considered the required modification in the perturbation formulas (1) or (6). Formula (1) is clearly an upper limit to the shift because the electronic charge density $\rho_e^{(0)}(r)$, Eq. (2), is larger everywhere in the nucleus than the true charge density,

$$\rho_e(r) = -(e/r^2)(F^2+G^2). \tag{8}$$

Here F and G are the exact solutions of the Dirac equations in the correctly modified field [also normalized as in (3)]. If the argument is applied in reverse by regarding the modified field as unperturbed, and the point-nucleus field as the perturbed field, then it is similarly clear that replacing $\rho_e^{(0)}(r)$ by $\rho_e(r)$, and $V_e^{(0)}(r)$ by $V_e(r)$, [$\nabla^2 V_e = -4\pi\rho_e$], in Eq. (1), leads to a lower limit on the energy shift. These obvious remarks are inserted in order to make reasonable the nearly exact formula of Broch.[15] Broch's formula is equivalent to the use in Eq. (1) of an effective electronic potential $V_e^B(r)$ satisfying

$$\nabla^2 V_e^B(r) = -4\pi\rho_e^B(r), \tag{9}$$

with

$$\rho_e^B(r) = -(e/r^2)(F_0F+G_0G). \tag{10}$$

Broch's result is in error only by a factor

$$4\pi \int_0^\infty (F_0F+G_0G) dr,$$

which is extremely close to 1 because of the very small fraction of the electronic charge which is within the nucleus.

The correct energy shift due to the finite extent of the nucleus at $Z=82$ is about 0.75 times the shift given by Eq. (6). The significant result of a number of exact calculations, for the present discussion, is that this correction factor is very nearly independent of the shape and size, R, of the nucleus. For potentials within the nucleus as widely different as zero (Broch[15]), $-Ze^2/R$, and $(-Ze^2/R)[(3/2)-\frac{1}{2}(r/R)^2]$ (Crawford and Schawlow[16]), the correction factor varies by only 4 percent. The exact results therefore are well represented by the form of Eq. (6):

$$\Delta E = \varphi(Z)\langle r^{2\sigma}\rangle_{Av}. \tag{11}$$

For any shape and size of nuclear charge distribution,

[13] R. F. Christy and J. M. Keller, Phys. Rev. **61**, 147 (1942).

[14] J. Rosenthal and G. Breit, Phys. Rev. **41**, 459 (1932).

[15] E. K. Broch, Arch. Math. Naturvidenskab. **48**, 25 (1945).

[16] M. F. Crawford and A. L. Schawlow, Phys. Rev. **76**, 1310 (1949).

[17] P. Brix and H. Kopfermann, Festschr. Akad. Wiss. Göttingen, Math.-Phys. Kl. **17** (1951); Phys. Rev. **85**, 1050 (1952).

the energy shift depends on the charge distribution only through the quantity $\langle r^{2\sigma}\rangle_{Av}$ defined by (7). The relation (11) appears to be equally valid for $p_{1/2}$ and $s_{1/2}$ states and is confirmed by recent exact calculations of Humbach[5] and of Schawlow and Townes.[4] Humbach examined distributions ranging from charge concentrated at center of nucleus to charge in a shell at edge of nucleus. His results are in good agreement with the relation (11). For example, at $Z=80$ he finds the shift for a shell of charge to be greater than the shift for uniform charge of the same radius by a factor 1.51. The ratio of $\langle r^{2\sigma}\rangle_{Av}$ for these two distributions is 1.54. For the same two distributions, Schawlow and Townes give the ratio of the $p_{1/2}$ shifts over the range $Z=70$ to 90 to be $11.2/7.32=1.53$. For these distributions, the ratios of $\langle r^{2\sigma}\rangle_{Av}$ are $(1/3)(3+2\sigma)=1.57$ at $Z=70$, 1.54 at $Z=80$, and 1.50 at $Z=90$. For comparison, the ratio of $\langle r^2\rangle_{Av}$ for the distributions is 1.67.

The useful relation (11) can be understood in part by noting that, for any given shape of charge distribution, the true charge density, Eq. (8), at the origin varies approximately as $R^{2\sigma-2}$. Thus the energy shift for the upper and lower limiting perturbation formulas and for the exact formula varies with nuclear size as $R^{2\sigma}$ for any shape of charge distribution. No simple argument has been found, however, to show that indeed the exact shift varies as $\langle r^{2\sigma}\rangle_{Av}$ from one shape to another.

2. Atomic Isotope Shift

The theoretical work referred to in the preceding section was directed mainly toward the explanation of the electronic isotope shift, but was equally applicable to the directly measured $2p_{1/2}$ shift. That part of the isotope shift (presumed to be the major part) arising from the nuclear volume effect is just the difference in the energy shifts (usually of an s electron) between isotopes of the same element. In order to see the dependence of the shift on the nuclear charge distribution, it is adequate to work from Eq. (11). The isotope shift is then

$$\delta\Delta E=\varphi(Z)\delta\langle r^{2\sigma}\rangle_{Av}. \tag{12}$$

If the shape of the charge distribution is the same for both isotopes, that is if

$$\rho_N(r)=\rho_0 f(r/r_0), \tag{13}$$

and if the function $f(x)$ is the same for both isotopes, then (12) becomes

$$\delta\Delta E=\Delta E[2\sigma\delta r_0/r_0]. \tag{14}$$

If, moreover, the nuclear size increases regularly as $A^{1/3}$, then

$$\delta r_0/r_0=\delta A/3A, \tag{15}$$

and

$$\delta\Delta E=(2\sigma/3A)\varphi(Z)\langle r^{2\sigma}\rangle_{Av}, \tag{16}$$

having the same dependence on the nuclear charge distribution as the direct shift ΔE. Equation (16) is incorrect for at least two reasons.[7] Nuclear deformation invalidates the assumption of a constant functional form $f(x)$ for the charge distribution and has a large effect. Nuclear compressibility invalidates the assumption of an $A^{1/3}$ law of radius and may also have a rather large effect. The first can be adequately corrected for and the second, which can be only roughly guessed, should not markedly affect the proportionality of $\delta\Delta E$ to $\langle r^{2\sigma}\rangle_{Av}$. Thus after correction for nuclear deformation, the isotope shift, like the direct shift, is proportional to $\langle r^{2\sigma}\rangle_{Av}$.

3. Medium-Energy Electron Scattering

Feshbach[18] has studied the dependence of "medium" energy electron scattering on the form of the nuclear charge distribution. "Medium" energy is defined by the conditions (a) electron energy$\gg$rest energy and (b) electron wavelength$\gg$nuclear radius, and therefore comprises for heavy nuclei about the range 5 to 40 Mev. Feshbach's results are that in this region only the s-wave phase shift is important in the deviation from Coulomb scattering, and that this phase shift depends only on the mean value of r^2 over the charge distribution, i.e., on

$$\langle r^2\rangle_{Av}=(Ze)^{-1}\int_0^\infty r^2\rho_N(r)4\pi r^2dr. \tag{17}$$

We give here a simpler derivation of the latter result, which makes more evident its limits of validity. The radial Dirac equations in a central field are:

$$\begin{aligned}(dF/d\xi)-(k/\xi)F+(\epsilon-1-U)G=0,\\ (dG/d\xi)+(k/\xi)G-(\epsilon+1-U)F=0,\end{aligned} \tag{18}$$

in which ϵ and U are the total energy and the potential energy in units of mc^2, ξ is the radius in units of $\hbar/mc$, and k, the angular quantum number, is $\pm(j+1/2)$ for $j=l\mp1/2$ (the negative of Feshbach's k). Equations (18) may be reduced to a single integral equation for the ratio F/G: either[19]

$$(F/G)=-\xi^{2k}\int_0^\xi[(\epsilon-1-U)+(\epsilon+1-U)(F/G)^2]\xi^{-2k}d\xi,\quad k<0, \tag{19}$$

or

$$(G/F)=\xi^{-2k}\int_0^\xi[(\epsilon-1-U)(G/F)^2+(\epsilon+1-U)]\xi^{2k}d\xi,\quad k>0. \tag{20}$$

Since the contribution of the kth partial wave to the scattering is determined[20] only by the ratio F/G at

[18] H. Feshbach, Phys. Rev. **84**, 1206 (1951).

[19] Here the upper limit of integration is chosen to be less than the first node of G (for $k<0$), or less than the first node of F (for $k>0$). See the asymptotic expressions in Appendix II of reference 1.

[20] George Parzen, Phys. Rev. **80**, 355 (1950).

some radius $\xi=a$ beyond which the potential is pure Coulomb, it follows that distributions which are equivalent for scattering must have equal values of the integrals

$$\int_0^a (\epsilon-1-U)\left[1+\frac{\epsilon+1-U}{\epsilon-1-U}\left(\frac{F}{G}\right)^2\right]\xi^{-2k}d\xi, \quad k<0; \quad (21)$$

or

$$\int_0^a (\epsilon+1-U)\left[1+\frac{\epsilon-1-U}{\epsilon+1-U}\left(\frac{G}{F}\right)^2\right]\xi^{2k}d\xi, \quad k>0. \quad (22)$$

These exact expressions go over to the equivalent integrals of Feshbach for the $s_{1/2}(k=-1)$ and $p_{1/2}(k=1)$ phase shifts if the second terms in the square brackets are negligible compared to 1. [Two integrations by parts then convert (21) and (22) to (17).] For electron *kinetic* energy within the nucleus great compared to mc^2, $(\epsilon\pm1-U)/(\epsilon\mp1-U)\cong1$; and for electron wavelength great compared to nuclear size, F/G (or G/F)$\ll1$ for $k<0$ (or $k>0$) at all positions in and near the nucleus. For $\epsilon-U=120$ within the nucleus (e.g., 40-Mev electrons on Pb), the second term in square brackets contributes only a few percent to the integrals (21) and (22). So long as only the $|k|=1$ partial waves are important, therefore, it is an excellent approximation to say that the electron scattering measures $\langle r^2\rangle_{Av}$. Higher partial waves of course measure higher moments of the charge distribution. The evident reason that bound state $s_{1/2}$ and $p_{1/2}$ energy shifts measure $\langle r^{2\sigma}\rangle_{Av}$, while $s_{1/2}$ and $p_{1/2}$ electron scattering measure $\langle r^2\rangle_{Av}$, is that the former depends on F^2+G^2, while the latter depends only on the ratio F/G.

It is to be noted that at small angles the electron scattering in the Born approximation also depends only on $\langle r^2\rangle_{Av}$. The Born approximation is proportional to the square of a form factor:[10]

$$F'=(Ze)^{-1}\int_0^\infty \rho_N(r)[\sin qr/qr]4\pi r^2dr, \quad (23)$$

where q is the momentum change of the electron divided by $\hbar$. At small angles (small q), this form factor is given approximately by:

$$F'=1-(1/6)q^2\langle r^2\rangle_{Av}, \quad (24)$$

with $\langle r^2\rangle_{Av}$ defined by (17).

4. Nuclear Coulomb Energy

In the absence of correlations among proton positions in the nucleus, the nuclear Coulomb energy is

$$E_c=[(Z-1)/2Z]\int_0^\infty \rho_N(r)V_N(r)d(\text{vol}), \quad (25)$$

where $V_N(r)$ is the electrostatic potential which satisfies

$$\nabla^2V_N=-4\pi\rho_N, \quad (26)$$

and approaches $-Ze/r$ outside the nucleus at large r. The Coulomb energy depends on the charge distribution in a more complicated way than do the other three effects discussed above. Since the integral on the right of (22) contains the product $\rho_N(r)\rho_N(r')$, the Coulomb energy cannot be expressed in terms of a single integral over the charge distribution. For any given shape of charge distribution, the Coulomb energy varies inversely as the radial extent of the distribution. For different distributions, intermediate in shape between uniform and exponential and having the same Coulomb energy, $\langle r^{0.8}\rangle_{Av}$ is roughly constant.

III. DEPENDENCE ON SHAPE OF CHARGE DISTRIBUTION

A convenient way to discuss the effect of changing the shape of the nuclear charge distribution is in terms of an equivalent radius of a uniform distribution. That is, if different experimental effects are interpreted in terms of a uniform distribution, a radius will be found for each, which we call the equivalent radius, R_{eq}. In case the distribution is in fact uniform, the R_{eq}'s should be the same for all effects and equal to the nuclear radius. Otherwise they will differ.

1. Charge distributions which are equivalent for isotope shift and x-ray fine structure have equal values of $\langle r^{2\sigma}\rangle_{Av}$ [Eq. (7)]. In order to treat the same set of functional forms for the charge distribution as considered in the preceding paper[1] (I), we turn to the dimensionless formulation introduced there. We introduce the new functional of the charge distribution f,

$$K_f(\sigma;x)=\int_0^x f(\xi)\xi^{2\sigma+2}d\xi. \quad (27)$$

Then

$$\langle r^{2\sigma}\rangle_{Av}=r_0^{2\sigma}K_f(\sigma;\infty)/I_f(\infty), \quad (28)$$

where $I_f(\infty)$ is defined by I, (6). For a uniform distribution,

$$\langle r^{2\sigma}\rangle_{Av}=R^{2\sigma}[3/(2\sigma+3)]. \quad (29)$$

Equating (28) and (29), one gets for the equivalent radius relevant to this first set of phenomena,

$$R_{eq}^{(1)}=\left[\frac{2\sigma+3}{3}\cdot\frac{K_f(\sigma;\infty)}{I_f(\infty)}\right]^{1/2\sigma}\cdot r_0. \quad (30)$$

Expressions for $K_f(\sigma;\infty)$ are given in an appendix to this paper, and expressions for $I_f(\infty)$ in an appendix to I.

2. Medium energy electron scattering (5–40 Mev) measures approximately $\langle r^2\rangle_{Av}$. The equivalent radii for charge distributions having equal values of $\langle r^2\rangle_{Av}$ are given by:

$$R_{eq}^{(2)}=\left[\frac{5}{3}\cdot\frac{K_f(1;\infty)}{I_f(\infty)}\right]^{\frac{1}{2}}r_0, \quad (31)$$

which follows immediately from (30).

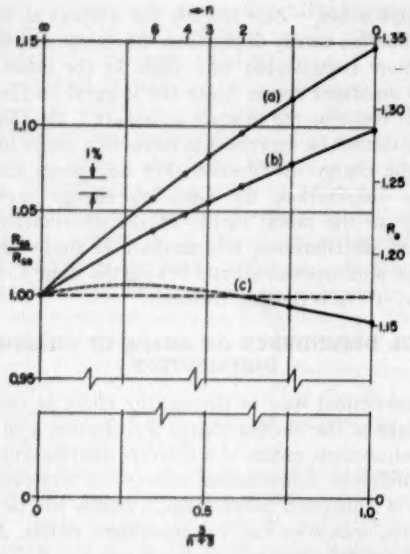

FIG. 1. Equivalent electrical radii of Pb for several nuclear charge-sensitive effects plotted *vs* an arbitrarily chosen shape parameter for family I of charge distributions. The right scale is $R_0=R_{eq}/A^{1/3}$ in units of 10^{-13} cm. (a) Radii determined from medium energy electron scattering. (b) Radii determined from x-ray fine structure effect and isotope shift. (c) Radii determined from nuclear Coulomb energy. Horizontal dashed line gives radii determined from mu-mesonic $2P\rightarrow 1S$ transition, to which the other curves are normalized.

3. For charge distributions possessing the same Coulomb energy, the integral

$$4\pi\int_0^\infty \rho_N(r)V_N(r)r^2dr \tag{32}$$

is constant. We introduce the corresponding dimensionless integral

$$L_f(\infty)=\int_0^\infty f(x)J_f(x)x^2dx. \tag{33}$$

$J_f(x)$ is the dimensionless potential defined by I, (7). Then the Coulomb energy is

$$E_c=\tfrac{1}{2}Z(Z-1)e^2r_0^{-1}[L_f(\infty)/I_f(\infty)]. \tag{34}$$

For a uniform distribution,

$$E_c=(3/5)Z(Z-1)e^2R^{-1}. \tag{35}$$

Therefore the equivalent radius for Coulomb energy is defined by

$$R_{eq}^{(3)}=(6/5)[I_f(\infty)/L_f(\infty)]r_0. \tag{36}$$

Expressions for $L_f(\infty)$ are given in the appendix.

Figures 1 and 2 show these three equivalent radii plotted as a function of a suitable shape parameter for charge distribution families I and II, subject to the condition that the mu-mesonic $2P_{3/2}\rightarrow 1S$ transition energy is a constant, 6.0 Mev. Z is taken to be 82. The left edge of each graph corresponds to the uniform distribution, the right, to the exponential. To make clear the meaning of these curves, we suppose for illustration that the Pb nucleus has an exponential charge distribution. If then the phenomena here considered are all interpreted exactly on the assumption of a uniform distribution, and the calculated radii put in the form $R=R_0A^{1/3}$, one should conclude from the electronic x-ray fine structure and isotope shift[21] that the nucleus has $R_0=1.28\times10^{-13}$ cm; from the mu-mesonic $2P\rightarrow1S$ transition that $R_0=1.17\times10^{-13}$ cm; from the Coulomb energy that $R_0=1.15\times10^{-13}$ cm; and from the medium energy electron scattering that $R_0=1.34\times10^{-13}$ cm. For small changes of the normalizing value 1.17×10^{-13} cm from the mu-meson experiment, the relative position of the curves is not appreciably altered.

The apparent qualitative features of Figs. 1 and 2 are: (a) The Coulomb energy is very insensitive to change of shape of the charge distribution. (b) The equivalent radii deduced from electronic x-ray data, isotope shift, and electron scattering are never smaller than that deduced from mu-mesonic transitions (exception: a distribution both peaked toward the edge of the nucleus and with a very rapid fall-off beyond the peak). (c) Radii deduced in these different ways should not differ by more than about 10 percent for any reasonable shape of charge distribution. The numbers plotted in Figs. 1 and 2 are given in Table I.

IV. COMPARISON WITH EXPERIMENT AND DISCUSSION

1. X-Ray Fine Structure

R_{eq} deduced from x-ray data by Schawlow and Townes[4] is $1.77\times10^{-13}A^{1/3}$ cm, with an assigned prob-

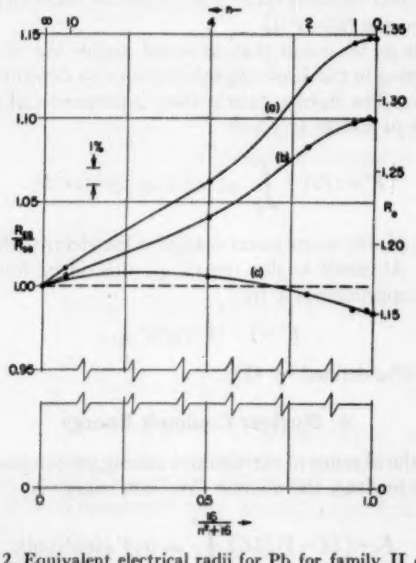

FIG. 2. Equivalent electrical radii for Pb for family II charge distributions. Labelling and significance of curves same as in Fig. 1.

[21] It is assumed for the moment that corrections for radiative effects and nuclear compressibility are known and included.

able error of 15 percent. This figure is to be contrasted with the much lower prediction from Figs. 1 and 2 of $(1.17 \text{ to } 1.29)\times10^{-13}A^{1/3}$. In discussing this and succeeding discrepancies, we retain the idea that the R_0 of 1.17×10^{-13} cm determined by the mu-mesonic experiment is accurate. (We note, however, that the mean R_0 for elements near Pb might be slightly larger than this value because of the closed shell structure and negligible deformation of the Pb^{208} nucleus.) That part of the $2p$ fine structure which is taken to be due to the finite extent of the nucleus is distinguished from the remainder by its greater Z dependence. Hence any large contributing error is to be sought in an effect with similar Z dependence, that is, an effect which depends on the $p_{1/2}$ electron density at the nucleus. One such effect is nuclear polarization. This effect, however, should act in the direction opposite to the finite volume effect and thereby increase the nuclear radius discrepancy. The effect has in any case been estimated to be small.[22] The Lamb shift probably provides the major uncertainty in $p_{1/2}$ energy shift. A part of the radiative correction may be attributed to an anomalous electron magnetic moment, which has been already included by Schawlow and Townes. The remainder of the radiative correction has its source in virtual events occurring within an electron Compton wavelength of the nucleus. This part of the Lamb shift has a Z dependence stronger than the leading term in the fine structure splitting, but weaker than the nuclear volume effect. In the absence of any detailed analysis of the Lamb shift in heavy elements, it is tempting to suspect that this effect may account for the large radius deduced by Schawlow and Townes.[23]

2. Isotope Shift

If one corrects for nuclear deformation,[7] but ignores nuclear compressibility, one may deduce from the comprehensive data of Brix and Kopfermann[17] a "spherically symmetric, incompressible" radius of heavy nuclei given by $0.92\times10^{-13}A^{1/3}$ cm, with a probable error of about 10 percent. This value is smaller than that given in reference 6 because of the assumption used there that isotope shift effect $\sim R^2$. The effect of a finite compressibility is to increase this number. If the nuclear radius varies as $A^{1/3}$ along the line of stable elements, the addition of neutrons only to a nucleus will increase the radius fractionally by[7]

$$\gamma[\delta A/3A], \tag{37}$$

where γ is a number less than 1.0. The equivalent nuclear radius will then be greater than that deduced on the incompressible assumption by a factor $(\gamma)^{-1/2\sigma}$.

[22] Breit, Arfken, and Clendenin, Phys. Rev. **78**, 390 (1950).
[23] The possible significance of the radiative corrections to the $p_{1/2}$ level has also been mentioned by N. M. Kroll, Phys. Rev. **94**, 747(T) (1954) and C. H. Townes, Phys. Rev. **94**, 773(T) (1954).

TABLE I. Equivalent radii for nonuniform charge distributions (near $Z=82$). R = radius of uniform distribution. r_0 = radial constant of distribution yielding same $2P_{3/2}\rightarrow1S$ mu-mesonic transition energy as uniform distribution. $R_{eq}^{(1)}$ = electrical radius determined by experiment which measures $\langle r^{2\sigma}\rangle_{Av}$. $R_{eq}^{(2)}$ = electrical radius determined by experiment which measures $\langle r^2\rangle_{Av}$. $R_{eq}^{(3)}$ = electrical radius determined by nuclear Coulomb energy.

Shape parameter	r_0/R	$R_{eq}^{(1)}/R$	$R_{eq}^{(2)}/R$	$R_{eq}^{(3)}/R$
		Family I		
$n=0$	0.2564	1.099	1.147	0.985
$n=1$	0.2039	1.079	1.117	0.994
$n=2$	0.1693	1.065	1.097	
$n=3$	0.1447	1.055	1.083	
$n=4$	0.1264	1.048	1.072	
$n=6$	0.1008	1.038	1.057	
$n=\infty$	1.0000	1.000	1.000	1.000
		Family II		
$n=0$	same as Family I			
$n=0.5$	0.2567	1.101	1.148	0.986
$n=1.0$	0.2551	1.098	1.145	0.986
$n=2.0$	0.4839	1.083	1.124	0.996
$n=4.0$	0.7554	1.041	1.062	1.006
$n=10.0$	0.9459	1.006	1.011	1.005
$n=\infty$	same as Family I			
		Family IV		
exp.	same as $n=0$			
mod. exp.	same as $n=1$, Family I			
Gaussian	0.6651	1.032	1.052	1.000
mod. Gauss.	0.5533	1.021	1.035	1.003
uniform	same as $n=\infty$			

Values of γ are given in Table III of reference 7. At $Z=80$, Feenberg's estimate[24] of nuclear compressibility ($E_0''=100A\ mc^2$) leads to $\gamma=0.683$, and therefore to an isotope shift equivalent radius of $R_0=1.16\times10^{-13}$ cm. The near agreement with the predicted R_0 (1.17 to 1.29×10^{-13}) is fortuitous. There is an uncertainty of 10 percent from the correction for nuclear deformation, and a change in the compressibility by 50 percent alters the radius by about 15 percent. The isotope shift does not provide at present an accurate way to measure nuclear radii, owing primarily to the uncertainty in nuclear compressibility. To the extent that the heavy element Lamb shift is a function of Z only and independent of the precise distribution of protons in the nucleus, the isotope shift will be unaffected by radiative corrections to the energy levels.

3. Electron Scattering

Bitter and Feshbach[6] analyze the experiments of Lyman *et al.*[25] and quote results of Raka *et al.*[26] on electrical radii deduced from medium energy electron scattering. For several heavy elements, values of R_0 from $(1.03 \text{ to } 1.2)\times10^{-13}$ cm are obtained. These are lower than predicted by the mu-mesonic experiment. According to Figs. 1 and 2, the radius deduced from elec-

[24] E. Feenberg, Revs. Modern Phys. **19**, 239 (1947).
[25] Lyman, Hanson, and Scott, Phys. Rev. **84**, 626 (1951).
[26] Hammer, Raka, and Pidd, Phys. Rev. **90**, 341 (1953).

TABLE II. Summary of radial measurements for Pb. Predicted electrical radii based on $2P_{3/2}\rightarrow 1S$ mu-mesonic transition energy of 6.0 Mev. Uncertainties in predicted and measured values discussed in text.

	$R_0=R_{rms}/A^{\frac{1}{3}}$ (units 10^{-13} cm)			
	Predicted		Measured	
Effect	Uniform	Exponential		Uniform
1. X-ray fine structure	1.17	1.29		1.77
2. Isotope shift	1.17	1.29	no compressibility	0.92
			standard compressibility	1.16
3. Medium energy Electron scattering	1.17	1.34		1.03–1.2
4. Coulomb energy	1.17	1.15		1.23

tron scattering should not be less than $1.17\times10^{-13}A^{1/3}$ cm for distributions with maximum charge density at $r=0$, and could be as large as about $1.3\times10^{-13}A^{1/3}$. The electron scattering results, therefore, although not yet of high accuracy, are suggestive of a charge distribution nearly uniform or even peaked at the edge of the nucleus.

4. Coulomb Energy

Charge distributions for Pb which are equivalent for the mu-mesonic transition are also approximately equivalent for Coulomb energy. In the realm of reasonable shapes, both measure approximately $\langle r^{0.8}\rangle_{Av}$. Proton correlation effects, important at low Z, are probably negligible for heavy elements.[5] But at high Z, there is no direct way to measure Coulomb energy. The balance of Coulomb repulsion vs effective surface tension, as deduced from fission thresholds[27] or collective rotational states of nuclei,[28] provides only a crude value for the Coulomb energy. The best measure of Coulomb energy in heavy elements is the semiempirical mass formula. A new determination of Coulomb energy from this source,[29] translated to equivalent radius by Bitter and Feshbach,[6] gives $R_0=1.23\times10^{-13}$ cm, in rather good agreement with the prediction of $(1.16$ to $1.18)\times10^{-13}$ cm—especially since the latter figure applies to Pb only, for which the mu-meson determined radius is somewhat smaller than the trend from other elements would imply.

The nuclear electrical radius data discussed here are summarized in Table II.

V. CONCLUSION

If one adopts the mu-mesonic $2P_{3/2}\rightarrow1S$ transition energy as an accurate constraint on the nuclear charge distribution, then: (a) the electrical radius deduced from x-ray fine structure is considerably larger than can be explained by a change of shape of the nuclear charge distribution; (b) the electrical radius deduced from atomic isotope shift can be brought into agreement with any reasonable shape of charge distribution, but is uncertain by about 25 percent owing to uncertainty in the magnitude of nuclear compressibility; (c) the electrical radius deduced from medium-energy electron scattering is inconsistent with a strong central peaking of the charge density, and is even suggestive of a peaking at the edge of the nucleus; (d) the electrical radius deduced from Coulomb energy is only a few percent too large. The major uncertainty in the x-ray effect is the radiative corrections. The electronic $2p_{1/2}$ shift may provide a better way of measuring the heavy-element Lamb shift than of measuring the electrical size of the nucleus. Similarly, the isotope shift provides a better way of measuring nuclear compressibility than of measuring nuclear electrical radius. No major uncertainties in the electron scattering effect or in the nuclear Coulomb energy are known, and these two measurements of nuclear electrical radius are not in serious disagreement with the mu-meson determined electrical radius. The Coulomb energy is a check of consistency on the nuclear electrical size, but can cast no additional light on the shape of the charge distribution. A refinement in the scattering effect to a point where the error in the electrical radial determination is less than about 3 percent will make possible a definite conclusion about the shape of the charge distribution or will else reveal a discrepancy in the mu-meson and electron determined electrical radii.

APPENDIX: SOME INTEGRALS

We list here the integrals $K_f(\sigma;\infty)$ and $L_f(\infty)$ defined by Eqs. (27) and (33). The weighted mean value of $r^{2\sigma}$ over the nuclear charge distribution is proportional to K_f; the nuclear Coulomb energy is proportional to L_f. The families of charge distribution considered are defined in I.[1]

Family I

$$K_f(\sigma;\infty)=\Gamma(2\sigma+4+n)/[n!(2\sigma+3)],$$

$$L_f(\infty)=\binom{n+2}{2}-\binom{n+3}{3}^{-1}S,$$

$$S=(n+1)\left(\frac{1}{2}\right)^{2n+2}\binom{2n+7}{n}$$
$$\times[(n+4)F(-n-1,6;n+8;-1)$$
$$-(n+2)F(-n,6;n+8;-1)]+4\binom{n+5}{5}$$
$$-(n+2)\left(\frac{1}{2}\right)^{2n+2}\binom{2n+6}{n}$$
$$\times[(2n+7)F(-n-1,6;n+7;-1)$$
$$-(2n+4)F(-n,6;n+7;-1)].$$

[27] D. L. Hill and J. A. Wheeler, Phys. Rev. **89**, 1102 (1953).
[28] A. Bohr and B. R. Mottelson, Kgl. Danske Videnskab. Selskab, Mat.-fys. Medd. **27**, No. 16 (1953).
[29] A. E. S. Green and N. A. Engler, Phys. Rev. **91**, 40 (1953).

Family IIa ($n \leqslant 1$)

$$K_f(\sigma;\infty)=\frac{\Gamma(2\sigma+3)}{1-\frac{1}{2}e^{-n}}\left[\frac{1}{2}-e^{n}-\sum_{k=0}^{\infty}\frac{n^{2\sigma+5+2k}}{\Gamma(2\sigma+6+2k)}\right],$$

$$L_f(\infty)=\{(2/15)n^5+(2/3)n^3+(5/4)n^2-2n+(21/8)+e^{-n}(n^2-2)-(5/16)e^{-2n}\}/\{(1-\tfrac{1}{2}e^{-n})[e^{-n}+2n+(1/3)n^3]\}.$$

Family IIb ($n \geqslant 1$)

$$[K_f(\sigma;\infty)]_{\mathrm{IIb}}=(1/n^{2\sigma+3})[K_f(\sigma;\infty)]_{\mathrm{IIa}},$$

$$[L_f(\infty)]_{\mathrm{IIb}}=(1/n^2)[L_f(\infty)]_{\mathrm{IIa}}.$$

Family IV

Exponential

$$K_f(\sigma;\infty)=\Gamma(2\sigma+3),\quad L_f(\infty)=\tfrac{5}{8}.$$

Modified Exponential

$$K_f(\sigma;\infty)=(2\sigma+4)\Gamma(2\sigma+3),\quad L_f(\infty)=63/32.$$

Gaussian

$$K_f(\sigma;\infty)=\tfrac{1}{2}\Gamma(\sigma+(3/2)),\quad L_f(\infty)=2^{-3/2}.$$

Modified Gaussian

$$K_f(\sigma;\infty)=\tfrac{1}{2}(\sigma+(5/2))\Gamma(\sigma+(3/2)),\quad L_f(\infty)=(83/80)2^{-1/2}.$$

Uniform

$$K_f(\sigma;\infty)=(1/2\sigma+3),\quad L_f(\infty)=\tfrac{2}{3}.$$

PHYSICAL REVIEW VOLUME 94, NUMBER 6 JUNE 15, 1954

Search for Anomalous Positively Charged Particles from P^{32}*

G. W. McCLURE
Bartol Research Foundation of The Franklin Institute, Swarthmore, Pennsylvania

(Received March 1, 1954)

With a small β-ray spectrometer of unique design, the electrically charged emanations of radioactive P^{32} have been analyzed in an attempt to verify evidence found by others of the emission of positively charged particles in concentrations of the order of 10^{-3} to 10^{-4} per β decay. The ratio of the yield of positively charged particles to that of negatively charged particles in the momentum interval $H\rho=700$ to 2700 gauss cm was found to be less than 8×10^{-6}. This ratio is about 100 times smaller than earlier determinations in the same momentum interval obtained with cloud chambers and small spectrometers, but agrees in order of magnitude with a previous result obtained with an ordinary-sized spectrometer. The hypothesis that the anomalous "positive particles" in question are unstable and detectable only at short distances from the source would account for a low positive-particle yield measured with an ordinary spectrometer but cannot account for the disparity between the present results and those arrived at repeatedly with cloud chambers and other "short path length" detectors. It appears that the previously reported "positive particle" ratios in the range 10^{-3} to 10^{-4} arise from spurious background effects.

INTRODUCTION

WHEN a β emitter is placed in a magnetic cloud chamber there appear among the tracks which ostensibly emanate from the source a certain small fraction which exhibit a sense of curvature characteristic of positively charged particles. Tracks of this nature have been observed in studies of such diverse substances as RaA, RaC, RaE, Th(C+C″), UX, and P^{32}.[1] In some cases[2,3] the positive particle yields (per β decay) from the same substance as determined with different source and chamber geometries have differed by several orders of magnitude, but to the best of our knowledge the lowest yield observed in any cloud chamber study is 10^{-4} "positives" per β decay. In every cloud chamber investigation the "positive" yield has exceeded by at least one order of magnitude that expected from positrons created in the source by electrons (electron pair-production), source bremsstrahlung or nuclear γ rays.

Some investigators have chosen to regard the "positives" as a completely spurious phenomenon attributable to one or more of the following effects: (1) electrons scattered from the walls back to the source, (2) electrons returning to the source after traversing a complete circle partially out of view, (3) electrons emerging from the source and being multiply scattered so as to assume a reversed curvature. Others have examined the spurious effects in more or less detail and have concluded that the "positive" tracks are really produced by positively charged particles—either positrons or some light particle distinct from the positron.

In recent years several cloud-chamber investiga-

* Supported in part by the joint program of the U. S. Office of Naval Research and the U. S. Atomic Energy Commission.

[1] As the present paper concerns only P^{32} and as extensive bibliographies relating to the other substances listed have been given elsewhere (see, e.g., reference 2) we omit references to the latter.

[2] L. Smith and G. Groetzinger, Phys. Rev. **70**, 96 (1946).

[3] G. Groetzinger and F. Ribe, Phys. Rev. **87**, 1003 (1952).

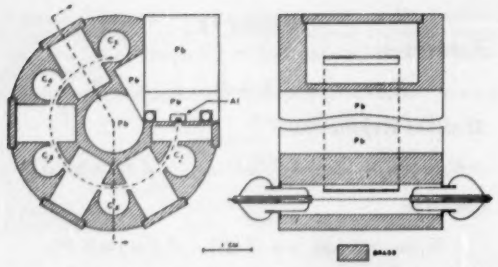

FIG. 1. Cross-sectional diagram of spectrometer showing G-M counters C, source S, and lead absorber Pb.

tions[3–6] of P^{32} (no nuclear γ rays) have given "positive-particle" yields between 10^{-3} and 10^{-4}. Of these studies perhaps the most thorough from the point of view of attention to spurious effects is that of Groetzinger and Ribe.[3] These investigators observed 2.9×10^{-4} positive particles per β decay and felt that the "positives" could not be explained by any of the effects enumerated above. An unsuccessful attempt to detect the particles in question with an ordinary β ray spectrometer[7] (upper limit 1.3×10^{-5} positives per β decay) led Groetzinger and Kahn[8] to suggest that the particles observed in the cloud chamber might be unstable and have so short a half-life that they would be difficult to detect in instruments (such as ordinary spectrometers) with distances greater than a few cm between source and detector. Groetzinger and Kahn[8] and also Yuasa[6] have sought to detect the "positives" with specially built small-sized spectrometers, and have arrived at yields of the same order of magnitude as given by the cloud chambers. The former investigators utilized an unevacuated 180° spectrometer with a 4-cm path length and an emulsion detector and the latter used an evacuated 180° instrument with a 7-cm path length and a G-M counter detector.

This communication describes an attempt to verify the last-mentioned results with a small spectrometer designed with particular care to eliminate some of the background effects which could give rise to an erroneous "positive-particle" indication.

APPARATUS

Two cross-sectional views of the spectrometer are shown in Fig. 1. The instrument is made of a brass cylinder with an internal annular channel. Around the annulus are spaced a series of five G-M counters so arranged that particles which start at the source S and pass completely around the channel traverse the sensitive volume of each counter. The channel has a central radius of curvature of 1.35 cm and a rectangular cross section measuring 0.16 cm by 1.59 cm. The distance along the channel between the source and the last counter C_5 is 6 cm. Rectangular cavities between adjacent pairs of counters serve to break up the continuity of the channel walls and thus reduce the probability that an electron which once impinges upon the wall can completely traverse the channel. The open space formed by the channel and counters is sealed at one end by a permanent plug and at the other end by a Pb block with an "O" ring gasket. The P^{32} source[9] was evaporated into a small $\frac{1}{32}$-in. thick Al boat which nested into the Pb block, exposing the bare source directly to the channel.

The entire instrument was filled with a self-quenching G-M counter gas mixture (90 percent argon, 10 percent butane) at a total pressure of 5 cm Hg. In traversing the 6-cm path length around the channel, a particle encounters no windows of solid material and is required to penetrate only 0.7 mg/cm² of gas.

The lead blocks behind the source and in the center of the spectrometer cylinder partially shield the counters from the source bremsstrahlung so as to minimize the probability of accidental coincidences and reduce the production in C_5 of photoelectrons which might traverse the channel in the backward direction and give spurious positive-particle counts.

The instrument was mounted in a magnetic field variable from 0 to 2000 gauss supplied by an electromagnet with 2.5-in. diameter pole faces spaced 2.5-in. apart. The field was measured by means of a ballistic galvanometer and flip-coil and was essentially uniform over the volume of the spectrometer.

PROCEDURE

The detection of fivefold coincidences between all of the circumferential G-M counters was originally conceived as a method of obtaining good suppression of cosmic-ray background and of insuring that only particles which completely traversed the channel would be counted. While the former objective was satisfactorily met by the original arrangement, there existed a weak tendency for adjacent counters to discharge one another by photoelectric interaction. Measurements of the cross-triggering probabilities between C_3 and C_4, and C_4 and C_5 (about 10^{-2} in each case) implied that an electron which traversed counters C_1, C_2, C_3, and not C_4, C_5 could give rise to a fivefold coincidence with probability of about 10^{-4}. While this effect introduced practically no distortion into the β spectrum, it led to excessive "positive-particle" yields in preliminary experiments.

After several unsuccessful attempts to eliminate the interactions between adjacent counters, it was decided to perform the experiment with twofold coincidences between counters C_3 and C_5 and to use an anticoincidence tray of G-M counters placed directly above the instrument as a means of rejecting cosmic-ray counts. This tray had a solid sensitive area measuring 4 in. by

[4] T. Pi and C. Chao, Phys. Rev. **72**, 639 (1947).
[5] J. Barlow and F. Rogers, Phys. Rev. **74**, 700 (1948).
[6] T. Yuasa, Compt. rend. **234**, 619 (1952).
[7] K. Bainbridge (report on Harwell Conference), Nature **160**, 492 (1947).
[8] G. Groetzinger and D. Kahn, Phys. Rev. **80**, 108 (1950).

[9] PO_4 in weak HCl. Procured from the U. S. Atomic Energy Commission, Isotope Division, Oak Ridge, Tennessee.

8 in. and was centered 3 inches above the central axis of the spectrometer. In this location the tray overlapped considerably the solid angle defined by counters C_3 and C_5, and was very effective in reducing cosmic-ray background.

EXPERIMENTAL RESULTS

The results of principal interest are shown in Fig. 2. Anticoincidence rates measured with the field oriented to favor the detection of β particles from the source are indicated by the $(-)$ curve, and rates with corresponding fields of the opposite polarity are indicated by the $(+)$ curve. The data were obtained over a period of approximately 10 days and were corrected for decay of the P^{32} source during the period. Within the statistical uncertainties the $(+)$ rates are independent of field strength.

The cosmic-ray background anticoincidence rate, measured with the source removed, was approximately 5×10^{-4} min^{-1}, or about one-tenth of the average rate represented by the $(+)$ points. Accidental coincidences and false anticoincidences caused by the "dead-time" of the anticoincidence tray were negligible in all experiments described herein.

Subsidiary experiments were performed to seek a correlation between the recorded $(+)$ rates and the rate at which counter 5 was discharged by P^{32} bremsstrahlung. It was discovered that an additional P^{32} source placed between the two Pb blocks behind the regular source increased the $(+)$ anticoincidence rate in about the same proportion as the bremsstrahlung rate of counter five at several different $(+)$ field-settings above 400 gauss. This suggested that many of the observed $(+)$ counts (at least 50 percent on the basis of rather crude statistics) were caused by bremsstrahlung-produced secondary electrons which were released in counter 5 and traversed the channel in the backward direction to counter 3. Even without correcting the $(+)$ data for this and other possible spurious effects which tend to enlarge the $(+)$ rates, the $(+)$ to $(-)$ ratios in the interval $H\rho=700$ to 2700 gauss cm are considerably smaller than expected from the cloud-chamber results and the prior small-spectrometer data.

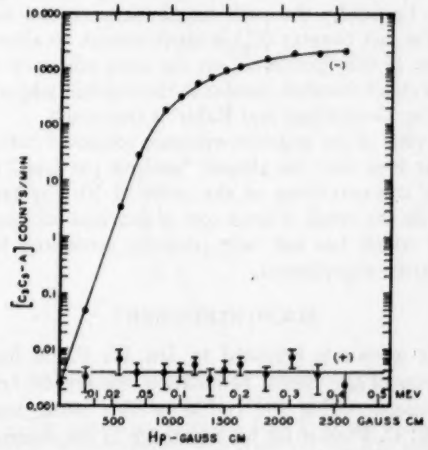

FIG. 2. Measured anticoincidence rates with P^{32} source. The $(-)$ curve was obtained with the magnetic field polarity favoring the passage through the spectrometer of negatively charged particles, and the $(+)$ curve with the opposite field polarity.

TABLE I. Efficiency of counter C_3 vs $H\rho$.

$H\rho$	820	1090	1370	1630	1870	2120	2350	2580
Efficiency of C_3	0.72	0.65	0.57	0.56	0.49	0.45	0.45	0.41

TABLE II. Calculated fraction of β rays removed from the channel by multiple scatterings vs $H\rho$.

$H\rho$	750	1000	1500	2000	2500	3000
Fraction removed	0.92	0.75	0.65	0.52	0.43	0.37

Because of the low pressure of the gas mixture and the short path length of the β rays through the G-M counters, particles which traversed the channel were not counted with 100 percent efficiency. The efficiency of counter C_3 was determined by taking the ratio of the threefold coincidence rate (C_3, C_4, C_5) to the twofold rate (C_4, C_5) at several different $(-)$ field settings. The results of these measurements, given in Table I, are affected only to the extent of about one percent by adjacent-counter interactions.

The variation of the counting efficiency over the $H\rho$ range investigated together with the scattering introduced by the gas and the finite thickness of the source render the $(-)$ curve in Fig. 2 only a crude approximation to the true β spectrum of P^{32}. A rough estimate of the multiple scattering loss as a function of $H\rho$ has been made by calculating the probability that a ray leaving the source with the proper direction and momentum to allow traversal of the center of the channel under the influence of the magnetic field alone will, owing to the presence of the gas, be scattered so as to miss the entrance slit of counter C_5. The results of this calculation, based upon empirical scattering data for argon[10] and a theoretical estimate of the (relatively small) contribution of the butane to the scattering, is shown in Table II.

The measured β spectrum corrected for: (1) the efficiency variation of counters C_3 and C_5 (the efficiency of C_5 is assumed identical to that of C_3 because of the similar geometries of the two counters), (2) the multiple-scattering loss as approximated above, and (3) the linear variation of the $\Delta H\rho$ acceptance interval as a function of $H\rho$ yields the dashed curve shown in Fig. 3. Comparison with the true spectrum of P^{32} as measured by Agnew[11] indicates fairly good agreement above $H\rho=1200$, but considerable departure at low momenta where the scattering calculation is least accurate and

[10] Groetzinger, Berger, and Ribe, Phys. Rev. 77, 584 (1952).
[11] H. Agnew, Phys. Rev. 77, 655 (1950).

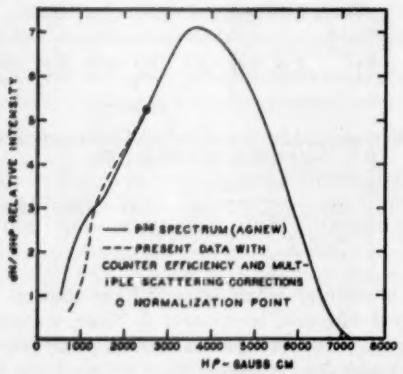
dN/dHρ RELATIVE INTENSITY
P32 SPECTRUM (AGNEW)
PRESENT DATA WITH COUNTER EFFICIENCY AND MULTIPLE SCATTERING CORRECTIONS
NORMALIZATION POINT
Hρ - GAUSS CM

FIG. 3. Comparison of present β spectrum of P^{32} (after corrections noted in text) with the more precise spectrum of Agnew (reference 11).

where the form of the spectrum is most sensitive to the thickness of the source and the nature of the source backing.

DISCUSSION

Since electrons and positrons of the same momentum are scattered similarly (if anything, positrons are somewhat less strongly scattered), the curves of Fig. 2 give directly at each $H\rho$ value an upper limit to the ratio of positrons to electrons emitted from the source. This ratio varies from 1.6×10^{-4} at $H\rho=700$ gauss cm to 2×10^{-6} at $H\rho=2700$ gauss cm.

At $H\rho=1600$ gauss cm the (+) to (−) ratio is 3×10^{-6}, while the corresponding value measured by Groetzinger and Kahn[5] with a small (unevacuated) spectrometer is 8×10^{-4}. For particles with $H\rho>700$ gauss cm, the cloud-chamber data of Groetzinger and Ribe[3] indicate an over-all positive-particle to negative-particle ratio of $\sim2\times10^{-4}$. If one breaks down the "positive-particle" spectrum of the aforementioned authors into momentum-intervals and assumes that the cloud-chamber electron spectrum is the same as that measured with a β-ray spectrograph, it is found that the positive-to-negative ratio in each of the $H\rho$ intervals 700–1400, 1400–2100, and 2100–2800 gauss cm exceeds the corresponding value measured with the present instrument by a factor of about 100. (Most of the "positive" tracks observed in the cloud chamber investigation[3] are included in the $H\rho$ intervals selected for comparison.)

The small spectrograph measurements of Yuasa[6] (250–2500 gauss cm) yield positive-to-negative ratios which are in agreement with the cloud-chamber data of the same author and also in rough agreement with the results of Groetzinger and Ribe.

If one chooses to adopt the point of view that the larger upper limits given by other investigators for the positive-particle yield from P^{32} reflect the presence of a real positively charged particle and not just a spurious effect, one must at the same time endow the particle with properties which might cause it to escape detection in the present instrument. One may propose, for example, that the particle is much more strongly scattered or has a much lower specific ionization than an electron of the same momentum. Although the existing data on multiple-scattering of the cloud chamber "positives"[12] are of somewhat limited statistical accuracy, it seems safe to say that the rms scattering angle of the positives in a given distance is not more than twice that of electrons of the same $H\rho$. If one assumes a factor of 2 for the sake of argument, it can be shown that the "positives" should not be suppressed in their passage through the instrument by more than a factor of 2 over the calculated electron suppression. The multiple scattering effect does not, therefore, seem adequate to explain the discrepancy between the present results and the cloud-chamber results.

The effect of specific ionization upon the detection efficiency of the instrument may be investigated by the use of an experimentally verified theoretical expression for the efficiency of a G-M counter as a function of the average number of primary-ionization events per incident-particle traversal.[13] From this expression, one finds that a specific ionization less than $\frac{1}{4}$ that of an electron of the same $H\rho$ must be attributed to the "positive" particle in question in order that its detection efficiency be suppressed by the amount required to explain the factor of discrepancy with the earlier results. Although there has been no detailed investigation of the ionization of the cloud chamber "positives" relative to electrons, if a ratio as high as 1 to 4 existed, it could hardly have escaped notice, for even electron tracks are quite thin and difficult to photograph clearly.

It is difficult to conceive of any factors other than those discussed above which could prevent the present instrument from detecting the positive particles if they exist. Certainly, the path length between the source and the last counter (C_5) is short enough to allow detection of the "positives" on the same efficiency basis as the cloud chamber, insofar as the instability hypothesized by Groetzinger and Kahn[5] is concerned.

In view of the negative evidence presented here, the author feels that the alleged "positive particles" from P^{32} in concentrations of the order of 10^{-4} or greater must be the result of some sort of spurious background effect which has not been properly accounted for in the earlier experiments.

ACKNOWLEDGMENT

The author is indebted to Dr. W. F. G. Swann, Director of the Bartol Foundation, for several helpful discussions during the course of this work, and to Mr. R. C. Pfeiffer for his assistance in the design and construction of the spectrometer.

[12] G. Groetzinger and F. Ribe, Phys. Rev. **79**, 904 (1950).
[13] See, e.g., G. McClure, Phys. Rev. **90**, 796 (1953).

Gamma Rays from Cu due to Neutron Inelastic Scattering*

L. A. Rayburn, D. L. Lafferty, and T. M. Hahn
Department of Physics, University of Kentucky, Lexington, Kentucky

(Received February 15, 1954)

Monoenergetic neutrons from the $H^2(d,n)He^3$ reaction were used to bombard a Cu scatterer in the form of a ring surrounding a gamma-ray spectrometer. An analysis of the gamma spectrum obtained by subtracting the background counting rate from the counting rate with the Cu scatterer in place yields gamma rays with energies of 0.965, 1.110, 1.67, 1.91, 2.42, and 2.58 Mev.

MONOENERGETIC neutrons from the $H^2(d,n)He^3$ reaction were used to bombard a Cu scatterer in the form of a ring surrounding a gamma-ray spectrometer. The deuterons were accelerated by the University of Kentucky 120-kv accelerator.[1] The gamma rays, resulting from the de-excitation of the Cu nuclei excited by inelastic scattering of the neutrons, were detected in a spectrometer consisting of a NaI(Tl) crystal mounted on a Du Mont 6292 photomultiplier tube. No shielding was used between the neutron source and the NaI crystal. A BF_3 counter was used to monitor the neutron flux.

The pulses from the photomultiplier were analyzed with a single-channel differential pulse-height analyzer. Gamma rays from Na^{22} (0.511 and 1.28 Mev) and Cs^{137} (0.661 Mev) were used to calibrate the spectrometer. The spectrometer had a resolution of 10 percent as measured for the 0.661-Mev gamma from Cs^{137}.

The gamma spectrum obtained by subtracting the background counting rate from the counting rate with the Cu scatterer in place is shown in Fig. 1. The gamma spectrum for the different energy regions is shown in Fig. 2, indicating the longer counting time that was necessary for the higher-energy regions.

As shown in the figures, there are gamma rays with energies of 0.965, 1.110, 1.67, 1.91, and 2.42 Mev, and a probable gamma ray at 2.58 Mev (the photoelectric peak for the 2.58-Mev gamma ray occurs at *A* in Fig. 2, the Compton at *B*, and the pair at *D*). The pair peak of the 1.91-Mev gamma ray and the Compton for the 1.110-Mev gamma ray are obscured by the 0.965-Mev photoelectric peak. The estimated probable error of these energy assignments is two or three percent.

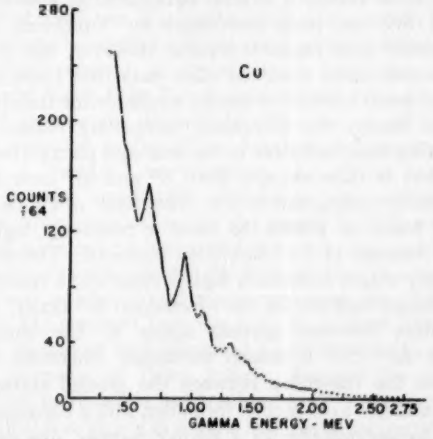

FIG. 1. The gamma-ray spectrum from a Cu scatterer. The ordinate has been normalized with respect to the BF_3 monitor counter.

TABLE I. Comparison of energy assignments. All energies are in Mev.

This paper	Reference 2	Reference 3	Reference 4	Reference 5	Reference 6	Reference 7
0.965	0.960				0.88	
1.110		1.11	1.12	1.1		1.13
1.67			1.49		1.47	1.53
1.91	1.89					
2.42				2.2		2.19
2.58	2.60					

The comparison of these results with those of other investigators[2-7] is shown in Table I.

The energies listed in references 2, 3, and 4 were found by investigation of radioactive decay; those listed in references 5, 6, and 7 are from neutron inelastic scattering.

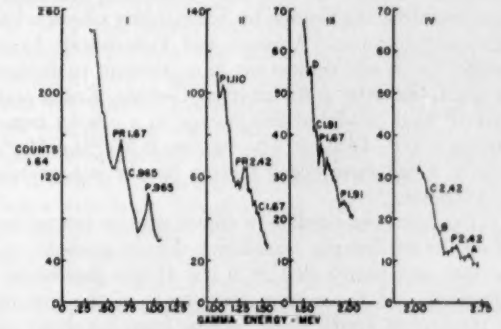

FIG. 2. The gamma-ray spectrum from a Cu scatterer shown in greater detail. The probable errors for region I are of the order of magnitude of the points of the curve. The channel width in region I was 0.022 Mev and in regions II, III, and IV 0.044 Mev. The ordinates have been normalized with respect to the BF_3 monitor counter. *P* refers to photoelectric peak; *C* to Compton edge; *PR* to pair peak. *A*, *B*, and *D* explained in the text.

* Sponsored by the Office of Ordnance Research, U. S. Army.

[1] Lafferty, Biggerstaff, Kern, and Hahn, Phys. Rev. **91**, 223 (1953).

[2] Huber, Medicus, Preiswerk, and Steffen, Helv. Phys. Acta **20**, 495 (1947).

[3] E. N. Jensen and L. J. Laslett, Phys. Rev. **75**, 458 (1949).

[4] K. Siegbahn and A. Ghosh, Phys. Rev. **76**, 307 (1949).

[5] Grace, Beghian, Preston, and Halban, Phys. Rev. **82**, 969 (1951).

[6] Scherrer, Smith, Allison, and Faust, Phys. Rev. **91**, 768 (1953).

[7] Garrett, Hereford, and Sloope, Phys. Rev. **92**, 1507 (1953).

Study of the Isobaric Triplet $Mg^{28}-Al^{28}-Si^{28}$†

RAYMOND K. SHELINE AND NOAH R. JOHNSON, *Chemistry Department, Florida State University, Tallahassee, Florida*

AND

P. R. BELL, R. C. DAVIS, AND F. K. MCGOWAN, *Physics Division, Oak Ridge National Laboratory, Oak Ridge, Tennessee*

(Received January 18, 1954)

The nuclide Mg^{28} has been produced by betatron irradiation and cyclotron bombardments in the following reactions: $Si^{30}(\gamma,2p)Mg^{28}$ and $Mg^{26}(\alpha,2p)Mg^{28}$. It is a 21.3±0.2 hour β^- emitter ($E_{max}=0.418\pm0.01$ Mev, log $ft=4.30$). Mg^{28} decays to Al^{28} with which it is in secular equilibrium. Milking experiments indicate that the Al^{28} daughter has a 2.3-min half-life, and confirm the mass assignment of Mg^{28}. Gamma-ray spectra of the $Mg^{28}-Al^{28}$ secular equilibrium mixture indicate gamma rays of the following energies in Mev (intensities in parentheses): 1.769±0.01 (0.98), 1.346±0.01 (0.70), 0.949±0.01 (0.29), 0.400±0.01 (0.31), 0.0319±0.001 (0.96). The 1.769-Mev gamma results from the decay of Al^{28}. Coincidence measurements show that the 1.346-, the 0.949-, and the 0.400-Mev gammas are each in coincidence with the 0.0319-Mev gamma, and that the 0.949- and 0.400-Mev gammas are in coincidence with each other. Delay coincidence measurements between the 1.346-Mev gamma and the 0.0319-Mev gamma indicate that the half-life of the latter is $<2\times10^{-9}$ sec. This information together with the $\alpha^K_{exp}=0.032\pm0.066$ indicates that the 0.0319-Mev gamma is an $M1$ transition as predicted if the ground-state doublet of Al^{28} is a $j-j$ doublet. A complete decay scheme for the isobaric triplet, $Mg^{28}-Al^{28}-Si^{28}$, is proposed. All spins and parities of ground and excited states are assigned. Assuming a mass of 27.985818±0.000043 amu for Si^{28}, the mass of Al^{28} is 27.990809±0.000045 and the mass of Mg^{28} is 27.992738±0.000047. On the basis of an empirical scheme of nuclear systematics the energy available for decay and the half-lives of the following nuclei are discussed: Si^{32}, Ne^{24}, O^{20}. A test for $j-j$ doublets is proposed. This test indicates that the ground state doublets of Al^{28} and P^{32} are true $j-j$ doublets, whereas the first excited state doublet of Al^{28} is not.

I. INTRODUCTION

Mg^{28} is a recently discovered[1,2] isotope with a considerable tracer usefulness because its half-life is so much longer than any other magnesium activity. Since its discovery a number of other studies of its various nuclear properties have been published. In particular, Marquez[3] has studied the beta spectra for the $Mg^{28}-Al^{28}$ isotopic pair. Both were found to have "allowed" shapes. In addition, Jones and Kohman[4] have produced the isotope by bombarding silicon with high-energy protons. Wapstra and Veenendaal[5] have studied the 31-kev gamma ray in an attempt to deduce its multipole order and character. Iwersen, Koski, and Rasetti[6] have produced this isotope in a pile by bombarding a Mg–Li alloy. The reaction is $Mg^{26}(t,p)Mg^{28}$. Finally, a tentative decay scheme for the isotope has been reported.[7]

It has now been possible to obtain relative intensities for all the gamma-ray transitions, definite evidence on the spin and parity change in the 31-kev gamma-ray transition, and a tentative assignment of the spin of all the excited states of Al^{28} arising from the decay of Mg^{28}. It is the purpose of this paper to report on these new experimental data and to give the details of the previous experimental evidence presented.[1,7]

In a chart of the nuclides, the isotopes Si^{32}, Mg^{28}, Ne^{24}, and O^{20} are an alpha particle apart in a sequence immediately below stable S^{36}. Each of these nuclei has two neutrons in excess of stability. At first glance one might believe, in spite of their even-even character, that these nuclei would be short lived, for they all lie further from the line of stability than the short-lived nuclei with one less neutron, Si^{31}, Mg^{27}, Ne^{23}, and O^{19}.

On the other hand, Suess[8] by an analysis of masses in this region of the chart of nuclides, felt there was a distinct possibility that Si^{32} and perhaps Mg^{28} would prove to be stable. A careful radiochemical search for stable Si^{32} has been performed by Turkevich and Tompkins[9] with negative results. However, one is led to the conclusion from the mass data that there is at most a small amount of energy available for transition in the decay. An additional compelling reason for expecting long half-lives is the spin and parity change expected in these decays. Both S^{32} and Si^{32} have spin and parity assignment of 0+. The decay of P^{32}, on the other hand, is known to have a relatively high ft value because of its l-forbidden character. Therefore, one may expect a similarly high ft value and a considerably longer half-life for the l-forbidden Si^{32} decay. The transition between ground states of the isobaric couple $Al^{28}-Si^{28}$ is second forbidden. Therefore, one expects the transition between the ground states of Mg^{28} and Al^{28} to be second forbidden with a correspondingly longer half-life. In a similar manner, one would expect Ne^{24} to have a forbidden transition to the ground state of Na^{24}. Also O^{20} could beta decay to the ground

† This research was partially supported under a contract between The Florida State University and the U. S. Atomic Energy Commission.

[1] R. K. Sheline and N. R. Johnson, Phys. Rev. **89**, 520 (1953).
[2] M. Lindner, Phys. Rev. **89**, 1150 (1953).
[3] L. Marquez, Phys. Rev. **90**, 330 (1953).
[4] J. W. Jones and T. P. Kohman, Phys. Rev. **90**, 495 (1953).
[5] A. H. Wapstra and A. L. Veenendaal, Phys. Rev. **91**, 426 (1953).
[6] Iwersen, Koski, and Rasetti, Phys. Rev. **91**, 1229 (1953).
[7] R. K. Sheline and N. R. Johnson, Phys. Rev. **90**, 325 (1953).
[8] H. Suess (private communication).
[9] A. Turkevich and A. Tompkins, Phys. Rev. **90**, 247 (1953).

state of F^{20} only by an *l*-forbidden transition. On the basis of these considerations, an attempt to produce one or more of these isotopes through cyclotron and betatron bombardments seemed justified. The logical choice to produce an activity long enough lived to be observed after the bombarded sample was air mailed hundreds of miles seemed to lie between Mg^{28} and Si^{32}. It was felt that Si^{32} lay so close to the line of stability that it might be extremely long lived and therefore difficult to observe. Accordingly we decide to look first for Mg^{28}. A betatron bombardment of ordinary elemental silicon was attempted with the University of Chicago betatron. First experiments were done with detecting equipment at the site of the betatron in an attempt to observe a possible short-lived activity. These results were negative, and therefore bombardments of longer duration were attempted both with the betatron at the University of Chicago and with the cyclotron of the University of California.

II. BOMBARDMENTS, CHEMICAL SEPARATION PROCEDURES, AND HALF-LIFE

In order to look for a very short-lived activity for Mg^{28}, a sample of elemental silicon in granular form was counted in place immediately after turning off the betatron beam. This sample in cylindrical form was mounted directly in the beam of the betatron in such a way that the axis of the cylinder was the axis of the beam. A Geiger tube shielded with 6 inches of lead was placed parallel to it, and 2 inches from the beam center. The betatron and Geiger tube were controlled by a motor-driven timing switch, and a brush recorder was used to record counts. The entire apparatus has previously been described.[10] In this way it was possible to irradiate samples for 3 seconds and then count them within milliseconds after the beam was turned off for a period of 5 seconds. If a Mg^{28} activity in the region from 0.02 second to several minutes were to be produced in this bombardment, it should have been observed. Only the region from 2 to 9 minutes and the region of 5 to 7 seconds are obscured by other known activities to be expected in the silicon betatron bombardment. Using a "rabbit" to transport the silicon sample quickly after irradiation and using the traditional Geiger tube counting setup, the longer half-life region from 9 minutes to 5 hours was explored. The region of 2.6 hours was obscured by the Si^{31} activity. The results from both of these experiments were negative. Therefore it was assumed that the half-life of Mg^{28} did not fall in the region 0.02 second to 5 hours, with the possible exception of those regions obscured by other activities produced in the bombardment.

With this evidence in mind a long betatron bombardment of silicon was undertaken. The expected nuclear reaction was $Si^{30}(\gamma,2p)Mg^{28}$. A sample of elemental granular silicon containing total impurities of less than 0.01 percent was obtained from the Institute of Metals

[10] R. K. Sheline, Phys. Rev. 87, 557 (1952).

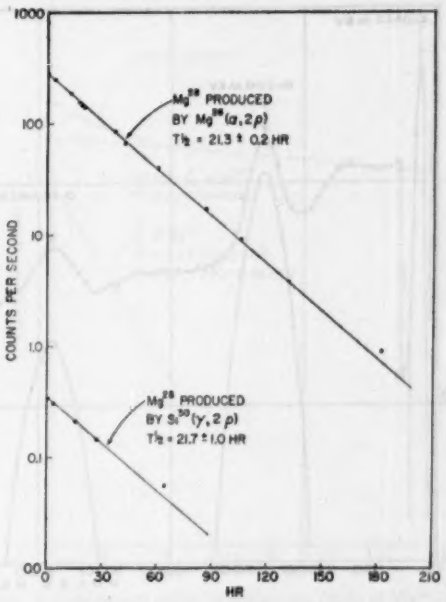

FIG. 1. Mg^{28} half-life determinations from betatron and cyclotron bombardments.

of the University of Chicago. It was irradiated for 8 hours in the gamma spectrum of the 100-Mev University of Chicago betatron. After dissolving the sample in hot concentrated sodium hydroxide, 15 mg of carrier magnesium chloride was added. Neutralization with HCl precipitated silicic acid. The slurry was then evaporated to dryness and warm distilled water added. The SiO_2 was filtered and the filtrate buffered with ammonium chloride and made slightly ammoniacal. The addition of 1 gram of primary ammonium phosphate precipitated magnesium ammonium phosphate. This precipitation was repeated twice to insure high purity. After transferring the precipitate to a planchet and drying, it was counted in a Geiger-Mueller counter. Counts were taken through only 3 half-lives due to the low specific activity. The resulting decay showed a single half-life of 21.7±1.0 hours (Fig. 1).

After this initial success, it seemed advisable to attempt a cross bombardment to confirm the observation of this new activity. The cross bombardment chosen was $Mg^{26}(\alpha,2p)Mg^{28}$.

A disk of magnesium of ordinary isotopic composition 1 and $\frac{5}{16}$ inches in diameter and 0.1 inch thick was bombarded for ten hours in an external beam of 39-Mev alpha particles of the University of California 60-inch cyclotron. The beam covered a one-inch by one-half-inch rectangular area on the disk and penetrated to a depth of ~0.0373 inch. Except for the area of beam penetration, the disk was coated with Krylon plastic spray. By means of a carefully timed procedure, approximately 0.013 inch of the active

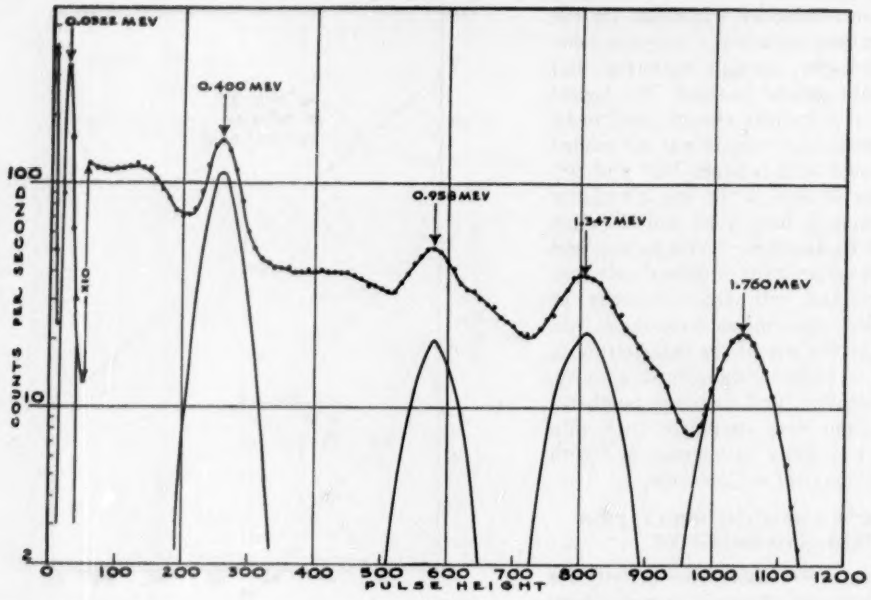

FIG. 2. Typical gamma-ray spectrum of Mg^{28} in secular equilibrium with Al^{28}.

portion was dissolved in 30 ml of 1:10 HCl. In this manner a higher specific activity was obtained. Four milligrams of NaCl were added to the solution as holdback carrier. After buffering the solution with NH_4Cl and making it ammoniacal, the magnesium was precipitated as magnesium ammonium phosphate by the addition of 15 ml of 1 molar primary ammonium phosphate. This precipitation was repeated four times to assure a minimum of impurity. Several samples were transferred to planchets, dried, and counted in Geiger-Mueller counters. The half-life for this bombardment was 21.3±0.2 hours over a decay curve covering 8.6 half-lives. The experimental data are shown in Fig. 1.

Jones and Kohman[4] have reported a half-life of 22.1±0.3 hours which differs significantly from our value. In additional bombardments we have repeated our half-life measurements, and find that 21.3±0.2 hours represents accurately all of our determinations. These additional bombardments were also used to study methods of producing the highest possible specific activity utilizing an isotopic target. Through the use of a 5-hour internal beam bombardment, it was possible to produce an initial magnesium activity of approximately 3.5×10^6 counts per minute per milligram of magnesium utilizing the technique of dissolving the active part of the target only. In summary, these experiments indicated the existence of a new 21.3-hour magnesium activity.

III. GAMMA-RAY SPECTRA, ABSORPTION MEASUREMENTS, AND MASS NUMBER ASSIGNMENT

Gamma-ray spectra of this new magnesium isotope were obtained using a sweep-type differential and integral discriminator similar to the one described by

TABLE I. Gamma-ray energies and intensities of Mg^{28} and Al^{28} in secular equilibrium with each other. These data are obtained from small crystal (1½ in.−1 in.) spectra only.

	Energies in Mev				
Gamma rays	γ_1	γ_2	γ_3	γ_4	γ_5
Run 1	~0.03[a]	0.40 ±0.02	0.95 ±0.02	1.35 ±0.02	1.78 ±0.02
Run 2	0.0316±0.001	0.40 ±0.01	0.940±0.01	1.340±0.01	1.766±0.01
Run 3	0.0322±0.001	0.40 ±0.01	0.958±0.01	1.347±0.01	1.760±0.01
Average	0.0319±0.001	0.40 ±0.01	0.949±0.01	1.346±0.01	1.769±0.01
	Intensities[b]				
Gamma rays	γ_1	γ_2	γ_3	γ_4	γ_5[c]
Run 1	Undetermined	0.30 ±0.03	0.28 ±0.03	0.71 ±0.05	1.00 ±0.05
Run 2	0.962 ±0.05	0.319±0.03	0.292±0.03	0.681±0.05	0.964±0.05
Average	0.962 ±0.05	0.309±0.03	0.286±0.03	0.696±0.05	0.982±0.05

[a] Not used in computing average.
[b] Intensity measurements were not determined in Run 3.
[c] Intensity measurements based on 17.0 percent of the 1.78-Mev gamma ray in the photopeak.

Fairstein.[11] In later bombardments the 20-channel pulse analyzer of Kelley, Bell, and Goss[12] was used to obtain the gamma-ray spectra. A typical gamma-ray spectrum is shown in Fig. 2. Several different determinations of the gamma rays, together with their energies and relative intensities, are listed in Table I. The relative intensities were obtained by correcting the areas in the photopeaks to account for the Compton distributions and by correcting for the geometry and efficiencies of the sodium iodide crystal. In addition, a correction was made for the absorption of the 30-kev gamma ray in the aluminum of the equipment. Jones and Kohman[4] found evidence for several gamma rays with energies extending to at least 2.5 Mev. A very careful search was made for these higher-energy gamma rays and we are able to say that gamma rays of energy greater than 2 Mev have an intensity less than one one-thousandth that of the 1.78-Mev gamma ray listed in Table I. The existence of these additional gamma rays in the spectra of Jones and Kohman may indicate contamination of their sample with a corresponding discrepancy in half-life.

Absorption measurements on the new magnesium activity shown in Fig. 3 indicate 2 betas, one of approximately 3 Mev, and the other of 0.40 ± 0.06 Mev. The actual absorption measurements on the 0.40-Mev beta do not in themselves indicate as large an experimental error as that noted. However, the inaccuracy resulting from subtracting the 3-Mev beta determines the high error. Both the 1.78-Mev gamma listed in Table I, and the approximately 3-Mev β^- observed in the absorption measurements agree almost perfectly with the nuclear data available for Al^{28}. Any Al^{28} produced in the initial bombardment would not be present in the Mg^{28} for two reasons. Its half-life is so short (2.3 min) that it would be dead at the time these separations were run. Also the chemical separation described in Sec. II would have separated it from the magnesium. Accordingly it is assumed that if Al^{28} is present it grows in as the daughter from the parent Mg^{28}. Such a supposition is easy to test through "milking" experiments.

A sample of the active magnesium ammonium phosphate was dissolved in HCl. This solution was made strongly basic with NaOH, causing the precipitation of $Mg(OH)_2$. The precipitate was dissolved in HCl and $AlCl_3$ carrier was added. After buffering with NH_4Cl the solution was made ammoniacal, resulting in the precipitation of aluminum hydroxide. The aluminum hydroxide was centrifuged, washed with a solution of NH_4Cl and NH_4OH, and centrifuged again. The procedure beginning with the dissolving of $Mg(OH)_2$ was carried out in a lusteroid tube. The tube was cut away just above the surface of the precipitate and the section containing the sample was mounted and

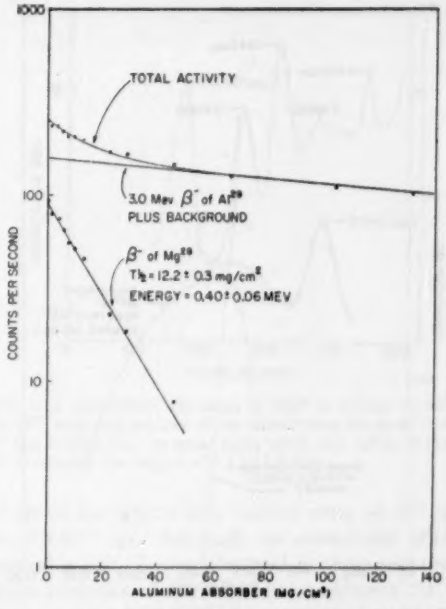

FIG. 3. Low-energy region of absorption curve of Mg^{28} and Al^{28} in secular equilibrium.

placed in a Geiger-Mueller counter. Four minutes elapsed from the time of the first precipitation of the $Al(OH)_3$ until the first count was taken. The decay curve shown in Fig. 4 consists of a 2.3-minute activity which drops off after 6 half-lives into a 21.3-hour background attributed to adsorbed Mg^{28}.

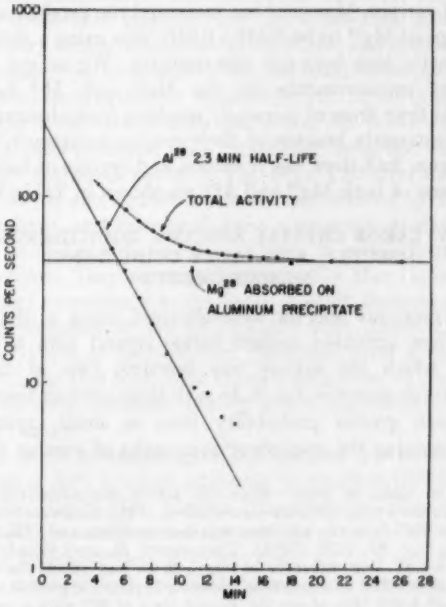

FIG. 4. The decay of the Al^{28} daughter milked from Mg^{28}.

[11] E. Fairstein, Rev. Sci. Instr. **22**, 76 (1951).
[12] Kelley, Bell, and Goss, Oak Ridge National Laboratory Report ORNL-1278, December 20, 1951 (unpublished), p. 27.

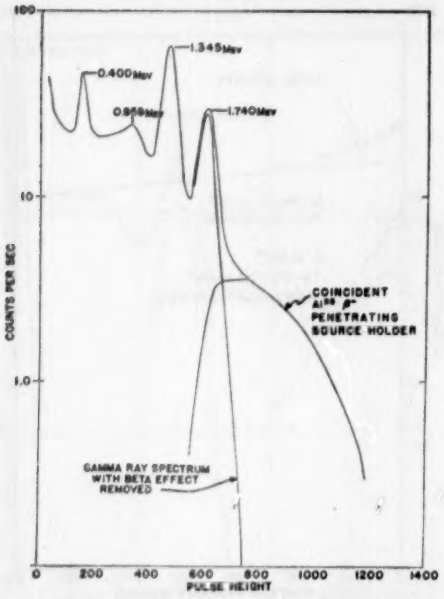

FIG. 5. A large crystal spectrum of Mg^{28} in secular equilibrium with Al^{28} used in coincidence determinations.

The presence of an Al^{28} daughter with a 2.3-minute half-life, approximately 3-Mev β^-, and a 1.78-Mev gamma in secular equilibrium with this new magnesium activity, is extremely strong evidence for its assignment as Mg^{28}.

The additional evidence from cross bombardments and nuclear systematics makes the Mg^{28} mass assignment certain. Marquez[3] has measured the maximum β^- energy of Mg^{28} to be 0.418 ± 0.010 Mev using a double magnetic lens beta-ray spectrometer. We accept his energy measurements for the Mg^{28} and Al^{28} betas rather than those of this study resulting from absorption measurements because of their greater accuracy.* The energies, half-lives, log *ft* values, and degrees of forbiddenness of both Mg^{28} and Al^{28} are shown in Table II.

IV. LARGE CRYSTAL SPECTRA, COINCIDENCE SPECTRA, AND DELAY COINCIDENCE MEASUREMENTS

Gamma-ray spectra were obtained using a $4\frac{3}{4}$-inch thallium activated sodium iodide crystal with a well into which the sample was inserted. One of these spectra is shown in Fig. 5. In such large crystals there is a much greater probability than in small crystals, of observing the coincident sum peaks of gamma rays emitted in coincidence. A comparison of the large crystal spectra and that obtained with a small crystal with the source outside the crystal shows which gamma rays are in coincidence. Figure 5 when compared with Fig. 2 shows quite definitely a decreased intensity of the 0.400- and 0.949-Mev photopeaks together with a corresponding increase in the 1.346-Mev photopeak. The 0.949-Mev gamma line is almost invisible since when a 0.949-Mev gamma ray is detected, the probability that the 0.400-Mev gamma ray (coincident with it) will escape, is quite small. On the other hand, when a 0.400-Mev gamma ray is detected, the probability of escape of the 0.949-Mev gamma is not as small. No line is observed at a pulse height corresponding to 2.7 Mev, showing that the 0.400–0.949 Mev cascade is not in coincidence with the 1.346-Mev gamma ray. The interpretation that the 0.400- and 0.949-Mev gamma rays are in coincidence seems unequivocal. Coincidence information on the 0.0319-Mev gamma ray using large crystal spectra is somewhat more difficult to obtain. Two large crystal spectra were obtained in which the Mg^{28} was surrounded by brass. In this case the majority of the 0.0319-Mev gamma rays did not get into the crystal.

In several other large crystal spectra an aluminum activity holder was used which allowed the majority of the 0.0319-Mev gamma rays to get into the crystal. These spectra are summarized in Table III. γ_2' and γ_4' refer to the energies when the activity is surrounded by aluminum, whereas γ_2 and γ_4 refer to the energies when surrounded by brass. The pertinent pieces of information in Table II are: (a) Both γ_2' and γ_4' have a higher energy than γ_2 and γ_4. (b) This difference in energies between γ_2', γ_4' and γ_2, γ_4 is very close to the energy of γ_1 (0.0319 Mev). (c) Surrounding the sample with either aluminum or brass makes no difference in the energy of γ_5. This information is interpreted as follows: γ_1 is in coincidence with γ_2 and γ_4. Therefore when the activity is surrounded by aluminum through which γ_1 can penetrate, the sum peaks are observed, namely γ_2' and γ_4'. These are slightly higher in energy than when the activity is surrounded by brass through which γ_1 cannot pass. The effect of the metal holder on the activity is not appreciable, as indicated by the fact that the Al^{28} γ_5 is exactly the same in both measurements. The comparison of the aluminum and brass differences of γ_4 and γ_5 indicates again a discrepancy of 0.03 Mev, just the energy of γ_1. Since it has previously been shown that γ_2 and γ_3 are in coincidence, and that

TABLE II. Data on the β^- decays of Mg^{28} and Al^{28}.

Isotope	Energy max of β^- (Mev)	Half-life (min)	log *ft*	Degree of forbiddenness
Mg^{28}	0.418	1278	4.30	Allowed
Al^{28}	2.865	2.3[a]	4.92[a]	Allowed[b]

[a] There is some indication from half-life measurements in milking experiments that Al^{28} has a slightly shorter half-life and correspondingly smaller log *ft* value.
[b] These values are from H. T. Motz and D. E. Alburger, Phys. Rev. **86**, 165 (1952).

* *Note added in proof.*—Since this article was submitted for publication a more accurate measurement of the maximum energy of the Mg^{28} beta ray has been obtained by Olsen and O'Kelley, Phys. Rev. **93**, 1125 (1954). They report $E_{max}=0.459\pm0.002$, log $ft=4.45$. This difference in energy in no way affects the conclusions reached in this article. However it puts the ground state of Mg^{28} 6.484 Mev above the ground state of Si^{28} with a consequent change of the mass of Mg^{28} to 27.992782 ± 0.000046.

γ_1 and γ_2 are in coincidence, a coincidence may be inferred between γ_1 and γ_3.

As a check on the coincidences between the 0.0319-Mev gamma ray and the 0.40- and 0.949-Mev gamma rays, a coincidence spectrum was obtained. One counter of the coincidence setup was set so as to accept only the 0.0319-Mev gamma rays. The other detector was used to monitor the region from 0.2 to 1.0 Mev. The spectrum so obtained is shown in Fig. 6.

It is noteworthy that it is almost identical with the ordinary spectrum from 0.2 to 1.0 Mev. This coincidence spectrum indicates definitely that the 0.0319-gamma ray is in coincidence both with the 0.400- and 0.949-Mev gamma rays. In the case of the 0.949-Mev gamma ray, this could only be inferred indirectly from the large crystal work.

The 0.0319-Mev gamma ray results from an excited state of Al^{28} which is so near the ground state that there is a distinct possibility that it might be metastable. Accordingly, delay coincidence measurements were made utilizing a delay coincidence scintillation spectrometer previously described.[13] In this case the delay coincidence scintillation spectrometer employed sodium-iodide thallium activated crystals with Type 5819 multiplier tubes as detectors. Coincidence measurements between the 1.346-Mev gamma ray and the 0.0319-Mev ray were made. In Fig. 7 (curve 2) the number of coincidences is plotted as a function of delay time for a sample of Mg^{28}. The slope of curve 2 indicates a half-life $\leq 2.27\times10^{-9}$ sec. Without a change in the apparatus, a resolution curve for prompt coincidences was obtained between the 1.28-Mev gamma ray of Na^{22}, and the 0.032-Mev electron pulses from the Compton distribution of positron annihilation with which the 1.28-Mev gamma is in prompt coincidence.

The half-life so observed is slightly shorter than in the case of Mg^{28}. (See Fig. 7, curve 1.) However, the difference is so small that it is possible to say that the half-life of the 0.0319-Mev excited state of Al^{28} is less than 2×10^{-9} sec. Although no metastable state of measurable half-life was observed in these experiments definite existence of the coincidence between the 1.35-Mev gamma and the 0.032-Mev gamma is indicated.

TABLE III. Gamma-ray energies in Mev as determined from large crystal spectra in which the activities were surrounded by aluminum or brass.

Activity surrounded by aluminum	Energy in Mev			
	γ_2'[a]	γ_4'[a]	γ_3'	$\gamma_3'-\gamma_4'$
Run 1	0.400	1.345	1.740	0.395
Run 2	0.401	1.356	1.755	0.399
Run 3	...	1.350	1.750	0.400
Run 4	...	1.350	1.735	0.385
Average	0.4005	1.350	1.745	0.392
Activity surrounded by brass	Energy in Mev			
	γ_2	γ_4	γ_3	$\gamma_3-\gamma_4$
Run 5	0.375	1.315	1.745	0.430
Run 6	0.390	1.325	1.745	0.420
Average	0.382	1.320	1.745	0.425

[a] The primes on gamma rays 2 and 4 indicate that the sample was surrounded by aluminum rather than brass; $\gamma_2'=(\gamma_2+\gamma_1)$, $\gamma_4'=(\gamma_4+\gamma_1)$.

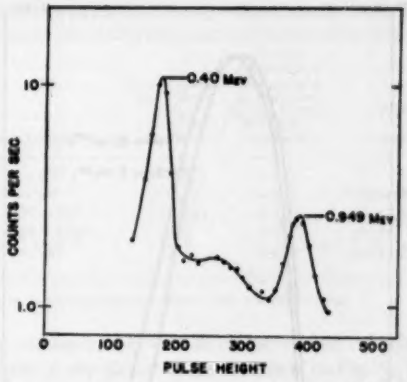

FIG. 6. A coincidence spectrum of Mg^{28} in secular equilibrium with Al^{28}, with one counter of the coincidence set so as to accept only the 0.0319-Mev gamma rays, while the other detector is used to monitor the region of 0.2 to 1.0 Mev.

V. DECAY SCHEME OF Mg^{28} AND THE MASSES OF Al^{28} AND Mg^{28}

The decay scheme for Mg^{28} must involve an energy level scheme in Al^{28} which will permit the following: (1) coincidences between the 1.346, 0.949, 0.400-Mev gammas, and the 0.0319-Mev gamma; (2) a coincidence between the 0.949-Mev gamma and 0.400-Mev gamma; (3) no coincidences between either the 0.949-Mev or the 0.400-Mev gammas and the 1.346-Mev gamma; (4) very similar intensities in the 0.944- and 0.400-Mev gammas; (5) an intensity for the 0.0319-Mev gamma which is approximately equal to the sum of the intensity of the 1.346-Mev gamma and either the 0.949- or the 0.400-Mev gammas; (6) a single Mg^{28} beta ray. Such a decay scheme is shown in Fig. 8(a). The level scheme for Al^{28} is almost identical with that derived by Enge, Buechner, and Sperduto[14] from a magnetic analysis of the $Al^{27}(d,p)Al^{28}$ reaction. There is one important exception. They report a level at 1.015 Mev for which we find no evidence in the decay of Mg^{28}. Because of its large intensity in the $Al^{27}(d,p)Al^{28}$ work, there can be little doubt of its existence. However, after a careful search for this level with enough resolution to observe it, we must conclude that it is not populated in the Mg^{28} decay.

In order to assign spins and parities to the various states of Al^{28}, it is first advisable to establish the nature of the 0.0319-Mev gamma transition. A delay coincidence measurement of the half-life of the 0.0319-Mev state indicates that it is less than 2×10^{-9} sec. From this measurement one may immediately conclude that

[13] F. K. McGowan, Phys. Rev. **79**, 404 (1950).

[14] Enge, Buechner, and Sperduto, Phys. Rev. **88**, 963 (1952).

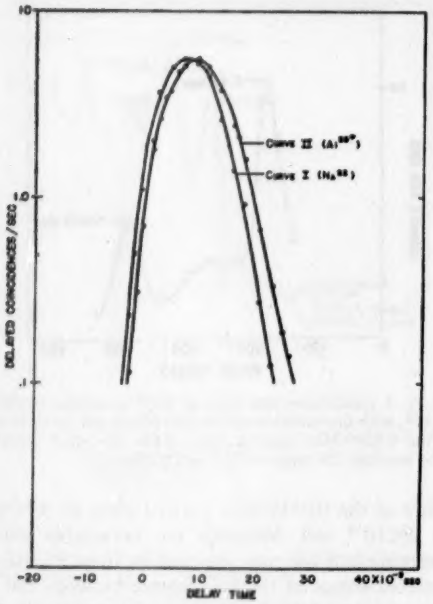

FIG. 7. The number of delayed coincidences as a function of delay time.

it is a dipole transition. Quadrupole or higher pole transitions of this energy would be expected to have much longer half-lives. It is then necessary to choose between $M1$ and $E1$ transitions. One sensitive method of distinguishing between these two transitions would be to observe the internal conversion coefficient. Smith and Anderson[15] have failed to observe internal conversion electrons, putting an upper limit on $\alpha^K_{exp} \leq 2$. By observing the intensity of the 0.0319-Mev gamma ray relative to the other gamma rays in the Mg^{28} decay, Wapstra and Veenendaal[5] set an $\alpha^K_{exp} = 0.30 \pm 0.20$, but were not able to draw a definite conclusion as to the nature of the transition. The results presented in Table I together with that part of the decay scheme indicated in Fig. 8(a) determine a value of $\alpha^K_{exp} = 0.032 \pm 0.066$ for the 0.0319-Mev gamma ray.

Although relativistic K-shell internal conversion coefficients for $E_\gamma < 150$ kev are not yet available, there is a method for obtaining extrapolated values of the coefficients at low energies. The ratio of the relativistic coefficients[16] to the nonrelativistic coefficients[17] is plotted for $E_\gamma \leq 150$ kev, and the ratio is extrapolated to one at zero electron energy.[18] Low-energy K-shell conversion coefficients for electric radiation are obtained by multiplying the nonrelativistic values by a correction factor from the ratio plot. Similarly, for magnetic radiation, extrapolated coefficients are obtained by multiplying the extrapolated coefficient for electric radiation by a correction factor from a plot of β_{l-1}/α_l extrapolated to zero electron energy.

The values obtained for these extrapolations indicate $\alpha_1^K = 0.31$, $\alpha_2^K = 10.8$, $\beta_1^K \lesssim 0.1$. The value for β_1^K is very uncertain because the extrapolated ratio of β_1^K to α_2^K is not known at very low energies. Fortunately the experimental data discriminate clearly against an internal conversion coefficient of 0.31. Therefore by elimination one is led to the conclusion that the 0.0319-Mev-gamma ray is an $M1$ transition. Since the spin and parity of the even-even Mg^{28} nucleus must be 0+, the allowed beta decay to the 1.375-Mev level determines its assignment as either 0+, or 1+. The ground state of Al^{28} with a $(d_{\frac{5}{2}})^{-1}s_{\frac{1}{2}}$ configuration should be 3+ according to the rules of Nordheim.[19] Furthermore, no other assignment for the ground state is completely consistent with the decay to the first excited state of Si^{28}, and with the gamma and beta decay energies and intensities of the Mg^{28} decay. The 0.0319-Mev excited state which goes to the 3+ ground state via an $M1$ transition must be 2+ rather than 4+, since it is populated by the 0+ or 1+ 1.375-Mev level, preferentially in comparison to the ground state. Finally the 0.978-Mev level must be 1−, 2−, or 2+ so that it can compete with the (2+) 0.031-Mev level for gamma rays, yet not be populated by the Mg^{28} beta decay. The various possible combinations of these spin possibilities together with the type of gamma-ray transitions which these combinations of spins determine are indicated in Figs. 8(b), (c), (d), (e), and (f). The measured ratio of the intensity of the 1.346-Mev gamma ray to the 0.400-Mev gamma ray is 2.25. By using the Weisskopf[20] formula it is possible to compute

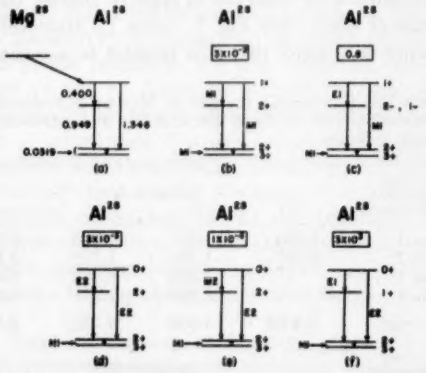

FIG. 8. Various possible assignments of Al^{28} energy levels, spins, and parities. (a) indicates the correct energy level assignment. (b), (c), (d), (e), and (f) indicate various possible spin and parity assignments. The numbers in the boxes above (b), (c), (d), (e), and (f) indicate the ratios of the intensities of the 1.346-Mev gamma to the 0.400-Mev gamma, calculated using the Weisskopf formula for each set of proposed parities and spins.

[15] R. D. Smith and R. A. Anderson, Nature **168**, 429 (1951).
[16] Rose, Goertzel, Spinrad, Harr, and Strong, Phys. Rev. **83**, 79 (1951).
[17] M. H. Hebb and E. Nelson, Phys. Rev. **58**, 486 (1940).
[18] P. Axel and R. F. Goodrich, U. S. Office of Naval Research Report (unpublished).
[19] L. W. Nordheim, Phys. Rev. **78**, 294 (1950).
[20] V. F. Weisskopf, Phys. Rev. **83**, 1073 (1951).

the theoretical ratio of intensities of the 1.346 Mev gamma to the 0.400-Mev gamma for the various combinations of spins. They are indicated in the boxes above the Figs. 8(b), (c), (d), (e), (f). Case (c) comes considerably closer than any of the others to predicting the experimental value. This would probably be a cleancut decision for 2−, or 1− for the 0.978-Mev level except for the experiments of Holt and Marsham.[21]

In their investigation of (d,p) stripping reactions on Al^{27} they observe an angular distribution of the unresolved proton groups going to the 0.0319-Mev and ground-state levels in which $l_n=0$. This indicates $J=2+$ and/or $3+$ for the ground state doublet, which agrees with the results obtained here from the Mg^{28} decay. However, Holt and Marsham[21] obtain an angular distribution of the unresolved proton groups going to the 0.978- and 1.015-Mev levels which could be fitted by a combination of about 10 percent of $l_n=0$ and about 90 percent $l_n=2$. Since the 0.978-Mev level populated in the Mg^{28} decay is produced in much less intensity in the (d,p) stripping reaction than the 1.015-Mev level, according to the work of Enge, Buechner, and Sperduto,[14] it is concluded that the 0.978-Mev level is responsible for the 10 percent $l_n=0$ angular distribution in the experiments of Holt and Marsham. Therefore, the spin and parity of the 0.978-Mev level should be $2+$ or $3+$. Since the Weisskopf formula is known to err by a large factor at times, and since the $2+$ state is the second choice from the calculation of the ratio of gamma-ray intensities (see Fig. 8), the most probable assignment of the 0.978-Mev level is $2+$. However, because of the calculations using the Weisskopf formula, an assignment as $2-$ or $1-$ is not completely ruled out and is indicated in the parentheses.

The first excited state of Si^{28} would be expected to be $2+$.[22] The entire decay scheme for the isobaric triplet $Mg^{28}-Al^{28}-Si^{28}$ is shown in Fig. 9.

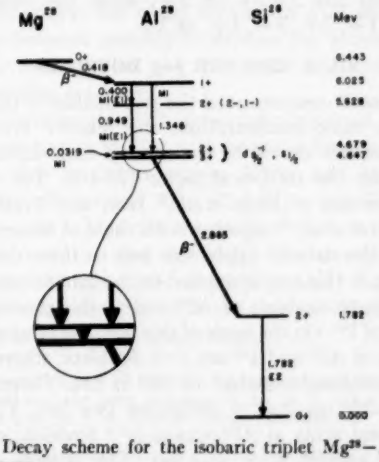

FIG. 9. Decay scheme for the isobaric triplet $Mg^{28}-Al^{28}-Si^{28}$.

[21] J. R. Holt and T. N. Marsham, Proc. Phys. Soc. (London) **A66**, 249 (1953).

[22] M. Goldhaber and A. W. Sunyar, Phys. Rev. **83**, 906 (1951).

TABLE IV. Energetic relationship between certain isobaric triplets.

Isobaric triplets	Prediction[a] of first couple energy differences in Mev	Energy differences of first couple as indicated by the Fermi-Weisäcker equation	Prediction of half-lives
$S^{36}-Cl^{36}-A^{36}$	(−0.97)	−3.2	...
$Si^{32}-P^{32}-S^{32}$	+0.12	−2.3	700±500 years
$Mg^{28}-Al^{28}-Si^{28}$	(1.76)	−1.3	(21.3 hours)
$Ne^{24}-Na^{24}-Mg^{24}$	4.4	−0.02	short
$O^{20}-F^{20}-Ne^{20}$	7.4	+1.6	very short

[a] Values in parentheses are known and not predictions.

The masses of Al^{28} and Mg^{28} have been calculated on the basis of the decay scheme shown in Fig. 9. Masses of 27.985810±0.000080,[23] 27.985792±0.000032,[24] and 27.985825±0.000016[25] have been reported for Si^{28}. A weighted mean gives a value of 27.985818±0.000043. Using the weighted mean, an energy transition of 4.647±0.0014 Mev, and 931.152[26] as the conversion factor, gives 27.990809±0.000045 as the mass of Al^{28}. An energy of 1.796±0.014 Mev is involved in the decay of Mg^{28} to the ground state of Al^{28}. From this the mass of Mg^{28} is determined as 27.992738±0.000047.††

VI. DISCUSSION

The search for Mg^{28} was undertaken on the assumption that O^{20}, Ne^{24}, Mg^{28}, and Si^{32}, whose decays are forbidden, might be sufficiently long-lived to serve as tracers. Its discovery has given new impetus to the search for the remaining isotopes of this group.

These unknown activities, together with other known activities and stable isobars, form the isobaric triplets shown in Table IV.

The energy differences between the second couples of the triplets (e.g., $Cl^{36}-A^{36}$, and $P^{32}-S^{32}$), are known, whereas in general the energy differences between the first couples (e.g., $Si^{32}-P^{32}$ and $Ne^{24}-Na^{24}$) are unknown. The energy differences between second couples can be plotted against mass number and then the energy coordinate changed to the energy differences between first couples. Only the decay energy of Mg^{28} and the mass difference between Cl^{36} and S^{36} can be used to define the first-couple energy differences coordinate. However, this is sufficient to predict energy differences for the rest of the first couples as shown in Table IV. It is interesting to note the comparison of the energies predicted using the method described and those predicted by the Fermi-Weisäcker equation. In general, the Fermi-Weisäcker equation predicts too little energy for the first couple by two or more Mev. Except

[23] H. E. Duckworth and R. S. Preston, Phys. Rev. **79**, 402 (1950).

[24] H. Ewald, Z. Naturforsch. **6a**, 293 (1951).

[25] K. Ogata and H. Matsuda, Phys. Rev. **89**, 27 (1953).

[26] J. W. M. Dumond and E. R. Cohen, Phys. Rev. **82**, 555 (1951).

†† See *Note added in proof*, p. 1646.

for $S^{36}-Cl^{36}$ and $O^{20}-F^{20}$, the Fermi-Weisäcker equation also predicts the wrong direction for the decay.

Unfortunately, since nothing is known about the decay scheme, it is not possible to predict half-lives for Ne^{24} and O^{20}. Since both Na^{24} and F^{20} have a number of excited states into which Ne^{24} and O^{20} can decay, it is probable that they will be short-lived in spite of the forbiddenness of their ground-state transitions. It should be stated that the one-particle shell model predicts even greater forbiddenness for the first several transitions from O^{20} to excited states of F^{20} than to the ground state. Therefore, because of the very great usefulness of a long-lived oxygen isotope, it would seem worth while to look for this isotope on the slim possibility that all energetically available transitions are forbidden. Si^{32} has such a small amount of energy available for decay that it must either decay into the ground state or to the 77-kev state of P^{32} described by Van Patter *et al.*[27] If one accepts the explanation of Inglis[28] for this ground-state doublet together with the accepted spin and parity assignment of the P^{32} ground state as 1+, then the 77-kev excited state should have a spin of 2+. Such an assignment of the doublet suggests that the Si^{32} decay should go to the ground state of P^{32} rather than to the 77-kev state. Since Si^{32} goes to the P^{32} ground state by a change of a $d_{\frac{1}{2}}$ neutron into an $s_{\frac{1}{2}}$ proton, and P^{32} goes to the ground state of S^{32} by exactly the same type of change, it is probable that the log ft value for these two beta decays would be very nearly the same. Using the log ft value of 7.9 for the P^{32} decay together with the 0.12 Mev of energy predicted for the Si^{32} decay, a half-life of 700 ± 500 years for Si^{32} is calculated. The large error is due to the large uncertainty in the energy.

Attempts to produce Si^{32} by successive (n,γ) reactions in the pile and by the reaction $Si^{30}(\alpha,2p)Si^{32}$ produced very small amounts of a long-lived activity. More recently, Lindner[29] has produced Si^{32} by high-energy proton spallation of chloride. He observed a simple beta decay of 0.10-Mev maximum energy and a 700-year half-life. The very close agreement between his experiments and the calculations presented here seems to justify them in spite of their empirical nature.

The implications of an $M1$ type transition from the 31-kev state to the ground state of Al^{28} are of considerable interest in addition to their worth in helping with spin assignments in the decay scheme.

According to Inglis,[28] the ground-state doublet of Al^{28} arises from neutron-proton $j-j$ coupling. The $d_{\frac{5}{2}}$ proton hole couples with the $s_{\frac{1}{2}}$ neutron. The splitting between the $J=2$ and $J=3$ levels is small because it is caused by a small term in the spin exchange operator. If these one-particle shell model arguments are correct, one would expect the 31.9-kev transition to be a magnetic dipole. The confirmation of this prediction by the experimental results presented here is gratifying.

In addition, Inglis suggests that the excited state doublet observed by Enge *et al.*[14] may be the result of the excitation of the odd proton from the $d_{\frac{5}{2}}$ orbital to the $d_{\frac{3}{2}}$ orbital. This leaves the spin of the s neutron to be oriented so that two states of $J=1+$ and 2+ are possibilities. The evidence presented here discriminates strongly against this interpretation. No population of the higher energy level of this doublet is observed from the decay of Mg^{28}. This is very strange if the interpretation of Inglis were correct. There are other indications that the excited state doublet is different from the ground-state doublet. The yield of the proton groups in the excited doublet is in the ratio 4.6 to 38.0, as observed by Enge *et al.*,[14] at 90° and 2.1-Mev bombarding energy. The proton groups going to the ground state and 31.9-kev level were in the ratio 100 to 69. Holt and Marsham[21] observed an angular distribution of the unresolved proton groups going to the excited doublet which can be fitted by a combination of $l_n=0$ and $l_n=2$. This result indicates that one of these two levels has $J=2+$ or 3+, while the other has $J=0+$, 1+, 2+, 3+, 4+, or 5+.

TABLE V. Tests for $j-j$ doublets.

Designation of doublet	Energy of levels in Mev	Spin and parity of levels	Relative[a] intensity of levels	Intensity $/(2J+1)$	$j-j$ doublet
Al^{28} ground-state doublet	0.000 0.0319	3+ 2+	100 69	14.3 13.8	Yes
Al^{28} first excited doublet	0.967 1.015	2+(2−,1−) >2	4.6 38.0	0.9(1.5) (5.4,4.2, 3.6)	No
P^{32} ground-state doublet	0.000 0.077	1+ 2+	1.0[b] 1.7[b]	3.3 3.4	Yes

[a] These numbers have meaning only for a given doublet but not for comparisons between doublets.
[b] Intensities for the P^{32} ground-state doublet were determined for 1.8-Mev bombarding deuterons; for 2.0-Mev deuterons the agreement is not quite as good.

VII. A TEST FOR $j-j$ DOUBLETS

Since each component of the $j-j$ doublet is captured into the same configuration, the relative intensities of the doublet should be the same if each intensity is divided by the statistical factor $(2J+1)$. The experimental results of Enge *et al.*,[14] Holt and Marsham,[21] Van Patter *et al.*,[27] together with those of this research provide the data to apply this test to three doublets. In Table V this test is applied to the ground- and first excited-state doublets of Al^{28} and to the ground-state doublet of P^{32}. On the basis of this test, the ground-state doublets of Al^{28} and P^{32} are $j-j$ doublets, whereas the first excited-state doublet of Al^{28} is not. There was a considerable qualitative indication (see Sec. VI) that the ground state of Al^{28} was a $j-j$ doublet, whereas the first excited state was not. The success of this quantitative test in verifying the conclusions about these doublets is not only gratifying but is an indication

[27] Van Patter, Endt, Sperduto, and Buechner, Phys. Rev. **86**, 502 (1952).
[28] D. R. Inglis, Revs. Modern Phys. **25**, 390 (1953).
[29] M. Lindner, Phys. Rev. **91**, 642 (1953).

that the test itself is a simple precise way of determining the nature of these doublets.

It is a pleasure to acknowledge the cooperation of the Radiation Laboratory of the University of California, and particularly of G. Bernard Rossi and the crew of the 60-in. cyclotron, in securing the many bombardments essential in this work. We are also grateful to the University of Chicago and the betatron operating crew for a bombardment received from them. Finally, the help of Dr. D. M. Van Patter and Dr. A. E. S. Green in the preparation of this paper is gratefully acknowledged.

PHYSICAL REVIEW VOLUME 94, NUMBER 6 JUNE 15, 1954

Systematics of Photoproton Reactions*

E. V. Weinstock and J. Halpern
University of Pennsylvania, Philadelphia, Pennsylvania
(Received March 3, 1954)

The photoproton yields from the elements Ta, Pt, Pb, W, and Au have been determined for betatron bremsstrahlung bombardment at 22-Mev peak energy by the use of zinc sulfide detectors and a 40-μsec betatron pulse duration. The yields, as measured in photoprotons per mole per roentgen, are as follows: Ta, 5.7×10^4; Pt, 2.9×10^4; Pb, 5.8×10^4; W, 5.2×10^4; and Au, 1.9×10^4. These values, along with previous determinations, permit a study of general behavior of photoproton yields for all Z values throughout the periodic table. Comparisons with calculations based on the evaporation model show good agreement with experimental trends up to a Z of 50, after which the measured yields are too high by factors ranging from 10 to 10^4. Calculations based on the direct photoelectric process give better agreement.

INTRODUCTION

In a systematic study of the proton yields from elements bombarded with bremsstrahlung radiation of moderate energy, almost all previous investigations have been limited to elements of either low or medium atomic number.[1–5] With the exception of cerium and bismuth, reported by Toms and Stephens, the elements studied have been confined to the region below a Z of 50. The present paper describes the measurement of photoproton yields from the elements tantalum, tungsten, platinum, gold, and lead. With these additions the systematics of yields as a function of Z is fairly complete except for a gap between a Z of 50 and 73. It now becomes possible to explore the general trend of the results with the proposed mechanisms for photonuclear reactions.

The twenty elements previously reported by this laboratory[1] were studied with betatron bremsstrahlung of 23.5-Mev maximum energy. Diven and Almy used 20.8 Mev, Butler and Almy 22.5 Mev, and Toms and Stephens 22.5 Mev for magnesium and 24 Mev for indium, cerium, and bismuth. The present work employed 22-Mev bremsstrahlung and the photoprotons were directly detected, as previously, with the use of zinc sulfide scintillators.

APPARATUS AND PROCEDURE

The experimental apparatus is essentially the same as that described in detail in reference 1. Briefly, a strongly collimated bremsstrahlung beam of maximum energy 22 Mev strikes the target, consisting of a thin sheet of the element under investigation, placed at an angle of 60 degrees with respect to two identical ZnS scintillators diametrically opposite each other. The detectors are kept fixed at an angle of 90 degrees to the photon beam and subtend an angle of 10 degrees at the target. After passing through the target, the photon beam strikes a 2-g/cm^2 tantalum target contained in a neutron detection assembly, and the number of neutrons from the $Ta(\gamma,n)$ reaction is used to monitor the bremsstrahlung intensity. Additional monitoring makes use of an ionization chamber and current integrator, which in turn are calibrated in terms of a Victoreen r thimble imbedded in 4 cm of Lucite.

The scintillation pulses from the ZnS screens are detected with the use of 5819 photomultiplier tubes feeding model-100 amplifiers with 1-μsec delay line clipping and into ten-channel integral pulse-height analyzers. For high-Z targets, the combination of low proton yield and large light particle scattering makes discrimination against light particle pileup critical, and with a one-microsecond betatron pulse duration the beam intensity must be reduced prohibitively to achieve sufficient discrimination for the proton pulses. It was this, in fact, which limited the previous study to elements with a Z below 50. By the use of tech-

* Supported in part by the U. S. Air Research and Development Command and the joint program of the U. S. Office of Naval Research and the U. S. Atomic Energy Commission.
[1] A. K. Mann and J. Halpern, Phys. Rev. **82**, 733 (1951).
[2] B. C. Diven and G. M. Almy, Phys. Rev. **80**, 407 (1950).
[3] W. A. Butler and G. M. Almy, Phys. Rev. **91**, 58 (1953).
[4] M. E. Toms and W. E. Stephens, Phys. Rev. **82**, 709 (1951).
[5] M. E. Toms and W. E. Stephens, Phys. Rev. **92**, 362 (1953).

TABLE I. Target characteristics and yield data.

Element	Z	A	Percent abundance	Target thickness (mg/cm²)	(γ,p) threshold (Mev)	Resonance peak energy	Measured yield (protons/mole/r)	Percent error	Predicted yield (evap.)
Tantalum	73	181	100	124	6.17	14.1	5.7×10^4	30	1.6×10^5
Tungsten	74			136		14.1	5.2×10^4	31	1.2×10^5
		180	0.14		6.62				
		182	26.2		7.08				
		183	14.3		7.30				
		184	30.7		7.52				
		186	28.7		7.96				
Platinum	78			157		13.9	2.9×10^4	51	40
		190	0.012		6.16				
		192	0.78		6.59				
		194	32.8		7.01				
		195	33.7		7.23				
		196	25.4		7.44				
		198	7.2		7.86				
Gold	79	197	100	112	5.72	13.8	1.9×10^4	83	29
Lead	82			140		13.7	5.8×10^4	30	13
		204	13		6.53				
		206	26		6.93				
		207	21		7.12				
		208	52		7.33				

niques similar to those reported by Keegan,[6] the betatron pulse duration was lengthened to 40 microseconds for the work reported herein, whereupon discrimination against pileup was unambiguous as indicated by the integral bias curve for tantalum shown in Fig. 1. Also included in the figure are a curve representing the background obtained without a target in the scattering chamber, and the net curve with background subtracted. These data were taken with a photon beam intensity of 5.9 roentgen per minute at the target, whereupon the net useful proton counting rate was 0.2 counts per minute for a tantalum target of 124-mg/cm² thickness, as obtained by extrapolation of the net curve to zero bias.

Targets were in the form of foils of commercial purity and natural isotopic composition. The low proton yield required the use of thick targets as listed in Table I, which necessitated a large target absorption correction calculated as outlined in reference 1. The calculated corrections increased the observed yield values by a factor of 2.5.

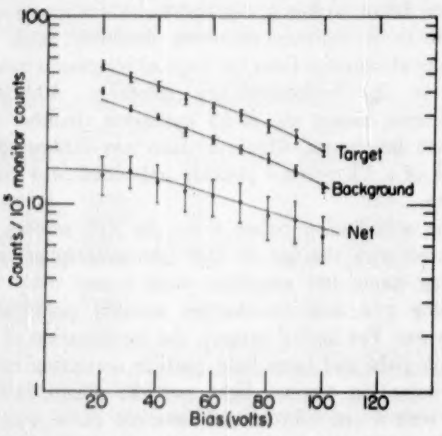

FIG. 1. Integral bias curves for a 124-mg/cm² tantalum target. Net count is obtained by subtracting background curve from target curve and extrapolating to zero bias.

Since measurements were made only at one angle, total yields were computed from the known geometry of the apparatus assuming spherical symmetry for the proton angular distributions. Although angular distribution data for heavy elements are sparse,[5,7,8] it is not believed that errors greater than 25 percent can enter as a result of the assumption of isotropy.

The possibility existed that some or all of the protons observed might arise from (n,p) reactions induced in the target by fast neutrons in the photon beam or present as background at the target position. Consequently it was deemed necessary to measure the fast neutron flux intercepted by the targets making use of the Lucite-zinc-sulfide fast neutron detector developed by Hornyak.[9] By further expansion of the betatron pulse duration to 100 microseconds and reduction of the photon beam intensity by a factor of 3000, it was possible to place the neutron detector in the direct betatron beam without excessive pileup. By calibration of the neutron detector efficiency using a radium-beryllium neutron source of known strength, and using reported (n,p) cross sections,[10] it was possible to show that any contribution to the measured proton yields from fast neutron reactions could not exceed a few percent at the most.

[6] T. J. Keegan, Rev. Sci. Instr. **24**, 472 (1953).

[7] Mann, Halpern, and Rothman, Phys. Rev. **87**, 146 (1952).

[8] M. M. Hoffman and A. G. W. Cameron, Phys. Rev. **92**, 1184 (1953).

[9] W. F. Hornyak, Rev. Sci. Instr. **23**, 264 (1952).

[10] B. L. Cohen, Phys. Rev. **81**, 184 (1951).

RESULTS AND DISCUSSION

The corrected absolute yield values are listed in Table I and plotted against Z in Fig. 2. The errors shown are those due to counting statistics as a result of the low yields inherent in heavy element photoproton emission. Also shown in the figure are all previous yield measurements made under comparable conditions. Included are the yields of Mann and Halpern taken using the method of this paper, and the photographically detected photoproton yields of Butler and Almy (B & A), Diven and Almy (D & A), and Toms and Stephens (T & S).

In a comparison of the data with the theories for photonuclear reactions we will be concerned with the general trends of the yields as opposed to individual fluctuations of neighboring elements. With increasing Z, the yields rise to a maximum at nickel ($Z=28$) and then drop rapidly until a Z of 50, whereupon they show a much slower drop at high Z values. An attempt will now be made to understand these trends on the basis of the evaporation model of nuclear reactions with corrections for the direct photoelectric ejection of a proton in the region of high Z, where this mechanism becomes relatively more important.

Following Weisskopf,[11] the (γ,p) cross section is:

$$\sigma(\gamma,p)=\sigma(\gamma)G_p. \tag{1}$$

Here $\sigma(\gamma)$ is the γ-ray absorption cross section and G_p the branching ratio, given by

$$G_p=F_p/\Sigma_b F_b, \tag{2}$$

where the summation is extended over all particles

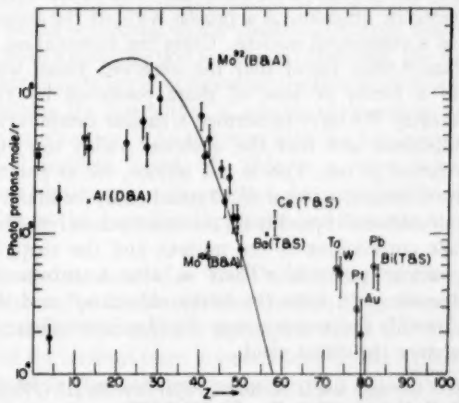

FIG. 2. Summary of published photoproton yield data. Unlabeled points are those of Mann and Halpern; crosses are data from Diven and Almy (D & A), Butler and Almy (B & A), and Toms and Stephens (T & S); points labeled only with chemical symbols are those obtained in the present work. The solid curve is the yield *vs* Z as predicted by the calculations described in the text.

[11] J. M. Blatt and V. F. Weisskopf, *Theoretical Nuclear Physics* (John Wiley and Sons, Inc., New York, 1952), pp. 340–374.

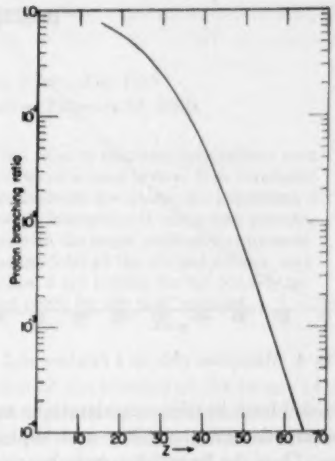

FIG. 3 Proton branching ratio as a function of Z.

that can be emitted in the reaction, and

$$F_b=\frac{2M_b}{\hbar^2}\int_0^{\epsilon_{\max}}\epsilon\sigma_{cb}(\epsilon)w(\epsilon_{\max}-\epsilon)d\epsilon. \tag{3}$$

M_b is the mass of the emitted particle, ϵ its energy upon emission, and $\epsilon_{\max}$ the maximum value that ϵ can assume (given in the present case by $\hbar w-S_p$, where S_p is the energy with which particle b is bound to the compound nucleus); σ_{cb} is the cross section for formation of the compound nucleus by particle b, and w is the density of energy levels of the residual nucleus.

The photoproton yield per mole per roentgen is then

$$Y_p=a\int_{E_{th}}^{E_\beta}\sigma(\gamma,p)N(E_\gamma,E_\beta)dE_\gamma$$
$$=a\int_{E_{th}}^{E_\beta}\sigma(\gamma)\frac{F_p}{\Sigma_b F_b}N(E_\gamma,E_\beta)dE_\gamma, \tag{4}$$

where $N(E_\gamma,E_\beta)$ is the bremsstrahlung distribution at the energy E_γ when the betatron energy is E_β; E_{th} is the threshold for the reaction, and a represents Avogadro's number.

A calculation of the proton yields therefore requires a knowledge of the energy dependence of the total absorption cross section for each element; and data for the various quantities that are contained in the F's, i.e., the particle binding energies, and capture cross sections and the level densities. Sufficient approximations to these quantities are available so that one can compute the order of magnitude of proton yields to be expected for the various Z values.

In computing the branching ratios, the assumption was first made that particle emission other than proton and neutron could be neglected. Except in the special case of copper, where a sizable deuteron emission has

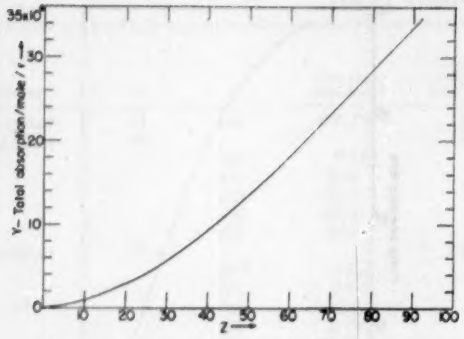

FIG. 4. Absorption yield as a function of Z.

been reported,[12] both barrier considerations and experiment rule out deuteron, triton, and alpha particle competition. Thus the branching ratio becomes simply $G_p=F_p/(F_p+F_n)$. Evaluation of the F functions involves ϵ_{max}, and thus the particle binding energies as well as the energies at which the photons are absorbed. Binding energies were computed from the mass formula,[13] and smooth curves were drawn through the values plotted as a function of Z. Since the photon absorption exhibits a resonance behavior, the peak position of the resonance as found from the systematic study of photoneutron reactions[14,15] was used for the photon energies. This approximation removed the branching ratios from the integral in Eq. (4) for the proton yield values.

F values have been plotted by Feld *et al.*,[16] with the assumption of exponential level densities for the residual nuclei. There is a further dependence on the nuclear radius which was chosen to be $1.3\times10^{-13}A^{\frac{1}{3}}$ cm for these evaluations. The resulting plot of the branching ratios as a function of Z is shown in Fig. 3.

There remains, then, the evaluation of the integral of the product of the absorption cross section and the bremsstrahlung distribution. The assumption of a narrow absorption resonance was again made through utilization of the bremsstrahlung intensity at the peak of the cross section *vs* energy curves. For the integrated cross section, the values predicted by Levinger and Bethe[17] from the dipole sum rules were inserted. The fraction of exchange in the neutron-proton interaction was assumed to be 0.5. The resultant absorption per mole per roentgen is plotted in Fig. 4 as a function of Z.

Since the absorption per mole per roentgen is an increasing function of Z and the branching ratio a decreasing function, the product of the two (representing the proton yield per mole per roentgen) will exhibit a peak as shown by the solid curve drawn through the measured values of Fig. 2. The peak occurs at $Z=23$, and between a Z of 28 and 50 the experimental points are in excellent agreement in absolute magnitude.

Even for the region below a Z of 28, the discrepancies with the above rough calculations is not serious especially in view of the fact that the level densities should depart radically from those assumed, the binding energies show large fluctuations, and it is known that the proton and neutron integrated cross sections up to 22 Mev do not add up to the predictions of the sum rules.[15]

The discrepancies, however, in the high-Z region are more serious as illustrated by the measured and predicted values listed in Table I. Observed yields are higher than those calculated by factors which get as large as three orders of magnitude, the agreement becoming progressively worse with increasing Z. Thus, even on the basis of such rough calculations, it is safe to say that the evaporation model as usually formulated is inadequate to explain the photoproton yields for elements of high atomic number.

As shown by Toms and Stephens[5] for the element bismuth, a considerable portion of the photoproton yield can be accounted for on the basis of the direct photoelectric emission of a proton without the formation of a compound nucleus. Using the formulation of Courant,[18] they found that the observed yields were within a factor of four of those predicted by this mechanism. We have performed a similar computation for tantalum and find the observed yields too high by a factor of ten. This is not serious, for as pointed out by Courant, a factor of 10 could easily be found in the calculations by modifying the assumptions regarding particle correlations in the nucleus and the shape of the nuclear potential. There is also a substantial quadrupole yield from the heavy elements,[19] and this could modify the proton energy distributions sufficiently to enhance the direct yield.

[12] P. R. Byerly and W. E. Stephens, Phys. Rev. **83**, 54 (1951).
[13] N. Metropolis and G. Reitwiesner, "Table of Atomic Masses," Los Alamos Scientific Laboratory Report NP-1980, 1950 (unpublished).
[14] Montalbetti, Katz, and Goldemberg, Phys. Rev. **91**, 659 (1953).
[15] R. Nathans and J. Halpern, Phys. Rev. **93**, 437 (1954).
[16] Feld, Feshbach, Goldberger, and Weisskopf, U. S. Atomic Energy Commission Report NYO-632 (unpublished).
[17] J. S. Levinger and H. A. Bethe, Phys. Rev. **78**, 115 (1950).
[18] E. D. Courant, Phys. Rev. **82**, 703 (1951).
[19] Halpern, Nathans, and Mann, Phys. Rev. **88**, 679 (1952).

Theory of the (d,p) Reaction*

W. TOBOCMAN
Laboratory of Nuclear Studies, Cornell University, Ithaca, New York
(Received October 23, 1953; revised manuscript received February 15, 1954)

The Born approximation treatment of the (d,p) reaction is modified so as to eliminate integrations over the interior of the target nucleus where the distortion of the incident wave is most severe. This treatment yields the S. T. Butler result when certain additional physical assumptions are made. An approximate expression for the (d,p) cross section is given in which (a) the Coulomb interaction is taken into account, (b) the effects due to the interaction of the deuterons and the protons with the target nucleus are expressed in terms of the boundary conditions for the wave functions of these particles at the nuclear surface, and (c) the effects arising from the fact that the mass of the target nucleus is not infinite are not entirely neglected. The methods presented can be used to get the corresponding result for the (d,n) reaction.

THERE are two approximate treatments of the (d,p) reaction that currently have been of interest. One is the boundary condition matching treatment introduced by Butler[1] and the other is the Born approximation treatment.[2] When the Coulomb interaction and the interaction between the proton and the residual nucleus are neglected, the boundary condition matching treatment gives a simple analytic expression for the (d,p) cross section which agrees surprisingly well with experiment. This result has proved to be a useful tool for determining the spins and parities of nuclear states. However, when the effects mentioned above are not neglected, the boundary condition matching cross section involves integrals which are very difficult to evaluate.

On the other hand, the Born approximation (d,p) cross section is not much more complicated when the Coulomb interaction and the interaction between liberated particle and the target nucleus are taken into account. It is also a simple matter to include the effects due to the scattering of the incident deuteron beam in the Born approximation treatment. However, the Born approximation involves replacing the true wave function describing the interaction of a beam of deuterons with the target nucleus Ψ by the wave function for the unperturbed incident beam Ψ^0. This is a very dubious approximation since there must be considerable distortion of the wave function inside and near the target nucleus.

We demonstrate below that the interior of the target nucleus can be eliminated from the Born approximation calculation. This cuts out the region where the distortion of the incident wave is most severe so that replacing Ψ by Ψ^0 in the modified treatment may not be a bad approximation.

Elimination of the interior of the target nucleus from the treatment introduces a set of parameters which may be approximately identified with the scattering amplitudes for free particles interacting with the residual nucleus. If one assumes that the liberated particles do not interact with the residual nucleus and sets these amplitudes equal to zero, neglects the Coulomb interaction, and assumes the n-p interaction to have zero range, then our (d,p) cross section reduces to the boundary condition matching expression for the (d,p) cross section.

We will discuss the (d,p) process only, but the extension of the discussion to the (d,n) process is straightforward.

II. GENERAL EXPRESSION FOR THE (d,p) CROSS SECTION

To simplify the following discussion we will neglect the Coulomb interaction, assume all the particles under discussion have zero spin, and assume that the mass of the target nucleus is infinite. These approximations will be removed in Sec. IV of this paper.

Our object is to calculate the cross section for a deuteron to interact with a target nucleus to yield a final state in which the neutron is captured by the target nucleus with (negative) energy $E_f=\hbar^2K_N^2/2M$ and the proton emerges with asymptotic momentum $\hbar\mathbf{K}_P$. K_N and K_P are related by the conservation of energy

$$\frac{\hbar^2K_N^2}{2M}+\frac{\hbar^2K_P^2}{2M}=E, \tag{1}$$

where E is the kinetic energy of the incident deuteron minus its binding energy. Consequently, all protons liberated with asymptotic momentum $\hbar\mathbf{K}_P$ must be associated with neutrons captured with energy $\hbar^2K_N^2/2M$. Thus our problem is simply to calculate the flux of protons liberated with asymptotic momentum $\hbar\mathbf{K}_P$.

Let $\Psi(\xi,\mathbf{r}_N,\mathbf{r}_P)$ be the wave function describing the interaction of a beam of deuterons with the target nucleus. $\mathbf{r}_N$ and $\mathbf{r}_P$ are the coordinates of the neutron and proton, respectively, measured from the center of

* Supported in part by the joint program of the U. S. Office of Naval Research and the U. S. Atomic Energy Commission.
[1] S. T. Butler, Proc. Roy. Soc. (London) **A208**, 559 (1951); F. L. Friedman and W. Tobocman, Phys. Rev. **92**, 93 (1953).
[2] A. B. Bhatia *et al.*, Phil. Mag. **43**, 485 (1952); R. Huby, Nature **166**, 552 (1950); Proc. Roy. Soc. (London) **A215**, 385 (1952); P. B. Daitsch and J. B. French, Phys. Rev. **87**, 900 (1952); N. Austern, Phys. Rev. **89**, 318 (1953); E. Gerjuoy, Phys. Rev. **91**, 645 (1953).

mass of the target nucleus. The coordinates of the A nucleons making up the target nucleus are lumped together in the symbol ξ. Let

$$\psi_f(\xi,\mathbf{r}_N)=\sum_{lm}\psi_f^{lm}(\xi,r_N)Y_l^m(\theta_N)$$

be the wave function for the residual nucleus. Then the wave function for the protons liberated as a result of neutrons being captured into the state ψ_f is

$$\mathfrak{f}_f(\mathbf{r}_P)=\int d\mathbf{r}_N d\xi\psi_f^*\Psi \tag{2}$$

for large r_P. The current per unit solid angle of these protons for large r_P is

$$F_f(\mathbf{K}_P)=\frac{h}{2Mi}r_P^2\left(\mathfrak{f}_f^*\frac{\partial}{\partial r_P}\mathfrak{f}_f-\mathfrak{f}_f\frac{\partial}{\partial r_P}\mathfrak{f}_f^*\right), \tag{3}$$

so that the (d,p) cross section is

$$\sigma(\mathbf{K}_p)=\sum_f\frac{F_f(\mathbf{K}_P)}{\mathcal{J}}. \tag{4}$$

$\mathcal{J}$ is the current density of the incident deuteron beam and the sum over f includes all states of the residual nucleus having energy E_f. We choose our normalization so that the asymptotic form of the incident deuteron beam is the plane wave,

$$\Psi^0=\chi(|\mathbf{r}_P-\mathbf{r}_N|)\Phi_I(\xi)\exp[i\mathbf{K}_D\cdot\tfrac{1}{2}(\mathbf{r}_P+\mathbf{r}_N)]. \tag{5}$$

Therefore

$$\mathcal{J}=hK_D/M_D \tag{6}$$

and

$$\sigma(\mathbf{K}_P)=\frac{M_D}{hK_D}\sum_f F_f(\mathbf{K}_P). \tag{7}$$

The wave function Ψ is a solution of the Schrödinger equation,

$$(H_I+T_N+T_P+V_{IN}+V_{IP}+V_{NP}-E)\Psi=0, \tag{8}$$

where H_I is the Hamiltonian operator for the target nucleus, T is the kinetic energy operator, and V_{ij} is the operator for the energy of interaction of particles i and j. Expand Ψ in terms of the complete set of eigenfunctions of the operator $H_I+T_N+V_{IN}$.

$$\Psi(\xi,\mathbf{r}_N,\mathbf{r}_P)=\sum_i\mathfrak{f}_i(\mathbf{r}_P)\psi_i(\xi,\mathbf{r}_N), \tag{9}$$

where the sum is understood to include an integral over the continuum of unbound states. Combining Eqs. (8) and (9) gives the Schrödinger equation for $\mathfrak{f}_f$:

$$\begin{aligned}\left(T_P-\frac{\hbar^2K_P^2}{2M}\right)\mathfrak{f}_f(\mathbf{r}_P)&=-\int d\mathbf{r}_N d\xi\psi_f^*[V_{NP}+V_{IP}]\Psi\\&=-\sum_i\langle f|V_{NP}+V_{IP}|i\rangle\mathfrak{f}_i(\mathbf{r}_P)\\&=-V_{FP}\mathfrak{f}_f(\mathbf{r}_P).\end{aligned} \tag{10}$$

This is just the form of the $(A+2)$-nucleon Schrödinger equation we would use to discuss the scattering of free protons by the residual nucleus.

Using the Green's function for the operator $T_P-(\hbar^2K_P^2/2M)$, we can transform Eq. (10) into an integral equation:

$$\begin{aligned}\mathfrak{f}_f(\mathbf{r})&=-\frac{M}{2\pi\hbar^2}\int d\mathbf{r}_P\frac{e^{iK_P|\mathbf{r}_P-\mathbf{r}|}}{|\mathbf{r}_P-\mathbf{r}|}V_{FP}\mathfrak{f}_f(\mathbf{r}_P)\\&=-\frac{M}{2\pi\hbar^2}\int d\mathbf{r}_P d\mathbf{r}_N d\xi\frac{e^{iK_P|\mathbf{r}_P-\mathbf{r}|}}{|\mathbf{r}_P-\mathbf{r}|}\psi_f^*[V_{NP}+V_{IP}]\Psi.\end{aligned} \tag{11}$$

Incorporated into Eq. (11) is the asymptotic boundary condition that all the liberated protons are outgoing at infinity. Now substituting Eq. (11) into Eq. (7) gives

$$\sigma(\mathbf{K}_P)=\frac{MM_DK_P}{(2\pi)^2\hbar^4K_D}\sum_f\left|\int d\mathbf{r}_P d\mathbf{r}_N d\xi e^{-i\mathbf{K}_P\cdot\mathbf{r}_P}\times\psi_f^*[V_{NP}+V_{IP}]\Psi\right|^2. \tag{12}$$

Replacing Ψ in Eq. (12) by Ψ^0, the wave function for the incident beam of deuterons, gives the Born approximation result for the (d,p) cross section. As long as the cross section for interaction with the target nucleus is small, Ψ^0 should be a fair approximation to Ψ outside the range of V_{IP} and V_{IN}. However, inside the target nucleus the wave function must be considerably distorted so that the Born approximation breaks down. Even if one believed the Born approximation, one would not be able to evaluate the stripping cross section because the form of ψ_f inside the target nucleus is not known.

We propose to modify the Born approximation treatment by eliminating (to a good approximation) the troublesome range of integration in favor of a set of parameters involving the logarithmic derivative of $\mathfrak{f}_f$ at the nuclear surface.

First we analyze $\mathfrak{f}_f$ into a sum of spherical harmonics:

$$\mathfrak{f}_f(\mathbf{r}_P)=\sum_{L,M}\mathfrak{f}_{fLM}(r_P)Y_L^M(\theta_P). \tag{13}$$

Introducing this expansion into Eq. (11) gives

$$\mathfrak{f}_{fLM}(r)=\frac{2K_PM}{i\hbar^2}\int d\mathbf{r}_P j_L(K_Pr_<)h_L^{(1)}(K_Pr_>)\times Y_L^{-M}(\theta_P)V_{FP}\mathfrak{f}_f(\mathbf{r}_P), \tag{14}$$

where

$$r_<=\begin{cases}r_P & r_P<r\\ r & r<r_P\end{cases}\quad\text{and}\quad r_>=\begin{cases}r_P & r_P>r\\ r & r>r_P\end{cases}.$$

In this expression j_L represents the spherical Bessel function and $h_L^{(1)}$ represents the spherical Hankel func-

tion of the first kind. Now for $r>R$, Eq. (14) may be written

$$\mathfrak{f}_{fLM}(r)=\frac{2K_PM}{i\hbar^2}\int_R^\infty d\mathbf{r}_P j_L(K_Pr_<)h_L^{(1)}(K_Pr_>)\times Y_L^{-M}(\theta_P)V_{FP}\mathfrak{f}_f(\mathbf{r}_P)-I_{fLM}h_L^{(1)}(K_Pr), \quad (15)$$

where I_{fLM} does not depend on r. I_{fLM} can be expressed in terms of the first term on the right of the above equation and the logarithmic derivative of $\mathfrak{f}_{fLM}$ at $r=R$. This can be accomplished by means of the Schrödinger equation and Green's theorem. However, it is simpler to take the logarithmic derivative of both sides of Eq. (15), set $r=R$, and solve for I_{fLM}. The result is

$$I_{fLM}=\beta_{fLM}{}^*\frac{2K_PM}{i\hbar^2}\int_R^\infty d\mathbf{r}_P h_L^{(1)}(x_Pr_P)Y_L^{-M}(\theta_P)\times V_{FP}\mathfrak{f}_f(r_P), \quad (16)$$

where

$$\beta_{fLM}{}^*=\left[\frac{\dfrac{\partial}{\partial r}j_L(K_Pr)-j_L(K_Pr)\dfrac{\partial}{\partial r}\log\mathfrak{f}_{fLM}(r)}{\dfrac{\partial}{\partial r}h_L^{(1)}(K_Pr)-h_L^{(1)}(K_Pr)\dfrac{\partial}{\partial r}\log\mathfrak{f}_{fLM}(r)}\right]_{r=R}. \quad (17)$$

Using Eq. (15) instead of Eq. (11) in Eq. (7) gives us an alternate expression for the (d,p) cross section:

$$\sigma(\mathbf{K}_P)=\frac{MM_DK_P}{(2\pi)^2\hbar^4K_D}\sum_f|A_f|^2, \quad (18)$$

$$A_f=\int d\mathbf{r}_N d\xi\int_R^\infty d\mathbf{r}_P\mathcal{S}^*(\mathbf{K}_P,\mathbf{r}_P)\times\psi_f^*(\xi,\mathbf{r}_N)[V_{NP}+V_{IP}]\Psi=\int_R^\infty d\mathbf{r}_P\mathcal{S}^*(\mathbf{K}_P,\mathbf{r}_P)V_{FP}\mathfrak{f}_f(\mathbf{r}_P),$$

where

$$\mathcal{S}^*(\mathbf{K}_P,\mathbf{r}_P)=e^{-i\mathbf{K}_P\cdot\mathbf{r}_P}-4\pi\sum_{L,M}i^{-L}Y_L{}^M(\theta_{KP})\times Y_L{}^{-M}(\theta_P)\beta_{fLM}{}^*h_L^{(1)}(K_Pr_P)=4\pi\sum_{L,M}i^{-L}Y_L{}^M(\theta_{KP})Y_L{}^{-M}(\theta_P)\times[j_L(K_Pr_P)-\beta_{fLM}{}^*h_L^{(1)}(K_Pr_P)]. \quad (19)$$

Associated with the target nucleus and the residual nucleus are characteristic radii R_I and R_F such that $V_{IP}=0$ for $r_P>R_I$ and $V_{FP}=0$ for $r_P>R_F$. We wish to choose R no smaller than R_I so that V_{IP} drops out of the stripping amplitude. We would like to choose R as large as possible since the difference between Ψ and Ψ^0 tends to decrease as we move away from the target nucleus, and we intend to replace Ψ by something like Ψ^0 eventually. However, we cannot choose $R>R_F$, since then our expression for the scattering amplitude A_f becomes simply $\mathfrak{f}_f(R)$ which is of no use to us. We will find that the choice $R=R_I$ is most convenient.

The elimination of V_{IP} by choosing $R=R_I$ leads to the opportunity for an important simplification of the scattering amplitude A_f. With V_{IP} absent, the integrand is proportional to V_{NP}. The short range of V_{NP} and the fact that $r_P>R_I$ cuts down the contribution to the integral due to the range $0<r_N<R_I$. In fact, assuming V_{NP} to have zero range, as is often done, completely removes the interior of the target nucleus from the ranges of the integrations over r_N and r_P. Thus we have to a good approximation eliminated the interior of the target nucleus by introducing the parameters $\beta_{fLM}{}^*$.

III. INTERPRETATION OF THE PARAMETERS $\beta_{fLM}{}^*$

We have seen that $\mathfrak{f}_f(\mathbf{r}_P)$ satisfies the Schrödinger equation for a proton interacting with the residual nucleus. However we cannot immediately conclude that $[(\partial/\partial r)\log\mathfrak{f}_{fLM}(r)]_{R_I}$ is the logarithmic derivative appropriate to the scattering of free protons out of an incident beam by the residual nucleus. First of all R_I is smaller than the radius of the residual nucleus and secondly the boundary conditions for the two problems are not obviously the same.

Actually the difference between R_I and R_F cannot be very great. Taking $R_I=NA^{\frac{1}{3}}$ and $R_F=N(A+1)^{\frac{1}{3}}$ gives

$$\frac{R_F-R_I}{R_F}\approx\frac{1}{3(A+1)}, \quad (20)$$

so that

for carbon, $R_F-R_I\approx0.026R_F$;
for aluminum, $R_F-R_I\approx0.012R_F$;
for iron, $R_F-R_I\approx0.006R_F$.

Since the logarithmic derivative of $\mathfrak{f}_{fLM}$ must be continuous, we expect that its value must be essentially the same at R_I as at R_F.

In order for the boundary conditions for $\mathfrak{f}_{fLM}(r_P)$ at $r_P=R_I$ to be that same as those for free incident protons, all the protons represented by $\mathfrak{f}_f$ must originate at values of r_P greater than R_I.

Because of the large extension of the deuteron and its small binding energy, the deuteron bond must be broken as soon as one member interacts with the target nucleus. In this process the other member of the deuteron is left free just outside the surface of the residual nucleus. Thus we can picture two sequences for the (d,p) process. (a) The neutron interacts with the target nucleus to form the residual nucleus leaving the proton outside. (b) The proton interacts with the target nucleus leaving the neutron free outside. The neutron is subsequently captured by the proton + target

nucleus system and following this the proton is ejected to leave the residual nucleus. Sequence (a) is called stripping. Clearly sequence (b) is much less probable than sequence (a). Sequence (a) is a one-step process while sequence (b) is a three-step process. The one step of (a) is equally as probable as the first step of (b). Taking the Coulomb interaction into account will tend to favor the one step of (a) over the first step of (b). But then the probability for each of the two succeeding steps of sequence (b) is much less than one. We conclude that sequence (b) is of little importance for the (d,p) reaction. Thus almost all the protons are liberated outside $r_P=R_I$. This is our reason for choosing $r_P=R_I$.

Assuming that all the protons are liberated outside the target nucleus allows us to identify $[(\partial/\partial r)\times\log f_{fLM}(r)]_{RI}$ with the logarithmic derivative appropriate for free protons incident on the residual nucleus. From what we have just said this assumption is equivalent to neglecting the contribution of compound nucleus formation to the (d,p) reaction. The extent to which $[(\partial/\partial r)\log f_{fLM}(r)]_{RI}$ can be identified with the logarithmic derivative for incident free protons is a measure of the importance of stripping for the (d,p) reaction.

We have shown that although R_I is smaller than R_F, the difference between them is very small so that the logarithmic derivative of f_{fLM} at R_I is very nearly the same as the logarithmic derivative at R_F. We have also shown that practically all the protons produced in the (d,p) process are liberated outside $r_P=R_I$. Consequently the logarithmic derivative of f_{fLM} at $r_P=R_I$ is essentially the same as the logarithmic derivative appropriate to the interaction of free protons incident on the residual nucleus.

The value of the logarithmic derivative of f_{fLM} is given by the particular theory of nuclear reactions we choose to employ. For example, we may assume that the surface of the residual nucleus presents an inpenetrable barrier to the liberated protons. This was done by J. Horowitz and A. M. L. Messiah [J. phys. radium **14**, 695 (1953)]. Alternatively, we may use the continuum theory of nuclear reactions[3] to estimate the logarithmic derivatives. According to this theory, we should write

$$\left[\frac{\partial}{\partial r}\log f_{fLM}(r)\right]_{RI}=-\frac{[1+iKR_I]}{R_I}, \tag{21}$$

where

$$K=(K_0^2+K_P^2)^{\frac{1}{2}},\quad K_0\approx 1\times 10^{-13}\ \text{cm}^{-1}.$$

Equation (17) now becomes

$$\beta_{fLM}{}^*=\frac{j_L(K_PR_I)}{h_L{}^{(1)}(K_PR_I)}\times\left[\frac{R_I(\partial/\partial r)\log j_L(K_Pr)+1+iKR_I}{R_I(\partial/\partial r)\log h_L{}^{(1)}(K_Pr)+1+iKR_I}\right]_{RI}. \tag{23}$$

If one supposes that the liberated protons have no interaction with the residual nucleus, one sets $\beta_{fLM}{}^*=0$. It will be shown below that this assumption leads to the boundary condition matching result for the (d,p) cross section.

IV. EFFECTS DUE TO SPIN, THE COULOMB INTERACTION, AND THE FINITE MASS OF THE TARGET NUCLEUS

The derivation of the previous sections can be carried out without neglecting the effects listed above. We will not give the details of the calculation, but we will merely state the results. For this purpose we write Eq. (18) for the (d,p) cross section in the following form:

$$\sigma(\mathbf{K}_P)=\frac{M^2M_DK_P}{2\pi^2\hbar^6RK_D}\sum_f\left|\sum_{l,m}\sqrt{\gamma_l}\,B_f{}^{lm}\right|^2, \tag{23}$$

where

$$B_f{}^{lm}=\int d\mathbf{r}_N d\xi\int_{RI}^{\infty}d\mathbf{r}_P\frac{\psi_f{}^{lm*}(\xi,r_N)}{\phi_f{}^{lm*}(R_I)}Y_l{}^{-m}(\theta_N)\times\mathcal{S}^*(\mathbf{K}_P,\mathbf{r}_P)[V_{NP}+V_{IP}]\Psi, \tag{24}$$

$$\gamma_l=\frac{\hbar^2R_I}{2M}|\phi_f{}^{lm}(R_I)|^2, \tag{25}$$

$$\phi_f{}^{lm}(R_I)=\int d\xi\Phi_I{}^*(\xi)\psi_f{}^{lm}(\xi,R_I),$$

$\Phi_I(\xi)$ = the wave function for the target nucleus.

To take the Coulomb interaction into account, one merely replaces the proton wave functions by their Coulomb analogs. Thus the function $\mathcal{S}^*(\mathbf{K}_P,\mathbf{r}_P)$ is replaced by

$$\mathcal{S}^{c*}(\mathbf{K}_P,\mathbf{r}_P)=4\pi\sum i^{-L}Y_L{}^M(\theta_{KP})Y_L{}^{-M}(\theta_P)\times e^{-i\sigma_L(\eta_P)}\left\{\frac{F_L(\eta_P,K_Pr_P)-\beta_{LM}{}^{c*}H_L(\eta_P,K_Pr_P)}{K_Pr_P}\right\}, \tag{26}$$

where

$$\beta_{LM}{}^{c*}=\left[\frac{\dfrac{\partial}{\partial r}\dfrac{F_L(\eta_P,K_Pr)}{K_Pr}-\dfrac{F_L(\eta_P,K_Pr)}{K_Pr}\dfrac{\partial}{\partial r}\log f_{fLM}(r)}{\dfrac{\partial}{\partial r}\dfrac{H_L(\eta_P,K_Pr)}{K_Pr}-\dfrac{H_L(\eta_P,K_Pr)}{K_Pr}\dfrac{\partial}{\partial r}\log f_{fLM}(r)}\right]_{r=RI},$$

[3] J. M. Blatt and V. F. Weisskopf, *Theoretical Nuclear Physics* (John Wiley and Sons, Inc., New York, 1952), p. 340.

$$\eta_P = Ze^2M/\hbar^2K_P,$$

$$\sigma_L(\eta_P) = \arg\{\Gamma(L+1+i\eta_P)\},$$

$$H_L(\eta,\rho) = F_L(\eta,\rho) - iG_L(\eta,\rho).$$

F_L and G_L are defined as the regular and irregular solutions of the differential equation

$$\left\{\frac{d^2}{d\rho^2} + \left[1 - \frac{2\eta}{\rho} - \frac{L(L+1)}{\rho^2}\right]\right\} F_L(\eta,\rho) = 0.$$

They are normalized so that they have the asymptotic forms

$$F_L(\eta,\rho) \to \sin[\rho - \eta \ln 2\rho - \tfrac{1}{2}L\pi + \sigma_L(\eta)],$$

$$G_L(\eta,\rho) \to \cos[\rho - \eta \ln 2\rho - \tfrac{1}{2}L\pi + \sigma_L(\eta)],$$

in the limit as $\rho \to \infty$.

The effect of taking the finiteness of the mass of the target nucleus into account is to

(a) introduce the factor

$$(1+M_D/M_I)^{-1}(1+M/M_I)^{-1}[1+M/(M+M_I)]^{-1}$$

into the expression for the cross section,

(b) replace $\mathbf{r}_P$ by $\boldsymbol{\varrho}_P = \mathbf{r}_P - \mathbf{r}_N M/(M+M_I)$ in the argument of $\mathcal{S}^{e*}$ and as the variable of integration in B_f^{lm}, and

(c) replace $V_{NP}+V_{IP}$ by $V_{NP}+\Delta V = V_{NP}+V_{IP} + Ze^2(1/r_P - 1/\rho_P)$ in B_f^{lm}.

For $M_I = \infty$, ΔV makes no contribution to B_f^{lm}. For finite M_I the contribution of ΔV to B_f^{lm} cannot be very large since while ρ_P ranges from R_I to ∞ the fact that ψ_f^{lm} describes a bound state of the residual nucleus means that r_N is restricted to a relatively small region around the origin. It follows that $\mathbf{r}_P - \boldsymbol{\varrho}_P \cong \mathbf{r}_N/(A+1)$ is small and consequently ΔV must be negligible over practically the entire range of integration.

Let I be the spin of the target nucleus, and let J be the spin of the residual nucleus. Taking the conservation of angular momentum and parity into account gives in place of Eq. (23)

$$\sigma(\mathbf{K}_P) = \frac{M^2M_DK_P}{2\pi^2\hbar^6R_IK_D} \sum_{l,m}{}' \frac{(2J+1)\gamma_l}{2(2I+1)(2l+1)} |B_f^{lm}|^2. \quad (27)$$

The primed summation symbol is used to indicate that the sum over l is restricted to the range $||I-J|-\frac{1}{2}| \leq l \leq I+J+\frac{1}{2}$, l being restricted to even integers or odd integers depending on the change of parity. This simple result is the consequence of the assumption that ΔV is not spin dependent and the assumption that it is a good approximation to replace Ψ by a wave function having the same spin dependence as the incident deuteron beam.

V. THE (d,p) CROSS SECTION

We conclude that the expression which should be compared with experiment is

$$\sigma(\mathbf{K}_P) = \frac{[1+M/(M+M_I)]^{-1}}{(1+M/M_I)(1+M_D/M_I)} \frac{M_DM^2}{(2\pi)^2\hbar^6R_I} \times \frac{(2J+1)}{(2I+1)} \frac{K_P}{K_D} \sum_{l,m}{}' \frac{\gamma_l}{2l+1} |B_f^{lm}|^2, \quad (28)$$

where

$$B_f^{lm} = \int d\mathbf{r}_N d\xi \int_{R_I}^{\infty} d\boldsymbol{\varrho}_P \frac{\psi_f^{lm*}(\xi,r_N)}{\phi_f^{lm*}(R_I)} Y_l^{-m}(\theta_N) \times \mathcal{S}^{e*}(\mathbf{K}_P,\boldsymbol{\varrho}_P)[V_{NP}+\Delta V]\Psi, \quad (29)$$

J = spin of the residual nucleus, I = spin of the target nucleus, and γ_l = the reduced width of the level into which the neutron is captured. The sum over l is restricted as in Eq. (27). If the level into which the neutron is captured is characterized by a definite value of l as well as definite values of J and parity, then only those terms in Eq. (28) corresponding to that value of l are to be retained.

To evaluate B_f^{lm} we introduce the following approximations. ΔV is neglected so that the effects due to the finite mass of the target nucleus are only partially taken into account. The (unknown) terms in Ψ representing the dissociation and distortion of deuterons are dropped. That is to say, Ψ is approximated by the expression $\Psi_{c.m.}(\frac{1}{2}(\mathbf{r}_N+\mathbf{r}_P))\cdot\chi(\mathbf{r}_P-\mathbf{r}_N)\Phi_I(\xi)$, where χ is the normalized wave function for the internal motion of an unperturbed deuteron, Φ_I is the wave function for the target nucleus, and $\Psi_{c.m.}$ describes the motion of the centers of mass of the incident and scattered deuterons. For $\Psi_{c.m.}$ we write

$$\Psi_{c.m.}(\mathfrak{R}) = 4\pi \sum_{L,M} i^L Y_L^{-M}(\theta_{K_D}) Y_L^M(\theta_{\mathfrak{R}}) e^{-i\sigma_L} \times \left\{\frac{F_L(\eta_D,K_D\mathfrak{R}) - \delta_L H_L(\eta_D,K_D\mathfrak{R})}{K_D\mathfrak{R}}\right\}, \quad (30)$$

where $\mathfrak{R} = (\mathbf{r}_P+\mathbf{r}_N)/2$. Lastly, V_{NP} is approximated by the zero range potential. This last step is the source of two important simplifications. First of all, the interior of the target nucleus is completely eliminated from the range of integration. Thus, since r_N is now restricted to a range in B_f^{lm} where it is always greater than R_I, ψ_f^{lm} can be replaced by $\Phi_I(\xi)h_l^{(1)}(K_Nr_N)$.

Secondly, our six-dimensional integral is reduced to a three-dimensional integral. In this three-dimensional integral the integration over angles can be performed leaving an expression for B_f^{lm} which is a sum of one-dimensional integrals.

The result of these approximations is

$$B_f{}^{lm}=-\frac{\hbar^2(8\pi\alpha)^{\frac{1}{2}}}{M|K_N|^3}\int_{R_I|K_N|(1+M/M_I)}^{\infty}d\mathbf{x}Y_l{}^{-m}(\theta_x)$$
$$\times\frac{h_l{}^{(1)}(ix)}{h_l{}^{(1)}(i|K_N|R_I)}\mathcal{E}^{c*}\left(\mathbf{K}_P,\frac{\mathbf{x}}{1+M/M_I}\right)\Psi_{c.m.}(\mathbf{K}_D,\mathbf{x}) \tag{31}$$
$$=-\frac{4\pi\hbar^2(1+M/M_I)[2\alpha(2l+1)]^{\frac{1}{2}}}{M|K_N|K_DK_P}\sum_{L,\lambda}P_L{}^{|m|}(\cos\theta_{K_P})$$
$$\times i^{\lambda-L}\exp(-i[\sigma_L(\eta_P)+\sigma_\lambda(\eta_D)])\Gamma_{L\lambda}{}^{lm}f_{L\lambda}{}^{l},$$

where

$$\Gamma_{L\lambda}{}^{lm}=\frac{(2\lambda+1)(2L+1)}{(2l+1)}\left(\frac{(L-|m|)!}{(L+|m|)!}\right)^{\frac{1}{2}}$$
$$\times(L\lambda00|L\lambda l0)(L\lambda m0|L\lambda lm),$$

$$f_{L\lambda}{}^{l}=\int_X^{\infty}dx\frac{h_l{}^{(1)}(ix)^*}{h_l{}^{(1)}\left(\frac{iX}{1+M/M_I}\right)}[F_\lambda(\eta_D,ax)$$
$$-\delta_\lambda H_\lambda(\eta_D,ax)][F_L(\eta_P,bx)-\beta_{Lm}{}^{c*}H_L(\eta_P,bx)],$$

$$a=\frac{K_D}{|K_N|},\quad b=\frac{K_P}{|K_N|(1+M/M_I)},$$

$$X=R_I|K_N|(1+M/M_I),$$

$$\eta_P=\frac{Ze^2M(M_I+M)}{\hbar^2K_P(M_I+2M)},$$

$$\eta_D=\frac{Ze^2M_DM_I}{\hbar^2K_D(M_I+M_D)},$$

$\sigma_L(\eta)=\arg\Gamma(1+L+i\eta)$,
$H_L(\eta,\rho)=F_L(\eta,\rho)-iG_L(\eta,\rho)$,
$F_L(\eta,\rho)=$ the regular radial Coulomb function,
$G_L(\eta,\rho)=$ the irregular radial Coulomb function,
$h_l{}^{(1)}(x)=$ the spherical Hankel function,
$\hbar^2\alpha^2/M=$ binding energy of the deuteron,
$M=$ the nucleon mass,
$M_D=$ the deuteron mass,
$M_I=$ the target nucleus mass,
$R_I=$ the radius of the target nucleus,
$\hbar\mathbf{K}_D=$ asymptotic momentum of the incident deuterons relative to the center of mass,
$\hbar\mathbf{K}_P=$ asymptotic momentum of the liberated protons relative to the center of mass,
$\hbar^2K_N{}^2(M+M_I)/2MM_I=$ energy of the captured neutron,
$(L\lambda m0|L\lambda lm)=$ the Clebsch-Gordan coefficient.

K_D, K_P, K_N, and α are related by the conservation of energy by

$$\frac{\hbar^2K_N{}^2(M+M_I)}{2MM_I}+\frac{\hbar^2K_P{}^2}{2M}\frac{(M_I+2M)}{(M_I+M)}$$
$$=\frac{\hbar^2K_D{}^2}{2M_D}\frac{(M_I+M_D)}{M_I}-\frac{\hbar^2\alpha^2}{M}. \tag{32}$$

$\beta_{Lm}{}^{c*}$ is defined after Eq. (26).

Setting $Z=0$, $\beta_{Lm}{}^{c*}=0$, and $\delta_\lambda=0$ causes Eq. (31) to have the form

$$B_f{}^{lm}=-\frac{\hbar^2(8\pi\alpha)^{\frac{1}{2}}}{Mh_l{}^{(1)}(K_NR_I)}\int_{R_I(1+M/M_I)}^{\infty}d\mathbf{r}Y_l{}^{-m}(\theta_r)$$
$$\times h_l{}^{(1)}(K_Nr)\exp\left[i\left(\mathbf{K}_D-\frac{\mathbf{K}_P}{1+M/M_I}\right)\cdot\mathbf{r}\right]. \tag{34}$$

Carrying out the integration over angles gives

$$B_f{}^{lm}=-\frac{4\pi\hbar^2i^l\delta_{m0}[2\alpha(2l+1)]^{\frac{1}{2}}}{Mh_l{}^{(1)}(K_NR_I)}\int_{R_I(1+M/M_I)}^{\infty}dr r^2$$
$$\times h_l{}^{(1)}(K_Nr)j_l(\kappa r), \tag{35}$$

where $\boldsymbol{\kappa}=\mathbf{K}_D-\mathbf{K}_P[1+(M/M_I)]^{-1}$ and δ_{m0} is the Kronecker delta symbol. The radial integral can be performed to give

$$B_f{}^{lm}=\frac{4\pi hi^l\delta_{m0}[2\alpha(2l+1)]^{\frac{1}{2}}}{M(K_N{}^2-\kappa^2)}\left\{r^2\left[\frac{\partial}{\partial r}j_l(\kappa r)\right.\right.$$
$$\left.\left.-j_l(\kappa r)\frac{\partial}{\partial r}\log h_l{}^{(1)}(K_Nr)\right]\right\}_{r=R_I(1+M/M_I)}. \tag{36}$$

By means of the conservation of energy the denominator is changed:

$$B_f{}^{lm}=-\frac{2\pi hi^l\delta_{m0}[2\alpha(2l+1)]^{\frac{1}{2}}}{M(\alpha^2+k_d{}^2)}\left\{r^2\left[\frac{\partial}{\partial r}j_l(\kappa r)\right.\right.$$
$$\left.\left.-j_l(\kappa r)\frac{\partial}{\partial r}\log h_l{}^{(1)}(K_Nr)\right]\right\}_{r=R_I(1+M/M_I)}, \tag{37}$$

where $\mathbf{k}_d=\mathbf{K}_P-\frac{1}{2}\mathbf{K}_D$. This expression is the boundary condition matching scattering amplitude when V_{NP} is assumed to have zero range.

We see that Eq. (31) gives a spherical harmonic expansion of $B_f{}^{lm}$ of the form

$$B_f{}^{lm}=\sum_L P_L{}^{|m|}(\cos\theta)\sum_\lambda A_{L\lambda}{}^{lm}f_{L\lambda}{}^{l}.$$

The fact that $A_{L\lambda}{}^{lm}$ is proportional to $(L\lambda00|L\lambda l0)$ limits the sum over λ to the values $\lambda=l+L$, $l+L-2$, $l+L-4$, $\cdots$, $|L-l|$. So for each value of L we must evaluate no more than $l+1$ radial integrals. For cases where the energy of the incident deuterons is about 15

Mev, the sum over L can be broken off at $L\approx 15$ without introducing great error. For smaller incident energies the range of L that is important is correspondingly smaller.

Since $h_l^{(1)}(ix)$ contains the factor e^{-x} we will usually introduce an error of about 1 percent if we replace the upper limit of infinity for the radial integrations by $X[1+(4.6/X)]$. X generally has values in the neighborhood of 4, so we see that the important range of integration for the radial integrals is from about $r=R$ to about $r=2R$.

The radial integrals appear to be suited to numerical evaluation. However, since the radial Coulomb functions are not adequately tabulated for this problem, the evaluation of these integrals will have to be done with an automatic computer or by means of some approximate method.

VI. AN ALTERNATE DERIVATION

We present here an alternate treatment of the (d,p) process. While this treatment leads to a result very similar to that given above, the approximations made are somewhat different and the final result is related very directly to the boundary condition matching result.

Again we neglect the Coulomb interaction, assume that all particles have zero spin, and assume that the mass of the target nucleus is infinite for the sake of simplicity. Let $\mathfrak{f}(\mathbf{K}_P,\mathbf{r}_P)$ be the wave function describing the motion of the liberated protons with asymptotic momentum $\hbar\mathbf{K}_P$. For large r_P the outgoing part of $\mathfrak{f}$ has the same form as the outgoing part of $e^{i\mathbf{K}_P\cdot\mathbf{r}_P}$. The (d,p) cross section is proportional to the rate at which deuterons are broken up to liberate protons with wave function $\mathfrak{f}(\mathbf{K}_P,\mathbf{r}_P)$

Assume $\mathfrak{f}$ is a member of a complete set of orthonormal functions. Then the wave function for the $A+1$ nucleons associated with the proton in the state $\mathfrak{f}(\mathbf{K}_P,\mathbf{r}_P)$ is

$$\psi(\mathbf{K}_P,\xi,\mathbf{r}_N)=\int d\mathbf{r}_P\mathfrak{f}^*(\mathbf{K}_P,\mathbf{r}_P)\Psi(\xi,\mathbf{r}_N,\mathbf{r}_P). \tag{38}$$

The rate at which protons are liberated into state $\mathfrak{f}(\mathbf{K}_P,\mathbf{r}_P)$ is just equal to the rate at which the nucleons described by $\psi(\mathbf{K}_P,\xi,\mathbf{r}_N)$ are forming residual nuclei. This is just the net flux of neutrons into the target nucleus predicted by ψ:

$$J(\mathbf{K}_P)=-\frac{\hbar R^2}{2Mi}\int d\xi d\Omega_N \times\left[\psi^*(\mathbf{K}_P,\xi,r_N)\frac{\partial}{\partial r_N}\psi(\mathbf{K}_P,\xi,\mathbf{r}_N) -\psi(\mathbf{K}_P,\xi,\mathbf{r}_N)\frac{\partial}{\partial r_N}\psi^*(\mathbf{K}_P,\xi,\mathbf{r}_N)\right]_{r_N=R}. \tag{39}$$

In terms of J the (d,p) cross section is

$$\sigma(\mathbf{K}_P)=\int_{K_P-}^{K_P+}dK\sigma_1(\mathbf{K}),$$
$$\sigma_1(\mathbf{K})=\frac{K^2}{\mathcal{J}}J(\mathbf{K})=\frac{M_D}{\hbar K_D}K^2J(\mathbf{K}). \tag{40}$$

The integration is over a resonance due to a level in the residual nucleus.

Equation (40) would provide an exact expression for the (d,p) cross section except for the fact that we must assume $\mathfrak{f}$ is a member of a complete set of functions. This means that the interaction between the proton and the residual nucleus is assumed to be elastic so that it can be represented by a real potential function $\bar{V}_{PP}(r_P)$. This assumption rules out the possibility for compound nucleus formation so that the (d,p) process is pictured in this treatment as going entirely by stripping.

To evaluate Eq. (40) for the cross section we proceed as before. Namely, we write the integral equation for $\psi(\mathbf{K}_P,\xi,\mathbf{r}_N)$, eliminate the interior of the target nucleus, and substitute the result into Eq. (40).

First we define $\mathfrak{f}(\mathbf{K}_P,\mathbf{r}_P)$ to be the solution of

$$\left(T_P+\bar{V}_{PP}-\frac{\hbar^2K_P^2}{2M}\right)\mathfrak{f}(\mathbf{K}_P,\mathbf{r}_P)=0, \tag{41}$$

which is the time reflection of the wave function for a beam of protons incident with momentum $-\hbar\mathbf{K}_P$ on the scattering center $\bar{V}_{PP}$. Let $\Phi_i(\xi)$ be the orthonormal regular solutions of

$$(H_I-E_i)\Phi_i(\xi)=0.$$

Then we expand the wave function $\Psi(\xi,\mathbf{r}_N,\mathbf{r}_P)$ as follows:

$$\Psi(\xi,\mathbf{r}_N,\mathbf{r}_P)=\int d\mathbf{K}_P\psi(\xi,\mathbf{r}_N,\mathbf{K}_P)\mathfrak{f}(\mathbf{K}_P,\mathbf{r}_P) =\sum_{l,m,i}\int d\mathbf{K}_P\phi_i^{lm}(\mathbf{K}_P,r_N) \times Y_l^m(\theta_N)\Phi_i(\xi)\mathfrak{f}(\mathbf{K}_P,\mathbf{r}_P). \tag{42}$$

Introducing this expansion into Eq. (8) gives the Schrödinger equation for ϕ_i^{lm}:

$$[T_N^{(l)}-E_{Ni}]\phi_i^{lm}(\mathbf{K}_P,r_N) =-\int d\mathbf{r}_P d\xi d\Omega_N\mathfrak{f}^*(\mathbf{K}_P,\mathbf{r}_P)\Phi_i^*(\xi)Y_l^{-m}(\theta_N) \times[V_{NP}+V_{IP}+V_{IN}-\bar{V}_{PP}]\Psi, \tag{43}$$

where

$$T_N^{(l)}=-\frac{\hbar^2}{2M}\left\{\frac{\partial^2}{\partial r_N^2}+\frac{2}{r_N}\frac{\partial}{\partial r_N}-\frac{l(l+1)}{r_N^2}\right\},$$
$$E_{Ni}=E-E_i-\frac{\hbar^2K_P^2}{2M}=\frac{\hbar^2K_{Ni}^2}{2M}.$$

By means of the Green's function for $T_N^{(1)}-E_{Ni}$ we get the integral equation for ϕ_i^{lm}:

$$\phi_i^{lm}(\mathbf{K}_P,\mathbf{r})=\frac{2K_{Ni}M}{i\hbar^2}\int d\mathbf{r}_N d\mathbf{r}_P d\xi\, j_l(K_{Ni}r_<)\times h_l^{(1)}(K_{Ni}r_>)Y_l^{-m}(\theta_N)\Phi_i^*(\xi)\times\mathfrak{f}^*(\mathbf{K}_P,\mathbf{r}_P)[V_{NP}+V_{IP}+V_{IN}-\bar{V}_{FP}]\Psi, \quad (44)$$

where

$$r_<=\begin{cases} r & r<r_N \\ r_N & r_N<r \end{cases}, \quad r_>=\begin{cases} r & r>r_N \\ r_N & r<r_N \end{cases}.$$

Equation (44) contains the asymptotic boundary condition that all the liberated neutrons at infinity are outgoing.

Let $V_{IN}=0$ for $r_N>R$. Proceeding as before we eliminate the contribution to ϕ_i^{lm} due to the range of integration $0\leq r_N\leq R$ by introducing the logarithmic derivative of ϕ_i^{lm} at $r_N=R$.

$$\phi_i^{lm}(\mathbf{K}_P,\mathbf{r})=\frac{2K_{Ni}M}{i\hbar^2}\int d\mathbf{r}_P d\xi\int_R^\infty d\mathbf{r}_N j_l(K_{Ni}r_<)\times h_l^{(1)}(K_{Ni}r_>)Y_l^{-m}(\theta_N)\Phi_i^*(\xi)\mathfrak{f}^*(\mathbf{K}_P,\mathbf{r}_P)\times[V_{NP}+V_{IP}-\bar{V}_{FP}]\Psi-\Pi_i^{lm}h_l^{(1)}(K_{Ni}r), \quad (45)$$

where $r>R$

$$\Pi_i^{lm}=\left[\frac{\frac{\partial}{\partial r}j_l(K_{Ni}r)-j_l(K_{Ni})\frac{\partial}{\partial r}\log\phi_i^{lm}(\mathbf{K}_P r)}{\frac{\partial}{\partial r}\log h_l^{(1)}(K_{Ni}r)-\frac{\partial}{\partial r}\log\phi_i^{lm}(\mathbf{K}_P r)}\right]_{R=r}\times\frac{2K_NM}{i\hbar^2}\bar{B}_i^{lm},$$

$$\bar{B}_i^{lm}=\int d\mathbf{r}_P d\xi\int_R^\infty d\mathbf{r}_N\frac{h_l^{(1)}(K_{Ni}r_N)}{h_l^{(1)}(K_{Ni}R)}Y_l^{-m}(\theta_N)\times\Phi_i^*(\xi)\mathfrak{f}^*(\mathbf{K}_P,\mathbf{r}_P)[V_{NP}+V_{IP}-\bar{V}_{FP}]\Psi.$$

For $r=R$, Eq. (45) becomes

$$\phi_i^{lm}(\mathbf{K}_P,R)=\frac{2M}{\hbar^2R^2}\bar{B}_i^{lm}\left[\frac{\partial}{\partial r}\log h_l^{(1)}(K_{Ni}r)-\frac{\partial}{\partial r}\log\phi_i^{lm}(\mathbf{K}_P,r)\right]_{r=R}^{-1}. \quad (46)$$

Substituting the expansion of $\psi(\xi,\mathbf{r}_N,\mathbf{K}_P)$ contained in Eq. (42) into Eq. (40) and using Eq. (46) gives

$$\sigma_1(\mathbf{K}_P)=-\frac{4K_P^2M_DM}{\hbar^4R^2K_D}\times\sum_{i,l,m}\frac{|\bar{B}_i^{lm}|^2 Im.\left[\frac{\partial}{\partial r}\log\phi_i^{lm}(\mathbf{K}_P,r)\right]_{r=R}}{\left|\frac{\partial}{\partial r}\log h_l^{(1)}(K_{Ni}r)-\frac{\partial}{\partial r}\log\phi_i^{lm}(\mathbf{K}_P,r)\right|^2_{R=r}}. \quad (47)$$

The (d,p) cross section due to a level of the residual nucleus results from integrating σ_1 over the corresponding resonance. To represent such a resonance we assume that for values of K_P near $K_{P'}$, the

$$[\partial\log\phi_i^{lm}(\mathbf{K}_P,r)/\partial r]_R$$

for one value of i, say $i=f$, become very nearly equal to $[\partial\log h_l^{(1)}(K_{Nf}r)/\partial r]_R$. In this energy region we can write

$$\left[\frac{\partial}{\partial r}\log\phi_f^{lm}(\mathbf{K}_P,r)-\frac{\partial}{\partial r}\log h_l^{(1)}(K_{Nf}r)\right]_R=-\frac{1}{R\gamma_{lf}}\left[E_{Nf}-E_{Nf'}+\frac{i\Gamma}{2}\right]. \quad (48)$$

We substitute Eq. (48) into Eq. (47), integrate $\sigma_1(\mathbf{K}_P)dK_P$ over a narrow range, and let $\Gamma\to 0$. The result is

$$\sigma(\mathbf{K}_P)=\frac{4\pi M^2K_PM_D}{\hbar^6RK_D}\sum_{l,m}\gamma_{lf}|\bar{B}_f^{lm}|^2. \quad (49)$$

Taking spin, the Coulomb interaction, and the finite mass of the target nucleus into account changes this to

$$\sigma(\mathbf{K}_P)=\frac{\left(1+\frac{M}{M+M_I}\right)^{-1}}{\left(1+\frac{M}{M_I}\right)\left(1+\frac{M_D}{M_I}\right)}\frac{M_DM^2}{\hbar^6R}\frac{(2J+1)}{(2I+1)}\frac{K_P}{K_D}\times\sum_{l,m}{}'\frac{\gamma_{lf}}{2l+1}|\bar{B}_f^{lm}|^2, \quad (50)$$

where

$$\bar{B}_f^{lm}=\frac{1}{h_l^{(1)}(K_NR)}\int d\varrho_P d\xi\int_R^\infty d\mathbf{r}_N h_l^{(1)}(K_N\mathbf{r}_N)\times Y_l^{-m}(\theta_N)\Phi_i^*(\xi)\mathfrak{f}^{c*}(\mathbf{K}_P,\varrho_P)\times\left[V_{NP}+V_{IP}+Ze^2\left(\frac{1}{r_P}-\frac{1}{\rho_P}\right)-\bar{V}_{FP}\right]\Psi, \quad (51)$$

$$\left[T_P+\bar{V}_{FP}+\frac{Ze^2}{\rho_P}-\frac{\hbar^2K_P^2}{2M}\right]\mathfrak{f}^c(\mathbf{K}_P,\varrho_P)=0.$$

Equation (50) is identical with Eq. (28) except for a factor of $(2\pi)^3$ due to the difference in normalization between $\mathfrak{f}$ and $\mathcal{S}$ and except for the difference in the definitions of B and $\bar{B}$.

Let us assume that V_{IP} can be approximated by a potential function $\bar{V}_{IP}(r_P)$. Then we would expect that $\bar{V}_{IP}$ is very nearly the same function of r_P as $\bar{V}_{FP}$ is of ρ_P. It follows that the contribution of

$$\Delta\bar{V}=V_{IP}-\bar{V}_{FP}+Ze^2\left(\frac{1}{r_P}-\frac{1}{\rho_P}\right)\approx\bar{V}_{IP}-\bar{V}_{FP}+Ze^2\left(\frac{1}{r_P}-\frac{1}{\rho_P}\right)$$

to $\bar{B}_f^{lm}$ is small and tends to vanish as $M_I \to \infty$. Upon dropping $\Delta\bar{V}$ we see that the range of integration $0 \leqslant \rho_P \leqslant R(1+M/M_I)$ will make a negligible contribution to $\bar{B}_f^{lm}$ because of the short range of V_{NP} so let us drop this range of integration. Since ρ_P is now always greater than R in $\bar{V}_f^{lm}$, the form of $\mathfrak{f}^{c*}(\mathbf{K}_P,\boldsymbol{\rho}_P)$ is

$$\mathfrak{f}^{c*}(\mathbf{K}_P,\boldsymbol{\rho}_P)=\frac{4\pi}{(2\pi)^{\frac{3}{2}}}\sum_{L,M} i^{-L}Y_L^{-M}(\theta_{\rho P})Y_L^{M}(\theta_{KP})e^{-i\sigma_L(\eta_P)}\left[\frac{F_L(\eta_P,K_P\rho_P)-\bar{\beta}_L{}^{c*}H_L(\eta_P,K_P\rho_P)}{K_P\rho_P}\right], \tag{52}$$

$$\bar{\beta}_L{}^{c*}=\left[\frac{\dfrac{\partial}{\partial r}\dfrac{F_L(\eta_P,K_Pr)}{K_Pr}-\dfrac{F_L(\eta_P,K_Pr)}{K_Pr}\dfrac{\partial}{\partial r}\log \mathfrak{f}_{LM}{}^{c*}(\mathbf{K}_P,r)}{\dfrac{\partial}{\partial r}\dfrac{H_L(\eta_P,K_Pr)}{K_Pr}-\dfrac{H_L(\eta_P,K_Pr)}{K_Pr}\dfrac{\partial}{\partial r}\log \mathfrak{f}_{LM}{}^{c*}(\mathbf{K}_P,r)}\right]_R;$$

$\mathfrak{f}^{c*}$ is the wave function describing the scattering of protons of momentum $-\hbar\mathbf{K}_P$ by the potential $\bar{V}_{FP}(\rho_P)$. Hence the $\bar{\beta}_L{}^{c*}$ are the scattering amplitudes for free protons incident on $\bar{V}_{FP}$. Thus if $\bar{V}_{FP}$ is a good approximation to V_{FP}, then $\mathfrak{f}^{c*}$ is a good approximation to $\mathcal{E}^{c*}$ defined in Eq. (26).

Setting $\Delta\bar{V}=0$, $V_{NP}=$ the zero range potential, and $\Psi=\Psi_{\text{s.m.}}\chi\Phi_I$ causes $\bar{B}_I^{lm}$ to be essentially equal to B_f^{lm} defined in Eq. (31) when $V_{FP}=\bar{V}_{FP}$. This derivation of Eq. (31) is not so satisfactory as our previous derivation since we are forced in the present derivation to replace V_{FP} by a real potential function of ρ_P and the contribution of $\Delta\bar{V}$ is not so obviously small as the contribution of ΔV. However in the present derivation the interpretation of $\bar{\beta}^{c*}$ is unambiguous and agrees with our previous interpretation of β^{c*}. γ_{iI} on the other hand can only approximately be identified with the reduced width of the level of the captured neutron in the residual nucleus.

The present derivation is also of interest because it is connected directly with the general boundary condition matching result. To demonstrate this we assume that $\bar{V}_{FP}=V_{IP}$ and $Z=0$. Then Eq. (51) becomes

$$\bar{B}_i^{lm}=\int d\boldsymbol{\rho}_P d\xi\int_R^\infty d\mathbf{r}_N\frac{h_l^{(1)}(K_Nr_N)}{h_l^{(1)}(K_NR)}Y_l^{-m}(\theta_N)\times\Phi_i^*(\xi)\mathfrak{f}^*(\mathbf{K}_P,\boldsymbol{\rho}_P)V_{NP}\Psi \tag{53}$$

$$=-\frac{\hbar^2R^2}{2M}\left[\frac{\partial}{\partial r}A_i^{lm}-A_i^{lm}\frac{\partial}{\partial r}\log h_l^{(1)}(K_Nr_N)\right]_{r=R},$$

where

$$A_i^{lm}=\frac{2MK_{Ni}}{i\hbar^2}\int d\boldsymbol{\rho}_P d\mathbf{r}_N d\xi\, j_l(K_Nr_<)h_l^{(1)}(K_Nr_>)\times Y_l^{-m}(\theta_N)\Phi_i^*(\xi)\mathfrak{f}^*(\mathbf{K}_P,\boldsymbol{\rho}_P)V_{NP}\Psi$$
$$=A_i^{lm}(\Psi).$$

Now set $\Psi=\Psi^0$, the wave function for the incident beam of deuterons and the target nucleus. But by Eq. (44) the transform of Ψ^0,

$$\phi_i^{0lm}(\mathbf{K}_P,\mathbf{r}_N)=\int d\boldsymbol{\rho}_P d\xi d\Omega_N Y_l^{-m}(\theta_N)\mathfrak{f}^*(\mathbf{K}_P,\boldsymbol{\rho}_P)\Phi_i^*(\xi)\Psi^0,$$

is the solution of the integral equation

$$\phi_i^{0lm}=\delta_{iI}A_i^{lm}(\Psi^0). \tag{54}$$

Therefore

$$\bar{B}_i^{lm}=-\frac{\delta_{iI}\hbar^2R^2}{2M}\left[\frac{\partial}{\partial r_N}\phi_I^{0lm}-\phi_I^{0lm}\frac{\partial}{\partial r_N}\times\log h_l^{(1)}(K_Nr_N)\right]_R, \tag{55}$$

which is the general form of the boundary condition matching result.

VII. ACKNOWLEDGMENT

I am grateful to H. A. Bethe, R. H. Dalitz, and N. Austern for many enlightening discussions on this topic. I also wish to thank J. Horowitz and A. M. L. Messiah for their helpful criticism of this work.

A Modified Shell Model of Odd-Even Nuclei*

A. B. VOLKOV†
University of Wisconsin, Madison, Wisconsin
(Received December 3, 1953)

Certain magnetic interaction data (static magnetic moments and "forbidden" magnetic dipole transitions) are interpreted on the basis of a modified shell model of odd-even nuclei. The nuclear wave function is assumed to be primarily an equally weighted admixture of states formed from all possible odd-particle configurations within the odd-particle open shell of the Mayer-Jensen shell model. These configurations are coupled in a prescribed manner so as to give the total angular momentum and parity of the nucleus. The agreement with the data represents a considerable improvement over the Mayer-Jensen model.

I. INTRODUCTION

THE independent-particle shell model of Mayer[1] and Haxel, Jensen, and Suess[2] has been remarkably successful in accounting for the angular momenta and parities of the low states of odd-even nuclei. However, there are many reasons to believe that nuclear wave functions are not accurately described by the model, that they contain important mixtures of terms other than that one suggested by the shell model. Evidence for this belief comes from almost any datum depending on the detailed structure of the wave function, the magnetic and quadrupole moments, the rates of isomeric transitions,[3] the reduced widths for neutron reactions,[4] and so on. When consideration is given to the way in which the shell model is to be modified to yield better wave functions, it is natural to start with modifications that change the model only slightly. Various modifications have been considered[5] in attempts to account for the data but none of the models seems to give an unambiguous account of the deviations of the nuclear magnetic moments from the Schmidt lines or the rate of the forbidden $M1$ transitions.[6] It has been suggested[7] that these effects can be ascribed to meson exchange currents, but Ross has presented arguments against this as a reasonable explanation of the deviations from the Schmidt lines.

Certain regularities in the behavior of the magnetic moment deviations suggest that the deviations of the wave function from the shell model primarily involve the sharing of angular momentum among several of the nucleons of odd type in the odd-even nuclei. This would mean that pairs of odd-type nucleons are not always coupled to zero angular momentum, but that the wave function contains terms in which three or more nucleons have their j values combined to form the total nuclear spin.

The regularities in question were first pointed out by Schawlow and Townes.[8] They called attention to the fact that the relative deviation from the Schmidt lines of the moment of an odd-even nucleus having an odd number Z of protons is about the same as that of the odd-even nucleus having Z neutrons, if the two (conjugate) nuclei have the same spin. This suggests some sort of mirror property of the moments of conjugate nuclei despite the fact that the numbers and configurations of even-type nucleons in the two nuclei are quite different. However such a mirroring might be expected to occur as long as the even-type nucleons do not share in the total angular momentum of the nucleus.

The simplest modification of the Mayer-Jensen model which would seem to be consistent with the mirror property would be to assume that the even-type nucleons are all coupled to zero angular momentum (without reference to detailed configurations) but that various combinations of the angular momenta of the odd-type nucleons contribute to the wave function. It seems reasonable to assume not only that states in which the angular momenta of pairs of odd-type nucleons are coupled to values different from zero contribute to the wave function, but that contributions also arise from all possible odd-nucleon configurations which can be formed within the shell structure of the Mayer-Jensen model.

This modification of the shell model is quite different from the various forms of the collective model[9] because no distinction is made between the even-type and odd-type nucleons in that model insofar as admixed terms in the wave functions are concerned. It is hard to see how the collective model can account for the mirror property in a natural way. However, it is possible that admixtures of both types must be considered, and that the collective motion makes only a small contribution to the magnetic moment but a large contribution to the quadrupole moment.

The modification of the shell model considered here

* This work was supported by the U. S. Atomic Energy Commission.
† Present address: University of Delaware, Newark, Delaware.
[1] M. G. Mayer, Phys. Rev. **78**, 16 (1950).
[2] Haxel, Jensen, and Suess, Z. Physik **128**, 295 (1950).
[3] S. A. Moszkowski, Phys. Rev. **89**, 474 (1953); V. B. Stech, Z. Naturforsh. **7a**, 401 (1952).
[4] T. Teichmann and E. P. Wigner, Phys. Rev. **87**, 123 (1952).
[5] See E. Feenberg, Ann. Rev. Nuclear Sci. **1**, 43 (1952).
[6] R. G. Sachs and M. Ross, Phys. Rev. **84**, 379 (1951).
[7] H. Miyazawa, Progr. Theoret. Phys. Japan **6**, 263 (1951); A. de-Shalit, Helv. Phys. Acta **24**, 296 (1951); F. Bloch, Phys. Rev. **83**, 839 (1951); A. Russek and L. Spruch, Phys. Rev. **87**, 1111 (1952); M. Ross, Phys. Rev. **88**, 939 (1952).
[8] A. L. Schawlow and C. H. Townes, Phys. Rev. **82**, 268 (1951); J. P. Davidson, Phys. Rev. **85**, 432 (1952).

involves the admixing of states[9] in which all but the last of the odd-type nucleons are coupled to angular momentum 2, since the evidence from even-even nuclei indicates[10] that this should be the energetically favored configuration. Furthermore, the angular momentum 2 states are assumed to be formed by even numbers of odd-type nucleons in equivalent states (having the same, n, j, and l quantum numbers). Many parameters are thereby introduced into the wave function and they can be adjusted to fit almost any magnetic moment. To reduce the ambiguity in the results it is assumed that every one of the possible configurations, of the type considered, contributes equally to the wave function and that interference terms in the magnetic moment average to zero. The resulting model will be referred to as the *statistical shell model*. It should not be considered as a model of a single nucleus but, instead, as a model giving the average behavior of a large group of nuclei having the same spin and the same unfilled shells of the Mayer-Jensen type. Thus, the average of the magnetic moments of nuclei in such a group is to be compared with the moment calculated by the statistical shell model. Fluctuations from one nucleus to another within the group are to be accounted for by deviations from the statistical form of the wave function.

The above described model is applied here with some success to calculation of the magnetic moments and to calculation of the rates of forbidden $M1$ transitions. A deviation from the model to allow for some sharing of the angular momentum by even-type nucleons is also considered. Indications are that deviations of this kind are largest for the heavy nuclei.

II. THE MIRROR PROPERTY

When comparing the experimentally observed magnetic moments of odd-even nuclei to the Schmidt lines, it is important to provide a scale in terms of which deviations can be measured. The following quantities provide an especially convenient measure of the deviations from the Schmidt lines:

$$\Delta^P = (\mu_s{}^P - \mu_{\exp}{}^P)/(\mu_p - \tfrac{1}{2}), \tag{1a}$$

$$\Delta^N = (\mu_s{}^N - \mu_{\exp}{}^N)/\mu_n, \tag{1b}$$

where Δ^P and Δ^N refer to odd-proton nuclei and odd-neutron nuclei, respectively, $\mu_s{}^P$ is the Schmidt value for the magnetic moment of the odd-proton nucleus, $\mu_s{}^N$ is the Schmidt value for the magnetic moment of the odd-neutron nucleus, $\mu_{\exp}{}^P$ and $\mu_{\exp}{}^N$ are the experimental magnetic moments of the corresponding nuclei and μ_n, μ_p are the neutron and proton moments. The quantities Δ^P and Δ^N will be referred to simply as "deviations" in the following discussion.

[9] Similar, but more restricted, wave functions have been used to study nuclear magnetic moments. A. de-Shalit, Phys. Rev. **90**, 83 (1953); Minoru Umezawa, Progr. Theoret. Phys. Japan **8**, 509 (1952).

[10] Gertrude Scharff-Goldhaber, Phys. Rev. **90**, 587 (1953).

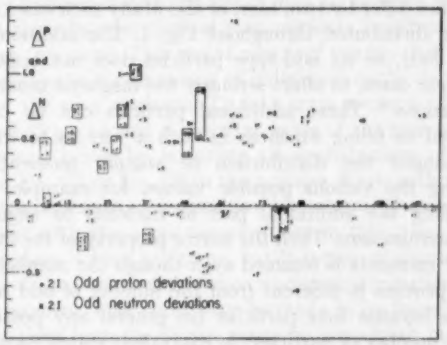

FIG. 1. The magnetic moment deviations of odd-even nuclei as a function of the number of the odd numbered nucleons. Twice the spin I of the nucleus is indicated beside each magnetic moment deviation.

The experimental magnetic moment deviations, as determined by Eqs. (1a) and (1b), are plotted[11] in Fig. 1 as a function of the number of odd particles in the odd-even nucleus. Odd-proton magnetic moment deviations are indicated by dots while odd-neutron magnetic moments are indicated by crosses. The total angular momentum I is written besides the indicated deviation. The Schmidt values are such that deviations inside the $I=L+\frac{1}{2}$ Schmidt line are *positive* (for both odd proton and odd neutron nuclei), while deviations inside the $I=L-\frac{1}{2}$ Schmidt lines are *negative*. Except for those nuclei with $\nu=1$, 7, and 113 odd nucleons, all the deviations plotted in Fig. 1 represent deviations *inside* the appropriate Schmidt line.

A number of systematic features of the magnetic moments are suggested by Fig. 1, and the one in which we are interested concerns those fifteen values of ν (excluding $\nu=1$ since these deviations are generally believed to be due to meson exchange currents) for which experimental deviations are recorded for both odd-proton and odd-neutron nuclei having the same ν and the same angular momentum I (conjugate pairs). The pairs (or in some cases, triplets) are boxed off[12] in Fig. 1. It is seen that the deviations for the odd-proton and odd-neutron nuclei with the same ν and I are generally close to each other.[5]

The close correlation of the majority of the conjugate pairs (or triplets) seems to indicate the mirror property discussed in the Introduction. Other, but less direct, evidence for such a mirror property is given by the near equality of the magnetic moment deviations for odd-proton and odd-neutron nuelci with the same I whose

[11] The experimental magnetic moments used to obtain this plot are from an unpublished compilation of nuclear moment data by Harold E. Walchli.

[12] The measured odd-neutron magnetic moments for $\nu=31$ ($_{26}Fe^{57}$) and $\nu=33$ ($_{28}Ni^{61}$) are quoted as $\mu_{\exp}\sim 0$ [P. F. A. Klinkenberg, Revs. Modern Phys. **24**, 63 (1952)] with a fairly large error possible. The conjugate pair with $\nu=33$ is boxed off because of the good correlation of the deviations, while the conjugate triplet with $\nu=31$ is not indicated because of the poor correlation. This procedure is highly arbitrary.

ν values differ by two, four, or six. Many such cases are found distributed throughout Fig. 1. The addition of two, four, or six odd-type particles does not appear, in these cases, to affect seriously the magnetic moment deviations.[13] These additional particles can be considered as filling subshells in such a way as to leave unchanged the distribution of angular momentum among the various possible values, for example, by coupling the additional pair of nucleons to angular momentum zero. Then the mirror property of the magnetic moments is retained even though the number of odd protons is different from the number of odd neutrons because four particles (in general any possible even number of particles) in equivalent states (same j and l) coupled to $J=2$ cannot be distinguished, with respect to any effect on the static magnetic moments, from two particles in equivalent states coupled to $J=2$.

The experimentally observed correlations of the conjugate pairs can be understood in terms of two conditions which are consistent with, but much more general than, the shell model. One of these is that *only the odd nucleons* carry the total angular momentum of the nucleons, the other, that the odd-nucleon wave functions satisfy a mirror condition. When the angular momentum I is assumed to be distributed only among the odd particles, the magnetic moment deviations as defined by Eqs. (1a) and (1b) are

$$\Delta^P=\frac{\epsilon(I)2I}{2L+1}-\langle\psi_I{}^I(P),\ \textstyle\sum_P \sigma_P{}^z\psi_I{}^I(P)\rangle, \tag{2a}$$

$$\Delta^N=\epsilon(I)\frac{2I}{2L+1}-\langle\psi_I{}^I(N),\ \textstyle\sum_N \sigma_N{}^z\psi_I{}^I(N)\rangle, \tag{2b}$$

where $\psi_I{}^I(P)$ and $\psi_I{}^I(N)$ are the wave functions of the odd protons of the odd-proton nucleus and of the odd neutrons of the odd-neutron nucleus respectively, and $\epsilon(j)=+1$ for $j=l+\frac{1}{2}$; $\epsilon(j)=-1$ for $j=l-\frac{1}{2}$. L is the orbital angular momentum that would be ascribed to the single odd nucleon on the basis of the nearest Schmidt line. If the wave functions $\psi_I{}^I(P)$ and $\psi_I{}^I(N)$ are the same when the number of protons is equal to the number of neutrons, then

$$\langle\psi_I{}^I(P),\ \textstyle\sum_P \sigma_P{}^z\psi_I{}^I(P)\rangle=\langle\psi_I{}^I(N),\ \sum_N \sigma_N{}^z\psi_I{}^I(N)\rangle. \tag{3}$$

This leads to the result

$$\Delta^P=\Delta^N.$$

Therefore, the experimentally observed correlations of the magnetic moment deviations can be understood by assuming that the even particles do not share the angular momentum I and that the odd-particle states are described by very similar wave functions.

The fact that the experimental deviations do not exactly satisfy Eq. (4) is not very surprising. Because the configurations of even-type nucleons are quite different, the wave functions of the odd nucleons cannot be expected to be just the same in the conjugate nuclei. Furthermore, any sharing of the nuclear angular momentum by the even nucleons would invalidate Eq. (4), even though the effect may be small if the even particle wave function is selected in just the right way. The point of view taken here is that the dominant contribution to admixtures in the wave function satisfy the conditions required for exact mirroring.

[13] In many instances there is also an additional increase in the number of even particles.

III. NUCLEAR MOMENTS

One advantage of a model in which just one kind of nucleon contributes to the angular momentum is that the calculation of the magnetic moment becomes very simple. For an odd-proton nucleus of total angular momentum I in which an even number of equivalent protons are coupled to an angular momentum 2, and which are in turn coupled to a final odd proton, the moment is

$$\mu^P=I+(\mu_p-\tfrac{1}{2})\left[\frac{\epsilon(j')2I}{2l'+1}+2\left(\frac{\epsilon(j)}{2l+1}-\frac{\epsilon(j')}{2l'+1}\right)\times\sum_m m|\langle j',2,I,I|j',2,I-m,m\rangle|^2\right], \tag{5}$$

where μ_p is the proton moment, j and l are the total and orbital angular momenta of the equivalent protons (in an unfilled shell) which are coupled to angular momentum 2, and j' and l' are the corresponding angular momenta of the final odd proton. The quantities $\langle j',2,I,I|j',2,I-m,m\rangle$ are the usual Clebsch-Gordan coefficients for the coupling of angular momenta j' and 2 to form angular momentum I (with magnetic quantum number I). For an odd-neutron nucleus the corresponding result is

$$\mu^N=\mu_n\left[\frac{\epsilon(j')2I}{2l'+1}+2\left(\frac{\epsilon(j)}{2l+1}-\frac{\epsilon(j')}{2l'+1}\right)\times\sum_m m|\langle j',2,I,I|j',2,I-m,m\rangle|^2\right]. \tag{6}$$

If the odd number of odd nucleons differs by more than one from a magic number there are a number of values that can be assigned to j, l and j', l' without removing a nucleon from the last (open) shell. If the moment (5) or (6) is calculated for each one of the possible assignments it is found that in by far the larger number of cases the resulting moment lies inside the corresponding Schmidt line. This result is interesting because the fact that nearly every observed magnetic moment lies between the Schmidt lines has always seemed mysterious. The present model, in which each of the possible assignments of j, l, and j', and l' values is given equal weight, is bound to lead to agreement with this qualitative fact.

It is useful to calculate contributions to the magnetic moment which arise when the even-type nucleons contribute to the nuclear angular momentum, because some insight into deviations from the statistical shell model may thereby be obtained. For the sake of simplicity, consideration is limited to that odd-nucleon configuration suggested by the Mayer-Jensen model. The even nucleons (in equivalent states) are coupled to angular momentum 2. The resulting magnetic moments are

$$\mu^P(\text{even}N)=\left[I-\frac{3}{I+1}\right]\left[1+\frac{\epsilon(I)2(\mu_p-\frac{1}{2})}{2L+1}\right]+\frac{\epsilon(j)6\mu_n}{(2l+1)(I+1)}, \quad (7)$$

$$\mu^N(\text{even}P)=\epsilon(I)\frac{2I\mu_n}{2L+1}+\left(1+\frac{2\epsilon(j)(\mu_p-\frac{1}{2})}{2l+1}-\frac{2\epsilon(I)}{2L+1}\mu_n\right)\frac{3}{I+1}, \quad (8)$$

where j and l are now characteristic of the equivalent nucleons in the open shell of the even type which are coupled to an odd-type particle having a total angular momentum $I=L\pm\frac{1}{2}$.

IV. THE STATISTICAL SHELL MODEL

The average magnetic moment of a class of nuclei having the same spin and the same open shells is now to be calculated by averaging the moments given by Eq. (5) or Eq. (6) over each of the possible[14] j, l and j', l' values. Equal weight is given to each such state and to the shell-model state. As we have remarked before, interference terms between the different configurations are neglected because their signs are expected to be as often negative as positive so their net contribution to the average should be small.

Although this statistical model is not expected to apply directly to any one nucleus, it is of some interest to note that in many cases the deviations of individual nuclei from the average behavior is not very great. It can be seen in Fig. 1 that the observed moments of nuclei in the same class do tend to lie close together. A striking example of this behavior is offered by the $I=7/2$ nuclei between $n=51$ and $n=57$. The discrepancy between $n=71$ and $n=73$ may be ascribed to the fact that the open shell of even nucleons is different in those two cases. This would mean, of course, that contributions to the moments of individual nuclei do arise from the even nucleons. To take some account of this possibility a second theoretical value of the moment is obtained below by including all contributions of the type Eq. (7) or Eq. (8) in the average. Each such term corresponding to each possible (j,l) value, is given equal weight with the other contributions in this case. This procedure is very arbitrary, but it serves to give some idea of the importance of even nucleon contributions to the moment. One point may be made in its favor: the deviations from the mirror property introduced in this way are quite small.

To compare the results of the model with the observed moments, eighty-five odd-even nuclei with measured magnetic moments and spins have been combined into 15 odd-proton–even-neutron classes and 15 odd-neutron–even-proton classes. These classes are indicated in Table I and in Table II, respectively. The total angular momentum I is indicated in the first column while the usually assigned shell-model state is given in the second column. The third and fourth columns indicate the unfilled neutron shell and proton shell respectively (the unfilled shell is indicated by the two closed shell numbers which constitute its upper and lower bounds). The fifth column gives the number of nuclei in the particular class being considered. The sixth column gives the average experimental magnetic moment, $\mu_{\text{exp}}{}^P(\text{av})$ or $\mu_{\text{exp}}{}^N(\text{av})$, of the nuclei in the class. The seventh column gives the calculated magnetic moment $\mu_1{}^P$ or $\mu_1{}^N$, obtained by considering admixtures of only odd-particle configurations in the statistical shell model, while the eighth column gives the calculated magnetic moment, $\mu_2{}^P$ or $\mu_2{}^N$ obtained from considering all possible admixtures in the statistical shell model. The ninth column gives the average of the absolute value of the magnetic moment deviations Δ^P or Δ^N for the nuclei in a given class which are to be compared to the deviations from the statistical shell model magnetic moments. The next two columns give the absolute deviations of the average experimental magnetic moments, $\mu_{\text{exp}}{}^P(\text{av})$ or $\mu_{\text{exp}}{}^N(\text{av})$, from $\mu_1{}^P$, and $\mu_2{}^P$, $\mu_2{}^N$ where these absolute deviations are defined as:

$$\delta_1{}^P=\frac{|\mu_1{}^P-\mu_{\text{exp}}{}^P(\text{av})|}{\mu_p-\frac{1}{2}}, \quad (9a)$$

$$\delta_1{}^N=\frac{|\mu_1{}^N-\mu_{\text{exp}}{}^N(\text{av})|}{\mu_n}, \quad (9b)$$

$$\delta_2{}^P=\frac{|\mu_2{}^P-\mu_{\text{exp}}{}^P(\text{av})|}{\mu_p-\frac{1}{2}}, \quad (10a)$$

$$\delta_2{}^N=\frac{|\mu_2{}^N-\mu_{\text{exp}}{}^N(\text{av})|}{\mu_n}. \quad (10b)$$

[14] When the shell is closed or one less or one more than closed, there is some ambiguity as to which configurations should be used in admixtures. In this work two particles are assumed to be promoted out of the closed or nearly closed shell (into equivalent states and usually coupled to zero), and the configurations of the now opened shell are used for admixture. In some cases, when there is one particle more than a closed shell, the closed shell is treated as still closed even though two particles have been promoted to what is then treated as the unfilled shell. This procedure is completely arbitrary.

Furthermore, for the very lightest nuclei admixtures of states from the next higher shell were also included in order to have enough states to speak meaningfully of a statistical shell model. In any event the statistical shell model prescription would not be expected to be really applicable for these very light nuclei.

TABLE I. Magnetic moment deviations of odd-proton nuclear classes.

I	Shell model state	N shell	P shell	No. of nuclei	$\mu_{\text{exp}}{}^P$(av)	$\mu_1{}^P$	$\mu_2{}^P$	Averaged Δ^P	$\delta_1{}^P$	$\delta_2{}^P$
1/2	$p_{1/2}$	50–82	20–50	4	−0.123	−0.320	−0.370	0.062	0.108	0.108
1/2	$s_{1/2}$	82–126	50–82	2	1.620	1.482	1.482	0.512	0.060	0.060
3/2	$p_{3/2}$	2–8	2–8	1	2.689	2.723	2.224	0.481	0.015	0.203
3/2	$d_{3/2}$	8–20	8–20	2	1.520	1.677	1.354	0.608	0.068	0.072
3/2	$d_{3/2}$	20–50	8–20	3	0.430	1.677	1.098	0.133	0.543	0.291
3/2	$p_{3/2}$	20–50	20–50	8	2.219	2.213	1.820	0.686	0.003	0.174
3/2	$d_{3/2}$	82–126	50–82	2	0.165	1.030	0.728	0.017	0.377	0.246
5/2	$d_{5/2}$	8–20	8–20	1	3.641	3.515	3.856	0.502	0.055	0.094
5/2	$f_{5/2}$	20–50	20–50	2	2.411	3.357	2.693	0.676	0.413	0.123
5/2	$d_{5/2}$	82–126	50–82	7	3.058	2.976	3.013	0.757	0.036	0.019
7/2	$f_{7/2}$	20–50	20–50	3	4.851	4.790	4.693	0.411	0.027	0.069
7/2	$g_{7/2}$	50–82	50–82	6	2.681	3.469	2.952	0.421	0.344	0.118
7/2	$g_{7/2}$	82–126	50–82	3	2.667	3.469	2.809	0.415	0.350	0.062
9/2	$g_{9/2}$	50–82	20–50	4	5.613	5.638	5.648	0.515	0.011	0.015
9/2	$h_{9/2}$	82–126	82–126	1	4.082	4.288	3.796	0.633	0.090	0.124

In Table III the weighted averages $\langle \text{av } \Delta^P \rangle$, $\langle \delta_1{}^P \rangle$, $\langle \delta_2{}^P \rangle$, $\langle \text{av } \Delta^N \rangle$, $\langle \delta_1{}^N \rangle$, and $\langle \delta_2{}^N \rangle$ of Table I and Table II are given. In the averaging process the weight for each class is given by the number of nuclei in the class. This procedure seems called for by the statistical nature of the theory. Thus, the average magnetic moment of a class which contains a large number of nuclei would be expected to agree with the theoretical magnetic moment on the statistical model better than that of a class composed of one or two nuclei. Individual differences in the ground states of nuclei within a class would be expected to average to zero if there is a sufficiently large number of nuclei in the class. A weighted average emphasizes this expectation.

Besides the simple weighted averages, Table III also gives the weighted averages of the $I=L+\frac{1}{2}$ and $I=L-\frac{1}{2}$ classes separately. When the averages $\langle \delta_1{}^P \rangle$, $\langle \delta_2{}^P \rangle$ and $\langle \delta_1{}^N \rangle$, $\langle \delta_2{}^N \rangle$ are compared to the appropriate averaged deviations from the Schmidt lines $\langle \text{av } \Delta^P \rangle$ and $\langle \text{av } \Delta^N \rangle$, it is seen that the statistical shell model gives a much better fit to the magnetic moment data than the Mayer-Jensen shell model. Thus in the best case, involving 26 nuclei, the $J=L+\frac{1}{2}$ odd-proton nuclei have $\langle \delta_1{}^P \rangle = 0.020$, i.e., an average deviation of the theoretical magnetic moments from the experimental magnetic moments of approximately 0.04 nuclear magnetons. This is to be compared to the average deviation from the Schmidt lines of $\langle \text{av } \Delta^P \rangle = 0.555$, i.e., over 1 nuclear magneton. The surprisingly good agreement in this case is probably fortuitous.

The moments of the $I=L+\frac{1}{2}$ nuclei are seen to be in generally better agreement with the statistical shell model than with the Mayer-Jensen model. There is also some improvement for the $I=L-\frac{1}{2}$ nuclei, but that is not so striking.

These averages, while quite significant, obscure some interesting features found in the body of Table I and and Table II. First, there is the fact that the variation of the average magnetic moments for classes with the same I and parity, but different unfilled shells, is in large measure predicted by the statistical shell model magnetic moments, e.g., the $p_{3/2}$ and $d_{5/2}$ classes in

TABLE II. Magnetic moment deviations of odd-neutron nuclear classes.

I	Shell model state	N shell	P shell	No. of nuclei	$\mu_{\text{exp}}{}^N$(av)	$\mu_1{}^N$	$\mu_2{}^N$	Average Δ^N	$\delta_1{}^N$	$\delta_2{}^N$
1/2	$p_{1/2}$	2–8	2–8	1	0.702	0.637	0.637	0.034	0.034	0.034
1/2	$s_{1/2}$	8–20	8–20	1	−0.555	−1.212	−1.212	0.710	0.343	0.343
1/2	$s_{1/2}$	50–82	50–82	8	−0.700	−1.050	−1.050	0.634	0.183	0.183
1/2	$p_{1/2}$	82–126	50–82	6	0.421	0.774	0.774	0.113	0.185	0.185
3/2	$p_{3/2}$	2–8	2–8	1	−1.177	−1.425	−0.679	0.385	0.130	0.286
3/2	$d_{3/2}$	8–20	8–20	1	0.643	0.626	0.856	0.264	0.009	0.111
3/2	$p_{3/2}$	20–50	20–50	1	−0.5	−0.621	−0.437	0.739	0.063	0.033
3/2	$d_{3/2}$	50–82	50–82	3	0.825	0.392	0.593	0.169	0.226	0.121
3/2	$p_{3/2}$	82–126	50–82	1	−0.613	−0.424	−0.171	0.680	0.099	0.231
5/2	$f_{5/2}$	28–50*	20–50	1	0.876	−0.170	0.669	0.257	0.547	0.108
5/2	$d_{5/2}$	50–82	20–50	3	−0.828	−0.532	−0.399	0.567	0.155	0.224
5/2	$f_{5/2}$	82–126	50–82	1	−0.66	−0.549	−0.169	1.060	0.058	0.257
7/2	$f_{7/2}$	20–50	20–50	2	−1.104	−1.076	−0.901	0.423	0.015	0.106
7/2	$f_{7/2}$	82–126	50–82	4	−0.713	−0.266	−0.377	0.627	0.234	0.176
9/2	$g_{9/2}$	20–50	20–50	2	−1.035	−0.928	−0.903	0.459	0.056	0.069

* The $f_{7/2}$ shell model level has been treated as a closed shell in this case in order to obtain satisfactory agreement.

Table I and the $p_{3/2}$ classes in Table II. Furthermore the δ_1 generally represent a better fit for the smaller unfilled shells (lighter nuclei), while the δ_2 represent a better fit for the larger unfilled shells (heavier nuclei), i.e., odd-particle admixtures alone give better agreement for lighter nuclei, while both odd-particle admixtures and even-particle admixtures give better agreement for heavier nuclei.

Agreement for nuclei in many classes could be improved by eliminating a few admixed states or by a judicious weighting of the admixed states, a weighting based on considerations of the shell model. However, such a detailed treatment does not seem warranted, since the theory is already rather arbitrary. The improved agreement by use of the statistical shell model with the experimental magnetic moments seems to indicate that a fairly large number of admixed states may be necessary to give an adequate description of the ground states of complex nuclei.

V. "FORBIDDEN" MAGNETIC DIPOLE TRANSITIONS

Graham and Bell[15] have measured the lifetimes of several isomeric magnetic dipole ($M1$) radiative transitions which should be forbidden on the basis of the Mayer-Jensen shell model. The measured lifetimes of these transitions were found to be comparable to the lifetimes of allowed $M1$ transitions. The experimental lifetimes of the forbidden transitions indicate that either the ground state and excited state are not adequately described by the Mayer-Jensen shell model or the magnetic moment operator has terms in addition to the ordinary magnetic moment operator, e.g., exchange magnetic moment operators, which are not subject to the selection rule $\Delta L=0$, as is the ordinary magnetic moment operator. The latter point of view was that considered by Sachs and Ross.[6]

TABLE III. Weighted averages of magnetic moment deviations.

	$\langle \text{av } \Delta^P \rangle$	$\langle \delta_1^P \rangle$	$\langle \delta_2^P \rangle$	$\langle \text{av } \Delta^N \rangle$	$\langle \delta_1^N \rangle$	$\langle \delta_2^N \rangle$
All nuclei	0.485	0.167	0.121	0.454	0.169	0.169
$I=L+\frac{1}{2}$	0.555	0.020	0.076	0.590	0.158	0.178
$I=L-\frac{1}{2}$	0.383	0.348	0.159	0.215	0.187	0.152

The investigation in Sec. IV of the magnetic moment deviations indicated that the Mayer-Jensen shell model may be quite inadequate in the description of the ground states of complex nuclei. If this is the case, then the excited states are probably also composed of admixtures somewhat similar to those of the ground states. The statistical shell model, used in the last section to account for the static magnetic moment deviations, will be investigated in this section as a possible explanation for the "forbidden" $M1$ radiative transitions. However, it should be kept in mind that the actual cause of the forbidden $M1$ transitions is probably a rather complicated combination of exchange moments and admixtures of states rather than a single one of the two.

The $M1$ radiative transition probability is given by the expression

$$w_\gamma = \frac{1}{(2I'+1)}\left(\frac{e^2}{\hbar c}\right)\left(\frac{m}{\mathfrak{M}}\right)^2\left(\frac{mc^2}{\hbar}\right) \times E_\gamma^3 \sum_{M,M'} |\langle \psi_{I'}{}^{M'} \mathbf{u}\cdot\boldsymbol{\mu}\psi_I{}^{M}\rangle|^2 \quad (11)$$

$$= \frac{1.68\times 10^{12}}{2I'+1} E_\gamma^3 |\boldsymbol{\mu}|^2 \text{ sec}^{-1},$$

where E_γ is the photon energy of the radiative transition in units of mc^2, I' and M' are the total angular momentum and z component of the total angular momentum of the initial (excited) state of the nucleus in the transition, I and M are the total angular momentum and z component of the total angular momentum of the final (ground) state of the nucleus, $\mathbf{u}$ is an arbitrary unit vector which will be taken as the z axis in further calculations, $\boldsymbol{\mu}$ is the appropriate magnetic moment operator which will be assumed to be the ordinary magnetic moment operator in all further work in this section, and

$$|\boldsymbol{\mu}|^2 = \sum_{M,M'} |\langle \psi_{I'}{}^{M'}, \mathbf{u}\cdot\boldsymbol{\mu}\psi_I{}^{M}\rangle|^2.$$

TABLE IV. Half-lives, assignments, and matrix elements for $M1$ transitions.

Nucleus	E (kev)	$T_{\frac{1}{2}}$ (sec)	α Total	Spins I'	Spins I	$\lvert\boldsymbol{\mu}\rvert^2$
Li^7	478	$(5.2\pm1.7)\times10^{-14}$	0	$p_{1/2}$	$p_{3/2}$	53.308
Fe^{57}	14	(1.1×10^{-7})	10	$p_{1/2}$	$p_{3/2}$	0.031
Te^{123}	159	$(1.9\pm0.3)\times10^{-10}$	0.21	$d_{3/2}$	$s_{1/2}$	0.223
Te^{125}	35.4	$(1.58\pm0.15)\times10^{-9}$	18	$d_{3/2}$	$s_{1/2}$	0.157
Xe^{131}	80	$(4.8\pm2.0)\times10^{-10}$	2.0	$s_{1/2}$	$d_{3/2}$	0.137
Cs^{133}	81	$(6.0\pm0.4)\times10^{-9}$	2.1	$d_{3/2}$	$g_{7/2}$	0.031
Cs^{135}	248	$(2.8\pm0.8)\times10^{-10}$	0.1	$d_{3/2}$	$g_{7/2}$	0.072
Pm^{147}	91.5	$(2.44\pm0.08)\times10^{-9}$	2.2	...	$d_{3/2}$	0.083

The experimental data and the experimental values for $|\boldsymbol{\mu}|^2$ are given in Table IV. In determining the experimental values of $|\boldsymbol{\mu}|^2$ from measured half-lives ($T_{1/2}$ in the third column of Table IV), the following relation between the transition probability and half-life is used:

$$w_\gamma(1+\alpha) = (\ln 2)/T_{1/2}, \quad (12)$$

where α is the total conversion coefficient.

All the nuclei listed in Table IV, with the exception of Li^7 and Fe^{57}, provide examples of the "forbidden" transitions. The value of $|\boldsymbol{\mu}|^2$ varies from $\sim$0.22 to $\sim$0.03 for the forbidden transitions. These values are smaller than the predicted value for $|\boldsymbol{\mu}|^2$ for allowed transitions by a factor of approximately 50 to 150 ($|\boldsymbol{\mu}|^2$

[15] R. L. Graham and R. E. Bell, Can. J. Phys. 31, 377 (1953).

TABLE V. Comparison of observed and calculated matrix elements for $M1$ transitions. Experimental and theoretical values of the magnetic moments of the nuclei are also given for comparison.

Nucleus	μ_s	μ_{exp}	μ_{ssm}	N	N'	$\|\psi\|_{exp}^2$	$\|\psi\|_{ssm}^2$
$_{53}Te^{123}$	−1.913	−0.736	−1.050	7	20	0.223	0.263
$_{52}Te^{125}$	−1.913	−0.887	−1.050	7	20	0.157	0.263
$_{54}Xe^{131}$	1.148	0.708	0.593	20	7	0.137	0.263
$_{55}Cs^{133}$	1.715	2.577	2.952	16	20	0.031	0.403
$_{55}Cs^{135}$	1.715	2.727	2.952	16	20	0.072	0.403

differs by a factor of 7 to 13). The experimental values of $|\psi|^2$ for the allowed transitions in Li^7 and Fe^{57} are larger than predicted in the first instance and smaller in the second. It is interesting to note that the experimental $|\psi|^2$ for Fe^{57}, a supposedly allowed transition, is equal to the smallest experimental value of $|\psi|^2$ for the "forbidden" transitions.[16] It should also be noted that the magnetic moment deviation of $Fe^{57}(\mu_{exp}\sim 0)$ is very large on the basis of the assumed $p_{3/2}$ ground state.

The nuclei involved in the measured "forbidden" magnetic dipole radiative transitions are of two types. The odd neutron nuclei $_{53}Te^{123}$, $_{52}Te^{125}$, and $_{54}Xe^{131}$ involve transitions between states having total angular momentum 3/2 and 1/2 ($d_{3/2}$ and $s_{1/2}$ states according to the Mayer-Jensen shell model) while the odd proton nuclei[17] $_{55}Cs^{133}$ and $_{55}Cs^{135}$ involve transitions between states having total angular momentum 5/2 and 7/2 ($d_{5/2}$ and $g_{7/2}$ states according to the Mayer-Jensen shell model). All the nuclei are in the statistical shell model classes of 50–82 even particles and 50–82 odd particles.

Table V gives the value of $|\psi|^2$ calculated on the basis of the statistical shell model including even-particle admixtures ($|\psi|_{ssm}^2$) as well as the experimental value of $|\psi|^2(|\psi|_{exp}^2)$. In the calculation of $|\psi|_{ssm}^2$ the prescription for choosing admixtures for the excited state is just the same as the prescription for obtaining the ground state. Also indicated in the table is μ_s the Schmidt value of the magnetic moment, μ_{exp} the experimental value of the magnetic moment, μ_{ssm} the statistical shell model magnetic moment, and N and N' the total number of states (including the shell model states) admixed in the ground state and excited state respectively.

[16] It is quite possible that the assignment for Fe^{57} given by Graham and Bell ($p_{1/2}\rightarrow p_{3/2}$) is incorrect. On the basis of the Mayer-Jensen shell model and the observed magnetic moments the transition may actually be $f_{5/2}\rightarrow p_{3/2}$, i.e., a "forbidden" $M1$ transition.

[17] $_{61}Pm^{147}$ will not be considered in detail because there has been no definite assignment of Mayer-Jensen shell model states for this nucleus. However, the results for this case are probably very similar to those obtained for the Cs isotopes.

It is seen that the values of μ_{ssm} represent a better fit to the experimental magnetic moments μ_{exp} than do the Schmidt magnetic moments μ_s. The theoretical values of $|\psi|_{ssm}^2$ are larger than the corresponding experimental values $|\psi|_{exp}^2$. The agreement is quite good for the odd-neutron isotopes while the agreement is poor for the odd-proton isotopes. The poorest agreement (for Cs^{133}) gives $|\psi|_{ssm}^2/|\psi|_{exp}^2\sim 10$ or $|\psi|_{ssm}/|\psi|_{exp}\sim 3$.

However, the fact that the theoretical values of $|\psi|_{ssm}^2$ are larger than $|\psi|_{exp}^2$ is satisfying, since almost any reasonable modification of the statistical shell model would tend to make $|\psi|_{ssm}^2$ smaller. Thus any additional mixing of even-particle states or of the shell-model state results in a decrease in the value of $|\psi|_{ssm}^2$.

It is interesting to note that on the basis of the statistical shell model the value of $|\psi|^2$ for supposedly allowed magnetic dipole transitions would be expected to be of the same order of magnitude as for the "forbidden" transitions. This would explain the rather small experimental value[16] of $|\psi|^2$ found for Fe^{57}. The large value of $|\psi|^2$ found for Li^7 can probably be attributed to the fact that the statistical shell model would not be expected to apply to so light a nucleus.

VI. CONCLUSION

The statistical shell model appears to offer at least a partial explanation of two anomalous features of magnetic dipole phenomena as interpreted by the Mayer-Jensen shell model. First, the deviations of the static magnetic moments of odd-even nuclei are in large measure predicted by means of the statistical shell model. Then, the supposedly forbidden magnetic dipole radiative transitions are found to be allowed by the statistical shell model and the theoretical values of the transition probability are of the same order of magnitude as the experimentally determined values. The statistical shell model is undoubtedly an oversimplification of the true physical situation, but the success of this comparatively simple model indicates that the Mayer-Jensen shell model probably gives a rather poor description of the ground-state wave function of complex nuclei. The great success of the Mayer-Jensen model in predicting spins and parities does not necessarily justify the assumption that it also gives an adequate representation of the dynamical features of complex nuclei.

The author wishes to express his appreciation to Dr. R. G. Sachs for his suggestions and helpful discussions related to this investigation and to Mr. Harold Almond for his aid in many of the calculations.

Magnetic Internal Compton Coefficients in the Born Approximation*

LARRY SPRUCH AND G. GOERTZEL
Physics Department, Washington Square College, New York University, New York, New York

(Received March 15, 1954)

The absolute and relative probabilities of a nuclear transition in which there is a simultaneous ejection of a K electron and emission of a gamma ray has been calculated quantum-mechanically for the case in which the virtual radiation field is a 2^L magnetic multipole. The process will be referred to as an internal Compton effect. The Born approximation has been used and hence the calculations are expected to be valid only if the nuclear charge Z is small and the nuclear energy level separation large. The ratio of the number of continuous energy gamma rays to the number of discrete energy K electrons is independent of the nuclear matrix element and *decreases* as Z or as L increases. This is true for any energy range and any angular range of the continuous energy gamma rays, where the angles are measured with respect to the coincident continuous energy K electron. The angular distribution is most sensitive to L for comparable electron and gamma-ray energies and for large angular separation. These conclusions are not much affected by inclusion of the L shell. In the limit of small gamma-ray energies, the results reduce to those predicted by semiclassical theory.

I. INTRODUCTION

THE transition of a nucleus to a lower state of the same nucleus by the emission of a gamma ray or by the ejectrion of an orbital electron, i.e., internal conversion, is very well known. Another possible mode of decay is the simultaneous emission of a gamma ray and ejection of an orbital electron; the electron and the nucleus exchange a virtual photon and the electron emits a real gamma ray. This process bears the same relationship to the Compton effect as internal pair production does to pair production, and will be referred to as the internal Compton effect. In the same sense, internal conversion is often referred to as the internal photoeffect. In all of these cases, the essential distinction between the internal and the external process is the presence of a virtual rather than a real photon.

The relative probability of the internal Compton effect is quite small and thus far the effect has been detected[1] only in the case of Ba^{137m}.[2] One should, nevertheless, have some quantitative estimate of its probability if only in order to be able to correct for the contributions due to this event in measurements of the internal conversion coefficient, or the angular correlation between a gamma ray and a beta particle emitted in cascade, or the angular correlation between a gamma ray and an internally converted electron emitted in cascade. In these latter cases the distinction between the process under consideration and the internal Compton effect can also be made by energy measurements, but this is often quite difficult.

The probability of an internal Compton transition was considered previously by Cooper and Morrison[3] who refer to the process as internal scattering. The calculation was limited to high-energy electric dipole transitions and is not valid over the entire range of permissible electron energies. Angular correlation between the electron and the photon was not considered.

A similar process, inner bremsstrahlung, i.e., photon production accompanying charged particle transformations, has been studied in the past in connection with nuclear β decay,[4,5] K capture,[6,7] charged meson production in high-energy nuclear collisions,[8,9] the decay of charged π mesons,[10,11] and μ decay.[12,13]

II. NOTATION

ψ_{N0}, ψ_{Nf}, ψ_0, and ψ_f are the initial and final nuclear and electronic wave functions, respectively.

$(p_0,\mathbf{p})$, $(E,\mathbf{P})$, $(q,\mathbf{q})$, and $(k_0,\mathbf{k})$ are the energy-momentum four-vectors of the electron in the intermediate state, the electron in the final state, the real photon, and the virtual photon, respectively.

E_0 = energy of the electron in the ground state.

W = energy given up by the nucleus.

ΔE and $\Delta E_K(e+\gamma)$ are the total width and the K shell internal Compton width, respectively, of the initial nuclear energy level.

$\mathbf{Q}=\mathbf{P}+\mathbf{q}$.

θ is the angle between $\mathbf{P}$ and $\mathbf{q}$.

$\mu=\cos\theta$.

$E'=E-P\mu$.

* One of the authors (L.S.) was partially supported by the U. S. Atomic Energy Commission.

[1] H. B. Brown and R. Stump, Phys. Rev. **90**, 1061 (1953).

[2] The present calculation cannot be expected to be valid for this nucleus. See L. Spruch and G. Goertzel, Phys. Rev. **93**, 642 (1954).

[3] E. P. Cooper and P. Morrison, Phys. Rev. **57**, 862 (1940). We would like to thank Dr. J. Levinger for calling our attention to this article.

[4] J. K. Knipp and G. E. Uhlenbeck, Physica **3**, 425 (1936); F. Bloch, Phys. Rev. **50**, 272 (1936).

[5] C. S. W. Chang and D. L. Falkoff, Phys. Rev. **76**, 365 (1949).

[5a] Madansky, Lipps, Bolgiano, and Berlin, Phys. Rev. **84**, 596 (1951).

[6] P. Morrison and L. I. Schiff, Phys. Rev. **58**, 24 (1940).

[7] J. M. Jauch, Oak Ridge National Laboratory Report ORNL-1102, 1951 (unpublished).

[8] S. Mayakawa and S. Tomonaga, Progr. Theoret. Phys. (Japan) **2**, 161 (1947).

[9] L. I. Schiff, Phys. Rev. **76**, 89 (1949).

[10] H. Primakoff, Phys. Rev. **84**, 1255 (1951).

[11] T. Eguchi, Phys. Rev. **85**, 943 (1952).

[12] D. B. Feer, Phys. Rev. **75**, 731 (1949).

[13] A. Lenard, Phys. Rev. **90**, 968 (1953).

α = fine structure constant.
Z = nuclear charge.
$\mathfrak{F}=[(Q^2-W^2)^2+(2mW\alpha Z)^2]^{-1}$.
K_+^{ν}, K_+, and δ_+ are the propagation kernels of an electron in a potential V, a free electron, and a photon, respectively.

$$K_+(\mathfrak{x}_7,\mathfrak{x}_6)=(i/16\pi^4)\int(\not{p}-m)^{-1}\exp(-i\mathfrak{p}\cdot\mathfrak{x}_{76})d^3\mathbf{p}dp_0$$

$$\delta_+[(\mathfrak{x}_6-\mathfrak{x}_5)^2]=-(1/4\pi^2)\int\exp(-i\mathfrak{k}\cdot\mathfrak{x}_{65})\mathfrak{k}^{-2}d^3\mathbf{k}dk_0.$$

M_1 and M_2 are the matrix elements corresponding to the two possible Feynman diagrams for an internal Compton transition.
J_0, m_0, J_f, m_f, and L, M are the angular momentum quantum numbers of the initial and final nuclear states and of the virtual radiation field, respectively.
$\mathbf{A}_{LM}^{(m)}$ and $\mathbf{B}_{LM}^{(m)}$ are the magnetic vector potentials of the radiation field multipoles which interact with the nucleus and electron, respectively.
$M_N(L,m_0,m_f,M)$ is a nuclear matrix element.
$|M_N(L)|^2$ is proportional to a sum of squares of nuclear matrix elements.

$$\mathbf{I}=\int\exp(-i\mathbf{Q}\cdot\mathbf{x})\mathbf{B}_{LM}^{(m)}(W\mathbf{x})e^{-m\alpha Z x}d^3\mathbf{x}.$$

$(\mathbf{F};\mathbf{G})=2(\mathbf{F}\cdot\mathbf{I})(\mathbf{G}\cdot\mathbf{I})$, for arbitrary F and G.
R_L is a radial integral.
K and L refer to the respective shells.
$\mathcal{P}_K$ is the absolute probability of an internal Compton transition.
$R_K(L;q_1,q_2;\theta)$ and $R_K(L;q_1,q_2)$ are magnetic internal Compton transition rates.
$B_K(L;q_1,q_2;\theta)$ and $B_K(L;q_1,q_2)$ are magnetic internal Compton coefficients.
$\mathfrak{N}_K(L)$ is a magnetic internal conversion rate.
$\beta_K(L)$ is a magnetic internal conversion coefficient.
$[\mathbf{n}]=(\mathbf{n}_1,\mathbf{n}_2,\mathbf{n}_3)$ represents a set of unit vectors fixed in space.

III. MATRIX ELEMENTS

We take as our initial state one in which the nucleus is in an excited state with angular momentum J_0 and the K shell is filled. We want to find the absolute and relative probabilities that after some time the nucleus is in a lower energy state with angular momentum J_f and that *either* K electron has been ejected and a coincident gamma ray has been emitted. We also want to find the energy distribution of these gamma rays and their angular correlation with respect to the electrons. It will be assumed that in the absence of orbital electrons the gamma ray emitted in the transition is a pure 2^L magnetic multipole. The angular momentum projections of the initial and final nuclear states, m_0 and m_f, and the projection of the spin of the electron, are defined with respect to the axis $\mathbf{n}_3$ of the set of unit vectors $\mathbf{n}_1$, $\mathbf{n}_2$, $\mathbf{n}_3$ fixed in space and denoted by $[\mathbf{n}]$.

The probability $\mathcal{P}_K$ that at some much later time this internal Compton process will have taken place is given by

$$\mathcal{P}_K=\int\mathcal{S}|M_1+M_2|^2(2\pi)^{-6}PEdEq^2dqd\omega_e d\omega_\gamma, \quad (1)$$

where

$$\mathcal{S}=(2J_0+1)^{-1}\sum_{m_0}\sum_{m_f}S_0S_fS_{\nu'}. \quad (2)$$

$\mathcal{S}$ represents the average over the initial state and the sum over the final state angular momentum projections of the nucleus, the sum over the initial and the final electron spin projections, and the sum over the states of polarization of the gamma ray. The matrix elements M_1 and M_2 follow immediately[14] from the Feynman diagrams 1 and 2 drawn in Fig. 1.

M_1 is given by

$$M_1=-e^2\int\bar{\psi}_{Nf}(\mathfrak{x}_6)\bar{\psi}_f(\mathfrak{x}_7)A(\mathfrak{x}_7)K_+^{\nu}(\mathfrak{x}_7,\mathfrak{x}_5)\gamma_{N\mu}\gamma_\mu \times\delta_+[(\mathfrak{x}_6-\mathfrak{x}_5)^2]\psi_{N0}(\mathfrak{x}_6)\psi_0(\mathfrak{x}_5)d^4\mathfrak{x}_5d^4\mathfrak{x}_6d^4\mathfrak{x}_7, \quad (3)$$

where

$$A(\mathfrak{x}_7)=\gamma_\nu S_\nu e(2\pi/q)^{\frac{1}{2}}e^{-i(\mathbf{q}\cdot\mathbf{x}_7-qt_7)}. \quad (4)$$

The S_ν represent the states of polarization of the real photon. We substitute in the explicit expressions for δ_+ and use the relationships

$$\int dk_0e^{-ik_0t_{65}}\int\frac{e^{i\mathbf{k}\cdot(\mathbf{x}_6-\mathbf{x}_5)}}{k_0^2-\mathbf{k}\cdot\mathbf{k}}d^3\mathbf{k} =-2\pi^2\int\frac{e^{i|k_0|x_{65}}}{x_{65}}e^{-ik_0t_{65}}dk_0, \quad (5)$$

where $x_{65}=|\mathbf{x}_6-\mathbf{x}_5|$, and $\gamma_{N\mu}\gamma_\mu=\beta_N\beta(1-\boldsymbol{\alpha}_N\cdot\boldsymbol{\alpha})$. By our assumption as to the nature of the nuclear states,

$$(1-\boldsymbol{\alpha}_N\cdot\boldsymbol{\alpha})e^{i|k_0|x_{65}}(x_{65})^{-1} \quad (6)$$

can be replaced by that portion of it which is proportional to the interactions of the nucleus and of the

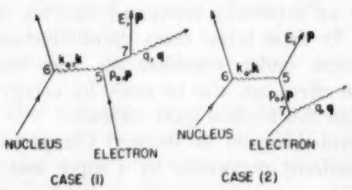

FIG. 1. Feynman diagrams for an internal Compton transition.

[14] We follow rather closely the methods and notation of Feynman, with some slight notational modifications as introduced by Baranger, Bethe, and Feynman. We use the normalization $u^\dagger u=1$. R. P. Feynman, Phys. Rev. **76**, 749, 769 (1949); Baranger, Bethe, and Feynman, Phys. Rev. **92**, 482 (1953), see in particular reference 8.

electron with a magnetic 2^L pole, that is, by[15]

$$2\pi^2 i|k_0|^{-1}[\alpha_N\cdot\mathbf{A}_{LM}{}^{*(m)}(|k_0|\mathbf{x}_6)]\times[\alpha\cdot\mathbf{B}_{LM}{}^{(m)}(|k_0|\mathbf{x}_5)], \quad (7)$$

where

$$M=m_\nu-m_f,$$

$$\mathbf{A}_{LM}{}^{(m)}(|k_0|\mathbf{x}_6)=Nj_L(|k_0|x_6)i\mathbf{L}Y_{LM}(\mathbf{x}_6,[\mathbf{n}]), \quad (8)$$

$$\mathbf{B}_{LM}{}^{(m)}(|k_0|\mathbf{x}_5)=Nh_L{}^{(1)}(|k_0|x_5)i\mathbf{L}Y_{LM}(\mathbf{x}_5,[\mathbf{n}]), \quad (9)$$

$$N=\{2/[\pi L(L+1)]\}^{\frac{1}{2}}|k_0|.$$

$Y_{LM}(\mathbf{x},[\mathbf{n}])$ is a spherical harmonic whose polar angles are those of the vector $\mathbf{x}$ with respect to the set of fixed axes $[\mathbf{n}]$. The spherical Bessel function, j_L, and the spherical Hankel function of the first kind, $h_L{}^{(1)}$, are defined as in Schiff.[16] In the above replacement, the quite negligible contribution due to those cases in which the orbital electron is ejected from within the nucleus has been ignored.

Since the initial state of the nucleus has a width ΔE (which is proportional to its initial rate of decay by any process whatever), we can write (see Appendix III)

$$\int_0^\infty e^{it_5(-k_0-W+i\Delta E)}dt_5=if', \quad (10)$$

where

$$f'=(-k_0-W+i\Delta E)^{-1}. \quad (11)$$

We now have

$$M_1=\pi e^2\int M_N'(L,m_0,m_f,M)|k_0|^{-1}\bar{\psi}_f(\chi_7)A(\chi_7)\times K_+{}^v(\chi_7,\chi_5)\beta\alpha\cdot\mathbf{B}_{LM}{}^{(m)}(|k_0|\mathbf{x}_5)e^{+ik_0t_5}\times\psi_0(\chi_5)f'd^4\chi_5dt^4\chi_7dk_0, \quad (12)$$

where we have defined a nuclear matrix element,

$$M_N'(L,m_0,m_f,M)=\int\bar{\psi}_{Nf}(\mathbf{x}_6)\beta_N\alpha_N\cdot\mathbf{A}_{LM}{}^{*(m)}(|k_0|\mathbf{x}_6)\times\psi_{N0}(\mathbf{x}_6)d^3\mathbf{x}_6. \quad (13)$$

At this point we make a number of approximations which should be valid when the nuclear charge is small, and when the energy given up by the nucleus, W, is of the order of or larger than m.

(1) It is assumed that the electron in the intermediate state is free, i.e., $K_+{}^v$ is replaced by K_+.

(2) It is assumed that the electron in the final state is free, i.e.,

$$\bar{\psi}_f(\chi_7)=\bar{\psi}_f(\mathbf{x}_7)e^{-iEt_7}\rightarrow u_fe^{-i(\mathbf{P}\cdot\mathbf{x}_7-Et_7)}, \quad (14)$$

where $P=(E^2-m^2)^{\frac{1}{2}}$.

(3) The small components of the electron ground state are neglected and the Dirac large components are replaced by the Schrödinger components, i.e.,

$$\psi_0(\chi_5)=\psi_0(\mathbf{x}_5)e^{-iE_0t_5}\rightarrow\pi^{-\frac{1}{2}}(m\alpha Z)^{\frac{1}{4}}e^{-m\alpha Zx_5-iE_0t_5}u_0, \quad (15)$$

where

$$u_0{}^\dagger=(1,0,0,0)\quad\text{or}\quad(0,1,0,0). \quad (16)$$

The neglect of the small components, unlike the first two approximations, does not greatly simplify the calculation. It is done since it is consistent with these approximations, where terms in αZ have already been neglected. The replacement of Dirac large components by Schrödinger components gives rise to an error of order $(\alpha Z)^2$.

(4) The binding energy of the electron in the ground state, which is of course proportional to $m(\alpha Z)^2$, is neglected with respect to its rest energy, i.e., E_0 is replaced by m.

With these approximations it is a trivial matter to carry through the integrations over t_7, t_5, k_0, p_0, $\mathbf{x}_7$, and $\mathbf{p}$, in the given order. We then find

$$M_1=i\pi^2e^2 2^{\frac{1}{2}}(m\alpha Z)^{\frac{1}{4}}(q^{\frac{1}{2}}W)^{-1}fM_N(L,m_0,m_f,M)(E')^{-1}T_1, \quad (17)$$

where

$$T_1=(u_f{}^\dagger\alpha\cdot\mathbf{S}[W+\alpha\cdot\mathbf{Q}]\alpha\cdot\mathbf{I}u_0), \quad (18)$$

$$\mathbf{Q}=\mathbf{P}+\mathbf{q}, \quad (19)$$

$$\mathbf{I}=\int\exp(-i\mathbf{Q}\cdot\mathbf{x})\mathbf{B}_{LM}{}^{(m)}(W\mathbf{x})e^{-m\alpha Zx}d^3\mathbf{x}, \quad (20)$$

$$E'=E-P\mu, \quad (21)$$

$$f=(-W-m+E+q+i\Delta E)^{-1} \quad (22)$$

$$M_N(L,m_0,m_f,M)=\int\bar{\psi}_{Nf}(\mathbf{x}_6)\beta_N\alpha_N\cdot\mathbf{A}_{LM}{}^{*(m)}(W\mathbf{x}_6)\psi_{N0}(\mathbf{x}_6)d^3\mathbf{x}_6. \quad (23)$$

In arriving at the above result, we have made use of the fact that $\gamma_\nu S_\nu$ represents a real photon so that

$$\gamma_\nu S_\nu=\beta\alpha\cdot\mathbf{S},$$

we have used $\beta u_0=u_0$, and we have dropped the subscript 5 on $\mathbf{x}_5$ in the expression for $\mathbf{I}$. We have further replaced $(E+q-m)$ by W in all terms other than f, which is permissible due to the form of f, as we shall see later.

Proceeding in the same manner, but making the further approximation that Fourier momentum components of the ground state of order m can be neglected (see Appendix IV), we find for M_2

$$M_2=i\pi^2e^2 2^{\frac{1}{2}}(m\alpha Z)^{\frac{1}{4}}(q^{\frac{1}{2}}W)^{-1}fM_N(L,m_0,m_f,M)m^{-1}T_2, \quad (24)$$

where

$$T_2=(u_f{}^\dagger\alpha\cdot\mathbf{I}[q+\alpha\cdot\mathbf{q}]\alpha\cdot\mathbf{S}u_0). \quad (25)$$

[15] N. Tralli and G. Goertzel, Phys. Rev. **83**, 399 (1951). See Appendix A.

[16] L. I. Schiff, *Quantum Mechanics* (McGraw-Hill Book Company, Inc., New York, 1949).

Performing sums in the usual way, we find

$$S_0 S_f S_\nu |M_1+M_2|^2 = \frac{8\pi^4 e^6 (m\alpha Z)^3 |M_N(L,m_0,m_f,M)|^2 |f|^2}{q^3 W^2 E} H, \quad (26)$$

where

$$H=(E')^{-2}|\mathbf{I}|^2[q^2E'+WP^2(1-\mu^2)] + (mE')^{-1}[|\mathbf{I}|^2 qP^2(\mu^2-1)-m(\mathbf{q};\mathbf{q})+q(\mathbf{P};\mathbf{P}) - P\mu \,\mathrm{Re}(\mathbf{P};\mathbf{q})]+(q/m^2)[|\mathbf{I}|^2 qE+\mathrm{Re}(\mathbf{P};\mathbf{q})], \quad (27)$$

where Re denotes the real part, and where, for arbitrary vectors $\mathbf{F}$ and $\mathbf{G}$,

$$(\mathbf{F};\mathbf{G})=2(\mathbf{F}\cdot\mathbf{I})(\mathbf{G}\cdot\mathbf{I}). \quad (28)$$

In the above expressions, the M in $M_N(L,m_0,m_f,M)$ and in the expressions of the form $(\mathbf{F};\mathbf{G})$ represents m_0-m_f. It is permissible, however, to consider M arbitrary and to sum over M, for only the one value m_0-m_f will contribute. If we now define $|M_N(L)|^2$ by the relation

$$(2J_0+1)^{-1}\textstyle\sum_{m_0}\sum_{m_f}|M_N(L,m_0,m_f,M)|^2 = |M_N(L)|^2, \quad (29)$$

$|M_N(L)|^2$ is independent of M and we obtain

$$\mathcal{P}_K = \frac{e^6(m\alpha Z)^3|M_N(L)|^2}{8\pi^2 W^2} \times \int q^{-1}|f|^2 P(\textstyle\sum_M H)\,dE\,dq\,d\omega_e\,d\omega_\gamma. \quad (30)$$

IV. RESULTS

It can be seen from the results derived in the appendices that the only angular dependence of the integrand of $\mathcal{P}_K$ is the dependence upon μ. The angular integrations thus reduce to

$$\int\cdots d\omega_e\,d\omega_\gamma=(4\pi)(2\pi)\int_{-1}^{1}\cdots d\mu. \quad (31)$$

Further, for any slowly varying function of E, $g(E)$, we have, ignoring terms in $(\Delta E)/(W-q)$,

$$\int_m^\infty g(E)|f|^2 dE = \int_m^\infty g(E)[(-W-m+E+q)^2+(\Delta E)^2]^{-1}dE = g(W+m-q)\pi(\Delta E)^{-1}. \quad (32)$$

$\mathcal{P}_K$ can now be expressed in the form $\Delta E_K(e+\gamma)/\Delta E$, where $\Delta E_K(e+\gamma)$ is that part of the width of the initial state which is due to the probability of decay via a K-shell internal Compton transition. Since an initial transition rate is given by twice the corresponding width, the initial transition rate for an internal Compton process in which the gamma ray has an energy between q_1 and q_2 and in which either K electron has been ejected is given by

$$R_K(L;q_1,q_2)=16\pi e^6(m\alpha Z)^3|M_N(L)|^2(2L+1) \times\int_{q_1}^{q_2}dq\int_{-1}^{1}d\mu q^{-1}P|R_{LL}|^2\mathfrak{C}, \quad (33)$$

where

$$\mathfrak{C}=(E')^{-2}[WP^2(1-\mu^2)+q^2E'] - (mE')^{-1}[qP^2(1-\mu^2)(mq+P^2+Pq\mu)Q^{-2}] + (q/m^2)[qE'-P^2q^2(1-\mu^2)Q^{-2}], \quad (34)$$

$$E=W+m-q, \quad (35)$$

$$|R_L|^2=(1/W^2)(Q^2/W^2)^L\mathfrak{F}, \quad (36)$$

$$\mathfrak{F}=[(Q^2-W^2)^2+(2mW\alpha Z)^2]^{-1}. \quad (37)$$

Use has been made of the results derived in the appendices. As in the notation for internal conversion, the dependence of the rate upon W and Z has been suppressed. A transition rate $R_K(L;q_1,q_2;\theta)$ per unit solid angle for an angle θ between the electron and the gamma ray can also be defined.

While in principle measurements can be made in which the lower limit q_1 approaches zero, the calculated rate diverges in this limit. There is no need, however, to modify the calculations so as to properly eliminate this infrared catastrophe, for experimentally it would be difficult to distinguish a very low-energy internal Compton gamma ray in coincidence with a continuous energy electron from an x-ray of comparable energy in coincidence with an "ordinary" internally converted electron with the maximum possible energy. The experimental procedure would then be to measure only those gamma rays above some minimum energy q_1, which is above the maximum x-ray energy for the given nucleus. It is to be noted that in a calculation of the energy imparted to the continuous gamma rays, the extra factor of q in the integrand automatically eliminates the infrared catastrophe. This energy calculation would probably be fairly accurate even though the number of very low-energy gamma rays is of course incorrectly given.

While the upper limits q_2 can be set equal to the true maximum W without any divergence, the calculations are not valid in this energy region for the electron energy is then so small that the Born approximation cannot be used.

To the same Born approximation, the transition rate for the internal conversion of either K electron is given by[17]

$$\mathfrak{N}_K(L)=8\pi^2 e^4 m(\alpha Z)^3(2L+1) \times|M_N(L)|^2(W+2m)^{L+1}(W)^{-L-5/2}. \quad (38)$$

[17] S. M. Dancoff and P. Morrison, Phys. Rev. 55, 122 (1939).

The coefficient of $|M_N(L)|^2$ is of course known exactly,[18] but the calculation of the probability of an internal Compton process relative to that of an internal conversion process will probably be more reliable if the inexact $\mathfrak{R}_K(L)$ is used, for it then involves approximations quite similar to those used in the evaluation of $R_K(L;q_1,q_2)$ and $R_K(L;q_1,q_2;\theta)$. In any event, the calculated relative probability will only be reliable in those regions for which the difference between the Born approximation and exact internal conversion rate is not too great.

The ratios,

$$B_K(L;q_1,q_2)=R_K(L;q_1,q_2)/\mathfrak{R}_K(L), \tag{39}$$

and

$$B_K(L;q_1,q_2;\theta)=R_K(L;q_1,q_2;\theta)/\mathfrak{R}_K(L), \tag{40}$$

will be referred to as the total and differential magnetic K-shell internal Compton coefficients, respectively, for a multipole of order L. The latter coefficient, for example, represents the ratio of the number of gamma rays emitted with energies between q_1 and q_2 per unit solid angle at an angle θ with respect to the coincident K electron to the number of discrete energy K electrons in the case of a 2^L magnetic multipole. The letter B is chosen in analogy with the magnetic internal conversion coefficient β. From their definitions, it follows that

$$B_K(L;q_1,q_2;\theta)=\frac{e^2m^2}{\pi^2W^{L-\frac{1}{2}}(W+2m)^{L+\frac{1}{2}}}\int_{q_1}^{q_2}dq\,\frac{P}{q}Q^{2L}\mathfrak{IC}\mathfrak{F}, \tag{41}$$

and

$$B_K(L;q_1,q_2)=2\pi\int_{-1}^{1}B_K(L;q_1,q_2;\theta)d\mu. \tag{42}$$

The corresponding quantities for the L shell follow immediately if, as is consistent with our previous approximations, we neglect the $2p$ contribution and the small components of the $2s$ electrons, and approximate the spatial dependence of the large components by the Schrödinger components with terms proportional to αZ neglected, in which case

$$\psi_{2s}(x,Z)=\psi_{1s}(x,Z/2). \tag{43}$$

The L-shell coefficients therefore follow from the K-shell coefficients by the replacement of Z by $(Z/2)$. However, $B_K(L;q_1,q_2;\theta)$ is roughly independent of Z except in the neighborhood of $Q=W$ where the dependence of $\mathfrak{F}$ upon Z is essential. If this region is then not included in the measurement, it follows, since

$$\beta_K(L)\approx 8\beta_L(L), \tag{44}$$

that

$$B_{K+L}(L;q_1,q_2;\theta)\approx(8/9)B_K(L;q_1,q_2;\theta)+(1/9)B_L(L;q_1,q_2;\theta)\approx B_K(L;q_1,q_2;\theta). \tag{45}$$

[18] Rose, Goertzel, Spinrad, Harr, and Strong, Phys. Rev. **76**, 1883 (1949).

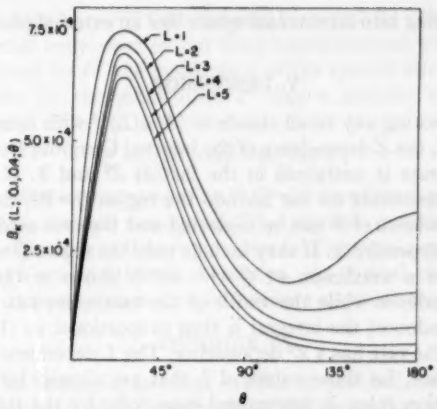

FIG. 2. $B_K(L;0.1,0.4;\theta)$ is the ratio of the number of gamma rays emitted per unit solid angle with energies between 0.1 mc^2 and 0.4 mc^2 to the number of discrete energy K electrons. The nucleus, of charge $Z=20$, makes a transition corresponding to a 2^L magnetic multipole of energy 1.29 mc^2. θ is the angle between the photon and the coincident K electron.

Although the L-shell maximum is four times that of the K shell, the factor (1/9) and the occurrence of the maxima in the same region cause this last relation to be approximately valid even when the region $Q=W$ is included. Obviously, to the same degree of validity, there exists the similar relation

$$B_{K+L}(L;q_1,q_2)\approx B_K(L;q_1,q_2).$$

The expression for $B_K(L;0.1,0.4;\theta)$ has been integrated numerically for one set of values of Z, W, q_1 and q_2. The results are shown in Fig. 2. The effect of a change in Z for these energies can be seen by a comparison with the results previously reported for Ba^{137m}.[2] For $\theta=0°$ or 180° $\mathfrak{IC}$ reduces to the very simple form

$$\mathfrak{IC}(\theta=0°\text{ or }180°)=2Eq^2/m^2. \tag{46}$$

The $B_K(L;q_1,q_2;\theta)$ can then be readily calculated for these angles.

As $q\to 0$, it is found that

$$B_K(L;q,q+dq;\theta)\to\frac{e^2}{4\pi^2}\frac{\beta^2(1-\mu^2)}{(1-\beta\mu)^2}\frac{dq}{q}, \tag{47}$$

where

$$\beta=P/E.$$

This is precisely the result derived semiclassically by Wang Chang and Falkoff[19] for the case of the inner bremsstrahlung associated with β decay, where it was shown to arise from the instantaneous acceleration of the electron. The relationship also follows quite generally,[20] in the limit as αZ and the photon energy approach zero, on comparing the squared matrix element for an arbitrary graph with one obtained from it by

[19] See reference 5. Note that our coefficient is defined per unit solid angle.

[20] See reference 13 and R. Jost, Phys. Rev. **72**, 815 (1947).

inserting into an external spinor line an external photon line.

V. DISCUSSION

Ignoring any small trends in $|M_N(L)|^2$ with increasing Z, the Z dependence of the internal Compton transition rate is contained in the factors Z^3 and $\mathfrak{F}$. If the measurements do not include the region $Q\approx W$, the Z dependence of $\mathfrak{F}$ can be neglected and the rate exhibits a Z^3 dependence. If they include only the region $Q\approx W$, $\mathfrak{F}$ has a maximum at $Q=W$ which shows a $(1/Z^2)$ dependence while the width of the maximum has a Z dependence; the integral is then proportional to $(1/Z)$ and the rate has a Z^3 dependence. The L dependence of the rate, for those values of L that are allowed by the selection rules, is determined essentially by the strong L dependence of $|M_N(L)|^2$, which decreases sharply with increasing L. This dependence cannot be offset by the factor $(2L+1)(Q^2/W^2)^L$ since for W of the order of or greater than m, for which the calculations are valid, (Q^2/W^2) cannot be more than about 3, the value it assumes for $W=m$, $q\approx 0$.

The Z dependence of the internal Compton coefficients is contained in the factor $\mathfrak{F}$. Therefore, unlike the internal conversion coefficients, they *decrease* as Z increases. However, $B_K(L;q_1,q_2;\theta)$ will be relatively independent of Z except in the region $Q\approx W$. Their L dependence is contained in the factor

$$[Q^2/(W^2+2Wm)]^L.$$

Since the argument within the square brackets is less than or equal to one, they *decrease* as L increases, again unlike the internal conversion coefficients. The L dependence of $B_K(L;q_1,q_2;\theta)$ will be strongest for large angles θ, due to the factor Q^{2L}. If θ and q_2 are small, $B_K(L;q_1,q_2;\theta)$ will be relatively insensitive to L.

Because the Born approximation was used, the results can be expected to be valid only if $maZ/P\ll 1$. A similar requirement holds for the intermediate states. For the Feynman diagrams 1 and 2, we have $\mathbf{p}=\mathbf{Q}$ and $\mathbf{p}=-\mathbf{q}$, respectively. These relations follow from conservation of momentum at the real photon junction. The calculation of M_1 is valid then only if $maZ/Q\ll 1$; however, if $Q\approx 0$, almost all of the small contribution (the total contribution vanishes at $Q=0$) comes from $|M_2|^2$. This can be seen by an analysis of $\mathfrak{IC}$, whose three terms originate in $|M_1|^2$, the cross term, and $|M_2|^2$, respectively, for, as $Q\to 0$,

$$P\to W(W+2m)\cdot\tfrac{1}{2}(m+W)^{-1},$$
$$P^2(1-\mu^2)Q^{-2}\to 1.$$

Similarly, the calculation of M_2 is valid only if $maZ/q\ll 1$; however, if $q\approx 0$, almost all of the contribution comes from $|M_1|^2$. Another possible criterion is that the calculations will be valid only for those values of Z and W for which the Born approximation calculations of the $\beta_K(L)$ are valid. On the one hand, the $B_K(L;q_1,q_2;\theta)$ can be expected to be more reliable than the $\beta_K(L)$, since the former involve the ratio of two calculations in which similar approximations have been made. On the other hand, the $B_K(L;q_1,q_2;\theta)$ refer to a more complicated process involving intermediate states which are also treated by the Born approximation.

The ratio of continuous gamma rays to discrete gamma rays is given by

$$B_K(L;q_1,q_2;\theta)\beta_K(L).$$

(This ratio, rather than the one chosen, might well have been called the internal Compton coefficient.) In this case, the exact $\beta_K(L)$ should be used.

Calculations of the electrical internal Compton coefficients are in progress. (See also reference 3.)

We would like to thank Miss Pearl Ehrlich for performing the numerical calculations.

APPENDIX I

Evaluation of $\sum_M|I|^2$ and of $\sum_M(F;G)$

The integral $\mathbf{I}$ is defined by Eqs. (9) and (20). If we define

$$(L\nu|\mathbf{L}|LM) \quad \text{by} \quad \mathbf{L}Y_{LM}(\mathbf{x},[\mathbf{n}]) = \sum_\nu Y_{L\nu}(\mathbf{x},[\mathbf{n}])(L\nu|\mathbf{L}|LM),$$

and note that

$$\exp(-i\mathbf{Q}\cdot\mathbf{x}) = 4\pi\sum_{l,p}(-i)^l j_l(Qx)Y_{lp}(\mathbf{Q},[\mathbf{n}])Y_{lp}^*(\mathbf{x},[\mathbf{n}]),$$

we may write

$$\mathbf{I}=\{32\pi/[L(L+1)]\}^{\frac{1}{2}}(-i)^{L-1}WR_L\mathbf{L}Y_{LM}(\mathbf{Q},[\mathbf{n}]),$$

where

$$R_L=\int_0^\infty h_L^{(1)}(Wx)j_L(Qx)e^{-maZ_2x^2}dx. \qquad \text{(A-1)}$$

Consider now the dyadic D defined by

$$D=\sum_M[\mathbf{L}Y_{LM}(\mathbf{Q},[\mathbf{n}])][\mathbf{L}Y_{LM}(\mathbf{Q},[\mathbf{n}])]^*.$$

Since

$$(L\sigma|\mathbf{L}|LM)^*=(LM|\mathbf{L}|L\sigma),$$

and since $\mathbf{L}$ connects only states with the same L, the expression becomes

$$D=\sum_{M,\nu,\sigma}Y_{L\nu}(\mathbf{Q},[\mathbf{n}]) \times(L\nu|\mathbf{L}|LM)(LM|\mathbf{L}|L\sigma)Y_{L\sigma}^*(\mathbf{Q},[\mathbf{n}])$$
$$=\sum_{\nu\sigma}Y_{L\nu}(\mathbf{Q},[\mathbf{n}])(L\nu|\mathbf{LL}|L\sigma)Y_{L\sigma}^*(\mathbf{Q},[\mathbf{n}]).$$

The basis $[\mathbf{n}]$ affects the terms in the sum only in determining the projections ν and σ; since ν and σ are summed over, D is independent of the basis. It is convenient to choose a basis $[\mathbf{u}]=(\mathbf{u}_1,\mathbf{u}_2,\mathbf{u}_3)$ in which $\mathbf{u}_3$ is in the direction of $\mathbf{Q}$. The polar angle is then 0 and D reduces to

$$D=|Y_{L0}(0,\phi)|^2(L0|\mathbf{LL}|L0)$$
$$=(2L+1)/(4\pi)(L0|\mathbf{LL}|L0).$$

The dyadic is then invariant under a rotation about $\mathbf{u}_3$

and is symmetric in the first and second unit vectors. It must then be possible to write

$$(L0|\mathbf{LL}|L0)=a(\mathbf{u}_1\mathbf{u}_1+\mathbf{u}_2\mathbf{u}_2)+b\mathbf{u}_3\mathbf{u}_3.$$

Since

$$L_{u_3}Y_{L0}(\mathbf{Q},[\mathbf{u}])=0,$$

the coefficient b vanishes. Taking the spur of both sides gives $L(L+1)=2a$, and thus

$$D=L(L+1)(2L+1)(1/8\pi)(\mathbf{u}_1\mathbf{u}_1+\mathbf{u}_2\mathbf{u}_2).$$

From the definition of D, it follows that

$$\sum_M|\mathbf{I}|^2=\{32\pi/[L(L+1)]\}W^2|R_L|^2\ \text{Spur}\ D$$
$$=8(2L+1)W^2|R_L|^2,$$

and that

$$\sum_M(\mathbf{F};\mathbf{G})=2\sum_M(\mathbf{F}\cdot\mathbf{I})(\mathbf{I}\cdot\mathbf{G})$$
$$=\{64\pi/[L(L+1)]\}W^2|R_L|^2\mathbf{F}\cdot D\cdot\mathbf{G}$$
$$=8W^2(2L+1)|R_L|^2[(\mathbf{F}\cdot\mathbf{G})$$
$$-Q^{-2}(\mathbf{F}\cdot\mathbf{Q})(\mathbf{G}\cdot\mathbf{Q})].$$

In particular

$$\sum_M(\mathbf{q};\mathbf{q})=\sum_M(\mathbf{P};\mathbf{P})=-\sum_M\mathrm{Re}(\mathbf{P};\mathbf{q})$$
$$=8W^2(2L+1)|R_L|^2P^2q^2(1-\mu^2)Q^{-2}.$$

APPENDIX II

Evaluation of $|R_L|^2$

$|R_L|^2$, where R_L is given by Eq. (A-1), must be evaluated. As is consistent with our previous approximations, correction terms in αZ are to be neglected. If $Q\neq W$ (i.e., if Q is not approximately equal to W), the exponential then simply serves as a convergence factor, i.e.,

$$R_L(Q\neq W)\approx\mathrm{Lim}(Z\to 0)R_L,$$

where the limiting process must be performed after the integration. This latter expression is equivalent to

$$\mathrm{Lim}(Z\to 0)\int_0^\infty j_L(Qx)h_L^{(1)}(W'x)x^2dx,$$

where $W'=W+im\alpha Zx$. In this form the integral can readily be performed, and we find

$$|R_L(Q\neq W)|^2\approx(1/W^2)(Q^2/W^2)^L(Q^2-W^2)^{-2}.$$

This approximation is obviously not valid for $Q=W$. Since the integrand is bounded, the divergence at $Q=W$ must be due to the infinite range of integration. It is then sufficient for our purposes, in the neighborhood of $Q=W$, to replace j_L and $h_L^{(1)}$ by their asymptotic forms, in which case the integration is trivial. Neglecting correction terms in αZ, and replacing Q by W in some terms, we find

$$|R_L(Q\approx W)|^2\approx(1/W^2)[(Q^2-W^2)^2+(2mW\alpha Z)^2]^{-1}.$$

A form which is applicable over the entire range is then

$$|R_L|^2\approx(1/W^2)(Q^2/W^2)^L[(Q^2-W^2)^2+(2mW\alpha Z)^2]^{-1}.$$

It is to be noted that the radial integral R_L arises in internal conversion in the Born approximation with Q replaced by P', the momentum of the ejected electron. Unlike Q, the momentum P' has a definite value, namely,

$$P'=[(W+m)^2-m^2]^{\frac{1}{2}}\neq W.$$

The situation corresponding to $Q=W$ therefore does not exist in internal conversion. The physical meaning of this difference is that in the internal Compton process, as opposed to internal conversion, the virtual photon can conserve energy even in the Born approximation.

APPENDIX III

The decay factor $\exp(-\Delta Et_0)$ is justified by the realization that the amplitudes of the states that we are interested in, namely, those which arise via an internal Compton transition, satisfy a set of differential equations in which they are coupled to the initial state but not to one another. The specification of the time dependence of the amplitude of the initial state then determines the time dependence of all of the other amplitudes. The use of the decay factor could have been avoided in a number of ways. One method would be the usual one of analyzing the time dependence of the initial state amplitude only for infinitesimal times after $t=0$. Another method would be the determination of the energy shift of the initial state by the use of Feynman diagrams in which the initial and final states involve the nucleus in its excited state and the K electron in its ground state and the intermediate states are those which arise in an internal Compton transition. The negative imaginary part of the energy shift, which is one-half of the initial transition rate, is found by considering those internal Compton intermediate states in which energy is conserved. There are four possible Feynman diagrams; two of the diagrams consist of one of the diagrams of Fig. 1 followed by its mirror image and two consist of one of the diagrams of Fig. 1 followed by the mirror image of the other.

APPENDIX IV

Evaluation of M_2

The expression for M_2 involves the integral

$$\int\exp(-m\alpha Zx_7-i\mathbf{q}\cdot\mathbf{x}_7-i\mathbf{p}\cdot\mathbf{x}_7+i\mathbf{p}\cdot\mathbf{x}_5)(\not{p}-m)^{-1}d^3\mathbf{x}_7d^3\mathbf{p}.$$

Unlike the situation for M_1, integration over $\mathbf{x}_7$ does not lead to a δ function, so that integration over $\mathbf{p}$ cannot readily be performed. However, it is permissible at the outset to replace the $\mathbf{p}$ which appears in $\not{p}$ by $(-\mathbf{q})$. This would be exact were it not for the factor $\exp(-m\alpha Zx_7)$. Integration over $\mathbf{p}$ and $\mathbf{x}_7$ is then trivial and one arrives at the result given in Eq. (24).

The factor $\exp(-m\alpha Zx_7)$ cannot simply be dropped, for it is ultimately required for convergence. The re-

placement of $\mathbf{p}$ by $(-\mathbf{q})$ in $\not{p}$ corresponds to the neglect of Fourier momentum components of order m, or, equivalently, to the neglect of residues due to the poles of $(\not{p}-m)^{-1}$. (A pole occurs on the real axis only if the real photon has an energy $q \geq 2m$, for if energy is to be conserved in the intermediate state the electron must jump into a negative energy state.) The error involved in the replacement of $\mathbf{p}$ by $(-\mathbf{q})$ in $\not{p}$ is of order αZ, and the approximation is therefore consistent with previous ones.

PHYSICAL REVIEW VOLUME 94, NUMBER 6 JUNE 15, 1954

Average Neutron Total Cross Sections in the 3- to 12-Mev Region*

NORRIS NERESON AND SPERRY DARDEN†
University of California, Los Alamos Scientific Laboratory, Los Alamos, New Mexico
(Received March 1, 1954)

Measurements of the average neutron total cross sections of N, F, Mg, P, Cl, Ti, Mn, Co, Ni, Zn, Se, Br, Mo, Ag, Cd, Sn, Sb, Te, La, Ta, W, Au, Hg, and Tl have been made over the 3- to 12-Mev energy range. The average energy spread of the measurements is approximately 10 percent and the over-all accuracy of the results is ±10 percent or better. The above data, together with those of a previous experiment, provide information on average cross-section behavior as a function of energy and atomic weight over most of the periodic table.

AVERAGE total cross sections for neutrons have been measured for a set of 24 elements over the 3- to 12-Mev energy region. The present measurements are an extension of a set of previous measurements made for 13 elements.[1] These earlier measurements showed that neighboring elements exhibit similar patterns in their average cross-section behavior. The aim of the present experiment was to supplement the previous data and to establish cross-section trends over the entire periodic table. Therefore, most of the elements were selected with the above objective in view; however, certain elements were chosen as a result of specific requests for total cross-section information.

The experimental arrangement for the present measurements was the same as that used in the previous measurements except for an improvement in the sample and detector geometry. In the present case, the distance from the sample to the detector was increased to 18 inches as compared to 11 inches in the earlier arrangement. All of the scattering samples were 1 inch in diameter and their length was chosen so as to give a neutron transmission of approximately 0.5. During the course of the work, the neutron source for the experiment was changed from one reactor to another reactor. The data from 6 to 13 Mev were obtained by using the Los Alamos fast reactor as previously described, while the 3- to 6-Mev data were acquired by using a U^{235} converter[2] placed in a hole which goes through the center of the Los Alamos water boiler. The neutron spectrum obtained from these two sources is the same over the energy region utilized for this experiment, i.e., above 3 Mev.

The results presented here retain the same characteristics as the previous measurements, i.e., the average energy spread is about 10 percent of the measured energy, and the over-all accuracy is at least ±10 percent over the 3- to 12-Mev energy range. Above 12 Mev the present data are subject to considerable error and the more accurate 14.1-Mev point obtained by Coon and others[3] has been weighted accordingly in determining the curve over the 12- to 14-Mev region. As previously, a smooth curve has been drawn through the data points and small fluctuations which are not well resolved by the experiment have been averaged over the curve. A curve has not been drawn where better-resolved data already exist. No corrections have been made on the measured cross sections for the effect of neutrons scattered into the detector by the sample. The geometry is such that this correction is probably less than 1.5 percent at 12 Mev.

The results obtained are shown in Figs. 1, 2, and 3 where the average neutron total cross section, σ_t, is plotted as a function of the neutron energy, E_n. In Fig. 1 the two sets of nitrogen data do not agree well over certain energy regions. The measurement employing melamine and polyethylene is probably

* This work was performed under the auspices of the U. S. Atomic Energy Commission.

† Present address: Department of Physics, University of Wisconsin, Madison, Wisconsin.

[1] N. Nereson and S. Darden, Phys. Rev. 89, 775 (1953).

[2] This converter was made by L. D. P. King of this laboratory and consisted of an assembly of 120 U^{235} disks each having a thickness of 0.01 inch and a diameter slightly less than 1 inch. This series of disks were sealed in an aluminum tube 3 feet long and 1 inch diameter and placed at the center of the reactor where the average thermal neutron flux is about 10^{12}. At a neutron energy of 3 Mev, this converter produced a collimated neutron flux at the wall of the reactor (77 inches distant from the converter) of 9×10^{6} neutrons cm^{-2} sec^{-1} Mev^{-1}. The above figures are for a water boiler power of 25 kilowatts.

[3] Coon, Graves, and Barschall, Phys. Rev. 88, 562 (1952).

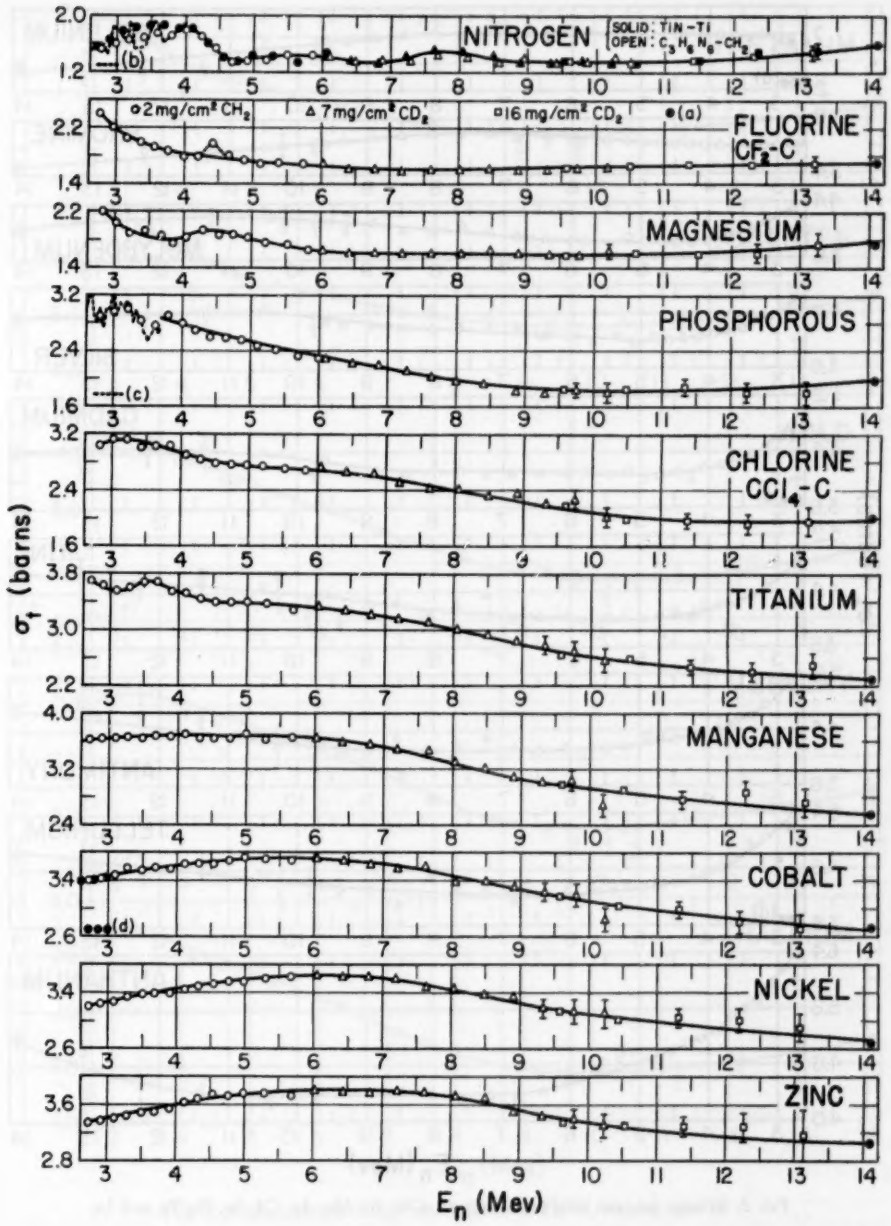

FIG. 1. Average neutron total cross sections of N, F, Mg, P, Cl, Ti, Mn, Co, Ni, and Zn. References to other experimental data shown in the figure are (a) Coon, Graves, and Barschall, Phys. Rev. 88, 562 (1952); (b) H. B. Willard, Oak Ridge National Laboratory, 1952 (unpublished data); (c) R. Ricamo, Nuovo cimento 8, 383 (1951); (d) Walt, Becker, Okazaki, and Fields, Phys. Rev. 89, 1271 (1953).

more subject to error on account of the carbon resonances in the 3 to 4 and 7 to 8 Mev regions. The data using titanium nitride and titanium are considered the more reliable since the titanium cross-section curve is smoother than the carbon curve. The latter data also agree better with the well-resolved data of Willard. The fluorine measurement (using Teflon and carbon) consistently showed a high point at 4.4 Mev; probably a resonance occurs in this vicinity. The fluctuations in the data points occurring over the low-energy sections of the Mg, P, Cl, and Ti curves are also indicative of resonance structure in this region. A

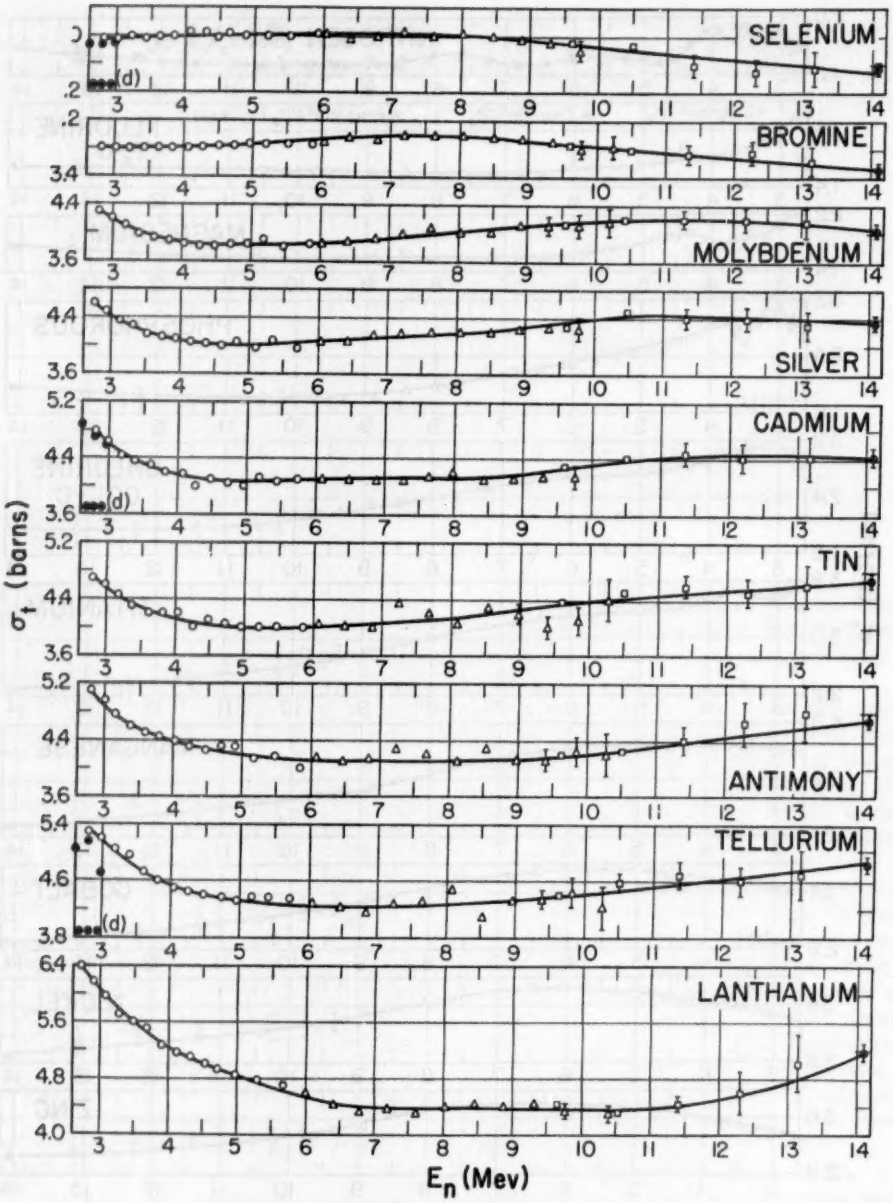

FIG. 2. Average neutron total cross sections of Se, Br, Mo, Ag, Cd, Sn, Sb, Te, and La.

comparison of the present data with the better resolved data of Ricamo in the case of P illustrates the type of average cross-section values obtained from the present experiment.

For neutron energies near 3 Mev, the present total cross-section values for some elements are about 10 percent higher than those measured by Miller *et al.*[4] As was pointed out by Miller, his results may be too low by as much as 10 percent in some cases because of forward scattering into the detector. That the observed discrepancies are probably due to this effect is borne out by the agreement between the present results and recent measurements made at Wisconsin (reference *d* in Figs. 1, 2, and 3). With the exception of Te, the results around 3 Mev for Co, Se, Cd, Au, and Hg all agree within 4 percent with the Wisconsin data for these

[4] Miller, Adair, Bockelman, and Darden, Phys. Rev. 88, 83 (1952).

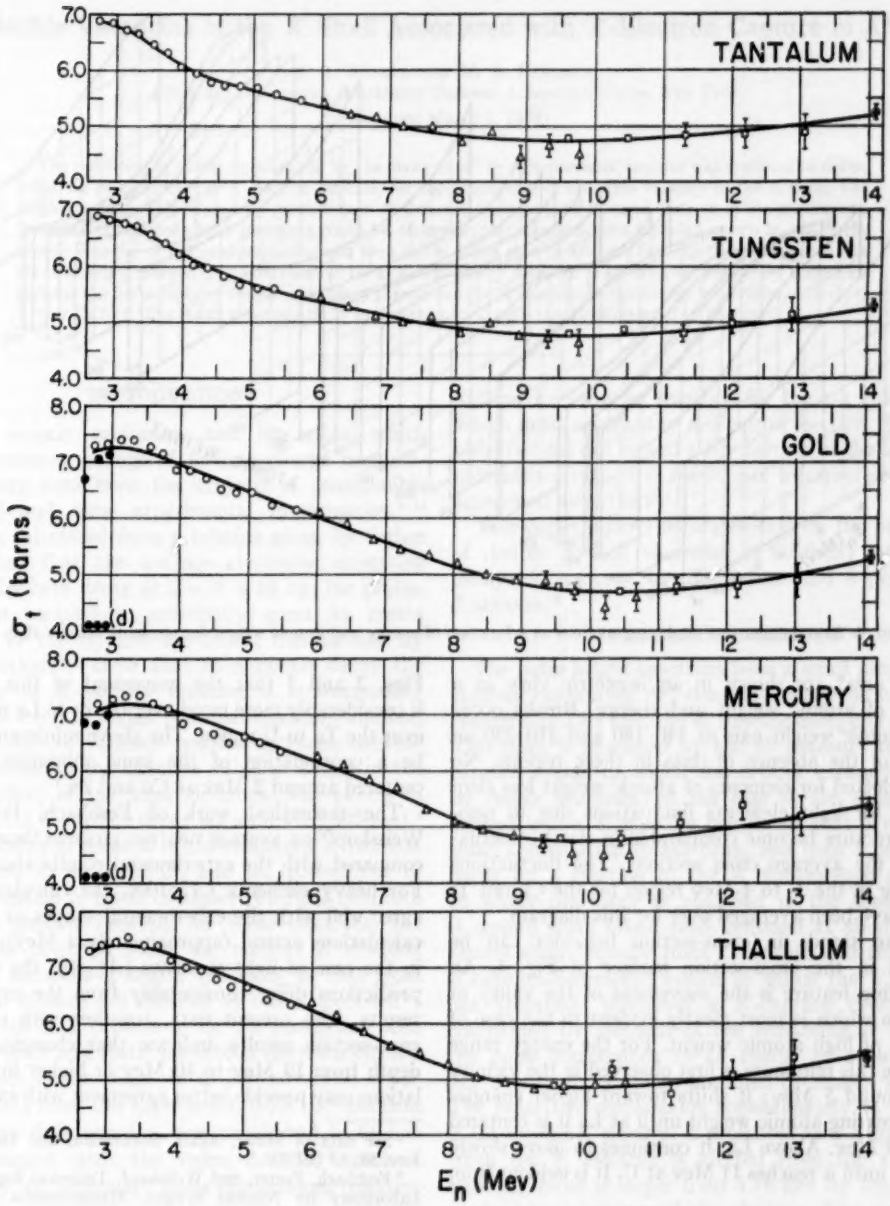

FIG. 3. Average neutron total cross sections of Ta, W, Au, Hg, and Tl.

elements; the latter average cross-section measurements were carried out in good geometry. Over the 12- to 13-Mev region, the present results join satisfactorily with the 14.1 Mev point[3] obtained with better geometry and higher statistical accuracy than the present experiment. The above correlations are considered important as verifications of the validity of the present cross-section measurements.

Average total cross-section trends for neutrons as a function of energy and atomic weight have been previously illustrated by Barschall[5] for the 0.1- to 3-Mev region. A similar presentation for the 3- to 14-Mev region can be made using the data of Figs. 1, 2, and 3, and those of the previous measurements.[1] Figure 4 shows such an illustration. In this figure, the measured cross sections divided by the nuclear geo-

[5] H. Barschall, Phys. Rev. 86, 431 (1952).

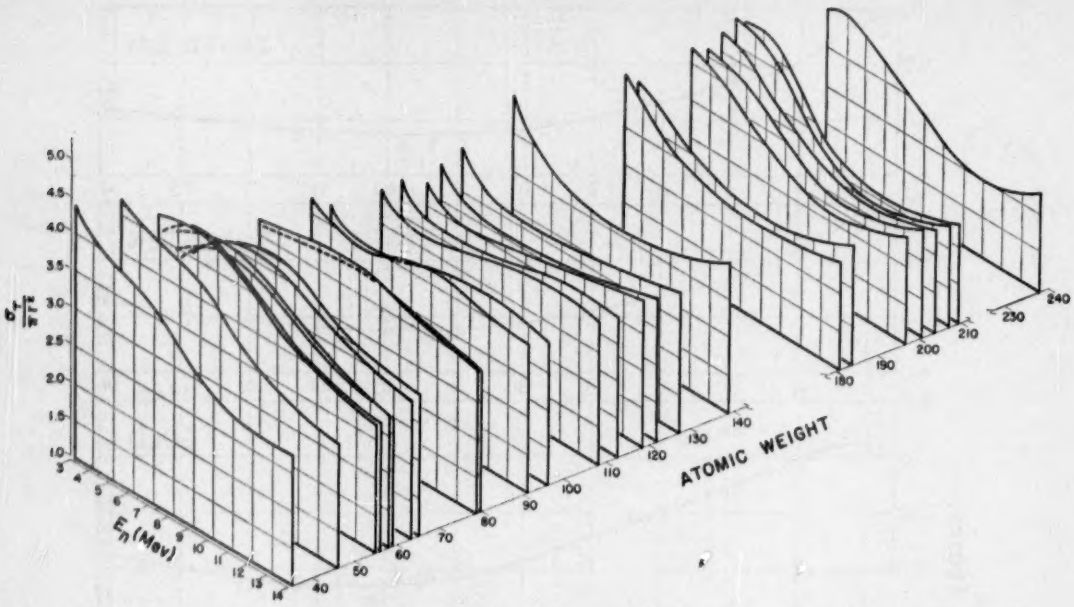

FIG. 4. Average neutron total cross sections as a function of energy and atomic weight for elements heavier than Cl.

metrical area[6] are shown in an isometric view as a function of atomic weight and energy. Breaks occur in the atomic weight axis at 140–180 and 210–230 on account of the absence of data in these regions. No data is plotted for elements of atomic weight less than 35 since for light elements fluctuations due to resonance structure become comparable in size to fluctuations in the average cross sections. The fluctuations appearing in the 3- to 4-Mev region for the Cl and Ti curves have been averaged over for this diagram.

Definite trends in cross-section behavior can be observed in the cross-section surface of Fig. 4. An outstanding feature is the movement of the valley or minimum which is most clearly evident in the case of elements of high atomic weight. For the energy range used here this minimum is first observed in the vicinity of Zr around 5 Mev; it shifts toward higher energies with increasing atomic weight until at La it is centered around 9 Mev. Above La, it continues to move slowly upwards until it reaches 11 Mev at U. It is evident from Figs. 2 and 3 that the movement of this minimum is considerably more rapid over the Zr to La region than over the Ta to U region. The above minimum seems to be a continuation of the same minimum which is centered around 2 Mev at Cu and Zn.[7]

The theoretical work of Feshbach, Porter, and Weisskopf[8] on average neutron cross sections has been compared with the experimental results above 3 Mev. For heavy elements ($A \gtrsim 100$), the calculated curves agree well with the experimental shapes as far as the calculations extend (approximately 4 Mev). However, in the case of light elements ($A \lesssim 50$), the theoretical predictions differ considerably from the experimental results. The present data, together with other total cross-section results, indicate that changing the well depth from 19 Mev to 40 Mev or higher in the calculations may provide better agreement with experiment.[9]

[6] The nuclear geometrical area was computed using a nuclear radius of $1.45 \times A^{\frac{1}{3}} \times 10^{-13}$ cm.

[7] See data of Miller, Adair, Bockelman, and Darden, Phys. Rev. 88, 83 (1952).

[8] Feshbach, Porter, and Weisskopf, Technical Report No. 62, Laboratory for Nuclear Science, Massachusetts Institute of Technology, 1953 (unpublished).

[9] R. K. Adair, Phys. Rev. 94, 737 (1954).

Double Vacancies in the K Shell Associated with K-Electron Capture in A^{37}†

J. A. MISKEL AND M. L. PERLMAN
Chemistry Department, Brookhaven National Laboratory, Upton, New York

(Received March 8, 1954)

The pulse-height spectrum produced by the decay of A^{37} in a proportional counter was analyzed to determine the probability, per K-electron capture, for the production of a double vacancy in the K shell. The double vacancy is produced by promotion of the second K electron to a bound state or to the continuum. In these experiments both processes could be observed; the measurements included events in which the kinetic energies of the promoted electrons were in the range zero to 4.0 kev. Seventy-three percent of the theoretically predicted total effect should occur in this energy interval. The data, appropriately corrected, give for the probability of double K-vacancy production per K capture, in the energy interval investigated, $3.9\pm0.7\times10^{-4}$. The result is substantially in agreement with the value calculated from theory.

INTRODUCTION

THE atomic excitation and ionization which accompany change of nuclear charge in radioactive decay have been the subjects of considerable theoretical and some experimental investigation.[1–12] It may be calculated from a relation given by Serber and Snyder[9] that the average electronic excitation produced by beta decay at $Z=18$ is 64 ev; the probabilities for excitations sufficiently great to create vacancies in the K shell are finite. Calculations by various workers[1–6] show that in negatron decay the probability of K-vacancy creation is approximately $0.5/Z^2$. For levels of higher principal quantum number, the probability of vacancy creation increases because of the decrease in the effective value of Z due to the shielding effect of the inner electrons. The effects to be expected in K-capture decay are somewhat different.[6] The probability of removal of the remaining K electron is calculated to be $0.125/Z^2$, and the probability of vacancy creation in levels of higher principal quantum number is smaller because, for these electrons, the electrostatic potential from the nucleus Z shielded by two K electrons is nearly the same as that from the product nucleus Z-1 shielded by one K electron.

In the case of K capture in Fe^{55}, a search has been made by Porter and Hotz[7] for orbital electrons ejected with energies in the range 30 to 205 kev. The upper limit resulting from this experiment, 0.6×10^{-6} electron ejections per disintegration, was considered to be not in disagreement with the value 3.6×10^{-6} derived from theory. G. Charpak,[12] using proportional counters and an Fe^{55} source, searched for the x-x coincidences which must accompany K-electron ejection. The effect observed did not exceed a few percent of the accidental coincidence rate; the result was interpreted to be in agreement with theory.

This paper reports measurements on the production of double K-shell vacancies in 35.0-day A^{37}, which decays 92 percent by K capture and 3 percent by L capture.[13]

EXPERIMENTAL METHOD

The pulse-height spectrum from a small proportional counter containing A^{37} consists mainly of one peak, centered at 2.83 kev, the K binding energy of chlorine. This peak is produced by the 89 percent[14] of the K-capture events in which the orbital vacancy is filled by Auger processes; in the case of the counters described below, it may be calculated that a relatively small contribution to the peak, less than 1 percent, is made by a fraction of the K fluorescence processes in which the x-ray is absorbed in the counter gas. A second small broad peak centered at about 200 ev results about equally from L capture and from those K-capture-fluorescent events in which the K x-ray is not absorbed. Whenever a K-capture event is accompanied by removal of the remaining K electron, the pulse corresponds to an energy of at least 5.76 kev if both K vacancies are filled by Auger processes. The pulse size corresponds approximately to 5.76 kev if the second K electron is promoted to a bound state; when the K electron is ejected from the atom the resulting pulse is larger than 5.76 kev by the amount of the kinetic energy of the electron. The value 5.76 kev for the double K vacancy with promotion to bound states has been taken to be somewhat larger than twice the K binding energy of chlorine, because one of the vacancies is filled in an atom which has no K electrons. Analysis of the pulse spectrum in the region of 6 kev and a comparison of the intensity in this region with that in the neighborhood of 3 kev, therefore, should give information about the probability

† Research carried out under the auspices of the U. S. Atomic Energy Commission.

[1] A. Migdal, J. Phys. (U.S.S.R.) **4**, 449 (1941).
[2] E. L. Feinberg, J. Phys. (U.S.S.R.) **4**, 423 (1941).
[3] A. Winther, Kgl. Danske Videnskab. Selskab, Mat.-fys. Medd. **27**, No. 2 (1952).
[4] J. S. Levinger, Phys. Rev. **90**, 11 (1953).
[5] H. M. Schwarz, J. Chem. Phys. **21**, 45 (1953).
[6] H. Primakoff and F. T. Porter, Phys. Rev. **89**, 930 (1953).
[7] F. T. Porter and H. P. Hotz, Phys. Rev. **89**, 938 (1953).
[8] T. B. Novey, Phys. Rev. **86**, 619 (1952).
[9] R. Serber and H. S. Snyder, Phys. Rev. **87**, 152 (1952).
[10] W. Rubinson and W. Bernstein, Phys. Rev. **86**, 545 (1952).
[11] M. L. Perlman and J. Miskel, Phys. Rev. **91**, 899 (1953).
[12] G. Charpak, Compt. rend. **237**, 243 (1953).
[13] Pontecorvo, Kirkwood, and Hanna, Phys. Rev. **75**, 982 (1949).
[14] Broyles, Thomas, and Haynes, Phys. Rev. **89**, 715 (1953).

of double-vacancy creation and about the kinetic energies of the ejected electrons.

The counters used for these measurements are similar to those described by Bernstein and Ballantine,[15] except for their size, which was made quite small (1-cm diameter, 4-cm length) in order to reduce background. One of the two counters was made with glass sleeves to define the central wire length; in the other counter metal sleeves, connected to the central wire, were used for this purpose. The counter gas mixture consisted of tracer amounts of A^{37} and a 60–40 mixture of argon and methane, at a total pressure of one atmosphere. The resolution of the two counters was the same. The operating characteristics of these tubes proved to be reproducible and stable over times of the order of months.

The high-voltage power supply used in these measurements has been described.[16] Counter pulses, after amplification by a linear, nonoverloading amplifier,[17] were measured with a single-channel analyzer. A nominal channel width of two volts, equivalent to approximately 250 ev, was used in all measurements. Corrections were made to the observed spectrum for a small variation of channel width with channel position. Good electrostatic shielding and careful treatment of insulating surfaces made it possible to reduce the effects of electrical leakage pulses to a fraction of one percent of the smallest measured rates. The distribution of the time intervals between pulses at the low count rates give no evidence for nonstatistical fluctuations. The over-all gain was monitored by observation of the location of the peak at 2.8 kev. Corrections were made for the small gain drift which occurred in one of the experiments.

In the energy region above the principal 2.8-kev peak there are four possible sources for pulses in addition to background and double-vacancy production. These are (a) inner bremsstrahlung, (b) statistical spread of the 2.8-kev pulse distribution, (c) accidental pulse addition, and (d) possible radioactive impurity.

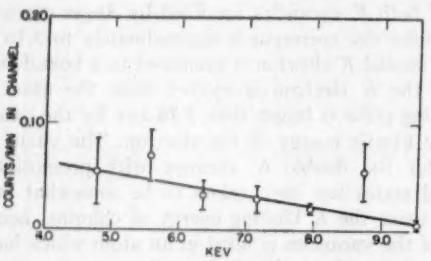

FIG. 1. Background pulse-height spectrum in small proportional counters.

(a) The energy distribution of the inner bremsstrahlung of A^{37} has recently been measured,[18] and the results are in agreement with theory.[19,20] The probability per K capture for the emission of a photon in the energy region of interest should be approximately 10^{-7}, or less than 0.1 percent of the expected double-vacancy effect.

(b) The statistical spread of the 2.8-kev peak was observed to give it a full width at half-maximum intensity of 30 percent. If the peak shape is assumed to represent a Gaussian distribution, it may be estimated that the area under the curve from 5 kev to infinity is 10^{-7} of the total area. Analysis of the peak shape, with allowance for accidental addition, showed that the distribution fell off on the high-energy side more rapidly than a Gaussian of equal width at half maximum.

(c) Pulses of size larger than those corresponding to 2.8 kev are produced whenever two 2.8-kev events occur within a sufficiently short time interval. The magnitude of this effect, which is proportional to the time duration of the pulses and to the square of the count rate, was made reasonably small by the avoidance of high rates and by the use of a short clipping-time constant ($\sim$0.3 μsec) in the amplifier; and it was evaluated by spectrum measurements made on samples of different strengths. The sample strengths, R and nR, were determined by measurement of the areas under the 2.8-kev peaks. In the spectral region between 4.5 kev and 10 kev the count rates, at any energy E, of the samples are

$$\text{for sample } R: \quad W_E = k_E R + c_E R^2,$$

and

$$\text{for sample } nR: \quad S_E = k_E nR + c_E (nR)^2,$$

where k_E is the factor for the double-vacancy production and c_E the factor for accidental pulse addition.[21] Then

$$W_E - S_E/n^2 = (n-1)k_E R/n.$$

The desired quantity $k_E R$ is thus evaluated because all other quantities in this relation are experimentally determined.

(d) Because small amounts of radioactive impurities in the A^{37} could produce pulses in the energy region of interest, complete sets of measurements were made with sources prepared in two different ways. In the first preparation the A^{37} was produced by neutron irradiation of calcium metal sealed in vacuum. Before irradiation the metal was cleaned and outgassed in vacuum at 600°C. The A^{37} was released by vacuum fusion of the calcium and was further purified by the

[15] W. Bernstein and R. Ballantine, Rev. Sci. Instr. **21**, 158 (1950).
[16] W. A. Higinbotham, Rev. Sci. Instr. **22**, 429 (1951).
[17] R. L. Chase and W. A. Higinbotham, Rev. Sci. Instr. **23**, 34 (1952); W. A. Higinbotham, Brookhaven National Laboratory Report BNL-234 (T-36) (unpublished).
[18] Anderson, Wheeler, and Watson, Phys. Rev. **90**, 606 (1953).
[19] P. Morrison and L. I. Schiff, Phys. Rev. **58**, 24 (1940).
[20] J. M. Jauch, Oak Ridge National Laboratory Report ORNL-1102, 1951 (unpublished).
[21] The factor c_E is energy-dependent because the pulse shape is not square and because all pulses under the 2.8-kev peak are not of one size.

TABLE I. Analysis of pulse-height spectrum representing events of energy between 4.5 kev and 10 kev from A^{37}. In column 7, n^2 represents the square of the ratio of the disintegration rate of Sample 2 on 11–21–53 to the disintegration rate of Sample 1 at the times listed in column 3. Column 11 is column 10 divided by $(n-1)/n$. All rates are given in counts/minute.

1[a]	2	3	4	5	6	7	8	9	10	11	12
		Sample 1			Sample 2 Net rate 11–21–53 0:00			Net Sample 1 corrected Col. 3– Col. 8	Col. 9 corr. for decay to 11–6–53, 14:00	Col. 10 corr. for excess accidental subtraction	Col. 11 corr. for channel width variation
Energy (kev)	Bkg rate	Date	Obs rate	Net rate		n^2	Column 6 / Column 7				
4.62	0.058±0.02	11–9–53 10:30	(0.80)[b]	(0.74)[b]	(3.88)[b]	13.4	(0.29)[b]	(0.45)[b]	(0.48)[b]	(0.66)[b]	(0.68)[b]
4.78	0.056±0.02	11–9 10:30	0.47 ±0.05	0.414±0.05	2.69±0.3	13.4	0.201±0.02	0.213±0.06	0.226±0.06	0.311±0.08	0.32±0.08
5.10	0.052±0.02	11–10 14:00	0.301±0.03	0.250±0.04	1.53±0.2	14.0	0.109±0.01	0.141±0.04	0.152±0.04	0.208±0.06	0.22±0.06
5.41	0.049±0.02	11–10 13:00	0.268±0.03	0.219±0.03	0.97±0.1	14.0	0.069±0.007	0.150±0.03	0.162±0.04	0.221±0.05	0.23±0.05
5.73	0.046±0.02	11–11 13:00	0.224±0.03	0.178±0.03	1.07±0.1	14.6	0.073±0.007	0.105±0.03	0.116±0.03	0.157±0.05	0.17±0.05
6.05	0.042±0.01	11–12 15:00	0.226±0.03	0.184±0.03	0.93±0.09	15.2	0.061±0.006	0.123±0.03	0.137±0.03	0.185±0.05	0.20±0.05
6.37	0.039±0.01	11–13 01:30	0.194±0.01	0.155±0.02	0.87±0.08	15.4	0.056±0.005	0.099±0.02	0.113±0.02	0.152±0.03	0.16±0.03
6.69	0.036±0.01	11–16 11:30	0.194±0.02	0.158±0.02	1.02±0.1	17.8	0.058±0.005	0.100±0.02	0.122±0.03	0.160±0.04	0.17±0.04
7.00	0.033±0.01	11–17 00:00	0.153±0.01	0.120±0.01	1.06±0.1	18.1	0.059±0.006	0.061±0.015	0.075±0.017	0.098±0.02	0.10±0.02
7.32	0.029±0.01	11–14 23:00	0.142±0.01	0.113±0.01	0.79±0.08	16.5	0.048±0.005	0.065±0.015	0.077±0.017	0.102±0.02	0.11±0.03
7.64	0.026±0.01	11–12 03:00	0.143±0.01	0.117±0.01	0.68±0.07	14.9	0.046±0.005	0.071±0.015	0.079±0.016	0.107±0.02	0.12±0.02
7.96	0.022±0.01	11–10 01:00	0.117±0.01	0.095±0.01	0.53±0.02	13.8	0.039±0.001	0.056±0.014	0.060±0.015	0.082±0.021	0.09±0.02
8.75	0.014±0.01	11–14 02:00	0.072±0.008	0.058±0.01	0.34±0.02	16.2	0.021±0.001	0.037±0.012	0.043±0.014	0.057±0.019	0.06±0.02
9.55	0.006±0.005	11–16 01:00	0.063±0.006	0.057±0.008	0.22±0.02	17.5	0.013±0.001	0.044±0.008	0.053±0.009	0.070±0.012	0.08±0.01

[a] The uncertainty in the energy values is about 2 percent.
[b] Values based on interpolation.

use of barium "getter" and by passage through a liquid-nitrogen-cooled trap. This material was six months old when used in the experiments. For the second preparation calcium fluoride, in the form of cleaned optical crystal material, was irradiated in vacuum. The irradiated material was transferred to a tantalum crucible and melted in vacuum, and the A^{37} was removed via a liquid-nitrogen-cooled trap. This A^{37} was used soon after preparation. Considerations of the purity of materials irradiated, of the nature of the purification process, and of the half-lives of possible products make it very unlikely that there was any measurable contribution by impurities to the observed pulse spectrum. Possible interference by 265-year A^{39} is ruled out because the results obtained from the two preparations are the same even though the A^{39}/A^{37} ratio was 30 times as large in the first preparation as it was in the second.

Background rates were measured when the counters were filled with inactive gas. The gas gain in the background measurements was made to equal that of the A^{37} measurements by adjustment of the high voltage; the pulse spectrum of an external Cd^{109} source was used as a monitor. The backgrounds of the two counters used, which were the same within the statistical errors, are shown in Fig. 1.

RESULTS AND DISCUSSION

In Table I are given the data and corrections obtained from the experiment with A^{37} produced from irradiated calcium fluoride. The data obtained with A^{37} from irradiated calcium metal were similar. Final results (column 12) are shown graphically in Figs. 2 and 3. The errors indicated in the table are derived from the counting statistics.

In the region below 5.5 kev the rates change so rapidly with energy that an energy uncertainty of a

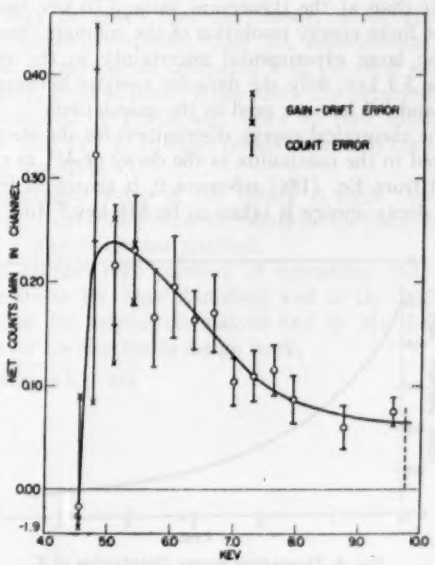

FIG. 2. Pulse-height spectrum representing events of energy 4.5 kev to 10 kev in the decay of A^{37}. (CaF_2 source).

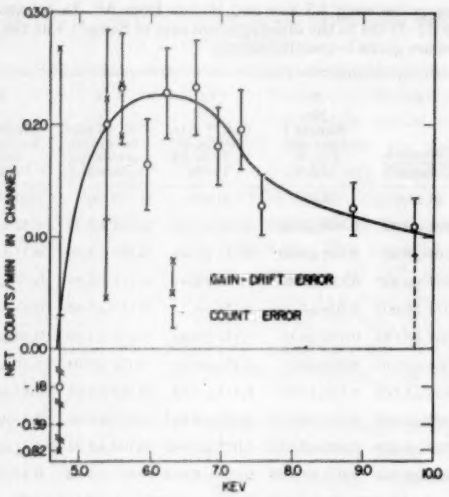

FIG. 3. Pulse-height spectrum representing events of energy 4.5 kev to 10 kev in the decay of A^{37}. (Ca metal source).

few percent, because of the subtraction which is involved in the calculation of column 9, gives rise to uncertainties larger than those shown in the table. Whenever the errors from this source become comparable with the tabulated errors, both are indicated in the figures. In the calculation of the errors caused by energy uncertainty, a 3 percent relative gain drift was assumed.

A smooth curve has been drawn through the experimental points (Figs. 2 and 3); and it has been made to reach the zero ordinate at approximately 4.7 kev rather than at the theoretical value 5.76 kev because of the finite energy resolution of the counters. Because of the large experimental uncertainty in the region below 5.4 kev, only the data for energies between 5.4 kev and 9.7 kev are used in the calculations.

The theoretical energy distribution for the electrons ejected to the continuum in the decay of A^{37}, as calculated from Eq. (18a) reference 6, is shown in Fig. 4. The decay energy is taken to be 816 kev.[22] In Fig. 5,

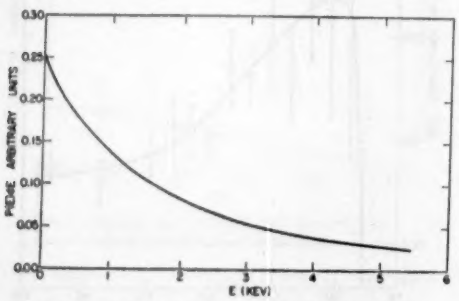

FIG. 4. Theoretical energy distribution of K electrons ejected in the decay of A^{37}.

[22] Richards, Smith, and Browne, Phys. Rev. **80**, 524 (1950).

Curve C shows this theoretical distribution as it appears when modified by the finite resolution of the counters and by the addition of the energy, 5.76 kev, derived from the filling of two K vacancies in chlorine. The energy of 5.76 kev appears only when both vacancies are filled by Auger cascades, for which the probability is $(0.89)^2$ or 0.79. Curve B is the pulse spectrum to be expected from the promotion of K electrons to bound states; the areas under B and C out to the end-point energy are normalized so that they are in the ratio 2:3, as given by reference 6, Eq. (17b) and Eq. (15) with the added factor $\frac{2}{3}$ as cited in the text. Curve A is the sum of B and C and represents the actual pulse-height distribution to be expected from the theory. In the calculation of B and C the resolution of the counter was computed from the observed resolution at 2.8 kev, with the assumption of an $E^{\frac{1}{2}}$ dependence.

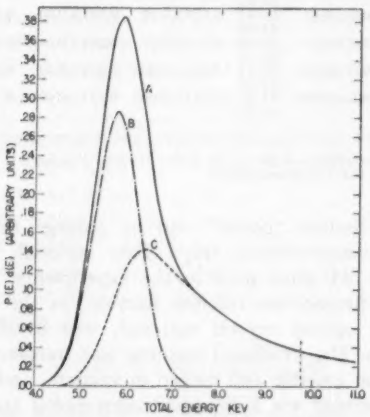

FIG. 5. Theoretical pulse-height distributions corrected for finite counter resolution. Curve C is the contribution of events in which the second K electron is ejected to the continuum. Curve B is the contribution of events in which the electron is promoted to a bound state. Curve A is the sum of B and C.

The vertical line at 9.73 kev, marking the high-energy limit of these experiments, corresponds to a kinetic energy for the ejected electron of 9.73–5.76 kev or 3.97 kev. From a graphical integration under the theoretical momentum-distribution curve it was found that 0.71 of all continuum-ejection events should be included in the experimental range 5.4 to 9.7 kev. Similarly 0.79 of the area under Curve B, Fig. 5, should be included. Thus the range of the measurements should include $(0.71)\frac{3}{5}+(0.79)\frac{2}{5}$ or 0.73 of all ejection and promotion events accompanied by double Auger cascade.

The final results are summarized in Table II. The various rates set down in Table II are obtained by division of the areas under the curves of Figs. 2 and 3 and under the 2.8-kev peaks by the channel width. The values given in column 5, however, do not depend on an accurate knowledge of this width.

A chlorine atom lacking two K electrons may complete its K shell in any of three ways: (a) double Auger process, probability $(0.89)^2$; (b) one fluorescent and one Auger process, probability $2(0.89)(0.11)$; and (c) double fluorescent process, probability $(0.11)^2$. The probability of completion of the K shell by path (b) is 25 percent as great as that by path (a), but the contribution by path (b) to the pulse distribution observed in these experiments is small, because the path (b) distribution has its maximum in the vicinity of 2.8 kev. Path (b) processes are estimated to contribute 8 percent of the areas under the curves of Figs. 2 and 3.

According to Primakoff and Porter,[6] the total probability per K capture for double K-vacancy production is

$$p^{(2)} \cong (3/4Z^2)(1-\gamma)^2(\alpha), \qquad (1)$$

where γ, a parameter, is given the value 0.50 to fit the electron space wave function used to that given by Hylleraas,[23] and α is a constant of value $\frac{2}{3}$ (but see below). For A^{37}, $p^{(2)}$ is calculated to be 3.86×10^{-4}; for comparison with the experiments this quantity is multiplied by 0.73 to give 2.82×10^{-4}. The value derived from the average experimental value (Table II, column 5), after correction for the path (b) contribution, is $3.9\pm0.7\times10^{-4}$.[24]

TABLE II. Summary of results for double K-vacancy production in A^{37}. In column 4 the rates of column 3 are corrected for fluorescence, factor $1/(0.89)^3$. Column 2 rates have been corrected for fluorescence, factor 1/0.89.

1	2	3	4	5
	K-capture rate (counts/min)	Rate of pulses in the interval between 5.38 kev and 9.73 kev (counts/min)	Column 3 corrected (counts/min)	Double K holes per K capture Col. 4/Col. 2
Exp. 1	6.65×10^3	2.35	2.97	4.47×10^{-4}
Exp. 2	5.26×10^3	1.66	2.10	3.99×10^{-4}
				av $4.2\pm0.7\times10^{-4}$ [a]

[a] The error value is estimated from a consideration of the possible sources of uncertainty; it is thought to be conservative.

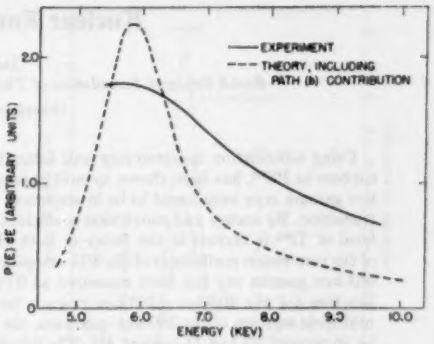

FIG. 6. Comparison of experiment and theory.

The probability per K capture for the ejection of the second K electron to the continuum as given in reference 6, Eq. (17b) is:

$$p_{\text{eject}} \cong 0.3(1-\gamma)^2/Z^2. \qquad (2)$$

The probability for promotion of the second K electron to bound states is then the difference between Eqs. (1) and (2). There is sufficient uncertainty in the value of α in Eq. (1) to make p_{bound} uncertain by a factor of at least 3. A comparison of the average experimental spectrum with the theoretical one, Fig. 6, seems to indicate that the ratio of p_{bound} to p_{eject} is smaller than that calculated; and if the value of α were chosen to be not $\frac{2}{3}$ but $\frac{1}{2}$, as suggested by Levinger,[25] the fit of the calculated curve with the observed spectrum would be much better. This choice, however, would give $p^{(2)}$ the value 2.9×10^{-4}, and $0.73p^{(2)}$ then would be 2.1×10^{-4}.

It may be noted that the theory, which gives a result somewhat smaller than the experimental one here at energies small compared with the total energy available, gives a result larger than the experimental one obtained by Porter and Hotz[7] in their measurements with Fe^{55} at energies comparable with the total energy available.

The present state of the theory is such that an attempt to determine accurate values for the parameters α and γ is probably not justified.

The authors take pleasure in expressing their appreciation to Dr. Max Wolfsberg and to Dr. William Rubinson for helpful discussions and to Mr. Robert Chase for his electronics design work.

[23] A value of 0.4 for γ, as given by E. A. Hylleraas, Z. Physik **54**, 347 (1929), could be used instead of the value 0.5. The choice $\gamma=0.4$ increases both $p^{(2)}$ and p_{eject} by a factor 1.44.

[24] Levinger's[5] expression is $p^{(2)}=0.16/Z^2$, which for A^{37} becomes 5.0×10^{-4}. The calculation of Primakoff and Porter, however, includes factors omitted by Levinger.

[25] Reference 6, p. 934.

Nuclear Energy Levels of Tl^{203}†

JAGDISH VARMA*
Bartol Research Foundation of The Franklin Institute, Swarthmore, Pennsylvania

(Received February 17, 1954)

Using scintillation spectrometry and coincidence counting techniques, Tl^{203}, formed by orbital electron capture in Pb^{203}, has been shown to emit gamma rays of energies 280, 403, and 683 kev. The 403- and 280-kev gamma rays were found to be in sequence; the 683-kev gamma ray represents the associated cross-over transition. By energy and conversion coefficient measurements, it has been shown that the same 280±2 kev level of Tl^{203} is excited in the decay of both Hg^{203} and Pb^{203}. A coincidence method for the measurement of the conversion coefficients of the 403-kev gamma rays is described. The K-shell conversion coefficient of the 403-kev gamma ray has been measured as 0.076, the $K/(L+M)$ ratio being 3.7. The angular correlation function for the 403-kev−280-kev cascade has the form $W(\theta)=1-(0.152\pm0.007)\cos^2\theta$. For the known multipole mixture of the 280-kev quantum, the correlation measurements indicate the 403-kev transition to be 76 percent $E2$ and 24 percent $M1$. The interference phases of the $E2$ and $M1$ matrices of both transitions are the same in Lloyd's notation. The angular correlation studies and the conversion coefficient measurements indicate the orbitals of the levels of Tl^{203} to be $d_{5/2}$, $d_{3/2}$, and $s_{1/2}$, in order of decreasing excitation energy. The spin of the ground state of Pb^{203} is shown to be $5/2(-)$.

INTRODUCTION

THE 46-day Hg^{203} has been shown[1–3] to decay by beta emission to a level at 280 kev in Tl^{203}. Early investigations of Pb^{203} showed[4] it to decay to Tl^{203} by orbital electron capture and subsequent emission of gamma rays of energies 270 and 470 kev. Magnetic spectrographic studies[5] of the radiations of the radio isotopes of lead have indicated that gamma rays of energies 153, 269, and 423 kev are emitted in the decay of the 52-hour Pb^{203}. From the energy and the measured K/L ratio of the 269-kev gamma ray, it was concluded[5] that the 269-kev level is different from the 280-kev level of Tl^{203} observed in the decay of Hg^{203}. It was also suggested by the same author that the 153- and 269-kev gamma rays are in cascade and that the 423-kev quantum is emitted in the cross-over transition.

In order to obtain further data concerning the levels of Tl^{203}, the radiations of Pb^{203} have been reinvestigated with thallium activated sodium iodide and anthracene scintillation spectrometers and coincidence methods.

CHEMICAL PROCEDURE

Pb^{203} was produced by the bombardment of metallic thallium by 14-Mev deuterons. To separate out the radioactive lead, the irradiated sample of thallium was dissolved in concentrated sulfuric acid; the sulfuric acid was then diluted to a 10N solution, and the lead sulfate thus precipitated was centrifuged out and washed with dilute sulfuric acid and a small quantity of water. The lead sulfate was then dissolved in an aqueous solution of ammonium acetate. Whenever a source in the solid state was needed, lead chromate was precipitated from the solution by addition of potassium chromate. In the course of some measurements, the lead chromate precipitate was dissolved in concentrated nitric acid with the addition of hydrogen peroxide.

ENERGIES AND RELATIVE INTENSITIES OF THE GAMMA RAYS

A strong source of Pb^{203} in solution was placed at a distance of 75 cm from a crystal of NaI(Tl) of thickness 3.5 cm which was mounted on a photomultiplier tube, RCA-5819. In Fig. 1 is plotted the pulse-height distribution generated in the crystal by the gamma rays of Pb^{203}. The source distance was large to avoid "pile up" of pulses arising from any coincident gamma rays. From the spectrogram it is clear that the quantum radiations of Pb^{203} consist of the 70-kev x-rays of thallium and gamma rays of energies 280, 403, and 683 kev. The small rise in counting rate at ~150 kev is produced by Compton secondaries in the crystal of the

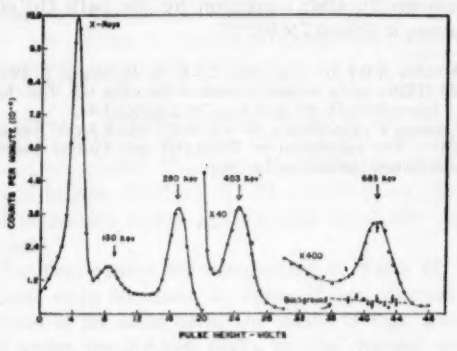

FIG. 1. Pulse-height distribution generated by gamma rays from Pb^{203} in a NaI(Tl) crystal of dimensions 3.5 cm×3.5 cm diameter.

† Assisted by the joint program of the U. S. Office of Naval Research, and the U. S. Atomic Energy Commission.

* Research Fellow, Bartol Research Foundation; permanent address, Morena (M.B.), India.

[1] H. Slätis and K. Siegbahn, Phys. Rev. **75**, 318 (1949).

[2] H. W. Wilson and S. C. Curran, Phil. Mag. **42**, 762 (1951).

[3] Cork, Martin, LeBlanc, and Branyan, Phys. Rev. **85**, 386 (1952).

[4] Lutz, Pool, and Kurbatov, Phys. Rev. **65**, 61 (1944).

[5] G. D. O'Kelley, Ph.D. thesis, University of California Radiation Laboratory Unclassified Report UCRL 1243, May, 1951 (unpublished).

280-kev quantum and by recoil photons resulting from backscattering in the source.

An experiment was performed to determine accurately the energy of the 280-kev gamma ray and to compare it with that of the gamma ray emitted in the decay of Hg^{203}. The photopeak produced in the crystal by the gamma ray of Hg^{203} was scanned just before and immediately after observing the same peak associated with a source of Pb^{203}. The same geometry was maintained throughout the course of these comparative measurements, and the sources of Hg^{203} and Pb^{203} were approximately equal in strength. To avoid changes in pulse height resulting from fluctuations in room temperature or line voltage, the measurements were performed in a relatively short time. As shown in Fig. 2, the energies of the gamma rays at about 280 kev emitted in the case of both Hg^{203} and Pb^{203} differ by not more than 0.5 kev. This small limit of difference suggests that the same 280-kev level of Tl^{203} is excited in the decay of either radionuclide. From the calibration of the scintillation spectrometer, the energy of the gamma ray is 280 ± 2 kev.

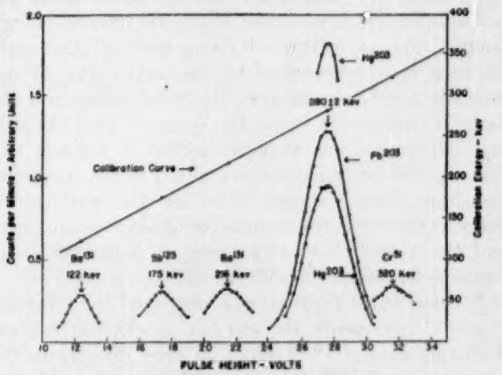

FIG. 2. Photopeaks due to gamma rays from Hg^{203} and Pb^{203}. The photopeak due to gamma ray from Hg^{203} was observed immediately before and after observing the peak due to gamma ray from Pb^{203}. The photopeaks due to gamma rays from Cr^{51}, Ba^{131}, and Sb^{125} were measured for calibration of the spectrometer.

To show that the rise in counting rate in the region of ~150 kev (Fig. 1) does not constitute evidence of the presence of the previously reported 153-kev radiation, a comparison was made between the gamma spectra of Hg^{203} and Pb^{203} using thin sources in which little backscattering occurred. In these measurements the peak at ~150 kev was found to be greatly reduced as compared with the intensity indicated in Fig. 1 and approximately what should be expected as the normal Compton contribution of a 280-kev gamma ray. The spectra of both radioelements were practically identical below 280 kev in energy, further substantiating that no appreciable 153-kev radiation is emitted by Pb^{203}, because Hg^{203} has been previously shown to emit a single gamma ray at 280 kev. From the ratio of the counting rate at ~150 kev to that at the photopeak, it was estimated that the 153-kev quantum could have an intensity of not more than two percent of that of the 280-kev quantum. Additional evidence of the absence of any 153-kev radiation was obtained from coincidence measurements limited to energies of 180 kev or less. A source of Pb^{203} was placed between the NaI(Tl) crystals of two coincident scintillation spectrometers. The channel of one of the spectrometers was fixed at the photopeak of the 280-kev gamma ray, while the channel of the other was allowed to traverse the interval of pulse heights corresponding to gamma-ray energies 20 and 180 kev. To avoid spurious coincidences arising from the backscattering of the 403- and 683-kev gamma rays from one crystal into the other, a lead absorber of thickness 2 g/cm² was placed between the source and the crystal of the spectrometer set at the photopeak of the 280-kev gamma ray. The presence of the lead absorber increased appreciably the single counting rate at ~150 kev. Only in the case of the 403-kev gamma ray does this scattering in the lead give rise to coincidences (it will later be shown that the 280- and 403-kev gamma rays are in cascade) at ~150 kev as indicated by the slight rise in the coincidence rate in that region of energy as shown in Fig. 3, where a spectrogram of quanta coincident with the 280-kev radiation is presented along with the single counting rate in the same energy interval. Any gamma ray of energy 153 kev of intensity even as little as one percent of that of the 280-kev line would have yielded a distinct photopeak in the coincidence rate.

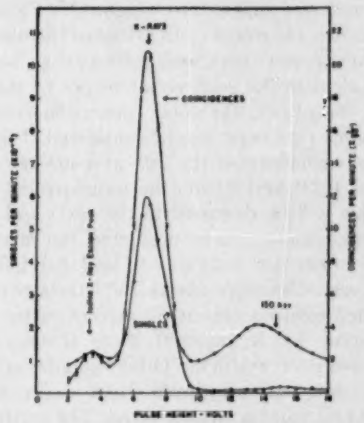

FIG. 3. Coincidence rate between the 280-kev gamma ray and the low-energy radiations from Pb^{203} where the statistical error, not shown, is less than the size of the point.

The relative intensities of the gamma rays from Pb^{203} were obtained from the areas of the photopeaks (really "full energy" peaks) shown in Fig. 1. In making the calculations, the variation with energy of the efficiency of the crystal for absorption of the full energy of the

gamma rays was taken into account.[6,7] From these measurements, the relative intensities of the 683-, 403-, and 280-kev gamma rays were estimated to be 1:5.1:120. To calculate the relative intensities of the corresponding transitions, the total conversion coefficients of the gamma rays must also be considered. Taking the conversion coefficients of the 280- and 403-kev gamma rays to be 0.24[2] and 0.098 (the measurement of this latter value will be discussed in the text) and that of the 683-kev quantum to be negligible, the ratio of the transition intensities was found to be 1:5.6:150.

With every disintegration of Pb^{203} through capture of a K-shell electron (about 80 percent of the transitions[8,9] occur by K capture) there is associated a K-series x-ray of thallium. Other quanta of 70-kev thallium x-rays may arise from the K-shell conversion of the several gamma rays emitted. The contribution to the x-ray intensity arising from internal conversion is appreciable only in the case of the 280-kev line. Because of the low intensities and small conversion coefficients, the remaining two gamma rays contribute little to the x-ray intensity. The Auger effect[10] reduces the intensity of the x-rays from thallium by about five percent. If one takes into account the efficiency of the crystal for full energy absorption of the 280-kev gamma ray and the 70-kev x-rays, the K-shell conversion coefficient of the 280-kev gamma ray, absorption of the 70-kev x-rays in the aluminum-magnesium oxide housing and in the source itself, and the Auger effect, a comparison of the areas under the 70-kev and 280-kev photopeaks indicates that with each disintegration (K and L capture included) there is associated roughly one 280-kev transition. On considering all possible errors resulting from the several corrections applied, it was concluded that perhaps as many as ten percent of the K-capture disintegrations might proceed to the ground state. However, as will be shown later in the text, coincidence measurements yield a much lower value for the upper limit of the probability of the ground-state transition.

From the pulse-height spectrum of the conversion electrons emitted from a source of Pb^{203} and observed in an anthracene crystal, the $K/(L+M)$ ratio for the 280-kev gamma ray was found to be 2.5. This value is in good agreement with recent measurements[11] of the corresponding ratio for the decay of Hg^{203}. Because the intensity of the conversion electrons related to the 403-kev gamma ray is quite low, its $K/(L+M)$ ratio could not be determined by this method.

COINCIDENCE MEASUREMENTS

To determine the relationship between the 280- and 403-kev gamma rays, coincidences between the two quanta were studied. Two NaI(Tl) scintillation spectrometers were placed in coincidence, and in the crystal of either spectrometer there was generated a pulse-height distribution like the one shown in Fig. 1 when a source of Pb^{203} was interposed between the two crystals. The channel of one of the spectrometers was set at the photopeak of the 280-kev gamma ray while the channel of the other was moved in steps of $\sim$9 kev from 335 to 445 kev. In Fig. 4 is plotted the coincidence rate (represented by open circles and calculated statistical probable errors) as observed in the above-cited energy interval. The points are to be compared with the single counting rate (represented by the solid curve). From the close agreement between the coincidences and the single counting rate, it can be concluded that the 403- and 280-kev gamma rays are indeed in cascade and that the 683-kev radiation is emitted in the cross-over transition. This is supported by the fact that coincidences were observed between the 683-kev gamma rays and the x-rays. No other quantum radiations were found to be coincident with the 683-kev gamma ray.

A coincidence method was employed in a further attempt to estimate the number of electron capture disintegrations of Pb^{203} which proceed directly to the ground state of Tl^{203}. A source of Pb^{203} was placed before the adjacent NaI(Tl) crystals of two scintillation spectrometers in coincidence. The crystals were shielded from each other by a thickness of one centimeter of lead.

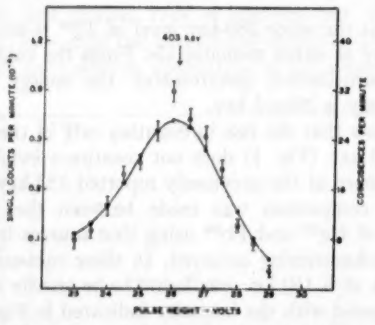

FIG. 4. Coincidence rate between the 280-kev gamma ray and the gamma spectrum at 403 kev. The solid curve represents the single counting rate. The points, shown with their statistical error, represent the coincidence rate in each position of the channel.

[6] The efficiency of a crystal for absorption of the total energy of a gamma ray is given by $E=RS$, where S is the total interaction cross section of the crystal for the gamma ray, and R is the ratio of the area of the full energy peak to that of the total contribution to the counting rate from the gamma ray. Both R and S vary with quantum energy and crystal size. The value of S was obtained from the curve given by Jordan,[7] while R was evaluated as a function of energy by observing the pulse-height distribution generated in the crystal by several different monoenergic gamma-ray sources. R is a function of the distance and geometry of the source, but for the gamma rays shown in Fig. 1, the relative values of R will change but little as the source geometry and distance is altered.

[7] W. H. Jordan, Ann. Rev. Nuclear Sci. **1**, 221 (1951).

[8] R. E. Marshak, Phys. Rev. **61**, 431 (1942).

[9] M. E. Rose and J. L. Jackson, Phys. Rev. **76**, 1540 (1949).

[10] E. H. S. Burhop, *The Auger Effect* (Cambridge University Press, Cambridge, 1952).

[11] F. R. Metzger (private communication, 1953). Data relating to the conversion coefficients of the gamma ray from Hg^{203} are $\alpha_K=0.163\pm0.006$, $K/L=3.5$, $L/M=3.2$.

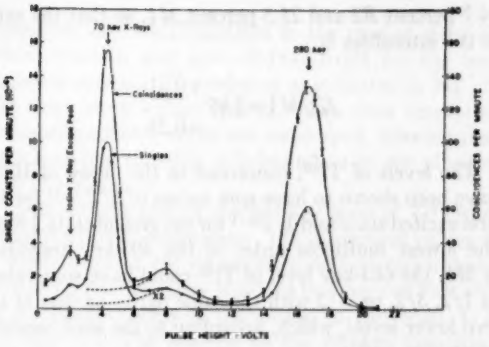

FIG. 5. Coincidence rate between Tl K x-rays and the low-energy gamma spectrum from Pb^{203}. The curve with points shown with statistical error represent the coincidence rate. The single counting rate is also plotted.

The channel of one spectrometer (hereafter denoted by the subscript "1") was fixed at the photopeak of the 70-kev x-rays while that of the other (henceforth to be indicated by the subscript "2") was moved over the region of energy lying between 20 kev and 350 kev. The single counting rate as well as the coincidence rate was recorded for each pulse-height setting of the channel as shown in Fig. 5. The two peaks in the coincidence rate at 70 and 280 kev represent coincidences between x-rays and x-rays, and x-rays and gamma rays.

If N_{xx} represents the number of coincidences between x-rays (two x-rays will be emitted when, after K capture, the 280-kev gamma ray is converted), $N_{x\gamma}$ the number of coincidences between 70-kev x-rays and 280-kev gamma rays, N_{x_2} the number of single counts due to x-rays, and $N_{\gamma 2}$ the number of single counts arising from 280-kev gamma rays recorded in the second spectrometer while measuring N_{xx} and $N_{x\gamma}$, an extension of the treatment given by Dunworth[12] yields

$$\frac{N_{xx}}{N_{x_2}}\cdot\frac{N_{\gamma 2}}{N_{x\gamma}}=\frac{2\alpha_K F}{K+K\alpha_T+\alpha_K F}, \tag{1}$$

where α_T and α_K are the total and the K-shell conversion coefficients of the 280-kev gamma ray, K the fraction of the disintegrations of Pb^{203} occurring through K-shell electron capture, and F the fraction of all the disintegrations of Pb^{203} in which the 280-kev transition is involved. From the calculations of Marshak[8] and the tables of Rose and Jackson,[9] the value of K is found to be 0.80 for the first forbidden transitions in question. The single counting rates at the energies of the x-ray peak and the 280-kev gamma-ray peak were properly corrected by extrapolations shown in Fig. 5 for the presence of counts arising from the Compton effect of radiations of higher energies. A similar extrapolation was necessary to remove x-ray—gamma coincidences from the apparent (x-ray)-(x-ray) coincidences. The extrapolation indicated in Fig. 5 corrects for coincidences between x-rays detected in spectrometer "1" and γ rays detected by way of the Compton effect in spectrometer "2." An additional correction is necessary to take into account $N_{x_2\gamma_1}$ the coincidences between gamma rays detected in spectrometer "1" and x-rays in spectrometer "2." The latter correction was obtained by observing the spectrum of "singles" in spectrometer "1" and extrapolating as in Fig. 5 to find the contributions of the gamma rays to the single counting rate in the x-ray peak; then $N_{x_2\gamma_1}$ can easily be calculated. In particular,

$$\frac{N_{x_2\gamma_1}}{N_{x_1\gamma_2}}=\frac{N_{x_2}}{N_{\gamma 2}}\cdot\frac{N_{\gamma 1}}{N_{x_1}}. \tag{2}$$

In practice, the actual calculation of the quantity $(N_{xx}/N_{x_2})(N_{\gamma 2}/N_{x\gamma})$ was made only at the three highest points of the peaks of Fig. 5. The average of the three computations 0.30 ± 0.010, was then employed to obtain F from Eq. (1), which becomes

$$F\alpha_K/(0.80+0.80\alpha_T+\alpha_K F)=0.150\pm0.005. \tag{3}$$

The conversion coeficients are taken to be those[11] of the 280-kev gamma ray of Hg^{203}, it being assumed that the gamma rays of this energy emitted by Hg^{203} and Pb^{203} are identical. This assumption appears valid from a consideration of the energies and of the $K/(L+M)$ ratios of the two transitions. From Eq. (3), the calculated value of F is 1.06 ± 0.05. Thus, the fraction of the total number of disintegrations proceeding to the ground state is small.‡

To determine the conversion coefficient of the 403-kev gamma ray, the coincidence rate between the conversion electrons and the 280-kev gamma ray from Pb^{203} was studied. To make these measurements a source of Pb^{203} of thickness about 1 mg/cm^2 was placed at a distance of 0.08 cm from an anthracene crystal 2.5 cm in diameter and 1 cm in thickness, mounted upon a Dumont 6292 photomultiplier tube. The conversion electrons were recorded over an energy interval extending from 250 to 450 kev. The gamma rays were detected in a NaI(Tl) scintillation spectrometer, the channel of which was set at the photopeak of the 280-kev gamma ray.

In Fig. 6 is plotted the value of $N_{\gamma e^-}/N_\gamma$ as a function of the pulse-height setting of the channel of the anthracene spectrometer. $N_{\gamma e^-}$ is the number of coincidences between the 280-kev gamma rays and the conversion electrons of the 403-gamma ray and N_γ is the number of single counts recorded simultaneously with the coincidences in the gamma-ray spectrometer fixed at the photopeak of the 280-kev gamma ray. To obtain the coincidence rate of Fig. 6, the coincidences due to Compton recoils produced in the anthracene crystal by the 403-kev gamma ray were subtracted from the observed coincidence rate. This Compton contribution to

[12] J. W. Dunworth, Rev. Sci. Instr. 11, 167 (1940).

‡ Since this paper was submitted for publication, a more detailed analysis of the statistics of the measurements has indicated that the relative probability is one-half that the value of F lie between 0.98 and 1.00.

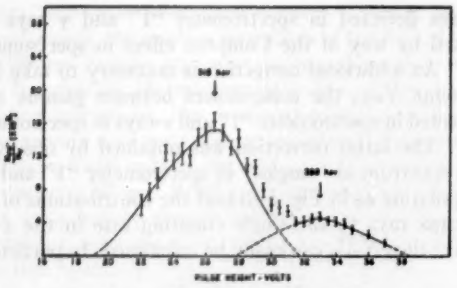

FIG. 6. Coincidence rate between the 280-kev gamma ray and the electrons from the conversion of the 403-kev gamma radiation.

the coincidence rate was obtained by interposing 0.08 centimeter of aluminum between the source and the anthracene crystal. In the coincidence curve of Fig. 6, the peaks arising from the K and L shell conversion electrons are well-resolved. The conversion electrons in the group centered at 388 kev include also those originating in the M shell. The slight asymmetry of the peak of K-shell electrons may be ascribed to non-uniformities in the anthracene crystal and to energy loss in the source. An extension of the treatment given by Dunworth[12] results in the equation

$$(N_{\gamma e^-}/N_\gamma)_\Sigma = f\omega_s\alpha_K/(1+\alpha_T), \tag{4}$$

where f is the fraction of the 280-kev transitions in sequence with the 403-kev radiation, converted and unconverted, ω_s the fractional solid angle subtended at the source by the anthracene crystal, and $(N_{\gamma e^-}/N_\gamma)_\Sigma$ the area under the K-shell peak of Fig. 6. From Fig. 1, f is estimated to be $5.1(1+\alpha_T)/150$, and ω_s is calculated to be 0.47. From Eq. (4) and the quantities defined above, α_K is calculated to be 0.063. An attempt was made to take into account backscattering in the source and at the surface of the crystal. The resulting value of α_K was found to be about 20 percent greater. This correction increases the value of α_K to 0.076.

A comparison of the areas of the two conversion electron peaks of Fig. 6 gives the ratio

$$\alpha_K/(\alpha_L+\alpha_M)=3.7. \tag{5}$$

The results of these conversion coefficient measurements were such as to suggest that the 403-kev transition is a mixture of $M1$ and $E2$ radiations. From the K-shell conversion coefficient and the curves of Rose *et al.*,[13] the 403-kev radiation is found to be a mixture, 74 percent $E2$ and 26 percent $M1$. By comparing the $K/(L+M)$ ratio with curves given by Goldhaber and Sunyar,[14] a similar mixture is obtained.

The value of the conversion coefficient of the 280-kev gamma ray identifies it also as a mixture of $E2$ in $M1$, 74.7 percent $E2$ and 25.3 percent $M1$, so that the ratio of the intensities is

$$E2/M1=2.95^{+0.31}_{-0.25}. \tag{6}$$

The levels of Tl^{203}, concerned in the decay of Hg^{203}, have been shown to have spin values of $3/2$[1,11,15] for the first excited state and $1/2$[16,17] for the ground state.§ Since the lowest multipole order of the 403-kev transition is $M1$, the 683-kev level of Tl^{203} could have spin values of 1/2, 3/2, or, 5/2 with the same parity as that of the two lower levels, which, according to the shell model,[18] have even parity.

ANGULAR CORRELATION STUDIES

To obtain more evidence concerning the spin values of the excited states of Tl^{203} excited in the decay of Pb^{203}, the spatial correlation of the two cascade gamma rays was investigated. Taking the orbital of the first excited level of Tl^{203} to be 3/2, the calculations of Ling and Falkoff[19] and Lloyd[20] show that the angular correlation function should contain only a $\cos^2\theta$ term in addition to the isotropic contribution; that is, it should be of the form

$$\omega(\theta)=1+a_2\cos^2\theta. \tag{7}$$

Because of this fact, the asymmetry in correlation was measured only at 135° and 180°. The experiment was performed with two NaI(Tl) scintillation spectrometers in coincidence. In one channel of the coincidence circuit, all pulses above the pulse height corresponding to a gamma-ray energy of 180 kev were accepted. In the other channel, all pulse heights greater than that of a pulse of a 330-kev gamma ray were accepted. The source employed in the measurements was in the form of powdered lead chromate. A "least squares" fit of the data yielded for $\omega(\theta)$

$$\omega(\theta)=1-(0.147\pm0.007)\cos^2\theta. \tag{8}$$

When corrected for the finite angular resolution of the detectors, the correlation function becomes

$$\omega(\theta)=1-(0.152\pm0.007)\cos^2\theta. \tag{9}$$

The asymmetry at 180° was observed using solutions of lead chromate in nitric acid and lead sulfate in an aqueous solution of ammonium acetate. The asymmetry after the resolution correction was found to be de-

[12] J. W. Dunworth, Rev. Sci. Instr. **11**, 167 (1940).
[13] Rose, Goertzel, and Perry, Oak Ridge National Laboratory Unclassified Report, ORNL-1023, July, 1951 (unpublished).
[14] M. Goldhaber and A. W. Sunyar, Phys. Rev. **83**, 906 (1951).
[15] Hollander, Perlman, and Seaborg, Revs. Modern Phys. **25**, 469 (1953).
§ Assignment of spin 3/2 to the first excited state of Tl^{203} is further supported by the asymmetric correlation function described in the next section.
[16] H. Schüler and J. E. Keystone, Z. Physik **70**, 1 (1931).
[17] D. A. Jackson, Z. Physik **75**, 223 (1932).
[18] Maria G. Mayer, Phys. Rev. **78**, 16, 22 (1950).
[19] D. S. Ling, Jr. and D. L. Falkoff, Phys. Rev. **76**, 1639 (1949).
[20] S. P. Lloyd, Ph.D. thesis, University of Illinois, 1951; see also Phys. Rev. **85**, 904 (1952).

scribed by $a_2=-0.175\pm0.028$ in the case of the lead sulfate solution and $a_2=-0.154\pm0.023$ for the lead chromate solution. The value of a_2 indicated in Eq. (9) and these latter values overlap when their respective statistical probable errors are considered, showing that the correlation function is independent of the physical state of the source.

To obtain the spin of the 683-kev level of Tl^{203} from the correlation measurements, the theoretical values of a_2 were obtained for dipole-mixture and quadrupole-mixture correlations from relations by Ling and Falkoff[17] for the possible spins of the second excited level, 1/2, 3/2, and 5/2. The mixture of the 280-kev transition was taken to be 74.7 percent $E2$ and 25.3 percent $M1$. Using these values of a_2, the mixture-mixture correlations for all the above mentioned spins were calculated for all possible mixtures in the 403-kev transition. In calculating the mixture-mixture correlation functions, the expressions given by Lloyd[20] were used. From these calculations, it can be seen that the observed correlation can be explained by any one of the following sets of conditions:

(a) The spin of the second excited state is 1/2 and the 403-kev gamma ray is a mixture of $E2$ and $M1$ such that $E2/M1=320$ or 0.16.

(b) The spin of the second excited state is 3/2 and the 403-kev transition is a mixture such that $E2/M1$ is approximately zero or greater than 800.

(c) The spin of the second excited level is 5/2 and the mixture of $E2$ with $M1$ in the 403-kev transition is such that $E2/M1=22$, 0, 0.11, or 3.1.

The fact that the previously discussed conversion coefficient measurements show the 403-kev transition to be 74 percent $E2$ and 26 percent $M1$ ($E2/M1=2.85$) rules out all conditions listed above except (c) where the spin of the 683-kev level is 5/2 and the 403-kev gamma ray is a mixture of $E2$ and $M1$ such that $E2/M1=3.1$. The conditions (a) and (b) are ruled out

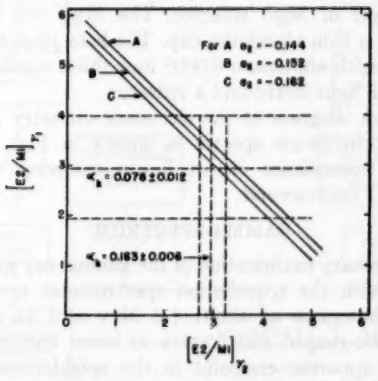

FIG. 7. The dependence of multipole mixture ($E2/M1$) in the first transition on the multipole mixture ($E2/M1$) in the second transition for the observed correlation function. The $E2/M1$ ratio allowed by the values of the conversion coefficients and their errors is shown by the dotted lines.

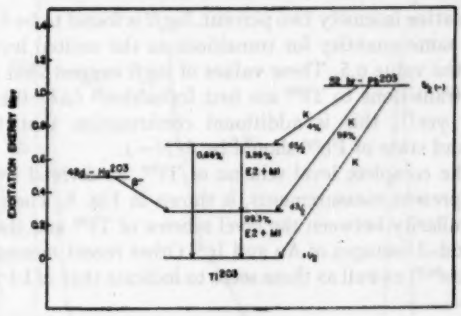

FIG. 8. Level scheme of Tl^{203}.

also by the observed intensities of the electron capture transitions and by the observed relative intensities of gamma rays originating from the second excited state of Tl^{203}.

For any given correlation function, the calculated ratio of $E2$ to $M1$ in the first transition is, of course, a function of the same ratio for the second transition. In Fig. 7 is shown the variation of the mixture in the first transition with the assumed mixture for the second transition, the correlation function being that observed in the present measurements. The curve was calculated taking as 180° (Lloyd's notation), the interference phase between $E2$ and $M1$ components of both transitions. The mixing ratio of the 403-kev transition can also be obtained from the curve of Fig. 7. The known mixture of the 280-kev transition and the observed correlation function give a value of 3.2 for $E2/M1$ in the case of the 403-kev gamma ray.

DISCUSSION

The angular correlation and conversion coefficient measurements establish the spins of the levels of Tl^{203} as 5/2, 3/2, and 1/2 in order of decreasing excitation energy. The parity for all the levels is even. In Tl^{203}, the number of protons is just one short of a magic number; so it is appropriate to write the orbitals as $d_{5/2}$, $d_{3/2}$, and $s_{1/2}$ in accord with the single-particle assignments of the shell model. The fact that few or no electron capture transitions to the ground state of Tl^{203} are observed excludes the possibility that the ground-state spin of Pb^{203} might be 1/2 or 3/2. If the spin of the ground state of Pb^{203} is assumed to be 7/2 or more, it is impossible to explain the relative intensities of the electron capture transitions which lead to the $d_{5/2}$ and $d_{3/2}$ levels of Tl^{203}. However, a spin of 5/2(−) does satisfactorily explain the relative intensities of the capture transitions forming Tl^{203}.

If the ft values of the transitions to the 683- and 280-kev levels are taken to be about equal, the energy release of the capture process terminating at the ground state of Tl^{203} is calculated[21] to be 1.03 Mev. For an electron capture transition to the ground state of Tl^{203}

[21] S. A. Moszkowski, Phys. Rev. 82, 35 (1951).

of relative intensity two percent, logft is found to be 8.0. The same quantity for transitions to the excited levels has the value 6.5. These values of logft suggest that all the transitions to Tl^{203} are first forbidden[22] ($\Delta I=0\pm1$; ±2, yes!); this is additional confirmation that the ground state of Pb^{203} should be $5/2(-)$.

The complete level scheme of Tl^{203}, as derived from the present measurements, is shown in Fig. 8. There is a similarity between the level scheme of Tl^{203} and those of odd-A isotopes of Au and Ir.[23] Other recent measurements[24,25] as well as these seem to indicate that $M1+E2$ mixtures are a general feature of transitions in odd-Z —even-N nuclei.

ACKNOWLEDGMENT

The writer wishes to thank Dr. F. R. Metzger for having suggested the problem, and for helpful advice during the course of the work. He also desires to express his appreciation to Dr. C. E. Mandeville for discussions concerning the measurements and for his kind assistance in preparation of the manuscript. The interest of Dr. W. F. G. Swann, Director of Bartol, is gratefully acknowledged. Chemical separations were performed by Dr. W. B. Keighton of Swarthmore College, and the radioactive material was prepared by the cyclotron group at the University of Pittsburgh. The author's visit to the United States was made possible by a fellowship granted by the Bartol Research Foundation.

[22] Mayer, Moszkowski, and Nordheim, Revs. Modern Phys. 23, 315 (1951).
[23] Gillon, Gopalakrishnan, DeShalit, and Mihelich, Phys. Rev. 93, 124 (1954).
[24] J. W. Mihelich and A. DeShalit, Phys. Rev. 93, 135 (1954).
[25] F. K. McGowan, Phys. Rev. 93, 163 (1954).

PHYSICAL REVIEW VOLUME 94, NUMBER 6 JUNE 15, 1954

Disintegration of Y^{91}

M. E. Bunker, J. P. Mize, and J. W. Starner
University of California, Los Alamos Scientific Laboratory, Los Alamos, New Mexico
(Received March 11, 1954)

The radiations of the fission product Y^{91} have been investigated with beta- and gamma-scintillation spectrometers. In addition to the well-known 1.55-Mev ground-state beta transition, there is a weak (0.3 percent) beta transition of energy 0.330 Mev which is followed by a gamma ray of energy 1.22±0.01 Mev. Definite assignment of these radiations to Y^{91} was established through exacting chemical procedures, measurement of the half-life of the gamma ray, and energy balance considerations. There is reason to believe that the 1.22-Mev level of $_{40}Zr^{91}$ is not a simple single-particle state.

INTRODUCTION

THERE has been considerable confusion in the literature as to whether or not there is weak γ radiation associated with the 60-day Y^{91} activity.[1–3] The recent measurements of Boley and Dunavan[3] suggest that the 1.2-Mev gamma ray ascribed to Y^{91} by Langer and Price is actually due to an impurity whose half-life is 160±30 days. Boley and Dunavan base their impurity argument not only on the half-life discrepancy but also on the fact that they found a beta-to-gamma ratio of ~20, whereas Langer and Price had found this ratio to be >1000. However, since an examination of highly purified Y^{91} (prepared at this laboratory) indicated the presence of 1.2-Mev gamma rays, it seemed worthwhile to investigate in detail the source of this gamma radiation.

APPARATUS

Scintillation spectrometers were used for the measurement of the beta- and gamma-ray spectra. NaI(Tl) crystals 2 inches in diameter and 2 inches thick were used for gamma detection, and a Pilot Plastic Scintillator-B[4] phosphor $1\frac{3}{4}$ inches in diameter and $\frac{3}{4}$ inch thick was used for beta detection. The scintillators were coupled directly to Dumont type 6292 photomultiplier tubes. Each NaI(Tl) crystal was surrounded by a layer of MgO reflector. The MgO was held in place by a thin aluminum cup. The beta phosphor was covered with aluminum 0.0005 inch thick which served both as a light shield and a reflector.

A block diagram of the electronic circuitry used to obtain coincidence spectra is shown in Fig. 1. The twofold coincidence circuit has a resolving time of about 0.2 microsecond.

GAMMA-SPECTRUM

Preliminary examination of the gamma-ray spectrum of Y^{91} with the scintillation spectrometer revealed a weak photopeak at about 1.2 Mev and an intense, hyperbolic-shaped distribution at lower energy which had an apparent endpoint in the neighborhood of 1 Mev. The bulk of the latter distribution was attributed to internal and external bremsstrahlung resulting from

[1] N. E. Ballou, *Radiochemical Studies: The Fission Products* (McGraw-Hill Book Company, Inc., New York, 1950), Paper No. 116, Natl. Nuclear Energy Ser., Plutonium Project Record 9, Div. IV.
[2] L. M. Langer and H. C. Price, Phys. Rev. 76, 641 (1949).
[3] F. I. Boley and D. S. Dunavan, Phys. Rev. 90, 158 (1953).
[4] Pilot Chemicals, Inc., 47 Felton Street, Waltham 54, Massachusetts.

emission of the well-known 1.55-Mev beta-ray group of Y^{91}. The scintillation spectrum shown in Fig. 2 was obtained with a source-detector geometry intended to minimize the contribution of the external bremsstrahlung. The source, which had a surface density of <0.2 mg/cm^2, was mounted on a thin rubber hydrochloride film and was positioned about 6 inches in front of the NaI(Tl) crystal. The only material (other than air) within several feet of the source which intercepted direct beta particles was a 0.25 inch thick Lucite beta-ray shield attached to the front of the crystal.

The photopeak appearing in Fig. 2 at a pulse height of about 87 volts is from a gamma ray of energy 1.22 ± 0.01 Mev. This energy value is based on a calibration of the scintillation spectrometer with the 1.277-Mev[5] gamma ray of Na^{22}. No other photopeaks could be found. A very careful search was made in the vicinity of 0.2 Mev, since a gamma ray of this energy had previously been assigned to Y^{91}.[2] The pulse height at which a 0.2-Mev photopeak would occur is indicated in Fig. 2. If there were equal numbers of quanta of energy 1.22 and 0.2 Mev, the 0.2-Mev photopeak would have a height about four times the height of the observed continuum at 0.2 Mev. If a 0.2-Mev gamma does exist, which seems very doubtful on the basis of gamma-gamma coincidence measurements described below, its intensity is certainly less than 5 percent of that of the 1.22-Mev gamma.

The source used in the above experiment was prepared by evaporating several drops of a stock solution of carrier-free Y^{91} obtained from Oak Ridge National Laboratory. As a preliminary check on whether any part of the spectrum of Fig. 2 could be due to source contamination, a portion of the Oak Ridge source material was subjected to additional chemical purification cycles and then reexamined with the scintillation spectrometer. No change was observed in the gamma spectrum or in the beta-to-gamma ratio. In addition, a source of long-lived fission product yttrium was prepared independently at this laboratory by chemical extraction from the gross fission products resulting from thermal neutron bombardment of a sample of U^{235}. The gamma spectrum of this source was found to be identical to that of the Oak Ridge source.

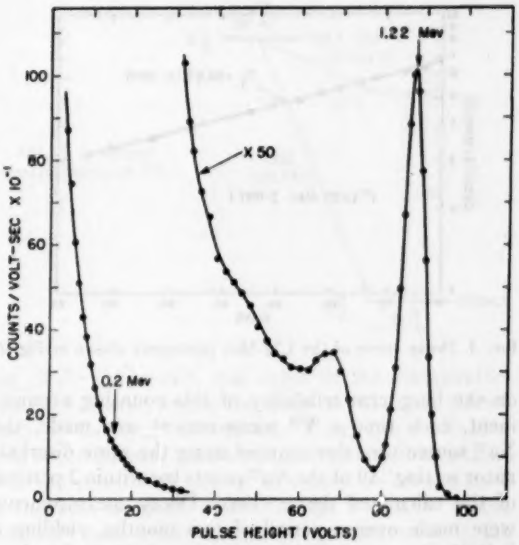

FIG. 2. γ-ray spectrum of Y^{91}, taken with a 2-inch NaI(Tl) crystal mounted on a Dumont type 6292 photomultiplier tube.

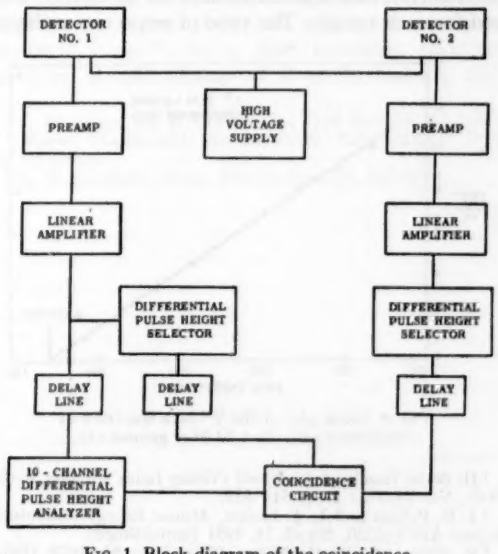

FIG. 1. Block diagram of the coincidence scintillation spectrometer.

Although the above experiments almost conclusively prove that the observed gamma spectrum is due entirely to the decay of a long-lived yttrium fission product (presumably Y^{91}), it was felt desirable to measure the half-life of the 1.22-Mev gamma ray before definitely assigning this gamma to Y^{91}. The decay data were taken with the scintillation spectrometer. The Y^{91} source used for this experiment was mounted rigidly inside a Lucite capsule which had wall thickness sufficient to stop the beta rays. An easily reproducible source-detector geometry was established which allowed alternate counting of the Y^{91} source and a Na^{22} monitor source. Each point on the decay curve (see Fig. 3) was obtained by first accurately calibrating the spectrometer and then measuring the total counting rate (minus background) above a discriminator setting corresponding in energy to 1.08 Mev which, in terms of pulse height, is at the minimum of the "valley" just to the left of the 1.22-Mev photopeak. Thus, the data of Fig. 3 represent essentially the decay of the 1.22-Mev photopeak. As a check

[5] D. E. Alburger, Phys. Rev. **76**, 435 (1949).

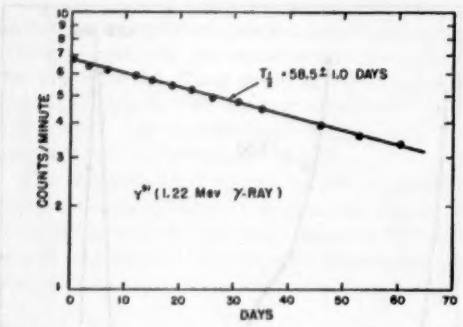

FIG. 3. Decay curve of the 1.22-Mev photopeak shown in Fig. 2.

on the long-term reliability of this counting arrangement, each time a Y^{91} measurement was made, the Na^{22} source was also counted using the same discriminator setting. All of the Na^{22} points lay within 2 percent of the calculated decay curve. Decay measurements were made over a period of two months, yielding a half-life for the 1.22-Mev gamma of 58.5±1.0 days which agrees quite well with the values reported for the half-life of Y^{91} (57 and 61 days).[6]

GAMMA-GAMMA COINCIDENCE SPECTRUM

Although there is no evidence from the simple pulse-height spectrum for any gamma rays except the one at 1.22 Mev, earlier measurements on Y^{91} had indicated that there were 1.2-Mev gamma—0.2-Mev gamma coincidences.[3] To investigate this possibility, a study was made of the gamma spectrum in coincidence with the 1.22-Mev gamma. The axes of the two scintillators were oriented at 90° to one another to eliminate coincidences resulting from 180° Compton scattering of the 1.22-Mev quanta. With the so-called "gate" spectrometer set to count all pulses representing 1.08 Mev or greater, all coincidences observed in the energy region 20 kev to 1 Mev were attributable to background plus chance coincidences. It is concluded that if gammas of energy other than 1.22 Mev are involved in the decay of Y^{91}, they are quite weak compared to the 1.22-Mev gamma and are probably not in coincidence with it.

BETA-GAMMA COINCIDENCE SPECTRUM

The above experiments indicate that there is a low intensity transition from Y^{91} to a 1.22-Mev excited state of Zr^{91}, implying that Y^{91} emits a weak beta group of end-point energy ~0.33 Mev. In order to verify this, the beta spectrum in coincidence with the 1.22-Mev photopeak was measured with the beta-scintillation spectrometer. The spectrometer was calibrated with the 624-kev K-conversion electron line of Ba^{137}. The coincidence counting rate was quite low, but the ratio of true to chance coincidences was >10 for points on the beta spectrum in the energy region below 200 kev. After correcting each point for energy loss[7] in the 0.0005-inch aluminum foil covering the beta scintillator, a Fermi plot was made of the coincidence spectrum. This is shown in Fig. 4. The end-point region has been corrected for the resolution of the spectrometer by the method of Palmer and Laslett.[8] The Fermi plot reveals only one beta-ray group with end-point energy 0.330±0.010 Mev, which confirms the hypothesis made at the beginning of this section.

DETERMINATION OF THE BRANCHING RATIO

The relative intensity of the 0.33-Mev beta group was determined by methods of absolute and comparison counting. A Na^{22} sample of known disintegration rate served as the comparison source. The source strength of 1.277-Mev gamma rays from this sample was determined by measuring the positron disintegration rate in a 4π proportional counter and then multiplying this result by 1.11 to correct for the K-capture branch to the 1.277-Mev level.[9] It was assumed, in agreement with the experiments of Sherr and Miller,[9] that Na^{22} K-capture events are not detected by the 4π counter. Two Y^{91} sources of very different strength were prepared from the same stock solution. The ratio of the activities of these two sources was known to be 5190 (±1 percent) by careful weighing of the amount of stock solution used for each source. The disintegration rate of the weaker source was measured in the 4π beta counter. Multiplication by 5190 then gave the disintegration rate of the stronger source. Next, the gamma-ray spectra of the stronger Y^{91} source and the Na^{22} source were examined with the scintillation spectrometer. Identical source-detector geometries were used for each sample. The ratio of respective emission

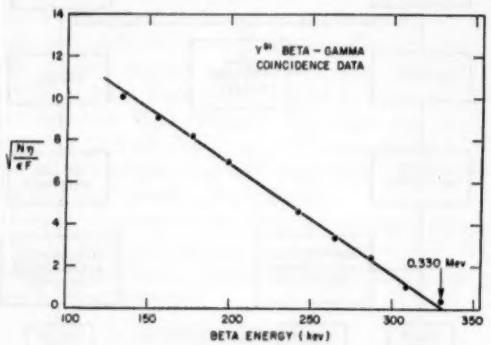

FIG. 4. Fermi plot of the Y^{91} beta spectrum in coincidence with the 1.22-Mev gamma ray.

[6] Hollander, Perlman, and Seaborg, Revs. Modern Phys. **25**, 469 (1953).

[7] H. Bethe, *Handbuch der Physik* (Verlag Julius Springer, Berlin, 1933), Vol. 24, Part 1, pp. 519–523.

[8] J. P. Palmer and L. J. Laslett, Atomic Energy Commission Report AECU-1220, March 14, 1951 (unpublished).

[9] R. Sherr and R. H. Miller, Phys. Rev. **93**, 1078 (1954). Private communication from Dr. R. Sherr to Dr. R. B. Day. We wish to thank Dr. R. Sherr and Mr. R. H. Miller for making their results available before publication.

rates of Y^{91} 1.22-Mev gamma rays and Na^{22} 1.277-Mev gamma rays was determined by comparing the areas of the two photopeaks and correcting for photopeak sensitivity of the crystal according to an empirical curve based on previous measurements of monoenergetic gamma-ray activities of known intensities. When the results of the experiments described above are combined, a value of 0.30 ± 0.05 percent is obtained for the strength of the Y^{91} decay branch involving the 0.33-Mev beta transition and the 1.22-Mev gamma transition.

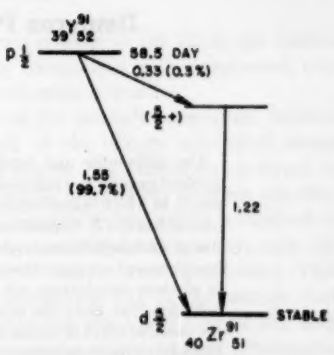

FIG. 5. proposed decay scheme of Y^{91}.

DISCUSSION

The decay scheme indicated by the measurements described above is shown in Fig. 5. Since the $_{40}Zr^{91}$ nucleus has only one particle outside a "magic" core, it seems reasonable to expect that the single-particle shell model would be particularly well suited for helping choose possible spin states for the low-lying levels of this nucleus. Odd-neutron levels in this shell are $d_{5/2}$, $g_{7/2}$, $h_{11/2}$, $d_{3/2}$, and $s_{1/2}$. The measured ground-state spin of Zr^{91} is 5/2, in accord with the $d_{5/2}$ shell-theory level. One can arrive at possible spin assignments for the 1.22-Mev level through consideration of beta-ray selection rules. The 1.55-Mev beta transition from Y^{91} has been identified as first forbidden $\Delta I=2$(yes),[10] so that the ground state of Y^{91} must be $p_{1/2}$, which is again consistent with shell-model predictions. The 0.330-Mev beta transition of Y^{91} has an associated logft value of 8.80, which classifies the transition as first forbidden. If the spin change involved is $\Delta I=0$, 1(yes), a single-particle assignment of $d_{3/2}$ or $s_{1/2}$ could be made for the 1.22-Mev level. However, it is noted that a logft value of 8.80 is considerably higher than one would expect on an empirical basis[11,12] for a first forbidden transition involving a spin change of 0 or 1. Instead, since $\log[(W_0^2-1)ft]=9.03$, the value of the comparative half-life falls well within the range of values for transitions of the type $\Delta I=2$(yes). Thus, the 0.330-Mev beta spectrum may have a unique first forbidden shape. It is not possible to answer this question on the basis of the beta-ray data shown in Fig. 4 because of the relatively poor resolution of the spectrometer. If the low-energy beta transition is indeed of the $\Delta I=2$(yes) type, one would expect the spin and parity of the 1.22-Mev level of Zr^{91} to be 5/2+. Since the $d_{5/2}$ level has already been assigned to the ground state, a 5/2+ excited state is not interpretable as a simple odd-particle level. It is quite possible that the 1.22-Mev level is associated with an excitation of the even-even core. In this connection, it is interesting to note that the first three excited states of Mo^{93} (also a 51-neutron nucleus) seem to result from core excitation.[13,14] The fact that study of the proton groups associated with the reaction $Zr^{90}(d,p)Zr^{91}$ seems to give no evidence for a level in Zr^{91} at 1.22 Mev[15] may be taken as an indication that this state has an unusual character.

The authors are indebted to Dr. Charles W. Stanley and Dr. Rene J. Prestwood for making the necessary chemical separations.

[10] L. M. Langer and H. C. Price, Jr., Phys. Rev. **76**, 186 (1949).
[11] Mayer, Moszkowski, and Nordheim, Revs. Modern Phys. **23**, 315 (1951).
[12] L. W. Nordheim, Revs. Modern Phys. **23**, 322 (1951).
[13] M. Goldhaber, Phys. Rev. **89**, 1146 (1953).
[14] J. J. Kraushaar, Phys. Rev. **92**, 318 (1953).
[15] F. B. Shull and C. E. McFarland, Phys. Rev. **87**, 216 (1952).

Deuteron Photodisintegration at Intermediate Energies*

J. M. BERGER†
Case Institute of Technology, Cleveland, Ohio
(Received February 9, 1954)

The differential and total cross sections for the photodisintegration of the deuteron are calculated for incident gamma-ray energies in the range from 6 to 28 Mev. The following cases are treated: (1) Approximation I, in which shape-independent wave functions are used corresponding to a 50 percent charge-exchange central force, (2) Approximation II-C, in which a central Hulthén potential with a variable percentage of charge exchange forces is used, (3) Approximation II-NC, in which approximate noncentral Hulthén wave functions and an approximate noncentral Hulthén potential with 50 percent charge-exchange force, is used. In all these calculations, use is made (where possible) of a form for the interaction between the deuteron and radiation that gives the results of the interaction to all multipole orders automatically. We also estimate the possible effect of exchange currents on the cross sections by a calculation making use of the phenomenologically derived exchange moments of Berger and Foldy.

The numerical results of these calculations are used to estimate the uncertainty in the theoretically calculated cross section at the present time. It is concluded that the uncertainty may be as large as 15 percent of the total cross section for these energies. About 5 percent of this arises from experimental uncertainties in empirically determined parameters, while the remainder arises from ignorance of the exact form of the neutron-proton interaction.

I. INTRODUCTION

THE problem of the experimental determination of absolute cross sections for photoprocesses in nuclei is complicated by the lack of a reliable method of fixing the spectrum of the incident gamma rays employed in the experiment. One promising method of obtaining a good absolute cross-section measurement is to use as a standard for calibration the simultaneously observed deuteron photodisintegration which may then be compared to the theoretical prediction for this process.[1] Unfortunately, although the deuteron is the simplest nuclear system of interest, it is far from being completely understood, and, as a result, there remain various sources of uncertainty in the theoretically predicted cross section. We wish, in this paper, to undertake a comprehensive and systematic calculation of the deuteron photodisintegration cross section. The results of such a calculation are, of course, of interest in themselves, but we hope that they will also serve to better evaluate the accuracy of our present knowledge of this problem and thereby to indicate the reliability of the above scheme as a calibration method.

We will restrict ourselves to the consideration of incident photon energies in the range from about 6 Mev to 30 Mev although, as will be indicated later, the methods used are applicable to lower and to higher energies and are perhaps even more valuable in the latter region. Our reasons for this choice of energy range are twofold: firstly, much of the investigation of photoprocesses is taking place in this energy region, and secondly, the Case betatron, which has been engaged in investigating such processes, is limited to energies of the order of 30 Mev. A further impetus to a careful analysis in this energy range is the growing accurcy of measurements of the total and differential cross sections for the photodisintegration of the deuteron at these energies.[2,3]

An accurate theoretical prediction of the photodisintegration cross section depends, of course, on knowledge of the correct form of the interaction of the deuteron with the electromagnetic field and further on knowledge of the initial and final wave functions for the deuteron system. Our knowledge of both these aspects of the problem is insufficient to allow an exact calculation to be made and it is therefore necessary to employe approximations, using with discretion what information is available. We are favored in this approach by several circumstances: We are cognizant of what are probably the most important terms in the interaction of the deuteron with radiation and we can at least estimate the effects of those terms of which our knowledge is more scanty. Furthermore, while detailed knowledge of the interaction potential between proton and neutron is necessary for an exact calculation of initial and final wave functions for the deuteron photodisintegration, yet many of the most important features of these wave functions, insofar as they determine the transition matrix element, can be derived on a semiempirical basis. Hence those features of the wave functions which depend on details of the potential interaction introduce considerably smaller uncertainties into the results than might otherwise be the case.

Before describing in detail the nature of our approach and approximations to this problem, we shall summarize briefly some of the more recent calculations of the deuteron photodisintegration cross section by Bethe

* From a thesis submitted to Case Institute of Technology in partial fulfillment of the requirements for the degree of Doctor of Philosophy.

† U. S. Atomic Energy Commission Pre-doctoral fellow, now at Forrestal Research Center, Princeton University, Princeton, New Jersey.

[1] V. E. Krohn, Jr., and E. F. Shrader, Phys. Rev. **87**, 685 (1952).

[2] Barnes, Carver, Stafford, and Wilkinson, Phys. Rev. **86**, 359 (1952).

[3] V. E. Krohn, Jr., and E. F. Shrader, Phys. Rev. **86**, 391 (1952).

and Longmire,[4] Schiff,[5] Marshall and Guth,[6] and Feshbach and Schwinger[7] in order to illuminate the distinguishing features of these and our own calculations.

Bethe and Longmire are concerned in their paper with energies less than 10 Mev and therefore they are able to express their results in a form largely independent of the specific internucleonic potential. They exhibit the electric and magnetic dipole matrix elements in terms of the triplet and singlet effective ranges, assuming a central force character for the internucleonic potential and the absence of interaction in odd parity states of the system (that is, they assume a Serber potential of half ordinary and half charge-exchange character). The results for the magnetic dipole term are checked by explicit calculations using different well shapes: square, Hulthén, and exponential. They also indicate that the electric dipole cross section is slightly smaller at these energies if 100 percent charge exchange forces are assumed in place of Serber forces.

Schiff calculates for the energy region of 20 to 140 Mev only the photoelectric effect, omitting the photomagnetic effect because of the uncertainty due to exchange currents. On the assumption of central forces of half charge-exchange, half ordinary, character, he examines the long-tailed potentials, exponential and Yukawa, and calculates in the electric dipole and quadrupole approximations. It is shown that the quadrupole term interferes with the dipole term so that the quadrupole term has an appreciable effect on the angular distribution. It is also shown that there is little difference between the cross sections obtained with the differently shaped wells, especially below 50 Mev.

Marshall and Guth have performed a similar calculation to that of Schiff, including the magnetic quadrupole term, obtaining essentially the same results. They also calculate the photodisintegration cross section for a square well with different percentages of charge exchange. The results they find for the square well with 50 percent charge exchange are quite different from those with the long-tailed potentials at high energies but are closely the same for energies below 30 Mev. The effect of large variations of the percentage of charge exchange they find to have a large effect at all energies.[8]

Feshbach and Schwinger have calculated the photodisintegration cross section for energies up to 20 Mev with noncentral forces having 50 percent charge-exchange character in the electric and magnetic dipole approximations. They find the electric dipole term to be essentially the shape-independent term of Bethe and Longmire. In the magnetic dipole calculation they include a term corresponding to the exchange current contribution, and by comparison with experiment, conclude that this contribution is small.

In our treatment of the photodisintegration problem we shall consider all of the effects mentioned above although in varying degree. Our calculation is based on an assumed form for the interaction between the deuteron and the electromagnetic field which is derived in an earlier paper.[9] (In the initial calculations only the so-called "one-particle" terms are considered.) This formulation of the interaction has the advantage that it allows us to include automatically and in one step all of the multipole orders in which the photodisintegration process takes place with relatively little extra labor. Estimates of the contributions of what are called in reference 9 "interaction terms" are made in the later calculations of the magnetic dipole matrix element by making use of results obtained from the phenomenological treatment of exchange moments by Berger and Foldy,[10] in the absence of exact expressions that would be predicted by a correct meson theory.

Once the form of the deuteron-radiation interaction has been assumed, the calculation of the matrix elements requires knowledge of the appropriate initial- and final-state wave functions for the deuteron. These are handled in our calculations in the following way: We assume, in what we shall call Approximation I, wave functions for the initial and final state which can be specified without any direct reference to the exact form of the interaction potential between neutron and proton. We do this as follows: For the initial wave function, representing the ground state of the deuteron, we follow Bethe and Longmire in employing a wave function appropriate to a zero-range interaction between neutron and proton but with a normalization adjusted by the employment of the empirical effective range of the neutron-proton interaction to corespond to that of a potential interaction of the proper effective range. This wave function can then be completely expressed once we are given the empirical triplet effective range and the deuteron binding energy. The final-state wave function, in this approximation, is assumed to be a plane wave as if the neutron and proton were free, but with one modification. The S-wave part of the plane wave is modified by the introduction of an empirical phase shift for both the singlet and triplet spin states so as to take partial account of the neutron-proton interaction. The final-state wave functions may therefore also be thought of as arising from a potential of zero range. The phase shifts employed are those deriving from the empirically known values of the zero energy scattering lengths and effective ranges of the singlet and triplet deuteron interactions, neglecting the contribution of "shape-dependent" terms. Thus the

[4] H. A. Bethe and C. Longmire, Phys. Rev. **77**, 647 (1950).
[5] L. I. Schiff, Phys. Rev. **78**, 733 (1950).
[6] J. F. Marshall and E. Guth, Phys. Rev. **78**, 738 (1950).
[7] H. Feshbach and J. Schwinger, Phys. Rev. **84**, 194 (1951).
[8] This result is in disagreement with our own results. It is believed to arise from several minor but numerically significant errors in the formulas of Marshall and Guth. See reference 14 of the present paper.
[9] L. L. Foldy, Phys. Rev. **92**, 178 (1953).
[10] J. M. Berger and L. L. Foldy, Tech. Report No. 18 at the Nuclear Physics Laboratory of Case Institute of Technology. These results will be published in a modified form.

final-state wave functions in this approximation can also be completely written down once these empirical parameters are given. We may also note that insofar as final states of odd parity are concerned, these assumed forms for the final-state wave functions correspond exactly to a Serber potential with 50 percent exchange force. The calculations in this Approximation I correspond then very closely to those of Bethe and Longmire but may be utilized over a higher energy range as a result of including automatically all multipoles in the calculation. This calculation, Approximation I, serves as a basis with which we may compare the changes that result from the more detailed calculations.

The second approximation in our calculation distinguishes between two cases corresponding to central and to noncentral forces between neutron and proton. In the first of these which we call Approximation II-C, we calculate the modification in the matrix elements and in the calculated cross sections resulting from the changes in the initial- and final-state wave functions when a specific radial dependence is assumed for a central interaction between the neutron and proton and when the percentage of charge-exchange character of this interaction is varied. The calculation is made with the choice of the Hulthén potential for the radial dependence of the interaction potential. The effects of modifications in the initial- and final-state wave functions are separately calculated. Where convenient and appropriate some additional approximations are made in these calculations. The contributions of exchange moment terms in the deuteron-radiation interaction are considered separately.

The second form of the second approximation, which is called Approximation II-NC, is similar to Approximation II-C, but the effects of a noncentral (tensor) character of the potential interaction between neutron and proton are examined instead.

In Sec. II the form of the interaction used is described together with the appropriate symbols. In Sec. III the details of the calculations are given excepting those for the exchange moments, and in Sec. IV the results are described. The details of the exchange moment contribution calculation are discussed in Sec. V. In Sec. VI we discuss the over-all results of this paper.

II. INTERACTION

To represent the interaction of radiation with the deuteron we will use the form of the general equations appropriate to the deuteron for the nuclear photoeffect derived by Foldy.[9] This form of the interaction will then give us the effects of all multipoles while involving very little more work for most of the calculations than is usually entailed in obtaining the matrix elements in the dipole approximation of the usual multipole expansion. Its only disadvantage is the somewhat more cumbersome form of the resultant matrix elements, although it is usually quite simple to reduce them to the corresponding dipole terms for comparison.

Our form of the interaction operator

$$\mathcal{H}'=-\int \mathbf{j}\cdot\mathbf{A}d\tau,$$

is conveniently expressed as the sum of four terms.

$$\mathcal{H}'=\mathcal{E}+\mathfrak{M}_c+\mathfrak{M}_s+\mathfrak{M}_x. \tag{1}$$

We label these terms in the following fashion. $\mathcal{E}$ is termed the electric interaction, $\mathfrak{M}_c$ is termed the magnetic convection interaction, $\mathfrak{M}_s$ is the magnetic spin interaction, and $\mathfrak{M}_x$ is the magnetic exchange interaction. In the next two sections we will confine our attention to the first three interactions: however, in Sec. V we will treat some aspects of the magnetic exchange interaction, although in only the dipole approximation.

Then the forms of the matrix elements corresponding to the interaction of a photon of wave vector $\boldsymbol{\kappa}$ with the deuteron in the center-of-mass (zero-momentum) system may be written as[9]

$$\begin{aligned}
E&=(\Psi_f|\mathcal{E}|\Psi_g)=\left(\frac{2\pi\hbar c}{\kappa V}\right)^{\frac{1}{2}}\frac{ie}{2\hbar c}(\epsilon_f-\epsilon_0)\\
&\times\left(\Psi_f\left|\int_0^1\boldsymbol{\varepsilon}\cdot\mathbf{r}\exp(i\boldsymbol{\kappa}\cdot\mathbf{R})[\tau_1{}^P\exp(is\boldsymbol{\kappa}\cdot\mathbf{r}/2)\right.\right.\\
&\qquad\left.\left.-\tau_2{}^P\exp(-is\boldsymbol{\kappa}\cdot\mathbf{r}/2)]ds\right|\Psi_g\right),\\
M_c&=(\Psi_f|\mathfrak{M}_c|\Psi_g)=\left(\frac{2\pi\hbar c}{\kappa V}\right)^{\frac{1}{2}}\frac{ie}{2\hbar c}(\epsilon_f-\epsilon_0)\\
&\times\left(\Psi_f\left|\frac{\hbar\kappa c}{\epsilon_0-\epsilon_f}\cdot\frac{1}{Mc}\int_0^1\{\tau_1{}^P([\mathbf{r}\times\mathbf{p}]\right.\right.\\
&\cdot\boldsymbol{\varepsilon}'\exp(is\boldsymbol{\kappa}\cdot\mathbf{r}/2)+\exp(is\boldsymbol{\kappa}\cdot\mathbf{r}/2)\boldsymbol{\varepsilon}'\cdot[\mathbf{r}\times\mathbf{p}])\\
&+\tau_2{}^P([\mathbf{r}\times\mathbf{p}]\cdot\boldsymbol{\varepsilon}'\exp(-is\boldsymbol{\kappa}\cdot\mathbf{r}/2)\\
&\left.\left.+\exp(-is\boldsymbol{\kappa}\cdot\mathbf{r}/2)\boldsymbol{\varepsilon}'\cdot[\mathbf{r}\times\mathbf{p}])\}\exp(i\boldsymbol{\kappa}\cdot\mathbf{R})sds\right|\Psi_g\right),\\
M_s&=(\Psi_f|\mathfrak{M}_s|\Psi_g)=\left(\frac{2\pi\hbar c}{\kappa V}\right)^{\frac{1}{2}}\frac{ie}{2\hbar c}(\epsilon_f-\epsilon_0)\\
&\times\left(\Psi_f\left|\frac{\hbar\kappa c}{(\epsilon_0-\epsilon_f)}\frac{\hbar}{Mc}\exp(i\boldsymbol{\kappa}\cdot\mathbf{R})\right.\right.\\
&\times\{(\mu_P\tau_1{}^P+\mu_n\tau_1{}^n)\boldsymbol{\sigma}_1\cdot\boldsymbol{\varepsilon}'\exp(i\boldsymbol{\kappa}\cdot\mathbf{r}/2)\\
&\left.\left.+(\mu_P\tau_2{}^P+\mu_n\tau_2{}^n)\boldsymbol{\sigma}_2\cdot\boldsymbol{\varepsilon}'\exp(-i\boldsymbol{\kappa}\cdot\mathbf{r}/2)\}\right|\Psi_g\right),
\end{aligned} \tag{2}$$

where Ψ_f and Ψ_g are the final- and ground-state wave functions, respectively.

In the above equations it will be noted that the multiplying factors outside the brackets have been written the same in all three cases, i.e., $(2\pi\hbar c/\kappa V)^{\frac{1}{2}}(ie/2\hbar c)(\epsilon_f-\epsilon_0)$, so that the quantities inside the brackets serve to indicate the relative magnitudes of these matrix elements. For the energies of interest in this paper the distinction between $\hbar\kappa c$, the photon energy, and $(\epsilon_f-\epsilon_0)$, the change in the internal energy of the deuteron, is negligible. Hence, for example, the magnitude of M_c relative to E is of order p/Mc, where p is the relative particle momentum.

The symbols used in the above expressions for the matrix elements represent the following: V is the normalization volume of the incident photon, $(\epsilon_f-\epsilon_0)$ is the difference between the internal energy states of the deuteron before and after the absorption of the photon, $\mathbf{R}$ is the center-of-mass coordinate, $\mathbf{r}$ is the relative coordinate of the neutron and proton, $\mathbf{p}$ is the momentum conjugate to $\mathbf{r}$, $\boldsymbol{\varepsilon}$ is the electric polarization vector of the incident photon, $\boldsymbol{\varepsilon}'=[\boldsymbol{\kappa}\times\boldsymbol{\varepsilon}]/\kappa$ is the magnetic polarization vector of the incident photon, M is the proton mass and is taken equal to the neutron mass, μ_P is the magnetic moment of the proton expressed in number of nuclear magnetons, μ_n is the magnetic moment of the neutron expressed in number of nuclear magnetons, $\boldsymbol{\sigma}_i$ is the spin operator associated with the ith nucleon, τ_i^P is the proton projection operator for the ith nucleon with $\tau_i^P=(1+\tau_i^z)/2$, τ_i^n is the neutron projection operator for the ith nucleon with $\tau_i^n=(1-\tau_i^z)/2$, τ_i^z is the z component of the isotopic spin operator, and s is a parameter of integration.

In the calculations that follow it will be convenient to separate the magnetic spin matrix element M_s into two terms, M_{st} corresponding to transitions due to the magnetic spin interaction $\mathfrak{M}_s$ to final triplet spin states, and M_{ss} corresponding to transitions to final singlet spin states.

III. CALCULATIONS

The wave functions that will be used in the calculation of the matrix elements described in the previous section, Eqs. (2), will be given here. The general form of the wave functions will be written in the following manner:

$$\Psi_g=\psi_g^0+\psi_g^1, \quad \Psi_f=\psi_f^0+\psi_f^1, \tag{3}$$

where ψ_g^0 is the shape-independent ground-state wave function and ψ_g^1 represents the correction to the shape-independent ground-state wave function due to the choice of a shape-dependent potential, in our case, a Hulthén potential. Similarly ψ_f^0 is the shape-independent final-state wave function corresponding to a plane wave except for a modified S state in which a phase shift is introduced to account for interaction, and ψ_f^1 is the correction introduced because of our specific choice of potential. It is more convenient to indicate the spin multiplicity of the final states explicitly. Thus, Ψ_{ft} is the triplet final-state wave function that is used in the calculation of the E, M_c, and M_{st} matrix elements, and Ψ_{fs} is the singlet final-state wave function that is used in the calculation of the M_{ss} matrix elements.

Thus the matrix elements described in II may be written as the sum of terms, in such a fashion that the introduction of each correction gives rise to an individual term so that the effects of each correction may be easily observed. Thus, for example, we may write E as

$$E=(\Psi_{ft}|\mathcal{E}|\Psi_g)={}_0E^0+{}_0E^1+{}_1E^0+{}_1E^1, \tag{4}$$

where

$$\begin{aligned} {}_0E^0&=(\psi_{ft}^0|\mathcal{E}|\psi_g^0), \quad {}_0E^1=(\psi_{ft}^0|\mathcal{E}|\psi_g^1),\\ {}_1E^0&=(\psi_{ft}^1|\mathcal{E}|\psi_g^0), \quad {}_1E^1=(\psi_{ft}^1|\mathcal{E}|\psi_g^1). \end{aligned} \tag{5}$$

We will speak of the calculation as being done in two approximations, Approximation I and Approximation II. In Approximation I only shape-independent effects are considered and thus it consists of the calculations of the ${}_0E^0$, ${}_0M_c^0$, ${}_0M_{st}^0$, ${}_0M_{ss}^0$ matrix elements. These terms will serve as a reference to which we may compare the effects calculated in the Approximation II. In the second Approximation the modifications that are introduced by the consideration of such effects as the explicitly Hulthén well shape, central and noncentral forces, and interactions in the final states, are calculated. These effects are introduced by the choice of the wave function corrections ψ_g^1, ψ_f^1. In this approximation the matrix elements we will actually calculate are ${}_0E^1$, ${}_1E^0$, ${}_0M_{ss}^1$, ${}_1M_{ss}^0$, ${}_1M_{ss}^1$. The details of these two approximations follow.

A. Approximation I

In this approximation we will calculate four matrix elements corresponding to the four interactions $\mathcal{E}$, $\mathfrak{M}_c$, $\mathfrak{M}_{st}$, $\mathfrak{M}_{ss}$ described in Sec. II, making use of only shape-independent wave functions. The $\mathfrak{M}_{st}$ and $\mathfrak{M}_{ss}$ interactions are, of course, exactly the same, both being the $\mathfrak{M}_s$ described in II. This notation is however convenient in denoting explicitly the spin multiplicity of the final-state wave function that is used with the $\mathfrak{M}_s$ interaction to obtain the matrix element M_{st} or M_{ss}. The wave functions we will use in this calculation are ψ_g^0 for the ground-state function and ψ_{ft}^0 or ψ_{fs}^0 for the final-state function, where ψ_{fs}^0 is used only with $\mathfrak{M}_{ss}$. For ψ_g^0 we will take the zero range form for the deuteron ground state, in which the correction for the finite range of forces is taken into account in the usual manner through the use of the effective range.[11] Thus

$$\psi_g^0=V^{-\frac{1}{2}}\exp(-i\boldsymbol{\kappa}\cdot\mathbf{R})\left[\frac{2\alpha}{4\pi(1-\alpha r_{0t})}\right]^{\frac{1}{2}}\frac{e^{-\alpha r}}{r}\cdot 2^{-\frac{1}{2}}(\xi_1\eta_2-\xi_2\eta_1)\chi_g^t. \tag{6}$$

For the final-state wave functions $\psi_{fs,t}^0$ we will use a plane wave except for replacing the S part by an S

[11] H. A. Bethe, Phys. Rev. 76, 38 (1949).

wave function in which the interaction in the final S state has been considered by the use of the phase shift δ_0. Therefore, we have for the triplet final-state wave function:

$$\psi_{fi}^0 = V^{-1}2^{-\frac{1}{2}}\left\{\xi_1\eta_2 e^{i\mathbf{k}\cdot\mathbf{r}} - \xi_2\eta_1 e^{-i\mathbf{k}\cdot\mathbf{r}} - [\xi_1\eta_2 - \xi_2\eta_1]\times\left[\frac{\sin kr}{kr} - e^{-i\delta_{0t}}\frac{\sin(kr+\delta_{0t})}{kr}\right]\right\}\chi_f^t, \quad (7)$$

and for the singlet final-state function:

$$\psi_{fs}^0 = V^{-1}2^{-\frac{1}{2}}\left\{\xi_1\eta_2 e^{i\mathbf{k}\cdot\mathbf{r}} + \xi_2\eta_1 e^{-i\mathbf{k}\cdot\mathbf{r}} - [\xi_1\eta_2 + \xi_2\eta_1]\times\left[\frac{\sin kr}{kr} - e^{-i\delta_{0s}}\frac{\sin(kr+\delta_{0s})}{kr}\right]\right\}\chi_f^s. \quad (8)$$

In the above, the symbols used mean the following: $\mathbf{k}$ is the propagation vector of the proton and k its magnitude, ξ_i and η_i are isotopic spin wave functions with ξ_i corresponding to the ith particle being in a proton state while η_i corresponds to the ith particle in a neutron state. The χ's are spin wave functions, with χ_g^t the ground-state triplet spin, while χ_f^t and χ_f^s are, respectively, the final-state triplet and singlet spin wave functions. Finally, r_{0t} is the triplet effective range, and δ_{0t} and δ_{0s} are, respectively, the phase shifts of the final-state triplet and singlet S wave functions obtained from the usual formula[11,12]

$$k\cot\delta_0 = -a^{-1} + \tfrac{1}{2}k^2 r_0,$$

where a is the appropriate scattering length and r_0 the appropriate effective range.

The values of the constants we use are, with the exception of r_{0t}, the same as used by Bethe and Longmire, and are

$$\alpha = 2.31\times10^{12}\ \text{cm}^{-1}, \quad a_t = 0.528\times10^{-12}\ \text{cm}, \quad a_s = -2.375\times10^{-12}\ \text{cm}, \quad r_{0t} = 1.70\times10^{-13}\ \text{cm}, \quad r_{0s} = 2.4\times10^{-13}\ \text{cm},$$

corresponding to a binding energy for the deuteron of 2.235 Mev.

The wave functions just described will now be used to evaluate the matrix elements ${}_0E^0$, ${}_0M_e^0$, ${}_0M_{et}^0$, ${}_0M_{es}^0$ where

$$ {}_0E^0 = (\psi_{fi}^0|\mathcal{E}|\psi_g^0), \quad {}_0M_e^0 = (\psi_{fi}^0|\mathfrak{M}|\psi_g^0), \quad {}_0M_{et}^0 = (\psi_{fi}^0|\mathfrak{M}|\psi_g^0), \quad {}_0M_{es}^0 = (\psi_{fs}^0|\mathfrak{M}|\psi_g^0). \quad (9)$$

The resulting matrix elements after integration but before the summation and averaging over the spin states and polarizations have been performed are

$${}_0E^0 = \left(\frac{2\pi\hbar c}{\kappa V^2}\cdot\frac{2\pi\alpha}{1-\alpha r_{0t}}\right)^{\frac{1}{2}}\frac{e}{\hbar c}(\epsilon_f-\epsilon_0)(\boldsymbol{\varepsilon}\cdot\mathbf{k}) \times 2\left[\frac{2c+b}{q(a+b+c)} - \frac{b}{qa} + \frac{4c}{q^3}\tan^{-1}\frac{q^3}{2a+b}\right](\chi_f^t,\chi_g^t),$$

$${}_0M_e^0 = \left(\frac{2\pi\hbar c}{\kappa V^2}\cdot\frac{2\pi\alpha}{1-\alpha r_{0t}}\right)^{\frac{1}{2}}\frac{e}{\hbar c}(\epsilon_f-\epsilon_0)(\boldsymbol{\varepsilon}\cdot\mathbf{k})\frac{\hbar\kappa c}{\epsilon_0-\epsilon_f} \cdot\frac{\hbar\kappa}{2Mc}\left[\frac{4a}{q^3}\tan^{-1}\frac{q^3}{2a+b} - \frac{2a+b}{q(a+b+c)}\right](\chi_f^t,\chi_g^t),$$

$${}_0M_{et}^0 = \left(\frac{2\pi\hbar c}{\kappa V^2}\cdot\frac{2\pi\alpha}{1-\alpha r_{0t}}\right)^{\frac{1}{2}}\frac{ie}{\hbar c}(\epsilon_f-\epsilon_0)\frac{\hbar\kappa c}{\epsilon_0-\epsilon_f} \cdot\frac{\hbar}{2Mc}\left\{\frac{\mu_P}{\alpha^2+K_1^2} + \frac{\mu_n}{\alpha^2+K_2^2} - (\mu_P+\mu_n)\left[\frac{(1-e^{i\delta_{0t}}\cos\delta_{0t})}{2k\kappa}\ln\left(\frac{\alpha^2+K_1'^2}{\alpha^2+K_2'^2}\right) - \frac{e^{i\delta_{0t}}\sin\delta_{0t}}{k\kappa}\tan^{-1}\frac{\alpha(K_1'-K_2')}{\alpha^2+K_1'K_2'} - \frac{e^{i\delta_{0t}}(k\cos\delta_{0t}+\alpha\sin\delta_{0t})}{k(\alpha^2+k^2)}\right]\right\} \times(\chi_f^t,\boldsymbol{\varepsilon}'\cdot(\boldsymbol{\sigma}_1+\boldsymbol{\sigma}_2)\chi_g^t), \quad (10)$$

$${}_0M_{es}^0 = \left(\frac{2\pi\hbar c}{\kappa V^2}\cdot\frac{2\pi\alpha}{1-\alpha r_{0t}}\right)^{\frac{1}{2}}\frac{ie}{\hbar c}(\epsilon_f-\epsilon_0)\cdot\frac{\hbar\kappa c}{\epsilon_0-\epsilon_f} \cdot\frac{\hbar}{2Mc}\left\{\frac{\mu_P}{\alpha^2+K_1^2} - \frac{\mu_n}{\alpha^2+K_2^2} - (\mu_P-\mu_n)\left[\frac{(1-e^{i\delta_{0s}}\cos\delta_{0s})}{2k\kappa}\ln\left(\frac{\alpha^2+K_1'^2}{\alpha^2+K_2'^2}\right) - \frac{e^{i\delta_{0s}}\sin\delta_{0s}}{k\kappa}\tan^{-1}\frac{\alpha(K_1'-K_2')}{\alpha^2+K_1'K_2'}\right]\right\} \times(\chi_f^s,\boldsymbol{\varepsilon}'\cdot(\boldsymbol{\sigma}_1-\boldsymbol{\sigma}_2)\chi_g^t),$$

where

$$a=\alpha^2+k^2, \quad b=-\boldsymbol{\kappa}\cdot\mathbf{k}, \quad c=\kappa^2/4, \quad q=4ac-b^2, \quad \mathbf{K}_1=\mathbf{k}-\tfrac{1}{2}\boldsymbol{\kappa}, \quad \mathbf{K}_2=\mathbf{k}+\tfrac{1}{2}\boldsymbol{\kappa}, \quad K_1'=k-\tfrac{1}{2}\kappa, \quad K_2'=k+\tfrac{1}{2}\kappa. \quad (11)$$

The calculations involved in obtaining these matrix elements are, for the most part, straightforward. Some care is required in the calculation of ${}_0M_{et}^0$ inasmuch as long wavelength magnetic dipole transitions between

[11] J. Schwinger, Harvard Lecture Notes (unpublished).

the initial triplet S state and final triplet S state are forbidden due to the orthogonality of these two states. Since the wave functions used are not themselves orthogonal the forbiddenness of the transition was accounted for in the following way. We actually used in this calculation a modified $\mathfrak{M}_{st}$ interaction $\mathfrak{M}_{st}'$ that was obtained by subtracting from the $\mathfrak{M}_{st}$ interaction given in Sec. II a term obtained by expanding the exponential $\exp(i\boldsymbol{\kappa}\cdot\mathbf{r}/2)$ occurring in the $\mathfrak{M}_{st}$ interaction and retaining only the first term. That is,

$$\mathfrak{M}_{st}'=\mathfrak{M}_{st}-\left(\frac{2\pi\hbar c}{\kappa V}\right)^{\frac{1}{2}}\frac{ie}{\hbar c}(\epsilon_f-\epsilon_0)\frac{\hbar\kappa c}{\epsilon_0-\epsilon_f}\frac{\hbar}{Mc}$$
$$\times\exp(i\boldsymbol{\kappa}\cdot\mathbf{R})[(\mu_P\tau_1{}^P+\mu_n\tau_1{}^n)\boldsymbol{\sigma}_1\cdot\boldsymbol{\epsilon}'$$
$$+(\mu_P\tau_2{}^P+\mu_n\tau_2{}^n)\boldsymbol{\sigma}_2\cdot\boldsymbol{\epsilon}'].\quad(12)$$

In this way we have eliminated this dipole transition.

It will be noted that the calculated matrix elements of this first approximation are not dependent upon any assumed details of potential shape, and therefore, that the accuracy with which these results may be determined is limited only by the accuracy of the experimental results for the binding energy, triplet and singlet scattering lengths, and effective ranges. The integrations performed have been exact; thus the results of this approximation has been to give the matrix elements in an essentially zero-range approximation assuming half exchange, half ordinary force, to all multipole orders.

B. Approximation II-C

We will now investigate in detail the deviations from the results of Approximation I that may be expected when a particular form for a central force potential is chosen. We will consider in detail only the Hulthén potential since it is most amenable to calculation, and since previous calculations[5,6] seem to indicate that its results would differ very little from the results that would be obtained with other long-tailed potentials. We have repeated some of the calculations using a square well potential, with parameters obtained from the curves of Blatt and Jackson,[12] to correspond to the same effective range as our Hulthén potentials. These square well calculations were performed as a check and are, therefore, not described in detail. The results will be discussed in the consideration of the parallel Hulthén calculations.

Explicitly, the calculations in this section involve the modification $\psi_g{}^1$ of the ground-state wave function that is obtained because of our use here of the Hulthén potential $\mathfrak{U}_T(r)$. That is, with

$$\mathfrak{U}_t(r)=\frac{(\alpha^2-\beta^2)}{e^{(\beta-\alpha)r}-1}=(\alpha^2-\beta^2)\frac{e^{-\mu r}}{1-e^{-\mu r}},\quad\mu=\beta-\alpha,\quad(13)$$

we have

$$\psi_g{}^1=V^{-\frac{1}{2}}\exp(-i\boldsymbol{\kappa}\cdot\mathbf{R})\left[\frac{2\alpha}{4\pi(1-\alpha r_{0t})}\right]^{\frac{1}{2}}$$
$$\times\left[\frac{e^{-\alpha r}-e^{-\beta r}}{r}-\frac{e^{-\alpha r}}{r}\right]2^{-\frac{1}{2}}(\xi_1\eta_2-\xi_2\eta_1)\chi_g{}^t,\quad(14)$$

where β is taken as $\beta=14.3\times10^{12}$ cm^{-1}, so that $\psi_g{}^1$ consists of only the difference between the Hulthén ground-state function and the shape-independent function used in Approximation I. In our modifications of the final-state S functions we keep in mind the fact that the transitions to the final singlet S state and to the final triplet P state are the dominant transitions since they correspond in the main to the magnetic and electric dipole transitions. In view of this the modification of the singlet final-state $\psi_{fs}{}^1$ is taken to represent only a modification of the final S state through the introduction of an *approximate* Hulthén final-state singlet S wave function. That is,

$$\psi_{fs}{}^1=V^{-\frac{1}{2}}2^{-\frac{1}{2}}[\xi_1\eta_2+\xi_2\eta_1]e^{-i\delta_{0s}}\left[\frac{(1-e^{-\eta r})}{kr}\sin(kr+\delta_{0s})\right.$$
$$\left.-\frac{\sin(kr+\delta_{0s})}{kr}\right]\chi_f{}^s,\quad(15)$$

where η is taken as $\eta=12.8\times10^{12}$ cm^{-1}. The modification of the final triplet-state wave function takes account of interaction in the general final state through a Born approximation calculation in which the final plane wave is perturbed by the Hulthén potential. In particular, we are interested in the final triplet P state so that we will be concerned with the effect of varying the percentage of ordinary and exchange forces present in the potential, from the previously assumed Serber form. The modification of the final triplet wave function $\psi_{ft}{}^1$ is then (from the Born approximation)

$$\psi_{ft}{}^1=-V^{-1}(2\pi)^{-3}2^{-\frac{1}{2}}$$
$$\times\left\{\xi_1\eta_2\int\int\frac{e^{i\mathbf{k}'\cdot(\mathbf{r}-\mathbf{r}')}}{k^2-k'^2}\mathfrak{U}_t(r')e^{i\mathbf{k}\cdot\mathbf{r}'}d\mathbf{k}'d\mathbf{r}'\right.$$
$$-\xi_2\eta_1\int\int\frac{e^{-i\mathbf{k}'\cdot(\mathbf{r}-\mathbf{r}')}}{k^2-k'^2}$$
$$\left.\times\mathfrak{U}_t(r')e^{-i\mathbf{k}\cdot\mathbf{r}'}d\mathbf{k}'d\mathbf{r}'\right\}\chi_f{}^t,\quad(16)$$

in which the nature of the force, exchange or ordinary, is still implicit in $\mathfrak{U}_t(r')$. For ease in performing the integrations indicated in (16) we have replaced the Hulthén potential by the corresponding Yukawa potential. That is, we have replaced $e^{-\mu r'}/(1-e^{-\mu r'})$ by $e^{-\mu r'}/\mu r'$. It will be noted that the modification of the final singlet state wave function does not include the possible effects of the variation of the percentage of charge exchange forces. This is consistent with the statement above that the dominant singlet final state

[12] J. M. Blatt and J. D. Jackson, Phys. Rev. **76**, 18 (1949).

is the S state where exchange force considerations have no effect.

As we have indicated above, it is well known that the electric and magnetic dipole interactions are by far the dominant effects for the energies we consider. Furthermore, it may be easily verified that the electric dipole interaction is included in $\mathcal{E}$ while the magnetic dipole interaction is included in $\mathfrak{M}_s$ (or alternatively $\mathfrak{M}_{ss}$). On this basis we expect that at these energies $\mathfrak{M}_c$ and $\mathfrak{M}_s$ employed with final triplet states (or alternatively $\mathfrak{M}_{st}$) will be relatively unimportant. The results of the numerical calculation of ${}_0M_c{}^0$ and ${}_0M_{st}{}^0$ bears this out. Therefore, in describing the effects of the wave function modification given above, we have restricted ourselves to the examination of only the E and M_{ss} matrix elements since it is clear that these will include all of the important effects. The matrix elements that we will calculate in this section are

$$\begin{aligned} &{}_0E^1=(\psi_{ft}{}^0|\mathcal{E}|\psi_g{}^1), \qquad {}_1E^0=(\psi_{ft}{}^1|\mathcal{E}|\psi_g{}^0),\\ &{}_1M_{ss}{}^0=(\psi_{fs}{}^1|\mathfrak{M}_s|\psi_g{}^0), \quad {}_0M_{ss}{}^1=(\psi_{fs}{}^0|\mathfrak{M}_s|\psi_g{}^1), \quad (17)\\ &\qquad\qquad {}_1M_{ss}{}^1=(\psi_{fs}{}^1|\mathfrak{M}_s|\psi_g{}^1). \end{aligned}$$

We have not calculated ${}_1E^1$ since both ${}_1E^0$ and ${}_0E^1$ are themselves quite small, and this would represent a higher-order correction. On the other hand both ${}_1M_{ss}{}^0$ and ${}_0M_{ss}{}^1$ are rather large so that it was necessary to calculate ${}_1M_{ss}{}^1$. Since the forms of the integrals encountered in the three M_{ss} terms were essentially the same we have actually calculated the three terms together as one term that we will refer to as $M_{ss}{}^1$.

The results of the calculations for these matrix elements are

$${}_0E^1=-\left(\frac{2\pi\hbar c}{\kappa V^2}\cdot\frac{2\pi\alpha}{1-\alpha r_{0t}}\right)^{\frac{1}{2}}\frac{e}{\hbar c}(\epsilon_f-\epsilon_0)2\boldsymbol{\epsilon}\cdot\mathbf{k}$$
$$\times\left[\frac{2c+b}{q'(a'+b+c)}-\frac{b}{q'a'}+\frac{4c}{q'^{\frac{1}{2}}}\tan^{-1}\frac{q'^{\frac{1}{2}}}{2a'+b}\right](\chi_f{}^t,\chi_g{}^t),$$

where $a'=\beta^2+k^2$, $q'=4a'c-b^2$.

$${}_1E^0=(-1)^v\left(\frac{2\pi\hbar c}{\kappa V^2}\cdot\frac{2\pi\alpha}{1-\alpha r_{0t}}\right)^{\frac{1}{2}}\frac{e}{\hbar c}(\epsilon_f-\epsilon_0)2\boldsymbol{\epsilon}\cdot\mathbf{k}\frac{(\alpha^2-\beta^2)}{2\mu\kappa}$$
$$\times\left\{i\left[\frac{\mu^2+2k^2}{4k^2(\alpha^2+k^2)^2}\ln\frac{\mu^2+4k^2}{\mu^2}-\frac{1}{\alpha^2+k^2}\right]\right.$$
$$+\frac{\mu^2+2k^2}{2k^2(\alpha^2+k^2)^2}\left[\tan^{-1}\frac{2k\mu}{\mu^2-k^2-\alpha^2}-\tan^{-1}\frac{2k}{\mu}\right.$$
$$\left.-\tan^{-1}\frac{2\alpha k}{\mu^2+k^2-\alpha^2}\right]+\frac{\alpha^2-k^2}{2\alpha k(\alpha^2+k^2)^2}$$
$$+\frac{(\mu^2+k^2-\alpha^2)(\mu^2+k^2+\alpha^2)}{2\alpha k(\alpha^2+k^2)[(\mu^2+k^2-\alpha^2)^2+4\alpha^2k^2]}$$
$$\left.-\frac{(\mu^2+k^2-\alpha^2)}{2k^2(\alpha^2+k^2)}\cdot\frac{2\mu k}{(\mu^2-k^2-\alpha^2)^2+4\mu^2k^2}\right\}(\chi_f{}^t,\chi_g{}^t). \quad (18)$$

Here, $v=0$ for pure charge exchange forces and $v=1$ for ordinary forces. Also

$$M_{ss}{}^1=-\left(\frac{2\pi\hbar c}{\kappa V^2}\cdot\frac{2\pi\alpha}{1-\alpha r_{0t}}\right)^{\frac{1}{2}}\frac{ie}{\hbar c}(\epsilon_f-\epsilon_0)$$
$$\cdot\frac{\hbar\kappa c}{\epsilon_0-\epsilon_f}\cdot\frac{\hbar}{2Mc}\left\{\frac{\mu_P}{\beta^2+K_1{}^2}-\frac{\mu_n}{\beta^2+K_2{}^2}\right.$$
$$+\frac{(\mu_P-\mu_n)}{k\kappa}\left[\frac{(e^{i\delta_{0s}}\cos\delta_{0s}-1)}{2}\ln\left(\frac{\beta^2+K_1{}'^2}{\beta^2+K_2{}'^2}\right)\right.$$
$$+\frac{e^{i\delta_{0s}}}{2}\cos\delta_{0s}\ln\left\{\frac{[(\eta+\alpha)^2+K_1{}'^2][(\eta+\beta)^2+K_2{}'^2]}{[(\eta+\alpha)^2+K_2{}'^2][(\eta+\beta)^2+K_1{}'^2]}\right\}$$
$$+e^{i\delta_{0s}}\sin\delta_{0s}\left\{\tan^{-1}\frac{\beta(K_1'-K_2')}{\beta^2+K_1'K_2'}\right.$$
$$+\tan^{-1}\frac{(\eta+\alpha)(K_1'-K_2')}{(\eta+\alpha)^2+K_1'K_2'}$$
$$\left.\left.\left.-\tan^{-1}\frac{(\eta+\beta)(K_1'-K_2')}{(\eta+\beta)^2+K_1'K_2'}\right\}\right]\right\}$$
$$\times(\chi_f{}^s,\boldsymbol{\epsilon}'\cdot(\boldsymbol{\sigma}_1-\boldsymbol{\sigma}_2)\chi_g{}^t).$$

The sums and averaging over spin states and polarizations have not yet been performed. It will be noted that in $M_{ss}{}^1$ one can easily separate out ${}_0M_{ss}{}^1$, ${}_1M_{ss}{}^0$, and ${}_1M_{ss}{}^1$ by referring to the constants β, η, and α. (That is, those terms which have β alone belong to ${}_0M_{ss}{}^1$, those terms involving η and α belong to ${}_1M_{ss}{}^0$, and those terms involving η and β belong to ${}_1M_{ss}{}^1$.)

In the calculation of ${}_1E^0$ another approximation was made, in addition to the use of the Yukawa form for the potential, in order that the contour integral involved be more tractable. We have not used in the calculation of this term the entire $\mathcal{E}$ interaction of Sec. II, but essentially only the dipole part that was obtained by expanding the exponential occurring in $\mathcal{E}$ and retaining only the first term. That is in $\mathcal{E}$, $[\tau_1{}^P\exp(is\boldsymbol{\kappa}\cdot\mathbf{r}/2)-\tau_2{}^P\exp(-is\boldsymbol{\kappa}\cdot\mathbf{r}/2)]$ was replaced by $\tau_1{}^P-\tau_2{}^P$. The error invoked by this simplification is very small since the term itself is quite small.

At this point we might indicate which square well calculations were performed, deferring the comparison of the two results to Sec. IV where the numerical results of the above calculations are given. We wished to check ${}_1E^0$ which at first sight appeared too small, and $M_{ss}{}^1$, which appeared too large. ${}_1E^0$ was compared to the result obtained using the formula[14] (45) of Marshall

[14] The formulas in the appendix of reference 6 are in error and should read

$$\tfrac{1}{2}M\ddot{x}_{01}=-(\partial V/\partial x)_{01}, \quad \ddot{x}_{01}=-(E_1-E_0)^2x_{01}/\hbar^2,$$
$$x_{01}=\frac{\hbar^2}{(E_0-E_1)^2}\int\psi_i\frac{\partial V}{\partial r}\cos\theta\psi_1d\tau,$$
$$\int\psi_i(\partial V/\partial r)\psi_i r^2d\tau=\psi_i(b_i)\psi_1(b_i)b_i{}^2V_0,$$

where V_0 is the depth of the square well. We believe that by use

and Guth for the matrix element with 100 percent ordinary force and using square well wave functions with the constants obtained from the curves of Blatt and Jackson so that the effective range was the same. $M_{ss}{}^1$ was compared to a straightforward magnetic dipole calculation in which the square well wave functions were used for both initial and final slates.

C. Approximation II-NC

The calculations treated in this section proceed in exactly the same manner as for Approximation II-C with central forces, with the obvious exception that where the explicit Hulthén central force potential and its associated wave functions occurred previously, it is understood that they are to be replaced by the appropriate noncentral terms. As before, we will calculate only the matrix elements, ${}_1E^0$, ${}_0E^1$, and $M_{ss}{}^1$ for exactly the same reasons as before. To distinguish between the results of these two second Approximations II, we will denote the matrix elements calculated here by ${}_0E_{NC}{}^1$, ${}_1E_{NC}{}^0$, and $M_{ss,NC}{}^1$.

It is not our intention, in this calculation with noncentral forces, to give a completely consistent result for the photodisintegration, but rather we intend merely to indicate the main effects of the introduction of the tensor force in the second Approximation. Thus, to fix the potential and wave functions, we nave not made any calculation of the electric quadrupole moment or magnetic moment of the deuteron, but instead we have chosen a potential and wave function that are probably reasonably correct and, at the same time, easily handled. The potential we have chosen is, in fact, somewhat more singular than is usually the case and, the wave functions we take for the ground state have been oversimplified. Explicitly, for the potential $\mathfrak{U}(\mathbf{r})$, we have taken[15]

$$\mathfrak{U}(\mathbf{r})=[1+\rho\{(\boldsymbol{\sigma}_1\cdot\nabla)(\boldsymbol{\sigma}_2\cdot\nabla)-\tfrac{1}{3}\boldsymbol{\sigma}_1\cdot\boldsymbol{\sigma}_2\nabla^2\}]\frac{(\alpha^2-\beta^2)e^{-\mu r}}{1-e^{-\mu r}},$$
$$(\mu=\beta-\alpha), \quad (19)$$

with the strength of the tensor portion $\rho=\mu^{-2}$. Indications are that this is about the right value for the strength.[16] It is a quite convenient choice, and in any event the numerical results are not very dependent upon this quantity.

In the modifications of the wave functions we have $\psi_{fs}{}^1$ and $\psi_{ft}{}^1$ of the same form as in the central force case. In $\psi_{ft}{}^1$ we must substitute the appropriate noncentral potential, and $\psi_{fs}{}^1$ remains exactly the same since the singlet potential remains central. For the ground-state wave function modification $\psi_g{}^1$ we now take

$$\psi_g{}^1=V^{-\frac{1}{2}}\exp(-i\boldsymbol{\kappa}\cdot\mathbf{R})\left(\frac{2\alpha}{4\pi(1-\alpha r_{0t})}\right)^{\frac{1}{2}}\times\left[u_{NC}(\mathbf{r})-\frac{e^{-\alpha r}}{r}\right]2^{-\frac{1}{2}}(\xi_1\eta_2-\xi_2\eta_1)\chi_g{}^t, \quad (20)$$

where

$$u_{NC}(\mathbf{r})=\left[1+(\tfrac{2}{8})^{-\frac{1}{2}}\times\left\{\frac{3(\boldsymbol{\sigma}_1\cdot\mathbf{r})(\boldsymbol{\sigma}_2\cdot\mathbf{r})}{r^2}-1\right\}\right]\frac{(e^{-\alpha r}-e^{-\beta r})}{r}. \quad (21)$$

The results for the calculations of the matrix elements, after integration but before the sums and averaging over spin states and polarizations have been performed, are

$$\begin{aligned}
{}_0E_{NC}{}^1=&[1-(\tfrac{2}{8})^{-\frac{1}{2}}]{}_0E^1-(\tfrac{2}{8})^{-\frac{1}{2}}{}_0E^0\\
&-\left(\frac{2\pi\hbar c}{\kappa V^2}\cdot\frac{2\pi\alpha}{1-\alpha r_{0t}}\right)^{\frac{1}{2}}\frac{e}{\hbar c}(\epsilon_f-\epsilon_0)\frac{3}{20}2^{-\frac{1}{2}}\\
&\times\boldsymbol{\epsilon}\cdot\nabla_k\times\left(\chi_f{}^t,\left\{[\sigma_1{}^x\sigma_2{}^x k_x+\sigma_1{}^y\sigma_2{}^y k_y\right.\right.\\
&+\sigma_1{}^z\sigma_2{}^z k_z]\frac{2}{k^4}\left(\alpha\tan^{-1}\frac{k}{\alpha}-\beta\tan^{-1}\frac{k}{\beta}\right)\\
&+(\boldsymbol{\sigma}_1\cdot\mathbf{k})(\boldsymbol{\sigma}_2\cdot\mathbf{k})\left[\frac{2}{k^4}\left(\frac{\alpha^2}{\alpha^2+k^2}-\frac{\beta^2}{\beta^2+k^2}\right)\right.\\
&\left.\left.\left.-\frac{6}{k^5}\left(\alpha\tan^{-1}\frac{k}{\alpha}-\beta\tan^{-1}\frac{k}{\beta}\right)\right]\right\}\chi_g{}^t\right),\\
{}_1E_{NC}{}^0=&[1-\rho\mu^2]{}_1E^0-(-1)^s\left(\frac{2\pi\hbar c}{\kappa V^2}\cdot\frac{2\pi\alpha}{1-\alpha r_{0t}}\right)^{\frac{1}{2}}\\
&\times\frac{e}{\hbar c}(\epsilon_f-\epsilon_0)\frac{4}{3}\frac{\rho(\alpha^2-\beta^2)}{\mu^2}\\
&\times\left(\chi_f{}^t,[(\boldsymbol{\sigma}_1\cdot\mathbf{k})(\boldsymbol{\sigma}_2\cdot\boldsymbol{\epsilon})-(\boldsymbol{\sigma}_2\cdot\mathbf{k})(\boldsymbol{\sigma}_1\cdot\boldsymbol{\epsilon})]\right.\\
&\times\left\{\frac{\alpha(\mu^2k^2-\alpha^4+k^4)}{(\mu^2-\alpha^2-k^2)^2(\alpha^2+k^2)^2}\right.\\
&-\frac{(\mu^2+k^2)^{\frac{1}{2}}}{2(\mu^2+2k^2)(\mu^2-\alpha^2+k^2)^2}\\
&\left.\left.-\frac{ik^3}{2(\mu^2+2k^2)(\alpha^2+k^2)^2}\right\}\chi_g{}^t\right),
\end{aligned} \quad (22)$$

of corrected formulas, the *large* difference found by Marshall and Guth for electric dipole cross sections with 50 percent ordinary −50 percent Majorana and with 100 percent ordinary forces, disappears.

[15] L. L. Foldy and R. E. Marshak, Phys. Rev. **75**, 1493 (1949); note added in proof.

[16] D. G. Padfield, Proc. Phys. Soc. (London) **A65**, 309 (1952).

$$M_{ss,NC}{}^{1}=[1-(\tfrac{2}{3})^{-\frac{1}{2}}]M_{ss}{}^{1}-(\tfrac{2}{3})^{-\frac{1}{2}}{}_{0}M_{ss}{}^{0}$$
$$+\left(\frac{2\pi\hbar c}{\kappa V^{2}}\cdot\frac{2\pi\alpha}{1-\alpha r_{0t}}\right)^{\frac{1}{2}}\frac{ie}{\hbar c}(\epsilon_{f}-\epsilon_{0})$$
$$\times\frac{\hbar\kappa c}{\epsilon_{0}-\epsilon_{f}}\cdot\frac{\hbar}{2M_{c}}\frac{(\mu_{P}-\mu_{n})}{20}2^{-\frac{1}{2}}$$
$$\times\Big(\chi_{f}{}^{*},\epsilon'\cdot(\sigma_{1}-\sigma_{2})\Big\{3[\sigma_{1}{}^{z}\sigma_{2}{}^{z}k_{x}+\sigma_{1}{}^{y}\sigma_{2}{}^{y}k_{y}$$
$$+\sigma_{1}{}^{z}\sigma_{2}{}^{z}k_{z}]\frac{2}{k^{4}}\left(\beta\tan^{-1}\frac{k}{\beta}-\alpha\tan^{-1}\frac{k}{\alpha}\right)$$
$$+2(\sigma_{1}\cdot\sigma_{2})\left[(e^{i\delta_{0s}}\cos\delta_{0s}-1)\left(\frac{1}{\alpha^{2}+k^{2}}-\frac{1}{\beta^{2}+k^{2}}\right)\right.$$
$$\left.+\frac{e^{i\delta_{0s}}\sin\delta_{0s}}{k}\left(\frac{\alpha}{\alpha^{2}+k^{2}}-\frac{\beta}{\beta^{2}+k^{2}}\right)\right]\Big\}\chi_{0}{}^{t}\Big).$$

In the above terms we have calculated in only the dipole approximation those integrals that involve the D-wave part of the ground-state wave function. That is, in those terms, we have used only the first term in the expansion of the exponential occurring in the $\mathcal{E}$ and $\mathfrak{M}_{s}$ interactions. This introduces no appreciable error and is consistent with the order of Approximation II.

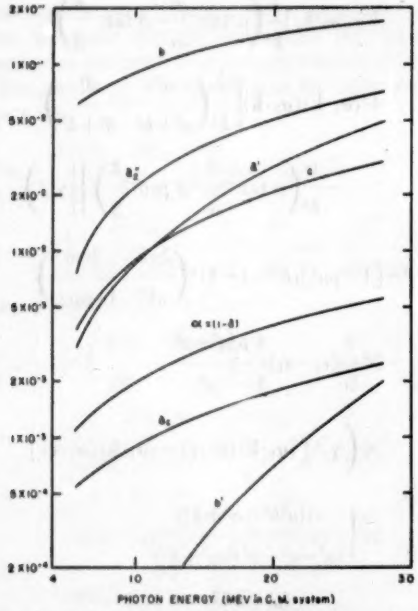

FIG. 1. Coefficients describing the departure from the matrix elements calculated in zero-range approximation in lowest multipole order due to our approximations and inclusion of all multipoles are plotted as a function of incident photon energy. The terms plotted here are those corresponding to ${}_{0}E^{0}$, ${}_{1}E^{0}$, ${}_{0}E^{2}$, and ${}_{0}M_{s}{}^{0}$. The form used is $(a+b\cos\theta+c\cos^{2}\theta)$ times the corresponding lowest multipole matrix element.

IV. RESULTS

The results of the calculations of the previous section are more easily interpreted if they are expressed in different form. The form we choose is to compare our results to the matrix elements that are obtained in the shape-independent theory using the lowest orders of the multipole expansion. Thus, we compare our E and M_{c} terms to the electric dipole matrix element, the M_{ss} terms are compared to the magnetic dipole matrix element, and the M_{st} term is compared to what is essentially the magnetic quadrupole matrix element. That is, we have written our results as the product of an appropriate multipole matrix element and a modifying expression composed of constants, for a given

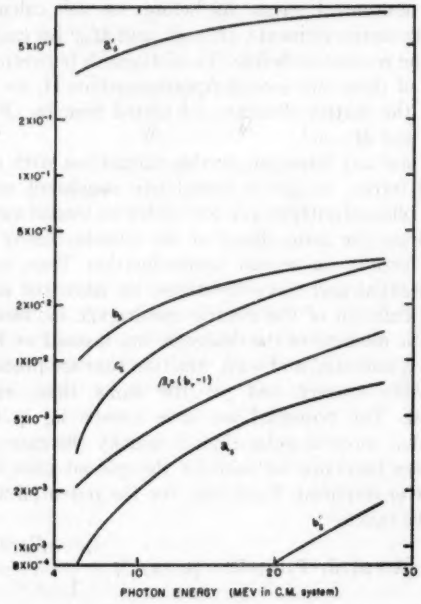

FIG. 2. The coefficients corresponding to ${}_{0}M_{ss}{}^{0}$, ${}_{0}M_{st}{}^{0}$, and $M_{ss}{}'$ are plotted in the same manner as for Fig. 1.

energy, and angular dependent terms. Then we may write for the central force matrix elements:

$${}_{0}E^{0}=\left(\frac{2\pi\hbar c}{\kappa V^{2}}\cdot\frac{2\pi\alpha}{1-\alpha r_{0t}}\right)^{\frac{1}{2}}\frac{e}{\hbar c}(\epsilon_{f}-\epsilon_{0})2\boldsymbol{\varepsilon}\cdot\mathbf{k}$$
$$\times\frac{1}{(\alpha^{2}+k^{2})^{2}}[a+b\cos\theta+c\cos^{2}\theta](\chi_{f}{}^{t},\chi_{0}{}^{t}),$$
$${}_{0}M_{c}{}^{0}=-\left(\frac{2\pi\hbar c}{\kappa V^{2}}\cdot\frac{2\pi\alpha}{1-\alpha r_{0t}}\right)^{\frac{1}{2}}\frac{e}{\hbar c}(\epsilon_{f}-\epsilon_{0})2\boldsymbol{\varepsilon}\cdot\mathbf{k}$$
$$\times\frac{1}{(\alpha^{2}+k^{2})^{2}}[a_{c}+b_{c}\cos\theta+c_{c}\cos^{2}\theta](\chi_{f}{}^{t},\chi_{0}{}^{t}),$$

$$
{}_0M_{st}{}^0=\left(\frac{2\pi\hbar c}{\kappa V^2}\cdot\frac{2\pi\alpha}{1-\alpha r_{0t}}\right)^{\frac{1}{2}}\frac{ie}{\hbar c}(\epsilon_f-\epsilon_0)
$$

$$
\times\frac{\hbar\kappa c}{(\epsilon_0-\epsilon_f)}\frac{\hbar}{2Mc}(\mu_P+\mu_n)\frac{\boldsymbol{\kappa}\cdot\mathbf{k}}{(\alpha^2+k^2)^2}
$$

$$
\times[b_t+c_t\cos\theta](\chi_f{}^t,\boldsymbol{\epsilon}'\cdot(\boldsymbol{\sigma}_1+\boldsymbol{\sigma}_2)\chi_0{}^t),
$$

$$
{}_0M_{ss}{}^0=\left(\frac{2\pi\hbar c}{\kappa V^2}\cdot\frac{2\pi\alpha}{1-\alpha r_{0t}}\right)^{\frac{1}{2}}\frac{ie}{\hbar c}(\epsilon_f-\epsilon_0)
$$

$$
\times\frac{\hbar\kappa c}{(\epsilon_0-\epsilon_f)}\frac{\hbar}{2Mc}\frac{(\mu_P-\mu_n)}{(\alpha^2+k^2)}\left[\cos\delta_{0s}+\frac{\alpha}{k}\sin\delta_{0s}\right] \quad (23)
$$

$$
\times[e^{i\delta_{0s}}-a_s+b_s\cos\theta+c_s\cos^2\theta]
$$

$$
\times(\chi_f{}^s,\boldsymbol{\epsilon}'\cdot(\boldsymbol{\sigma}_1-\boldsymbol{\sigma}_2)\chi_0{}^t),
$$

$${}_0E'=-\left(\frac{2\pi\hbar c}{\kappa V^2}\cdot\frac{2\pi\alpha}{1-\alpha r_{0t}}\right)^{\frac{1}{2}}\frac{e}{\hbar c}(\epsilon_f-\epsilon_0)2\boldsymbol{\epsilon}\cdot\mathbf{k}$$

$$
\times\frac{1}{(\alpha^2+k^2)^2}[a'+b'\cos\theta](\chi_f{}^t,\chi_0{}^t),
$$

$${}_1E^0=(-1)^0\left(\frac{2\pi\hbar c}{\kappa V^2}\cdot\frac{2\pi\alpha}{1-\alpha r_{0t}}\right)^{\frac{1}{2}}\frac{e}{\hbar c}(\epsilon_f-\epsilon_0)2\boldsymbol{\epsilon}\cdot\mathbf{k}$$

$$
\times\frac{1}{(\alpha^2+k^2)^2}[a_1''+ia_2'']({\chi_f}^t,{\chi_0}^t),
$$

$$
M_{ss}{}'=-\left(\frac{2\pi\hbar c}{\kappa V^2}\cdot\frac{2\pi\alpha}{1-\alpha r_{0t}}\right)^{\frac{1}{2}}\frac{ie}{\hbar c}(\epsilon_f-\epsilon_0)
$$

$$
\times\frac{\hbar\kappa c}{(\epsilon_0-\epsilon_f)}\frac{\hbar}{2Mc}\frac{(\mu_P-\mu_N)}{(\alpha^2+k^2)}\left[\cos\delta_{0s}+\frac{\alpha}{k}\sin\delta_{0s}\right]
$$

$$
\times[a_s'e^{i\delta_{0s}}+b_s'\cos\theta](\chi_f{}^s,\boldsymbol{\epsilon}'\cdot(\boldsymbol{\sigma}_1-\boldsymbol{\sigma}_2)\chi_0{}^t).
$$

Thus the results of our calculations are readily evident from the magnitudes of the coefficients of the angular terms. These coefficients are plotted against the incident gamma-ray energy in Figs. 1, 2, and 3.

In the expressions above it is clear that the expressions of the form $(a+b\cos\theta+c\cos^2\theta)$ demonstrate the effects of the additional consideration we have made; i.e., higher multipoles, explicit Hulthén shape, and interaction in the final states. The remaining factor of the terms are, in the case of ${}_0E^0$, ${}_0M_c{}^0$, ${}_0E^1$, and ${}_1E^0$ the electric dipole matrix element between the shape-independent ground-state function $\psi_0{}^0$ and the free-particle final triplet P-state function. In the case of ${}_0M_{ss}{}^0$ and $M_{ss}{}^1$, the remainder is the magnetic dipole matrix element between the shape-independent ground-state wave function $\psi_0{}^0$ and the final singlet S-state wave function in which a correction for interaction has been introduced by means of the phase shift. Both of

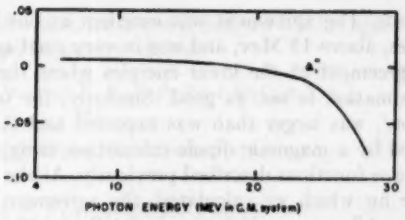

FIG. 3. A term corresponding to ${}_1E^0$ is plotted in the same manner as in Fig. 1.

these cases may be easily obtained from our interaction by using only the first term of the expansion for the exponentials occurring in the $\mathcal{E}$ and $\mathfrak{M}_s$ interactions. This is just what we have been calling the dipole approximation for our interaction. The remainder in the ${}_0M_{st}{}^0$ expression has been obtained by replacing, in the original calculation of ${}_0M_{st}{}^0$, the exponential occurring in the $\mathfrak{M}_{st}$ interaction by the second term of its expansion. This is the analogous term to the magnetic quadrupole term. The coefficients of the angular terms in the modifying expression were arrived at in the following way. The original expressions, Eqs. (10) and (18), for the different matrix elements were numerically calculated at five energies in the range from 5 Mev to 30 Mev, i.e., 5.66 Mev, 11.23, 16.53, 22.44, and 28.06 Mev, and for seven angles at each energy; i.e., 0°, 30°, 60°, 90°, 120°, 150°, and 180°. For each energy the results for each matrix element were numerically fitted to the corresponding term of the above expressions, Eqs. (23), in this way obtaining the coefficients. In all cases these expressions represent the calculated terms to better than one percent at all angles. The coefficients thus obtained were then plotted as a function of the incident gamma-ray energy in Figs. 1, 2, and 3. Actually, only those coefficients whose effects are noticeable are plotted. Higher-order terms in such an expansion in powers of the cosine than those given are at least an order of magnitude smaller than the smallest of the terms given.

Referring to these curves and Eqs. (23), it will be observed that the first coefficient in the modifying expression for each matrix element is the dominant term. This is expected since the more complicated angular behaviour corresponds to the higher multipoles. These first coefficients in the cases of ${}_0E^0$ and ${}_0M_{st}{}^0$ are very nearly equal to unity so that in these cases we have plotted their departures from unity, i.e., for a we plot $\alpha=1-a$, for b_t we plot $\beta_t=b_t-1$. The first coefficients of ${}_0E^1$ and ${}_0M_c{}^0$, a^1 and a_c, respectively, are as expected much smaller although still not negligible because they will interfere with ${}_0E^0$. The term of importance in ${}_1E^0$, that is, a_1'', is smaller than had been anticipated, but this result has been corroborated by an alternative calculation using the method of Marshall and Guth[14] for calculating the electric dipole matrix element with 100 percent ordinary forces and using square well wave

functions. The agreement was excellent at our higher energies, above 15 Mev, and was in very good qualitative agreement at the lower energies where the Born approximation is not as good. Similarly, the term in M_{s}', a_s', was larger than was expected and this was checked by a magnetic dipole calculation using square well wave functions described previously. At the lowest energy for which we calculated, the agreement is excellent while at our higher energies the agreement is is within 10 percent of the calculated correction term.

The second and third terms in the modifying expressions reflect the presence of the higher multipoles. It is evident that though these terms are small they will not be negligible in their effects on the angular distribution, even at our lowest energies. This is more clearly seen by writing the differential cross section for the photodisintegration in terms of these coefficients. It is to be understood that by the Approximation II-C cross section we mean the calculated cross section in which the second Approximation terms are included. Obviously, the first Approximation terms are also included. Thus, we have for the differential cross section in the second Approximation with central forces, and for an unpolarized γ-ray beam:

$$\frac{d\Omega_{II}}{d\Omega}=\frac{M}{2\hbar^2}\frac{e^2}{\hbar^2c^2}\frac{\alpha}{1-\alpha r_{0t}}(\epsilon_f-\epsilon_0)^2\frac{k}{\kappa}\left\{\frac{2k^2\sin^2\theta}{(\alpha^2+k^2)^4}\right.$$
$$\times[(a-a'-a_e+(-1)^s a_1'')$$
$$+(b-b')\cos\theta+c\cos^2\theta]^2$$
$$+\left[\frac{\hbar\kappa c}{(\epsilon_0-\epsilon_f)}\frac{\hbar}{2Mc}\frac{(\mu_P-\mu_n)}{(\alpha^2+k^2)}\right]^2\left[\left(\cos\delta_{0s}+\frac{\alpha}{k}\sin\delta_{0s}\right)^2\right.$$
$$\times\left.\left.\frac{4}{3}[(1-a_s')e^{i\delta_{0s}}-a_s+(b_s-b_s')\cos\theta+c_s\cos^2\theta]^2\right.\right.$$
$$\left.\left.+\frac{k^2\kappa^2}{(\alpha^2+k^2)^4}\cos^2\theta\cdot\frac{8}{3}b_t^2\right]\right\},\quad(24)$$

where θ is the angle between the direction of the incident γ ray and the emergent proton.

The differential cross section in Approximation I, $d\sigma_I/d\Omega$, is easily obtained from the above expression Approximation II by simply omitting a', a_1'', a_s', b_s' where they occur. It is not convenient to express the differential cross section obtained from Approximation II-NC in the above form because of the more complicated spin dependence of the matrix elements. This results in a greater degree of interference between the different terms entering in the calculation of the cross section. For a similar reason we have not felt it particularly illuminating to express the noncentral case matrix elements in the form of Eqs. (23) either. However, in discussing the numerical results for the angular distribution of the different differential cross sections it is more convenient to write the differential cross section in the form

$$d\sigma/d\Omega=A+B\sin^2\theta+C\sin^2\theta\cos\theta$$
$$+D\sin^2\theta\cos^2\theta+E\sin^4\theta\cos\theta,\quad(25)$$

and this form applies equally well for the noncentral as well as central force cases.

The angular distribution is then easily described in terms of the ratio of each of the other coefficients to B, where B is the dominant term corresponding in the main to the electric dipole contribution. Thus A/B gives the measure of the isotropy in the angular distribution, C/B and E/B measure the forward asymmetry, and D/B measures the broadening of the peak of the angular distribution. These ratios are plotted as a function of incident γ-ray energy in the center-of-mass system for the three cases in Fig. 4. The subscript I refers to the quantities in Approximation I, II to the Approximation II-C cross-section, and N.C. to Approximation II-NC. E/B is plotted in only the case of Approximation II-NC since it is only in this case that it is appreciable.

The resultant total cross section can, of course, be written as

$$\sigma=4\pi[A+\tfrac{2}{3}B+(2/15)D].\quad(26)$$

The calculated total cross sections are given in Figs. 5 and 6 as a function of incident gamma-ray energy. In Fig. 5 three curves appear, one for σ_I, the result from Approximation I, for σ_{II} (50 percent), the result from Approximation II with central forces that are 50 percent charge-exchange, 50 percent ordinary, and for $\sigma_{N.C.}$, the result of Approximation II-N.C. with forces that are

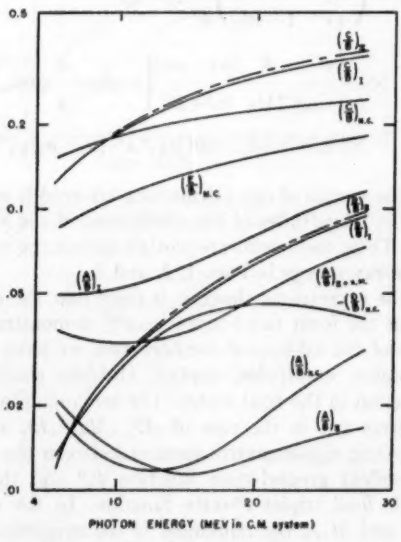

FIG. 4 The angular dependence of the differential cross sections in the three approximations I, II, and IINC, and including the effects of exchange moments in II+X.M. is plotted as a function of incident photon energy. The form assumed for the cross section is $d\sigma/d\Omega=A+B\sin^2\theta+C\sin^2\theta\cos\theta+D\sin^2\theta\cos^2\theta+E\sin^4\theta\cos\theta$.

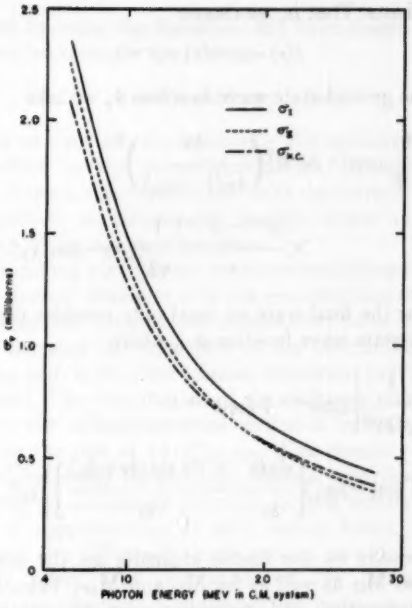

FIG. 5. The total cross section in millibarns is plotted as a function of the incident photon energy for the three approximations calculated, I, II, and IINC.

50 percent charge exchange, and 50 percent ordinary. In Fig. 6, we have plotted the case of Approximation II-C with central forces and 0 percent charge exchange forces, $\sigma_{II}(0 \text{ percent})$, in the form of the ratio $\sigma_{II}(0 \text{ percent})/\sigma_{II}(50 \text{ percent})$ of this cross section to the cross section from Approximation II-C with central forces, and 50 percent charge exchange which appears in Fig. 5. From the curves of the differential and total cross sections, Figs. 4, 5, and 6 and the appropriate equations, (25) and (26), it is clear that the values of the coefficients A, B, C, D, and E may easily be obtained for each case and for any of the energies in the range calculated.

V. EXCHANGE-MOMENT CONTRIBUTION

In the preceding sections we have not treated the interaction due to exchange currents in the deuteron, arising from the charge-exchange character of nuclear forces, even though it is to be expected that such effects are present, because the explicit form for the interaction must depend upon the choice of meson theory to be used. In the absence of a suitable meson theory, it is, however, still possible to obtain some information from a phenomenological approach. In a recent paper[10] such a phenomenological method was described, in which, on the basis of differential charge conservation and reasonable symmetry restrictions on the nuclear Hamiltonian, consideration was given to the possible operational forms for the two-body exchange current operators. The resultant magnetic moment operators were obtained which, for convenience, we will list again here. They are, for general nuclei:

$$\mathbf{M}_I=(e/4\hbar c)\sum_{i\neq j}V_{ij}(\tau_i{}^z\tau_j{}^y-\tau_i{}^y\tau_j{}^z)[\mathbf{x}_i\times\mathbf{x}_j],$$

$$\mathbf{M}_{\mathrm{I}}=\tfrac{1}{4}\sum_{i<j}F_{\mathrm{I}}(r_{ij})(\tau_i{}^z\tau_j{}^y-\tau_i{}^y\tau_j{}^z)(\boldsymbol{\sigma}_i\times\boldsymbol{\sigma}_j),$$

$$\mathbf{M}_{\mathrm{I}'}=\tfrac{1}{4}\sum_{i<j}F_{\mathrm{I}'}(r_{ij})(\tau_i{}^z\tau_j{}^y-\tau_i{}^y\tau_j{}^z)\times\{3[\mathbf{r}_{ij}\cdot(\boldsymbol{\sigma}_i\times\boldsymbol{\sigma}_j)]\mathbf{r}_{ij}/r_{ij}{}^2-(\boldsymbol{\sigma}_i\times\boldsymbol{\sigma}_j)\},$$

$$\mathbf{M}_{\mathrm{II}}=\tfrac{1}{4}\sum_{i<j}F_{\mathrm{II}}(r_{ij})(\tau_i{}^z-\tau_j{}^z)(\boldsymbol{\sigma}_i-\boldsymbol{\sigma}_j),$$

$$\mathbf{M}_{\mathrm{II}'}=\tfrac{1}{4}\sum_{i<j}F_{\mathrm{II}'}(r_{ij})(\tau_i{}^z-\tau_j{}^z)\times\{3[\mathbf{r}_{ij}\cdot(\boldsymbol{\sigma}_i-\boldsymbol{\sigma}_j)]\mathbf{r}_{ij}/r_{ij}{}^2-(\boldsymbol{\sigma}_i-\boldsymbol{\sigma}_j)\},$$

$$\mathbf{M}_{\mathrm{III}}=\tfrac{1}{4}\sum_{i<j}F_{\mathrm{III}}(r_{ij})(\tau_i{}^z+\tau_j{}^z)(\boldsymbol{\sigma}_i+\boldsymbol{\sigma}_j),$$

$$\mathbf{M}_{\mathrm{III}'}=\tfrac{1}{4}\sum_{i<j}F_{\mathrm{III}'}(r_{ij})(\tau_i{}^z+\tau_j{}^z)\times\{3[\mathbf{r}_{ij}\cdot(\boldsymbol{\sigma}_i+\boldsymbol{\sigma}_j)]\mathbf{r}_{ij}/r_{ij}{}^2-(\boldsymbol{\sigma}_i+\boldsymbol{\sigma}_j)\}, \quad (27)$$

$$\mathbf{M}_{\mathrm{IV}}=\tfrac{1}{4}\sum_{i<j}F_{\mathrm{IV}}(r_{ij})(1+\tau_i{}^z\tau_j{}^z)(\boldsymbol{\sigma}_i+\boldsymbol{\sigma}_j),$$

$$\mathbf{M}_{\mathrm{IV}'}=\tfrac{1}{4}\sum_{i<j}F_{\mathrm{IV}'}(r_{ij})(1+\tau_i{}^z\tau_j{}^z)\times\{3[\mathbf{r}_{ij}\cdot(\boldsymbol{\sigma}_i+\boldsymbol{\sigma}_j)]\mathbf{r}_{ij}/r_{ij}{}^2-(\boldsymbol{\sigma}_i+\boldsymbol{\sigma}_j)\},$$

$$\mathbf{M}_{\mathrm{V}}=\tfrac{1}{4}\sum_{i<j}F_{\mathrm{V}}(r_{ij})(1-\tau_i{}^z\tau_j{}^z)(\boldsymbol{\sigma}_i+\boldsymbol{\sigma}_j),$$

$$\mathbf{M}_{\mathrm{V}'}=\tfrac{1}{4}\sum_{i<j}F_{\mathrm{V}'}(r_{ij})(1-\tau_i{}^z\tau_j{}^z)\times\{3[\mathbf{r}_{ij}\cdot(\boldsymbol{\sigma}_i+\boldsymbol{\sigma}_j)]\mathbf{r}_{ij}/r_{ij}{}^2-(\boldsymbol{\sigma}_i+\boldsymbol{\sigma}_j)\},$$

$$\mathbf{M}_{\mathrm{VI}}=-\tfrac{1}{4}\sum_{i<j}F_{\mathrm{VI}}(r_{ij})(\tau_i{}^z\tau_j{}^z+\tau_i{}^y\tau_j{}^y)(\boldsymbol{\sigma}_i+\boldsymbol{\sigma}_j),$$

$$\mathbf{M}_{\mathrm{VI}'}=-\tfrac{1}{4}\sum_{i<j}F_{\mathrm{VI}'}(r_{ij})(\tau_i{}^z\tau_j{}^z+\tau_i{}^y\tau_j{}^y)\times\{3[\mathbf{r}_{ij}\cdot(\boldsymbol{\sigma}_i+\boldsymbol{\sigma}_j)]\mathbf{r}_{ij}/r_{ij}{}^2-(\boldsymbol{\sigma}_i+\boldsymbol{\sigma}_j)\},$$

with the general expression for the magnetic moment operator of the nuclear system being

$$\mathbf{M}=\mathbf{M}_I+\textstyle\sum_N C_N\mathbf{M}_N, \quad (28)$$

where the C_N are arbitrary constants.

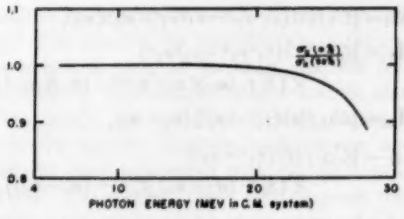

FIG. 6. The ratio of the total cross section calculated in Approximation II with 100 percent ordinary forces to the total cross section calculated in Approximation II with 50 percent charge-exchange forces (which appears in Fig. 5) is plotted as a function of incident photon energy.

We see that aside from $\mathbf{M}_I$, the remaining twelve exchange-moment operators $M_1-M_{VI'}$ have within them an arbitrary function of r_{ij}, the separation of the ith and jth nucleons. It was there assumed that all twelve of these functions were the same and of the form of a Gaussian function. Choosing a reasonable value for the range of the Gaussian it was then possible, by referring to the experimental data on the magnetic moment anomalies of the deuteron, triton, He^3, and heavy odd nuclei, to obtain some information on the values of the multiplicative constants C_N which represent the strengths of the different terms. It is our purpose to utilize these numerical results for estimating the magnitude of the contribution of exchange moment effects on the matrix elements for photodisintegration in the magnetic dipole approximation.

For the deuteron it may readily be verified that the exchange moment operators $\mathbf{M}_I$, $\mathbf{M}_{III}$, $\mathbf{M}_{III'}$, $\mathbf{M}_{IV}$, and $\mathbf{M}_{IV'}$ can give no contribution to the matrix elements for photodisintegration. $\mathbf{M}_I$ cannot contribute for any two-nucleon system, while the other four terms have a null contribution because the deuteron has a singlet isotopic spin ground-state wave function which, when operated upon by the isotopic spin operator parts of $\mathbf{M}_{III}$, $\mathbf{M}_{III'}$, $\mathbf{M}_{IV}$, and $\mathbf{M}_{IV'}$, yields zero identically. If we assume that the ground state of the deuteron is completely an S state, as we shall in this calculation, the selection rules for the remainder of the exchange moment operators may readily be obtained. Thus $\mathbf{M}_I$ and $\mathbf{M}_{II}$ give rise to transitions to a final singlet S state, while $\mathbf{M}_{I'}$ and $\mathbf{M}_{II'}$ give rise to transitions to final singlet S or singlet D states. $\mathbf{M}_V$ and $\mathbf{M}_{VI}$ give rise to transitions to final triplet S states, while $\mathbf{M}_{V'}$ and $\mathbf{M}_{VI'}$ may give rise to transitions to either final triplet S or triplet D states in the deuteron.

Since $\mathbf{M}_V$, $\mathbf{M}_{V'}$, $\mathbf{M}_{VI}$, and $\mathbf{M}_{VI'}$ would give exchange contributions to the magnetic moment of the deuteron, the conclusion arrived at was that the strengths of these terms are probably very small. On the other hand, the strengths of $\mathbf{M}_I$, $\mathbf{M}_{I'}$, $\mathbf{M}_{II}$, and $\mathbf{M}_{II'}$ may be quite a bit larger, by at least an order of magnitude. For our purpose of merely estimating the magnitudes of these contributions to the photodisintegration it will be sufficient to consider only the terms $\mathbf{M}_I$, $\mathbf{M}_{I'}$, $\mathbf{M}_{II}$, $\mathbf{M}_{II'}$. That is, for the deuteron we consider

$$\begin{aligned}
&C_I\mathbf{M}_I=\tfrac{1}{4}C_I f(r)(\tau_1{}^x\tau_2{}^y-\tau_1{}^y\tau_2{}^x)(\boldsymbol{\sigma}_1\times\boldsymbol{\sigma}_2),\\
&C_{I'}\mathbf{M}_{I'}=\tfrac{1}{4}C_{I'}f(r)(\tau_1{}^x\tau_2{}^y-\tau_1{}^y\tau_2{}^x)\\
&\qquad\times\{3[\mathbf{r}\cdot(\boldsymbol{\sigma}_1\times\boldsymbol{\sigma}_2)]\mathbf{r}/r^2-(\boldsymbol{\sigma}_1\times\boldsymbol{\sigma}_2)\},\\
&C_{II}\mathbf{M}_{II}=\tfrac{1}{4}C_{II}f(r)(\tau_1{}^z-\tau_2{}^z)(\boldsymbol{\sigma}_1-\boldsymbol{\sigma}_2),\\
&C_{II'}\mathbf{M}_{II'}=\tfrac{1}{4}C_{II'}f(r)(\tau_1{}^z-\tau_2{}^z)\\
&\qquad\times\{3[\mathbf{r}\cdot(\boldsymbol{\sigma}_1-\boldsymbol{\sigma}_2)]\mathbf{r}/r^2-(\boldsymbol{\sigma}_1-\boldsymbol{\sigma}_2)\}.
\end{aligned}\tag{29}$$

In our calculations we will assume for simplicity that $C_I=3C_{I'}$ and $C_{II}=3C_{II'}$, and we will choose for $f(r)$ a Hulthén form rather than a Gaussian, although this causes some further uncertainty in the values of the coefficients. That is, we choose

$$f(r)=e^{-\mu r}/(1-e^{-\mu r}).\tag{30}$$

For the ground-state wave function ψ_g we take

$$\psi_g=\frac{1}{\sqrt{V}}\exp(-i\boldsymbol{\kappa}\cdot\mathbf{R})\left(\frac{2\alpha}{4\pi(1-\alpha r_{0t})}\right)^{\frac{1}{2}}\times\frac{(e^{-\alpha r}-e^{-\beta r})}{r}\frac{1}{\sqrt{2}}(\xi_1\eta_2-\xi_2\eta_1)\chi_g{}^t,\tag{31}$$

and for the final state we need only consider the final singlet-state wave function ψ_{fs}, where

$$\psi_{fs}=\frac{1}{\sqrt{2V^2}}\left\{\xi_1\eta_2e^{i\mathbf{k}\cdot\mathbf{r}}+\xi_2\eta_1e^{-i\mathbf{k}\cdot\mathbf{r}}-[\xi_1\eta_2+\xi_2\eta_1]\left[\frac{\sin kr}{kr}-\frac{e^{-i\delta_{0s}}\sin(kr+\delta_{0s})}{kr}\right]\right\}\chi_f{}^s.\tag{32}$$

The results for the matrix elements are the same for $\mathbf{M}_I$ and $\mathbf{M}_{II}$ as well as for $\mathbf{M}_{I'}$ and $\mathbf{M}_{II'}$. Thus, before the summation and averaging over spin states and polarizations we have

$$\begin{aligned}
&(\psi_f|C_I(M_I+M_{I'})|\psi_g)=(\psi_f|C_{II}(M_{II}+M_{II'})|\psi_g)\\
&=\left(\frac{2\pi\hbar c}{\kappa V^2}\cdot\frac{2\pi\alpha}{1-\alpha r_{0t}}\right)^{\frac{1}{2}}\frac{e}{2\hbar c}(\epsilon_f-\epsilon_0)\frac{\hbar\kappa c}{(\epsilon_0-\epsilon_f)}\frac{h}{Mc}2C_N\\
&\times\chi_f{}^s\left\{\boldsymbol{\epsilon}'\cdot\mathbf{S}_N\left[\frac{e^{-i\delta_{0s}}}{\beta^2+k^2}\left(\cos\delta_{0s}+\beta/k\,\sin\delta_{0s}-\frac{e^{i\delta_{0s}}}{4}\right)\right]\right.\\
&+\frac{\boldsymbol{\epsilon}'\cdot\mathbf{k}}{k^2}(\mathbf{S}_N\cdot\mathbf{k})\left[\frac{1}{k^2}\left(\frac{2+k^2/\beta^2}{1+k^2/\beta^2}\right)+\frac{1}{k^2}-\frac{3\beta}{k^3}\tan^{-1}\frac{k}{\beta}\right]\\
&\left.+\frac{(\epsilon_x'S_{Nx}k_x+\epsilon_y'S_{Ny}k_y)}{k}\left[\frac{\beta}{k^3}\tan^{-1}\frac{k}{\beta}-\frac{1}{k^2}\right]\right\}\chi_g{}^t,
\end{aligned}\tag{33}$$

where C_N is either C_I or C_{II}, and S_N is the corresponding spin operator, $\mathbf{S}_I=(\boldsymbol{\sigma}_1\times\boldsymbol{\sigma}_2)$ and $\mathbf{S}_{II}=(\boldsymbol{\sigma}_1-\boldsymbol{\sigma}_{II})$; however, $\mathbf{S}_I$ and $\mathbf{S}_{II}$ have exactly the same effects operating on the deuteron ground-state triplet spin function $\chi_g{}^t$.

The original calculations[10] to determine the magnitudes of the C_N's performed with a Gaussian for $f(r)$ indicated magnitudes for C_I and C_{II} of the order of a nuclear magneton. We have estimated the effect on the C_N's of the use of the Hulthén form for $f(r)$ instead of the Gaussian by two methods. The first consisted of equating the expectation values for the magnetic moment of the deuteron for the two forms, and the second consisted of normalizing both interaction forms to the same volume and then equating them. Neither method is completely satisfactory but both methods do indicate that the constants, i.e., strengths, to be used with the Hulthén form should be somewhat larger than those

obtained by using the Gaussian. We have chosen as a conservative estimate the relation

$$C_{\mathrm{I}}+C_{\mathrm{II}}=2.0 \text{ nm} \tag{34}$$

to serve as our basis for estimating the exchange moment effect on the photodisintegration. Though, of course, inexact, this value should be of the correct order of magnitude to indicate the possible extent of the influence of the exchange moments.

The resulting contribution to the photodisintegration matrix element interferes with the contributions of the $\mathfrak{M}_{ss}$ interaction. Despite the complicated form of the matrix elements the main part of the contribution is isotropic, and, in fact, the angular dependent part may be ignored. The contribution of the exchange moment terms to the differential cross section is indicated in Fig. 4 by the plot of $(A/B)_{\mathrm{II+XM}}$. This quantity was obtained by adding the exchange-moment contribution, considered as completely isotropic, to the matrix elements of Approximation II with central forces, thus yielding a new differential cross section to which this quantity refers. The magnitude of the exchange-moment contribution is indicated by comparison of $(A/B)_{\mathrm{II+XM}}$ to the quantity $(A/B)_{\mathrm{II}}$. The contribution of the exchange moments to the total cross section is indicated in Fig. 7 where the difference between the total cross section given by Approximation II with central forces and 50 percent charge exchange with the inclusion of the exchange moment and the quantity σ_{II} (50 percent) without the exchange-moment contribution is plotted as a function of the incident gamma-ray energy.

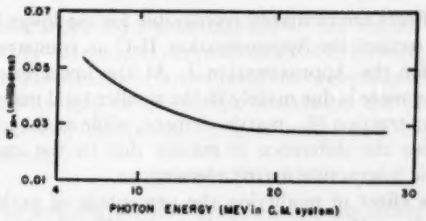

FIG. 7. The contribution to the total cross section due to the inclusion of exchange moments is plotted as a function of incident photon energy. σ_{XM} is the difference between the cross section given by Approximation II with 50 percent charge-exchange forces and including the exchange moments and the same Approximation without the exchange moments.

VI. DISCUSISON OF RESULTS

All of the salient results of this paper are summarized in the Figs. 1 through 7. In this section we will discuss these results in the order in which we have presented them.

A. Approximation I

The results obtained in Approximation I are characterized by the curves for α, b, c, a_c, β_t, a_s, b_s, and c_s in Figs. 1 and 2 which describe the behavior of the matrix elements; the curves for $(A/B)_{\mathrm{I}}$, $(C/B)_{\mathrm{I}}$, and $(D/B)_{\mathrm{I}}$ in Fig. 4 which yields the angular distribution of the differential cross section; and the curve for σ_{I} in Fig. 5 which gives the total cross section in this approximation. The results in Figs. 1 and 2 corresponding to Approximation I show most clearly the effects of including all of the multipoles. At the low energies it may be seen that the magnitude of the final result, the total cross section, is essentially the same as obtains in the simple dipole approximations. As the energy increases the disparity between this and the dipole calculation becomes more pronounced, as indicated for example, by the curves of α and a_s, but the difference is still fairly insignificant at the highest energy we consider. The curves of Fig. 4 representing the angular dependence of the differential cross section show more significant results. There it is observed that even at the lowest energies the forward asymmetry $(C/B)_{\mathrm{I}}$ is appreciable. Thus, it is seen that higher multipoles may have appreciable effects on the angular distribution before they have signiñcant effects on the total cross section. These remarks obtain equally well for Approximation II.

All of the results of Approximation I are independent of any explicit knowledge of the nature of the forces in the deuteron and are dependent upon only the numerical choice of the constants used, i.e., effective ranges, scattering lengths, and binding energy of the deuteron, these values (with the exception of the last) having been obtained from experiments other than photodisintegration. Of these experimental quantities, the triplet effective range, r_{0t} is probably responsible for the largest contribution to the error. As an overall estimate it would seem reasonable to conclude that the numerical results of Figs. 4 and 5 are correct to within 5 percent, this error being due to the uncertainties in the experimental quantities that are used in the numerical calculation. Essentially the same error arises in Approximation II.

B. Approximation II-C

The modifications introduced through Approximation II-C are apparent in Fig. 4 for the effect on the differential cross section, and in Fig. 5 for the effect on the total cross section. The effects of individual terms that are calculated in Approximation II-C are seen in Figs. 1, 2, and 3. The effect of the introduction of the specific potential shape is seen to be most marked for the magnetic spin to final singlet states matrix element M_{ss}'. This result, as indicated before, seems independent of the specific Hulthén form chosen, as evidenced by the good agreement with calculations using a square well. The greatest effect is to decrease the isotropic term as is evidenced by comparison of $(A/B)_{\mathrm{II}}$ to $(A/B)_{\mathrm{I}}$ in Fig. 4. The curve for a' in Fig. 1 shows that the total electric interaction $\mathcal{E}$ matrix element is also decreased by the destructive interference of ${}_0E^1$, though almost negligibly at the lower energies. These

two effects are primarily responsible for the lower total cross section for Approximation II-C as compared to that for the Approximation I. At the lower energies this decrease is due mainly to the smaller total magnetic spin interaction $\mathfrak{M}_{ss}$ matrix element, while at the higher energies the difference is mainly due to the smaller electric interaction matrix element.

The effect of modifying the percentage of exchange force from 50 percent is indicated in Fig. 3 where the dominant term in the matrix element ${}_1E^0, a_1''$, is plotted as a function of energy, and in Fig. 6 where the ratio of the total cross section in Approximation II with 0 percent exchange force, to the total cross section in Approximation II-C with 50 percent exchange force, $\sigma_{II}(0 \text{ percent})/\sigma_{II}(50 \text{ percent})$ is plotted. Both curves indicate the same behavior. Below about 20 Mev the effect of varying the percentage is negligible and therefore difficult to detect experimentally. In fact, the 0 percent cross section is slightly greater than the 50 percent exchange cross section. Above 20 Mev the effects become more pronounced with the 0 percent exchange cross section smaller than the 50 percent exchange cross section, the ratio being 0.87 at 28 Mev. This general result does not seem dependent upon the choice of potential shape[17] since, as mentioned before, the same behavior is obtained with a square well calculation.

Essentially the same arguments apply to the reliability of the numerical results of Approximation II-C as were used for the first Approximation, although the use of the Hulthén wave function diminishes to some degree the error due to the uncertainty in the triplet effective range. We will, however, estimate the error as the same as for the First Approximation.

C. Approximation II-NC

Inasmuch as only approximate wave functions and potentials were used in the noncentral force calculation, the results obtained can only serve to indicate the changes that occur upon the introduction of the tensor force. The most significant modifications to the second Approximation cross section due to the inclusion of a noncentral force are to the angular distribution and may be seen in Fig. 4. Comparing to the terms from Approximation II-C, we see the following changes. First, the isotropic component becomes considerably larger at the higher energies. Thus, the ratio of $(A/B)_{N.C.}$ to $(A/B)_{II}$ is about unity up to around 15 Mev but is nearly two at 28 Mev. Secondly, the forward asymmetry, represented by the two terms $(C/B)_{NC}$ and $(E/B)_{NC}$, is greater at the very low energies, around 6 Mev, but becomes about the same as the central-force case, with the peak slightly shifted, at the higher energies. Finally, the width of the peak in the angular distribution is decreased due to the fact that $(D/B)_{NC}$ is negative in this energy range while it is positive in the central force cases. The total cross section σ_{NC}, Fig. 5, is smaller than σ_{II} at the lowest energies as would be expected due to the lower percentage of S state in the ground state. The fact that the difference between the two cross sections, σ_{NC} and σ_{II}, becomes smaller as the energy increases seems to be a reflection of the relative increase of the isotropic term, both effects apparently being due to the increased importance of transitions from the D state. It is more difficult in this case to see the causes of small changes in the cross sections because of the more complicated spin and angular dependence of the matrix elements and the resultant mixing and interference between terms entering into the calculation of the cross sections.

[17] J. S. Levinger and H. A. Bethe, Phys. Rev. **78**, 115 (1950).

D. Exchange Moment Contribution

The estimated exchange moment contributions to the cross sections are indicated by $(A/B)_{II+XM}$ in Fig. 4 for the effect on the angular distribution, and by the contribution to the second Approximation for central forces total cross section in Fig. 7 where essentially $\sigma_{II+XM}-\sigma_{II}$ is plotted. Since our choice of the strengths for the exchange moments was somewhat arbitrary, these calculations can only serve to indicate the order of magnitude of the effects to be expected. However, these results show that the exchange moment effects may not be inappreciable. Our calculated contribution to the total cross section gives an increase of almost 10 percent of σ_{II} at 28 Mev and the increase of the isotropy in Approximation II-C is nearly fivefold. Unfortunately, because of the other uncertainties of the deuteron problem these effects may not be clearly distinguishable experimentally, if they are present. However, these contributions seem to become more important as the energy increases and it is possible that they may become quite significant at energies above those calculated here.

E. Extension to Higher Energies

The methods used in obtaining our results are expected to be particularly appropriate for similar calculations at higher energies where the higher multipoles would be relatively more important. In fact, Eqs. (10), (18), (22), and (32) could be used in their present form to calculate the corresponding matrix elements, with reasonable accuracy, up to energies of the order of 100 Mev. The Born approximation used for Eq. (16) will, in fact, be better at the high energies. If desired, the calculation could easily be somewhat improved for higher energies by the inclusion of the phase shifts for the D final states, etc.

F. Conclusion

We may conclude, from the results of this paper, that the theoretical estimates for the deuteron photodisintegration, in the energy range here considered, may be

considered to be fairly well bracketed, as is most clearly shown by Fig. 5 for the total cross sections. Certainly, greater accuracy in the experimental quantities used in numerically fixing these cross sections will be almost a prerequisite before refined photodisintegration measurements can distinguish the presence of such effects as are due to tensor forces, exchange forces, exchange currents, or particular well shape. However, as a standard to be used for determining other photo-process cross sections the present calculations indicate that such a calculated result as σ_{II}, as our best approximation to the correct total cross section, can only be considered to be accurate to within 15 percent. About 5 percent of this arises from uncertainties in the values of empirically determined parameters (effective ranges, etc.), while the remainder arises from the uncertainties introduced by lack of knowledge concerning the potential interaction, noncentral interactions, and exchange moments.

ACKNOWLEDGMENTS

The writer gratefully acknowledges his indebtedness to Professor L. L. Foldy for suggesting this problem, and for his invaluable advice throughout the course of the work. The writer is also indebted to Professor M. L. Goldberger for pointing out an error in the original manuscript.

PHYSICAL REVIEW VOLUME 94, NUMBER 6 JUNE 15, 1954

New Neutron-Deficient Isotope of Silver*

B. C. Haldar† and Edwin O. Wiig
Department of Chemistry, University of Rochester, Rochester, New York

(Received February 1, 1954)

Silver-103 of 1.1-hour half-life, produced by bombarding silver with high-energy protons, was identified by following the decay with β-proportional, scintillation, and x-ray proportional counters and by milking the daughter, 17-day Pd^{103}, through seven half-lives. Measurements with a β-ray survey spectrometer showed the presence of conversion electrons of 0.6-Mev energy and positrons of 1.3-Mev maximum energy, both of which decayed with a half-life of 1.1 hours. Aluminum absorption measurements also gave 1.3 Mev as the maximum β^+ energy. Ag^{103} decays in part by K capture.

THE existence of previously unknown Ag^{103} of 1.1-hour half-life was investigated by bombarding silver with protons of energy 80, 100, and 170 Mev in the internal beam of the 130-inch synchrocyclotron of the University of Rochester. Bendel *et al.*[1] have reported bombardment of Pd foil with 12-Mev deuterons and examination of the activity associated with the silver fraction. They observed that conversion lines of 530- and 740-kev associated with the silver activity decayed with half-lives of 1.1 hours, which they could not assign to any known silver isotope. In view of the present results it seems quite likely that they synthesized 1.1-hour Ag^{103} from Pd^{102} by a (d,n) reaction.

EXPERIMENTAL

Silver powder, determined by spectrochemical analysis to contain only traces of copper and possible traces of lead, was wrapped in a 5-mil aluminum foil envelope and bombarded, usually for one hour.

The bombarded sample was dissolved in hot nitric acid containing ions of In, Cd, Pd, Y, Sr, and Rb as carriers. The resulting solution was diluted with water and AgCl precipitated by addition of HCl. The washed solid was dissolved in NH_4OH and the solution scavenged twice with $Fe(OH)_3$. Addition of H_2S to the solution gave a precipitate of Ag_2S, which was washed and dissolved in hot concentrated HNO_3. Dilution and addition of HCl resulted in precipitation of AgCl, which was dissolved in NH_4OH and the $Fe(OH)_3$, Ag_2S, AgCl purification cycle repeated. The final AgCl precipitate was washed with water, alcohol and ether and suitably mounted for counting with β-proportional, scintillation, and x-ray proportional counters. Samples were also prepared for β-ray spectrometer and aluminum absorption measurements.

In milking experiments a known amount of $Pd(NO_3)_2$ as carrier in solution was added to a known weight of purified active AgCl. The mixture was allowed to stand for 45 minutes and then dissolved in NH_4OH solution. At the end of 1.1 hours from the previous precipitation of AgCl, the NH_4OH solution was made acid with HCl and AgCl reprecipitated and separated. The supernatant was scavenged with AgCl, after which palladium dimethylglyoxime was precipitated, separated, and washed. A solution of the precipitate in hot concentrated HNO_3 was again scavenged with AgCl. After dilution of the supernatant, palladium was separated as palladium dimethylglyoxime, washed, dried, mounted, and weighed. The

* This research was supported by a contract with the U. S. Atomic Energy Commission
† Postdoctoral Research Associate in Chemistry.
[1] Bendel, Shore, Brown, and Becker, Phys. Rev. **90**, 888 (1953).

K-capture decay of 17-day Pd^{103} was followed with an x-ray proportional counter.

RESULTS

Half-Life and Mass Number

The decay curve for the silver activity produced by bombardment with 100-Mev protons and followed with a β-proportional counter is illustrated in Fig. 1. Similar curves were obtained with a scintillation counter and for all three proton energies. Besides long-lived activity, the silver sample was found to decay with half-lives of 1.1 hours and 25 minutes. The latter activity presumably indicates the presence of the known isotopes[2] Ag^{106} (24 minutes) and/or Ag^{104} (27 minutes). Measurements with an x-ray proportional counter also showed the 1.1-hour activity along with other activities (Fig. 2, curve A). Silver activities of 16.3 minutes and 1.2 hours were originally assigned by Ens[3] to Ag^{104} and Ag^{102}, respectively. However, he expressed doubt concerning the assignment of the 1.2-hour activity, which was of low intensity. In the most recent "Table of Isotopes"[2] the 16-minute decay is assigned to Ag^{102} and the 1.2-hour to Ag^{104}. It would now appear that perhaps Ens' 1.2-hour Ag activity was actually 57-minute Rh^{103m}, which was unknown at the time. The latter has since been prepared by a

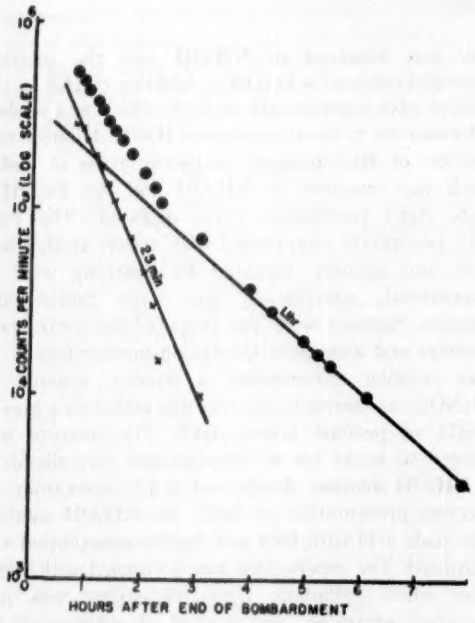

FIG. 1. Decay curve of active silver as observed with a beta-proportional counter.

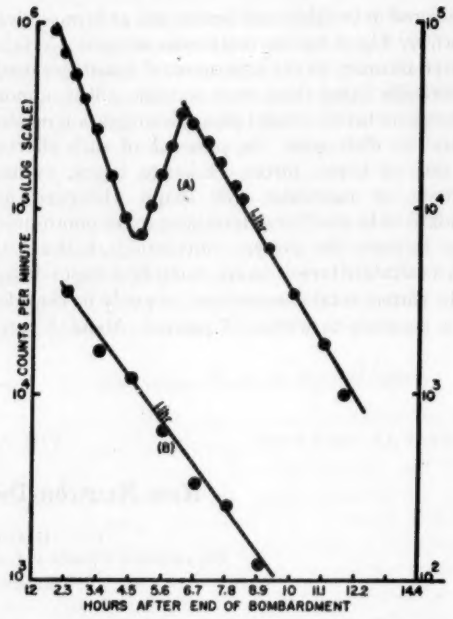

FIG. 2. (A) Decay of active silver as observed with an x-ray proportional counter. (B) Yields of Pd^{103} daughter extracted from chemically purified active silver.

(p,p) reaction[4] on Rh^{103}, and Rh was present in Ens' Pd target. No data have as yet appeared for the more recently reported[2] 1.2-hour Ag activity. At any rate, in view of the relatively short half-life of Ag^{104} and of the energy available in the transition from the ground state of Ag^{102} to that of Pd^{102} (5.3 Mev, calculated by the β-decay systematics of Coryell[5]), Ag^{102} should have a short half-life. This suggested that our observed 1.1-hour Ag activity was due to Ag^{103}, a conclusion which was confirmed by extraction of the known 17-day Pd^{103} daughter.

The results of the Pd milking experiments are summarized in Fig. 2, curve B. The yield of Pd activity decreases with a 1.1-hour half-life. The separated Pd decayed by K capture and with a 17-day half-life.

Mode of Decay and Radiation Characteristics

Measurements made with a β-ray survey spectrometer indicated that the 1.1-hour Ag activity emits positrons of 1.3-Mev maximum energy. At the magnet current corresponding to 0.52 Mev, the peak of the 1.3-Mev β^+ emission, the activity was found to decay with a 1.1-hour half-life. Aluminum absorption data (Fig. 3) also gave 1.3 Mev as the maximum positron energy. The 0.4-Mev β^- rays of 24-minute Ag^{106} were also seen but were allowed to decay out before starting measurements on Ag^{103}. The high count remaining in

[2] Hollander, Perlman, and Seaborg, Revs. Modern Phys. **25**, 469 (1953).
[3] T. Ens, Phys. Rev. **56**, 872 (1939).
[4] N. Hole, Arkiv. Mat. Astron. Fysik **36A**, No. 2 (1948).
[5] C. D. Coryell, Ann. Rev. Nuclear Sci. **2**, 305 (1953).

Fig. 3 is due to γ rays from 8.3-day Ag^{106} and 40-day Ag^{105}, and to a soft component equivalent to betas of ~0.75-Mev maximum energy. The latter was not observable until 2 days after the bombardment and was possibly due to some other silver isotope or to the presence of impurity activity.

A calculation by Coryell's β-decay systematics[5] gives 1.72 Mev as the total disintegration energy of Ag^{103} in the positron ground state transition. This would suggest that Ag^{103} decays by emission of 1.3-Mev β^+ to an excited state of Pd^{103}, which then decays to the ground state by gamma emission. Conversion electrons of 0.6-Mev energy observed in the β-ray spectrometer data were found to decay with a half-life of 1.1 hours. Thus the observed total energy, 1.92 Mev,

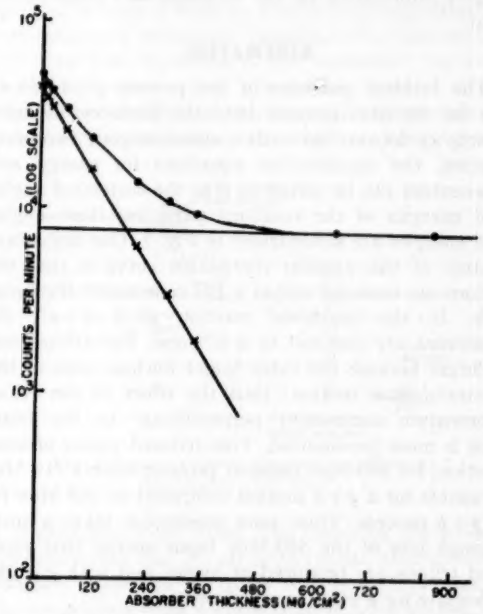

FIG. 3. Aluminum absorption curve of active silver 7 hours after end of bombardment.

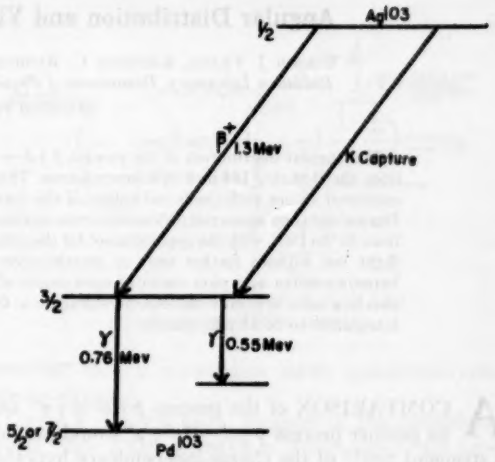

FIG. 4. Suggested decay scheme for silver-103.

is within the limits of error in agreement with the estimated energy.

By way of summary, the experiments reported here show 1.1-hour Ag^{103} to decay by emission of 1.3-Mev β^+, ~0.6-Mev γ rays and K capture.

By combining our data and the 530- and 740-kev conversion lines of Bendel *et al.*,[1] which our results show are associated with Ag^{103}, the tentative decay scheme shown in Fig. 4 may be suggested for Ag^{103}. The value of log ft is ~4.8, as calculated from Feenberg and Trigg.[6] From the shell model the spin of Ag^{103} in the ground state is expected to be $\frac{1}{2}$ due to the 47th proton in the $p_{\frac{1}{2}}$ state. The spin of the ground state of Pd^{103} is due to its 57th neutron which may occupy the $d_{\frac{3}{2}}$ or $g_{7/2}$ state.

We wish to express our thanks to Professor S. W. Barnes, Mr. W. Coombs, and the members of the operating crew of the Rochester 130-inch synchrocyclotron for their assistance with the bombardments.

[6] E. Feenberg and G. Trigg, Revs. Modern Phys. **22**, 401 (1950).

Angular Distribution and Yield of the Process $p+d\rightarrow t+\pi^+$

WILSON J. FRANK, KENNETH C. BANDTEL, RICHARD MADEY,* AND BURTON J. MOYER
Radiation Laboratory, Department of Physics, University of California, Berkeley, California

(Received Februrary 23, 1954)

The angular distribution of the process $p+d\rightarrow t+\pi^+$ has been determined for 340-Mev incident protons from the Berkeley 184-inch synchrocyclotron. The process was identified at one angle by a comparison of measured values with predicted values of the correlated angles, particle ranges, and triton time of flight. During one continuous run differential cross sections were measured at six pion center-of-mass angles ranging from 30° to 150°, with the apparatus set for the predicted correlated angles, minimum ranges, and triton time flight but without further tests of identification. The cross section is constant at about 0.45 microbarns/steradian over pion center-of-mass angles of 180° to 90°. The cross section rises in the forward direction to a value around 5 microbarns/steradian at 0°. The total yield of the process is estimated by numerical integration to be 15 microbarns.

A COMPARISON of the process $p+d\rightarrow t+\pi^+$ and its partner process $p+d\rightarrow He^3+\pi^0$ would provide a stringent test[1,2] of the charge-independence hypothesis. If nuclear interactions are charge-independent in this energy region, the angular distributions of these two processes should be identical, and the ratio of the total cross sections, or the differential cross sections at any center-of-mass angle, should be 2:1. As an exploratory experiment, the angular distribution of the process $p+d\rightarrow t+\pi^+$ was measured.

This process, however, is of interest for its own sake, since its relation to the analogous process $p+p\rightarrow d+\pi^+$ makes it amenable to theoretical treatment. A prediction[1,3] of its angular distribution and yield involves some assumptions about the deuteron and triton wave functions and an estimate of the angular distribution and yield of the process $p+p\rightarrow d+\pi^+$ for pions with a center-of-mass energy of 78 Mev. Once the experimental data on the $p+d\rightarrow t+\pi^+$ process are available, the theoretical treatment can be reversed or modified to give information on the estimates and assumptions used.

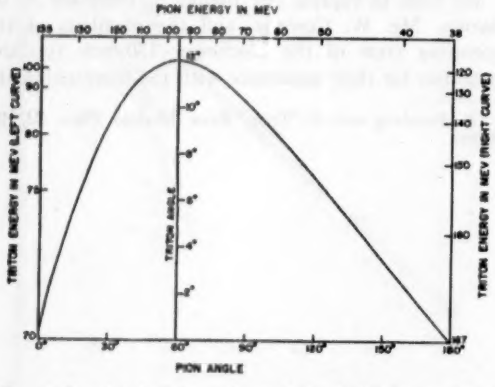

FIG. 1. Correlated angles and energies in the laboratory system for the process $p+d\rightarrow t+\pi^+$. The incident proton energy is 340 Mev.

KINEMATICS

The incident particles in the process $p+d\rightarrow t+\pi^+$ are the 340-Mev protons from the Berkeley 184-inch synchrocyclotron. For such a monoenergetic two-body process, the conservation equations for energy and momentum can be solved to give the correlated angles and energies of the resultant particles; these angles and energies are summarized in Fig. 1. One important feature of this angular correlation curve is that the tritons are confined within a 12° cone about the beam axis. In the analogous reaction $p+p\rightarrow d+\pi^+$, the deuterons are confined to a 6° cone. The triton cone is larger because the extra target nucleon reduces the center-of-mass motion; thus the effect of the triton momentum component perpendicular to the beam axis is more pronounced. This reduced center-of-mass motion, for 340-Mev incident protons, makes 219 Mev available for a $p+d$ process compared to 163 Mev for a $p+p$ process. Thus, pion production takes a small enough bite of the 340-Mev input energy that pions and tritons are produced at angles and with energies adequate for a counter experiment.

The concentration of tritons within a small angular region in the forward direction makes possible a triton time-of-flight measurement without a sacrifice in counting rate. For example, consider the correlated angles of 8.0° for the triton and 110° for the pion. In this region of Fig. 1, a 9° center-of-mass angular interval for tritons is compressed into a 1° laboratory angular interval; in the same transformation, the pion angular interval is changed only slightly. If, then, the distance of the triton counters from the target is nine times that of the pion counters, the same center-of-mass polar angular interval will be subtended by triton and pion counters of equal horizontal dimensions. Also, even though the triton counters are considerably farther from the target than the pion counters, both sets of counters will be about the same perpendicular distance from the beam axis; therefore, triton and pion counters of roughly the same vertical dimensions

* Now at the Brookhaven National Laboratory, Upton, New York.

[1] M. Ruderman, Phys. Rev. **87**, 383 (1952).
[2] A. M. L. Messiah, Phys. Rev. **86**, 430 (1952).
[3] S. Bludman, following paper, Phys. Rev. **94**, 1722 (1954).

will intercept the same azimuthal interval. This fact is illustrated qualitatively in a scale drawing of the experiment arrangement in Fig. 2. In summary, the solid angle determined by the pion counters at a distance of 14 in. from the target is not reduced by placing similar-sized triton counters 11 ft from the target. This large triton-counter distance allows the triton time of flight to be measured.

EXPERIMENTAL APPARATUS

The experimental arrangement at a typical angle is illustrated in Fig. 2. The incident 340-Mev protons were collimated to a 2-in. diameter beam. The beam was monitored by an ionization chamber; the ion current was integrated on a calibrated condenser and recorded in units of volts by a recording millivoltmeter. The targets of deuterated paraffin (CD_2) and carbon (C) were 3 in. in diameter and contained the same number of carbon atoms. The particle detector at the triton angle consisted of two trans-stilbene phosphors; each phosphor was 2 in. by 4 in. and was viewed by two

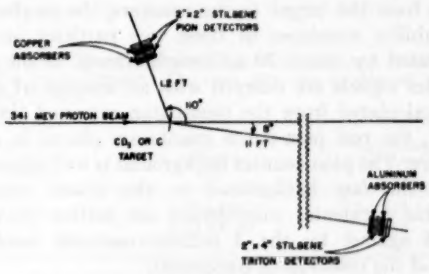

FIG. 2. Experimental arrangement for observing the process $p+d\rightarrow t+\pi^+$.

1P21 photomultiplier tubes. The phosphor thicknesses were selected so that the expected tritons, after suitable absorber, would lose 20 to 30 Mev in each phosphor. The two signals from a given counter were shaped by clipping to a width of 3 millimicroseconds and added together. Figure 3 shows this pulse shaping and adder circuit, together with the last dynode stage of the photomultiplier. The high impedance (259-ohm) coaxial cable was used to increase the signal transmitted from the photomultiplier and help eliminate the need for amplifiers between the photomultiplier and the coincidence circuit.

The particle detector at the pion angle consisted of two trans-stilbene phosphors; each phosphor was 2 in. square and was viewed by one 1P21 photomultiplier tube. The phosphor thicknesses were selected so that the expected pions, after suitable absorber, would lose 10 to 15 Mev in each. Each pion signal was clipped to a width of 3 millimicroseconds and delayed by a length of coaxial line calculated to match the expected triton-signal time of arrival at the coincidence circuit. The two triton signals and the two delayed pion signals

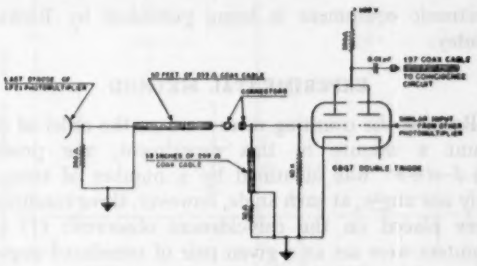

FIG. 3. Circuit used to shape, limit, and add photomultiplier pulses.

were fed into a germanium diode quadruple coincidence circuit.

Figure 4 is a schematic diagram of the coincidence circuit. The IN38 germanium diode inputs are used instead of vacuum tubes to increase the circuit sensitivity. The diode circuit can be driven directly from the output of the pulse-shaping circuit without the aid of distributed amplifiers. The three parallel IN56 diodes and the associated capacitor are due to Garwin.[4] They increase the discrimination ratio by clamping the output voltage in all cases in which less than four of the input diodes are cut off. The IN54A diode in the grid of the output tube is introduced to increase further the discrimination of the circuit and, with the grid resistance, provide a pulse-lengthening action. The ratio of quadruple to triple coincidence output pulse heights is better than sixteen.

The output signal of the coincidence circuit is amplified and lengthened with a secondary emission tube (Phillips type EFP-60) and recorded on two scaling units. The discriminator for each scaler is calibrated so that the two different discriminator bias settings provide a measure of the bias plateau. If only one discriminator were used, the running time would be increased. The efficiency of the counting equipment has been measured to be almost 100 percent. The resolution time of the overall system is about 3 millimicroseconds. A more detailed account of the

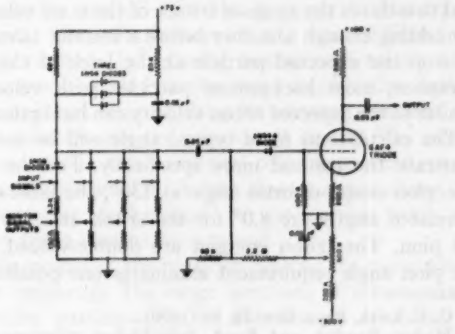

FIG. 4. Germanium diode quadruple coincidence circuit.

[4] R. L. Garwin, Rev. Sci. Instr. **21**, 569 (1950).

electronic equipment is being published by Richard Madey.

EXPERIMENTAL METHOD

Because the counting rates were on the order of one count a minute in this experiment, the process $p+d \rightarrow t+\pi^+$ was identified by a number of tests at only one angle; at each angle, however, three conditions were placed on the coincidences observed: (1) the counters were set at a given pair of correlated angles; (2) a time-of-flight requirement was placed on the triton by delaying the pion signals relative to the triton signals according to the calculated relative velocities; (3) the absorbers added to each counter telescope were selected to stop any particles with ranges below the minimum calculated ranges.

The 340-Mev scattered deflected external proton beam[5] pulses from the Berkeley cyclotron have envelopes of roughly 25 microseconds duration. The pulse repetition rate is about 60 per second. Within this pulse envelope, a fine structure exists with the 16-Mc frequency of a phase-stable bunch of protons circulating near the machine's maximum radius. Thus, the fine-structure interval between proton pulses is 60 millimicroseconds; the width at half-maximum of a single pulse of protons is 4 millimicroseconds.[6] The bunched protons in the beam produce bunched background processes in the target that have cross sections several orders of magnitude larger than the cross section of the process $p+d \rightarrow t+\pi^+$; however, the time-of-flight method used for measuring the triton velocity also separates background processes by means of their different velocities.

The time-of-flight method will discriminate only against background particles with velocities different enough from the expected triton velocity to separate the two particles at the triton counter by a time comparable to the resolution time of the coincidence circuit. However, background particles with the same velocity as the triton can be absorbed out if their masses are less than the triton mass. For example, protons and deuterons have respectively one-third and two-thirds the range of tritons of the same velocity. By adding enough absorber before a counter telescope to stop the expected particle at the back of the last phosphor, most background particles with velocities similar to the expected triton velocity can be eliminated.

The calculations for a typical angle will be used to illustrate the method more specifically. For the case of a pion center-of-mass angle at 130°, the laboratory correlated angles are 8.0° for the triton and 110° for the pion. The triton energies are double-valued, but the pion angle requirement eliminates one possibility. The geometry is shown in Fig. 2. Suppose a time origin is taken when a proton pulse passes through the target. Assume that a triton-pion pair or a miscellaneous pair of background particles is created at some time within a radiofrequency proton beam pulse. The triton and pion are created simultaneously, but the background particles occur separately, spaced at most by the width of the radiofrequency envelope. (This condition is somewhat idealized, but most of the background trouble might be expected and was found to arise from the many protons in the peak of the radiofrequency beam pulse rather than from the few protons in the trough between pulses.) The pion velocity at 110° is 69 percent of the velocity of light, or 0.69c; the pion arrives at its counter in two millimicroseconds. The pion-counter background travels more slowly, except for electron and gamma rays, but is not debunched much over the short distance from the target to the counters. The time sequence of events being described is illustrated in Fig. 5. The triton velocity at 8.0° is 0.31c, while the velocity of elastically scattered protons is about 0.67c. Over the 11 ft from the target to the counters, the production probability envelopes of these two particles become separated by about 20 millimicroseconds. If the pion counter signals are delayed with an amount of delay line calculated from the pion-triton expected time of flight, the real pion-triton counts are placed in coincidence. The pion-counter background is well separated from the fast background at the triton counter; possible accidental coincidences are further discriminated against by the 3 millimicroseconds resolving time of the coincidence equipment.

Absorbers calculated to stop the expected particle at the back of the last phosphor were added to each counter telescope; the larger pulse height obtained from the expected particle's increased energy loss in the phosphor allows less energy-loss background to be biased out. The aluminum absorber calculated for tritons at 8.0° will stop 85-Mev protons. Figure 5 shows that protons of this energy and greater are in the fast-background category and are discriminated against by the coincidence-circuit resolving time.

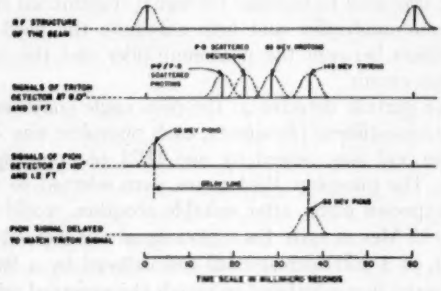

FIG. 5. Time sequence of particles arriving at the counters. The time origin is taken as the arrival of a single radiofrequency proton pulse at the target.

[5] C. E. Leith, Phys. Rev. 78, 89 (1950).

[6] Madey, Bandtel, and Frank (unpublished measurements). For the method, compare "The Radiofrequency Fine Structure of the Photon Beam from the Berkeley Synchrotron" to be published in the *Review of Scientific Instruments* by the same authors.

In summary, the method is this: two particles are detected in coincidence at angles correlated for the process $p+d\rightarrow t+\pi^+$; greater-velocity background is eliminated by a time-of-flight requirement; similar-velocity background is eliminated by a range requirement. The success of the method is seen in the fact that a CD_2-to-C ratio of 5:1 was obtained at most angles without using unreasonably low beam intensities.

EXPERIMENTAL RESULTS

Identification

When the method described above was first developed, a number of identification tests were made at one angle in order to be certain that the process $p+d\rightarrow t+\pi^+$ was really being observed. The correlated angles of 8.0° for the triton and 110° for the pion were chosen at that time for two reasons. First, since pion production from nucleon-nucleon collisions typically has an $(a+b\cos^2\theta)$-type of angular distribution, pion angles away from 90° in the center-of-mass system or 70° in the laboratory system were to be preferred in order to utilize the possibly higher cross section. Second, since the cross section for $p+d\rightarrow t+\pi^+$ might

TABLE I. CD_2-C difference counting rate as a function of relative beam intensity. The rate units are counts per unit of integrated beam.

Relative beam intensity	CD_2-C difference rate	Approximate CD_2-to-C ratio
6	1.00±0.20	3:1
1	1.25±0.30	6:1

be one or two orders of magnitude lower than the $p+p\rightarrow d+\pi^+$ process, accidental coincidences could be expected to be one of the major experimental difficulties. This source of trouble could be reduced by selecting a pion angle in the back quadrant correlated with a large triton angle. Unfortunately, the largest triton angle in the laboratory system is in the region of 90° in the center-of-mass system. The correlated angles for the identification test were chosen as a compromise between a possible low real counting rate and a possible high accidental counting rate. As it turned out, this pair of angles was among the most difficult at which data were obtained.

As the first step, a difference in the coincidence counting rates from CD_2 and C targets was obtained, with the calculated absorbers and delay lines, at the correlated laboratory angles of 8.0° for the triton and 110° for the pion. The result of varying the proton beam intensity is given in Table I. The target-out counting rate was a factor of five below the carbon rate at the higher intensity. The fact that the difference counting rate was constant over a large variation in intensity indicates that a real process from protons on deuterons was being observed. The identification tests

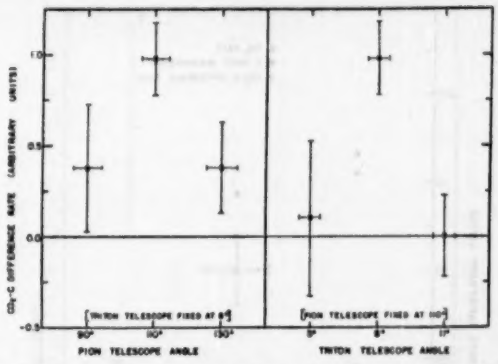

FIG. 6. Angular correlation test for the process $p+d\rightarrow t+\pi^+$. The correlated angles are 8° for the triton and 110° for the pion.

for this real process were made by changing the angles, absorbers, and delay lines from the calculated values and observing the reduction in the difference counting rate.

The angular correlation of the process was tested by moving each counter telescope separately from its calculated angle. The results, plotted in Fig. 6, show that the difference was properly reduced in each case. The large amount of triton multiple scattering and the fact that the pion counters were moved only two counter widths to each side while the triton counters were changed by three counter widths account for the incomplete disappearance of the counting rate in the pion-angle correlation test. The coplanarity of the process was tested by raising the triton counters one counter height out of the plane formed by the beam axis and the pion counters; the difference rate dropped to 0.00±0.30 from the normal 1.00±0.20 counts per integrated beam unit.

The time-of-flight correlation of the process was tested by changing the arrival time of the pion signal relative to the triton signal. The results of varying the length of pion delay line are given in Fig. 7. The difference counting rate is a maximum when the length of delay line in the pion counters is chosen to match the expected triton velocity; the difference rate disappears for particle velocities larger or smaller by 12 percent. The effectiveness of the time-of-flight and range methods in reducing background counts may be appreciated by noting how rapidly the carbon counting rate rises as delay is removed between the pion counters and the coincidence circuit. The reason for the rise in this accidental coincidence rate can be understood from Fig. 5; the shorter delay allows the pion-counter background to synchronize with the faster triton-counter background.

The ranges of the particles causing the coincidences were measured. The range spectrum of triton-counter particles participating in coincidences is shown in Fig. 8; the calculated triton ranges are indicated for comparison. The spread in the expected ranges is

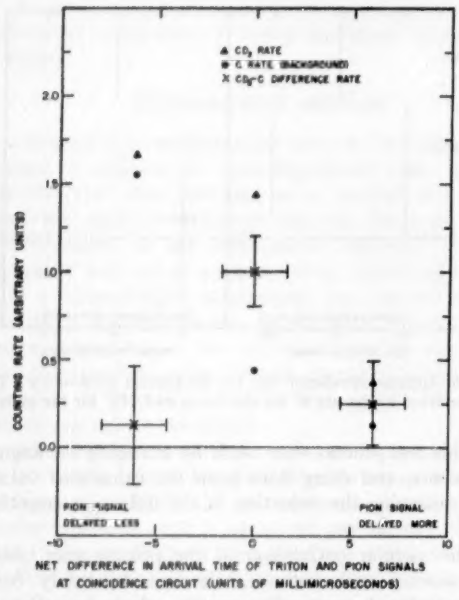

FIG. 7. Time correlation test for the process $p+d \rightarrow t+\pi^+$. Zero time is based on pion and triton calculated times of flight.

caused by production at different target depths. The measured range agrees with the calculated triton energy to within 10 percent. The effectiveness of the range method in reducing accidental coincidences due to similar-velocity background is illustrated by the fact that the CD_2-to-C ratio of 3:1 with the absorber drops to 4:3 without the absorber. The range of pion-counter particles participating in coincidences was measured by adding more absorber to the pion counters; the measured range agrees with the predicted pion energy to within 10 percent.

When CH_2 was substituted for C, the CD_2-CH_2 difference remained the same as the CD_2-C difference. Thus, all these identification tests show a real process from protons on deuterons. This process is a monoenergetic two-body reaction that is consistent with the process $p+d \rightarrow t+\pi^+$. Because of the low counting rates in this experiment, such a series of tests could not be made for each angle without excessive use of cyclotron time. The general method of imposing the conditions of correlated angles, expected triton time of flight, and minimum ranges for both particles was extended to the other angles at which cross sections were obtained; however, no further tests were made.

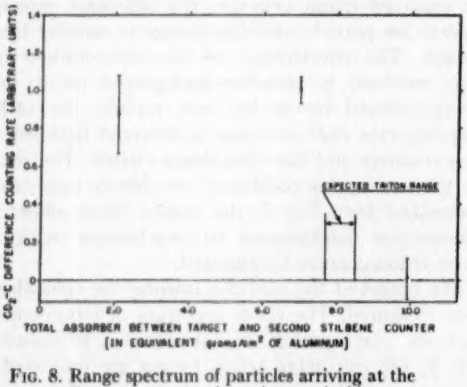

FIG. 8. Range spectrum of particles arriving at the triton counters, and causing a coincidence.

Angular Distribution

Seven laboratory angles, corresponding to equally spaced center-of-mass angles, were chosen for the angular distribution; one of the middle angles, however, was omitted because of data-taking time limitations. The data were originally obtained in terms of counts per unit of integrated beam, but for interest are listed in Table II in terms of counts per minute. Three corrections were made to the data: (a) pion loss by decay in flight; (b) pion loss by absorption in the copper absorbers defining the minimum range; (c) triton loss and—to a lesser extent—pion loss by multiple scattering in the target.

TABLE II. The various counting rates (in units of counts/minute) as a function of pion center-of-mass angle.

Pion center-of-mass angle	CD_2 rate	C rate	CD_2/C ratio	CD_2-C difference rate
30	0.420	0.075	6	0.345±0.085
50	0.985	0.095	10	0.890±0.060
70	0.640	0.070	9	0.570±0.080
90	0.990	0.065	15	0.925±0.100
130	3.23	0.85	4	2.38 ±0.31
150	0.700	0.360	2	0.340±0.093

In the present experiment, the pion is detected only as a charged particle satisfying certain correlated angle, minimum-range, and time-of-flight requirements. Its muon decay product is charged and can produce a coincidence if it meets these requirements. Only about one-quarter of the muons can cause coincidences; even so, the pion decay correction never amounts to more than 5 percent because of the short pion flight path.

Because of the minimum range requirement placed on the pion, the pion passes through an appreciable amount of copper absorber before being detected. Some of the pions interact with the copper nuclei and are absorbed, or scattered at large angles. The recent data of Stork[7] at this laboratory on π^+ absorption in copper was plotted in the form of the absorption coefficient, μ, *versus* the absorber thickness, t, in radiation lengths; the integral $\int_{t_1}^{t_2} \mu dt$ was evaluated numerically over the absorber thickness to give the correction factor, $\exp\int_{t_1}^{t_2} \mu dt$. This factor increases with the pion energy, and at most, amounts to 1.40, corresponding to a 30 percent pion loss. If this correction

[7] D. Stork (private communication).

were avoided by removing the minimum range requirement, the higher accidental coincidence rate and consequently the lower CD_2-to-C ratio would increase the data-taking time requirements severalfold and make the experiment unfeasible from the standpoint of available cyclotron time.

In passing through the target and the eleven feet of air between the target and the counter system, the triton undergoes multiple scattering which sometimes destroys the angular correlation with its paired pion. Ordinarily this loss would be avoided by making the triton counters large enough to intercept all the scattered particles, while allowing the pion counters to define the solid angle. There are several difficulties with such a procedure in the present experiment. In order to identify the process and suppress the background, a long time-of-flight path is required for the triton; even so, equal-sized pion and triton counters subtend approximately the same center-of-mass solid angle. To eliminate a multiple-scattering correction, the pion counter must be reduced in size or the triton counter extended in size. The change should be by at least a factor of two in linear dimensions, or a factor of four in area. If the pion counters are made smaller, the already marginal counting rate becomes unreasonably low. Larger triton counters are difficult to make with a uniform detection efficiency for short resolution time and short deadtime coincidence counting; moreover, this extra area represents a fourfold increase in the accidental counting rate, but a less than double increase in the real counting rate. A further complication is provided by the double-valued angular correlation curve if the same counters are used at all the desired data-taking angles. In the actual experimental arrangement, the solid angle was determined by the pion counter while the triton counter usually subtended a somewhat larger area. The correction factor for scattering loss is about 1.80 at 90° (pion center-of-mass angle) and falls to around 1.50 at 30° and 150°. The total correction factors applied to the data, as well as the final differential cross sections, are given in Table III. The errors shown are the statistical standard deviations related to the number of counts in the original data.

TABLE III. Correction factors and differential cross sections at various pion center-of-mass angles for the process $p+d\rightarrow t+\pi^+$.

Pion center-of-mass angle	Total correction factor	$d\sigma/d\Omega_0$ (microbarns/steradian)
30	1.94	3.95±0.97
50	2.21	2.55±0.18
70	2.24	0.77±0.11
90	2.21	0.44±0.05
130	1.82	0.46±0.07
150	1.66	0.41±0.12

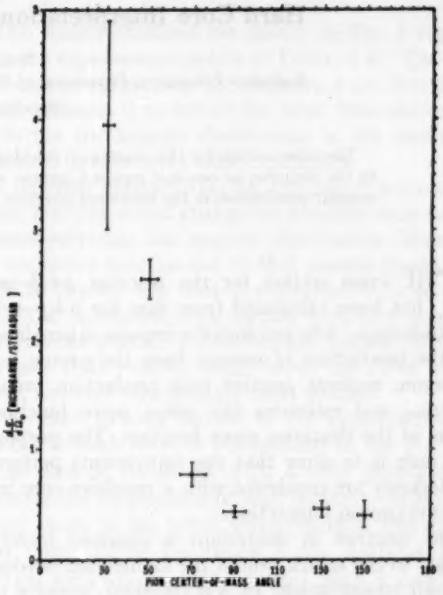

FIG. 9. Experimental angular distribution for the process $p+d\rightarrow t+\pi^+$.

The angular distribution data have been plotted in Fig. 9. If a reasonably smooth curve is drawn through the points, the total cross section is estimated by numerical integration to be 15 microbarns. The total error in the integrated number of protons, the target particle density, and the solid angle subtended is estimated to be 10 percent. Since the counting equipment is nearly 100 percent efficient, this cross section can be taken as the absolute yield within 25 percent.

CONCLUSIONS

The most noticeable feature of the $p+d\rightarrow t+\pi^+$ angular distribution is the constant cross section part from 90° to 180°. Ruderman's theoretical distribution,[1] derived in terms of the $p+p\rightarrow d+\pi^+$ experimental distribution by using an impulse approximation method, has a 90° minimum with a large 0° peak, and a lesser 180° peak. In reconsidering the problem, Bludman[3] has been able to fit the experimental data quite well by introducing Jastrow's nucleon model[4] of a short-range repulsive force surrounded by the usual longer-range attractive force. A comparison of the theoretical and experimental results is given in the following article.

[4] R. Jastrow, Phys. Rev. **81**, 165 (1951).

Hard Core Interpretation of the Reaction $p+d\rightarrow\pi^{+}+t$

SIDNEY A. BLUDMAN
Radiation Laboratory, Department of Physics, University of California, Berkeley, California

(Received February 23, 1954)

The cross section for this reaction is calculated for three Hulthén deuteron wave functions. A hard core in the deuteron at one-half meson Compton wavelength reduces the total cross section and flattens the angular distribution in the backward direction in agreement with experiment.

THE cross section for the reaction $p+d\rightarrow\pi^{+}+t$ has been calculated from that for $p+p\rightarrow\pi^{+}+d$ by Ruderman,[1] who employs the impulse approximation for the production of mesons from the proton in the deuteron, neglects positive pion production from the neutron, and estimates the triton wave function in terms of the deuteron wave function. The purpose of this note is to show that the experiments performed[2] at Berkeley are consistent with a repulsive core in the neutron-proton interaction.

The neutron in deuterium is assumed merely to impart to the struck proton the momentum needed for over-all conservation. In p-n collisions, positive pions can be produced only via intermediate states of isotopic spin $\frac{1}{2}$, while from p-p collisions the isotopic spin state $\frac{3}{2}$ is available as well. The evidence, from experiments on complex nuclei, for the suppression of $p+n\rightarrow\pi^{-}$, and by charge symmetry $p+n\rightarrow\pi^{+}$, relative to $p+p\rightarrow\pi^{+}$ is by now compelling. The large momentum transfers involved in meson production suggest the applicability of the impulse approximation and imply a short-range encounter between the incident and struck protons.

Under these assumptions, the transition rate for meson production in deuterium can be calculated[1] from that in hydrogen, giving in the center-of-mass system of proton and deuteron:

$$\frac{d\sigma}{d\Omega}(pd\pi^{+}t)=\frac{1}{v_{pd}}[f(\theta)]^{2}\frac{1}{3}\frac{E_t}{E_\pi+E_t}\left[v_{pp}\frac{E_\pi+E_d}{E_d}\frac{d\sigma}{d\Omega}(pp\pi^{+}d)\right].$$

Here the E's and v's are the energies and relative velocities occurring in the phase space and flux factors of the cross sections. The quantities in brackets are to be evaluated in the center-of-mass system of the two protons for that energy which produces a meson of momentum $\mathbf{q}$.

The form factor,

$$f(\theta)=\int\psi_D(\mathbf{x})\exp(i\boldsymbol{\Delta}\cdot\mathbf{x}/\hbar)\frac{\psi_T(\mathbf{x},0)}{\psi_D(0)}d\mathbf{x},$$

depends on the deuteron and triton wave functions $\psi_D(\mathbf{x})$, $\psi_T(\mathbf{Z},\mathbf{x})$ where $\mathbf{x}$ is the neutron-proton relative coordinate and $\mathbf{Z}$ the coordinate of the neutron in the triton relative to the center of mass of the proton and remaining neutron. With $\mathbf{k}$ the momentum of the incident proton, $\boldsymbol{\Delta}=\frac{1}{2}\mathbf{k}-\frac{1}{3}\mathbf{q}$ is the relative momentum in the struck deuteron which is required by momentum conservation. The integral $f(\theta)$ is the amplitude for finding in the original deuteron such a relative momentum that the original neutron and the deuteron from $p+p\rightarrow\pi^{+}+d$ will form a bound triton in the final state.

For 341-Mev protons, which produce mesons of 78 Mev in the center of mass, Δ varies from 1.5 to $2.3\mu c$ for meson angles θ from 0° to 180°, so that $f(\theta)$ is sensitive to the deuteron and triton wave functions for $x=0.4$ to 0.6 meson Compton wavelengths. In the absence of information concerning the triton wave function at these distances, one can only show that the cross section observed is consistent with a repulsive core in the interior of the deuteron.

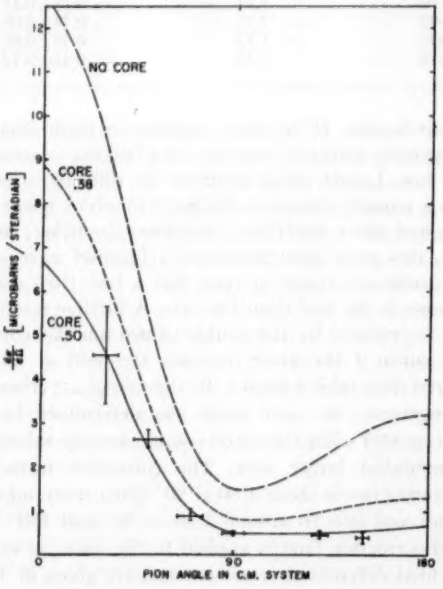

FIG. 1. Differential cross section in the center-of-mass system for $p+d\rightarrow\pi^{+}+t$ with 341-Mev incident protons. The three curves are for deuteron wave functions with hard core at $0.50\hbar/\mu c$, $0.38\hbar/\mu c$, and no core. The experimental points are those of reference 2.

[1] M. Ruderman, Phys. Rev. 87, 383 (1952). There are several numerical errors in the calculation of the cross section by Ruderman, who considered no core, which prevent comparison of his results with experiment, even in this case.

[2] Frank, Bandtel, Madey, and Moyer, preceding paper [Phys. Rev. 94, 1716 (1954)].

For the triton wave function, Fröhlich *et al.*[3] find that the simple form

$$\psi_T=N_t\exp\{-\tfrac{1}{2}\alpha(x_{12}+x_{22}+x_{31})\},$$

where x_{ij} is the distance between nucleons i and j, gives 90 percent of the triton binding energy when calculated with nuclear potentials fitted to the two-body data. The optimum value of the parameter α is $\alpha=1.270\mu c/\hbar$, and the correct normalization constant is

$$N_t=(2/7)^{\frac{1}{2}}\alpha^3/\pi.$$

For the deuteron three different Hulthén wave functions,

$$\psi_D=(e^{-\beta r}-e^{-\gamma r})/r,$$

were employed: the foregoing function, and similar functions made to vanish at core radii $r_c=0.38$ and at $0.50\hbar/\mu c$. In each case the Hulthén parameters β and γ were chosen to fit the deuteron binding energy and triplet range. While the differential cross section for meson production is strongly anisotropic, this is probably more evidence for the important role of intermediate states of isotopic spin and angular momentum $\frac{3}{2}$ than for the effects of D state in the deuteron.

The cross section for the production of 78-Mev mesons in the $p+p\rightarrow\pi^{+}+d$ reaction has been extrapolated from the data of Schulz,[4] Durbin, Loar, and Steinberger,[5] and Crawford and Stevenson[6] to be

$$\frac{d\sigma}{d\Omega}(pp\pi^{+}d)=210(\tfrac{1}{3}+\cos^2\theta)\qquad\mu\text{b/steradian}.$$

The results obtained are shown in Fig. 1 together with the experimental points of Frank *et al.*[2] The effect of a core in suppressing the deuteron wave function at small distances is to reduce the total cross section and to flatten the angular distribution in the backwards direction, in agreement with experiment.

A different extrapolation for the proton-proton excitation function would change the absolute cross section without affecting the angular distribution. However, the excitation function for 78-Mev mesons would have to be 50 percent less than as extrapolated in order to bring the calculated cross section anywhere near the experimental points. A less isotropic angular distribution, say $(0.15+\cos^2\theta)$, would lower the curve at 90° where, however, the data are most reliable.

The most striking feature of the experiments, the forward to back ratio, is independent of the p-p cross section and is consistent with a core phenomenon. (Because the suppression of high momenta might just as well reside in the triton wave function, this experiment might probe the triton if the deuteron wave function were known well enough.) Such a core phenomenon seems indicated by the high-energy scattering[7] and by some forms of pseudoscalar meson theory.[8]

I am indebted to Dr. B. J. Moyer, Dr. R. Madey, Dr. W. J. Frank, and Mr. K. C. Bandtel for access to the preliminary results of their experiment. Mr. Donald Criley carried out the numerical calculations. This work was performed under the auspices of the U. S. Atomic Energy Commission.

[3] Fröhlich, Huang, and Sneddon, Proc. Roy. Soc. (London) **191**, 61 (1947). These authors give the parameter α in terms of an old meson mass and employ a different normalization for the wave function.

[4] A. G. Schulz, Jr., University of California Radiation Laboratory Report UCRL-1756 (unpublished).

[5] Durbin, Loar, and Steinberger, Phys. Rev. **84**, 581 (1951).

[6] F. S. Crawford, Jr., and M. L. Stevenson, Phys. Rev. **91**, 468 (1953).

[7] R. Jastrow, Phys. Rev. **79**, 389 (1950).

[8] M. Levy, Phys. Rev. **88**, 725 (1952); A. Klein, Phys. Rev. **90**, 1101 (1953).

Nuclear Events at High Energies

JOSEPH V. LEPORE AND RICHARD N. STUART
Radiation Laboratory, Department of Physics, University of California, Berkeley, California

(Received March 12, 1954)

The statistical model, introduced by Fermi, is used to calculate the probabilities for various nuclear events at high energies. A general method for evaluating the phase integrals is proposed and used to find to some extent the consequences of neglect of pion momentum conservation. The effect of pion indistinguishability is studied and tables giving the probabilities for various processes are presented together with the energy spectra of the corresponding final nucleons.

I. INTRODUCTION

A STATISTICAL model has been introduced by Fermi[1] to study multiple processes occurring in high-energy nucleon encounters. The method is based on the assumption that in such an encounter there is a localization of energy in a small spatial volume which decays into the various possible final states, compatible with the constants of motion, with relative *a priori* probabilities proportional to their statistical weights. In view of the mathematical and physical uncertainties involved in field-theoretic approaches to such problems, the method may provide a simple means of providing a much needed background for discussion of nuclear events at the moderately high energies now accessible to laboratory study by means of the various high-energy particle accelerators. Fermi has explored the consequences of the model most fully for cases of extremely high energy where the statistical model may be treated by using thermodynamics. When using the more detailed approach, he has treated nucleons as being nonrelativistic, pions as being extremely relativistic; furthermore, the momentum of the pions is neglected.

In this paper a general approach to the calculation of phase volumes is proposed. This method is used to study the consequences of including momentum conservation in the simple case of extremely relativistic particles. Tables are presented giving the probabilities for pion and heavy meson production using the Fermi approximations. The effect of indistinguishability of the pions is also treated.

II. METHOD

Following Fermi, the statistical weight of a state leading to n particles of masses $M_1, \cdots, M_n$ is computed according to the following rule:

$$S_n=\frac{\mathcal{S}}{\mathcal{G}}\frac{\Omega^{n-1}}{(2\pi)^{3(n-1)}}\int\prod_{i=1}^{n}d^3\mathbf{p}_i. \tag{1}$$

(We are using units such that $\hbar=c=1$.) The integration extends over that region of momentum space compatible with the constraints on the system. The configurational space volume Ω is taken to depend on the energy E in the center-of-mass system:

$$\Omega=(2M/E)\Omega_0;\quad \Omega_0=(4\pi/3)R^3. \tag{2}$$

The factor $2M/E$ represents the Lorentz contraction of the pion cloud surrounding a nucleon whose radius, in its proper coordinate system, is R. Although R is expected to be about $\hbar/m_\pi c$, it may be regarded as an adjustable parameter. The symbol $\mathcal{S}$ represents the weight factors due to conservation of spin and isotopic spin. The factor[2] $\mathcal{G}$ converts the specific phase space volume into a generic one appropriate to indistinguishable particles.

The constraints on the momentum integration are those due to conservation of momentum, energy, and angular momentum. To simplify the calculations in what follows, angular momentum conservation is disregarded. There are other statistical factors which enter into the computation of reaction probabilities: conservation of spin, isotopic spin, and the effect of indistinguishability of emitted particles. Also some rule must be accepted regarding conservation of nucleons. If one believes in the possibility of nucleon pair production, this means that the difference between the numbers of nucleons and antinucleons is conserved:

$$N-N'=\text{constant}. \tag{3}$$

The requirements of momentum and energy conservation may be imposed on the statistical weight by inserting discontinuous factors in the integrand of Eq. (1) and then allowing the integrations to go over the entire momentum space:

$$S_n=\frac{\mathcal{S}}{\mathcal{G}}\frac{\Omega^{n-1}}{(2\pi)^{3n+1}}\frac{d}{d(iE)}\int_{-\infty-i\epsilon}^{\infty-i\epsilon}\frac{d\alpha}{\alpha}\int_{-\infty}^{\infty}d^3\boldsymbol{\lambda}\prod_i d^3\mathbf{p}_i$$
$$\times\exp\{i[\boldsymbol{\lambda}\cdot\textstyle\sum_i\mathbf{p}_i+\alpha(E-\sum_i(p_i^2+M_i^2)^{\frac{1}{2}})]\}, \tag{4}$$

where ϵ is a small positive number which insures that S_n is well defined. It is taken to be zero after the integrations are performed.

Each momentum integral occurring in Eq. (4) has the form

$$I=\int d^3\mathbf{p}\exp\{i[\boldsymbol{\lambda}\cdot\mathbf{p}-\alpha(p^2+M^2)^{\frac{1}{2}}]\}. \tag{5}$$

[1] Enrico Fermi, Progr. Theoret. Phys. (Japan) **5**, 570 (1950).

[2] For example, $\mathcal{G}=1/n!$ if the state is one of n identical pions.

The angular integration may be carried out and yields

$$I=-\frac{2\pi}{\lambda}\frac{d}{d\lambda}\int_{-\infty}^{\infty}dp\,\exp\{i[\lambda p-\alpha(p^2+M^2)^{\frac{1}{2}}]\}. \quad (6)$$

In this expression λ is the magnitude of the vector $\boldsymbol{\lambda}$.

In order to evaluate this integral, it is convenient to introduce a change of variable:

$$p=M\sinh\theta. \quad (7)$$

One finds from Eq. (6):

$$I=\frac{-2\pi M}{\lambda}\frac{d}{d\lambda}\int_{-\infty}^{\infty}d\theta\cosh\theta \times\exp[iM(\lambda\sinh\theta-\alpha\cosh\theta)]. \quad (8)$$

Depending on the relative values of λ and α, the argument of the exponential in (8) may be written in three different ways:

(i) $\alpha>\lambda>0$:

$$\lambda\sinh\theta-\alpha\cosh\theta=-(\alpha^2-\lambda^2)^{\frac{1}{2}}\cosh(\theta-\phi_1),$$
$$\cosh\phi_1=\alpha/(\alpha^2-\lambda^2)^{\frac{1}{2}};$$

(ii) $|\alpha|<\lambda>0$:

$$(\lambda\sinh\theta-\alpha\cosh\theta)=(\alpha^2-\lambda^2)^{\frac{1}{2}}\sinh(\theta-\phi_2),$$
$$\sinh\phi_2=\alpha/(\lambda^2-\alpha^2)^{\frac{1}{2}};$$

(iii) $-\alpha>\lambda>0$:

$$(\lambda\sinh\theta-\alpha\cosh\theta)=(\alpha^2-\lambda^2)^{\frac{1}{2}}\cosh(\theta+\phi_3),$$
$$\cosh\phi_3=-\alpha/(\alpha^2-\lambda^2)^{\frac{1}{2}}. \quad (9)$$

The integrals may be reduced to standard forms if the parameters lie in the first or the last region. For $\alpha>\lambda>0$,

$$I=\frac{-2\pi M}{\lambda}\frac{d}{d\lambda}\int_{-\infty}^{\infty}d\theta\cosh\theta \times\exp[-iM(\alpha^2-\lambda^2)^{\frac{1}{2}}\cosh(\theta-\phi_1)]. \quad (10)$$

If a change of variable $\theta'=\theta-\phi_1$ is made, one obtains

$$I=\frac{-2\pi M}{\lambda}\frac{d}{d\lambda}\frac{\alpha}{(\alpha^2-\lambda^2)^{\frac{1}{2}}}\int_{-\infty}^{\infty}d\theta'\cosh\theta' \times\exp[-i(\alpha^2-\lambda^2)^{\frac{1}{2}}\cosh\theta'].$$

Thus, I is expressible in terms of the Hankel functions,[3]

$$I=2\pi^2M^2\alpha\frac{H_2^{(2)}(M(\alpha^2-\lambda^2)^{\frac{1}{2}})}{\alpha^2-\lambda^2}. \quad (11)$$

[3] G. N. Watson, *Bessel Functions* (MacMillan Company, New York, 1948), p. 180, Eq. (11); p. 74, Eq. (10).

In the region $-\alpha>\lambda>0$, the integral may be evaluated in the same manner:

$$I=-2\pi^2M^2\alpha\frac{H_2^{(1)}(M(\alpha^2-\lambda^2)^{\frac{1}{2}})}{\alpha^2-\lambda^2}. \quad (12)$$

In the region $\lambda>|\alpha|>0$, we may infer the value of the integral by observing that I is an analytic function of α and λ and by appealing to the principle of continuation. That choice of phases of the square root $(\alpha^2-\lambda^2)^{\frac{1}{2}}$ must be made which joins the first and last regions through the other. A careful examination shows that I may be compactly represented in any region as

$$I=2\pi^2M^2\alpha\frac{H_2^{(2)}(M(\alpha^2-\lambda^2)^{\frac{1}{2}})}{\alpha^2-\lambda^2}, \quad (13)$$

if it is understood that the phase of the square root is chosen according to the following scheme:

$$\begin{aligned}&(\alpha^2-\lambda^2)^{\frac{1}{2}}, && \alpha>\lambda>0\\ &e^{-i\pi/2}(\lambda^2-\alpha^2)^{\frac{1}{2}}, && \lambda>|\alpha|>0\\ &e^{-i\pi}(\alpha^2-\lambda^2)^{\frac{1}{2}}, && -\alpha>\lambda>0.\end{aligned} \quad (14)$$

If Eq. (13) is combined with Eq. (4), one finds for the density of states:

$$S_n=\frac{8}{9}\frac{\Omega^{n-1}}{2^{2n-1}}\frac{\prod_i M_i^2}{\pi^n}\int_{-\infty-i\epsilon}^{\infty-i\epsilon}d\alpha\cdot\alpha^n e^{i\alpha E} \times\int_0^{\infty}\frac{d\lambda\cdot\lambda^2}{(\alpha^2-\lambda^2)^n}\prod_i H_2^{(2)}(M_i(\alpha^2-\lambda^2)^{\frac{1}{2}}). \quad (15)$$

S_n may be evaluated readily only when the masses of all particles are small compared to E. In this case $H_2^{(2)}$ may be replaced by[4]

$$H_2^{(2)}(z)\cong 4i/\pi z^2. \quad (16)$$

One finds

$$S_n=\frac{8}{9}\frac{2\Omega^{n-1}i^n}{\pi^{2n}}\int_{-\infty-i\epsilon}^{\infty-i\epsilon}d\alpha\cdot\alpha^n e^{i\alpha E}\int_0^{\infty}\frac{d\lambda\cdot\lambda^2}{(\alpha^2-\lambda^2)^{2n}}. \quad (17)$$

This may be evaluated by applying the method of residues. The integral over λ may be evaluated by closing the contour above the real axis. There are poles of order $2n$ at $\lambda=\pm\alpha$ but since $\epsilon>0$ only the pole at $\lambda=-\alpha$ will be encircled. One finds

$$\int\frac{d\lambda\cdot\lambda^2}{(\lambda^2-\alpha^2)^{2n}}=\frac{-\pi i(4n-3)!}{2^{4n-3}(2n-1)!(2n-2)!\alpha^{4n-3}}. \quad (18)$$

The remaining integral over α in the expression for S_n may be similarly evaluated by closing the contour

[4] See reference 3, p. 84.

above the real axis,

$$\oint d\alpha \frac{e^{i\alpha E}}{\alpha^{3n-3}} = \frac{2\pi i (iE)^{3n-4}}{(3n-4)!}. \tag{19}$$

The expression for the density of states in the extremely relativistic limit is therefore

$$S_n = \frac{8\Omega^{n-1}(4n-3)!E^{3n-4}}{9\pi^{2n-2}2^{4n-4}(2n-1)!(2n-2)!(3n-4)!}. \tag{20}$$

This is to be compared with the corresponding formula of Fermi's paper[5] which neglects momentum conservation:

$$S_n = \frac{\Omega^{n-1}}{\pi^{2n}} \frac{E^{3n-1}}{(3n-1)!}. \tag{21}$$

For large values of n, Stirling's approximation may be applied to evaluate Eq. (20).

$$S_n = \frac{8\Omega^{n-1}}{9\pi^{2n}} \left(\frac{2\pi^3}{n}\right)^{\frac{1}{2}} \frac{E^{3n-4}}{(3n-4)!}. \tag{22}$$

III. APPROXIMATE EVALUATION OF THE STATISTICAL WEIGHT

It is not clear how to evaluate the expression for S_n when the masses of the particles cannot be neglected. In order to obtain some numerical results, Fermi has suggested that one divide particles into two classes: (1) pions and (2) nucleons and heavy mesons. He treats the pions as being extremely relativistic and neglects the momentum carried away by them; the other particles are taken as nonrelativistic and it is assumed that they carry most of the momentum.

If these approximations are made in the expression for I, Eq. (5), one finds

$$\left.\begin{aligned} I_{ER} &= 4\pi \int_0^\infty dp p^2 \exp(-i\alpha|p|) \\ &\qquad \text{(extremely relativistic)} \\ I_{NR} &= \frac{-2\pi}{\lambda} e^{-i\alpha M} \frac{d}{d\lambda} \int_{-\infty}^{\infty} dp \exp[i(\lambda p - \alpha p^2/2M)] \\ &\qquad \text{(nonrelativistic)} \end{aligned}\right\}. \tag{23}$$

One finds

$$\left.\begin{aligned} I_{ER} &= 8\pi i/\alpha^3, \\ I_{NR} &= -\pi^{\frac{1}{2}} e^{i\pi/4} (2M/\alpha)^{\frac{1}{2}} e^{-i\alpha M} \exp(iM\lambda^2/2\alpha). \end{aligned}\right\} \tag{24}$$

By using these approximations, the expression for S_n may be evaluated by the method of the preceding section. One finds the result given by Fermi

$$S_n = \frac{8}{9}\Omega^{n-1} \times \frac{\prod_i M_i^{3/2}(E-\sum_i M_i)^{3s/2+3m-5/2}}{(\sum_i M_i)^{3/2}2^{3s/2-1/2}\pi^{3s/2+2m-3/2}\Gamma(3s/2+3m-3/2)}, \tag{25}$$

where Γ is the ordinary Γ function, s is the number of heavy particles, and m the number of light ones.

It is of some interest to derive an expression for the energy spectrum of inelastically scattered nucleons (see Fig. 1). Since nucleon pair formation and heavy meson production presumably contribute inappreciably to the totality of the observed processes at moderate energies, one may write down the expression for the case when two nucleons and m pions are formed. Using the Fermi approximations, one finds

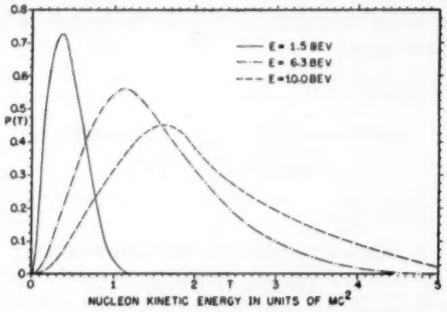

FIG. 1. Graph showing energy spectrum of inelastic nucleons resulting from a high-energy collision. The curves are normalized so that their areas represent the total probability at the indicated energy of all inelastic processes.

$$S_{m+2} = \frac{8M^{3/2}\Omega^{m+1}}{9 2^{7/2}\pi^{2m+5}(3n-1)!} \times \int dT_M (T_M)^{\frac{1}{2}}(E-2M-2T_M)^{3n-1}. \tag{26}$$

Here T_n is the kinetic energy of one of the two heavy particles of mass M in the center-of-momentum system. The coefficient of dT_M therefore represents the spectrum

$$S_{m+2}(T_M) = \frac{8M^{3/2}\Omega^{m+1}(T_M)^{\frac{1}{2}}}{9 2^{7/2}\pi^{2m+5}(3n-1)!}(E-2M-2T_M)^{3n-1}. \tag{27}$$

IV. APPLICATIONS

The foregoing results may be used to compute the probabilities of various processes. The probability for formation of particles of masses $M_1, \cdots, M_n$ is

$$P_n(M_1 \cdots M_n) = \frac{S_n(M_1 \cdots M_n)}{\sum_n' S_n(M_1 \cdots M_n)}. \tag{28}$$

[5] See reference 3, p. 576, Eq. (13). Fermi omits explicit reference to the factor $8/9$.

TABLE I. Probabilities for emission of m_1, m_2, m_3 particles of mass $M_1=176$, $M_2=967$, $M_3=1848$ (in units of the electron mass) at the indicated energy E (laboratory system). Case of distinguishable particles.

m_1	m_2	m_3	2.5 Bev	3.9 Bev	4.71 Bev
0	0	2	0.5846	0.007388	0.0008
1			0.4127	0.2302	0.0647
2			0.0027	0.3679	0.2957
3			0	0.09187	0.2547
4				0.00503	0.0601
5				0.00007	0.0046
0	1	2		0.05910	0.0111
1				0.1391	0.0936
2				0.03006	0.0954
3				0.0010	0.0207
4				0.000005	0.0012
0	2	2		0.0562	0.0288
1				0.00942	0.0365
2				0.00013	0.0071
3				0	0.0003
0	3	2		0.00248	0.0148
1	3	2		0.000005	0.0024
0	4	2			0.0008
0	0	4			0.0063
1	0	4			0
0	1	4			0.0001
1	1	4			0

TABLE II. Probabilities for emission of m_1, m_2, m_3 particles of mass $M_1=176$, $M_2=967$, $M_3=1848$ (in units of the electron mass) at the indicated energy E (laboratory system). Case of indistinguishable particles.

m_1	m_2	m_3	2.5 Bev	3.9 Bev	4.71 Bev
0	0	2	0.5854	0.0108	0.0018
1			0.4132	0.3367	0.1412
2			0.0014	0.2690	0.3228
3			0	0.0224	0.0927
4				0.0003	0.0055
5				0	0
0	1	2		0.08642	0.0242
1				0.2035	0.2042
2				0.02198	0.1042
3				0.00024	0.0075
4				0	0.0001
0	2	2		0.0411	0.0315
1				0.0069	0.0398
2				0.0001	0.0039
3				0	0
0	3	2		0.0006	0.0054
1	3	2		0	0.0009
0	4	2			0.0001
0	0	4			0.0138
1	0	4			0.0001
0	1	4			0.0003
1	1	4			0

$\sum_n'$ is to be derived from the statistical weights S_n by omitting those terms, from the sum over all states, which are incompatible with heavy-particle conservation.

Since the total cross section is assumed to be fixed, that part of it leading to a given final state is

$$\sigma_n(M_1\cdots M_n)=P_n(M_1\cdots M_n)\sigma_{\text{total}}. \tag{29}$$

Tables I and II give the probabilities for emission of various numbers of neutral pions and a possible heavy meson of mass $967mc$. For purposes of comparison they have been computed assuming particles of a given mass are: (a) distinguishable, (b) indistinguishable. Spin and isotopic spin conservation have been neglected.[6] For the case of distinguishable particles they differ somewhat from those given in Fermi's article, since the pion rest mass has been included in the sum occurring in Eq. (25). This amounts to writing $E=|\mathbf{p}|+\mu$ for extremely relativistic particles and has the effect of insuring that not more pions are emitted than are compatible with the available energy. The curves giving the energy spectra of inelastically scattered neutrons have been similarly handled. They have been transformed to the laboratory system by using the fact that this model, which neglects angular momentum conservation, yields an isotropic angular distribution in the center-of-mass system.

We are grateful to Dr. Maurice Neuman who contributed much to all parts of this paper and to Dr. Warren Heckrotte for helpful discussions. This work was performed under the auspices of the U. S. Atomic Energy Commission.

[6] This corresponds to setting $g=1$ in the expression for S_n.

Range and Specific Ionization for High-Energy Protons in Nuclear Emulsions*

OTTO HEINZ†
Radiation Laboratory, Department of Physics, University of California, Berkeley, California

(Received March 9, 1954)

Stacks of nuclear emulsion varying in thickness from 18.35 g/cm² to 56.83 g/cm² were exposed in the external proton beam of the Berkeley cyclotron, and the average specific ionization dT/dx [in Mev $(g/cm^2)^{-1}$] was measured by determining the equivalent thickness of Cu needed to remove the same amount of energy from the beam as a given thickness of emulsion. The energies range from 230 to 320 Mev. The emulsion stacks consisted of layers of 200-μ Ilford C-2 stripped emulsions of average density 3.81±0.01 g/cm³. The specific ionization was found to be 1.5 percent higher for emulsion than for Cu measured over the same energy interval. From these data the ratio of the mean ionization potentials for emulsion and Cu was determined as $I_E/I_{Cu}=0.89\pm0.09$. The range of 342.5-Mev protons in emulsion was found to be 92.68 ±0.25 g/cm², which is 1.1 percent lower than the measured range of the same beam in Cu (93.65±0.20 g/cm²). The measured range in emulsion is about 1.5 percent shorter than the value calculated by Vigneron (and extended to higher energies by Barkas). They assumed 332 ev as the mean ionization potential of emulsion.

I. INTRODUCTION

THE recent introduction of nuclear emulsion stacks into work with cosmic rays and with high-energy accelerators has led to the systematic investigation of very long tracks. The range-energy relation for such tracks becomes of considerable importance in many problems such as the decay schemes of heavy mesons and hyperons or the energy balance in nuclear stars; it was thus decided to extend the experimental measurements of the range-energy relation to higher energies.

Considerable experimental data exist for proton energies up to about 40 Mev,[1] including an accurate measurement recently performed at this laboratory at 33.64-Mev proton energy.[2] These energies correspond to track lengths of the order of 0.5 cm, whereas the tracks studied in emulsion stacks may be 10 cm and more in length. A calculation of the proton ranges up to 230 Mev has been carried out by Vigneron[1] and extended by Barkas[3] to 30 Bev.

The purpose of this experiment is thus (1) to measure a point on the range-energy curve at a proton energy corresponding to a track length of about 25 cm which would serve as an experimental check on the calculated value of the range and (2) to measure the specific ionization of emulsion relative to that of copper. We shall define specific ionization to mean the quantity dT/dx expressed in units of Mev $(g/cm^2)^{-1}$. The latter measurement allows one to calculate the mean ionization potential of emulsion, assuming some previously determined value for the mean ionization potential of copper.

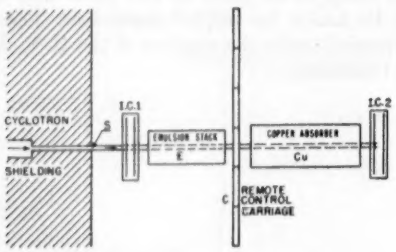

FIG. 1. Experimental arrangement.

II. EXPERIMENTAL PROCEDURE

Let us first consider the experimental procedure for the measurement of the specific ionization. The experimental arrangement is shown in Fig. 1. The external proton beam of the 184-in. cyclotron passes through a collimator, 40 in. long and of adjustable opening, and emerges from the concrete shielding surrounding the machine at the snout S. The beam next passes through a thin ion chamber (I. C. 1), through a known thickness of emulsion E, and then through a variable thickness of copper consisting of a thick copper absorber Cu and thin copper absorbers mounted on the carriage C. This carriage is remote-controlled, and the amount of copper in the beam at any one time can be changed from 0.56 g/cm² to 3.36 g/cm² in six equal steps of 0.56 g/cm². Finally the beam passes through a second ion chamber (I. C. 2) identical with the first one.

If we make a plot of the ratio of the ion chamber outputs I_2/I_1 as a function of absorber thickness we obtain the well-known Bragg curve (see Fig. 2). We first determine the amount of energy ΔT removed from the beam by a thickness of emulsion ΔR_E. This is done by simply measuring the range of the beam (in copper) with and without the emulsion in the position shown in Fig. 1. The difference between the two range values for copper gives the thickness of copper ΔR_{Cu} needed to remove the same increment of energy ΔT from the beam as the emulsion. The quantities $\Delta T/\Delta R_E$ and $\Delta T/\Delta R_{Cu}$ give us the average specific ionization in emulsion and in copper measured over the same energy interval.

* This work was done under the auspices of the U. S. Atomic Energy Commission.

† Now at Bell Telephone Laboratories, Holmdel, New Jersey.

[1] L. Vigneron, J. phys. et radium **14**, 145 (1953).

[2] W. H. Barkas, University of California Radiation Laboratory Report No. UCRL-2327, September, 1953 (unpublished).

[3] W. H. Barkas (private communication).

The apparatus for the measurement of the range in emulsion was the same as described above except that all the copper, including the absorbers on the carriage, was replaced by emulsion. Using this arrangement another Bragg curve was run. Here again the energy of the beam was determined by its range in copper.

The emulsion absorber consisted of layers of 200-μ C-2 Ilford stripped emulsions held in a clamping device. Their size varied from 2 in.$\times$2 in. at the front to 4 in.$\times$5 in. at the back, to allow for the broadening of the beam due to multiple Coulomb scattering as the protons slow down. The entire emulsion stack was machined and weighed after it was clamped together to determine the thickness in the direction of the beam. The density was

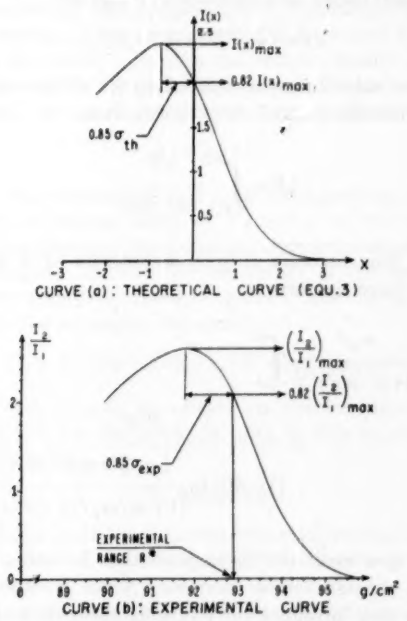

FIG. 2. Ion chamber response *vs* range.

determined from the known volume and weight of the emulsion stack, and in addition the water content was determined by a chemical analysis before and after each run

The ion chambers were filled with argon at slightly higher than atmospheric pressure. The collecting foils are about 2 in. apart and 4 in. in diameter, and are operated at 1000 v positive with respect to a grounded foil in the center of the chamber.

III. DISCUSSION

The experimental results consist of curves giving the ratio of the ion-chamber outputs as a function of absorber thickness, as illustrated in Fig. 2. From a curve of this type we now wish to obtain the "range" of the particles in the absorber and—for copper—determine

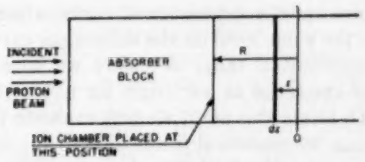

FIG. 3. Residual range R and position variable r in absorber block.

the energy of the particles by use of the known range-energy relations. We shall here outline only very briefly the method employed for obtaining the range, further details of which are given by Aron[4] and Mather and Segrè.[5]

The response of the ion chamber placed at a distance R from the end of the range in the absorber material is of the form

$$I(R)=N_0\int_{-\infty}^{\infty}P(r,R)i(r,R)dr, \qquad (1)$$

where $P(r,R)$ is the probability that a particle in the interval between r, and $r+dr$ has an energy corresponding to a residual range R (see Fig. 3), and $i(r,R)$ is the response of the ion chamber to a particle which has the residual range R when it passes the position r. Both r and R are measured from the end of the range of the particle, being positive towards the source of the beam. The total number of particles is N_0, which we assume to be constant. We thus neglect the attenuation of the beam due to large-angle scattering and other nuclear interactions in going from one experimental point to the next. It can be shown that this introduces only a very minor change in the shape of the curve.

We now substitute the usual Gaussian range-straggling distribution (with a standard deviation α) for $P(r,R)$ and an empirical relation[5] of the form

$$i(r,R)=i(r')=\text{constant}\,(r')^{-0.46} \qquad (2)$$

as the ion chamber response for a single particle. The variable $r'=2R-r$ represents the total residual range of the particle (in the absorber material) as it passes through the ion chamber. It is easy to see that $i(r')=0$ for negative values of r'.

Making another substitution of variables in order to obtain the curve in units of α, we get, as the final response of the ion chamber,

$$I(x)=(\text{const})\int_0^{\infty}\exp[-\tfrac{1}{2}(x+t)^2]t^{-0.46}dt, \qquad (3)$$

where $x=-R/\alpha$ and $t=r'/\alpha$. Thus, if we assume only statistical straggling to be present the curve of $I(x)$ *versus* x should be identical with the experimentally observed Bragg curve. Note that the curve $I(x)$ *versus* x is independent of α.

[4] Walter A. Aron, University of California Radiation Laboratory Report No. UCRL-1325, May, 1951 (unpublished).
[5] R. Mather and E. Segrè, Phys. Rev. **84**, 191 (1951).

The point on the experimental curve which corresponds to the value $x=0$ on the theoretical curve gives us the experimental range R^*, since we have chosen the end of the range as our origin for x. (See curve a, Fig. 2.) To locate this point we first evaluate the ratio $I(0)/I(x)_{\max}$ by numerical integration of Eq. (3). This ratio turns out to be 0.82. We thus choose a point on the experimental curve whose ordinate is 0.82 times the peak ordinate, and the abscissa of this point represents the experimental range R^*.

From the experimental range R^* determined above, we obtain the rectified experimental range R by correcting for the shortening of the tracks by multiple small-angle scattering in the absorber. It can be shown[5] that this correction is fairly small, and for protons it is approximately given by

$$(R-R^*)/R=Z/6400,$$

or about $\frac{1}{2}$ percent for copper.

A comparison of the shapes of the theoretical and experimental response curves of the ion chamber yields an estimate of the energy spread of the proton beam. If we assume that the energy spread of the proton beam is Gaussian, we may fold this Gaussian into the statistical straggling Gaussian, and we again obtain a Gaussian but with a larger standard deviation. We thus ascribe any broadening of the experimental curve with respect to the theoretical curve to the energy spread of the beam, and hence,

$$\sigma_{\text{beam}}=(\sigma_{\text{exp}}{}^2-\sigma_{\text{th}}{}^2)^{\frac{1}{2}}=\frac{\Delta T}{(dT/dx)}. \tag{4}$$

In the above expression σ_{th} is obtained by a numerical integration of the relativistic straggling formula,[6]

$$\sigma_{\text{th}}{}^2=4\pi z^2e^4N_aZ\int_0^T\left(\frac{dT}{dR}\right)^{-3}\left(\frac{1-\beta^2/2}{1-\beta^2}\right)dT. \tag{5}$$

The experimental standard deviation σ_{exp} is obtained by noting that the horizontal distance between $I(x)_{\max}$ and $I(0)$ is $0.85\sigma_{\text{th}}$ on the theoretical curve (curve a, Fig. 2). The same relation holds to a good approximation for the experimental curve, and we thus take the difference between the abscissa of the peak and the range as $0.85\sigma_{\text{exp}}$. Substituting the values of σ_{exp}, σ_{th}, and the value of dT/dx in Cu for 340-Mev protons, we obtain $\Delta T=\pm 1.5$ Mev.

Since the experiment indicated that both the ranges and the specific ionization are very closely the same for nuclear emulsions and for copper, the average ionization potential I_E for emulsion was evaluated relative to that of copper using the method outlined below.

At the energies we are considering, the rate of energy loss of a proton in matter can be written in the form[7]

$$\frac{dT}{dx}=\left(\frac{4\pi}{\beta^2}\right)\left(\frac{e^2}{mc^2}\right)^2N\ln\frac{2mc^2\beta^2\exp(-\beta^2)}{(1+m/m_p)^2(1-\beta^2)I}\times(mc^2/\text{cm}), \tag{6}$$

where $\beta=v/c$ for the incident particle, e^2/mc^2 = classical electron radius, N = number of electrons/cm^3 of absorber, m = electron mass, m_p = proton mass, I = mean ionization potential, and T = kinetic energy of incident particle. In this formulation the units of dT/dx are mc^2/cm rather than the usual Mev/cm. From the kinematical relationship between T and β we obtain an expression for dT as a function of β and $d\beta$:

$$dT=(m_pc^2)\beta d\beta/(1-\beta^2)^{\frac{1}{2}}. \tag{7}$$

We now substitute the expressions for dT/dx and dT from formulas 6 and 7, respectively, into

$$\Delta R=\int_{T_1}^{T_2}\frac{dT}{(dT/dx)}, \tag{8}$$

which thus becomes entirely a function of β and I. It will have the form

$$\Delta R=\frac{m_pc^2}{4\pi(e^2/mc^2)^2N}\int_{\beta_1}^{\beta_2}\times\frac{\beta^3d\beta}{(1-\beta^2)^{\frac{1}{2}}\ln\dfrac{2mc^2\beta^2\exp(-\beta^2)}{(1+m/m_p)^2(1-\beta^2)I}}. \tag{9}$$

We now make the assumption that $I_E=\lambda I_{\text{Cu}}$ where λ is a constant whose numerical value is close to 1. Let us now introduce the following abbreviations:

$$A(\beta)=\frac{\beta^3}{(1-\beta^2)^{\frac{1}{2}}},\quad B(\beta)=\frac{2mc^2\beta^2\exp(-\beta^2)}{(1+m/m_p)^2(1-\beta^2)},\text{ and }I=I_{\text{Cu}}.$$

We can then write

$$\frac{N_E\Delta R_E}{N_{\text{Cu}}\Delta R_{\text{Cu}}}=\frac{\displaystyle\int_{\beta_1}^{\beta_2}\frac{A(\beta)d\beta}{\ln[B(\beta)/I]-\ln\lambda}}{\displaystyle\int_{\beta_1}^{\beta_2}\frac{A(\beta)d\beta}{\ln[B(\beta)/I]}}. \tag{10}$$

However, since $\ln[B(\beta)/I]\gg\ln\lambda$, we can expand the integrand in the numerator of (10) in terms of the small quantity $\ln\lambda/\ln[B(\beta)/I]$. This enables us to solve for

[6] J. Lindhard and M. Scharff, Kgl. Danske Videnskab. Selskab, Mat.-fys. Medd. **27**, No. 15 (1953).

[7] H. H. Bethe and T. Ashkin, *Experimental Nuclear Physics* (John Wiley and Sons, Inc., New York, 1953), p. 223.

$\ln\lambda$, which is given by

$$\left\langle\left(\ln\frac{2mc^2\beta^2\exp(-\beta^2)}{(1+m/m_p)(1-\beta^2)I_{Cu}}\right)^{-1}\right\rangle\ln\lambda = \left(\frac{N_E\Delta R_E}{N_{Cu}\Delta R_{Cu}}-1\right), \quad (11)$$

where the ln term has been averaged over the range of β appropriate to the ΔR under consideration. The ln term in Eq. (11) is a slowly varying function of both β and I, but λ is a fairly sensitive function of the electron densities N_E and N_{Cu} and the experimentally measured ratio $\Delta R_E/\Delta R_{Cu}$.

The density and composition of a nuclear emulsion is a function of its water content and we thus have to find a relation that gives us the electron density N_E for a given value of the physical density ρ. We assume that for small variations in ρ this relation may be written

$$N_E=a\rho+b, \quad (12)$$

where the constants a and b are evaluated by substituting the known values of N_E and ρ at two points. The manufacturer[8] furnishes the chemical composition of emulsions at two different values of the density: for dry emulsion, ($\rho=4.18$ g/cm^3), and for $\rho=3.92$ g/cm^3. The expression becomes

$$N_E=(0.253\rho+0.080)\times10^{24}\text{ electrons/cm}^3. \quad (13)$$

From this formula we obtain an electron density of 1.044×10^{24} for the emulsion used in this experiment ($\rho=3.81$ g/cm^3).

IV. RESULTS

In Table I are listed the experimental results for the measurement of the average specific ionization in emulsion over the energy intervals indicated. The beam energies were determined from the proton ranges in Cu and the range-energy curves of Aron.[4] The energies listed in Col. 2 are the mid-point energies of the intervals listed in Col. 1. The values of dT/dx shown in Cols. 5 and 6 were obtained by dividing ΔT (Col. 1) by ΔR (Cols. 3 and 4, resp.). The values of λ listed were calculated from Eq. (11). The average value of λ is 0.89 ± 0.09 and the average percent difference between $(dT/dx)_{EM}$ and $(dT/dx)_{Cu}=1.36$ percent. The estimated error of 10 percent in the value of λ is based on the estimated accuracy in the measurements of ΔR_E, ΔR_{Cu} and the values of N_E and N_{Cu}.

[8] Ilford Limited, Ilford, London, England.

TABLE I. Experimental results for measurement of specific ionization.

Col. 1 ΔT (Mev)	Col. 2 Mid-point energy T_M	Col. 3 $(\Delta R)_{EM}$ g/cm^2	Col. 4 $(\Delta R)_{Cu}$ g/cm^2	Col. 5 $(dT/dx)_{EM}$ Mev (g/cm^2)$^{-1}$	Col. 6 $(dT/dx)_{Cu}$ Mev (g/cm^2)$^{-1}$	Col. 7 λ
345–302	323.5	18.35	18.53	2.34	2.32	0.91
298–272	285.0	10.45	10.65	2.53	2.48	0.86
342–272	307.0	28.80	29.28	2.43	2.39	0.87
272–193	232.5	28.03	28.30	2.82	2.79	0.92
342–193	267.5	56.83	57.58	2.62	2.59	0.89

The second measurement was of the range of high-energy protons in emulsion. The experimental results and the calculated range (rectified experimental ranges $\bar{R}$) are:

Range of beam in Cu	93.65 ± 0.20 g/cm^2
Energy of beam	342.5 ± 1.5 Mev
Range in emulsion	92.68 ± 0.25 g/cm^2
Calculated range	94.22 g/cm^2.

The energy of the beam is again obtained from the curves of Aron,[4] and the calculated value of the range in emulsion is from the work of Vigneron[1] and Barkas.[8]

The experiment thus indicates that the specific ionization [in Mev (g/cm^2)$^{-1}$] for protons in the energy region of 200 to 300 Mev is about 1 percent higher than the same quantity measured in Cu. It was also found that the range of 342-Mev protons in emulsion is about 1 percent lower than their range in Cu, which is in agreement with the dT/dx measurements.

This fact is of some practical utility, since it permits one to substitute the well-known range energy and dT/dx curves of copper for the corresponding emulsion curves whenever calculations do not call for a high degree of accuracy.

The value of the mean ionization potential of emulsion upon which Vigneron based his range-energy calculations is $I_E=332\pm25$ ev. We found that $I_E=(0.89\pm0.09)I_{Cu}$, and if we take Aron's value[4] for I_{Cu} (309.9 ev) which is based on the experiment of Mather and Segrè, we obtain for the mean ionization potential of emulsion $I_E=276\pm28$ ev.

V. ACKNOWLEDGMENTS

I wish to thank Professor Chaim Richman, under whose supervision the experiment was carried out, and Dr. Donald H. Perkins, who suggested the experiment to me. I am especially indebted to Dr. Walter H. Barkas, who made many valuable suggestions during the course of the experiment and made available to me his unpublished calculations on high-energy proton ranges.

Cloud-Chamber Observations of Some Unusual Neutral V Particles Having Light Secondaries*

V. A. J. VAN LINT, C. D. ANDERSON, E. W. COWAN, R. B. LEIGHTON, AND C. M. YORK, JR.
California Institute of Technology, Pasadena, California

(Received March 15, 1954)

From six cloud-chamber photographs of unusual V^0 decay events, the following conclusions are drawn: (1) there is a neutral V particle that decays into two particles lighter than κ mesons with a Q value too small to be consistent with a $\theta^0(\pi,\pi, 214$ Mev) particle; (2) some of these events cannot be explained in terms of the decay of a $\tau^0(\pi^0,\pi^-,\pi^+, Q\sim 80$ Mev) particle; (3) these events can be explained by any one of a number of three-body decay schemes, but two different types of V particles must be postulated if two-body decays are assumed.

I. INTRODUCTION

SINCE the discovery of neutral V particles it has become clear that at least two decay schemes must be postulated to explain the experimental data. The majority of V^0 decay events can be interpreted in terms of a decay into a proton and a negative π meson as the observable secondaries: $\Lambda^0\rightarrow p^+ + \pi^-$. Many laboratories have also observed decays which cannot be interpreted in terms of the Λ^0 mode because the ionization and momentum of the positive decay product imply a mass smaller than the proton mass. The work of Thompson and others has established that a large fraction of these V^0 decays are consistent with the decay scheme $\theta^0\rightarrow\pi^\pm + \pi^\pm$ (or $\mu^\mp$) with an energy release $Q(\pi,\pi)=214\pm 5$ Mev.[1] The Caltech group also observes that most of the cases in which the positive secondary is lighter than a proton are consistent with the above θ^0 decay scheme.

However, many laboratories have observed decays which cannot be Λ^0 decays, and for which $Q(\pi,\pi)$ is clearly less than 200 Mev.[1-5] Some of these cases can be explained by the decay scheme $V_3^0\rightarrow\pi^+ + \kappa^-$ postulated by Leighton, *et al.*[6] However, some events have been observed recently in which both secondaries are clearly less massive than a κ or τ meson and for which $Q(\pi,\pi)$ is clearly inconsistent with 214 Mev.

The purpose of this paper is to report some cases which are inconsistent with both the $\Lambda^0(p,\pi)$ and $\theta^0[\pi,L,214(\pi,\pi)]$[7] decay schemes. The events have been observed in the 18-inch magnet cloud chambers operating at Mount Wilson (1750-m elevation), the 21-inch magnet cloud chamber operating at Pasadena (220 m), and the 48-inch magnet cloud chambers operating at Pasadena (220 m). The data from the best individual cases will be presented in detail, a summary of the data from a few other cases given, and tentative conclusions drawn from this evidence.

II. MEASUREMENT TECHNIQUE

The curvatures of the tracks were measured by determining coordinates of points on the tracks with a precision comparator and plotting these points on graph paper with the transverse dimension magnified ten times more than the longitudinal dimension. The resulting plots were compared with standard curves to determine the best fit. Angles between tracks were determined by projecting onto a plane at full size and graphically constructing an orthogonal view of the tracks.[6] The calculation of the momentum of a particle included corrections for effects of magnetic-field inhomogeneity and the conical projection involved in the photography. The errors in the momentum measurements were calculated from the estimated maximum detectable momentum in each chamber at the times the photographs were taken.

III. PHOTOGRAPH 8796 (18-INCH MAGNET)

Figure 1 is a reproduction of the first of these unusual V^0 decays observed in this laboratory.[5] The V^0 particle decays in the lower chamber and was undoubtedly produced in the interaction in the lead plate between the two chambers. The energy release calculated assuming the products to be two π mesons is 116 ± 30 Mev. The momentum of the positive particle (curved clockwise) would have to be doubled in order to make the calculated Q value of this event 214 Mev, or to make it consistent with the decay of a Λ^0 particle at

* Supported in part by the joint program of the U. S. Office of Naval Research and the U. S. Atomic Energy Commission.

[1] Thompson, Buskirk, Etter, Karzmark, and Rediker, Phys. Rev. **90**, 1122 (1953); Thompson, Buskirk, Cohn, Karzmark, and Rediker, Report B-2 at Bagnères Conference (unpublished).

[2] Armenteros, Barker, Butler, and Cachon, Phil. Mag **42**, 1113 (1951); K. H. Barker, Report B-3 at Bagnères Conference (unpublished)

[3] Thompson, Buskirk, Etter, Karzmark, and Rediker, Phys. Rev. **90**, 329 (1953).

[4] Ballam, Harris, Hodson, Rau, Reynolds, Treiman, and Vidale, Phys. Rev. **91**, 1019 (1953); G. T. Reynolds, Report B-5 at Bagnères Conference (unpublished).

[5] Leighton, Wanlass, and Alford, Phys. Rev. **83**, 843 (1951).

[6] Leighton, Wanlass, and Anderson, Phys. Rev. **89**, 148 (1953).

[7] In order to specify concisely what characteristics are assumed when a particular particle is mentioned, the assumed decay products and energy release are stated in brackets or parentheses. For example, the notation $\Lambda^0(p,\pi)$ refers to a class of particles decaying into a proton and π meson only, irrespective of their energy release. The notation $\theta^0[\pi,L,214(\pi,\pi)]$ refers to a class of particles which decay into a π and an L meson (π or μ), whose energy release is calculated as 214 Mev on the assumption that two π mesons are the decay products. The term V particle is used as a general term to include both K mesons and hyperons.

35 Mev. The plane of the decay products contains the interaction in the lead plate within the large errors of measurement introduced by the shortness of the line of flight of the unstable particle. Also the components of the momenta perpendicular to the assumed line of flight of the V^0 particle balance within experimental accuracy. This statement would not be true if the positive momentum were doubled.

IV. PHOTOGRAPH 12590 (21-INCH MAGNET)

Figure 2 shows the decay of a V^0 particle into two light secondaries. On the original film the individual droplets are clearly resolved along all tracks in the chamber.[8] Therefore the relative ionization of the V-particle secondaries and comparison tracks can be determined. If the identity and momenta of the particles producing the comparison tracks are known, then through the application of a theoretical expression for the dependence of ionization on velocity, the specific ionization of the V-particle secondaries can be determined. In the present case the two highly curved comparison tracks are identified as electrons, and the resulting values for the ionizations of the positive and negative secondaries of the V particle are $1.4\pm0.2\times$ minimum and $1.3\pm0.2\times$minimum, respectively. These values are probably too high, since a preliminary study of the ionization of electrons in the velocity range of the comparison tracks has indicated the actual ionization to be somewhat less than that given by the theoretical formula.

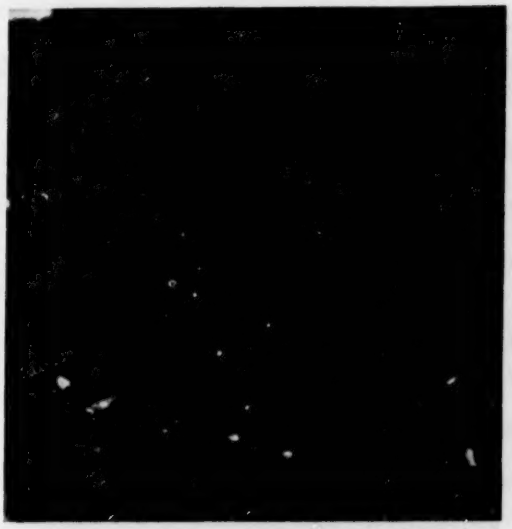

FIG. 2. Photograph 12 590 (21-inch magnet). The V^0 decay is in the upper left corner and the secondaries both leave the chamber through the rear wall. Individual droplets can be counted on the original photograph permitting a comparison of the ionizations of the secondaries and the two curved electron tracks. A negative particle corresponds to a clockwise curvature.

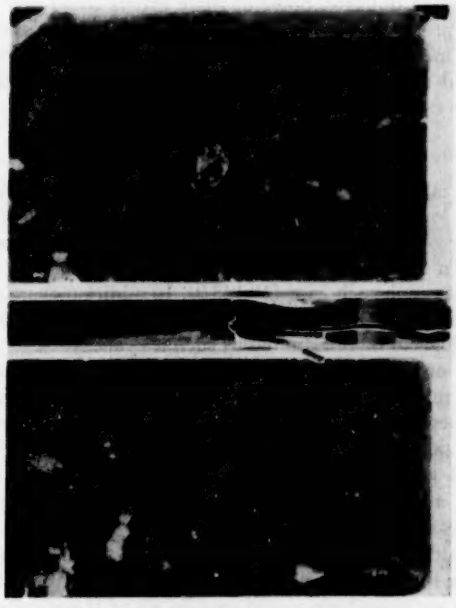

FIG. 1. Photograph 8796 (18-inch magnet). The V^0 decay is observed just below the lead plate. The V^0 particle probably originated at the interaction in the plate. A positive particle corresponds to a clockwise curvature.

[8] E. W. Cowan, Phys. Rev. **94**, 161 (1954).

The measured momentum of the negative secondary is 249 ± 12 Mev/c and if it is assumed to be a π or μ meson, its specific ionization is $1.1\times$minimum. If this track is used as a comparison track, the specific ionization of the positive secondary is $1.2\pm0.2\times$minimum. The momentum of the positive track is 493 ± 33 Mev/c. If it is assumed to be a κ meson, its specific ionization is $1.6\times$minimum. Therefore, the present measurements make unlikely the possibility that the secondaries are a π or μ meson and a κ meson, although the possibility that either or both might be *electrons* cannot be excluded from ionization measurements.

The energy release calculated assuming the secondaries to be two π mesons is 79 ± 10 Mev. The short straight track and the longer electron track appear to intersect in the lead above the chamber, although the exact intersection is uncertain because of the large possible multiple scattering of the electron. This possible origin lies in the plane of decay of the V^0 particle and the components of momentum transverse to the assumed lines of flight of the V^0-particle balance within experimental error.

V. PHOTOGRAPH 19143 (48-INCH MAGNET)

Figure 3 shows two decay events which occurred at points A and B in the large upper cloud chamber of the 48-inch magnet. The decay at point A is consistent with the usual θ^0 decay scheme. Its energy release,

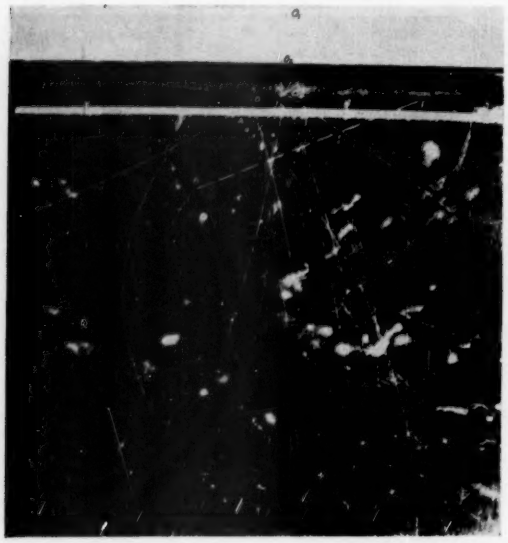

FIG. 3. Photograph 19 143 (48-inch magnet). Two V^0 decays are observed at points A and B. All tracks other than those due to electrons project back to one of the four intersections O_1, O_2, O_3, O_4 in the chamber wall and lead plate. The line PB represents the presumed line of flight of the primary if the decay at point B is a two-body decay.

assuming the products to be two π mesons, is 238±30 Mev.

The decay which appears at point B in this photograph has a Q value of 41±5 Mev, calculated assuming two π mesons as the only decay products. If this event actually represents a two-body decay, momentum balance requires that the point of production of the parent particle lie on the extension of the line BP which lies within the illuminated region of the chamber. Extensions of the lines of flight of all charged particles in the chamber other than electrons and heavily ionizing tracks locate two intersections in the lead plate above the chambers at O_1 and O_2. In addition there are two more nuclear interactions at O_3 and O_4 in the upper chamber wall from which only heavily ionizing tracks emanate. Whereas event A shows good coplanarity and transverse momentum balance if O_2 is assumed to be its origin, it is clear for event B that there is no evidence for any interaction along the extension BP. Furthermore, the locations of the interactions above the chamber indicate that the penetrating shower was probably initiated by a single primary interacting at O_1, with secondaries producing further interactions at O_2, O_3, and O_4. It seems quite improbable that a secondary from one of these events was emitted at nearly 90° to the primary direction, interacted at the right of the lead plate and emitted an energetic unstable particle in a backward direction along the line PB and furthermore produced no charged secondaries which entered the chambers.

We thus conclude that this event is probably not a two-body decay. The possibility that it is a three-body decay will now be considered.

If one assumes the origin of the parent particle to be any of the four observed interactions, the component of momentum of the neutral secondary perpendicular to the primary line of flight lies in the range 170±20 Mev/c to 210±25 Mev/c. This information, together with the assumption of the mass of the neutral secondary, determines a lower limit to the Q value of the three-body decay.

If one assumes the neutral secondary to be a π^0 meson, by analogy with the charged τ-decay scheme, the lower limit on the Q value is 165±20 Mev. The Q value of the *charged* τ meson is known to be 75±1 Mev, and thus the interpretation of this event as a $\tau^0(\pi^0,\pi^+,\pi^-,80)$ decay is inconsistent with the assumption that the particle originated in one of the four observed interactions.

VI. SUMMARY OF CASES

Table I summarizes the important data from the events described and a few others. The ionization of all tracks except those of No. 12 590 were estimated visually.

The three cases that have been added to this tabulation have no clear origin for the parent particle. Nevertheless, the estimated ionizations and the orientations make such possible alternatives as the decay of a $\kappa^\pm$ meson unlikely. Some of these events could also be interpreted as the decay of a neutral particle into a π or μ meson and a κ meson. However, no simplification would result from such an assumption since the best cases cannot be so interpreted.

VII. DISCUSSION

It is tempting to interpret the cases which have a very low Q value as representing the decay of a neutral τ meson into three π mesons. However, it has been shown that such an interpretation is very unlikely for at least one such case (19 143B). In addition there are a number of cases whose two-body Q values are already too high to be interpreted as such a τ^0 decay.

If one wishes to retain the simplifying assumption that most of these cases are decays of the same particle, a scheme with a much higher energy release is required. One possible decay scheme which satisfies this requirement is an alternate mode of decay of the θ^0 particle into $\pi+\mu+\nu$. The computed energy release for this decay is about 244 Mev.

Calculation of the minimum Q value assuming $\theta^0\rightarrow\pi+\mu+\nu$ for case 19 143B yields 245±30 Mev. Thus such an hypothesis would explain all of these unusual cases. It should be pointed out, however, that this decay scheme is certainly not a unique one. For example, another decay scheme which can explain all of these cases is θ^0 or $\tau^0\rightarrow\pi^0+\mu^++\mu^-+(\sim 148$ Mev). Both of

TABLE I. Data on unusual V^0 decays.

Event	Secondary	Momentum (Mev/c)	Specific ionization (×minimum)	Mass (units of m_e)	Angle between secondaries	$Q(\pi,\pi)$ (Mev)
8796 (18 in.)	+	570±130	1−1.7	<1200	44°	116±30
	−	120±5	1.5−3	220−420		
56 337 (18 in.)	+	240±65	1−1.7	<600	63°	148±30
	−	390±30	1−1.7	<830		
59 824 (18 in.)	+	124±10	1−2	<310	61°	96±16
	−	365±55	1−1.7	<780		
12 590 (21 in.)	+	493±33	1.4±1.2[a]	840±150[a]	34°	79±10
	−	249±12	1.3±1.2[a]	385±130[a]		
15 329 (48 in.)[b]	+	940±100	1−1.7	<2000	8°	45^{+25}_{-12}
	−	1420±300	1−2	<3500		
19 143 (48 in.)A	+	375±30	1−2	<970	46°	238±30
	−	820±70	1−1.7	<1700		
19 143 (48 in.)B	+	260±20	1−2	<640	40°	41±5
	−	87±4.5	1.5−3	160−300		

[a] These values are calculated assuming the dubious theoretical electron ionization and are therefore probably too high.
[b] This case is included here because $Q(p,\pi)$ would be 343±80 Mev.

these hypotheses are so broad that they can explain almost any individual event of the type considered here. To confirm or to disprove either of them would require a large amount of accurate data on these rare events.

It is possible that the $\theta^0(\pi,\pi)$ decays having Q values near 214 Mev represent a part of the same three-body decay distribution. However, if this were the case it is unlikely that the observed $Q(\pi,\pi)$ value distribution should be as sharply peaked as present experimental measurements appear to indicate.

VIII. SUMMARY

There is evidence for the existence of a neutral particle which decays into two charged L mesons which cannot be explained by the scheme $\theta^0\rightarrow\pi^+ + \pi^-$ + (214 Mev). If only two-body decays are considered, at least two different new particles have to be postulated with $Q(\pi,\pi)$ near 41 Mev and 90 Mev, respectively, and under this assumption a question as to the point of production in at least one case still remains. Not all of these cases can be explained by the decay of a neutral τ meson into three π mesons. Hence a decay scheme with a higher energy release is indicated. One scheme which might explain these cases in terms of an alternate mode of decay of a known particle is $\theta\rightarrow\pi^{\pm}+\mu^{\mp}+\nu+$ (∼244 Mev). Of course, many other decay schemes might be postulated, but there is no direct experimental evidence for any particular one of these.

ACKNOWLEDGMENTS

The authors gratefully acknowledge the efforts of Mr. E. K. Björnerud, Mr. J. D. Sorrels, Mr. G. H. Trilling, and Dr. S. D. Wanlass in carrying out some of the preliminary analysis of these data.

Meson-Nucleon Scattering. I

R. J. RIDDELL, JR., AND B. D. FRIED*
Radiation Laboratory, Physics Department, University of California, Berkeley, California
(Received October 14, 1953)

An approximate quantum-mechanical solution of the meson-nucleon scattering problem for intermediate values of the coupling constant is presented. The particular case treated here is that of charged scalar mesons interacting with a static nucleon. In finding the cross section, attention is focused upon the matrix elements of the field and isotopic spin operators and on the equations of motion, no attempt being made to calculate explicitly the scattering state vector. It is shown that in *both* the weak and strong coupling limits the procedure described here gives the scattering correctly. For intermediate coupling the cross section must be found numerically. Computations have been carried out for several intermediate values of the coupling constant and the results are presented in the form of curves showing cross section *vs* meson energy. Since certain information about the one-nucleon problem (i.e., one real nucleon and no real mesons) is needed for these calculations, a detailed numerical solution of that problem has been carried out using the Tomonaga approximation. The relevant results of this work are presented in several graphs. Although it is not a part of the scattering problem, the calculation of the isobar separation in the strong coupling limit can be carried out so easily by the methods of this paper that a brief account of it is also given. In the appendix, a variational method of calculating the scattering-state vector for intermediate coupling is described. It is shown that this, however, fails to give the correct strong coupling limit.

1. INTRODUCTION

ONE of the most fundamental problems of meson field theory is the task of giving a quantitatively satisfactory explanation of the increasingly abundant and detailed experimental data on the scattering of pions by nucleons. Since all qualitative estimates of the meson-nucleon coupling indicate that it is neither very large nor very small, it is imperative to develop a technique for calculating the scattering cross section which is valid for intermediate values of the coupling constant. Although it is clear that the problem must eventually be treated in a completely relativistic manner, using pseudoscalar meson theory, to date this has proved so formidable a task that a critical examination of the intermediate coupling region for the much simpler problem of an infinitely heavy nucleon seems worth while. Even with this restriction no exact solution for all values of the coupling has been found, and so we must look for suitable approximations.

In this paper we shall study the question of meson scattering from a fixed nucleon for intermediate values of the coupling constant g. In order to avoid the algebraic complications involved in treating both spin and isotopic spin, we shall first discuss the simplest nontrivial case, the charged scalar field, although the same methods can be used in the more complicated cases, e.g., the pseudoscalar, charge symmetric field, which will be discussed in a subsequent paper.

The nonrelativistic one-body problem (i.e., one real, fixed nucleon and no real mesons) can be treated by Tomonaga's variational procedure,[1] which uses as trial function a state vector in which only a few meson states are occupied (although no restriction is placed on the occupation numbers). The crucial point in the justification of this method is its validity in both the weak and strong coupling limits. The assumption that all mesons are in the same spatial state is certainly correct if, as in the weak coupling case, the probability of having more than one meson is very small. That this same approximation will also be successful for large values of the coupling constant is less obvious and a demonstration of the agreement between the strong coupling limit of the Tomonaga approximation and the conventional strong coupling (s.c.) theory[2] is essential in any attempt to make plausible the validity of the Tomonaga assumption for the intermediate coupling region. In his original paper[1] on the subject, Tomonaga showed that his method does indeed give the correct s.c. value for the isobar separation.

Going on to the two-body problem of one real meson and one real nucleon, it seems natural to look for a consistent method of calculating the scattering cross section which shall satisfy the following three criteria:

(1°) For small values of g the cross section is the same as that obtained from ordinary perturbation theory.

(2°) For large g the cross section agrees with the result of the conventional strong coupling theory.[2]

(3°) For intermediate values of g a numerical calculation of the scattering cross section is feasible.

The first requirement is satisfied by almost any reasonable procedure, and it is quite easy to find some which also fulfill the third condition, since an approximate calculation, e.g., Tomonaga's, may be used to supply such information about the one-body problem as is needed in the scattering calculation. However, it is considerably more difficult to find a method which in addition gives the correct s.c. limit. It may well happen, of course, that a procedure which fulfills only two of the

* Now at the Ramo-Wooldridge Corporation, Los Angeles, California.

[1] S. Tomonaga, Progr. Theoret. Phys. (Japan) 2, 6 (1947).

[2] G. Wentzel, Helv. Phys. Acta 13, 269 (1940); W. Pauli and S. M. Dancoff, Phys. Rev. 62, 85 (1942); A. Kaufman, Phys. Rev. 92, 468 (1953).

conditions will be closer to the exact answer in the intermediate coupling region than one which satisfies all three. In particular, our insistence that condition (2°) be satisfied may seem unjustified since from qualitative indications, such as the failure to detect stable isobars, it appears that the actual value of g cannot be large enough to make s.c. theory applicable. However, it is equally certain that g is not small enough to justify the use of perturbation theory and in the absence of evidence to the contrary it seems reasonable to place more confidence in a method which is correct in *both* the weak and strong coupling limits.

In this paper we shall describe a procedure (i.e., a set of approximations) for solving the meson-nucleon scattering problem which satisfies all three of these requirements. Subsequent papers will deal with the application of this same method to the scattering problem for pseudoscalar mesons and with its extension to the case of nonstatic nucleons. In Sec. II we discuss briefly the Tomonaga solution of the one-body problem including some features which, to our knowledge, have not been described before. The solution of the scattering problem is described in Sec. III, and graphs showing the variation of $d\sigma/d\Omega$ with energy and coupling constant are presented. Section IV shows how the same techniques may be used to find the s.c. isobar separation. A general discussion of the method and results is given in Sec. V.

In Appendix I a variational approach to the scattering problem is discussed. This method satisfies conditions (1°) and (3°) but gives only order of magnitude agreement with the s.c. result. Still another way of finding the scattering has recently been proposed by Maki, Sato, and Tomonaga.[3] They have shown that it satisfies requirements (1°) and (3°), but they have found it necessary to treat the strong coupling case by a method[4] somewhat different from that used for the weak or intermediate coupling regions. Thus, they "have given no formula which connects continuously the weak, intermediate, and strong coupling cases."[5]

2. THE ONE-BODY PROBLEM IN THE TOMONAGA APPROXIMATION

In terms of momentum-space annihilation operators $A(\mathbf{k})$, $B(\mathbf{k})$ for positive and negative mesons, respectively, and the usual Pauli isotopic spin matrices, $\tau_\pm$, the Hamiltonian for the charged scalar field is[6]

$$H=\int d\mathbf{k}\{A^*(\mathbf{k})\omega A(\mathbf{k})+B^*(\mathbf{k})\omega B(\mathbf{k}) -gR(\mathbf{k})[A(\mathbf{k})\tau_-+B(\mathbf{k})\tau_++\text{cc}]\}, \quad (1)$$

where

$$R(\mathbf{k})\equiv\rho(\mathbf{k})(2\omega)^{-\frac{1}{2}}, \quad \omega=(k^2+\mu^2)^{\frac{1}{2}},$$

and $\rho(\mathbf{k})$ is the Fourier transform of the nucleon source density $\rho(\mathbf{x})$ satisfying

$$\int d\mathbf{x}\rho(\mathbf{x})=1.$$

As usual,

$$[A(\mathbf{k}), A^*(\mathbf{k}')]=[B(\mathbf{k}), B^*(\mathbf{k}')]=\delta(\mathbf{k}-\mathbf{k}'), \quad (2)$$

and other commutators are zero. [We use units in which $\hbar$, c, and μ (meson mass) have the value one.]

To solve the Schrödinger equation $HF=EF$ for a state of total charge Q, we introduce Tomonaga's assumption:

$$F=\sum_n c_{n+Q,n}\frac{(a^*)^{n+Q}(b^*)^n}{[n!(n+Q)!]^{\frac{1}{2}}}N +\sum_n c_{n+Q-1,n}\frac{(a^*)^{n+Q-1}(b^*)^n}{[n!(n+Q-1)!]^{\frac{1}{2}}}P, \quad (3)$$

where

$$a=\int d\mathbf{k}\phi_+(\mathbf{k})A(\mathbf{k}), \quad (4)$$

and b is defined similarly. The state vector N (or P) denotes the state: "bare neutron (or proton) plus meson vacuum." The $\phi_\pm$ (which we take to be real functions) and the $c_{n,m}$ are to be determined by minimizing $\langle F|H|F\rangle$ subject to

$$\langle F|F\rangle=1 \quad \text{and} \quad \int d\mathbf{k}[\phi_\pm(\mathbf{k})]^2=1,$$

i.e.,

$$\delta\left\{\langle F|H|F\rangle-\nu\langle F|F\rangle-\nu_+\int\phi_+^2-\nu_-\int\phi_-^2\right\}=0. \quad (5)$$

where ν and $\nu_\pm$ are Lagrange multipliers. Since

$$\langle F|H|F\rangle=\langle F|H^T|F\rangle, \quad (6)$$

with

$$H^T=a^*a\omega_++b^*b\omega_--[\tau_-(g_+a+g_-b^*)+\text{c.c.}], \quad (7)$$

and

$$\omega_\pm=\int d\mathbf{k}\omega\phi_\pm^2, \quad g_\pm=g\int d\mathbf{k}R\varphi_\pm,$$

the variation with respect to the $c_{n,m}$ just leads to a simplified Schrödinger equation,

$$H^TF=\mathcal{E}F, \quad (8)$$

which can be solved analytically in the weak and strong coupling limits and numerically in the intermediate coupling region. (The Lagrange multiplier ν, of course, is just $\mathcal{E}$.)

[3] Maki, Sato, and Tomonaga, Progr. Theoret. Phys. (Japan) **9**, 614 (1953). We are indebted to Dr. T. Kinoshita for informing us of this work prior to its publication.

[4] Z. Maki and M. Sato, Progr. Theoret. Phys. (Japan) **10**, 386 (1953).

[5] S. Tomonaga (private communication).

[6] G. Wentzel, *Quantum Theory of Fields* (Interscience Publishers, Inc., New York, 1949).

In carrying out the variation with respect to $\phi_\pm$ it is convenient to use the easily verified relation

$$\delta\phi_+ F=\left[\int d\mathbf{k}\delta\phi_+(\mathbf{k})A^*(\mathbf{k})a\right]F, \tag{9}$$

for the change in F produced by a small variation,

$$\phi_+(\mathbf{k})\to\phi_+(\mathbf{k})+\delta\phi_+(\mathbf{k}).$$

We then have, from (5),

$$\langle F|H-\mathcal{E}|A^*(\mathbf{k})aF\rangle+\text{c.c.}-\nu_+\phi_+(\mathbf{k})=0.$$

Using the commutation relations (2) and noting that by (3) and (4)

$$A(\mathbf{k})F=a\phi_+(\mathbf{k})F, \tag{10}$$

we obtain

$$[\langle F|a^*(H-\mathcal{E})a|F\rangle\phi_+ +\langle F|\omega\phi_+ a^*-gR\tau_-|aF\rangle +\text{c.c.}]-\nu_+\phi_+=0.$$

As in (6), H can now be replaced by H^τ, so we find

$$[N_+(\omega-\omega_+)+M_+g_+-\nu_+]\phi_+-gM_+R=0, \tag{11}$$

with

$$N_+=\langle F|a^*a|F\rangle,\quad M_+=\tfrac{1}{2}[\langle F|a\tau_-|F\rangle+\text{c.c.}].$$

Since multiplying (11) by $\phi_+(\mathbf{k})$ and integrating gives $\nu_+=0$, we have finally

$$\phi_+(\mathbf{k})=\frac{gM_+}{N_+}\cdot\frac{R(\mathbf{k})}{(\omega-\omega_+ +gM_+/N_+)},$$

or

$$\phi_+(\mathbf{k})=(gM_+/N_+)R(\mathbf{k})[\omega-\lambda_+]^{-1}, \tag{12}$$

where λ_+ is given in terms of gM_+/N_+ by the normalization requirement on ϕ_+,

$$\left(\frac{gM_+}{N_+}\right)^2\int d\mathbf{k}\frac{R^2(\mathbf{k})}{(\omega-\lambda_+)^2}=1. \tag{13}$$

A similar equation holds for ϕ_-.

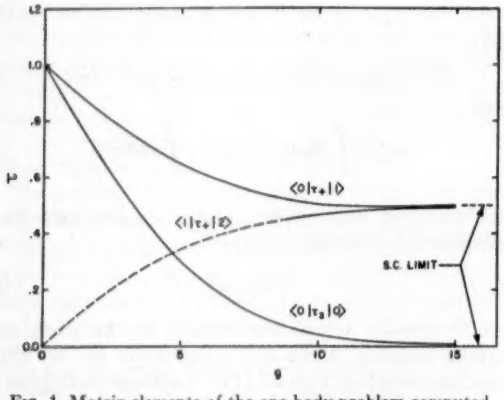

FIG. 1. Matrix elements of the one-body problem computed from the Tomonaga approximation.

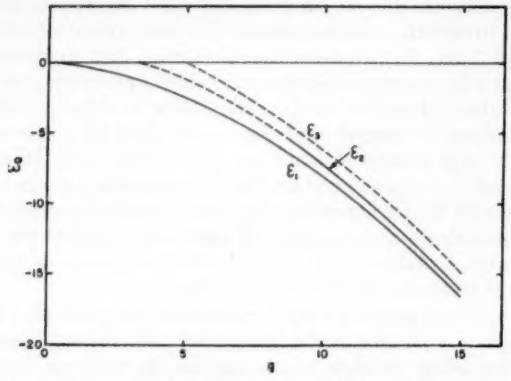

FIG. 2. Nucleon isobar energies computed from the Tomonaga approximation. The charge-2 isobar is stable for $g>8.66$.

Numerical calculations for $\phi_\pm$ and F have been carried out using the IBM Card Programmed Computer at the University of California Radiation Laboratory, Livermore, California. In Figs. 1 through 4 we have presented some of the results of this work. Curves corresponding to the charge-2 isobar have been dotted for values of g below 8.66, where that state becomes unstable with respect to meson emission. For the same reason, the entire $\mathcal{E}_3$ curve is dotted since $\mathcal{E}_3-\mathcal{E}_1>\mu$ for all values of g which we used.

Actually, the scattering calculations to be described in Sec. III require very little information about the one-body problem. Besides the isobar energy separations, we need only the matrix elements $\langle 0|\tau_+|1\rangle$ and $\langle 1|\tau_3|1\rangle$ (for ordinary scattering) and $\langle 1|\tau_+|2\rangle$ and $\langle 2|\tau_+|3\rangle$ (for charge-exchange scattering). Since the variational calculation of the Tomonaga state described above is to be carried out anew for each value of the total charge Q of (3), $\phi_\pm$ and all quantities related to them—$\lambda_\pm$, a, b, H^τ, $\mathcal{E}$, $N_\pm$, etc.—depend on Q and really ought to carry a label Q which we have omitted in this section for simplicity. Because of the charge symmetry of the Hamiltonian it is sufficient to solve the one-body problem for $Q\geqslant 1$, since $\mathcal{E}_Q=\mathcal{E}_{1-Q}$; $\lambda_{Q\pm}=\lambda_{1-Q,\mp}$; $N_{Q\pm}=N_{1-Q,\mp}$; etc.

Since we have used a static approximation for the nucleon, it is necessary to introduce a cutoff in all of the calculations. We have chosen the one which seems most convenient for computations:

$$\rho(\mathbf{k})=\frac{1}{(2\pi)^{\frac{3}{2}}}\int d\mathbf{x}\rho(\mathbf{x})e^{i\mathbf{k}\cdot\mathbf{x}}=\begin{cases}(2\pi)^{-\frac{3}{2}}, & |\mathbf{k}|<M\\ 0, & |\mathbf{k}|>M,\end{cases} \tag{14}$$

where $M=6.62\mu$ is the nucleon mass.

3. MESON SCATTERING

Of the three requirements discussed in Sec. I, the most difficult to satisfy seems to be that of agreement with s.c. theory. Thus, using a technique reminiscent

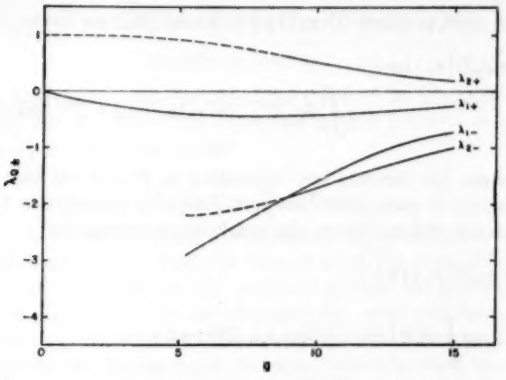

FIG. 3. $\lambda_\pm$ *vs* g for the isobars of charge 1 and charge 2 in the Tomonaga approximation as computed from (13).

of that theory, we shall work directly with the matrix elements of the field and isotopic spin operators in solving the scattering problem. In contrast to the approach customary in perturbation theory, we shall not attempt to calculate explicitly the relevant state vectors. The latter contain more information than we actually require, whereas the matrix elements are closely related to observable quantities. For instance, suppose that $|Q\rangle$ is the state vector of a physical nucleon ($Q=1$ for proton, $Q=0$ for neutron), while $|Q+1, \mathbf{p}+\rangle$ represents a state of total charge $Q+1$ in which a positive meson of momentum $\mathbf{p}$ is incident upon the charge Q nucleon. (It is to be emphasized that we mean these to be exact eigenstates of the *total* Hamiltonian:

$$H|Q\rangle=E_Q|Q\rangle, \quad H|Q\mathbf{p}+\rangle=E_{Q\mathbf{p}+}|Q\mathbf{p}+\rangle.) \tag{15}$$

Then $\langle Q|A(\mathbf{x})|Q+1, \mathbf{p}+\rangle$ is asymptotically equal to the wave function of the scattered positive meson, i.e.,

$$\langle Q|A(\mathbf{x})|Q+1, \mathbf{p}+\rangle \rightarrow (2\pi)^{-\frac{3}{2}}[e^{i\mathbf{p}\cdot\mathbf{x}}+\alpha e^{ip'r}/r], \tag{16}$$

for $r=|\mathbf{x}|\rightarrow\infty$, and $|\alpha|^2$ gives the scattering cross section. If the coupling is strong enough so that stable isobars of higher charge, e.g., $Q=2$ and $Q=3$, exist, then charge-exchange scattering may also occur for $\omega'=(\omega_p-E_{Q+2}+E_Q)>\mu$. In a similar way we can then find the cross section for that process from

$$\langle Q+2|B(\mathbf{x})|Q+1, \mathbf{p}+\rangle,$$

which is asymptotically the wave function of the outgoing negative meson,

$$\langle Q+2|B(\mathbf{x})|Q+1, \mathbf{p}+\rangle \rightarrow (2\pi)^{-\frac{3}{2}}\alpha' e^{ip'r}/r, \tag{17}$$

where $p'=(\omega'^2-\mu^2)^{\frac{1}{2}}$. In the following we need consider only the case where the incident meson is positive, since it follows from the charge symmetry of the Hamiltonian that $\sigma(\pi^+ + P)=\sigma(\pi^- + N)$, etc.

In order to find these matrix elements, we turn to the equations of motion. From the Hamiltonian (1), we obtain the operator equations

$$-i\dot{A}\equiv[H,A]=-\omega A+gR\tau_+, \tag{18}$$

$$-i\dot{B}=-\omega B+gR\tau_-, \tag{19}$$

$$-i\dot{\tau}_+=g\int d\mathbf{k}R\tau_3(A+B^*), \tag{20}$$

$$-i\dot{\tau}_3=2g\int d\mathbf{k}R[\tau_+(A^*+B)-(A+B^*)\tau_-], \tag{21}$$

together with corresponding relations for the Hermitian conjugate operators, A^*, B^*, and τ_-. In a matrix representation of these operators which uses as basis a complete set of energy eigenstates, these equations give rise to a set of coupled integral equations for the matrix elements. Of course, in addition to the matrix elements (16) and (17), an infinite number of others are included in this set.

Since we cannot solve these coupled equations exactly, we shall introduce the approximation of neglecting all but a few of the matrix elements involved. We shall demonstrate that this procedure can be carried out in such a way that *all* of the requirements set forth in Sec. I are satisfied.

The basis of energy eigenstates will consist of the following states:

$$\left.\begin{aligned} &|Q\rangle\sim\text{nucleon isobar of charge } Q;\\ &|Q+1, \mathbf{p}+\rangle\sim\text{positive meson of momentum } \mathbf{p} \text{ incident on a nucleon isobar of charge } Q;\\ &|Q-1, \mathbf{p}-\rangle\sim\text{negative meson of momentum } \mathbf{p} \text{ incident on a nucleon isobar of charge } Q; \end{aligned}\right\} \tag{22}$$

together with states similar to these representing two, three, $\cdots$incident mesons. For small values of g, Q may assume only the values 0 and 1. However, when g

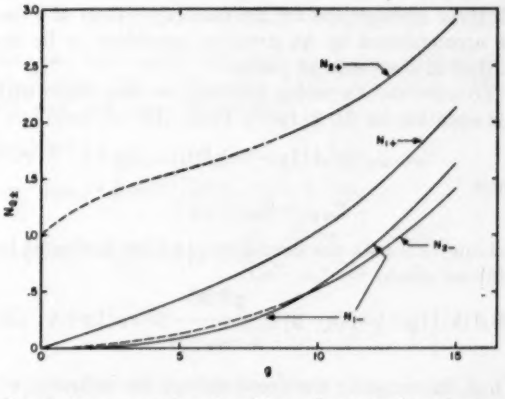

FIG. 4. Average number of positive and negative bound mesons in the meson cloud surrounding the charge-1 and charge-2 nucleon isobars.

is large, isobars of higher charge are stable, and in that case Q must be allowed to take on all integral values from Q_m to $1-Q_m$ where Q_m is the largest charge for which

$$E_{Q_m}-E_1\leqslant\mu.$$

(In the extreme s.c. limit $Q_m\to\infty$, since E_Q-E_{Q-1} is of order g^{-2}.)

The approximations which we shall make are the following, in which C represents any of the operators A, B, τ_+, τ_3, etc.:

I. We neglect all matrix elements involving states with more than one incident meson.

II. We set

$$\langle Q\mathbf{p}j|C|Q'\mathbf{p}'j'\rangle=\delta_{jj'}\delta(\mathbf{p}-\mathbf{p}')\langle Q\pm1|C|Q'\pm1\rangle, \quad (23)$$

where j, j' are $+$ or $-$ and the upper sign is to be used for $j=-$, the lower for $j=+$.

III. We approximate one-body matrix elements by the values obtained from the Tomonaga solution of the one-body problem,

$$\langle Q|C|Q'\rangle=\langle F_Q|C|F_{Q'}\rangle, \quad (24)$$

where F_Q is the lowest charge-Q eigenstate of the Tomonaga Hamiltonian,

$$H_Q{}^TF_Q=\mathcal{E}_QF_Q. \quad (25)$$

In addition, the isobar energies,

$$E_Q=\langle Q|H|Q\rangle, \quad (26)$$

are approximated by the corresponding Tomonaga values $\mathcal{E}_Q$.

By actually computing the values of the matrix elements which have been neglected, it can be shown, *a posteriori*, that the approximations I and II are valid in both the weak and strong coupling limits. (That III is correct in both limits follows from Tomonaga's work.[1]) In general, I and II correspond to the assumption that the physical nucleon is not affected very much by the incident meson. The quantitative justification of all three assumptions for intermediate values of g can be accomplished by an iterative procedure to be described in a subsequent paper.

To solve the scattering problem, we may begin with the equation for $\langle 0|A|1\mathbf{p}+\rangle$. From (18) we find

$$(\omega-\omega_p)\langle 0|A|1\mathbf{p}+\rangle=gR\langle 0|\tau_+|1\mathbf{p}+\rangle, \quad (27)$$

since

$$E_{Q\mathbf{p}\pm}=E_{Q\mp1}+\omega_p.$$

Solving (27) with the boundary condition indicated by (16) we obtain

$$\langle 0|A(\mathbf{k})|1\mathbf{p}+\rangle=\delta(\mathbf{k}-\mathbf{p})+\frac{gR(\mathbf{k})}{\omega-\omega_p-i\epsilon}\langle 0|\tau_+|1\mathbf{p}+\rangle. \quad (28)$$

Thus, to compute the cross section for ordinary π^+-neutron scattering,

$$d\sigma/d\Omega=|4\pi^2\omega_pgR(\mathbf{p})\langle 0|\tau_+|1\mathbf{p}+\rangle|^2, \quad (29)$$

we need to know $\langle 0|\tau_+|1\mathbf{p}+\rangle$. From (20), we have

$$-\omega_p\langle 0|\tau_+|1\mathbf{p}+\rangle=g\int d\mathbf{k}[R\sum_n\langle 0|\tau_3|n\rangle\langle n|A+B^*|1\mathbf{p}+\rangle,$$

where $|n\rangle$ denotes any eigenstate of H and the summation is over all values of n. Invoking assumption I, we can reduce this to the much simpler equation

$$-\omega_p\langle 0|\tau_+|1\mathbf{p}+\rangle=g\int d\mathbf{k}R\Big\{\langle 0|\tau_3|0\rangle\langle 0|A+B^*|1\mathbf{p}+\rangle+\sum_{j=\pm}\int d\mathbf{p}'\langle 0|\tau_3|0\mathbf{p}'j\rangle\langle 0\mathbf{p}'j|A+B^*|1\mathbf{p}+\rangle\Big\}.$$

Then, using assumption II, we find

$$-\omega_p\langle 0|\tau_+|1\mathbf{p}+\rangle=g\int d\mathbf{k}R\{\langle 0|\tau_3|0\rangle\langle 0|A+B^*|1\mathbf{p}+\rangle+\beta\langle 0|\tau_3|0\mathbf{p}+\rangle\langle -1|A+B^*|0\rangle\}, \quad (30)$$

where $\beta=1$ if a stable isobar of charge -1 exists, and $\beta=0$ otherwise. In addition to the one-body matrix elements, which by assumption III are to be considered as known, we have now introduced the new matrix elements $\langle 0|\tau_3|0\mathbf{p}+\rangle$ and $\langle 0|B^*|1\mathbf{p}+\rangle$, so we continue writing equations of motion until we have a closed set (number of equations equal to the number of unknown matrix elements).

Before carrying out this procedure in general, we shall consider the two limiting cases (small g and large g) in order to illustrate the method for simple cases and also to demonstrate that conditions (1°) and (2°) are satisfied.

(a) Weak Coupling

In this case, the Tomonaga solution of the one-body problem (which here coincides with ordinary perturbation theory) tells us that $\langle 0|A+B^*|1\rangle$ is of order g, $\beta=0$, and $\langle 0|\tau_3|0\rangle=1+O(g^2)$. Furthermore, we have from (19)

$$\langle 0|B^*|1\mathbf{p}+\rangle=\frac{gR}{\omega+\omega_p}\langle 0|\tau_+|1\mathbf{p}+\rangle, \quad (31)$$

so that if in (30) we retain only the terms of lowest order in g we get

$$-\omega_p\langle 0|\tau_+|1\mathbf{p}+\rangle=g\int d\mathbf{k}R\langle 0|A|1\mathbf{p}+\rangle,$$

or, using (28),

$$\langle 0|\tau_+|1\mathbf{p}+\rangle=-gR(\mathbf{p})/\omega_p, \quad (32)$$

where again terms of higher order in g have been dropped. Substituting (14) and (32) into (29), we find

for $\pi^+ + n \to \pi^+ + n$ the cross section,

$$d\sigma/d\Omega = g^4(16\pi^2\omega^2)^{-1}, \tag{33}$$

in agreement with perturbation theory.[6] In a similar way we can show that the cross section for $\pi^+ + p \to \pi^+ + p$ is also given by (33).

(b) Strong Coupling

When g is very large, the isobars of higher charge are stable so $\beta = 1$. In fact, the first term on the right side of (30) is smaller by two orders of g than the second term, in contrast to the situation for weak coupling. To see this we note first that according to the Tomonaga solution of the one-body problem (which is here the same as conventional s.c. theory to leading order in g^{-1}), $\langle 0|\tau_3|0\rangle$ is of order g^{-4}, while $\langle -1|A+B^*|0\rangle$ is of order g.[7] In addition, we shall see[8] that $\langle 0|\tau_3|0\mathbf{p}+\rangle$ is of order g^{-3} while $\langle 0|A+B^*|1\mathbf{p}+\rangle$ is of order g^0, so the first term within the curly brackets of (30) is of order g^{-4} while the second is of order g^{-2}. Neglecting the first term, we have from (30)

$$\langle 0|\tau_+|1\mathbf{p}+\rangle = -g\omega_p^{-1}\int d\mathbf{k}R\langle 0|\tau_3|0\mathbf{p}+\rangle\langle -1|A+B^*|0\rangle. \tag{34}$$

From (18) and (19) we find

$$\langle -1|A|0\rangle = \langle -1|B^*|0\rangle = gR\langle -1|\tau_+|0\rangle\omega^{-1} = \tfrac{1}{2}gR\omega^{-1}, \tag{35}$$

since the Tomonaga (or s.c.) solution of the one-body problem gives[9]

$$\langle 0|\tau_+|1\rangle = \langle -1|\tau_+|0\rangle = \tfrac{1}{2}. \tag{36}$$

Then from (34),

$$\langle 0|\tau_+|1\mathbf{p}+\rangle = -g^2K_1\langle 0|\tau_3|0\mathbf{p}+\rangle\omega_p^{-1}, \tag{37}$$

where

$$K_n \equiv \int d\mathbf{k}R^2\omega^{-n}. \tag{38}$$

Evidently we now need an equation for $\langle 0|\tau_3|0\mathbf{p}+\rangle$. From (21) we obtain

$$\begin{aligned}-\omega_p\langle 0|\tau_3|0\mathbf{p}+\rangle &= 2g\int d\mathbf{k}R\{\langle 0|\tau_+|1\rangle\langle 1|A^*+B|0\mathbf{p}+\rangle \\ &+\langle 0|\tau_+|1\mathbf{p}+\rangle\langle 0|A^*+B|-1\rangle \\ &-\langle 0|A+B^*|1\rangle\langle 1|\tau_-|0\mathbf{p}+\rangle \\ &-\langle 0|A+B^*|1\mathbf{p}+\rangle\langle 0|\tau_-|-1\rangle\},\end{aligned} \tag{39}$$

where, as in the derivation of (30), we have made use of assumptions I and II. Although (39) contains several new matrix elements, it is quite easy to express them all in terms of $\langle 0|\tau_3|0\mathbf{p}+\rangle$ and so obtain the desired closed set. Thus, from (19) we have

$$(\omega - \omega_p + E_1 - E_{-1})\langle 1|B|0\mathbf{p}+\rangle = gR\langle 1|\tau_-|0\mathbf{p}+\rangle,$$

which, with the boundary condition (17), gives

$$\langle 1|B|0\mathbf{p}+\rangle = \frac{gR}{\omega - \omega_p + E_1 - E_{-1} - i\epsilon}\langle 1|\tau_-|0\mathbf{p}+\rangle. \tag{40}$$

In the s.c. limit, where the isobar separation is of order g^{-2}, this reduces to

$$\langle 1|B|0\mathbf{p}+\rangle = \frac{gR}{\omega - \omega_p - i\epsilon}\langle 1|\tau_-|0\mathbf{p}+\rangle. \tag{41}$$

In a similar fashion we find

$$\langle 1|A^*|0\mathbf{p}+\rangle = \frac{gR}{\omega + \omega_p}\langle 1|\tau_-|0\mathbf{p}+\rangle, \tag{42}$$

$$\langle 0|B^*|1\mathbf{p}+\rangle = \frac{gR}{\omega + \omega_p}\langle 0|\tau_+|1\mathbf{p}+\rangle, \tag{43}$$

where in (42) we have again neglected the isobar separation. From (18), (19), and (36), we have also

$$\langle 0|A|1\rangle = \langle 0|B^*|1\rangle = \frac{gR}{\omega}\langle 0|\tau_+|1\rangle = \frac{gR}{2\omega}. \tag{44}$$

Finally, using the Hermitian conjugate of (20) and assumptions I and II, we find

$$\begin{aligned}(E_1 - E_{-1} - \omega_p)&\langle 1|\tau_-|0\mathbf{p}+\rangle \\ &= -g\int d\mathbf{k}R\{\langle 1|A^*+B|0\rangle\langle 0|\tau_3|0\mathbf{p}+\rangle \\ &\quad +\langle 1|A^*+B|0\mathbf{p}+\rangle\langle -1|\tau_3|-1\rangle\}.\end{aligned} \tag{45}$$

In consequence of (44) and the remarks preceding (34),[10] this reduces to

$$\langle 1|\tau_-|0\mathbf{p}+\rangle = g^2K_1\omega_p^{-1}\langle 0|\tau_3|0\mathbf{p}+\rangle, \tag{46}$$

where we have again neglected the isobar separation. Substituting (28), (35), (36), (37), (41), (42), (43), (44), and (46) into (39) we find

$$\begin{aligned}\langle 0|\tau_3|0\mathbf{p}+\rangle &= -2g\omega_p^{-1}\int d\mathbf{k}R\Big\{[\langle 0|\tau_+|1\rangle\langle 1|\tau_-|0\mathbf{p}+\rangle \\ &\quad -\langle 0|\tau_-|-1\rangle\langle 0|\tau_+|1\mathbf{p}+\rangle]\left[\frac{2gR\omega}{\omega^2 - \omega_p^2 - i\epsilon} - \frac{2gR\omega}{\omega^2}\right] \\ &\quad -\langle 0|\tau_-|-1\rangle\delta(\mathbf{k}-\mathbf{p})\Big\} \\ &= g\omega_p^{-1}R(\mathbf{p}) - 2g^4\omega_p^{-2}K_1\langle 0|\tau_3|0\mathbf{p}+\rangle[I(\omega_p) - I(0)],\end{aligned} \tag{47}$$

[7] These statements can also be justified directly from the equations of motion without recourse to the Tomonaga approximation—see Sec. IV.

[8] The *a posteriori* justification of assumptions concerning the relative magnitude of various terms is characteristic of most s.c. calculations (see reference 2).

[9] This corresponds to the fact that for large g the physical nucleon involves a large number of bound mesons and it is equally likely for the bare nucleon to be either a proton or a neutron.

[10] Like $\langle 0|\tau_3|0\rangle$, the term $\langle -1|\tau_3|-1\rangle$ is of order g^{-4}.

where

$$I(x)\equiv\int d\mathbf{k}\frac{2K^2\omega}{\omega^2-x^2-i\epsilon}=\int d\mathbf{k}\frac{\rho^2(\mathbf{k})}{\omega^2-x^2-i\epsilon}. \quad (48)$$

(For our choice of ρ,

$$I(\omega_p)=\tfrac{1}{2}\pi^{-2}\{M+\tfrac{1}{2}p\log[(M-p)(M+p)^{-1}]+\pi ip/2\}.) \quad (49)$$

Solving (47), we obtain

$$\langle 0|\tau_3|0\mathbf{p}+\rangle = gR(p)\omega_p[\omega_p{}^2+2g^4K_1\{I(\omega_p)-I(0)\}]^{-1}, \quad (50)$$

which in the s.c. limit gives

$$\langle 0|\tau_3|0\mathbf{p}+\rangle = R(p)\omega_p[2g^3K_1\{I(\omega_p)-I(0)\}]^{-1}. \quad (51)$$

Although $I(\omega_p)$ diverges for $M\to\infty$, the denominator of (51) remains finite, since

$$J(\omega_p)\equiv I(\omega_p)-I(0)=\omega_p{}^2\int d\mathbf{k}\frac{\rho^2(\mathbf{k})}{\omega^2(k^2-p^2-i\epsilon)} \quad (52)$$

is convergent. From (37) and (51) we have, finally,

$$\langle 0|\tau_+|1\mathbf{p}+\rangle=-R(p)[2gJ(\omega_p)]^{-1}, \quad (53)$$

so that the cross section (29) is

$$(d\sigma/d\Omega)_{\pi^+,\,n}=|2\pi^2\omega_pR^2(p)/J(\omega_p)|^2. \quad (54)$$

In the point source limit, $M\to\infty$, we have

$$J(\omega_p)\to(\mu+ip)/4\pi. \quad (55)$$

Also, with our choice (14) for the nucleon density,

$$R^2(p)=(16\pi^3\omega_p)^{-1} \quad (56)$$

so

$$\langle 0|\tau_+|1\mathbf{p}+\rangle\to-2\pi R(p)g^{-1}(\mu+ip)^{-1}, \quad (57)$$

and

$$d\sigma/d\Omega\to(4\omega_p{}^2)^{-1}, \quad (58)$$

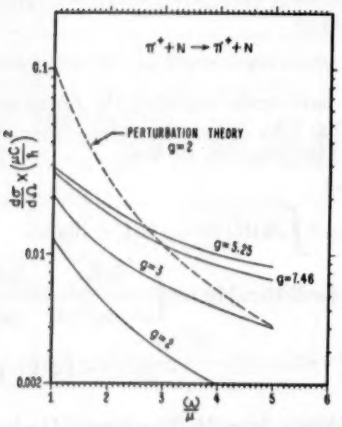

FIG. 5. Cross section *vs* total energy for π^+-neutron scattering with $g=2$, 3, 5.25, and 7.46. The result of lowest-order perturbation theory for $g=2$ is also shown for comparison.

in agreement with the usual s.c. theory.[2] The matrix elements for the other possible scattering processes—$\langle 1|\tau_+|2\mathbf{p}+\rangle$ for the π^+ proton scattering, $\langle 2|\tau_-|1\mathbf{p}+\rangle$ which corresponds to the charge-exchange π^+ neutron scattering $\pi^++n\to\pi^-+p^{++}$, etc.—can be found in the same way. They all give the correct cross section (58).

We have now demonstrated that our approximations I, II, and III leads to results for meson scattering which agree with both the perturbation and s.c. theories in the appropriate limits. The general nature of our procedure should by now be fairly clear, so we shall simply outline the derivation of the formulas for the cross sections in the general case (g arbitrary).

(c) General Case

In contrast to our procedure in (a) and (b), we must now retain in our equations *all* matrix elements which remain after assumptions I and II have been invoked. For instance, both of the terms on the right side of (3) must be retained for, as we have seen, one is important for small g, the other for large g, and we may expect them to be of comparable magnitude in the intermediate coupling region. In addition, assumption III now assumes its full importance, for while the necessary one-body matrix elements

$$\langle 0|\tau_+|1\rangle,\quad \langle 1|\tau_3|1\rangle,\quad \langle 1|\tau_+|2\rangle,\quad \text{and}\quad \langle 2|\tau_3|2\rangle$$

can be found analytically in the weak and strong coupling limits, for intermediate values of g they must be computed numerically from some solution (e.g., Tomonaga's) of the one-body problem. We also need to know the values of g at which the various excited isobars become stable. For instance, using the Tomonaga approximation we find that the isobars of charge 2 and -1 are stable only for $g>8.66$, while those of charge 3 and -2 are not stable for any value of g up to 15.

When $g<8.66$, so that $\beta=0$, (30) becomes

$$\langle 0|\tau_+|1\mathbf{p}+\rangle=-g\omega_p{}^{-1}\int d\mathbf{k}R\langle 0|\tau_3|0\rangle\langle 0|A+B^*|1\mathbf{p}+\rangle.$$

Using (28) and (43), we find

$$\langle 0|\tau_+|1\mathbf{p}+\rangle=-g\omega_p{}^{-1}\langle 0|\tau_3|0\rangle \times[R(p)+gI(\omega_p)\langle 0(\tau_+|1\mathbf{p}+)\rangle],$$

so that

$$\langle 0|\tau_+|1\mathbf{p}+\rangle=\frac{-gR(p)\langle 0|\tau_3|0\rangle}{\omega_p+g^2I(\omega_p)\langle 0|\tau_3|0\rangle}.$$

In the same way, we find

$$\langle 1|\tau_+|2\mathbf{p}+\rangle=\frac{gR(p)\langle 0|\tau_3|0\rangle}{\omega_p-g^2I(\omega_p)\langle 0|\tau_3|0\rangle}. \quad (59)$$

Thus, for $g<8.66$ the π^+ cross sections are

$$d\sigma/d\Omega=[4\pi|I(\omega_p)\pm g^{-2}\omega_p/\langle 0|\tau_3|0\rangle|]^{-2}, \quad (60)$$

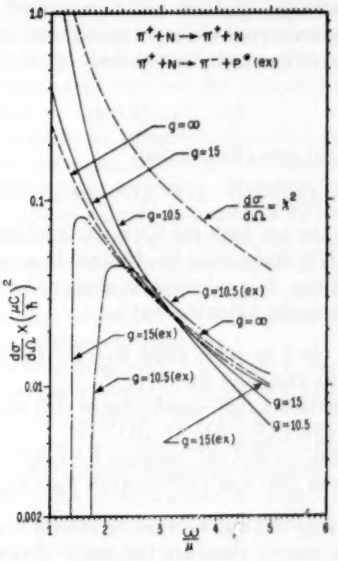

FIG. 6. Cross section *vs* total energy for π^+ neutron scattering with $g=10.5$ and 15. The charge-exchange cross section for the latter two coupling constants is labeled (ex). The s.c. theory result and the maximum S-wave cross section are also shown.

where the + sign is to be used for π^+ neutron, the − sign for π^+-proton scattering.

When $g>8.66$, the procedure is quite similar to that of section (b), although the algebra is slightly more complicated since we can no longer use (36) or neglect the isobar separation,

$$\Delta = E_2 - E_1. \tag{61}$$

The results are most easily expressed in terms of the simultaneous equations,

$$y(p) = -\frac{\langle 0|\tau_3|0\rangle \pm 2g^2 I(\Delta)|\langle 1|\tau_+|2\rangle|^2 z(p)}{\pm\omega_p g^{-2} + \langle 0|\tau_3|0\rangle I(\omega_p)},$$
$$z(p) = \frac{1+[I(\omega_p)-I(\Delta)]y(p)}{\omega_p \pm \Delta + C[I(\omega_p \pm \Delta) - I(0)] \times [\omega_p \pm \Delta \pm g^2\langle 2|\tau_3|2\rangle I(\omega_p \pm \Delta)]^{-1}}, \tag{62}$$

where

$$C = 2g^4 I(0)|\langle 0|\tau_+|1\rangle|^2.$$

If y_+ and z_+ denote the solutions obtained by using the upper sign everywhere in (62), then we have

$$\langle 0|\tau_+|1\mathbf{p}+\rangle = g^{-1}R(p)y_+(p),$$
$$\langle 0|\tau_3|0\mathbf{p}+\rangle = 2gR(p)\langle 1|\tau_+|2\rangle z_+(p), \tag{63}$$

while from the solutions y_-, z_- corresponding to the lower sign we find

$$\langle 1|\tau_+|2\mathbf{p}+\rangle = g^{-1}R(p)y_-(p), \tag{64}$$
$$\langle 2|\tau_3|2\mathbf{p}+\rangle = 2gR(p)\langle 2|\tau_-|1\rangle z_-(p). \tag{65}$$

Substituting (63) into (29) we obtain the ordinary π^+ neutron scattering cross section. If we replace $\langle 0|\tau_+|1\mathbf{p}+\rangle$ in (29) by $\langle 1|\tau_+|2\mathbf{p}+\rangle$ and use (64) we obtain the ordinary π^+ proton cross section. The matrix element $\langle 2|\tau_-|1\mathbf{p}+\rangle$ needed for the π^+ neutron exchange scattering can be obtained from (65) and the relation

$$\langle 2|\tau_-|1\mathbf{p}+\rangle = \frac{g^2 I(0)\langle 1|\tau_-|0\rangle\langle 2|\tau_3|2\mathbf{p}+\rangle}{\omega_p - \Delta - g^2\langle 2|\tau_3|2\rangle I(\omega_p - \Delta)}, \tag{66}$$

which we get from the τ_- equation of motion. Since this charge-exchange scattering, $\pi^+ + n \to \pi^- + p^{++}$, is an inelastic process, the cross section is given by

$$d\sigma/d\Omega = |4\pi^2\omega_p g R\langle 2|\tau_-|1\mathbf{p}+\rangle|^2 p'/p, \tag{65}$$

where $p' \equiv [(\omega-\Delta)^2-\mu^2]^{\frac{1}{2}}$ is the momentum of the outgoing meson.

In Figs. 5 through 8 the results of these calculations are presented in the form of curves showing $d\sigma/d\Omega$ [in units $(\hbar/\mu c)^2$] *vs* ω/μ for several values of g. A semilog plot has been used so that all curves could be drawn to the same scale. In Figs. 5 and 7, the ordinary π^+-neutron and π^+-proton cross sections are given for $g=2$, 3, 5.25, and 7.46. The cross sections for higher g values are given in Figs. 6 and 8. Since the charge-2 isobar is stable for $g>8.66$ (see Fig. 2), the π^+, neutron charge-exchange cross sections are also shown for $g=10.5$ for $g=15$. (The charge-3 isobar is not stable for the range of coupling constants which we used and so the π^+, proton charge-exchange scattering is not considered.) For $g=5.25$, 7.46, 10.5, and 15 the one-body matrix elements needed in the scattering calculation,

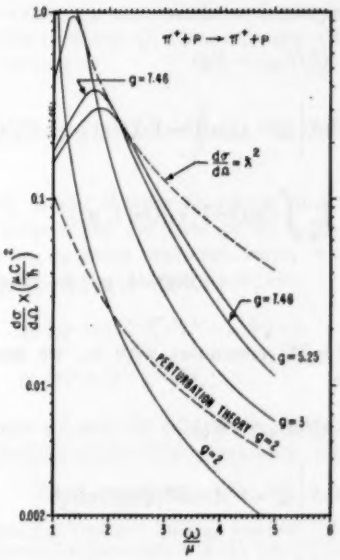

FIG. 7. Cross section *vs* total energy for π^+-proton scattering with $g=2$, 3, 5.25, and 7.46. The result of perturbation theory for $g=2$ and the maximum S-wave cross section are also shown.

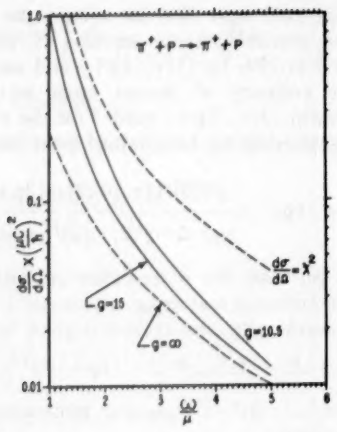

FIG. 8. Cross section for π^+-proton scattering with $g=10.5$ and 15. The s.c. theory result and the maximum S-wave cross section are also shown.

$\langle\langle 0|\tau_+|1\rangle, \langle 0|\tau_3|0\rangle = -\langle 1|\tau_3|1\rangle, \langle 1|\tau_+|2\rangle$, and $\langle 2|\tau_3|2\rangle\rangle$, have been found from the numerical solution of the Tomonaga problem described in Sec. 2. These were also used to draw the curves of Fig. 1, the matrix elements for other choices of g then being obtained from Fig. 1.

4. THE S.C. ISOBAR SEPARATION

It is of interest to note that once the matrix elements for the scattering cross section have been found, the isobar separation can be determined by similar techniques. Here we shall carry this through for the s.c. limit where an analytic solution is possible. From (20) and assumption I we obtain

$$\langle Q-1|\tau_+|Q\rangle(E_{Q-1}-E_Q)$$
$$=g\int d\mathbf{k}R\Big\{\langle Q-1|\tau_3|Q-1\rangle\langle Q-1|A+B^*|Q\rangle$$
$$+\sum_{j=\pm}\int d\mathbf{p}\langle Q-1|\tau_3|Q-1,\,\mathbf{p}j\rangle$$
$$\times\langle Q-1,\,\mathbf{p}j|A+B^*|Q\rangle\Big\}. \quad (68)$$

Since $(A+B^*)$ commutes with τ_3, we may equally well write

$$\langle Q-1|\tau_+|Q\rangle(E_{Q-1}-E_Q)$$
$$=g\int d\mathbf{k}R\Big\{\langle Q-1|A+B^*|Q\rangle\langle Q|\tau_3|Q\rangle$$
$$+\sum_{j=\pm}\int d\mathbf{p}\langle Q-1|A+B^*|Q\mathbf{p}j\rangle\langle Q\mathbf{p}j|\tau_3|Q\rangle\Big\}. \quad (69)$$

If the scattering problem has been solved, then the only unknown matrix elements in (68) and (69) are the isobar separation and the one-body matrix elements. Now[9]

$$\langle Q-1|\tau_+|Q\rangle=\tfrac{1}{2},$$

so using (18) and (19), we find

$$\langle Q-1|A|Q\rangle=\langle Q-1|B^*|Q\rangle^*=\tfrac{1}{2}gR\omega^{-1}+O(g^{-1}).$$

However, the s.c. limit for $\langle Q|\tau_3|Q\rangle$ is of much higher order in $(1/g)$ and cannot be obtained from such simple considerations. We calculate it along with the isobar separation in the following way:

(i) Set $Q=1$ in (68). Since $E_1=E_0$, the left side is zero and we can solve for $\langle 0|\tau_3|0\rangle$.

(ii) Equate the right-hand sides of (68) and (69) and solve for $\langle Q|\tau_3|Q\rangle-\langle Q-1|\tau_3|Q-1\rangle$.

(iii) From (i) and (ii) compute $\langle Q|\tau_3|Q\rangle$.

(iv) From (69) and (iii) compute E_Q-E_{Q-1}.

In carrying this out we must be careful to use for the scattering matrix elements the result obtained before letting $M\to\infty$, since in (68) and (69) $|\mathbf{p}|$ ranges from O to M. For instance, we must use (53) for $\langle 0|\tau_+|1\mathbf{p}+\rangle$ and not the $M\to\infty$ form (57). The limit $M\to\infty$ must be taken only *after* the integrations in (68) and (69) have been performed.

The result of step (i) is

$$\langle 0|\tau_3|0\rangle=\tfrac{1}{2}(g^4K_1)^{-1}\int d\mathbf{p}p^2(\mathbf{p})\,|J(\omega_p)|^{-2}, \quad (70)$$

where $J(\omega_p)$ is defined by (52). The integral (70) has been evaluated by Kaufman.[2] Using his result we have

$$\langle 1|\tau_3|1\rangle=-(4g^4K_1)^{-1}[K_3^{-1}-\tfrac{1}{2}K_1^{-2}]$$
$$\underset{M\to\infty}{\to}-(4g^4K_1K_3)^{-1}, \quad (71)$$

where K_n is given by (38).

From (ii) and (iii) we then find

$$\langle Q|\tau_3|Q\rangle=(1-2Q)(4g^4K_1K_3)^{-1}, \quad (72)$$

so that

$$E_Q-E_{Q-1}=(Q-1)/g^2K_3, \quad (73)$$

and

$$E_Q=(Q-\tfrac{1}{2})^2(2g^2K_3)^{-1}+\text{const.} \quad (74)$$

This is in agreement with conventional s.c. theory.[2]

5. DISCUSSION OF METHOD AND RESULTS

In the preceding sections we have seen that our approximate method of solving the matrix equations of motion is correct in both the weak and strong coupling limits. To establish its validity in the intermediate region, the approximations of Sec. 3 could be investigated by an iterative procedure in which one-body matrix elements and those of the form $\langle Q|C|Q'$, $\mathbf{p}j,\,\mathbf{p}'j'\rangle$ or $\langle Q\mathbf{p}j|C|Q'\mathbf{p}'j'\rangle$ are calculated from the

equations of motion, using for $\langle Q'|C|Q\mathbf{p}j\rangle$, etc., the values found previously. Since the latter are only known numerically in the intermediate region, this calculation is fairly complicated and will be discussed in a subsequent paper.

In some respects our procedure resembles the Tamm-Dancoff approximation, since states with more than one incident meson are neglected. However, the total number of mesons allowed is considerably larger than in most Tamm-Dancoff calculations, for no limitation is placed on the number of mesons bound to the nucleon. Any such restriction would, in fact, preclude agreement with s.c. theory, where the average number of bound mesons is approximately $g^2K_2/2$.

As can be seen from Figs. 5 through 8, the shape of the cross section *vs* energy curves for intermediate values of g is quite different from the $d\sigma/\Omega \propto 1/\omega^2$ which characterizes the two limiting cases. The general character of the curves suggests "resonance" with a virtual isobar level. In such a case, we expect the phase shift[11] to go through 90° giving a cross section

$$d\sigma/d\Omega = p^{-2} = \lambda^2. \tag{75}$$

For values of g smaller than 8.66 the π^+-proton cross section (Fig. 7) does indeed attain this value, while the π^+-neutron cross section (Fig. 5) does not. This is consistent with the resonance picture, for in the proton case the total charge is 2, so there could be a resonance with a virtual isobar state of charge 2. However, there is no low-lying virtual state of charge 1 with which the π^+-neutron scattering could resonate. For $g>8.66$ the π^+-proton scattering curves (Fig. 8) show no resonance effects. This is consistent with the fact that the lowest-lying charge-2 isobar is stable and so its energy is too low to allow any resonance with the scattering state.

As g increases from about 6 to 8.66, the value of ω for which $d\sigma/d\Omega=\lambda^2$ decreases. This lends further support to the resonance idea, since the excitation of the virtual level would also decrease with increasing g. Unfortunately, between $g\approx 2.2$ and $g=6$ the "resonance" energy increases with increasing g. Thus the interpretation in terms of a simple resonance with a virtual isobar is less successful for these smaller values of g.

The essential test of any theory—comparison with experiment—cannot be applied to our results since we have used scalar mesons. Moreover, since the scattering problem for intermediate values of g has not been extensively studied heretofore, it is difficult to say whether our results are "reasonable." This question will be resolved, however, by a comparison of the experimental pion-nucleon scattering data with the results of the calculations for pseudoscalar mesons which are now in progress.

One of the most unpleasant consequences of our static approximation for the nucleon is the necessity for a cutoff. Since this cannot be avoided in a nonrelativistic treatment, we can simply hope that it is not very important for the low-energy mesons. Preliminary calculations indicate that the results are not very sensitive to the choice of cut off. Moreover, a generalization of the methods described in this paper to include recoil and relativistic effects is now being investigated. If a renormalization procedure can be found, it will be possible to eliminate the cutoff altogether. In this connection, it may be noted that even in its present, static form this matrix formulation has the advantage that only energy *differences*, and not the energies themselves, appear in the equations.

We wish to express our very sincere appreciation to Mr. James Baker and Mrs. Joan Lafon for their excellent computational work on both the scattering and the one-body problems, and to Mr. Robert Oeder and Mr. Lawrence Lasnik who carried out the solution for the one-body state vectors on the IBM Card Programmed Calculator at the University of California Radiation Laboratory, Livermore. We are also indebted to Dr. J. Lepore for many interesting discussions of the Tomonaga approximation and the strong coupling theory.

APPENDIX I. VARIATIONAL CALCULATION OF MESON SCATTERING

The problem of meson scattering can also be treated by a modification of the Hulthén variational principle.[12,13] For the state vector describing the scattering of a positive meson of initial momentum $\mathbf{p}$ by a proton, we make the assumption

$$\psi = a_*^*|1\rangle + b_*^*|3\rangle + \eta|2\rangle, \tag{A.1}$$

where $|Q\rangle$ is again the state vector corresponding to the nucleon isobar of charge Q. The scattering operators a_* and b_* are defined by

$$a_* = \int d\mathbf{k}\chi_+^*(\mathbf{k})A(\mathbf{k}), \quad b_* = \int d\mathbf{k}\chi_-^*(\mathbf{k})B(\mathbf{k}), \tag{A.2}$$

where $\chi_+(\mathbf{k})$ is the Fourier transform of a function which for large r has the form of an incident plane wave plus an outgoing scattered wave, while χ_- is asymptotically just a scattered wave; *viz.*,

$$\begin{aligned} &\chi_+(\mathbf{x}) \to (2\pi)^{-\frac{3}{2}}\left[e^{i\mathbf{p}\cdot\mathbf{x}} + \alpha e^{ipr}/r\right], \\ &\chi_-(\mathbf{x}) \to \alpha' e^{ipr}/r(2\pi)^{\frac{3}{2}}. \end{aligned} \tag{A.3}$$

The functions $\chi_\pm$ and the constant η are to be determined by making $\langle\psi|E-H|\psi\rangle$ stationary, with

$$E = E_1 + \omega_p = E_1 + (p^2+\mu^2)^{\frac{1}{2}}. \tag{A.4}$$

[11] Of course only S waves are scattered in this scalar theory.

[12] L. Hulthén, Kgl. Fysiograf. Sällskap. Lund Förh. **14**, 1 (1944).

[13] This approach has been used by T. D. Lee and R. Christian in their work on the Tomonaga approximation, Phys. Rev. **94**, 1760 (1954). We wish to thank these authors for informing us of their work prior to its publication.

Before carrying out this variation, we shall make a few remarks concerning the choice of the assumption (A.1). The first term in (A.1) corresponds to the ordinary π^+, proton scattering while the second term takes account of the charge-exchange scattering which can occur when the coupling is sufficiently strong. (Since we are primarily interested in the s.c. limit for this method we shall consider first the case in which g is large enough to make the $Q=2$ and $Q=3$ isobars stable.) The role of the third term can be appreciated if the variation with respect to η is carried out. We obtain

$$(\delta\eta^*)\langle 2|\psi\rangle=0,$$

which shows that the value of η simply makes ψ orthogonal to ψ_2,

$$\eta=-\langle 2|a_s^*|1\rangle-\langle 2|b_s^*|3\rangle. \tag{A.5}$$

The importance of including this term may be understood from the following:

1. The scattering problem for a neutral scalar field, which is closely related to the s.c. limit of charged theory, may be treated by an assumption analogous to (A.1). (Of course, it can also be solved exactly.) If a term corresponding to the $\eta|2\rangle$ of (A.1) is included, the correct answer, $d\sigma/d\Omega=0$, is obtained. However, if this term is omitted, the cross section is no longer zero. Instead, we find

$$(d\sigma/d\Omega)_{\text{neutral}}=|\omega_p/\pi-(p/\pi)\times\log(p+\omega_p)/\mu+\mu/2+ip|^{-2}. \tag{A.6}$$

2. As shown below, the charged meson scattering may be calculated by approximating the $|Q\rangle$ in (A.1) by the corresponding Tomonaga state vector, F_Q. If we consider the s.c. limit of the H^T problem and retain only the leading-order terms in g, then we obtain $d\sigma/d\Omega=0$, indicating that higher-order corrections to the Tomonaga state vector must be considered. If, however, the $\eta|2\rangle$ term is omitted, then the cross section turns out to be just $\frac{1}{4}$ of $(d\sigma/d\Omega)_{\text{neutral}}$ which does not agree with the correct s.c. result (59). This discrepancy has been pointed out by Christian and Lee.[13] In this case it is clear that higher-order corrections to the Tomonaga approximation could not remove this lack of agreement.

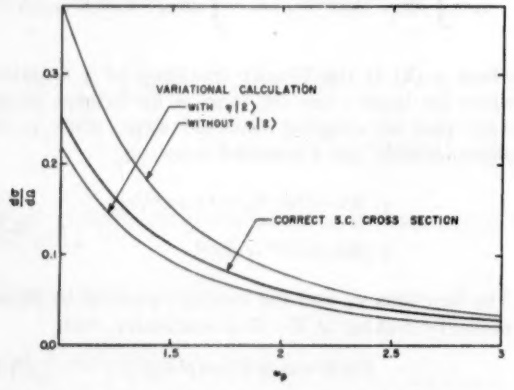

FIG. 9. S.C. limit of the variational scattering calculation described in Appendix I. The lower curve is a plot of (A.14) while the upper curve shows the result obtained if the $\eta|2\rangle$ term is omitted from the assumption (A.1). The s.c. theory (see reference 2) cross section is also shown for comparison.

A final point concerning the assumption (A.1) is that we shall consider only the case $\mu\leqslant\omega_p\leqslant 2\mu$. At higher energies, additional terms would of course be needed in (A.1) to take account of meson production, etc.

Returning now to the variational problem,

$$\delta\langle\psi|E-H|\psi\rangle=0,$$

we see that variation with respect to χ_+^* gives

$$\int d\mathbf{k}\delta\chi_+^*(\mathbf{k})\langle 1|A(\mathbf{k})[E-H]|\psi\rangle=0.$$

Commuting $A(\mathbf{k})$ with $(E-H)$ and taking account of (15) and (A.4) we find

$$\omega_p\langle 1|A(\mathbf{k})|\psi\rangle-\langle 1|\omega A(\mathbf{k})-g\tau_+R(\mathbf{k})|\psi\rangle=0,$$

which by manipulations similar to those used in Sec. 2, can be reduced to

$$\begin{aligned}(\omega_p-\omega)\chi_+&+(\omega_p-\omega)\Big\{\langle F_1|a_1^*a_1|F_1\rangle\phi_{1+}\int\chi_+\phi_{1+}\\&+\langle F_1|b_1^*a_3|F_3\rangle\phi_{3+}\int\chi_-\phi_{1-}+\eta\langle F_1|a_2|F_2\rangle\phi_{2+}\Big\}\\&+gR\Big\{\langle F_1|a_1^*\tau_+|F_1\rangle\int\chi_+\phi_{1+}\\&+\langle F_1|b_1^*\tau_+|F_3\rangle\int\chi_-\phi_{1-}+\eta\langle F_1|\tau_+|F_2\rangle\Big\}=0,\end{aligned} \tag{A.7}$$

where, according to (A.5),

$$\eta=-\langle F_2|a_2^*|F_1\rangle\int\chi_+\phi_{2+}-\langle F_2|b_2^*|F_3\rangle\int\chi_-\phi_{2-}. \tag{A.8}$$

Here we have made the approximation of replacing $|Q\rangle$ by the corresponding eigenstate, F_Q, of $H_Q{}^T$. The integral equation for χ_- can be obtained from (A.7) by the substitutions

$$a\leftrightarrow b,$$
$$1\leftrightarrow 3 \text{ (in all subscripts)},$$
$$\omega_p\rightarrow\omega_p-\Delta_{13},$$

where $\Delta_{13}=E_3-E_1$.

These coupled integral equations for χ_+ and χ_- can be solved once the Tomonaga matrix elements appearing in (A.7) and (A.8) are known. Using Tomonaga's s.c. solution[1] of (8), we have evaluated these

matrix elements in the s.c. limit. Table I shows the leading term, and also the first (i.e., $1/g^2$) correction thereto, for all of the relevant matrix elements. (The $\lambda_\pm$ calculated from (13), which are also listed for convenience, agree with the expressions given by Tomonaga,[1] who obtained them in a somewhat different way.)

From Table I, we see at once that the right side of (A.7) contains terms of order g^2, g^0, $\cdots$. However, upon substituting the various matrix elements into (A.7) we find that *all terms of order g^2 cancel*. Without the g^{-2} corrections to the matrix elements there would be *no scattering*. (As pointed out above, this cancellation does not occur if the $\eta|2\rangle$ term is omitted from (A.1).) With the aid of Eq. (12) and Table I we obtain

$$(\omega-\omega_p)\chi_+(\mathbf{k})=-(\omega-\omega_p+\Delta_{13})\chi_-(\mathbf{k})=J_1(\mathbf{k})$$
$$\equiv\frac{R(\mathbf{k})}{4\omega}\left\{\left[\frac{1}{K_3}+\frac{\omega_p K_4}{2(K_3)^2}-\frac{\omega_p}{2K_2}\right]\int\frac{R\chi}{\omega}-\frac{\omega_p}{K_3}\int\frac{R\chi}{\omega^2}\right\}$$
$$-\frac{R(\mathbf{k})\omega_p}{4\omega^2K_3}\int\frac{R\chi}{\omega}+\frac{R(\mathbf{k})}{8K_2}\int\frac{R\chi}{\omega},\quad\text{(A.9)}$$

where $\chi\equiv\chi_+-\chi_-$. Since we are concerned with terms of order g^0, we may drop Δ_{13} which is of order g^{-2}. Taking the sum and difference of the χ_+ and χ_- equations we find two elementary uncoupled equations:

$$(\omega-\omega_p)(\chi_++\chi_-)=0,\quad\text{(A.10)}$$
$$(\omega-\omega_p)\chi=2J_1.\quad\text{(A.11)}$$

According to (A.10),

$$\chi_+(\mathbf{k})+\chi_-(\mathbf{k})=\delta(\mathbf{k}-\mathbf{p}),$$

i.e., χ_+ and $(-\chi_-)$ can differ only by a plane wave so that the direct and charge-exchange scattering cross sections are equal, in agreement with s.c. theory. From (A.11) it is easy to obtain a solution of the form

$$\chi(\mathbf{k})=\delta(\mathbf{k}-\mathbf{p})-\frac{f(\omega)}{\omega-\omega_p-i\epsilon},\quad\text{(A.12)}$$

where $f(\omega)$ can be found explicitly by solving a pair of algebraic equations. In the limit of a point source, $\rho(\mathbf{x})\to\delta(\mathbf{x})$, the scattering amplitude $f(\omega_p)$ has the value

$$f(\omega_p)=[R(\mathbf{p})]^2\omega_p^{-2}[K_3+C(\omega_p)]^{-1},$$

where

$$C(\omega_p)\equiv\int d\mathbf{k}\frac{R^2(\mathbf{k})}{\omega^2(\omega-\omega_p-i\epsilon)}=(4\pi^2\omega_p^2)^{-1}$$
$$\times[\omega_p-p\log[(p+\omega_p)/\mu]+\pi\mu/2+\pi ip].\quad\text{(A.13)}$$

Consequently, both the ordinary and charge-exchange cross sections have the value

$$\frac{d\sigma}{d\Omega}=\frac{1}{4}\left|\frac{\omega_p^2}{4\mu}+\frac{\omega_p}{\pi}-\frac{p}{\pi}\log\frac{p+\omega_p}{\mu}+\frac{\mu}{2}+ip\right|^{-2}.\quad\text{(A.14)}$$

TABLE I. Matrix elements for the single-nucleon problem as computed from the s.c. limit of the Tomonaga approximation.

$$N_{Q+}\equiv\langle F_Q|a_Q^*a_Q|F_Q\rangle=\tfrac{1}{2}V^2[1+2(Q-1)V^{-2}]$$
$$N_{Q-}\equiv\langle F_Q|b_Q^*b_Q|F_Q\rangle=\tfrac{1}{2}V^2[1-2QV^{-2}]$$
$$M_{Q+}\equiv\langle F_Q|a_Q\tau_-|F_Q\rangle=\tfrac{1}{2}V[1+(Q-\tfrac{1}{2})V^{-2}]$$
$$M_{Q-}\equiv\langle F_Q|b_Q\tau_+|F_Q\rangle=\tfrac{1}{2}V[1-(Q-\tfrac{1}{2})V^{-2}]$$
$$\langle F_1|b_1^*a_3|F_3\rangle=\tfrac{1}{2}V^2(1+V^{-2})\exp(LV^{-2})$$
$$\langle F_1|a_2|F_2\rangle=\tfrac{1}{2}V(1+V^{-2})\exp(\tfrac{1}{2}LV^{-2})$$
$$\langle F_3|b_2|F_2\rangle=\tfrac{1}{2}V(1+2V^{-2})\exp(\tfrac{1}{2}LV^{-2})$$
$$\langle F_1|b_1^*\tau_+|F_3\rangle=\tfrac{1}{2}V(1-\tfrac{3}{2}V^{-2})\exp(LV^{-2})$$
$$\langle F_1|\tau_+|F_2\rangle=\langle F_2|\tau_+|F_3\rangle=\tfrac{1}{2}\exp(\tfrac{1}{2}LV^{-2})$$
$$\langle F_3|a_3^*\tau_-|F_1\rangle=\tfrac{1}{2}V(1+\tfrac{3}{2}V^{-2})\exp(LV^{-2})$$
$$\lambda_{Q\pm}=[\pm(Q-\tfrac{1}{2})-K_1K_3(K_2)^{-2}]/g^2K_3$$

where

$$V=g(K_2)^{\frac{1}{2}}\{1+g^{-2}[1-K_1K_3(K_2)^{-2}](K_2)^{-1}\},$$
$$L=1-K_2K_4(K_3)^{-2},$$
$$K_n=\int d\mathbf{k}R^2(\mathbf{k})\omega^{-n}.$$

In Fig. 9 we have plotted the s.c. limit of $d\sigma/d\Omega$ as a function of incident meson energy. The solid curve is the correct s.c. result, (59). The one below it represents Eq. (A.14) which is seen to be correct only in order of magnitude. Lest we be tempted to accept this as a partial fulfillment of condition (2°) of the introduction, we have plotted in Fig. 9 also $\frac{1}{4}(d\sigma/d\Omega)_{\text{neutral}}$ as given by (A.6), i.e., the result obtained by omitting the $\eta|2\rangle$ term from the assumption (A.1). It seems to us that this spurious neutral scalar cross section has very little to do with the actual charged scalar problem and yet it, too, shows what might be called order of magnitude agreement with the correct charged scalar s.c. result. We conclude from this that nothing less than exact agreement with the s.c. answer can be accepted as fulfillment of condition (2°).

Finally, in the weak coupling limit the isobars of charge 2 and 3 do not exist so that no question concerning the $\eta|2\rangle$ term arises. The assumption (A.1) then simplifies to

$$\psi=a_+^*|1\rangle,\quad\text{(A.15)}$$

and an analysis like that which led to (21) gives

$$(\omega_p-\omega)\left[\chi_++N_{1+}\phi_{1+}\int d\mathbf{k}\chi_+\phi_{1+}\right]$$
$$+gRM_{1+}\int d\mathbf{k}\chi_+\phi_{1+}=0.\quad\text{(A.16)}$$

As Christian and Lee[13] have shown, the cross section obtained from (A.16) for small g agrees with that given by ordinary perturbation theory, so that condition (1°) is satisfied. For intermediate values of g the cross section can be found numerically by using for the various Tomonaga matrix elements required in (A.7) or (A.16) the values computed from a numerical solution

of the one-body problem, and so this method also satisfies condition (3°).

So far we have discussed only the π^+ proton scattering. However, the problem of π^+ neutron can be treated in an exactly analogous fashion. The appropriate assumption there is

$$\psi = a_s^*|0\rangle + b_s^*|2\rangle + \eta'|1\rangle$$

for large g, or

$$\psi = a_s^*|0\rangle + \eta'|1\rangle$$

for small g. In this case, the $\eta'|1\rangle$ term should be included for all values of g, since $|1\rangle$ (real proton) and $|0\rangle$ (real neutron) are always stable. Again, conditions (1°) and (3°) are satisfied but not (2°).

PHYSICAL REVIEW VOLUME 94, NUMBER 6 JUNE 15, 1954

Renormalization of Meson Theory with a Fixed Extended Source*

GEOFFREY F. CHEW
Department of Physics, University of Illinois, Urbana, Illinois, and Brookhaven National Laboratory, Upton, New York
(Received January 18, 1954)

It is shown that the procedures for mass and charge renormalization developed by Dyson, Ward, and others for a covariant local field theory can be applied in the static or fixed source approximation where the interaction is nonlocal. Reasons are given to show that, although charge renormalization is not necessary in this case because the theory is not divergent, it is nevertheless a very sensible procedure.

INTRODUCTION

A WELL-DEFINED and often discussed form of meson theory treats the nucleon as an infinitely heavy source of pions and completely ignores recoil effects.[1] This form of the theory, sometimes called the static approximation, cannot be reached from conventional local pseudoscalar theory by a straightforward limiting process of setting $M = \infty$. Even after renormalization, integrals occurring in the local theory will diverge for an infinite nucleon mass. In the static approximation, convergence is achieved by inserting a cut-off factor, but it has often been pointed out that this factor cannot represent simply a damping due to nucleon recoil.[2] Nevertheless, there are at least two reasons to justify an examination of the static approximation: (1) Mathematically it is much simpler than the relativistic case and can yield a qualitative understanding of many important general features of field theory. (2) A number of experiments suggest that the actual damping of high-energy virtual effects is stronger than that produced by nucleon recoil alone in the local theory.[3] Thus it is possible that in some sense the correct and complete theory will be nonlocal. For example, if three fundamental fields rather than two are required, an approximate theory for the pion-nucleon interaction which does not specifically introduce the third field would have to be nonlocal. If this is the case the cut-off factor in the static approximation, which is equivalent to "spreading out" the region of the pion-nucleon interaction in space, may have a real physical significance.

The main interest in the static approximation thus far has been for the case of strong or intermediate strength coupling, where the relativistic theory has defied attempts at solution. No discussion has heretofore been given of the possibility of renormalizing the static approximation because the theory is finite without charge renormalization and the mass of the nucleon does not appear explicitly. Actually, the identification of self-energies *must* always be done in any field theory and has been done in past treatments of the static approximation. The point is merely that words other than "mass renormalization" have been used to describe the process. However, the technique of mesonic *charge* renormalization has up to now been stated only for a covariant local theory[4,5] and it is the purpose of this paper to show that the same methods can be applied to the static approximation.

The result of renormalizing the static approximation is not to render an infinite theory finite. The theory is finite before and after renormalization. However, renormalization eliminates many unobservable high-frequency effects and shows that observable quantities are much less "cut-off dependent" than is often thought. Also the renormalized coupling constant turns out to be substantially smaller than the original one, so that now perturbation methods become possible. Another way of describing the situation is to say that one has divided the infinite series given by perturbation theory

* This research was supported by the U. S. Office of Naval Research and the U. S. Atomic Energy Commission.

[1] See, for example, W. Pauli, *Meson Theory of Nuclear Forces* (Interscience Publishers, Inc., New York, 1946).

[2] The point here is that nucleon recoil can damp out momenta much larger than M, if M is the nucleon rest mass, but momenta of the order of M will remain very important. Thus a nonrelativistic approximation to a local pseudoscalar theory is impossible.

[3] J. S. Blair and G. F. Chew, Ann. Rev. Nuc. Sci. **2**, 163 (1953).

[4] F. J. Dyson, Phys. Rev. **75**, 1736 (1949).

[5] J. C. Ward, Proc. Phys. Soc. (London) **A64**, 54 (1951).

into two subseries, one of which converges much more rapidly than the other. The slowly converging series has been summed completely and the net result shown to be equivalent to reducing the value of the coupling constant appearing in the more rapidly converging series.

FORMULATION OF THE STATIC APPROXIMATION

With a pseudoscalar pion field, linearly and symmetrically coupled to the nucleon source, the interaction energy is

$$\mathcal{H}=(4\pi)^{\frac{1}{2}}\frac{f}{\mu}\sum_{\lambda=1}^{3}\tau_\lambda\int d\tau\rho(\mathbf{r})\boldsymbol{\sigma}\cdot\boldsymbol{\nabla}\varphi_\lambda(\mathbf{r}), \qquad (1)$$

where $\boldsymbol{\sigma}$ and $\boldsymbol{\tau}$ are the Pauli spin and isotopic spin matrices, φ_λ is the pion field, and $\rho(\mathbf{r})$ is the source distribution function. We shall make our discussion in terms of the specific interaction form (1), but it will become apparent that the only essential feature of (1) is the linearity in φ, which means that $\mathcal{H}$ annihilates or creates pions *one at a time*.

Suppose that we begin by thinking in terms of a conventional perturbation approach. That is to say, we imagine that all transition matrix elements are expanded in powers of the interaction energy $\mathcal{H}$. There will then be a one-to-one correspondence between the terms in this series and diagrams to be drawn according to the following rules: (1) A single solid line running upward (time runs upward) denotes the nucleon. Unlike the nucleon lines in a Feynman diagram,[6] the nucleon line here never turns around, since pair formation is excluded. (2) The pions are denoted by dotted lines which can begin (creation) or end (annihilation) at points along the nucleon line. Dotted lines entering the diagram from below correspond to free pions in the initial state, while dotted lines leaving at the top correspond to free pions in the final state. A moment's thought shows that the pion lines also only move upward (forward in time), and for a virtual pion, creation always precedes annihilation. This, again, is a feature not present in Feynman diagrams, where all time orderings of the vertices are understood.

For purposes of orientation, let us consider a particular fourth-order diagram, Fig. 1a, which occurs in the problem of pion-nucleon scattering. According to the well-known formula of conventional perturbation theory, this diagram corresponds to the following term in the expansion of the transition matrix:

$$\frac{\mathcal{H}_{fn}\mathcal{H}_{nm}\mathcal{H}_{ml}\mathcal{H}_{li}}{(E_i-E_n)(E_i-E_m)(E_i-E_l)}, \qquad (2)$$

where the state i contains *one* pion of momentum $\mathbf{k}_i$, the state l contains two pions, one of momentum $\mathbf{k}_i$ and one of momentum $\mathbf{k}$, the state m contains *one* pion of momentum $\mathbf{k}$, and so on. It is clear that we are

[6] R. Feynman, Phys. Rev. **76**, 749 (1949).

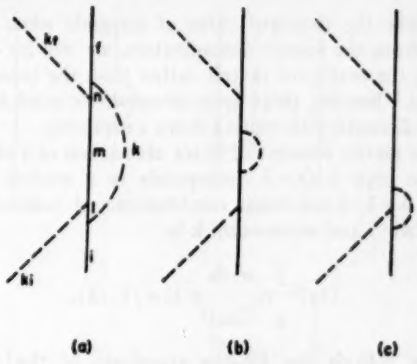

FIG. 1. Some typical diagrams occurring in the pion-nucleon scattering problem.

using the diagram purely as a counting device, to keep track of all possible intermediate states. For each vertex one has a matrix element of $\mathcal{H}$ corresponding to the emission or absorption of a pion. For each segment of the nucleon line between vertices we have an energy denominator.

It is legitimate to think of the energy denominators as propagation functions in a sense very similar to that of Feynman. Let us introduce the function

$$S(E)=1/(E+i\epsilon), \qquad (3)$$

where E is defined as the net energy which the nucleon has "absorbed" from the various pions which it has created or annihilated. E is zero for a "real" nucleon at the beginning or end of a diagram but for intermediate virtual nucleon states may be either positive or negative, to be calculated as if energy were conserved at each vertex. It follows that E is exactly the conventional energy denominator associated with the nucleon line in question.

It has been pointed out[7] that the simple expansion of which (2) is a sample term, is correct, strictly speaking, only in the absence of self-energies. It can easily be shown, however, that the correct expansion is obtained merely by adding the self-energy into each energy denominator.[8] In our problem, therefore, we should define the argument E of the nucleon propagation function as the *total* nucleon energy, including the self-energy. For "real" nucleons, we now have $E=E_S$, where E_S is the self-energy. Later E_S will be removed by a renormalization procedure.

The quantity ϵ, appearing in (3), is an infinitesimal real positive number which is to approach zero after sums over intermediate virtual states are performed. As usual, ϵ guarantees that the proper boundary conditions are satisfied by the transition matrix. If we omit ϵ

[7] M. Gell-Mann and M. L. Goldberger, Phys. Rev. **91**, 398 (1953).

[8] This rule ignores "end effects," that is, terms corresponding to the self-energy acting as a perturbation either at the beginning or the end of a process. It is well known, however, that conventional charge renormalization causes these effects to cancel out.

and take the principal value of integrals when poles arise from the energy denominators, we will be calculating the reactance matrix rather than the transition matrix.[9] Bearing these facts in mind, we shall henceforth dispense with writing down ϵ explicitly.

The matrix element of $\mathcal{H}$ for absorption of a pion of charge type λ ($\lambda=3$ corresponds to a neutral pion, while $\lambda=1, 2$ are linear combinations of positive and negative[10]) and momentum $\mathbf{k}$ is

$$(4\pi)^{\frac{1}{2}}\frac{f}{\mu}\tau_\lambda\frac{\boldsymbol{\sigma}\cdot i\mathbf{k}}{(2\omega_k)^{\frac{1}{2}}}v(k)=fV_\lambda(\mathbf{k}), \tag{4}$$

where $v(k)$ is the Fourier transform of the source function $\rho(r)$.[11] Conventionally, $\int\rho(r)d\mathbf{r}$ is normalized to unity, so that $v(0)=1$. The corresponding creation operator is the complex conjugate of (4). Thus we may write out (2) as follows, if the initial pion is in the state i, the intermediate pion in the state j, and the final pion in the state f:

$$f^4\sum_j V_fS(E_s+\omega_i-\omega_j-\omega_f)V_j^*S(E_s+\omega_i-\omega_j)\times V_iS(E_s-\omega_j)V_j^*. \tag{2'}$$

Comparing (2') to Feynman's formalism,[6] note that we have no propagation function for the pions. Actually one could perfectly well introduce a pion propagation function, but, since all lines move forward in time, it is possible immediately to do the integrals over pion energy and get only a residue at the *positive* value, $\omega_k=+(k^2+\mu^2)^{\frac{1}{2}}$. The factor, $1/2\omega_k$, which occurs in $|V_k|^2$ is precisely this residue. The concept of a *nucleon* propagation function is useful here because many of the renormalization effects will be identified as radiative modifications of the function $S(E)$. There are no modifications of the *pion* propagation function in the static approximation, however, since there are no nucleon pairs.

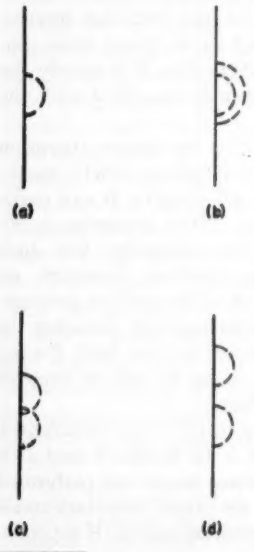

FIG. 2. Some diagrams contributing to $S'(E)$, the modified nucleon propagation function.

People familiar with Dyson's approach[4] will now see how the corresponding idea works here. We have two primary quantities, the propagation function $S(E)$ and the vertex operator V_j. By using diagrams we determine how to combine these quantities to form all the possible terms in the expansion of the transition matrix. One is next led to the notion of reducible and irreducible parts of diagrams. That is to say, certain combinations of lines and vertices can be thought of as merely producing a modification in the functions S and V. For example, among the fourth-order diagrams for pion-nucleon scattering, Fig. 1b corresponds to a modification of the intermediate nucleon propagation in a second-order diagram. Correspondingly Fig. 1c may be interpreted as a modification of one of the *vertices* in second-order scattering. Note on the other hand that Fig. 1a is irreducible. No parts may be interpreted merely as modifications of S or V.

Thus our problem, just as did Dyson's, breaks into two parts: (1) The determination of the modified nucleon propagation function, which we shall call $S'(E)$, and the modified vertex operator, which we shall call V_j'. (2) The evaluation of the irreducible diagrams in terms of S' and V_j'. The problem of renormalization is entirely concentrated in the first part. The remainder of this paper, then, will give an explicit recipe for calculating S' and V_j', taking proper account of mass renormalization and incorporating a mesonic charge renormalization which, as stated before, is not necessary but is extremely useful.

THE MODIFIED NUCLEON PROPAGATION FUNCTION

Following Ward,[5] we base our treatment of the modified nucleon propagation function $S'(E)$ on an auxiliary function, to be called $\Gamma_0(E)$ and to be defined by

$$\Gamma_0(E)=\partial/\partial E[1/S'(E)]. \tag{5}$$

In order to understand the significance of $\Gamma_0(E)$, note that we may write

$$S'(E)=\frac{1}{E-\sum(E)}, \tag{6}$$

where $\sum(E)$ is the sum of all modifications of a bare nucleon line due to overlapping meson lines. For example, the term in $\sum(E)$ of lowest order in f (second order) corresponds to Fig. 2a and is given by

$$f^2\sum_j V_jS(E-\omega_j)V_j^*. \tag{7}$$

Similarly the fourth-order terms in $\sum(E)$ correspond to Figs. 2b and 2c which each contain four vertex

[9] B. A. Lippmann and J. Schwinger, Phys. Rev. **79**, 398 (1953).

[10] See, for example, G. Wentzel, *Quantum Theory of Fields* (Edwards Bros., Inc., Ann Arbor, 1946), p. 61.

[11] For reasons of economy, the two variables $\mathbf{k}$ and λ will usually be summarized by the single index j. For example, instead of $V_\lambda(\mathbf{k})$ we shall write V_j and instead of $\sum_\lambda\int d\mathbf{k}/(2\pi)^3$, we write $\sum_j$.

operators and three propagation functions. Note, however, that there is *no* term in $\sum(E)$ corresponding to Fig. 2d, which contains *nonoverlapping* pions. Such diagrams are produced by expanding (6) in powers of $\sum(E)$. That is,

$$S'(E)=\frac{1}{E}+\frac{1}{E}\sum(E)\frac{1}{E}+\frac{1}{E}\sum(E)\frac{1}{E}\sum(E)\frac{1}{E}+\cdots. \quad (8)$$

From Eqs. (5) and (6), it follows that

$$\Gamma_0(E)=1+\Lambda_0(E),$$

where

$$\Lambda_0(E)=-\frac{\partial}{\partial E}\sum(E), \quad (9)$$

which leads to an interpretation of $\Gamma_0(E)$ if one remembers that in each term which makes up $\sum(E)$ the dependence on E arises solely from the nucleon propagation functions. If n propagation functions occur in a particular term, then taking the derivative with respect to E splits that term into n pieces. A particular piece

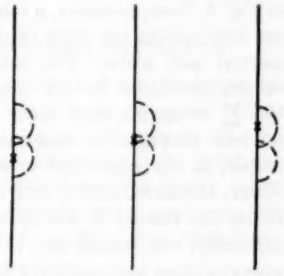

FIG. 3. Sample second-order contributions to $\Lambda_0(E)$.

can be represented by a diagram with an x on the nucleon line which has been differentiated. Thus, for example, the term in $\sum(E)$ corresponding to Fig. 2c is split by differentiation into the three pieces, shown in Fig. 3, which contribute to $\Lambda_0(E)$. Finally note that the operation $-\partial/\partial E$ on a particular propagation function $1/(E-\Omega)$ gives simply $1/(E-\Omega)^2$, so that $\Gamma_0(E)$ is just the so-called vertex modification of the effective coupling of the nucleon to a hypothetical neutral scalar field of low frequency.

In other words, suppose we wanted to calculate the matrix element of interaction of a nucleon with a neutral scalar field containing only very low frequencies so that it cannot change the proton energy appreciably. We would then evaluate a series of terms corresponding to the diagrams in Fig. 4, in which each pion overlaps with at least one other and the point of interaction with the "external" field, indicated by the x, is interlocked with the virtual pions. (One must also calculate diagrams involving nonoverlapping pions, but these would be treated most naturally by modifying the propagation function for the incoming and outgoing nucleon.) The sum of the above diagrams is called the vertex modification of the nucleonic coupling to the external field and is evidently identical with $\Gamma_0(E)$. For example, to second order in f, the vertex modification of the coupling to the external field from Fig. 4 is

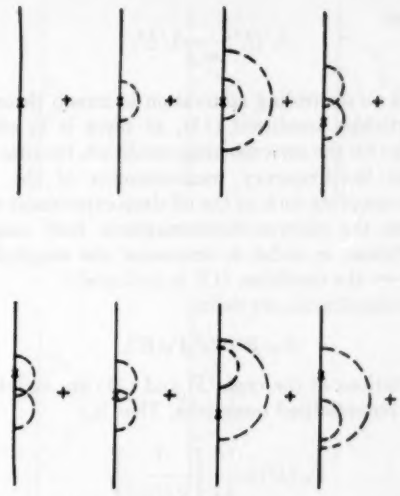

FIG. 4. Vertex modifying diagrams up to fourth order.

$$1+f^2\sum_j V_j S(E-\omega_j)S(E-\omega_j)V_j^*, \quad (7')$$

which also follows immediately from (9) and (7).

NUCLEON ENERGY (MASS) RENORMALIZATION

It is convenient both physically and mathematically to shift the scale of the nucleon energy so that it is always referred to the self-energy. That is, if E_S is the self-energy of a single nucleon due to the associated pion field, then we define $E'=E-E_S$. Now from exactly the same considerations as apply to the relativistic theory, E_S may be identified as the position of the pole of $S'(E)$. In other words E_S is the solution of the equation

$$E_S=\sum(E_S), \quad (10)$$

and if S' is now considered as a function of E', then $S'(E')$ has its pole at $E'=0$.[12]

With the boundary condition that $1/S'(E')$ shall vanish at $E'=0$, we may integrate Eq. (5) to obtain an explicit formula for S' in terms of Γ_0,

$$1/S'(E')=\int_0^{E'} d\lambda'\Gamma_0(\lambda'). \quad (11)$$

THE RENORMALIZED PROPAGATION FUNCTION

Following Dyson, we now wish to introduce a renormalized nucleon propagation function,

$$S_r'(E')=Z_2^{-1}S'(E'), \quad (12)$$

[12] We here violate accepted mathematical notation in favor of maintaining physical simplicity. We mean by $S'(E')$ a quantity *equal* to $S'(E)$ for $E'=E-E_S$.

such that

$$S_r'(E') \xrightarrow[E'\to 0]{} 1/E'. \tag{13}$$

There is no overriding motivation in meson theory for the particular condition (13), as there is in electrodynamics for the corresponding condition, because there exist no low-frequency measurements of the pion-nucleon coupling such as the oil-drop experiment which measures the electron-electromagnetic field coupling. Nevertheless, in order to maximize the simplicity of the theory the condition (13) is indicated.[13]

If we simultaneously define

$$\Gamma_{0r}(E') = Z_2\Gamma_0(E'), \tag{14}$$

then relations of the type (5) and (11) are maintained for the renormalized quantities. That is,

$$\Gamma_{0r}(E') = \frac{\partial}{\partial E'}\left[\frac{1}{S_r'(E')}\right], \tag{15}$$

$$\frac{1}{S_r'(E')} = \int_0^{E'} d\lambda'\Gamma_{0r}(\lambda'). \tag{16}$$

From Eq. (15), we see that the requirement (13) implies that

$$\Gamma_{0r}(E') \xrightarrow[E'\to 0]{} 1, \tag{17}$$

and the latter relation allows us to determine Z_2 in terms of $\sum$, or, as will turn out to be convenient later, in terms of $\sum_r = Z_2\sum$ or $\Lambda_{0r} = Z_2\Lambda_0$. Substituting (14) into (9), we obtain

$$Z_2^{-1}\Gamma_{0r}(E') = 1 - \frac{\partial}{\partial E'}\sum(E') = 1 + Z_2^{-1}\Lambda_{0r}(E').$$

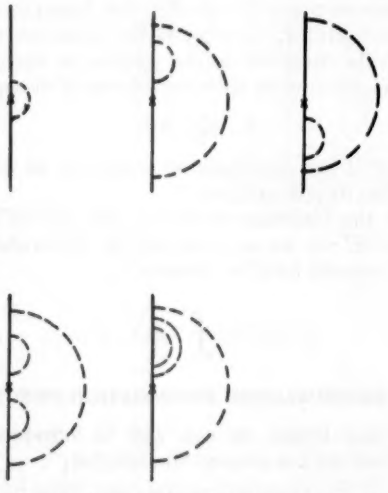

FIG. 5. Sample diagrams illustrating propagation function modification *within* a "fundamental" vertex diagram.

[13] For example, without condition (13) one could not neglect the "end effects" mentioned in footnote 8.

Taking the limit $E'\to 0$ then gives

$$Z_2 = 1 - \Lambda_{0r}(0). \tag{18}$$

It can be shown[14] that Z_2 represents the probability of finding the bare nucleon (zero pion configuration) in a single physical nucleon. Thus we know that $Z_2 < 1$.

An important problem still remains: to find a procedure for evaluating Γ_{0r}, and thus S_r', in which only renormalized quantities occur, Z_2 itself having been completely eliminated. Such a procedure is of course necessary in a divergent theory such as quantum electrodynamics. Here it is useful in eliminating uninteresting high-frequency effects which tend to obscure the essential aspects of the problem. To formulate the desired procedure, however, we must first construct the modified vertex operator.

THE MODIFIED VERTEX OPERATOR AND ITS RENORMALIZATION

The series of diagrams whose sum yields the modified vertex operator is in exact topological correspondence to the series which produces Γ_0 and which is indicated in Fig. 4. Now, however, a relation of the type (5) does *not* hold unless the pion field happens actually to be neutral and scalar. The insertion of an "external" vertex (indicated by the cross in Fig. 4) into one of the $\sum$ diagrams does more than simply square the nucleon propagation function at that point. For example, if the pion field is symmetrical and pseudoscalar, the absorption of one of its quanta may change either the charge or the spin of the nucleon. Mathematically, one would say that the "external" vertex operator does not commute with the "internal" vertex operators. In spite of this fact, it is not hard to convince oneself that the dependence of the modified vertex operator V_j' on $\mathbf{k}$, $\boldsymbol{\sigma}$, and λ will be exactly the same as that of V_j. The difference is that V_j' will also depend on E_1' and E_2', the nucleon energies before and after the vertex. We may summarize these statements by defining $L(E_2',E_1')$ such that

$$V_j'(E_2',E_1') = V_jL(E_2',E_1'). \tag{19}$$

This factorization of V_j' will be justified later by its self-consistency. Note that we consider E_2' and E_1' as independent of $\mathbf{k}$ although in any actual calculation $E_2' - E_1' = \omega_k$.

The failure of the vertex operators to commute will manifest itself in numerical factors not present in the case of Γ_0. For example, to second order in the coupling constant for the symmetrical pseudoscalar theory,

$$L(E_2',E_1') = 1 + (1/9)f^2\textstyle\sum_j V_jS(E_2'-\omega_j) \times S(E_1'-\omega_j)V_j^*. \tag{20}$$

[14] This fact was pointed out to the author by F. Low and its proof can easily be achieved with the techniques developed by M. Gell-Mann and F. Low in a forthcoming paper.

Comparing to (7′), one might say that to this order, only 1/9 as many pions contribute to the vertex modification as contribute to $\sum$, which gives the propagation function modification. In general, we shall express the function $L(E_2',E_1')$ as

$$L(E_2',E_1')=1+\Lambda(E_2',E_1'), \tag{21}$$

where $\Lambda(E_2',E_1')$ is the sum of contributions from all diagrams of the type shown in Fig. 4.

Still following Dyson's scheme, we next define a renormalized vertex operator L_r by

$$L_r(E_2',E_1')=Z_1L(E_2',E_1') \tag{22}$$

and require that

$$L_r(0,0)=1, \tag{23}$$

again following the convention established in electrodynamics. If we simultaneously define $\Lambda_r=Z_1\Lambda$, then we find

$$Z_1=1-\Lambda_r(0,0). \tag{24}$$

We are now in a position to formulate a general procedure for calculating S_r' and L_r, which does not involve Z_1 and Z_2.

RENORMALIZED INTEGRAL EQUATIONS

We shall find it worth while to make the remaining discussion in terms of certain integral equations rather than straightforward expansions in powers of the coupling constant. It seems likely that these equations have a more general validity than the power series expansions but no such claim is being made at this time. Our chief motive here in employing integral equations is to simplify the discussion.

Consider first the quantity $\Gamma_0(E')$ or $\Lambda_0(E')$ from which $S'(E)$ may be derived. The infinite series of diagrams which make up $\Gamma_0(E')$ may be split up into subseries in a systematic manner. For example, a well-defined subseries corresponds to taking the second diagram of Fig. 4, which has the value

$$f^2\sum_j V_jS(E'-\omega_j)S(E'-\omega_j)V_j^* \tag{25}$$

and modifying the two nucleon propagation functions. This would generate diagrams of the type shown in Fig. 5. One may alternatively modify the two vertex operators, generating diagrams of the type shown in Fig. 6. Or one may do both and note that simultaneous modifications of S and V does not repeat any diagrams. Each diagram occurs only once. Making both modifications replaces (25) by

$$\begin{aligned}f^2\sum_j V_j'S'(E'-\omega_j)S'(E'-\omega_j)V_j'^*&\\ =(Z_2f/Z_1)^2\sum_j V_jL_r(E',E'-\omega_j)S_r'(E'-\omega_j)&\\ \times S_r'(E'-\omega_j)V_j^*L_r(E'-\omega_j,E').&\end{aligned} \tag{26}$$

This series of diagrams may be enlarged even further by inserting at the position of the cross the function $\Gamma_0(E'-\omega_j)$ itself, which gives us an integral equation

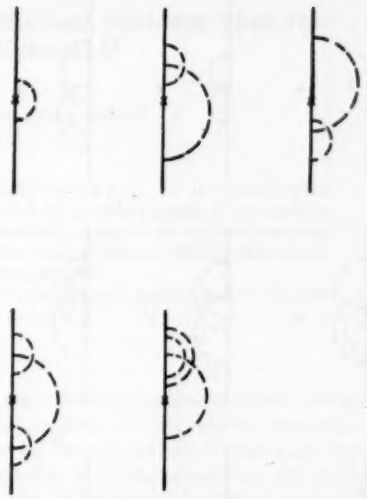

FIG. 6. Sample diagrams illustrating vertex modification *within* a "fundamental" vertex diagram.

for Γ_0. Again no repetitions of diagrams are generated. One might hope that, by modifying S, V, *and* the external vertex, one has included everything but this is unfortunately not so. One cannot, for example, generate in this way the sixth diagram of Fig. 4. This diagram, in fact, can itself be used to generate an entirely new series of terms by modifying within it the four propagation functions, the four internal vertices, and the one external vertex. In fact one can enumerate an infinite series of "fundamental" diagrams which each must be completely modified in order to generate the entire series of terms. The "fundamental" diagrams involving up to three pions are shown in Fig. 7.

Each "fundamental" diagram contains Γ_0 once and a number of V's equal to the number of S's. After modification and renormalization, therefore, each term will contain a factor, $Z_2(Z_2Z_1^{-1}f)^n$, so that it is natural to define a renormalized coupling constant,

$$f_r=Z_2Z_1^{-1}f, \tag{27}$$

as well as $\Lambda_{0r}=Z_2\Lambda_0$, which we have already done. The equation for Γ_{0r} then reads

$$\Gamma_{0r}(E')=Z_2+\Lambda_{0r}(E'), \tag{28}$$

where $\Lambda_{0r}(E')$ is to be evaluated entirely with the renormalized functions S_r' and L_r and the renormalized coupling constant f_r. Using (18) we may eliminate Z_2 from (28), obtaining the final equation

$$\Gamma_{0r}(E')=1+\Lambda_{0r}(E')-\Lambda_{0r}(0). \tag{29}$$

This is formally a linear integral equation for Γ_{0r}, but it contains of course the functions S_r' and L_r which must be codetermined. Equation (16) gives the recipe for obtaining S_r' and already entirely in terms of renormalized quantities. The problem of obtaining a re-

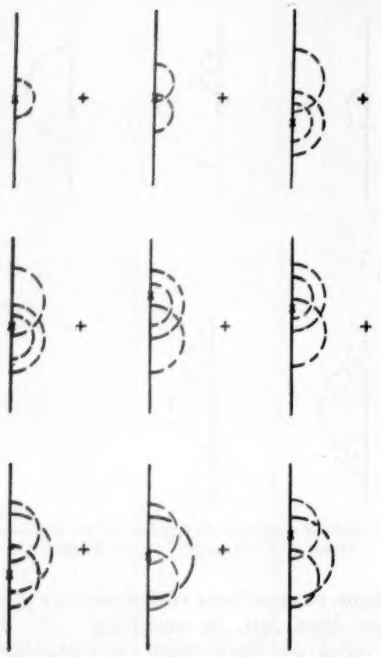

FIG. 7. The fundamental vertex diagrams involving up to three virtual pions.

normalized equation for L_r is completely analogous to that for Γ_{0r}, so we write down the result immediately

$$L_r(E_2',E_1')=1+\Lambda_r(E_2',E_1')-\Lambda_r(0,0). \quad (30)$$

The quantity Λ_r is to be evaluated by the same recipe as that for Λ_{0r} except that, for the external vertex, L_rV_j is to be used in place of Γ_0. The operator V_j is to be factored out only after the appropriate commutations have been performed to bring it outside the summation over virtual pions.

CONCLUSION

It has been demonstrated explicitly that charge and mass renormalization can be performed even in the static approximation of field theory. The particular recipe given for the renormalization is in terms of coupled integral equations of infinite order for the exact vertex and propagation functions but, as usual, perturbation methods can be applied. In the following paper, one such method will be formulated.

In the final renormalized equations, the nucleon self-energy and the original coupling constant are completely eliminated. It will be shown in the following paper that in a perturbation calculation integrals over virtual pion momenta are now linearly dependent on the cutoff in momentum space, whereas without charge renormalization, quadratically dependent terms would appear. Thus the performance of explicit charge renormalization in advance shows that the theory is less cutoff dependent than might appear at first sight. It will also be demonstrated in the following paper that the renormalized coupling constant in the pseudoscalar theory is sufficiently smaller than the original constant that perturbation approaches have a good chance of success. Our conclusion, then, is that, although charge renormalization is not required in a finite theory, it can be performed and is in many respects a very sensible procedure.

From a practical point of view it is possible that if the static approximation to meson theory is to have a chance of actually corresponding to physical reality it will be necessary to include a quadratic term in the coupling so as to produce S-wave pion-nucleon scattering. The author has every confidence that renormalization procedures can be developed for such a quadratic term, but to date no attempt has been made in this direction.

ACKNOWLEDGMENTS

This paper would not have been possible without constant help from Professor Francis Low, who has shown great patience in explaining to the author the intricacies of relativistic renormalization theory. Part of the writing up was carried out at the 1953 session of the Summer School for Theoretical Physics in Les Houches, France, where the author was a Fulbright lecturer.

Method of Approximation for the Meson-Nucleon Problem when the Interaction is Fixed and Extended*

GEOFFREY F. CHEW
Department of Physics, University of Illinois, Urbana, Illinois
(Received January 18, 1954)

It is proposed that a consistent and satisfactory method for evaluating the fixed extended source meson problem is: (a) first to renormalize the calculation by the method of the preceding paper; (b) to evaluate the fundamental quantities L_τ and Σ_τ by the usual weak coupling method; (c) also to use standard perturbation theory for the irreducible diagrams except when poles occur in integrations over intermediate states. Sums of diagrams in which repeated poles occur should be evaluated exactly.

The proposed method is similar to but not identical with the Tamm-Dancoff approximation. The new method is applied to the pion-nucleon scattering problem.

I. INTRODUCTION

IN the preceding paper, hereafter to be referred to as I, it has been shown that explicit mass and charge renormalization may be performed in advance even for the static limit of a meson theory, that is, for a theory with a fixed source. The purpose of the present paper is to outline a practical method of approximate calculation especially suitable to the solution of the renormalized fixed source problem.

It must be realized, first of all, that the static approximation can make sense only for energies substantially smaller than the nucleon rest energy, which is $\sim$1 Bev. Not only must the initial and final energies be small, however, but also the energies of all intermediate pions. That means that the Fourier transform of the source function, which is the cut-off factor in momentum space, must restrict pion energies to values well below 1 Bev. Under these conditions the Tamm-Dancoff[1] type of approach becomes promising. For example, Blair and Chew[2] have shown explicitly that after renormalization the dominant fourth-order contributions to pion-nucleon scattering are those whose intermediate states all involve less than three pions. This is only true for low values of the momentum cutoff, but fortunately a low cutoff seems required not only by the nonrelativistic nature of the theory but also apparently by experiment.[3]

A study of the results of Blair and Chew[2] suggests that, with the required large source and with charge renormalization, the effective coupling between pions and nucleons is by no means strong. In fact the dimensionless number which characterizes the rate of convergence of the perturbation expansion is $\sim$0.2. Why, then, are higher-order terms so important in the pion-nucleon scattering problem? The answer lies in those special intermediate states which can have an energy very close to the initial energy and whose magnitude consequently is anomalously large. Except for these states a perturbation expansion would converge fairly well. The validity of the above argument is substantiated by the calculations of Brueckner and Watson[4] and of Henley and Ruderman[5] on the nuclear force problem and by Friedman[6] on the nucleon magnetic moment problem.

Therefore we shall now propose a new criterion of approximation, similar to but not identical with the Tamm-Dancoff approximation.

(a) After renormalization, ordinary perturbation theory (i.e., an expansion in powers of the coupling constant) is to be applied, except when intermediate states occur which may have an energy coincident with the initial energy and which therefore give rise to poles in the integrations over intermediate states.

(b) For each pole the order of the corresponding diagram must be considered as *lowered* by one power of f^2. Thus, for example, the diagrams of Fig. 1 which contribute to pion-nucleon scattering, are all to be considered as of the same order in this sense, namely, of order f^2. (By chance, in this theory, the actual numerical order of magnitude of the "resonance" denominators, relative to "ordinary" denominators, turns out to be approximately equivalent to a factor f^2. Even if the resonance denominators were much smaller, however, our criterion would still make sense because we never treat any resonant state as weak.) For low-

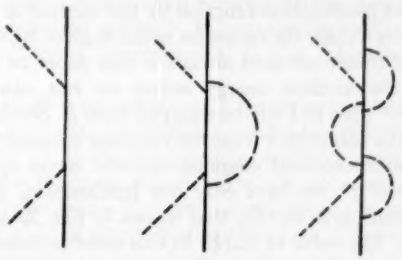

FIG. 1. Sample diagrams contributing to pion-nucleon scattering, all of which are of order f^4 in the sense of this paper.

* This research was supported by the U. S. Office of Naval Research.

[1] S. M. Dancoff, Phys. Rev. **78**, 382 (1950); I. Tamm, J. Phys. U.S.S.R. **9**, 449 (1945).

[2] J. S. Blair and G. F. Chew, Phys. Rev. **90**, 1065 (1953).

[3] J. S. Blair and G. F. Chew, Ann. Rev. Nuc. Sci. **2**, 163 (1953); G. F. Chew, Phys. Rev. **89**, 591 (1953).

[4] K. Brueckner and K. Watson, Phys. Rev. **92**, 1023 (1953).

[5] E. Henley and M. Ruderman, Phys. Rev. **92**, 1036 (1953).

[6] M. H. Friedman (private communication).

FIG. 2. A typical pion-nucleon scattering diagram which illustrates the difference between the Tamm-Dancoff approximation and that proposed here.

energy pion-nucleon scattering the criterion can be better stated as follows: In first approximation, only those virtual pions are considered which *at some time are alone* in the field. Pions which are never alone may be treated by a perturbation expansion. This criterion differs from that of Tamm and Dancoff who in lowest order would keep all diagrams in which no intermediate state involves more than two pions. For example, the diagram in Fig. 2 would be kept by the lowest-order Tamm-Dancoff approximation but omitted by that proposed here. After renormalization, we consider this diagram of order f^4 and therefore small compared to those of Fig. 1.

In the nuclear force problem, we would regard the diagrams Fig. 3a, b, c, as all being of the order f^2 but consider Fig. 3d, e, f, as being of order f^4.

Charge renormalization is enormously important in justifying our approximation. For example, Fig. 2 without charge renormalization would be much too large to neglect. The point is that having made charge renormalization, we have actually taken most of Fig. 2 into account and neglected only a part which is rather small.

Many diagrams do not involve poles and in such cases it is sufficient to expand the modified vertex and propagation functions in powers of the coupling constant. Let us begin, therefore, by examining the lowest-order modifications of these functions.

II. THE f^2 MODIFICATION OF THE NUCLEON PROPAGATION FUNCTION

The starting point for calculating the modified nucleon propagation function by the method of I is the quantity $\Gamma_0(E)$, the recipe for which is given by formula (I-29). (Since we shall always in this paper be dealing with the nucleon energy *minus its rest energy* the "prime" used in I will be dropped from E. Similarly we drop the subscript r from the coupling constant f since the unrenormalized coupling constant never appears.) To order f^2, we have only one fundamental diagram contributing to $\Lambda_{0r}(E)$, that shown in Fig. 2a of reference I. The value of $\Lambda_{0r}(E)$ to this order is therefore

$$\Lambda_{0r}(E)=f^2\sum_j V_j\frac{1}{E-\omega_j}\frac{1}{E-\omega_j}V_j^*, \qquad (1)$$

since we replace L_r and S_r' by their zeroth-order values. From (I-29) we then get

$$\Gamma_{0r}(E)=1+f^2\sum_j V_jV_j^*\left[\frac{1}{(E-\omega_j)^2}-\frac{1}{\omega_j^2}\right], \qquad (2)$$

which by (I-16) leads to

$$1/S_r'(E)=E-f^2\sum_j V_jV_j^*\left[\frac{1}{E-\omega_j}+\frac{1}{\omega_j}+\frac{E}{\omega_j^2}\right] \qquad (3)$$

$$=E[1+f^2\Delta(E)],$$

where

$$\Delta(E)=\frac{3}{\pi}\int_\mu^\infty d\omega\frac{k^3}{\mu^2\omega^2}\frac{E}{\omega-E}v^2(k). \qquad (4)$$

The function $\Delta(E)$ is plotted in Fig. 4 for the square cut-off function $v(k)$ with $\omega_{max}=3.2\mu$, as determined by Chew[3] in fitting the P-wave pion-nucleon scattering. In evaluating $\Delta(E)$ in the "resonance" region, the principal value of the integral has been taken. This is correct if we are interested eventually in the reactance matrix. It is seen that only for $\mu<E<\omega_{max}$ does the magnitude of $\Delta(E)$ become substantially greater than unity. (We may disregard the region for $E>\omega_{max}$ because the theory should not be applied to external energies close to or greater than ω_{max} and the internal nucleon energy can never be greater than the total external energy.) This corresponds to the fact that only in this region can the virtual pion "resonate" with the energy E. It seems, therefore, with $f^2\sim0.2$ as determined by Chew,[3] that for E not in this region a weak coupling expansion is adequate.

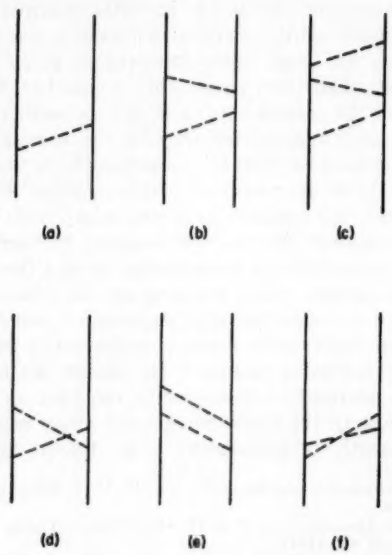

FIG. 3. Sample diagrams contributing in second and fourth order to the nuclear force problem.

III. THE f^3 MODIFICATION OF THE VERTEX FUNCTION

The lowest-order correction to the vertex function is obtained from Eq. (I-30) in the same manner as we obtained Γ_{0r} from (I-29). The difference is that the failure of the external vertex operator to commute with the internal vertex operators leads to a numerical factor of 1/9,

$$L_r(E_2,E_1)=1+(f^2/9)\sum_j V_jV_j^*\left[\frac{1}{E_2-\omega_j}\frac{1}{E_1-\omega_j}-\frac{1}{\omega_j^2}\right]$$

$$=1+(f^2/9)\Delta(E_2,E_1), \tag{5}$$

where

$$\Delta(E_2,E_1)=\frac{3}{\pi}\int_\mu^\infty d\omega\frac{k^2}{\mu^2\omega^2}\frac{(E_2+E_1)\omega-E_2E_1}{(\omega-E_2)(\omega-E_1)}v^2(k). \tag{6}$$

It is easy to verify that $\Delta(E_2,0)=\Delta(E_2)$ and $\Delta(0,E_1)=\Delta(E_1)$, so that for the correction to the first or last vertex in a diagram, the discussion given above for the propagation function modification is certainly valid here. The discussion for internal vertices is more complicated but leads to the same conclusions. The quantity $\Delta(E_2,E_1)$ can be large only when one or the other of the energies lies in the range between μ and $\omega_{\max}$. In addition, however, the numerical factor 1/9 in formula (5) should not be overlooked. Whenever pion lines cross, as they do in the vertex modification, the effective coupling strength is reduced because the nucleon may not be able to reabsorb every pion which it emits. For example, suppose a proton emits a positive pion, becoming a neutron. It can obviously reabsorb the original pion if nothing else happens; but, if in the meantime it emits a negative pion or absorbs a positive, it can no longer reabsorb the original positive pion. A similar situation prevails with respect to angular momentum, so that actually only 1/9 as many pions can cross a vertex as can contribute to propagation modification in lowest order. This extra factor of smallness means that we can always treat vertex modifications by perturbation theory, regardless of the energy situation.[7]

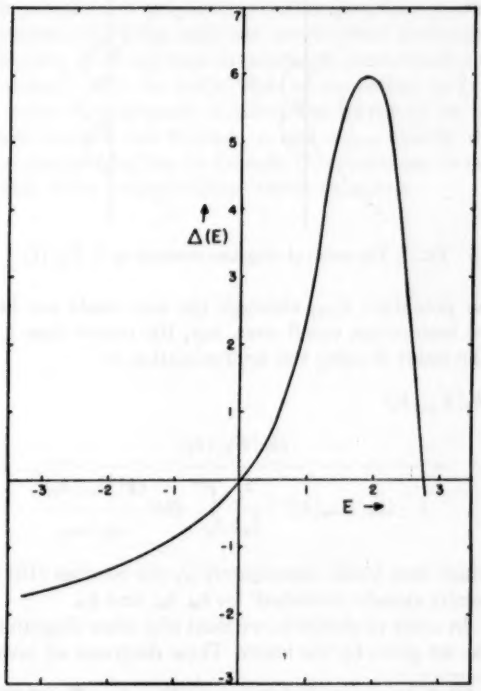

FIG. 4. The function $\Delta(E)$, defined in Eq. (4), for a "square" cutoff with $\omega_{\max}=3.2\mu$.

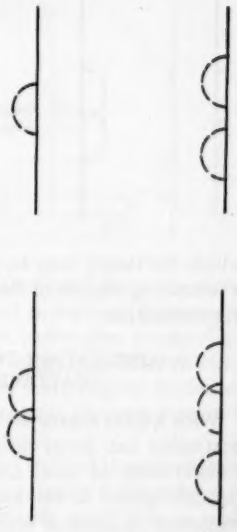

FIG. 5. Sample diagrams contributing to S_r'.

IV. PROPAGATION FUNCTION MODIFICATION FOR $\mu<E<\omega_{\max}$

We now turn to the problem of the nucleon propagation modification in the "resonance" region, when $\mu<E<\omega_{\max}$. According to our original criterion we must, in lowest order, take account of the series of diagrams indicated in Fig. 5. This means keeping in $\sum_r$ a series of terms corresponding to the diagrams of Fig. 6.

However, since each new pion line crosses one vertex, we are assured that the coupling constant is effectively $(1/9)f^2$, not f^2, so that we actually need keep only the lowest-order diagram, where there are no crossings. Thus formula (3) is still correct, if no attempt is made to treat $f^2\Delta(E)$ as small. Notice that with $f^2=0.2$, no new singularities are introduced in the range of E for

[7] This numerical factor of 1/9 also means that Z_2/Z_1 is substantially smaller than 1, in contrast to electrodynamics where gauge invariance insures that $Z_2=Z_1$. The consequence that the renormalized coupling constant here is smaller than the original coupling constant is one of the main practical reasons for renormalizing the static approximation.

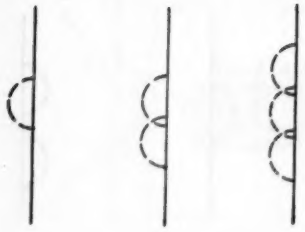

FIG. 6. Sample diagrams contributing to Σ_r.

which the theory may be sensible, i.e., $E<\omega_{\max}$. This is a reassuring feature of the theory and of our method of approximation.

V. APPLICATION TO THE PION-NUCLEON SCATTERING PROBLEM

With a fixed source and linear coupling, pion-nucleon scattering can occur only in P-states; and using the conservation of total angular momentum as well as isotopic spin it is well known that the problem can be expressed in terms of four eigenstates, which have been labeled with the notation, 33, 31, 13, 11. The first number is twice the total isotopic spin and the second is twice the total angular momentum. Now the *bare nucleon* is a 11 state, so that from the conservation laws it follows that diagrams containing at any point a bare nucleon line can contribute only to the 11 scattering. A little thought then suffices to show that by the criteria we have set up one needs to keep *only* the sequence of diagrams shown in Fig. 7 for the 33, 31, and 13 states; no propagation or vertex modifications are needed. If we denote the sum of all such diagrams by $(f|K|0)$, then an integral equation for $(f|K|0)$ may be written down

$$(f|K|0)=(f|U_0|0)+\sum_n (f|U_0|n)\frac{1}{\omega_0-\omega_n}(n|K|0), \quad (7)$$

where

$$(m|U_0|n)=f^2(V_nV_m^*)/(\omega_0-\omega_n-\omega_m).$$

The first step in solving (7) is to use the conservation laws to break the single equation in many variables into four separate equations each depending only on the magnitude of the momentum. The result is as follows:

$$(k_f|K_{0\alpha}|k_0)=(k_f|U_{0\alpha}|k_0)+\frac{1}{2\pi^2}\times\int_0^\infty dkk^2\frac{(k_f|U_{0\alpha}|k)(k|K_{0\alpha}|k_0)}{\omega_0-\omega_k}, \quad (8)$$

where

$$(k_n|U_{0\alpha}|k_m)=C_\alpha 2\pi\frac{f^2}{\mu^2}\frac{k_nk_m}{(\omega_n\omega_m)^{\frac{1}{2}}}\frac{v(k_n)v(k_m)}{\omega_0-\omega_n-\omega_m}, \quad (9)$$

with $C_{33}=4/3$, $C_{31}=-2/3$, $C_{13}=-2/3$, and $C_{11}=1/3$. If the principal value of the integral in (8) is taken, then the relation between all phase shifts, except δ_{11}, and the matrix K_0 is as follows:[8]

$$\tan\delta_\alpha=-(k_0\omega_0/2\pi)(k_0|K_{0\alpha}|k_0). \quad (10)$$

To calculate δ_{11} we have to add more diagrams which involve internal bare nucleon lines, but before proceeding to this problem, let us write down an approximate solution of the integral equation (8).

This solution is based on an application of one of Schwinger's variational principles which has recently been discussed in detail by Altshuler[9] and by Chew.[10] Sufficient conditions for the validity of the approximation appear to be: (1) that no more than one bound state shall be possible; (2) that the potential function U shall be of a single sign and have important components only over a logarithmically small range of momenta. All of these conditions are well satisfied by

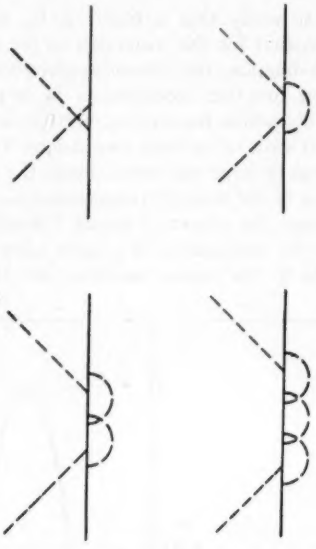

FIG. 7. The series of diagrams summed up in Eq. (7).

our potentials $U_{0\alpha}$, although the last would not be if the momentum cutoff were, say, 10μ rather than 3.2μ. The result of using this approximation is

$$(k_0|K_{0\alpha}|k_0)=\frac{(k_0|U_{0\alpha}|k_0)}{1-(k_0|U_{0\alpha}|k_0)^{-1}\frac{1}{2\pi^2}\int_0^\infty dkk^2\frac{(k|U_{0\alpha}|k_0)^2}{\omega_0-\omega_k}}, \quad (11)$$

which then yields immediately by the relation (10) the results already published[8] for δ_{33}, δ_{31}, and δ_{13}.

In order to obtain δ_{11} we must add other diagrams to the set given by the above. These diagrams all involve

[8] B. A. Lippmann and J. Schwinger, Phys. Rev. **79**, 469 (1950).
[9] S. Altshuler, Phys. Rev. **89**, 1278 (1953).
[10] G. F. Chew, Phys. Rev. **93**, 341 (1954).

a bare nucleon line at some internal point and thus they are all reducible to the diagram shown in Fig. 8, whose value is given by

$$f^2V_f^*L_r(0,\omega_0)S_r'(\omega_0)V_0L_r(\omega_0,0). \tag{12}$$

Now it has been shown that our zeroth-order approximation amounts to replacing L_r by 1 and $S_r'(E)$ by formula (5). Thus (12) becomes

$$\frac{f^2V_f^*V_0}{\omega_0[1+f^2\Delta(\omega_0)]}, \tag{13}$$

the projection of which onto the 11 state is

$$2\pi\left(\frac{3f^2}{\mu^2}\right)\frac{k_fk_0}{(\omega_f\omega_0)^{\frac{1}{2}}}\frac{v(k_f)v(k_0)}{\omega_0[1+f^2\Delta(\omega_0)]}. \tag{14}$$

The result already published[3] for δ_{11} is a rough approximation to the sum of (14) and (11), motivated by the fact that (14) carries a numerical factor 9 times as great as that for (11). Note that the relation between the function $\Delta-$ of reference 3 and the function Δ of the present paper is as follows: $f^2\Delta(E)=+(9/2)\Delta-(E)$.

SUMMARY AND CONCLUSION

An approximation procedure has been formulated which allows a relatively simple evaluation of the fixed source meson problem with an accuracy of ~20 percent. The procedure is as follows: (1) Disregard all reducible diagrams. (2) Keep only the lowest-order irreducible diagrams, counting each intermediate state which can "resonate" with the initial state as equivalent to $1/f^2$ in order of magnitude. 3 When the energy of an internal nucleon lies between μ and ω_{max}, modify the propagation function by formula (5); otherwise do not modify either propagation or vertex functions.

FIG. 8. The main diagram for scattering in the 11 state.

This procedure has here been applied to the pion-nucleon scattering problem and in separate papers will be applied to the problems of photo pion production, anomalous nucleon magnetic moments, neutron-electron interaction, and Compton scattering by nucleons. Higher-order corrections will eventually be calculated by standard perturbation methods.

It should be remembered that in all of these problems the fixed-source model cannot possibly make sense for energies greater than the cut-off energy ω_{max} and probably should be restricted to energies well below ω_{max}. At higher energies it will certainly be necessary to take account of nucleon recoil as well as the existence of heavier mesons. It is also possible that even at low energies an S-wave pion-nucleon interaction cannot consistently be ignored. An S-state interaction can be included in the fixed source theory via a term quadratic in the pion field, but the charge dependence is not determined by general principles, nor is the amplitude relative to the linear term. For reasons of simplicity, therefore, we have not here considered a quadratic interaction term.

Note added in proof.—Recent developments incline the author now to use a larger cutoff ($\omega_{max}=5.6\,\mu$) and a smaller coupling constant ($f^2=0.058$). The only aspect of this paper to be seriously affected by this change is the accuracy of the variational result (11).

Intermediate Coupling Method for Meson-Nucleon Scattering*

T. D. LEE, *Columbia University, New York, New York,*

AND

R. CHRISTIAN, *Los Alamos Scientific Laboratory, Los Alamos, New Mexico*

(Received March 1, 1954)

It is shown that for the meson-nucleon scattering processes an intermediate-coupling method can be applied which joins smoothly the results obtained from the weak- and strong-coupling limits. The method is illustrated by a detailed study of the charged scalar meson field with fixed nucleon.

I. INTRODUCTION

AN intermediate-coupling approximation that is applicable to the bound states of a nucleon-meson system, i.e., a "physical" nucleon and its possible isobars, has been given by Tomonaga.[1] This method is limited to a nonrelativistic treatment of the nucleon but does afford some insight into the problem when the coupling constant is not sufficiently small or large that either the usual weak- or strong-coupling treatment is trustworthy. Furthermore, in the limit of very small or very large values of the coupling constant the result of the intermediate-coupling treatment agrees with that of the correct weak- and strong-coupling calculation.

This intermediate-coupling method is a simple Hartree-Fock approximation in which the total number of mesons is not limited, but all mesons of the same type are assumed to be only in a finite number of orbital states. These orbital state functions, together with the probability amplitude for finding any number of virtual mesons in the nucleon state, are determined by minimizing the total energy. Calculations so far have been limited to determining the self-energies of the stable state of a nucleon with charged scalar mesons neglecting recoil[1] and obtaining the interaction between a nucleon with neutral scalar mesons including recoil.[2]

The purpose of the present note is to extend Tomonaga's method to the scattering of a meson by a nucleon.[3] The charged scalar meson field with fixed nucleon is chosen to illustrate the essential features. The extension of this method to the pseudoscalar meson with pseudovector coupling will be discussed in a subsequent paper.

For the scattering system of a free meson plus a "physical" nucleon we first assume that we have a wave function in the Fock space representing the "physical" nucleon. This wave function is multiplied by a scattering function of the meson which represents an incident and scattered wave. This product function is then symmetrized with respect to all the mesons, and the best functional form of the scattering function is determined by the usual variational technique. As such, the approximation allows for a distortion of the meson wave but does not allow for a "polarization" of the "physical" nucleon.

In the weak-coupling limit the results for the cross section agree with those of the perturbation method. In the strong-coupling limit the results differ from the rigorous strong-coupling results by numerical factors close to unity (depending slightly upon the source size and incident meson energy).

For intermediate values of the coupling constant the procedure is to calculate (numerically) the Tomonaga wave function for the bound states from which one determines the scattering function and consequently the cross section by solving the variational problem. As the coupling constant varies from small to large values it is found that resonance features may occur. It is interesting to note that in the scattering calculation the effect of self-energy and renormalization of coupling constant appear in a very natural way so that they can be identified and eliminated in an unambiguous manner.

II. BOUND STATE

We consider a charged scalar meson field with the Hamiltonian

$$H=\int \omega_k(\alpha_k^\dagger\alpha_k+\beta_k^\dagger\beta_k)d^3k - g\int u(k)[\tau_+(\alpha_k+\beta_k^\dagger)+\tau_-(\alpha_k^\dagger+\beta_k)]d^3k, \quad (1)$$

where $\alpha_k^\dagger$, α_k, and $\beta_k^\dagger$, β_k are the creation and annihilation operators of the positive and negative mesons of momentum k, and

$$u(k)=(4\pi^2\omega_k)^{-\frac{1}{2}}\int U(r)e^{ik\cdot r}d^3r, \quad (2)$$

where $U(r)$ is the normalized source function. ω_k is the total energy of the meson, $\omega_k=(k^2+\mu^2)^{\frac{1}{2}}$.

In order to introduce our notation and have at hand some results already found by Tomonaga, we shall summarize his method for the bound state.

* Publication assisted by the Ernest Kempton Adams Fund.

[1] S. Tomonaga, Prog. Theoret. Phys. **2**, 6 (1947). F. Harlow and B. Jacobson, Phys. Rev. **93**, 333 (1954).

[2] T. D. Lee and D. Pines, Phys. Rev. **92**, 883 (1953).

[3] During the completion of this paper, a similar extension of the intermediate-coupling method to include scattering problem has been worked out by S. Tomonaga, Abstract Book, International Conference of Theoretical Physics, Kyoto and Tokyo, 1953 (unpublished).

TABLE I. Various quantities for the ground state of the nucleon, as functions of g.

g^2	E_0/μ	$\mathfrak{N}_+^0$	$\mathfrak{N}_-^0$	$\mathfrak{M}_+^0$	$\mathfrak{M}_-^0$	λ_+^0/μ	λ_-^0/μ
$\ll 1$	$-g^2\int\frac{u^2}{\omega}d^3k$	$g^2\int\frac{u^2}{\omega^2}d^3k$	$O(g^4)$	$g\left(\int\frac{u^2}{\omega^2}d^3k\right)^{\frac{1}{2}}$	$O(g^3)$	0	$\sim M/\mu$
2	-1.75	0.385	0.05	0.465	0.12	0.2	4
6	-5.45	0.77	0.33	0.555	0.32	0.2	1.8
$\gg 1$	$-\frac{g^2}{2}\int\frac{u^2}{\omega}d^3k$[a]	$\frac{g^2}{4}\int\frac{u^2}{\omega^2}d^3k$	$\frac{g^2}{4}\int\frac{u^2}{\omega^2}d^3k$	$\frac{g}{4}\left(\int\frac{u^2}{\omega^2}d^3k\right)^{\frac{1}{2}}$	$\frac{g}{4}\left(\int\frac{u^2}{\omega^2}d^3k\right)^{\frac{1}{2}}$	$\frac{1.22}{g^2}$[b]	$\frac{10.8}{g^2}$[b]

[a] See Eq. (3.38), reference 1, for the complete expression.
[b] See Eq. (3.37), reference 1, for the complete expression.

The values of the various integrals occurring in the table are

$$\int\frac{u^2(k)}{\omega_k}d^3k=1.34;\quad\int\frac{u^2(k)}{\omega_k^2}d^3k=0.410;\quad\int\frac{u^2(k)}{\omega_k^3}d^3k=0.167.$$

A brief derivation of the form $\mathfrak{N}_+^0$ and $\mathfrak{M}_+^0$ is given in Appendix I.

We denote the probability amplitude for finding n positive and m negative mesons with wave numbers $k_1^+\cdots k_n^+$; $k_1^-\cdots k_m^-$ in the ground state of a single nucleon by

$$\psi_{n,m}^0\equiv\langle k_1^+,\cdots k_n^+;k_1^-,\cdots k_m^-|\Psi^0\rangle. \tag{3}$$

For definiteness we suppose Ψ^0 to be a proton state (the superscript 0 indicates a ground state); thus, the difference $n-m$ can only be 0 or 1, depending upon the charge of the "bare" nucleon.

Following Tomonaga we apply the Ritz variational principle,

$$\delta\langle\Psi^0|H-E_0|\Psi^0\rangle=0,$$

with trial functions of the form

$$\begin{aligned}\psi_{n,n}^0&=C_{n,n}^0\prod_{i=1}^{n}f_+^0(k_i^+)\prod_{j=1}^{n}f_-^0(k_j^-),\\ \psi_{n,n-1}^0&=C_{n,n-1}^0\prod_{i=1}^{n}f_+^0(k_i^+)\prod_{j=1}^{n-1}f_-^0(k_j^-),\end{aligned} \tag{4}$$

where $f_+^0(k)$ and $f_-^0(k)$ are normalized but otherwise arbitrary functions to be determined, together with the numerical constants $C_{n,m}^0$, by the application of the Ritz principle. It is easy to carry out the variation with respect to $f_\pm^0$ and show that the best forms of f_+^0 and f_-^0 are

$$f_\pm^0(k)=N_\pm^0u(k)/(\omega_k+\lambda_\pm^0), \tag{5}$$

where λ_+^0 and λ_-^0 are numerical constants depending on the coupling constant and $N_\pm^0$ are normalization constants. The result of carrying out the variation with respect to the constants $C_{n,m}^0$, λ_+^0, and λ_-^0 leads to a set of difference equations[4] in $C_{n,m}^0$, which can be evaluated analytically in the weak- and strong-coupling limits and give *identical* results for the binding energy with the rigorous treatments in these two limits.[5] For the intermediate value of coupling constant these equations can only be solved numerically.

As shall be shown later, the determination of the quantities,

$$\begin{aligned}\mathfrak{N}_+^0&\equiv\sum_{n=1}^{\infty}\sum_{m=n-1}^{n}|C_{n,m}^0|^2n,\\ \mathfrak{N}_-^0&\equiv\sum_{n=1}^{\infty}\sum_{m=n-1}^{n}|C_{n,m}^0|^2m,\\ \mathfrak{M}_+^0&\equiv\sum_{n=0}^{\infty}C_{n+1,n}^0C_{n,n}^0(n+1)^{\frac{1}{2}},\\ \mathfrak{M}_-^0&\equiv\sum_{n=0}^{\infty}C_{n+1,n+1}^0C_{n+1,n}^0(n+1)^{\frac{1}{2}},\end{aligned} \tag{6}$$

and $\lambda_\pm^0$ will be necessary for the evaluation of the meson-nucleon scattering cross section. With these definitions the normalization $N_\pm^0$, may be written as

$$N_\pm^0=g\mathfrak{M}_\pm^0/\mathfrak{N}_\pm^0. \tag{7}$$

The analytical forms of these quantities in the strong- and weak-coupling limits, together with some of their numerical values for the intermediate region, are listed in Table I and shown graphically in Figs. 1

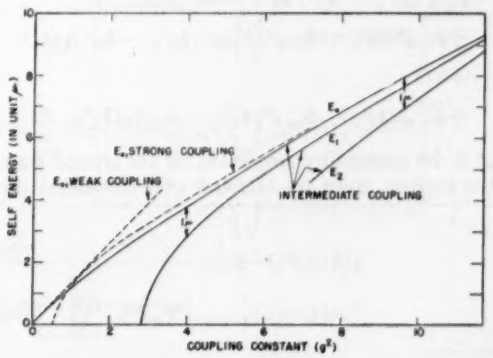

FIG. 1. The self-energy as calculated with the intermediate coupling approximation for the lowest state, E_0; 1st excited state with $m=\pm\frac{1}{2}$, E_1; and 2nd excited state with $m=\pm5/2$, E_2.

[4] See reference 1, Eq. (3.15).

[5] The weak-coupling result is well known. The strong-coupling result is discussed by: G. Wentzel, Helv. Phys. Acta **13**, 269 (1940); **14**, 633 (1941); R. Serber and S. Dancoff, Phys. Rev. **63**, 143 (1943); S. Tomonaga, Prog. Theoret. Phys. **1**, 109 (1946).

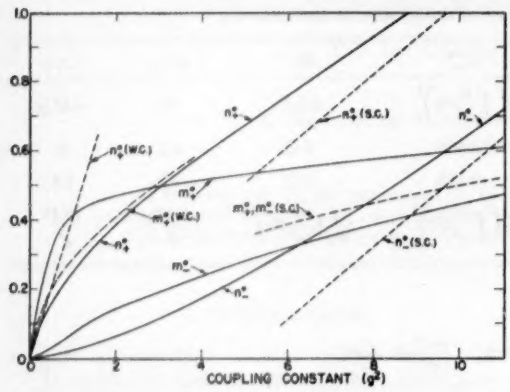

FIG. 2. Various quantities arising in meson-nucleon scattering as determined by the intermediate coupling approximation (solid lines).

and 2. For the numerical calculations the source function $U(r)=[M^2\exp(-M/r)]/4\pi r$, was used where $\mu/M=1/7$.

III. ELASTIC SCATTERING

To illustrate the extension of Tomonaga's method to meson-nucleon scattering, we shall consider first only elastic scattering and restrict ourselves to energies less than 2μ and to values of the coupling constant g such that no *stable* isobars exist. The method used can be easily extended to inelastic scattering and will be discussed in the next section.

The functional form of the state Ψ, representing the scattering process $\pi^+ + p \to \pi^+ + p$, is assumed to be[6]:

$$\psi_{n+1,m} \equiv \langle k_1^+, \cdots k_n^+, k_{n+1}^+; k_1^-, \cdots k_m^- | \Psi \rangle = (n+1)^{-\frac{1}{2}} S_+ [\psi_{n,m}{}^0 \chi(k_{n+1}^+)], \tag{8}$$

where S_+ is the symmetrization operator with respect to positive meson, given by

$$\begin{aligned} S_+[\psi_{n,m}{}^0\chi(k_{n+1}^+)] &= \psi_{n,m}{}^0(k_1^+, \cdots k_n^+; k_1^-, \cdots k_m^-)\chi(k_{n+1}^+) \\ &+ \psi_{n,m}{}^0(k_1^+, \cdots k_{n-1}^+, k_{n+1}^+; k_1^-, \cdots k_m^-)\chi(k_n^+) \\ &+ \cdots \\ &+ \psi_{n,m}{}^0(k_2^+, \cdots k_{n+1}^+; k_1^-, \cdots k_m^-)\chi(k_1^+). \end{aligned}$$

$\psi_{n,m}{}^0$ is the probability amplitude for the ground state of the nucleon given by (3), and $\chi(k)$ represents the wave function of the free meson. To determine the functional form of $\chi(k)$, we use the variational principle for scattering, which may be *formally* written[7] as

$$J \equiv \langle \Psi | H - E_0 - \omega_0 | \Psi \rangle, \qquad \delta J/\delta\chi = 0, \tag{9}$$

where ω_0 is the energy of the incident meson and E_0 is the self-energy of the proton.

For computational purposes it is convenient to write Eq. (8) in the equivalent form,

$$\Psi = \int d^3k \chi(k) \alpha_k{}^\dagger \Psi^0. \tag{10}$$

J may then be easily calculated by commuting $\alpha_k{}^\dagger$ in Eq. (10) with the Hamiltonian, H, and noting that Ψ^0 is an eigenfunction of H with eigenvalues E_0. Thus

$$2J = \left\langle \Psi^0 \middle| \int d^3k' \chi^*(k') \alpha_{k'} \int d^3k (\omega_k - \omega_0) \chi(k) \alpha_k{}^\dagger \middle| \Psi^0 \right\rangle - g \left\langle \Psi^0 \middle| \int d^3k' \chi^*(k') \alpha_{k'} \int d^3k \tau_+ u(k) \chi(k) \middle| \Psi^0 \right\rangle + \text{c.c.} \tag{11}$$

Upon varying J with respect to $\chi(k)$, we find the integral equation

$$(\omega_k - \omega_0)\chi(k) = \int K(k, k')\chi(k') d^3k', \tag{12}$$

where

$$\begin{aligned} 2K(k, k') = g\langle \Psi^0 | [\alpha_{k'} u(k) + \alpha_k u(k')]\tau_+ | \Psi^0 \rangle \\ - \langle \Psi^0 | \alpha_k{}^\dagger (\omega_{k'} - \omega_0)\alpha_{k'} | \Psi^0 \rangle \\ - \langle \Psi^0 | \alpha_{k'}{}^\dagger (\omega_k - \omega_0)\alpha_k | \Psi^0 \rangle. \end{aligned} \tag{12a}$$

By using the Tomonaga approximate form for Ψ^0, Eq. (4), and the expressions for $\langle \alpha^\dagger \alpha \rangle_{Av}$ and $\langle \alpha \tau_+ \rangle_{Av}$ given by Eqs. (A.3) and (6), Eq. (12a) becomes

$$\begin{aligned} 2K(k,k') = g\mathfrak{M}_+{}^0[f_+{}^0(k)u(k') + u(k)f_+{}^0(k')] \\ - \mathfrak{N}_+{}^0[\omega_k + \omega_{k'} - 2\omega_0] f_+{}^0(k) f_+{}^0(k'). \end{aligned}$$

Finally upon using Eqs. (5) and (7) we find,

$$K(k,k') = \mathfrak{N}_+{}^0(\omega_0 + \lambda_+{}^0) f_+{}^0(k) f_+{}^0(k'). \tag{13}$$

The solution for the scattering problem of Eq. (12) is

$$\chi(k) = \delta^3(k - k_0) + \frac{\mathfrak{N}_+{}^0(\omega_0 + \lambda_+{}^0) f_+{}^0(k) f_+{}^0(k_0)}{(\omega_k - \omega_0 - i\epsilon)\left[1 - \mathfrak{N}_+{}^0(\omega_0 + \lambda_+{}^0)\int d^3k' |f_+{}^0(k')|^2/(\omega_{k'} - \omega_0 - i\epsilon)\right]}, \tag{14}$$

[6] For $\pi^- + p$, an additional term corresponding to the formation of a neutron must be included. See Appendix II for a detailed discussion.

[7] A rigorous formulation of the variational principle is given in Appendix III.

corresponding to a differential cross section given by (see Appendix III):

$$\frac{d\sigma}{d\Omega}=\frac{[4\pi^2\omega_0 u^2(k_0)Rg^2]^2}{[4\pi^2\omega_0 k_0 u^2(k_0)Rg^2]^2+(\omega_0+\lambda_+{}^0)^2\left[1-Rg^2(\omega_0+\lambda_+{}^0)\mathrm{P}\int d^3k u^2/(\omega+\lambda_+{}^0)^2(\omega-\omega_0)\right]^2}, \tag{15}$$

where P indicates that the principal value of the integral is to be taken and $R=(\mathfrak{M}_+{}^0)^2/\mathfrak{N}_+{}^0$.

It may be emphasized that the self-energy E_0 has been explicitly eliminated in the kernel $K(k,k')$, Eq. (12), and that in (15), R is always multiplied by g^2 and plays the role of a charge renormalization factor. The result (15) is then completely convergent even for a delta function source.

Weak-Coupling Limit

For a sufficiently small coupling constant, $R=1$ and $\lambda_+{}^0=0$ so that with a delta function source the cross section becomes

$$d\sigma/d\Omega=g^4/\omega_0{}^2,$$

which agrees exactly with the usual weak-coupling calculation.

IV. INELASTIC SCATTERING

For sufficiently large value of the coupling constant a *stable* isobaric state of the nucleon with charge 3 is possible and the scattering will be inelastic; that is, the reaction

$$\text{(A)}\quad \pi^++p\rightarrow\pi^-+p^{+++}$$

competes with the scattering process

$$\text{(B)}\quad \pi^++p\rightarrow\pi^++p.$$

Therefore, instead of Eq. (9) we use the trial function[8]

$$\psi_{n+1,m}=(n+1)^{-\frac{1}{2}}S_+[\psi_{n,m}{}^0\chi_+(k_{n+1}{}^+)]+m^{-\frac{1}{2}}S_-[\psi_{n+1,m-1}{}^1\chi_-(k_m{}^-)], \tag{16}$$

where $\psi_{n+1,m-1}{}^1$ is the probability amplitude of the triply charged stable isobaric state p^{+++} for finding $n+1$ positive mesons and $m-1$ negative mesons. The procedure for the determination of the isobaric state wave function is identical with that used for the ground state. We shall in this paper use superscript 0 for quantities connected with the ground state and the superscript 1 for the corresponding quantities associated with the isobaric state p^{+++}. $\chi_-(k)$ represents the outgoing wave of a negative meson and $\chi_+(k)$ is defined as before.

Applying the variational principle (9) to the trial function (16) with independent variations of $\chi_+(k)$ and $\chi_-(k)$ we have

$$\begin{aligned}(\omega_k-\omega_0)\chi_+(k)&=\int K_{++}(k,k')\chi_+(k')d^3k'+\int K_{+-}(k,k')\chi_-(k')d^3k',\\ (\omega_k-\omega_1)\chi_-(k)&=\int K_{-+}(k,k')\chi_+(k')d^3k'+\int K_{--}(k,k')\chi_-(k')d^3k',\end{aligned} \tag{17}$$

where ω_0 and ω_1 are the total energy of the free positive meson and the outgoing negative meson, respectively. The kernels are

$$2K_{++}(k,k')=\mathfrak{M}_+{}^0g[f_+{}^0(k)u(k')+u(k)f_+{}^0(k')]-\mathfrak{N}_+{}^0(\omega_k+\omega_{k'}-2\omega_0)f_+{}^0(k)f_+{}^0(k'),$$

$$\begin{aligned}2K_{+-}(k,k')&=2K_{-+}(k',k)\\&=g\mathcal{O}f_+{}^1(k)u(k')+g\mathcal{P}u(k)f_-{}^0(k')-\mathcal{Q}(\omega_k+\omega_{k'}-\omega_0-\omega_1)f_+{}^1(k)f_-{}^0(k'),\end{aligned}$$

and

$$2K_{--}(k,k')=\mathfrak{M}_+{}^1g[f_-{}^1(k)u(k')+u(k)f_-{}^1(k')]-\mathfrak{N}_+{}^1(\omega_k+\omega_{k'}-2\omega_1)f_-{}^1(k)f_-{}^1(k'),$$

where $\mathfrak{M}_+{}^0$, $\mathfrak{N}_+{}^0$ are defined by Eq. (6) and $\mathfrak{M}_+{}^1$, $\mathfrak{N}_+{}^1$ are the corresponding quantities for the state p^{+++}. The constants $\mathcal{O}$, $\mathcal{P}$, $\mathcal{Q}$, are

$$\begin{aligned}\mathcal{O}&\equiv\sum_{n=1}^{\infty}C_{n,n-1}{}^0C_{n+1,n-1}{}^1(n+1)^{\frac{1}{2}}\left[\int f_+{}^1(k)f_+{}^0(k)d^3k\right]^n\times\left[\int f_-{}^1(k)f_-{}^0(k)d^3k\right]^{n-1},\\ \mathcal{P}&\equiv\sum_{n=1}^{\infty}C_{n+1,n-1}{}^1C_{n+1,n}{}^0n^{\frac{1}{2}}\left[\int f_+{}^0(k)f_+{}^1(k)d^3k\right]^{n+1}\times\left[\int f_-{}^0(k)f_-{}^1(k)d^3k\right]^{n-1},\end{aligned} \tag{18}$$

and

$$\mathcal{Q}\equiv\sum_{n=1}^{\infty}\sum_{m=n-1}^{n}C_{n,m}{}^0C_{n+1,m-1}{}^1[(n+1)m]^{\frac{1}{2}}\times\left[\int f_+{}^1(k)f_+{}^0(k)d^3k\right]^n\left[\int f_-{}^1(k)f_-{}^0(k)d^3k\right]^{m-1},$$

[8] For simplicity we have restricted ourselves to energy less than 2μ. At greater energy, multiple production of mesons is possible which must be taken into account by adding additional outgoing waves in the trial function.

where $C_{n,m}{}^0$ and $C_{n,m}{}^1$ are the total probability amplitude for finding n positive mesons and m negative mesons in the ground state and the triply charged isobaric state of the nucleon, respectively.

Upon noticing that the kernels of the integral equation (17) can be written as a sum of product functions each having only one variable, the solution for χ_+ and χ_- must, therefore, be of the form

$$\chi_+(k)=\delta^3(k-k_0)+\alpha_+{}^0 f_+{}^0(k)+\alpha_+{}^1 f_+{}^1(k) +[\beta_+{}^0 f_+{}^0(k)+\beta_+{}^1 f_+{}^1(k)+\gamma_+ u(k)] \times[\omega-\omega_0-i\epsilon]^{-1}, \quad (19)$$

and

$$\chi_-(k)=\alpha_-{}^0 f_-{}^0(k)+\alpha_-{}^1 f_-{}^1(k) +[\beta_-{}^0 f_-{}^0(k)+\beta_-{}^1 f_-{}^1(k)+\gamma_- u(k)][\omega-\omega_1-i\epsilon]^{-1},$$

where $\alpha_\pm{}^i$, $\beta_\pm{}^i$ $(i=0, 1)$, and $\gamma_\pm$ are numerical constants which can be determined by substituting Eq. (19) back into the integral equation (17).

Strong-Coupling Limit

It is of interest to examine the solution when the coupling constant is very large. In this case the energy separation $(\omega_0-\omega_1)$ of the isobaric state with the ground state is of the order g^{-2} and is neglected. Furthermore, the distribution functions of mesons around the nucleon becomes identical for the isobaric and the ground state as $g\to\infty$. We can then *in this limit*[9] set

$$\mathfrak{N}_+{}^0=\mathfrak{N}_+{}^1=\mathfrak{Q},$$

$$\mathfrak{M}_+{}^0=\mathfrak{M}_+{}^1=\mathfrak{O}=\mathfrak{P},$$

and

$$f_+{}^1=f_+{}^0=f_-{}^1=f_-{}^0=(u(k)/\omega)\left(\int d^3k u^2/\omega^2\right)^{-\frac{1}{2}}.$$

Thus the kernels become

$$K_{++}=K_{+-}=K_{-+}=K_{--}=K(k,k'),$$

where K is identical with that in Eq. (12). By forming the linear combinations $\chi_+\pm\chi_-$ we readily find

$$(\omega-\omega_0)[\chi_+(k)-\chi_-(k)]=0, \quad (20)$$

and

$$(\omega-\omega_0)[\chi_+(k)+\chi_-(k)] =2\int K(k,k')[\chi_+(k')+\chi_-(k')]d^3k'.$$

The first equation shows that the difference between $\chi_+(k)$ and $\chi_-(k)$ can only be a $\delta^3(k-k_0)$ so that *in the strong-coupling limit the charge exchange and nonexchange cross sections are equal*. The second equation can now be solved by casting $\chi_+(k)+\chi_-(k)$ into the same form as $\chi(k)$ in Eq. (14). On using the limiting values for $\mathfrak{N}_\pm{}^0$ and $\mathfrak{M}_\pm{}^0$ as tabulated in Table I we find the differential cross section $d\sigma_{++}/d\Omega$ and $d\sigma_{+-}/d\Omega$ for the reaction (A) and (B) to be

$$d\sigma_{++}/d\Omega=d\sigma_{+-}/d\Omega =4\pi^4\frac{f^4(k_0)\omega_0{}^2}{m^{-2}+[4\pi^2 f^2(k_0)k_0\omega_0]^2}+O(\mu/M), \quad (21)$$

where M^{-1} is the size of the source function and

$$m^{-1}=\mathrm{P}\int[f^2(k)/(\omega-\omega_0)]d^3k, \quad (22)$$

where P indicates that the principal value of the integral is to be taken. For a δ-function source (i.e., $M\to\infty$) we get for the total cross section when $\omega_0=\mu$

$$\sigma_{++}=\sigma_{+-}=\pi\mu^{-2}(2^{-1}+\pi^{-1})^{-2}, \quad (23)$$

while the rigorous treatment in the strong-coupling limit[4] yields

$$\sigma_{++}=\sigma_{+-}=\pi\mu^{-2}. \quad (24)$$

Hence, unlike Tomonaga's treatments on the bound states where the variational method leads to exact agreement with both the rigorous calculations for weak- and strong-coupling limits, our calculations for meson scattering give exact agreement only in the weak-coupling limit while in the strong-coupling limit the rigorous treatment differs from our result by the factor[10]

$$(\tfrac{1}{2}+1/\pi)^2$$

at zero energy. At other energy this factor is

$$\left[\left(\frac{1}{2}+\frac{1}{\pi}\right)+\frac{\mu-\omega_0}{2\omega_0}+\frac{(\omega_0{}^2-\mu^2)^{\frac{1}{2}}}{\pi\omega_0}\ln\frac{(\omega_0+\mu)^{\frac{1}{2}}-(\omega_0-\mu)^{\frac{1}{2}}}{(\omega_0+\mu)^{\frac{1}{2}}+(\omega_0-\mu)^{\frac{1}{2}}}\right]^2 +\left[\frac{\omega_0{}^2-\mu^2}{\omega_0{}^2}\right],$$

which only varies from about 0.7 to 0.8 as ω_0 increases from μ to 2μ.

V. INTERMEDIATE-COUPLING RANGE

In this section we shall present the results of the numerical calculations in the intermediate-coupling range. Figure 3 shows $k^2(d\sigma/d\Omega)$ as a function of energy for π^++p and π^-+p scattering. It is of interest to notice that even as $g^2=10$ the deviation in cross section from the strong-coupling limit is still substantial. Thus, at least throughout the range $1<g^2<10$, both the weak-

[9] The constants $\lambda_\pm{}^i$ in the strong-coupling limit are of the order g^{-2}. Thus, their influence on each of the overlapping integrals in (18) is of order g^{-4} which can be neglected in the present calculation. On the other hand, in the calculation of isobaric separation it is necessary to include $\lambda_\pm{}^i$ since the isobaric separation energy is itself of the order g^{-2}.

[10] This discrepancy presumably is due to the absence of polarization effect in our approximation. The inclusion of such effect, though desirable, tends to make the calculations at intermediate coupling range much more complicated.

and strong-coupling results are in very poor agreement with the intermediate-coupling results. In Fig. 4, $k\cot\delta$ is plotted against energy and shows that the scattering amplitudes for $\pi^+ + p$ and $\pi^- + p$ are very similar to *that of a short-range attractive potential and a short-range repulsive potential, respectively*, while for $\pi^+ + p$, a 90° phase shift is always possible at a suitable value of the energy, provided $g^2 \geq 4.0$. Yet the phase shift for $\pi^- + p$ would always be smaller than 90° except may be at the region of extremely large g values. Figure 5 shows the manner in which the scattering amplitude for zero incident kinetic energy ($\omega_0 = \mu$) changes smoothly from weak-coupling value to the strong-coupling value. It may be noted that for zero-energy $\pi^+ + p$ scattering, a phase shift of 90° will occur at a value of $g^2 = 4.0$. From Fig. 1 one sees that, by using the Tomonaga's technique for bound state, also at $g^2 = 4.0$, the first excited state p^{++} has a zero binding energy. Thus, at least in this case, the method for the bound state agrees with that for the scattering state.

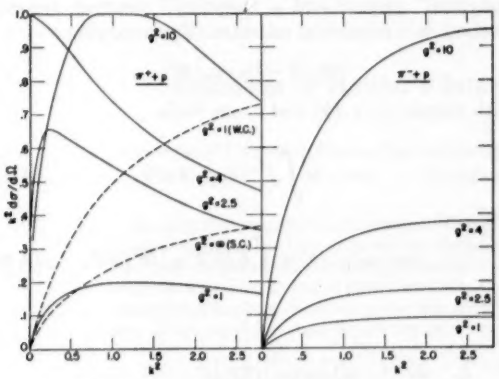

FIG. 3. $k^3 d\sigma/d\Omega$ *versus* k^2. Solid lines refer to intermediate coupling calculations.

While the detailed results are essentially of a numerical nature, some approximate expressions are found useful in understanding the over-all behavior of the cross sections. For $\pi^+ + p$ scattering it is found that with λ_+^0 in (15) taken equal to zero the phase shift δ may be written as[11]

$$\tan\delta = \frac{4\pi^2 (Rg^2) k_0 u^2(k_0)}{1-\Delta}, \qquad \Delta = Rg^2 \omega_0 \mathrm{P} \int [u^2/\omega^2(\omega-\omega_0)] d^3k. \tag{25}$$

Since the integral is in general positive (if $\omega_0 < 2\mu$), it is possible to find one resonance at any energy less than 2μ for some value of g. On the other hand, since the integral is a decreasing function of ω_0, the phase shift will be less than $\pi/2$ if g is smaller than the value of g required to give a resonance at zero energy, $\omega_0 = \mu$.

[11] A similar form for the phase shifts is obtained by G. Chew for pseudoscalar meson theory, using the Dancoff-type wave functions [Phys. Rev. **89**, 591 (1952)].

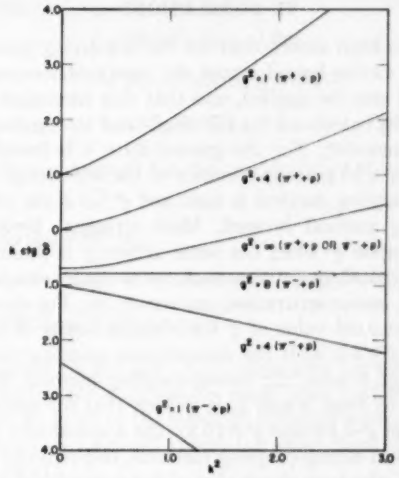

FIG. 4. $k\cot\delta$ *vs* k^2 for various g values.

Examination of the simplified form of the cross section indicates that essentially two distinct conditions must be satisfied to validate a perturbation calculation. These are (1) that the number of mesons about a nucleon be sufficiently small that the perturbation result agrees with the intermediate coupling result, namely

$$\mathfrak{N}_+^0 \cong g^2 \int [u^2(k)/\omega_k^2] d^3k < 1, \tag{26}$$

and (2) that the damping terms in the denominator be small compared with unity, i.e.,

$$\Delta < 1. \tag{27}$$

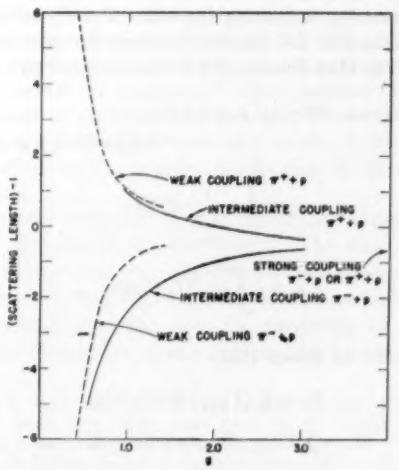
WEAK COUPLING $\pi^+ + p$
INTERMEDIATE COUPLING $\pi^+ + p$
STRONG COUPLING $\pi^- + p$ OR $\pi^+ + p$
INTERMEDIATE COUPLING $\pi^- + p$
WEAK COUPLING $\pi^- + p$
(SCATTERING LENGTH)$^{-1}$
g

FIG. 5. (Scattering length)$^{-1}$ *vs* g for $\omega_0 = \mu$.

VI. CONCLUSIONS

It has been shown that for the scattering processes as well as the bound states the intermediate-coupling method may be applied, and that this treatment joins all results calculated for the weak- and strong-coupling limits smoothly. For the ground state it is found that $g^2 \lesssim 1$ for a 10 percent accuracy in the self-energy if the weak-coupling method is used and $g^2 \lesssim 3$ if the strong-coupling method is used. More stringent limits are placed upon g^2 when the same accuracy is desired for more critical quantities such as average number of mesons, isobar separation, scattering, etc. For example, the calculated value of g^2 for a stable isobar of charge two is $g^2 \geq 4.0$ with the intermediate-coupling method and $g^2 \geq 5.8$ with the strong-coupling method. By referring to Figs. 3 and 5, it is seen that for scattering processes $g^2 < 1.0$ and $g^2 \gg 10$ for the applicability of the weak- and strong-coupling methods, respectively.

It has also been shown that $\pi^+ + p$ scattering is similar to scattering by a short-range attractive potential and that $\pi^- + p$ is similar to scattering by a repulsive potential.

The authors wish to thank Dr. C. N. Yang for some helpful discussions and express their gratitude to Professor Oppenheimer for the hospitality extended to them by the Institute for Advanced Study.

APPENDIX I

To derive the explicit forms of $\mathfrak{N}_\pm{}^0$ and $\mathfrak{M}_\pm{}^0$ we consider an alternative formulation of the Tomonaga method. In this formulation one approximates the annihilation and creation operators of the mesons by

$$\begin{aligned} &\alpha_k = f_+(k)\alpha; \quad \alpha_k{}^\dagger = f_+(k)\alpha^\dagger, \\ &\beta_k = f_-(k)\beta; \quad \beta_k{}^\dagger = f_-(k)\beta^\dagger, \end{aligned} \tag{A.1}$$

where α, β, and $\alpha^\dagger$, $\beta^\dagger$ are annihilation and creation operators independent of k. (In this section we omit the superscript indicating the state of the total charge as all equations are identical in form for any isobaric state.) The Hamiltonian (1) is then reduced to

$$H = \omega_+\alpha^\dagger\alpha + \omega_-\beta^\dagger\beta - \tau_+[g_+\alpha + g_-\beta^\dagger] - \tau_-[g_+\alpha^\dagger + g_-\beta], \tag{A.2}$$

where

$$\omega_\pm = \int \omega_k f_\pm{}^2(k)d^3k,$$

$$g_\pm = g\int u(k)f_\pm(k)d^3k.$$

It can then be shown that

$$\mathfrak{N}_+ = \sum |C_{n,m}|^2 n = \langle \alpha^\dagger\alpha \rangle_M,$$

and

$$\mathfrak{M}_+ = \sum C_{n+1,n}C_{n,n}(n+1)^{\frac{1}{2}} = \langle \alpha\tau_+ \rangle_M, \tag{A.3}$$

where $\langle\ \rangle_M$ means the diagonal matrix element. These averages can be obtained explicitly by converting α, β into real canonical conjugate variables, and the problem of determining the eigenstates of H [Eq. (A.2)] reduces to the problem of two coupled harmonic oscillators. In the strong-coupling limit, one may neglect higher orders in g^{-1} and set $f_+(k) = f_-(k)$. The results are listed in Table I.

APPENDIX II

The trial function Ψ representing the process,

$$\pi^- + p \to \pi^- + p,$$

differs slightly from that for π^+ scattering, Eq. (10), due to the possibility of finding a neutron with no mesons. The assumed form is now a combination of

$$\Psi = \int \chi_-(k)\beta_k{}^\dagger\Psi_P d^3k + c\Psi_N, \tag{A.4}$$

where Ψ_P and Ψ_N are the state vectors representing a "physical" proton and a "physical" neutron, respectively. c is a numerical constant. Upon varying

$$\langle \Psi | H - E_0 - \omega_0 | \Psi \rangle$$

with respect to $\chi_-(k)$ and c, one finds

$$c = -\mathfrak{R}\int f_+{}^0(k)\chi_-(k)d^3k, \tag{A.5}$$

and

$$(\omega - \omega_0)\chi_-(k) = \int K(k,k')\chi_-(k')d^3k', \tag{A.6}$$

where

$$\mathfrak{R} = \sum_{n=0}^{\infty}\sum_{m=n-1}^{n} C_{n,m}{}^0 C_{m+1,n}{}^0 (m+1)^{\frac{1}{2}} \times \left(\int f_+{}^0 f_-{}^0 d^3k\right)^{n+m}, \tag{A.7}$$

and

$$K(k,k') = \mathfrak{N}_-{}^0(\omega_0 + \lambda_-{}^0)f_-{}^0(k)f_-{}^0(k') - \mathfrak{R}^2\omega_0 f_+{}^0(k)f_+{}^0(k'). \tag{A.8}$$

Equation (A.6) can then be solved by assuming a form for $\chi_-(k)$ similar to that of Eq. (14). In the weak-coupling limit it yields the rigorous scattering amplitude.

APPENDIX III

In the case of elastic scattering (i.e., $\omega < 2\mu$ and no stable isobar of the nucleon exists), the rigorous Schrödinger wave function for the scattering of a positive meson with incident wave number k_0 by a proton can be written as

$$\psi_{n,m} = n^{-\frac{1}{2}} S_+\{\psi_{n-1,m}{}^0(k_1{}^+, \cdots, k_{i-1}{}^+, k_{i+1}{}^+, \cdots, k_n{}^+; k_1{}^-, \cdots, k_m{}^-) \times [\delta^3(k_i - k_0) + B_{n,m}{}^i(\omega_k{}^+ - \omega_0 - i\epsilon)^{-1}]\}, \tag{A.8}$$

where $B_{n,m}{}^{i}$ is a regular function of $k_1{}^{+}\cdots k_n{}^{+}$ and $k_1{}^{-}\cdots k_m{}^{-}$. The value of $B_{n,m}{}^{i}$ when $k_i{}^{+}=k_0$ represents the scattering amplitude of the ith meson; consequently

$$B_{n,m}{}^{i}|_{k_i{}^{+}=k_0}=B(k_0)$$

depends on k_0 only. These conditions are physically necessary for any elastic scattering problem and can be readily verified by a direct substitution into the Schrödinger equation. The differential cross section $d\sigma/d\Omega$ and the phase shift η are related to $B(k_0)$ by the relations:

$$\begin{aligned} d\sigma/d\Omega&=(4\pi^2)^2|B(k_0)|^2\omega_0{}^2, \\ B(k_0)&=(e^{2i\eta}-1)/8i\pi^2k_0\omega_0. \end{aligned} \tag{A.9}$$

Following Kohn's[12] variational treatment for scattering problem in momentum space, we find for the correct solution

$$\begin{aligned} J&=\langle\Psi|H-E_0-\omega|\Psi\rangle \\ &=B(k_0)-4i\pi^2k_0\omega_0|B(k_0)|^2 \\ &=\sin2\eta/8\pi^2k_0\omega_0, \end{aligned} \tag{A.10}$$

and the variation of J in the neighborhood of the correct Ψ is

$$\begin{aligned} \delta J&=\delta B(k_0)+\delta B^*(k_0) \\ &\quad+4i\pi^2k_0\omega_0[-B^*(k_0)\delta B(k_0)+B(k_0)\delta B^*(k_0)] \\ &=(4\pi^2k_0\omega_0)^{-1}(1+\cos2\eta)\delta\eta. \end{aligned} \tag{A.11}$$

Equations (A.10) and (A.11) then give the variational calculation for η. It can be easily seen that if one assumes Ψ to be of the form (8) a formal variation with respect to χ [Eq. (9)] gives the same result as (A.10) and (A.11).

[12] W. Kohn, Phys. Rev. **84**, 495 (1951).

PHYSICAL REVIEW VOLUME 94, NUMBER 6 JUNE 15, 1954

Solutions of Heitler's Integral Equation by Iteration Method

S. N. Biswas
Department of Theoretical Physics, Indian Association for the Cultivation of Science, Jadavpur, Calcutta, India
(Received August 28, 1953)

An iterative procedure analogous to Wagner's method for the numerical evaluation of the Fredholm integral equation has been proposed for the solution of Heitler's integral equation on radiation damping. It has been applied to the scattering of mesons by nucleons. The solution for the scattering of π^+ mesons by neutrons agrees with that of Hsueh and Ma, and Goldberger. For the scattering of π^+ mesons by protons, the solution has been taken up to the first approximation; the energy dependence and the angular distribution of the scattering cross section are shown in the accompanying figures.

1. INTRODUCTION

THE consideration of radiation reaction in quantum-mechanical collisional problems is absolutely necessary to remove the divergence difficulties inherent in collisions. The effect of radiation reaction is taken into account by an integral equation which cannot be solved exactly except in a very few cases; the difficulty of solving such an integral equation is due to the complicated nature of the kernel.

In view of this difficulty we are led to consider an approximate method for the solution of the integral equation. One approximate method that is often used for the treatment of scattering processes is the variational principle. But a serious objection to the variational techniques is that no definite mathematical statement can be made as to the error involved in the solution. On the other hand, the ordinary iterative procedure (Neumann sequence) is very slowly convergent and it suffers from the difficulty that the higher-order terms in the integral equation for the scattering process are very involved for computational purposes and in most cases the resulting series cannot even be summed. Hence there arises the necessity of considering a modified sequence for the iterational procedure so that it may converge rapidly and that only a few iterations should suffice.

The semivariational technique of Hsüeh and Ma[1] has been applied to the scattering of neutrons by protons[2] and mesons by nucleons.[1,3] Their solution shows the influence of radiation reaction only in the energy dependence of the total cross section but it fails to give any effect on the angular distribution of the scattered particle.

Another improved type of variational technique has been formulated by Goldberger.[4] The superiority of this method over that of Hsüeh and Ma has been shown by the fact that the solution obtained by Goldberger's variational procedure for the scattering of negative mesons by protons agrees with the exact solution of the

[1] C. F. Hsüeh and S. T. Ma, Phys. Rev. **67**, 303 (1945).
[2] D. Basu, Proc. Roy. Irish Acad. **53**, 31 (1950); D. Basu, Indian J. Phys. **25**, 246 (1951).
[3] S. N. Biswas, Indian J. Phys. **26**, 617 (1952).
[4] M. L. Goldberger, Phys. Rev. **84**, 99 (1951).

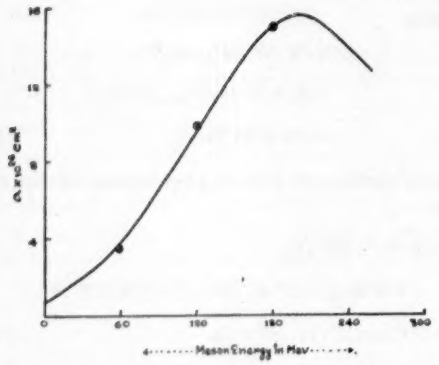

FIG. 1. Variation of the total scattering cross section with the energy of the incident meson.

integral equation as obtained by Hsüeh and Ma.[5] The same method has also been applied to the solution of the scattering of charged scalar mesons by nucleons.[6]

As an improvement we have here developed a method for the solution of the integral equation based on the iterative procedure for the numerical evaluation of the Fredholm's equation of the second kind, as recently proposed by Wagner.[7] This method consists in defining a modified sequence of approximations to the solution in such a way that the average of the absolute deviations of the approximate solutions from the true solution converges towards zero.

As an application of this method we have studied the scattering of negative mesons by protons and that of positive mesons by protons. It has been found that for the first process, an exact solution is obtained by only a single iteration after assuming an arbitrary initial approximate solution. The result obtained is in agreement with the solutions of Goldberger[4] and of Hsüeh and Ma.[5]

In another section we have considered the influence of radiation damping on the scattering of positive mesons by protons using the pseudoscalar meson field with pseudovector coupling. It is found that the inclusion of the radiation reaction prevents the indefinite increase of the scattering cross section with increasing energy as obtained from the pseudovector coupling when radiation reaction is neglected.

The variation of the total scattering cross section with the energy of the incident meson is shown in Fig. 1. Assuming the value of the coupling constant, g^2, to be 0.448, we see that the result agrees well with the experimental findings of Chedester *et al.*[8] In Fig. 2 the angular distribution of the scattered particle at 60-Mev incident meson energy under the influence of radiation damping is compared with a similar distribution without damping reaction. It may be remarked that this present method of solution shows that the angular distribution of the scattered particle is essentially altered by the radiation reaction, whereas the method of Hsüeh and Ma failed to give this alteration of the angular distribution. Curve I of the angular distribution indicates that the value of the scattering cross section falls sharply from 0° to 180°, showing a preponderance of forward scattering, while in curve II, the scattering cross section under the influence of radiation damping at first decreases and then begins to increase after 90°.

2. APPROXIMATION METHOD

Following Blatt[9] and Goldberger,[4] we write the well-known integral equation of Heitler for radiation damping in scattering processes in a more convenient way as follows:

$$\mathfrak{R}(\mathbf{k},\mathbf{k}_0)=\mathcal{G}(\mathbf{k},\mathbf{k}_0) -\rho_{k'}(k_0/4\pi i)\int \mathcal{G}(\mathbf{k},\mathbf{k}')\mathfrak{R}(\mathbf{k}',\mathbf{k}_0)d\Omega'. \quad (2.1)$$

The units $\hbar=c=1$ have been used throughout. We assume that an approximate solution $\mathfrak{R}^{(0)}(\mathbf{k},\mathbf{k}_0)$ is known for (2.1), where $\mathcal{G}(\mathbf{k},\mathbf{k}_0)$ and $\mathcal{G}(\mathbf{k},\mathbf{k}')$ stand respectively for the first Born approximation and the kernel of Eq. (2.1) and $\rho_{k'}$ is the density of the energy level. We now seek a closer approximation than $\mathfrak{R}^{(0)}$. We consider a modified sequence of functions for successive approximations suitable for the iterative procedure in the following way:

$$\mathfrak{R}^{(n+1)}(\mathbf{k},\mathbf{k}_0)=\mathfrak{R}^{(n)}(\mathbf{k},\mathbf{k}_0)+\Gamma^{(n+1)}(\mathbf{k},\mathbf{k}_0), \quad (2.2)$$

where $\Gamma^{(n+1)}(\mathbf{k},\mathbf{k}_0)$ represents the correction amplitude to be added to the preceding approximation $\mathfrak{R}^{(n)}(\mathbf{k},\mathbf{k}_0)$. Hence the true solution, $\mathfrak{R}(\mathbf{k},\mathbf{k}_0)$, is given by

$$\mathfrak{R}(\mathbf{k},\mathbf{k}_0)=\mathfrak{R}^{(0)}(\mathbf{k},\mathbf{k}_0)+\Gamma^{(1)}(\mathbf{k},\mathbf{k}_0) +\Gamma^{(2)}(\mathbf{k},\mathbf{k}_0)+\cdots. \quad (2.3)$$

Now, if Eq. (2.1) be approximated by $\mathfrak{R}^{(n)}(\mathbf{k},\mathbf{k}_0)$, then the deviation of the approximate solution from the true solution is given by

$$\Delta^{(n)}(\mathbf{k},\mathbf{k}_0)=\mathfrak{R}^{(n)}(\mathbf{k},\mathbf{k}_0)+\rho_{k'}(k_0/4\pi i) \times\int \mathcal{G}(\mathbf{k},\mathbf{k}')\mathfrak{R}^{(n)}(\mathbf{k}',\mathbf{k}_0)d\Omega'-\mathcal{G}(\mathbf{k},\mathbf{k}_0). \quad (2.4)$$

[5] C. F. Hsüeh and S. T. Ma, Proc. Cambridge Phil. Soc. **40**, 167 (1944).
[6] S. N. Biswas, Indian J. Phys. **27**, 197 (1953).
[7] C. Wagner, J. Math. and Phys. **30**, 23 (1951).
[8] Chedester, Isaacs, Sachs, and Steinberger, Phys. Rev. **82**, 958 (1951).
[9] J. M. Blatt, Phys. Rev. **72**, 466 (1949).

Each correction amplitude may be regarded as proportional to $\Delta^{(n)}(\mathbf{k},\mathbf{k}_0)$; hence

$$\Gamma^{(n+1)}(\mathbf{k},\mathbf{k}_0) = C(\mathbf{k},\mathbf{k}_0)\Delta^{(n)}(\mathbf{k},\mathbf{k}_0) = C(\mathbf{k},\mathbf{k}_0)\Big[\Re^{(n)}(\mathbf{k},\mathbf{k}_0)+\rho_{k'}(k_0/4\pi i)\times\int \mathcal{G}(\mathbf{k},\mathbf{k}')\Re^{(n)}(\mathbf{k}',\mathbf{k}_0)d\Omega' - \mathcal{G}(\mathbf{k},\mathbf{k}_0)\Big]. \quad (2.5)$$

We now set

$$C(\mathbf{k},\mathbf{k}_0) = -1\Big/\Big[1+\rho_{k'}(k_0/4\pi i)\int \mathcal{G}(\mathbf{k},\mathbf{k}')d\Omega'\Big],$$

such that

$$\int \mathcal{G}(\mathbf{k},\mathbf{k}')d\Omega' > 0, \qquad \int \mathcal{G}(\mathbf{k},\mathbf{k}')d\Omega' \neq 4\pi/(ik_0\rho_{k'}). \quad (2.6)$$

Putting this value of $C(\mathbf{k},\mathbf{k}_0)$ in (2.5), we get from (2.2) the following modified sequence for successive approximation:

$$\Re^{(n+1)}(\mathbf{k},\mathbf{k}_0) = \frac{\mathcal{G}(\mathbf{k},\mathbf{k}_0)+\rho_{k'}(k_0/4\pi i)\Re^{(n)}(\mathbf{k},\mathbf{k}_0)\int \mathcal{G}(\mathbf{k},\mathbf{k}')d\Omega' - \rho_{k'}(k_0/4\pi i)\int \mathcal{G}(\mathbf{k},\mathbf{k}')\Re^{(n)}(\mathbf{k}',\mathbf{k}_0)d\Omega'}{1+\rho_{k'}(k_0/4\pi i)\int \mathcal{G}(\mathbf{k},\mathbf{k}')d\Omega'}. \quad (2.7)$$

If we assume arbitrarily an initial function $\Re^{(n)}(\mathbf{k},\mathbf{k}_0)$ which is not dependent on angles, then (2.7) reduces to the simple form

$$\Re^{(n+1)}(\mathbf{k},\mathbf{k}_0) = \frac{\mathcal{G}(\mathbf{k},\mathbf{k}_0)}{1+\rho_{k'}(k_0/4\pi i)\int \mathcal{G}(\mathbf{k},\mathbf{k}')d\Omega'}. \quad (2.8)$$

The necessary criterion of convergence may be deduced in the same way as was done by Wagner.[7] Let the deviation of the nth approximation $\Re^{(n)}(\mathbf{k},\mathbf{k}_0)$ from $\Re(\mathbf{k},\mathbf{k}_0)$ be given by $E^{(n)}(\mathbf{k},\mathbf{k}_0)$, i.e.,

$$E^{(n)}(\mathbf{k},\mathbf{k}_0) = \Re^{(n)}(\mathbf{k},\mathbf{k}_0) - \Re(\mathbf{k},\mathbf{k}_0). \quad (2.9)$$

Inserting the value of $\Re^{(n)}(\mathbf{k},\mathbf{k}_0)$ from (2.9) into (2.5), we have

$$\Gamma^{(n+1)}(\mathbf{k},\mathbf{k}_0) = C(\mathbf{k},\mathbf{k}_0)\Big[\Re(\mathbf{k},\mathbf{k}_0)+E^{(n)}(\mathbf{k},\mathbf{k}_0) + \rho_{k'}(k_0/4\pi i)\int \mathcal{G}(\mathbf{k},\mathbf{k}')\Re(\mathbf{k}',\mathbf{k}_0)d\Omega' + \rho_{k'}(k_0/4\pi i)\int \mathcal{G}(\mathbf{k},\mathbf{k}')E^{(n)}(\mathbf{k}',\mathbf{k}_0)d\Omega' - \mathcal{G}(\mathbf{k},\mathbf{k}_0)\Big]. \quad (2.10)$$

With the help of (2.1), Eq. (2.10) reduces to

$$\Gamma^{(n+1)}(\mathbf{k},\mathbf{k}_0) = C(\mathbf{k},\mathbf{k}_0)\Big[E^{(n)}(\mathbf{k},\mathbf{k}_0)+\rho_{k'}(k_0/4\pi i)\times\int \mathcal{G}(\mathbf{k},\mathbf{k}_0')E^{(n)}(\mathbf{k}',\mathbf{k}_0)d\Omega'\Big]. \quad (2.11)$$

Now if $|\mathcal{G}(\mathbf{k},\mathbf{k}')|>0$ and $|\rho_{k'}(k_0/4\pi i)|>0$, it follows that

$$\Big|E^{(n)}(\mathbf{k},\mathbf{k}_0)+\rho_{k'}(k_0/4\pi i)\int \mathcal{G}(\mathbf{k},\mathbf{k}')E^{(n)}(\mathbf{k}',\mathbf{k}_0)d\Omega'\Big| \leq E_{\max}{}^{(n)}\Big[1+\rho_{k'}(k_0/4\pi i)\int \mathcal{G}(\mathbf{k},\mathbf{k}')d\Omega'\Big], \quad (2.12)$$

where $E_{\max}{}^{(n)}$ is the maximum of all deviations of the approximate solutions from the exact solution. Substituting the values of (2.6) and (2.12) into (2.11), we get

$$|\Gamma^{(n+1)}(\mathbf{k},\mathbf{k}_0)| \leq E_{\max}{}^{(n)}. \quad (2.13)$$

Next let us find the necessary condition for which the average of absolute deviations of the approximate amplitude from the exact one would tend to zero.

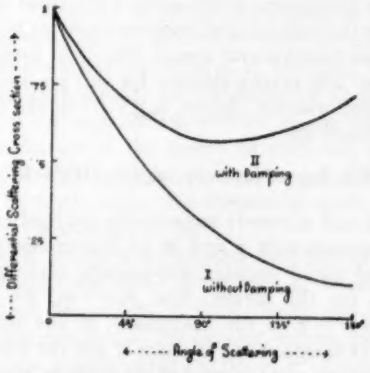

FIG. 2. Angular distribution of the scattered particle at 60-Mev incident meson energy; I, neglecting the influence of radiation damping; II, including this effect.

From Eq. (2.11) it follows that

$$|E^{(n+1)}(\mathbf{k},\mathbf{k}_0)| = |E^{(n)}(\mathbf{k},\mathbf{k}_0)+\Gamma^{(n+1)}(\mathbf{k},\mathbf{k}_0)|$$
$$\leq |1+C(\mathbf{k},\mathbf{k}_0)|\,|E^{(n)}(\mathbf{k},\mathbf{k}_0)|$$
$$+|C(\mathbf{k},\mathbf{k}_0)|\,\rho_{k'}(k_0/4\pi i)$$
$$\times\int |\mathcal{G}(\mathbf{k},\mathbf{k}')|\,|E^{(n)}(\mathbf{k}',\mathbf{k}_0)d\Omega'. \quad (2.14)$$

After obtaining the integral of the absolute value of $E^{(n+1)}(\mathbf{k},\mathbf{k}_0)$, we get

$$\int |E^{(n+1)}(\mathbf{k},\mathbf{k}_0)|\,d\Omega \leq \int |1+C(\mathbf{k},\mathbf{k}_0)|\,|E^{(n)}(\mathbf{k},\mathbf{k}_0)|\,d\Omega$$
$$+\int |E^{(n)}(\mathbf{k},\mathbf{k}_0)|\,\rho_{k'}(k_0/4\pi i)$$
$$\times\left[\int |C(\mathbf{k},\mathbf{k}_0)|\,|\mathcal{G}(\mathbf{k}_0,\mathbf{k}')|\,d\Omega\right]d\Omega'. \quad (2.15)$$

Hence

$$\int |E^{(n+1)}(\mathbf{k},\mathbf{k}_0)|\,d\Omega \leq U\int |E^{(n)}(\mathbf{k},\mathbf{k}_0)|\,d\Omega, \quad (2.16)$$

where U is such that

$$\left[|1+C(\mathbf{k},\mathbf{k}_0)|+\rho_{k'}(k_0/4\pi i)\right.$$
$$\left.\times\int |C(\mathbf{k}_0,\mathbf{k}')|\,|\mathcal{G}(\mathbf{k}',\mathbf{k}_0)|\,d\Omega'\right]\leq U.$$

Thus we see that the average of the absolute deviations $E^{(n)}(\mathbf{k},\mathbf{k}_0)$, $E^{(n+1)}(\mathbf{k},\mathbf{k}_0)$, $\cdots$ converges towards zero if U in (2.17) be less than unity, in which case the convergence will be rapid.

3. THE SCATTERING OF NEGATIVE MESONS BY PROTONS $(\pi^-+p)\rightarrow(\pi^-+p')$

As an illustration of the method described above, we consider the scattering of negative π mesons by protons, using the pseudoscalar meson field with pseudovector coupling. The matrix element for this process, according to perturbation theory, is given[10] in the center-of-mass system by

$$(\mathbf{p},\mathbf{k}|\,\mathbf{G}\,|\,\mathbf{p}_0,\mathbf{k}_0) = \bar{u}(a_1+a_2\gamma_4)u_0/[2\epsilon_0(W_0^2-M^2)], \quad (3.1)$$

where $\bar{u}$ and u_0 denote respectively the final and initial Dirac spinors with $\mathbf{p}$ and $\mathbf{p}_0$ as four-momenta of the final and initial nucleon, respectively, and similarly $\mathbf{k}$ and $\mathbf{k}_0$ for the meson. Also $p_0=-k_0$, $\mathbf{p}=-\mathbf{k}$, and $\epsilon_0=(\mu^2+p^2)^{\frac{1}{2}}\cdot p$ is the magnitude of the momentum and μ the meson mass. W_0 and M are the total energy of the system and the mass of the nucleon, respectively.

[10] Ashkin, Simon, and Marshak, Progr. Theoret. Phys. (Japan) 5, 634 (1950).

For pseudovector coupling, the parameters a_1 and a_2 of Eq. (3.1) have the following values:

$$a_1 = g^2M(M^2+3W_0^2)/\mu^2,$$
$$a_2 = g^2W_0(W_0^2+3M^2)/\mu^2, \quad (3.2)$$

where g is the coupling constant. The Heitler integral equation may be written as[4]

$$\mathcal{R}(\mathbf{p},\mathbf{k};\,\mathbf{p}_0,\mathbf{k}_0) = \mathcal{G}(\mathbf{p},\mathbf{k};\,\mathbf{p}_0,\mathbf{k}_0)+(ip/32W\pi^2)$$
$$\times\int d\Omega'\mathcal{G}(\mathbf{p},\mathbf{k};\,\mathbf{p}',\mathbf{k}')\Lambda(p')\mathcal{R}(\mathbf{p}',\mathbf{k}';\,\mathbf{p}_0,\mathbf{k}_0), \quad (3.3)$$

with the notation

$$(\mathbf{p},\mathbf{k}|\,\mathbf{G}\,|\,\mathbf{p}_0,\mathbf{k}_0) = (1/2\epsilon_0)\bar{u}\,\mathcal{G}(\mathbf{p},\mathbf{k};\,\mathbf{p}_0,\mathbf{k}_0),$$
$$(\mathbf{p},\mathbf{k}|\,\mathbf{R}\,|\,\mathbf{p}_0,\mathbf{k}_0) = (1/2\epsilon_0)\bar{u}\,\mathcal{R}(\mathbf{p},\mathbf{k};\,\mathbf{p}_0,\mathbf{k}_0).$$

$\Lambda(p)$ is the usual Feynman projection operator,

$$\Lambda(p) = (-i\gamma_\mu p_\mu+M).$$

We now propose to solve (3.3) with the help of our new method. According to (2.8), we write the solution as

$$\mathcal{R}(\mathbf{p},\mathbf{k};\,\mathbf{p}_0,\mathbf{k}_0) = \frac{\mathcal{G}(\mathbf{p},\mathbf{k};\,\mathbf{p}_0,\mathbf{k}_0)}{1-i(p/32W\pi^2)\int \mathcal{G}(\mathbf{p},\mathbf{k};\,\mathbf{p}',\mathbf{k}')\Lambda(p')d\Omega'} \quad (3.4)$$
$$=[\mathcal{G}(\mathbf{p},\mathbf{k};\,\mathbf{p}_0,\mathbf{k}_0)]/(1-i\lambda),$$

where

$$\lambda = (p/8\pi W)\,\mathcal{G}(\mathbf{p},\mathbf{k};\,\mathbf{p}_0,\mathbf{k}_0)(E_0\gamma_4+M),$$

E_0 being the nucleon energy. Hence

$$(\mathbf{p},\mathbf{k}|\,\mathbf{R}\,|\,\mathbf{p}_0,\mathbf{k}_0)$$
$$=\bar{u}\left\{\left[\frac{1+iK_1+iK_2\gamma_4}{(1+iK_1)^2+K_2^2}\right]\left[\frac{a_1-a_2\gamma_4}{(W_0^2-M^2)2E_0}\right]\right\}u_0. \quad (3.5)$$

Now by the usual procedure we obtain for the total cross section the following result:

$$\sigma = (8\pi/p^2)\left[\frac{K_1^2+K_2^2+(K_2^2-K_1^2)^2}{1+2(K_1^2+K_2^2)+(K_2^2-K_1^2)^2}\right], \quad (3.6)$$

where

$$K_1 = (p/8\pi W_0)\cdot(E_0a_2-Ma_1)/(W_0^2-M^2);$$
$$K_2 = (p/8\pi W_0)(E_0a_1-Ma_2)/(W_0^2-M^2).$$

The same result (3.6) has also been obtained by Hsüeh and Ma[1] and Goldberger[3] using different methods.

It may be mentioned here that we can easily verify that the solution (3.4) is an exact one, for if we iterate Eq. (2.7) once again, substituting in (2.7) the value (3.4) for $\mathcal{R}^{(n)}(\mathbf{k},\mathbf{k}_0)$, we will get the same result (3.4).

4. THE SCATTERING OF POSITIVE MESONS BY PROTONS $(\pi^+ + p) \rightarrow (\pi^{+\prime} + p')$

The Heitler integral equation for this scattering process is given by[11]

$$\mathfrak{R}(\mathbf{p},\mathbf{k};\,\mathbf{p}_0\mathbf{k}_0) = \mathcal{G}(\mathbf{p},\mathbf{k};\,\mathbf{p}_0,\mathbf{k}_0) - i(p/16\pi^2 W) \times \int d\Omega' \mathcal{G}(\mathbf{p},\mathbf{k};\,\mathbf{p}_0\mathbf{k}_0)\Lambda(\mathbf{p}')\mathfrak{R}(\mathbf{p}',\mathbf{k}';\,\mathbf{p}_0,\mathbf{k}_0), \quad (4.1)$$

where

$$(\mathbf{p},\mathbf{k}|\,\mathbf{R}\,|\,\mathbf{p}_0,\mathbf{k}_0) = \bar{u}\mathfrak{R}(\mathbf{p},\mathbf{k};\,\mathbf{p}_0,\mathbf{k}_0)u_0,$$
$$(\mathbf{p},\mathbf{k}|\,\mathbf{G}\,|\,\mathbf{p}_0,\mathbf{k}_0) = \bar{u}\mathcal{G}(\mathbf{p},\mathbf{k};\,\mathbf{p}_0\mathbf{k}_0)u_0.$$

The matrix element $(\mathbf{p},\mathbf{k}|\,\mathbf{G}\,|\,\mathbf{p}_0,\mathbf{k}_0)$ refers to the first nonvanishing approximation. According to pseudoscalar meson theory with pseudovector coupling, the relevant matrix element may be written in the center-of-mass system, with the usual notation (as in Sec. 3 and reference 9), in the following way:

$$\mathcal{G}(\mathbf{p},\mathbf{k};\,\mathbf{p}_0,\mathbf{k}_0) = i(g^2/\mu^2)[2M - R_2(\gamma_4\epsilon + \boldsymbol{\gamma}\cdot\mathbf{p}_0)], \quad (4.2)$$

with

$$R_2 = \frac{4M^2+\mu^2-2(p_0\cdot k)}{2(p_0\cdot k)-\mu^2}.$$

Now for the solution of (4.1) we have, according to (2.7),

$$\mathfrak{R}(\mathbf{p},\mathbf{k};\,\mathbf{p}_0,\mathbf{k}_0) = \frac{\mathcal{G}(\mathbf{p},\mathbf{k};\,\mathbf{p}_0,\mathbf{k}_0)}{1+(p/16\pi^2W)\int d\Omega'\mathcal{G}(\mathbf{p},\mathbf{k};\,\mathbf{p}',\mathbf{k}')\Lambda(p')}. \quad (4.3)$$

Substituting the values of $\mathcal{G}(\mathbf{p},\mathbf{k};\,\mathbf{p}_0,\mathbf{k}_0)$ and $\Lambda(p')$ from (4.2) and (3.3), we get

$$1+(p/16\pi^2W)\int d\Omega'\mathcal{G}(\mathbf{p},\mathbf{k};\,\mathbf{p}',\mathbf{k}')\Lambda(p') = K_1+K_2\gamma_4+K_3(\boldsymbol{\gamma}\cdot\mathbf{p})+K_4\gamma_4(\boldsymbol{\gamma}\cdot\mathbf{p}),$$

where K_1, K_2, K_3, and K_4 are given in the Appendix. Hence the solution of (4.1) is given by

$$\mathfrak{R}(\mathbf{p},\mathbf{k};\,\mathbf{p}_0,\mathbf{k}_0) = \frac{\mathcal{G}(\mathbf{p},\mathbf{k};\,\mathbf{p}_0,\mathbf{k}_0)}{[K_1+K_2\gamma_4+K_3(\boldsymbol{\gamma}\cdot\mathbf{p})+K_4\gamma_4(\boldsymbol{\gamma}\cdot\mathbf{p})]}.$$

Thus the matrix element is

$$(\mathbf{p},\mathbf{k}|\,\mathbf{R}\,|\,\mathbf{p}_0,\mathbf{k}_0) = i(g^2/\mu^2)\bar{u}\left\{\frac{[K_1-K_2\gamma_4-K_3(\boldsymbol{\gamma}\cdot\mathbf{p})-K_4\gamma_4(\boldsymbol{\gamma}\cdot\mathbf{p})][2M-R_2(\gamma_4\epsilon+(\boldsymbol{\gamma}\cdot\mathbf{p}_0))]}{K_1^2+K_2^2+p^2(K_3^2+K_4^2)}\right\}u_0.$$

The differential cross section for this process is

$$d\sigma = d\Omega/(32\pi^2W^2)\cdot \mathrm{Tr}(\Lambda(p)\mathfrak{R}\Lambda(p_0)\gamma_4\mathfrak{R}^\dagger\gamma_4), \quad (4.4)$$

where we have taken the average of the initial spin states and performed the summation over the final spin of the nucleon. Thus

$$d\sigma = d\Omega\{g^4/[4\pi^2\mu^2(x_1+x_2)^2R(x)]\} \times\{A(x)+B(x)\cos\theta+C(x)R_2+D(x)R_2\cos\theta +[E(x)+F(x)\cos\theta]R_2^2\}. \quad (4.5)$$

After integrating over all angles the total cross section becomes

$$\sigma = \frac{g^4}{2\pi(x_1+x_2)^2\mu^2R(x)}\cdot\left[A(x)+\tfrac{1}{2}C(x)\left(1-\frac{\rho^2}{x^2}\ln\frac{2x^2+1}{2x^2-1}\right) - D(x)\left(4x^2+\ln\frac{2x^2+1}{2x^2-1}\right)\frac{\rho^2}{4x^4} + E(x)\left(1-\frac{4\rho^2}{x^2(4x^4-1)}-\frac{2\rho^2}{x^2}\ln\frac{2x^2+1}{2x^2-1}\right) +F(x)\frac{\rho^2}{x^4}\left(3\ln\frac{2x^2+1}{2x^2-1}+\frac{4}{4x^4-1}+4x\right)\right], \quad (4.6)$$

where $x=p/\mu$; $x_1=E/\mu$; $x_2=\epsilon/\mu$; $\rho=M/\mu$; and the functions $R(x)$, $A(x)$, $B(x)$, $C(x)$, $D(x)$, $E(x)$, and $F(x)$ are given in the Appendix.

[11] N. Fukuda and T. Miyazima, Progr. Theoret. Phys. (Japan) 5, 849 (1950).

5. DISCUSSION AND COMPARISON WITH EXPERIMENT

From the theoretical values obtained according to Eq. (4.6), the energy dependence of the total cross section for the scattering of positive mesons by protons is shown in Fig. 1. To bring the theoretical result into agreement with the experimental findings, the pseudovector coupling constant g^2 is taken to be 0.448. The ratio M/μ, denoted by ρ, is taken to be 6.67 by using for the meson mass the value $276m_e$ (m_e = mass of electron). The effect of radiation damping is to bring down the value of the scattering cross section after it has reached a maximum value at an energy of 180 Mev for the incident meson; the prevention of an indefinite increase of the cross section with increasing energy is a desirable feature of the theory of radiation reaction. The experimental points of Steinberger[5] have been marked by small circles; the theoretical result is represented by the continuous line.

In Fig. 2, we show the angular distribution of positive π mesons scattered by protons at 60 Mev. We have drawn two curves to show clearly the influence of radiation reaction on the angular distribution; curve II gives the angular distribution of π^+ mesons when radiation reaction has been included, whereas curve I is obtained from the second-order perturbation method

without the consideration of radiation damping. The latter result has been taken from the calculations of Ashkin, Simon, and Marshak.[10]

From curve I of Fig. 2, it is evident that the differential cross section (without radiation damping) falls sharply from 0° to 180° and shows a general tendency toward forward scattering. When we consider the effect of radiation reaction the nature of the curve is changed; it is approximately symmetrical about 90°. The effect of including radiation reaction is to give more backward scattering than would be obtained without radiation damping. As the experimental data are not available, we cannot discuss the significance of this result.

ACKNOWLEDGMENT

The author wishes to express his sincere gratitude to Dr. D. Basu for the suggestion of the problem and for his valuable advice and his sympathetic interest throughout the preparation of this work.

APPENDIX

$$A(x)=2\Gamma_1(x)(K_1\rho x_1-K_2\rho^2)+2\Gamma_2(x)(K_1-K_2)\rho^2 +2\Gamma_3(x)(K_4x_1-K_3\rho)x^2\rho-2\Gamma_4(x)(K_4x_1-K_3x_2)x^2\rho.$$

$$B(x)=\Gamma_1(x)x^2\rho K_4-2\Gamma_2(x)K_3x^2x_1 +2\Gamma_3(x)K_1x^2\rho+2\Gamma_4(x)K_2x^2\rho.$$

$$C(x)=\Gamma_1(x)(K_2x_2-K_1\rho)x_1+\Gamma_2(x)(K_2x^2-K_1x_1x_2) +\Gamma_3(x)(K_3x^4+K_4x^4+K_4x^2x_1\rho) +\Gamma_4(x)(K_3\rho+K_4x_1)x^2\rho+2T_1(x)(K_1\rho x_1-K_2\rho^2) +2T_2(x)(K_1-K_2)\rho^2-2T_3(x)K_2\rho x^2 +2T_4(x)(K_3\rho-K_4x_1)x^2\rho+2T_5(x)(K_4x-K_3x_1)x^2\rho -2T_6(x)K_3x^4-2T_7(x)K_1x^2\rho-2T_8(x)K_4x^2\rho.$$

$$D(x)=2[T_6(x)(K_1\rho-K_3x_2)+T_7(x)(K_3x-K_4x_2) +T_8(x)(K_1x_1-K_3x)-T_1(x)K_4-T_2(x)K_1 -T_4(x)K_1-T_5(x)K_2]x^2\rho-2T_2(x)K_3x^2x_1.$$

$$E(x)=T_1(x)(K_2x_2-K_1\rho)x_1+T_2(x)(K_2x^2-K_1x_1x_2 -K_1x^2+K_2\rho x_2)-T_3(x)K_2\rho x^2-T_4(x)(K_3x^2 +K_4x^2-K_4\rho x_1)x^2-T_5(x)(K_3\rho+K_4x_1)x^2x_2 -T_6(x)(K_1x_1+K_3\rho-K_4x_2+K_4\rho) +T_7(x)(K_1\rho+K_2x_1-K_1x_2-K_2x_2)x^2 +T_8(x)(K_3x_2+K_4x_1)x^4.$$

$$F(x)=T_1(x)(K_3x_2+K_4x_1)x^2+T_2(x)(K_3x_1+K_4\rho)x^2 -T_3(x)(K_3\rho+K_4x_1)x^2x_2+T_4(x)(K_1\rho+K_2x_1 +K_3x_1x_2)x^2+T_5(x)(K_1x_2-K_2\rho)x^2 +T_6(x)K_2\rho x^2x_2+T_7(x)(K_3x_1+K_4\rho)x^2x_1 -T_8(x)(K_1\rho-K_2x_1)x^2\rho.$$

$$\Gamma_1(x)=2\rho(K_1x_1-K_2\rho+K_4x^2);$$

$$\Gamma_2(x)=2\rho(K_1\rho-K_2x_1+K_3\rho);$$

$$\Gamma_3(x)=-2\rho(K_1+K_3\rho+K_4x_1);$$

$$\Gamma_4(x)=-2\rho(K_2+K_3x_1+K_4x_1).$$

$$T_1(x)=x_2(K_2x_1-K_1\rho+K_3x^2);$$

$$T_2(x)=x_2(K_2\rho-K_1x_1+K_4x^2);$$

$$T_3(x)=(K_2\rho-K_1x_1);$$

$$T_4(x)=x_2(K_3x_1-K_2-K_4\rho);\quad T_5(x)=x_2(K_3\rho-K_4x_1);$$

$$T_6(x)=(K_4\rho-K_1);$$

$$T_7(x)=-(K_4x^2+K_2x_2+K_1\rho);$$

$$T_8(x)=(K_4x_1+K_3x_1+K_2).$$

$$K_1=1+g^2x(4\pi)^{-1}(x_1+x_2)^{-1}(2\rho^2+x^2+x_1x_2) -J_1x\rho^2g^2(2\pi)^{-2}(x_1+x_2)^{-1}(x^2+x_1x_2);$$

$$K_2=g^2\rho x(4\pi)^{-1}(x_1+x_2)^{-1}[(2x_1+x_2)-J_2\rho^2x_2];$$

$$K_3=-J_2xg^2x_2\rho^3(2\pi)^{-2}(x_1+x_2)^{-1};\quad K_4=x_2x_3$$

$$R(x)=[(K_1^2+K_2^2)+x^2(K_3^2+K_4^2)]^2.$$

$$J_1=\pi\ln\frac{\Lambda^2}{\Lambda^2+4p^2};\quad J_2=\pi\left\{1+\left(\frac{2p^2+\Lambda^2}{\Lambda^2}\right)\ln\frac{\Lambda^2}{\Lambda^2+4p^2}\right\};$$

with

$$\Lambda^2=M^2+2\mu^2-W^2.$$

Some Applications of the Mass Operator in Quantum Electrodynamics*

ROGER G. NEWTON†‡
Harvard University, Cambridge, Massachusetts
(Received October 20, 1953)

The one-photon mass operator is calculated explicitly up to the second order in the applied field, once for the purpose of taking matrix elements between states that satisfy the complete Dirac equation, and once for free-electron states. The former is manifestly gauge-invariant. The part linear in the applied field is also calculated for matrix elements, only one side of which satisfies the Dirac equation; it is seen, in application, to cancel precisely the non-gauge invariant part (for free electrons) of the second-order mass operator. A systematic procedure for carrying out the photon integration at the very beginning of the calculation is described and used. After the (nonperturbation) derivation of a cross-section formula in terms of the mass operator, the latter is used to rederive the integrated Klein-Nishina formula and also applied to the simple case of a constant field. The use of the mass operator technique for the calculation of inelastic cross sections is demonstrated and it is proved that, except for virtual processes induced by the radiation field (in contrast to the static field), the low-energy limit of the bremsstrahlung cross section is a multiple of the one for elastic scattering (to all orders). Finally, the lowest order-radiative corrections to Coulomb scattering are rederived.

I. INTRODUCTION

SCHWINGER has shown[1] that the interaction of electrons with the fluctuating radiation field can be described by means of a modified (and no longer second-quantized) Dirac equation in which the numerical mass is replaced by an operator in the ordinary quantum-mechanical sense, that is to say, an integral operator in the coordinate representation. The present paper has the dual purpose of explicitly exhibiting the one-photon part of this mass operator up to the second power in the external field, and of illustrating the mass operator technique by means of some simple applications. The result of the first part is somewhat more general and at the same time simpler than that previously known.[2] It has been applied to the calculation of radiation corrections to Coulomb scattering up to terms quadratic in the Coulomb field. This calculation will be dealt with in a future paper.

In the first approximation, so far as the intermediate presence of photons is concerned, the mass operator is given by (in the coordinate representation)[3]:

$$M(x,x')=m\delta(x-x')+ie^2\gamma_\mu G(x,x')\gamma_\mu D(x,x'), \quad (1.1)$$

where G and D are the outgoing wave Green's functions of the Dirac field and the Maxwell field, respectively. Equation (1) may be written in operator form:

$$M=m+ie^2\int\frac{(dK)^4}{(2\pi)^4}\frac{1}{K^2}e^{iKx}\gamma_\mu(m+\gamma\pi)^{-1}\gamma_\mu e^{-iKx},$$

and for the representation of the inverse operators with the outgoing-wave boundary condition the proper time procedure is used:

$$M=m-ie^2\int_0^\infty ds\int_0^\infty dt\int\frac{(dK)^4}{(2\pi)^4}\exp(-itK^2)e^{iKx}\gamma_\mu \cdot\tfrac{1}{2}\{(m-\gamma\pi),\exp[-is(m^2-(\gamma\pi)^2)]\}\gamma_\mu e^{-iKx}. \quad (1.2)$$

The fact that s and t extend to $+\infty$ implies that, strictly speaking, the masses of the electron and the photon are to be supplemented by small negative imaginary quantities in order to insure convergence of the integrals; it is therefore proper to the outgoing-wave Green's function.

For calculational purposes G must be expanded in powers of the applied field. The part of the mass operator linear in the latter will in the future be called "the first-order mass operator," the part quadratic in it "the second-order mass operator." Section II will be concerned with the derivation and explicit exhibition of these two for arbitrary fields. They are manifestly gauge-invariant when gauge-invariant matrix elements are taken. A relatively simple new technique of carrying out the photon integration at the beginning of the calculation is used. (The systematic calculational process involved is described in Appendix I.) Section IV will show the application of the second-order mass operator to the special cases of the uniform field and the pure radiation field, the latter being applied to a rederivation of the integrated Klein-Nishina formula. Using the result of Sec. III, which contains the rigorous derivation of a cross-section formula in terms of field dependent operators in the Dirac equation, Sec. V concerns itself with that part of the inelastic cross section which describes the scattering accompanied by the emission of exactly one low-energy photon (there called the "slightly inelastic cross section"). It is needed as a supplement to the elastic cross section (resulting in the "essentially elastic cross section") in order to eliminate

* Based, for the most part, on part of a thesis presented in partial fulfillment of the requirements for the degree of Doctor of Philosophy at Harvard University, September, 1953.

† Most of this work was done while the author was an Eastman Kodak predoctoral fellow.

‡ Now at the Institute for Advanced Study, Princeton, New Jersey.

[1] J. Schwinger, Proc. Natl. Acad. Sci. U. S. **37**, 452 ff (1951).

[2] R. Karplus and A. Klein, Phys. Rev. **85**, 978 ff (1952).

[3] Reference 1, Eq. (48).

the infrared divergencies. A general result, expressing the low-energy limit of the bremsstrahlung cross section as a multiple of the elastic one, is proved and the first-order slightly inelastic cross sections derived. Section VI treats the first-order radiative corrections to the cross section and contains a rederivation of Schwinger's result.

The notation used is the following. "Natural units" are used, in which $\hbar=c=1$ and $\alpha=e^2/4\pi$. The Dirac matrices are anti-Hermitian when $\mu=1, 2, 3, 4$; γ_0 is Hermitian. The summation convention is employed throughout and, generally, indices are suppressed. No special notation will be used to indicate four-vectors, but three-vectors are usually distinguished from them by the use of bold-face type. FF will in general stand for $F_{\mu\nu}F_{\mu\nu}$, and σF means $\sigma_{\mu\nu}F_{\mu\nu}$, where $\sigma_{\mu\nu}=\frac{1}{2}i[\gamma_\mu,\gamma_\nu]$. In Sec. II, p will denote the four-momentum *operator*, and x, the coordinate *operator*.

II. THE MASS OPERATOR

If the Dirac equation, modified to include radiation effects, is written symbolically:

$$(\gamma\pi+M)\psi=0,$$

then the mass operator M must, in the absence of any electromagnetic field, yield the numerical mass of the electron. The difference between M and m does not tend to zero as F tends to zero, but it tends to a function of the momentum, which, upon operating on a solution of the Dirac equation (in the absence of a field), equals a numerical function of m (to the present order of calculation). The sum of this function and m must therefore be the experimental mass of the electron. If, then, by the mass of an electron a number is meant that is independent of the external field, an operator must be subtracted from the radiative mass operator which, when operating on a solution of the Dirac equation in the presence of a field, equals precisely the same function of m (to the present order) as does the radiative mass operator in the absence of a field. At the same time this "renormalization operator" is added to m, the sum of which two is then a number (when operating on a solution of the Dirac equation) independent of the electromagnetic field. In addition to the physical reasonableness of the renormalization, it has the effect of leaving a finite radiative mass operator while all the divergencies originally occurring in it are now shifted to the numerical part where they are relatively harmless.

The radiative mass operator is given by

$$\Delta M=-ie^2\int_0^\infty ds\int_0^\infty dt\int\frac{(dK)^4}{(2\pi)^4}\times\exp(-itK^2)\mathfrak{M}(K), \quad (2.1)$$

where

$$\mathfrak{M}=\tfrac{1}{2}e^{iKx}\gamma_\mu\{(m-\gamma\pi),\exp[-is(m^2-(\gamma\pi)^2)]\}\gamma_\mu e^{-iKx}. \quad (2.2)$$

In the absence of an electromagnetic field $A_\mu=[p_\mu,B]$, $[\pi_\mu,\pi_\nu]=0$ where B is a scalar function of x. It is then easily possible to carry out the photon summations, i.e., the K integration and the $\gamma_\mu\cdots\gamma_\mu$ summation. The result is a function of $\gamma\pi$:

$$\Delta M_0=-ie^2\int_0^\infty ds\int_0^\infty dt\int\frac{(dK)^4}{(2\pi)^4}\exp[-i(s+t)K^2]\times\{\exp[-is(m^2-(1-u)(\gamma\pi)^2)],[-2m-(1-u)\gamma\pi]\},$$

where $u=s(s+t)^{-1}$. Then, to the present order:

$$\Delta M_0\psi_0=2ie^2m\int_0^\infty ds\int_0^\infty dt\int\frac{(dK)^4}{(2\pi)^4}\times\exp[-i(s+t)K^2](1+u)\exp(-isum^2)\psi_0. \quad (2.3)$$

Hence, the renormalization operator is

$$\Delta M_0=ie^2\int_0^\infty ds\int_0^\infty dt\int\frac{(dK)^4}{(2\pi)^4}\times\exp[-i(s+t)K^2]\{[2m+(1-u)\gamma\pi],\exp[-is(m^2-(1-u)(\gamma\pi)^2)]\}, \quad (2.4)$$

because it satisfies (3) when ψ_0 is replaced by ψ.

The K integration is directly carried out in (4), because it was possible to shift the origin of K_μ by π_μ, all of which commuted and thus could be treated like numbers. In (1), which can be written:

$$\Delta M=-ie^2\int_0^\infty ds\int_0^\infty dt\int\frac{(dK)^4}{(2\pi)^4}\exp(-itK^2)\tfrac{1}{2}\gamma_\mu\times\{[m-\gamma(\pi-K)],\exp[-is[m^2-(\gamma(\pi-K))^2]]\}\gamma_\mu,$$

no such shift can be made. As a result it has in the past been considered impossible to do the K integration at this stage.[4] Since it is desirable to be rid of the photon integration before doing any calculation of mass operator terms, we have at this point departed from that view and carried out the K integration first.

The integral $\int(dK)^4\exp(iK^2+iA\cdot K)$, where the vector A is a set of numbers, is customarily carried out by completing the square and then shifting the origin of the K integration, after which it becomes the well-known Gaussian integral, with the value $i\pi^2\exp(-iA^2/4)$. It can, however, be evaluated differently. One may expand $e^{iA\cdot K}$ and then integrate the series term by term. Afterwards the series is summed again and the result is, as it must be, the same as the one obtained by the first method. In case the vector A is not a set of numbers, but a set of noncommuting operators, the first method is not applicable, but the second one is. From the expansion of $e^{iA\cdot K}$, in which all terms must be quite

[4] R. Karplus and A. Klein, Phys. Rev. **86**, 290 (1952).

symmetrically distributed, it is clear that the same must be the case for the result after the integration. The result will therefore be:

$$\int (dK)^4 \exp(iK^2+iA\cdot K)=i\pi^2\exp(-iA_\mu|A_\mu/4), \quad (2.5)$$

where the bar indicates that in the expansion it is not A^2 that is to be symmetrized with respect to the other squares, but each component has to be symmetrized separately with respect to all others, so that A_ν's will get to stand between two equal factors: $\cdots A_\mu\cdots A_\nu\cdots A_\mu\cdots$. A very convenient way of dealing with this kind of situation is the use of Feynman's position integrals.[5] That method, of course, could have been used in the first place to derive (5) very easily. Every operator is provided with an attached parameter variable running, say, from zero to one, and then immediately integrated over. The only purpose of the parameter is to indicate its position, with the understanding that the ones with the lower value stand to the right. The position of such operators with integrals attached can then be changed freely; in short, they can be treated like numbers. In order for the results to be useful, after an expansion, say, it must be possible to convert the position integral notation into the more usual one. That, of course, is the main problem. In the case of the integration problem one could have attached such an integral to A:

$$\int (dK)^4 \exp\left\{iK^2+iK\cdot\int_0^1 A(t)dt\right\},$$

and then proceeded as though $\int_0^1 A_\mu(t)dt$ were a set of numbers, with the result:

$$i\pi^2\exp\left\{(i/4)\left[\int_0^1 A_\mu(t)dt\int_0^1 A_\mu(t)dt\right]\right\}.$$

This is the same as (5) since the integrals attached on each component separately also means complete symmetrization in the expansion.

The application of this procedure to the mass operator results in the following:

$$\Delta\bar{M}=\Delta M-\Delta M_0=-\frac{\alpha}{4\pi}\int_0^\infty\frac{ds}{s}\int_0^1 du\mathfrak{M}(u,s),\qquad \mathfrak{M}=\mathfrak{M}-\mathfrak{M}_0,$$

$$\mathfrak{M}=\tfrac{1}{2}\gamma_\mu\left\{\left(m-\gamma\pi+u\gamma\int\pi\right),\right. \quad (2.6)$$

$$\left.\exp\left[-is\left(m^2-\int(\gamma\pi)^2-u\int\pi_\mu\int\pi_\mu\right)\right]\right\}\gamma_\mu,$$

$$\mathfrak{M}_0=-\{(2m+(1-u)\gamma\pi),\qquad \exp[-is(m^2-(1-u)(\gamma\pi)^2)]\}.$$

[5] R. Feynman, Phys. Rev. **84**, 108 ff (1951).

Appendix I describes a systematic procedure for converting such terms as the above into the ordinary notation after the exponential is expanded.

In the following the exponential in the mass operator will be expanded in powers of the field and only the first and second powers will be kept. Then the potential is Fourier analyzed. The first-order terms have one Fourier integral, the second-order terms, two, which are taken outside. Thus every field variable $A(x)$ is replaced by

$$A(k)e^{ikx}=\int(dx')^4(2\pi)^{-2}e^{ik(x-x')}A_\mu(x').$$

This facilitates commuting functions of the momentum with the field variables when the relation,

$$f(x)g(p)=g\left(p+i\frac{\partial}{\partial x}\right)f(x)=g(p)f\left(x+i\frac{\partial}{\partial p(\leftarrow)}\right), \quad (2.7)$$

is used. (This equation is readily proved for powers of x and p and then extended by expanding other functions in power series.) The left-hand field always carries k_1, the right, k_2. Furthermore, we are at present interested only in the application of the mass operator to solutions of the zero-order Dirac equation, i.e., matrix elements between free electron states. Another way of stating this is that the mass operator is flanked on both sides by $(m-\gamma p)$, where p is the momentum of an electron. Therefore $(m+\gamma p)$ will be set equal to zero whenever it occurs on the outside of an expression. If one is interested in the application to solutions of the complete Dirac equation, in the presence of a field, further contributions to the second order will come from the first-order term. These are also calculated. There is no further contribution from the second-order terms, since those would be of the third order.

The conversion of the position integrals into normal notation introduces the usual integrations over as many auxiliary parameters as there are factors to be symmetrized. In the first-order terms the exponentials look as follows:

$$\int_0^1 dv_1\exp\{-is(1-v_1)\times[H-u(p_1^2(1-v_1)+v_1p_1p_2)]\}\cdots\times\exp\{-isv_1[H-u(p_2^2v_1+(1-v_1)p_1p_2)]\},$$

where the subscripts on p indicate their position on the left, if 1, or on the right, if 2, of the entire expression. In the center stands a field variable, i.e., $f(k)e^{ikx}$, and $H=m^2+p^2$. The use of (7) reduces this to:

$$\int_0^1 dv e^{-is(1-v)(1-u)H}\ldots e^{-isv(1-u)H}\times\exp\{-isu[m^2+v(1-v)k^2]\}.$$

For the purpose of matrix elements between states that satisfy the field free Dirac equation, this further sim-

plifies to

$$\int_0^1 dv\,\exp\{-isu[m^2+v(1-v)k^2]\}\cdots.$$

For states in the presence of a field, the relations:

$$\mathbf{H}=m^2-(\gamma\pi)^2,\quad p^2=-(\gamma\pi)^2-e\{\gamma p,\gamma A\},$$

$$e^{a\mathbf{H}}=\exp(a\mathbf{H})$$

$$-ea\int_0^1 dv\,\exp[a(1-v)\mathbf{H}]\{\gamma p,\gamma A\}\exp(av\mathbf{H}),$$

are used, where now $\mathbf{H}$ on the outside can be set equal to zero. There will then always be a factor with an $\mathbf{H}$ left in the center. The variables will be labeled so that the center term is $\exp\{-isv_1(1-v_2)(1-u)\mathbf{H}\}$ and then variables are changed as $v_1v_2\to v_2$.

Most of the second-order terms are of the form

$$\int_0^1 dv_1\int_0^{v_1} dv_2\,\exp\{-is(1-v_1)[H-u((1-v_1)p_1p_1+Vp_1p_2+v_2p_1p_2)]\}A$$
$$\times\exp\{-isV[H-u((1-v_1)p_1p_2+Vp_2p_2+v_2p_2p_2)]\}B$$
$$\times\exp\{-isv_2[H-u((1-v_1)p_1p_2+Vp_2p_2+v_2p_2p_2)]\},$$

which, with the use of (7) and $H=0$ when on the outside, reduces to

$$\int_0^1 dv_1\int_0^{v_1} dv_2 Ae^{-is(1-u)VH}B\exp\{-isu(m^2+\varphi)\},$$

where

$$\varphi=k_1^2v_1(1-v_1)+k_2^2v_2(1-v_2)+2k_1\cdot k_2v_2(1-v_1),$$

and $V=v_1-v_2$. For the purpose of carrying out the photon summation the following relations are used:

$$\gamma_\mu^2=-4,\quad \gamma_\mu\gamma A\gamma_\mu=2\gamma A,\quad \gamma_\mu\sigma F\gamma_\mu=0,$$
$$\gamma_\mu\gamma A\sigma F\gamma_\mu=-2\sigma F\gamma A,\quad \gamma_\mu\{\gamma p,\gamma A\}\gamma_\mu=4\{p;A\},$$
$$\gamma_\mu\{\gamma p,\gamma A\}\cdots\{\gamma p,\gamma A\}\gamma_\mu$$
$$=4(\{\gamma p,\gamma A\}\cdots\{p;A\}+\{p;A\}\cdots\{\gamma p,\gamma A\})$$
$$+4\{\gamma p,\gamma A\}\cdots\{\gamma p,\gamma A\}-4\gamma F\cdots F\gamma,$$

where the dots indicate operators which commute with γ_μ; and

$$\tfrac{1}{2}\gamma_\mu\{(m-\gamma p),(\ )\}\gamma_\mu$$
$$=\tfrac{1}{2}\{(m+\gamma p),\gamma_\mu(\ )\gamma_\mu\}+p_\mu(\ )\gamma_\mu+\gamma_\mu(\ )p_\mu$$
$$\to\{\gamma p,(\ )\}-[p_\mu,[\gamma_\mu,(\ )]]$$
$$\to-2m(\ )-[\gamma\bar{k},(\ )],\quad(\bar{k}=k_1+k_2)$$

since $H=0$ on the outside and the parentheses contain $\cdots e^{ik_1x}\cdots e^{ik_2x}\cdots$. A list of further useful relations between occurring combinations of field variables is given in Appendix II.

The functions of v_1 and v_2 occurring are:

$$\left.\begin{aligned}
&\varphi=v_1(1-v_1)k_1^2+v_2(1-v_2)k_2^2, && V=v_1-v_2,\quad \bar{v}=1-2v,\\
&\varphi'=v_1(1-v_1)k_2^2+v_2(1-v_2)k_1^2, && \bar{\varphi}=2v_2(1-v_1)k_1\cdot k_2,\quad \varphi=\bar{\varphi}+\varphi',\\
&\psi_1=\exp[-isuv(1-v)k_1^2], && \psi_2=\exp[-isuv(1-v)k_2^2],\quad \bar{\psi}=\exp[-isuv(1-v)\bar{k}^2],\\
&\phi=\bar{\phi}\cdot\phi=\exp(-isu\varphi), && \bar{\phi}=\exp(-isu\bar{\varphi}),\quad \phi=\exp(-isu\varphi),\quad \phi'=\exp(-isu\varphi'),\\
&\phi'=\bar{\phi}\cdot\phi', && \psi=\tfrac{1}{2}(\psi_1+\psi_2),\quad E=e^{-is(1-u)VH}.
\end{aligned}\right\}\tag{2.8}$$

When there is only one v involved, $E=e^{-is(1-u)vH}$.

Extensive use was made of the symmetry:

$$\int_0^1 dv_1\int_0^{v_1} dv_2 f(v_1,v_2)=\int_0^1 dv_1\int_0^{v_1} dv_2 f(1-v_2,1-v_1).\tag{2.9}$$

Thus an interchange $v_1\to1-v_2$, $v_2\to1-v_1$ will not be explicitly mentioned in the following, but a dash on ϕ indicates such an interchange. The following partial integrations were used (wherever a function of both v_1 and v_2 occurs, integration $\int_0^1 dv_1\int_0^{v_1} dv_2\cdots$ is implied; where only one v occurs it is implied to be integrated from zero to one. All partial integrations are on v_2).

$$E\phi=\frac{\phi}{is(1-u)H}\frac{\partial}{\partial v_2}E\to\frac{1}{is(1-u)H}(\bar{\psi}-E\psi_1)$$
$$+\frac{u}{1-u}\frac{E}{H}\phi[\bar{v}_2k_2^2+2(1-v_1)k_1\cdot k_2]$$
$$=\frac{\phi'}{is(1-u)H}\frac{\partial}{\partial v_2}E\to\frac{1}{is(1-u)H}(\bar{\psi}-E\psi_2)$$
$$+\frac{u}{1-u}\frac{E}{H}\phi[-\bar{v}_1k_1^2+2v_2k_1\cdot k_2],$$

$$E\phi V\to\bar{v}\frac{E\psi}{is(1-u)H}-\frac{1}{2}\frac{u}{1-u}\frac{E}{H}\phi[\bar{v}_1\bar{v}_2(k_1^2+k_2^2)$$
$$+2k_1\cdot k_2(\bar{v}_1(1-v_1)+\bar{v}_2v_2)],$$

$$[1+\tfrac{1}{2}is(1-u)(1-V)H-2k_1\cdot k_2isuv_2(1-v_1)]E\phi$$
$$=\tfrac{1}{2}(\phi+\phi')\frac{\partial}{\partial v_2}(v_2E\bar{\phi})$$
$$\to\bar{\psi}vE+\tfrac{1}{2}isu[v_2\bar{v}_2k_2^2-\bar{v}_1(1-v_1)k_1^2]E\phi,$$

$$v_2E\phi\to\bar{v}\frac{E}{is(1-u)H}\psi_2+\frac{u}{1-u}\frac{E}{H}\phi\bar{v}_2(2v_2k_1\cdot k_2-\bar{v}_1k_1^2),$$

$$is(1-u)HE\psi\to-(E_0-1)-isuE(\psi_1k_1^2+\psi_2k_2^2),$$

and many others of similar type.

Extensive rearrangement by means of all these relations finally yields the following result for the renormalized mass operator. (In the following every field variable stands for a Fourier transform:

$$A_\mu \equiv A_\mu(k) = \int (dx)^4 (2\pi)^{-2} A_\mu(x) e^{-ikx}.$$

Where two field variables occur, the one of the left always carries k_1 and the one on the right, k_2.)

$$\Delta\bar{M} = i\frac{\alpha}{4\pi}\int_0^\infty ds \int_0^1 du \exp(-isum^2)\mathfrak{M}(u,s), \tag{2.10}$$

$$\mathfrak{M} = e\int \frac{(dk)^4}{(2\pi)^2} e^{ikx}\mathfrak{M}_1(u,s,k) + e^2\int\frac{(dk_1)^4}{(2\pi)^2}\int\frac{(dk_2)^4}{(2\pi)^2}e^{ik_1x} \times \mathfrak{M}_2(u,s,k_1,k_2)e^{ik_2x}. \tag{2.11}$$

$\mathfrak{M}$ has two distinct forms, depending upon whether matrix elements between free electron states, i.e., those that satisfy $(m+\gamma p)\psi=0$, are to be taken, or whether matrix elements between states that satisfy $(m+\gamma\pi)\psi=0$ are to be taken. If we write

$$\mathfrak{M}_2 = \mathfrak{M}_2{}^1 + \mathfrak{M}_2{}^2 + \mathfrak{M}_2{}^3, \tag{2.12}$$

then $\mathfrak{M}_1$, $\mathfrak{M}_2{}^1$, $\mathfrak{M}_2{}^3$ are the same in both cases, namely:

$$\mathfrak{M}_1 = \int_0^1 dv\bar{\psi}[mu(u-1)\sigma F + (2-u+2u^2v\bar{v}-4ism^2u(u^2-1)v\bar{v})\gamma J], \tag{2.13}$$

$$\mathfrak{M}_2{}^1 = \int_0^1 dv\bar{\psi}\{4uv\bar{v}[u+2ism^2(1-u^2)]\gamma FGF\gamma + mu(u-1)[(\gamma J/k_1^2)G\sigma F + \sigma FG(\gamma J/k_2^2)] + [(2-u)+2u^2v\bar{v}+4ism^2u(1-u^2)v\bar{v}] \times (k_1^{-2}+k_2^{-2})\gamma JG\gamma J\}. \tag{2.14}$$

For $\gamma\pi$ states:

$$\mathfrak{M}_2{}^2 = \int_0^1 dv\{[(u-2)-2u^2v\bar{v}][\psi_1/k_2^2+\psi_2/k_1^2]\gamma JG\gamma J - u(u-1)m\sigma FG\gamma J\psi_1/k_2^2 + \gamma JG\sigma F\psi_2/k_1^2\}. \tag{2.15}$$

For γp states:

$$\mathfrak{M}_2{}^{2'} = \int_0^1 dv\{(u-2+u\bar{v}(1-2uv)) \cdot[\gamma AGE\gamma J\psi_2+\gamma JGE\gamma A\psi_1] + 2u(1+u)\bar{v}m(\gamma AG^2E\gamma J\psi_2+\gamma JG^2E\gamma A\psi_1) + (u-1)(uv-1)(\sigma FE\gamma A\psi_1+\gamma AE\sigma F\psi_2) - u(u-1)m(\sigma FGE\gamma A\psi_1+\gamma AGE\sigma F\psi_2)\}, \tag{2.16}$$

$$\mathfrak{M}_2{}^3 = \int_0^1 dv_1\int_0^{v_1} dv_2\phi\{4ismu^2(1+u)(v_1-1)v_2FEF + 4isu^2(1-v_1)v_2(1+uV)F(m+\gamma p)EF + 4ismu\gamma FEF\gamma + 2is(1-u)[2+u(V-1) + u^2V(V-1)]\gamma F(m-\gamma\pi)EF\gamma + 2u^2(1-V)\gamma FGEF\gamma + 2isu(1-u^2) \times (1-V)m\gamma FHG^2EF\gamma - \tfrac{1}{2}ismu^2(3-u)\sigma FE\sigma F - \tfrac{1}{2}isu(1-u)(2-u)V\sigma F(m+\gamma\pi)E\sigma F + 2su^2v_2[(1-v_2)+(u-2)V]\gamma Fk_2E\sigma F - 2su^2(1-v_1)[v_1+(u-2)V]\sigma FEk_1F\gamma + 2su^2(1-u)v_2m\gamma Fk_2GE\sigma F - 2su^2(1-u) \times (1-v_1)m\sigma FGEk_1F\gamma - isu^2[v_1(1-v_2) + v_2(1-v_1)+(2-u)\bar{v}_1V]\gamma JE\sigma F - isu^2[v_1(1-v_2)+v_2(1-v_1)-(2-u)\bar{v}_2V]\sigma FE\gamma J + isu^2(1-u)\bar{v}_1m\gamma JGE\sigma F - isu^2(1-u)\bar{v}_2m\sigma FGE\gamma J + 2su(1-v_1)[2-u\bar{v}_1(1+uV)]JEF\gamma + 2suv_2[2+u\bar{v}_2(1+uV)]\gamma FEJ + 2su^2(1+u)(1-v_1)\bar{v}_1mJGEF\gamma - 2su^2(1+u)v_2\bar{v}_2m\gamma FGEJ - 2su^2(1+u)(1-v_1)\bar{v}_1m\gamma JG^2Ek_1F\gamma - 2su^2(1+u)v_2\bar{v}_2m\gamma Fk_2G^2E\gamma J + 2su(1-v_1)[2-u+u^2V\bar{v}_1]\gamma JGEk_1F\gamma - 2suv_2[2-u-u^2V\bar{v}_2]\gamma Fk_2GE\gamma J + 2isuV[2-u+u^2\bar{v}_1\bar{v}_2]\gamma JGE\gamma J - 2isu^2(1+u)\bar{v}_1\bar{v}_2m\gamma JG^2E\gamma J\}, \tag{2.17}$$

where G is the Green's function,

$$G = (\gamma\pi+m)^{-1} \sim (\gamma p+m)^{-1}.$$

In addition, the first-order mass operator is needed for the purpose of taking matrix elements between states, only one of which is an electron state. The calculation is of the same type, except that $m+\gamma p=0$ only on one side. The resulting first-order mass operator for the purpose of taking matrix elements between states, only the right-hand one of which is an electron

state, is as follows:

$$\Delta\bar{M}_r = i\frac{\alpha e}{4\pi}\int_0^\infty ds\int_0^1 du\,\exp(-isum^2)\int\frac{(dk)^4}{(2\pi)^2}$$
$$\times e^{-isv(1-u)H}e^{ikx}\exp[-isuv(1-v)k^2]$$
$$\times\{[2-u-u^2\bar{v}^2-u(1-u)\bar{v}]\gamma J$$
$$-mu(1-u)\sigma F-2m(1+u)u\bar{v}G\gamma J$$
$$-(1-u)(1-uv)(m+\gamma p)\sigma F\}. \quad (2.18)$$

The one for electron states on the left is the same expression, except that $\exp\{-isv(1-u)H\}$ stands on the right of $\exp(ikx)$. This result is significant in that it proves

$$\Delta M_2^{3\prime} = -e(M_1G_0\gamma A+\gamma AG_0M_1), \quad (2.19)$$

which leads to a cancellation of $\Delta M_2^{3\prime}$ in the scattering operator H, (3.4).

It will be noticed that, for the purpose of taking matrix elements between states that satisfy $m+\gamma\pi=0$, the mass operator is explicitly gauge-invariant. When matrix elements between free electron states are taken, this is not so, as (16) shows. That is, of course, not surprising, since neither is p. The results (13) to (17) are in a form significantly simpler than the one previously known.[2]

III. DERIVATION OF THE CROSS-SECTION FORMULA

Suppose that the Dirac equation is modified by the addition of an integral operator which expresses radiation effects of the electromagnetic field:

$$(\gamma\pi+M)\psi\equiv(\gamma p+m+\mathfrak{IC})\psi=0, \quad (3.1)$$

where $\mathfrak{IC}$ stands symbolically for an integral operator, a special case of which, of course, is a potential function multiplying ψ.

The solution of the Dirac equation in the absence of any electromagnetic field will be called ψ_0:

$$(\gamma p+m)\psi_0=0. \quad (3.2)$$

Then one may write

$$(\gamma\pi+M)(\psi_0-\psi)=\mathfrak{IC}\psi_0, \quad \psi=\psi_0-G\mathfrak{IC}\psi_0,$$

where G is the Green's function of the modified Dirac equation, symbolically written as the inverse of an operator, and expressible, symbolically, in terms of the known zero-order Green's function and the additional integral operator:

$$G=(\gamma p+m+\mathfrak{IC})^{-1}=(m+\gamma p)^{-1}(1+\mathfrak{IC}G_0)^{-1}$$
$$=G_0(1+\mathfrak{IC}G_0)^{-1}.$$

Thus solutions to (1) in terms of those of (2) are symbolically

$$\psi=\psi_0-G_0(1+\mathfrak{IC}G_0)^{-1}\mathfrak{IC}\psi_0. \quad (3.3)$$

Not all solutions to (1) will be thus expressible. Equation (3) is not applicable to bound-state solutions. It must be interpreted physically as stating that ψ either was equal to ψ_0 in the remote past when no electromagnetic field was present, or is equal to ψ_0 at large distances. Neither of these statements is true for bound-state solutions and there is no ψ_0 from which ψ "evolves." However, we are dealing with a scattering problem and in that case (3) is applicable in principle. The relevant operator shall be abbreviated:

$$H=(1+\mathfrak{IC}G_0)^{-1}\mathfrak{IC}. \quad (3.4)$$

Then (3) says

$$(m+\gamma p)\psi=-H\psi_0,$$

or, more explicitly

$$\left(m-i\gamma\cdot\nabla-i\gamma_0\frac{\partial}{\partial t}\right)\psi_{p\lambda}(\mathbf{r},t)$$
$$=-\int(dx')(\mathbf{r},t|H|x')\psi_{0p\lambda}(x'), \quad (3.5)$$

where p and λ identify the state by means of the momentum and spin at infinity; i.e., $\psi_{p\lambda}$ is the state which "evolved" from an eigenstate of the momentum with eigenvalue p, and of the spin, with λ. Equation (5) is then multiplied on the left by $\bar{\psi}_{q\mu}$, integrated over $\mathbf{r}$, and on the left-hand side once integrated by parts (the boundary terms are assumed to vanish). Then, since

$$\bar{\psi}_0\left(m+i\gamma\cdot\nabla(\leftarrow)+i\gamma_0\frac{\partial}{\partial t(\leftarrow)}\right)=0,$$

(with an obvious symbolism), it follows that

$$-i\frac{\partial}{\partial t}\int(d\mathbf{r})\psi_{0q\mu}{}^*(\mathbf{r},t)\psi_{p\lambda}(\mathbf{r},t)$$
$$=-\int(dx')(d\mathbf{r})\bar{\psi}_{0q\mu}(\mathbf{r},t)(\mathbf{r},t|H|x')\psi_{0p\lambda}(x'). \quad (3.6)$$

$\int(d\mathbf{r})\psi_{0q\mu}{}^*(\mathbf{r},t)\psi_{p\lambda}(\mathbf{r},t)$ is the probability amplitude for the particle to be in the definite (q,μ) state, knowing that it is in the general (p,λ) state, that is to say, for the particle to be found on measurement with the momentum q and the spin μ, provided that it was prepared (at "infinity") with the momentum p and the spin λ. This will be called $f(q,\mu|p,\lambda)$. Then (6) states:

$$\frac{\partial}{\partial t}f(q,\mu|p,\lambda)=\frac{1}{i}\int(dx')(d\mathbf{r})\bar{\psi}_{0q\mu}(\mathbf{r},t)(x|H|x')\psi_{0p\lambda}(x').$$

Assuming that the field was adiabatically turned on, we know that at $t=-\infty$ the particle was in the state (p,λ), whence it follows that

$$f(q,\mu|p,\lambda)_{t=-\infty}=\delta_{\mu\lambda}\delta(\mathbf{p}-\mathbf{q}).$$

Therefore,

$$f(q,\mu|p,\lambda)_t=\frac{1}{i}\int(dx'')\int(d\mathbf{r}')\int_{-\infty}^{t}dt'\bar{\psi}_{0q\mu}(x')$$
$$\times(x'|H|x'')\psi_{0p\lambda}(x'')+\delta_{\mu\lambda}\delta(\mathbf{p}-\mathbf{q}). \quad (3.7)$$

$|f(q,\mu|p,\lambda)|^2$ is the probability for the particle to be in the (q,μ) state, if it was originally in the (p,λ) state; it is a function of the time. The relevant quantity is the probability per unit time, since the scattering cross section states the number of particles that emerge in the (q,μ) state per unit time, provided that a steady unit flux of particles originally in the (p,λ) state enters the scattering center. The probability per unit time is

$$W(q,\mu|p,\lambda)=\frac{\partial}{\partial t}|f|^2=2\,\mathrm{Re}f^*\frac{\partial}{\partial t}f,$$

and, therefore,

$$\begin{aligned}W(q,\mu|p,\lambda)=2\,\mathrm{Re}\int&(dx')(dx'')(d\mathbf{r}''')(d\mathbf{r})\\&\times\int_{-\infty}^{t}dt'''\bar{\psi}_{0q\mu}(x''')(x'''|\gamma_0H^1\gamma_0|x'')\psi_{0p\lambda}(x'')\\&\times\bar{\psi}_{0p\lambda}(x')(x'|H|x)\psi_{0q\mu}(x)\\&+2\,\mathrm{Im}\delta_{\mu\lambda}\delta(\mathbf{p}-\mathbf{q})\int(dx')(d\mathbf{r})\\&\times\bar{\psi}_{0p\lambda}(x)(x|H|x')\psi_{0p\lambda}(x'). \quad (3.8)\end{aligned}$$

Since $\gamma_\mu^\dagger=\gamma_0\gamma_\mu\gamma_0$, the combination $\gamma_0H^1\gamma_0$ means taking the Hermitian conjugate of H as though the γ's appearing in it were Hermitian. Interest centers on the scattering from the momentum p to the momentum q, irrespective of the spin, i.e., the average over the two initial spin states and the sum over the two final ones (both positive energy states). As is well known, the selection of the positive energy states is accomplished by the insertion of the projection operator $(m-\gamma p)\gamma_0/2p_0$ and then summation over all spin states. The completeness of the solutions of $(m+\gamma p)u^\lambda=0$, with numerical p's, and the fact that the solutions of (2) are $u^\lambda e^{-ix\cdot p}/(2\pi)^3$ enable the probability of scattering from momentum p to q to be written as

$$\begin{aligned}W(q|p)=(4p_0q_0)^{-1}\,\mathrm{Re}\int&(dx')(dx'')(d\mathbf{r})(d\mathbf{r}''')\\&\times\int_{-\infty}^{t}dt'''e^{-iq(x'''-x)}(2\pi)^{-3}e^{-ip(x'-x'')}(2\pi)^{-3}\\&\times\mathrm{tr}(m-\gamma q)(x'''|\gamma_0H^1\gamma_0|x'')\\&\times(m-\gamma p)(x'|H|x)+(2p_0)^{-1}\,\mathrm{Im}\delta(\mathbf{p}-\mathbf{q})\\&\times\int(dx')(d\mathbf{r})e^{-ip(x-x')}(2\pi)^{-3}\\&\times\mathrm{tr}(m-\gamma p)(x|H|x')=(16\pi^2p_0q_0)^{-1}\\&\times\mathrm{Re}\int(d\mathbf{r})(d\mathbf{r}')\int_{-\infty}^{t}dt'e^{-iq(x'-x)}\\&\times\mathrm{tr}(m-\gamma q)(x'|\gamma_0H^1\gamma_0|p)(m-\gamma p)(p|H|x)\\&+(4\pi p_0)^{-1}\,\mathrm{Im}\delta(\mathbf{p}-\mathbf{q})\int(d\mathbf{r})e^{-ipx}\\&\times\mathrm{tr}(m-\gamma p)(x|H|p). \quad (3.9)\end{aligned}$$

More precisely, $W(d\mathbf{q})^3$ is the probability that the particle will be found in the momentum interval $(d\mathbf{q})^3$. But since

$$(d\mathbf{q})^3=\mathbf{q}^2d|\mathbf{q}|d\Omega,\qquad q_0=(\mathbf{q}^2+m^2)^{\frac{1}{2}},$$
$$dq_0q_0=d|\mathbf{q}||\mathbf{q}|,\qquad (d\mathbf{q})^3=|\mathbf{q}|q_0dq_0d\Omega,$$

where $d\Omega$ is the element of solid angle into which scattering is measured. Since this angle is the only point of interest in most cases, q_0 is integrated over from zero to infinity. The normalization of the ψ_0's used here is such that the probability for the particle to be in the Vol. V is $V/(2\pi)^3$, i.e., one particle per $(2\pi)^3$ units of volume. Hence the incident flux is $v/(2\pi)^3=|\mathbf{p}|/p_0(2\pi)^3$. Division by this factor normalizes the cross section correctly to unit incident flux:

$$d\sigma/d\Omega=(2\pi)^3\int_0^\infty dq_0Wp_0q_0|\mathbf{q}|/|\mathbf{p}|, \quad (3.10)$$

and hence

$$\begin{aligned}d\sigma/d\Omega=\frac{\pi}{2}\,\mathrm{Re}\int_0^\infty&dq_0(|\mathbf{q}|/|\mathbf{p}|)\int_{-\infty}^{t}dt'e^{-iq_0(t-t')}\\&\times\mathrm{tr}(m-\gamma q)(\mathbf{q},t'|\gamma_0H^1\gamma_0|p)(m-\gamma p)(p|H|\mathbf{q},t)\\&+2\pi^2(2\pi)^{\frac{1}{2}}\int_0^\infty dq_0q_0\delta(\mathbf{p}-\mathbf{q})\,\mathrm{Im}e^{ip_0t}\\&\times\mathrm{tr}(m-\gamma p)(\mathbf{p},t|H|p). \quad (3.11)\end{aligned}$$

In the special case in which H is independent of time, the time-energy transformation function can be taken out of the H-matrix elements, leaving the latter three dimensional. The origin of the t' integration in the first term is then shifted by t, leaving it extended from $-\infty$ to 0. The trace is real, since it is the sum of numbers multiplied by their complex conjugates, and thus all that is needed is

$$\mathrm{Re}\int_{-\infty}^{0}dt'e^{i(q_0-p_0)t'}=\pi\delta(q_0-p_0).$$

In the second term the time exponentials cancel. Furthermore,

$$\delta(\mathbf{q})=\delta(|\mathbf{q}|)|\mathbf{q}|^{-2}\delta(\Omega),\quad \delta(\Omega)=\delta(\varphi)\delta(\vartheta)/\sin\vartheta,$$

and hence

$$\int_0^\infty dq_0q_0\delta(\mathbf{p}-\mathbf{q})=\int_0^\infty d|\mathbf{q}||\mathbf{q}|\frac{\delta(|\mathbf{p}|-|\mathbf{q}|)}{|\mathbf{q}|^2}\delta(\Omega)=\delta(\Omega)|\mathbf{p}|^{-1}.$$

Therefore, the differential scattering cross section is given by

$$\begin{aligned}d\sigma/d\Omega=2\pi^4&\,\mathrm{tr}(m-\gamma p)(\mathbf{p}|H|\mathbf{q})(m-\gamma q)(\mathbf{q}|\gamma_0H^1\gamma_0|\mathbf{p})\\&-4\pi^3|\mathbf{p}|^{-1}\delta(\Omega)\,\mathrm{Im}\,\mathrm{tr}(\mathbf{p}|H|\mathbf{p})(\gamma p-m), \quad (3.12)\end{aligned}$$

where in H, the operator p_0 must be commuted through to the outside and replaced by the number $p_0=q_0$. (The fact that H is time-independent does not imply that the applied field is so. It just means that, after all p_0's have been commuted to the outside, all time-dependent factors have canceled.)

It will be noticed that (12) is not an approximation, but is an exact formula; this is at the expense, however, of containing the symbolically defined operator H. For actual calculation H will have to be approximated. If it is expanded symbolically in powers of $\mathcal{H}$, then the successive terms in the expansion yield, when inserted in (12), the successive Born approximations.

Equation (12) is interpreted as follows: the first term is the actual scattering, while the second, which is different from zero only in the forward direction, describes the amount taken out of the forward wave and scattered. This must then be equal to the total amount scattered. Therefore (12) yields for the total scattering cross section:

$$\sigma=4\pi^3|\mathbf{p}|^{-1}\,\mathrm{Im}\,\mathrm{tr}(\gamma p-m)(\mathbf{p}|H|\mathbf{p}). \qquad (3.13)$$

In case H is not time-independent, but contains the total frequency k_0, the differential cross section (without the forward part) will be

$$d\sigma/d\Omega=2\pi^4(|\mathbf{q}|/|\mathbf{p}|)\,\mathrm{tr}(m-\gamma p)(\mathbf{p}|H|\mathbf{q}) \times(m-\gamma q)(\mathbf{q}|\gamma_0 H^\dagger\gamma_0|\mathbf{p}), \qquad (3.14)$$

where in H the operator p_0 is moved through to the outside and then replaced by the number p_0 or $q_0=p_0-k_0$, respectively. Of course,

$$|\mathbf{q}|=(q_0^2-m^2)^{\frac{1}{2}}=((p_0-K_0)^2-m^2)^{\frac{1}{2}}.$$

IV. APPLICATION TO SPECIAL CASES

A. The Uniform Field

The simplest special case to which the second-order mass operator may be applied is that of a uniform field. The proper time integration can be carried out immediately and the resultant expression contains a term in u^{-2}, as well as two in u^{-1}. It will be recalled that the origin of the u integration was setting $u=s(s+t)^{-1}$, and t was the variable used in the photon Green's function:

$$D(x)=(4\pi)^{-2}\int_0^\infty dt t^{-2}\exp(ix^2/4t).$$

If the photon had a finite mass ϵ, the Green's function would have been

$$D(x)=(4\pi)^{-2}\int_0^\infty dt t^{-2}\exp\left\{i\left(\frac{x^2}{4t}-\epsilon^2 t\right)\right\}.$$

This would have introduced an additional factor of $\exp\{-i\epsilon^2 t\}=\exp\{-is\epsilon^2(u^{-1}-1)\}$ everywhere; since the divergence occurs at small u, only the additional factor $\exp\{-i\epsilon^2 s/u\}$ matters. Since every u in the denominator arises from the s integration, namely, the factor $\exp\{-isum^2\}$, this shows that the introduction of the small photon mass ϵ replaces every u^{-1} by $u[u^2+(\epsilon/m)^2]^{-1}$. The introduction of a finite photon mass thus prevents all divergencies at u equal to zero. These divergencies are, then, clearly of an infrared nature, which are customarily cut off by means of a finite photon mass.

If this procedure is followed and only terms which do not vanish in the limit as ϵ tends to zero are kept, the u integration can be carried out and the resulting second-order mass operator becomes

$$\Delta M=\frac{\alpha^2}{m^3}\Big[\tfrac{1}{12}FF-\tfrac{1}{6}\sigma F\sigma F+2\gamma FF\frac{p}{m}+\tfrac{2}{3}\pi\left(\frac{m}{\epsilon}\right)\gamma FF\frac{p}{m} +\frac{4}{3}\left(FF-4\gamma FF\frac{p}{m}\right)\log(m/\epsilon)\Big]. \qquad (4.1)$$

Since $(\sigma F)^2$ can be expressed in terms of γ_5 and the adjoint field tensor, $F_{\mu\nu}{}^*$:

$$(\sigma F)^2=2(FF+\gamma_5 FF^*),$$

this can also be written as

$$\Delta M=\frac{\alpha^2}{m^3}\Big[2\gamma FF\frac{p}{m}-\frac{5}{4}\gamma_5 FF^*-\frac{7}{6}FF+\tfrac{2}{3}\pi\left(\frac{m}{\epsilon}\right)\gamma FF\frac{p}{m} +\frac{4}{3}\left(FF-4\gamma FF\frac{p}{m}\right)\log(m/\epsilon)\Big]. \qquad (4.1a)$$

The logarithmic infrared divergence is not surprising and occurs for any static field. The ϵ^{-1} divergence, however, which happens to this order to be a peculiarity of the uniform field, should be recognized to be spurious in the following sense. The occurrence of all infrared divergencies is due to the nonallowed expansion of a function such as $e\log(\epsilon+eA)$ in powers of e:

$$e\log(\epsilon+eA)=e\log\epsilon+e^2A/\epsilon+\cdots.$$

It is clear, then, that an ϵ^{-n} in the mth order properly belongs to the $(n-m)$th order where it should not have been expanded but kept as $\log(\epsilon+eA)\to\log(eA)$.

In the present case, therefore, $\epsilon^{-1}\gamma FF\pi$ really is a first-order term:

$$\gamma F(\log(\epsilon+F))\pi\to\gamma F(\log F)\pi$$

(matrix notation). This, however, vanishes precisely as does $\gamma F\pi\log\epsilon$, which is the reason for the nonoccurrence of an infrared divergence in the first order (for the uniform field):

$$\gamma F\pi=-\tfrac{1}{2}\gamma F\gamma\gamma\pi+\tfrac{1}{2}\gamma\pi\gamma F\gamma+\pi F\gamma \to+\tfrac{1}{2}\gamma F\gamma m-\tfrac{1}{2}m\gamma F\gamma-\gamma F\pi,$$

whence $\gamma F\pi=0$. $\gamma F(\log F)\pi=0$ in the same way, since $(\log F)^T=\log F+$ (a multiple of the unit matrix).

Note added in proof.—A method of eliminating these infrared divergencies completely will be published by the author in the near future.

B. The Pure Radiation Field (Compton Scattering)

We shall apply the second-order mass operator to a rederivation of the total cross section for Compton scattering (the integrated Klein-Nishina formula). Equation (3.13) expressed the total cross section normalized to unit electron flux. For the purpose of photon scattering by a central electron, the free electron wave functions must instead be given the continuum normalization $[dp/(2\pi)^3]^{\frac{1}{2}}e^{ixp}$ and the electromagnetic field entering H must be a pure radiation field normalized to unit photon flux. Equation (3.13) then becomes

$$\sigma=\tfrac{1}{2}p_0^{-1}\,\mathrm{Im}\,\mathrm{tr}(\gamma p-m)(\mathbf{p}|H|\mathbf{p})(d\mathbf{p})^3, \qquad (4.2)$$

where naturally $\delta(\mathbf{p}-\mathbf{p})(d\mathbf{p})^3$ will be interpreted as equal to unity.

The reason why (3.13) is applicable in spite of the nonstatic nature of the field is that only diagonal 3-momentum matrix elements occur in the forward part of (3.11). Therefore only those terms in which the radiation field occurs twice, once in the form e^{ikx} and once in the form e^{-ikx}, contribute to these matrix elements anyway, and in these terms the time dependence cancels also. It will be noticed, incidentally, that the present treatment is a calculation of the scattering of photons by electrons via the description of the electrons' behavior in the presence of photons.

According to (2), then,

$$\mathrm{Im}\,\mathrm{tr}(m-\gamma p)(\mathbf{p}|H|\mathbf{p})$$

must be calculated, where

$$H=(1+\mathfrak{K}G_0)^{-1}\mathfrak{K}=\mathfrak{K}-\mathfrak{K}G_0\mathfrak{K}+\cdots, \qquad (4.3)$$

and

$$\mathfrak{K}=-e\gamma A+\Delta M.$$

Therefore the contributions to H, second order in the field, are

$$\Delta M_2+e(\gamma AG_0\Delta M_1+\Delta M_1G_0\gamma A)-e^2\gamma AG_0\gamma A.$$

In Sec. II it has been shown that

$$e(\gamma AG_0\Delta M_1+\Delta M_1G_0\gamma A)=-\Delta M_2{}^{2'}.$$

Therefore the second-order contributions arising from the first-order mass operator and γA always cancel the contribution from $\Delta M_2{}^{2'}$.

The external field in $\mathfrak{K}$ is

$$A_\mu=\epsilon_\mu(2|k_0|)^{-\frac{1}{2}}(e^{ikx}+e^{-ikx}),$$
$$k^2=0,\quad \mathbf{k}\cdot\boldsymbol{\epsilon}=0,\quad \boldsymbol{\epsilon}^2=1, \qquad (4.4)$$

which represents unit photon flux. (The average energy density is k_0, and hence the photon flux is 1, since their velocity is 1.) The scattering electrons will be assumed to be at rest. Then $\mu=|k_0|/m$ represents the ratio of the photon energy to the electronic rest mass.

The second-order mass operator simplifies very much for the pure radiation field:

$$\phi=\psi=\psi_1=\psi_2=\bar{\psi}=1,$$
$$H=m^2+p^2\to m^2+(p-k_2)^2=-2p\cdot k_2=2mk_0,$$
$$E\to\exp\{-2isV(1-u)mk_0\},$$

when the negative exponential in the radiation field is used on the right. Furthermore,

$$F\cdots F=\gamma F\cdots F\gamma=\sigma F\cdots\sigma F=\gamma Fk\cdots\sigma F$$
$$=\sigma F\cdots kF\gamma=\gamma A(m-\gamma p)\sigma F=0,$$
$$\sigma F\cdots(m+\gamma p)\sigma F=4m\gamma k,\quad \gamma F\cdots(m-\gamma p)F\gamma=m\gamma k,$$
$$\sigma F\cdots\gamma A=\gamma A\cdots\sigma F=\gamma k/k_0,$$
$$\mathrm{tr}(\gamma p-m)\gamma k=-4p\cdot k.$$

Thus, without $\mathfrak{M}_2{}^{2'}$,

$$\mathrm{tr}(\gamma p-m)\mathfrak{M}\to 4m(k_0/|k_0|)$$
$$\times\left\{\int_0^1 dvE[-2(m/k_0)u(1+u)(1-v)+2(uv-1)\right.$$
$$\left.+u^2(1-2v^2)]+(m/k_0)u(1+u)+\frac{4}{3}-u+\frac{5}{3}u^2\right\}. \qquad (4.5)$$

The expression then needed is

$$\mathrm{Im}\,i(\alpha/4\pi)\int_0^\infty ds\int_0^1 du\exp(-isum^2)\,\mathrm{tr}(m-\gamma p)\mathfrak{M}.$$

Since

$$\mathrm{Re}\int_0^\infty dse^{-isA}=\pi\delta(A),$$

the last term contains $(\pi/m^2)\delta(u)$ and therefore yields $-(4/3)\alpha(k_0/|k_0|)$. When the positive exponential part of the radiation field is used on the right, k_0 changes sign, and therefore the above contribution cancels when the two terms are added. The first part, containing E, is of the form

$$\int_0^1 dv\int_0^1 du[\ ]\delta(v(1-u)+um/2k_0).$$

Introduction of the new variables $uv\to w$, $u\to 1-u$ changes this to

$$\int_0^1\frac{du}{u}\int_0^u dw[\ ]\delta(w-(u-1)m/2k_0).$$

This expression differs from zero only if

$$0<m(2k_0)^{-1}(u-1)<u,$$

which inequality requires that $k_0<0$. Since physically an incoming photon wave requires $k_0>0$, the above inequality implies that contributions come only from the positive exponential on the right.

The evaluation of the integrals is direct and yields

$$-\frac{\alpha}{2m\mu^3}\Big\{(2+2\mu-\mu^2)\log(1+2\mu)+\frac{\mu(\mu+1)}{(1+2\mu)^2}(1+4\mu+2\mu^2)-5\mu-\mu^2\Big\}. \quad (4.6)$$

The only other term needed is $\mathrm{Im}\,\mathrm{tr}(m-\gamma p)\times(\mathbf{p}|\gamma A G_0\gamma A|\mathbf{p})$. But since A is real, this equals $\pi\,\mathrm{tr}(m-\gamma p)(\mathbf{p}|\gamma A(m-\gamma p)\delta(m^2+p^2)\gamma A|\mathbf{p})$, which vanishes because the requirements,

$$m^2+p^2=0, \quad k^2=0, \quad m^2+(p+k)^2=0,$$

are inconsistent with each other.

The total cross section for Compton scattering is thus found to be

$$\sigma=\pi r_0^2\Gamma/\mu^3, \quad (4.7)$$

where

$$\Gamma=(\mu^2-2\mu-2)\log(1+2\mu)+\frac{4\mu(1+\mu)^2}{1+2\mu}-\frac{2\mu^3(1+3\mu)}{(1+2\mu)^2}. \quad (4.8)$$

This result agrees precisely with the previously known one.[6] The only purpose for rederiving it here was for the sake of the technique and as a check on the second-order mass operator.

V. THE INELASTIC CROSS SECTION

The mass operator technique is applicable to the calculation of an inelastic cross section in the following manner. In addition to the static field a pure radiation field is introduced. Thus, one is in fact calculating a cross section for the reverse process of bremsstrahlung, since the electron absorbs photons initially present. If the initially present radiation field contains exactly one photon per allowed state (in a "box normalization," say), detailed balancing shows that the probability for the absorption of one of them is equal to the probability of one emission if none had been initially present. In this case the additional introduction of the radiation field as part of the external field simulates the description of photon emission.

The relevant cross-section formula is now (3.11), where

$$H=(1+\mathfrak{M}G_0)^{-1}\mathfrak{M}, \qquad \mathfrak{M}=\Delta M-e\gamma A,$$

$$\gamma_0 H^\dagger\gamma_0=(1+\mathfrak{M}_-G_0)\mathfrak{M}_-, \quad \mathfrak{M}_-=\Delta M_--e\gamma A,$$

and $A=A^a+A^r$. Consider cross terms between parts of H with frequency k_0 in the second matrix and k_0' in the first. The fourth component transformation function can be taken out and, after a shift of t' by t, the time integral involved is

$$(2\pi)^{-1}\int_{-\infty}^{0}dt'e^{i(q_0-p_0-k_0')t'}\times e^{it(k_0-k_0')}.$$

The time average of this is zero unless $k_0=k_0'$, in which case its real part is $\frac{1}{2}\delta(q_0-p_0-k_0)$. In other words, cross terms with different frequencies vanish. The products with frequency k_0 describe transitions in which the energy k_0 has been absorbed.

Furthermore, other fields beside one pure radiation field must be present on one side, since the set of equations,

$$q^2+m^2=p^2+m^2=k^2=(p+k-q)=0,$$

is inconsistent. (A free electron cannot radiate or absorb energy.)

The lowest-order term that may contribute is therefore of the form

$$\cdots(e\gamma A^r G_0 e\gamma A^r)\cdots(e\gamma A^r G_0 e\gamma A^r)\cdots.$$

This, however, is independent of the static potential and properly belongs to the Compton scattering cross section. The lowest-order relevant contribution is of the form

$$\cdots(e\gamma A^r G_0 e\gamma A^a+e\gamma A^a G_0 e\gamma A^r)\cdots\times(e\gamma A^r G_0 e\gamma A^a+e\gamma A^a G_0 e\gamma A^r)\cdots,$$

which is of order $Z^2\alpha^3$. The next term will be of order $Z^3\alpha^4$, i.e., another static field will be added:

$$\cdots(e\gamma A^r G_0 e\gamma A^a)\cdots(e\gamma A^r G_0 e\gamma A^a G_0 e\gamma A^a)\cdots,$$

plus terms of different arrangement.

The first-order contribution is

$$d\sigma/d\Omega=2\pi^4(|\mathbf{q}|/|\mathbf{p}|)e^4\,\mathrm{tr}(m-\gamma q)\times(\mathbf{q}|\gamma_0(\gamma A^r G_0\gamma A^a+\gamma A^a G_0\gamma A^r)^\dagger\gamma_0|\mathbf{p})\times(m-\gamma p)(\mathbf{p}|\gamma A^r G_0\gamma A^a+\gamma A^a G_0\gamma A^r|\mathbf{q}), \quad (5.1)$$

where $q_0=p_0+k_0$. Parts containing the imaginary part of G_0 vanish, and therefore the $\gamma_0\cdots\gamma_0$ and the Hermitian conjugation in the first matrix element cancel each other. Insertion of

$$A^r=\epsilon(e^{iKx}+e^{-iKx}), \qquad \epsilon\cdot K=K^2=0, \quad \epsilon_4=0,$$

$$A_a^a=0, \ a=1,2,3, \qquad A_0^a(\mathbf{r})=\int\frac{(d\mathbf{k})^3}{(2\pi)^3}e^{i\mathbf{k}\cdot\mathbf{r}}A_0(\mathbf{k}),$$

yields, for the matrix elements:

$$(\mathbf{q}|\gamma A^r G_0\gamma A^a|\mathbf{p})\to\Big(\mathbf{q}\Big|\gamma\epsilon e^{iK\cdot r}\frac{m-\gamma p}{m^2+p^2}e^{i\mathbf{k}\cdot\mathbf{r}}\gamma A^a\Big|\mathbf{p}\Big)$$

$$=\delta(\mathbf{p}+\mathbf{k}+\mathbf{K}-\mathbf{q})\gamma\epsilon\frac{m-\gamma p-\gamma k}{m^2+(p+k)^2}\gamma A,$$

$$(\mathbf{q}|\gamma A^a G_0\gamma A^r|\mathbf{p})\to\delta(\mathbf{p}+\mathbf{k}+\mathbf{K}-\mathbf{q})\gamma A\frac{m-\gamma q+\gamma k}{m^2+(q-k)^2}\gamma\epsilon.$$

[6] W. Heitler, *The Quantum Theory of Radiation* (Oxford, University Press, Oxford, 1944), p. 157.

Therefore the terms which describe the absorption of energy are

$$d\sigma/d\Omega=2\alpha^2(|\mathbf{q}|/|\mathbf{p}|)\tfrac{1}{4}\,\mathrm{tr}(m-\gamma q)\times\left(\gamma_0\frac{m-\gamma p-\gamma K}{m^2+(p+K)^2}\gamma\epsilon+\gamma\epsilon\frac{m-\gamma q+\gamma K}{m^2+(q-K)^2}\gamma_0\right)\times(m-\gamma p)\left(\gamma_0\frac{m-\gamma q+\gamma K}{m^2+(q-K)^2}\gamma\epsilon+\gamma\epsilon\frac{m-\gamma p-\gamma K}{m^2+(p+K)^2}\gamma_0\right)|A_0(\mathbf{q}-\mathbf{K}-\mathbf{p})|^2, \quad (5.2)$$

for $K_0>0$, and the same with $K\rightarrow -K$, for $K_0<0$.

The cross section for spontaneous emission of radiation is obtained from this as discussed above. The probability of emission into a radiation field in which n photons are present in each state is equal to the probability of absorption from a field in which $n+1$ photons are present per state (except for the interchange of initial and final states). Hence, if ϵ is chosen such that $A_\mu=\epsilon_\mu(e^{iKx}+e^{-iKx})$ represents one photon per allowed state, then the cross section for absorption from this radiation field is equal to that for radiation into the photon vacuum, if initial and final states are interchanged.

There are $(dK)/(2\pi)^3$ allowed states per unit volume in the range (dK). The energy density represented by $A_\mu=\epsilon_\mu(e^{iKx}+e^{-iKx})$ is $2K_0^2\epsilon^2$, i.e., there are $2|K_0|\epsilon^2$ photons per unit volume. Thus, to have one photon per allowed state requires $2|K_0|\epsilon^2=(d\mathbf{K})^3/(2\pi)^3$; i.e.,

$$\epsilon^2=\tfrac{1}{2}(d\mathbf{K})^3(2\pi)^{-3}|\mathbf{K}|^{-1}=\int_0^\infty dK_0\delta(K^2)(d\mathbf{K})^3(2\pi)^{-3}, \quad K_0>0;$$
$$=\int_{-\infty}^0 dK_0\delta(K^2)(d\mathbf{K})^3(2\pi)^{-3}, \quad K_0<0. \quad (5.3)$$

In the presence of the full radiation field, i.e., with all momentum ranges and both signs of the frequency, (2) then becomes

$$d\sigma/d\Omega=4\alpha^2(2\pi)^{-3}\int_{K_0>0}(dK)\delta(K^2)\times(|\mathbf{q}|/|\mathbf{p}|)|A_0(\mathbf{q}-\mathbf{K}-\mathbf{p})|^2\times\tfrac{1}{4}\,\mathrm{tr}(m-\gamma q)\times\left(\gamma_0\frac{m-\gamma p-\gamma K}{2p\cdot K}\gamma\epsilon-\gamma\epsilon\frac{m-\gamma q+\gamma K}{2q\cdot K}\gamma_0\right)\times(m-\gamma p)\left(\gamma\epsilon\frac{m-\gamma p-\gamma K}{2p\cdot K}\gamma_0-\gamma_0\frac{m-\gamma q+\gamma K}{2q\cdot K}\gamma\epsilon\right), \quad (5.4)$$

where ϵ is the unit polarization vector of the radiation. For an unpolarized radiation field (4) has to be averaged over two perpendicular polarization directions. For that purpose choose $\epsilon^{(1)}$, $\epsilon^{(2)}$, and $\mathbf{n}=\mathbf{K}/|\mathbf{K}|$ as an orthogonal basis. Then, for any two vectors a and b

$$\mathbf{a}\cdot\mathbf{b}=\mathbf{a}\cdot\epsilon^{(1)}\mathbf{b}\cdot\epsilon^{(1)}+\mathbf{a}\cdot\epsilon^{(2)}\mathbf{b}\cdot\epsilon^{(2)}+\mathbf{a}\cdot\mathbf{n}\mathbf{b}\cdot\mathbf{n}.$$

Hence in particular

$$\sum_{\text{pol.}}\gamma\epsilon\cdots\gamma\epsilon=\gamma_i\cdots\gamma_i-K_0^{-2}\gamma\cdot\mathbf{K}\cdots\gamma\cdot\mathbf{K}=\gamma_\mu\cdots\gamma_\mu-K_0^{-2}\gamma\cdot K\cdots\gamma\cdot K-K_0^{-1}\gamma_0\cdots\gamma\cdot K-K_0^{-1}\gamma\cdot K\cdots\gamma_0. \quad (5.5)$$

The identity

$$(m-\gamma q)\left[\gamma_0\frac{m-\gamma p-\gamma K}{2p\cdot K}\gamma K-\gamma K\frac{m-\gamma q+\gamma K}{2q\cdot K}\gamma_0\right](m-\gamma q)=(m-\gamma q)\left[\gamma_0+\gamma_0\gamma K\frac{m+\gamma p}{2p\cdot K}+\gamma_0\frac{K^2}{2p\cdot K}-\gamma_0-\frac{m+\gamma q}{2q\cdot K}\gamma K\gamma_0+\frac{K^2}{2q\cdot K}\gamma_0\right](m-\gamma p)=0$$

shows that the last three terms of (5) do not contribute and thus, effectively,

$$\sum_{\text{pol.}}\gamma\epsilon\cdots\gamma\epsilon=\gamma_\mu\cdots\gamma_\mu.$$

Therefore,

$$d\sigma/d\Omega=2\alpha^2(2\pi)^{-3}\int_{K_0>0}(dK)\delta(K^2)\times(|\mathbf{q}|/|\mathbf{p}|)|A_0(\mathbf{q}-\mathbf{K}-\mathbf{p})|^2\times\tfrac{1}{4}\,\mathrm{tr}(m-\gamma q)\times\left(\gamma_0\frac{m-\gamma p-\gamma K}{2p\cdot K}\gamma_\mu-\gamma_\mu\frac{m-\gamma q+\gamma K}{2q\cdot K}\gamma_0\right)\times(m-\gamma p)\left(\gamma_\mu\frac{m-\gamma p-\gamma K}{2p\cdot K}\gamma_0-\gamma_0\frac{m-\gamma q+\gamma K}{2q\cdot K}\gamma_\mu\right). \quad (5.6)$$

As discussed above, the interchange of initial and final states (i.e., q and p, except for the factor $|\mathbf{q}|/|\mathbf{p}|$, which arises from the normalization), which is equivalent to replacement of K by $-K$, yields the cross section for emission in the absence of initial photons. Thus the

cross section for emission of unpolarized radiation is

$$d\sigma/d\Omega = 2\alpha^2(2\pi)^{-3}\int_{K_0>0}(dK)\delta(K^2)$$
$$\times(|\mathbf{q}|/|\mathbf{p}|)|A_0(\mathbf{q}+\mathbf{K}-\mathbf{p})|^2\times\tfrac{1}{4}\,\mathrm{tr}(m-\gamma q)$$
$$\left(\gamma_0\frac{m-\gamma p+\gamma K}{2p\cdot K}\gamma_\mu-\gamma_\mu\frac{m-\gamma q-\gamma K}{2q\cdot K}\gamma_0\right)$$
$$\times(m-\gamma p)\left(\gamma_\mu\frac{m-\gamma p+\gamma K}{2p\cdot K}\gamma_0\right.$$
$$\left.-\gamma_0\frac{m-\gamma q-\gamma K}{2q\cdot K}\gamma_\mu\right), \quad (5.7)$$

where $q_0=p_0-K_0$. If A is the field due to point charge Ze, then

$$A_0(\mathbf{k})=-\frac{Ze}{\mathbf{k}^2},$$

and therefore, in this case,

$$d\sigma/d\Omega=\alpha\pi^{-2}\int(dK)\delta(K^2)(|\mathbf{q}|/|\mathbf{p}|)$$
$$\times\left|\frac{Z\alpha}{|\mathbf{q}+\mathbf{K}-\mathbf{p}|^2}\right|^2\times\tfrac{1}{4}\,\mathrm{tr}\cdots, \quad (5.8)$$

which is precisely Schwinger's result.[7]

For essentially elastic scattering, i.e., in the limit as K tends to zero, this goes over into[8]

$$\frac{d\sigma}{d\Omega}=\frac{\alpha}{2\pi^2}\left(\frac{Z\alpha}{2|\mathbf{p}|\beta}\csc^2\tfrac{1}{2}\vartheta\right)^2(1-\beta^2\sin^2\tfrac{1}{2}\vartheta)$$
$$\times\int_{K_0=0}^{K}(dK)\delta(K^2)\left(\frac{p}{p\cdot K}-\frac{q}{q\cdot K}\right). \quad (5.9)$$

We shall, in this work, only be interested in this limit, that is to say, that part of the inelastic cross section which describes scattering accompanied by the emission of one soft photon.

Since the integrals in (9) are evaluated elsewhere,[9] the only point that need be mentioned here is the method for cutting off the infrared divergence occurring in (9). In order to facilitate fitting this result to the elastic cross section which will be derived in the next section, the low-energy cutoff will not be made by means of a lower limit to the frequency, as in Schwinger's work, but via the introduction of a finite photon mass. Equation (2.88) of Schwinger's paper then becomes

$$\int(dk)\,{}^4k_0{}^{-2}\delta(k^2+\epsilon^2)$$
$$=\int_0^K dk_0 d|k|\,|k|^2 d\Omega k_0{}^{-2}\delta(k_0{}^2-\mathbf{k}^2-\epsilon^2)$$
$$=2\pi\int_0^K\frac{dkk^2}{(k^2+\epsilon^2)^{\frac{1}{2}}}$$
$$=2\pi\left(\log\frac{2K}{\epsilon}-1\right), \quad (5.10)$$

and therefore, (2.93) goes over into

$$\int_{k_0=0}^{k_0=K}(dk)\,{}^4\delta(k)\left(\frac{p}{pk}-\frac{q}{qk}\right)^2$$
$$=4\pi\frac{|\mathbf{p}|^2}{m^2}\sin^{-1}\left(\frac{\vartheta}{2}\right)\left[\left(\log\left(\frac{K}{\epsilon}\right)\right.\right.$$
$$\left.\left.-\log\left(\frac{p_0}{m}\right)\right)(F_0+F_1)+F_1+H+\tfrac{1}{2}G\right], \quad (5.11)$$

with the functions involved defined in that paper.

It will now be proved that *to the extent to which virtual radiation processes induced by the radiation field are neglected, the low-energy bremsstrahlung cross section is a multiple of the elastic scattering cross section.* It is to be noted that this statement is not an approximation, either in the number of emitted photons or in the strength of the static field. It includes all virtual processes due purely to the static field (i.e., the complete mass operator as a function of the static field alone), but excludes those contributions which describe the effects of the radiation field on the virtual processes (i.e., the mass operator as a function of the radiation field either alone or in conjunction with the static field).

Consider $\mathfrak{M}$ broken up into two parts, $\mathfrak{M}=\mathfrak{M}_r+\mathfrak{M}_s$, where $\mathfrak{M}_r$ is the radiation field and $\mathfrak{M}_s$ involves only the static field. The possibility of such a breakup excludes automatically the use of the radiation field in the mass operator, since the latter is not linear in the field. $\mathfrak{M}_s$ may, however, include the mass operator as a function of the static field alone. Then

$$H=\{1+(\mathfrak{M}_r+\mathfrak{M}_s)G_0\}^{-1}(\mathfrak{M}_r+\mathfrak{M}_s), \quad (5.12)$$

and we set

$$H_r=(1+\mathfrak{M}_rG_0)^{-1}\mathfrak{M}_r, \quad (5.13)$$

$$H_s=(1+\mathfrak{M}_sG_0)^{-1}\mathfrak{M}_s. \quad (5.14)$$

[7] J. Schwinger, Phys. Rev. **76**, 790 ff (1949), Eq. (2.78).
[8] Reference 7, Eq. (2.80).
[9] Reference 7, pp. 811 ff.

H can then be written (with $\mathfrak{F}\equiv(1-H_rG_0H_sG_0)^{-1}$, $\mathfrak{F}'\equiv(1-G_0H_rG_0H_s)^{-1}$, $\mathfrak{G}\equiv H_sG_0H_rG_0H_s$):

$$\begin{aligned}H&=[(1-H_sG_0)^{-1}+H_rG_0(1-H_rG_0)^{-1}]^{-1}\\&\quad\times[(1-H_rG_0)^{-1}H_r+(1-H_sG_0)^{-1}H_s]\\&=(1-H_sG_0)\mathfrak{F}(H_r+H_s-2H_rG_0H_s)(1-G_0H_s)^{-1}\\&=H_s+(1-H_sG_0)\mathfrak{F}H_r(1-G_0H_s)\\&=H_s+H_r+H_rG_0H_sG_0H_r+\mathfrak{F}H_rG_0\mathfrak{G}G_0H_r\\&\quad-H_sG_0H_r-\mathfrak{G}G_0\mathfrak{F}H_r-H_rG_0H_s\\&\quad-\mathfrak{F}H_rG_0\mathfrak{G}+\mathfrak{G}\mathfrak{F}'.\end{aligned}\tag{5.15}$$

Consider the component $\mathfrak{G}=H_s[G_0\mathcal{K}_rG_0-G_0\mathcal{K}_rG_0\mathcal{K}_rG_0+\cdots]H_s$. $\mathcal{K}_r$ cannot be flanked on both sides by the imaginary parts of G_0 and yield a nonvanishing result, since $\cdots\delta(K^2)\delta(m^2+p^2)e^{iKx}\delta(m^2+p^2)\cdots=0$. Moreover,

$$\cdots\delta(K_1^2)\cdots\delta(K_n^2)\delta(m^2+p^2)e^{iK_1x}\cdots e^{iK_nx}\delta(m^2+p^2)$$

fails to vanish only on a set of measure zero (the relevant measure being the volume of the $K_1\times\cdots\times K_n$ space; the set of measure zero is a hypersurface in it). Since all K's are integrated over, it therefore effectively vanishes. Hence it follows that at most one imaginary part of a G_0 contributes. However,

$$\cdots\mathrm{Im}G_0\mathcal{K}_r\,\mathrm{Re}G_0\cdots+\cdots\mathrm{Re}G_0\mathcal{K}_r\,\mathrm{Im}G_0\cdots=0,$$

since

$$\begin{aligned}&\cdots\delta(m^2+p^2)(m-\gamma p)\gamma\epsilon e^{iKx}\frac{m-\gamma P}{m^2+p^2}\cdots\\&\quad=\cdots\delta(m^2+p^2)\frac{m-\gamma p}{-2pK}\gamma\epsilon e^{iKx}(m-\gamma p)\to\cdots\\&\qquad\times(m^2+p^2)(m-\gamma p)\frac{p\epsilon}{-pK}\cdots,\end{aligned}$$

and

$$\begin{aligned}&\cdots\frac{m-\gamma p}{m^2+p^2}e^{iKx}\gamma\epsilon(m-\gamma p)\delta(m^2+p^2)\to\cdots\\&\qquad\times\frac{p\epsilon}{pK}(m-\gamma p)\delta(m^2+p^2),\end{aligned}$$

where the arrow indicates the limit as $K\to0$. Therefore, the only contribution of $\mathfrak{G}$ comes from the use of *real* G_0 everywhere. That part, however, is of the form

$$\cdots(m^2+p^2)^{-1}e^{iKx}(m^2+p^2)^{-1}\cdots,$$

and thus stays finite as $K\to0$. Hence, as K is integrated from $K_0=0$ to $K_0=\Delta E$ this will tend to zero, even if the second e^{iKx} entering the integral comes from an "outside" $\mathcal{K}_r$ which leads to K^{-1}. Since all divergencies are logarithmic, such a factor, tending to zero at least linearly, will make every term containing $\mathfrak{G}$ vanish in the limit.

It follows that effectively

$$\begin{aligned}H&=H_s-H_sG_0H_r-H_rG_0H_s+H_rG_0H_sG_0H_r\\&=(1-H_rG_0)H_s(1-G_0H_r)\\&=(1+\mathcal{K}_rG_0)^{-1}H_s(1+G_0\mathcal{K}_r)^{-1},\end{aligned}\tag{5.16}$$

since by the same reasoning as above, H_r alone does not contribute. Now in the limit as $K\to0$,

$$\left(p\left|\gamma\epsilon e^{iKx}\frac{\gamma p-m}{m^2+p^2}\cdots\right|\right)=\frac{\epsilon p}{Kp}(p|\cdots|),\tag{5.17}$$

where the left-hand state is an electron state ($m+\gamma p=0$), and therefore $(p|(\mathcal{K}_rG_0)^n|)$ is a multiple of $(p|)$. Thus it follows that for electron states,

$$(p|H|q)=f(p,q)(p|H_s|q),\tag{5.18}$$

as was to be proved.

The present interest centers on the one-photon approximation. In that case, (16) and (18) become explicitly:

$$\begin{aligned}H-H_s&=\mathcal{K}_rG_0H_s+H_sG_0\mathcal{K}_r\to e\left[H_s\frac{p\epsilon}{pK}-\frac{p\epsilon}{pK}H_s\right]\\&=-e\left[\frac{p\epsilon}{pK},H_s\right],\end{aligned}\tag{5.19}$$

$$(p|H-H_s|q)=-e\left(\frac{p\epsilon}{pK}-\frac{q\epsilon}{qK}\right)(p|H_s|q).\tag{5.20}$$

After the necessary average over both polarization directions has been taken, the cross section for scattering accompanied by the emission of one low-energy photon is therefore expressible as a multiple of the elastic cross section:

$$\begin{aligned}\left(\frac{d\sigma}{d\Omega}\right)_{\Delta E}&=\frac{\alpha}{2\pi^2}\int_{K_0=0}^{\Delta E}(dK)\delta(K^2)\\&\quad\times\left(\frac{p}{pK}-\frac{q}{qK}\right)^2\left(\frac{d\sigma}{d\Omega}\right)_{el}.\end{aligned}\tag{5.21}$$

The essentially elastic cross section, for scattering that is accompanied at most by the emission of one soft quantum of energy ΔE, can thus be written

$$\begin{aligned}(d\sigma/d\Omega)&=[1+\delta(\Delta E)]2\pi^4\,\mathrm{tr}(m-\gamma q)\\&\quad\times(\mathbf{q}|\gamma_0H^\dagger\gamma_0|\mathbf{p})(m-\gamma p)(\mathbf{p}|H|\mathbf{q}),\\\delta(\Delta E)&=\frac{\alpha}{2\pi^2}\int_{K_0=0}^{\Delta E}(dK)^4\delta(K^2)\left(\frac{p}{pK}-\frac{q}{qK}\right)^2.\end{aligned}\tag{5.22}$$

δ contains an infrared divergence and so does $(d\sigma)_{el}$. These two cancel in the following sense: δ, being due to the emission of one photon, times that part of $(d\sigma)_{el}$ which contains no intermediate photons will cancel the divergencies in that part of $(d\sigma)_{el}$ due to the intermediate existence of one photon. For the cancelation of infrared divergencies occurring in higher-order virtual processes, the cross section for scattering accompanied by the emission of more than one photon is needed.

The following combination which occurs in the essentially elastic cross section will not contain any di-

vergencies:

$$\delta(\Delta E)(\mathbf{q}|(1-e\gamma AG_0)^{-1}e\gamma A|\mathbf{p})(\mathbf{p}|(1-e\gamma AG_0)^{-1}e\gamma A|\mathbf{q})$$
$$-2\,\mathrm{Re}(\mathbf{q}|(1-e\gamma AG_0)^{-1}e\gamma A|\mathbf{p})$$
$$\times(\mathbf{p}|(1-e\gamma AG_0)^{-1}\Delta M(1-eG_0\gamma A)^{-1}|\mathbf{q}).$$

It can be shown that this combination is equivalent to the use of a mass operator in which the small interval from $K_0=-\Delta E$ to $K_0=\Delta E$ is cut out of the photon integration. The physical interpretation of this is clearly that the limiting energy of photon emission is precisely equal to the size of the "energy hole" through which they are allowed to escape in the fluctuation processes described in the mass operator. For calculational purposes, however, it would be quite inconvenient to use such a mutilated mass operator.

VI. THE ELASTIC CROSS SECTION

The radiative corrections to the elastic cross section are obtained from (3.14) by setting

$$H=-e\gamma A-e\gamma A'+\Delta M, \tag{6.1}$$

where A is the external potential; A', the vacuum polarization potential induced by A; and ΔM, the mass operator, as given in Sec. III. The lowest-order radiative corrections consist of terms which contain one matrix element of γA alone and one of either the first-order mass operator or the vacuum polarization potential alone. The calculation of the first-order mass operator contribution, with the Coulomb potential used in the result of Sec. III, is straightforward and need not detain us:

$$(d\sigma/d\Omega)_{M1}=\left(\frac{Z\alpha}{2|\mathbf{p}|\beta}\csc^2\tfrac{1}{2}\vartheta\right)^2(1-\beta^2\sin^2\tfrac{1}{2}\vartheta)a$$

$$a=\frac{2\alpha\lambda^2}{\pi}\left\{-\tfrac{1}{2}\gamma^{-2}\lambda^{-2}F_0+\tfrac{1}{2}F_0+F_1 \right.\tag{6.2}$$
$$\left.+2\int_0^1 du\int_0^1 dv\left[\frac{v^2}{l^2}-\frac{1}{l}\right]\right\},$$

with

$$\lambda=\frac{|p-q|}{2m},\quad \gamma^2=\frac{p_0^2}{m^2\lambda^2}-1,\quad l=1+\lambda^2(1-v^2),$$

and F_0 and F_1 as defined in the previously mentioned Schwinger paper.[10] The divergent u integral is treated as explained in Sec. IV. Thus,

$$\int_0^1\frac{du}{u}\int_0^1 dv\left[\frac{v^2}{l^2}-\frac{1}{l}\right]\to\int_0^1\frac{du}{u}\int_0^1 dv$$
$$\times\left[v^2\left(l+\frac{(\epsilon/m)^2}{u^2}\right)^{-2}-\left(l+\frac{(\epsilon/m)^2}{u^2}\right)^{-1}\right],$$

the integration of which is accomplished by setting

$$u=(\epsilon/m)(l-1)^{-\frac{1}{2}}.$$

It is then found in a straightforward manner that

$$2\int_0^1 du\int_0^1 dv\left[\frac{v^2}{l^2}-\frac{1}{l}\right]\to(F_0+F_1)\log(\epsilon/m)$$
$$-\tfrac{1}{2}(2+\lambda^{-2})\int_0^1 dv\frac{\log l}{l}. \tag{6.3}$$

In terms of the function G used in the Schwinger paper,

$$G=\int_0^1 dv(1+v^2)\frac{\log l}{l} \tag{6.4}$$

(2) results in

$$a=\frac{2\alpha\lambda^2}{\pi}\left[-\tfrac{1}{2}\gamma^{-2}\lambda^{-2}F_0+\tfrac{1}{2}F_0\right.$$
$$\left.-\tfrac{1}{2}G+(F_0+F_1)\log(\epsilon/m)\right]. \tag{6.5}$$

The current induced in the vacuum by the external current J is given by[11]

$$j_\mu'(x)=-\frac{\alpha}{2\pi}\int\frac{(dk)^4}{(2\pi)^2}e^{ikx}J_\mu(k)\int_0^1 dv(1-v^2)\int_0^\infty\frac{ds}{s}$$
$$\times\exp\left\{-is\left[m^2+\frac{k^2}{4}(1-v^2)\right]\right\}. \tag{6.6}$$

The potential is obtained from this by means of the well-known Green's function

$$A'(r)=\frac{1}{(2\pi)^3}\int\frac{(d\mathbf{k})}{\mathbf{k}^2}\int(dr')e^{i\mathbf{k}(r-r')}j_0(\mathbf{r}').$$

The cross section is easily seen to be

$$(d\sigma/d\Omega)_v=\left(\frac{Z\alpha}{2|\mathbf{p}|\beta}\csc^2\tfrac{1}{2}\vartheta\right)^2(1-\beta^2\sin^2\tfrac{1}{2}\vartheta)b,$$
$$b=-\frac{2(2\pi)^{\frac{1}{2}}}{eZ}(\mathbf{p}-\mathbf{q})^2\,\mathrm{Re}A_0'(\mathbf{q}-\mathbf{p}),$$
$$|p|=|q|. \tag{6.7}$$

For a point charge, then,

$$A_0'(\mathbf{q}-\mathbf{p})=\frac{Ze\alpha}{(2\pi)^{5/2}}\int_0^1 dv(1-v^2)$$
$$\times\int_0^\infty\frac{ds}{s}e^{-isl}(\mathbf{p}-\mathbf{q})^{-2}, \tag{6.8}$$

$$b=-\frac{\alpha}{\pi}\,\mathrm{Re}\int_0^1 dv(1-v^2)\int_0^\infty\frac{ds}{s}e^{-isl}. \tag{6.9}$$

[10] Reference 7, p. 809.

[11] J. Schwinger, Phys. Rev. 82, 678 (1951).

An integration by parts with respect to v yields

$$b=-\frac{2}{3}\frac{\alpha}{\pi}\mathrm{Re}\int_0^\infty dss^{-1}e^{-is}+\frac{2\alpha\lambda^2}{\pi}\mathrm{Re}i\int_0^\infty ds\int_0^1 dvv^2(1-v^2/3)e^{-isl}. \quad (6.10)$$

The first term is the charge renormalization term and will be disregarded. The remainder has the finite value,

$$b=\frac{2\alpha\lambda^2}{\pi}(F_1-\tfrac{1}{3}F_2). \quad (6.11)$$

Equations (2) and (9) lead to the first-order radiative corrections to elastic Coulomb scattering:

$$a+b=(2\alpha\lambda^2/\pi)\{-\tfrac{1}{2}\gamma^{-2}\lambda^{-2}F_0+\tfrac{1}{2}F_0-\tfrac{1}{3}F_2+F_1-\tfrac{1}{2}G+(i'_0+F_1)\log(\epsilon/m)\}. \quad (6.12)$$

When this is combined with the slightly inelastic cross section, (5.11), the terms containing the photon mass cancel, and the result agrees perfectly with Schwinger's.[12]

ACKNOWLEDGMENTS

The author takes pleasure in acknowledging his indebtedness to Professor Julian Schwinger for advice and encouragement during the present work. Most of the investigation was carried out under an Eastman Kodak Fellowship.

APPENDIX I

Symmetrization

Expressions of the type

$$B=\int_0^1 dv_1A_1(v_1)\cdots\int_0^1 dv_nA_n(v_n)\exp\left\{\int_0^1 H(t)dt\right\},$$

where $A_1,\cdots,A_n,H$ are noncommuting operators and the integrals are Feynman position integrals, are easily converted into customary notation. There are $n!$ different possible orders of the variables $v_1,\cdots,v_n$. To each such order there corresponds an order of the A's. The t integral is broken up into $n+1$ ranges, fitting between the values of the v's attached to the A's, and exponentials with these parts of the integration over H are placed between the A's. After that is done the position integrals have no longer any purpose and the operators are again considered independent of them. Thus the t integrals are immediately carried out and the result is

$$\Sigma\int_0^1 dv_1\int_0^{v_1} dv_2\cdots\int_0^{v_{n-1}} dv_ne^{(1-v_1)H}A_1e^{(v_1-v_2)H}A_2\cdots\times A_{n-1}e^{(v_{n-1}-v_n)H}A_ne^{v_nH},$$

where the summation extends over all possible permutations of $A_1,\cdots,A_n$ (the v's are always labeled the same as here, for convenience). In case all A's are the same, the $n!$ permutations have equal values and it follows that

$$e^{A+B}=\exp\left(\int A+\int B\right)=\exp\left(\int A\right)\sum_{n=0}^\infty\frac{1}{n!}\left(\int B\right)^n=\sum_{n=0}^\infty\int_0^1 dv_1\cdots\int_0^{v_{n-1}} dv_ne^{(1-v_1)A}Be^{(v_1-v_2)A}\cdots Be^{v_nA},$$

which is the customary expression for the expansion of such an exponential.

Suppose that A_1 commutes with H. In the summation term where A_1 stands in the Kth place, it is flanked by

$$e^{(v_{K-1}-v_K)H}\cdots e^{(v_K-v_{K+1})H},$$

which now contracts to $\exp[(v_{K-1}-v_{K+1})H]$. Thus v_K does not occur in the integrand and the v_K integral can be carried out by one partial integration:

$$\cdots\int_0^{v_{K-2}} dv_{K-1}\int_0^{v_{K-1}} dv_K\int_0^{v_K} dv_{K+1}\cdots=\cdots\int_0^{v_{K-2}} dv_{K-1}(v_{K-1}-v_{K+1})\int_0^{v_{K-1}} dv_{K+1}\cdots.$$

Therefore, if A_1 commutes with H, then in the summation term where A_1 stands in the Kth place, the Kth integral is deleted and $(v_{K-1}-v_{K+1})$ is substituted for it. This rule holds also for the first and last place, if one sets $v_0=1$, $v_{n+1}=0$.

Thus,

$$B=\Sigma\int_0^1 dv_1\int_0^{v_1} dv_2\cdots\int_0^{v_{n-1}} dv_ne^{(1-v_1)H}A_{m(1)}e^{(v_1-v_2)H}\times A_{m(2)}\cdots A_{m(K)}A_{m(K+1)}e^{(v_{K+1}-v_{K+2})H}\cdots(v_{K-1}-v_{K+1}),$$

where the summation runs through all permutations of $m_1,\cdots,m_n$; $m_K=1$, and the Kth integral is missing.

Suppose that, in addition, A_2 commutes with H. Then, if $m_L=2$, the Lth integral is without exponential integrand and the same as above is obtained, except in the case where $L=K-1$ or $K+1$. In case $L=K-1$,

$$\cdots\int_0^{v_{K-3}} dv_{K-2}\int_0^{v_{K-2}} dv_{K-1}\times\int_0^{v_{K-1}} dv_{K+1}\cdots(v_{K-1}-v_{K+1})=\cdots\int_0^{v_{K-3}} dv_{K-2}\int_0^{v_{K-2}} dv_{K+1}\tfrac{1}{2}(v_{K+1}-v_{K-2})^2\cdots,$$

[12] Reference 7, p. 812.

and if $L=K+1$,

$$\cdots\int_0^{v_{K-2}} dv_{K-1}\int_0^{v_{K-1}} dv_{K+1}\times\int_0^{v_{K+1}} dv_{K+2}(v_{K-1}-v_{K+1})\cdots$$
$$=\cdots\int_0^{v_{K-2}} dv_{K-1}\int_0^{v_{K-1}} dv_{K+2}\tfrac{1}{2}(v_{K-1}-v_{K+2})^2\cdots.$$

Thus these two terms will have the form

$$\int dv_1\cdots\int dv_{K-2}\int dv_{K+1}\cdots e^{(v_{K-2}-v_{K-1})H}$$
$$A_{m(K-1)}A_{m(K)}A_{m(K+1)}e^{(v_{K+1}-v_{K+2})H}$$
$$\times\tfrac{1}{2}(v_{K+1}-v_{K-2})^2\cdots\begin{bmatrix}m_{(K)}=1\\ m_{(K-1)}=2\end{bmatrix}$$
$$+\int dv_1\cdots\int dv_{K-2}\int dv_{K+1}\cdots e^{(v_{K-2}-v_{K-1})H}$$
$$A_{m(K-1)}A_{m(K)}A_{m(K+1)}e^{(v_{K+1}-v_{K+2})H}$$
$$\times\tfrac{1}{2}(v_{K-1}-v_{K+1})^2\cdots\begin{bmatrix}m_{(K)}=2\\ m_{(K-1)}=1\end{bmatrix}$$
$$=\int dv_1\cdots\int dv_{K-2}\int dv_{K+1}\cdots e^{(v_{K-2}-v_{K-1})H}$$
$$\times\tfrac{1}{2}\{A_1,A_2\}(v_{K+1}-v_{K-2})^2e^{(v_{K+1}-v_{K+2})H}\cdots.$$

In other words, if A_1 and A_2 commute with H, then the Kth and the Lth integrals are missing if they stand in the Kth and Lth place, and $(v_{K-1}-v_{K+1})$ is substituted for the Kth, $(v_{L-1}-v_{L+1})$ for the Lth integral. When they stand next to each other, i.e., when $m_K=1$, $m_{K-1}=2$ and when $m_{K-1}=1$, $m_K=2$, then one must take $\frac{1}{2}\{A_1,A_2\}(v_{K+1}-v_{K-2})^2$.

This process can be continued and it can be seen that if $A_1\cdots A_m$ commute with H, then the integrals belonging to the places they occupy are deleted and for every Kth integral deleted, $(v_{K-1}-v_{K+1})$ is substituted. If j A's are situated next to each other, they are symmetrized, and if their places are $K-j+1,\cdots,K$, then $(v_{K-j}-v_{K+1})^j$ is substituted.

This has the disadvantage that not all terms have equally labeled integrals. They may readily be relabeled. If s A's commute with H, then only $(n-s)$ integrals are needed. The s A's commuting with H are called $B_1,\cdots,B_s$, and the rest $A_1,\cdots,A_m$, with $m=n-s$. They can be permuted separately, in the sense that first all the A's are permuted; then all permutations of the B's are distributed in all possible ways among the A's. If we fix our attention on a given distribution of the B set among the A set, then all terms due to varying permutations of the B's have the same integrals. If the B's are distributed in groups of $J(1),\cdots,J(j)$, after the $K(1),\cdots,K(j)$th A's, then the $[K(1)+1]$th, $\cdots$, $[K(1)+J(1)]$th, $[K(2)+1]$th, $\cdots[K(2)+J(2)]$th, $\cdots$, integrals are deleted and

$$(J(1)!)^{-1}(v_{K(1)}-v_{K(1)+J(1)+1})^{J(1)}\cdot(J(2)!)^{-1}(v_{K(2)}-v_{K(2)+J(2)+1})^{J(2)}\cdots$$

substituted for it. Then all permutations of the A's and B's among themselves are summed over, and finally all distributions of J's are summed over with the above weighting factors. We shall now relabel the integrals so that they all read from v_1 to v_m. Thus the following procedure has to be followed: The set of B's is cut into groups of sizes $J(1),\cdots,J(j)$, with the group i standing after the $L(i)$th A. Then its factor is

$$(v_{L(i)}-v_{L(i)+1})^{J(i)}/J(i)!.$$

The product of all such factors belonging to each group of B's is taken. Then the A's and B's are permuted among themselves without changing the B groups or their positions. Finally, one must sum over all possible groupings, each weighted according to the above.

A slightly more general kind of term that will be needed is of the form

$$C=\int A_1\int A_2\cdots\int A_n\exp\Big[\int H+\int P\int P\Big],$$

where H and P commute. It will easily be seen that conversion to ordinary notation leads to

$$C=\sum\int_0^1 dv_1\cdots\int_0^{v_{n-1}} dv_n\exp\{(1-v_1)[H+(1-v_1)p_1p_1+(v_1-v_2)p_1p_2+\cdots+v_np_1p_{n+1}]\}A_1$$
$$\times\exp\{(v_1-v_2)[H+(1-v_1)p_1p_2+\cdots+v_np_2p_{n+1}]\}\cdots,$$

where P_j means P standing between the $(j-1)$st and the jth A. The above considerations are immediately applicable to this case too.

TABLE I. An example of symmetrization.

J_1	J_2	L_1	L_2	Factor	Terms
1	1	0	1	$(1-v_1)(v_1-v_2)$	$p_\mu\{\gamma p,\gamma A\}p_\nu A_\nu+p_\nu\{\ \}p_\mu A_\nu$ $+p_\mu A_\nu p_\nu\{\ \}+p_\nu A_\nu p_\mu\{\ \}$
1	1	0	2	$(1-v_1)v_2$	$p_\nu\{\ \}A_\nu p_\nu+p_\nu\{\ \}A_\nu p_\mu$ $+p_\nu A_\nu\{\ \}p_\mu+p_\mu A_\nu\{\ \}p_\nu$
1	1	1	2	$(v_1-v_2)v_2$	$A_\nu p_\mu\{\ \}p_\nu+A_\nu p_\nu\{\ \}p_\mu$ $+\{\ \}p_\nu A_\nu p_\mu+\{\ \}p_\mu A_\nu p_\nu$
2	0	0		$\frac{1}{2}(1-v_1)^2$	$p_\mu p_\nu A_\nu\{\ \}+p_\nu p_\mu A_\nu\{\ \}$ $+p_\mu p_\nu\{\ \}A_\nu+p_\nu p_\mu\{\ \}A_\nu$
2	0	1		$\frac{1}{2}(v_1-v_2)^2$	$2A_\nu p_\mu p_\nu\{\ \}+2\{\ \}p_\mu p_\nu A_\nu$
2	0	2		$\frac{1}{2}v_2^2$	$2A_\nu\{\ \}p_\nu p_\mu+2\{\ \}A_\nu p_\nu p_\mu$

The outlined procedure will be demonstrated by the calculation of $\int\{\gamma p,\gamma A\}\int p_\mu\int p_\nu\int A_\nu\exp(\cdots\int H)$ which occurs in the mass operator. Table I yields:

$$\int\{\gamma p,\gamma A\}\int p_\mu\int p_\nu\int A_\nu\exp\Big(\cdots\int H\Big)$$

$$=\int_0^1 dv_1\int_0^{v_1} dv_2 e^{\cdots(1-v_1)H}\sum(\,)e^{\cdots(v_1-v_2)H}(\,)e^{\cdots v_2 H},$$

$$\begin{aligned}\sum(\,)\cdots(\,)=&(1-v_1)p_\mu[\{\,\}\cdots(Ap)+(Ap)\cdots\{\,\}]\\&+v_2[\{\,\}\cdots(Ap)+(Ap)\cdots\{\,\}]p_\mu\\&+(v_1-v_2)[(Ap)p_\mu\cdots\{\,\}+\{\,\}\cdots p_\mu(Ap)]\\&+(1-v_1)^2p_\mu\{\,\}\cdots A_2\cdot k_1-(1-v_1)\\&\times v_2[p_\mu A_1\cdot k_2\cdots\{\,\}-\{\,\}\cdots A_2\cdot k_1p_\mu]\\&-v_2^2A_1\cdot k_2\cdots\{\,\}p_\mu-v_2(v_1-v_2)A_1\cdot k_2\\&\cdots p_\mu\{\,\}+(1-v_1)(v_1-v_2)\{\,\}\cdots p_\mu A_2\cdot k_1\\&+\tfrac{1}{2}\{(1-v_1)\bar v_2p_\mu\{\,\}\cdots B\\&+(1-v_1)\bar v_1p_\mu B\cdots\{\,\}+v_2\bar v_2\{\,\}\cdots Bp_\mu\\&+v_2\bar v_1B\cdots\{\,\}p_\mu+(v_1-v_2)\bar v_1Bp_\mu\cdots\{\,\}\\&+(v_1-v_2)\bar v_2\{\,\}\cdots p_\mu B\},\end{aligned}$$

where $B=A\cdot k$, $\bar v=1-2v$. The other terms of similar type are calculated in a similar manner.

APPENDIX II

Every field variable in the following carries the operator e^{ikx} with it; the ones on the left, e^{ik_1x}, and the ones on the right, e^{ik_2x}. The dots in the center indicate an operator which commutes with p and γ. We set $(\gamma p+m)=0$ on the outside of any expression. Every Ap stands for $\frac{1}{2}\{p;A\}$; whenever a k occurs multiplying a field variable on the left of the dots, it is meant to be k_2, and *vice versa*; kk stands for $k_1\cdot k_2$.

The following relations were used in simplifying the second-order mass operator:

$$\begin{aligned}Ak\cdots\gamma A&=-iA\cdots F\gamma+A(\gamma p+m)\cdots A,\\\gamma A\cdots Ak&=i\gamma F\cdots A-A(\gamma p+m)\cdots A,\\Ak\cdots Ak&=\tfrac{1}{2}F\cdots F+kkA\cdots A,\\\gamma Fk\cdots Ak&=-i\gamma F\cdots Fk+kk\gamma F\cdots A\\&=-\tfrac{1}{2}i\gamma F(m+\gamma p)\cdots F\gamma+kk\gamma F\cdots A,\\\sigma F\gamma k&=-2\gamma J,\quad \gamma A\gamma k=\tfrac{1}{2}\sigma F-Ak,\\\gamma Fp+pF\gamma&=i\gamma J,\quad \gamma Fp-pF\gamma=-\tfrac{1}{2}i[\gamma p,\sigma F],\\p_\mu A_\nu p_\mu&=\tfrac{1}{2}\{p^2,A_\nu\}-\tfrac{1}{2}J_\nu-\tfrac{1}{2}k_\nu Ak,\\\gamma Fk\cdots Ap&=-\tfrac{1}{2}\gamma F\cdots J-i\gamma F\cdots Fp\\&\quad+\tfrac{1}{2}\gamma F\cdots m^2+p^2A,\\kk\gamma A_1&=-ik_2F_1\gamma+[\gamma p,A_1k_2],\\Fp&=-\tfrac{1}{2}ik\{\gamma p,\gamma A\}-\tfrac{1}{4}ik\sigma F\\&\quad+\tfrac{1}{2}iJ-\tfrac{1}{2}i[p^2,A],\\\gamma Fp\cdots\sigma F&=\tfrac{1}{2}i\gamma J\cdots\sigma F+\tfrac{1}{2}i\sigma F(m+\gamma p)\cdots\sigma F,\\\gamma F\cdots Fk&=-kF\cdots F\gamma=\tfrac{1}{2}F(m+\gamma p)\cdots F,\\\gamma A\cdots kF\gamma&=i\gamma F\cdots F\gamma-A(m+\gamma p)\cdots F\gamma,\\i\gamma F(\gamma p-m)\cdots F\gamma&=-\gamma F\cdots J-2i\gamma F\cdots Fp\\&\quad+\tfrac{1}{2}\gamma Fk\cdots\sigma F,\\\gamma Fp\cdots\gamma A&=\tfrac{1}{2}i\gamma J\cdots\gamma A+\tfrac{1}{4}i\sigma F\cdots(m+\gamma p)\gamma A,\\\gamma Fp\cdots Ak&=\tfrac{1}{2}i\gamma J\cdots Ak+\tfrac{1}{4}i\sigma F(m+\gamma p)\cdots Ak,\\kk\gamma A\cdots\gamma A&=\gamma F\cdots F\gamma+i\gamma F(m+\gamma p)\cdots A\\&\quad+iA\cdots(m+\gamma p)F\gamma-A(m+\gamma p)^2\cdots A.\end{aligned}$$

Letters to the Editor

PUBLICATION of brief reports of important discoveries in physics may be secured by addressing them to this department. The closing date for this department is five weeks prior to the date of issue. No proof will be sent to the authors. The Board of Editors does not hold itself responsible for the opinions expressed by the correspondents. Communications should not exceed 600 words in length and should be submitted in duplicate.

Variety of Our Sources of Information on Avogadro's Number and Other Constants*

JESSE W. M. DUMOND, *California Institute of Technology, Pasadena, California*

AND

E. RICHARD COHEN, *North American Aviation, Downey, California*

(Received April 12, 1954)

IN a recent article[1] Straumanis has stated that the most precise value of Avogadro's number, N, is obtained by means of crystal lattice parameter and crystal density measurements. In support of this statement he cites articles[2] by Birge in 1942 and by Stille, 1943 and 1948. One of the chief purposes of this note is to emphasize the fact that this statement is definitely no longer true, a circumstance which, undoubtedly, most physicists and physical chemists do not yet realize. We here enumerate no less than thirteen different ways of obtaining N beside the one cited by Straumanis, all of comparable accuracy. The method cited by Straumanis employing grating values of x-ray wavelengths to measure crystal parameters we shall refer to as the x-ray-crystal-density method or, for brevity, the X.R.C.D. method. Of the thirteen other methods ten are more accurate than the X.R.C.D. method, and the most accurate of the fourteen has nothing whatever to do with crystals but involves such diverse experimental information as the Faraday by electrochemistry, the "omegatron" (or inverse cyclotron) determinations of the magnetic moment of the proton, the Rydberg constant, and the fine structure splitting in deuterium. For this reason we believe that Straumanis' proposal to conventionalize the value of N on the basis of the density and lattice parameter of "purest calcite" would be an extremely arbitrary and objectionable step.

For the sake of brevity we here adopt the same symbols and equation numbers used in a recent paper[3] by the authors. The thirteen independent equations on page 701 of that paper, Eqs. (8.1) to (8.13), comprise a statement of the bulk of our present precise information bearing on the constants and conversion factors of physics, their sources being indicated by the numbers in parentheses and in brackets to the left of each equation. We shall work, however, with the linearized forms of these Eqs. (8.14) to (8.26) on page 702 of reference 3. We adopt a fixed value for the velocity of light ($x_3=10$ or $c=2.99793\times10^{10}$ cm sec^{-1}), thus eliminating one of the five variables and two of the thirteen equations. We further simplify by combining all equations of the same kind such as the pair (8.16) and (8.17) or the triplet (8.22), (8.23), and (8.24), equating each kind to a weighted average value of the numerics. This gives the following seven equations in the four unknowns, x_1, x_3, x_4, x_5, corresponding to α, e, N and λ_g/λ_*. The numbers on the left refer to the observational data in reference 3 on which each equation reposes.

(6.2)(6.3)(6.4)		x_3+x_4	$=84.2\pm10.9=a_1.$
(6.2)(6.5)(6.6)[7.5][7.6][7.8][7.9]	$-3x_1+2x_3+x_4$		$=145.0\pm10.5=a_2.$
(6.2)(6.7)[7.5][7.6][7.8][7.9]	$3x_1-x_3$		$=-23.\pm22.9=a_3.$
(6.8)		$x_3=$	$0.0\pm30.1=a_4.$
(6.2)(6.9)(6.10)(6.11)[7.7]	$-x_1+x_3$	$-x_5=$	$-65.4\pm29.5=a_5.$
(6.12)		$x_4+3x_5=$	$35.\pm37.8=a_6.$
(6.2)(6.13)[7.3][7.4][7.5]	$2x_1$	$=$	$80.\pm9.0=a_7.$

Even after this simplification the numbers of solutions for α, e, N, and λ_g/λ_* which can be formed from appropriately chosen subsets of these seven equations are no less than 11, 11, 14, and 11, respectively. We list below[4] only the solutions for x_4 (i.e., for N) in the order of increasing accuracy:

	(s.d.)
$x_4=(6a_2-12a_5-4a_6+3a_7)/2;$	$N=0.602980\pm0.000118.$
$x_4=3a_3+3a_4+a_6-3a_7$;	$N=0.602217\pm0.000073.$
$x_4=2a_1-a_3-3a_5-a_6$;	$N=0.602712\pm0.000061.$
$x_4=a_6-3a_4$; (X.R.C.D. solution)	$N=0.602521\pm0.000059.$
$x_4=a_1+a_3-3a_5-a_6$;	$N=0.602735\pm0.000058.$
$x_4=(2a_2-4a_4-4a_5+a_7)/2;$	$N=0.602619\pm0.000051.$
$x_4=(a_1+a_2-3a_4-3a_5)/2;$	$N=0.602628\pm0.000044.$
$x_4=(2a_1-a_3-3a_4-3a_6)/2;$	$N=0.602617\pm0.000039.$
$x_4=(2a_2+a_3-3a_4-3a_6)/2;$	$N=0.602639\pm0.000039.$
$x_4=(6a_1-6a_3-2a_6-3a_7)/4;$	$N=0.602588\pm0.000031.$
$x_4=(2a_3+4a_4-3a_7)/2$;	$N=0.602487\pm0.000030.$
$x_4=(2a_1-2a_4-2a_5-a_7)/2;$	$N=0.602566\pm0.000026.$
$x_4=(2a_1+2a_3-3a_7)/2$;	$N=0.602465\pm0.000017.$
$x_4=(4a_1-2a_2-3a_7)/2$;	$N=0.602442\pm0.000017.$

These results are also shown in Fig. 1.

The subscripts to the a's indicate the subset used in each solution. Most emphatically we do not recommend any of the above just-determinate solutions because each utilizes only a fragment of our total budget of information and arbitrarily ignores the remainder. It would also be a serious error in principle to take an ordinary weighted average of these solutions, using weights inversely as the square of the error measures, because the solutions are not independent but are observationally correlated. The fourteen solutions cannot, of course, be independent since there are only seven independent input data. Nevertheless, any one of these solutions has just as good a claim to validity as the X.R.C.D. solution.

Undoubtedly at least some of the observational data still contain small systematic errors and we are working on the difficult problem of detecting, if possible, where these are by exploration of the consistency measures, χ^2, of all possible overdetermined subsets by digital computer. The normalized residues, R_i/σ_i listed in Table III, page 702, reference 3, are so small, however, that we feel there is at present no sufficient criterion for rejection of any of the input data used in our November 1952 least-squares adjustment.[3] We recommend our least-squares adjusted values ($N=0.602472\pm0.000036)\times10^{24}$ (g mole)$^{-1}$) in preference to any just-determinate single track solutions (such as X.R.C.D.) because the least-squares adjustment makes the least arbitrary and most impartially inclusive use of all our sources of knowledge at any given epoch. It is most gratifying to observe the good compatibility of results derived from such diverse sources of information, for it gives a direct proof of the inner consistency of physical units beyond the arbitrariness of man-made cgs units.

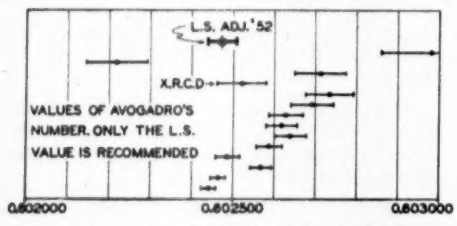

FIG. 1. The least-squares adjusted 1952 value of Avogadro's number (top) compared with fourteen just-determinate values each of which is based on a different subgroup combination of seven distinct and independent types of experimental measurement. Only the least-squares adjusted value is recommended.

* Jointly supported by the U. S. Office of Naval Research and the U. S. Atomic Energy Commission.

[1] M. E. Straumanis, Phys. Rev. **92**, 1155 (1953).

[2] R. T. Birge, Phys. Rev. **62**, 301 (1942); U. Stille, Z. Physik **121**, 142 (1943); **125**, 174 (1948).

[3] J. W. M. DuMond and E. R. Cohen, Revs. Modern Phys. **25**, 691 (1953).

[4] These values of N are per g-mole on the physical scale of atomic weights and should be followed by 10^{24}.

Photoconductivity and Photoelectromagnetic Effects in InSb†

S. W. KURNICK, A. J. STRAUSS, AND R. N. ZITTER
Chicago, Midway Laboratories, Chicago, Illinois
(Received April 30, 1954)

PHOTOCONDUCTIVE and photoelectromagnetic[1-3] responses have been observed at 300°K and 77°K in p-type samples of InSb which are intrinsic at room temperature. The data reported here were obtained in experiments on rectangular plates measuring $0.028\times0.26\times1.0$ cm³ with an effective impurity concentration of approximately 7×10^{15} acceptors/cm³ (as determined by Hall measurements at 77°K) and with a resistivity of 0.015 ohm-cm at 300°K and 1.1 ohm-cm at 77°K. Samples were placed in a cryostat with a rocksalt window and mounted between the pole pieces of an electromagnet. Illumination of approximately 0.05 watt/cm², chopped at 525 cps, was supplied by a Nernst glower with a brightness temperature of about 1600°C. The sample length, magnetic field, and illumination were mutually perpendicular. A bias voltage could be applied across the sample for photoconductivity measurements. At 300°K the sample was connected through a transformer with impedance ratio 1:1600 to a Hewlett Packard Model 450A amplifier and then to a Hewlett Packard Model 300A harmonic wave analyzer. For measurements at 77°K, the sample was connected directly to the amplifier and wave analyzer. The results are more directly interpreted in terms of i_s, the "short-circuit" current. To obtain i_s from the observed current i_o, the formula $i_s=i_oR/R_s$ is employed, where R_s is the resistance of the illuminated portion of the sample and R is the total resistance in the circuit. In cases where magnetoresistance effects (large μB) are important, the resistance must be evaluated at the appropriate value of magnetic field.

On the basis of the simple model given by Moss, the short-circuit current generated by the photoelectromagnetic (PEM) effect is given by

$$i_s=\frac{\eta Qe B\mu}{1+\mu^2B^2}\frac{(D\tau)^{\frac{1}{2}}}{L}, \tag{1}$$

where η is the quantum efficiency, Q the photon flux, e the electronic charge, B the magnetic flux density, and L the length of the illuminated portion of the sample; μ, D, τ are, respectively, the mobility, diffusion constant, and effective lifetime of the excited electrons produced by the illumination. Since the electron mobility in InSb is much higher than the hole mobility, the contribution of the excited holes to the photocurrent at low magnetic fields may be neglected. It should be noted that the factor $1/(1+\mu^2B^2)$ does not appear in Moss' expression for the short-circuit current because Moss applied the expression to data for PbS where $\mu B\ll1$.

Figures 1 and 2 show that the observed variation of i_s with B is in good agreement with Eq. (1). The curves in Fig. 1 were

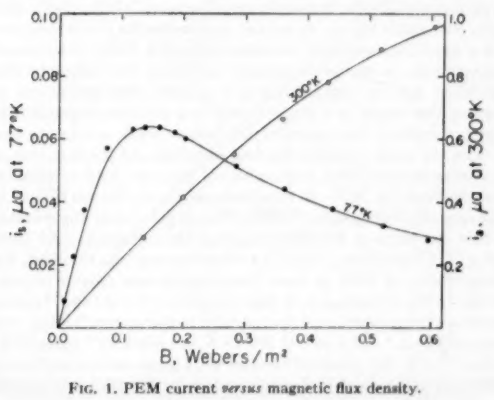

FIG. 1. PEM current *versus* magnetic flux density.

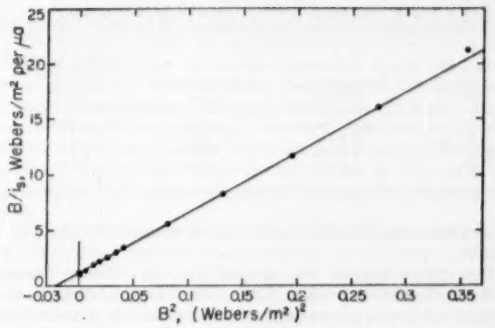

FIG. 2. Plot of B/i_s *versus* B^2.

calculated from the equation $i_s=KB/(1+\mu^2B^2)$ using the values of K and μ best fitting the experimental data. These parameters were found by plotting B/i_s *versus* B^2 as shown in Fig. 2 for the results at 77°K. The mobilities found in this manner were 1.0 and 6.8 m²/v-sec at 300°K and 77°K, respectively. The former value is about one-fifth of the Hall mobility reported by Tanenbaum and Maita[4] for electrons in intrinsic single crystals at 300°K, while the latter is only about 10 percent less than the Hall mobility reported by these authors for electrons in an n-type single crystal. The value for 300°K agrees qualitatively with the electron mobility of 1.5 m²/v-sec derived from the magnetoresistance data of Pearson and Tanenbaum.[5]

Effective lifetimes estimated from the PEM data on the basis of Eq. (1), utilizing the derived mobilities, are about 10^{-10} and 10^{-12} sec at 300°K and 77°K, respectively. When lifetimes are derived from the photoconductive short-circuit current

$$i'=\eta Qe\mu F\tau/L \tag{2}$$

where F is the electric field, the values are 10^{-6} and 10^{-10} sec at 300°K and 77°K, respectively. The discrepancies between the photoconductive and PEM lifetimes may result at least in part from errors in the estimation of the photon flux Q. However, it seems unlikely that this is sufficient to account for all the inconsistencies since the ratio of photoconductive to PEM lifetime increases from 10^2 at 300°K to 10^3 at 77°K. Alternatively there may be real differences between the two effective lifetimes due to enhanced surface recombination in the magnetic field (Suhl effect).

† This research was supported in whole by the United States Air Force under a contract.
[1] Moss, Pincherle, and Woodward, Proc. Phys. Soc. (London) **B66**, 743 (1953).
[2] T. S. Moss, Proc. Phys. Soc. (London) **B66**, 993 (1953).
[3] P. Aigrain and H. Bulliard, Compt. rend. **236**, 595 and 672 (1953).
[4] M. Tanenbaum and J. P. Maita, Phys. Rev. **91**, 1009 (1953).
[5] G. L. Pearson and M. Tanenbaum, Phys. Rev. **90**, 153 (1953).

Recombination of Holes and Electrons at Lineage Boundaries in Germanium

F. L. VOGEL, W. T. READ, AND L. C. LOVELL
Bell Telephone Laboratories, Murray Hill, New Jersey
(Received April 20, 1954)

SMALL-angle-of-misfit grain boundaries are made up of arrays of dislocations, which, in certain lineage boundaries in germanium, have been revealed by etch pits.[1] Dislocations in or near the edge orientation act like rows of closely spaced acceptor centers with energies slightly above the middle of the gap.[2,3] An occupied acceptor is a hole trap and an empty acceptor, an electron trap. Thus excess holes and electrons should recombine at a small-angle grain boundary made up of edge dislocations, and the boundary should have a characteristic recombination velocity. This letter describes some studies of recombination at grain boundaries in germanium. The dislocations, which are parallel

TABLE I. Boundary recombination velocities for several specimens.

Spec. no.	Resistivity, ρ ohm-cm	Body lifetime, τ μsec	Crystal boundary recombination velocity, v cm/sec
A	16 $-n$	1100	2.0×10^3
B	9.0 $-n$	450	1.2
C	7.1 $-n$	310	2.6
D	3.0 $-p$	250	1.6

and in the edge orientation, are spaced at intervals of about a micron.

The recombination was studied by the Morton-Haynes[4] method, illustrated in Fig. 1(a). The (movable) light source generates excess carriers and their concentration is measured as a function of the position x_l of the light source. In an n-type specimen the excess hole concentration at the (fixed) collector point is proportional to the collector current which is measured as the voltage, V, across a resistor in series with the collector. The straight-line portion of the V *vs* x_l plot gives body lifetime. Figure 1(b) shows V *vs* x_l for a fixed position, x_b, of the grain boundary. As the light approaches the grain boundary, the slope of the V *vs* x_l curve becomes steeper—indicating that the boundary is a sink for holes; that is, a greater fraction of the light-generated holes moves to the right, or toward the boundary, rather than to the left, or toward the collector.

At the top in Fig. 1(a) are the solutions to the diffusion equation giving the excess hole concentration $\delta p(x)$ in the three regions shown. The bulk diffusion length is taken as unit length. A_1, A_2, B_2, B_3 are functions of x_l and x_b, and are determined by the following boundary conditions: $\delta p(x)$ is continuous at x_l and x_b; the discontinuity in hole current at x_l is the rate of hole generation and the discontinuity at x_b is $v\delta p(x_b)$, where v is the recombination velocity. Using the fact that δp at the collector ($x=0$) is proportional to V, we find

$$\ln[1-(V/V_0)]+\ln[(2v_l/v)+1]=-2(x_b-x_l),$$

where V_0 is the potential that would be observed in the absence of the grain boundary and $v_l=$(diffusion length)/(lifetime) in the bulk material. When the light is 40 or more mils to the left of the collector, the points in Fig. 1(b) fall on a straight line, which reflected about $x=0$ gives V_0 for corresponding positions of the light to the right of the collector. Figure 2 shows a semilog plot of $[1-(V/V_0)]$ *vs* (x_b-x_l). The points are well fitted by a straight line of slope -2. The intercept at $x_b-x_l=0$ gives v. Comparable agreement with the theory was obtained for three other specimens. Table I gives the resistivity, conductivity type, lifetime, and recombination velocity for the four specimens.

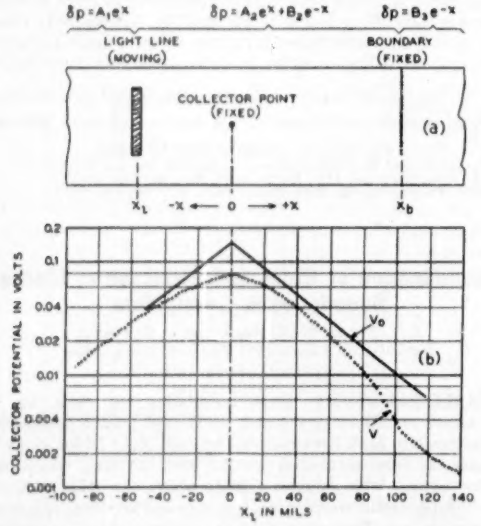

FIG. 1(a) Diagram of the positions of the fixed collector point and grain boundary and the movable light line on an n-type specimen. At the top of the figure are the solutions of the diffusion equation for excess hole concentration δp *vs* distance x from the collector in the three regions indicated. (b) The collector potential plotted as a function of the position x_l of the movable light line for specimen B.

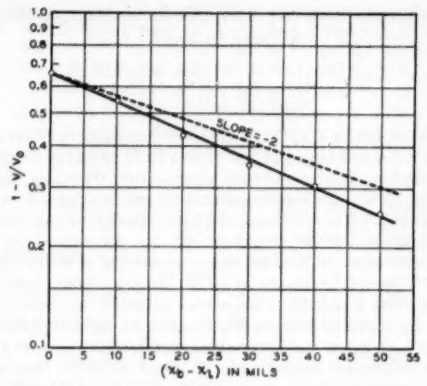

FIG. 2. Plot of $1-(V/V_0)$ *versus* (x_b-x_l), where V is collector potential and V_0 is the potential that would be observed in the absence of a grain boundary. Both V and V_0 are found from Fig. 1(b). The theory predicts a straight line of slope -2.

The existence of a surface recombination velocity at the crystal boundary indicates a concentration of recombination centers in the boundary. The density of these centers cannot, however, be calculated from the data because of uncertainties in (1) the carrier concentration in the space-charge region at the boundary, (2) the capture cross section, and (3) the number of traps which are charged.

[1] Vogel, Pfann, Corey, and Thomas, Phys. Rev. **90**, 489–489 (1953).
[2] W. Shockley, Phys. Rev. **91**, 228 (1953).
[3] Pearson, Read, and Morin, Phys. Rev. **93**, 666 (1954).
[4] L. B. Valdes, Proc. Inst. Radio Engrs. **40**, 1420 (1952).

Magnetic Anisotropy of NiF_2

L. M. MATARRESE AND J. W. STOUT
Institute for the Study of Metals and Department of Chemistry, The University of Chicago, Chicago, Illinois
(Received April 26, 1954)

IN an investigation of the magnetic anisotropy of a single crystal of NiF_2 we have observed phenomena which are unlike those found[1,2] in the isomorphous substances MnF_2, FeF_2, and CoF_2, and which lead us to believe that below the Curie temperature a small ferromagnetic moment appears in NiF_2. In a normal paramagnetic or antiferromagnetic substance the magnetic susceptibility may be represented by a second-order tensor and in this case the torque on a single crystal in a uniform magnetic field is proportional to the square of the field strength and to the sine of twice the angle between the field direction and the direction of maximum susceptibility in the plane of rotation. Such a behavior was observed for NiF_2 at temperatures above the maximum in heat capacity[3] occurring at 73.2°K. The single crystal was oriented so that the plane of rotation contained the tetragonal [001] axis and a [110] direction. Unlike the other isomorphous fluorides, the susceptibility of NiF_2 at room temperature was greater perpendicular to the tetragonal axis than parallel to it and the difference between the perpendicular and parallel molal susceptibilities rose gradually from 1.102×10^{-4} at 301.15°K to 1.890×10^{-4} at 90.07°K. Below 73.2°K the observed torques were large and anomalous in their dependence on field strength and angle. The torque measured

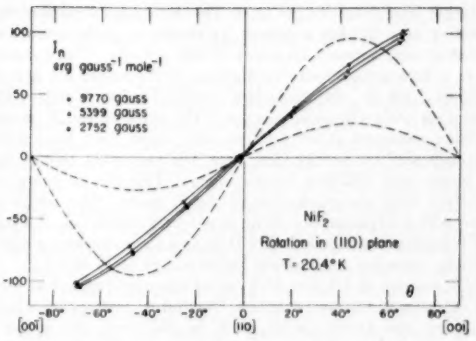

FIG. 1. Molal perpendicular magnetization of nickel fluoride *versus* angle between field and [110] direction. Rotation in (110) plane. Dashed curves indicate typical antiferromagnetic behavior.

by the torsion balance[4] is proportional to I_n, the component of the magnetization which is perpendicular both to the field direction and to the axis of the suspension. In Fig. 1 are shown values of I_n at 20.4°K and for three field strengths. The observed torques were identical at positions 180° from one another. The dashed curves in Fig. 1 illustrate the behavior expected for an antiferromagnetic substance with no permanent moment and a susceptibility independent of field strength. In this case I_n is proportional to the field strength and the two dashed curves correspond to 2752 and 9770 gauss. The magnitude of the dashed curves is calculated from the powder susceptibility data of de Haas, Schultz, and Koolhaas[5] at 20.4°K, assuming that the susceptibility parallel to the tetragonal axis is essentially zero. The observed values of I_n vary little with field strength and are suggestive of that expected from a permanent moment whose projection in the (110) plane lies preferentially in a [110] direction but which can be rotated somewhat from this position by a magnetic field.

Measurements were then made of the torques with the crystal mounted so its tetragonal axis was parallel to the axis of the suspension. In this orientation no torques are expected for a normal paramagnetic or antiferromagnetic crystal and only very small ones, amounting to 1.5 percent of the torques in the first orientation and attributable to a misorientation of a small portion of the crystal, were found above 73.2°K. Below this temperature, however, large torques were observed in this second orientation. These torques had a periodicity of 90°. Values of I_n at 20.4°K are shown in Fig. 2. These curves may be fitted by a model[6] such as is used to interpret ferromagnetic anisotropy. In the (110) plane the easy directions of magnetization are ⟨100⟩. The moment

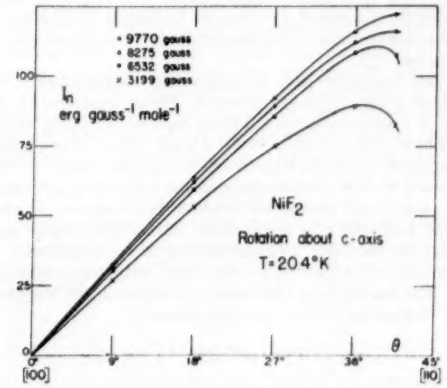

FIG. 2. Molal perpendicular magnetization of nickel fluoride *versus* angle between field and [100] direction. Rotation about tetragonal axis.

is assumed constant in magnitude and its direction is determined by the balance between the torque exerted by the magnetic field and that arising from the crystal anisotropy which will have a periodicity of 90°. The curves are consistent with a permanent moment whose magnitude is about 350 erg gauss^{-1} mole^{-1}. However, the crystalline anisotropy "constant" turns out to increase slightly more than proportionally to the field strength. The reason for this is obscure and there is therefore some question as to the applicability of the usual model for ferromagnetic anisotropy to NiF_2.

Erickson[7] has observed in neutron diffraction measurements on NiF_2 a small peak which was not found in the other antiferromagnetic fluorides of the iron group and which he interpreted as indicating that in the ordered alignment the spins, instead of being strictly parallel and antiparallel to the tetragonal axis as in MnF_2, FeF_2, and CoF_2, are in NiF_2 inclined at an angle of 10° from this axis. If one assumes that the cocking of one sublattice is in the [110] direction and that of the other sublattice at right angles in the [1$\bar{1}$0] direction, then there is a net moment in the [100] direction. The moment of 350 erg gauss^{-1} mole^{-1}, which is 3 percent of the saturation moment of the nickel ions, would on such a model correspond to a cocking of 2.5°.

The crystal used for the measurements weighed 17 mg and contained impurities of 0.02 percent Co; 0.02 percent Fe; 0.01 percent Al; 0.005 percent Cu; and 0.001 percent Mn, Mg, and Si. In order to see if the observed effects were dependent on the impurity content, some measurements were made on a large crystal containing about 1 percent Fe. The magnetizations observed below the Curie temperature with this impure crystal agreed within 0.7 percent with those found with the small purer crystal, so we do not believe that impurities are the cause of the observed phenomena.

[1] M. Griffel and J. W. Stout, J. Chem. Phys. **18**, 1455 (1950).
[2] J. W. Stout and L. M. Matarrese, Revs. Modern Phys. **25**, 338 (1953).
[3] J. W. Stout and E. Catalano, Phys. Rev. **92**, 1575 (1953).
[4] J. W. Stout and M. Griffel, J. Chem. Phys. **18**, 1449 (1950).
[5] de Haas, Schultz, and Koolhaas, Physica **7**, 57 (1940).
[6] See F. Bitter, *Introduction to Ferromagnetism* (McGraw-Hill Book Company, Inc., New York, 1937), Chap. VI; R. M. Bozorth, *Ferromagnetism* (D. Van Nostrand Company, Inc., New York, 1951), Chap. 12.
[7] R. A. Erickson, Phys. Rev. **90**, 779 (1953).

Radiogenic Argon Measurements

H. A. SHILLIBEER, R. D. RUSSELL, R. M. FARQUHAR, AND E. A. W. JONES
Geophysics Laboratory, Department of Physics, University of Toronto, Toronto, Canada
(Received April 14, 1954)

SOME of the writers recently published the results of an experiment to determine the branching ratio of potassium by the extraction and measurement of radiogenic argon from dated potassium minerals.[1] The value of 0.06 obtained in this way is appreciably lower than the value obtained in many recent gamma-ray counting experiments. Errors in our experiment could have arisen from loss of argon during the purification process, incomplete extraction of the argon from the minerals, or incorrect dating of the minerals.

We have since carried out a number of yield runs in the purification apparatus and found that in all cases no measurable loss occurred. The argon extractions had been carried out by heating the sample to 850°C in vacuum with a sodium metal flux. To test the efficiency of this procedure we sent a second sample of Bessner microcline to G. J. Wasserburg at the University of Chicago who

TABLE I. Comparison of fluxes.

Locality	A^{40}/K^{40} Sodium flux Result	No. of runs	Sodium hydroxide flux Result	No. of runs
Varala, Finland	0.119	2	0.140	6
Lee Lake, Saskatchewan	0.087	3	0.131	2
Dill Township, Ontario	0.0421	3	0.0522	6

uses an entirely different procedure for the extraction and measurement of radiogenic argon. He obtained an A^{40}/K^{40} ratio approximately 35 percent larger than our value.[2] We now find that this difference was caused by the fact that our sodium flux extracted less argon than the sodium hydroxide flux used by Wasserburg. Comparison runs have now been carried out at Toronto using both sodium metal and sodium hydroxide fluxes. The following results are typical of those obtained. In each case sodium hydroxide extracted more of the argon than metallic sodium.

The Lee Lake microcline was the same sample used for our previous measurements.[1] Using the same age of 1750 million years we obtain with the sodium hydroxide flux a branching ratio of 0.090. For our Bessner sample Wasserburg's measurements give a branching ratio of 0.088, assuming an age of 940 million years. This age we determined on a uraninite collected with the feldspar. These estimates of the branching ratio suggest that the radiogenic argon measurements as now carried out at Chicago and at Toronto are in reasonable agreement.

Both the ages quoted above were determined at Toronto by the lead ratio method applied to uraninites found in the same pegmatites as the potassium feldspars. It has been our experience that the lead ratio method generally gives the most reasonable ages for old minerals.[3]

As pointed out by Wasserburg and Hayden,[2] Nier[4] has dated a specimen identified as "Bessner Ontario uraninite" by the lead ratio method and obtained an age of only 825 million years. Through the kindness of J. P. Marble, Chairman, Committee on the Measurement of Geologic Time, we obtained some of Nier's original Bessner sample and for it found an age of 860 million years in agreement with Nier. Thus there are either uraninites of two ages at Bessner or Nier's sample was collected for him at some other locality. For this reason we have used our age for Bessner determined on the uraninite which we collected.

Additional potassium-argon measurements and a more detailed discussion are being published elsewhere.

This research was assisted by grants from the National Research Council and Geological Survey of Canada, the Research Council of Ontario, and Imperial Oil Limited.

[1] Russell, Shillibeer, Farquhar, and Mousuf, Phys. Rev. **91**, 1223 (1953).
[2] G. J. Wasserburg and R. J. Hayden, Phys. Rev. **93**, 645 (1954).
[3] Collins, Farquhar, and Russell, Bull. Geol. Soc. Am. **65**, 1 (1954).
[4] A. O. Nier, Phys. Rev. **55**, 153 (1939).

K-Particle Production by Protons of 2.2 and 3.0 Bev*

R. D. Hill,† E. O. Salant, and M. Widgoff
Brookhaven National Laboratory, Upton, New York
(Received April 27, 1954)

STACKS of Ilford 400 μ *G5* stripped emulsions have been exposed to radiations from a 6 mm thick copper target bombarded by the circulating proton beam of the BNL Cosmotron. No magnetic analysis was used.

Four events attributed to stopping K mesons have been found in area-scanning of the emulsions. Preliminary values of the masses of these mesons have been determined from range, ionization, and multiple scattering measurements. Each K particle was observed to enter the emulsion in the target-to-emulsion direction.

At one stack position, (a), the target-to-emulsion path, 28 cm long, made an angle of 90° with the proton beam direction; at another position, (b), the target-to-emulsion path was 50 cm long and made an angle of 45° with the proton beam. At both positions the radiations incident on the stacks from the target traversed the steel wall (1.1 cm) of the Cosmotron, and at position (b) they traversed an additional 7.5 cm of copper.

With protons of 2.2 Bev, and emulsions at (b), one stopping K^- meson (range in the emulsion 31 mm) has been found in a scanned area of 36.2 cm², in which 231 stopping π and μ mesons were observed. In these emulsions, the flux of fast particles coming from the target was about 5×10^3 cm^{-2}. The K^- meson formed a star consisting of a 50-Mev π meson (as shown by grain count and scattering) and a heavy fragment of 600 μ range. The π meson makes a two-pronged star in flight after traversing 3.1 mm of emulsion. This K^- star resembles closely the one found at the Cosmotron with magnetic selection.[1] The mass of the K^-meson has been measured as $970\pm150\ m_e$. If it came from the target, as is indicated by its direction, then it is estimated that it left the target with 270-Mev kinetic energy. This kinetic energy is consistent with the production of the K meson either single or paired with a hyperon; it is inconsistent with production of a pair of K mesons of mass as low as 920 m_e in a single nucleon-nucleon collision, assuming a maximum Fermi energy of 25 Mev.[2]

With protons of 3.0 Bev, 10.8 cm² of emulsion exposed at position (a) have so far been scanned. The flux of fast particles from the target was about 3×10^3 cm^{-2}. In this area, 386 π and μ meson endings have been found and three tracks due to stopping heavy mesons (ranges in emulsion 19 mm, 40 mm, 46 mm) have been identified. In each of these events the heavy meson gave rise to a single minimum ionizing particle, with no visible recoil or electron track. The events are, then, typical of positive K meson decays. It is not yet known whether the decay particles are π mesons or μ mesons. The measured masses of these three K mesons are in the range $1050\pm250\ m_e$, and their kinetic energies on leaving the copper target lie between 90 and 130 Mev.

All the K mesons observed lived at least 2×10^{-9} sec before coming to rest in the emulsion.

Emulsions exposed at position (b), with 3.0-Bev protons, have not yet been scanned.

We wish to thank Mrs. M. Carter and Mr. J. E. Smith for processing these emulsions, and Mrs. M. Hall, B. Cozine, A. Lea, and M. Bracker for invaluable aid in the microscopy.

* Work performed under the auspices of the U. S. Atomic Energy Commission.
† On leave from the University of Illinois, Urbana, Illinois.
[1] J. Hornbostel and E. O. Salant, Phys. Rev. **93**, 902 (1954).
[2] R. M. Sternheimer, Phys. Rev. **93**, 642 (1954); Brookhaven National Laboratory Report No. RS-41, March 8, 1954 (unpublished).

Beta-Decay Interaction*

Henry Brysk
Vanderbilt University, Nashville, Tennessee
(Received March 5, 1954)

EXISTING arguments, presented exhaustively by Mahmoud and Konopinski[1] and since supplemented and firmly established by the electron-neutrino angular correlation experiments on helium-6[2] and neon-19,[3] indicate that the beta-decay interaction contains tensor and scalar contributions (in a ratio of the order of unity), but no vector or axial vector. Previous conclusions concerning the pseudoscalar interaction are largely invalidated by a recent re-examination of the theory[4] whose consequences are discussed below.

The new treatment gives a pseudoscalar contribution to the l-forbidden group ($\Delta j=\pm1$, $\Delta l=\pm2$). Direct evidence for the validity of l assignments comes from deuteron stripping experiments which yield the shell model l even when lower l values could compete,[5] as in phosphorus-32.[6] A mixture of single-particle states, with a $\Delta l=0$ contribution of the order of a percent or less, is possible and sometimes expected. If we ascribe the whole transition probability to pseudoscalar interaction (despite competition from the other interactions and $\Delta l=0$ admixture), we shall find an upper limit to g_P consistent with the observed ft values. The pseudoscalar l-forbidden correction factor is approximately (neglecting nuclear force corrections):

$$C_{lP}=g_P^2(4M^2)^{-1}(\alpha Z/2\rho)^2\left|\rho^{-2}\int\mathbf{r}(\boldsymbol{\sigma}\cdot\mathbf{r})\right|^2,$$

as against the allowed tensor $C_{0T}=g_T^2|\int\boldsymbol{\sigma}|^2$ and Rose and Osborn's first-forbidden pseudoscalar correction factor, which is ap-

proximately

$$C_{1P}=g_P^2(4M^2)^{-1}(\alpha Z/2\rho)^2(\alpha Z)^2\left|\rho^{-1}\int\boldsymbol{\sigma}\cdot\boldsymbol{\tau}\right|^2.$$

As a fair estimate, we consider $|\int\boldsymbol{\sigma}|\approx|\rho^{-1}\int\boldsymbol{\sigma}\cdot\boldsymbol{\tau}|\approx|\rho^{-2}\int\boldsymbol{\tau}(\boldsymbol{\sigma}\cdot\boldsymbol{\tau})|$, where we take for the tensor matrix element the ordinary allowed (not superallowed) value of the matrix element—i.e., we consider all transitions to be subject to the same "unfavored factor." Repeated occurrence of fortuitously extremely small matrix elements is unlikely, as ft values in any group tend to be pretty uniform, and major irregularities here would lead us to expect them elsewhere as well. The presence of a large nuclear force contribution to the pseudoscalar interaction would depress g_P in order to fit of the observed l-forbidden ft values. From the ratio C_{1P}/C_{0T} determined from observed ft values for the extensively studied carbon-14[7] and phosphorus-32 and neighboring allowed nuclides, we obtain $|g_P/g_T|\approx4$ and 20, respectively; the $Z\approx30$ group yields a ratio near 15. Even a ratio of 20, however, leads to log $ft\approx8$ for C_{1P} for the highest Z—a trifle small to compete equally with the other interactions, and certainly inadequate to account for log $ft\approx5.5$ among the high-Z $\Delta j=0$ (yes) group. Thus it appears that the pseudoscalar interaction does not play a detectable role in beta decay, if it is present at all.

I wish to thank Dr. M. E. Rose for making his results available to me ahead of publication and for a number of fruitful discussions.

* Work supported in part by the U. S. Atomic Energy Commission.

[1] H. M. Mahmoud and E. J. Konopinski, Phys. Rev. **88**, 1266 (1952).
[2] B. M. Rustad and S. L. Ruby, Phys. Rev. **89**, 880 (1953).
[3] W. P. Alford and D. R. Hamilton, Phys. Rev. **94**, 779 (1954).
[4] M. E. Rose and R. K. Osborn, Phys. Rev. **93**, 1315 (1954).
[5] H. A. Bethe and S. T. Butler, Phys. Rev. **85**, 1045 (1952).
[6] Parkinson, Beach, and King, Phys. Rev. **87**, 387 (1952).
[7] A. M. L. Messiah, Phys. Rev. **88**, 151 (1952).

Ground State of Al^{26}

J. C. Kluyver, C. van der Leun, and P. M. Endt
Physisch Laboratorium der Rijksuniversiteit, Utrecht, Netherlands
(Received April 19, 1954)

IT has recently been suggested[1,2] that the state in Al^{26}, which decays by positron emission with a half-life of 6.7 sec, and which was generally accepted as the ground state, might be the $T_z=0$ component of the lowest triplet with isobaric spin $T=1$ and ordinary spin $J=0^+$. The lowest $T=0$ state in Al^{26}, which might well have an ordinary spin $J=5^+$,[3] might be situated either above or below the 6.7-second state. In Li^6, B^{10}, N^{14} and Na^{22} the ground state is a $T=0$ state, while in Cl^{34} the ground state has $T=1$. In any case such a low $J=5^+$ state would have a very long half-life.

There is much conflicting experimental evidence[4–11] about the lowest levels in Al^{26} (see Table I). The differences in the threshold measured by neutron detection and by positron detection both for $Al^{27}(\gamma,n)Al^{26}$ and $Mg^{26}(p,n)Al^{26}$ point to a long-lived state in Al^{26}. Moreover, it is found that the neutron yield of the $Al^{27}(\gamma,n)Al^{26}$ reaction is three times larger than the positron yield.[12,1]

In the present investigation the $Mg^{25}(p,\gamma)Al^{26}$ reaction was used to obtain more information on the lowest states in Al^{26}. By bombarding thin targets of separated Mg^{24}, Mg^{25}, and Mg^{26} (obtained from Dr. M. L. Smith, Atomic Energy Research Establishment, Harwell, England) by protons in the energy region from $E_p=200$ to 700 kev, it was possible to assign six resonances to Mg^{25}, *viz.*, at $E_p=315$, 389, 436, 508 (possibly unresolved doublet), 586, and 620 kev. The first four resonances have been observed previously from natural magnesium targets by Tangen[13] and by Hunt and Jones.[14] Tangen assigned the 436-kev resonance to Mg^{25}, as he did not detect positrons at this resonance. Hunt and Jones interpreted also the 315- and 387-kev resonances as Mg^{26} resonances.

TABLE I. Experimental data about the position of the two lowest states in Al^{26} relative to the Mg^{26} ground state.

Reaction	$Al^{26}-Mg^{26}$ (Mev)	$Al^{26*}-Mg^{26}$ (Mev)	Ref.
$Al^{26}(\beta^+)Mg^{26}$		4.4 ±0.5	4, 5
$Al^{26}(\beta^+)Mg^{26}$		(3.8)[a]	6
$Al^{26}(\beta^+)Mg^{26}$		(4.01)	7
$Al^{27}(\gamma,n)Al^{26}$	3.70 ±0.20		8
$Al^{27}(\gamma,n)Al^{26}$		5.0 ±0.4	9
$Mg^{25}(d,n)Al^{26}$	2.51 ±0.10	4.51 ±0.18	10
$Mg^{26}(p,n)Al^{26}$	~2.6	(4.3)	11

[a] The value has been put between parentheses, when the isotopic assignment is doubtful.

Gamma-ray energies were measured with a scintillation spectrometer (2×2×3 cm³ NaI crystal). Pulses were fed both to a one-channel differential discriminator and to an ordinary discriminator, used as a monitor. Energy calibrations were performed with a Po-Be source ($E_\gamma=4.44$ Mev) and with γ rays from the $F^{19}(p,\alpha\gamma)O^{16}$ reaction ($E_\gamma=6.13$ Mev) and from the $C^{13}(p,\gamma)N^{14}$ reaction ($E_\gamma=8.06$ Mev).

At the 436-kev resonance a γ ray of $E_\gamma=6.77\pm0.08$ Mev is observed indicating an Al^{26} state (the ground state) 3.96±0.08 Mev above the Mg^{26} ground state. At all resonances a γ ray was found proceeding to an Al^{26} level 4.42±0.08 Mev above the Mg^{26} ground state, corresponding to 0.46±0.08 Mev above the Al^{26} ground state (see Table II). No higher energy γ rays were found

TABLE II. Observed γ rays at six $Mg^{25}(p,\gamma)Al^{26}$ resonances.

Resonance proton energy (kev)	$E_{\gamma1}$ (Mev)	$Mg^{25}+p-Al^{26}$ (Mev)	Rel.[a] int.	$E_{\gamma2}$ (Mev)	$Mg^{25}+p-Al^{26*}$ (Mev)	Rel.[a] int.
315			≦3	6.28	5.98	18
389			≦2	6.20	5.83	8
436	6.77	6.35	25	6.28	5.86	6
508			≦2	6.38	5.89	10
586			≦2	6.43	5.87	18
620			≦2	6.50	5.90	19

[a] The relative intensity is given in percents of the number of γ-ray pulses larger than 1 Mev.

at any of the six resonances investigated. There are certainly present several lower energy γ rays, but their energy has not yet been accurately determined. In a preliminary survey positrons from the Al^{26} decay were observed at all of the investigated resonances. However at the 436-kev resonance the yield is certainly low, in agreement with Tangen's observation.[13]

All experimental evidence cited in this letter is compatible with the assumption that the Al^{26} ground state has isobaric spin $T=0$ and the level at 0.46 Mev $T=1$. If the ground state really has a spin $J=5^+$, it probably decays by a second forbidden β^+ transition to the Mg^{26} level at 1.83 Mev (assumedly with $J=2^+$) with a β^+ endpoint of 1.11±0.08 Mev. Taking log $ft=13.0$ leads to an estimated half-life of 4×10^4 years.

[1] P. Stähelin, Helv. Phys. Acta **26**, 691 (1953), and Phys. Rev. **92**, 1076 (1953).
[2] S. A. Moszkowski and D. C. Peaslee, Phys. Rev. **93**, 455 (1954).
[3] R. W. King and D. C. Peaslee, Phys. Rev. **90**, 1001 (1953).
[4] O. R. Frisch, Nature **133**, 721 (1934).
[5] E. Bleuler and W. Zünti, Helv. Phys. Acta **19**, 375 (1946).
[6] H. R. Allan and C. A. Wilkinson, Proc. Roy. Soc. (London) **A194**, 131 (1948).
[7] White, Delsasso, Fox, and Creutz, Phys. Rev. **56**, 512 (1939).
[8] Sher, Halpern, and Mann, Phys. Rev. **84**, 387 (1951).
[9] McElhinney, Hanson, Becker, Duffield, and Diven, Phys. Rev. **75**, 542 (1949).
[10] Swann, Mandeville, and Whitehead, Phys. Rev. **79**, 598 (1950).
[11] P. Stähelin (private communication).
[12] Montalbetti, Katz, and Goldemberg, Phys. Rev. **91**, 659 (1953).
[13] R. Tangen, Kgl. Norske Videnskab. Selskabs Skrifter No. 1 (1946).
[14] S. E. Hunt and W. M. Jones, Phys. Rev. **89**, 1283 (1953).

Proton-Proton Scattering from 40 to 95 Mev*

U. E. Kruse,† J. M. Teem,‡ and N. F. Ramsey
Harvard University, Cambridge, Massachusetts
(Received April 26, 1954)

PROTON-PROTON scattering has been studied with the external beam of the Harvard cyclotron, using scintillation counters to detect the protons scattered from hydrocarbon targets

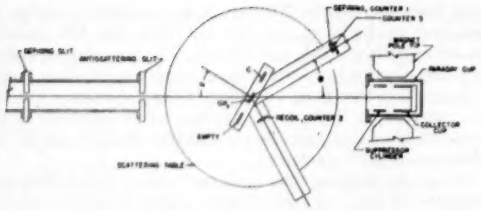

FIG. 1. Experimental equipment.

and a Faraday cup to measure the incident proton flux. The angular distribution from 90° to 40° in the center-of-mass system was observed at 95 Mev. The cross section at 90° for lower energies was obtained by degrading the beam with lithium hydride absorbers.

The experimental arrangement is shown in Fig. 1. To detect both of the protons as in the method of Wilson and Creutz[1] two arms whose angles could be accurately adjusted were mounted on the circular scattering platform. Fastened to the arms were supports for the detectors consisting of stilbene crystals mounted on 1P21 photomultiplier tubes. The pulses from the photomultipliers were fed into diode bridge coincidence circuits.[2] Coincidences between the defining counter 1 and counter 3 directly behind the defining counter as well as coincidences between the defining counter and the recoil counter 2 were obtained from the diode bridge coincidence circuits. These could then be mixed in a slow coincidence circuit to obtain threefold coincidences. At the lower energies the protons did not have sufficient energy to pass through the defining counter, and only twofold coincidences between the defining and recoil counters were measured. Throughout the experiment suitable checks on efficiency and accidentals were performed. Also, to eliminate any effects due to polarization of protons in the beam or misalignment of the scattering table, the defining counter was placed alternately on the right and left side of the beam.

The targets employed in this phase of the experiment were two thicknesses of polyethylene with carbon targets of approximately equal stopping power. At 90° in the center-of-mass system the cross section was also checked with a polystyrene target. Because of the low incident beam intensity it was necessary to use a geometry in which genuine coincidences from carbon could not be neglected, and this contribution to the coincidence rate in the polyethylene was therefore suitably subtracted. With the thickness of targets necessary to obtain reasonable counting rates it was impossible to detect both protons corresponding to angles smaller than 40° in the center-of-mass system. It is hoped that this region as well as the angles up to 90° will be investigated soon with liquid hydrogen targets.

The number of protons in the beam was measured with a Faraday cup. The energy of the incident particles was determined by finding the fraction of particles penetrating known amounts of aluminum. In this way it was found that the full width at half-maximum was 2 Mev at the full energy of 95 Mev and increased to a width of 4.8 Mev at a mean energy of 41 Mev. The total charge collected on the Faraday cup was measured using a Brown vibrating reed electrometer modified to operate with a specially constructed capacitor mounted in the Faraday cup vacuum system. It was found that the charge collected on the cup was independent of parameters of the cup system such as electrical and magnetic suppression of secondaries as well as distance of the front foil and other geometrical considerations.

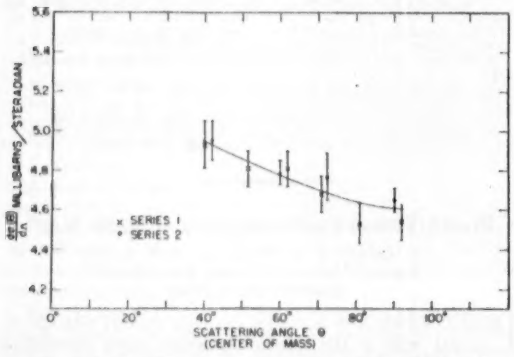

FIG. 2. Angular distribution at 95 Mev—counting statistics only.

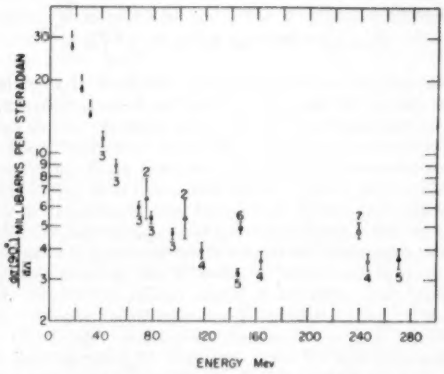

FIG. 3. Cross sections at 90° center-of-mass. 1. Berkeley, reference 7; 2. Harvard, reference 6; 3. Harvard, present data; 4. Berkeley, reference 3; 5. Chicago, reference 8; 6. Harwell, reference 5; 7. Rochester, reference 4.

The angular distribution obtained at 95 Mev is shown in Fig 2; counting statistics only are shown. When possible systematic errors are included, the reliability of the ratio of the cross sections at 90° and 40° is estimated to be 4 percent. In Fig. 3, the cross sections at 90° in the center-of-mass system are compared to results previously reported.[3-8] The estimated errors for the absolute cross section listed by the authors are shown except in the Chicago results where only a preliminary estimate is available.

* Supported by the joint program of the U. S. Office of Naval Research and the U. S. Atomic Energy Commission.
† Society of Fellows.
‡ National Science Foundation Predoctoral Fellow.
[1] R. R. Wilson and E. C. Creutz, Phys. Rev. **71**, 339 (1947).
[2] Karl Strauch, Rev. Sci. Instr. **24**, 283 (1953).
[3] Chamberlain, Segrè, and Wiegand, Phys. Rev. **83**, 923 (1951).
[4] C. L. Oxley and R. D. Schamberger, Phys. Rev. **85**, 416 (1952); O. A. Towler, Jr., Phys. Rev. **85**, 1024 (1952).
[5] Cassels, Pickavance, and Stafford, Proc. Roy. Soc. (London) **214**, 262 (1952).
[6] Birge, Kruse, and Ramsey, Phys. Rev. **83**, 274 (1951).
[7] Bruce Cork, Phys. Rev. **80**, 321 (1950).
[8] Marshall, Marshall, and Nedzel, Phys. Rev. **92**, 834 (1953).

Polarization by p-p Collision at 439 Mev*

H. G. DE CARVALHO, E. HEIBERG, J. MARSHALL, AND L. MARSHALL
Institute for Nuclear Studies, The University of Chicago, Chicago, Illinois
(Received April 30, 1954)

PREVIOUS measurements of asymmetry of p-p scattering for polarized protons of 340[1] and 310[2] Mev indicate that at these energies triplet states of angular momentum greater than 1 have become important in p-p collisions. This is made evident by the fact that the asymmetry of scattering varies as $\sin\theta\cos\theta$ if only ^3P states act, but at 310 and 340 Mev it is fitted by $\sin\theta\cos\theta(a+b\cos^2\theta+c\cos^4\theta+\cdots)$ where b and c are probably larger than a. Terms other than the first can arise only by interference in triplet states of angular momentum greater than 1.

We report here a measurement of asymmetry of p-p scattering with 439-Mev polarized protons, from which we hoped to learn

more about the additional triplet angular momentum states acting. We used an external proton beam of fifty percent polarized protons of 439±6 Mev, produced when protons of 435-Mev average energy (in the 450-Mev equilibrium orbit of the cyclotron) were scattered at 14° to the right from a beryllium target in the cyclotron. An estimate of the degree of polarization of the beam was obtained by measuring the asymmetry of second scattering from a beryllium target in the experimental area. The scattering was measured at 14°, excluding the nucleon-scattered component by filtration of the scattered protons through 5¾ inches of copper. (The mean range of the 439-Mev incident beam was 6¼ inches of copper). We assumed the first and second events to be similar in nature, and estimated the polarization of the beam as (¼ asymmetry)$^{\frac{1}{2}}$=fifty percent polarized.

Next the asymmetry of scattering of the 439-Mev beam from liquid hydrogen was measured and found to be as shown in Fig. 1.

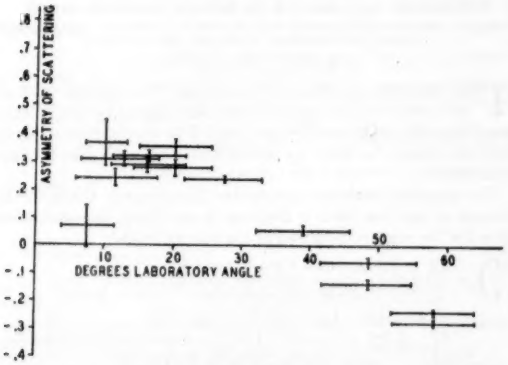

FIG. 1. Asymmetry of scattering [defined as $(R-L)/\frac{1}{2}(R+L)$] from liquid hydrogen for 439-Mev 50-percent-polarized protons, shown plotted against laboratory angle. A best curve through the data crosses the axis at 43°, as it should, owing to the relativistic nature of the protons. For the above data, the polarization P_H is equal to the asymmetry.

The horizontal dimensions of the data represent geometrical width of the counters, and the vertical dimensions are the statistical counting errors. For laboratory angles greater than 26°, the two scattered protons were measured in coincidence with each other (and with the incident proton) in order to exclude meson production events. At smaller angles such a coincidence measurement is no longer useful because it can be triggered by an event in which a meson enters one counter and a proton enters the counter on the other side of the beam. At angles of 8° or less, the situation becomes even more ambiguous in that events may be recorded in which a meson enters one counter while a deuteron enters the other counter.

In order to eliminate uncertainties introduced by meson production, the following measurements were made. The asymmetry of meson production at 58°±6.5° and 48.5°±8.5° was measured for the process $p+p\rightarrow\pi^++d$. For these measurements 4 counters were connected in quadruple coincidence, counters A and B forming a telescope in the incident beam, counter K extending from 3.1° to 13.8° laboratory angle, and counter C on the other side of the beam placed one time from 41.5° to 64.5° and in the next measurement from 40° to 57° laboratory angle. The quadruple coincidence ABCK then detected events in which a meson was produced at 58°±6.5° or at 48.5°±8.5° and accompanied by a deuteron. Under these conditions the deuteron goes forward approximately at 8°. This quadruple coincidence also detected approximately 78 percent of the "unbound" reaction $p+p\rightarrow\pi^++p+n$. The observed asymmetries asym=$\{[I(R)-I(L)]/\frac{1}{2}[I(R)+I(L)]\}$ were (+7.5±11) percent at 58° and (−21±12) percent at 48.5°. These laboratory angles respectively correspond to 98° and 85° in the barycentric system of meson and deuteron.

The asymmetry of meson production which arises from an interference between s and p angular momentum states of the pion-nucleon system, varies to a first approximation[3] as $\sin\theta$, and hence is maximal in the region where we measured it. Because the asymmetry varies as $\sin\theta$, we can average these two values which are approximately equally removed from 90°, and obtain thereby the statistically more accurate value of (−7±8.5) percent asymmetry.

Although this number is not of high accuracy, still it suffices to demonstrate that at small angles one can measure the asymmetry of scattering of total charged particles and interpret it as asymmetry of scattered protons, with very little error introduced from asymmetry in meson production. The argument follows. The meson asymmetry measurement included also an absolute measurement of meson production cross section calculated from the average intensity scattered to right and to left. We found 0.143±0.010 mb/sterad at 100° barycentric angle and 0.125 ±0.008 mb/sterad at 85° barycentric angle.

The asymmetric part of the meson production has the value therefore of $0.07\times0.134\sin\theta=0.01\sin\theta$ mb/sterad. The asymmetric part of the proton cross section from 10−25° is ∼4 mb/sterad×forty percent=1.60 mb/sterad. At 25° it follows that 0.01 sin25°/1.60 or less than one percent of the asymmetry is due to meson production. At smaller angles the meson contribution is smaller.

This amount of ambiguity we considered negligible, and we proceeded to measure the asymmetries below 25° using a telescope of two counters to catch the scattered particles in coincidence with a telescope of two counters in the incident beam, with the resulting asymmetries shown in Fig. 1. The polarization of hydrogen is calculated from the relation $P_H=\frac{1}{2}$(asym/0.50) where 0.50 represents polarization of the incident beam. In this case it follows that P_H=asymmetry.

The results of this experiment seem to be little different from those of 340[1] and 310[2] Mev. There seems to be little tendency for higher angular momentum states to increase their contribution. In fact if there is any difference at all, the angular distribution is more nearly $\sin\theta\cos\theta$ (triplet p interaction) than it was at the lower energy.

Assuming an angular dependence of $0.2+\cos^2\theta$ for the bound and unbound meson production, and assuming the bound meson production cross section $(p+p\rightarrow d+\pi^+)$ to be 1.0 mb,[4] we compute a value of 3.75±0.24 mb for the unbound reaction. Let the total meson production cross section be written as $\sigma(p+p\rightarrow\pi^++\text{nucleons})=\sigma_{10}(\pi^++d)+\sigma_{10}(\pi^++p+n)+\sigma_{11}(\pi^0+p+p)$. Then the branching ratio is defined[4] as $[\sigma_{10}(\pi^++p+n)+\sigma_{10}(\pi^++n+p)+\sigma_{10}(\pi^++d)]$. We use 0.22 mb for σ_{11} and compute for the branching ratio the value of 3.5.

* Research supported by a joint program of the U. S. Office of Naval Research and the U. S. Atomic Energy Commission.

[1] Chamberlain, Segrè, Tripp, Wiegand, and Ypsilantis, Phys. Rev. **93**, 1430 (1954).
[2] Marshall, Marshall, and de Carvalho, Phys. Rev. **93**, 1430 (1954).
[3] R. E. Marshak and A. M. L. Messiah, Phys. Rev. (to be published).
[4] A. H. Rosenfeld, Phys. Rev. (to be published).

Polarization of Elastically Scattered Nucleons from Nuclei in the Born Approximation*

WARREN HECKROTTE
Radiation Laboratory, Department of Physics, University of California, Berkeley, California

(Received April 13, 1954)

RECENT experiments on the polarization of high-energy nucleons elastically scattered from nuclei[1] have led to the interpretation of these results in terms of an effective spin-orbit nuclear potential[2] in addition to the usual central nuclear potential used to explain[3] the total and experimental cross sections of the high-energy nuclear scattering. A small spin-orbit potential is sufficient to account for the large polarization observed.

At these high energies (∼300 Mev) and at least for lighter nuclei, it has been pointed out that the Born approximation or

equivalent simple arguments[2] yield a qualitative estimate of the amount and character of the polarization phenomena. The fact that the first Born approximation yields a polarization is a consequence of the use of a complex central potential. The polarization is a result of the selective absorption of nucleons scattered with spins up ($j=l+\frac{1}{2}$) and with spins down ($j=l-\frac{1}{2}$).

It is the purpose of this note to point out that the Born approximation result for the polarization is independent of the shape of the nuclear potential if the spin-orbit potential is taken to be proportional to the gradient of the central nuclear potential.[4] The central potential is taken to be $V_c(r)=-(u_0+iw_0)\rho(r)$ in Mev, where $\rho(r)$ represents the radial dependence of the potential. The spin-orbit potential is taken to be $V_s=-U_s(r)\boldsymbol{\sigma}\cdot\mathbf{L}/\hbar$, where $U_s(r)=-(\mu a^2/r)(d\rho/dr)$. Roughly speaking, μ can be considered as the depth of an equivalent square well of radius a.

In Born approximation, the scattered amplitude $f(\theta)$ is given by

$$(2m/\hbar^2)f(\theta)=A(\theta)+i\boldsymbol{\sigma}\cdot\mathbf{n}\sin\theta B(\theta),$$

where

$$A(\theta)=\int j_0(gr)V_c(r)r^2dr,$$

$$B(\theta)=-\frac{k^2}{g}\int j_1(gr)U_s(r)r^2dr.$$

$\mathbf{n}$ is the unit vector normal to the plane of scattering, k is the incident wave number, g is the momentum transfer, and j_0 and j_1 are spherical Bessel functions.[5] Using the fact that $x^2j_0(x)=(d/dx)[x^2j_1(x)]$ and performing a partial integration on $A(\theta)$, one can show that

$$A(\theta)=-\frac{1}{g}\int j_1(gr)\left(\frac{1}{r}\frac{d}{dr}V_c\right)r^3dr.$$

Accordingly, $A(\theta)$ and $B(\theta)$ have the same functional form and the scattered amplitude can be written as

$$\frac{2m}{\hbar^2}f(\theta)=\left(1-i\boldsymbol{\sigma}\cdot\mathbf{n}\sin\theta\frac{k^2a^2\mu}{u_0+iw_0}\right)A(\theta).$$

The polarization is given then by

$$P=\frac{-2k^2a^2\mu w_0/(u_0^2+w_0^2)}{1+(k^4a^4\mu^2\sin^2\theta)/(u_0^2+w_0^2)}\sin\theta.$$

The polarization is thus independent of the shape of the nuclear potential, except that u_0, w_0, and μ must be adjusted to yield the total and absorption cross sections for a particular choice of the radial dependence, $\rho(r)$. The result is also independent of the target nucleus unless such a dependence is introduced into μa^2 (say, for example, $a\sim A^{\frac{1}{3}}$).

If we take, for example, a square well, the constants obtained in fitting the total nuclear cross sections for 300-Mev neutrons are $u_0\cong 0$ and $w_0=18$ Mev.[3] If we use $\mu a^2=5\times10^{-26}$ Mev cm^2 which corresponds to $\mu=\frac{1}{2}$ Mev when a is equal to the radius of carbon, the polarization is given by

$$P=\frac{-8.5}{1+18.1\sin^2\theta}\sin\theta.$$

The polarization obtained in the Born approximation can be expected to hold only for forward scattering angles. For larger angles the angular dependence of $B(\theta)$ relative to $A(\theta)$ changes sufficiently to introduce large corrections to the Born approximation result, particularly in the region of the diffraction minima. Thus, it is principally in these latter regions that model-dependent features of the polarization can be expected to appear. In addition, if non-square well shapes are taken, it has been found that u_0 and w_0 must be increased over their square well values in order to fit the observed cross sections. In some cases the increase is sufficient to invalidate the Born approximation. The results of more accurate calculations for neutrons and protons and for a number of well shapes is in the course of preparation.

I wish to thank Dr. Burton Fried for a discussion during which the observation on the polarization in Born approximation was made.

* This work was performed under the auspices of the U. S. Atomic Energy Commission.

[1] Oxley, Cartwright, and Rouvina, Phys. Rev. **93**, 806 (1954); Chamberlain, Segrè, Tripp, Weigand, and Ypsilantis (unpublished results).

[2] E. Fermi, Nuovo cimento **11**, 407 (1954); B. Malenka, Bull. Am. Phys. Soc. **29**, No. 4, 32 (1954); and W. Heckrotte and J. V. Lepore, Phys. Rev. **94**, 500 (1954).

[3] Fernbach, Serber, and Taylor, Phys. Rev. **75**, 1352 (1949); S. Fernbach, thesis, University of California Radiation Laboratory Report 1382 (unpublished).

[4] W. Heisenberg, *Theorie Des Atomkernes* (Göttingen, 1951), p. 22.

[5] L. Schiff, *Quantum Mechanics* (McGraw-Hill Book Company, Inc., New York, 1949), p. 77.

Hyperfine Structure of I^{127}. Nuclear Magnetic Octupole Moment*

V. Jaccarino, J. G. King, R. A. Satten,† and H. H. Stroke
Research Laboratory of Electronics and Department of Physics, Massachusetts Institute of Technology, Cambridge, Massachusetts

(Received April 22, 1954)

THE hyperfine structure of the atomic $^2P_{3/2}$ ground state of the stable isotope of iodine has been studied by the atomic-beam magnetic-resonance method. As will be shown, the measured intervals cannot be fitted by dipole and quadrupole-like interactions alone.

The hyperfine structure interaction Hamiltonian, which in the absence of external fields is diagonal in an F, m_F representation, gives for the relative positions of the energy levels[1]:

$$\left(\frac{W}{h}\right)_F=\frac{aK}{2}+b\frac{\frac{3}{4}K(K+1)-I(I+1)J(J+1)}{2I(2I-1)J(2J-1)}+c\frac{5}{4}\left\{\frac{K^3+4K^2+\frac{1}{4}K[-3I(I+1)J(J+1)+I(I+1)+J(J+1)+3]-4I(I+1)J(J+1)}{I(I-1)(2I-1)J(J-1)(2J-1)}\right\}, \quad (1)$$

where a and b are the nuclear magnetic dipole and electric quadrupole interaction constants, respectively,[2,3] and c is the nuclear magnetic octupole interaction constant. It can be expressed as

$$hc=\langle r^3P_3\,\mathrm{div}\mathbf{M}\rangle_{I,I}\langle r^{-4}P_3\,\mathrm{div}\mathbf{M}\rangle_{J,J}. \quad (2)$$

(Here $\mathbf{M}$ is defined by the relation $\mathrm{curl}\mathbf{M}=\mathbf{i}/c$. The current density includes spin as well as orbital currents.) We have defined

$$\langle\tfrac{1}{4}(5z^3-3zr^2)\,\mathrm{div}\mathbf{M}\rangle_{I,I}$$

as the octupole moment.

By using second-order perturbation theory, matrix elements of the dipole and quadrupole moment operators which, for a given F, are nondiagonal with respect to J, may be calculated.[4] The effects of these perturbations by the neighboring $^2P_{1/2}$ fine-structure level,

$$[E(P_{1/2})-E(P_{3/2})]/h=2.28\times10^8\ \mathrm{Mc/sec},$$

must be included. The measured zero-field intervals are:

	Uncorrected	Corrected
$F=4\leftrightarrow F=3$:	4226.172±0.015 Mc/sec;	4226.161±0.015 Mc/sec,
$F=3\leftrightarrow F=2$:	1965.884±0.010 Mc/sec;	1965.895±0.010 Mc/sec,
$F=2\leftrightarrow F=1$:	737.492±0.008 Mc/sec;	737.492±0.008 Mc/sec.

Experimental values for each of the three intervals were obtained by observing transitions for which $\Delta F=\pm1$, in the region of zero external magnetic field.

The corrected intervals give the following values for the interaction constants:

$$a=\ 827.265\ \ \pm0.003\ \mathrm{Mc/sec},$$

$$b=1146.356\ \ \pm0.010\ \mathrm{Mc/sec},$$

$$c=\ 0.00245\pm0.00037\ \mathrm{Mc/sec}\ \text{(all errors rms)}.$$

From this value of c the nuclear magnetic octupole moment is calculated:

$$\langle\tfrac{1}{4}(5z^3-3zr^2)\,\mathrm{div}\mathbf{M}\rangle_{I,I}=+0.3\mu_n\times10^{-24}\ \mathrm{cm}^3.$$

This result is not inconsistent either in magnitude or sign with the octupole moment to be expected for iodine. In fact, it is in good agreement with the result predicted from a detailed theory for a $d_{5/2}$ proton in a single-particle orbit.[5] The authors would like to point out that this result has no relation to that found by Tolansky from a study of the optical spectrum of ionized iodine.[6]

Consideration of the form of the octupole interaction shows why, for a given octupole moment, the interaction energy is appreciably larger in iodine than in the elements of group III or the remaining halogens. The hyperfine structure of some of these elements has been studied by atomic-beam methods with comparable precision and no octupole-like departures have been found.[8] Details of this and other considerations (relativistic effects, configuration interactions, etc.) will be discussed in a forthcoming paper, which will describe the experimental method as well. It will be accompanied by a paper by C. Schwartz on the theory of the hyperfine structure interaction.

We are indebted to Charles Schwartz for his valuable cooperation.

* This work was supported in part by the Signal Corps, the Air Materiel Command, and the U. S. Office of Naval Research.

† On leave from the University of California at Los Angeles. Present address, Physics Department, University of California at Los Angeles, Los Angeles, California.

[1] Here $K=F(F+1)-I(I+1)-J(J+1)$. For $J=3/2$ only these *interactions* exist. This does not preclude, for $I=5/2$, the existence of an electric nuclear 2^4 *moment*.

[2] For a closed shell minus an electron the interaction constants may be expressed as:

$$ha=\mu_0\mu_I\frac{2L(L+1)}{I\,J(J+1)}\langle r^{-3}\rangle,$$

$$hb=-e^2Q\frac{2L}{2L+3}\langle r^{-3}\rangle,$$

$$hc=\mu_0\left\langle\frac{(3z^2-3r^2)}{2}\,\mathrm{div}\mathbf{M}\right\rangle_{I,I}\frac{2L(L-1)(2L+2)(2L+4)}{(2J+2)(2J+3)(2J+4)}\langle r^{-5}\rangle,$$

The indeterminate form of c for the case of a $p_{3/2}$ electron may be evaluated following reference 3.

[3] H. B. G. Casimir and G. Karreman, Physica **9**, 494 (1942).

[4] The results of these calculations were also obtained independently by C. Schwartz.

[5] Paper on the theory of the hyperfine structure interaction to be published by C. Schwartz.

[6] S. Tolansky, Proc. Roy. Soc. (London) **A170**, 214 (1939). In a detailed paper in which the theory of the hyperfine structure involving the nuclear magnetic octupole moment was first presented, Casimir and Karreman (reference 3) pointed out that the Tolansky octupole moment was some 300 times larger than that expected. Other optical investigations (reference 7) did not support Tolansky's results.

[7] T. Schmidt, Z. Physik **112**, 199 (1939); K. Murakawa, Z. Physik **112**, 234 (1939).

[8] The results of recent high-precision measurements of the hyperfine structure of In^{115}, when suitably corrected for the effects of the neighboring fine-structure level, show the existence of a nuclear magnetic octupole moment in In^{115}, though some four times smaller than the value expected for a $g_{9/2}$ proton. Since, in the group III elements, the effects of configuration interactions for large Z must be considered, this result may not be surprising. We wish to express our gratitude to Professor P. Kusch of Columbia University for making his data available to us before publication [P. Kusch and T. G. Eck, following letter, Phys. Rev. **94**, 1799 (1954)].

Hyperfine Structure of In^{115}. Evidence of a Nuclear Octupole Moment*

P. Kusch and T. G. Eck
Department of Physics, Columbia University, New York, New York
(Received April 22, 1954)

THE hyperfine structure intervals in the $^2P_{3/2}$ state of In^{115} have been measured with a high precision in a search for effects arising from a nuclear magnetic octupole moment. Previous measurements[1] allowed the description of the observed intervals in terms of a magnetic dipole and an electric quadrupole interaction only, within experimental error. The present measurements were made on an apparatus in which the weak field, ranging from 0.43 to 1.48 gauss in the several runs, which determined the magnetic splitting of the lines is extremely uniform. The lines are thus sharp and free of asymmetries and it is possible to determine their frequencies to very high precision. The inhomogeneous deflecting fields of the apparatus are sufficiently low so that the atoms are in the (F,m_F) quantization in these fields. Accordingly almost all transitions $\Delta F=\pm1$, $\Delta m_F=\pm1,0$ are accompanied by significant changes in magnetic moment and it is possible to observe a large number of the Zeeman components of each line. The quadratic terms in the energy levels were small in all cases.

The measured frequencies of the zero field lines are as follows:

$$F=6\leftrightarrow F=5:\quad f_6=1752.6851\pm0.0006\ \text{Mc/sec},$$

$$F=5\leftrightarrow F=4:\quad f_5=1117.1693\pm0.0005\ \text{Mc/sec},$$

$$F=4\leftrightarrow F=3:\quad f_4=\ 668.9638\pm0.0005\ \text{Mc/sec}.$$

It is remarkable that these three frequencies can be very accurately represented by an expression for the energy levels which includes only the dipole and quadrupole interaction. In fact, if f_6 and f_4 are assumed as given, f_5 becomes 1117.1692 Mc/sec. However, the levels of the $^2P_{3/2}$ state are perturbed by the $^2P_{1/2}$ state. The perturbation[2] serves to shift the $F=5$ level upwards by 8.2 kc/sec and the $F=4$ level upwards by 1.0 kc/sec. The attempt to describe the corrected line frequencies by an expression which includes only dipole and quadrupole interaction terms leaves residual discrepancies between observed and calculated line frequencies of the order of 5 kc/sec, far beyond the uncertainties of the experimental data.

If we use the expression for the energy levels given by Jaccarino *et al.* in the preceding letter and which includes magnetic dipole, electric quadrupole, and magnetic octupole terms, we find

$$a=242.16485\pm0.00006\ \text{Mc/sec},$$

$$b=449.5524\pm0.0006\ \text{Mc/sec},$$

$$c=0.000497\pm0.000033\ \text{Mc/sec},$$

where, in each case, the quoted uncertainty is the rms sum of the uncertainties in each of the terms of the linear equation which determines the quantity in terms of the line frequencies. No attempt is made to include uncertainties in the small correction terms which have been applied to the observed frequencies. The quantity c is about fourteen times the uncertainty in that quantity and the reality of an octupole-like interaction term is, therefore, not subject to significant doubt. The determination of the octupole moment itself from the interaction constant cannot be made without further extensive calculation.

These measurements were made in consequence of the observation of a much larger octupole interaction energy in I^{127} by the group at the Massachusetts Institute of Technology whose letter appears immediately before the present letter.[3]

* This work was supported in part by the U. S. Office of Naval Research.

[1] A. K. Mann and P. Kusch, Phys. Rev. **77**, 427 (1950).

[2] We are indebted to Dr. V. Jaccarino and Mr. Charles Schwartz for access to their calculations of the relevant perturbation energies.

[3] V. Jaccarino *et al.*, preceding letter [Phys. Rev. **94**, 1798 (1954)].

Coulomb Effects in Pion-Proton Scattering at Relativistic Energies

Frank T. Solmitz
Institute for Nuclear Studies, University of Chicago, Chicago, Illinois
(Received April 22, 1954)

VAN HOVE[1] and Ashkin and Smith[2] have shown how to separate Coulomb and nuclear effects in pion-proton scattering at nonrelativistic energies. One simply considers the Coulomb force negligible inside the region (of radius of the order of the meson Compton wavelength) in which the nuclear forces act, and uses the appropriate Coulomb wave functions outside. It then turns out that the scattering amplitude for not too low energies can be written, to quite good approximation, as the sum of the nuclear amplitude in terms of phase shifts and the Coulomb Born approximation amplitude.

Thus the cross section in the center-of-mass system (including nuclear s and p waves only) is of the form

$$d\sigma/d\Omega=|(1/2ik)(P+Q\cos\theta)+f^{(n,f)}(\theta)|^2 +|(1/2ik)R\sin\theta+f^{(f)}(\theta)|^2; \quad (1)$$

k and θ are the momentum and scattering angle in the c.m.

system; for $\pi^+ + p \to \pi^+ + p$,

$$P = \exp(2i\alpha_3) - 1,$$
$$Q = \exp(2i\alpha_{31}) + 2\exp(2i\alpha_{33}) - 3,$$
$$R = \exp(2i\alpha_{33}) - \exp(2i\alpha_{31}),$$

and for $\pi^- + p \to \pi^- + p$,

$$P = \tfrac{1}{3}[2\exp(2i\alpha_1) + \exp(2i\alpha_3)] - 1,$$
$$Q = \tfrac{1}{3}[2\exp(2i\alpha_{11}) + \exp(2i\alpha_{31}) + 4\exp(2i\alpha_{13}) + 2\exp(2i\alpha_{33})] - 3,$$
$$R = \tfrac{1}{3}[2\exp(2i\alpha_{13}) + \exp(2i\alpha_{33}) - 2\exp(2i\alpha_{11}) - \exp(2i\alpha_{31})].$$

The Coulomb non-spin-flip and spin-flip amplitudes can be written in the following form:

$$f^{(ns)}(\theta) = \mp \frac{e^2}{2pV_\pi \sin^2(\theta/2)}, \quad f^{(s)}(\theta) = 0; \tag{2}$$

here $p = \hbar k$ is the momentum in the c.m. system, and V_π is the pion velocity in the laboratory system. The upper and lower signs refer to scattering of positive and negative pions, respectively.

There has been some question about the correct relativistic generalization of the above result. For small angles and high energy, a classical relativistic calculation should give the correct Coulomb cross section; such a calculation yields $(d\sigma/d\Omega)_C = [(e^2/2pV_\pi)(2/\theta)^2]^2$. Comparison of this expression with Eq. (2) shows that the amplitude, as written there, is also correct relativistically for small angles. [Note that the amplitude is given in a different form in references 1 and 2 and hence differs from Eq. (2) at relativistic energies.]

An alternate approach, valid also for large angles, is to write down the scattering amplitudes to first order in $e^2/\hbar c$ for the electromagnetic interaction Hamiltonian:

$$\mathcal{H}^{EM} = -(4\pi)^{\frac{1}{2}} e \psi_p^\dagger \gamma_\nu \psi_p A_\nu + \frac{(4\pi)^{\frac{1}{2}} e\hbar}{2Mc}(\mu_p - 1)\psi_p^\dagger \gamma_\mu \gamma_\nu \psi_p \times \left(\frac{\partial}{\partial x_\mu} A_\nu - \frac{\partial}{\partial x_\nu} A_\mu\right) + \frac{i(4\pi)^{\frac{1}{2}} ec}{\hbar}\left(\varphi^* \frac{\partial \varphi}{\partial x_\nu} - \varphi \frac{\partial \varphi^*}{\partial x_\nu}\right) A_\nu + \frac{4\pi e^2}{\hbar^2} \varphi^* \varphi (A_\nu A_\nu - A_4^2);$$

here ψ_p, φ are the proton and meson wave functions, respectively, and A_ν is the 4-vector potential of the electromagnetic field. We have included a "Pauli term" for the anomalous magnetic moment of the proton (μ_p is the magnetic moment in nuclear magnetons). Using standard methods, we obtain

$$f^{(ns)} = \frac{\mp e^2}{2p(v_\pi + v_p)\sin^2(\theta/2)} \times \left[1 + \tfrac{1}{2}\frac{v_\pi v_p}{c^2}(1 + \cos\theta) - \tfrac{1}{4}(2\mu_p - 1)\frac{v_p^2}{c^2}(1 - \cos\theta)\right],$$

$$f^{(s)} = \frac{\pm e^2}{2p(v_\pi + v_p)\sin^2(\theta/2)}\left[\tfrac{1}{2}\mu_p \frac{v_\pi v_p}{c^2} + \tfrac{1}{4}(2\mu_p - 1)\frac{v_p^2}{c^2}\right]\sin\theta; \tag{3}$$

v_π, v_p are the pion and proton velocities in the c.m. system. We have neglected terms of order $(v_p/c)^3$. It can be seen that the Coulomb cross section based on Eq. (3) reduces correctly to the classical relativistic expression for small angles.

The author is indebted to Professor E. Fermi and Dr. J. Orear for valuable discussion of this problem.

[1] L. van Hove, Phys. Rev. **88**, 1358 (1952).
[2] J. Ashkin and L. Smith, Coulomb Interference Effects in the Scattering of Mesons by Protons, Technical Report No. 1, Carnegie Institute of Technology, February 2, 1953 (unpublished).

Scintillation Response of Anthracene to Soft X-Rays

J. B. BIRKS AND F. D. BROOKS
Physics Department, Rhodes University, Grahamstown, South Africa
(Received April 20, 1954)

BIRKS[1,2] has predicted a difference between the scintillation response of organic phosphors to external electrons and to internal photoelectrons of the same energy. The scintillation response of anthracene to secondary characteristic x-rays of energies between 6 kev and 25 kev has therefore been studied. The scintillations were observed with an E.M.I. type 5060 photomultiplier, and the output pulse amplitude distribution was obtained using a "gray-wedge" pulse-height analyzer, based on the instrument originally developed by Bernstein *et al.*[3] Secondary characteristic x-rays of known energies were obtained by placing a series of scattering foils of different elements in the path of a beam of "white" x-radiation, and were detected at right angles to the primary beam direction by a 2 mm thick crystal of anthracene.

The pulse amplitude distribution photographs, obtained from the analyzer, showed that it was possible to resolve the photoelectron peaks produced by incident x-rays of energy >11 kev, when the photomultiplier was operating at room temperature (20°C). By cooling the photomultiplier to dry ice temperatures, to reduce the dark noise background, adequate resolution was obtained at lower energies from 6 kev to 11 kev.

The mean scintillation pulse height S is plotted as a function of the x-ray energy E in Fig. 1. The experimental data of Taylor

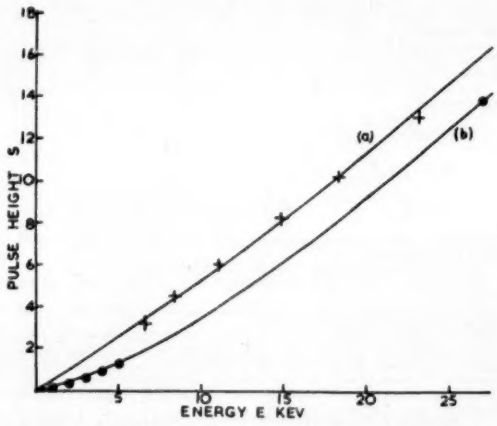

FIG. 1. Scintillation response of anthracene. (a) X-rays. Experimental +; theoretical ——. (b) Electrons. Experimental ●; theoretical ——.

et al.[4] on the scintillation response of anthracene to electrons of energy E, incident externally on the crystal, have been normalized to the same scale of S, and these are also plotted in Fig. 1 for comparison.

The theoretical response curve for photoelectrons, produced internally by x-rays, has been calculated from the formula[2,5]

$$\left(\frac{dS}{dr}\right)_x = \frac{A(dE/dr)}{1 + kB(dE/dr)},$$

by using experimentally determined values of the constants A and kB, and the range-energy data for electrons, given by Curie.[6] The theoretical response curve for external electrons has been calculated from the formula[1,2] for particles of range r,

$$(dS/dr)_e = \phi(dS/dr)_x,$$

where $\phi = 1 - \tfrac{1}{2}[\exp(-r/a_0) - (r/a_0)\,\mathrm{Ei}(r/a_0)]$, $\mathrm{Ei}(r/a_0)$ being the exponential integral. A value of $a_0 = 3$ mm air equivalent has been taken, corresponding to a mean free path for the primary photons[2] of about 3 microns.

The two theoretical response curves, which are plotted in Fig. 1, are in excellent agreement with the experimental data. These results provide further evidence in favor of the photon cascade theory of the scintillation process, proposed by Birks.[2,7] Further measurements are in progress on the scintillation response of anthracene and other organic phosphors to x-rays and electrons.

THE PHYSICAL REVIEW

A journal of experimental and theoretical physics established by E. L. Nichols in 1893

VOLUME 94

Second Series

APRIL 1–JUNE 15, 1954

Published for the

AMERICAN PHYSICAL SOCIETY

by the

AMERICAN INSTITUTE OF PHYSICS

Incorporated

THE PHYSICAL REVIEW

A journal of experimental and theoretical physics established by E. L. Nichols in 1893

Published by the American Institute of Physics for the

AMERICAN PHYSICAL SOCIETY

Officers

President

H. A. BETHE
Cornell University
Ithaca, New York

Vice-President

R. T. BIRGE
University of California,
Berkeley, California

Secretary

K. K. DARROW
Bell Telephone Laboratories
Office:
Columbia University
New York 27, New York

Treasurer

G. B. PEGRAM
Columbia University
New York 27, New York

Local Secretary for the Pacific Coast

J. KAPLAN
University of California at Los Angeles
Los Angeles, California

Managing Editor

S. A. GOUDSMIT
Brookhaven National Laboratory
Upton, Long Island
New York

BOARD OF EDITORS

Editor

S. A. GOUDSMIT

Assistant Editor

S. PASTERNACK

Associate Editors

1952–1954	*1953–1955*	*1954–1956*
W. P. ALLIS	W. A. FOWLER	P. G. BERGMANN
F. G. BRICKWEDDE	KENNETH GREISEN	GREGORY BREIT
W. B. FRETTER	CHARLES KITTEL	F. J. DYSON
CONYERS HERRING	R. E. MARSHAK	P. KUSCH
H. W. LEVERENZ	W. K. H. PANOFSKY	R. SMOLUCHOWSKI
ARNOLD NORDSIECK	V. F. WEISSKOPF	J. C. STREET

Manuscripts for publication should be submitted to S. A. GOUDSMIT, Brookhaven National Laboratory, Upton, Long Island, New York. The authors' institutions are requested to pay a publication charge of $15 per page which, if honored, entitles them to 100 free reprints. Instructions will be sent with galley proofs.

Proof and all correspondence concerning papers in the process of publication should be addressed to the Publication Manager, American Institute of Physics, 57 East 55 Street, New York 22, New York.

Subscription Price

United States and Canada $30.00
Elsewhere $32.00

Back Numbers[1]

Yearly back number rate when complete year is available:
Prior to 1949: $25.00
Thereafter: $33.00
Single copies: $3.00 each, prior to July, 1929;
$1.50 each, July, 1929–December, 1941;
$3.00 each, January, 1942–December, 1946;
$1.50 each, thereafter.
General index, 1893–1920: $4.00.

Subscriptions, renewals, and orders for back numbers should be addressed to the American Institute of Physics, 57 East 55 Street, New York 22, New York.

Changes of address in the case of members of the American Physical Society should be addressed to the Treasurer; in the case of other subscribers to the American Institute of Physics.

[1] For Series 1 inquire of Physics Department, Cornell University, Ithaca, New York.

The Physical Review is published semi-monthly at Prince and Lemon Streets, Lancaster, Pennsylvania.

Entered as second-class matter March 6, 1947, at the Post Office at Lancaster, Pennsylvania, under the Act of March 3, 1879.

Acceptance for mailing at special rate of postage provided for in paragraph (d-2), section 34.40, P. L. & R. of 1948, authorized January 27, 1933.

We are indebted to the South African Council for Scientific and Industrial Research for a grant, and for a bursary to one of us (F.D.B.).

[1] J. B. Birks, Phys. Rev. **86**, 569 (1952); **90**, 1131 (1953).
[2] J. B. Birks, *Scintillation Counters* (Pergamon Press, London; McGraw-Hill Book Company, Inc., New York, 1953).
[3] Bernstein, Chase, and Schardt, Rev. Sci. Instr. **24**, 437 (1953).
[4] Taylor, Jentschke, Remley, Eby, and Kruger, Phys. Rev. **84**, 1034 (1951).
[5] J. B. Birks, Phys. Rev. **84**, 364 (1951); Proc. Phys. Soc. (London) **A64**, 874 (1951).
[6] M. Curie, *Radioactivité* (Hermann et Cie., Paris, 1935).
[7] J. B. Birks, Phys. Rev. **94**, 1567 (1954).

Errata

Paramagnetic Scattering of Neutrons by Rare Earth Oxides, W. C. KOEHLER AND E. O. WOLLAN [Phys. Rev. **92**, 1380 (1953)]. The diffraction patterns of Fig. 4, page 1383, and Fig. 6, page 1384, should be interchanged with the figure numbers and captions held in their present location.

Small-Angle X-Ray Scattering from Liquid Helium I and Liquid Helium II, ARTHUR G. TWEET [Phys. Rev. **93**, 15 (1954)]. In the "note added in proof" on page 20, the last line should read "... at 4.16°K shown in Fig. 3 to 0.61." The number 0.61 appears incorrectly as 0.16.

The Half-Life of Lanthanum-140, H. W. KIRBY AND MURRELL L. SALUTSKY [Phys. Rev. **93**, 1051 (1954)]. In the first sentence of the fifth paragraph, instead of "... having a resolution time of 0.1 microsecond" read "... having a resolution time of 0.1 microminute." In the second sentence of the same paragraph, instead of "... a mixture of 90 percent methane and 10 percent argon" read "... a mixture of 90 percent argon and 10 percent methane." These errors do not affect either the data or the results.

The Scattering of Neutrons by Systems of Heavy Nuclei, G. PLACZEK [Phys. Rev. **86**, 377 (1952)]. Dr. von Dardel[1] and Professor Wick[2] have kindly directed the author's attention to the fact that Eqs. (7.20) and (5.17) contain elementary errors which are readily eliminated by correctly carrying out the substitutions indicated in the text above these equations.

The second and third lines of Eq. (7.20) for the contribution of the interference terms to the total cross section should be replaced by

$$+v_0^{-2}\langle(\cos 2k_0z_{ss'}-2k_0z_{ss'}\sin 2k_0z_{ss'})v_{s''}v_{s'''}\rangle_{kl}$$
$$+\frac{1}{\mu_s\mu_{s'}}\left\langle\frac{\sin 2k_0r_{ss'}}{k_0r_{ss'}}+\cos 2k_0r_{ss'}\right\rangle_{kl}.$$

The corresponding expressions (7.22) and (7.23) for the differential cross section, however, are given correctly.

The expression (5.17) for the average energy transfer should read as follows:

$$\langle E_l\rangle_{kl}=\frac{2\mu}{(\mu+1)^2}\left\{E_0-\frac{4}{3}K_{kl}\left(1-\frac{1}{4\mu}\right)+\frac{B_{kl}}{8E_0}\right.$$
$$\left.+\frac{4}{9}\frac{K_{kl}^3-\frac{3}{2}\langle K^3\rangle_{kl}+\frac{3}{2}B_{kl}}{\mu E_0}+O\left(\frac{K_{kl}^3}{\mu^2E_0}\right)\right\}.$$

The conclusions reached in the discussion of Eqs. (7.20) and (5.17) are in no way affected.

[1] G. von Dardel (private communication); see also G. F. von Dardel, *The Interaction of Neutrons with Matter Studied with a Pulsed Neutron Source* (Elanders Boktryckeri Aktiebolag, Goteborg, 1953).
[2] G. C. Wick (private communication).

Density Fluctuations at Low Temperatures, P. J. PRICE [Phys. Rev. **94**, 257 (1954)]. In Eq. (8) and the equation directly above it, S^z should be N.

Author Index to Volume 94

References with (A) are to abstracts of papers presented at meetings of the American Physical Society; references with (T) designate title only. References with (L) are to Letters to the Editor. References with (E) are to Errata.

Aamodt, L. C., P. C. Fletcher, G. Silvey, and C. H. Townes. Spin and quadrupole moment of Se^{75}—789(A)
Abraham, Bernard M. (see Osborne, Darrell W.)—202(L)
Adair, Robert K. Nuclear potential well depth—737(L)
Adams, R. K. (see Fields, R. E.)—389
Ajzenberg, Fay and Wolfgang Franzen. Neutrons from proton bombardment of N^{14}—409
Albrecht, H. O. and C. E. Mandeville. Luminescence of BeO—776(A)
Albrecht, H. O. (see Mandeville, C. E.)—494(L)
Aldrich, R. (see Marvin, Robert S.)—1413(A)
Alford, W. L. (see Newman, E.)—748(A)
Alford, W. Parker and Donald R. Hamilton. Recoil spectrum in β decay of Ne^{19}—779(A)
Alfvén, Hannes. Magnetic storm effect on cosmic radiation—1182(L)
Allen, Harry C., Jr., and Earle K. Plyler. Infrared spectrum of hydrogen sulfide in 5100 cm^{-1} region—1423(A)
—— (see Risser, J. R.)—810(A)
Allen, James (see Coulter, George A.)—782(A)
Allison, B. A. (see Scherrer, V. E.)—791(A)
Alvarez, Luis W. (see Gow, J. D.)—365
Ament, W. S. and G. T. Rado. Electromagnetic effects of spin wave resonance—1411(A)
Ander, Paul (see Mesrobian, Robert B.)—1413(A)
Anderson, C. D. (see van Lint, V. A.)—1732
Anderson, G. W., P. S. Freier, and J. E. Naugle. Time and directional study of primary heavy nuclei—1317
—— (see Freier, P. S.)—677
Anderson, James L. "Dressed" particles in quantum field theory—745(A)
—— Green's-functions in quantum electrodynamics—703
Anderson, W. A. and J. T. Arnold. Line-narrowing experiment—497(L)
Andrew, J. F. and S. Mrozowski. Photoresponse of aromatic films—1438(A)
Andrews, R. D. Measure of orientation in polystyrene monofilaments by means of double refraction—1412(T)
Annis, Martin, Homer C. Wilkins, and John D. Miller. Nuclear interaction of fast μ mesons—1038
Anthony, R. L. (see Baldwin, F. P.)—1425(A)
Argence, E. (see Rawer, K.)—253
Arné, L. A. (see Smith, R. L.)—1407(A)
Arnold, Charles W. and F. A. Matsen. Infrared spectra of C_3D_4O—804(A)
Arnold, J. T. (see Anderson, W. A.)—497(L)
Arnowitt, R. and S. Deser. Virtual states of two-meson systems—798(A)
—— **and S. Gasiorowicz.** Effect of negative energy components in two-nucleon system—746(A); 1057
Arrott, A. Method for measuring magnetization and susceptibility at low temperatures—781(A)
—— (see Goldman, J. E.)—782(A)
Asaro, Frank and I. Perlman. α- and γ-ray spectra of Pu^{238}—381
Aschner, J. F. Self-diffusion in KCl—771(A)
Ashkin, Arthur, Lorne A. Page, and W. M. Woodward. Electron-electron and positron-electron scattering measurements—357
Askey, C. M. (see Palmatier, E. D.)—766(A)
Augustyniak, W. (see McReynolds, A. W.)—1417(A)
Auth, W. J., W. S. Emmerich, and J. D. Kurbatov. Nuclear spectra of Ce^{144} and Pr^{144}—794(A)
—— (see Emmerich, W. S.)—110
Auverman, Harry J. and Arthur E. Lockenvitz. Mechanical electric computer for solving polynomial equations—811(A)
Azuma, Toshio. β-ray spectrum of Ag^{110}—638
Azumi, K. and J. E. Goldman. Volume magnetostriction in Ni and its alloys—781(A)

Babiskin, J. (see Steele, M. C.)—1394(L)
Badar, L. J. and V. P. Jacobsmeyer. Electrical characteristics of polycrystalline boron—808(A)
Bagchi, S. N. (see Hosemann, R.)—71
Bair, J. K. (see Willard, H. B.)—786(A)
Baker, E. (see Friedlander, G.)—727(L); 775(A)
Baldwin, F. P., J. Ivory, and R. L. Anthony. Experimental investigation of statistical theory of rubber elasticity—1425(A)
Ballantine, David S. (see Mesrobian, Robert B.)—1413(A)
Bandtel, Kenneth C. (see Frank, Wilson J.)—1716
Banister, J. R., S. Legvold, and F. H. Spedding. Structure of Gd, Dy, and Er at low temperatures—1140
Banta, H. E. and R. L. Macklin. Search for $Li^7(n,t)$ reaction—807(A)
Barber, W. A., P. Debye, and B. H. Eckstein. Field-induced diffraction method for molecular weight determinations—1412(A)
Bardeen, John. Surface barrier effects in semiconductors—1419(T)
—— Theory of boundary effects of super-conductors—554
Barnes, C. A. (see Peterson, R. W.)—1075(L)
—— (see Thirion, J.)—1076(L)
Barnes, J. M. Multiple diffraction patterns in glass produced by ultrasonic waves of high intensity—1434(A)
Barnes, R. G., P. J. Bray, and N. F. Ramsey. Variations of hydrogen rotational magnetic moments with rotational quantum number and with isotopic mass—893
Barrett, Paul H. K-meson and hyperon decays—1328
Bartholomew, G. A. (see Gove, H. E.)—749(A)
—— (see Paul, E. B.)—749(A)
Battey, J. F. and R. M. Baum. Energy of high-lying acceptor level in Cu-doped Ge—1393(L)
Bauer, Ernest and Ta-You Wu. Cooling of gas by radiation—1424(A)
Baum, R. M. (see Battey, J. F.)—1393(L)
Bay, Z., V. P. Henri, and F. McLernon. Upper limits for lifetimes of Ni^{60}—780(A)
Bayard, Robert T. and J. L. Yntema. Elastic scattering of electrons from nuclei—757(A)
Beard, D. B. Level densities in heavy nuclei of 10- to 20-Mev excitation—738(L)
Becker, J. H. (see Blunt, R. F.)—1431(A)
Becker, Milton. Growth of long-lifetime Ge crystals—1420(A)
Becker, R. L. (see Fields, R. E.)—389
Becker, Stewart and Melvin Eisner. Paramagnetic resonance absorption in diphenyl picryl hydrazyl at low values of splitting field—811(A)
Beer, A. C. (see Harman, T. C.)—1065(L)
Beers, Yardley (see Sterzer, Fred)—1410(A)
Beghian, L. E. (see Eliot, E. A.)—144
Beguin, Gilbert and Kasimir Fajans. Influence of charge distribution on repulsive forces and internuclear distances between ions—1434(A)
Belinfante, F. J. Avoiding perturbation methods in quantum electrodynamics, meson theory, etc.—745(A)
Bell, P. R. (see Sheline, Raymond K.)—1642
Bemski, G., W. A. Nierenberg, and H. B. Silsbee. Spin-orbit interaction in RbF and CsF—767(A)

Benedek, G. B. (see Paul, W.)—1415(A)
Benedict, W. S. and Shirleigh Silverman. Line shapes in infrared—752(A)
Bengston, J. (see Thaler, R. M.)—679; 683
Bennett, W. E. Spallation studies of Bi—997
Bennett, Willard H. Mapping particle paths in earth's magnetic field—796(A)
Beresovski, T. (see Cuykendall, T. R.)—1421(A)
Berger, J. M. Deuteron photodisintegration at intermediate energies—1698
Bergmann, Peter G. Restrictions on invariant transformation groups in Lagrangian and Hamiltonian formalisms—788(A)
Beringer, Robert, E. B. Rawson, and Allan F. Henry. Microwave resonance in NO: λ doubling and hfs—343
Berkowitz, A. E. Effect on diffusion measurements of some β-ray absorption phenomena—1407(A)
——, **F. E. Jaumot, Jr., and F. C. Nix.** Diffusion of Co^{60} in some Ni-Al alloys containing excess vacancies—1407(A)
—— (see Franklin, A. D.)—1432(A)
Berlincourt, Ted G. de Haas-van Alphen effect in Cd—1172
Bernardini, G. and E. L. Goldwasser. Photoproduction of π^+ mesons from H near threshold—729(L)
—— (see Goldwasser, E. L.)—755(A)
Bernstein, Eugene. Production of *L*-shell x-rays by protons—774(A)
Bernstein, Ira B. and T. Holstein. Electron energy distributions in stationary discharges—1475
Bernstein, Seymour, L. D. Roberts, C. P. Stanford, J. W. T. Dabbs, and T. E. Stephenson. Interaction of polarized neutrons with polarized Mn^{55} nuclei—1243
—— (see Sherwood, J. E.)—791(A)
—— (see Stanford, C. P.)—374
—— (see Wilkinson, M. K.)—772(A)
Bestul, A. B. Energy requirements of mechanical shear degradation in concentrated polymer solutions—1425(A)
Betchov, R. Triple correlations in isotropic turbulence—783(A)
Beyen, Werner J. (see Mitchell, Dean L.)—1430(A)
Bhatnagar, P. L., E. P. Gross, and M. Krook. Model for collision processes in gases. I. Small amplitude processes in charged and neutral one-component systems—511
Bichsel, H. and R. F. Mozley. Range of protons in Be, Al, Cu, Ag, and Au—764(A)
Bickford, L. R., Jr., J. Pappis, and J. L. Stull. Permeability and magnetostriction of cation-substituted magnetite—1433(A)
Biedenharn, L. C. (see Gluckstern, R. L.)—768(A)
—— (see Hull, M. H., Jr.)—768(A)
—— (see Major, J. K.)—779(A)
Bilpuch, E. G. (see Block, R. C.)—774(A)
Binder, D. and W. J. Sturm. Equivalence of x-ray lattice parameter and density changes in neutron-irradiated LiF—760(A)
Binnie, W. P. and A. M. Liebschutz. Elastic constants of Si before and after neutron bombardment from x-ray diffuse scattering—1410(A)
Biondi, Manfred A. and Lorne M. Chanin. Mobilities of atomic and molecular ions in noble gases—910
Bird, G. R. and C. H. Townes. S bonds and quadrupole moments of O, S, and Se isotopes—1203
Birks, J. B. Energy transfer in organic phosphors—1567
—— **and F. D. Brooks.** Scintillation response of anthracene to soft x-rays—1800(L)
Biswas, N. N. and M. S. Sinha. Mean lives of positive and negative μ mesons—1400(L)
Biswas, S. N. Solutions of Heitler's integral equation by iteration method—1767
Bittner, J. W., R. G. Herb, R. D. Moffat, and J. A. Weinman. Doubly ionized He ion source—769(A)
—— (see Haberle, W.)—769(A)
Bjerregaard, Jørgen H. and Torben Huus. Coulomb excitation by means of bombardment with various particles—204(L)
Blackman, V. H. and D. K. Weimer. Reflection of shock waves from blunt wedge—508
Blair, J. M. (see Holmgren, H. D.)—748(A)
Blatt, J. M. (see Kalos, M. H.)—762(A)
Bleil, D. F. and A. R. Butz. Magnetostriction in nickel ferrite-aluminates and nickel ferrite-gallates—1440(A)
Blewett, J. P. Design of 25-Bev proton synchrotron for European organization for nuclear research—792(T)
Bloch, F. Line-narrowing by macroscopic motion—496(L)
Block, R. C., J. H. Gibbons, E. G. Bilpuch, and D. F. Herring. Total neutron cross sections in kev region: As, Zr, Nb, La, Ce, Pr, and Au—774(A)
Bloembergen, N. Nuclear magnetic relaxation in semiconductors—1411(A)
—— Nuclear magnetic resonance and structure of metals and alloys—1416(T)
Bloom, Arnold L. and Owen Chamberlain. Scattering of 190-Mev deuterons on protons—659
Bloom, M. "Slow beats" in nuclear quadrupole induction—1396(L)
Bludman, Sidney A. Reaction $p+d \rightarrow \pi^+ + t$—1722
Blunt, R. F., H. P. R. Frederikse, and J. H. Becker. Optical absorption of AlSb—1431(A)
Bockelman, C. K. and J. J. Jung. Energies of excited states of Be^{10}—748(A)
Bode, Donald E. and Henry Levinstein. Effect of oxygen on PbTe films—1430(A)
Bode, Donald E. (see Mitchell, Dean L.)—1430(A)
Boley, F. I. Short-lived isomeric states of Ag^{119} and In^{116}—1078(L)
Bolsterli, Mark. Photon splitting in nuclear electrostatic field—367
Bonfiglioli, G., A. Ferro, G. Montalenti, and G. Rosa. Behavior of ferromagnetic domains under stress—316
Bonner, T. W. and C. F. Cook. Neutron thresholds in Li^7-$(d,n)Be^8$ and $Be^9(d,n)B^{10}$—807(A)
—— (see Cook, C. F.)—651; 807(A)
—— (see Marion, J. B.)—807(A)
—— (see McCrary, J. H.)—808(A)
—— (see Taylor, H. L.)—807(A)
Boorse, H. A. Recent studies of heat capacities of superconducting elements—771(T)
Boorse, H. A. (see Smith, B.)—772(A)
Bothe, W. and H. Kraemer. Shower structure in higher shower maxima—1402(L)
Bowen, D. B. and H. Hori. Change of resistivity of Cu with elastic strain—1422(A)
—— (see Dixon, C. E.)—1418(A)
Boyer, R. F. Physical properties of polymeric glasses—1425(T)
Bozorth, R. M. and R. C. Sherwood. Magnetostriction of Co—1439(A)
—— (see Nesbitt, E. A.)—1440(A)
Braams, C. M. Energy levels in Ca^{41} from $Ca^{40}(d,p)Ca^{41}$ reaction—763(A)
Bradshaw, B. C. and R. A. Shuttleworth. Mechanism of adsorption. I. Theory—753(A)
—— (see Shuttleworth, R. A.)—753(A)
Bransden, B. H. Rearrangement collisions—726(L)
Brattain, W. H. and C. G. B. Garrett. Electrical properties of interface between Ge single crystal and electrolyte—750(A)
Bray, P. J. Self-quenching superregenerative rf spectrometers—767(A)
—— (see Barnes, R. G.)—893
Brebrick, R. F. and W. W. Scanlon. Interdiffusion in PbS crystals—1430(A)
—— (see Scanlon, W. W.)—1430(A)
Breit, G. Longitudinal and transverse stability in linear accelerator systems—768(A)
—— (see Thaler, R. M.)—683

Brentano, J. C. M. and Colman Goldberg. Electrical conductance of pressed powders, in particular of ZnO—56
—— **and J. D. Richards.** Evaporated multiple layers with semiconductor properties—1427(A)
Brice, M. K. (see Cork, J. M.)—1218
Bridgman, P. W. Effects of pressure on twelve rare-earth metals—759(T)
Brockhouse, B. N. Antiferromagnetism in CuO—781(A)
Brockman, Karl W., Jr. p-α scattering at 17.5 Mev—785(A)
Broder, J. D. (see Wolff, G.)—753(A)
Brolley, J. E., Jr., and W. C. Dickinson. Angular distribution of fragments from neutron-induced fission—640
Brooks, F. D. (see Birks, J. B.)—1800(L)
Brooks, Harvey. Theory of g factor and spin-lattice relaxation time in alkali metals—1411(A)
—— (see Paul, William)—1128; 1415(A)
Broudy, R. and H. Levinstein. High-frequency resistance of photoconducting films—290
—— **and H. Levinstein.** High-frequency resistance of thin films—285
Brown, Douglas E. (see Hobbs, Lindsey M.)—1412(A)
Brown, Edmond. Electronic energy bands in crystals—1434(A)
Brown, H. (see Ruderman, M. A.)—746(A)
Brown, Sanborn (see Weinstein, Roy)—758(A)
Browne, C. P. (see Zimmerman, S. F., Jr.)—749(A)
Brueckner, K. A. and J. S. Kovacs. Effect of deuteron formation on multiple meson production—726(L)
Brysk, Henry. β-decay interaction—1794(L)
Buchdahl, Rolf and Lawrence E. Nielsen. Multiple dispersion regions in rigid polymeric systems—1414(A)
Bueche, F. Mechanics of molecular motion in bulk polymers—1425(T)
Bulliard, Hubert H. Photomagnetoelectric effect in Ge and Si—1564
Bunker, M. E., J. P. Mize, and J. W. Starner. Disintegration of Y^{91}—1694
Burch, D. E., J. N. Howard, and Dudley Williams. Effect of foreign gas broadening on total absorption by 6.3μ band of water vapor—1424(A)
Burns, F. P. Kinetics of ordering and disordering process in Cu_3Au—1429(A)
Burson, S. B., W. C. Jordan, and J. M. LeBlanc. Decay of $_{65}Tb^{160}$ (71 days)—103
—— (see LeBlanc, J. M.)—1436(A)
Burstein, Elias. Anomalous optical absorption limit in InSb—1431(A)
——, **B. W. Henvis, and N. Sclar.** Infrared properties of p-type Ge—750(A)
Butz, A. R. (see Bleil, D. F.)—1440(A)

Cadenhead, C. P. (see Little, R. N., Jr.)—807(A)
Caird, Robert S. and Allan C. G. Mitchell. Disintegration of Co^{58} and I^{130}—412
—— **and Allan C. G. Mitchell.** Disintegration of I^{130}—780(A)
Caldwell, David O. and J. Reginald Richardson. Mean excitation potentials—79
Caldwell, R. S. and H. Y. Fan. Infrared absorption of Te—1427(A)
Calhoun, B. A. Magnetic and electric properties of magnetite at low temperatures—1577
Callen, Earl. Configuration interaction applied to hydrogen molecule—1423(A)
Callen, Herbert B. (see Kriessman, C. J.)—781(A); 837
Campbell, R. C., J. D. Korsmeyer, and D. C. Ralph. Neutron yields from d-d reaction in various target materials—791(A)
Carlson, B. C. (see Gerhart, J. B.)—917
Carlson, R. R., E. H. Geer, and E. B. Nelson. Scintillation counter study of γ rays from proton capture in Na—1311
Carr, H. Y. and E. M. Purcell. Effects of diffusion on free precession in nuclear magnetic resonance experiments—630
Carter, R. S. (see Palevsky, H.)—1088(L)
Case, K. M. Nonrelativistic limit of half-integral-spin wave equations—1442(A)
—— Two extensions of Foldy-Wouthuysen transformation—786(A)
—— (see Mendlowitz, H.)—1436(A)
Castle, J. G., Jr. Paramagnetic resonance absorption in carbons—1410(A)
Caswell, R. S., R. F. Gabbard, W. P. Doering, and D. W. Padgett. Attenuation of 14.1-Mev neutrons in water—786(A)
Chaberski, A. (see Mrozowski, S.)—1427(A)
Chamberlain, Owen and James W. Easley. Small angle neutron-proton scattering at 90 Mev—208(L)
——, **G. W. Farwell, and E. Segrè.** $_{94}Pu^{240}$ and its spontaneous fission—156
—— **and Martin O. Stern.** Elastic scattering of 190-Mev deuterons by protons—666
—— (see Bloom, Arnold L.)—659
—— (see Clark, David D.)—785(A)
Chanin, Lorne M. (see Biondi, Manfred A.)—910
Charlesby, A. Effect of high-energy radiation on polymers—1412(T)
Charpie, R. A. (see Cohen, B. L.)—620
—— (see Cohen, B. L.)—953
Chase, D. M. and F. Rohrlich. Elastic scattering of protons by nuclei—81
Chen, F. F., C. P. Leavitt, and A. M. Shapiro. Attenuation of 870-Mev protons by various elements—784(A)
Chester, G. V. Theory of liquid He—246
Chew, Geoffrey F. Method of approximation for meson-nucleon problem when interaction is fixed and extended—1755
—— Renormalization of meson theory with fixed extended source—1748
Choppin, G. R., S. G. Thompson, A. Ghiorso, and B. G. Harvey. Nuclear properties of some isotopes of Cf, elements 99 and 100—1080(L)
—— (see Ghiorso, S. G.)—1081(L)
Christian, R. (see Lee, T. D.)—1760
Christian, Russell H. and Robert G. Shreffler. Hugoniot of gases by shock wave measurements—783(A)
Christy, R. F. Low excited states of F^{19}. IV. Angular distributions—1077(L)
—— (see Sherr, R.)—1076(L)
Chuoke, Robert L. Electron interactions in metals—808(A)
Church, E. L. and J. E. Monahan. Internal conversion in L and M sub-shells—762(A)
Claassen, H. H. (see Nielsen, J. Rud)—805(A)
Clark, A. F. (see Grandey, R. A.)—766(A)
Clark, David D. and Owen Chamberlain. Elastic scattering of 340-Mev protons by deuterons—785(A)
Clarke, Edward N. Electron traps on Ge surfaces produced by heating in oxygen—1420(A)
Clarkson, Henry Neal and Arthur E. Lockenvitz. Accurate determination of tidal variations of gravity—811(A)
Class, C. M. Coulomb excitation of nuclei—809(T)
——, **C. F. Cook, and J. T. Eisinger.** Coulomb excitation of heavy nuclei—747(A); 809(A)
—— (see Cohen, L.)—419
—— (see Dudley, J. D.)—807(A)
—— (see Eisinger, J. T.)—735(L)
Clauser, Francis H. Design of diffusers to avoid turbulent boundary layer separation—783(A)
Cleland, J. W. and J. H. Crawford, Jr. Radiation effects in InSb—1410(A)
—— (see Stevens, D. K.)—1409(A)
Clendenin, W. W. Gyromagnetic ratio in hfs of doublet states—1590
Cocconi, Giuseppe. Influence of earth magnetic field on extensive air showers—796(A)

—— Strange particles and multiple meson production—741(L)
Cochran, L. W. (see Stanford, C. P.)—374
Cohen, Bernard L. K^{44}—117
—— Angular distribution of products from 22-Mev proton reactions—803(T)
—— Diffraction scattering of 22-Mev protons—773(T)
——, **R. A. Charpie, T. H. Handley, and E. L. Olson.** Mn^{57}—953
——, **W. H. Jones, G. H. McCormick, and B. L. Ferrell.** Angular distributions of fission fragments from 22-Mev proton-induced Th fission—625; 758(A)
——, **E. Newman, R. A. Charpie, and T. H. Handley.** (p,pn) and $(p,\alpha n)$ excitation functions—620
Cohen, E. Richard (see DuMond, Jesse W. M.)—1790(L)
Cohen, L., S. S. Hanna, and C. M. Class. Angular correlations in $Be^9(d,p\gamma)Be^{10}$ and $Be^9(d,\alpha\gamma)Li^7$—419
Cohen, M. H. and F. Keffer. Dipolar ferromagnetism in cubic lattices—1412(A)
Coles, D. K. (see Gunther-Mohr, G. R.)—1184
Collins, G. B. Cosmotron as research tool—745(T)
Collins, R. L. and J. Rud Nielsen. Vibrational spectra of $H_3C\text{-}SiF_3$—805(A)
Collins, T. L., Walter H. Johnson, Jr., and Alfred O. Nier. Atomic masses in intermediate region—398
Conway, John G. and Ralph D. McLaughlin. Nuclear spin of Am^{240} and isotope shift in Am spectrum—498(L)
Conwell, Esther M. Electrical properties of p-type Ge—1416(A)
—— High-field effects in Ge—1068(L)
Cook, C. F. and T. W. Bonner. Neutron thresholds from $Cu^{65}(p,n)Zn^{65}$, $Cu^{63}(p,n)Zn^{63}$, and $Li^7(p,n)Be^7$—807(A)
—— **and T. W. Bonner.** Scattering of fast neutrons in light nuclei—651
—— (see Bonner, T. W.)—807(A)
—— (see Class, C. M.)—747(A); 809(A)
—— (see Eisinger, J. T.)—735(L)
—— (see Marion, J. B.)—807(A)
Cooke, Claude E. Study of electrokinetic relations using sinusoidal pressure and voltage—812(A)
Cooley, William C. (see Van Horn, David D.)—1418(A)
Coon, J. B. and J. K. Ward. Application of Franck-Condon principle to bent XY_2 molecule—805(A)
Coon, J. H. and R. W. Davis. Elastic scattering of 14-Mev neutrons—785(A)
Cooper, Daniel I., David H. Frisch, and Robert L. Zimmerman. p-p scattering near interference minimum—1209
Cooper, H. G., J. S. Koehler, and J. W. Marx. Resistivity changes in Cu, Ag, and Au produced by deuteron irradiation near 10°K—496(L)
Cooper, J. N. (see Green, D. W.)—764(A)
—— (see Smith, J. A.)—749(A)
Coor, T. (see Hill, D. A.)—791(A)
—— (see Snow, G. A.)—791(A)
Corben, H. C. Lamb shift in mesic atoms—787(A)
Corenzwit, E. (see Matthias, B. T.)—1069(L)
Cork, Bruce and Walter Hartsough. p-p scattering at 9.7 Mev—1300
Cork, J. M., M. K. Brice, L. C. Schmid, G. D. Hickman, and H. Nine. Neutron capture in separated isotopes of Pt—1218
—— (see LeBlanc, J. M.)—1436(A)
Corliss, L. (see Weiss, R. J.)—1420(A)
Cormack, A. M. Interference of Rayleigh and nuclear Thomson scattering—1398(L)
Corrsin, Stanley. Measure of area of homogeneous random surface in space—783(A)
—— (see Kistler, Alan)—783(A)
Corson, D. R. (see Davis, H. L.)—756(A)
Cotter, T. P. Structure of detonation in some liquid explosives—765(T)
Coulter, George A. and James Allen. Diffraction of step shocks through double slits—782(A)
Courant, E. D. Interaction of high-energy pions with nuclei—1081(L)
—— Particle orbits in alternating gradient synchrotron—792(T)
Courant, H. γ rays associated with S-particle decay—797(A)
Cowan, Alvin E. and Arthur E. Lockenvitz. Time rate of change for transformation of monoclinic Se into hexagonal—809(A)
Cowan, C. L., Jr., and F. Reines. Status of experiment to detect free neutrino—751(T)
Cowan, E. W. Properties of new V particles—796(T)
—— V-decay event with heavy negative secondary, and identification of secondary V-decay event in cascade—161
—— (see van Lint, V. A.)—1732
Cowen, J. A. and R. D. Spence. Ferromagnetic resonance relaxation times in single crystals of Ni and Fe—1411(A)
Cranberg, L. (see Henkel, R. L.)—141
Crane, H. R. Design of precision experiment on gyromagnetic ratio of free electron—1426(T)
—— Initiation of discharge in CO_2-filled GM counter by negative ions—1437(A)
—— (see Louisell, W. H.)—7
Crane, W. W. T. (see Higgins, G. H.)—735(L)
Crawford, J. H. Nucleon bombardment of semiconductors—803(T)
Crawford, J. H., Jr., and D. K. Stevens. Effective mass and degeneracy of carriers in Ge from diamagnetic behavior—1415(A)
—— (see Cleland, J. W.)—1410(A)
—— (see Stevens, D. K.)—1409(A)
Crittenden, E. C., Jr., and H. Dieckamp. Change of elastic constants of Cu on annealing after plastic deformation at 78°K—1421(A)
—— (see Dieckamp, H.)—1418(A)
Crownfield, Frederic R., Jr., and Peter Havas. Classical equations of motion of point particles in neutral meson fields—471
Crussard, J., W. D. Walker, and M. Koshiba. π^--p interactions at 1.5 Bev—736(L)
—— (see Hill, R. D.)—797(A)
Curtis, J. P. Absorption coefficients of air and nitrogen for extreme uv—908
Cuykendall, T. R., T. Beresovski, and H. S. Sack. Internal friction in single metal crystals at audiofrequencies—1421(A)
—— (see Sack, H. S.)—1414(A)

Dabbs, J. W. T. (see Bernstein, S.)—1243
Dailey, B. P. (see Kraitchman, J.)—788(A)
—— (see Solimene, N.)—789(A)
Daitch, P. B. (see Gluckstern, R. L.)—768(A)
—— (see Hull, M. H., Jr.)—768(A)
Dalby, F. W., H. H. Nielsen, and F. P. Dickey. Absorption spectra of water vapor in 2.7μ and 6.0μ regions—1423(A)
Dalitz, R. H. Decay of τ mesons of known charge—1046
D'Altroy, F. A. and H. Y. Fan. Microwave transmission in p-type Ge—1415(A)
Damask, A. C. and A. S. Nowick. Internal friction associated with precipitation in Al-Ag alloy—1421(A)
Danforth, W. E. (see Goldwater, D. L.)—754(A)
Danos, M. Čerenkov radiation from extended electron beams—758(A)
Darden, Sperry (see Nereson, Norris)—1678
Darrow, K. K. American Physical Society at Columbia University—776(T)
Dash, Jay Gregory. Critical and supercritical flow of liquid helium II—771(T); 772(A)

—— Superfluidity and dissipative processes in liquid He II—825
—— Superfluid dynamics of liquid He II—1091
Date, Muneyuki (see Okamura, Tosihiko)—314
Daunt, J. G. (see Gordon, W. L.)—771(A)
Davis, H. L. and D. R. Corson. Elastic production of π^0 photomesons from deuterium—756(A)
Davis, Marguerite. Range measurement of low voltage electrons—243
Davis, R. C. (see Sheline, Raymond K.)—1642
Davis, R. E. (see Goldberg, Colman)—1121
Davis, R. W. (see Coon, J. H.)—785(A)
Davisson, J. W. Electrical breakdown paths in nonpolar crystals—1437(A)
Daw, Harold. Generalized absorption coefficients of water vapor—1424(A)
Dayton, I. E. and P. C. Gugelot. Elastic scattering of 18.5-Mev protons by nuclei—785(A)
Deal, W. E., Jr. Shock Hugoniot of air—811(A)
DeBenedetti, S. and R. T. Siegel. 3-photon annihilation of positrons and electrons—955
——, **M. B. Stearns, M. Stearns, and H. J. Richings.** Spectroscopy of π- and μ-meson x-rays—766(A)
—— (see Stearns, M.)—766(A)
—— (see Sugarman, R.)—795(A)
deBretteville, A. P., Jr. Threshold field and free energy for antiferroelectric-ferroelectric phase transition in $PbZrO_3$—1125
—— **and E. D. Harris.** Heat of transition of $BaTiO_3$ at Curie point—1408(A)
Debye, P., P. P. Debye, and B. H. Eckstein. Dielectric high-frequency method for molecular weight determinations—1412(A)
—— (see Barber, W. A.)—1412(A)
Debye, P. P. and T. Kohane. Hall mobility of electrons and holes in Si—724(L)
—— (see Debye, P.)—1412(A)
de Carvalho, H. G., E. Heiberg, J. Marshall, and L. Marshall. Polarization by p-p collision at 439 Mev—1796(L)
de Groot, S. R. and P. Mazur. Extension of Onsager's theory of reciprocal relations. I—218
—— (see Mazur, P.)—224
Dekker, A. J. Energy and temperature dependence of secondary emission of MgO—1179
DeMarco, J. J. (see Weiss, R. J.)—1420(A)
Denney, J. M. Experimental evidence for melted regions in metal crystals resulting from particle bombardment—1417(A)
De-Saussure, G. and L. S. Osborne. Elastic photoproduction of π^0 in He—756(A)
Deser, S. and W. E. Thirring. Low-energy limits of meson processes—746(A)
——, **W. E. Thirring, and M. L. Goldberger.** Low-energy limits and renormalization in meson theory—711
—— (see Arnowitt, R.)—798(A)
de-Shalit, A. (see Schwartz, C.)—1257
Detwiler, D. P. Conductivity, Hall effect, and rectification of GaSb—1431(A)
Deutsch, Martin (see Weinstein, Roy)—758(A)
DeWire, J. W. (see Wolfe, B.)—756(A)
Dexter, D. L. Tunneling of electrons in alkali halides—771(A)
Diamond, H., L. B. Magnusson, J. F. Mech, C. M. Stevens, A. M. Friedman, M. H. Studier, P. R. Fields, and J. R. Huizenga. Identification of Cf isotopes 249, 250, 251, and 252 from pile-irradiated Pu—1083(L)
—— (see Fields, P. R.)—209(L)
—— (see Stevens, C. M.)—974
Dibeler, Vernon H. and Fred L. Mohler. Mass spectra of deuteroethylenes—754(A)
Dick, J. (see Sakai, M.)—779(A)
Dickey, F. P. (see Dalby, F. W.)—1423(A)
—— (see France, W. L.)—1423(A)
Dickinson, W. C. (see Brolley, J. E., Jr.)—640
DiDonato, A. R., A. A. MacLeod, and A. C. Webber. Creep and relaxation of plastics—770(A)
—— (see MacLeod, A. A.)—769(A)
Dieckamp, H. and E. C. Crittenden, Jr. Shear modulus of irradiated Cu—1418(A)
—— (see Crittenden, E. C., Jr.)—1421(A)
Dienes, G. J. (see Levy, Paul W.)—1409(A)
—— (see Mesrobian, Robert B.)—1413(A)
—— (see Rosenblatt, D. B.)—1417(A)
Dillon, J. A., Jr., and H. E. Farnsworth. Adsorption of CO_2 on Ni single crystal faces using radiotracer technique—753(A)
Dixon, C. E. and D. B. Bowen. Radiation ordering by cyclotron particles—1418(A)
Doering, W. P. (see Caswell, R. S.)—786(A)
Dolecek, R. L. Latent heat of transition of superconducting Pb—540
Domenicali, C. A. and F. A. Otter. Thermoelectric power and resistivity of dilute Cu-Si, Ni-Si, and Fe-Si alloys—1421(A)
Donahoe, F. J. (see Steijn, R. P.)—1432(A)
Dorfman, Leon M. and B. A. Hemmer. Ion-yield of tritium-oxygen reaction—754(A)
Dosanjh, Darshan (see Kovásznay, Leslie S. G.)—784(A)
Douglas, R. A. (see Jones, K. W.)—947
Dousmanis, G. C. Microwave spectrum of free OD radical—789(A)
Douthett, E. M. and D. H. Templeton. Ranges of fragments from high-energy fission of U—128
—— (see Templeton, D. H.)—759(A)
Dreicer, H. (see Strandberg, M. W. P.)—1393(L)
Dresden, M. and Martin Gutzwiller. Renormalization questions in curved spaces—745(A)
Dresner, Joseph. Spectral energy distribution of 2-Mev x-rays—751(A)
Dropkin, J. J. (see Watson, W. R.)—777(A)
Drost-Hansen, W. and E. J. Workman. Theory of volume rectification in ice—770(A)
—— (see Workman, E. J.)—770(A); 1073(L)
Drougard, M. E. and D. R. Young. Domain clamping effect in $BaTiO_3$ single crystals—1408(A); 1561
Drummond, W. E. and C. S. Gardner. Point-source kernel for diffusion with small-angle scattering—149
Dudley, J. D. and C. M. Class. $N^{14}(n,2n)N^{13}$ cross-section measurement with 14-Mev neutrons—807(A)
Dudziak, Walter F. $\pi^{\pm}$ production cross sections from deuterium—756(A)
—— (see Sagane, Ryokichi)—755(A)
Duerig, William H. Rate of production of color centers in KCl and KBr by x-rays at 78°K—65
Duff, Russell E. and H. T. Knight. Observations of Taylor instability in gases—784(A)
—— (see Knight, Herbert T.)—784(A)
Duffield, Robert B. and Nathan Sugarman. Disintegration of heavy elements by 2.2-Bev protons—776(A)
—— (see Gindler, James)—759(A)
Duller, N. M., W. D. Walker, J. W. Graham, and J. R. Risser. Sea-level zenith-angle dependence of high-energy μ mesons—810(A)
DuMond, Jesse W. M. and E. Richard Cohen. Variety of our sources of information on Avogadro's number and other constants—1790(L)
Dunlap, W. C., Jr. Diffusion of impurities in Ge—1531
—— Properties of Zn-, Cu-, and Pt-doped Ge—1419(A)
—— (see Leifer, H. N.)—1431(A)
Dunnington, F. G., C. L. Hemenway, and J. D. Rough. Determination of h/e by new method—592
Dvorak, Henry R. (see Wills, James E.)—810(A)

Easley, James W. (see Chamberlain, Owen)—208(L)
Eatherly, W. P. Radiation damage effects on electronic properties of graphite—1432(T)
Eck, T. G. (see Kusch, P.)—1799(L)
Eckerman, J. (see Schwartz, R. N.)—1441(A)
Eckstein, B. H. (see Barber, W. A.)—1412(A)
—— (see Debye, P.)—1412(A)
Efremov, N. New method of approximate calculation of atomic radii—753(A)
—— Role of principal quantum number (n) in calculations of radii for ions with high (4, 5, 6, 7) valence—1424(A)
—— Role of Rydberg constant in calculation of ionic radii—813(A)
Eggleston, R. R. (see Meechan, C. J.)—1406(A)
Eisberg, R. M. Energy spectra of nucleons evaporated from compound nucleus—739(L)
—— (see Palevsky, H.)—1088(L)
Eisele, J. A. and F. Keffer. Effects of anisotropy on thermodynamic properties of antiferromagnets—1440(A)
Eisenstein, Albert S. X-ray induced luminescence in MgO—776(A)
Eisinger, J. T., C. F. Cook, and C. M. Class. Electric excitation of Ta—735(L)
—— (see Class, C. M.)—747(A); 809(A)
—— (see Gossett, C. R.)—807(A)
Eisner, Melvin (see Becker, Stewart)—811(A)
—— (see Mitchell, R. W.)—811(A)
Ekstein, H. Unitarity of U operator—1063
—— **and J. Kelly.** Rapid remagnetization of thin Mo permalloy strips—1440(A)
Elcock, E. W. Molecular field treatment of magnetic ordering transitions—1070(L)
Eliot, E. A., D. Hicks, L. E. Beghian, and H. Halban. Inelastic scattering of neutrons—144
Elliott, J. F., S. Legvold, and F. H. Spedding. Magnetic properties of Dy metal—1143
——, **S. Legvold, and F. H. Spedding.** Magnetic susceptibility of Nd metal—50
Elliott, L. G., R. L. Graham, J. Walker, and J. L. Wolfson. Energy levels of Pb^{208}—795(A)
Elliott, R. J. Resistance anomalies in some rare earth metals—564
El-Sabban, M. Z. and J. Rud Nielsen. Vibrational spectra of cyclobutforene—805(A)
Elsasser, Walter M. Magnetohydrodynamics of earth and sun—1440(T)
Emmerich, W. S., W. J. Auth, and J. D. Kurbatov. Nuclear spectra of Ce^{144} and Pr^{144}—110
——, **S. E. Singer, and J. D. Kurbatov.** Radiative electron capture of Fe^{55}, A^{37}, and Ni^{59}—113
—— (see Auth, W. J.)—794(A)
—— (see Singer, S. E.)—779(A)
Endt, P. M. (see Kluyver, J. C.)—1795(L)
Enge, Harald A. Spins of lowest states of K^{40}, P^{32}, and Al^{28} nuclei—730(L)
Engelbrecht, Alfred (see Lotspeich, J. F.)—789(A)
Engelkemeir, D. and L. B. Magnusson. Existence of 3.7×10^{-8}-sec metastable state in Pa^{232}—1395(L)
Enright, Dorothy (see Talley, Robert M.)—1431(A)
Epstein, A. and H. Fritzsche. Hall effect and thermoelectric power of pure Te at melting point and in liquid state—1426(A)
Ewald, A. W. Effect of impurities on conductivity of gray tin—1428(A)
Ewing, R. and J. C. Lee. Proton magnetic resonance in compounds having several liquid crystal phases—1411(A)

Fader, W. J. and A. Sperduto. Energy levels, from reaction $B^{10}(\alpha,p)C^{13}$—748(A)
Fagen, E., J. Goff, and N. Pearlman. Thermal conductivity and thermoelectric power of Ge at low temperatures—1415(A)
Fairhall, A. W., I. Halpern, and E. J. Winhold. Angular anisotropy of specific Th photofission fragments—733(L)
Fajans, Kasimir (see Beguin, Gilbert)—1434(A)
—— (see Caldwell, R. S.)—1427(A)
Fan, H. Y. (see D'Altroy, F. A.)—1415(A)
—— (see Kaiser, W.)—1431(A)
Farnsworth, H. E. (see Dillon, J. A., Jr.)—753(A)
—— (see Wallis, G.)—777(A)
Farquhar, R. M. (see Shillibeer, H. A.)—1793(L)
Farwell, G. W., J. E. Roberts, and A. C. Wahl. Half-lives of Pu^{240} and Pu^{239}—363
—— (see Chamberlain, O.)—156
Faust, W. R. (see Scherrer, V. E.)—791(A)
Feld, B. T., R. D. Godbole, A. Odian, F. Scherb, P. C. Stein, and A. Wattenberg. High-energy photoproton production by 325-Mev bremsstrahlung radiation—1000
Fermi, Enrico. Physics at Columbia University: genesis of nuclear-energy project—776(T)
—— What can we learn with high-energy accelerators?—773(T)
Ferrell, B. L. (see Cohen, B. L.)—625; 758(A)
Ferrell, R. A. (see Schulten, R.)—739(L)
Ferro, A. (see Bonfiglioli, G.)—316
Ferry, John D., Malcolm L. Williams, and Donald M. Stern. Slow relaxation mechanisms in concentrated polymer solutions—1413(A)
—— (see Williams, Malcolm L.)—1413(A)
Feshbach, Herman. Relativistic wave equations—786(A)
Feynman, R. P. Atomic theory of two-fluid model of liquid He—262
—— **and G. Speisman.** p-n mass difference—500(L)
Fields, P. R., M. H. Studier, J. F. Mech, H. Diamond, A. M. Friedman, L. B. Magnusson, and J. R. Huizenga. Additional properties of isotopes of elements 99 and 100—209(L)
—— (see Diamond, H.)—1083(L)
—— (see Stevens, C. M.)—974
Fields, R. E., R. L. Becker, and R. K. Adams. Measurement of n-p cross section at 1.0 and 2.5 Mev—389
Fine, M. E. and Nancy T. Kenney. Moduli and internal friction of magnetite as affected by low temperature transformation—1573
Fink, Richard W. and Edwin O. Wiig. Reactions of Cs with 240-Mev protons—1357
Fireman, E. L. and D. Schwarzer. Measurement of T concentration in natural waters by diffusion cloud chamber—385
Firor, John W. Cosmic radiation intensity-time variations and their origin. IV. Increases associated with solar flares—1017
——, **W. H. Fonger, and J. A. Simpson.** Cosmic radiation intensity-time variations and their origin. V. Daily variation of intensity—1031
Fisher, L. H. (see Menes, M.)—1
Fiske, Milan D. Effect of hydrostatic pressure on superconducting transition of Sn and Tl—495(L)
Fivel, Daniel I. and Gilbert N. Plass. Radiation flux in planetary atmosphere—752(A)
Fleeman, Jerome. $\beta\rightarrow\alpha$ transformation in Sn—1422(A)
Fletcher, P. C. (see Aamodt, L. C.)—789(A)
Fletcher, R. C., W. A. Yager, G. L. Pearson, A. N. Holden, W. T. Read, and F. R. Merritt. Spin resonance of donors in Si—1392(L)
Folen, V. J., F. C. Nix, and F. E. Jaumot, Jr. Ferromagnetic properties and order-disorder in Fe-Pd alloys—1432(A)
Foley, H. M. (see Sessler, A. M.)—761(A)
Fonger, W. H. (see Firor, J. W.)—1031
Foote, H. L., Jr. Te resonance scattering—790(A)

Ford, Kenneth W. and David L. Hill. Non-uniform nuclear charge distributions and measurements of nuclear electrical radius—1630
—— (see Hill, David L.)—1617; 787(A)
Forster, H. K. and N. Zuber. Bubble dynamics in superheated liquid—754(A)
Foster, B. P., G. S. Stanford, and L. L. Lee. γ rays from Ne^{22} 804(A)
Fowler, C. M., H. W. Kruse, V. Keshishian, R. J. Klotz, and G. P. Mellor. Energy levels in W^{182}—1082(L)
Fowler, Charles A., Jr., and Edward M. Fryer. Magnetic domains by longitudinal Kerr effect—52
Fowler, E. C., H. L. Kraybill, R. M. Walker, and R. S. Preston. Interaction with A and Pb of neutrons with energies up to 2.3 Bev—791(A)
Fowler, W. A. (see Peterson, R. W.)—1075(L)
Fox, David. Production of antiprotons in p-p collisions—499(L)
Fox, T. G. Effect of structural variables on specific volume and glass temperature—1425(T)
France, W. L. and F. P. Dickey. 2.7μ bands of CO_2—1423(A)
Frank, P. J. (see Gutowsky, H. S.)—1067(L)
Frank, Wilson J., Kenneth C. Bandtel, Richard Madey, and Burton J. Moyer. Angular distribution and yield of process $p+d \rightarrow t+\pi^+$—1716
Franklin, A. D., A. E. Berkowitz, and E. Klokholm. Ferromagnetism and order in Fe-Pt alloys near Fe_3Pt—1432(A)
Franzen, Wolfgang (see Ajzenberg, Fay)—409
Fraser, J. S. and J. C. D. Milton. Rates of decay of observed anisotropies in Am^{241} α-γ and Cd^{111} γ-γ angular correlations—795(A)
Fraser, P. A. (see Nicholls, R. W.)—1423(A)
Frazer, B. C., Marilyn McKeown, and Ray Pepinsky. Neutron diffraction studies of Rochelle-salt single crystals—1435(A)
Frederikse, H. P. R. (see Blunt, R. F.)—1431(A)
Freidman, M. B. (see Ludloff, J. F.)— 763(T)
Freier, P. S., G. W. Anderson, and J. E. Naugle. Decay of heavy nuclear fragment—677
—— (see Anderson, G. W.)—1317
Freistadt, Hans. Quantized interaction of relativistic fields—746(A)
Frenzen, P. (see Fultz, D.)—1471
Frerichs, Rudolf. Dielectric changes in crystal-phosphor condensers irradiated with x-rays—1408(A)
Fried, Burton D. and R. J. Riddell, Jr. Meson-nucleon scattering. II—746(A)
—— (see Riddell, R. J., Jr.)—1736; 745(A)
Friedlander, G., E. Baker, J. Hudis, J. M. Miller, and R. Wolfgang. Radioactive products from interaction of 2.2-Bev protons with Cu—775(A)
——, **J. M. Miller, R. Wolfgang, J. Hudis, and E. Baker.** Nuclear reactions of Cu with 2.2-Bev protons—727(L)
—— (see Hudis, J.)—775(A)
—— (see Wolfgang, R.)—775(A)
Friedman, A. M. (see Diamond, H.)—1083(L)
—— (see Fields, P. R.)—209(L)
—— (see Stevens, C. M.)—974
Friedman, Abraham S. and Lester Haar. General method for high-speed machine computation of ideal gas thermal properties. Isotopic water molecules—1423(A)
Frisch, David H. (see Cooper, Daniel I.)—1209
Fritzsche, H. Hall effect and resistivity of Ge at low temperatures—1415(A)
—— (see Epstein A.)—1426(A)
Frost, Albert D. (see Mingins, Charles R.)—770(A)
Fryer, Edward M. (see Fowler, Charles A., Jr.)—52
Fuller, C. S. (see Severiens, J. C.)—750(A)
Fuller, E. G. and Evans Hayward. Elastic scattering of photons—732(L)
Fultz, D., Y. Nakagawa, and P. Frenzen. Instance in thermal convection of Eddington's "overstability"—1471
Furst, Milton and Hartmut Kallmann. Energy transfer by means of collision in liquid organic solutions under high energy and uv excitations—503

Gabbard, R. F. (see Caswell, R. S.)—786(A)
Garber, M. and D. E. Mapother. Effect of hydrostatic pressure on superconducting transition of Sn—1065(L)
Gardner, C. S. (see Drummond, W. E.)—1491
Gardner, J. W. Effect of knock-on electrons on ionization loss—746(A)
Garrett, C. G. B. (see Brattain, W. H.)—750(A)
Garrison, Gerald R. (see Miller, Charles E.)—167
Gasiorowicz, S. (see Arnowitt, R.)—746(A); 1057
Gates, Halbert. Determination of ratio of photo-elastic constants of glasses by means of ultrasonic waves—1434(A)
Geballe, T. H. and G. W. Hull. Seebeck effect in Ge—1134
Geer, E. H. (see Carlson, R. R.)—1311
Gehatia, Matatiahu. Low even configurations of Hf II—618
Gellman, H. (see Sharp, W. T.)—762(A)
Geltman, S. Interpretation of ionic mobilities in N_2—1072(L)
George, Waller (see McLean, E. A.)—761(A); 1428(A)
Gerhart, J. B., B. C. Carlson, and R. Sherr. Annihilation of positrons in flight—917
Gerjuoy, E. and David S. Saxon. Application of variational methods to intermediate and high-energy scattering—478
—— **and David S. Saxon.** Variational principles for acoustic field—1445
Ghiorso, A., S. G. Thompson, G. R. Choppin, and B. G. Harvey. New isotopes of Am, Bk, and Cf—1081(L)
—— (see Choppin, G. R.)—1080(L)
Gibbons, J. H. Improved apparatus for high resolution neutron cross-section measurements—773(A)
—— (see Block, R. C.)—774(A)
Gibbs, Julian H. Electric polarization of charged particles in square potential wells—292
Gilbert, Richard S. (see Hicks, Harry G.)—371
Gilmer, T. E. (see Patterson, J. R.)—774(A)
Gindler, James and Robert B. Duffield. Photofission cross sections—759(A)
Ginzbarg, Arthur S. and William L. Roever. Transmission of pulses through elastic plate—812(A)
Givens, M. Parker (see Woodruff, Robert W.)—752(A)
Glasser, R. G. (see Sprague, A. D.)—994
Glassgold, Alfred E. Elastic scattering of high-energy electrons by nuclei—757(A)
Glauber, R. J. Scattering by lattices of deformable atoms—751(A)
—— (see Zemach, A. C.)—790(A)
Glendenin, L. E. (see Keller, R. N.)—969
Glicksman, Maurice. Scattering of 217-Mev negative pions by hydrogen—1335
Gluckstern, R. L., P. B. Daitch, L. C. Biedenharn, and M. H. Hull, Jr. Continuous parameter approximation in linear accelerator with independently excited cavities—768(A)
—— (see Feld, B. T.)—1000
—— (see Hull, M. H., Jr.)—768(A)
Godfrey, T. N. K. Negative μ-meson capture in carbon—756(A)
Goertzel, G. (see Spruch, Larry)—1671
Goff, J. (see Fagen, E.)—1415(A)
Gold, R. (see Lidofsky, L.)—780(A)
Goldberg, Colman and R. E. Davis. New galvanomagnetic effect—1121
—— (see Brentano, J. C. M.)—56
Goldberger, M. L. (see Deser, S.)—711
Goldburg, W. I. and R. M. Williamson. Energy dependence of Coulomb excitation of Ta and Au—747(A)

Goldman, J. E. and A. Arrott. Magnetic susceptibility of Ni-Cu and Ni-Cr alloys—782(A)
—— (see Azumi, K.)—781(A)
Goldwasser, E. L. and G. Bernardini. Photoproduction of π^+ mesons near threshold—755(A)
—— (see Bernardini, G.)—729(L)
—— (see Nicolai, V. O.)—755(A)
Goldwater, D. L. and W. E. Danforth. Electrolysis of sintered ThO—754(A)
Good, R. H., Jr. Effect of atomic electron screening on shape of forbidden β spectra—931
Good, W. E. (see Gunther-Mohr, G. R.)—1184
Good, W. M., W. E. Kunz, and C. D. Moak. He^3+He^3 reactions—87
Goodman, Clark (see McClelland, C. L.)—1437(A)
Goodman, P. Concentration dependence of mechanical shear degradation—1425(A)
Goodrich, Max. Recent scintillation-spectrometer measurements at Louisiana State University—803(T)
—— **and Wilbur B. Payne.** Internal bremsstrahlung from P^{32}—405
Gordon, W. L., C. H. Shaw, and J. G. Daunt. Structure of liquid He by x-ray scattering—771(A)
Gordy, Walter. Mm and sub-mm wave spectroscopy—803(T)
Gossett, C. R., G. C. Phillips, and J. T. Risinger. Nuclear energy levels by absolute magnetic analysis of inelastically scattered protons—807(A)
Gossick, B. R. Transient response of p-n junction rectifiers—1427(A)
Gove, H. E., E. B. Paul, G. A. Bartholomew, and A. E. Litherland. Angular distribution of γ rays from $Al^{27}(p,\gamma)Si^{28}$—749(A)
—— (see Paul, E. B.)—749(A)
Gow, J. D. and Luis W. Alvarez. Ne^{18}—365
Graham, J. W. (see Duller, N. M.)—810(A)
Graham, R. L. and J. Walker. Disintegration of Sm^{153}—794(A)
—— (see Elliott, L. G.)—795(A)
Graham, Walter J. and Arthur J. Ruhlig. Calculated values of parameters of noble gas discharges—25
Grandey, R. A. and A. F. Clark. Elastic scattering of 160-Mev pions in emulsions—766(A)
Grannemann, W. W., C. W. Horton, and R. B. Watson. Diffraction of electromagnetic waves by metallic wedge of acute dihedral angle—812(A)
—— (see Horton, C. W.)—812(A)
Green, D. W., J. N. Cooper, and J. C. Harris. Stopping power of several elements for protons—764(A)
Green, Melville. Boltzmann equation from statistical mechanical point of view—792(A)
Grimsal, E. G. (see Levinger, J. S.)—772(A)
Grodzins, L. Scattering of 2.7-Mev positrons by Au and Al foils—758(A)
Gross, B. Theory of thermodielectric effect—1545
Gross, E. P. Shape of collision-broadened spectral lines—1424(A)
—— **and M. Krook.** Propagation of waves in ionized gases—778(A)
—— (see Bhatnagar, P. L.)—511
Gugelot, P. C. (see Dayton, I. E.)—785(A)
Gummel, Hermann and Melvin Lax. Thermal ionization of trapped electrons—1419(A)
Günther, Marian. Relativistic configuration space formulation of multi-electron problem. II—1347
Gunther-Mohr, G. R., C. H. Townes, and J. H. Van Vleck. Hfs in spectrum of $N^{14}H_3$. II. Theoretical discussion—1191
——, **R. L. White, A. L. Schawlow, W. E. Good, and D. K. Coles.** Hfs in spectrum of $N^{14}H_3$. I. Experimental results—1184
Gurnee, E. F. Theory of orientation and double refraction in polymers—1412(T)
Gutowsky, H. S. and P. J. Frank. Electron spin resonance in metals at low fields—1067(L)
Gutzwiller, Martin (see Dresden, M.)—745(A)

Haar, Lester (see Friedman, Abraham S.)—1423(A)
Haberle, W., J. W. Bittner, and R. D. Moffat. Elastic scattering of α particles by carbon—769(A)
Haber-Schaim, U., Y. Yeivin, and G. Yekutieli. Production of K mesons—184
Hagstrum, H. D. Theory concerning secondary electrons ejected from metals by ions—749(T)
Hahn, B. (see McIntyre, J. A.)—1084(L)
Hahn, T. M. (see Rayburn, L. A.)—1641
Halban, H. (see Eliot, E. A.)—144
Haldar, B. C. and Edwin O. Wiig. New neutron-deficient isotope of Ag—1713
Halpern, I. (see Fairhall, A. W.)—733(L)
Halpern, J. (see Weinstock, E. V.)—1651
Halpern, Otto. Magnetic quenching of positronium decay—904
Halpin, A. T. (see Watson, W. R.)—777(A)
Hamilton, Donald R. (see Alford, W. Parker)—779(A)
Hammel, Edward F. (see Kilpatrick, John E.)—1103
Hammerle, W. G. Theory of viscoelastic behavior—1425(T)
Handley, Thomas H. Neutron-deficient activities of Ho—945
—— **and Elmer L. Olson.** Yb^{169}—968
—— (see Cohen, B. L.)—620; 953
Hanna, S. S. (see Cohen, L.)—419
Hans, H. S. (see Rothman, M. A.)—791(A)
Hanson, A. O. (see Schriever, Barbara Dwight)—763(A)
—— (see Scott, M. B.)—763(A)
Harman, T. C., R. K. Willardson, and A. C. Beer. Hall coefficient in Ge—1065(L)
Harris, E. D. (see deBretteville, A.)—1408(A)
Harris, J. C. (see Green, D. W.)—764(A)
—— (see Smith, J. A.)—749(A)
Hartley, R. V. L. Corrected theory of relativity and its classical interpretation—792(A)
Hartmann, N. (see Sheer, C.)—769(A)
Hartsough, Walter (see Cork, Bruce)—1300
Harvey, B. G. (see Choppin, G. R.)—1080(L)
—— (see Ghiorso, S. G.)—1081(L)
Haskin, D. M. (see Sprague, A. D.)—994
Hastings, J. (see Weiss, R. J.)—1420(A)
Hatalkar, M. M. Theory of elementary particles in general relativity—1472
Havas, Peter (see Crownfield, Frederic R., Jr.)—471
Havens, W. W., Jr. (see Melkonian, E.)—790(A)
Haxby, R. O. (see Murray, P. C.)—764(A)
Hayes, W. D. Pseudo-transonic similitude and first-order wave structure—763(T)
Haynes, J. R. and J. A. Hornbeck. Decay in photoconductivity associated with hole traps in n-type Si—1438(A)
—— (see Hornbeck, J. A.)—1437(A)
Hayward, Evans (see Fuller, E. G.)—732(L)
Heaps, C. W. Electrical properties of molybdenite—809(A)
Heckrotte, Warren. Polarization of elastically scattered nucleons from nuclei in Born approximation—1797(L)
—— **and Joseph V. Lepore.** Polarization of elastically scattered nucleons from nuclei—500(L)
—— (see Schecter, Larry)—1086(L)
Hedgran, Arne and Sölve Hultberg. Angular distribution of photoelectrons from γ radiation of 0.4 and 1.3 Mev—498(L)
Heiberg, E. (see de Carvalho, H. G.)—1796(L)
Heidemann, E. A. (see Leitner, A.)—1441(A)
Heinz, Otto. Range and specific ionization for high-energy protons in nuclear emulsions—1728
Heller, Wilfried. Analysis of reduced viscosity equations—1426(A)

Hellund, E. J. and Katsumi Tanaka. Quantized space-time—192
Hemenway, C. L. (see Dunnington, F. G.)—592
Hemmer, B. A. (see Dorfman, M.)—754(A)
Hempstead, C. F. (see Parratt, L. G.)—1593
Henderson, Joseph E. (see Miller, Charles E.)—167
Henkel, R. L., L. Cranberg, G. A. Jarvis, R. Nobles, and J. E. Perry. Total neutron cross section for U from 20 kev to 20 Mev—141
Henri, V. P. (see Bay, Z.)—780(A)
Henry, Allan F. (see Beringer, Robert)—343
Henry, Warren E. Antiferromagnetic *H-T* boundaries and apparent molecular fields for $MnCl_2 \cdot 4H_2O$ and $MnBr_2 \cdot 4H_2O$—1146
—— High-field non-Brillouin moments for cobalt sulfate heptahydrate—781(A)
—— Magnetization of $CuK_2(SO_4)_2 \cdot 6H_2O$ at liquid He temperatures and in strong magnetic fields—1433(A)
Hensley, E. B. Conduction mechanism in oxide-coated cathodes—790(T)
Henvis, B. W. (see Burstein, E.)—750(A)
Herb, R. G. (see Bittner, J. W.)—769(A)
Hereford, F. L. Photoelectron production by polarized γ rays—806(T)
—— (see McMaster, W. H.)—757(A)
Herman, R. C., S. Silverman, and R. F. Wallis. Vibration-rotation line intensities of diatomic molecules—752(A)
Herring, D. F. (see Block, R. C.)—774(A)
Hersh, S. P. and D. J. Montgomery. Static electrification of filaments: dependence of charge transferred on normal force and velocity—1413(A)
Herwig, Lloyd O. and Glenn H. Miller. α-particle ionization yields in gridded chamber—1183
Hesketh, R. V. and E. E. Schneider. Restoration of F and V_1 centers following low-temperature bleaching—494(L)
Heybey, W. H. Theoretical determination of shock distances in ideal and real gases—1441(A)
Heydenburg, N. P. and G. M. Temmer. γ rays from inelastic scattering of α particles by Li and F—748(A)
—— **and G. M. Temmer.** γ rays from Li^7, F^{19}, Ne^{22}, and Na^{23} produced by α-particle bombardment of Li and F—1252
—— (see Temmer, G. M.)—1399(L); 747(A)
Hickman, G. D. (see Cork, J. M.)—1218
Hicks, D. (see Eliot, E. A.)—144
Hicks, Harry G. and Richard S. Gilbert. New isotope of Pd, 1.5-minute Pd^{113}—371
Hiedemann, E. A. (see Leitner, A.)—1441(A)
Higgins, G. H. and W. W. T. Crane. Thermal neutron fission cross section of Am^{242m}—735(L)
Hildebrandt, Alvin F. Narrow gap electromagnet for high-resolution nuclear resonance spectrometry—811(A)
Hill, D. A., T. Coor, W. F. Hornyak, L. W. Smith, and G. A. Snow. Experiments with neutrons from the Cosmotron. I—791(A)
—— (see Snow, G. A.)—791(A)
Hill, David L. and Kenneth W. Ford. μ-mesonic x-rays and shape of nuclear charge distribution—1617
—— **and Kenneth W. Ford.** Nuclear charge distribution—787(A)
—— (see Ford, Kenneth W.)—1630
Hill, R. D., E. O. Salant, and M. Widgoff. K-particle production by protons of 2.2 and 3.0 Bev—1794(L)
——, **E. O. Salant, M. Widgoff, L. S. Osborne, A. Pevsner, D. M. Ritson, J. Crussard, and W. D. Walker.** Unstable heavy particles from Cosmotron—797(A)
Hobbs, Lindsey M., Douglas E. Brown, and David W. Pletcher. Effects of Co^{60} γ radiation on formation and degradation of polymers—1412(A)
Hoch, Michael and Herrick L. Johnston. Germanium-oxygen system—749(A)
Hoff, E. A. W. Dynamic properties of high polymers—1425(T)
Hoffman, J. D. Rotation of chain molecules in crystals—1425(T)
Hoffman, R. W. and N. S. Rasor. Annealing kinetics of lattice imperfections using evaporated metal films—1406(A)
Hofstadter, Robert. Nuclear determinations from electron scattering—773(T)
—— (see McIntyre, J. A.)—1084(L)
Holden, A. N. (see Fletcher, R. C.)—1392(L)
—— (see Kunz, F. W.)—1417(A)
Holmes, John R. and Leon Pape. Pressure shift in He λ5875—902
Holmgren, H. D., J. M. Blair, B. E. Simmons, and R. V. Stuart. Differential cross sections for $C^{13}(d,t)C^{13}$ reaction—748(A)
Holstein, T. (see Bernstein, Ira B.)—1475
Honnold, V. R., F. McCaffrey, and B. A. Mrowca. Measurement of nuclear induction relaxation times in polymers—1414(A)
Hori, H. (see Bowen, D. B.)—1422(A)
Hornbeck, J. A. and J. R. Haynes. Decay in photo-conductivity associated with deep electron traps in p-type Si—1437(A)
—— (see Haynes, J. R.)—1438(A)
Hornig, D. F. Characteristics of shock fronts in liquids and gases—765(T)
Hornyak, W. F. (see Hill, D. A.)—791(A)
—— (see Snow, G. A.)—791(A)
Horton, C. W. and W. W. Grannemann. Diffraction measurements at 1.25 cm—812(A)
—— (see Grannemann, W. W.)—812(A)
Horton, G. K. and E. Phibbs. Perturbation theory with Sommerfeld-Maue wave function—1402(L)
Hosemann, R. and S. N. Bagchi. Diffraction effects of crystals with deformation faults—71
Houston, W. V. Variation method applied to wave functions in crystals—808(A)
Howard, J. N. (see Burch, D. E.)—1424(A)
Hoyer, W. A. Compressibility of liquid cholesterol benzoate at isotropic-anisotropic transition—812(A)
Hudis, J., R. Wolfgang, N. Sugarman, and G. Friedlander. Reactions of Al with 2.2-Bev protons—775(A)
—— (see Friedlander, G.)—727(L); 775(A)
Hudspeth, Emmett L. (see Rickard, James A.)—806(A)
—— (see Spearman, K. R.)—806(A)
Hughes, D. J. Statistical factors in radiation widths of nuclear energy levels—740(L)
—— (see Palevsky, H.)—1088(L)
Hughes, D. S. Thermodynamic properties of solids deduced from high-pressure measurements—803(T)
Hughes, Vernon W. and Werner B. Teutsch. Relativistic contributions to magnetic shielding of nuclei in atoms—761(A)
Huizenga, John R. Spontaneous fission systematics—158
—— (see Diamond, H.)—1083(L)
—— (see Fields, P. R.)—209(L)
—— (see Stevens, C. M.)—974
Hull, G. W. (see Geballe, T. H.)—1134
Hull, M. H., Jr., L. C. Biedenharn, P. B. Daitch, and R. L. Gluckstern. Stability of linear accelerator with independently excited cavities—768(A)
—— (see Gluckstern, R. L.)—768(A)
Hulm, John K. Superconductivity of pure metallic Re—1390(L)
Hultberg, Sölve (see Hedgran, Arne)—498(L)
Hunter, L. P. Graphical representation of semiconductor Hall effect—1426(A); 1157
Hurlbut, F. C. Molecular beam investigation of scattering of molecules from surfaces—754(A)

Huus, Torben (see Bjerregaard, Jørgen H.)—204(L)
—— (see Zupančič, Črtomir)—205(L)
Hyde, Earl K. Radiations of AcK—1221

Ingersoll, L. R. and D. H. Liebenberg. Faraday effect in gases—754(A)
Innes, Frederick R. Spin-other-orbit interaction in theory of complex spectra—761(A)
Ishiguro, Eiichi and Shoichiro Koide. Magnetic properties of H_2 molecules—350
Ivey, D. G. and A. Kwei. Stress-temperature-time studies through second-order transition region—1414(A)
Ivory, J. (see Baldwin, F. P.)—1425(A)

Jaccarino, Vincent, J. G. King, R. A. Satten, and H. H. Stroke. Hfs of I^{127}. Nuclear magnetic octupole moment—1798(L)
—— (see King, John Gordon)—1610
Jacobsen, E. H. Elastic spectrum of Cu from temperature scattering of x-rays—1420(A)
Jacobsmeyer, V. P. (see Badar, L. J.)—808(A)
James, Hubert M. (see Lehman, Guy W.)—1428(A)
Jarmain, W. R. (see Nicholls, R. W.)—1423(A)
Jarvis, G. A. (see Henkel, R. L.)—141
Jaumot, F. E., Jr., and A. Sawatzky. Order-disorder and cold-work phenomena in Cu-Pd alloys—1429(A)
—— (see Berkowitz, A. E.)—1407(A)
—— (see Folen, V. J.)—1432(A)
—— (see Smith, R. L.)—1407(A)
—— (see Sutcliffe, C. H.)—1429(A); 1429(A)
Javan, Ali (see Lotspeich, J. F.)—789(A)
Jenkins, T. L., D. Luckey, and R. R. Wilson. Photomeson production from hydrogen—755(A)
Jensen, E. N. (see Nichols, R. T.)—369
Jesse, William P. and John Sadauskis. α-particle ionization in noble gases and formation of metastable atoms—764(A)
Johnson E. J. and W. G. Spitzer. Optical properties of Ge in far infrared—1415(A)
Johnson, Noah R. (see Sheline, Raymond K.)—1642
Johnson, Peter D. Optical properties of MgO in vacuum uv—845
Johnson, V. A. Resistivity, thermoelectric power, and Hall effect in semiconductor with hexagonal structure—1427(A)
Johnson, Walter H., Jr. (see Collins, T. L.)—398
Johnston, Herrick L. (see Hoch, Michael)—749(A)
Johnston, R. W. and D. H. Tomboulian. Absorption spectrum of Be in neighborhood of K edge—1585
Jona, F., G. Shirane, and R. Pepinsky. Measurements of ferroelectric transition in single crystals of $Cd_2Nb_2O_7$—1408(A)
Jones, E. A. W. (see Shillibeer, H. A.)—1793(L)
Jones, H. Soft x-ray emission bands in metals—1072(L)
Jones, K. W., R. A. Douglas, M. T. McEllistrem, and H. T. Richards. Comparison of nuclear and γ-ray energy scales—947
Jones, L. W. and K. M. Terwilliger. Electromechanical analog for study of strong-focusing orbits—1436(A)
Jones, Royce J. (see Livingston, Robert S.)—1436(A)
Jones, W. H. (see Cohen, B. L.)—625; 758(A)
Jordan, W. C. (see Burson, S. B.)—103
Joyner, W. T. (p,γ) coincidence measurements utilizing proton time-of-flight—774(A)
Joynson, R. E. Elastic spectrum of Zn from temperature scattering of x-rays—851
Jung, J. J. (see Bockelman, C. K.)—748(A)

Kaenzig, Werner. Properties of very small ferroelectric particles—1408(T)
Kaiser, H. F. Microtron resonators—768(A)
Kaiser, W. and H. Y. Fan. Infrared properties of InSb—1431(A)
Kallmann, Hartmut (see Furst, Milton)—503
Kalos, M. H. and J. M. Blatt. Phenomenological n-p interaction—762(A)
Kane, Evan O. Thermionic emission and semiconduction in single crystals of BaO—1439(A)
Känzig, Werner (see Ueta, Masayasu)—1390(L)
Kao, L. P. and E. Katz. Magnetoresistance—1433(A)
Karplus, R. (see Luttinger, J. M.)—782(A)
Kasnitz, Harold L. and Kurt Sitte. Structure and composition of air shower cores—977
Katcoff, Seymour (see McKeown, Michael)—965
Katz, E. Theory of photographic intermittence effect at low light intensities—1441(A)
—— (see Kao, L. P.)—1433(A)
—— (see Schamp, H. W., Jr.)—828
Kauzman, W. D. Nature of liquid and glassy states—1425(T)
Keating, D. T. Diffraction studies of possible ordering in α brass—1429(A)
Keck, P. H. (see Wolff, G.)—753(A)
Keffer, F. (see Cohen, M. H.)—1412(A)
—— (see Eisele, J. A.)—1440(A)
Keller, R. N., E. P. Steinberg, and L. E. Glendenin. Yields of fission products from U^{233} irradiated with fission spectrum neutrons—969
Keller, William E. (see Kilpatrick, John E.)—1103
Kelly, John, James Ray, and Richard A. Ogg, Jr. Nuclear magnetic resonance spectra of boranes and derivatives—767(A)
—— (see Ekstein, H.)—1440(A)
Kenney, Nancy T. (see Fine, M. E.)—1573
Kerst, D. W. (see Scott, M. B.)—763(A)
Keshishian, V. (see Fowler, C. M.)—1082(L)
Kessler, John O. and Leon M. Lederman. Interactions of negative pions in C and Pb—689
Keuffel, J. W. and L. Mezzetti. Search for K particles using Čerenkov counters—797(A)
Keyes, R. J. and T. G. Maple. Variation of recombination velocity of Ge surfaces with ambient gases—1416(A)
Keyes, R. J. (see Stevenson, D. T.)—1416(A)
Keyes, Robert W. Diffusion of lattice defects in temperature gradient—1389(L)
Kies, J. A. and H. L. Smith. Methods for determining the energy for fracture propagation in plates—760(A)
—— (see Smith, H. L.)—760(A)
Kilpatrick, John E., William E. Keller, Edward F. Hammel, and Nicholas Metropolis. Second virial coefficients of He^3 and He^4—1103
Kim, Y. B. Energy distribution of neutral mesons produced in cosmic-ray stars—797(A)
King, John Gordon and Vincent Jaccarino. Hfs and nuclear moments of stable Br isotopes—1610
—— (see Jaccarino, V.)—1798(L)
King, R. W. and D. C. Peaslee. First forbidden matrix element in β decay—1284
—— **and D. C. Peaslee.** Spin of RaE—795(A)
Kingston, R. H. "Channels" in n-p-n junction transistors: new results and proposed model—1146(A)
Kington, J. D. (see Willard, H. B.)—786(A)
Kinoshita, Toichiro. Effect of Coulomb . . .—1331
—— V particles and γ decay of neutral pion—1384
—— **and Yoichiro Nambu.** Collective description of many-particle . . .—598
Kip, A. F. Electron spin resonance in semiconductors and metals—1416(T)
Kirby, H. W. and Murrell L. Salutsky. Half-life of La^{140}—1801(E)
Kistler, Alan, Vivian O'Brien, and Stanley Corrsin. Isotropic temperature fluctuations in isotropic turbulence—783(A)
Kittel, Charles. Solid-state cyclotron—768(T)
Klein, Abraham. Configuration space methods for construction of potentials—195

—— Single-time formalisms from covariant equations—1052
Klein, Ralph. Surface migration of C on W—1407(A)
Klick, Clifford C. Search for *F*-center luminescence—1541
—— Search for luminescent emission from *F* center—1438(A)
Klokholm, E. (see Franklin, A. D.)—1432(A)
Klontz, E. (see Pepper, R.)—1410(A)
Klotz, R. J. (see Fowler, C. M.)—1082(L)
Kluyver, J. C., C. van der Leun, and P. M. Endt. Ground state of Al^{26}—1795(L)
Knight, Herbert T. and Russell E. Duff. Precision measurement of detonation and strong shock velocity in gases—784(A)
—— (see Duff, R. E.)—784(A)
Knight, W. D. Nuclear resonance in ferroelectric crystals—1408(T)
Knowles, J. W. New method for measuring short γ-ray lifetimes—795(A)
Koehler, J. S. Pauli principle scattering and resistivity minimum—1071(L)
—— (see Cooper, H. G.)—496(L)
—— (see Sosin, A.)—1422(A)
Koehler, W. C. and E. O. Wollan. Paramagnetic scattering of neutrons by rare earth oxides—1801(E)
Kofsky, Irving L. (see Sitte, Kurt)—988
Kohane, T. (see Debye, P. P.)—724(L)
Kohn, W. Bombardment damage of Ge crystals by fast electrons—1409(A)
—— **and N. Rostoker.** Solution of Schrödinger equation in periodic lattices with application to metallic Li—1111
—— (see Lakin, W.)—787(A)
Koide, Shoichiro (see Ishiguro, Eiichi)—350
Konopinski, E. J. Possible relation between pseudoscalar β coupling and nuclear spin-orbit coupling—492
Korringa, J. Electron resonance in *F* centers—1388(L)
—— Orientation of nuclei by saturation of paramagnetic resonance—1388(L)
Korsmeyer, J. D. (see Campbell, R. C.)—791(A)
Koshiba, M. (see Crussard, J.)—736(L)
Koster, G. F. and J. C. Slater. Wave functions for impurity levels—1392(L)
—— (see Slater, J. C.)—1498
Kovacs, J. S. (see Brueckner, K. A.)—726(L)
Kovásznay, Leslie S. G. and Darshan Dosanjh. Shock tube experiments on grid flow—784(A)
Kraemer, H. (see Bothe, W.)—1402(L)
Kraitchman, J. and B. P. Dailey. Microwave spectrum of ethyl fluoride—788(A)
Kraus, Alfred A., Jr. γ rays from $N^{15}(p,\alpha\gamma)C^{12}$ and $N^{15}(p,\gamma)O^{16}$—975
Kraus, Olen. Solutions of Helmholtz and Schrödinger equations in sphero-conal coordinates—1442(A)
Kraybill, H. L. (see Fowler, E. C.)—791(A)
Kriessman, C. J. and Herbert B. Callen. Magnetic susceptibility of transition elements—781(A); 837
Krimm, S. Infrared spectrum of polyethylene—1426(A)
Kroll, N. M. Survey of quantum electrodynamics—747(T)
Krook, M. (see Bhatnagar, P. L.)—511
—— (see Gross, E. P.)—778(A)
Kruse, H. W. (see Fowler, C. M.)—1082(L)
Kruse, U. E., J. M. Teem, and N. F. Ramsey. Proton-proton scattering from 40 to 95 Mev—1795(L)
Kuczynski, G. C. Effect of elastic strain on electrical resistance of metals—61
Kunz, F. W. and A. N. Holden. Effect of short-time moderate-flux neutron irradiation on mechanical properties of some metals—1417(A)
Kunz, W. E. (see Good, W. M.)—87
Kurbatov, J. D. (see Auth, W. J.)—794(A)
—— (see Emmerich, W. S.)—110; 113
—— (see Murray, B. B.)—780(A)
—— (see Sakai, M.)—779(A)
—— (see Singer, S. E.)—779(A)
Kurnick, S. W., A. J. Strauss, and R. N. Zitter. Photoconductivity and photoelectromagnetic effects in InSb—1791(L)
Kurşunoğlu, Behram. Interaction between two nucleons—746(A)
Kusch, P. and T. G. Eck. Hfs of In^{115}. Evidence of nuclear octupole moment—1799(L)
Kwei, A. (see Ivey, D. G.)—1414(A)

Lafferty, D. L. (see Rayburn, L. A.)—1641
Lakin, W. and W. Kohn. Distortion of nucleus in μ-mesic atoms—787(A)
Landauer, Rolf. Bound states in dislocations—1386(L)
Lander, J. J. Chemical observations on non-stoichiometric ZnO and interpretation of its conductivity—803(T)
Landon, H. H. Doppler effect in slow neutron resonance in Rh—1215
Landsberg, Peter T. Basic principles of quantum statistical mechanics—1442(A)
—— Continuous spectrum approximation in quantum statistics—469
Lane, R. O. and D. J. Zaffarano. Transmission of 0–40 kev electrons by thin films with application to β-ray spectroscopy—959
Lark-Horovitz, K. Nucleon bombardment of semiconductors—1432(T)
—— (see Pepper, R.)—1410(A)
Lauritsen, C. C. (see Peterson, R. W.)—1075(L)
—— (see Thirion, J.)—1076(L)
Lax, Melvin. Localized perturbations—1391(L)
—— **and R. Toupin.** Lattice of partly permanent dipoles—780(A)
—— (see Gummel, Hermann)—1419(A)
—— (see Toupin, R.)—781(A)
Lazarus, D. Solute diffusion in metals—1407(A)
Leaderman, Herbert and M. Wales. Steady-state elastic shear compliance and molecular weight distribution in polyisobutylene—1414(A)
Leavitt, C. P. (see Chen, F. F.)—784(A)
LeBlanc, J. M., J. M. Cork, and S. B. Burson. Activities of Zn^{71}—1436(A)
—— (see Burson, S. B.)—103
Leder, Lewis B. and L. Marton. Energy losses of electrons in passage through thin films—777(A)
—— (see Marton, L.)—203(L); 778(A)
Lederman, Leon M. Meson reactions in hydrogen—745(T)
—— (see Kessler, John O.)—689
Lee, J. C. (see Ewing, R.)—1411(A)
Lee, L. L. (see Foster, B. P.)—804(A)
Lee, T. D. and R. Christian. Intermediate coupling method for meson-nucleon scattering—1760
Legvold, S. (see Banister, J. R.)—1140
—— (see Elliott, J. F.)—50; 1143
Lehman, Guy W. and Hubert M. James. Interaction of impurities and mobile carriers in semiconductors—1428(A)
Lehnert, Bo. Magneto-hydrodynamic waves in liquid Na—815
Lehovec, Kurt. Electric breakdown of crystals in high-temperature region—770(A)
—— Theory of thermionic emission.—1439(A)
Leifer, H. N. and W. C. Dunlap. Properties of *p*-type GaSb between 15°K and 925°K—1431(A)
Leighton, R. B. (see van Lint, V. A.)—1732
Leipuner, L. (see Stearns, M.)—766(A)
Leitner, A. and E. A. Hiedemann. Symmetric modes of tapered reed—1441(A)
Leivo, W. and R. Smoluchowski. Color centers in KCl crystals produced by high-energy protons—771(A)
—— (see Smith, W. J.)—1435(A)

Leonard, B. P., Jr. (see Little, R. N., Jr.)—807(A)
Lepore, Joseph V., Maurice Neuman, and Richard N. Stuart. High-energy events—788(A)
—— **and Richard N. Stuart.** Nuclear events at high energies—1724
—— (see Heckrotte, Warren)—500(L)
Levinger, J. S. and E. G. Grimsal. Low-temperature oscillatory Hall effect—772(A)
Levinstein, Henry (see Bode, Donald E.)—1430(A)
—— (see Broudy, R.)—285; 290
—— (see Silverman, Searl J.)—871; 1430(A)
Levinthal, Cyrus. Structure and function in molecular biophysics—1426(T)
Levy, Harris B. and I. Perlman. Long-lived isomer of RaE (Bi^{210})—152
Lévy, Maurice M. Covariant treatment of meson-nucleon scattering—460
Levy, Paul W. and G. J. Dienes. Irradiation-induced optical absorption in Al_2O_3—1409(A)
Lewis, J. A. (see Mason, W. P.)—1439(A)
Li, C. W. (see Sherr, R.)—1076(L)
Li, Yin-Yuan and R. Smoluchowski. Diffraction of x-rays by lattice imperfections—751(A)
—— **and R. Smoluchowski.** Fourier analysis of x-rays small-angle scattering—1435(A)
—— **and R. Smoluchowski.** Theory of x-ray small-angle scattering—866
—— (see Robinson, W. H.)—1435(A)
Lide, David R., Jr. Microwave spectrum of methyl amine—788(A)
Lidiard, A. B. Ionic conductivity of impure polar crystals—29
Lidofsky, L., R. Gold, and C. S. Wu. Radiations of 18-min Br^{80}—780(A)
Liebenberg, D. H. (see Ingersoll, L. R.)—754(A)
Lieberman, D. S., M. S. Wechsler, and T. A. Read. Cubic to orthorhombic diffusionless phase change—experimental and theoretical studies of AuCd—760(A)
—— (see Read, T. A.)—759(A)
—— (see Wechsler, M. S.)—759(A)
Liebschutz, A. M. (see Binnie, W. P.)—1410(A)
Lindenbaum, J. Seymour (see Pevsner, Aihud)—765(A)
—— (see Williams, Ross)—765(A)
Lindner, M. and R. N. Osborne. Some studies of products of high-energy fission process—1323
Lindsay, Robert. Field-dependent magnetic susceptibility of MnSe—808(A)
Lindsley, John. Flux of primary cosmic-ray α particles—796(A)
Litherland, A. E. (see Gove, H. E.)—749(A)
—— (see Paul, E. B.)—749(A)
Little, R. N., Jr., C. P. Cadenhead, B. P. Leonard, Jr., J. T. Prud'homme, L. D. Vincent, and J. E. Wills. Angular distribution of $D(d,n)$ neutrons scattered from C, Al, S, Fe, Cd, Cu, W, and Pb—807(A)
Livingston, M. S. Design study for 15-Bev accelerator by Cambridge design study group—792(A)
Livingston, Ralph, Henry Zeldes, and Ellison H. Taylor. Atomic hydrogen hfs in irradiated acids—725(L)
Livingston, Robert S. and Royce J. Jones. Design features of high-current cyclotron—1436(A)
Lloyd, J. P. and G. E. Pake. Spin relaxation in free radical solutions exhibiting hfs—579
Lockenvitz, Arthur E. (see Auverman, Harry J.)—811(A)
—— (see Clarkson, Henry Neal)—811(A)
—— (see Cowan, Alvin E.)—809(A)
Loeb, Leonard B. Some aspects of breakdown streamers—227
Loebner, E. E. 2-phase graphitization—1435(A)
Logan, John K. Low-temperature magnetoresistance of Au in fields up to 50 kilogauss—1433(A)
Lomont, J. S. Time reversal *vs* Boltzmann equation—792(A)
Longini, R. L. (see McKelvey, J. P.)—750(A)
Lönsjö, O. (see Taylor, H. L.)—807(A)
Lotspeich, J. F., Ali Javan, and Alfred Engelbrecht. Microwave spectrum of ReO_3F—789(A)
Louisell, W. H., R. W. Pidd, and H. R. Crane. Experimental measurement of gyromagnetic ratio of free electron—7
Love, Temple and Fred Maienschein. γ-ray spectrum of Po-B source—795(A)
—— (see Maienschein, Fred)—778(A)
Lovell, L. C. (see Vogel, F. L.)—1791(L)
Löwdin, Per-Olov. Studies of atomic self-consistent fields. II. Interpolation problems—1600
Lu, Daniel C. and M. L. Wiedenbeck. Summation of γ-ray energies with single-crystal spectrometer—501(L)
Luckey, D. (see Jenkins, T. L.)—755(A)
Luckey, P. D. Production of charged mesons by γ rays on H and D—755(T)
Ludloff, J. F. and M. B. Freidman. Aerodynamics of blasts: Diffraction of blast around finite corners—763(T)
Lummis, F. L. (see Petritz, R. L.)—1430(A)
Luttinger, J. M. and R. Karplus. Hall effect in ferromagnetics—782(A); 1434(T)

MacGregor, M. H. and M. L. Wiedenbeck. Third forbidden β spectrum of Rb^{87}—138
MacKay, J. (see Pepper, R.)—1410(A)
Mackin, R. J., Jr. γ rays and internal pairs from Be^9+H^1—648
Macklin, R. L. (see Banta, H. E.)—807(A)
MacLeod, A. A., A. R. DiDonato, and A. C. Webber. Viscoelasticity in complex static stress systems—769(A)
—— (see DiDonato, A. R.)—770(A)
Madansky, L. and F. Rasetti. Radiative electron capture in Fe^{55}—407
Madey, Richard (see Frank, Wilson J.)—1716
Magnusson, L. B. (see Diamond, H.)—1083(L)
—— (see Engelkemeir, D.)—1395(L)
—— (see Fields, P. R.)—209(L)
Maienschein, Fred and Temple Love. γ-ray spectrum of Bulk Shielding Reactor—778(A)
—— (see Love, Temple)—795(A)
Maita, J. P. (see Morin, F. J.)—1525
Major, J. K. and L. C. Biedenharn. Sargent diagram and ft values for electron capture transitions—779(A)
Mandeville, C. E. and H. O. Albrecht. Luminescence of BeO—494(L)
—— **and Jagdish Varma.** Disintegration of Mo^{93}—780(A)
—— (see Albrecht, H. O.)—776(A)
—— (see Rothman, M. A.)—791(A)
—— (see Varma, Jagdish)—91
Maple, T. G. (see Keyes, R. J.)—1416(A)
Mapother, D. E. (see Garber, M.)—1065(L)
Marcus, Paul M. Theory of temperature waves—771(A)
Marion, J. B. LiI(Eu) crystals as neutron detectors—808(A)
——, **C. F. Cook, and T. W. Bonner.** Neutrons from proton bombardment of Be^9 and H^2—807(A)
Mark, Hans. Inelastic scattering of charged particles in electric excitation processes—1436(A)
Markham, Jordan J. Multiphonon transitions in F center—1395(L)
Marshak, H. Total neutron cross sections in kev region: Cu, Cu^{63}, Cu^{65}, and Ga—774(A)
Marshall, J. (see de Carvalho, H. G.)—1796(L)
Marshall, J. F. (see Shatas, R. A.)—757(A)
Marshall, L. (see de Carvalho, H. G.)—1796(L)
Martin, Don S., Jr. (see Schupp, Fritz D.)—80
Martin, R. L. Phase shift analysis of scattering of negative pions by H—765(A)
Marton, L. and Lewis B. Leder. Energy loss of electrons in passage through thin films—203(L)

—— **and Lewis B. Leder.** Penetration of medium fast electrons into photographic emulsions—778(A)
—— (see Leder, Lewis B.)—777(A)
Marvin, Robert S. Introductory remarks—1425(T)
——, **H. S. Sack, and R. Aldrich.** Calculation of dynamic bulk modulus of polyisobutylene—1413(A)
Marx, J. W. (see Cooper, H. G.)—496(L)
Mason, W. P. and J. A. Lewis. Equations for magneto-striction and anisotropic energy for hexagonal crystal of class $D_{4h}(6/m, 2/m, 2/m)$—1439(A)
Matarrese, L. M. and J. W. Stout. Magnetic anisotropy of NiF_2—1792(L)
Matheson, Max S. (see Smaller, Bernard)—202(L)
Matossi, Frank. Interpretation of electroluminescence effects in excited phosphor—1151
Matsen, F. A. (see Arnold, Charles W.)—804(A)
—— (see Miller, J. M.)—804(A)
—— (see Streetman, J. R.)—805(A)
Matthews, P. T. and Abdus Salam. Renormalization—185
Matthias, B. T. and E. Corenzwit. Superconducting alloys—1069(L)
Maxwell, Louis R. and Stanley J. Pickart. Magnetization in nickel ferrite indates—1433(A)
Mayburg, Sumner. Interstitial Ge in heat-treated Ge—750(A)
Mazur, P. and S. R. de Groot. Extension of Onsager's theory of reciprocal relations. II—224
—— (see de Groot, S. R.)—218
McCaffrey, F. (see Honnold, V. R.)—1414(A)
McClelland, C. L. and Clark Goodman. Electric excitation of Pt—1437(A)
McClure, G. W. Distribution of specific ionization of primary cosmic rays at $\lambda = 10°$N—796(A)
—— Search for anomalous positively-charged particles from P^{32}—1637
McCormick, G. H. (see Cohen, B. L.)—625; 758(A)
McCrary, J. H., H. L. Taylor, and T. W. Bonner. Fast neutron counter with energy resolution—808(A)
McEllistrem, M. T. (see Jones, K. W.)—947
McGinnis, C. L. Disintegration of In^{117}—780(A)
McGowan, F. K. (see Sheline, Raymond K.)—1642
McIntyre, J. A., B. Hahn, and R. Hofstadter. Inelastic scattering of 190-Mev electrons in Be—1084(L)
McKay, K. G. Avalanche breakdown in Si—877; 1437(T)
McKelvey, J. P. and R. L. Longini. Volume and surface recombination rates in Ge—750(A)
McKeown, Marilyn (see Frazer, B. C.)—1435(A)
McKeown, Michael and Seymour Katcoff. Radiations of 53-min I^{134} and 86-sec I^{136}—965
—— (see McReynolds, A. W.)—1417(A)
—— (see Mihelich, J. W.)—794(A)
McLaughlin, Ralph D. (see Conway, John G.)—498(L)
McLean, E. A. and Waller George. Nucleation of fracture origins—761(A)
—— **and Waller George.** Size effects found in nucleation of fracture origins—1428(A)
McLernon, F. (see Bay, Z.)—780(A)
McMaster, W. H. and F. L. Hereford. Angular distribution of photoelectrons—757(A)
McReynolds, A. W., W. Augustyniak, M. McKeown, and D. B. Rosenblatt. Neutron irradiation effects at low temperature—Cu and Al—1417(A)
—— (see Riste, T.)—1433(A)
Mech, J. F. (see Diamond, H.)—1083(L)
—— (see Fields, P. R.)—209(L)
—— (see Stevens, C. M.)—974
Meechan, C. J. and R. R. Eggleston. Formation energy of vacancies in Au—1406(A)
Meem, J. L. Measurement of energy released per fission in Bulk Shielding Reactor—759(A)
Meers, J. T. (see Palmatier, E. D.)—766(A)
Melchor, J. L. and A. A. Petrauskas. Ultrasonic properties of Hycar OS-10 and Paracril 35—1414(A)
Melkonian, E. and W. W. Havens, Jr. Calculation of effect of finite resolution on neutron transmission near resonance—790(A)
Mellor, G. P. (see Fowler, C. M.)—1082(L)
Melnick, Donald A. Photoconduction of ZnO semiconductor: oxygen adsorption process—1438(A)
Mendlowitz, H. and K. M. Case. Double scattering of electrons with magnetic perturbation—1436(A)
Menes, M. and L. H. Fisher. Positive point-to-plane corona studies in air—1
Merritt, F. R. (see Fletcher, R. C.)—1392(L)
Meshkov, Sydney. d^3 and d^4 configurations of V—761(A)
—— **and C. W. Ufford.** Complete Bacher and Goudsmit method—75
—— (see Ufford, C. W.)—761(A)
Mesrobian, Robert B., Paul Ander, David S. Ballantine, and G. J. Dienes. γ-ray polymerization of acrylamide in solid state—1413(A)
Metropolis, Nicholas (see Kilpatrick, John E.)—1103
Metzger, F. R. and W. B. Todd. Resonance fluorescence with nuclei: Hg^{199}—794(A)
Meyer, D. I. and F. H. Schmidt. Precise momentum measurement of F line of Th B—927
Mezzetti, L. (see Keuffel, J. W.)—797(A)
Mifsud, J. F. Absorption of ultrasonic waves in liquids under pressure—812(A)
Mihelich, J. W., Gertrude Scharff-Goldhaber, and Michael McKeown. Decay scheme of 5.5-hr isomer of Hf^{180m}—794(A)
—— (see Tomlinson, E. P.)—794(A)
Miller, Charles E., Joseph E. Henderson, Gerald R. Garrison, David S. Potter, Wayne M. Sandstrom, and Jay Todd, Jr. Cosmic-ray protons at 3.4 km—167
Miller, Glenn H. (see Herwig, Lloyd O.)—1183
Miller, J. M. and F. A. Matsen. Molecular-wave-functions in e-notation—804(A)
—— (see Friedlander, G.)—727(L); 775(A)
Miller, John D. (see Annis, Martin)—1038
Miller, S. C., Jr. Normalization of WKB-type approximation—1345
Millett, Walter E. Decay of positrons in superconducting Pb—809(A)
Milton, J. C. D. (see Fraser, J. S.)—795(A)
Mingins, Charles R., Robert W. Perry, and Albert D. Frost. Effects of stepped surfaces on motional parameters of piezoelectric filter plates—770(A)
Minton, George H. Lifetime for annihilation of positrons in Al and Pb—758(A)
Miskel, J. A. and M. L. Perlman. Double vacancies in K shell associated with K-electron capture in A^{37}—1683
Mitchell, A. C. G. Recent advances in nuclear spectroscopy—803(T)
Mitchell, Allan C. G. (see Caird, Robert S.)—412
—— (see Caird, R. S.)—780(A)
Mitchell, Dean L., Werner J. Beyen, and Donald E. Bode. Current oscillations in photoconductive films of PbTe—1430(A)
Mitchell, R. W. and Melvin Eisner. Nuclear resonance absorption in weak, homogeneous fields—811(A)
Mittelman, Phillip S. Decay scheme of Zr^{93}—99
Mize, J. P. (see Bunker, M. E.)—1694
Mizushima, Masataka. Theory of hfs of NO molecule—569; 789(A)
Moak, C. D. (see Good, W. M.)—87
Mobley, R. C. (see Patterson, J. R.)—774(A)
Moffat, R. D. (see Bittner, J. W.)—769(A)
—— (see Haberle, W.)—769(A)
Mohler, Fred L. (see Dibeler, Vernon H.)—754(A)

Monahan, J. E. (see Church, E. L.)—762(A)
Montalenti, G. (see Bonfiglioli, G.)—316
Montgomery, D. J. (see Hersh, S. P.)—1413(A)
Moran, Norma B. (see Nielsen, J. Rud)—805(A)
Morgan, I. L. (see Spearman, K. R.)—806(A)
Morin, F. J. and J. P. Maita. Conductivity and Hall effect in intrinsic range of Ge—1525
—— (see Pearson, G. L.)—750(A)
Morrison, Philip, Stanislaw Olbert, and Bruno Rossi. Origin of cosmic rays—440
H. E. Moses. Determination of perturbation from scattering operator—1442(A)
Moyer, Burton J. (see Frank, Wilson J.)—1716
Mozley, R. F. (see Bichsel, H.)—764(A)
Mrowca, B. A. (see Honnold, V. R.)—1414(A)
Mrozowski, S. and A. Chaberski. Hall effect and magnetoresistivity in carbons—1427(A)
—— (see Andrew, J. F.)—1438(A)
Murray, B. B. and J. D. Kurbatov. Disintegration of As^{74}—780(A)
Murray, P. C., R. I. Scace, R. O. Haxby, and T. R. Palfrey, Jr. Photoprotons from 300-Mev bremsstrahlung—764(A)

Nagamatsu, H. T. Recent galcit hypersonic experimental investigations—763(T)
Nakagawa, Y. (see Fultz, D.)—1471
Nambu, Yoichiro (see Kinoshita, Toichiro)—598
Nanda, V. S. Heat of mixing of He^3 and He^4 solutions—241
Naugle, J. E. (see Anderson, G. W.)—1317
—— (see Freier, P. S.)—677
Naumann, R. A. 10.5-day isotope of Pt—794(A)
—— (see Tomlinson, E. P.)—794(A)
Neamtan, S. M. Quantum mechanical definition of refractive index—327
Nedzel, V. Alexander. Total cross sections for 410-Mev neutrons—174
Neighbours, John R. and Charles S. Smith. Elastic constants of Cu alloys—1421(A)
Nelson, E. B. (see Carlson, R. R.)—1311
Nereson, Norris. Survey of average total neutron cross sections in 3–12 Mev region—806(T)
—— **and Sperry Darden.** Average neutron total cross sections in 3- to 12-Mev region—1678
Nesbitt, E. A., H. J. Williams, and R. M. Bozorth. Factors determining permanent magnet properties of single crystals of Fe_2NiAl—1440(A)
Neufeld, Jacob. Bohr's theory of energy losses of moving charged particles—792(A)
—— (see Snyder, W. S.)—760(A)
Neuman, Maurice (see Lepore, Joseph V.)—788(A)
Newman, E. and W. L. Alford. Angular distribution of α particles from (p,α) reactions—748(A)
—— (see Cohen, B. L.)—620
Newman, Roger. Photoconductivity in Au-doped Si—1530
—— Photoconductivity in Au-Ge alloys—278
—— **and W. W. Tyler.** Photoconduction in Fe-, Co-, and Ni-doped Ge—1419(A)
—— (see Tyler, W. W.)—1419(A)
Newson, Henry W. and Robert H. Rohrer. Shell effects in highly excited nuclei—654
——, **R. M. Williamson, A. L. Toller, and P. F. Nichols.** Total neutron cross sections in kev region: Se, Br, Y, I, and Cs—774(A)
—— (see Patterson, J. R.)—774(A)
Newton, Roger G. Applications of mass operator in quantum electrodynamics—1773
—— Radiative corrections to electron scattering—788(A)
Nicholls, R. W., P. A. Fraser, R. G. Turner, and W. R. Jarmain. Intensities, electronic transition moments, and vibrational transition probabilities of diatomic molecules—1423(A)
Nichols, M. H. Growth and surface properties of Ta crystals—309
Nichols, P. F. (see Newson, H. W.)—774(A)
Nichols, R. T. and E. N. Jensen. Radioisotope P^{33}—369
Nicolai, V. O. and E. L. Goldwasser. Photodisintegration of He above meson threshold—755(A)
Nielsen, H. H. (see Dalby, F. W.)—1423(A)
Nielsen, J. Rud, H. H. Claassen, and Norma B. Moran. Infrared and Raman spectra of fluorinated ethanes. VIII. CF_3CF_2H—805(A)
—— (see Collins, R. L.)—805(A)
—— (see El-Sabban, M. Z.)—805(A)
Nielsen, John P. Origin of recrystallization nuclei—1428(A)
Nielsen, Lawrence E. Effect of crystallinity on dynamic mechanical properties of polyethylenes—1414(A)
—— (see Buchdahl, Rolf)—1414(A)
Nier, Alfred O. (see Collins, T. L.)—398
Nierenberg, W. A. (see Bemski, G.)—767(A)
Nine, H. (see Cork, J. M.)—1218
Nix, F. C. (see Berkowitz, A. E.)—1407(A)
—— (see Folen, V. J.)—1407(A); 1432(A)
Nobles, R. (see Henkel, R. L.)—141
Noland, James A. Optical absorption of single-crystal $SrTiO_3$—724(L)
Nolle, A. W. Effect of hydrostatic pressure in two-state model of compressional relaxation in liquids—812(A)
Norberg, R. E. Nuclear magnetic resonance in alkali metals—1416(T)
Nowick, A. S. Interpretation of recovery phenomena in cold-worked metals—760(A)
—— (see Damask, A. C.)—1421(A)
Noyes, H. P. and A. E. Woodruff. Phenomenology of pion-nucleon S waves—1401(L)
Nozick, Seymour. Writing speed and tonal range of dark trace tubes—778(A)
Nussbaum, Allen. Electrical properties of pure Te and Te-Se alloys—337

O'Brien, Vivian (see Kistler, Alan)—783(A)
Odian, A. (see Feld, B. T.)—1000
Ogg, Richard A., Jr. Nuclear magnetic resonance as criterion of chemical bonding—767(A)
—— (see Kelly, John)—767(A)
Okamura, Tosihiko and Muneyuki Date. Paramagnetic resonance of Cu complex salts—314
Olbert, Stanislaw (see Morrison, Philip)—440
Olson, Elmer L. (see Cohen, B. L.)—953
—— (see Handley, Thomas H.)—968
Ord-Smith, R. J. Symmetry relations of 12-j symbol—1227
Oriani, R. A. Thermodynamics of ordering alloys, II. Ordered and disordered solid solutions of Au and Cu system—760(A)
Orvis, A. L. and M. M. D. Williams. Coincidences in scintillation counter—810(A)
Osborne, Darrell W., Bernard M. Abraham, and Bernard Weinstock. Heat capacity and entropy of liquid He^3 from 0.42°K to 1.06°K—202(L)
Osborne, L. S. (see De-Saussure, G.)—756(A)
—— (see Hill, R. D.)—797(A)
Osborne, R. N. (see Lindner, M.)—1323
Oser, A. W., Jr. (see Peacock, C. L.)—372; 804(A)
Otter, F. A. (see Domenicali, C. A.)—1421(A)
Overhauser, Albert W. Polarization of nuclei in metals by magnetic resonance—768(T)
—— Stored energy in irradiated Cu—1432(T)
—— Stored energy measurements in irradiated Cu—1551

Padgett, D. W. (see Caswell, R. S.)—786(A)
Page, Lorne A. (see Ashkin, Arthur)—357
Pai, Shih I. Stability of vortex sheet in inviscid compressible fluid—782(A)

Pake, G. E. (see Lloyd, J. P.)—579
Palevsky, H., R. S. Carter, R. M. Eisberg, and D. J. Hughes. Neutron absorption cross section of U^{235} at 2200 m/sec—1088(L)
Palfrey, T. R., Jr. (see Murray, P. C.)—764(A) 257; 1801(E)
Palmatier, E. D., J. T. Meers, and C. M. Askey. Density effect for ionization energy losses in gases—766(A)
Pandya, S. P. Classical scattering of mesons—1037
Pape, Leon (see Holmes, John R.)—902
Pappis, J. (see Bickford, L. R., Jr.)—1433(A)
Parker, E. N. Tensor virial equations—1441(A)
Parkinson, W. C. Recent experimental results from stripping reactions—1436(T)
Parratt, L. G. and C. F. Hempstead. Anomalous dispersion and scattering of x-rays—1593
Parzen, Philip. Energy equation for sinusoidal solutions of Maxwell's equations with electron beams—793(A)
Patterson, J. R., H. W. Newson, R. C. Mobley, and T. E. Gilmer. Total neutron cross sections in kev region: Li, F, Cl, Sc, Rb, Mo, Ag, and Ta—774(A)
Paul, E. B., H. E. Gove, G. A. Bartholomew, and A. E. Litherland. Partial widths for reactions $Al^{27}(p,\gamma)Si^{28}$ and $Al^{27}(p,p')Al^{27}$—749(A)
—— (see Gove, H. E.)—749(A)
Paul, William, G. B. Benedek, and H. Brooks. Pressure dependence of Hall effect in Ge—1415(A)
—— **and Harvey Brooks.** Pressure dependence of resistivity of Ge—1128
Payne, Wilbur B. (see Goodrich, Max)—405
Peacock, C. L., A. W. Oser, and J. F. Quin. Disintegration of La^{140}—804(A)
——, **J. F. Quin, and A. W. Oser, Jr.** Radiations of La^{140}—372
Pearlman, N. (see Fagen, E.)—1415(A)
Pearlstein, Edgar. Change of electrical conductivity of alkali halides upon irradiation with 350-Mev protons—1409(A)
Pearson, G. L., W. T. Read, Jr., and F. J. Morin. Electrical properties of dislocations in plastically deformed Ge—750(A)
—— (see Fletcher, R. C.)—1392(L)
Peaslee, D. C. Pion production ratios—1085(L)
—— (see King, R. W.)—795(A); 1284
Pegram, G. B. Physics at Columbia University: early years—776(T)
Penning, J. R. and F. H. Schmidt. β spectra of O^{14}—779(A)
Pepinsky, Ray. X-ray and neutron diffraction investigations on ferroelectric crystal transitions—1408(T)
—— (see Frazer, B. C.)—1435(A)
—— (see Jona, F.)—1408(A)
—— (see Vand, V.)—1435(A)
Pepper, R., E. Klontz, K. Lark-Horovitz, and J. MacKay. Hall and resistivity measurements during electron bombardment of Ge and In-Sb—1410(A)
Percus, Jerome K. and George J. Yevick. New approach to classical and quantum theory of many interacting particles. II—787(A)
—— (see Yevick, George J.)—787(A)
Perlman, I. Nuclear spectroscopic states deduced from α decay—803(T)
—— (see Asaro, Frank)—381
—— (see Levy, Harris B.)—152
Perlman, M. L. (see Miskel, J. A.)—1683
Perry, J. E. (see Henkel, R. L.)—141
Perry, Leo F. (see Venable, Douglas)—784(A)
Perry, Robert W. (see Mingins, Charles R.)—770(A)
Peterson, R. W., C. A. Barnes, W. A. Fowler, and C. C. Lauritsen. Low excited states of F^{19}. I. Proton inelastic scattering—1075(L)
Petrauskas, A. A. (see Melchor, J. L.)—1414(A)
Petritz, R. L., W. W. Scanlon, and F. L. Lummis. Mobility and mean free path of electrons and holes in PbS crystals—1430(A)
Pevsner, Aihud, James Rainwater, Ross Williams, and Seymour J. Lindenbaum. Elastic scattering of 80-Mev π mesons on Al—765(A)
—— (see Hill, R. D.)—797(A)
—— (see Williams, Ross)—765(A)
Phibbs, E. (see Horton, G. K.)—1402(L)
Philipp, H. R. Photoelectric emission from BaO—777(A)
Phillips, G. C. (see Gossett, C. R.)—807(A)
—— (see Reich, C. W.)—804(A)
—— (see Russell, J., Jr.)—804(A)
—— (see Windham, Pat M.)—803(A)
Phillips, J. A. Equilibrium charge-exchange ratios for low-energy protons—806(T)
Pickart, Stanley J. (see Maxwell, Louis R.)—1433(A)
Picus, Gerald S. Film flow in liquid He II at low level differences—1459
Pidd, R. W. (see Louisell, W. H.)—7
Pinnick, H. T. Magnetic susceptibility of carbons and polycrystalline graphites—319
Piper, William W. and Ferd E. Williams. Theory of electroluminescence of ZnS crystals—777(A)
Placzek, G. Scattering of neutrons by systems of heavy nuclei—1801(E)
Plaskett, J. S. Peculiarity of electron density near impurity in metal and its effect on x-ray spectra—1420(A)
Plass, Gilbert N. (see Fivel, Daniel I.)—752(A)
Pletcher, David W. (see Hobbs, Lindsey M.)—1412(A)
Plint, C. A., R. M. B. Small, and H. L. Welsh. Density effects in Raman spectrum of ammonia—805(A)
Plyler, Earle K. (see Allen, Harry C., Jr.)—1423(A)
Pomerantz, M. A. (see Shatas, R. A.)—757(A)
Pomerantz, W. A. Cosmic radiation at very high altitudes near geomagnetic equator—796(A)
Pond, T. A. Annihilation of positrons in condensed materials—758(A)
Potter, David S. (see Miller, Chares E.)—167
Powell, W. M. Neutron-proton scattering cross sections at high energies—786(T)
Power, E. A. Nonadiabatic corrections to scalar theory—1442(A)
Pratt, William W. Some (d,p) reactions in Ni and statistical theory of nuclear reactions—1086(L)
Preston, R. S. (see Fowler, E. C.)—791(A)
Price, P. J. Density fluctuations at low temperatures—257; 1801(E)
Prud'homme, J. T. (see Little, R. N., Jr.)—807(A)
Purcell, E. M. (see Carr, H. Y.)—630

Quin, J. F. (see Peacock, C. L.)—372
—— (see Peacock, C. L.)—804(A)

Rabi, I. I. Physics at Columbia University: recent years—776(T)
Rado, G. T. and J. R. Weertman. Exchange interactions in spin wave resonance—1411(A)
—— **and J. R. Weertman.** Observation of exchange interaction effects in ferromagnetics by spin wave resonance—1386(L)
—— (see Ament, W. S.)—1411(A)
Rainwater, James. Nuclear size from mesonic atoms—773(T)
—— (see Pevsner, Aihud)—765(A)
—— (see Williams, Ross)—765(A)
Ralph, D. C. (see Campbell, R. C.)—791(A)
Ramsey, N. F. Rotational reorientation spectra of molecular hydrogen and deuterium—751(T)
—— (see Barnes, R. G.)—893
—— (see Kruse, U. E.)—1795(L)
Randall, H. M. Early days of infrared spectroscopy at University of Michigan—1426(T)

Rank, D. H., J. N. Shearer, and T. A. Wiggins. Precision determination of velocity of light derived from band spectrum method. II—575
Rappaport, P. Minority carrier lifetime in semiconductors as sensitive indicator of radiation damage—1409(A)
Rasetti, F. (see Madansky, L.)—407
Rasor, N. S. (see Hoffman, R. W.)—1406(A)
Rawer, K. and E. Argence. Origin of ionospheric *E* layer—253
Rawson, E. B. (see Beringer, Robert)—343
Ray, James (see Kelly, John)—767(A)
Rayburn, L. A., D. L. Lafferty, and T. M. Hahn. Energy levels of Cu from inelastic neutron scattering—1641
Read, T. A., M. S. Wechsler, and D. S. Lieberman. Experimental studies of diffusionless cubic—tetragonal phase changes—759(A)
—— (see Lieberman, D. S.)—760(A)
—— (see Wechsler, M. S.)—759(A)
Read, W. T. (see Fletcher, R. C.)—1392(L)
—— (see Pearson, G. L.)—750(A)
—— (see Vogel, F. L.)—1791(L)
Redfield, Alfred G. Electronic Hall effect in alkali halides—537
—— Electronic Hall effect in diamond—526
Reich, C. W., J. Russell, and G. C. Phillips. Differential pumping system for gas targets—804(A)
—— (see Russell, J., Jr.)—804(A)
Reiffel, L. Pressure effects in phosphorescence—856
Reines, F. (see Cowan, C. L., Jr.)—751(T)
Reitz, R. A. (see Whalin, E. A.)—752(A)
Reynolds, George T. and S. B. Treiman. Kinematics of Λ^0 production—207(L); 797(A)
Reynolds, H. L. (see Scott, D. W.)—810(A)
—— (see Zucker, A.)—748(A)
Reynolds, J. M. Periodic Hall effect at low temperatures—803(T)
Ribe, F. L. and J. D. Seagrave. Pickup reactions $B^{10}(n,d)Be^9$ for 14-Mev neutrons—934
Richards, H. T. (see Jones, K. W.)—947
Richards, J. D. (see Brentano, J. C. M.)—1427(A)
Richardson, J. Reginald (see Caldwell, David O.)—79
Richings, H. J. (see DeBenedetti, S.)—766(A)
Rickard, James A. and Emmett L. Hudspeth. Excitation function and *Q* value for $C^{14}(d,p)C^{15}$—806(A)
Riddell, R. J., Jr., and Burton D. Fried. Meson-nucleon scattering. I—745(A); 1736
—— (see Fried, Burton D.)—746(A)
Risser, J. R. and H. C. Allen, Jr. NaI γ-ray spectrometry techniques applied to outlining of brain tumors—810(A)
—— (see Duller, N. M.)—810(A)
—— (see Thompson, L. C.)—941
Riste, T. and A. W. McReynolds. Magnetic neutron diffraction in Fe_3O_4—1433(A)
Ritland, H. N. Relation between refractive index and density in glass—1434(A)
Ritson, D. M. (see Hill, R. D.)—797(A)
Rittner, Edmund S. Extension of theory of junction transistor—1161
—— Review of interface compound formation in oxide cathodes—790(T)
Roberts, A. and J. Tinlot. Angular distribution of π^--proton charge exchange scattering at 40 Mev. I. Apparatus—766(A)
—— (see Tinlot, J.)—766(A)
Roberts, J. E. (see Farwell, G. W.)—363
Roberts, L. D. (see Bernstein, S.)—1243
—— (see Wilkinson, M. K.)—772(A)
Robinson, W. H., Yin-Yuan Li, and R. Smoluchowski. Small-angle scattering of x-rays by irradiated diamond—1435(A)
Rodeback, G. W. Imperfections in Cu in terms of electrical resistivity and thermoelectric power—1406(A)
Roesch, William C. Age-diffusion theory for β-ray problems—779(A)
Roever, William L. (see Ginzbarg, Arthur S.)—812(A)
Rohrer, Robert H. (see Newson, Henry W.)—654
Rohrlich, F. (see Chase, D. M.)—81
Rollier, Mario A. and Einar Saeland. Half-life and β decay of long-lived Nb^{94}—1079(L)
Rollwitz, William L. Analysis of phase detectors for display of nuclear magnetic resonance signals—810(A)
Rorden, H. C. (see Wegel, R. L.)—782(A)
Rorschach, H. E., Jr. (see Swim, R. T.)—809(A)
Rosa, G. (see Bonfiglioli, G.)—316
Rosenblatt, D. B., R. Smoluchowski, and G. J. Dienes. Radiation-induced changes in electrical resistivity of α brass—1417(A)
—— (see McReynolds, A. W.)—1417(A)
Ross, Donald. Unnecessary, restrictive concept in turbulent boundary layer theory—783(A)
Ross, Marc. Connection between pion photoproduction and scattering phase shifts—454
Rossi, Bruno (see Morrison, Philip)—440
Rostoker, N. (see Kohn, W.)—1111
Rothman, M. A., H. S. Hans, and C. E. Mandeville. γ rays excited by inelastic scattering of fast neutrons in Bi, Ni, and Cu—791(A)
Rothstein, Jerome. Application of bimolecular kinetics to relaxation of order below Curie point—1429(A)
—— Application of group theory to statistical mechanics—792(A)
Rough, J. D. (see Dunnington, F. G.)—592
Ruderman, M. A. and H. Brown. Classical theory of high-energy processes—746(A)
Ruhlig, Arthur J. (see Graham, Walter J.)—25
Rumsey, V. H. Reaction concept in electromagnetic theory—1483
Russell, J., Jr., C. W. Reich, and G. C. Phillips. Large volume scattering chamber for angular distribution experiments—804(A)
—— (see Reich, C. W.)—804(A)
Russell, R. D. (see Shillibeer, H. A.)—1793(L)
Russell, R. K. Vibrational analysis of 3400–4000A absorption spectrum of SO_2—805(A)
Rustad, B. M. Electron-neutrino angular-correlation coefficient in decay of He^6—751(T)

Sack, H. S., T. R. Cuykendall, and T. J. Woods. Elastic and dielectric losses of some high polymers near and below second-order transition temperature—1414(A)
—— (see Cuykendall, T. R.)—1421(A)
—— (see Marvin, Robert S.)—1413(A)
Sadauskis, John (see Jesse, William P.)—764(A)
Saeland, Einar (see Rollier, Mario A.)—1079(L)
Sagalyn, Paul L. Hfs of $3P_{3/2}$ state of Na^{23}—885
Sagane, Ryokichi and Walter F. Dudziak. π^+/π^- ratios at low energies from complex nuclei—755(A)
Sakai, M., J. Dick, and J. D. Kurbatov. Disintegration of Co^{58}—779(A)
Salam, Abdus (see Matthews, P. T)—185
Salant, E. O. (see Hill, R. D.)—1794(L); 797(A)
Salkovitz, Edward I. and Paul L. Smith. X-ray study of prismatic punching in TlCl—770(A)
Salter, L. Simon melting equation and effective intermolecular potential—1434(A)
Salutsky, Murrell L. (see Kirby, H. W.)—1801(E)
Sampson, J. B. (see Tucker, C. W., Jr.)—1418(A)
Samuels, Arthur (see Turkevich, Anthony)—364
Sandstrom, Wayne M. (see Miller, Charles E.)—167
Saraf, Babulal. Inner bremsstrahlung in Cs^{131}—642; 793(A)
Satchler, G. R. Angular correlation of 3 nuclear radiations—1304

Satten, R. A. (see Jaccarino, V.)—1798(L)
Sawatzky, A. (see Jaumot, F. E., Jr.)—1429(A)
Saxon, David S. (see Gerjuoy, E.)—1445; 478
Scace, R. I. (see Murray, P. C.)—764(A)
Scanlon, W. W. and R. F. Brebrick. Preparation of PbS crystals of controlled electrical properties—1430(A)
—— (see Brebrick, R. F.)—1430(A)
—— (see Petritz, R. L.)—1430(A)
Schamp, H. W., Jr., and E. Katz. Self-diffusion and ionic conductivity in NaBr—828
Scharff-Goldhaber, Gertrude (see Mihelich, J. W.)—794(A)
Schawlow, A. L. (see Gunther-Mohr, G. R.)—1184
Schecter, Larry and Warren Heckrotte. Correction to deuteron stripping cross sections—1086(L)
Schein, Marcel (see Sprague, A. D.)—994
Schensted, Craige. Electromagnetic scattering by paraboloid of revolution—793(A)
Scherb, F. (see Feld, B. T.)—1000
Scherrer, V. E., B. A. Allison, and W. R. Faust. γ-γ coincidences from interaction of 3.1-Mev neutrons with various materials—791(A)
Schiessler, R. W. (see Webb, W.)—753(A)
Schindler, A. I. Hall effect of Pd-Ag alloy system—1422(A)
Schmid, L. C. (see Cork, J. M.)—1218
Schmidt, F. H. (see Meyer, D. I.)—927
—— (see Penning, J. R.)—779(A)
Schneider, E. E. Microwave resonance in color centers—768(T)
—— (see Hesketh, R. V.)—494(L)
Schrieffer, J. Robert. Effective carrier mobility in surface well—1420(A)
Schriever, Barbara Dwight, E. A. Whalin, and A. O. Hanson. Photodisintegration of deuterium by 60-280 Mev x-rays—763(A)
Schulten, R. and R. A. Ferrell. Nuclear shell model *ft* values for intermediate coupling—739(L)
Schulz, L. G. Effective mass of conduction electrons in Ag, Au, and Cu—1422(A)
Schupp, Fritz D. and Don S. Martin, Jr. $Mg^{24}(\gamma,3p3n)F^{18}$ reaction induced by 70-Mev bremsstrahlung—80
Schwartz, C. Ground states of odd-odd nuclei—95
—— **and A. de-Shalit.** Many-particle configurations in central field—1257
Schwartz, Robert M. 3-dimensional calculation of vibrational relaxation times in gases—793(A)
—— **and J. Eckerman.** Real gas effects by measurement of shock detachment distance—1441(A)
Schwarzer, D. (see Fireman, E. L.)—385
Schweber, S. S. Covariant formulation of Tamm-Dancoff method—1089(L)
Schwinger, Julian. Theory of quantized fields—1362
Sclar, N. (see Burstein, E.)—750(A)
Scott, D. W., H. L. Reynolds, and A. Zucker. Range and charge of energetic nitrogen ions in Ni—810(A)
Scott, M. B., A. O. Hanson, and D. W. Kerst. Electrodisintegration of Cu^{63}—763(A)
Seagrave, J. D. (see Ribe, F. L.)—934
Secrest, E. L. (see Smith, D. M.)—806(A)
Segrè, Emilio and Clyde Weigand. Energy spectrum of spontaneous fission fragments—157
—— (see Chamberlain, O.)—156
Seitz, Frederick. Nature of lattice defects in metals—1406(A)
—— Theory of radiation damage—1432(T)
Sellers, P. A., C. M. Stevens, and M. H. Studier. Half-life of U^{232}—952
—— (see Stevens, C. M.)—974
Serber, R. L. Interpretation of high-energy experiments—745(T)
Sessler, A. M. and H. M. Foley. Interaction current contribution to hfs of tritium—761(A)
Severiens, J. C. and C. S. Fuller. Mobility of impurity ions in Ge and Si—750(A)
Shapiro, A. M. (see Chen, F. F.)—784(A)
Sharp, W. T., H. Gellman, and G. E. Tauber. Intermediate coupling in B^{10}—762(A)
Shatas, R. A., J. F. Marshall, and M. A. Pomerantz. Energy distribution of secondary electrons produced by 1.3-Mev primary electrons—757(A)
Shaw, C. H. (see Gordon, W. L.)—771(A)
—— (see Spielberg, N.)—752(A)
Shearer, J. N. (see Rank, D. H.)—575
Sheer, C., A. Zinn, and N. Hartmann. Variable Hg delay line equipment for measurement of short half-lives—769(A)
Sheline, Raymond K., Noah R. Johnson, P. R. Bell, R. C. Davis, and F. K. McGowan. Study of isobaric triplet Mg^{28}-Al^{28}-Si^{28}—1642
—— **and Joseph R. Wilkinson.** Nuclide V^{53}—729(L)
Sherr, R., C. W. Li, and R. F. Christy. Low excited states of F^{19}. III. Coulomb excitation by α particles—1076(L)
—— (see Gerhart, J. B.)—917
Sherwood, J. E., T. E. Stephenson, C. P. Stanford, and Seymour Bernstein. Stern-Gerlach experiment on polarized neutrons—791(A)
Sherwood, R. C. (see Bozorth, R. M.)—1439(A)
Shillibeer, H. A., R. D. Russell, R. M. Farquhar, and E. A. W. Jones. Radiogenic A measurements—1793(L)
Shirane, R. (see Jona, F.)—1408(A)
Shockley, W. (see van Roosbroeck, W.)—1558
Shreffler, Robert G. (see Christian, Russell H.)—783(A)
Shull, C. G. and M. K. Wilkinson. Small-angle neutron scattering by Fe at high temperatures—1439(A)
—— (see Wilkinson, M. K.)—1439(A); 772(A)
Shutt, R. P. Heavy unstable particles and multiple meson production observed in cloud chamber at cosmotron—745(T)
Shuttleworth, R. A. and B. C. Bradshaw. Mechanism of adsorption. II. Application—753(A)
—— (see Bradshaw, B. C.)—753(A)
Siegel, R. T. (see DeBenedetti, S.)—955
Silsbee, H. B. (see Bemski, G.)—767(A)
Silver, E. G. and R. W. Waniek. Use of wires embedded in nuclear emulsions to investigate reactions induced by high-energy neutrons—769(A)
Silverman, A. (see Wolfe, B.)—756(A)
Silverman, Searl J. and H. Levinstein. Electrical properties of single crystals and thin films of PbSe and PbTe—871
—— **and Henry Levinstein.** Electrical properties of single crystals and thin films of PbTe—1430(A)
Silverman, Shirleigh (see Benedict, W. S.)—752(A)
—— (see Herman, R. C.)—752(A)
Silvey, G. (see Aamodt, L. C.)—789(A)
Simmons, B. E. (see Holmgren, H. D.)—748(A)
Simon, A. and T. A. Welton. Polarization from isolated resonances—943
Simpson, J. A. Cosmic radiation intensity-time variations and their origin. III. The origin of 27-day variations—426
—— (see Firor, J. W.)—1031
Singer, S. E., W. S. Emmerich, and J. D. Kurbatov. Radiative electron capture in Fe^{55}, A^{37}, and Ni^{59}—779(A)
—— (see Emmerich, W. S.)—113
Singwi, K. S. and B. M. Udgaonkar. Polaron self-energy and Bloch-Nordsieck method—38
Sinha, M. S. (see Biswas, N. N.)—1400(L)
Sitte, Kurt, Don L. Stierwalt, and Irving L. Kofsky. Development of air showers in atmosphere—988
—— (see Kasnitz, Harold L.)—977
Skinner, Selby M. Contact potential, work function, and surface states—1428(A)
Slater, J. C. and G. F. Koster. Simplified LCAO method for periodic potential problem—1498

—— (see Koster, G. F.)—1392(L)
Slifkin, L. (see Tomizuka, C. T.)—1406(A)
Small, R. M. B. (see Plint, C. A.)—805(A)
Smaller, Bernard, Max S. Matheson, and Edward L. Yasaitis. Paramagnetic resonance in irradiated ice—202(L)
Smart, J. Samuel. Cation distributions in mixed ferrites—847
Smiley, E. F. Measurements of vibrational relaxation times in Cl_2 and Cl_2-He mixtures—1441(A)
Smith, Alan W. and John Turkevich. Effect of neutron bombardment on ZnS phosphor—857
—— Effect of radiation damage on thermal conductivity of graphite—1417(A)
Smith, B. and H. A. Boorse. Role of substrate and surface finish in He II film transport—772(A)
Smith, Charles S. Piezoresistance effect in Ge and Si—42
—— (see Neighbours, John R.)—1421(A)
Smith, Cyril Stanley. Properties of plutonium metal—1068(L)
Smith, D. M. and E. L. Secrest. Variation wave function for Na—806(A)
Smith, George F. Thermionic and surface properties of W crystals—295
Smith, H. L. and J. A. Kies. Energy to create fracture surfaces in glass—760(A)
—— (see Kies, J. A.)—760(A)
Smith, J. A., J. N. Cooper, and J. C. Harris. γ-ray energies from Al^{27} and S^{32}—749(A)
Smith, J. F. Electrostatic energy calculations for sodium tungsten bronze (Na_xWO_3)—1407(A)
Smith, L. W. (see Hill, D. A.)—791(A)
—— (see Snow, G. A.)—791(A)
Smith, Paul L. (see Salkovitz, Edward I.)—770(A)
Smith, R. L., F. E. Jaumot, Jr., and L. A. Arné, Jr. Comparison of diffusion techniques employing radioisotopes—1407(A)
Smith, Robert S. Dielectric constants of powders at uhf—1438(A)
Smith, W. J., W. J. Leivo, and R. Smoluchowski. Interferometric study of surface of x-ray and proton irradiated KCl crystals—1435(A)
Smoluchowski, R. Influence of nuclear radiation on electrical conductivity of alkali halides—1409(A)
—— Radiation effects in ionic and valence crystals—1432(T)
—— (see Leivo, W.)—771(A)
—— (see Li, Yin-Yuan)—1435(A); 751(A); 866
—— (see Robinson, W. H.)—1435(A)
—— (see Rosenblatt, D. B.)—1417(A)
—— (see Smith, W. J.)—1435(A)
Snow, G. A., T. Coor, D. A. Hill, W. F. Hornyak, and L. W. Smith. Experiments with neutrons from Cosmotron. II—791(A)
——, **R. M. Sternheimer, and C. N. Yang.** Polarization of nucleons elastically scattered from nuclei—1073(L)
—— (see Hill, D. A.)—791(A)
Snowdon, S. C. and W. D. Whitehead. Angular distribution of neutrons scattered from Cd, Sn, and Bi—786(A); 1267
Snyder, W. S. and Jacob Neufeld. Disordering of solids by heavy corpuscular radiation—760(A)
Solimene, N. and B. P. Dailey. Microwave spectrum of 1,1 difluoroethane—789(A)
Solmitz, Frank T. Coulomb effects in pion-proton scattering at relativistic energies—1799(L)
Sosin, A. and J. S. Koehler. Electrical resistivity of cold-worked Al single crystals—1422(A)
Soules, J. A. (see Spielberg, N.)—752(A)
Spearman, K. R., E. L. Hudspeth, and I. L. Morgan. γ-ray spectrum of C^{15} and γ rays from proton bombardment of C^{14}—806(A)
Spedding, F. H. (see Banister, J. R.)—1140
—— (see Elliott, J. F.)—50; 1143
Speisman, G. (see Feynman, R. P.)—500(L)
Spence, R. D. (see Cowen, J. A.)—1411(A)
—— (see Tahsin, Salah)—1442(A)
Spencer, J. W. (see Webb, W.)—753(A)
Sperduto, A. (see Fader, W. J.)—748(A)
Spetner, L. M. Errors in power spectra due to finite sample—778(A)
Spielberg, N., Shaw, C. H., and J. A. Soules. L-emission spectrum of Zr(40)—752(A)
Spiess, Fred Noel. α-emitting isomer: Po^{211}—1292
Spitzer, W. G. (see Johnson, E. J.)—1415(A)
Sprague, A. D., D. M. Haskin, R. G. Glasser, and Marcel Schein. Analysis of 405-Mev proton and 222-Mev negative pion stars—994
Sproull, R. L. Review of electronic processes in BaO crystals—790(T)
Spruch, Larry and G. Goertzel. Magnetic internal Compton coefficients in Born approximation—1671
Spry, W. Charge exchange scattering of negative pions at 42, 30, and 20 Mev in hydrogen—766(A)
Squire, C. F. Effect of pressure on superconductivity—803(T)
—— Solid state at low temperatures: survey of 1953 International Congress on Low Temperature-Physics—1426(T)
St. John, Robert M. and J. G. Winans. Motion of arc cathode spot in magnetic field—1097
Standing, K. G. Angular distribution of deuterons from N^{14}-$(p,d)N^{13}$—731(L)
Stanford, C. P., T. E. Stephenson, L. W. Cochran, and S. Bernstein. Neutron polarization—374
—— (see Bernstein, S.)—1243
—— (see Sherwood, J. E.)—791(A)
Stanford, G. S. (see Foster, B. P.)—804(A)
Starner, J. W. (see Bunker, M. E.)—1694
M. Stearns, M. B. Stearns, S. DeBenedetti, and L. Leipuner. Yields of π- and μ-meson x-rays in low Z materials—766(A)
—— (see DeBenedetti, S.)—766(A)
Stearns, M. B. (see DeBenedetti, S.)—766(A)
—— (see Stearns, M.)—766(A)
Steele, M. C. and J. Babiskin. Magneto-thermoelectric behavior of Bi at liquid He temperatures—1394(L)
Steijn, R. P. and F. J. Donahoe. Resistance studies of phase transformations in Fe-Pt alloys near composition Fe_3Pt—1432(A)
Stein, P. C. (see Feld, B. T.)—1000
Steinberg, E. P. (see Keller, R. N.)—969
Stephenson, T. E. (see Bernstein, S.)—1243
—— (see Sherwood, J. E.)—791(A)
—— (see Stanford, C. P.)—374
Stern, Donald M. (see Ferry, John D.)—1413(A)
Stern, Frank. Spin waves in antiferromagnetic face-centered cubic lattices—1412(A)
Stern, Martin O. (see Chamberlain, Owen)—666
Sternheimer, R. M. (see Snow, G. A.)—1073(L)
Sterzer, Fred and Yardley Beers. Pure quadrupole spectrum of methyl iodide vapor—1410(A)
Stevens, C. M., M. H. Studier, P. R. Fields, J. F. Mech, P. A. Sellers, A. M. Friedman, H. Diamond, and J. R. Huizenga. Cm isotopes 246 and 247 from pile-irradiated plutonium—974
—— (see Diamond, H.)—1083(L)
—— (see Sellers, P. A.)—952
Stevens, D. K., J. W. Cleland, and J. H. Crawford, Jr. Magnetic susceptibility of fast-neutron-bombarded Ge—1409(A)
—— (see Crawford, J. H., Jr.)—1415(A)
Stevenson, D. T. and R. J. Keyes. Measurement of lifetimes and diffusion constants in Ge—1416(A)
Stewart, J. W. and C. A. Swenson. Compressibilities of solid H_2 and D_2 at 4.2°K—772(A)
—— **and C. A. Swenson.** Compression to 10 000 atmos of solid hydrogen and deuterium at 4.2°K—1069(L)
Stierwalt, Don L. (see Sitte, Kurt)—988

Stout, J. W. (see Matarrese, L. M.)—1792(L)
Strandberg, M. W. P. and H. Dreicer. Doppler line width reduction—1393(L)
Strauch, K. and F. Titus. Scattering of 96-Mev protons from light nuclei. II. Angular distribution—785(A)
—— (see Titus, F.)—785(A)
Strauss, A. J. (see Kurnick, S. W.)—1791(L)
Streetman, J. R. and F. A. Matsen. United atom-separated atom treatment of H_3^+—805(A)
Stroke, H. H. (see Jaccarino, V.)—1798(L)
Stuart, R. V. (see Holmgren, H. D.)—748(A)
Stuart, Richard N. (see Lepore, Joseph V.)—1724; 788(A)
Studier, M. H. (see Diamond, H.)—1083(L)
—— (see Fields, P. R.)—209(L)
—— (see Sellers, P. A.)—952
—— (see Stevens, C. M.)—974
Stull, J. L. (see Bickford, L. R., Jr.)—1433(A)
Stump, Robert (see Talley, Harry)—809(A)
Sturm, W. J. (see Binder, D.)—760(A)
Sueoka, Seiichi. Decay of χ meson—1397(L)
Sugarman, Nathan and Anthony Turkevich. Production of Ga, Ge, and As nuclides by 2.2-Bev protons on Cu—775(A)
—— (see Duffield, Robert B.)—776(A)
—— (see Hudis, J.)—775(A)
—— (see Turkevich, Anthony)—728(L)
Sugarman, R. and S. DeBenedetti. Time structure of extensive air showers—796(A)
Suita, T. Dielectric properties of colored KCl crystals—1497
Suits, G. H. Metal-insulator-metal junction—1427(A)
Sutcliffe, C. H. and F. E. Jaumot, Jr. Long-range order in Cu-Au alloys of nonstoichiometric compositions—1429(A)
—— **and F. E. Jaumot, Jr.** Nature of order-disorder transformation in Cu-Au alloys of nonstoichiometric compositions—1429(A)
Sutherland, G. B. B. M. Infrared analysis of structure of large molecules—1426(T)
Swann, C. P. Initial performance of large Bartol Van de Graaff—768(A)
Swenson, C. A. (see Stewart, J. W.)—772(A); 1069(L)
Swim, R. T. and H. E. Rorschach, Jr. Flow of He II under hydrostatic pressure head—809(A)

Tahsin, Salah and R. D. Spence. Propagation of sound pulse in medium with complex elastic modulus—1442(A)
Takeda, G. and K. M. Watson. Polarization of fast protons scattered by nuclei—1087(L)
Talley, Harry and Robert Stump. Lifetime of positrons in superconductors—809(A)
Talley, Robert M. and Dorothy Enright. Optical and electrical measurements on InAs—1431(A)
Tamor, S. Polarization of high-energy protons scattered by complex nuclei—1087(L)
Tanaka, Katsumi (see Hellund, E. J.)—192
Taub, A. H. General relativistic variational principle for perfect fluids—1468
Tauber, G. E. and Ta-You Wu. Magnetic moment of K^{40} in intermediate coupling—762(A); 1307
—— (see Sharp, W. T.)—762(A)
Taylor, Ellison H. (see Livingston, Ralph)—725(L)
Taylor, H. L., O. Lönsjö, and T. W. Bonner. Nonelastic scattering of fast neutrons—807(A)
—— (see McCrary, J. H.)—808(A)
Taylor, T. B. Interpretation of measurements of total cross sections for nuclear scattering of high-energy neutrons—785(A)
Tchen, C. M. 1-dimensional walk with correlation by saturation for description of diffusion phenomena—1442(A)
Teem, J. M. (see Kruse, U. E.)—1795(L)
Temmer, G. M. and N. P. Heydenburg. Coulomb excitation of heavy and medium nuclei by α particles—747(A)
—— **and N. P. Heydenburg.** Rotational nuclear energy levels from Coulomb excitation—1399(L)
—— (see Heydenburg, N. P.)—748(A); 1252
Templeton, Charles C. Thickness of films left on capillary wall during displacement of one fluid by another—812(A)
Templeton, D. H. and E. M. Douthett. Measurement of fission fragment ranges in Al—759(A)
—— (see Douthett, E. M.)—128
Terwilliger, K. M. (see Jones, L. W.)—1436(A)
Teutsch, Werner B. (see Hughes, Vernon W.)—761(A)
Thaler, R. M. and J. Bengston. Phase shift analysis of high-energy nucleon-nucleon scattering experiments—679
——, **J. Bengston, and G. Breit.** Intermediate state coupling and interpretation of high-energy nucleon-nucleon scattering—683
Thirion, J., C. A. Barnes, and C. C. Lauritsen. Low excited states of F^{19}. II. Lifetime measurements—1076(L)
Thirring, W. E. (see Deser, S.)—711; 746(A)
Thompson, L. C. and J. R. Risser. γ rays from inelastic scattering of 14-Mev neutrons in C^{12} and O^{16}—941
Thompson, S. G. (see Choppin, G. R.)—1080(L)
—— (see Ghiorso, A.)—1081(L)
Thorn, R. N. Production of proton pairs—501(L)
Thulin, Sigvard. Decay scheme of Xe^{138}—734(L)
Tinlot, J. and A. Roberts. Angular distribution of π^--proton charge exchange scattering at 40 Mev. II. Analysis of results—766(A)
—— (see Roberts, A.)—766(A)
Titterton, E. W. Low-lying states of Be^8—206(L)
Titus, F. and K. Strauch. Scattering of 96-Mev protons from light nuclei. I. Energy distribution—785(A)
—— (see Strauch, K.)—785(A)
Tobocman, W. Theory of deuteron stripping—762(A)
—— Theory of the (d,p) reaction—1655
Todd, Jay, Jr. (see Miller, Charles E.)—167
Todd, W. B. (see Metzger, F. R.)—794(A)
Toller, A. L. (see Newson, H. W.)—774(A)
Tomboulian, D. H. (see Johnston, R. W.)—1585
Tomizuka, C. T. and L. Slifkin. Diffusion in Ag single crystals—1406(A)
Tomlinson, E. P., R. A. Naumann, and J. W. Mihelich. Decay of Pt^{191}—794(A)
Toupin, R. and M. Lax. Critical temperature and susceptibility of dipole lattices—781(A)
—— (see Lax, M.)—780(A)
Townes, C. H. Nuclear size from x-ray fine structure—773(T)
—— (see Aamodt, L. C.)—789(A)
—— (see Bird, G. R.)—1203
—— (see Gunther-Mohr, G. R.)—1191
—— (see Wang, T. C.)—767(A)
Treiman, S. B. Solar magnetic moment and cosmic-ray effects associated with solar flares—1029
—— (see Reynolds, George T.)—207(L); 797(A)
Truby, Frank K. (see Workman, E. J.)—1073(L)
Trumble, R. E., Jr. (α,n) reactions in Be^9, B^{11}, and C^{13}—748(A)
Tucker, C. W., Jr., and J. B. Sampson. Interstitial content of radiation-damaged metals from precision x-ray lattice parameter measurements—1418(A)
Turkevich, Anthony. Estimation of beam intensity and cross sections at Cosmotron from gross radioactivity in Cu—775(A)
—— **and Arthur Samuels.** Evidence for Si^{32}, long-lived β emitter—364
—— **and Nathan Sugarman.** Ga, Ge, and As nuclides produced in bombardment of Cu with 2.2-Bev protons—728(L)
—— (see Sugarman, Nathan)—775(A)
Turkevich, John (see Smith, Alan W.)—857
Turner, R. G. (see Nicholls, R. W.)—1423(A)

Tweet, Arthur G. Small angle x-ray scattering from liquid He I and liquid He II—1801(E)
Tyler, W. W., H. H. Woodbury, and R. Newman. Properties of Ge doped with Fe or Co—1419(A)
—— (see Newman, R.)—1419(A)

Uberoi, M. S. Effect of wind-tunnel contraction on free stream turbulence—763(T)
Udgaonkar, B. M. (see Singwi, K. S.)—38
Uehling, Edwin A. (see Young, J. A., Jr.)—544
Ueta, Masayasu and Werner Känzig. Effect of plastic flow upon color centers in alkali halide crystals—1390(L)
Ufford, C. W. and S. Meshkov. Complete Bacher and Goudsmit method—761(A)
—— (see Meshkov, Sydney)—75

Vallarta, M. S. Diurnal variation of cosmic radiation—806(T)
van der Leun, C. (see Kluyver, J. C.)—1795(L)
Van der Ziel, A. Noise mechanisms in oxide-coated cathodes—790(T)
Van Horn, David D. and William C. Cooley. Dimensional changes of α brass on dezincification and lattice strain in Cu introduced by vacancies—1418(A)
van Krzywoblocki, M. Z. New approach to theory of turbulence in gases—783(A)
van Lint, V. A. J., C. D. Anderson, E. W. Cowan, R. B. Leighton, and C. M. York, Jr. Cloud-chamber observations of some unusual neutral V particles having light secondaries—1732
van Roosbroeck, W. and W. Shockley. Photo-radiative recombination of electrons and holes in Ge—1558
Van Vleck, J. H. (see Gunther-Mohr, G. R.)—1191
Vand, V. and R. Pepinsky. Evaluation of statistical approach to phase determination in x-ray analysis—1435(A)
Varma, Jagdish. Nuclear energy levels of Tl^{203}—795(A); 1688
—— **and C. E. Mandeville.** Disintegration of Mo^{99}—91
—— (see Mandeville, C. E.)—780(A)
Venable, Douglas and Leo F. Perry. Statistical uncertainties in radiographic determination of gas densities—784(A)
Vilain, J. H. and Robert W. Williams. μ-meson decay spectrum—1011
—— (see Williams, Robert W.)—757(A)
Villars, F. and V. F. Weisskopf. Scattering of electromagnetic waves by turbulent atmospheric fluctuations—232
Vincent, L. D. (see Little, R. N., Jr.)—807(A)
Vineyard, G. H. Small-angle scattering—751(T)
Vogel, F. L., W. T. Read, and L. C. Lovell. Recombination of holes and electrons at lineage boundaries in Ge—1791(L)
Vogt, Erich and Gregory H. Wannier. Quantum mechanics of scattering by a r^{-4} attractive potential—793(A)
Volkov, A. B. Modified shell model of odd-even nuclei—1664
von Dardel, G. F. Interaction of neutrons with moderating materials—1272

Wahl, A. C. (see Farwell, G. W.)—363
Wales, M. (see Leaderman, Herbert)—1414(A)
Walker, J. (see Elliott, L. G.)—795(A)
—— (see Graham, R. L.)—794(A)
Walker, R. M. (see Fowler, E. C.)—791(A)
Walker, W. D. (see Crussard, J.)—736(L)
—— (see Duller, N. M.)—810(A)
—— (see Hill, R. D.)—797(A)
Wall, C. N. Metaphysics of physics teacher—773(T)
Wall, N. S. Deuteron-induced reaction studies—763(A)
Wallenmeyer, W. Study of cloud-chamber distortions—768(A)
Wallis, G. and H. E. Farnsworth. Effect of strain on work function of polycrystalline Ag—777(A)
Wallis, R. F. (see Herman, R. C.)—752(A)
Walsh, J. M. Metal equation of state from shock-wave studies—765(T)
Wang, T. C. and C. H. Townes. Ratios of quadrupole coupling constants of isotopes and their variation with temperature—767(A)
Waniek, R. W. (see Silver, E. G.)—769(A)
Wannier, Gregory H. (see Vogt, Erich)—793(A)
Ward, J. K. (see Coon, J. B.)—805(A)
Warekois, E. P. X-ray measurements of cold-worked α brass—1421(A)
Watson, K. M. (see Takeda, G.)—1087(L)
Watson, R. B. (see Grannemann, W. W.)—812(A)
Watson, W. R., J. J. Dropkin, and A. T. Halpin. Electroluminescence in ZnS single crystals—777(A)
Wattenberg, A. (see Feld, B. T.)—1000
Way, Katharine and Marion Wood. β-decay energy systematics—119
Webb, W., J. W. Spencer, and R. W. Schiessler. Effect of structure and molecular weight on viscosity of higher hydrocarbons at high pressures—753(A)
Webber, A. C. (see DiDonato, A. R.)—770(A)
—— (see MacLeod, A. A.)—769(A)
Weber, J. Quantum theory of damped electrical oscillator and noise. II—211
—— Quantum theory of radiation resistance—793(A)
—— Vacuum fluctuation noise—213
Wechsler, M. S., D. S. Lieberman, and T. A. Read. Theory of crystal geometry of cubic—tetragonal phase changes—759(A)
—— (see Lieberman, D. S.)—760(A)
—— (see Read, T. A.)—759(A)
Weertman, J. R. (see Rado, G. T.)—1411(A); 1386(L)
Wegel, R. L. and H. C. Rorden. Structure of vibration pattern of transverse waves in slow circular jets—782(A)
Weimer, D. K. (see Blackman, V. H.)—508
Weinman, J. A. (see Bittner, J. W.)—769(A)
Weinstein, Roy, Martin Deutsch, and Sanborn Brown. Fine structure of positronium—758(A)
Weinstock, Bernard (see Osborne, Darrell W.)—202(L)
Weinstock, E. V. and J. Halpern. Systematics of photoproton reactions—1651
Weiss, R. J., J. J. DeMarco, G. Weremchuk, J. Hastings, and L. Corliss. Anisotropic Debye-Waller factors in cubic crystals—1420(A)
Weisskopf, V. F. (see Villars, F.)—232
Weller, Charles E. Improved spark counter for detecting α radiation—810(A)
Welsh, H. L. (see Plint, C. A.)—805(A)
Welton, T. A. (see Simon, A.)—943
Weremchuk, G. (see Weiss, R. J.)—1420(A)
Wert, C. (see Wruck, D.)—1417(A)
Westervelt, D. R. R', colloidal, and Z bands in KCl—1438(A)
Whalin, E. A. and R. A. Reitz. Liquefied gas x-ray target—752(A)
—— (see Schriever, Barbara Dwight)—763(A)
Whaling, Ward. Energy loss of protons and deuterons in gases—806(T)
Wheeler, J. A. Fields and particles—773(T)
White, M. G. Summary of other accelerator studies in progress—792(T)
White, Robert L. Hfs in DCC, Cl, DCN, and HCN due to deuteron quadrupole coupling and field asymmetries—789(A)
—— (see Gunther-Mohr, G. R.)—1184
Whitehead, W. D. (see Snowdon, S. C.)—786(A); 1267
Wick, G. C. Scattering of neutrons by systems containing light nuclei—1228
Widgoff, M. (see Hill, R. D.)—1794(L); 797(A)
Wiedenbeck, M. L. (see Lu, Daniel C.)—501(L)
—— (see MacGregor, M. H.)—138

—— (see Segrè, Emilio)—157
Wiggins, T. A. (see Rank, D. H.)—575
Wigner, Eugene P. Application of Rayleigh-Schrödinger perturbation theory to hydrogen atom—77
—— Problem of multiple scattering—17
Wilg, Edwin O. (see Fink, Richard W.)—1357
—— (see Haldar, B. C.)—1713
Wilkins, Homer C. (see Annis, Martin)—1038
Wilkinson, Joseph R. (see Sheline, Raymond K.)—729(L)
Wilkinson, M. K. and C. G. Shull. Neutron diffraction observations on Fe at high temperatures—1439(A)
——, **C. G. Shull, L. D. Roberts, and S. Bernstein.** Neutron diffraction investigations on superconducting elements —772(A)
—— (see Shull, C. G.)—1439(A)
Willard, H. B., J. K. Bair, and J. D. Kington. Angular distributions of 0.2–1.5 Mev neutrons elastically scattered by light nuclei—786(A)
Willardson, R. K. (see Harman, T. C.)—1065(L)
Williams, Dudley. Recent developments in rf spectroscopy—803(T)
—— (see Burch, D. E.)—1424(A)
Williams, Ferd E. (see Piper, William W.)—777(A)
Williams, H. J. (see Nesbitt, E. A.)—1440(A)
Williams, M. M. D. (see Orvis, A. L.)—810(A)
Williams, Malcolm L. and John D. Ferry. Dynamic mechanical properties of polyvinyl acetate—1413(A)
—— (see Ferry, John D.)—1413(A)
Williams, Robert W. and J. H. Vilain. Spectrum of electrons from μ-meson decay—757(A)
—— (see Vilain, J. H.)—1011
Williams, Ross, Aihud Pevsner, James Rainwater, and Seymour J. Lindenbaum. Elastic scattering of positive and negative pions in Li—765(A)
—— (see Pevsner, Aihud)—765(A)
Williamson, R. M. (see Goldburg, W. I.)—747(A)
—— (see Newson, H. W.)—774(A)
Willig, F. J. Applications of high explosives and high-speed photography to physical research problems—765(T)
Wills, James E. and Henry R. Dvorak. Analyzing magnet for 100-kv modified Cockcroft-Walton accelerator—810(A)
—— (see Little, R. N., Jr.)—807(A)
Wilson, R. R. (see Jenkins, T. L.); 755(A)
Winans, J. G. (see St. John, Robert M.)—1097
Windham, Pat M. and G. C. Phillips. Angular correlation apparatus for $Li^7(p,\gamma,\alpha)He^4$—803(A)
Winhold, E. J. (see Fairhall, A. W.)—733(L)
Winkler, Stanley. Nonuniform microwave transmission lines and solutions of Riccati equations—778(A)
Winston, Harvey. Studies on localized orbitals—328
Witmer, Enos E. Nuclear masses as integral or rational multiples of electron mass—764(A)
Wolfe, B., J. W. DeWire, and A. Silverman. Elastic photoproduction of neutral mesons from deuterium—756(A)
Wolfenstein, L. Possible angular correlations involving V particles—786(A)
Wolff, G. Triboluminescence in crystals—777(A)
——, **P. H. Keck, and J. D. Broder.** Preparation and properties of III–V compounds—753(A)
Wolff, P. A. Theory of energy distribution of secondary electrons—749(T)
Wolfgang, R. and G. Friedlander. Momentum transfer in high-energy nuclear interactions in Al—775(A)
—— (see Friedlander, G.)—727(L); 775(A)
—— (see Hudis, J.)—775(A)
Wolfson, J. L. (see Elliott, L. G.)—795(A)
Wollan, E. O. (see Koehler, W. C.)—1801(E)
Wood, John G. Bubble tracks in hydrogen-filled Glaser chamber—731(L)
Wood, Marion (see Way, Katharine)—119
Wood, R. E. Activation measurements in Eu with monoenergetic neutrons—794(A)
Woodbury, H. H. (see Tyler, W. W.)—1419(A)
Woodruff, A. E. (see Noyes, H. P.)—1401(L)
Woodruff, Robert W. and M. Parker Givens. Soft x-ray absorption of Te—752(A)
Woods, T. J. (see Sack, H. S.)—1414(A)
Woodward, W. M. (see Ashkin, Arthur)—357
Workman, E. J. and W. Drost-Hansen. Electrical conduction and dielectric properties of ice—770(A)
——, **Frank K. Truby, and W. Drost-Hansen.** Electrical conduction in halide-contaminated ice—1073(L)
—— (see Drost-Hansen, W.)—770(A)
Wruck, D. and C. Wert. Crystal structure as factor in radiation damage—1417(A)
Wu, C. S. (see Lidofsky, L.)—780(A)
Wu, Ta-You. Theory of directed valence—1424(A)
—— (see Bauer, Ernest)—1424(A)
—— (see Tauber, G. E.)—762(A); 1307

Yager, W. A. (see Fletcher, R. C.)—1392(L)
Yang, C. N. (see Snow, G. A.)—1073(L)
Yasaitis, Edward L. (see Smaller, Bernard)—202(L)
Yeivin, Y. (see Haber-Schaim, U.)—184
Yekutieli, G. (see Haber-Schaim, U.)—184
Yevick, George J. and Jerome K. Percus. New approach to classical and quantum theory of many interacting particles. I—787(A)
—— (see Percus, Jerome K.)—787(A)
Yntema, J. L. (see Bayard, Robert T.)—757(A)
York, C. M., Jr. (see van Lint, B. A.)—1732
Young, D. R. (see Drougard, M. E.)—1408(A); 1561
Young, J. A., Jr., and Edwin A. Uehling. Tensor formulation of ferromagnetic resonance—544

Zacharias, J. R. Precision measurements with molecular beams—751(T)
Zaffarano, D. J. (see Lane, R. O.)—959
Zeldes, Henry (see Livingston, Ralph)—725(L)
Zemach, A. C. and R. J. Glauber. Neutron scattering by rotators—790(A)
Zimmerman, Robert L. (see Cooper, Daniel I.)—1209
Zimmerman, S. F., Jr., and C. P. Browne. Energy levels of Al^{27}—749(A)
Zinn, A. (see Sheer, C.)—769(A)
Zitter, R. N. (see Kurnick, S. W.)—1791(L)
Zuber, N. (see Forster, H. K.)—754(A)
Zucker, A. and H. L. Reynolds. Excitation functions for nitrogen-induced nuclear reactions in C—748(A)
—— (see Scott, D. W.)—810(A)
Zumino, Bruno. Collision matrix for Dirac particles—747(A)
Zupančič, Črtomir and Torben Huus. Emission of δ- and x-rays from targets bombarded by accelerated ions—205(L)

Analytic Subject Index to Volume 94

References with (A) are to abstracts of papers presented at meetings of the American Physical Society; references with (L) are to Letters to the Editor; references with (E) are to Errata. Items are listed under the following categories:

Acoustics
Astrophysics
Atomic and Molecular Beams
Atomic Mass and Abundance
Atomic Structure and Spectra
Biophysics
Chemical Effects and Properties
Constants, Standards, Units
Cosmic Radiation
Crystalline State
Dielectrics and Dielectric Properties
Diffraction
Diffusion
Elasticity and Plasticity
Electrical Conductivity and Resistance
Electrical Discharges
Electrical Properties
Electromagnetic Theory and Electrodynamics
Electrons and Positrons
Elementary Particle Interactions
Errata
Field Theory
Films, Properties
Fluid Dynamics
Gamma Rays
Gases
Geophysics
Helium, Liquid
Imperfections in Solids
Ionization
Ions
Ions and Electrons, Mobility
Liquids
Luminescence
Magnetic Properties
Magnetic Resonance
Mathematical Methods
Mechanics
Mesons
Methods and Instruments
Microwaves
Miscellaneous
Molecular Aggregates
Molecular Structure and Spectra
Neutrino
Noise
Nuclear Fission
Nuclear Moments and Spin
Nuclear Photoeffects
Nuclear Reactions, General
Nuclear Reactions Induced by α Particles and He^3
Nuclear Reactions Induced by Deuterons and Tritons
Nuclear Reactions Induced by Mesons
Nuclear Reactions Induced by Neutrons
Nuclear Reactions Induced by Protons
Nuclear Spectra
Nuclear Structure Theory
Optical Properties
Proceedings of the American Physical Society
Quantum Electrodynamics
Quantum Mechanics
Radiation
Radioactivity
Range and Energy Loss of Particles
Relativity and Gravitation
Scattering, General
Scattering of α Particles
Scattering of Deuterons
Scattering of Electrons and Positrons
Scattering of Mesons
Scattering of Neutrons
Scattering of Protons
Semiconductors
Spectra, General
Statistical Mechanics and Thermodynamics
Superconductivity
Thermal Properties
X-Rays

Absorption of Radiation (see **Radiation**)

Acoustics

Absorption of ultrasonic waves in liquids under pressure, J. F. Mifsud—812(A)

Compressibility of liquid cholesterol benzoate at isotropic-anisotropic transition, W. A. Hoyer—812(A)

Determination of ratio of photoelastic constants of glasses by means of ultrasonic waves, Halbert Gates—1434(A)

Multiple diffraction patterns in glass produced by ultrasonic waves of high intensity, J. M. Barnes—1434(A)

Propagation of sound pulse in medium with complex elastic modulus, Salah Tahsin and R. D. Spence—1442(A)

Symmetric modes of tapered reed, A. Leitner and E. A. Hiedemann—1441(A)

Ultrasonic properties of Hycar OS-10 and Paracril 35, J. L. Melchor and A. A. Petrauskas—1414(A)

Variational principles for acoustic field, E. Gerjuoy and David S. Saxon—1445

Adsorption (see **Gases**)

Aerodynamics (see **Fluid Dynamics**)

Afterglow (see **Electrical Discharges**)

Alloys (see **Crystalline State**)

Annihilation (see **Electrons and Positrons**)

Antiferroelectric Phenomena (see **Dielectrics and Dielectric Properties**)

Antiferromagnetism (see **Magnetic Properties**)

Arcs (see **Electrical Discharges**)

Astrophysics

Cosmic radiation intensity-time variations and their origin. IV. Increases associated with solar flares, John Firor—1017

Dimensional relations in magnetohydrodynamics, W. M. Elsasser—1440(A)

Radiation flux in planetary atmosphere, Daniel I. Fivel and Gilbert N. Plass—752(A)

Solar magnetic moment and cosmic-ray effects associated with solar flares, S. B. Treiman—1029

Atmosphere (see **Geophysics**)

Atomic and Molecular Beams

Doppler line-width reduction, M. W. P. Strandberg and H. Dreicer—1393(L)

Hfs and nuclear moments of stable Br isotopes, John Gordon King and Vincent Jaccarino—1610

Hfs of I^{127}. Nuclear magnetic octupole moment, V. Jaccarino, J. G. King, R. A. Satten, and H. H. Stroke—1798(L)

Hfs of In^{113}. Evidence of nuclear octupole moment, P. Kusch and T. G. Eck—1799(L)

Molecular beam investigation of scattering of molecules from surfaces, F. C. Hurlbut—754(A)

Stern-Gerlach experiment on polarized neutrons, J. E. Sherwood, T. E. Stephenson, C. P. Stanford, and Seymour Bernstein—791(A)

Variations of hydrogen rotational magnetic moments with rotational quantum number and with isotopic mass, R. G. Barnes, P. J. Bray, and N. F. Ramsey—893

Atomic Mass and Abundance

Atomic masses in intermediate region, T. L. Collins, Walter H. Johnson, Jr., and Alfred O. Nier—398

Nuclear masses as integral or rational multiples of electron mass, Enos E. Witmer—764(A)

T concentration in natural waters by diffusion cloud chamber, E. L. Fireman and D. Schwarzer—385

Atomic Structure and Spectra

Application of Rayleigh-Schrödinger perturbation theory to hydrogen atom, Eugene P. Wigner—77

Atomic Structure and Spectra (Continued)
Atomic self-consistent fields. II. Interpolation problems, Per-Olov Löwdin—1600
Complete Bacher and Goudsmit method, Sydney Meshkov and C. W. Ufford—75; C. W. Ufford and S. Meshkov —761(A)
Determination of h/e by new method, F. G. Dunnington, C. L. Hemenway, and J. D. Rough—592
Distortion of nucleus in μ-mesic atoms, W. Lakin and W. Kohn—787(A)
Fine structure of positronium, Roy Weinstein, Martin Deutsch, and Sanborn Brown—758(A)
Gyromagnetic ratio in hfs of doublet states, W. W. Clendenin—1590
Hfs and nuclear moments of stable Br isotopes, John Gordon King and Vincent Jaccarino—1610
Hfs of I^{127}. Nuclear magnetic octupole moment, J. Jaccarino, J. G. King, R. A. Satten, and H. H. Stroke—1798(L)
Hfs of In^{115}. Evidence of nuclear octupole moment, P. Kusch and T. G. Eck—1799(L)
Hfs of $3P_{3/2}$ state of Na^{23}, Paul L. Sagalyn—885
Interaction current contribution to hfs of tritium, A. M. Sessler and H. M. Foley—761(A)
Lamb shift in mesic atoms, H. C. Corben—787(A)
Low even configurations of Hf II, Matatiahu Gehatia—618
Magnetic quenching of positronium decay, Otto Halpern —904
μ-mesonic x-rays and shape of nuclear charge distribution, David L. Hill and Kenneth W. Ford—1617
New method of approximate calculation of atomic radii, N. Efremov—753(A)
Nuclear spin of Am^{242} and isotope shift in Am spectrum, John G. Conway and Ralph D. McLaughlin—498(L)
Pressure shift in He λ5875, John R. Holmes and Leon Pape—902
Relativistic contributions to magnetic shielding of nuclei in atoms, Vernon W. Hughes and Werner B. Teutsch —761(A)
Spectroscopy of π- and μ-meson x-rays, S. de Benedetti, M. B. Stearns, M. Stearns, and H. J. Richings—766(A)
Spin-other-orbit interaction in theory of complex spectra, Frederick R. Innes—761(A)
V d^3 and d^4 configurations, Sydney Meshkov—761(A)
Variation wave function for Na, D. M. Smith and E. L. Secrest—806(A)
Yields of π- and μ-meson x-rays in low-Z materials, M. Stearns, M. B. Stearns, S. De Benedetti, and L. Leipuner—766(A)
Aurora (see **Astrophysics; Geophysics**)

Barkhausen Effect (see **Magnetic Properties**)
Biophysics
NaI γ-ray spectrometry techniques applied to outlining of brain tumors, J. R. Risser and H. C. Allen, Jr.—810(A)
Range measurement of low-voltage electrons, Marguerite Davis—243
Boson Theory (see **Field Theory**)
Bremsstrahlung (see **Radiation**)
Broadening of Spectral Lines (see **Atomic Structure and Spectra; Molecular Structure and Spectra; Spectra, General**)

Capture Cross Sections (see **Electrons and Positrons; Nuclear Reactions; Radiation**)
Čerenkov Effect (see **Radiation**)
Chemical Effects and Properties
Adsorption of CO_2 on Ni single crystal faces using radiotracer technique, J. A. Dillon, Jr., and H. E. Farnsworth —753(A)
Effect of structure and molecular weight on viscosity of higher hydrocarbons at high pressures, W. Webb, J. W. Spencer, and R. W. Schiessler—753(A)
Electrolysis of sintered ThO, D. L. Goldwater and W. E. Danforth—754(A)
Ion-yield of tritium-oxygen reaction, Leon M. Dorfman and B. A. Hemmer—754(A)
Mechanism of adsorption. I. Theory, B. C. Bradshaw and R. A. Shuttleworth—753(A); II. Application, R. A. Shuttleworth and B. C. Bradshaw—753(A)
Nuclear magnetic resonance as criterion of chemical bonding, Richard A. Ogg, Jr.—767(A)
Preparation and properties of III-V compounds, G. Wolff, P. H. Keck, and J. D. Broder—753(A)
Theory of directed valence, Ta-You Wu—1424(A)
Chemical Reactions (see **Chemical Effects and Properties**)
Chemiluminescence (see **Luminescence**)
Cold Emission (see **Electrical Properties**)
Colloids (see **Chemical Effects and Properties; Molecular Aggregates**)
Compton Effect (see **Radiation**)
Conductivity, Electrical (see **Electrical Conductivity and Resistance**)
Conductivity, Thermal (see **Thermal Properties**)
Constants, Standards, Units
Comparison of nuclear and γ-ray energy scales, K. W. Jones, R. A. Douglas, M. T. McEllistrem, and H. T. Richards—947
Determination of h/e by new method, F. G. Dunnington, C. L. Hemenway, and J. D. Rough—592
Precision determination of velocity of light derived from band spectrum method. II, D. H. Rank, J. N. Shearer, and T. A. Wiggins—575
Variety of our sources of information on Avogadro's number and other constants, Jesse W. M. DuMond, and E. Richard Cohen—1790(L)
Cosmic Radiation
Cloud-chamber observations of unusual neutral V particles having light secondaries, V. A. J. van Lint, C. D. Anderson, E. W. Cowan, R. B. Leighton, and C. M. York, Jr. —1732
Cosmic radiation at very high altitudes near geomagnetic equator, W. A. Pomerantz—796(A)
Cosmic radiation intensity-time variations and their origin. III. Origin of 27-day variations, J. A. Simpson—426; IV. Increases associated with solar flares, John Firor—1017; V. Daily variation of intensity, J. W. Firor, W. H. Fonger, and J. A. Simpson—1031
Cosmic-ray protons at 3.4 km, Charles E. Miller, Joseph E. Henderson, Gerald R. Garrison, David S. Potter, Wayne M. Sandstrom, and Jay Todd, Jr.—167
Decay of heavy nuclear fragment, P. S. Freier, G. W. Anderson, and J. E. Naugle—677
Development of air showers in atmosphere, Kurt Sitte, Don L. Stierwalt, and Irving L. Kofsky—988
Distribution of specific ionization of primary cosmic rays at $\lambda = 10°$N, G. W. McClure—796(A)
Energy distribution of neutral mesons produced in cosmic-ray stars, Y. B. Kim—797(A)
Flux of primary cosmic-ray α particles, John Lindsley—796(A)
Influence of earth-magnetic field on extensive air showers, Giuseppe Cocconi—796(A)
Kinematics of Λ^0 production, George T. Reynolds and S. B. Treiman—207(L); 797(A)
K-meson and hyperon decays, Paul H. Barrett—1328
Magnetic storm effect on cosmic radiation, Hannes Alfven —1082(L)

Mean lives of positive and negative μ mesons, N. N. Biswas and M. S. Sinha—1400(L)
Negative μ-meson capture in carbon, T. N. K. Godfrey—756(A)
Nuclear interaction of fast μ mesons, Martin Annis, Homer C. Wilkins, and John D. Miller—1038
Origin of cosmic rays, Philip Morrison, Stanislaw Olbert, and Bruno Rossi—440
Sea-level zenith-angle dependence of high-energy μ mesons, N. M. Duller, W. D. Walker, J. W. Graham, and J. R. Risser—810(A)
Search for K particles using Čerenkov counters, J. W. Keuffel and L. Mezzetti—797(A)
Shower structure in higher shower maxima, W. Bothe and H. Kraemer—1402(L)
Solar magnetic moment and cosmic-ray effects associated with solar flares, S. B. Treiman—1029
Structure and composition of air shower cores, Harold L. Kasnitz and Kurt Sitte—977
Time and directional study of primary heavy nuclei, G. W. Anderson, P. S. Freier, and J. E. Naugle—1317
Time structure of extensive air showers, R. Sugarman and S. De Benedetti—796(A)
V-decay event with heavy negative secondary, and identification of secondary V-decay event in cascade, E. W. Cowan—161

Cosmology (see **Astrophysics; Relativity and Gravitation**)

Critical Potentials (see **Atomic Structure and Spectra; Molecular Structure and Spectra**)

Cross Section (see **Electrons and Positrons; Nuclear Reactions; Radiation; Scattering**)

Crystal Counters (see **Methods and Instruments**)

Crystalline State (see also **Electrical Properties; Imperfections in Solids; Magnetic Properties; Semiconductors;** etc.)

Absorption spectrum of Be in neighborhood of K edge, R. W. Johnston and D. H. Tomboulian—1585
Anisotropic Debye-Waller factors in cubic crystals, R. J. Weiss, J. J. DeMarco, G. Weremchuk, J. Hastings, and L. Corliss—1420(A)
Annealing kinetics of lattice imperfections using evaporated metal films, R. W. Hoffman and N. S. Rasor—1406(A)
Application of bimolecular kinetics to relaxation of order below Curie point, Jerome Rothstein—1429(A)
$\beta \rightarrow \alpha$ transformation in Sn, Jerome Fleeman—1422(A)
Bombardment damage of Ge crystals by fast electrons, W. Kohn—1409(A)
Bound states in dislocations, Rolf Landauer—1386(L)
Change of elastic constants of Cu on annealing after plastic deformation at 78°K, E. C. Crittenden, Jr., and H. Dieckamp—1421(A)
Change of resistivity of Cu with elastic strain, D. B. Bowen and H. Hori—1422(A)
Crystal geometry of cubic—tetragonal phase changes, theory, M. S. Wechsler, D. S. Lieberman, and T. A. Read—759(A)
Crystal structure as factor in radiation damage, D. Wruck and C. Wert—1417(A)
Cubic to orthorhombic diffusionless phase change—experimental and theoretical studies of AuCd, D. S. Lieberman, M. S. Wechsler, and T. A. Read—760(A)
Diffraction effects of crystals with deformation faults, R. Hosemann and S. N. Bagchi—71
Diffraction of x-rays by lattice imperfections, Yin-Yuan Li and R. Smoluchowski—751(A)
Diffraction studies of possible ordering in α brass, D. T. Keating—1429(A)
Diffusion in Ag single crystals, C. T. Tomizuka and L. Slifkin—1406(A)
Diffusion of Co^{60} in some Ni-Al alloys containing excess vacancies, A. E. Berkowitz, F. E. Jaumot, Jr., and F. C. Nix—1407(A)
Diffusion of lattice defects in temperature gradient, Robert W. Keyes—1389(L)
Diffusionless cubic—tetragonal phase changes, T. A. Read, M. S. Wechsler, and D. S. Lieberman—759(A)
Dimensional changes of α brass on dezincification and lattice strain in Cu introduced by vacancies, David D. Van Horn and William C. Cooley—1418(A)
Disordering of solids by heavy corpuscular radiation, W. S. Snyder and Jacob Neufeld—760(A)
Effect of plastic flow upon color centers in alkali halide crystals, Masayasu Ueta and Werner Känzig—1390(L)
Effect of short-time moderate-flux neutron irradiation on mechanical properties of some metals, F. W. Kunz and A. N. Holden—1417(A)
Effective mass of conduction electrons in Ag, Au, and Cu, L. G. Schulz—1422(A)
Elastic constants of Cu alloys, John R. Neighbours and Charles S. Smith—1421(A)
Elastic constants of Si before and after neutron bombardment from x-ray diffuse scattering, W. P. Binnie and A. M. Liebschutz—1410(A)
Elastic spectrum of Cu from temperature scattering of x-rays, E. H. Jacobsen—1420(A)
Elastic spectrum of Zn from temperature scattering of x-rays, R. E. Joynson—851
Electric breakdown of crystals in high-temperature region, Kurt Lehovec—770(A)
Electrical breakdown paths in nonpolar crystals, J. W. Davisson—1437(A)
Electrical characteristics of polycrystalline boron, L. J. Badar and V. P. Jacobsmeyer—808(A)
Electrical properties of single crystals and thin films of PbSe and PbTe, S. J. Silverman and H. Levinstein—871
Electrical resistivity of cold-worked Al single crystals, A. Sosin and J. S. Koehler—1422(A)
Electrolysis of sintered ThO, D. L. Goldwater and W. E. Danforth—754(A)
Electron interactions in metals, Robert L. Chuoke—808(A)
Electron resonance in F centers, J. Korringa—1388(L)
Electronic energy bands in crystals, Edmond Brown—1434(A)
Electrostatic energy calculations for sodium tungsten bronze (Na_xWO_3), J. F. Smith—1407(A)
Energy for fracture propagation in plates, J. A. Kies and H. L. Smith—760(A)
Equations for magnetostriction and anisotropic energy for hexagonal crystal of class $D_{6h}(6/m, 2/m, 2/m)$, W. P. Mason and J. A. Lewis—1439(A)
Equivalence of x-ray lattice parameter and density changes in neutron-irradiated LiF, D. Binder and W. J. Sturm—760(A)
Formation energy of vacancies in Au, C. J. Meechan and R. R. Eggleston—1406(A)
Germanium-oxygen system, Michael Hoch and Herrick L. Johnston—749(A)
Growth and surface properties of Ta crystals, M. H. Nichols—309
Hall effect of Pd-Ag alloy system, A. I. Schindler—1422(A)
Imperfections in Cu in terms of electrical resistivity and thermoelectric power, G. W. Rodeback—1406(A)
Influence of charge distribution on repulsive forces and internuclear distances between ions, Gilbert Beguin and Kasimir Fajans—1434(A)
Interferometric study of surface of x-ray and proton-irradiated KCl crystals, W. J. Smith, W. J. Leivo, and R. Smoluchowski—1435(A)

Crystalline State (Continued)
Internal friction associated with precipitation in Al-Ag alloy, A. C. Damask and A. S. Nowick—1421(A)
Internal friction in single metal crystals at audiofrequencies, T. R. Cuykendall, T. Beresovski, and H. S. Sack—1421(A)
Interstitial content of radiation-damaged metals from precision x-ray lattice parameter measurements, C. W. Tucker, Jr., and J. B. Sampson—1418(A)
Ionic conductivity of impure polar crystals, A. B. Lidiard—29
Kinetics of ordering and disordering process in Cu_3Au, F. P. Burns—1429(A)
Lattice defects in metals, Frederick Seitz—1406(A)
Localized orbitals, Harvey Winston—328
Localized perturbations, Melvin Lax—1391(L)
Long-range order in Cu-Au alloys of nonstoichiometric compositions, C. H. Sutcliffe and F. E. Jaumot, Jr.—1429(A)
Magnetic neutron diffraction in Fe_3O_4, T. Riste and A. W. McReynolds—1433(A)
Magnetic susceptibility of carbons and polycrystalline graphites, H. T. Pinnick—319
Melted regions in metal crystals resulting from particle bombardment, J. M. Denney—1417(A)
Moduli and internal friction of magnetite as affected by low temperature transformation, M. E. Fine and Nancy T. Kenney—1573
Multiphonon transitions in F center, Jordan J. Markham—1395(L)
Neutron diffraction investigations on superconducting elements, M. K. Wilkinson, C. G. Shull, L. D. Roberts, and S. Bernstein—772(A)
Neutron diffraction observations on Fe at high temperatures, M. K. Wilkinson and C. G. Shull—1439(A)
Neutron diffraction studies of rochelle-salt single crystals, B. C. Frazer, Marilyn McKeown, and Ray Pepinsky—1435(A)
Nucleation of fracture origins, E. A. McLean and Waller George—761(A)
Order-disorder and cold-work phenomena in Cu-Pd alloys, F. E. Jaumot, Jr., and A. Sawatzky—1429(A)
Order-disorder transformation in Cu-Au alloys of nonstoichiometric compositions, C. H. Sutcliffe and F. E. Jaumot, Jr.—1429(A)
Orientation of nuclei by saturation of paramagnetic resonance, J. Korringa—1388(L)
Origin of recrystallization nuclei, John P. Nielsen—1428(A)
Pauli principle scattering and resistivity minimum, J. S. Koehler—1071(L)
Peculiarity of electron density near impurity in metal and its effect on x-ray spectra, J. S. Plaskett—1420(A)
Polaron self-energy and Bloch-Nordsieck method, K. S. Singwi and B. M. Udgaonkar—38
Preparation and properties of III-V compounds, G. Wolff, P. H. Keck, and J. D. Broder—753(A)
Pu metal properties, Cyril Stanley Smith—1068(L)
R', colloidal, and Z bands in KCl, D. R. Westervelt—1438(A)
Radiation ordering by cyclotron particles, C. E. Dixon and D. B. Bowen—1418(A)
Radiation-induced changes in electrical resistivity of α brass, D. B. Rosenblatt, R. Smoluchowski, and G. J. Dienes—1417(A)
Rate of production of color centers in KCl and KBr by x-rays at 78°K, William H. Duerig—65
Recovery phenomena in cold-worked metals, A. S. Nowick—760(A)
Resistivity changes in Cu, Ag, and Au produced by deuteron irradiation near 10°K, H. G. Cooper, J. S. Koehler, and J. W. Marx—496(L)
Restoration of F and V_1 centers following low temperature bleaching, R. V. Hesketh and E. E. Schneider—494(L)
Role of Rydberg constant in calculation of ionic radii, N. Efremov—813(A)
Scattering by lattices of deformable atoms, R. J. Glauber—751(A)
Self-diffusion and ionic conductivity in NaBr, H. W. Schamp, Jr., and E. Katz—828
Self-diffusion in KCl, J. F. Aschner—771(A)
Simon melting equation and effective intermolecular potential, L. Salter—1434(A)
Simplified LCAO method for periodic potential problem, J. C. Slater and G. F. Koster—1498
Size effects in nucleation of fracture origins, E. A. McLean and Waller George—1428(A)
Small-angle scattering of x-rays by irradiated diamond, W. H. Robinson, Yin-Yuan Li, and R. Smoluchowski—1435(A)
Soft x-ray emission bands in metals, H. Jones—1072(L)
Solute diffusion in metals, D. Lazarus—1407(A)
Solution of Schrödinger equation in periodic lattices with application to metallic Li, W. Kohn and N. Rostoker—1111
Statistical approach to phase determination in x-ray analysis, V. Vand and R. Pepinsky—1435(A)
Stored energy measurements in irradiated Cu, Albert W. Overhauser—1551
Structure of Gd, Dy, and Er at low temperatures, J. R. Banister, S. Legvold, and F. H. Spedding—1140
Surface migration of C on W, Ralph Klein—1407(A)
Theory of x-ray small-angle scattering, Yin-Yuan Li and R. Smoluchowski—866
Thermal ionization of trapped electrons, Hermann Gummel and Melvin Lax—1419(A)
Thermionic and surface properties of W crystals, George F. Smith—295
Thermionic emission and semiconduction in single crystals of BaO, Evan O. Kane—1439(A)
Thermodynamics of ordering alloys. II. Ordered and disordered solid solutions of Au and Cu system, R. A. Oriani—760(A)
Thermoelectric power and resistivity of dilute Cu-Si, Ni-Si, and Fe-Si alloys, C. A. Domenicali and F. A. Otter—1421(A)
Time rate of change for transformation of monoclinic Se into hexagonal, Alvin E. Cowan and Arthur E. Lockenvitz—809(A)
Time reversal *vs* Boltzmann equation, J. S. Lomont—792(A)
Tunneling of electrons in alkali halides, D. L. Dexter—771(A)
2-phase graphitization, E. E. Loebner—1435(A)
Variation method applied to wave functions in crystals, W. V. Houston—808(A)
Wave functions for impurity levels, G. F. Koster and J. C. Slater—1392(L)
X-ray measurements of cold-worked α brass, E. P. Warekois—1421(A)

Diamagnetism (see **Magnetic Properties**)
Dielectrics and Dielectric Properties
Dielectric changes in crystal-phosphor condensers irradiated with x-rays, Rudolf Frerichs—1408(A)
Dielectric constants of powders at uhf, Robert S. Smith—1438(A)

Dielectric high-frequency method for molecular weight determinations, P. Debye, P. P. Debye, and B. H. Eckstein—1412(A)
Dielectric properties of colored KCl crystals, T. Suita—1497
Domain clamping effect in $BaTiO_3$ single crystals, M. E. Drougard and D. R. Young—1408(A); 1561
Effects of stepped surfaces on motional parameters of piezoelectric filter plates, Charles R. Mingins, Robert W. Perry, and Albert D. Frost—770(A)
Electric polarization of charged particles in square potential wells, Julian H. Gibbs—292
Electrical conduction and dielectric properties of ice, E. J. Workman and W. Drost-Hansen—770(A)
Ferroelectric transition in single crystals of $Cd_2Nb_2O_7$, F. Jona, G. Shirane, and R. Pepinsky—1408(A)
Heat of transition of $BaTiO_3$ at Curie point, A. DeBretteville and E. D. Harris—1408(A)
Neutron diffraction studies of rochelle-salt single crystals, B. C. Frazer, Marilyn McKeown, and Ray Pepinsky—1435(A)
Piezoresistance effect in Ge and Si, Charles S. Smith—42
Static electrification of filaments: dependence of charge transferred on normal force and velocity, S. P. Hersh and D. J. Montgomery—1413(A)
Theory of thermodielectric effect, B. Gross—1545
Theory of volume rectification in ice, W. Drost-Hansen and E. J. Workman—770(A)
Threshold field and free energy for antiferroelectric-ferroelectric phase transition in $PbZrO_3$, A. P. deBretteville, Jr.—1125

Diffraction (see also **Scattering**)
Anisotropic Debye-Waller factors in cubic crystals, R. J. Weiss, J. J. DeMarco, G. Weremchuk, J. Hastings, and L. Corliss—1420(A)
Diffraction effects of crystals with deformation faults, R. Hosemann and S. N. Bagchi—71
Diffraction measurements at 1.25 cm, C. W. Horton and W. W. Grannemann—812(A)
Diffraction of electromagnetic waves by metallic wedge of acute dihedral angle, W. W. Grannemann, C. W. Horton, and R. B. Watson—812(A)
Diffraction of step shocks through double slits, George A. Coulter and James Allen—782(A)
Diffraction of x-rays by lattice imperfections, Yin-Yuan Li and R. Smoluchowski—751(A)
Diffraction studies of possible ordering in α brass, D. T. Keating—1429(A)
Field-induced diffraction method for molecular weight determinations, W. A. Barber, P. Debye, and B. H. Eckstein—1412(A)
Magnetic neutron diffraction in Fe_3O_4, T. Riste and A. W. McReynolds—1433(A)
Multiple diffraction patterns in glass produced by ultrasonic waves of high intensity, J. M. Barnes—1434(A)
Neutron diffraction investigations on superconducting elements, M. G. Wilkinson, C. G. Shull, L. D. Roberts, and S. Bernstein—772(A)
Neutron diffraction observations on Fe at high temperatures, M. K. Wilkinson and C. G. Shull—1439(A)
Neutron diffraction studies of rochelle-salt single crystals, B. C. Frazer, Marilyn McKeown, and Ray Pepinsky—1407(A)
Scattering by lattices of deformable atoms, R. J. Glauber—751(A)

Diffusion
Age-diffusion theory for β-ray problems, William C. Roesch—779(A)
Comparison of diffusion techniques employing radioisotopes, R. L. Smith, F. E. Jaumot, Jr., and L. A. Arné, Jr.—1407(A)
Design of diffusers to avoid turbulent boundary layer separation, Francis H. Clauser—783(A)
Diffusion in Ag single crystals, C. T. Tomizuka and L. Slifkin—1406(A)
Diffusion of Co^{60} in some Ni-Al alloys containing excess vacancies, A. E. Berkowitz, F. E. Jaumot, Jr., and F. C. Nix—1407(A)
Diffusion of impurities in Ge, W. C. Dunlap, Jr.—1531
Diffusion of lattice defects in temperature gradient, Robert W. Keyes—1389(L)
Effect on diffusion measurements of some β-ray absorption phenomena, A. E. Berkowitz—1407(A)
Electrostatic energy calculations for sodium tungsten bronze (Na_xWO_3), J. F. Smith—1407(A)
Extension of Onsager's theory of reciprocal relations. I, S. R. de Groot and P. Mazur—218; II, P. Mazur and S. R. de Groot—224
Interdiffusion in PbS crystals, R. F. Brebrick and W. W. Scanlon—1430(A)
Lifetimes and diffusion constants in Ge, D. T. Stevenson and R. J. Keyes—1416(A)
1-dimensional walk with correlation by saturation for description of diffusion phenomena, C. M. Tchen—1442(A)
Point-source kernel for diffusion with small-angle scattering, W. E. Drummond and C. S. Gardner—1491
Self-diffusion and ionic conductivity in NaBr, H. W. Schamp, Jr., and E. Katz—828
Self-diffusion in KCl, J. F. Aschner—771(A)
Solute diffusion in metals, D. Lazarus—1407(A)
Surface migration of C on W, Ralph Klein—1407(A)

Discharge of Electricity in Gases (see **Electrical Discharges**)

Disintegration and Excitation of Nucleus (see **Nuclear Reactions**)

Dynamics (see **Mechanics**)

Elasticity and Plasticity (see also **Molecular Associates**)
Behavior of ferromagnetic domains under stress, G. Bonfiglioli, A. Ferro, G. Montalenti, and G. Rosa—316
Change of elastic constants of Cu on annealing after plastic deformation at 78°K, E. C. Crittenden, Jr., and H. Dieckamp—1421(A)
Compressibilities of solid H_2 and D_2 at 4.2°K, J. W. Stewart and C. A. Swenson—772(A)
Compression to 10 000 atmos of solid hydrogen and deuterium at 4.2°K, J. W. Stewart and C. A. Swenson—1069(L)
Creep and relaxation of plastics, A. R. DiDonato, A. A. MacLeod, and A. C. Webber—770(A)
Determination of ratio of photoelastic constants of glasses by means of ultrasonic waves, Halbert Gates—1434(A)
Effect of elastic strain on electrical resistance of metals, G. C. Kuczynski—61
Effect of plastic flow upon color centers in alkali halide crystals, Masayasu Ueta and Werner Känzig—1390(L)
Effect of short-time moderate-flux neutron irradiation on mechanical properties of some metals, F. W. Kunz and A. N. Holden—1417(A)
Elastic constants of Cu alloys, John R. Neighbours and Charles S. Smith—1421(A)
Elastic constants of Si before and after neutron bombardment from x-ray diffuse scattering, W. P. Binnie and A. M. Liebschutz—1410(A)
Energy for fracture propagation in plates, J. A. Kies and H. L. Smith—760(A)

Elasticity and Plasticity (Continued)
Energy to create fracture surfaces in glass, H. L. Smith and J. A. Kies—760(A)
Experimental investigation of statistical theory of rubber elasticity, F. P. Baldwin, J. Ivory, and R. L. Anthony—1425(A)
Internal friction associated with precipitation in Al-Ag alloy, A. C. Damask and A. S. Nowick—1421(A)
Internal friction in single metal crystals at audiofrequencies, T. R. Cuykendall, T. Beresovski, and H. S. Sack—1421(A)
Moduli and internal friction of magnetite as affected by low temperature transformation, M. E. Fine and Nancy T. Kenney—1573
Neutron irradiation effects at low temperature—Cu and Al, A. W. McReynolds, W. Augustyniak, M. McKeown, and D. B. Rosenblatt—1417(A)
Nucleation of fracture origins, E. A. McLean and Waller George—761(A)
Pu metal properties, Cyril Stanley Smith—1068(L)
Shear modulus of irradiated Cu, H. Dieckamp and E. C. Crittenden, Jr.—1418(A)
Stress-temperature-time studies through second-order transition region, D. G. Ivey and A. Kwei—1414(A)
Transmission of pulses through elastic plate, Arthur S. Ginzbarg and William L. Roever—812(A)
Viscoelasticity in complex static stress systems, A. A. MacLeod, A. R. DiDonato, and A. C. Weber—769(A)
X-ray study of prismatic punching in TlCl, Edward I. Salkovitz and Paul L. Smith—770(A)

Electrical Breakdown (see **Dielectrics and Dielectric Properties; Electrical Discharges**)

Electrical Conductivity and Resistance (see also **Semiconductors; Superconductors**)
Change of electrical conductivity of alkali halides upon irradiation with 350-Mev protons, Edgar Pearlstein—1409(A)
Change of resistivity of Cu with elastic strain, D. B. Bowen and H. Hori—1422(A)
Crystal structure as factor in radiation damage, D. Wruck and C. Wert—1417(A)
Effect of elastic strain on electrical resistance of metals, G. C. Kuczynski—61
Effect of impurities on conductivity of gray tin, A. W. Ewald—1428(A)
Electrical characteristics of polycrystalline boron, L. J. Badar and V. P. Jacobsmeyer—808(A)
Electrical conduction and dielectric properties of ice, E. J. Workman and W. Drost-Hansen—770(A)
Electrical conduction in halide-contaminated ice, E. J. Workman, Frank K. Truby, and W. Drost-Hansen—1073(L)
Electrical properties of single crystals and thin films of PbTe, Searl J. Silverman and Henry Levinstein—1430(A)
Electrical resistivity of cold-worked Al single crystals, A. Sosin and J. S. Koehler—1422(A)
Electrokinetic relations using sinusoidal pressure and voltage, Claude E. Cooke—812(A)
Electronic Hall effect in alkali halides, Alfred G. Redfield—537
Electronic Hall effect in diamond, Alfred G. Redfield—526
Extension of Onsager's theory of reciprocal relations. II, P. Mazur and S. R. de Groot—224
Hall effect and magnetoresistivity in carbons, S. Mrozowski and A. Chaberski—1427(A)
Hall effect in ferromagnetics, J. M. Luttinger—782(A)
Hall effect of Pd-Ag alloy system, A. I. Schindler—1422(A)
High-frequency resistance of photoconducting films, R. Broudy and H. Levinstein—290
High-frequency resistance of thin films, R. Broudy and H. Levinstein—285
Imperfections in Cu in terms of electrical resistivity and thermoelectric power, G. W. Rodeback—1406(A)
Influence of nuclear radiation on electrical conductivity of alkali halides, R. Smoluchowski—1409(A)
Ionic conductivity of impure polar crystals, A. B. Lidiard—29
Low-temperature magnetoresistance of Au in fields up to 50 kilogauss, John K. Logan—1433(A)
Low-temperature oscillatory Hall effect, J. S. Levinger and E. G. Grimsal—772(A)
Magnetic and electric properties of magnetite at low temperatures, B. A. Calhoun—1577
Magnetoresistance, L. P. Kao and E. Katz—1433(A)
Metal-insulator-metal junction, G. H. Suits—1427(A)
Neutron irradiation effects at low temperature—Cu and Al, A. W. McReynolds W. Augustyniak, M. McKeown, and D. B. Rosenblatt—1417(A)
New galvanomagnetic effect, Colman Goldberg and R. E. Davis—1121
Pauli principle scattering and resistivity minimum, J. S. Koehler—1071(L)
Photoresponse of aromatic films, J. F. Andrew and S. Mrozowski—1438(A)
Pu metal properties, Cyril Stanley Smith—1068(L)
Radiation-induced changes in electrical resistivity of α brass, D. B. Rosenblatt, R. Smoluchowski, and G. J. Dienes—1417(A)
Recovery phenomena in cold-worked metals, A. S. Nowick—760(A)
Resistance anomalies in some rare earth metals, R. J. Elliott—564
Resistance studies of phase transformations in Fe-Pt alloys near composition Fe_3Pt, R. P. Steijn and F. J. Donahoe—1432(A)
Resistivity changes in Cu, Ag, and Au produced by deuteron irradiation near 10°K, H. G. Cooper, J. S. Koehler, and J. W. Marx—496(L)
Self-diffusion and ionic conductivity in NaBr, H. W. Schamp, Jr., and E. Katz—828
Self-diffusion in KCl, J. F. Aschner—771(A)
Theory of volume rectification in ice, W. Drost-Hansen and E. J. Workman—770(A)
Thermoelectric power and resistivity of dilute Cu-Si, Ni-Si, and Fe-Si alloys, C. A. Domenicali and F. A. Otter—1421(A)
2-phase graphitization, E. E. Loebner—1435(A)

Electrical Discharges
Aspects of breakdown streamers, Leonard B. Loeb—227
Calculated values of parameters of noble gas discharges, Walter J. Graham and Arthur J. Ruhlig—25
Electron energy distributions in stationary discharges, Ira B. Bernstein and T. Holstein—1475
Initiation of discharge in CO_2-filled G-M counter by negative ions, H. R. Crane—1437(A)
Motion of arc cathode spot in magnetic field, Robert M. St. John and J. G. Winans—1097
Positive point-to-plane corona studies in air, M. Menes and L. H. Fisher—1
Propagation of waves in ionized gases, E. P. Gross and M. Krook—778(A)

Electrical Properties (see also **Dielectrics and Dielectric Properties; Electrical Conductivity and Resistance; Semiconductors; Superconductors**)
Angular distribution of photoelectrons, W. H. McMaster and F. L. Hereford—757(A)

Angular distribution of photoelectrons from γ radiation of 0.4 and 1.3 Mev, Arne Hedgran and Sölve Hultberg —498(L)
Contact potential, work function, and surface states, Selby M. Skinner—1428(A)
Effect of oxygen on PbTe films, Donald E. Bode and Henry Levinstein—1430(A)
Effect of strain on work function of polycrystalline Ag, G. Wallis and H. E. Farnsworth—777(A)
Electric breakdown of crystals in high-temperature region, Kurt Lehovec—770(A)
Energy and temperature dependence of secondary emission of MgO, A. J. Dekker—1179
Energy distribution of secondary electrons produced by 1.3-Mev primary electrons, R. A. Shatas, J. F. Marshall, and M. A. Pomerantz—757(A)
Growth and surface properties of Ta crystals, M. H. Nichols—309
Hall effect and thermoelectric power of pure Te at melting point and in liquid state, A. Epstein and H. Fritzsche—1426(A)
Imperfections in Cu in terms of electrical resistivity and thermoelectric power, G. W. Rodeback—1406(A)
Interpretation of electroluminescence effects in excited phosphor, Frank Matossi—1151
Magneto-thermoelectric behavior of Bi at liquid He temperatures, M. C. Steele and J. Babiskin—1394(L)
Photoconductivity and photoelectromagnetic effects in InSb, S. W. Kurnick, A. J. Strauss, and R. N. Zitter—1791(L)
Photoelectric emission from BaO, H. R. Philipp—777(A)
Photomagnetoelectric effect in Ge and Si, Hubert H. Bulliard—1564
Resistivity, thermoelectric power, and Hall effect in semiconductor with hexagonal structure, V. A. Johnson—1427(A)
Seebeck effect in Ge, T. H. Geballe and G. W. Hull—1134
Theory of thermionic emission, Kurt Lehovec—1439(A)
Thermal conductivity and thermoelectric power of Ge at low temperatures, E. Fagen, J. Goff, and N. Pearlman —1415(A)
Thermionic and surface properties of W crystals, George F. Smith—295
Thermionic emission and semiconduction in single crystals of BaO, Evan O. Kane—1439(A)
Thermoelectric power and resistivity of dilute Cu-Si, Ni-Si, and Fe-Si alloys, C. A. Domenicali and F. A. Otter —1421(A)
2-phase graphitization, E. E. Loebner—1435(A)

Electrodynamics (see **Electromagnetic Theory and Electrodynamics**)

Electrolysis (see **Chemical Effects and Properties**)

Electromagnetic Theory and Electrodynamics

Continuous parameter approximation in linear accelerator with independently excited cavities, R. L. Gluckstern, P. B. Daitch, L. C. Biedenharn, and M. H. Hull, Jr.—768(A)
Diffraction measurements at 1.25 cm, C. W. Horton and W. W. Grannemann—812(A)
Diffraction of electromagnetic waves by metallic wedge of acute dihedral angle, W. W. Grannemann, C. W. Horton, and R. B. Watson—812(A)
Electrokinetic relations using sinusoidal pressure and voltage, Claude E. Cooke—812(A)
Electromagnetic scattering by paraboloid of revolution, Craige Schensted—793(A)
Electromechanical analog for study of strong-focusing orbits, L. W. Jones and K. M. Terwilliger—1436(A)
Energy equation for sinusoidal solutions of Maxwell's equations with electron beams, Philip Parzen—793(A)
Longitudinal and transverse stability in linear accelerator systems, G. Breit—768(A)
Mapping particle paths in earth's magnetic field, Willard H. Bennett—796(A)
Quantum theory of damped electrical oscillator and noise. II, J. Weber—211
Quantum theory of radiation resistance, J. Weber—793(A)
Reaction concept in electromagnetic theory, V. H. Rumsey —1483
Scattering of electromagnetic waves by turbulent atmospheric fluctuations, F. Villars and V. F. Weisskopf—232
Stability of linear accelerator with independently excited cavities, M. H. Hull, Jr., L. C. Biedenharn, P. B. Daitch, and R. L. Gluckstern—768(A)

Electron diffraction (see **Diffraction: Scattering of Electrons and Positrons**)

Electron Optics (see **Electromagnetic Theory and Electrodynamics**)

Electronic Tubes (see **Methods and Instruments**)

Electrons and Positrons (see also **Electromagnetic Theory and Electrodynamics; Elementary Particle Interactions; Scattering of Electrons and Positrons**)

Annihilation of positrons in condensed materials, T. A. Pond—758(A)
Annihilation of positrons in flight, J. B. Gerhart, B. C. Carlson, and R. Sherr—917
Decay of positrons in superconducting Pb, Walter E. Millett—809(A)
Experimental measurement of gyromagnetic ratio of free electron, W. H. Louisell, R. W. Pidd, and H. R. Crane —7
Fine structure of positronium, Roy Weinstein, Martin Deutsch, and Sanborn Brown—758(A)
Lifetime for annihilation of positrons in Al and Pb, George H. Minton—758(A)
Lifetime of positrons in superconductors, Harry Talley and Robert Stump—809(A)
Magnetic quenching of positronium decay, Otto Halpern, —904
3-photon annihilation of positrons and electrons, S. De-Benedetti and R. T. Siegel—955

Electrons, Mobility (see **Ions and Electrons, Mobility**)

Electrons, Scattering of (see **Scattering of Electrons and Positrons**)

Electrons, Secondary (see **Electrical Properties**)

Electrons, Thermionic (see **Electrical Properties**)

Electro-Optical Effects (see **Optical Properties**)

Electrostriction (see **Dielectrics and Dielectric Properties**)

Elementary Particle Interactions

Angular distribution of π^--proton charge exchange scattering at 40 Mev. I. Apparatus, A. Roberts and J. Tinlot—766(A); II. Analysis of results, J. Tinlot and A. Roberts—766(A)
Annihilation of positrons in flight, J. B. Gerhart, B. C. Carlson, and R. Sherr—917
Charge exchange scattering of negative pions at 42, 30, and 20 Mev in hydrogen, W. Spry—766(A)
χ-meson decay, Seiichi Sueoka—1397(L)
Classical theory of high-energy processes, M. A. Ruderman and H. Brown—746(A)
Configuration space methods for construction of potentials, Abraham Klein—195
Coulomb effects in pion-proton scattering at relativistic energies, Frank T. Solmitz—1799(L)
Effect of negative energy components in 2-nucleon system, R. Arnowitt and S. Gasiorowicz—746(A); 1057
Experiments with neutrons from the Cosmotron. I, D. A. Hill, T. Coor, W. F. Hornyak, L. W. Smith, and G. A. Snow—791(A)

Elementary Particle Interactions (Continued)
High-energy events, Joseph V. Lepore, Maurice Neuman, and Richard N. Stuart—788(A)
Interaction between 2 nucleons, Behram Kurşunoğlu—746(A)
Intermediate coupling method for meson-nucleon scattering, T. D. Lee and R. Christian—1760
Intermediate state coupling and interpretation of high-energy nucleon-nucleon scattering, R. M. Thaler, J. Bengston, and G. Breit—683
Kinematics of Λ^0 production, George T. Reynolds and S. B. Treiman—207(L); 797(A)
K-particle production by protons of 2.2 and 3.0 Bev, R. D. Hill, E. O. Salant, and M. Widgoff—1794(L)
Meson-nucleon problem when interaction is fixed and extended, Geoffrey F. Chew—1755
Meson-nucleon scattering, I, R. J. Riddell, Jr., and Burton D. Fried—745(A); 1736; II, Burton D. Fried and R. J. Riddell, Jr.—746(A)
n-p cross section at 1.0 and 2.5 Mev, R. E. Fields, R. L. Becker, and R. K. Adams—389
Nuclear events at high energies, Joseph V. Lepore and Richard N. Stuart—1724
Phase shift analysis of high-energy nucleon-nucleon scattering experiments, R. M. Thaler and J. Bengston—679
Phase shift analysis of scattering of negative pions by hydrogen, R. L. Martin—765(A)
Phenomenological n-p interaction, M. H. Kalos and J. M. Blatt—762(A)
Phenomenology of pion-nucleon S waves, H. P. Noyes and A. E. Woodruff—1401(L)
Photomeson production from hydrogen, T. L. Jenkins, D. Luckey, and R. R. Wilson—755(A)
Photoproduction of π^+ mesons from H near threshold, G. Bernardini and E. L. Goldwasser—729(L); E. L. Goldwasser and G. Bernardini—755(A)
π^+ production cross sections from deuterium, Walter F. Dudziak—756(A)
Pion production ratios, D. C. Peaslee—1085(L)
π^--p interactions at 1.5 Bev, J. Crussard, W. D. Walker, and M. Koshiba—736(L)
Polarization by p-p collision at 439 Mev, H. G. de Carvalho, E. Heiberg, J. Marshall, and L. Marshall—1796—(L)
Polarization of elastically scattered nucleons from nuclei in Born approximation, Warren Heckrotte—1797(L)
Possible angular correlations involving V particles, L. Wolfenstein—786(A)
p-p scattering at 9.7 Mev, Bruce Cork and Walter Hartsough—1300
p-p scattering from 40 to 95 Mev, U. E. Kruse, J. M. Teem, and N. F. Ramsey—1795(L)
p-p scattering near interference minimum, Daniel I. Cooper, David H. Frisch, and Robert L. Zimmerman—1209
Production of antiprotons in p-p collisions, David Fox—499(L)
Production of K mesons, U. Haber-Schaim, Y. Yeivin, and G. Yekutieli—184
Production of proton pairs, R. N. Thorn—501(L)
Scattering of 217-Mev negative pions by hydrogen, Maurice Glicksman—1335
Small angle n-p scattering at 90 Mev, Owen Chamberlain and James W. Easley—208(L)
Strange particles and multiple meson production, Giuseppe Cocconi—741(L)
3-photon annihilation of positrons and electrons, S. De-Benedetti and R. T. Siegel—955
V particles and γ decay of neutral pion, Toichiro Kinoshita—1386
Elements (see **Atomic Mass and Abundance**)
Energy Loss of Particles (see **Range and Energy Loss of Particles**)
Energy States of Atoms (see **Atomic Structure and Spectra**)
Energy States of Molecules (see **Molecular Structure and Spectra**)
Energy States of Nucleus (see **Nuclear Reactions; Nuclear Spectra; Nuclear Structure Theory**)
Equations of State (see **Chemical Effects and Properties**)
Errata
Density fluctuations at low temperatures, P. J. Price—1801(E)
La^{140} half-life, H. W. Kirby and Murrell L. Salutsky—1801(E)
Paramagnetic scattering of neutrons by rare earth oxides, W. C. Koehler and E. O. Wollan—1801(E)
Scattering of neutrons by systems of heavy nuclei, G. Placzek—1801(E)
Small angle x-ray scattering from liquid He I and liquid He II, Arthur G. Tweet—1801(E)
Errors of Measurement (see **Methods and Instruments**)
Evaporation (see **Liquids**)
Excitation of Atoms (see **Atomic Structure and Spectra**)
Excitation of Molecules (see **Molecular Structure and Spectra**)
Excitation of Nucleus (see **Nuclear Reactions; Nuclear Spectra; Nuclear Structure Theory**)
Explosion Phenomena (see **Fluid Dynamics**)

Faraday Effect (see **Optical Properties**)
Ferroelectric Phenomena (see **Dielectrics and Dielectric Properties**)
Ferromagnetism (see **Magnetic Properties**)
Field Emission (see **Electrical Properties**)
Field Theory (see also **Quantum Electrodynamics**)
Avoiding perturbation methods in quantum electrodynamics, meson theory, etc., F. J. Belinfante—745(A)
Classical equations of motion of point particles in neutral meson fields, Frederic R. Crownfield, Jr., and Peter Havas—471
Classical theory of high-energy processes, M. A. Ruderman and H. Brown—746(A)
Configuration space methods for construction of potentials, Abraham Klein—195
Covariant formulation of Tamm-Dancoff method, S. S. Schweber—1089(L)
Covariant treatment of meson-nucleon scattering, Maurice M. Lévy—460
"Dressed" particles in quantum field theory, James L. Anderson—745(A)
Effect of negative energy components in 2-nucleon system, R. Arnowitt and S. Gasiorowicz—746(A); 1057
Interaction between 2 nucleons, Behram Kurşunoğlu—746(A)
Intermediate coupling method for meson-nucleon scattering, T. D. Lee and R. Christian—1760
Low-energy limits and renormalization in meson theory, S. Deser, W. E. Thirring, and M. L. Goldberger—711
Low-energy limits of meson processes, S. Deser and W. E. Thirring—746(A)
Meson-nucleon problem when interaction is fixed and extended, Geoffrey F. Chew—1755
Meson-nucleon scattering, R. J. Riddell, Jr., and Burton D. Fried—745(A); I, R. J. Riddell, Jr., and Burton D. Fried—1736; II, Burton D. Fried and R. J. Riddell, Jr.—746(A)

Nonadiabatic corrections to scalar theory, E. A. Power—1442(A)
Nonrelativistic limit of half-integral spin-wave equations, K. M. Case—1442(A)
p-n mass difference, R. P. Feynman and G. Speisman—500(L)
Production of proton pairs, R. N. Thorn—501(L)
Quantized interaction of relativistic fields, Hans Freistadt—746(A)
Relativistic wave equations, Herman Feshbach—786(A)
Renormalization, P. T. Matthews and Abdus Salam—185
Renormalization of meson theory with fixed extended source, Geoffrey F. Chew—1748
Renormalization questions in curved spaces, M. Dresden and Martin Gutzwiller—745(A)
Restrictions on invariant transformation groups in Lagrangian and Hamiltonian formalisms, Peter G. Bergmann—788(A)
Single-time formalisms from covariant equations, Abraham Klein—1052
Theory of elementary particles in general relativity, M. M. Hatalkar—1472
Theory of quantized fields, Julian Schwinger—1362
Two extensions of Foldy-Wouthuysen transformation, K. M. Case—786(A)
Unitarity of *U* operator, H. Ekstein—1063
V particles and γ decay of neutral pion, Toichiro Kinoshita—1386
Virtual states of 2-meson systems, R. Arnowitt and S. Deser—798(A)

Films, Properties
Annealing kinetics of lattice imperfections using evaporated metal films, R. W. Hoffman and N. S. Rasor—1406(A)
Current oscillations in photoconductive films of PbTe, Dean L. Mitchell, Werner J. Beyen, and Donald E. Bode—1430(A)
Effect of oxygen on PbTe films, Donald E. Bode and Henry Levinstein—1430(A)
Electrical properties of single crystals and thin films of PbSe and PbTe, S. J. Silverman and H. Levinstein—871
Electrical properties of single crystals and thin films of PbTe, Searl J. Silverman and Henry Levinstein—1430(A)
Energy loss of electrons in passage through thin films, L. Marton and Lewis B. Leder—203(L); Lewis B. Leder and L. Marton—777(A)
Evaporated multiple layers with semiconductor properties, J. C. Brentano and J. D. Richards—1427(A)
High-frequency resistance of photoconducting films, R. Broudy and H. Levinstein—290
High-frequency resistance of thin films, R. Broudy and H. Levinstein—285
Photoresponse of aromatic films, J. F. Andrew and S. Mrozowski—1438(A)
Thickness of films left on capillary wall during displacement of one fluid by another, Charles C. Templeton—812(A)

Fine Structure (see **Atomic Structure and Spectra**)
Fission of Nucleus (see **Nuclear Fission**)
Fluctuation Phenomena (see **Noise**)

Fluid Dynamics
Compressibility of liquid cholesterol benzoate at isotropic-anisotropic transition, W. A. Hoyer—812(A)
Design of diffusers to avoid tuburlent boundary layer separation, Francis H. Clauser—783(A)
Detonation and strong shock velocity in gases, Herbert T. Knight and Russell E. Duff—784(A)
Diffraction of step shocks through double slits, George A. Coulter and James Allen—782(A)
Effect of hydrostatic pressure in 2-state model of compressional relaxation in liquids, A. W. Nolle—812(A)
General relativistic variational principle for perfect fluids, A. H. Taub—1468
Hugoniot of gases by shock wave measurements, Russell H. Christian and Robert G. Shreffler—783(A)
Instance in thermal convection of Eddington's "overstability," D. Fultz, Y. Nakagawa, and P. Frenzen—1471
Isotropic temperature fluctuations in isotropic turbulence, Alan Kistler, Vivian O'Brien, and Stanley Corrsin—783(A)
Magneto-hydrodynamic waves in liquid Na, Bo Lehnert—815
Propagation of waves in ionized gases, E. P. Gross and M. Crook—778(A)
Real gas effects by measurement of shock detachment distance, R. N. Schwartz and J. Eckerman—1441(A)
Reflection of shock waves from blunt wedge, V. H. Blackman and D. K. Weimer—508
Scattering of electromagnetic waves by turbulent atmospheric fluctuations, F. Villars and V. F. Weisskopf—232
Shock Hugoniot of air, W. E. Deal, Jr.—811(A)
Shock tube experiments on grid flow, Leslie S. G. Kovásznay and Darshan Dosanjh—784(A)
Stability of vortex sheet in inviscid compressible fluid, Shih I. Pai—782(A)
Taylor instability in gases, R. E. Duff and H. T. Knight—784(A)
Theoretical determination of shock distances in ideal and real gases, W. H. Heybey—1441(A)
Theory of turbulence in gases, M. Z. van Krzywoblocki—783(A)
Triple correlations in isotropic turbulence, R. Betchov—783(A)
Turbulent boundary layer theory, Donald Ross—783(A)
Vibration pattern of transverse waves in slow circular jets, R. L. Wegel and H. C. Rorden—782(A)
Vibrational relaxation times in Cl_2 and Cl_2-He mixtures, E. F. Smiley—1441(A)

Fluorescence (see **Luminescence**)
Friction (see **Mechanics**)

Galvanomagnetic Effect (see **Magnetic Properties**)
Gamma Rays (see also **Nuclear Reactions; Nuclear Spectra**)
Angular distribution of photoelectrons from γ radiation of 0.4 and 1.3 Mev, Arne Hedgran and Sölve Hultberg—498(L)
γ-ray spectrum of Bulk Shielding Reactor, Fred Maienschein and Temple Love—778(A)
Interference of Rayleigh and nuclear Thomson scattering, A. M. Cormack—1398(L)

Gases
Adsorption of CO_2 on Ni single crystal faces using radiotracer technique, J. A. Dillon, Jr., and H. E. Farnsworth—753(A)
Cooling of gas by radiation, Ernest Bauer and Ta-You Wu—1424(A)
Faraday effect in gases, L. R. Ingersoll and D. H. Liebenberg—754(A)
High-speed machine computation of ideal gas thermal properties. Isotopic water molecules, Abraham S. Friedman and Lester Haar—1423(A)
Mechanism of adsorption. I. Theory, B. C. Bradshaw and R. A. Shuttleworth—753(A); II. Application, R. A. Shuttleworth and B. C. Bradshaw—753(A)

Gases (Continued)
Model for collision processes in gases. I. Small amplitude processes in charged and neutral one-component systems, P. L. Bhatnagar, E. P. Gross, and M. Krook—511
Propagation of waves in ionized gases, E. P. Gross and M. Krook—778(A)
Statistical uncertainties in radiographic determination of gas densities, Douglas Venable and Leo F. Perry—784(A)
Theoretical determination of shock distances in ideal and real gases, W. H. Heybey—1441(A)
3-dimensional calculation of vibrational relaxation times in gases, Robert N. Schwartz—793(A)
Vibrational relaxation times in Cl_2 and Cl_2-He mixtures, E. F. Smiley—1441(A)
Geophysics
Accurate determination of tidal variations of gravity, Henry Neal Clarkson and Arthur E. Lockenvitz—811(A)
Mapping particle paths in earth's magnetic field, Willard H. Bennett—796(A)
Origin of ionispheric *E* layer, K. Rawer and E. Argence—253
Radiogenic A measurements, H. A. Shillibeer, R. D. Russell, R. M. Farquhar, and E. A. W. Jones—1793(L)
Scattering of electromagnetic waves by turbulent atmospheric fluctuations, F. Villars and V. F. Weisskopf—232
Glasses (see **Molecular Aggregates**)
Gravitation (see **Relativity and Gravitation**)
Gyromagnetization (see **Magnetic Properties**)

Hall Effect (see **Electrical Conductivity and Resistance; Semiconductors**)
Heat Capacity (see **Thermal Properties**)
Heat Conduction (see **Thermal Properties**)
Heat of Dissociation and Formation (see **Molecular Structure and Spectra**)
Heat of Fusion (see **Thermal Properties**)
Heat of Vaporization (see **Thermal Properties**)
Helium, Liquid
Atomic theory of 2-fluid model of liquid He, R. P. Feynman—262
Critical and supercritical flow in liquid He II, Jay Gregory Dash—772(A)
Film flow in liquid He II at low level differences, Gerald S. Picus—1459
Flow of He II under hydrostatic pressure head, R. T. Swim and H. E. Rorschach, Jr.—809(A)
Heat capacity and entropy of liquid He^3 from 0.42°K to 1.06°K, Darrell W. Osborne, Bernard M. Abraham, and Bernard Weinstock—202(L)
Heat of mixing of He^3 and He^4 solutions, V. S. Nanda—241
Role of substrate and surface finish in He II film transport, B. Smith and H. A. Boorse—772(A)
Second virial coefficients of He^3 and He^4, John E. Kilpatrick, William E. Keller, Edward F. Hammel, and Nicholas Metropolis—1103
Simon melting equation and effective intermolecular potential, L. Salter—1434(A)
Small angle x-ray scattering from liquid He I and liquid He II, Arthur G. Tweet—1801(E)
Structure of liquid He by x-ray scattering, W. L. Gordon, C. H. Shaw, and J. G. Daunt—771(A)
Superfluid dynamics of liquid He II, J. G. Dash—1091
Superfluidity and dissipative processes in liquid He II, J. G. Dash—825
Theory of liquid He, G. V. Chester—246

High Voltage Tubes and Machines (see **Methods and Instruments**)
Hydrodynamics (see **Fluid Dynamics**)
Hyperfine Structure (see **Atomic Structure and Spectra; Molecular Structure and Spectra; Nuclear Moments and Spin**)

Imperfections in Solids (see also **Crystalline State; Electrical Conductivity and Resistance; Luminescence; Semiconductors**)
Annealing kinetics of lattice imperfections using evaporated metal films, R. W. Hoffman and N. S. Rasor—1406(A)
$\beta \rightarrow \alpha$ transformation in Sn, Jerome Fleeman—1422(A)
Bombardment damage of Ge crystals by fast electrons, W. Kohn—1409(A)
Bound states in dislocations, Rolf Landauer—1386(L)
Change of elastic constants of Cu on annealing after plastic deformation at 78°K, E. C. Crittenden, Jr., and H. Dieckamp—1421(A)
Change of electrical conductivity of alkali halides upon irradiation with 350-Mev protons, Edgar Pearlstein—1409(A)
Change of resistivity of Cu with elastic strain, D. B. Bowen and H. Hori—1422(A)
Color centers in KCl crystals produced by high-energy protons, W. Leivo and R. Smoluchowski—771(A)
Crystal structure as factor in radiation damage, D. Wruck and C. Wert—1417(A)
Dielectric changes in crystal-phosphor condensers irradiated with x-rays, Rudolf Frerichs—1408(A)
Dielectric properties of colored KCl crystals, T. Suita—1497
Diffraction effects of crystals with deformation faults, R. Hosemann and S. N. Bagchi—71
Diffraction of x-rays by lattice imperfections, Yin-Yuan Li and R. Smoluchowski—751(A)
Diffusion of Co^{60} in some Ni-Al alloys containing excess vacancies, A. E. Berkowitz, F. E. Jaumot, Jr., and F. C. Nix—1407(A)
Diffusion of lattice defects in temperature gradient, Robert W. Keyes—1389(L)
Dimensional changes of α brass on dezincification and lattice strain in Cu introduced by vacancies, David D. Van Horn and William C. Cooley—1418(A)
Disordering of solids by heavy corpuscular radiation, W. S. Snyder and Jacob Neufeld—760(A)
Effect of neutron bombardment on ZnS phosphor, Alan W. Smith and John Turkevich—857
Effect of plastic flow upon color centers in alkali halide crystals, Masayasu Ueta and Werner Känzig—1390(L)
Effect of radiation damage on thermal conductivity of graphite, Alan W. Smith—1417(A)
Effect of short-time moderate-flux neutron irradiation on mechanical properties of some metals, F. W. Kunz and A. N. Holden—1417(A)
Elastic constants of Si before and after neutron bombardment from x-ray diffuse scattering, W. P. Binnie and A. M. Liebschutz—1410(A)
Electrical characteristics of polycrystalline boron, L. J. Badar and V. P. Jacobsmeyer—808(A)
Electrical properties of dislocations in plastically deformed Ge, G. L. Pearson, W. T. Read, Jr., and F. J. Morin—750(A)
Electrical resistivity of cold-worked Al single crystals, A. Sosin and J. S. Koehler—1422(A)
Electron resonance in *F* centers, J. Korringa—1388(L)
Electron traps on Ge surfaces produced by heating in oxygen, Edward N. Clarke—1420(A)
Energy and temperature dependence of secondary emission of MgO, A. J. Dekker—1179

Equivalence of x-ray lattice parameter and density changes in neutron irradiated LiF, D. Binder and W. J. Sturm—760(A)
Formation energy of vacancies in Au, C. J. Meechan and R. R. Eggleston—1406(A)
Hall and resistivity measurements during electron bombardment of Ge and In-Sb, R. Pepper, E. Klontz, K. Lark-Horovitz, and J. MacKay—1410(A)
Imperfections in Cu in terms of electrical resistivity and thermoelectric power, G. W. Rodeback—1406(A)
Influence of nuclear radiation on electrical conductivity of alkali halides, R. Smoluchowski—1409(A)
Interferometric study of surface of x-ray and proton irradiated KCl crystals, W. J. Smith, W. J. Leivo, and R. Smoluchowski—1435(A)
Internal friction associated with precipitation in Al-Ag alloy, A. C. Damask and A. S. Nowick—1421(A)
Interpretation of electroluminescence effects in excited phosphor, Frank Matossi—1151
Interstitial content of radiation-damaged metals from precision x-ray lattice parameter measurements, C. W. Tucker, Jr., and J. B. Sampson—1418(A)
Interstitial Ge in heat-treated Ge, Sumner Mayburg—750(A)
Ionic conductivity of impure polar crystals, A. B. Lidiard—29
Irradiation-induced optical absorption in Al_2O_3, Paul W. Levy and G. J. Dienes—1409(A)
Lattice defects in metals, Frederick Seitz—1406(A)
Magnetic susceptibility of fast-neutron-bombarded Ge, D. K. Stevens, J. W. Cleland, and J. H. Crawford, Jr.—1409(A)
Melted regions in metal crystals resulting from particle bombardment, J. M. Denney—1418(A)
Minority carrier lifetime in semiconductors as sensitive indicator of radiation damage, P. Rappaport—1410(A)
Moduli and internal friction of magnetic as affected by low temperature transformation, M. E. Fine and Nancy T. Kenney—1573
Multiphonon transitions in F center, Jordan J. Markham—1395(L)
Neutron irradiation effects at low temperature—Cu and Al, A. W. McReynolds, W. Augustyniak, M. McKeown, and D. B. Rosenblatt—1417(A)
Order-disorder and cold-work phenomena in Cu-Pd alloys, F. E. Jaumot, Jr., and A. Sawatzky—1429(A)
Paramagnetic resonance in irradiated ice, Bernard Smaller, Max S. Matheson, and Edward L. Yasaitis—202(L)
Pauli principle scattering and resistivity minimum, J. S. Koehler—1071(L)
Peculiarity of electron density near impurity in metal and its effect on x-ray spectra, J. S. Plaskett—1420(A)
R', colloidal, and Z bands in KCl, D. R. Westervelt—1438(A)
Radiation effects in InSb, J. W. Cleland and J. H. Crawford, Jr.—1410(A)
Radiation ordering by cyclotron particles, C. E. Dixon and D. B. Bowen—1418(A)
Radiation-induced changes in electrical resistivity of α brass, D. B. Rosenblatt, R. Smoluchowski, and G. J. Dienes—1418(A)
Rate of production of color centers in KCl and KBr by x-rays at 78°K, William H. Duerig—65
Recombination of holes and electrons at lineage boundaries in Ge, F. L. Vogel, W. T. Read, and L. C. Lovell—1791(L)
Recovery phenomena in cold-worked metals, A. S. Nowick—760(A)
Resistivity changes in Cu, Ag, and Au produced by deuteron irradiation near 10°K, H. G. Cooper, J. S. Koehler, and J. W. Marx—496(L)
Restoration of F and V_3 centers following low temperature bleaching, R. V. Hesketh and E. E. Schneider—494(L)
Search for F-center luminescence, Clifford C. Klick—1541
Search for luminescent emission from F center, Clifford C. Klick—1438(A)
Self-diffusion and ionic conductivity in NaBr, H. W. Schamp, Jr., and E. Katz—828
Self-diffusion in KCl, J. F. Aschner—771(A)
Shear modulus of irradiated Cu, H. Dieckamp and E. C. Crittenden, Jr.—1418(A)
Small-angle scattering of x-rays by irradiated diamond, W. H. Robinson, Yin-Yuan Li, and R. Smoluchowski—1435(A)
Stored energy measurements in irradiated Cu, Albert W. Overhauser—1551
Tunneling of electrons in alkali halides, D. L. Dexter—771(A)
X-ray measurements of cold-worked α brass, E. P. Warekois—1421(A)
X-ray study of prismatic punching in TlCl, Edward I. Salkovitz and Paul L. Smith—770(A)
Inelastic Scattering (see **Nuclear Reactions; Scattering**)
Instruments (see **Methods and Instruments**)
Internal Conversion (see **Nuclear Spectra**)
Ionization (see also **Electrical Discharges; Range and Energy Loss of Particles**)
α-particle ionization in noble gases and formation of metastable atoms, William P. Jesse and John Sadauskis—764(A)
α-particle ionization yields in gridded chamber, Lloyd O. Herwig and Glenn H. Miller—1183
Distribution of specific ionization of primary cosmic rays at $\lambda = 10°$N, G. W. McClure—796(A)
Production of L-shell x-rays by protons, Eugene Bernstein—774(A)
Range and specific ionization for high-energy protons in nuclear emulsions, Otto Heinz—1728
Ionization Potentials of Atoms (see **Atomic Structure and Spectra**)
Ionization Potentials of Molecules (see **Molecular Structure and Spectra**)
Ionosphere (see **Geophysics**)
Ions (see also **Electrical Discharges**)
Propagation of waves in ionized gases, E. P. Gross and M. Krook—778(A)
Range and charge of energetic nitrogen ions in Ni, D. W. Scott, H. L. Reynolds, and A. Zucker—810(A)
Role of Rydberg constant in calculation of ionic radii, N. Efremov—813(A)
United atom-separated atom treatment of H_2^+, J. R. Streetman and F. A. Matsen—805(A)
Ions and Electrons, Mobility (see also **Semiconductors**)
Electronic Hall effect in alkali halides, Alfred G. Redfield—537
Electronic Hall effect in diamond, Alfred G. Redfield—526
Hall mobility of electrons and holes in Si, P. P. Debye and T. Kohane—724(L)
Interpretation of ionic mobilities in N_2, S. Geltman—1072(L)
Mobilities of atomic and molecular ions in noble gases, Manfred A. Biondi and Lorne M. Chanin—910
Mobility and mean free path of electrons and holes in PbS crystals, R. L. Petritz, W. W. Scanlon, and F. L. Lummis—1430
Mobility of impurity ions in Ge and Si, J. C. Severiens and C. S. Fuller—750(A)
Isobars (see **Atomic Mass and Abundance**)

Isomers, Molecular (see **Molecular Structure and Spectra**)
Isomers, Nuclear (see **Nuclear Spectra**)
Isotopes (see **Atomic Mass and Abundance; Radioactivity**)

Kerr Effect (see **Optical Properties**)
Kinetic Theory of Gases (see **Gases**)

Liquid Helium (see **Helium, Liquid**)
Liquids
Absorption of ultrasonic waves in liquids under pressure, J. F. Mifsud—812(A)
Analysis of reduced viscosity equations, Wilfried Heller —1426(A)
Bubble dynamics in superheated liquid, H. K. Forster and N. Zuber—754(A)
Compressibility of liquid cholesterol benzoate at isotropic-anisotropic transition, W. A. Hoyer—812(A)
Density fluctuations at low temperatures, P. J. Price—257; 1801(E)
Effect of hydrostatic pressure in two-state model of compressional relaxation in liquids, A. W. Nolle—812(A)
Effect of structure and molecular weight on viscosity of higher hydrocarbons at high pressures, W. Webb, J. W. Spencer, and R. W. Schiessler—753(A)
Theory of thermodielectric effect, B. Gross—1545
Thickness of films left on capillary wall during displacement of one fluid by another, Charles C. Templeton—812(A)
Luminescence
BeO luminescence, H. O. Albrecht and C. E. Mandeville —776(A); C. E. Mandeville and H. O. Albrecht—494(L)
Dielectric changes in crystal-phosphor condensers irradiated with x-rays, Rudolf Frerichs—1408(A)
Effect of neutron bombardment on ZnS phosphor, Alan W. Smith and John Turkevich—857
Electroluminescence in ZnS single crystals, W. R. Watson, J. J. Dropkin, and A. T. Halpin—777(A)
Energy transfer by means of collision in liquid organic solutions under high energy and uv excitations, Milton Furst and Hartmut Kallmann—503
Interpretation of electroluminescence effects in excited phosphor, Frank Matossi—1151
Optical properties of MgO in vacuum uv, Peter D. Johnson—845
Pressure effects in phosphorescence, L. Reiffel—856
Scintillation response of anthracene to soft x-rays, J. B. Birks and F. D. Brooks—1800(L)
Search for *F*-center luminescence, Clifford C. Klick—1438(A); 1541
Theory of electroluminescence of ZnS crystals, William W. Piper and Ferd E. Williams—777(A)
Triboluminescence in crystals, G. Wolff—777(A)
X-ray induced luminescence in MgO. Albert S. Eisenstein —776(A)

Magnetic Fields (see **Electromagnetic Theory and Electrodynamics**)
Magnetic Properties
Antiferromagnetic H–T boundaries and apparent molecular fields for $MnCl_2 \cdot 4H_2O$ and $MnBr_2 \cdot 4H_2O$, Warren E. Henry—1146
Antiferromagnetism in CuO, B. N. Brockhouse—781(A)
Behavior of ferromagnetic domains under stress, G. Bonfiglioli, A. Ferro, and G. Rosa—316
Cation distributions in mixed ferrites, J. Samuel Smart —847
Critical temperature and susceptibility of dipole lattices, R. Toupin and M. Lax—781(A)
de Haas-van Alphen effect in Cd, Ted G. Berlincourt—1172
Dipolar ferromagnetism in cubic lattices, M. H. Cohen and F. Keffer—1412(A)
Effective mass and degeneracy of carriers in Ge from diamagnetic behavior, J. H. Crawford and D. K. Stevens —1415(A)
Effects of anisotropy on thermodynamic properties of antiferromagnets, J. A. Eisele and F. Keffer—1440(A)
Electromagnetic effects of spin wave resonance, W. S. Ament and G. T. Rado—1411(A)
Equations for magnetostriction and anisotropic energy for hexagonal crystal of class $D_{6h}(6/m,\ 2/m,\ 2/m)$, W. P. Mason and J. A. Lewis—1439(A)
Exchange interactions in spin wave resonance, G. T. Rado and J. R. Weertman—1411(A)
Factors determining permanent magnet properties of single crystals of Fe_2NiAl, E. A. Nesbitt, H. J. Williams, and R. M. Bozorth—1440(A)
Ferromagnetic properties and order-disorder in Fe-Pd alloys, V. J. Folen, F. C. Nix, and F. E. Jaumot, Jr. —1432(A)
Ferromagnetic resonance relaxation times in single crystals of Ni and Fe, J. A. Cowen and R. D. Spence—1411(A)
Ferromagnetism and order in Fe-Pt alloys near Fe_3Pt, A. D. Franklin, A. E. Berkowitz, and E. Klokholm—1432(A)
Field-dependent magnetic susceptibility of MnSe, Robert Lindsay—808(A)
Hall effect in ferromagnetics, J. M. Luttinger and R. Karplus—782(A)
High-field non-Brillouin moments for cobalt sulfate heptahydrate, Warren E. Henry—781(A)
Interaction of polarized neutrons with polarized Mn^{55} nuclei, S. Bernstein, L. D. Roberts, C. P. Stanford, J. W. T. Dabbs, and T. E. Stephenson—1243
Lattice of partly permanent dipoles, M. Lax and R. Toupin —780(A)
Magnetic and electric properties of magnetite at low temperatures, B. A. Calhoun—1577
Magnetic anisotropy of NiF_2, L. M. Matarrese and J. W. Stout—1792(L)
Magnetic domains by longitudinal Kerr effect, Charles A. Fowler, Jr., and Edward M. Fryer—52
Magnetic neutron diffraction in Fe_3O_4, T. Riste and A. W. McReynolds—1433(A)
Magnetic properties of Dy metal, J. F. Elliott, S. Legvold, and F. H. Spedding—1143
Magnetic properties of H_2 molecules, Eiichi Ishiguro and Shoichiro Koide—350
Magnetic susceptibility of carbons and polycrystalline graphites, H. T. Pinnick—319
Magnetic susceptibility of fast-neutron-bombarded Ge, D. K. Stevens, J. W. Cleland, and J. H. Crawford, Jr.—1409(A)
Magnetic susceptibility of Nd metal, J. F. Elliott, S. Legvold, and F. H. Spedding—50
Magnetic susceptibility of Ni-Cu and Ni-Cr alloys, J. E. Goldman and A. Arrott—782(A)
Magnetic susceptibility of transition elements, C. J. Kriessman and Herbert B. Callen—781(A); 837
Magnetization in nickel ferrite indates, Louis R. Maxwell and Stanley J. Pickart—1433(A)
Magnetization of $CuK_2(SO_4)_2 \cdot 6H_2O$ at liquid He temperatures and in strong magnetic fields, Warren E. Henry—1433(A)

Magnetostriction in nickel ferrite-aluminates and nickel ferrite-gallates, D. F. Bleil and A. R. Butz—1440(A)
Magnetostriction of Co, R. M. Bozorth and R. C. Sherwood—1439(A)
Magneto-thermoelectric behavior of Bi at liquid He temperatures, M. C. Steele and J. Babiskin—1394(L)
Melted regions in metal crystals resulting from particle bombardment, J. M. Denney—1417(A)
Method for measuring magnetization and susceptibility at low temperatures, A. Arrott—781(A)
Moduli and internal friction of magnetite as affected by low-temperature transformation, M. E. Fine and Nancy T. Kenney—1573
Molecular field treatment of magnetic ordering transitions, E. W. Elcock—1070(L)
Neutron diffraction observations on Fe at high temperatures, M. K. Wilkinson and C. G. Shull—1439(A)
Neutron polarization, C. P. Stanford, T. E. Stephenson, L. W. Cochran, and S. Bernstein—374
Observation of exchange interaction effects in ferromagnetics by spin wave resonance, G. T. Rado and J. R. Weertman—1386(L)
Paramagnetic scattering of neutrons by rare earth oxides, W. C. Koehler and E. O. Wollan—1801(E)
Permeability and magnetostriction of cation-substituted magnetite, L. R. Bickford, Jr., J. Pappis, and J. L. Stull—1433(A)
Rapid remagnetization of thin Mo permalloy strips, H. Ekstein and J. Kelly—1440(A)
Resistance studies of phase transformations in Fe-Pt alloys near composition Fe_3Pt, R. P. Steijn and F. J. Donahoe—1432(A)
Small-angle neutron scattering by Fe at high temperatures, C. G. Shull and M. K. Wilkinson—1439(A)
Spin waves in antiferromagnetic face-centered cubic lattices, Frank Stern—1412(A)
Structure of Gd, Dy, and Er at low temperatures, J. R. Banister, S. Legvold, and F. H. Spedding—1140
Tensor formulation of ferromagnetic resonance, J. A. Young, Jr., and Edwin A. Uehling—544
Volume magnetostriction in Ni and its alloys, K. Azumi and J. E. Goldman—781(A)

Magnetic Resonance (see also **Nuclear Moments and Spin**)

Analysis of phase detectors for display of nuclear magnetic resonance signals, William L. Rollwitz—810(A)
Atomic hydrogen hfs in irradiated acids, Ralph Livingston, Henry Zeldes, and Ellison H. Taylor—725(L)
Effects of diffusion on free precession in nuclear magnetic resonance experiments, H. Y. Carr and E. M. Purcell—630
Electromagnetic effects of spin wave resonance, W. S. Ament and G. T. Rado—1411(A)
Electron resonance in *F* centers, J. Korringa—1388(L)
Electron spin resonance in metals at low fields, H. S. Gutowsky and P. J. Frank—1067(L)
Exchange interactions in spin wave resonance, G. T. Rado and J. R. Weertman—1411(A)
Ferromagnetic resonance relaxation times in single crystals of Ni and Fe, J. A. Cowen and R. D. Spence—1411(A)
g factor and spin-lattice relaxation time in alkali metals, Harvey Brooks—1411(A)
Hfs and nuclear moments of stable Br isotopes, John Gordon King and Vincent Jaccarino—1610
Hfs in spectrum of $N^{14}H_3$. I. Experimental results, G. R. Gunther-Mohr, R. L. White, A. L. Schawlow, W. E. Good, and D. K. Coles—1184; II. Theoretical discussion, G. R. Gunter-Mohr, C. H. Townes, and J. H. Van Vleck—1191
Hfs of I^{127}. Nuclear magnetic octupole moment, V. Jaccarino, J. G. King, R. A. Satten, and H. H. Stroke—1798(L)
Hfs of In^{115}. Nuclear octupole moment, P. Kusch and T. G. Eck—1799(L)
Line-narrowing by macroscopic motion, F. Bloch—496(L)
Line-narrowing experiment, W. A. Anderson and J. T. Arnold—497(L)
Microwave resonance in NO: λ doubling and hfs, Robert Beringer, E. B. Rawson, and Allan F. Henry—343
Narrow gap electromagnet for high-resolution nuclear resonance spectrometry, Alvin F. Hildebrandt—811(A)
Nuclear induction relaxation times in polymers, V. R. Honnold, F. McCaffrey, and B. A. Mrowca—1414(A)
Nuclear magnetic relaxation in semiconductors, N. Bloembergen—1411(A)
Nuclear magnetic resonance as criterion of chemical bonding, Richard A. Ogg, Jr.—767(A)
Nuclear magnetic resonance spectra of boranes and derivatives, John Kelly, James Ray, and Richard A. Ogg, Jr.—767(A)
Nuclear resonance absorption in weak, homogeneous fields, R. W. Mitchell and Melvin Eisner—811(A)
Observation of exchange interaction effects in ferromagnetics by spin wave resonance, G. T. Rado and J. R. Weertman—1386(L)
Orientation of nuclei by saturation of paramagnetic resonance, J. Korringa—1388(L)
Paramagnetic resonance absorption in carbons, J. G. Castle, Jr.—1410(A)
Paramagnetic resonance absorption in diphenyl picryl hydrazyl at low values of splitting field, Stewart Becker and Melvin Eisner—811(A)
Paramagnetic resonance in irradiated ice, Bernard Smaller, Max S. Matheson, and Edward L. Yasaitis—202(L)
Paramagnetic resonance of Cu complex salts, Tosihiko Okamura and Muneyuki Date—314
Proton magnetic resonance in compounds having several liquid crystal phases, R. Ewing and J. C. Lee—1411(A)
Ratios of quadrupole coupling constants of isotopes and their variation with temperature, T. C. Wang and C. H. Townes—767(A)
Self-quenching superregenerative spectrometers, P. J. Bray—767(A)
"Slow beats" in nuclear quadrupole induction, M. Bloom—1396(L)
Spin relaxation in free radical solutions exhibiting hfs, J. P. Lloyd and G. E. Pake—579
Spin resonance of ionized donors in Si, R. C. Fletcher, W. A. Yager, G. L. Pearson, A. N. Holden, W. T. Read, and F. R. Merritt—1392(L)
Spin waves in antiferromagnetic face-centered cubic lattices, Frank Stern—1412(A)
Spin-orbit interaction in RbF and CsF, G. Bemski, W. A. Nierenberg, and H. B. Silsbee—767(A)
Tensor formulation of ferromagnetic resonance, J. A. Young, Jr., and Edwin A. Uehling—544
Variations of hydrogen rotational magnetic moments with rotational quantum number and with isotopic mass, R. G. Barnes, P. J. Bray, and N. F. Ramsey—893

Magneto-Optical Effects (see **Optical Properties**)

Magnetoresistance (see **Electrical Conductivity and Resistance**)

Magnetostriction (see **Magnetic Properties**)

Mass Defects (see **Atomic Mass and Abundance**)

Mass Spectroscopy (see **Atomic Mass and Abundance; Methods and Instruments**)

Mathematical Methods
Fourier analysis of x-ray small-angle scattering, Yin-Yuan Li and R. Smoluchowski—1435(A)
Measure of area of homogeneous random surface in space, Stanley Corrsin—783(A)
Mechanical electric computer for solving polynomial equations, Harry J. Auverman and Arthur E. Lockenvitz—811(A)
Solutions of Helmholtz and Schrödinger equations in sphero-conal coordinates, Olen Kraus—1442(A)
Statistical approach to phase determination in x-ray analysis, V. Vand and R. Pepinsky—1435(A)
Measurements (see **Methods and Instruments**)
Mechanics
Classical and quantum theory of many interacting particles. I, George J. Yevick and Jerome K. Percus—787(A); II, Jerome K. Percus and George J. Yevick—787(A)
Tensor virial equations, E. N. Parker—1441(A)
Mechanics, Quantum—Atomic Structure and Spectra (see **Atomic Structure and Spectra**)
Mechanics, Quantum—General (see **Quantum Mechanics**)
Mechanics, Quantum—Molecular Structure and Spectra (see **Molecular Structure and Spectra**)
Mechanics, Quantum—Nuclear (see **Nuclear Structure Theory**)
Mechanics, Quantum—of Solid Bodies (see **Crystalline State**)
Mechanics, Statistical (see **Statistical Mechanics and Thermodynamics**)
Meson Field Theory (see **Field Theory**)
Mesons (see also **Cosmic Radiation; Elementary Particle Interactions; Nuclear Reactions Induced by Mesons; Scattering of Mesons**)
Cloud-chamber observations of some unusual neutral V particles having light secondaries, V. A. J. van Lint, C. D. Anderson, E. W. Cowan, R. B. Leighton, and C. M. York, Jr.—1732
Connection between pion photoproduction and scattering phase shifts, Marc Ross—454
Decay of χ meson, Seiichi Sueoka—1397(L)
Decay of heavy nuclear fragment, P. S. Freier, G. W. Anderson, and J. E. Naugle—677
Decay of τ mesons of known charge, R. H. Dalitz—1046
Density effect for ionization energy losses in gases, E. D. Palmatier, J. T. Meers, and C. M. Askey—766(A)
Distortion of nucleus in μ-mesic atoms, W. Lakin and W. Kohn—787(A)
Effect of Coulomb barrier on meson production by nucleon-nucleus collisions, Toichiro Kinoshita—1331
Effect of deuteron formation on multiple meson production, K. A. Brueckner and J. S. Kovacs—726(L)
Elastic photoproduction of neutral mesons from deuterium, B. J. W. Wolfe, B. J. W. DeWire, and A. Silverman—756(A)
Elastic production of π^0 photomesons from deuterium, H. L. Davis and D. R. Corson—756(A)
Energy distribution of neutral mesons produced in cosmic-ray stars, Y. B. Kim—797(A)
γ rays associated with S-particle decay, H. Courant—797(A)
Interaction with A and Pb of neutrons with energies up to 2.3 Bev, E. C. Fowler, H. L. Kraybill, R. M. Walker, and R. S. Preston—791(A)
Kinematics of Λ^0 production, George T. Reynolds and S. B. Treiman—207(L); 797(A)
K-meson and hyperon decays, Paul H. Barrett—1328
K-particle production by protons of 2.2 and 3.0 Bev, R. D. Hill, E. O. Salant and M. Widgoff—1794(L)
Low-energy limits of meson processes, S. Deser and W. E. Thirring—746(A)
Mean lives of positive and negative μ mesons, N. N. Biswas and M. S. Sinha—1400(L)
μ-meson decay spectrum, J. H. Vilain and Robert W. Williams—1011
μ-mesonic x-rays and shape of nuclear charge distribution, David L. Hill and Kenneth W. Ford—1617
Nuclear events at high energies, Joseph V. Lepore and Richard N. Stuart—1724
$p+d\rightarrow\pi^{+}+t$ reaction, Sidney A. Bludman—1722
$p+d\rightarrow t+\pi^{+}$ angular distribution and yield, Wilson J. Frank, Kenneth C. Bandtel, Richard Madey, and Burton J. Moyer—1716
Phenomenology of pion-nucleon S waves, H. P. Noyes and A. E. Woodruff—1401(L)
Photomeson production from hydrogen, T. L. Jenkins, D. Luckey, and R. R. Wilson—755(A)
Photoproduction of π^{+} mesons from H near threshold, G. Bernardini and E. L. Goldwasser—729(L)
Photoproduction of π^{+} mesons near threshold, E. L. Goldwasser and G. Bernardini—755(A)
$\pi^{\pm}$ production cross sections from deuterium, Walter F. Dudziak—756(A)
π^{+}/π^{-} ratios at low energies from complex nuclei, Ryokichi Sagane and Walter F. Dudziak—755(A)
Pion production ratios, D. C. Peaslee—1085(L)
Possible angular correlations involving V particles, L. Wolfenstein—786(A)
Production of K mesons, U. Haber-Schaim, Y. Yeivin, and G. Yekutieli—184
Sea-level zenith-angle dependence of high-energy μ mesons, N. M. Duller, W. D. Walker, J. W. Graham, and J. R. Risser—810(A)
Search for K particles using Čerenkov counters, J. W. Keuffel and L. Mezzetti—797(A)
Spectroscopy of π^{-} and μ-meson x-rays, S. De Benedetti, M. B. Stearns, M. Stearns, and H. J. Richings—766(A)
Spectrum of electrons from μ-meson decay, R. W. Williams and J. H. Vilain—757(A)
Strange particles and multiple meson production, Giuseppe Cocconi—741(L)
Unstable heavy particles from Cosmotron, R. D. Hill, E. O. Salant, M. Widgoff, L. S. Osborn, A. Pevsner, D. M. Ritson, J. Crussard, and W. D. Walker—797(A)
V-decay event with heavy negative secondary, and secondary V-decay event in cascade, E. W. Cowan—161
V particles and γ decay of neutral pion, Toichiro Kinoshita—1386
Yields of π^{-} and μ-meson x-rays in low-Z materials, M. Stearns, M. B. Stearns, S. De Benedetti, and L. Leipuner—766(A)
Metals (see **Crystalline State**)
Metastable Atoms (see **Atomic Structure and Spectra**)
Metastable Molecules (see **Molecular Structure and Spectra**)
Meteorology (see **Geophysics**)
Methods and Instruments
Analysis of phase detectors for display of nuclear magnetic resonance signals, William L. Rollwitz—810(A)
Analyzing magnet for 100-kv modified Cockcroft-Walton accelerator, James E. Wills and Henry R. Dvorak—810(A)
Angular correlation apparatus for $Li^{7}(p,\gamma,\alpha)He^{4}$, Pat M. Windham and G. C. Phillips—803(A)
Bubble tracks in hydrogen-filled Glaser chamber, John G. Wood—731(L)

Cloud-chamber distortions, W. Wallenmeyer—768(A)
Coincidences in scintillation counter, A. L. Orvis and M. M. D. Williams—810(A)
Comparison of diffusion techniques employing radioisotopes, R. L. Smith, F. E. Jaumot, Jr., and L. A. Arné, Jr.—1407(A)
Continuous parameter approximation in linear accelerator with independently excited cavities, R. L. Gluckstern, P. B. Daitch, L. C. Biedenharn, and M. H. Hull, Jr.—768(A)
Design features of high-current cyclotron, Robert S. Livingston and Royce J. Jones—1436(A)
Design of diffusers to avoid turbulent boundary layer separation, Francis H. Clauser—783(A)
Design study for 15-Bev accelerator by Cambridge design study group, M. S. Livingston—792(A)
Dielectric changes in crystal-phosphor condensers irradiated with x-rays, Rudolf Frerichs—1408(A)
Dielectric high-frequency method for molecular weight determinations, P. Debye, P. P. Debye, and B. H. Eckstein—1412(A)
Differential pumping system for gas targets, C. W. Reich, J. Russell, and G. C. Phillips—804(A)
Doppler line-width reduction, M. W. P. Strandberg and H. Dreicer—1393(L)
Doubly ionized He ion source, J. W. Bittner, R. G. Herb, R. D. Moffat, and J. A. Weinman—769(A)
Electromechanical analog for study of strong-focusing orbits, L. W. Jones and K. M. Terwilliger—1436(A)
Estimation of beam intensity and cross sections at Cosmotron from gross radioactivity in Cu, Anthony Turkevich—775(A)
Fast neutron counter with energy resolution, J. H. McCrary, H. L. Taylor, and T. W. Bonner—808(A)
Field-induced diffraction method for molecular weight determinations, W. A. Barber, P. Debye, and B. H. Eckstein—1412(A)
Growth of long-lifetime Ge crystals, Milton Becker—1420(A)
High-speed machine computation of ideal gas thermal properties. Isotopic water molecules, Abraham S. Friedman and Lester Haar—1423(A)
Improved apparatus for high-resolution neutron cross-section measurements, J. H. Gibbons—773(A)
Improved spark counter for detecting α radiation, Charles E. Weller—810(A)
Initial performance of large Bartol Van de Graaf, C. P. Swann—768(A)
Initiation of discharge in CO_2-filled G-M counter by negative ions, H. R. Crane—1437(A)
Large volume scattering chamber for angular distribution experiments, J. Russell, Jr., C. W. Reich, and G. C. Phillips—804(A)
LiI(Eu) crystals as neutron detectors, J. B. Marion—808(A)
Line-narrowing by macroscopic motion, F. Bloch—496(L)
Line-narrowing experiment, W. A. Anderson and J. T. Arnold—497(L)
Liquefied gas x-ray target, E. A. Whalin and R. A. Reitz—752(A)
Longitudinal and transverse stability in linear accelerator systems, G. Breit—768(A)
Mechanical electric computer for solving polynomial equations, Harry J. Auverman and Arthur E. Lockenvitz—811(A)
Method for measuring magnetization and susceptibility at low temperatures, A. Arrott—781(A)
Microtron resonators, H. F. Kaiser—768(A)
NaI γ-ray spectrometry techniques applied to outlining of brain tumors, J. R. Risser and H. C. Allen, Jr.—810(A)
Narrow gap electromagnet for high-resolution nuclear resonance spectrometry, Alvin F. Hildebrandt—811(A)
New method for measuring short γ-ray lifetimes, J. W. Knowles—795(A)
Preparation of PbS crystals of controlled electrical properties, W. W. Scanlon and R. F. Brebrick—1430(A)
Scintillation response of anthracene to soft x-rays, J. B. Birks and F. D. Brooks—1800(L)
Self-quenching superregenerative rf spectrometers, P. J. Bray—767(A)
Stability of linear accelerator with independently excited cavities, M. H. Hull, Jr., L. C. Biedenharn, P. B. Daitch, and R. L. Gluckstern—768(A)
Summation of γ-ray energies with single-crystal spectrometer, Daniel C. Lu and M. L. Wiedenbeck—501(L)
Theory of photographic intermittence effect at low light intensities, E. Katz—1441(A)
Use of wires embedded in nuclear emulsions to investigate reactions induced by high-energy neutrons, E. G. Silver and R. W. Waniek—769(A)
Variable Hg delay line equipment for measurement of short half-lives, C. A. Sheer, A. Zinn, and N. Hartmann—769(A)
Writing speed and tonal range of dark trace tubes, Seymour Nozick—778(A)

Microwaves (see also **Atomic Structure and Spectra; Magnetic Resonance; Molecular Structure and Spectra; Nuclear Moments and Spin**)
Doppler line-width reduction, M. W. P. Strandberg and H. Dreicer—1393(L)
Nonuniform microwave transmission lines and solutions of Riccati equations, Stanley Winkler—778(A)

Miscellaneous

Mobility of Ions and Electrons (see **Ions and Electrons, Mobility**)

Molecular Aggregates
Analysis of reduced viscosity equations, Wilfried Heller—1426(A)
Calculation of dynamic bulk modulus of polyisobutylene, Robert S. Marvin, H. S. Sack, and R. Aldrich—1413(A)
Concentration dependence of mechanical shear degradation, P. Goodman—1425(A)
Creep and relaxation of plastics, A. R. DiDonato, A. A. MacLeod, and A. C. Webber—770(A)
Determination of ratio of photoelastic constants of glasses by means of ultrasonic waves, Halbert Gates—1434(A)
Dielectric high-frequency method for molecular weight determinations, P. Debye, P. P. Debye, and B. H. Eckstein—1412(A)
Dynamic mechanical properties of polyvinyl acetate, Malcolm L. Williams and John D. Ferry—1413(A)
Effect of crystallinity on dynamic mechanical properties of polyethylenes, Lawrence E. Nielsen—1414(A)
Effect of structure and molecular weight on viscosity of higher hydrocarbons at high pressures, W. Webb, J. W. Spencer, and R. S. Schiessler—753(A)
Effects of Co^{60} γ radiation on formation and degradation of polymers, Lindsey M. Hobbs, Douglas E. Brown, and David W. Pletcher—1412(A)
Elastic and dielectric losses of high polymers near and below second-order transition temperature, H. S. Sack, T. R. Cuykendall, and T. J. Woods—1414(A)
Energy requirements of mechanical shear degradation in concentrated polymer solutions, A. B. Bestul—1425(A)
Energy to create fracture surfaces in glass, H. L. Smith and J. A. Kies—760(A)

Molecular Aggregates (Continued)
Experimental investigation of statistical theory of rubber elasticity, F. P. Baldwin, J. Ivory, and R. L. Anthony—1425(A)
Field-induced diffraction method for molecular weight determinations, W. A. Barber, P. Debye, and B. H. Eckstein—1412(A)
γ-ray polymerization of acrylamide in solid state, Robert B. Mesrobian, Paul Ander, David S. Ballantine, and G. J. Dienes—1413(A)
Infrared spectrum of polyethylene, S. Krimm—1426(A)
Multiple diffraction patterns in glass produced by ultrasonic waves of high intensity, J. M. Barnes—1434(A)
Multiple dispersion regions in rigid polymeric systems, Rolf Buchdahl and Lawrence E. Nielsen—1414(A)
Nuclear induction relaxation times in polymers, V. R. Honnold, F. McCaffrey, and B. A. Mrowca—1414(A)
Relation between refractive index and density in glass, H. N. Ritland—1434(A)
Slow relaxation mechanisms in concentrated polymer solutions, John D. Ferry, Malcolm L. Williams, and Donald M. Stern—1413(A)
Steady-state elastic shear compliance and molecular weight distribution in polyisobutylene, Herbert Leaderman and M. Wales—1414(A)
Stress-temperature-time studies through second-order transition region, D. G. Ivey and A. Kwei—1414(A)
Ultrasonic properties of Hycar OS-10 and Paracril 35, J. L. Melchor and A. A. Petrauskas—1414(A)
Viscoelasticity in complex static stress systems, A. A. MacLeod, A. R. DiDonato, and A. C. Webber—769(A)
Molecular Beams (see **Atomic and Molecular Beams**)
Molecular Structure and Spectra
Absorption spectra of water vapor in 2.7μ and 6.0μ regions, F. W. Dalby, H. H. Nielsen, and F. P. Dickey—1423(A)
Application of Franck-Condon principle to bent XY_2 molecule, J. B. Coon and J. K. Ward—805(A)
Configuration interaction applied to hydrogen molecule, Earl Callen—1423(A)
Density effects in Raman spectrum of ammonia, C. A. Plint, R. M. B. Small, and H. L. Welsh—805(A)
Effect of foreign gas broadening on total absorption by 6.3μ band of water vapor, D. E. Burch, J. N. Howard, and Dudley Williams—1424(A)
Generalized absorption coefficients of water vapor, Harold Daw—1424(A)
Hfs in DCC, Cl, DCN, and HCN due to deuteron quadrupole coupling and field asymmetries, Robert L. White—789(A)
Hfs in spectrum of $N^{14}H_3$. I. Experimental results, G. R. Gunther-Mohr, R. L. White, A. L. Schawlow, W. E. Good, and D. K. Coles—1184; II. Theoretical discussion, G. R. Gunther-Mohr, C. H. Townes, and J. H. Van Vleck—1191
Infrared and Raman spectra of fluorinated ethanes. VIII. CF_3CF_2H, J. Rud Nielsen, H. H. Claassen, and Norma B. Moran—805(A)
Infrared spectra of C_6D_4O, Charles W. Arnold and F. A. Matsen—804(A)
Infrared spectrum of hydrogen sulfide in 5100 cm^{-1} region, Harry C. Allen, Jr., and Earle K. Plyler—1423(A)
Intensities, electronic transition moments, and vibrational transition probabilities of diatomic molecules, R. W. Nicholl, P. A. Fraser, R. G. Turner, and W. R. Jarmain—1423(A)
Line shapes in infrared, W. S. Benedict and Shirleigh Silverman—752(A)
Magnetic properties of H_3 molecules, Eiichi Ishiguro and Shoichiro Koide—350
Mass spectra of deuteroethylenes, Vernon H. Dibelar and Fred L. Mohler—754(A)
Microwave resonance in NO: λ doubling and hfs, Robert Beringer, E. B. Rawson, and Allan F. Henry—343
Microwave spectrum of ethyl fluoride, J. Kraitchman and B. P. Dailey—788(A)
Microwave spectrum of free OD radical, G. C. Dousmanis—789(A)
Microwave spectrum of methyl amine, David R. Lide, Jr.—788(A)
Microwave spectrum of 1,1 difluoroethane, N. Solimene and B. P. Dailey—789(A)
Microwave spectrum of ReO_3F, J. F. Lotspeich, Ali Javan, and Alfred Engelbrecht—789(A)
Molecular wave-functions in *e*-notation, J. M. Miller and F. A. Matsen—804(A)
NO hfs theory, Masataka Mizushima—569; 789(A)
Precision determination of velocity of light derived from band spectrum method. II, D. H. Rank, J. N. Shearer, and T. A. Wiggins—575
Pure quadrupole spectrum of methyl iodide vapor, Fred Sterzer and Yardley Beers—1410(A)
Role of principal quantum number (n) in calculations of radii for ions with high (4, 5, 6, 7) valence, N. Efremov—1424(A)
S bonds and quadrupole moments of O, S, and Se isotopes, G. R. Bird and C. H. Townes—1203
Se^{77} spin and quadrupole moment, L. C. Aamodt, P. C. Fletcher, G. Silvey, and C. H. Townes—789(A)
Shape of collision-broadened spectral lines, E. P. Gross—1424(A)
Theory of directed valence, Ta-You Wu—1424(A)
3-dimensional calculation of vibrational relaxation times in gases, Robert N. Schwartz—793(A)
2.7μ bands of CO_2, W. L. France and F. P. Dickey—1423(A)
United atom-separated atom treatment of H_3^+, J. R. Streetman and F. A. Matsen—805(A)
Variations of hydrogen rotational magnetic moments with rotational quantum number and with isotopic mass, R. G. Barnes, P. J. Bray, and N. F. Ramsey—893
Vibrational analysis of 3400–4000A absorption spectrum of SO_2, R. K. Russell—805(A)
Vibrational spectra of cyclobutforene, M. Z. El-Sabban and J. Rud Nielsen—805(A)
Vibrational spectra of H_3D-SiF_3, R. L. Collins and J. Rud Nielsen—805(A)
Vibration-rotation line intensities of diatomic molecules, R. C. Herman, S. Silverman, and R. F. Wallis—752(A)
Moments, Nuclear (see **Nuclear Moments and Spin**)
Moments of Molecules (see **Molecular Structure and Spectra**)

Neutrino (see also **Nuclear Spectra; Radioactivity**)
Neutron Diffraction (see **Diffraction; Scattering of Neutrons**)
Neutrons (see **Elementary Particle Interactions**)
Noise
Current oscillations in photoconductive films of PbTe, Dean L. Mitchell, Werner J. Beyen, and Donald E. Bode—1430(A)
Errors in power spectra due to finite sample, L. M. Spetner—778(A)
Quantum theory of damped electrical oscillator and noise, II, J. Weber—211
Quantum theory of radiation resistance, J. Weber—793(A)
Vacuum fluctuation noise, J. Weber—215

Nuclear Fission
Angular anisotropy of specific Th photofission fragments, A. W. Fairhall, I. Halpern, and E. J. Winhold—733(L)
Angular distribution of fragments from neutron-induced fission, J. E. Brolley, Jr., and W. C. Dickinson—640
Angular distributions of fission fragments from 22-Mev proton-induced Th fission, B. L. Cohen, W. H. Jones, G. H. McCormick, and B. L. Ferrell—625; 758(A)
Energy released per fission in Bulk Shielding Reactor, J. L. Meem—759(A)
Energy spectrum of spontaneous fission fragments, Emilio Segrè and Clyde Wiegand—157
Fission fragment ranges in Al, D. H. Templeton and E. M. Douthett—759(A)
Identification of Cf isotopes 249, 250, 251, and 252 from pile-irradiated Pu, H. Diamond, L. B. Magnusson, J. F. Mech, C. M. Stevens, A. M. Friedman, M. H. Studier, P. R. Fields, and J. R. Huizenga—1083(L)
New isotopes of Am, Bk, and Cf, A. Ghiorso, S. G. Thompson, G. R. Choppin, and B. G. Harvey—1081(L)
Nuclear properties of some isotopes of Cf, elements 99 and 100, G. R. Choppin, S. G. Thompson, A. Ghiorso, and B. G. Harvey—1080(L)
Photofission cross sections, James Gindler and Robert B. Duffield—759(A)
Products of high-energy fission, M. Lindner and R. N. Osborne—1323
$_{94}Pu^{240}$ and its spontaneous fission, O. Chamberlain, G. W. Farwell, and E. Segrè—156
Ranges of fragments from high-energy fission of U, E. M. Douthett and D. H. Templeton—128
Spontaneous fission systematics, John R. Huizenga—158
Thermal neutron fission cross section of Am^{242m}, G. H. Higgins and W. W. T. Crane—735(L)
Yields of fission products from U^{235} irradiated with fission spectrum neutrons, R. N. Keller, E. P. Steinberg, and L. E. Glendenin—969
Nuclear Forces (see **Elementary Particle Interactions; Field Theory; Nuclear Structure Theory**)
Nuclear Induction (see **Magnetic Resonance; Nuclear Moments and Spin**)
Nuclear Isomers (see **Nuclear Spectra; Radioactivity**)
Nuclear Moments and Spin
Hfs and nuclear moments of stable Br isotopes, John Gordon King and Vincent Jaccarino—1610
Hfs in DCC, Cl, DCN, and HCN due to deuteron quadrupole coupling and field asymmetries, Robert L. White—789(A)
Hfs of $3P_{3/2}$ state of Na^{23}, Paul L. Sagalyn—885
Magnetic moment of K^{40} in intermediate coupling, G. E. Tauber and Ta-You-Wu—262(A); 1307
NO hfs theory, Masataka Mizushima—569; 789(A)
Nuclear spin of Am^{243} and isotope shift in Am spectrum, John G. Conway and Ralph D. McLaughlin—498(L)
Orientation of nuclei by saturation of paramagnetic resonance, J. Korringa—1388(L)
RaE spin, R. W. King and D. C. Peaslee—795(A)
S bonds and quadrupole moments of O, S, and Se isotopes, G. R. Bird and C. H. Townes—1203
Se^{76} spin and quadrupole moment, L. C. Aamodt, P. C. Fletcher, G. Silvey, and C. H. Townes—789(A)
Spin relaxation in free radical solutions exhibiting hfs, J. P. Lloyd and G. E. Pake—579
Spins of lowest states of K^{40}, P^{32}, and Al^{26} nuclei, Harald A. Enge—730(L)
Nuclear Photoeffects
Angular anisotropy of specific Th photofission fragments, A. W. Fairhill, I. Halpern, and E. J. Winhold—733(L)
Connection between pion photoproduction and scattering phase shifts, Marc Ross—454
Deuteron photodisintegration at intermediate energies, J. M. Berger—1698
Elastic photoproduction of neutral mesons from deuterium, B. Wolfe, J. W. DeWire, and A. Silverman—756(A)
Elastic photoproduction of π^0 in He, G. De-Saussure and L. S. Osborne—756(A)
Elastic production of π^0 photomesons from deuterium, H. L. Davis and D. R. Corson—756(A)
Electrodisintegration of Cu^{65}, M. B. Scott, A. O. Hanson, and D. W. Kerst—763(A)
High-energy photoproton production by 325-Mev bremsstrahlung radiation, B. T. Feld, R. D. Godbole, A. Odian, F. Scherb, P. C. Stein, and A. Wattenberg—1000
Stern-Gerlach experiment on polarized neutrons, J. E. Sherwood, T. E. Stephenson, C. P. Stanford, and Seymour Bernstein—791(A)
$Mg^{24}(\gamma,3p3n)F^{18}$ reaction induced by 70-Mev bremsstrahlung, Fritz D. Schupp and Don S. Martin, Jr.—80
Photodisintegration of deuterium by 60–280 Mev x-rays, Barbara Dwight Schreiber, E. A. Whalin, and A. O. Hanson—763(A)
Photodisintegration of He above meson threshold, V. O. Nicolai and E. L. Goldwasser—755(A)
Photofission cross sections, James Gindler and Robert B. Duffield—759(A)
Photomeson production from hydrogen, T. L. Jenkins, D. Luckey, and R. R. Wilson—755(A)
Photoproduction of π^+ mesons from H near threshold, G. Bernardini and E. L. Goldwasser—729(L)
Photoproduction of π^+ mesons near threshold, E. L. Goldwasser and G. Bernardini—755(A)
Photoprotons from 300-Mev bremsstrahlung, P. C. Murray, R. I. Scace, R. O. Haxby, and T. R. Palfrey, Jr.—764(A)
Systematics of photoproton reactions, E. B. Weinstock and J. Halpern—1651
Nuclear Reactions, General (see also **Elementary Particle Interactions; Scattering**)
Coulomb excitation by means of bombardment with various particles, Jørgen H. Bjerregaard and Torben Huus—204(L)
Decay of heavy nuclear fragment, P. S. Freier, G. W. Anderson, and J. E. Naugle—677
Electrodisintegration of Cu^{65}, M. B. Scott, A. O. Hanson, and D. W. Kerst—763(A)
Emission of δ- and x-rays from targets bombarded by accelerated ions, Črtomir Zupančič and Torben Huus—205(L)
Energy spectra of nucleons evaporated from compound nucleus, R. M. Eisberg—739(L)
Excitation functions for nitrogen-induced nuclear reactions in C, A. Zucker and H. L. Reynolds—748(A)
High-energy events, Joseph V. Lepore, Maurice Neuman, and Richard N. Stuart—788(A)
Inelastic scattering of charged particles in electric excitation processes, Hans Mark—1436(A)
Inelastic scattering of 190-Mev electrons in Be, J. A. McIntyre, B. Hahn, and R. Hofstadter—1084(L)
Level densities in heavy nuclei of 10- to 20-Mev excitation, D. B. Beard—738(L)
Nuclear events at high energies, Joseph V. Lepore and Richard N. Stuart—1724
Nuclear potential well depth, Robert K. Adair—737(L)
Polarization from isolated resonances, A. Simon and T. A. Welton—943
Statistical factors in radiation widths of nuclear energy levels, D. J. Hughes—740(L)

Nuclear Reactions Induced by α Particles and He^3 (see also **Scattering of α Particles**)

(α-n) reactions in Be^9, B^{11}, and C^{13}, R. E. Trumble, Jr.—748(A)

$B^{10}(\alpha,p)C^{13}$ energy levels, W. J. Fader and A. Sperduto—748(A)

Coulomb excitation of heavy and medium nuclei by α particles, G. M. Temmer and N. P. Heydenburg—747(A)

γ-ray spectrum of Po-B source, Temple Love and Fred Maienschein—795(A)

γ rays from inelastic scattering of α particles by lithium and fluorine, N. P. Heydenburg, and G. M. Temmer—748(A)

γ rays from Li^7, F^{19}, Ne^{20}, and Na^{22} produced by α-particle bombardment of lithium and fluorine, N. P. Heydenburg and G. M. Temmer—1252

γ rays from Ne^{20}, B. P. Foster, G. S. Stanford, and L. L. Lee—804(A)

$He^3 + He^3$ reactions, W. M. Good, W. E. Kunz, and C. D. Moak—87

Low excited states of F^{19}. III. Coulomb excitation by α particles, R. Sherr, C. W. Li, and R. F. Christy—1076(L)

Rotational nuclear energy levels from Coulomb excitation, G. M. Temmer and N. P. Heydenburg—1399(L)

Nuclear Reactions Induced by Deuterons and Tritons (see also **Scattering of Deuterons**)

Angular correlations in $Be^9(d,p\gamma)Be^{10}$ and $Be^9(d,\alpha\gamma)Li^7$, L. Cohen, S. S. Hanna, and C. M. Class—419

Be^{10} energies of excited states, C. K. Bockelman and J. J. Jung—748(A)

$C^{13}(d,t)C^{12}$ differential cross sections, H. D. Holmgren, J. M. Blair, B. E. Simmons, and R. V. Stuart—748(A)

Correction to deuteron stripping cross sections, Larry Schecter and Warren Heckrotte—1086(L)

(d,p) reactions in Ni and statistical theory of nuclear reactions, William W. Pratt—1086(L)

Deuteron stripping theory, W. Tobocman—762(A)

Deuteron-induced reaction studies, N. S. Wall—763(A)

Energy levels in Ca^{41} from $Ca^{40}(d,p)Ca^{41}$ reaction, C. M. Braams—763(A)

Excitation function and Q value for $C^{14}(d,p)C^{15}$, James A. Rickard and Emmett L. Hudspeth—806(A)

Neutron thresholds in $Li^7(d,n)Be^8$ and $Be^9(d,n)B^{10}$, T. W. Bonner and C. F. Cook—807(A)

Neutron yields from d-d reaction in various target materials, R. C. Campbell, J. D. Korsmeyer, and D. C. Ralph—791(A)

Scattering of 190-Mev deuterons on protons, Arnold L. Bloom and Owen Chamberlain—659

Spins of lowest states of K^{40}, P^{32}, and Al^{28} nuclei, Harald A. Enge—730(L)

Nuclear Reactions Induced by Mesons (see also **Elementary Particle Interactions; Mesons; Scattering of Mesons**)

Analysis of 405-Mev proton and 222-Mev negative pion stars, A. D. Sprague, D. M. Haskin, R. G. Glasser, and Marcel Schein—994

Angular distribution of π^--proton charge exchange scattering at 40 Mev. I. Apparatus, A. Roberts and J. Tinlot—766(A); II. Analysis of results, J. Tinlot and A. Roberts—766(A)

Charge exchange scattering of negative pions at 42, 30, and 20 Mev in hydrogen, W. Spry—766(A)

Interaction of high-energy pions with nuclei, E. D. Courant—1081(L)

Interactions of negative pions in C and Pb, John O. Kessler and Leon M. Lederman—689

Negative μ-meson capture in carbon, T. N. K. Godfrey—756

Nuclear interaction of fast μ mesons, Martin Annis, Homer C. Wilkins, and John D. Miller—1038

π^--p interactions at 1.5 Bev, J. Crussard, W. D. Walker, and M. Koshiba—736(L)

Possible angular correlations involving V particles, L. Wolfenstein—786(A)

Unstable heavy particles from Cosmotron, R. D. Hill, E. O. Salant, M. Widgoff, L. S. Osborne, A. Pevsner, D. M. Ritson, J. Crussard, and W. D. Walker—797(A)

Nuclear Reactions Induced by Neutrons (see also **Elementary Particle Interactions; Scattering of Neutrons**)

Activation measurements in Eu with monoenergetic neutrons, R. E. Wood—794(A)

Angular distribution of D(d,n) neutrons scattered from C, Al, S, Fe, Cd, Cu, W, and Pb, R. N. Little, Jr., C. P. Cadenhead, B. P. Leonard, Jr., J. T. Prud'homme, L. D. Vincent, and J. E. Wills—807(A)

Angular distribution of fragments from neutron-induced fission, J. E. Brolley, Jr., and W. C. Dickinson—640

Average neutron total cross sections in 3- to 12-Mev region, Norris Nereson and Sperry Darden—1678

Cm isotopes 246 and 247 from pile-irradiated plutonium, C. M. Stevens, M. H. Studier, P. R. Fields, J. F. Mech, P. A. Sellers, A. M. Friedman, H. Diamond, and J. R. Huizenga—974

Doppler effect in slow neutron resonance in Rh, H. H. Landon—1215

Effect of finite resolution on neutron transmission near resonance, E. Melkonian and W. W. Havens, Jr.—790(A)

Energy levels of Cu from inelastic neutron scattering, L. A. Rayburn, D. L. Lafferty, and T. M. Hahn—1641

Energy spectra of nucleons evaporated from compound nucleus, R. M. Eisberg—739(L)

Evidence for Si^{32}, long-lived β emitter, Anthony Turkevich and Arthur Samuels—364

Experiments with neutrons from the Cosmotron. I, D. A. Hill, T. Coor, W. F. Hornyak, L. W. Smith and G. A. Snow—791(A); II, G. A. Snow, T. Coor, D. A. Hill, W. F. Hornyak, and L. W. Smith—791(A)

γ rays excited by inelastic scattering of fast neutrons in Bi, Ni, and Cu, M. S. Rothman, H. S. Hans, and C. E. Mandeville—791(A)

γ rays from inelastic scattering of 14-Mev neutrons in C^{13} and O^{16}, L. C. Thompson and J. R. Risser—941

γ-γ coincidences from interaction of 3.1-Mev neutrons with various materials, V. E. Scherrer, B. A. Allison, and W. R. Faust—791(A)

Improved apparatus for high-resolution neutron cross-section measurements, J. H. Gibbons—773(A)

Inelastic scattering of neutrons, E. A. Eliot, D. Hicks, L. E. Beghian, and H. Halban—144

Interaction of polarized neutrons with polarized Mn^{56} nuclei, S. Bernstein, L. D. Roberts, C. P. Stanford, J. W. T. Dabbs, and T. E. Stephenson—1243

Interaction with A and Pb of neutrons with energies up to 2.3 Bev, E. C. Fowler, H. L. Kraybill, R. M. Walker, and R. S. Preston—791(A)

Interpretation of measurements of total cross sections for nuclear scattering of high-energy neutrons, T. B. Taylor—785(A)

Level densities in heavy nuclei of 10- to 20-Mev excitation, D. B. Beard—738(L)

$N^{14}(n,2n)N^{13}$ cross-section measurement with 14-Mev neutrons, J. D. Dudley and C. M. Class—807(A)

Neutron absorption cross section of U^{235} at 2200 m/sec, H. Palevsky, R. S. Carter, R. M. Eisberg, and D. J. Hughes—1088(L)
Neutron capture in separated isotopes of Pt, J. M. Cork, M. K. Brice, L. C. Schmid, G. D. Hickman, and H. Nine—1218
Nonelastic scattering of fast neutrons, H. L. Taylor, O. Lönsjö, and T. W. Bonner—807(A)
n-p cross section at 1.0 and 2.5 Mev, R. E. Fields, R. L. Becker, and R. K. Adams—389
Nuclear potential well depth, Robert K. Adair—737(L)
Pickup reactions $B^{10}(n,d)Be^9$ for 14-Mev neutrons, F. L. Ribe and J. D. Seagrave—934
Search for $Li^7(n,t)$ reaction, H. E. Banta and R. L. Macklin—807(A)
Shell effects in highly excited nuclei, Henry W. Newson and Robert H. Rohrer—654
Te resonance scattering, H. L. Foote, Jr.—790(A)
Total cross sections for 410-Mev neutrons, V. Alexander Nedzel—174
Total neutron cross section for U from 20 kev to 20 Mev, R. L. Henkel, L. Cranberg, G. A. Jarvis, R. Nobles, and J. E. Perry—141
Total neutron cross sections in kev region: As, Zr, Nb, La, Ce, Pr, and Au, R. C. Block, J. H. Gibbons, E. G. Bilpuch, and D. F. Herring—774(A)
Total neutron cross sections in kev region: Cu, Cu^{63}, Cu^{65}, and Ga, H. Marshak—774(A)
Total neutron cross sections in kev region: Li, F, Cl, Sc, Rb, Mo, Ag, and Ta, J. R. Patterson, H. W. Newson, R. C. Mobley, and T. E. Gilmer—774(A)
Total neutron cross sections in kev region: Se, Br, Y, I, and Cs, H. W. Newson, R. M. Williamson, A. L. Toller, and P. F. Nichols—774(A)

Nuclear Reactions Induced by Protons (see also **Elementary Particle Interactions; Scattering of Protons**)

Al^{28} ground state, J. C. Kluyver, C. van der Leun and P. M. Endt—1795(L)
Al^{27} energy levels, S. F. Zimmerman, Jr., and C. P. Browne—749(A)
Analysis of 405-Mev proton and 222-Mev negative pion stars, A. D. Sprague, D. M. Haskin, R. G. Glasser, and Marcel Schein—994
Angular correlation apparatus for $Li^7(p,\gamma,\alpha)He^4$, Pat M. Windham and G. C. Phillips—803(A)
Angular distribution of α particles from (p,α) reactions, E. Newman and W. L. Alford—748(A)
Angular distribution of deuterons from $N^{14}(p,d)N^{13}$, K. G. Standing—731(L)
Angular distribution of γ rays from $Al^{27}(p,\gamma)Si^{28}$, H. E. Gove, E. B. Paul, G. A. Bartholomew, and A. E. Litherland—749(A)
Angular distributions of fission fragments from 22-Mev proton-induced Th fission, B. L. Cohen, W. H. Jones, G. H. McCormick, and B. L. Ferrell—625; 758(A)
Attenuation of 870-Mev protons by various elements, F. F. Chen, C. P. Leavitt, and A. M. Shapiro—784(A)
Comparison of nuclear and γ-ray energy scales, K. W. Jones, R. A. Douglas, M. T. McEllistrem, and H. T. Richards—947
Coulomb excitation of heavy nuclei, C. M. Class, C. F. Cook, and J. T. Eisinger—747(A); 809(A)
Disintegration of heavy elements by 2.2-Bev protons, Robert B. Duffield and Nathan Sugarman—776(A)
Effect of Coulomb barrier on meson production by nucleon-nucleus collisions, Toichiro Kinoshita—1331
Electric excitation of Pt, C. L. McClelland and Clark Goodman—1437(A)
Electric excitation of Ta, J. T. Eisinger, C. F. Cook, and C. M. Class—735(L)
Energy dependence of Coulomb excitation of Ta and Au, W. I. Goldburg and R. M. Williamson—747(A)
Energy spectra of nucleons evaporated from compound nucleus, R. M. Eisberg—739(L)
Estimation of beam intensity and cross sections at Cosmotron from gross radioactivity in Cu, Anthony Turkevich—775(A)
Experiments with neutrons from the Cosmotron. I, D. A. Hill, T. Coor, W. F. Hornyak, L. W. Smith, and G. A. Snow—791(A)
Ga, Ge, and As nuclides produced in bombardment of Cu with 2.2-Bev protons, Anthony Turkevich and Nathan Sugarman—728(L)
γ-ray energies from Al^{27} and S^{32}, J. A. Smith, J. N. Cooper, and J. C. Harris—749(A)
γ-ray spectrum of C^{13} and γ rays from proton bombardment of C^{14}, K. R. Spearman, E. L. Hudspeth, and I. L. Morgan—806(A)
γ rays and internal pairs from $Be^9 + H^1$, R. J. Mackin, Jr.—648
γ rays from $N^{15}(p,\alpha\gamma)C^{12}$ and $N^{15}(p,\gamma)O^{16}$, Alfred A. Kraus, Jr.—975
K-particle production by protons of 2.2 and 3.0 Bev, R. D. Hill, E. O. Salant, and M. Widgoff—1794(L)
Low excited states of F^{19}. I. Proton inelastic scattering, R. W. Peterson, C. A. Barnes, W. A. Fowler, and C. C. Lauritsen—1075(L); II. Lifetime measurements, J. Thirion, C. A. Barnes, and C. C. Lauritsen—1076(L); IV. Angular distributions, R. F. Christy—1077(L)
Momentum transfer in high-energy nuclear interactions in Al, R. Wolfgang and G. Friedlander—775(A)
Neutron thresholds from $Cu^{63}(p,n)Zn^{63}$, $Cu^{65}(p,n)Zn^{65}$, and $Li^7(p,n)Be^7$, C. F. Cook and T. W. Bonner—807(A)
Neutrons from proton bombardment of Be^9 and H^3, J. B. Marion, C. F. Cook, and T. W. Bonner—807(A)
Neutrons from proton bombardment of N^{14}, Fay Ajzenberg and Wolfgang Franzen—409
Nuclear energy levels by absolute magnetic analysis of inelastically scattered protons, C. R. Gossett, G. C. Phillips, and J. T. Eisinger—807(A)
Nuclear reactions of Cu with 2.2-Bev protons, G. Friedlander, J. M. Miller, R. Wolfgang, J. Hudis, and E. Baker—727(L)
$p + d \rightarrow \pi^+ + t$ reaction, Sidney A. Bludman—1722
$p + d \rightarrow t + \pi^+$ angular distribution and yield, Wilson J. Frank, Kenneth C. Bandtel, Richard Madey, and Burton J. Moyer—1716
(p,γ) coincidence measurements utilizing proton time-of-flight, W. T. Joyner—774(A)
(p,pn) and $(p,\alpha n)$ excitation functions, B. L. Cohen, E. Newman, R. A. Charpie, and T. H. Handley—620
Partial widths for reactions $Al^{27}(p,\gamma)Si^{28}$ and $Al^{27}(p,p')Al^{27}$, E. B. Paul, H. E. Gove, G. A. Bartholomew, and A. E. Litherland—749(A)
π^0 production cross sections from deuterium, Walter F. Dudziak—756(A)
π^+/π^- ratios at low energies from complex nuclei, Ryokichi Sagane and Walter F. Dudziak—755(A)
Pion production ratios, D. C. Peaslee—1085(L)
Production of antiprotons in p-p collisions, David Fox—499(L)
Production of Ga, Ge, and As nuclides by 2.2-Bev protons on Cu, Nathan Sugarman and Anthony Turkevich—775(A)
Radioactive products from interaction of 2.2-Bev protons with Cu, G. Friedlander, E. Baker, J. Hudis, J. M. Miller, and R. Wolfgang—775(A)

Nuclear Reactions Induced by Protons (Continued)
Reactions of Al with 2.2-Bev protons, J. Hudis, R. Wolfgang, N. Sugarman, and G. Friedlander—775(A)
Reactions of Cs with 240-Mev protons, Richard W. Fink and Edwin O. Wiig—1357
Scattering of 96-Mev protons from light nuclei. I. Energy distribution, F. Titus and K. Strauch—785(A); II. Angular distribution, K. Strauch and F. Titus—785(A)
Scintillation counter study of γ rays from proton capture in Na, R. R. Carlson, E. H. Geer, and E. B. Nelson —1311
Spallation studies of Bi, W. E. Bennett—997
Nuclear Scattering (see **Scattering**)
Nuclear Spectra (see also **Nuclear Reactions; Radioactivity**)
AcK radiation, Earl K. Hyde—1221
Additional properties of isotopes of elements 99 and 100, P. R. Fields, M. H. Studier, J. F. Mech, H. Diamond, A. M. Friedman, L. B. Magnusson, and J. R. Huizenga —209(L)
Al^{26} ground state, J. C. Kluyver, C. van der Leun, and P. M. Endt—1795(L)
Ag neutron-deficient isotope, B. C. Haldar and Edwin O. Wiig—1713
Ag^{110} β-ray spectrum, Toshio Azuma—638
Al^{27} energy levels, S. F. Zimmerman, Jr., and C. P. Browne—749(A)
Angular correlation of 3 nuclear radiations, G. R. Satchler —1304
Angular distribution of γ rays from $Al^{27}(p,\gamma)Si^{28}$, H. E. Gove, E. B. Paul, G. A. Bartholomew, and A. E. Litherland—749(A)
Angular distribution of photoelectrons from γ radiation of 0.4 and 1.3 Mev, Arne Hedgran and Sölve Hultberg —498(L)
β-decay energy systematics, Katharine Way and Marion Wood—119
β-decay interaction, Henry Brysk—1794(L)
Ce^{144} and Pr^{144} nuclear spectra, W. S. Emmerich, W. J. Auth, and J. D. Kurbatov—110; W. J. Auth, W. S. Emmerich, and J. D. Kurbatov—794(A)
Co^{55} and I^{130} disintegration, Robert S. Caird and Allan C. G. Mitchell—412
Co^{56} disintegration, M. Sakai, J. Dick, and J. D. Kurbatov —779(A)
Coulomb excitation by means of bombardment with various particles, Jørgen H. Bjerregaard and Torben Huus—204(L)
Cs^{131} inner bremsstrahlung, Babulal Saraf—642; 793(A)
Decay scheme of 5.5-hr. isomer of Hf^{180m}, J. W. Mihelich, Gertrude Scharff-Goldhaber, and Michael McKeown—794(A)
Double vacancies in K shell associated with K-electron capture in A^{37}, J. A. Miskel and M. L. Perlman—1683
Effect of atomic electron screening on shape of forbidden β spectra, R. H. Good, Jr.—931
Electric excitation of Pt, C. L. McClelland and Clark Goodman—1437(A)
Energy levels of Cu from inelastic neutron scattering, L. A. Rayburn, D. L. Lafferty, and T. M. Hahn—1641
First forbidden matrix element in β decay, R. W. King and D. C. Peaslee—1284
γ-γ coincidences from interaction of 3.1-Mev neutrons with various materials—791(A)
γ-ray energies from Al^{27} and S^{32}, J. A. Smith, J. N. Cooper, and J. C. Harris—749(A)
γ-ray spectrum of C^{13} and γ rays from proton bombardment of C^{14}, K. R. Spearman, E. L. Hudspeth, and I. L. Morgan—806(A)
γ-ray spectrum of Po-B source, Temple Love and Fred Maienschein—795(A)
γ rays and internal pairs from $Be^9 + H^1$, R. J. Mackin, Jr. —648
γ rays excited by inelastic scattering of fast neutrons in Bi, Ni, and Cu, M. A. Rothman, H. S. Hans, and C. E. Mandeville—791(A)
γ rays from inelastic scattering of α particles by Li and F, N. P. Heydenburg and G. M. Temmer—748(A)
γ rays from Li^7, F^{19}, Ne^{22}, and Na^{23} produced by α-particle bombardment of Li and F, N. P. Heydenburg and G. M. Temmer—1252
γ rays from $N^{15}(p,\alpha\gamma)C^{12}$ and $N^{15}(p,\gamma)O^{16}$, Alfred A. Kraus, Jr.—975
Half-life and β decay of long-lived Nb^{94}, Mario A. Rollier and Einar Saeland—1079(L)
Ho neutron-deficient activities, Thomas H. Handley—945
I^{130} disintegration, R. S. Caird and Allan C. G. Mitchell —780(A)
Identification of Cf isotopes 249, 250, 251, and 252 from pile-irradiated Pu, H. Diamond, L. B. Magnusson, J. F. Mech, C. M. Stevens, A. M. Friedman, M. H. Studier, P. R. Fields, and J. R. Huizenga—1083(L)
In^{117} disintegration, C. L. McGinnis—780
Intermediate coupling in B^{10}, W. T. Sharp, H. Gellman, and G. E. Tauber—762(A)
Internal bremsstrahlung from P^{32}, Max Goodrich and Wilbur B. Payne—405
Internal conversion in L and M sub-shells, E. L. Church and J. E. Monahan—762(A)
Isobaric triplet Mg^{25}-Al^{25}-Si^{25}, Raymond K. Sheline, Noah R. Johnson, P. R. Bell, R. C. Davis, and F. K. McGowan—1642
K^{44}, Bernard L. Cohen—117
La^{140} disintegration, C. L. Peacock, A. W. Oser, and J. F. Quin—804(A)
La^{140} radiation, C. L. Peacock, J. F. Quin, and A. W. Oser, Jr.—372
Long-lived isomer of RaE (Bi^{210}), Harris B. Levy and I. Perlman—152
Low excited states of F^{19}, I. Proton inelastic scattering, R. W. Peterson, C. A. Barnes, W. A. Fowler and C. C. Lauritsen—1075(L); II. Lifetime measurements, J. Thirion, C. A. Barnes, and C. C. Lauritsen—1076(L); III. Coulomb excitation by α particles, R. Sherr, C. W. Li, and R. F. Christy—1076(L); IV. Angular distributions, R. F. Christy—1077(L)
Low-lying states of Be^9, E. W. Titterton—206(L)
Magnetic internal Compton coefficients in Born approximation, Larry Spruch and G. Goertzel—1671
Mn^{57}, B. L. Cohen, R. A. Charpie, T. H. Handley, and E. L. Olson—953
Mo^{99} disintegration, Jagdish Varma and C. E. Mandeville —91; C. E. Mandeville and Jagdish Varma—780(A)
Modified shell model of odd-even nuclei, A. B. Volkov—1664
Ne^{18}, J. D. Gow and Luis W. Alvarez—365
Ne^{20} γ rays, B. P. Foster, G. S. Stanford, and L. L. Lee —804(A)
Neutron capture in separated isotopes of Pt, J. M. Cork, M. K. Brice, L. C. Schmid, G. D. Hickman, and H. Nine—1218
New isotopes of Am, Bk, and Cf, A. Ghiorso, S. G. Thompson, G. R. Choppin, and B. G. Harvey—1081(L)
New method for measuring short γ-ray lifetimes, J. W. Knowles—795(A)
Nuclear properties of some isotopes of Cf, elements 99 and 100, G. R. Choppin, S. G. Thompson, A. Ghiorso, and B. G. Harvey—1080(L)

Nuclear shell model *ft* values for intermediate coupling, R. Schulten and R. A. Ferrell—739(L)
O^{14} β spectra, J. R. Penning and F. H. Schmidt—779(A)
P^{28} radioisotope, R. T. Nichols and E. N. Jensen—369
Pa^{234} 3.7×10^{-6}-sec metastable state, D. Engelkemeir and L. B. Magnusson—1395(L)
Partial widths for reactions $Al^{27}(p,\gamma)Si^{28}$ and $Al^{27}(p,p')Al^{27}$, E. B. Paul, H. E. Gove, G. A. Bartholomew, and A. E. Litherland—749(A)
Pb^{209} energy levels, L. G. Elliott, R. L. Graham, J. Walker, and J. L. Wolfson—795(A)
Po^{211} α-emitting isomer, Fred Noel Spiess—1292
Precise momentum measurement of *F* line of ThB, D. I. Meyer and F. H. Schmidt—927
Pt 10.5-day isotope, R. A. Naumann—794(A)
Pt^{191} decay, E. P. Tomlinson, R. A. Naumann, and J. W. Mihelich—794(A)
Pu^{238} α- and γ-ray spectra, Frank Asaro and I. Perlman —381
Radiations of 18-min Br^{80}, L. Lidofsky, R. Gold, and C. S. Wu—780(A)
Radiations of 53-min I^{134} and 86-sec I^{136}, Michael McKeown and Seymour Katcoff—965
Radiative electron capture in Fe^{55}, L. Madansky and F. Rasetti—407
Radiative electron capture of Fe^{55}, A^{37}, and Ni^{59}, W. S. Emmerich, S. E. Singer, and J. D. Kurbatov—113; S. E. Singer, W. S. Emmerich, and J. D. Kurbatov—779(A)
RaE spin, R. W. King and D. C. Peaslee—795(A)
Rates of decay of observed anisotropies in Am^{241} α-γ and Cd^{111} γ-γ angular correlations, J. S. Fraser and J. C. D. Milton—795(A)
Rb^{87} third forbidden β spectrum, M. H. MacGregor and M. L. Wiedenback—138
Recoil spectrum in β decay of Ne^{19}, W. Parker Alford and Donald R. Hamilton—779(A)
Resonance fluorescence with nuclei: Hg^{199}, F. R. Metzger and W. B. Todd—794(A)
Rotational nuclear energy levels from Coulomb excitation, G. M. Temmer and N. P. Heydenburg—1399(L)
Sargent diagram and *ft* values for electron capture transitions, J. K. Major and L. C. Biedenharn—779(A)
Scintillation counter study of γ rays from proton capture in Na, R. R. Carlson, E. H. Geer, and E. B. Nelson —1311
Search for anomalous positively-charged particles from P^{32}, G. W. McClure—1637
Short-lived isomeric states of Ag^{110} and In^{116}, F. I. Boley —1078(L)
Sm^{152} disintegration, R. L. Graham and J. Walker—794(A)
Summation of γ-ray energies with single-crystal spectrometer, Daniel C. Lu and M. L. Wiedenbeck—501(L)
Symmetry relations of 12-*j* symbol, R. J. Ord-Smith—1227
Tb^{160} (71-day) decay, S. B. Burson, W. C. Jordan, and J. M. LeBlanc—103
Tl^{208} nuclear energy levels, Jagdish Varma—795(A); 1688
Transmission of 0–40 kev electrons by thin films with application to β-ray spectroscopy, R. O. Lane and D. J. Zaffarano—959
Upper limits for lifetimes of Ni^{59}, Z. Bay, V. P. Henri, and F. McLernon—780(A)
V^{48} nuclide, Raymond K. Sheline and Joseph R. Wilkinson —729(L)
W^{180} energy levels, C. M. Fowler, H. W. Kruse, V. Keshishian, R. J. Klotz, and G. P. Mellor—1082(L)
Xe^{135} decay scheme, Sigvard Thulin—734(L)
Y^{91} disintegration, M. E. Bunker, J. P. Mize, and J. W. Starner—1694
Yb^{169}, Thomas H. Handley and Elmer L. Olson—968
Zn^{71} activities, J. M. LeBlanc, J. M. Cork, and S. B. Burson—1436(A)
Zr^{95} decay scheme, Phillip S. Mittelman—99

Nuclear Structure Theory (see also **Nuclear Reactions; Nuclear Spectra**)
Distortion of nucleus in μ-mesic atoms, W. Lakin and W. Kohn—787(A)
Ground states of odd-odd nuclei, C. Schwartz—95
Interaction of high-energy pions with nuclei, E. D. Courant —1081(L)
Level densities in heavy nuclei of 10- to 20-Mev excitation, D. B. Beard—738(L)
Magnetic moment of K^{40} in intermediate coupling, G. E. Tauber and Ta-You Wu—762(A); 1307
Many-particle configurations in central field, C. Schwartz and A. de-Shalit—1257
Modified shell model of odd-even nuclei, A. B. Volkov—1664
μ-mesonic x-rays and shape of nuclear charge distribution, David L. Hill and Kenneth W. Ford—1617
Non-uniform nuclear charge distributions and measurements of nuclear electrical radius, Kenneth W. Ford and David L. Hill—1630
Nuclear charge distribution, David L. Hill and Kenneth W. Ford—787(A)
Nuclear potential well depth, Robert K. Adair—737(L)
Nuclear shell model *ft* values for intermediate coupling—739(L)
Phenomenological interaction, M. H. Kalos and J. M. Blatt—762(A)
Possible relation between pseudoscalar β coupling and nuclear spin-orbit coupling, E. J. Konopinski—550
Spins of lowest states of K^{40}, P^{32}, and Al^{26} nuclei, Harald A. Enge—730(L)
Statistical factors in radiation widths of nuclear energy levels, D. J. Hughes—740(L)

Optical Instruments (see **Methods and Instruments**)
Optical Properties (see also **Luminescence**)
Anomalous optical absorption limit in InSb, Elias Burstein —1431(A)
Color centers in KCl crystals produced by high-energy protons, W. Leivo and R. Smoluchowski—771(A)
Dielectric properties of colored KCl crystals—T. Suita —1497
Effect of plastic flow upon color centers in alkali halide crystals, Masayasu Ueta and Werner Känzig—1390(L)
Effective mass of conduction electrons in Ag, Au, and Cu, L. G. Schulz—1422(A)
Faraday effect in gases, L. R. Ingersoll and D. H. Liebenberg—754(A)
Infrared absorption of Te, R. S. Caldwell and H. Y. Fan —1427(A)
Infrared properties of InSb, W. Kaiser and H. Y. Fan —1431(A)
Infrared properties of *p*-type Ge, E. Burstein, B. W. Henvis, and N. Sclar—750(A)
Irradiation-induced optical absorption in Al_2O_3, Paul W. Levy and G. J. Dienes—1409(A)
Multiphonon transitions in *F* center, Jordan J. Markham —1395(L)
Optical absorption of AlSb, R. F. Blunt, H. P. R. Frederikse, and J. H. Becker—1431(A)
Optical absorption of single-crystal $SrTiO_3$, James A. Noland—724(L)
Optical and electrical measurements on InAs, Robert M. Talley and Dorothy Enright—1431(A)

Optical Properties (Continued)
Optical properties of Ge in far infrared, E. J. Johnson and W. G. Spitzer—1415(A)
Optical properties of MgO in vacuum uv, Peter D. Johnson—845
Photomagnetoelectric effect in Ge and Si, Hubert H. Bulliard—1564
Photoresponse of aromatic films, J. F. Andrew and S. Mrozowski—1438(A)
Quantum-mechanical definition of refractive index, S. M. Neamtan—327
R', colloidal, and Z bands in KCl, D. R. Westervelt—1438(A)
Rate of production of color centers in KCl and KBr by x-rays at 79°K, William H. Duerig—65
Relation between refractive index and density in glass, H. N. Ritland—1434(A)
Restoration of F and V_1 centers following low temperature bleaching, R. V. Hesketh and E. E. Schneider—494(L)
Search for F-center luminescence, Clifford C. Klick—1438(A); 1541
Tunneling of electrons in alkali halides, D. L. Dexter—771(A)

Pair Production (see **Electrons and Positrons**)
Phosphors and Phosphorescence (see **Luminescence**)
Photoconductivity (see **Electrical Conductivity and Resistance; Semiconductors**)
Photodisintegration (see **Nuclear Photoeffects**)
Photoelasticity (see **Elasticity and Plasticity**)
Photoelectric Effect (see **Electrical Properties**)
Photography and Photographic Emulsions (see **Methods and Instruments**)
Photometry (see **Methods and Instruments**)
Photons (see **Radiation**)
Photovoltaic Effect (see **Electrical Properties**)
Piezoelectric Effect (see **Dielectrics and Dielectric Properties**)
Plasticity (see **Elasticity and Plasticity**)
Polarization, Electrical (see **Dielectrics and Dielectric Properties**)
Polymers (see **Molecular Aggregates**)
Positrons (see **Electrons and Positrons**)
Probability (see **Mathematical Methods**)
Proceedings of the American Physical Society
Annual Meeting at Columbia University, New York City, New York, January 28–30, 1954—742
Austin Meeting at Austin, Texas, February 26–27, 1954—802
Michigan Meeting at Detroit and Ann Arbor, Michigan, March 18–20, 1954—1404
Protons (see **Elementary Particle Interactions**)

Quantum Electrodynamics (see also **Field Theory**)
Applications of mass operator in quantum electrodynamics, Roger G. Newton—1773
Avoiding perturbation methods in quantum electrodynamics, meson theory, etc., F. J. Belinfante—745(A)
Collision matrix for Dirac particles, Bruno Zumino—747(A)
Green's functions in quantum electrodynamics, James L. Anderson—703
Interaction current contribution to hfs of tritium, A. M. Sessler and H. M. Foley—761(A)
Lamb shift in mesic atoms, H. C. Corben—787(A)
Photon splitting in nuclear electrostatic field, Mark Bolsterli—367
p-n mass difference, R. P. Feynman and G. Speisman—500(L)
Production of antiprotons in p-p collisions, David Fox—499(L)
Production of proton pairs, R. N. Thorn—501(L)
Rearrangement collisions, B. H. Bransden—726(L)
Relativistic configuration space formulation of multi-electron problem. II, Marian Günther—1347
Relativistic wave equations, Herman Feshbach—786(A)
Renormalization, P. T. Matthews and Abdus Salam—178
Solutions of Heitler's integral equation by iteration method, S. N. Biswas—1767
Two extensions of Foldy-Wouthuysen transformation, K. M. Case—786(A)
Unitarity of U operator, H. Ekstein—1063

Quantum Mechanics
Application of Rayleigh-Schrödinger perturbation theory to hydrogen atom, Eugene P. Wigner—77
Atomic self-consistent fields. II. Interpolation problems, Per-Olov Lödwin—1600
Classical and quantum theory of many interacting particles. I, George J. Yevick and Jerome K. Percus—787(A); II, Jerome K. Percus and George J. Yevick—787(A)
Collective description of many-particle systems (generalized theory of Hartree fields), Toichiro Kinoshita and Yoichiro Nambu—598
Complete Bacher and Goudsmit method, Sydney Meshkov and C. W. Ufford—75; C. W. Ufford and S. Meshkov—761(A)
Determination of perturbation from scattering operator, H. E. Moses—1442(A)
Effect of negative energy components in two-nucleon system, R. Arnowitt and S. Gasiorowicz—746(A); 1057
Localized orbitals, Harvey Winston—328
Molecular wave functions in e-notation, J. M. Miller and F. A. Matsen—804(A)
New approach to classical and quantum theory of many interacting particles. I, George J. Yevick and Jerome K. Percus—787(A); II, Jerome K. Percus and George J. Yevick—787(A)
Nonrelativistic limit of half-integral-spin wave equations, K. M. Case—1442(A)
Normalization of WKB-type approximation, S. C. Miller, Jr.—1345
Perturbation theory with Sommerfeld-Maue wave function, G. K. Horton and E. Phibbs—1402(L)
Quantized space-time, E. J. Hellund—192
Quantum mechanical definition of refractive index, S. M. Neamtan—327
Quantum mechanics of scattering by a r^{-4} attractive potential, Erich Vogt and Gregory H. Wannier—793(A)
Quantum theory of radiation resistance, J. Weber—793(A)
Radiative corrections to electron scattering, Roger G. Newton—788(A)
Restrictions on invariant transformation groups in Lagrangian and Hamiltonian formalisms, Peter G. Bergmann—788(A)
Simplified LCAO method for periodic potential problem, J. C. Slater and G. F. Koster—1498
Solutions of Helmholtz and Schrödinger equations in sphero-conal coordinates, Olen Kraus—1442(A)
Spin-other-orbit interaction in theory of complex spectra, Frederick R. Innes—761(A)
Theory of elementary particles in general relativity, M. M. Hatalkar—1472
Two extensions of Foldy-Wouthuysen transformation, K. M. Case—786(A)
United atom-separated atom treatment of H_2^+, J. R. Streetman and F. A. Matsen—805(A)

Variation method applied to wave functions in crystals, W. V. Houston—808(A)
Quenching of Radiation (see **Radiation**)

Radar (see **Methods and Instruments; Radiation**)
Radiation
Absorption coefficients of air and nitrogen for extreme uv, J. P. Curtis—908
Čerenkov radiation from extended electron beams, M. Danos—758(A)
Cooling of gas by radiation, Ernest Bauer and Ta-You Wu —1424(A)
Cs^{131} inner bremsstrahlung, Babulal Saraf—642; 793(A)
Elastic scattering of photons, E. G. Fuller and Evans Hayward—732(L)
Emission of δ- and x-rays from targets bombarded by accelerated ions, Črtomir Zupančič and Torben Huus —205(L)
High-energy photoproton production by 325-Mev bremsstrahlung radiation, B. T. Feld, R. D. Godbole, A. Odian, F. Scherb, P. C. Stein, and A. Wattenberg—1000
Interference of Rayleigh and nuclear Thomson scattering, A. M. Cormack—1398(L)
Internal bremsstrahlung from P^{32}, Max Goodrich and Wilbur B. Payne—405
Magnetic internal Compton coefficients in Born approximation, Larry Spruch and G. Goertzel—1671
Photon splitting in nuclear electrostatic field, Mark Bolsterli—367
Radiation flux in planetary atmosphere, Daniel I. Fivel and Gilbert N. Plass—752(A)
Radiative electron capture in Fe^{55}, L. Madansky and F. Rasetti—407
Resonance fluorescence with nuclei: Hg^{199}, F. R. Metzger and W. B. Todd—794(A)
Scattering of electromagnetic waves by turbulent atmospheric fluctuations, F. Villars and V. F. Weisskopf— 232
Search for *K* particles using Čerenkov counters, J. W. Keuffel and L. Mezzetti—797(A)
Theory of x-ray small-angle scattering, Yin-Yuan Li and R. Smoluchowski—866
Radio Waves (see **Radiation**)
Radioactivity (see also **Nuclear Spectra**)
AcK radiations, Earl K. Hyde—1221
Additional properties of isotopes of elements 99 and 100, P. R. Fields, M. H. Studier, J. F. Mech, H. Diamond, A. M. Friedman, I. B. Magnusson, and J. R. Huizenga —209(L)
Ag neutron-deficient isotope, B. C. Haldar and Edwin O. Wiig—1713
Age-diffusion theory for β-ray problems, William C. Roesch—779(A)
β-decay energy systematics, Katharine Way and Marion Wood—119
Cm isotopes 246 and 247 from pile-irradiated plutonium, C. M. Stevens, M. H. Studier, P. R. Fields, J. F. Mech, P. A. Sellers, A. M. Friedman, H. Diamond, and J. R. Huizenga—974
Evidence for Si^{32}, long-lived β emitter, Anthony Turkevich and Arthur Samuels—364
Half-life and β decay of long-lived Nb^{94}, Mario A. Rollier and Einar Saeland—1079(L)
Ho neutron-deficient activities, Thomas H. Handley—945
Identification of Cf isotopes 249, 250, 251, and 252 from pile-irradiated Pu, H. Diamond, L. B. Magnusson, J. F. Mech, C. M. Stevens, A. M. Friedman, M. H. Studier, P. R. Fields, and J. R. Huizenga—1083(L)
K^{44}, Bernard L. Cohen—117
La^{140} half-life, H. W. Kirby and Murrell L. Salutsky— 1801(E)
Long-lived isomer of RaE (Bi^{210}), Harris B. Levy and I. Perlman—152
Mn^{57}, B. L. Cohen, R. A. Charpie, T. H. Handley, and E. L. Olson—953
Ne^{18}, J. D. Gow and Luis W. Alvarez—365
Neutron capture in separated isotopes of Pt, J. M. Cork, M. K. Brice, L. C. Schmid, G. D. Hickman, and H. Nine—1218
New isotopes of Am, Bk, and Cf, A. Ghiorso, S. G. Thompson, G. R. Choppin, and B. G. Harvey—1081(L)
New method for measuring short γ-ray lifetimes, J. W. Knowles—795(A)
Nuclear properties of some isotopes of Cf, elements 99 and 100, G. R. Choppin, S. G. Thompson, A. Ghiorso, and B. G. Harvey—1080(L)
P^{32} radioisotope, R. T. Nichols and E. N. Jensen—369
Pd isotope, 1.5-minute Pd^{118}, Harry G. Hicks and Richard S. Gilbert—371
Po^{211} α-emitting isomer, Fred Noel Spiess—1292
Precise momentum measurement of *F* line of ThB, D. I. Meyer and F. H. Schmidt—927
Pt 10.5-day isotope, R. A. Naumann—795(A)
Pu^{238} α- and γ-ray spectra, Frank Asaro and I. Perlman —381
Pu^{240} and Pu^{239} half-lives, G. W. Farwell, J. E. Roberts, and A. C. Wahl—363
Radiogenic A measurements, H. A. Shillibeer, R. D. Russell, R. M. Farquhar, and E. A. W. Jones—1793(L)
RaE spin, R. W. King and D. C. Peaslee—795(A)
Rates of decay of observed anisotropies in Am^{241} α-γ and Cd^{111} γ-γ angular correlations, J. S. Fraser and J. C. D. Milton—795(A)
T concentration in natural waters by diffusion cloud chamber, E. L. Fireman and D. Schwarzer—385
U^{232} half-life, P. A. Sellers, C. M. Stevens, and M. H. Studier—952
V^{50}, Raymond K. Sheline and Joseph R. Wilkinson— 729(L)
Raman Spectra (see **Molecular Structure and Spectra**)
Range and Energy Loss of Particles (see also **Scattering**)
α-particle ionization yields in gridded chamber, Lloyd O. Herwig and Glenn H. Miller—1183
Attenuation of 14.1-Mev neutrons in water, R. S. Caswell, R. F. Gabbard, W. P. Doering, and D. W. Padgett— 786(A)
Bohr's theory of energy losses of moving charged particles, Jacob Neufeld—792(A)
Density effect for ionization energy losses in gases, E. D. Palmatier, J. T. Meers, and C. M. Askey—766(A)
Effect of knock-on electrons on ionization loss, J. W. Gardner—764(A)
Energy loss of electrons in passage through thin films, L. Marton and Lewis B. Leder—203(L); Lewis B. Leder and L. Marton—777(A)
Interaction of neutrons with moderating materials, G. F. von Dardel—1272
Mean excitation potentials, David O. Caldwell and J. Reginal Richardson—79
Penetration of medium fast electrons into photographic emulsions, L. Marton and Lewis B. Leder—778(A)
Range and charge of energetic nitrogen ions in Ni, D. W. Scott, H. L. Reynolds, and A. Zucker—810(A)
Range and specific ionization for high-energy protons in nuclear emulsions, Otto Heinz—1728
Range measurement of low voltage electrons, Marguerite Davis—243
Range of protons in Be, Al, Cu, Ag, and Au, H. Bichsel and R. F. Mozley—764(A)

Range and Energy Loss of Particles (Continued)
Stopping power of several elements for protons, D. W. Green, J. N. Cooper, and J. C. Harris—764(A)
Transmission of 0–40 kev electrons by thin films with application to β-ray spectroscopy—959
Recombination (see **Molecular Structure and Spectra**)
Rectifiers (see **Electrical Conductivity and Resistance; Semiconductors**)
Relativity and Gravitation
Accurate determination of tidal variations of gravity, Henry Neal Clarkson and Arthur E. Lockenvitz—811(A)
Corrected theory of relativity and its classical interpretation, R. V. L. Hartley—792(A)
General relativistic variational principle for perfect fluids, A. H. Taub—1468
Theory of elementary particles in general relativity, M. M. Hatalkar—1472
Resistance, Electrical (see **Electrical Conductivity and Resistance**)
Resonance Radiation (see **Radiation**)

Scattering, General (see also **Diffraction; Elementary Particle Interaction; Nuclear Reactions; Range and Energy Loss of Particles**)
Application of variational methods to intermediate and high-energy scattering, E. Gerjuoy and David S. Saxon—478
Determination of perturbation from scattering operator, H. E. Moses—1442(A)
Inelastic scattering of charged particles in electric excitation processes, Hans Mark—1436(A)
Interference of Rayleigh and nuclear Thomson scattering, A. M. Cormack—1398(L)
Molecular beam investigation of scattering of molecules from surfaces, F. C. Hurlbut—754(A)
Point source kernel for diffusion with small-angle scattering, W. E. Drummond and C. S. Gardner—1491
Polarization of elastically scattered nucleons from nuclei, Warren Heckrotte and Joseph V. Lepore—500(L)
Polarization of elastically scattered nucleons from nuclei in Born approximation, Warren Heckrotte—1797(L)
Polarization of nucleons elastically scattered from nuclei, G. A. Snow, R. M. Sternheimer, and C. N. Yang—1073(L)
Problem of multiple scattering, E. P. Wigner—17
Quantum mechanics of scattering by r^{-4} attractive potential, Erich Vogt and Gregory H. Wannier—793(A)
Rearrangement collisions, B. H. Bransden—726(L)
3-dimensional calculation of vibrational relaxation times in gases, Robert N. Schwartz—793(A)
Variational principles for acoustic field, E. Gerjuoy and David S. Saxon—1445
Scattering of α Particles (see also **Nuclear Reactions Induced by α Particles and He^3**)
Elastic scattering of α particles by carbon, W. Haberle, J. W. Bittner, and R. D. Moffat—769(A)
γ rays from inelastic scattering of α particles by Li and F, N. P. Heydenburg and G. M. Temmer—748(A)
Scattering of Atoms and Molecules (see **Atomic and Molecular Beams**)
Scattering of Deuterons (see also **Nuclear Reactions Induced by Deuterons and Tritons**)
Elastic scattering of 190-Mev deuterons by protons, Owen Chamberlain and Martin O. Stern—666
Scattering of 190-Mev deuterons on protons, Arnold L. Bloom and Owen Chamberlain—659
Scattering of Electrons and Positrons (see also **Electrons and Positrons**)
Double scattering of electrons with magnetic perturbation, H. Mendlowitz and K. M. Case—1436(A)
Elastic scattering of electrons from nuclei, Robert T. Bayard and J. L. Yntema—757(A)
Elastic scattering of high-energy electrons by nuclei, Alfred E. Glassgold—757(A)
Electron-electron and positron-electron scattering measurements, Arthur Ashkin, Lorne A. Page, and W. M. Woodward—357
Experimental measurement of gyromagnetic ratio of free electron, W. H. Louisell, R. W. Pidd, and H. R. Crane—7
Inelastic scattering of 190-Mev electrons in Be, J. A. McIntyre, B. Hahn, and R. Hofstadter—1084(L)
Radiative corrections to electron scattering, Roger G. Newton—788(A)
Scattering of 2.7-Mev positrons by Au and Al foils, L. Grodzins—758(A)
Scattering of Mesons (see also **Mesons; Nuclear Reactions Induced by Mesons**)
Angular distribution of π^--proton charge exchange scattering at 40 Mev. I. Apparatus, A. Roberts and J. Tinlot—766(A); II. Analysis of results, J. Tinlot and A. Roberts—766(A)
Classical scattering of mesons, S. P. Pandya—1037
Connection between pion photoproduction and scattering phase shifts, Marc Ross—454
Coulomb effects in pion-proton scattering at relativistic energies, Frank T. Solmitz—1799(L)
Covariant treatment of meson-nucleon scattering, Maurice M. Lévy—460
Elastic scattering of 80-Mev π mesons on Al, Aihud Pevsner, James Rainwater, Ross Williams, and Seymour J. Lindenbaum—765(A)
Elastic scattering of 160-Mev pions in emulsions, R. A. Grandey and A. F. Clark—766(A)
Elastic scattering of positive and negative pions in Li, Ross Williams, Aihud Pevsner, James Rainwater, and Seymour J. Lindenbaum—765(A)
Interaction of high-energy pions with nuclei, E. D. Courant—1081(L)
Interactions of negative pions in C and Pb, John O. Kesler and Leon M. Lederman—689
Intermediate coupling method for meson-nucleon scattering, T. D. Lee and R. Christian—1760
Low-energy limits of meson processes, S. Deser and W. E. Thirring—746(A)
Meson-nucleon problem when interaction is fixed and extended, Geoffrey F. Chew—1755
Meson-nucleon scattering. I, R. J. Riddell, Jr., and Burton D. Fried—745(A); 1736; II. Burton D. Fried and R. J. Riddell, Jr.—746(A)
Phase shift analysis of scattering of negative pions by H, R. L. Martin—765(A)
Phenomenology of pion-nucleon S waves, H. P. Noyes and A. E. Woodruff—1401(L)
Scattering of 217-Mev negative pions by hydrogen, Maurice Glicksman—1335
Solutions of Heitler's integral equation by iteration method, S. N. Biswas—1767
Scattering of Neutrons (see also **Nuclear Reactions Induced by Neutrons**)
Angular distribution of $D(d,n)$ neutrons scattered from C, Al, S, Fe, Cd, Cu, W, and Pb, R. N. Little, Jr., C. P. Cadenhead, B. P. Leonard, Jr., J. T. Prud'homme, L. D. Vincent, and J. E. Wills—807(A)

Angular distribution of neutrons scattered from Cd, Sn, and Bi, S. C. Snowdon and W. D. Whitehead—786(A); 1267
Angular distributions of 0.2–1.5 Mev neutrons elastically scattered by light nuclei, H. B. Willard, J. K. Bair, and J. D. Kington—786(A)
Elastic scattering of 14-Mev neutrons, J. H. Coon and R. W. Davis—785(A)
Energy levels of Cu from inelastic neutron scattering, L. A. Rayburn, D. L. Lafferty, and T. M. Hahn—1641
γ rays excited by inelastic scattering of fast neutrons in Bi, Ni, and Cu, M. A. Rothman, H. S. Hans, and C. E. Mandeville—791(A)
Inelastic scattering of neutrons, E. A. Eliot, D. Hicks, L. E. Beghian, and H. Halban—144
Interaction of neutrons with moderating materials, G. F. von Dardel—1272
Interpretation of measurements of total cross sections for nuclear scattering of high-energy neutrons, T. B. Taylor—785(A)
Neutron polarization, C. P. Stanford, T. E. Stephenson, L. W. Cochran, and S. Bernstein—374
Neutron scattering by rotators, A. C. Zemach and R. J. Glauber—790(A)
Nonelastic scattering of fast neutrons, H. L. Taylor, O. Lönsjö, and T. W. Bonner—807(A)
Polarization of elastically scattered nucleons from nuclei, Warren Heckrotte and Joseph V. Lepore—500(L)
Polarization of elastically scattered nucleons from nuclei in Born approximation, Warren Heckrotte—1797(L)
Polarization of nucleons elastically scattered from nuclei, G. A. Snow, R. M. Sternheimer, and C. N. Yang—1073(L)
Scattering of fast neutrons in light nuclei, C. F. Cook and T. W. Bonner—651
Scattering of neutrons by systems containing light nuclei, G. C. Wick—1228
Scattering of neutrons by systems of heavy nuclei, G. Placzek—1801(E)
Small-angle neutron scattering by Fe at high temperatures, C. G. Shull and M. K. Wilkinson—1439(A)
Small-angle n-p scattering at 90 Mev, Owen Chamberlain and James W. Easley—208(L)
Te resonance scattering, H. L. Foote, Jr.—790(A)

Scattering of Protons (see also **Nuclear Reactions Induced by Protons**)

Elastic scattering of 18.5-Mev protons by nuclei, I. E. Dayton and P. C. Gugelot—785(A)
Elastic scattering of protons by nuclei, D. M. Chase and F. Rohrlich—81
Elastic scattering of 340-Mev protons by deuterons, David D. Clark and Owen Chamberlain—785(A)
Intermediate state coupling and interpretation of high-energy nucleon-nucleon scattering, R. M. Thaler, J. Bengston, and G. Breit—683
Low excited states of F^{19}. I. Proton inelastic scattering, R. W. Peterson, C. A. Barnes, W. A. Fowler, and C. C. Lauritsen—1075(L); II. Lifetime measurements, J. Thirion, C. A. Barnes, and C. C. Lauritsen—1076(L); IV. Angular distributions, R. F. Christy—1077(L)
Nuclear energy levels by absolute magnetic analysis of inelastically scattered protons, C. R. Gossett, G. C. Phillips, and J. T. Eisinger—807(A)
p-α scattering at 17.5 Mev, Karl W. Brockman, Jr.—785(A)
Phase shift analysis of high-energy nucleon-nucleon scattering experiments, R. M. Thaler and J. Bengston—679
Polarization by p-p collision at 439 Mev, H. G. de Carvalho, E. Heiberg, J. Marshall, and L. Marshall—1796(L)
Polarization of elastically scattered nucleons from nuclei, Warren Heckrotte and Joseph V. Lepore—500(L)
Polarization of elastically scattered nucleons from nuclei in Born approximation, Warren Heckrotte—1797(L)
Polarization of fast protons scattered by nuclei, G. Takeda and K. M. Watson—1087(L)
Polarization of high-energy protons scattered by complex nuclei, S. Tamor—1087(L)
Polarization of nucleons elastically scattered from nuclei, G. A. Snow, R. M. Sternheimer, and C. N. Yang—1073(L)
p-p scattering at 9.7 Mev, Bruce Cork and Walter Hartsough—1300
p-p scattering from 40 to 95 Mev, U. E. Kruse, J. M. Teem, and N. F. Ramsey—1795(L)
p-p scattering near interference minimum, Daniel I. Cooper, David H. Frisch, and Robert L. Zimmerman—1209
(p,pn) and $(p,\alpha n)$ excitation functions, B. L. Cohen, E. Newman, R. A. Charpie, and T. H. Handley—620
Scattering of 96-Mev protons from light nuclei. I. Energy distribution, F. Titus and K. Strauch—785(A); II. Angular distribution, K. Strauch and F. Titus—785(A)

Scattering of Radiation (see **Radiation; X-Rays**)
Scintillation Counters (see **Methods and Instruments**)
Secondary Emission (see **Electrical Properties**)

Semiconductors

Anomalous optical absorption limit in InSb, Elias Burstein—1431(A)
Avalanche breakdown in Si, K. G. McKay—877
Bombardment damage of Ge crystals by fast electrons, W. Kohn—1409(A)
Bound states in dislocations, Rolf Landauer—1386(L)
"Channels" in n-p-n junction transistors: new results and proposed model, R. H. Kingston—1416(A)
Conductivity and Hall effect in intrinsic range of Ge, F. J. Morin and J. P. Haita—1525
Conductivity, Hall effect, and rectification of GaSb, D. P. Detwiler—1431(A)
Contact potential, work function, and surface states, Selby M. Skinner—1428(A)
Current oscillations in photoconductive films of PbTe, Dean L. Mitchell, Werner J. Beyen, and Donald E. Bode—1430(A)
Decay in photoconductivity associated with deep electron traps in p-type Si, J. A. Hornbeck and J. R. Haynes—1437(A)
Decay in photoconductivity associated with hole traps in n-type Si, J. R. Haynes and J. A. Hornbeck—1438(A)
Diffusion of impurities in Ge, W. C. Dunlap, Jr.—1531
Diffusion of lattice defects in temperature gradient, Robert W. Keyes—1389(L)
Effect of impurities on conductivity of gray tin, A. W. Ewald—1428(A)
Effect of oxygen on PbTe films, Donald E. Bode and Henry Levinstein—1430(A)
Effective carrier mobility in surface well, J. Robert Schrieffer—1420(A)
Effective mass and degeneracy of carriers in Ge from diamagnetic behavior, J. H. Crawford, Jr., and D. K. Stevens—1415(A)
Electrical conductance of pressed powders, in particular of ZnO, J. C. M. Brentano and Colman Goldberg—56
Electrical properties of dislocations in plastically deformed Ge, G. L. Pearson, W. T. Read, Jr., and F. J. Morin—750(A)

Semiconductors (Continued)
Electrical properties of interface between Ge single crystal and electrolyte, W. H. Brattain and C. G. B. Garrett —750(A)
Electrical properties of molybdenite, C. W. Heaps—809(A)
Electrical properties of p-type Ge, Esther M. Conwell—1416(A)
Electrical properties of pure Te and Te-Se alloys, Allen Nussbaum—337
Electrical properties of single crystals and thin films of PbSe and PbTe, S. J. Silverman and H. Levinstein—871
Electrical properties of single crystals and thin films of PbTe, Searl J. Silverman and Henry Levinstein—1430(A)
Electron traps on Ge surfaces produced by heating in oxygen, Edward N. Clarke—1420(A)
Energy of high-lying acceptor level in Cu-doped Ge, J. F. Battey and R. M. Baum—1393(L)
Evaporated multiple layers with semiconductor properties, J. C. M. Brentano and J. D. Richards—1427(A)
Germanium-oxygen system, Michael Hoch and Herrick L. Johnston—749(A)
Graphical representation of semiconductor Hall effect, L. P. Hunter—1426(A); 1157
Growth of long-lifetime Ge crystals, Milton Becker—1420(A)
Hall and resistivity measurements during electron bombardment of Ge and InSb, R. Pepper, E. Klontz, K. Lark-Horovitz, and J. MacKay—1410(A)
Hall coefficient in Ge, T. C. Harman, R. K. Willardson, and A. C. Beer—1065(L)
Hall effect and resistivity of Ge at low temperatures, H. Fritzsche—1415(A)
Hall effect and thermoelectric power of pure Te at melting point and in liquid state, A. Epstein and H. Fritzsche —1426(A)
Hall mobility of electrons and holes in Si, P. P. Debye and T. Kohane—724(L)
High-field effects in Ge, Esther M. Conwell—1068(L)
Infrared absorption of Te, R. S. Caldwell and H. Y. Fan —1427(A)
Infrared properties of InSb, W. Kaiser and H. Y. Fan —1431(A)
Infrared properties of p-type Ge, E. Burstein, B. W. Henvis, and N. Sclar—750(A)
Interaction of impurities and mobile carriers in semiconductors, Guy W. Lehman and Hubert M. James—1428(A)
Interdiffusion in PbS crystals, R. F. Brebrick and W. W. Scanlon—1430(A)
Interstitial Ge in heat-treated Ge, Sumner Mayburg—750(A)
Lifetimes and diffusion constants in Ge, D. T. Stevenson and R. J. Keyes—1416(A)
Microwave transmission in p-type Ge, F. A. D'Altroy and H. Y. Fan—1415(A)
Minority carrier lifetime in semiconductors as sensitive indicator of radiation damage, P. Rappaport—1409(A)
Mobility and mean free path of electrons and holes in PbS crystals, R. L. Petritz, W. W. Scanlon, and F. L. Lummis—1430
Mobility of impurity ions in Ge and Si, J. C. Severiens and C. S. Fuller—750(A)
New galvanomagnetic effect, Colman Goldberg and R. E. Davis—1121
Nuclear magnetic relaxation in semiconductors, N. Bloembergen—1411(A)
Optical absorption of AlSb, R. F. Blunt, H. P. R. Frederikse, and J. H. Becker—1431(A)
Optical and electrical measurements on InAs, Robert M. Talley and Dorothy Enright—1431(A)
Optical properties of Ge in far infrared, E. J. Johnson and W. G. Spitzer—1415(A)
Photoconduction in Fe-, Co-, and Ni-doped Ge, R. Newman and W. W. Tyler—1419(A)
Photoconduction of ZnO semiconductor: oxygen adsorption process, Donald A. Melnick—1438(A)
Photoconductivity and photoelectromagnetic effects in InSb, S. W. Kurnick, A. J. Strauss, and R. N. Zitter —1791(L)
Photoconductivity in Au-doped Si, R. Newman—1530
Photoconductivity in Au-Ge alloys, Roger Newman—278
Photomagnetoelectric effect in Ge and Si, Hubert H. Bulliard—1564
Photo-radiative recombination of electrons and holes in Ge, W. van Roosbroeck and W. Shockley—1558
Piezoresistance effect in Ge and Si, Charles S. Smith—42
Preparation and properties of III-V compounds, G. Wolff, P. H. Keck, and J. D. Broder—753(A)
Preparation of Pbs crystals of controlled electrical properties, W. W. Scanlon and R. F Brebrick—1430(A)
Pressure dependence of Hall effect in Ge, W. Paul, G. B. Benedek, and H. Brooks—1415(A)
Pressure dependence of resistivity of Ge, William Paul and Harvey Brooks—1128
Properties of Ge doped with Fe or Co, W. W. Tyler, H. H. Woodbury, and R. Newman—1419(A)
Properties of p-type GaSb between 15°K and 925°K, H. N. Leifer and W. C. Dunlap—1431(A)
Properties of Zn-, Cu-, and Pt-doped Ge, W. C. Dunlap, Jr.—1419(A)
Radiation effects in InSb, J. W. Cleland and J. H. Crawford, Jr.—1410(A)
Recombination of holes and electrons at lineage boundaries in Ge, F. L. Vogel, W. T. Read, and L. C. Lovell—1791(L)
Resistivity, thermoelectric power, and Hall effect in semiconductor with hexagonal structure, V. A. Johnson—1427(A)
Seebeck effect in Ge, T. H. Geballe and G. W. Hull—1134
Spin resonance of donors in Si, R. C. Fletcher, W. A. Yager, G. L. Pearson, A. N. Holden, W. T. Read, and F. R. Merritt—1392(L)
Theory of junction transistor, Edmund S. Rittner—1161
Thermal conductivity and thermoelectric power of Ge at low temperatures, E. Fagen, J. Goff, and N. Perlman —1415(A)
Thermal ionization of trapped electrons, Hermann Gummel and Melvin Lax—1419(A)
Thermionic emission and semiconduction in single crystals of BaO, Evan O. Kane—1439(A)
Transient response of p-n junction rectifiers, B. R. Gossick —1427(A)
Variation of recombination velocity of Ge surfaces with ambient gases, R. J. Keyes and T. C. Maple—1416(A)
Volume and surface recombination rates in Ge, J. P. McKelvey and R. L. Longini—750(A)
Shock Waves (see **Fluid Dynamics**)
Solid State (see **Crystalline State**)
Solutions (see **Liquids**)
Sound (see **Acoustics**)
Spallation (see **Nuclear Reactions**)
Spark Discharge (see **Electrical Discharges**)
Specific Heat (see **Thermal Properties**)
Spectra, Atomic (see **Atomic Structure and Spectra**)

Spectra, General
Errors in power spectra due to finite sample, L. M. Spetner—778(A)
γ-ray spectrum of Bulk Shielding Reactor, Fred Maienschein and Temple Love—778(A)
Precision determination of velocity of light derived from band spectrum method. II, D. H. Rank, J. N. Shearer, and T. A. Wiggins—575
Shape of collision-broadened spectral lines, E. P. Gross —1424(A)
Spectra, Molecular (see **Molecular Structure and Spectra**)
Spectra, Nuclear (see **Nuclear Spectra**)
Spectroscopy Technique (see **Methods and Instruments**)
Spinor Fields (see **Field Theory**)
Standards (see **Constants, Standards, Units**)
Stark Effect (see **Atomic Structure and Spectra**)
Statistical Mechanics and Thermodynamics
Application of group theory to statistical mechanics, Jerome Rothstein—792(A)
Basic principles of quantum statistical mechanics, P. T. Landsberg—1442(A)
Boltzmann equation from statistical mechanical point of view, Melville Green—792(A)
Continuous spectrum approximation in quantum statistics, Peter T. Landsberg—469
Density fluctuations at low temperatures, P. J. Price— 257; 1801(E)
High-speed machine computation of ideal gas thermal properties. Isotopic water molecules, Abraham S. Friedman and Lester Haar—1423(A)
1-dimensional walk with correlation by saturation for description of diffusion phenomena, C. M. Tchen— 1442(A)
Simon melting equation and effective intermolecular potential, L. Salter—1434(A)
Time reversal *vs* Boltzmann equation, J. S. Lomont— 792(A)
Statistical Methods (see **Mathematical Methods**)
Superconductivity
Decay of positrons in superconducting Pb, Walter E. Millett—809(A)
Effect of hydrostatic pressure on superconducting transition of Sn, M. Garber and D. E. Mapother—1065(L)
Effect of hydrostatic pressure on superconducting transition of Sn and Tl, Milan D. Fiske—495(L)
Latent heat of transition of superconducting Pb, R. L. Dolecek—540
Lifetime of positrons in superconductors, Harry Talley and Robert Stump—809(A)
Neutron diffraction investigations on superconducting elements, M. K. Wilkinson, C. G. Shull, L. D. Roberts, and S. Bernstein—772(A)
Superconducting alloys, B. T. Matthias and E. Corenzwit —1069(L)
Superconductivity of pure metallic Re, John K. Hulm— 1390(L)
Theory of boundary effects of superconductors, J. Bardeen —554
Supersonics (see **Fluid Dynamics**)

Thermal Conductivity (see **Thermal Properties**)
Thermal Diffusion (see **Diffusion**)
Thermal Expansion (see **Thermal Properties**)
Thermal Properties
Effect of radiation damage on thermal conductivity of graphite, Alan W. Smith—1417(A)
Effects of anisotropy on thermodynamic properties of antiferromagnets, J. A. Eisele and F. Keffer—1440(A)
Heat capacity and entropy of liquid He^3 from 0.42°K to 1.06°K, Darrell W. Osborne, Bernard M. Abraham, and Bernard Weinstock—202(L)
High-speed machine computation of ideal gas thermal properties. Isotopic water molecules, Abraham S. Friedman and Lester Haar—1423(A)
Theory of temperature waves, Paul M. Marcus—771(A)
Thermal conductivity and thermoelectric power of Ge at low temperatures, E. Fagen, J. Goff, and N. Perlman —1415(A)
Thermal Radiation (see **Radiation**)
Thermionic Emission (see **Electrical Properties**)
Thermodynamics (see **Statistical Mechanics and Thermodynamics**)
Thermoelectric Effect (see **Electrical Properties**)
Thermoluminescence (see **Luminescence**)
Thermomagnetic Effect (see **Magnetic Properties**)
Total Cross Sections (see **Electrons and Positrons; Nuclear Reactions**)
Transmutation (see **Nuclear Reactions**)

Uncertainty Principle (see **Quantum Mechanics**)
Units (see **Constants, Standards, Units**)

Vacuum Tubes (see **Methods and Instruments**)
Van der Waals Forces (see **Molecular Structure and Spectra**)
Viscosity (see **Liquids**)

Wave Mechanics (see **Quantum Mechanics**)
Work Function (see **Electrical Properties**)

X-Rays
Absorption spectrum of Be in neighborhood of *K* edge, R. W. Johnston and D. H. Tomboulian—1585
Anomalous dispersion and scattering of x-rays, L. G. Parratt and C. F. Hempstead—1593
Diffraction effects of crystals with deformation faults, R. Hosemann and S. N. Bagchi—71
Diffraction of x-rays by lattice imperfections, Yin-Yuan Li and R. Smoluchowski—751(A)
Elastic constants of Si before and after neutron bombardment from x-ray diffuse scattering, W. P. Binnie and A. M. Liebschutz—1410(A)
Elastic spectrum of Cu from temperature scattering of x-rays, E. H. Jacobsen—1420(A)
Elastic spectrum of Zn from temperature scattering of x-rays, R. E. Joynson—851
Emission of δ- and x-rays from targets bombarded by accelerated ions, Črtomir Zupančič and Torben Huus —205(L)
Equivalence of x-ray lattice parameter and density changes in neutron-irradiated LiF, D. Binder and W. J. Sturm —760(A)
Fourier analysis of x-ray small-angle scattering, Yin-Yuan Li and R. Smoluchowski—1435(A)
Interstitial content of radiation-damaged metals from precision x-ray lattice parameter measurements, C. W. Tucker, Jr., and J. B. Sampson—1418(A)
L-emission spectrum of Zr (40), N. Spielberg, C. H. Shaw, and J. A. Soules—752(A)
Liquefied gas x-ray target, E. A. Whalin and R. A. Reitz —752(A)
μ-mesonic x-rays and shape of nuclear charge distribution, David L. Hill and Kenneth W. Ford—1617
Peculiarity of electron density near impurity in metal and its effect on x-ray spectra, J. S. Plaskett—1420(A)
Photodisintegration of deuterium by 60–280 Mev x-rays, Barbara Dwight Schriever, E. A. Whalin, and A. O. Hanson—763(A)

X-Rays (Continued)
Production of *L*-shell x-rays by protons, Eugene Bernstein —774(A)
Rate of production of color centers in KCl and KBr by x-rays at 78°K, William H. Duerig—65
Scattering by lattices of deformable atoms, R. J. Glauber —751(A)
Scintillation response of anthracene to soft x-rays, J. B. Birks and F. D. Brooks—1800(L)
Small-angle scattering of x-rays by irradiated diamond, W. H. Robinson, Yin-Yuan Li, and R. Smoluchowski —1435(A)
Small-angle x-ray scattering from liquid He I and liquid He II, Arthur G. Tweet—1801(E)
Soft x-ray absorption of Te, Robert W. Woodruff and M. Parker Givens—752(A)
Soft x-ray emission bands in metals, H. Jones—1072(L)
Spectral energy distribution of 2-Mev x-rays, Joseph Dresner—751(A)
Spectroscopy of π- and μ-meson x-rays, S. DeBenedetti, M. B. Stearns, M. Stearns, and J. J. Richings—766(A)
Statistical approach to phase determination in x-ray analysis, V. Vand and R. Pepinsky—1435(A)
Structure of liquid He by x-ray scattering, W. L. Gordon, C. H. Shaw and J. G. Daunt—771(A)
Theory of x-ray small-angle scattering, Yin-Yuan Li and R. Smoluchowski—866
X-ray measurements of cold-worked α brass, E. P. Warekois—1421(A)
X-ray study of prismatic punching in TlCl, Edward I. Salkovitz and Paul L. Smith—770(A)
Yields of π- and μ-meson x-rays in low-Z materials, M. Stearns, M. B. Stearns, S. DeBenedetti, and L. Leipuner—766(A)